Proceedings
PRO 118

ADVANCES IN CONSTRUCTION MATERIALS AND SYSTEMS

Vol. 2

Proceedings of
an **International Conference (ICACMS)**
Chennai, INDIA

September 3 - 8, 2017




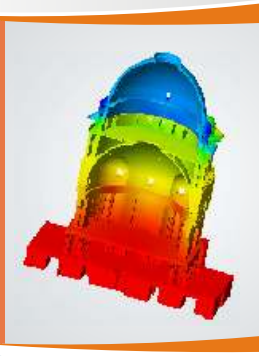

Organised by

INDIAN INSTITUTE OF TECHNOLOGY MADRAS
सिद्धिर्भवति कर्मजा

Edited by:
Manu Santhanam
Ravindra Gettu
Radhakrishna G. Pillai
Sunitha K. Nayar

RILEM Publications S.A.R.L.

Advances in Construction Materials and Systems

Proceedings of International Conference, Chennai, Sep 3 – 8, 2017

Published by RILEM Publications S.A.R.L.
4 avenue du Recteur Poincaré 75016 Paris - France
Tel : + 33 1 42 24 64 46 Fax : + 33 9 70 29 51 20
http://www.rilem.net E-mail: dg@rilem.net

ISBN: 978-2-35158-194-0
ISBN: 978-2-35158-190-2 (Set)
e-ISBN: 978-2-35158-191-9

RILEM, The International Union of Laboratories and Experts in Construction Materials, Systems and Structures, is a non profit-making, non-governmental technical association whose vocation is to contribute to progress in the construction sciences, techniques and industries, essentially by means of the communication it fosters between research and practice. RILEM's activity therefore aims at developing the knowledge of properties of materials and performance of structures, at defining the means for their assessment in laboratory and service conditions and at unifying measurement and testing methods used with this objective.

RILEM was founded in 1947, and has a membership of over 900 in some 70 countries. It forms an institutional framework for co-operation by experts to:

- optimise and harmonise test methods for measuring properties and performance of building and civil engineering materials and structures under laboratory and service environments,
- prepare technical recommendations for testing methods,
- prepare state-of-the-art reports to identify further research needs,
- collaborate with national or international associations in realising these objectives.

RILEM members include the leading building research and testing laboratories around the world, industrial research, manufacturing and contracting interests, as well as a significant number of individual members from industry and universities. RILEM's focus is on construction materials and their use in building and civil engineering structures, covering all phases of the building process from manufacture to use and recycling of materials.

RILEM meets these objectives through the work of its technical committees. Symposia, workshops and seminars are organised to facilitate the exchange of information and dissemination of knowledge. RILEM's primary output consists of technical recommendations. RILEM also publishes the journal *Materials and Structures* which provides a further avenue for reporting the work of its committees. Many other publications, in the form of reports, monographs, symposia and workshop proceedings are produced.

International Conference on Advances in Construction Materials and Systems

In conjunction with 71st RILEM Annual Week

Chennai, India
3 – 8 September

Proceedings Vol. 2

Edited by
Manu Santhanam
Ravindra Gettu
Radhakrishna G. Pillai
Sunitha K. Nayar

RILEM Publications S.A.R.L.

RILEM Publications

The following list is presenting the global offer of RILEM Publications, sorted by series. Each publication is available in printed version and/or in online version.

RILEM PROCEEDINGS (PRO)

PRO 1: Durability of High Performance Concrete (ISBN: 2-912143-03-9); *Ed. H. Sommer*

PRO 2: Chloride Penetration into Concrete (ISBN: 2-912143-00-04); *Eds. L.-O. Nilsson and J.-P. Ollivier*

PRO 3: Evaluation and Strengthening of Existing Masonry Structures (ISBN: 2-912143-02-0); *Eds. L. Binda and C. Modena*

PRO 4: Concrete: From Material to Structure (ISBN: 2-912143-04-7); *Eds. J.-P. Bournazel and Y. Malier*

PRO 5: The Role of Admixtures in High Performance Concrete (ISBN: 2-912143-05-5);
Eds. J. G. Cabrera and R. Rivera-Villarreal

PRO 6: High Performance Fiber Reinforced Cement Composites - HPFRCC 3 (ISBN: 2-912143-06-3); *Eds. H. W. Reinhardt and A. E. Naaman*

PRO 7: 1st International RILEM Symposium on Self-Compacting Concrete (ISBN: 2-912143-09-8); *Eds. Å. Skarendahl and Ö. Petersson*

PRO 8: International RILEM Symposium on Timber Engineering (ISBN: 2-912143-10-1); *Ed. L. Boström*

PRO 9: 2nd International RILEM Symposium on Adhesion between Polymers and Concrete ISAP '99 (ISBN: 2-912143-11-X); *Eds. Y. Ohama and M. Puterman*

PRO 10: 3rd International RILEM Symposium on Durability of Building and Construction Sealants (ISBN: 2-912143-13-6); *Eds. A. T. Wolf*

PRO 11: 4th International RILEM Conference on Reflective Cracking in Pavements (ISBN: 2-912143-14-4); *Eds. A. O. Abd El Halim, D. A. Taylor and El H. H. Mohamed*

PRO 12: International RILEM Workshop on Historic Mortars: Characteristics and Tests (ISBN: 2-912143-15-2); *Eds. P. Bartos, C. Groot and J. J. Hughes*

PRO 13: 2nd International RILEM Symposium on Hydration and Setting (ISBN: 2-912143-16-0); *Ed. A. Nonat*

PRO 14: Integrated Life-Cycle Design of Materials and Structures - ILCDES 2000 (ISBN: 951-758-408-3); (ISSN: 0356-9403); *Ed. S. Sarja*

PRO 15: Fifth RILEM Symposium on Fibre-Reinforced Concretes (FRC) - BEFIB'2000 (ISBN: 2-912143-18-7); *Eds. P. Rossi and G. Chanvillard*

PRO 16: Life Prediction and Management of Concrete Structures (ISBN: 2-912143-19-5); *Ed. D. Naus*

PRO 17: Shrinkage of Concrete – Shrinkage 2000 (ISBN: 2-912143-20-9); *Eds. V. Baroghel-Bouny and P.-C. Aïtcin*

PRO 18: Measurement and Interpretation of the On-Site Corrosion Rate (ISBN: 2-912143-21-7); *Eds. C. Andrade, C. Alonso, J. Fullea, J. Polimon and J. Rodriguez*

PRO 19: Testing and Modelling the Chloride Ingress into Concrete (ISBN: 2-912143-22-5); *Eds. C. Andrade and J. Kropp*

PRO 20: 1st International RILEM Workshop on Microbial Impacts on Building Materials (CD 02) (e-ISBN 978-2-35158-013-4); *Ed. M. Ribas Silva*

PRO 21: International RILEM Symposium on Connections between Steel and Concrete (ISBN: 2-912143-25-X); *Ed. R. Eligehausen*

PRO 22: International RILEM Symposium on Joints in Timber Structures (ISBN: 2-912143-28-4); *Eds. S. Aicher and H.-W. Reinhardt*

PRO 23: International RILEM Conference on Early Age Cracking in Cementitious Systems (ISBN: 2-912143-29-2); *Eds. K. Kovler and A. Bentur*

PRO 24: 2nd International RILEM Workshop on Frost Resistance of Concrete (ISBN: 2-912143-30-6); *Eds. M. J. Setzer, R. Auberg and H.-J. Keck*

PRO 25: International RILEM Workshop on Frost Damage in Concrete (ISBN: 2-912143-31-4); *Eds. D. J. Janssen, M. J. Setzer and M. B. Snyder*

PRO 26: International RILEM Workshop on On-Site Control and Evaluation of Masonry Structures (ISBN: 2-912143-34-9); *Eds. L. Binda and R. C. de Vekey*

PRO 27: International RILEM Symposium on Building Joint Sealants (CD03); *Ed. A. T. Wolf*

PRO 28: 6th International RILEM Symposium on Performance Testing and Evaluation of Bituminous Materials - PTEBM'03 (ISBN: 2-912143-35-7; e-ISBN: 978-2-912143-77-8); *Ed. M. N. Partl*

PRO 29: 2nd International RILEM Workshop on Life Prediction and Ageing Management of Concrete Structures (ISBN: 2-912143-36-5); *Ed. D. J. Naus*

PRO 30: 4th International RILEM Workshop on High Performance Fiber Reinforced Cement Composites - HPFRCC 4 (ISBN: 2-912143-37-3); *Eds. A. E. Naaman and H. W. Reinhardt*

PRO 31: International RILEM Workshop on Test and Design Methods for Steel Fibre Reinforced Concrete: Background and Experiences (ISBN: 2-912143-38-1); *Eds. B. Schnütgen and L. Vandewalle*

PRO 32: International Conference on Advances in Concrete and Structures 2 vol. (ISBN (set): 2-912143-41-1); *Eds. Ying-shu Yuan, Surendra P. Shah and Heng-lin Lü*

PRO 33: 3rd International Symposium on Self-Compacting Concrete (ISBN: 2-912143-42-X); *Eds. Ö. Wallevik and I. Nielsson*

PRO 34: International RILEM Conference on Microbial Impact on Building Materials (ISBN: 2-912143-43-8); *Ed. M. Ribas Silva*

PRO 35: International RILEM TC 186-ISA on Internal Sulfate Attack and Delayed Ettringite Formation (ISBN: 2-912143-44-6); *Eds. K. Scrivener and J. Skalny*

PRO 36: International RILEM Symposium on Concrete Science and Engineering – A Tribute to Arnon Bentur (ISBN: 2-912143-46-2); *Eds. K. Kovler, J. Marchand, S. Mindess and J. Weiss*

PRO 37: 5th International RILEM Conference on Cracking in Pavements – Mitigation, Risk Assessment and Prevention (ISBN: 2-912143-47-0); *Eds. C. Petit, I. Al-Qadi and A. Millien*

PRO 38: 3rd International RILEM Workshop on Testing and Modelling the Chloride Ingress into Concrete (ISBN: 2-912143-48-9); *Eds. C. Andrade and J. Kropp*

PRO 39: 6th International RILEM Symposium on Fibre-Reinforced Concretes - BEFIB 2004 (ISBN: 2-912143-51-9); *Eds. M. Di Prisco, R. Felicetti and G. A. Plizzari*

PRO 40: International RILEM Conference on the Use of Recycled Materials in Buildings and Structures (ISBN: 2-912143-52-7); *Eds. E. Vázquez, Ch. F. Hendriks and G. M. T. Janssen*

PRO 41: RILEM International Symposium on Environment-Conscious Materials and Systems for Sustainable Development (ISBN: 2-912143-55-1); *Eds. N. Kashino and Y. Ohama*

PRO 42: SCC'2005 - China: 1st International Symposium on Design, Performance and Use of Self-Consolidating Concrete (ISBN: 2-912143-61-6); *Eds. Zhiwu Yu, Caijun Shi, Kamal Henri Khayat and Youjun Xie*

PRO 43: International RILEM Workshop on Bonded Concrete Overlays (e-ISBN: 2-912143-83-7); *Eds. J. L. Granju and J. Silfwerbrand*

PRO 44: 2nd International RILEM Workshop on Microbial Impacts on Building Materials (CD11) (e-ISBN: 2-912143-84-5); *Ed. M. Ribas Silva*

PRO 45: 2nd International Symposium on Nanotechnology in Construction, Bilbao (ISBN: 2-912143-87-X); *Eds. Peter J. M. Bartos, Yolanda de Miguel and Antonio Porro*

PRO 46: ConcreteLife'06 - International RILEM-JCI Seminar on Concrete Durability and Service Life Planning: Curing, Crack Control, Performance in Harsh Environments (ISBN: 2-912143-89-6); *Ed. K. Kovler*

PRO 47: International RILEM Workshop on Performance Based Evaluation and Indicators for Concrete Durability (ISBN: 978-2-912143-95-2); *Eds. V. Baroghel-Bouny, C. Andrade, R. Torrent and K. Scrivener*

PRO 48: 1st International RILEM Symposium on Advances in Concrete through Science and Engineering (e-ISBN: 2-912143-92-6); *Eds. J. Weiss, K. Kovler, J. Marchand, and S. Mindess*

PRO 49: International RILEM Workshop on High Performance Fiber Reinforced Cementitious Composites in Structural Applications (ISBN: 2-912143-93-4); *Eds. G. Fischer and V.C. Li*

PRO 50: 1st International RILEM Symposium on Textile Reinforced Concrete (ISBN: 2-912143-97-7); *Eds. Josef Hegger, Wolfgang Brameshuber and Norbert Will*

PRO 51: 2nd International Symposium on Advances in Concrete through Science and Engineering (ISBN: 2-35158-003-6; e-ISBN: 2-35158-002-8); *Eds. J. Marchand, B. Bissonnette, R. Gagné, M. Jolin and F. Paradis*

PRO 52: Volume Changes of Hardening Concrete: Testing and Mitigation (ISBN: 2-35158-004-4; e-ISBN: 2-35158-005-2); *Eds. O. M. Jensen, P. Lura and K. Kovler*

PRO 53: High Performance Fiber Reinforced Cement Composites - HPFRCC5 (ISBN: 978-2-35158-046-2); *Eds. H. W. Reinhardt and A. E. Naaman*

PRO 54: 5th International RILEM Symposium on Self-Compacting Concrete (ISBN: 978-2-35158-047-9); *Eds. G. De Schutter and V. Boel*

PRO 55: International RILEM Symposium Photocatalysis, Environment and Construction Materials (ISBN: 978-2-35158-056-1); *Eds. P. Baglioni and L. Cassar*

PRO 56: International RILEM Workshop on Integral Service Life Modelling of Concrete Structures (ISBN 978-2-35158-058-5); *Eds. R. M. Ferreira, J. Gulikers and C. Andrade*

PRO 57: RILEM Workshop on Performance of cement-based materials in aggressive aqueous environments (e-ISBN: 978-2-35158-059-2); *Ed. N. De Belie*

PRO 58: International RILEM Symposium on Concrete Modelling - CONMOD'08 (ISBN: 978-2-35158-060-8); *Eds. E. Schlangen and G. De Schutter*

PRO 59: International RILEM Conference on On Site Assessment of Concrete, Masonry and Timber Structures - SACoMaTiS 2008 (ISBN set: 978-2-35158-061-5); *Eds. L. Binda, M. di Prisco and R. Felicetti*

PRO 60: Seventh RILEM International Symposium on Fibre Reinforced Concrete: Design and Applications - BEFIB 2008 (ISBN: 978-2-35158-064-6); *Ed. R. Gettu*

PRO 61: 1st International Conference on Microstructure Related Durability of Cementitious Composites 2 vol., (ISBN: 978-2-35158-065-3); *Eds. W. Sun, K. van Breugel, C. Miao, G. Ye and H. Chen*

PRO 62: NSF/ RILEM Workshop: In-situ Evaluation of Historic Wood and Masonry Structures (e-ISBN: 978-2-35158-068-4); *Eds. B. Kasal, R. Anthony and M. Drdácký*

PRO 63: Concrete in Aggressive Aqueous Environments: Performance, Testing and Modelling, 2 vol., (ISBN: 978-2-35158-071-4); *Eds. M. G. Alexander and A. Bertron*

PRO 64: Long Term Performance of Cementitious Barriers and Reinforced Concrete in Nuclear Power Plants and Waste Management - NUCPERF 2009 (ISBN: 978-2-35158-072-1); *Eds. V. L'Hostis, R. Gens, C. Gallé*

PRO 65: Design Performance and Use of Self-consolidating Concrete - SCC'2009 (ISBN: 978-2-35158-073-8); *Eds. C. Shi, Z. Yu, K. H. Khayat and P. Yan*

PRO 66: 2nd International RILEM Workshop on Concrete Durability and Service Life Planning - ConcreteLife'09 (ISBN: 978-2-35158-074-5); *Ed. K. Kovler*

PRO 67: Repairs Mortars for Historic Masonry (e-ISBN: 978-2-35158-083-7); *Ed. C. Groot*

PRO 68: Proceedings of the 3rd International RILEM Symposium on 'Rheology of Cement Suspensions such as Fresh Concrete (ISBN 978-2-35158-091-2); *Eds. O. H. Wallevik, S. Kubens and S. Oesterheld*

PRO 69: 3rd International PhD Student Workshop on 'Modelling the Durability of Reinforced Concrete (ISBN: 978-2-35158-095-0); *Eds. R. M. Ferreira, J. Gulikers and C. Andrade*

PRO 70: 2nd International Conference on 'Service Life Design for Infrastructure' (ISBN set: 978-2-35158-096-7, e-ISBN: 978-2-35158-097-4); *Ed. K. van Breugel, G. Ye and Y. Yuan*

PRO 71: Advances in Civil Engineering Materials - The 50-year Teaching Anniversary of Prof. Sun Wei' (ISBN: 978-2-35158-098-1; e-ISBN: 978-2-35158-099-8); *Eds. C. Miao, G. Ye, and H. Chen*

PRO 72: First International Conference on 'Advances in Chemically-Activated Materials – CAM'2010' (2010), 264 pp, ISBN: 978-2-35158-101-8; e-ISBN: 978-2-35158-115-5, *Eds. Caijun Shi and Xiaodong Shen*

PRO 73: 2nd International Conference on 'Waste Engineering and Management - ICWEM 2010' (2010), 894 pp, ISBN: 978-2-35158-102-5; e-ISBN: 978-2-35158-103-2, *Eds. J. Zh. Xiao, Y. Zhang, M. S. Cheung and R. Chu*

PRO 74: International RILEM Conference on 'Use of Superabsorsorbent Polymers and Other New Addditives in Concrete' (2010) 374 pp., ISBN: 978-2-35158-104-9; e-ISBN: 978-2-35158-105-6; *Eds. O.M. Jensen, M.T. Hasholt, and S. Laustsen*

PRO 75: International Conference on 'Material Science - 2nd ICTRC - Textile Reinforced Concrete - Theme 1' (2010) 436 pp., ISBN: 978-2-35158-106-3; e-ISBN: 978-2-35158-107-0; *Ed. W. Brameshuber*

PRO 76: International Conference on 'Material Science - HetMat - Modelling of Heterogeneous Materials - Theme 2' (2010) 255 pp., ISBN: 978-2-35158-108-7; e-ISBN: 978-2-35158-109-4; *Ed. W. Brameshuber*

PRO 77: International Conference on 'Material Science - AdIPoC - Additions Improving Properties of Concrete - Theme 3' (2010) 459 pp., ISBN: 978-2-35158-110-0; e-ISBN: 978-2-35158-111-7; *Ed. W. Brameshuber*

PRO 78: 2nd Historic Mortars Conference and RILEM TC 203-RHM Final Workshop – HMC2010 (2010) 1416 pp., e-ISBN: 978-2-35158-112-4; *Eds J. Válek, C. Groot, and J. J. Hughes*

PRO 79: International RILEM Conference on Advances in Construction Materials Through Science and Engineering (2011) 213 pp., e-ISBN: 978-2-35158-117-9; *Eds Christopher Leung and K.T. Wan*

PRO 80: 2nd International RILEM Conference on Concrete Spalling due to Fire Exposure (2011) 453 pp., ISBN: 978-2-35158-118-6, e-ISBN: 978-2-35158-119-3; *Eds E.A.B. Koenders and F. Dehn*

PRO 81: 2nd International RILEM Conference on Strain Hardening Cementitious Composites (SHCC2-Rio) (2011) 451 pp., ISBN: 978-2-35158-120-9, e-ISBN: 978-2-35158-121-6; *Eds R.D. Toledo Filho, F.A. Silva, E.A.B. Koenders and E.M.R. Fairbairn*

PRO 82: 2nd International RILEM Conference on Progress of Recycling in the Built Environment (2011) 507 pp., e-ISBN: 978-2-35158-122-3; *Eds V.M. John, E. Vazquez, S.C. Angulo and C. Ulsen*

PRO 83: 2nd International Conference on Microstructural-related Durability of Cementitious Composites (2012) 250 pp., ISBN: 978-2-35158-129-2; e-ISBN: 978-2-35158-123-0; *Eds G. Ye, K. van Breugel, W. Sun and C. Miao*

PRO 85: RILEM-JCI International Workshop on Crack Control of Mass Concrete and Related issues concerning Early-Age of Concrete Structures – ConCrack 3 – Control of Cracking in Concrete Structures 3 (2012) 237 pp., ISBN: 978-2-35158-125-4; e-ISBN: 978-2-35158-126-1; *Eds F. Toutlemonde and J.-M. Torrenti*

PRO 86: International Symposium on Life Cycle Assessment and Construction (2012) 414 pp., ISBN: 978-2-35158-127-8, e-ISBN: 978-2-35158-128-5; *Eds A. Ventura and C. de la Roche*

PRO 87: UHPFRC 2013 – RILEM-fib-AFGC International Symposium on Ultra-High Performance Fibre-Reinforced Concrete (2013), ISBN: 978-2-35158-130-8, e-ISBN: 978-2-35158-131-5; *Eds F. Toutlemonde*

PRO 88: 8th RILEM International Symposium on Fibre Reinforced Concrete (2012) 344 pp., ISBN: 978-2-35158-132-2, e-ISBN: 978-2-35158-133-9; *Eds Joaquim A.O. Barros*

PRO 89: RILEM International workshop on performance-based specification and control of concrete durability (2014) 678 pp, ISBN: 978-2-35158-135-3, e-ISBN: 978-2-35158-136-0; *Eds. D. Bjegović, H. Beushausen and M. Serdar*

PRO 90: 7th RILEM International Conference on Self-Compacting Concrete and of the 1st RILEM International Conference on Rheology and Processing of Construction Materials (2013) 396 pp, ISBN: 978-2-35158-137-7, e-ISBN: 978-2-35158-138-4; *Eds. Nicolas Roussel and Hela Bessaies-Bey*

PRO 91: CONMOD 2014 - RILEM International Symposium on Concrete Modelling (2014), ISBN: 978-2-35158-139-1; e-ISBN: 978-2-35158-140-7; *Eds. Kefei Li, Peiyu Yan and Rongwei Yang*

PRO 92: CAM 2014 - 2nd International Conference on advances in chemically-activated materials (2014) 392 pp., ISBN: 978-2-35158-141-4; e-ISBN: 978-2-35158-142-1; *Eds. Caijun Shi and Xiadong Shen*

PRO 93: SCC 2014 - 3rd International Symposium on Design, Performance and Use of Self-Consolidating Concrete (2014) 438 pp., ISBN: 978-2-35158-143-8; e-ISBN: 978-2-35158-144-5; *Eds. Caijun Shi, Zhihua Ou, Kamal H. Khayat*

PRO 94 (online version): HPFRCC-7 - 7th RILEM conference on High performance fiber reinforced cement composites (2015), e-ISBN: 978-2-35158-146-9; *Eds. H.W. Reinhardt, G.J. Parra-Montesinos, H. Garrecht*

PRO 95: International RILEM Conference on Application of superabsorbent polymers and other new admixtures in concrete construction (2014), ISBN: 978-2-35158-147-6; e-ISBN: 978-2-35158-148-3; *Eds. Viktor Mechtcherine, Christof Schroefl*

PRO 96 (online version): XIII DBMC: XIII International Conference on Durability of Building Materials and Components(2015), e-ISBN: 978-2-35158-149-0; *Eds. M. Quattrone, V.M. John*

PRO 97: SHCC3 – 3rd International RILEM Conference on Strain Hardening Cementitious Composites (2014), ISBN: 978-2-35158-150-6; e-ISBN: 978-2-35158-151-3; *Eds. E. Schlangen, M.G. Sierra Beltran, M. Lukovic, G. Ye*

PRO 98: FERRO-11 – 11th International Symposium on Ferrocement and 3rd ICTRC - International Conference on Textile Reinforced Concrete (2015), ISBN: 978-2-35158-152-0; e-ISBN: 978-2-35158-153-7; *Ed. W. Brameshuber*

PRO 99 (online version): ICBBM 2015 - 1st International Conference on Bio-Based Building Materials (2015), e-ISBN: 978-2-35158-154-4; *Eds. S. Amziane, M. Sonebi*

PRO 100: SCC16 - RILEM Self-Consolidating Concrete Conference (2016)**,** ISBN: 978-2-35158-156-8; e-ISBN: 978-2-35158-157-5; *Ed. Kamal H. Kayat*

PRO 101 (online version): III Progress of Recycling in the Built Environment (2015), e-ISBN: 978-2-35158-158-2; *Eds I. Martins, C. Ulsen and S. C. Angulo*

PRO 102 (online version): RILEM Conference on Microorganisms-Cementitious Materials Interactions (2016), e-ISBN: 978-2-35158-160-5; *Eds. Alexandra Bertron, Henk Jonkers, Virginie Wiktor*

PRO 103 (online version): ACESC'16 - Advances in Civil Engineering and Sustainable Construction (2016), e-ISBN: 978-2-35158-161-2

PRO 104 (online version): SSCS'2015 - Numerical Modeling - Strategies for Sustainable Concrete Structures (2015), e-ISBN: 978-2-35158-162-9

PRO 105: 1st International Conference on UHPC Materials and Structures (2016), ISBN: 978-2-35158-164-3, e-ISBN: 978-2-35158-165-0

PRO 106: AFGC-ACI-fib-RILEM International Conference on Ultra-High-Performance Fibre-Reinforced Concrete – UHPFRC 2017 (2017), ISBN: 978-2-35158-166-7, e-ISBN: 978-2-35158-167-4; *Eds. François Toutlemonde & Jacques Resplendino*

PRO 107 (online version): XIV DBMC – 14th International Conference on Durability of Building Materials and Components (2017), e-ISBN: 978-2-35158-159-9; *Eds. Geert De Schutter, Nele De Belie, Arnold Janssens, Nathan Van Den Bossche*

PRO 108: MSSCE 2016 - Innovation of Teaching in Materials and Structures (2016), ISBN: 978-2-35158-178-0, e-ISBN: 978-2-35158-179-7; *Ed. Per Goltermann*

PRO 109 (two volumes): MSSCE 2016 - Service Life of Cement-Based Materials and Structures (2016), ISBN Vol. 1: 978-2-35158-170-4, Vol. 2: 978-2-35158-171-4, Set Vol. 1&2: 978-2-35158-172-8, e-ISBN : 978-2-35158-173-5; *Eds. Miguel Azenha, Ivan Gabrijel, Dirk Schlicke, Terje Kanstad and Ole Mejlhede Jensen*

PRO 110: MSSCE 2016 - Historical Masonry (2016), ISBN: 978-2-35158-178-0, e-ISBN: 978-2-35158-179-7; *Eds. Inge Rörig-Dalgaard and Ioannis Ioannou*

PRO 111: MSSCE 2016 - Electrochemistry in Civil Engineering (2016), ISBN: 978-2-35158-176-6, e-ISBN: 978-2-35158-177-3; *Ed. Lisbeth M. Ottosen*

PRO 112: MSSCE 2016 - Moisture in Materials and Structures (2016), ISBN: 978-2-35158-178-0, e-ISBN: 978-2-35158-179-7; *Eds. Kurt Kielsgaard Hansen, Carsten Rode and Lars-Olof Nilsson*

PRO 113: MSSCE 2016 - Concrete with Supplementary Cementitious Materials (2016), ISBN: 978-2-35158-178-0, e-ISBN: 978-2-35158-179-7; *Eds. Ole Mejlhede Jensen, Konstantin Kovler and Nele De Belie*

PRO 114: MSSCE 2016 - Frost Action in Concrete (2016), ISBN: 978-2-35158-182-7, e-ISBN: 978-2-35158-183-4; *Eds. Marianne Tange Hasholt, Katja Fridh and R. Doug Hooton*

PRO 115: MSSCE 2016 - Fresh Concrete (2016), ISBN: 978-2-35158-184-1, e-ISBN: 978-2-35158-185-8; *Eds. Lars N. Thrane, Claus Pade, Oldrich Svec and Nicolas Roussel*

PRO 116: BEFIB 2016 – 9th RILEM International Symposium on Fiber Reinforced Concrete (2016), ISBN: 978-2-35158-187-2, e-ISBN: 978-2-35158-186-5;

PRO 117: 3rd International RILEM Conference on Microstructure Related Durability of Cementitious Composites (2016), ISBN: 978-2-35158-188-9, e-ISBN: 978-2-35158-189-6; *Eds. Changwen Miao, Wei Sun, Jiaping Liu, Huisu Chen, Guang Ye and Klaas van Breugel*

RILEM REPORTS (REP)

Report 19: Considerations for Use in Managing the Aging of Nuclear Power Plant Concrete Structures (ISBN: 2-912143-07-1); *Ed. D. J. Naus*

Report 20: Engineering and Transport Properties of the Interfacial Transition Zone in Cementitious Composites (ISBN: 2-912143-08-X); *Eds. M. G. Alexander, G. Arliguie, G. Ballivy, A. Bentur and J. Marchand*

Report 21: Durability of Building Sealants (ISBN: 2-912143-12-8); *Ed. A. T. Wolf*

Report 22: Sustainable Raw Materials - Construction and Demolition Waste (ISBN: 2-912143-17-9); *Eds. C. F. Hendriks and H. S. Pietersen*

Report 23: Self-Compacting Concrete state-of-the-art report (ISBN: 2-912143-23-3); *Eds. Å. Skarendahl and Ö. Petersson*

Report 24: Workability and Rheology of Fresh Concrete: Compendium of Tests (ISBN: 2-912143-32-2); *Eds. P. J. M. Bartos, M. Sonebi and A. K. Tamimi*

Report 25: Early Age Cracking in Cementitious Systems (ISBN: 2-912143-33-0); *Ed. A. Bentur*

Report 26: Towards Sustainable Roofing (Joint Committee CIB/RILEM) (CD 07) (e-ISBN 978-2-912143-65-5); *Eds. Thomas W. Hutchinson and Keith Roberts*

Report 27: Condition Assessment of Roofs (Joint Committee CIB/RILEM) (CD 08) (e-ISBN 978-2-912143-66-2); *Ed. CIB W 83/RILEM TC166-RMS*

Report 28: Final report of RILEM TC 167-COM 'Characterisation of Old Mortars with Respect to Their Repair (ISBN: 978-2-912143-56-3); *Eds. C. Groot, G. Ashall and J. Hughes*

Report 29: Pavement Performance Prediction and Evaluation (PPPE): Interlaboratory Tests (e-ISBN: 2-912143-68-3); *Eds. M. Partl and H. Piber*

Report 30: Final Report of RILEM TC 198-URM 'Use of Recycled Materials' (ISBN: 2-912143-82-9; e-ISBN: 2-912143-69-1); *Eds. Ch. F. Hendriks, G. M. T. Janssen and E. Vázquez*

Report 31: Final Report of RILEM TC 185-ATC 'Advanced testing of cement-based materials during setting and hardening' (ISBN: 2-912143-81-0; e-ISBN: 2-912143-70-5); *Eds. H. W. Reinhardt and C. U. Grosse*

Report 32: Probabilistic Assessment of Existing Structures. A JCSS publication (ISBN 2-912143-24-1); *Ed. D. Diamantidis*

Report 33: State-of-the-Art Report of RILEM Technical Committee TC 184-IFE 'Industrial Floors' (ISBN 2-35158-006-0); *Ed. P. Seidler*

Report 34: Report of RILEM Technical Committee TC 147-FMB 'Fracture mechanics applications to anchorage and bond' Tension of Reinforced Concrete Prisms – Round Robin Analysis and Tests on Bond (e-ISBN 2-912143-91-8); *Eds. L. Elfgren and K. Noghabai*

Report 35: Final Report of RILEM Technical Committee TC 188-CSC 'Casting of Self Compacting Concrete' (ISBN 2-35158-001-X; e-ISBN: 2-912143-98-5); *Eds. Å. Skarendahl and P. Billberg*

Report 36: State-of-the-Art Report of RILEM Technical Committee TC 201-TRC 'Textile Reinforced Concrete' (ISBN 2-912143-99-3); *Ed. W. Brameshuber*

Report 37: State-of-the-Art Report of RILEM Technical Committee TC 192-ECM 'Environment-conscious construction materials and systems' (ISBN: 978-2-35158-053-0); *Eds. N. Kashino, D. Van Gemert and K. Imamoto*

Report 38: State-of-the-Art Report of RILEM Technical Committee TC 205-DSC 'Durability of Self-Compacting Concrete' (ISBN: 978-2-35158-048-6); *Eds. G. De Schutter and K. Audenaert*

Report 39: Final Report of RILEM Technical Committee TC 187-SOC 'Experimental determination of the stress-crack opening curve for concrete in tension' (ISBN 978-2-35158-049-3); *Ed. J. Planas*

Report 40: State-of-the-Art Report of RILEM Technical Committee TC 189-NEC 'Non-Destructive Evaluation of the Penetrability and Thickness of the Concrete Cover' (ISBN 978-2-35158-054-7); *Eds. R. Torrent and L. Fernández Luco*

Report 41: State-of-the-Art Report of RILEM Technical Committee TC 196-ICC 'Internal Curing of Concrete' (ISBN 978-2-35158-009-7); *Eds. K. Kovler and O. M. Jensen*

Report 42: 'Acoustic Emission and Related Non-destructive Evaluation Techniques for Crack Detection and Damage Evaluation in Concrete' - Final Report of RILEM Technical Committee 212-ACD (e-ISBN: 978-2-35158-100-1); *Ed. M. Ohtsu*

Report 45: Repair Mortars for Historic Masonry - State-of-the-Art Report of RILEM Technical Committee TC 203-RHM (e-ISBN: 978-2-35158-163-6); *Eds. Paul Maurenbrecher and Caspar Groot*

Organizing Committee

Manu Santhanam, IIT Madras	Chair
Ravindra Gettu, IIT Madras	Co-chair
Arun Menon, IIT Madras	Co-chair
Benny Raphael, IIT Madras	Co-chair
J. Murali Krishnan, IIT Madras	Co-chair
Radhakrishna G. Pillai, IIT Madras	Co-chair
S. P. Shah, Northwestern University, USA	Co-chair

Atul Narayan, IIT Madras
A. Veeraraghavan, IIT Madras
Bhaskar Sangoju, SERC, Chennai
Carlos Espina, Lafarge-Holcim, France
Dali Naidu Arnepalli, IIT Madras
Geert de Schutter, Ghent University, Belgium
Haji Sheikh Mohammed, BSAR University
K. Jayasankar, Ultratech Cement
K. P. Jaya, Anna University
K. Ramamurthy, IIT Madras
K. G. K. Moorthy, Totale Global Pvt. Ltd.
Madhavi Tadepalli, SRM University
Muhammed Salman, IIT Bombay
Nicolas Roussel, IFSTTAR, France
Nigel Pradeep Narayan, The Masterbuilder
Prakash Nanthagopalan, IIT Bombay
Shashank Bishnoi, IIT Delhi
Sivakumar Palaniappan, IIT Madras
Soumen Maity, TARA, New Delhi
Sunitha K. Nayar, IIT Madras
Vaibhav Rathi, TARA, New Delhi
Venkatraman, Ultratech Cement
Viswanathan Mahadevan, BASF

Scientific Committee

Abhijit P. Deshpande, India
Ahmed Asif, USA
Ambili P. S, India
Amit Chatterjee, India
Amlan Sengupta, India
Ananth Ramaswamy, India
Anjan K. Chatterjee, India
Anjan Kumar, India
Antonio Aguado, Spain
Antonio Figueirado, Brazil
Appa Rao G, India
Aravind K. Swamy, India
Aravind Narayanaswamy, India
Arijit Basu, India
Arnon Bentur, Israel
Arun Menon, India
Atul Narayan, India
Bahurudeen A, India
Balaguru P, USA
Balasubramanian K, India
Benny Raphael, India
Betiglu Eshete Jimma, USA
Bharatkumar H, India
Bhattacharya S. K, India
Bhupinder Singh, India
Bishwajit Bhattacharjee, India
Bruno D'Souza, Australia
Bryan Barragan, Spain
Caijun Shi, China
Carlos Aire, Mexico
Carmen Andrade, Spain
Cedric Sauzeat, France
Chandra Kishen J. M, India
Chris Leung, Hong Kong
Christophe Cortinovis, Spain
Chrysl Aranha, India
Climent Molins, Spain
Dali Naidu Arnepalli, India
Daniela Ciancio, Australia
Dhanya B S, India
Massimo Borsa, Italy
Mazen Tabbara, USA
Dharamveer Singh, India
Dinakar P, India
Doug Hooton R, Canada
Elson John, India
Enric Vazquez, Spain
Erik Schlangen, Netherlands
Esperanza Menendez, Madrid
Francois de Larrard, France
Frank Dehn, Germany
Gabriele Tebaldi, USA
Ganesan N, India
Ganesh Chaudhari, USA
Geert de Schutter, Belgium
Geetha Selva, India
Geoff Rowe, Canada
Girish Bonde, India
Hakim Abdelgader, Libya
Hemanta Doloi, India
Herve Benedetto, France
Hussain Bahia, USA
Ignacio Carol, Spain
Ignasi Casanova, Spain
Ioan Pepenar, Romania
Jay Sanjayan, Australia
Jayachandran K, India
Jayasree C, Kuwait
Joan Ramon Casas, Spain
Joana Roncero, Spain
John Bolander, USA
Jorge Debrito, Portugal
José Sena-Cruz, Portugal
José Turmo, Spain
Kingsley Ernest, India
Kolluru Subramaniam, India
Leung K. Y, Hong Kong
Liberato Ferrara, Italy
Manu Santhanam, India
Maricruz Alonso, Spain
Mark Alexander, South Africa
Mohammed Haneefa, India

Muhammed Basheer, UK
Murali Krishnan J, India
Murty C V R, India
Narayanan Neithalath, USA
Neal Berke, USA
Neethu Roy, India
Nele de Belie, Belgium
Nemy Banthia, Canada
Nivedya M. K, USA
Padmarekha A, India
Pascal Boustingorry, France
Pascal Casanova, France
Paulo Cruz, Portugal
Pedro Castro Borges, Mexico
Pedro Serna Ros, Spain
Pierre-Claude Aitcin, Canada
Prakash Nanthagopalan, India
Prannoy Suraneni, USA
Prasad Rangaraju, USA
Praveen Kumar, India
Priya Nair, India
Radhakrishna G. Pillai, India
Raghavan N, India
Rajamane N. P, India
Rajan N. K, India
Ramamurthy K, India
Ranganath R. V, India
Raúl Zerbino, Argentina
Ravindra Gettu, India
Remya Varma K, India
Roberto Torrent, Argentina
Sangoju Bhaskar, India
Sanjay Bahadur, India
Saravanan U, India
Senthilkumar V, UAE
Sergio Pialarissi Cavalaro, Spain
Shashank Bishnoi, India
Sivakumar Babu G, India
Sivakumar Palaniappan, India
Smitha Gopinath, India
Soumen Maity, India
Sunitha K. Nayar, India
Ta-Peng Chang, Taiwan
Tejash Gandhi, USA
Tulio Bittencourt, Brazil
Vasugi V, India
Veeraragavan A., India
Venkaiah Chowdary, India
Victor Oscar Garcia Alvarez, Spain
Visalakshi T, India
Viswanath Mahadevan, China
Vivek Agnihotri, India
Vivek Bindiganavile, Canada
Yong-Rak Kim, USA
Yunus Ballim, South Africa

Proceedings Editing Team

Dyana Joseline	Sripriya R	Sundar R
Divya Rani	Sujatha Jose	Aswathy R
K P Ramaswamy	Sunitha K. Nayar	Manu Mohan
Prabha M	Yuvaraj Dhandapani	Resmi G
R Priyadharshini	Uma Chakkoth	Anand G
Saarthak Surana	M Murugan	Gopakumar K
Sachin Paul	A V Rahul	Ananth Sundararaman
Sooraj Nair	Deepak Kamde	

Conference Secretariat

Ramya Lakshmanan
Lakshmi R

Table of Contents

Preface

The International Conference on Advances in Construction Materials and Systems (ICACMS 2017) is part of the prestigious RILEM Annual Week, which is the annual meeting of the standing committees of RILEM *(International Union of Testing and Research Laboratories for Materials and Structures*). Such meetings occur every year in conjunction with a major international conference. The recent RILEM weeks were held in Copenhagen (2016), Melbourne (2015), São Paulo (2014), Paris (2013), Cape Town (2012), Hong Kong (2011).

The conference covers several themes related to construction materials and systems, with the objective of providing the state of the art coverage on cement and asphalt concrete, heritage materials, and building systems. The specific conference themes include: Advances in supplementary cementing materials, Concrete durability and performance specifications, Early age behaviour and rheology of cementitious systems, Special concretes and applications, Advances in characterization of construction materials, Sustainable building systems, Bituminous binders and mixtures, Repair and conservation of heritage structures, Corrosion control and corrosion monitoring in concrete structures, Repair materials and repair systems for concrete structures. The themes selected for the conference are reflective of the scientific coverage provided by the different Technical Clusters within RILEM.

The 250+ papers received from academics and industry professionals from more than 50 countries across the world are assembled into 4 volumes. The first volume deals with the papers from the invited (keynote) speakers, while the remaining three volumes – arranged in appropriate sub-sections, deal with the specific themes of the conference. The onerous task of compilation of these papers into the four volumes was performed by our editing team comprising of students. The abstracts submitted for the conference were subjected to independent peer review by two experts from the international scientific committee, and subsequently, the selected papers were also thoroughly reviewed by the editing team followed by members from the scientific committee. The successful compilation of the proceedings is largely owing to the efforts of the editing team and the experts from the scientific committee.

The support by our sponsors and organizational partners has enabled us to put together the largest of its kind conference in India, and we are extremely thankful.

We wish you all a highly productive and engaging conference!

Manu Santhanam
Ravindra Gettu
Radhakrishna G. Pillai
Sunitha K. Nayar

Thixotropic Effects During Large-scale Concrete Pump Tests on Site

Geert De Schutter

Magnel Laboratory for Concrete Research, Ghent University, Belgium.

Abstract

During recent years, the fundamentals of pumping fresh concrete have been intensively studied worldwide. New insights have been gained concerning the important role of the lubrication layer near the surface pipe. The influence of rheological properties of the fresh concrete, like yield stress, viscosity, and shear thickening behavior, is now well understood, and can be fairly accurately modelled. One major challenge is found in the potential effect of thixotropy while pumping fresh concrete, especially in case the pumping operation is temporarily paused and resumed after a while. Due to thixotropic effects, restarting the pumping operation can be a very challenging task. This paper reports on a large-scale concrete pump test on a construction site, specifically focusing on the risk of thixotropy. Fresh concrete has been pumped in a horizontal closed-loop pumping pipe with a total length of 600 meter. In steady-state pumping conditions, the pumping operation was very successful, and in agreement with the expectations. However, the thixotropic effects, occurring during a short stop of the pumping operations, showed to provoke major problems while trying to resume pumping. The lessons-learnt helped to define a successful pumping procedure for this major construction site.
Keywords: Concrete, pumping, thixotropy, rheology.

1 INTRODUCTION

Pumping of fresh concrete is a commonly used technique to cast structural elements on site. With the introduction of new types of concrete, such as self-compacting concrete, new research insights have been obtained in the pumping behaviour of fresh concrete, explaining the important role of the lubrication layer near the pipe surface, the effect of internal shear in the concrete, and the occurrence of a plug zone in the centre of the pipe. A recent update on the basic understanding and remaining challenges of pumping of fresh concrete can be found in [1].

The in-regime pumping of fresh concrete seems well understood now, and pressure-discharge relations can be simulated in a reasonable way. Practical difficulties typically occur during the starting phase of the pumping process. In order to prepare the pipe surface and facilitate the formation of the lubrication layer, a cement mortar is typically pumped first. Afterwards, the concrete is entered into the pipes, and a lubrication layer is properly formed thanks to the presence of a thin paste layer on the pipe surface, and due to further shear-induced particle migration inside the concrete. Without a proper start-up procedure involving cement mortar, the risk of blocking inside the concrete pipe is very high.

Less known and less understood is the fact that blocking can also occur after a short stand-still of the pumping process (e.g. due to delay of a concrete truck), during the restarting phase. Short interruptions of the pumping process can lead to significant problems in resuming pumping operations because of internal structural build-up in the fresh concrete,

also called thixotropy.The physical origin of thixotropic behavior is discussed in [2], but is beyond the scope of this paper. A pragmatic model to describe thixotropy is given in [3], and is reprinted in equations (1) and (2).

$$\tau = (1+\lambda)\tau_0 + \mu_p\dot{\gamma} \tag{1}$$

$$\frac{\partial\lambda}{\partial t} = \frac{1}{T} - \alpha\lambda\dot{\gamma} \tag{2}$$

In equation (1), λ is the flocculation state of the material, τ is the shear stress, τ_0 is the yield stress, μ_p is the plastic viscosity, and $\dot{\gamma}$ is the shear rate. The first term in the right hand side of equation (2) is the structuration rate, while the second term can be seen as the de-structuration rate. When the concrete is at rest, e.g. when the pumping operations are being paused, the evolution of the apparent yield stress as a function of time t is given by equation (3).

$$\tau_0(t) = (1+\lambda)\tau_0 = \tau_0\left(1+\frac{t}{T}\right) = \tau_0 + A_{thix}t \tag{3}$$

The parameter A_{thix}, also equal to τ_0/T, is the structuration rate, expressed in Pa/s. By means of this thixotropy model, some experimentally obtained results in a large-scale pump test on a construction site will be analysed to further illustrate the effect of thixotropy on pumping operations.

2 LARGE-SCALE PUMPING CIRCUIT

For the construction of a railway tunnel in Belgium, concrete needed to be pumped over a distance of about 1 km, into the tunnel. Before the start of the real pumping operations, a large-scale trial pump test was set up on the construction site. A closed-loop horizontal pumping circuit was installed with a total length of 600 m. The setup is illustrated in figure 1, showing the powerful concrete pump, the sequence of concrete pipes, and the final pipe returning the fresh concrete to the pump, closing the loop.

A powerful piston pump was used, with a capacity of about 350 bar. During each single stroke of the pump, a concrete volume of 0.063 m³ was pushed into the pumping pipe. The steel pipes had a diameter of 125 mm, and have been prepared by firstly pumping a specially prepared cement mortar. Afterwards, the concrete was introduced into the pump and the pipes, and during a couple of minutes, the concrete was pumped around, and some measurements were performed, including conventional workability tests on the pumped concrete (see further).

The main goal of the large-scale pump test however, was to test the effect of a stand-still of the fresh concrete during 15 to 20 minutes, the maximum waiting time which was estimated to occur in the real production in case of delay of a truck mixer. So, after the first cycle of steady-state pumping, the pumping operation was halted, and the concrete remained at rest within the pipes. After the prescribed waiting time, the pumping operation was to be resumed, monitoring required pump pressures.

Figure 1: Layout of the closed-loop pumping circuit with a total length of 600 m

3 CONCRETE

A conventional vibrated concrete was used in the pump test, with a composition as given in table 1. Blast furnace slag cement of European type CEM III/A 42.5 N LA has been used. The strength class of the concrete is C30/37 according to the European standard EN 206.

Table 1: Concrete mix design

Material	**Amount (kg/m³)**
Cement CEM III/A 42.5 N LA	365
Fly ash	90
Limestone aggregate 2/6	195
Granite aggregate 2/22	765
Coarse sand 0/4	496
Fine sand 0/1	210
Plasticizer (naphtalene-based)	6
Retarder	0.5
Water	195

On arrival at the construction site, conventional workability measurements have been performed on the fresh concrete. The slump of the concrete was equal to 220 mm (Figure 2), and the flow was equal to 640 mm (Figure 3). It is important to mention that the concrete was retarded in order to avoid the influence of workability loss within the duration of the pump trials.

Figure 2: Slump measurement on fresh concrete at construction site

Figure 3: Flow measurement on fresh concrete at construction site

4 PUMP TEST RESULTS

After preparation of the pumping pipes with a cement mortar consisting per m³ of 800 kg CEM III/A 43.5 N LA, 150 kg fly ash, 822 kg fine sand 0/1 and 335 kg water, the fresh concrete with composition given in table 1 was introduced into the pump and the pipes. The concrete was then pumped in the closed-loop during about 2 minutes, having 120 pump strokes. This means that the entire concrete volume of about 7.5 m³ present in the pumping pipes made about one loop. At one stroke per second, the discharge rate was 63 l/s, or about 227 m³/h. The required pumping pressure in steady-state regime was 220 bar in the pump. The real concrete pressure in the pipe was not measured directly, but according to previous experiences of the pump operators, the concrete pressure at the inlet of the pipe is estimated to be about 60% of the pump pressure, which means about 135 bar.

After one full pumping cycle, the workability of the concrete has been measured again, resulting in a slump value equal to 260 mm and a flow equal to 670 mm. This means that the concrete coming out of the pumping pipe showed a slight increase in workability. This could be explained by some intermixing with the cement mortar previously introduced into the pumping pipes in order to prepare the pipe surface. However, other effects could also occur, e.g. linked to the role of air [4]. Temperature effects can also intervene. The temperature of the concrete after one cycle of pumping increased to 26°C (coming from about 20°C on arrival on site) (Figure 4).

Figure 4: Temperature measurement on fresh concrete at construction site

After a second full cycle of pumping, with steady-state pump pressures now equalling 235 bar (estimated concrete pressure at inlet equalling about 140 bar), the concrete temperature increased to 27°C, while the slump flow value decreased to 220 mm from 570 mm.

At this stage, the pumping was paused for 20 minutes, simulating a delay in concrete delivery. After 20 minutes, the pumping pressures were increased again in order to resume pumping operation. At the maximum pump pressure capacity of 350 bar, it showed not possible to bring the fresh concrete in the pumping pipes into motion again. At this moment the estimated concrete pressure at the inlet of the pipes was about 210 bar, which was about 50% higher than the corresponding pressure in steady-state pumping conditions. Attempts to increase the applied pressure by circumventing the safety settings of the pump, assisted by the pump producer present on site, unfortunately did not help. Finally, the pumping pipes had to be dismounted for proper cleaning, and no further pumping cycles could be performed.

5 DISCUSSION

As retarder was added to the concrete, avoiding workability loss due to hydration during the pump test, the fact that the pumping operation could not be resumed after a pause of 20 minutes is mainly due to the thixotropic behaviour of the fresh concrete. Due to internal clustering and structure formation, the fresh concrete becomes stiffer, and shows a larger resistance against flow. Considering the fresh concrete as a homogeneous material in a cylindrical pumping pipe with diameter R, it can be shown that the shear stress τ_w at the pipe wall can be calculated by means of equation (4), as explained in [5].

$$\tau_w = \frac{\Delta p_{tot}}{L} \cdot \frac{R}{2} \quad (4)$$

In this equation, Δp_{tot} is the total pressure loss over the length L of the pipe with radius R. With the experimentally obtained pressure results mentioned in previous section, it can be calculated in this way that the shear stress at the pipe wall, having a total pressure loss of 210 bar over a length of 600 m, was equal to about 1100 Pa. Indicatively, it can thus be concluded by applying equation (4) that the apparent yield stress of the concrete at that moment, at the end of the 20 minutes waiting period, was at least equal to 1100 Pa.

During the steady-state pumping cycle preceding the 20 minutes waiting period, the total pressure loss was equal to 140 bar, which would indicate a yield stress of about 730 Pa (assuming that the yield stress in these flowing conditions could be estimated by the same conditions as in equation (4), neglecting the non-homogenous situation caused by the existence of a lubrication layer during active flow, which is questionable but acceptable in an indicative way).

Applying equation (3), and considering an increase in apparent yield stress from 730 Pa to 1100 Pa in 20 minutes (1200 seconds), it can be estimated that A_{thix} in this case was equal to about 0.3 Pa/s. While for reasons of formwork pressure reduction in freshly cast concrete walls a significant structuration rate A_{thix} is desirable, during pumping operations it can mean a significant problem and risk.

As only one pump test was performed (because of limited budget), the obtained values can only be considered as indicative. Nevertheless, the obtained results illustrate the potential order of magnitude of the thixotropic effects while pumping.

6 ERC ADVANCED GRANT PROJECT 'SMARTCAST'

As illustrated in this large-scale pumping test, short interruptions of the pumping process can lead to major difficulties in resuming pumping operations due to the sometimes tremendous effect of internal structural build-up or thixotropy. During a pause in the pumping operations, current practices do not allow for the active control of the concrete rheology. The pumping operator can only passively consider the evolution of the rheological properties of the cementitious material, in steady-state conditions or in rest, and has no means to adjust the material properties.

A potential solution to overcome this problem is currently studied in the ERC Advanced Grant Project 'SmartCast'[6], which aims to introduce a ground-breaking approach by developing an innovative concrete mix design containing responsive polymer admixtures interacting with applied electromagnetic fields, enabling the active rheology control (ARC) of the fresh concrete while being placed, and the active stiffening control (ASC) as soon as the concrete is in final position in the formwork. These active control features would bring a relevant solution for contradicting requirements e.g. related to the structuration rate A_{thix} as shown with the experiment described in this paper. Active control would limit the structuration while placing the concrete, and increase the structuration rate after casting, all of this with the same concrete mixture.

7 CONCLUSIONS

By performing a large-scale closed-loop pumping test on site, with a total pipe length of 600 m, some relevant conclusions can be summarized:

It was shown that short interruptions of the pumping process (e.g. due to the delay of a concrete truck) can lead to major difficulties in resuming pumping operations due to the

effect of internal structural build-up or thixotropy. As the tested concrete was retarded, workability loss due to hydration could be excluded as significant factor.

Requirements limiting the structuration rate of the fresh concrete, in order to limit the risk of blocking after pausing and facilitating the restart of pumping operations, are contradictory to requirements in view of obtaining fast reductions in formwork pressures.

Active rheology control (ARC) and active stiffening control (ASC) of fresh concrete, as currently studied within the ERC Advanced Grant Project 'SmartCast', would make concrete pumping (and formwork casting) safer and more reliable.

8 ACKNOWLEDGEMENTS

The financial support of the European Research Council (ERC), as provided through the Advanced Grant Project 'SmartCast' (2016-2021) awarded to the author of this paper, is gratefully acknowledged.

9 REFERENCES

[1] De Schutter, G. and Feys, D., 'Pumping of Fresh Concrete: Insights and Challenges', RILEM Technical Letters (2016) 1, 76 – 81, DOI: http://dx.doi.org/10.21809/rilemtechlett.2016.15.

[2] Roussel, N., 'Understanding the rheology of concrete', Woodhead Publishing Limited, 2012, ISBN 978-0-85709-028-7.

[3] Roussel, N., 'A thixotropy model for fresh fluid concretes: theory, validation and applications', Cement and Concrete Research (2006) 36, 1797-1806.

[4] Feys, D., De Schutter, G., Khayat, K.,Verhoeven, R., 'Changes in Rheology of Self-Consolidating Concrete Induced by Pumping', Materials and Structures (2016) 49, 2016, 4657–4677, DOI 10.1617/s11527-016-0815-7.

[5] Feys, D., 'Interactions between rheological properties and pumping of self-compacting concrete', PhD thesis, Magnel Laboratory for Concrete Research, Ghent University, Belgium, 2009.

[6] De Schutter, G., "Smart casting of concrete structures by active control of rheology, Smartcast," ERC Advanced Grant Project, European Research Council, 2016-2021.

Modeling Fly Ash Based Geopolymer Flow for 3D Printing Applications

Biranchi Panda, Li Mingyang, Yi Wei Daniel Tay, Suvash Chandra Paul and Ming Jen Tan

Singapore Centre for 3D Printing, School of Mechanical & Aerospace Engineering, Nanyang Technological University, Singapore

ABSTRACT

3D printing is gaining attraction in the construction industry because of its significant benefits over the traditional construction methods. Present construction methods are dependent on the large amount of manpower and time to erect formwork and place concrete, and it is believed that by using a 3D printing technique, these can be significantly reduced. 3D concrete printing is a formwork less construction method, where concrete is deposited layer by layer as per the design specified in a computer aided design (CAD) model. Literature reveals that it requires combination of appropriate rheology, advanced delivery and control system for the successful application. Therefore, this paper aims to study the rheological properties of geopolymer mortar and propose a flow model for 3D printing application. Results conclude that, the material must possess thixotropic behaviour, which will allow a decrease in viscosity during pumping and quick reflocculation to recover under static conditions after deposition. Considering global demand for a sustainable built environment, 3D printing of geopolymer could be a major breakthrough for faster and eco-friendly construction.

Keywords: Sustainable construction materials, thixotropy, 3D printing, digital construction, rheology

1 INTRODUCTION

The construction industry is responsible for almost half of the country's carbon emissions, half of our water consumption, and one quarter of all raw materials used in the economy. Traditionally, the construction industry has relied on two-dimensional (2D) drawings and scale models for evaluation of the design process. Increasingly, 2D drawings and prototypes are being replaced by three-dimensional (3D) modelling in the virtual environment of building information modelling (BIM) [1, 2]. BIM can be used to illustrate the entire building life-cycle, from cradle to cradle, from inception and design to demolition while preventing errors creeping in at the various stages of development/ construction. A benefit in the use of BIM, backed up by 3D modelling, is that they can be used in combination with digital fabrication methods. Digital fabrication includes the use of 3D printing (3DP) or additive manufacturing (AM) which uses a layer by layer deposition strategy to build complex 3D objects directly from the computer aided design (CAD) model in a reasonable build time. Latterly, this technology has shown the potential to be used in building and construction (B&C) sectors due to significant advantages in terms of reduced build time, less wastage and less human resources when compared to traditional methods [3]. The first published evidence of 3D concrete printing was in 1997 with an innovative

approach suggested by Pegna [4]. However, the actual development started in the mid-1990s in California, USA, when Khoshnevis introduced a technique termed Contour Crafting (Figure 1 (a)). Contour crafting (CC) is a gantry based robotic system that extrudes material in a layer by layer manner to construct on-site structures [5]. Like CC, using another technology called concrete printing, a concrete bench was printed at Loughborough University, UK with high-performance fibre-reinforced concrete material (Figure 1 (b)) [6]. Besides Khoshnevis and the University of Loughborough, pioneering work was done by Shanghai based contractor Winsun, and the company Total Kustom, Minnesota, USA. An alternative to working with single, large robot/gantry was introduced by the Institute of Advanced Architecture of Catalonia (IAAC) in 2014 where a group of small robots were printing together using swarm base group technology (Figure 2). Currently, developments are going so fast that any overview of existing techniques and examples is out-of-date almost as soon as it is published. Some noteworthy extrusion based concrete printing is shown in figure 2 [7].

Figure 1. (a) Contour crafting (CC) [5] (b) Concrete printing processes [6]

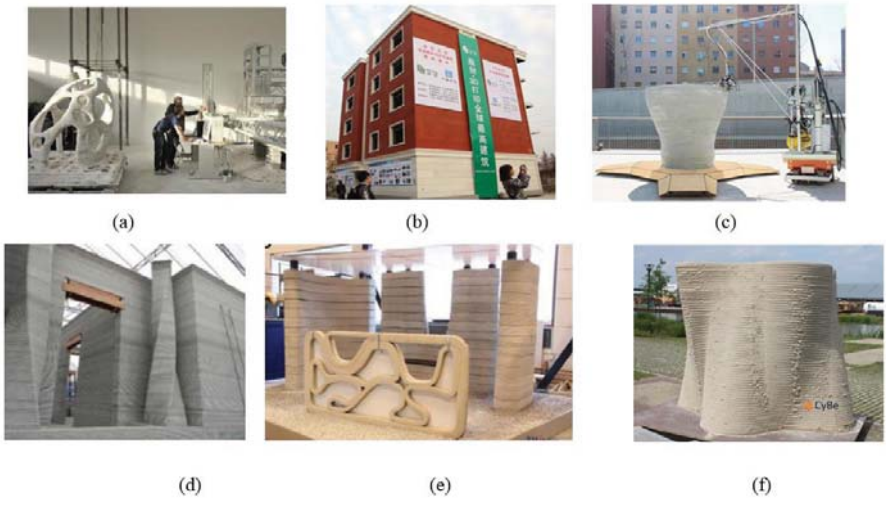

Figure 2. Concrete printing by (a) D-shape (b) Winsun, China (c) IAAC, Spain (d) Total Kustom, USA (e) Tu/e Eindhoven, Netherlands (f) Cybe, Netherlands [7]

The main challenge associated with extrusion based printing is to develop appropriate material that can be extruded continuously and stacked up over one another without causing any deformation in the printed structure. In this regard, University of Loughborough, UK presented essential benchmarking properties while developing right mix design for concrete printing [8]. A close look at these properties reveals that rheology of the material plays very important role for concrete printing application. Though there are few studies that have been done in the past [9-10], concrete printing needs a different set of rheology i.e., discussed in the following section.

2 RHEOLOGY

Rheology is the science of deformation and flow of matter, and is related to stress, strain and time. In terms of fresh concrete, the field of rheology is related to the flow properties of concrete and its mobility before setting takes place. Concrete is generally considered as non-Newtonian fluid and its rheology can be described by Bingham plastic model given by [11]

$$\tau = \tau_0 + k\dot{\gamma} \quad (1)$$

Where τ_0(Pa) is the yield stress, k (Pa·s) is the plastic viscosity, and $\dot{\gamma}$(1/s) is the shear stress. Both τ_0 and k are related to the resistance to flow of fresh concrete and it is affected by many factors such as particle size, packing density, w/b ratio, additives etc. Use of rotational rheometer is among some well-established testing methods to measure yield stress and viscosity by varying shear stress and shear rate. Results from rheometer tests shows that mortar can be considered as shear thinning liquid, in which the viscosity decreases when the shear rate increases. It also possesses a yield value: a minimum shear stress that must be applied before the mortar can begin to flow. If this shear thinning effect is permanent, then this behaviour is known as thixotropic. Thixotropy is a reversible, isothermal, time-dependent decrease in viscosity when a fluid is subjected to increased shear stress or shear rate [12]. It is due to two main aspects a) structural build-up when concrete is at rest; and b) structural break-down, when concrete is under a shear or flow. This behaviour of concrete is helpful for 3D printing application where during extrusion, viscosity will be lower down and once the material is out of nozzle it can recover its original state again [13].

Thixotropic property can be measured by calculating the surface area between up and down curves of the torque-rpm graph obtained from rheometer. More area indicates higher thixotropy which assures easy pumping and layering up the material followed by CAD model. However, thixotropy changes with progress of time since the material begins to harden substantially after the mixing process. Simultaneously, yield stress and viscosity also increases, which may limit the material for pumping and thus making the material incompatible for 3D printing. Therefore, it is necessary to track the material property changes with time so that printing can be done without the material getting hardened inside the hose. Figure 3 shows the typical strength development of concrete material where the area limited by two dotted lines indicates the allowable stress zone for extruding concrete. Below this line, the material is too liquid and above the line it is too stiff for which pump pressure goes high during extrusion process. To avoid this rise in pressure, a prediction model is developed in this work using material fresh properties so that a smooth extrusion can be assured during printing process.

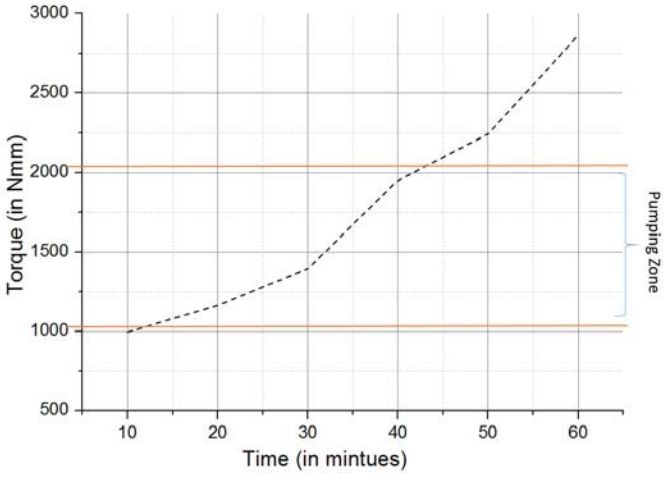

Figure 3. Geopolymer strength development vs time

3 MATERIALS AND MODELS

3.1 Material

Geopolymer mortar is prepared in this study by considering fly ash as main precursor element. For ambient curing, a part of fly ash is replaced with slag supplied by Engro. Singapore. Silica fume provided by Elkem Private Ltd. also added in to the dry components and mixed uniformly for 2-3 minutes. As alkaline reagent, potassium (K) silicate with molar ratio 1.85 is added to the dry components to make geopolymer binder. Later fine river sand of maximum particle of 2 mm and small amount of water are mixed with the binder to formulate mortar of desired workability. The complete mix design is shown in Table 1.

Table 1. Mix design

Materials	**Dry Components**					**Liquid Components**	
	Fly ash	Slag (GGBS)	Silica Fume	Sand	Additives	K-Silicate	Water
Weight (by Percentage)	22.42	3.27	6.54	49.0	0.50	13.25	4.90

Once material is ready, it is loaded in the rheometer cell to measure yield stress and plastic viscosity. In this research, Viskomat XL rheometer from Schleibinger testing Systems, Germany is used to conduct flow curve test at increasing speed of 60 rpm up to two minute followed by two-minute constant speed and then reducing to zero again in two minutes. The area of T (Torque) - N (rotation, rpm) graph is used to measure thixotropic index whereas the down curve is considered to calculate Bingham parameters of the mortar i.e. plastic viscosity, and shear stress.

3.2 Model

In order to explore the change in fresh property of geopolymer mortar, two sets of rheology test are conducted in fifteen minutes' interval. Using the torque-rpm graph, thixotropy is measured to ensure the fitness of material for the 3D printing process.

Torque is determined for steady state -flow using the relationship

$$T = \frac{4\pi R_1^2 R_2^2 H}{R_2^2 - R_1^2}\left[\tau_0 \ln\frac{R_2}{R_1} + k(\omega_2 - \omega_1)\right] \quad (2)$$

where T (*N-mm*) is the torque, $R_1$and $R_2(m)$,$\omega_1$and ω_2 (*rad/s*) are the radius and rotational speed of the inner and outer cylinders, respectively, and H (m) is the length of the cylinders. Later, using material property (yield stress, plastic viscosity) and hose pipe length (3 m length), diameter (1 inch) pressure drop is estimated using the following steady state equation [14]:

$$\Delta p = \left(\frac{8\tau_0}{3R_h} + \frac{8k}{\pi R_h^4}Q\right)L \quad (3)$$

Where Δp (Pa) is the pressure drop along the hose, R_h (m) is the radius of the hose, Q (m^3/s) is the flow rate passing through the hose, and L (m) is the length of the hose.

Due to rapid hardening nature of the material, only two tests results are considered in this study to investigate the material behaviour with progress of time.

4 RESULTS AND DISCUSIONS

Results from the rheometer for two different time intervals are shown in figure 4. It is clear from the figure that thixotropy decreases with time as the area between up and down curves are getting reduced due to strength development in the material.

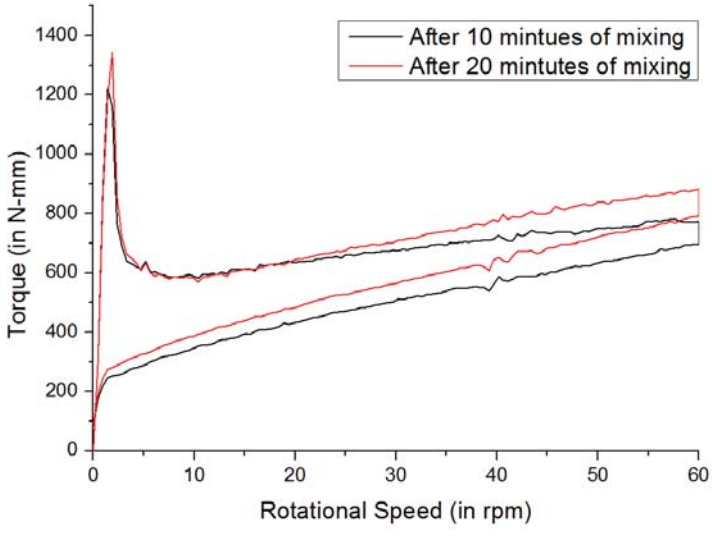

Figure 4. Torque-rpm graph obtained from rheometer

From several trials, it has been found that a minimum thixotropic area of 10000 is necessary for smooth extrusion of geopolymer during printing. This surface area held between up and down curve, only indicates preliminary thixotropy behaviour, but do not provide a good basis for quantitative treatments. Therefore, authors are currently exploring other methods to quantitatively measure thixotropy of the material. It is worth mention that, before conducting rheology test, shear rate at the nozzle must be known, since it affects the thixotropy and structural break down of the geopolymer mortar [15,16].

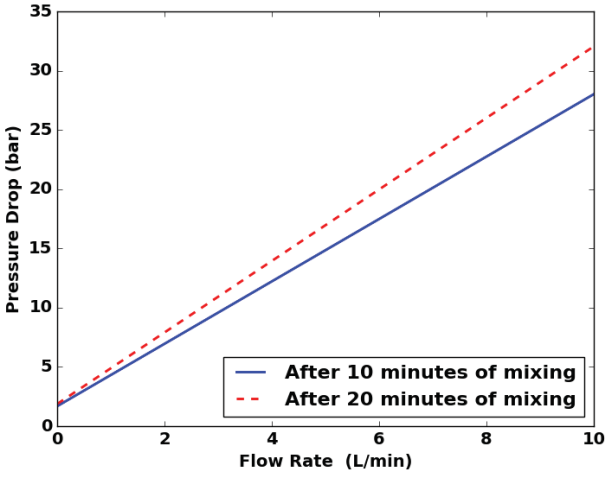

Figure 5. Pressure drop variation at two different time intervals

Figure 5 shows the pressure drop values for our current pump set up (MAI2PUMP Pictor by MAI International GmbH) predicted using the Equation (3). Following this graph, flow is controlled with time for depositing material in different parts of structure. Pressure drop for three-meter hose pipe at two different intervals indicates that geopolymer mortar can be pumped smoothly up to 6 lit/min flow rate even after twenty minutes of mixing. After this time interval, pump need to apply comparatively more pressure to extrude out the material which may exceed out of the safe limit of pump. High flow rate increases the pressure in the hose pipe and as per safety manual of the pump; it should not cross 30 bar during delivery operation. In this case, both material and flow control plays a crucial role for ensuring smooth flow of material out of nozzle. Using the pressure drop model, concrete printing experts now can predict the flow behaviour prior to printing task which will help them to adjust their mix formulation as per pump and hose specification.

5 CONCLUSIONS

With global demands for faster and sustainable construction, 3D printing of geopolymer is one of the potential way to fulfil the desire of building and construction sectors. For printing geopolymer layer by layer, fresh property need to be improved considering the capabilities of printing system and pump. Due to sticky nature of the alkaline reagent, geopolymer flow properties are completely different from conventional Portland cement. In this regard, printable geopolymer has been developed in the current study while modelling the flow using rheology information. Future work involves in optimizing the printer path planning according to material changes with time so that builders can take the actual benefit of 3D printing for future construction projects.

6 ACKNOWLEDGEMENTS

The authors would like to acknowledge SempCrop Architects & Engineers Pte Ltd and National Research Foundation, Singapore (NRF) for funding and support.

7 REFERENCES

[1] Stewart, M. G., Wang, X., & Nguyen, M. N., 'Climate change impact and risks of concrete infrastructure deterioration'. *Engineering Structures*, **33**(4), (2011) 1326-1337.

[2] Cerovsek, T. A review and outlook for a 'Building Information Model'(BIM): A multi-standpoint framework for technological development'. *Advanced engineering informatics*, **25**(2), (2011) 224-244

[3] Labonnote, N., Rønnquist, A., Manum, B., &Rüther, P., 'Additive construction: State-of-the-art, challenges and opportunities'. *Automation in Construction*, **72**, (2016) 347-366.

[4] Pegna, J., 'Exploratory investigation of solid freeform construction'. *Automation in construction*, **5**(5), (1997) 427-437.

[5] Khoshnevis, B., Hwang, D., Yao, K. T., & Yeh, Z., 'Mega-scale fabrication by contour crafting'. *International Journal of Industrial and Systems Engineering*, **1**(3), (2006) 301-320.

[6] Lim, S., Buswell, R. A., Le, T. T., Austin, S. A., Gibb, A. G., & Thorpe, T. 'Developments in construction-scale additive manufacturing processes'. *Automation in construction*, **21** (2012) 262-268.

[7] Bos, F., Wolfs, R., Ahmed, Z., & Salet, T., 'Additive manufacturing of concrete in construction: potentials and challenges of 3D concrete printing'. *Virtual and Physical Prototyping*, **11**(3), (2016) 209-225.

[8] Le, T. T., Austin, S. A., Lim, S., Buswell, R. A., Gibb, A. G., & Thorpe, T., 'Mix design and fresh properties for high-performance printing concrete'. *Materials and structures*, **45**(8), (2012) 1221-1232.

[9] Di Carlo, T., Khoshnevis, B., & Chen, Y., 'Manufacturing Additively, With Fresh Concrete'. *In ASME 2013 International Mechanical Engineering Congress and Exposition*, *American Society of Mechanical Engineers* (2013) pp. V02AT02A007-V02AT02A007

[10] Perrot, A., Rangeard, D., & Pierre, A., 'Structural built-up of cement-based materials used for 3D-printing extrusion techniques'. *Materials and Structures*, **49**(4), (2016) 1213-1220.

[11] Banfill, P. F. G., 'Rheology of fresh cement and concrete'. *Rheology reviews*, **61**(2006).

[12] Mewis, J., 'Thixotropy-a general review'. *Journal of Non-Newtonian Fluid Mechanics*, **6**(1), (1979) 1-20.

[13] Tay Yi, W., Panda, B., Paul, S.C., Tan, M.J., Qian, S., Leong, K.F., and Chua, C.K., 'Processing and properties of construction materials for 3D printing'. *Materials Science Forum*, **861**, (2016)177-181.

[14] Raj P Chhabra and John Francis Richardson. 'Non-Newtonian flow and applied rheology: engineering applications' (Butterworth-Heinemann, 2011).

[15] Li, H., Liu, S., & Lin, L. 'Rheological study on 3D printability of alginate hydrogel and effect of graphene oxide'. *International Journal of Bioprinting*, 2(2), (2016).

[16] Wallevik, J. E., &Wallevik, O. H. 'Analysis of shear rate inside a concrete truck mixer. *Cement and Concrete Research*', **95**, (2017) 9-17.

Understanding Ionic Dependence on the Water Absorption by Superabsorbent Polymer in Early Age Concrete

Moon, Juhyuk[(1)], Kang, Sung-Hoon[(2)] and Hong, Sung-Gul[(2)]

[(1)]Department of Civil & Environmental Engineering, National University of Singapore, Singapore

[(2)]Department of Architecture and Architectural Engineering, Seoul National University, Korea

ABSTRACT

The effects of ion composition and concentration of cement-based solutions on the absorption and retention capacities of superabsorbent polymer (SAP) are investigated. The ion concentration history and SAP absorbency tests verify that the reduction of long-term swelling occurs from an irreversible ion exchange between Ca^{2+} and the anionic groups of SAP; thus, the Ca^{2+} concentration in a solution is a decisive factor for swelling reduction or retention. Furthermore, this reduction is also highly dependent on the concentrations of the other ions in the solution. The retention capacity is improved as the total ion concentration (TIC), which is influenced by these concentrations, increases because a higher TIC indicates a weaker osmotic pressure, which reduces the maximum absorbency along with the effect of the trapped Ca^{2+} in SAP. With the help of herein determined ionic factors for the prepared pore solutions, the complicated absorption and retention behaviors of SAP in concrete can be understood.

Keywords: Superabsorbent polymer, absorption, retention, cement admixture, water-entraining admixture

1 INTRODUCTION

Jensen and Hansen [1] have been demonstrated that it is possible to reduce the autogenous shrinkage and the risk of cracks in the early age of ultra-high performance Concrete (UHPC) by internal curing using superabsorbent polymer (SAP). Since that, extensive studies on the internal curing effect using SAP, such as cement hydration, autogenous shrinkage, mechanical properties and durability have been widely conducted [2, 3].

The SAP in UHPC absorbs initially available water during mixing, then provides the absorbed water to prevent the loss of internal relative humidity (IRH) at later stage. The prevention of IRH loss leads to the reduction of autogenous shrinkage. However, it should affect the water/cement (W/C) ratio, accurate prediction of absorbed amount of water is crucial for the use of SAP as an internal curing admixture.

For instance, two situations can arise when the absorption capacity is mispredicted. First, SAP can absorb more water than designed during the mixing of concrete if its capacity was underestimated. In this case, a part of free water to satisfy the target slump or slump flow value is absorbed by SAP, causing a severe reduction in workability. Also, when SAP has not reached equilibrium swelling at the time of the slump test, even if the target level is satisfied, severe workability loss can occur beyond that point due to the increasing absorption of SAP

[4]. The second situation involves the overestimation of the capacity. In this case, due to the extra water added with SAP, the actual W/C of concrete after mixing exceeds its designed value. This increase can cause unwanted strength loss, and can even lead to problems in structural performance of internally cured concretes. The compressive strength loss due to such over estimation has been demonstrated previously in [5], and by Hasholt et al. [6].

In current study, we attempt to understand the absorption kinetics of solution by the SAP using a tea-bag method and simulated pore solutions. Several cement filtrates were manufactured considering different W/C ratios and the addition of silica fume (SF). Then accurate measurement of compositions and concentrations of the solutions were obtained through inductively coupled plasma-optical emission spectroscopy (ICP-OES) experiments.

2 EXPERIMENTAL SET-UP

Poly acrylic acid type of SAP (MG-2800W, LG Chem., Korea) is used for current study (Figure1). This is one of the most commonly used commercial types of SAP, mainly for personal hygine products such as diapers. This type of polymer has been successfully used for decades due to its productivity, safety, and suitability for diapers application, along with low price and great absorption capacity. The particle size distribution of the SAP ranges from100 μm to 700 μm.

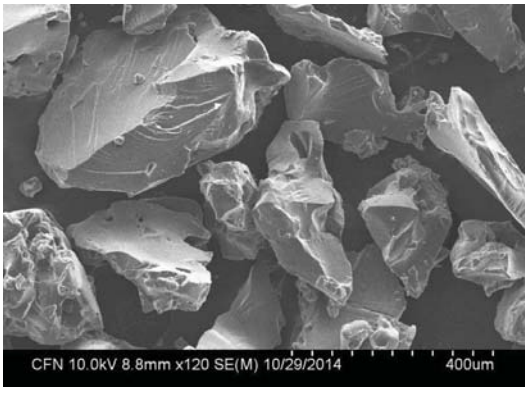

Figure 1: Superabsorbent polymer (SAP)

Several cement filtrates were manufactured (Table 1). When preparing the cement filtrates, SF (SF/cement of 0.25) was mixed with the cement slurry to reflect the ion concentration of pore solution in low W/C concrete accurately. In addition, the various W/C ratios of the slurry such as 1, 2, and 4 were planned to investigate the dilution effect of ions, which was due to the inclusion of large amounts of water compared to the concrete pore solution. Furthermore, solution A was manufactured by dissolving KOH, NaOH, Na_2SO_4, and $Ca(OH)_2$ powders in distilled water by following the previous study [7]. It designed to simulate the concrete pore solution in a long–term age (e.g. > 28 d). As can be seen in Table 1, solution A has a negligible Ca^{2+}concentration (0.02 mM), and contains primarily monovalent cations such as Na^+ (35 mM) and K^+ (169 mM). For absorption test, prepared tea-bag was completely submerged in the prepared solution. After a predetermined time (1, 10, 30, 60, and 180 min), the tea-bag was removed and the liquid on surface was gently wiped. Then 1 min of centrifugation time was applied to remove any entrapped solution between SAP particles or particle and tea-bag. Details of experimental procedures can be found in our previous paper [8].

Table 1: Manufactured solutions for absorption tests.

Solution label	W/C	SF/C	Ion concentration by ICP-OES [mM]							
			Na	K	Ca	Mg	Al	Fe	Si	S
Solution A	n.a	n.a	35.5	169.2	0.0	0.0	0.0	0.0	0.3	10.7
Cement Filt._1	1	0	15.1	124.8	15.4	0.0	0.0	0.0	0.0	52.8
Cement Filt._2	2	0	8.1	65.3	23.1	0.0	0.0	0.0	0.0	31.3
Cement Filt._2_SF	2	0.25	11.0	68.5	21.0	0.0	0.0	0.0	0.0	31.4
Cement Filt._4	4	0	4.3	31.0	25.9	0.0	0.0	0.0	0.0	20.7
Cement Filt._4_SF	4	0.25	5.8	31.9	23.9	0.0	0.0	0.0	0.0	21.0

3 EFFECT OF ION CONCENTRATION ON SAP ABSORBENCY

Figure 2: compares measured absorption behaviors of SAP in distilled water and the solution A. As a preliminary test, it can be observed that the absorption kinetics is not changed by the concentrations of monovalent cations. However, the absolute absorbency under distilled water is almost 7 times higher than that in solution A. This can be explained by absorption of monovalent cations in SAP [8]. The monovalent cation can exchange its proton with anionic group in SAP, causing the absorption reduction [9]. However, no reduction of absorbency was observed in both distilled water and solution A where there are no multivalent cations.

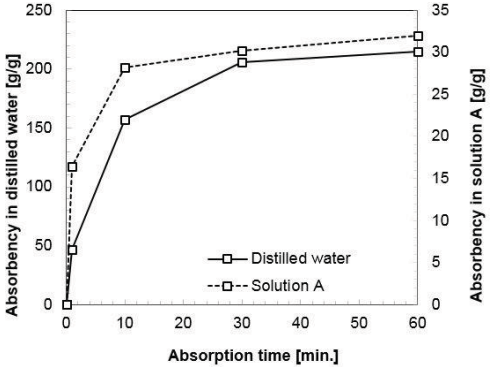

Figure 2: Solution absorbency of SAP in distilled water and solution A

The influence of W/C of cement filtrates on the absorption kinetics of SAP can be understood in Figure 3(left). As the W/C of cement filtrates increases from 1 to 4, the initial absorbency (up to 30 min) increased, whereas the long–term absorbency (30 min to 180 min) decreased. In other words, the absorption kinetics varies based on the W/C of cement filtrates. It suggests a potential underestimation of absorption capacity of SAP if cement filtrate of a high W/C is used to predict the long-term absorbency. Furthermore, as shown in the Table 1, the concentrations of the four ions (Na^+, K^+, SO_4^{2-}, and OH^-) decreased in higher W/C. This increases the osmotic pressure [10] and mitigates the charge screening effect [11]. Thus, the initial absorbency is expected to be improved. After 30 minute, the swelling

reduction was further accelerated with the increase of W/C, which caused the change of the long–term absorbency. Such changes in the swelling reduction and absorption kinetics after 30 min arisen due to the multivalent cation, Ca^{2+}, rather than monovalent cations or anions [9, 10]. More specifically, the ion exchange by Ca^{2+} leads to the increase of the cross–linker density and the shrinkage of the SAP network, as well. As a result, additional uptake of solution is blocked and the swelling reduction is accelerated; this can change the long–term absorbency and absorption kinetics[8].

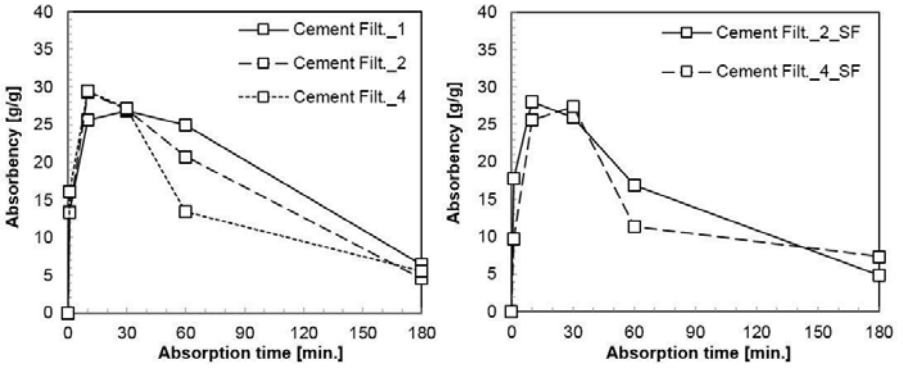

Figure 3: Effect of W/C of cement filtrates on SAP: (left) without silica fume (right) with silica fume

Figure 3(right) shows the absorption kinetics of SAP as a function of W/C in a given SF addition (SF/C = 0.25). The addition of SF was intended to better simulate the ion concentration of pore solution of concrete with low W/C ratio. For instance, silica fume is typically used to achieve the properties of UHPC. As can be seen in Table 1, the concentrations of Na^+, K^+, and SO_4^{2-} in the cement filtrate slightly increase as a result of SF addition, while the Ca^{2+} concentration decreases. The degree of this increase and decrease was minor when compared with other influential factors such as W/C. Thus, the addition of SF did not change the absorption kinetics of SAP dramatically. The absorbency of the SAP decreased slightly before the 60 min by the SF addition, since the concentration of monovalent cations increased. However, the absorbency increased and reached similar absorbency compared to them without SF addition.

The effect of the cationic charge number (1 or 2) on the absorptivity and absorption kinetics of SAP is presented in Fig. 4(left) at the given cation concentration (24.5±0.8 mM). Certainly, the maximum absorbency decreased and the absorption kinetics changed by the increase of the charge number. The initial absorption speed up to 1 min is slightly decreased because the total ion concentration (TIC) increased by 40%, and the maximum absorbency after 1 min remarkably decreased because of the increased ionic strength. In particular, the chosen SAP_AA shows a consistent swelling reduction after 10 min. This indicates that the absorption kinetics of SAP with a high density of anionic groups is sensitive to the cationic charge number, i.e., the absorption capacity of this type of SAP can be dramatically decreased by the effect of multivalent cations[10].

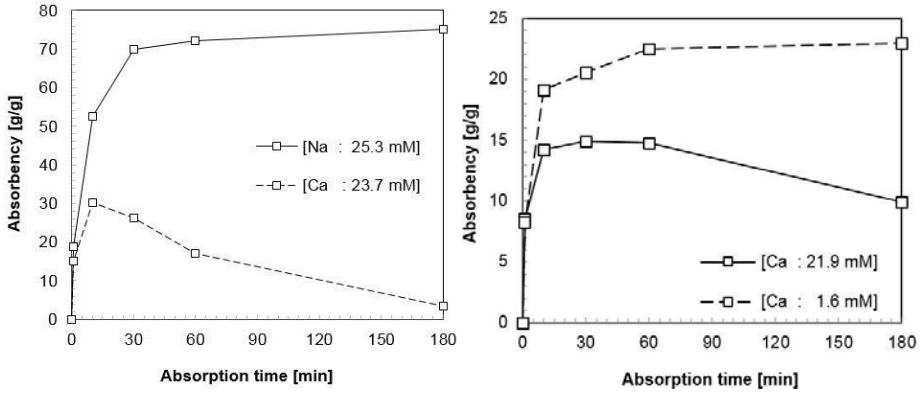

Figure 4: Effects of (left) cation charge number and (right) Ca^{2+} concentration on absorption kinetics of SAP under the given conditions of (left) cation concentration and (right) total ion concentration

At the given TIC (982.5±12.3 mM), Figure 4 (right) shows the absorption kinetics of the SAP that depends on the Ca^{2+} concentration. The Ca^{2+} concentration to TIC ratio of solid-line in the Fig. is 2.2%, which is 11 times higher than that of dot-line (0.2%). Nevertheless, the two solutions are composed of mostly (> 97.8%) of monovalent ions (Na^+, Cl^-, and NO_3^-). The initial absorbency at 1 min in the two solutions is similar because of the fixed TIC value. However, absolute 2% of the increase (from 0.2% to 2.2%) of the Ca^{2+} concentration to the TIC ratio caused the change of the absorption kinetics because of the ionic cross-linking effect. This result indicates that the change of the kinetics caused by the 20.3 mM increase of the Ca^{2+} concentration. Both this change and reduction of the absorption capacity were especially noticeable for the chosen SAP herein. After 30 min, this SAP could not absorb any additional solution, and from 60 min it released the absorbed solution by reducing the swelling. As a result, the absorbency at 180 min decreased by 57%.

4 CONCLUSIONS

- Tea-bag test was performed on various cement filtrates to understand absorption kinetics of SAP in concrete. Available monovalent cations in a solution will be absorbed by SAP, causing the significant reduction of absorption capacity of SAP compared with distilled water.
- SF addition does not change the ionic concentration or composition significantly so negligible change of absorption kinetics is observed. Ca^{2+} concentration plays a key role for absorption capacity as well as swelling reduction or retention. Tested SAP shows highly sensitivity of maximum absorbency and retention capacity to the cationic charge number. At the given TIC, although absolute portion of Ca^{2+} is smaller in the solution, it governs the volumetric behaviors of the retention and shrinkage due to the divalent cation exchange.

5 ACKNOWLEDGEMENTS

This research was supported by Singapore Ministry of Education Academic Research Fund Tier 1.

6 REFERENCES

[1] O.M. Jensen, P.F. Hansen, Water-entrained cement-based materials: II. Experimental observations, Cement and Concrete Research, 32 (2002) 973-978.

[2] L. Dudziak, V. Mechtcherine, Mitigation of volume changes of ultra-high performance concrete (UHPC) by using super absorbent polymers, Proceedings of the 2nd international symposium on ultra high performance concrete. Kassel University Press, Kassel, 2008, pp. 425-432.

[3] J. Justs, M. Wyrzykowski, D. Bajare, P. Lura, Internal curing by superabsorbent polymers in ultra-high performance concrete, Cement and Concrete Research, 76 (2015) 82-90.

[4] L.P. Esteves, On the absorption kinetics of superabsorbent polymers, International RILEM conference on use of superabsorbent polymers and other new additives in concrete, RILEM Publications SARL, Lyngby, 2010, pp. 77-84.

[5] B. Craeye, M. Geirnaert, G. De Schutter, Super absorbing polymers as an internal curing agent for mitigation of early-age cracking of high-performance concrete bridge decks, Construction and Building Materials, 25 (2011) 1-13.

[6] M.T. Hasholt, O.M. Jensen, K. Kovler, S. Zhutovsky, Can superabsorent polymers mitigate autogenous shrinkage of internally cured concrete without compromising the strength?, Construction and Building Materials, 31 (2012) 226-230.

[7] D. Addari, B. Elsener, A. Rossi, Electrochemistry and surface chemistry of stainless steels in alkaline media simulating concrete pore solutions, Electrochimica Acta, 53 (2008) 8078-8086.

[8] S.-H. Kang, S.-G. Hong, J. Moon, Absorption kinetics of superabsorbent polymers (SAP) in various cement-based solutions, Cement and Concrete Research, 97 (2017) 73-83.

[9] Q. Zhu, C.W. Barney, K.A. Erk, Effect of ionic crosslinking on the swelling and mechanical response of model superabsorbent polymer hydrogels for internally cured concrete, Materials and Structures, 48 (2015) 2261-2276.

[10] C. Schröfl, V. Mechtcherine, M. Gorges, Relation between the molecular structure and the efficiency of superabsorbent polymers (SAP) as concrete admixture to mitigate autogenous shrinkage, Cement and Concrete Research, 42 (2012) 865-873.

[11] W.M. Jignesh H. Trivedi, Young Huang and Harikrishna C. Trivedi, Photo-induced sodium salt of partially carboxymethylated psyllium-g-polyacrylonitrile: II. Synthesis, characterization and swelling behaviour of its superabsorbent hydrogel, International Journal of Scientific and Research Publications (IJSRP), 5 (2015) 14.

Parametric Study on the Influence of Cement Replacement Materials on the Rheology of Cement Paste using Brookfield Viscometer

Kalyana Rama, J. S.[(1)], Saikrishna Pallerla[(1)], Sivakumar, M. V. N.[(2)], Vasan, A.[(1)] and Ramachandra Murthy, A.[(3)]

[(1)]BITS Pilani Hyderabad Campus, BITS Pilani, India

[(2)]National Institute of Technology, Warangal

[(3)]CSIR-Structural Engineering Research Centre (CSIR-SERC)

ABSTRACT

The main focus of this study is to develop the rheological model of cement paste by the addition of various mineral additives and chemical admixtures as cementitious materials. This is important because the fresh properties that are as important as the hardened properties to yield a good performance of the concrete are governed by their rheology. The rheological properties are believed to be affected by the chemical composition. This study tries to estimate the two rheological properties. Plastic viscosity and yield stress using various models like Bingham model. Brookfield viscometer is used for the purpose of the study. Using this, shear stress-shear rate flow tests are conducted on a number of cement paste samples. Among various models available to describe the rheological properties of cement paste, the study is mainly restricted to one single model i.e. Bingham model where linear regression method is used to obtain the Bingham parameters (plastic viscosity and yield stress). The rheological properties of cement paste obtained are further used to study the flow properties of self-compacting concrete (SCC). A successful attempt is made for the first time in measuring the rheological properties of cement paste with different combinations using Brookfield Viscometer.

Keywords: Rheology, plastic viscosity, yield stress, viscometer, GGBS, fly ash.

1 INTRODUCTION

Rheology which deals with the deformation and flow behaviour of materials is important because of the scope it offers for characterising fresh cement paste, grout, mortar and concrete, and for understanding how they perform in practical applications. In describing the flow behaviour of concrete, rheological study using parameters like plastic viscosity, yield stress etc. is much better than workability which is calculated by conducting slump flow test, compaction factor test etc. In SCC, which is a complex mixture containing many constituents, workability changes with the properties of the constituents and their proportions. Here it is not always possible to determine the workability of the concrete at the test site due to high cost. Rheological study and developing models is thus important for a material like SCC to estimate its workability. Also, in the mix design of SCC, rheological parameters are to be given as an input. All the above stated reasons drive us to study the rheological behaviour of cement and thus in turn the rheology of SCC.

When high calcium fly ash was used as a SCM, with the increase in fly ash content, yield stress and plastic viscosity of the paste have seen an increase [3]. It was observed that fine fraction content was a better parameter than the specific surface area to describe the fluidity of the paste. Kurita et al. observed that use of fly ash improves rheological behaviour and reduces the possibility of cracking of concrete because less amount of heat is generated during the process of hydration. Using viscosity modifying agents or increasing the solid fraction of the cement paste, viscosity of the paste can be increased which will help to meet the requirements of SCC mix [6]. It is proved that, it is too difficult to compute shear stress at zero shear rate i.e. yield stress. Thus to overcome these problems, rheological models serves as a good statistical approximation [7]. Rheology of cement paste is affected by the properties of cement, SCMs, chemical admixtures, water content in the paste and on the reaction between cement and admixtures used [8]. Importance of proper compatibility between the cement and chemical admixtures used in the mix, which is a function of rheology of the cement paste is studied to some extent [9]. Experimental studies are conducted to observe the rheological behaviour of cement paste when rice husk ash (RHA) is used as a SCM. It was observed that with the addition of RHA, there was an improvement in the rheological and mechanical properties of concrete [10]. In the same study, mechanical and rheological properties of concrete were also studied when a percentage of natural sand (fine aggregates) were replaced by crushed fine aggregates (CGA). It was observed that the compressive strength of the concrete mix has seen a significant increase when about 50% of natural sand was replaced by CGA. Also, when the CGA content was increased, there was a reduction in segregation of the material.

The mixing samples used for the present study are 100% OPC, 80% OPC + 20% FA, 75% OPC + 25% GGBS, 50% OPC + 25% FA + 25% GGBS. Water to cementitious ratios (w/cm) used for the study are 0.35, 0.40, 0.45, 0.5 and 0.55. Glenium 8233 is used as a superplasticizer which is a light brown liquid made of a new generation based on modified polycarboxylic ether. Brookfield viscometer is used for conducting the rheological tests on all the samples. The conditions at which the tests were conducted remained same throughout the course of study.

2 RESULTS AND OBSERVATIONS

2.1 Chemical Analysis and Physical Properties

Chemical compositions of individual cementitious materials extracted from X-ray fluorescence along with their physical properties are given in Table 1 and the chemical compositions of blended cementitious materials are given in Table 2.

Table 1: Chemical composition of ordinary Portland cement, fly ash and GGBS

Chemical Composition (%)	OPC	Fly Ash	GGBS
CaO	65.2	1.7	40.6
SiO_2	18.6	60.1	35.1
Al_2O_3	5.7	28.	19.6
Fe_2O_3	4.5	5.10	0.5
SO_3	4.3	0.1	1.9
K_2O	0.6	2.1	0.4
TiO_2	0.5	1.4	0.9
Physical Properties			
Specific Gravity	3.15	2.16	2.85

Table 2: Chemical composition of blended cements

Chemical Composition (%)	80% OPC + 20% FA	75% OPC + 25% GGBS	50% OPC + 25% GGBS + 25% FA
CaO	43.8	49.7	39.4
SiO_2	30.8	28.0	34.5
Al_2O_3	14.6	13.5	16.6
Fe_2O_3	5.0	3.8	4.1
SO_3	2.5	2.1	2.1
K_2O	1.3	1.0	1.2
TiO_2	1.2	1.1	1.2

2.2 Rheological properties using Brookfield Viscometer

Brookfield rotational viscometer DV3T as shown in Figure 1 is used for the entire testing sequence. The viscometer was equipped with a vane geometry spindle of 2.53 mm height and 0.64 mm radius. The rheological properties of cement pastes are measured with varying shear rates for different intervals of time at a constant room temperature.

Figure 1. Brookfield Viscometer DV3T

Plastic viscosity of the cement pastes as shown in Table 3 to Table 6 followed a decreasing trend with the increase in w/cm ratio due to the reaction between cementitious molecules and water.

Table 3: Bingham parameters for OPC paste

W/cm	0.35	0.4	0.45	0.5	0.55
Yield Stress	1.67	5.48	0.04	11.03	9.39
Plastic Viscosity	0.39	0.22	0.18	0.12	0.09

Table 4: Bingham parameters for 75% OPC + 25% GGBS paste

W/cm	0.35	0.4	0.45	0.5	0.55
Yield Stress	5.72	2.53	5.36	8.98	10.54
Plastic Viscosity	0.28	0.27	0.26	0.24	0.19

Table 5: Bingham parameters for 80% OPC + 20% FA paste

W/cm	0.35	0.4	0.45	0.5	0.55
Yield Stress	2.85	2.15	4.59	9.06	8.80
Plastic Viscosity	0.39	0.27	0.25	0.16	0.11

Table 6: Bingham parameters for ternary 50% OPC + 25% FA + 25% GGBS paste

W/cm	0.35	0.4	0.45	0.5	0.55
Yield Stress	2.1204	4.1353	4.86	5.99	6.87
Plastic Viscosity	0.284	0.175	0.189	0.1025	0.07

The full hydration process will happen at a w/cm of 0.38 to 0.42 for a pure OPC paste which directly indicates that there will be a sudden decrease in plastic viscosity till 0.4 followed by a gradual decrease as shown in Figure 2. But in the case of paste with 25% GGBS as a replacement, due to the flaky nature of particles, paste with GGBS requires more water resulting in a gradual decrease of plastic viscosity which follows a convex trend as shown in Figure 3. For 20% fly ash as replacement, reaction of water with fly ash requires more time resulting in concave curve leading to a gradual decrease of plastic viscosity as shown in Figure 3. For ternary mix as shown in Figure 4, the total contribution of fly ash and GGBS are 25% and with the increase in water to cement ratio a decreasing trend of plastic viscosity is observed.

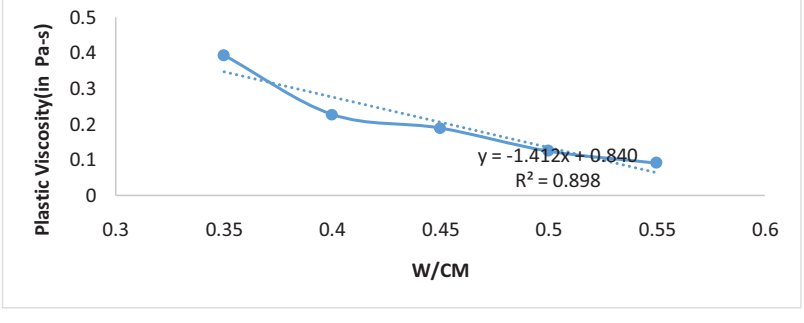

Figure 2. Plastic viscosity vs w/cm ratio for OPC

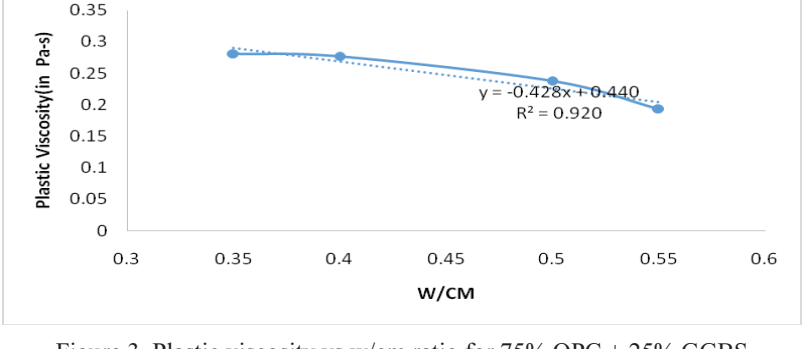

Figure 3. Plastic viscosity vs w/cm ratio for 75% OPC + 25% GGBS

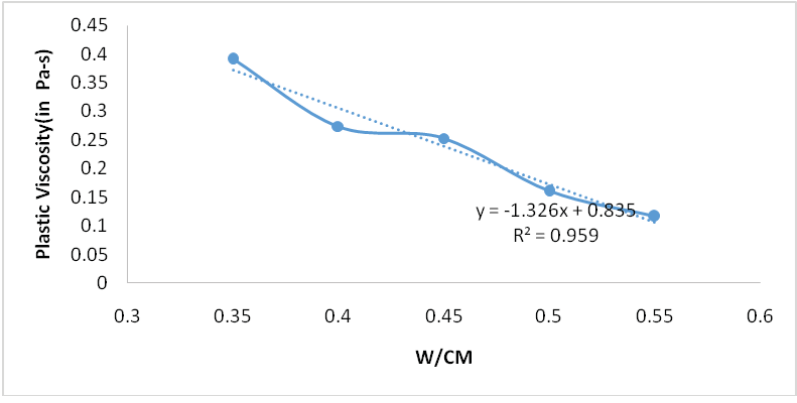

Figure 3. Plastic viscosity vs w/cm ratio for 80% OPC + 20% FA

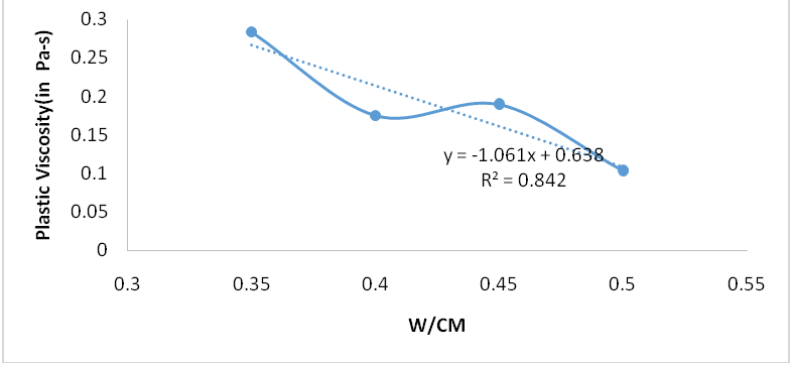

Figure 4. Plastic viscosity vs w/cm ratio for ternary/triple blend Mix (50% OPC + 25% FA + 25% GGBS)

3 CONCLUSION

The study successfully used Brookfield Viscometer for the first time to estimate the plastic viscosity of cement paste with various supplementary cementitious materials. There was a significant improvement in the rheological parameters with the addition of SCMs and was greatest in the case of ternary or triple blend and triple blended mix containing cement, fly ash and GGBS. Flow curves suggest us clearly that the plastic viscosity of the paste decreases with the increase in w/cm ratio. Further, Bingham model was able to approximately describe the behaviour of cementitious pastes containing SCMs when subjected to varying shear rates.

REFERENCES

[1] Barnes, H.A., Hutton, J.F. and Walters, K., 1989. *An introduction to rheology* (**Vol. 3**). Elsevier.

[2] Tattersall G.H. (1991), "Workability and Quality Control of Concrete", E&FN Spon, London

[3] Grzeszczyk, S. and Lipowski, G., 1997. Effect of content and particle size distribution of high-calcium fly ash on the rheological properties of cement pastes. *Cement and concrete research*, 27(6), pp.907-916.

[4] Yahia A., Tanimura M., Shimabukura A., Shimoyama Y. (1999), "Effect of Rheological Parameters on Self-Compatibility of Concrete Containing Various Mineral Admixture", Proceeding of the first Rilem International Symposium on Self-Compacting Concrete, Stockholm, September, 523-535

[5] Kurita M., Nomura T. (1999), "Highly Flowable Steel Fiber-Reinforced Concrete Containing Fly Ash", Special Publication 178, June, 159-176

[6] Billberg P. (1999a), "Fine Mortar Rheology in Mix Design of SCC", Proceedings of First International RILEM Symposium on Self-Compacting Concrete, Stockholm, 1999, 47-58

[7] Nehdi, M. and Rahman, M.A., 2004. Estimating rheological properties of cement pastes using various rheological models for different test geometry, gap and surface friction. *Cement and concrete research*, 34(11), pp.1993-2007.

[8] SHEINN, A.M.M., 2007. *Rheological modelling of self-compacting concrete* (Doctoral dissertation, NATIONAL UNIVERSITY OF SINGAPORE).

[9] Mukhopadhyay, A.K. and Jang, S., 2009. *Using cement paste rheology to predict concrete mix design problems: Technical Report* (No. FHWA/TX-09/0-5820-1). Texas Transportation Institute, Texas A & M University System.

[10] Cordeiro, G.C., de Alvarenga, L.M.S.C. and Rocha, C.A.A., 2016. Rheological and mechanical properties of concrete containing crushed granite fine aggregate. *Construction and Building Materials*, 111, pp.766-773

Factors Influencing the Interactions between PCE Superplasticizers and Portland Cement

Pascal Boustingorry [(1)], Caroline Autier [(1)] and Nathalie Azema [(2)]

[(1)]CHRYSO, 7 rue de l'Europe, 45300 Sermaises, France

[(2)]Centre C2MA, Ecole des Mines d'Alès, 6 Avenue de Clavières, 30319 Alès Cedex, France

ABSTRACT

The so-called incompatibility between a PCE superplasticizer and a given cement often leads to technical problems such as rise in required dosage, thus in cost, workability increase through time, decrease in early strength, etc. This paper aims at illustrating two different root causes for incompatibility, one linked to a polymer structure which is unfit for a sufficient dispersing effect, the other to a cement-related parameter which changes the pore solution composition. In the first part, the influence of polymer structure, and precisely grafting ratio at constant graft length, is shown to induce a non-monotonous influence on the sedimentation regimes and dispersion states of cement suspensions. This behaviour may be explained by observing how adsorption is affected by polymer structure. In a second part, following the seminal work by Yamada et al. [1], it is shown that the sulphate ions released by cement into the pore solution interfere with PCE adsorption, leading to a decreased state of dispersion at equal dosage. This phenomenon is correlated to a very precise cement property.

Keywords: PCE, superplasticizer, polymer structure, compatibility, sulphate.

1 INTRODUCTION

PCE superplasticizers have brought new possibilities in terms of water reducing ability, workability retention while retaining early strength, and their remarkably versatile chemistry allows addressing a broad range of concrete properties.

However, these advantages come with an apparent greater sensitivity to the mineral composition of cement, aggregate quality, water-to-cement ratio, etc., and the very broad range of available products sometimes makes it difficult to choose or design the right superplasticizer for a given case.

The objective of this paper is to shed some light on the interactions between superplasticizers and cements, first through a selection of polymers differing by their structure, and secondly by focusing on the pore solution properties of different cements.

2 MATERIALS AND METHODS

2.1 Materials

Four PCEs provided by the CHRYSO company (France) were studied and called A, B, C and D later in this paper. They are composed of a poly (methacrylic acid) backbone, responsible for adsorption, partially esterified with methoxy-terminated poly-oxyethylene side-chains (PEO) responsible for steric repulsion. The chemical structure is shown in Fig. 1. The ester grafting ratio (m/n + m) increases from 10 to 40 % through polymers A to D with a fixed PEO length (p) of 45 monomers. This series of polymers was chosen in order to study

the influence of grafting ratio on the efficiency of PCE while keeping graft length constant. The details of the polymer structures are given in Table 1.

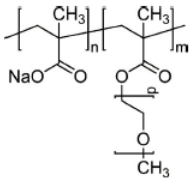

Figure 1: General scheme of a PCE structure

Table 1 : PCE structure parameters

PCE marking	Average grafting ratio m/(m+n)	Average graft length P
A	0.1	45
B	0.2	45
C	0.3	45
D	0.4	45

2.2 Cement suspension preparation

Cement suspensions were prepared by adding 200 g of cement powder to admixture solutions in deionized water (liquid chosen to control the water quality: pH, ionic conductivity, etc.) with a water to cement ratio of 0.5 (including the amount of water provided by the admixture). Each polycarboxylate was tested through a dosage range up to 1% of dry active matter with respect to cement weight.

The mixing equipment consisted in a twisted mixing anchor blade adapted to a Stuart SS 30 mixer and a stainless steel beaker. The suspension was mixed at a speed of 185 rpm during 20 minutes before analysis, which must be done during the 2 h of the dormant period (checked by conductivity and calcium concentration measurements).

For suspension stability and total organic carbon (TOC) measurements, paste samples were first diluted in deionized water. This perturbation may modify the ionic strength and solid-solution equilibrium of studied system, but it was neglected in a first approximation. The dilution was the same (30% by weight of suspension diluted in 70% deionized water) for suspension stability and TOC analyses, which allows a fair comparison between measurements.

2.3 Characterization of the cement pastes by TOC analysis

The PCE adsorption amounts were measured according to the depletion method. For that purpose, suspensions were diluted and let to settle in the same conditions as for the settling measurement. Then, the liquid phase at the top of the column was extracted and the pore solution was separated from the particles by filtration with a 0.2 µm membrane filter and neutralized with concentrated hydrochloric acid. The quantity of remaining PCE was determined by total organic carbon (TOC) analysis using a commercial TOC-VCPN analyser (Shimadzu, Japan). Solutions of PCE with the same dosages as in the pastes were analysed and used as an initial concentration measurement. The quantity of consumed polymer was estimated by difference between the quantity of PCE introduced in the paste and the measured quantity of PCE remaining in pore solution.

In order to take the amount of organic carbon released by the cement (coming from grinding aids) into account, the TOC value of the unadmixtured paste was considered as a background and subtracted from all measurements.

2.4 Multiple light scattering analysis

A Turbiscan MA 2000 analyser (Formulaction, France) was used to quantify the settling kinetics of the different suspensions. The device is designed to detect nascent instability phenomena in concentrated dispersions (e.g. suspensions and emulsions) faster and more accurately than the naked eye.

This technique is based on the detection of the transmitted and backscattered light intensity as a function of the height in the suspension column. The device is composed of a light sensor (wavelength of 850 nm) which moves vertically with a step of 40 µm along a cylindrical cell (15 mm diameter and 110 mm height) containing the sample. Two measurements at 0° and 135° from the incident beam direction are performed and correspond respectively to the intensity of transmitted and backscattered light.

Both signals allow a distinction between the formation of a sediment and the presence of a sparsely concentrated hazy supernatant, since the technique is both sensitive to the size and the concentration of the particles [2–4].

2.5 Sulphate concentration in solution

Precisely weighed samples of pore solutions were diluted in enough (ca. 40 ml) Ultrapure water (Millipore) for a conductivity electrode to be dipped in a glass beaker. The sample was then titrated by a barium nitrate 0.05 mol/L solution using an automated 888 Titrino device with an 856 conductivity adapter (Metrohm, Switzerland). Sulphates are precipitated under the form of the scarcely soluble barium sulphate, yielding a decrease in solution conductivity up to the equivalent point, beyond which conductivity increases again due to excess barium nitrate ions.

The minimum of the conductivity curve plotted against added moles of barium yields the equivalent point in moles of sulphate, eventually expressed in millimoles per litre of pore solution.

2.6 Soluble alkali concentration

Precisely weighed samples of pore solutions were diluted in Ultrapure water (Millipore) fed into a PFP7 Flame Photometer equipped with monochromatic filters for sodium and potassium. The device is first calibrated with reference solutions of known concentrations prior to measurement.

3 THE INFLUENCE OF THE GRAFTING RATIO ON THE INTERACTION WITH CEMENT

3.1 Introduction

The polymer structure parameters have been shown to have a tremendous influence on the dispersing performance of PCE molecules, both initially and through the so-called workability window [5–7]. The influence of the grafting ratio will be illustrated here through a very simple test consisting in observing the settling regimes of cement suspensions prepared with increasing PCE dosages.

3.2 Suspension settling regimes through visual inspection and multiple light scattering measurements

After preparation according to the protocol described in paragraph 2.2, the suspensions were poured into glass tubes and visually inspected after 20 minutes of rest. As Figure 2 shows, suspensions feature discriminated aspects depending upon PCE dosage. More specifically the reference tube shows a large clear supernatant, while an increase in PCE dosage yields a decreasing clear supernatant with a hazy lower phase until for an intermediate dosage, the suspension appears almost homogeneous (around 0.1% dry polymer by weight of cement on Figure 2). Beyond this regime, supernatant haziness is almost constant, but a dense sediment appears.

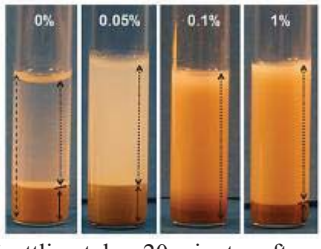

Figure 2: Visual inspection of settling tubes 20 minutes after mixing with increasing dosages of PCE superplasticizer. Dosages are expressed in dry polymer by weight of cement

As mentioned in paragraph 2.4, multiple light scattering is more accurate for determining the different settling regimes. More precisely, a clear supernatant is characterized by a high transmitted signal, while a hazy supernatant and a dense sediment may be distinguished by a strong difference in backscattered intensity. Raw curve examples may be found in Autier et al. [3].

A simple way of quantifying settling is to merely plot the relative thicknesses of clear supernatant on the one hand, and dense sediment on the other hand, as a function of polymer dosage. Data are represented according to this approach on Figure 3.

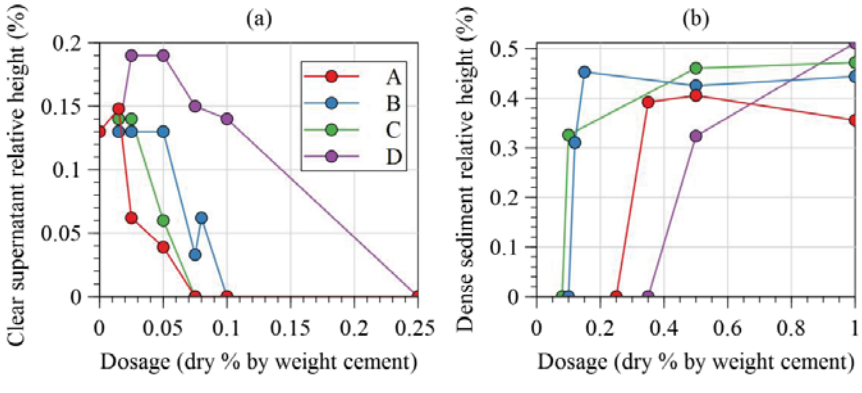

Figure 3: Settling regimes as afuntion of polymer dosage. (a) relative clear supernatant thickness, (b) relative dense sediment thickness

No clear monotonous trend may be observed on the data. As a matter of fact, the critical dosage beyond which a clear supernatant disappears (Figure 3a) does not follow the grafting ratio at all. The critical dosage beyond which a dense sediment appears (Figure 3b) seems to

reach a minimum for the intermediate grafting ratios of polymers B and C. There clearly exists different optimum dosage ranges, leading to a whole stable suspension, that depend on the polymer structure: this optimum is reached for example between 0.25% and 0.35% for polymer D, and rather between 0.075% and 0.1% for polymer C. One may then infer that polymer C presents a more efficient dispersing ability without falling into sedimentation.

As far as the grafting ratio is concerned, the more is not necessarily the better. The root causes of this fact may be further investigated by observing the different adsorbing behaviours.

3.3 Adsorbed amounts and settling regimes

The same data as in Figure 3 were plotted against the measured adsorbed amounts, yielding the plots on Figure 4.

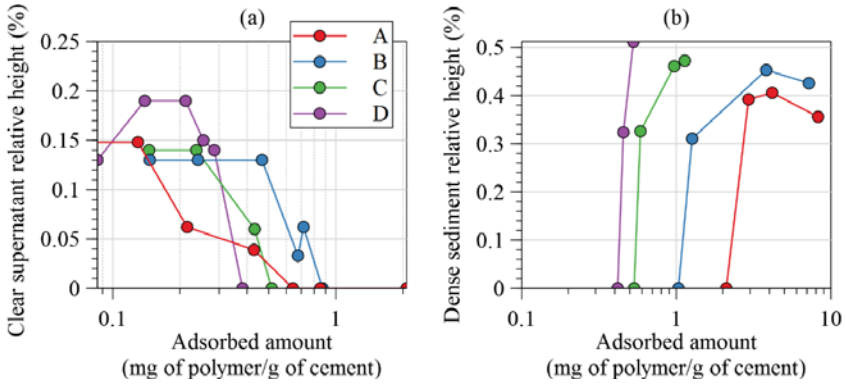

Figure 4: Settling regimes as a function of polymer adsorbed amounts. (a) relative clear supernatant thickness, (b) relative dense sediment thickness

Here, monotonous trends are retrieved: the higher the grafting ratio, the lower the critical dosages for both clear supernatant disappearance and dense sediment appearance. This means that at equal adsorbed amount, the polymer with the highest grafting ratio (D) is the most efficient dispersant, while the polymer with the lowest grafting ratio (A) is the least efficient.

This is reminiscent of previous work by Sakai et al.[5] or more recently by Zingg et al.[8] or Flatt et al. [9], showing that polymer structure may influence the adsorbed layer thickness, hence the range of steric repulsion forces. Here, the authors propose that an increase of the grafting ratio induces an increase in the adsorbed layer thickness, but a decrease in the adsorbed amount.

As a result, polymer A is adsorbed in very high amounts, but forms a very flat and weakly dispersing layer, while polymer D is able to form quite thick layers at the surface, yet requires very high dosages in order to reach a sufficient adsorbed amount. Polymers B and C lie in the optimal range which leads, at medium dosages, to an appreciable adsorption of thick enough layers, explaining the non-monotonous trend observed in paragraph 3.2.

3.4 Conclusion

This very simple test, only involving the observation of suspension settling in tubes, seems to be efficient for estimating an optimum dosage range of a superplasticizer for the dispersion of a given cement. It relies upon sound principles of physical chemistry, and may prove to be a valuable tool for quickly ranking admixtures according to their dispersion ability.

4 THE INFLUENCE OF SOLUBLE SULPHATES ON PCE EFFICIENCY

4.1 Introduction

The sensitivity of superplasticizers towards cements has been observed throughout the past decades, whatever the technology involved [1,10–14]. Among the abundant literature, a landmark study is the paper by Yamada and Hanehara [1] where a demonstration is given of the influence of pore solution sulphate ions on the adsorption of superplasticizers. A spectacular experiment is presented, which consists in alternatively increasing and decreasing sulphate concentration by adding respectively sodium sulphate and calcium chloride, resulting respectively in decreasing and increasing polymer adsorption. A competitive adsorption mechanism between sulphate ions and polymers is proposed to explain the phenomenon.

This part of the paper proposes to illustrate this point through some examples, and to propose a simple rule to assess the potential compatibility between a cement and a PCE molecule.

4.2 Sensitivity of adsorption to sulphate concentration

Adsorption isotherms of any polymer onto cement may be constructed by plotting the adsorbed amount as a function of the remaining polymer concentration in the pore solution. A series of experiments was performed with a single cement but with additions of potassium sulphate (Sigma Aldrich, Germany), to artificially increase sulphate concentration in the pore solution.

The results obtained with PCE C five minutes after mixing are plotted in Figure 5.

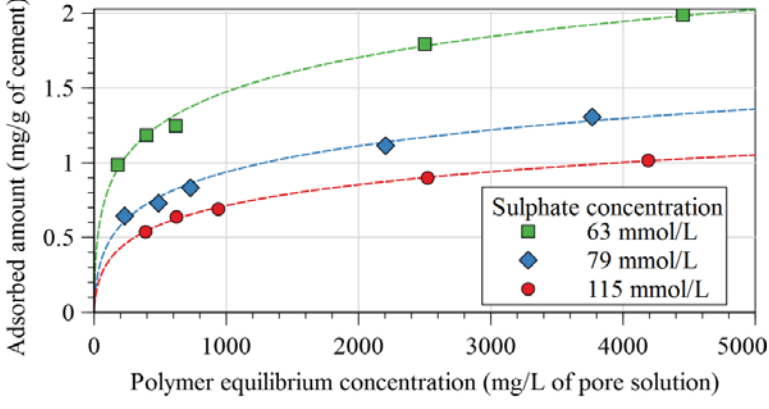

Figure 5: Adsorption isotherms of PCE C as a function of sulphate concentration in solution. Dashed lines are guides to the eye.

The data show clearly that adsorption equilibria are shifted towards lower adsorbed amounts when sulphate ion concentration increases in the aqueous phase. Adsorption at five minutes governs workability at the same concrete age, it may then be inferred that sulphate concentration will have a huge influence on the PCE dosage required to reach a target workability.

The authors experience shows that for extremely high values of sulphate concentration, the required dosage increase may be far too high for a reasonable performance. Previous work shows that the sensitivity to sulphate concentration is decreased if a PCE with a higher degree of carboxylic acid, thus a lower grafting ratio, is chosen [5]. Once again this is confirmed by the authors experience as well as the data presented in the first part of the

paper, where low-grafting ratio polymers were shown to be stronger adsorbers, hence better sulphate competitors.

4.3 Relationship between sulphate concentration and cement characteristics

There remains to establish a link between sulphate concentration in water and some cement characteristics, to have an easy reading of the potential incompatibility between a PCE admixture and a given cement.

Figure 6 shows the concentrations in sulphate ion measured in pore solutions five minutes after mixing, obtained from three different OPCs coming from French factories, at three different water-to-OPC ratios. It is also shown that, provided data are plotted against the OPC-to-water ratio, they fall on a straight line whose slope and intercept only depend upon the cement origin.

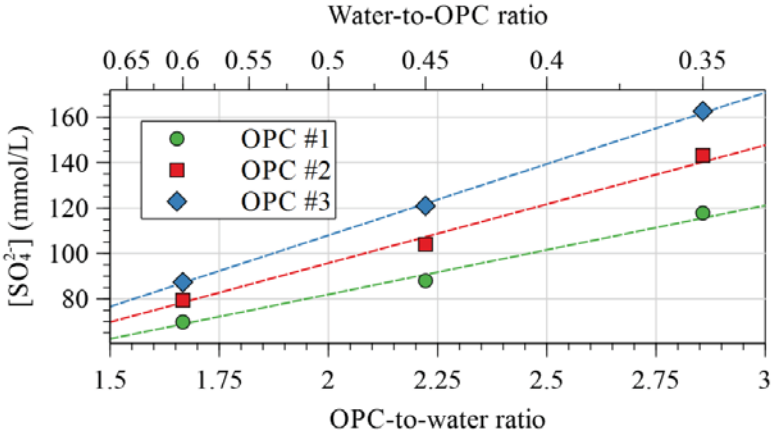

Figure 6: Relationship between the actual sulphate concentration in pore water and the cement-to-water ratio for three cements. The upper horizontal axis shows units in terms of the more usual Water-to-Cement ratio.

This clearly demonstrates that sulphate concentration in the batching water follows a cement dilution rule, which states that the higher the water-to-cement ratio, the lower the sulphate concentration, the less the potential influence on PCE adsorption, and the other way around.

The influence of cement nature was investigated further on. In a Portland cement, sources of sulphate may be the calcium sulphate (gypsum, anhydrite) addition to clinker. However, gypsum or anhydrite solubility only accounts for a few mmol/L of sulphate in water at 25°C (see e.g. [15] mentioning a solubility product of $10^{-4.58}$). There is indeed another source of highly soluble sulphates in cement, namely alkali (sodium, potassium) sulphates.

To verify this assumption, the concentration of sodium and potassium in pore solution was measured by flame photometry, and the results were expressed as the relative weight of equivalent sodium oxide by weight of cement (see Table 2).

Table 2: Equivalent soluble Na_2O values of the three considered OPCs

Cement	$Na_2O_{eq,sol}$, by weight of cement
OPC #1	0.39%
OPC #2	0.44%
OPC #3	0.51%

The values above were multiplied by the cement-to-water ratio of the different suspensions, yielding a number which roughly estimates the concentration in alkali ions released into the pore solution by the cements.

Sulphate concentrations were then plotted against the parameter defined above, to obtain Figure 7.

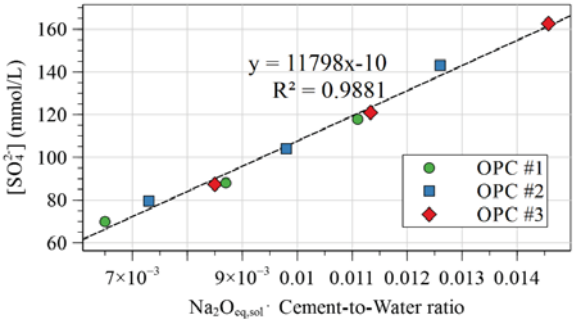

Figure 7: Relationship between the actual sulphate concentration in pore water and the product $Na_2O_{eq,\,sol}$ x (OPC-to-water ratio) for the same three cements

All data fall on a straight line with a very good correlation coefficient, which shows that the sulphate concentration in water is primarily driven by the alkali amount of the three studied cements and the water-to-cement ratio. The alkali amount is most often displayed on a cement datasheet, or if not, the total active alkali is provided. The authors experience shows that the latter is well correlated to the former.

4.4 Conclusion

The authors infer that the simple knowledge of the soluble alkali amount of a cement and of the water-to-cement ratio of the application may allow estimating the sulphate concentration in the water of the corresponding concrete. Henceforth, the choice of the most suitable PCE may be more straightforward, by choosing strong adsorbers for the high sulphate cases, and weak adsorbers for the low sulphate cases.

5 GENERAL CONCLUSIONS

This paper essentially shows that not any PCE superplasticizer may be used on any cement. The compatibility between both is the result of a subtle balance between polymer structure and the solution chemistry provided by the cement mineral composition.

Whenever a PCE must be chosen for an unknown cement, and especially in cases when the cement supply for trials is scarce, a simplified workflow may be designed:

- Check the alkali amount of cement and multiply it by the cement-to-water ratio of the application to assess the sulphate conditions through the linear law provided in Figure 7.

- If the above number is too high, discard all 'low water reducers' i.e. superplasticizers which usually have high dosages
- Carry out a series of settling experiments per the first part of this paper and pick the admixtures which yield a homogeneous suspension for the lowest dosages.

6 REFERENCES

[1] K. Yamada, S. Hanehara, Interaction mechanism of cement and superplasticizers- The roles of polymer adsorption and ionic conditions of aqueous phase., Concr. Sci. Eng. 3 (2001) 135–145.

[2] C. Autier, N. Azema, J.-M. Taulemesse, L. Clerc, Mesostructure evolution of cement pastes with addition of superplasticizers highlighted by dispersion indices, Powder Technol. 249 (2013) 282–289. doi:10.1016/j.powtec.2013.08.036.

[3] C. Autier, N. Azéma, P. Boustingorry, Using settling behaviour to study mesostructural organization of cement pastes and superplasticizer efficiency, Colloids Surf. Physicochem. Eng. Asp. 450 (2014) 36–45.

[4] Y. Peng, R.A. Lauten, K. Reknes, S. Jacobsen, Bleeding and sedimentation of cement paste measured by hydrostatic pressure and Turbiscan, Cem. Concr. Compos. 76 (2017) 25–38. doi:10.1016/j.cemconcomp.2016.11.013.

[5] E. Sakai, K. Yamada, A. Ohta, Molecular structure and dispersion-adsorption mechanisms of comb-type superplasticizers used in Japan, J. Adv. Concr. Technol. 1 (2003) 16–25.

[6] F. Winnefeld, S. Becker, J. Pakusch, T. Götz, Polymer structure/concrete property relation of HRWRA, in: Montréal, CA, 2006.

[7] F. Winnefeld, S. Becker, J. Pakusch, T. Götz, Effects of the molecular architecture of comb-shaped superplasticizers on their performance in cementitious systems, Cem. Concr. Compos. 29 (2007) 251–262.

[8] A. Zingg, F. Winnefeld, L. Holzer, J. Pakusch, S. Becker, L. Gauckler, Adsorption of polyelectrolytes and its influence on the rheology, zeta potential, and microstructure of various cement and hydrate phases, J. Colloid Interface Sci. 323 (2008) 301–312. doi:10.1016/j.jcis.2008.04.052.

[9] R.J. Flatt, I. Schober, E. Raphael, C. Plassard, E. Lesniewska, Conformation of Adsorbed Comb Copolymer Dispersants, Langmuir. 25 (2009) 845–855. doi:10.1021/la801410e.

[10] K. Yamada, T. Takahashi, S. Hanehara, M. Matsuhisa, Effects of the chemical structure on the properties of polycarboxylate-type superplasticizer, Cem. Concr. Res. 30 (2000) 197–207.

[11] S. Hanehara, K. Yamada, Rheology and early age properties of cement systems, Cem. Concr. Res. 38 (2008) 175–195. doi:10.1016/j.cemconres.2007.09.006.

[12] C. Bedard, N.P. Mailvaganam, The Use of Chemical Admixtures in Concrete. Part I: Admixture-Cement Compatibility, J. Perform. Constr. Facil. 19 (2005) 263–266.

[13] M.H. Li, J.M. Zhao, H. Jin, G.Q. Li, Y.S. Wang, Review: The Effect Factors of Compatibility of Cement and Superplasticizer, Adv. Mater. Res. 450 (2012) 193–196.

[14] L.N. Tang, Study on the Compatibility between Naphthalene-Based Superplasticizer and Low Alkali Cement, Adv. Mater. Res. 639 (2013) 309–312.

[15] D. Rothstein, J.J. Thomas, B.J. Christensen, H.M. Jennings, Solubility behavior of Ca-, S-, Al-, and Si-bearing solid phases in Portland cement pore solutions as a function of hydration time, Cem. Concr. Res. 32 (2002) 1663–1671.

Evaluation of Delayed Addition of Superplasticizer in Standard Concrete

Mohit R, Sourabh T, Mohit K, Devender K, and Pardeep K

Department of Civil Engineering, National Institute of Technology Hamirpur, India

ABSTRACT

Superplasticizer (SP) has become the most important as well as a mandatory ingredient in modern concrete. It is known for increasing the workability with lower water content. Although the operational methods and techniques, including the mechanisms of superplasticizer's potential and performance in concrete are well known, issues regarding cement-superplasticizer incompatibility are recurrently seen in field applications. In this study, laboratory findings on cement concrete were reported which includes the effect of delayed addition of superplasticizer in concrete from the time of adding water into the mix. Outcomes of previous researches which studied the effect of SP on fresh concrete, for example, slump loss, have been reviewed prior to this study. Comparison of effect of delayed addition of two superplasticizers with a different chemical composition based on modified lignosulphonate polymers (MLP) and sulphonated naphthalene polymers (SNP) has been carried out. A design mix of M30 grade was evaluated for the change in the physical properties: (a) compressive strength and (b) split-tensile strength, on delayed addition of these superplasticizers. The effect of delay in addition of superplasticizers was manifested which was observed in terms of variation in the physical properties of concrete.

Keywords: Superplasticizer, cement-superplasticizer interactions, compressive strength, split-tensile strength.

1 INTRODUCTION

Almost every concrete made nowadays has admixtures in it. Making desirable concrete for a specified application is common with the presence of various chemical and mineral admixtures. Specifically, chemical admixtures as water reducers are universally used to improve the characteristics of concrete. Apart from the presence of various chemical admixtures, different types of cement are also available in the market nowadays. With this effusive variety of cement, as well as variants of water-reducers, there are issues that arise related to the compatibility between these two ingredients of concrete. Most users perform trial-and-error method to these chemicals, often resulting in a hapless negative experience and/or low cost-effectiveness, which make a bias against admixtures in general.

Admixture incompatibility of cement (OPC) is due to a high specific surface area which in turn is related to a large intrinsic porosity of cement clinker and to the presence of significant amounts of highly reactive C_3A. This rapid reaction, enhanced by the huge specific surface area, induces the early production of abundant ettringite, which provides additional surface for the adsorption of polycarboxylic ether (PCE) superplasticizer macromolecules [1]. Superplasticizers based on lignosulphonates (LS), sulphonated melamine formaldehyde (SMF), and sulphonated naphthalene formaldehyde (SNF) work by decreasing zeta potential. However, polycarboxylic ether (PCE), acrylic esters, and cross-linked acrylic polymers, disperse the cement grains by steric hindrance [2]. This hindrance produces electrostatic repulsion which depends on the amount of SP adsorbed (for better repulsion greater should be adsorption) [3]. Superplasticizer hinders the reaction of silicate and aluminate. The distinctive progression of the aluminate reaction remains unaffected by the addition of the superplasticizer, although all reactions are ominously retarded. It is generally assumed that there is a preferred adsorption of anionic superplasticizers on those cement surfaces displaying opposite charge (C_3A, ettringite). This is an evident prerequisite for the mode of action of superplasticizers [4]. However, it is reported that the degree of hindrance varies with the type and dosage of the admixtures. The modified lignosulphonates (MLS) based SP has much stronger retarding effect as compared to the polycarboxylic ether (PCE) and poly naphthalene superplasticizers (PNS). The initial setting times of the cement pastes with the PCE and PNS superplasticizers determined by the penetration depth method were reported much shorter than those with the MLS superplasticizers. Although the cement pastes with MLS admixture had longer workable time, the longer setting time has to be taken into attention in practice whenever early strength growth is indispensable [5]. Ettringite undergo crystallization under large dosages of SP and forms substantial clusters. The amount of admixture adsorbed reduces when cement hydrates meaning that adsorption is greater on unhydrated compounds compared to the hydrated ones [6]. Superplasticizers are soluble macromolecules, which are hundreds of times bigger than a H_2O molecule and with the addition of SP beyond 2%, compressive strength decreases with the increase of dosages of SP. It has also been recorded that with overdoses, lignosulphonates used mixtures fresh unit weight values are decreased marginally, while naphthalene sulphonate used mixtures fresh unit weight values were decreased significantly. It was established that this condition was a consequent from air entrainment in the specimens. [7,8]. The effect of SP on porosity and pore size distribution among different curing systems suggested that the superplasticizer in cement paste leads in lowering the total pore volume.

Due to the presence of SP the size of pore is unaffected but the threshold diameter is decreased. Different curing systems has a significant influence on porosity and pore structure of cement paste in which SP is added [9]. In the study of the effect of addition period of an SNF based SP on the adsorption manners of Portland cement and on the concrete workability, it was recorded that the amount of SNF adsorption decreases with the increase in the time. This endorses that the optimum addition time of SNF in concrete should be 10-15 minutes [10]. In terms of fineness of cement, the interaction on SP-cement interface appears to be chiefly reliant on the chemical composition of cement. It has been seen that influence of fineness of cement is more noticeable when the cement is incompatible with the superplasticizer [11]. Hence, it can be concluded that appropriate and suitable assortment of superplasticizer is essential, the selected admixture should be compatible with the cement to

be used. The dosage suggested by the manufacturer may or may not hold suitable with the materials and their proportions to be used in a specific work. Thus, confirmation checks with the given material are mandatory. Hence, the suitability of a superplasticizer with a particular cement must be established before embarking on the use in large scale concrete works [12]. The effect of SPs on the early age of concrete when studied using ordinary portland cement (OPC) and portland pozzolana cement (PPC) exhibits a complex nature of interactions between cement and superplasticizers in concrete [13]. The compatibility between the superplasticizer and Portland slag cements as a suitable combination for use in concrete, especially when high workability, slump retention and early age strength are required must be investigated [14].

2 EXPERIMENTAL INVESTIGATION

2.1 Material used and mix Proportions

The OPC, Grade 43, confirming to IS 8112: 2013 [15] was used in this study. The specific gravities of cement, fine aggregate and coarse aggregate are given in Table 1. The fineness moduli of fine and coarse aggregates were 2.76 and 6.98 respectively. River sand was used as fine aggregate which was well graded, clean and uncrushed while the coarse aggregate was angular crushed stone with 20 mm nominal maximum size. 20 mm and 10 mm aggregates were mixed in 60 % and 40 % ratio to get the required grading. The cement had a normal consistency of 33 %. The initial and final setting times of the cement were 35 and 480 min respectively. Potable water was used for mixing and curing of concrete.

Table 1: Specific gravities of materials used in the study

Material	Specific Gravity
Cement (OPC Grade - 43)	3.15
Coarse Aggregates (20 mm and 10 mm)	2.65, 2.66
Sand (Zone II) conforming to IS 383 (1970)	2.61

Two plasticizers, first SNP based and second, MLS based, termed SP1 and SP2 herafter, were used in the study. The SNP based superplasticizer**,** Conplast SP430 G8 (SP1) has been specially formulated to give high water reductions up to 25% without loss of workability. The properties of SP1 used are given in Table 2. The MLS based superplasticizer, Plastiment 2001 NS (SP2) is based on Modified Lignosulphonate polymer. Its properties are described as in Table 3.

All the tests were performed as per the Indian standard specifications contained in various codes of practice [16-19]. In order to study the effect of the delayed addition of the two different superplasticizers SP1 and SP2, only one mix (M30) was designed with the design stipulations given in Table 4. The design mix was carried out as per the recommendations of IS 10262: 2009 [20].

Table 2: Properties of SNP-based SP as supplied by the manufacturer.

Specific gravity	1.24 to 1.26	**Flash Point**	None.
Chloride content	Nil to IS:456	**Auto flammability**	Not applicable
Air entrainment	Approx. 1%	**Explosive Properties**	Not applicable
Physical State	Liquid	**Vapour Pressure**	2.3 (water)
Colour	Brown	**Water Solubility**	Soluble
Specific Gravity	1.250 – 1.270		

Table 3: Properties of MLS based SP

Appearance/ Colour	Dark brown liquid
Chemical base	Modified lignosulphonate
Relative density	1.12 kg/l at 25°C
Storage conditions/ Shelf –life	12 months from date of production if stored properly in undamaged unopened, originally sealed packaging, in dry conditions at temperatures between +10°C and +40°C

Table 4: Parameters for mix design

Grade designation	M30
Type of cement	OPC-43 grade
Maximum nominal size of coarse aggregates	20 mm
Minimum cement content	As per IS 456: 2000
Maximum water-cement ratio	As per IS 456: 2000
Workability	Up to 75 mm slump loss
Exposure condition	As per Table 4 and 5 of IS: 456
Maximum temperature of concrete at the time of placing	Room temperature
Type of aggregate	Crushed natural aggregate
Type of admixture	SP1 and SP2
Fine aggregate	Zone-II
Minimum cement	450 kg/m3
Maximum water-cement ratio	0.45

Based on above stipulations, after the trials a mix proportions yielding strength of mix above the target strength and passing the acceptance criteria as per IS 456: 2000 were fixed to be water: cement: F.A.: C.A. = 0.4: 1: 1.65: 2.92 with 1.2 % of SP dosage.

2.2 Preparation, casting and testing of specimens

The standard cube specimens and standard cylinders were cast in the laboratory by hand mixing. The standard size of 150 mm × 150 mm × 150 mm for cubes and 150 mm × 300 mm for cylinders was adopted for testing compressive strength and split tensile strength respectively. The moulded samples were kept in the curing pond. In this study out of total 70 specimens cast, 54 cubes and 16 cylinders were investigated. The specimen was tested at the age of 3 days, 7 days and 28 days. All the tests were performed as per the Indian standard specifications contained in various codes of practice [16-19]. The superplasticiser was added

after the addition of water with a delay of 5 min, 20 min and 40 min. Primarily, focus of study was to investigate the hardened properties of concrete. The effect of delayed addition on the fresh properties is not reported here.

a) Casting of Cubes

b) Curing of Cubes

Figure 1: Preparation of sample

3 TEST FOR HARDENED CONCRETE PROPERTIES

3.1 Compressive strength test

The concrete cube specimens were used for testing the compressive strength. A total of 27 cubes were cast for each mix to achieve strength at 3rd, 7th and 28th day. The tests were conducted on 300 ton compression testing machine (CTM) after drying at room temperature as per IS 516: 1959. The value of compressive strength at a particular age was considered as the average strength of 3 cubes. All the specimens were tested at a constant loading rate of 5.2 kN/s. The load was applied smoothly and uniformly without impacts and jerks. The strength of each specimen was recorded.

3.2 Split tensile strength test

The cylindrical specimens of size 150 mm × 300 mm cast for measuring split tensile strength were tested at the age of 7 days and 28 days using standard procedure after drying at room temperature as per IS 516: 1959. The compressive line load along the opposite faces of a concrete cylinder which is placed in between the two compressive plates is applied. The magnitude of tensile stress is obtained from the formula as per IS 5816: 1970.

$$T = 2P/\pi LD \quad (1)$$

Where T- Split Tensile Strength (N/mm^2)

P- Failure Load (N)

L- Length of the cylinder (mm)

D- Diameter of the cylinder (mm)

4 RESULTS AND DISCUSSIONS

4.1 Compressive strength of concrete with SP1 and SP2

The delayed addition of SP1 reduced the compressive strength at all ages i.e. 3, 7 and 28 days for all the specimens, decreased as the time of addition of superplasticizer was increasing. The results are shown in Figures 2 and 3 for SP1 and SP2.

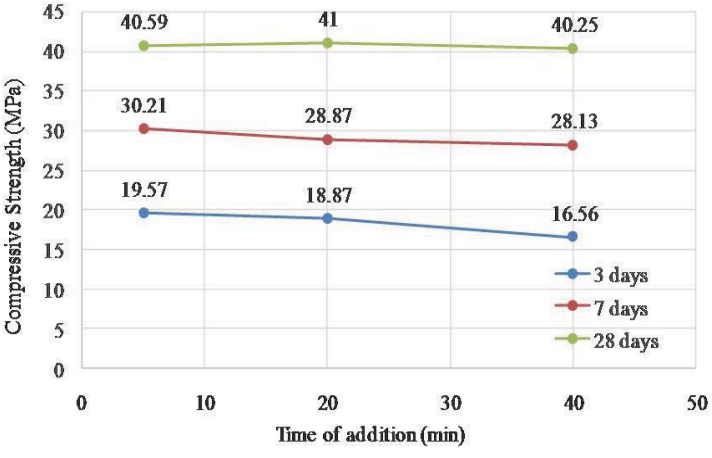

Figure 2: Compressive strength of concrete with different time of addition of SNP-based SP1

Among all the same aged cubes, the one having 5 minutes (minimum) of delayed addition was found to be have the highest strength and the cubes having 40 minutes of delay showed the least compressive strength. The cubes with 20 minutes of delay in addition of superplasticizer were having the strength in between the cubes of 5 minutes and 40 minutes of delay. The variation of compressive strength on addition of SP1 and SP2 are shown in Figure 2 and Figure 3 respectively.

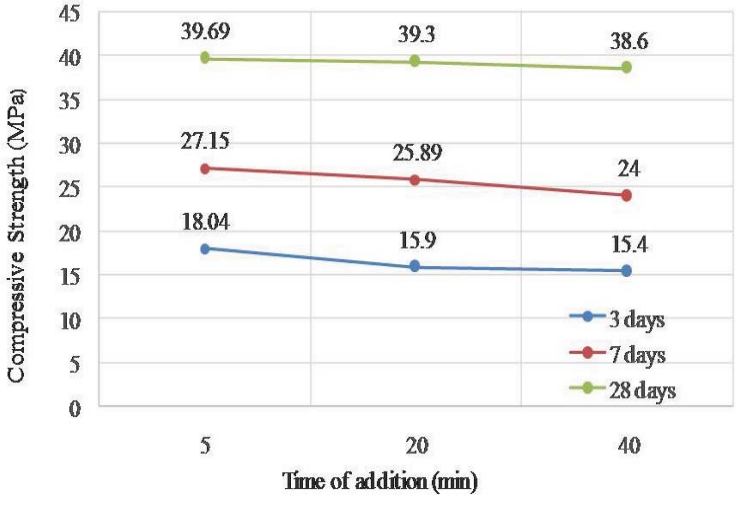

Figure 3: Compressive Strength of concrete with different time of addition of MLS based SP2

4.2 Split tensile strength of concrete with SP1 and SP2

The split tensile strength tests were conducted on concrete cylinders on 7 and 28 days age on addition of SP1 and SP2. The split tensile strengths are tabulated in Table 6.

Table 6: Split tensile strength of concrete with delayed addition of SP1 and SP2

Split tensile strength		5 min delayed addition of SP (MPa)	20 min delayed addition of SP (MPa)
SNP based SP1	7^{th} day	2.92	2.74
	28^{th} day	4.88	4.9
MLS based SP2	7^{th} day	2.63	2.35
	28^{th} day	4.66	4.6

The delayed addition of the superplasticizer in concrete makes it weaker in strength as is evident from the results of both compressive and split tensile strength during early days. A possible reason for this may be that the amount of admixture adsorbed reduces when cement hydrates; in other words, adsorption is greater on unhydrated compounds compared to the hydrated phases. As a result, when a delayed addition is done, there is more admixture available in the solution to maintain the fluidity and hence it loses its strength. The delayed addition has been shown to result in the lesser participation of the polymer in the formation of the organo-mineral phase.

5 CONCLUSIONS

In this limited experimental programme tests were conducted on hardened concrete on delayed addition of SP1 and SP2 and following conclusions were made from the study:

1. The MLS and SNP based superplasticizers were able to influence only early age strength i.e. 3rd and 7th day strength of the concrete.
2. It was found that none of the superplasticizer SP1 or SP2 (MLS based and SNP based) used in the study had any significant effect on the 28-day compressive strength as well as the split tensile strength of the concrete.
3. The delayed addition of the superplasticizer in concrete makes it weaker in strength as is evident from the results of both compressive and split tensile strength during early days.
4. On comparison of the performance of the two plasticizers in the study, it was found that sulphonated naphthalene polymer-based SP (SP1) was more effective by providing more early days' strength to concrete than modified lignosulphonate based SP (SP2). In addition to this, it was found SP1 was slightly more sensitive to the delayed addition than the SP2.

6 ACKNOWLEDGEMENTS

This work has been carried out by group of students in Concrete and Structural Engineering Laboratory at Civil Engineering Department of NIT Hamirpur. The help rendered by the staff of the department is duly acknowledged.

7 REFERENCES

[1] Ferrari, G., Valentini, L., Russo, V., Dalconi, M.C., Favero, M., and Artioli, G., 'Improving the performance of PCE Superplasticizer in early stiffening of OPC', Construction and Building Materials. **130** (2017) 83-91.

[2] Uchikawa, H., Sawaki, D., and Hanehara, S., 'Influence of kind and added timing of of organic admixture on the composition, Structure, and property of fresh cement paste', Cement and Concrete Research Journal. **25** (1995) 353-364.

[3] Nakajima, Y., and K. Yamada, K., 'The Effect of the Kind of Calcium Sulfate in cements on the dispersing ability of poly ß-napthalene sulfonate condensate superplasticizer', *Cement and Concrete Research.* **34** (2004) 839 – 844.

[4] Jansen, D., Neubauer, J., Goetz-Neunhoeffer, F., Haerzschel, R., and Hergeth, W. D., 'Change in reaction kinetics of a Portland Cement caused by superplasticizer – Calculation of Heat Flow curves from XRD data' *Cement and Concrete Composites*. **42** (2012) 327-332

[5] Zhang, M.H., Sisomphon K., Ng T.S., and Sun D.J., 'Effect of Superplasticizer on workability retention and initial setting time of the cement pastes' , *Construction and Building Materials.* **24** (2010) 1700-1707

[6] Flatt, R.J., Houst, Y.F., Bowen, P., Hofmann, H., Widmer, J., Sulser, U., Maeder, U., and Burge, T.A., 'Analysis of superplasticizers used in concrete'. *Analusis Magazine*. **26** (1998) 28-34

[7] Kumar, P. and Dubey, R., 'Effect of superplasticizer dosages on compressive strength of self compacting concrete', *International Journal of Civil and Structural Engineering,* Vol. **3** (2012) 360-366.

[8] Atesin, O., and Topcu, I.B., 'Effect of high dosages of lignosulphonate and naphthalene sulphonate based plasticizer usage on micro concrete properties.' *Construction and Building Materials.* **120** (2016) 189-197

[9] Khatib, J.M., and Mangat, P.S., 'Influence of Superplasticizer and curing on porosity and pore structure of cement paste' , *Cement and Concrete Composites*. **21** (1999) 431-437

[10] Hsu, K.C., Chiu, J.J., Chen, S.D., and Tseng, Y.C., 'Effect of addition time of a Superplasticizer on cement adsorption and on concrete workability' , *Cement and Concrete Composites*. **21** (1999) 425-430

[11] Aydin, S., Aytac, A.H., and Ramyar, K., 'Effects of fineness of cement on polynaphthalene sulphonate based SP-cement interaction' , *Construction and Building Materials.* **23** (2009) 2402-2408

[12] Agarwal, S.K., Masood, I., and Malhotra, S.K., 'Compatibility of Superplasticizer with different cements' , *Construction and Building Materials.* **14** (2000) 253-259

[13] Santhanam, Manu, 'Evaluation of Superplasticizer Performance in Concrete', Third International Conference on Sustainable Construction Materials and Technologies, (2013), Kyoto Research Park, Kyoto, Japan.

[14] Maganti, Janardhana and Raju, V. Siva Prasada, 'Compatibility of Sulphonated Naphthalene Formaldehyde and Lignosulphonates based Superplasticizer with Portland Slag Cements', (2013), Kyoto Research Park, Kyoto, Japan.

[15] IS 8112 (2013), Indian Standard on Ordinary Portland Cement-Specifications, Bureau of Indian Standards, New Delhi.

[16] IS 456 (2000), Indian Standard code of practice for plain and reinforced concrete, Bureau of Indian standards, New Delhi, India.

[17] IS 2386 (1963), Methods of test of aggregates for concrete, Bureau of Indian standard, New Delhi, India.

[18] IS 383 (1970), Specification for coarse and fine aggregates from natural sources for concrete Bureau of Indian Standards, New Delhi.

[19] IS 516:1959 (2008), Methods of test for strength of concrete, Bureau of Indian Standards, New Delhi.

[20] IS 10262 (2009), Concrete Mix Proportioning Guidelines, Bureau of Indian Standards, New Delhi.

Comparison of Different Beneficiation Techniques to Improve Utilization Potential of Municipal Solid Waste Incineration Fly ash Concrete

Aneeta Mary Joseph[1,2], Philip Van den Heede[1], Ruben Snellings[3], Andres Van Brecht[4], Stijn Matthys[1] and Nele De Belie[1]

[1]Magnel Laboratory for Concrete Research, Ghent University, Belgium.

[2]Strategic Initiative Materials (SIM vzw), project ASH-CEM within the program 'MARES', Technologiepark Zwijnaarde 935, Ghent B-9052, Belgium.

[3]VITO Vlaamse Instelling Voor Technologisch Onderzoek Research Institute, Boeretang 200, 2400 Mol, Belgium

[4]Indaver nv, Dijle 17/A, 2800 Mechelen, Belgium

ABSTRACT

A large volume of waste is generated in urban areas. Waste treatment techniques are being adopted in developed countries including recycling of wastes (such as paper, plastic, metals, etc.), composting organic waste and incineration of the remaining fraction. Ash generated as a result of incineration processes presently goes mainly into landfill, increasing both land use and resource wastage. Municipal solid waste incineration (MSWI) fly ash could alternatively be used as a supplementary cementitious material (SCM) in cement. The major hurdle that currently prevents its use are the expansion of concrete due to elemental aluminium (Al) and also its non-negligible chloride, sulphate, and heavy metal content. Washing with water is the simplest and most effective technique to remove chloride. To prevent Al expansion washing with water and alkali, or washing with a moderate heat treatment were effective. In this research, MSWI fly ash generated in a fluidized bed incinerator was tested in combination with Portland cement. This paper discusses the conducted experiments with varying parameters and the obtained test results in brief.

Keywords: Municipal solid waste incineration ash, pozzolana, elemental aluminium

1 INTRODUCTION

Waste management is an integral part of urban management, and its refinement is closely related to the socio-economic development of a country. Most waste management protocols consist of the following steps: generation, processing at source, collection, transport sorting, processing and disposal. Lansink's ladder, which is a thumb rule for effective sequencing of these processes when aiming at reducing wastage of resources, indicates the chain of preference as source reduction, reuse, recycling, incineration and landfill. Incineration comes at the bottom of the ladder and is mostly opted for residual waste in developed countries [1]. The incineration process has several advantages over landfilling, i.e. it aids in disinfection, and in volume and mass reduction by 90% and 70% respectively. On average, out of the 1.3 billion tonnes of waste generated per year, around 130 million tonnes are incinerated [2]. The characteristics of the residues vary greatly depending upon the type and operating

parameters and the input. The residues are broadly classified based on the point of collection. Coarser waste collected at the bottom of the incinerator is called bottom ash or slag. Residue from the flue gas collected at the boiler is called boiler ash and that from electrostatic precipitators or baghouses is called fly ash. In many countries, the bottom ash is utilized as road sub base material. Fly ash and boiler ash which contain questionable constituents like heavy metals and PCBs are landfilled presently. These residues have reasonable amounts of amorphous silica and alumina that induce pozzolanic properties. Various technical and environmental obstacles prevent its utilization such as presence of metallic aluminium, salts and heavy metals. Results from preliminary investigation of some beneficiation techniques to solve these problems, especially expansion due to metallic aluminium and the undesirable high chloride content in fly ash are discussed in this paper.

2 MATERIALS

The fly ash (FA) used for this study was collected from the fluidized bed furnace in the Indaver incineration facility in Doel, Belgium. CEM I 52.5 N cement conforming to EN 197-1 was used for the study, and was produced by VVM cements, Rieme, Belgium.

3 CHARACTERIZATION

The chemical composition of the ashes was determined by using the X-ray fluorescence (XRF) equipment available at the laboratories of Indaver nv. The elemental composition obtained was converted into its oxide form for certain elements as can be seen in Table 1.

Table 1. Chemical analysis of fly ash and cement

Property		FA
% by mass (m. %)	CaO	39.4
	SiO_2	23.8
	Al_2O_3	10.8
	Fe_2O_3	12.2
	Cl	3.5
	S	4.3
	K	1.1
	MgO	3.1
	MnO	0.3
	Equivalent Elemental Al	0.32
Density (kg/m^3)		2.75
Specific surface area (m^2/kg)		4.68

4 METHODS

Quantification of the equivalent elemental Al content was conducted indirectly based on the volume of gas generated on reaction with 1M NaOH, which was then related to the stoichiometry of the reaction. A set-up similar to the one mentioned in CUR recommendation 116 was used (Fig. 1) [3]. The term equivalent Al is used to account for zinc present in the ash, which also gives a similar evolution of hydrogen on reaction with water. The molecular mass and stoichiometry of Al was used for calculation. Acid soluble chloride content was determined by means of potentiometric titration, after boiling the ash sample in nitric acid solution for mobilizing bound chlorides. As such, the total chloride content was determined.

Figure 1: Set-up for equivalent elemental Al quantification

5 CHLORIDE REMOVAL

Salts are present in fly ash, mainly as chlorides and sulphates. They are rarely present in the bottom ash fraction. The reason for that is that metal chlorides and sulfides have a lower boiling point than their oxides and phosphates. The chloride content in MSWI fly ash varies between 0.5 to 15% [4]. Chlorides are contained, not only in soluble salts such as halite or sylvine, but also exist as lowly soluble hydrate phases such as Friedel's salt and hydrocalumnite [5]. Lowly soluble phases cannot be removed by washing with water. It is reported that calcination and carbonation can mobilise these insoluble chlorides [6]. In this study, a washing process was combined with three additional treatments for removal of chlorides. The parameters investigated were:

- Effect of carbonation
- Effect of temperature
- Effect of water – solid ratio

The washing process was conducted by immersing the fly ash in specified temperatures and stirred for few minutes, and the supernatant liquid was removed and the results are shown in Figure 2. Raw ash has a chloride content of 3.4 m. %. It can be observed that ~40% of chlorides are insoluble, since they could not be removed by simple washing. No change was noted increasing the water–solid ratio from 8:1 to 20:1. Increasing the temperature of the washing water from 20 to 40°C only slightly enhanced the removal of chloride. This may be explained by a combination of an increased solubility and more rapid dissolution kinetics of the salts. Carbonation of the ash was conducted at 1% CO_2 content for a period of 30 days. Subsequently, the ash was washed with water at a solid to liquid ratio of 1:10, which resulted in partial removal of insoluble chlorides. This treatment only slightly enhanced the removal of the chlorides. Further tests need to be conducted to check the releasability of bound chlorides during the utilization period.

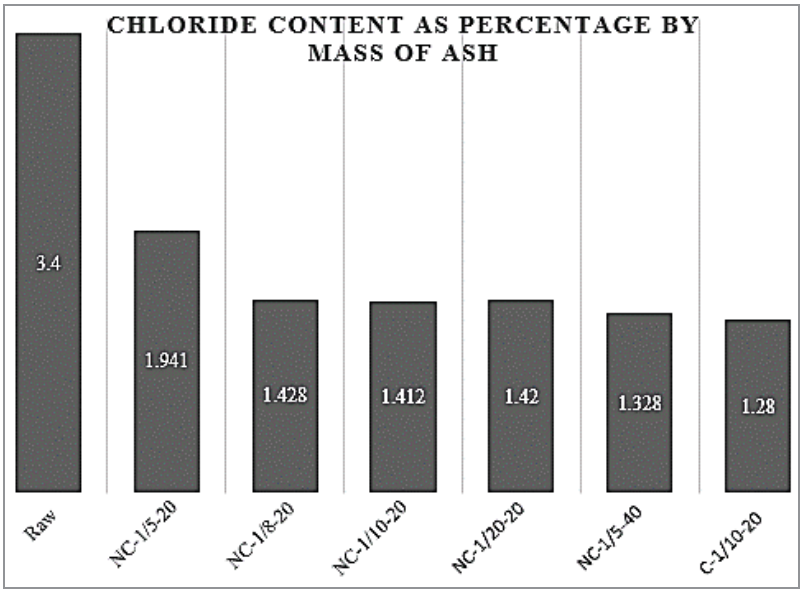

Figure 2: Effect of various parameters on chloride removal

NC – Non carbonated, C – Carbonated; Fraction represents the solid to water ratio;

Third digit represents temperature in °C (20°C & 40°C)

6 EXPANSION REDUCTION

Metallic aluminium in MSWI ash originates from aluminium foils, nails, etc., present in the waste. Attrition in the waste processing reduces it into finer sizes. When used as a pozzolan, it gets mixed with cement solution which is highly alkaline, and releases hydrogen gas. It reduces the effectiveness of the ashes as SCM in terms of strength increase and pore structure since it creates large air voids. It reacts with water to generate hydrogen gas in alkaline condition as shown in Eq. 1, 2, and 3. As a consequence, the air content of the mortar increases before it sets and thus a higher porosity in hardened state is eventually obtained.

$$Al + 2OH^- + H_2O \rightarrow [AlO(OH)_2]^- + H_2\uparrow \qquad pH > 7 \tag{1}$$

$$2Al + 2OH^- + 6H_2O \rightarrow 2[Al(OH)_4]^-_{aq} + 3H_2 \tag{2}$$

$$Zn + 2OH^- \rightarrow ZnO_2^{2-} + H_2 \tag{3}$$

This problem can be resolved in two ways, i.e. by:

1. Removing the metallic aluminium from the ash prior to the use
2. Accelerating the hydration of aluminium prior to its use

Removal of non-ferrous metals like aluminium is done in incineration plants by eddy current separation. But the effectiveness of this technique is restricted by the size and

orientation of metal particles. As a result, a part of it remains in the bulk. Since fly ash particles are small, they cannot be subjected to the eddy current separation technique. Electrochemical separation, where aluminium is first brought into solution as ions and then separated using current or sacrificial electrodes, is a possible technique to recover aluminium from the bulk of fly ash. Nevertheless, this will be costly. A cheaper alternative to prevent expansion is to accelerate the hydration process of aluminium prior to its use. The process can be accelerated either by increasing the temperature, or the alkalinity of the solution used for hydrating aluminium. Preliminary tests for both the processes were conducted and the results are shown in Figure 3.

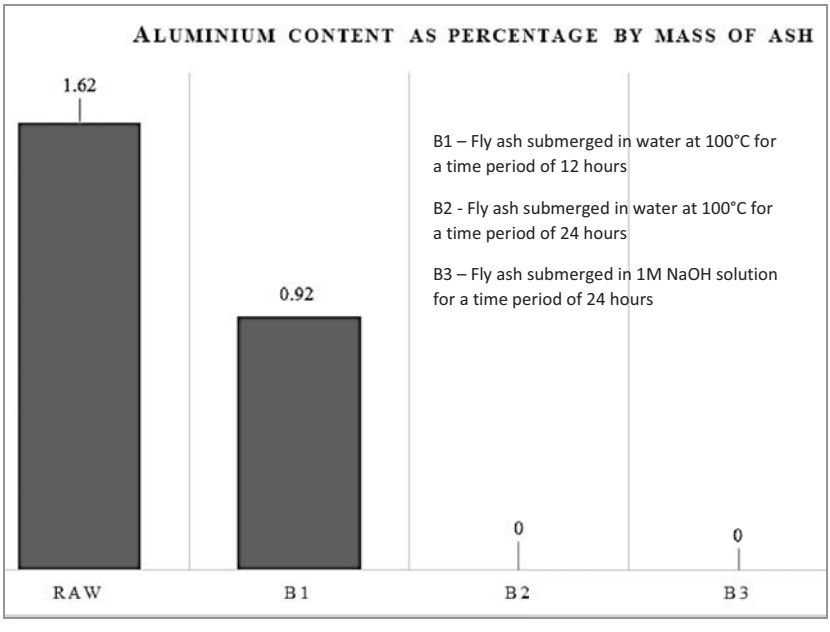

Figure 3: Effect of different beneficiation techniques on the metallic aluminium content

It can be seen that complete removal of metallic aluminium is possible by washing at 100°C for 24 hours, or by washing in 1N NaOH solution at room temperature.

7 CONCLUSIONS

1. Around 40% of chlorides are bound.
2. Carbonation and higher temperature (40°C) treatments can slightly mobilize bound chlorides in fly ash.
3. High temperature and high alkalinity accelerate the process of aluminium hydration to release hydrogen gas. In fly ash with 1.62 m. % of aluminium, all the aluminium got hydrated within 24 hours when submerged in water at 100 °C, and 1N NaOH at room temperature.

8 ACKNOWLEDGEMENTS

The authors are grateful to Mr. Guy Watzeels from Indaver for helping in conducting chemical analysis of ash samples. This research is a part of ASHCEM project, which in itself is a part of the bigger program MaRes aimed at creating and demonstrating an operational, flexible toolbox to recover metals and valorize the residual matrix into building materials funded by SIM (Strategic Initiative Materials in Flanders) and VLAIO (Flanders Innovation & Entrepreneurship). The financial support from the foundations for this study is gratefully appreciated.

9 REFERENCES

[1] R. E. Marshall and K. Farahbakhsh, "Systems approaches to integrated solid waste management in developing countries," Waste Manag., **33** (4) (2013) 988–1003.

[2] H. Cheng and Y. Hu, "Municipal solid waste (MSW) as a renewable source of energy: Current and future practices in China," Bioresour. Technol., **101 (**11) (2010) 3816–3824.

[3] CUR, Bouwen met kennis materiaal voor beton for concrete. 2012.

[4] S. Wu, Y. Xu, J. Sun, Z. Cao, J. Zhou, Y. Pan, and G. Qian, "Inhibiting evaporation of heavy metal by controlling its chemical speciation in MSWI fly ash," Fuel, **158** (2015) 764–769.

[5] K. Inkaew, A. Saffarzadeh, and T. Shimaoka, "Modeling the formation of the quench product in municipal solid waste incineration (MSWI) bottom ash," Waste Manag., **52** (2015) 159–168.

[6] S. Yang, A. Saffarzadeh, T. Shimaoka, and T. Kawano, "Existence of Cl in municipal solid waste incineration bottom ash and dechlorination effect of thermal treatment," J. Hazard. Mater., **267** (2014) 214–220.

[7] U. Müller and K. Rübner, "The microstructure of concrete made with municipal waste incinerator bottom ash as an aggregate component," Cem. Concr. Res., **36** (8) (2006) 1434–1443.

[8] I. Garcia-Lodeiro, V. Carcelen-Taboada, A. Fernández-Jiménez, and A. Palomo, "Manufacture of hybrid cements with fly ash and bottom ash from a municipal solid waste incinerator," Constr. Build. Mater., **105** (2016) 218–226.

The Effect of Nanomagnetite on the Shielding Properties of Cementitious Composites

E. Horszczaruk[(1)], P. Brzozowski[(1)], P. Sikora[(1)], K. Cendrowski[(2)] and E. Mijowska[(2)]

[(1)]Faculty of Civil Engineering and Architecture, West Pomeranian University of Technology, Szczecin, Poland

[(2)]Faculty of Chemical Technology and Engineering, West Pomeranian University of Technology, Szczecin, Poland

ABSTRACT

Concrete is an economical and effective material for shielding stationary reactors. Due to possible accidental conditions such as steam leakage, fire or terrorist attacks requires satisfactory shielding properties along with high thermal resistance are desired parameters in such structures. One of the novel additives which can find its potential application leading to improvement of strength and microstructure are nanomaterials. In the present work the effect of nanomagnetite (nano-Fe_3O_4) addition to cement pastes cured in normal conditions and exposed to temperature of 300 and 450°C on its gamma-ray shielding characteristics are investigated. Cement pastes containing addition of 5% and 10% (by mass of cement) of nanomagnetite have been prepared. The gamma-ray attenuation coefficients were measured as a function of the additive percentage of nanomagnetite for gamma-ray energy using 0.662 MeV ^{137}Cs source. The obtained data revealed that the incorporation of nanomagnetite increase the density of cement pastes, therefore, improves the gamma-ray attenuation coefficient. Moreover, addition of nanomagnetite improved the thermal resistance of samples by reducing amount of cracks. This contributed to much denser structure resulting in better shielding properties while compared to plain cement paste. Radiation tests have been supported with visual inspection of samples.

Keywords: Nanomagnetite, elevated temperature, cement paste, Gamma-ray shielding.

1 INTRODUCTION

Concrete is one of the most popular and relatively cheap material used for radiation shielding in medical infrastructure, facilities containing radioactive sources and radiation generating equipment. Compared with other construction materials, concrete has a high shielding capacity against nuclear radiation, good long-term durability and it easier to manufacture while compared to pure lead blocks or neutron shielding materials. This material in its simplest form is a mixture of Portland cement, sand, coarse aggregates and water. Portland cement is a component responsible for the binding properties in concrete.

For efficient neutron shielding, concrete must contain some heavy elements, which are capable to slow down fast neutrons, and a sufficient quantity of hydrogen to slow down the intermediate neutrons and to absorb the slow neutrons. As high-density materials are needed to shield against gamma rays, a high-density concrete is often favoured over the low density one. The probability of the interaction of γ-rays depends on the incident photon energy, the

atomic number and the density of the shielding materials therefore, to improve the shielding properties of the concretes the heavyweight aggregate (containing heavy elements) is widely applied (e.g. magnetite, hematite, goethite and barite) [1]. Study on the influence on the aggregate type on the shielding properties has been already extensively studied by various researchers [2-3].

Another factor which is taken in account in case of shielding materials is its thermal resistance. Possible accidental conditions such as steam leakage, fire or terrorist attacks require proper designing of the structure. Elevated temperature significantly affects the properties of concretes by reducing its mechanical properties, density and increasing its porosity. This results in decrement of shielding properties of cement-based composites [4]. Therefore, satisfactory shielding properties along with high thermal resistance are desired parameters in the development of modern radiation shielding structures.

Recently, the development of nanotechnology and the subsequent availability of new nanomaterials have opened up novel applications in numerous fields of industry including modern building materials. The nanoparticles exhibit unique chemical and physical properties relative in comparison to the same material in microscopic or macroscopic scale [5]. Moreover, the incorporation of a few percentage of the nanosized particles can influence the properties of the building materials significantly [6]. The recent research in the field of radiation shielding is concentrated on the development of denser concrete with improved microstructure by adding the suitable percentage of additives [1,7-9]. The studies presented by the researchers show that use of admixture results in the improvement of the microstructure and increase of the density of concrete which can lead to improvement of shielding properties.

One of recently aroused interest in this field is focused on the enhancement of the shielding properties when nanomaterials are applied. Their surface area, the number of dangling bond atoms, and unsaturated coordination on the surface of the nanoparticles lead to the interface polarization and multiple scattering (which are useful for absorption of electromagnetic radiations) [6]. In addition, the increased number of particles per gram has a very beneficial effect for radiation attenuation of nanomaterials at lower energies.

For this application, lead and iron oxides gathered considerable attention. Although, there are high amount of reports on the application of lead in the concrete [10-11], there are only few studies related to the influence of lead nanopowders on the shielding properties of the concrete [1,12]. The studies show that application of lead nanoparticles has a very positive influence of gamma-ray shielding properties. Although, lead nanoparticles seem to be very promising material for shielding application, exposure to lead is very hazardous and it may leads to several health problems [9]. The long-term exposure to lead or its salts (e.g., lead oxide, lead acetate, etc.) may cause accumulation of the heavy metal within the body. big efforts are made to replace the conventional lead-based materials what led to the development of ‘‘lead-equivalent’’ materials [5,13] which might be utilized instead of toxic lead and lead composites.

Therefore, the nanoparticles of iron oxides (i. e. nanomagnetite) focused its attention in this field. The application of nano-Fe_3O_4 or other magnetic elements [5] in polymer nanocomposites exhibit enhanced radiation shielding response. The nanocomposites combine the excellent functional properties of the nanoparticles with desired properties of host polymers [6]. The use of cementitious materials as a host for the nanomaterials seems to be very effective due to its strong binding properties and ability to immobilize the nanostructure within the matrix.

So far, there is no information available regarding the influence of nano-Fe_3O_4 on the shielding properties of concretes, however, study held by Cao et al. (2004) on the influence of micro particles of Fe_3O_4 and Fe_2O_3 (particle size smaller than 40 μm) on shielding properties

showed very successful results [14]. It is already widely reported that nano-Fe_2O_3 in cementitious composites exhibits positive influence on the mechanical and micro structural properties [15-20]. Moreover, researchers state that the application of nanosized iron oxide particles in a dispersed phase may also play an important role in the future production of heavyweight concretes [21]. Application of nanosized materials enable to extend the concrete particles grading from five decades to seven decades enabling to create much more denser a heavier structure.

Data regarding the effect of nanomagnetite is pretty limited. Researchers report that that the application of nano-Fe_3O_4 in a small amount (up to 0.3 wt%) can lead to the enhancement of the mechanical properties and refinement of the pore structure [15, 22-23]. Recently Sikora et al. (2016) have reported that 3 wt% of nano-Fe_3O_4 can be beneficial for improving the compressive strength and refining the pore structure of cement mortars [24]. Studies undertaken by Shekari et al. (2001) show that introduction of 1.5 wt% of nano-Fe_3O_4 improved the compressive strength as well as reduced the chloride penetration and water absorption [23].

Both Fe_3O_4 and Fe_2O_3 nanoparticles might contribute to improve the thermal resistance of cementitious composites [25]. Recently, Heikal et al. (2016) has reported that even small amount (1 wt%) of nano-Fe_2O_3 can be beneficial for improving fire resistance of cement pastes modified with this nanoparticle and diminish the cracks length [26].

Presented study is devoted to characterize the effect of nanomagnetite particles on the shielding properties against gamma-ray radiation of cement-based composites in ambient temperature and elevated temperature of 300 and 450^{o}C.

2 MATERIALS AND METHODS

2.1 Materials

For cement pastes preparation Rapid Hardening Portland Cement (RHPC) CEM I 42.5R conforming to EN 197-1 was used as received. Tap water was used as a mixing water. The nanomagnetite structures in size of 50–100 nm (purity 97 %) were purchased from Sigma Aldrich (637106) and were used as received. Transmission electron micrographs (TEM) and powder X-ray diffraction (XRD) diagrams of the Fe_3O_4 nanoparticles are shown in Fig. 1. The TEM (Fig. 1a) image of the magnetite shows that the iron oxide nanoparticles are in a cubic shape with a diameter in the range of 50–100 nm. The magnetite phase of the nanosized iron oxide was confirmed via XRD (Fig. 1b).

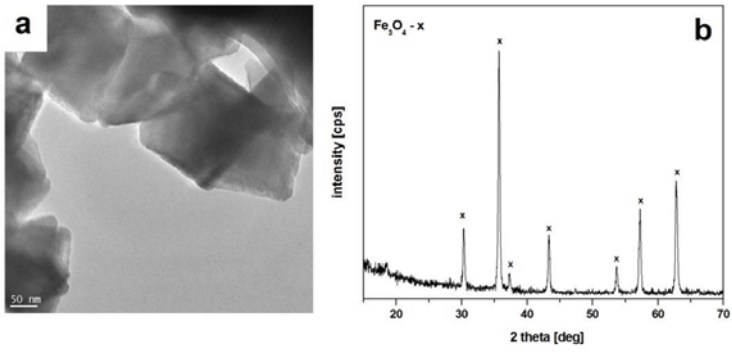

Figure 1: TEM (a) micrograph and X-ray diffraction pattern (b) of the nano-Fe_3O_4

No additional admixtures and additives were used in order to solely determine the influence of the nanomagnetite presence in the cementitious composite.

2.2 Cement paste preparation

Three types of cement pastes were designated as: R – plain (reference) cement paste, RF5 – cement paste containing addition of 5 wt% of nanomagnetite and RF10 – cement paste containing addition of 10 wt% of nanomagnetite were prepared (Table 1). The water to cement (w/c) ratio was fixed at 0.5.

Cement pastes were mixed with rotary mixer in a following procedure: 30 seconds slow mixing, 1 minute of fast mixing, 1 minute break, 1 minute of fast mixing. All cement pastes were mixed for a total time of 4.5 min.

Table 1: The weight fraction of cement pastes and density of the samples before and after heating

Sample designation	Cement	Nanomagnetite	Water	Density [g/cm^3]		
				20°C	300°C	450°C
R	1.0	0	0.5	1.67	1.50	1.48
RF5	1.0	0.05	0.5	1.68	1.52	1.49
RF10	1.0	0.1	0.5	1.69	1.53	1.51

Before the introduction of the nanomaterials into the cement mortars, the nano-Fe_3O_4 particles were sonicated in the mixing water for 10 min to obtain a uniform dispersion of nanomaterials. All cement pastes were cast in two layers into 80 x 80 mm cylinders. Three cylinders of R, RF5, RF10 cement pastes for each testing temperature were prepared. After casting, specimens were covered with plastic membrane to avoid water evaporation and thereafter kept in the laboratory for 24 hours at ambient temperature. After demoulding specimens were stored for 28 days in a standard water bath at a temperature of 20 °C ± 2 °C.

2.3 Heating and cooling regimes

After 28 days of curing, the specimens were weighed and dried in a chamber at a constant temperature, to obtain a dry mass of the specimens. Afterwards, one set of cylinders were subjected to gamma ray shielding test. Rest of the specimens were exposed to temperature of 300°C and 450°C. Heating of the specimens was performed using a medium-temperature furnace, with a thermostat allowing regulation of the rate of heating. The specimens were set separately in the bottom of a furnace chamber, far from the heating source, to enable uniform heat distribution across the specimens. The heating procedure conformed to RILEM guidelines [27] aimed at limiting thermal stresses due to the thermal gradient in specimens.

In the first stage, a constant rate of heating of 1°C/min was maintained in the furnace. After reaching the desired temperature, the samples were left in the furnace for 1 hour in order to stabilize the temperature over their entire cross-section. Afterwards, to avoid any thermal shocks, the samples were slowly cooled with an approximate rate of cooling of 1°C/min. The cooled specimens were visually observed to estimate the degree of damage sustained and weight loss was determined. Upon the calculations of the specimens densities the accuracy of the measurements were ±0.1 g for the mass determination and ±0.05 mm for the geometrical dimensions.

2.4 Radiation attenuation test

Linear attenuation coefficient has been determined with use of experimental setup presented in Figure 2a. Specimens were irradiated by gamma ray source of ^{137} Cs with activity of 10 mCi and photon energy of 0.662 MeV. A scintillation detector coupled with spectrometer has been used to detect passing gamma-ray. Experimental data was recorded with lab software on PC. Distance between the gamma source and detector has been set to 35 cm. Cement pastes after cooling were placed between the gamma source and detector and the measurements were conducted for 60 min counting time for each specimen. Photograph of experimental setup while testing the sample is presented in Figure 2b.

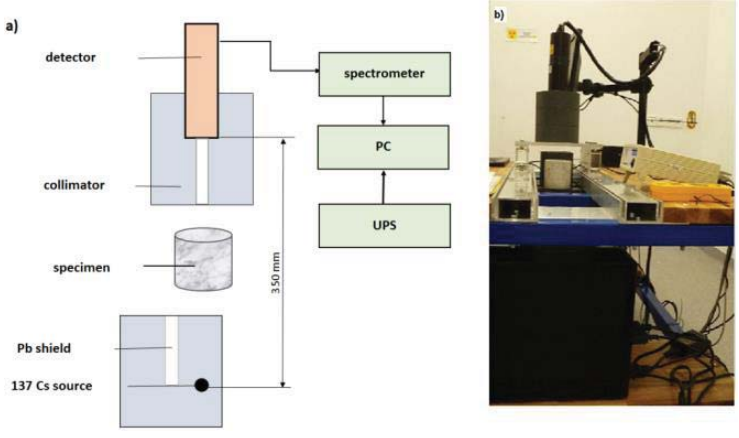

Figure 2: Experimental setup for determination of gamma-ray shielding properties of cementitious composites: a) graphic scheme of experimental setup, b) cement paste during the testing procedure

The incident intensity, I_0, of the gamma ray was reduced to intensity, I, after the cement paste specimens were placed between the source and the detector. We then obtained the linear attenuation coefficient, μ (cm^{-1}) values using Beer-Lambert's law as follows:

$$I = I_0 e^{(-\mu x)} \quad (1)$$

where x is the thickness of the paste specimen.

Once the μ values were determined, additional radiation shielding parameters, such as the *HVL* and *TVL*, were used to evaluate the gamma ray shielding ability of the cement paste. The *HVL* and *TVL* values represent the thickness of an absorber that will reduce the gamma radiation to one-half and to one-tenth of its original intensity, respectively The *HVL* and *TVL* values can be determined from the μ by using the following equations:

$$HVL = \chi_{1/2} = \frac{ln2}{\mu} \quad (2)$$

$$TVL = \chi_{1/10} = \frac{ln10}{\mu} \quad (3)$$

3 RESULTS AND DISCUSSION

3.1 Gamma-rays attenuation coefficient

Results of gamma ray shielding properties of cement pastes are presented in Table 2. From the following results it can be observed that addition of nanomagnetite even in small quantities (up to 10 %) has contributed to slight improvement of shielding properties of cement pastes. The relative linear attenuation coefficient as a function of temperature of cement pastes is presented in Figure 3.

Table 2: Results of shielding properties of cement pastes

Coefficient	μ [cm^{-1}]			*HVL* [cm]			TVL [cm]		
Temperature [°C]	20	300	450	20	300	450	20	300	450
R	0.133	0.116	0.113	5.21	5.98	6.13	17.31	19.85	20.38
RF5	0.134	0.118	0.114	5.17	5.87	6.08	17.18	19.51	20.20
RF10	0.137	0.121	0.116	5.06	5.73	5.97	16.80	19.03	19.85

With increment of temperature μ is decreasing as a results of density loss of samples caused by elevated temperature. Density measurements in the specimens are summarized in Table 1. Although, specimens containing nanomagnetite exhibit higher linear attenuation coefficient in all tested temperatures. It can be observed that increment of nanomagnetite content contributes to increase the shielding properties of cement pastes.

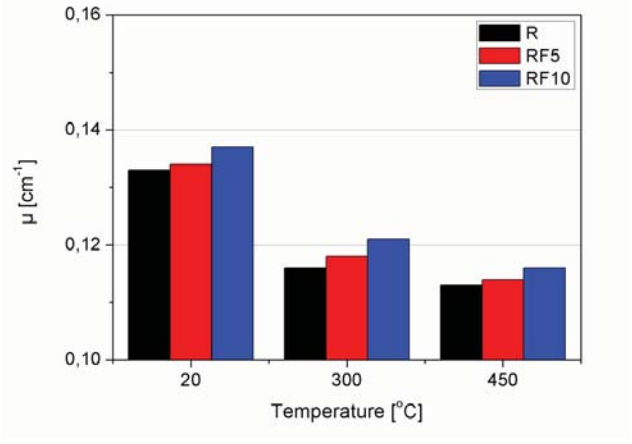

Figure 3. Relative linear attenuation coefficient (%) of tested cement pastes before and after exposure to 300°C and 450°C

3.2 Visual inspection

Figure 4 presents surface of tested cylinders. Unfortunately presence of nanomagnetite particles in the cement paste caused darkening of samples, therefore cracks cannot to be precisely observed in the figure. For cracks analysis optical microscope was incorporated. As it can be observed with the increase of the temperature amount of surface cracks has been increased. However, the presence of nanomagnetite in samples RF5 and RF10 reduced the

crack width and amount especially at temperature of 300°C. After exposure to 450°C samples RF10 exhibited similar amount of cracks as plain reference sample R. Surface of RF5 had the lowest amount of surface cracks.

This observation confirms the findings of Heikal (2016) that iron oxide nanoparticles can be beneficial for diminishing amount of cracks and reducing their width [26].

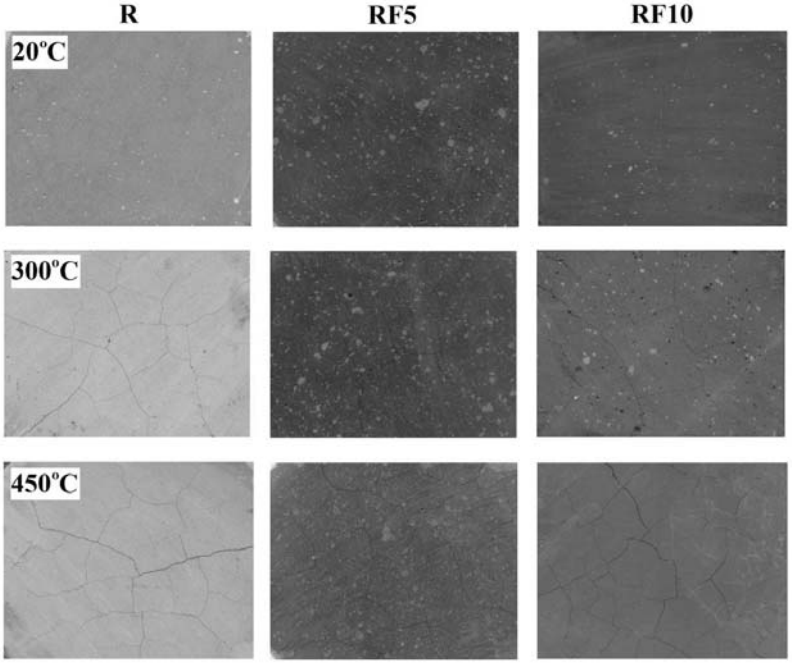

Figure 4: Surface of investigated samples before and after exposure to 300°C and 450°C

4 CONCLUSIONS

From the results obtained, it can be concluded that:

- Incorporation of small amount of nano-Fe_3O_4 increase the linear attenuation coefficient of gamma ray,
- Presence of nano-Fe_3O_4 in cement pastes helps to reduce the amount of surface cracks and diminish width of cracks of samples exposed to 300°C.
- After exposure to 450°C on the surface of samples R and RF10 similar amount of cracks have been observed, however, linear attenuation coefficient was higher for sample RF10,
- Nanomagnetite exhibits potential to be used as an additional nanosized (besides heavyweight aggregate and micro powders) admixture to various cementitious composites for improving shielding properties.

ACKNOWLEDGEMENTS

This research was funded by the National Science Centre within 2014/13/B/ST8/03875 (OPUS 7).

REFERENCES

[1] Hassan, H.E., Badran, H.M., Aydarous, A. and Sharshar, T., 'Studying the effect of nano lead compounds additives on the concrete shielding properties for γ-rays', *Nucl. Instr. Meth. B.* **360** (2015) 81-89.

[2] Demir, F., Budak, G., Sahin, R., Karabulut, A., Oltulu, M. and Un, A., 'Determination of radiation attenuation coefficients of heavyweight- and normal-weight concretes containing colemanite and barite for 0.663 MeV γ-rays', *Ann. Nucl. Energy* **38** (2011) 1274-1278.

[3] Ouda, A.S., 'Development of high-performance heavy density concrete using different aggregates for gamma-ray shielding', *Prog. Nucl. Energy* **79** (2015) 48-55.

[4] Sakr, K. and El-Hakim, E., (2005) 'Effect of high temperature or fire on heavy weight concrete properties', *Cem. Concr. Res.* **35** (2005) 590-596.

[5] Nambiar, S., Osei, E.K. and Yeow, J.T.W., 'Polymer nanocomposite-based shielding against diagnostic X-rays', *J. Appl. Polym. Sci.* **127** (6) (2013) 4939–4946.

[6] Badawy, S.M. and El-Latif, A.A.A., 'Synthesis and characterizations of magnetite nanocomposite films for radiation shielding', *Polym. Compos.* 2015 DOI: 10.1002/pc.23660.

[7] Yilmaz, E., Baltas, H., Kiris, E., Ustabas, I., Cevik, U. and El-Khayatt, A.M., 'Gamma ray and neutron shielding properties of some concrete materials', *Ann. Nucl. Energy* **38** (2011) 2204-2212.

[8] Rezaei-Ochbelagh, D., Azimkhani, S. and Gasemzadeh Mosavinejad, H., 'Shielding and strength tests of silica fume concrete', *Ann. Nucl. Energy* **45** (2012) 150-154.

[9] Yao, Y., Zhang, X., Li, M., Yang, R., Jiang, T. and Lv, J., 'Investigation of gamma ray shielding efficiency and mechanical performances of concrete shields containing bismuth oxide as an environmentally friendly additive', *Rad. Phys. Chem.* **127** (2016) 188-193.

[10] Rezaei-Ochbelagh, D. and Azimkhani, S. 'Investigation of gamma-ray shielding properties of concrete containing different percentages of lead'. *Appl. Radiat. Isot.* **70** (2012) 2282-2286.

[11] Rezaei-Ochbelagh, D., Azimkhani, S. and Gasemzadeh Mosavinejad, H., 'Gamma-ray shielding properties of concrete with different percentages of lead', *Nucl. Sci. Tech.* **23** (4) (2012) 215-218.

[12] Rajavikraman, R.S., 'Novel method for radiation shielding using nano-concrete composite', *Int. J. Mater. Sci. Eng.* **1** (1) (2013) 20-23.

[13] Gülbiçim, H., Tufan, M.Ç. and Türkan, M.N., 'The investigation of vermiculite as an alternating shielding material for gamma rays'. Rad. Phys. Chem. **130** (2017) 112–117.

[14] Cao, J. and Chung, D.D.L., 'Use of fly ash as an admixture for electromagnetic interference shielding', *Cem. Concr. Res.* **34** (2004) 1889–1892.

[15] Rashad, A.M., 'A synopsis about the effect of nano-Al2O3, nano-Fe2O3, nano-Fe3O4 and nano-clay on some properties of cementitious materials – A short guide for Civil Engineer', *Mater. Des.* **52** (2013)143–57.

[16] Khoshakhlagh, A., Nazari, A. and Khalaj, G., 'Effects of fe2o3 nanoparticles on water permeability and strength assessments of high strength self-compacting concrete', *J. Mater. Sci. Technol.* **28** (1) (2012) 73-82.

[17] Nazari, A., Riahi, S., Shamekhi, S.F. and Khademno, A., 'Benefits of Fe2O3 nanoparticles in concrete mixing matrix', *J. Am. Sci.* **6** (4) (2010) 102-106.

[18] Yazdi, N.A., Arefi, M.R., Mollaahmadi, E. and Nejand, B.A., 'To study the effect of adding Fe2O3 nanoparticles on the morphology properties and microstructure of cement mortar', *Life Sci. J.* **8** (4) (2011) 550-554.

[19] Oltulu, M. and Sahin, R., 'Single and combined effects of nano-SiO2, nano-Al2O3 and nano-Fe2O3 powders on compressive strength and capillary permeability of cement mortar containing silica fume', *Mater. Sci. Eng. A* **528** (2011) 7012–7019.

[20] Oltulu, M. and Sahin, R., 'Effect of nano-SiO2, nano-Al2O3 and nano-Fe2O3 powders on compressive strengths and capillary water absorption of cement mortar containing fly ash: A comparative study', *Energy Build.* **58** (2013) 292-301.

[21] Silvestre, J., Silvestre, N. and de Brito, J., 'Review on concrete nanotechnology', *Eur. J. Environ. Civ. Eng.* **20** (4) 2015 1-31.

[22] Amin, M.S., El-Gamal, S.M.A. and Hashem, F.S., 'Effect of addition of nano-magnetite on the hydration characteristics of hardened Portland cement and high slag cement pastes', *J. Therm. Anal. Calorim.* **112** (3) 2013 1253-1259.
[23] Shekari, A.H. and Razzaghi, M.S., 'Influence of nano particles on durability and mechanical properties of high performance concrete', *Proc. Eng.* **14** 2001 3036–3041.
[24] Sikora, P., Horszczaruk, E., Cendrowski, K. and Mijowska, E., 'The influence of nano-fe3o4 on the microstructure and mechanical properties of cementitious composites', *Nanoscale Res. Lett.* **11** (182) (2016).
[25] Amer, A.A., El-Sokkary, T.M. and Abdullah, N.I., 'Thermal durability of OPC pastes admixed with nano iron oxide', *HBRC J.* **11** (2) 2015 299-305.
[26] Heikal, M., 'Characteristics, textural properties and fire resistance of cement pastes containing Fe2O3 nano-particles', *J. Therm. Anal. Calorim.* **126** (3) 2016 1077-1087.
[27] Rilem Technical Committees 129-MHT. Test methods for mechanical properties of concrete at high temperatures, part 1: introduction, part 2: stress–strain relation, part 3: compressive strength for service and accident conditions. *Mater. Struct.* **28** (1995).

Characterization of Building Derived Materials for Ground Improvement of Contaminated Soils

Stuti Mondal[(1)], Arkamitra Kar[(1)], Anasua Guharay[(1)] and Naveen James[(2)]

[(1)]Department of Civil Engineering, Birla Institute of Technology and Science (BITS)-Pilani, Hyderabad, India

[(2)]Department of Civil Engineering, Indian Institute of Technology (IIT), Ropar, India

ABSTRACT

Building derived materials (BDM) are waste materials that are generated during constructions and demolition of structural components of buildings. Management and proper disposal of these wastes has assumed prime concern for modern civil engineers. The present study is aimed at characterization of BDM to ensure their recycling and reuse in practical purposes. One possible mode of reusing BDM is ground improvement. At present, BDM are used in the form of recycled coarse aggregates, after subjecting the former through various physical and chemical refinements, which incur extra cost. To address this issue, the present study emphasizes on the use of virgin BDM, which conserves natural aggregate, reduces the impact on landfills, saves energy, and thus can provide cost benefit. Hence, in this study, BDM are characterized to assess their compatibility when used in conjunction with local soil. It depends upon the type of soil and the contaminants present in the soil. The BDM in this study are characterized through physical investigations, microscopy, and exposure to chemically aggressive environment like acids, salts, and seawater to study their response. The results thus obtained show that BDM are highly susceptible to aggressive environment and appropriate measures must be adopted while using BDM in chemically aggressive environment.

Keywords: Building derived materials (BDM), chemical aggressive environment

1 INTRODUCTION

Due to rapid urbanization and development of infrastructure, huge volume of construction waste is generated. Additionally, periodic renovation and modification of these structures produce large quantities of demolition waste. Further, natural calamities like earthquake may also lead to destruction of structures, creating significant amount of solid demolition waste. U.S. Environmental Protection Agency (USEPA) defines construction and demolition waste (CDW) as waste materials consisting of the debris generated during the construction, renovation, and demolition of buildings, roads, and bridges [1]. Major component of these CDW is building derived materials (BDM), which is primarily composed of rejected concrete and brick. As the construction industry greatly contributes to the present environmental unbalances, it is necessary to: i) drastically reduce the consumption of non-renewable natural resources; and ii) limit the dumping of rejected BDM that takes up ever more limited space.

In existing practice, BDM are used in the form of recycled coarse aggregates, after subjecting the former through various physical and chemical refinements. The application of recycled aggregates has started in several Asian and Western countries for construction

projects [2]. Recycled aggregates have previously been used in limited quantities to enhance the performance of pavements, with the goal of using BDM in the near future [3]. However, there are no available studies regarding their physical and chemical characterizations. Moreover, no studies have been reported about their utilization for ground improvement. Behaviour of BDM in the soil will depend upon the type of soil and the contaminants present in the soil. Chemicals like sulphate and chloride are well known for their detrimental effect on concrete [4]. If the soil belongs to coastal region, seawater may cause deterioration of the BDM. If soil is near industrial or agricultural area it may contain nitrate. Due to rapid urbanization, these sites, which were once considered marginal, are now being extensively considered for infrastructure development. Thus, to use BDM in such soil, the present study characterizes them through physical investigations, microscopy, and exposure to chemically aggressive environment like sulphate, chloride, sea water and nitrate to study their response.

Concrete is by far the most important, versatile, and widely used building material in the world. Every year, over ten billion tons of concrete are being produced in the world. In the United States, the annual production of concrete is over 500 million tons. Such volumes require huge quantity of natural resources for aggregate and cement production. It has been estimated that the production of one ton of Portland cement causes the release of one ton of CO_2 into the atmosphere. CO_2 is known to be a greenhouse gas that contributes to global warming, and the cement industry alone generates about 7% of it [5]. In 2004–2005, BDM generation in Australia was 15.1 million tons, of which 7.6 million tons was recycled materials (timber, steel, concrete, rubble and soil) and 7.5 million tons was residual waste to landfill [5]. A report generated by Northeast Waste Management Officials' Association in 2009 claims that more than 52% of recycled waste Australia is those from construction and demolition activities [6]. While Germany, Denmark, Ireland, the Netherlands and the United Kingdom have recycling rates which are higher than 70%, Spain, Poland and Greece currently recycle less than 20% of their BDM [5-7]. On the other hand there exists places like Connecticut, USA, where construction wastes are not recycled at all [8].

BDM in India for the year 2010 may be estimated as 22-26 million tons [9]. Presently, BDM generation in India accounts up to 23.75 million tons annually and these figures were expected to have doubled by 2016 [10]. According to a study commissioned by Technology Information, Forecasting and Assessment Council (TIFAC), 70% of the construction industry is not aware of recycling techniques [11]. IS 383 (1970) ("Specification for coarse and fine aggregates from natural sources for concrete") stipulates that concrete can be made only with naturally accessed materials. Construction agencies cite this rule to avoid using recycled BDM [12]. The Union ministry of housing and urban poverty alleviation had told the Rajya Sabha in 2012 about the shortage of building material, especially for aggregates and concrete. The shortage has been so severe that several civic projects in India are facing delays [11]. In collaboration with MCD, a pilot project has been developed by IL&FS Environmental Infrastructure & Services Ltd. (IEISL) on public private partnership basis at Burari to demonstrate the potential of a scientifically managed process in relation to the collection and recycling of BDM in Delhi. The BDM is thereafter being recycled into aggregates at the waste management facility, which is in turn converted to ready mix concrete, pavement blocks, kerb stones and concrete bricks. Apart from this there is no document available advocating recycling of BDM.

In the work done by Corinaldesi et al. (2007), materials coming from BDM recycling were used instead of sand for the production of bedding mortars. This proved to be profitable not only for the obvious environmental advantages but also in terms of improvement of the mortar–brick interface. Experimental studies have been reported on BDM samples containing recycled concrete aggregate (RCA), crushed brick (CB), and waste rock (WR) for geotechnical assessment and suitability of usage of the sample for subbase layer of pavement.

The tests performed included particle size distribution, particle density, water absorption, compaction, Los Angeles abrasion, post-compaction sieve analysis, flakiness index, hydraulic conductivity, California bearing ratio (CBR) tests and triaxial test. It was found in another study that RCA and WR were good enough to be used as replacements of natural aggregates [13].

Results from another study showed that the properties of recycled concrete made with high percentages of coarse RCA (80%, 100%) and natural fine, were lower than those of ordinary concrete, while properties of recycled concrete made with 50% and 20% of coarse recycled aggregates, are similar to normal concrete [14]. The feasibility of building derived concrete (BDC) debris for highway construction has been studied by [15]. The gradation, optimum water content, unit weight, and resilient modulus were measured for the BDC and for the control materials, which were a crushed stone and sand. It was concluded that BDC had potential for use in highway construction, and they justified further testing and characterization. The use of coarse RCA as a replacement for natural aggregate did not significantly increase the drying shrinkage of concrete when incorporated into the mixture [16]. Another study concluded that there is clear increase in carbonation depths with increasing replacement levels when RCA concrete mixes are made with a similar mix design to that of the control natural aggregate concrete [17]. Investigations on the role of 0–2 mm size fine aggregate on the compressive and splitting tensile strengths of (RCA) concrete with normal and high strengths were conducted by [18]. The reduction in the splitting tensile strength was more pronounced than for the compressive strength. However, both strengths could be improved by incorporating silica fume and/or normal fine aggregates of 0–2 mm size in the RCA concrete mixture. The positive effect of the contribution of normal sand of 0–2 mm in RCA concrete was more pronounced in the compressive strength of a normal strength concrete and in the splitting tensile strength of high strength concrete.

In the recent 'Sustainable Geotechnical Applications' webinar conducted by ASCE, Melton (2015) suggested another possible solution to utilizing RCA and BDC by mixing them with soil to improve its shear strength characteristics. The barriers in construction and demolition waste management in developing countries taking the case of Iran were studied by [19]. The major findings were lack of awareness among contractors, lack of regulations and building codes to mandate waste management, and lack of budget in managing waste and low costs of spending materials to landfill.

Hence the present study emphasizes on the use of virgin BDM to conserve natural aggregate, reduce the impact on landfills, and provide cost and energy benefits. Load carrying and durability characteristics of BDM need to be assessed if they are to be used for ground improvement. The present study investigates the durability characteristics BDM after immersion in aggressive chemicals to simulate the different conditions that can be present in soil. There is a lack of available data for BDM. Hence, the results obtained from these tests are compared with those corresponding to the standard natural aggregate values for concrete pavement. The materials and experimental methodology used for this study are presented in the next section.

2 MATERIALS AND EXPERIMENTAL METHODOLOGY

2.1 Materials

The primary source of BDM was the local construction sites inside the campus. As the Hyderabad campus of Birla Institute of Science and Technology (BITS)-Pilani is undergoing extension it is producing huge amounts of construction as well as demolition wastes. Thus demolition of some existing structural elements that were no longer serviceable, and the rejected specimens (cubes, cylinders, and prism) from the concrete laboratory constituted the

main sources of BDM used in the study. The BDM used in the present study are thus predominantly concrete wastes, i.e., mixture of cement, sand, and coarse aggregates.

According to the suggestions from existing literature for inclusion of foreign materials in soil, the procured concrete wastes were crushed into particles having sizes of 10 mm or less However, to perform aggregate impact value (AIV) test, the concrete was crushed to a size that could pass 12 mm sieve was retained on 10 mm sieve. Seawater used in this work was procured from the Bay of Bengal. Commercially available laboratory grade sulphuric acid, hydrochloric acid, and nitric acid (in the laboratory) were mixed with measured amounts of deionised water to prepare 5% *v/v* solutions for each of those acids.

The BDM samples were tested for exposure to each of the following aggressive chemicals: i) seawater, ii) sulphuric acid, iii) hydrochloric acid, and iv) nitric acid. To study the extent of attack the samples were tested for the following after seven days of immersion in the agents mentioned above.

2.2 Study of surface under stereo microscope

Particles of BDM were studied under an Olympus SXZ7 stereomicroscope to check surface condition of the sample before immersing it into aggressive chemicals. After immersion for seven days, the BDM samples were observed under stereomicroscope to check for changes in surface characteristics. The minimum dimension that can be identified by this microscope is 20 μm.

2.3 Assessment of change in strength of BDM due to aggressive chemicals

Strength of natural aggregates can be measured by conducting aggregate impact value (AIV) test as per the guidelines of the Ministry of Road Transport and Highway (MoRTH). The same guidelines were adopted for BDM in this study. After immersing the BDM into aggressive chemicals for seven days, the samples were tested for impact value (as per IS: 2386 (Part IV) – 1963). The difference in the impact values of these samples before and after immersion was studied to assess change in strength.

2.4 Check for change in weight of BDM due to aggressive chemicals

Depending on the composition of the virgin BDM and aggressive chemicals, the samples reacted differently in each solution. The change in weight of BDM as a result of 7 – day immersion in aggressive chemicals was determined by comparing their weights before and after immersion in the chemicals. The differences were expressed in percentages with respect to the weight of BDM before immersion. The results obtained from these tests are presented in the following section.

3 RESULTS AND OBSERVATIONS

3.1 Study of surface under stereo microscope

Figures 1 through 5 present the observations made under stereo microscope. Figure 1 shows the unaffected surface of the virgin BDM aggregates. The greyish white colour on the surface shows the presence of cement paste on the aggregates.

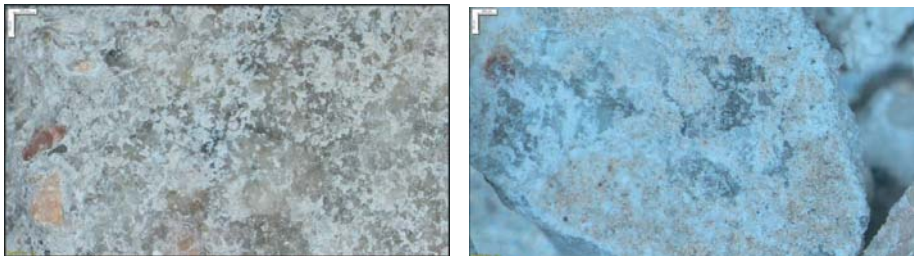

Figure 1: Samples before chemical exposure

Figures 2 to 5 show the chemically affected surfaces of the BDM samples. The change in colour and apparent increase in the surface deposits indicate adverse reactions between the BDM sample and the salts in the solutions.

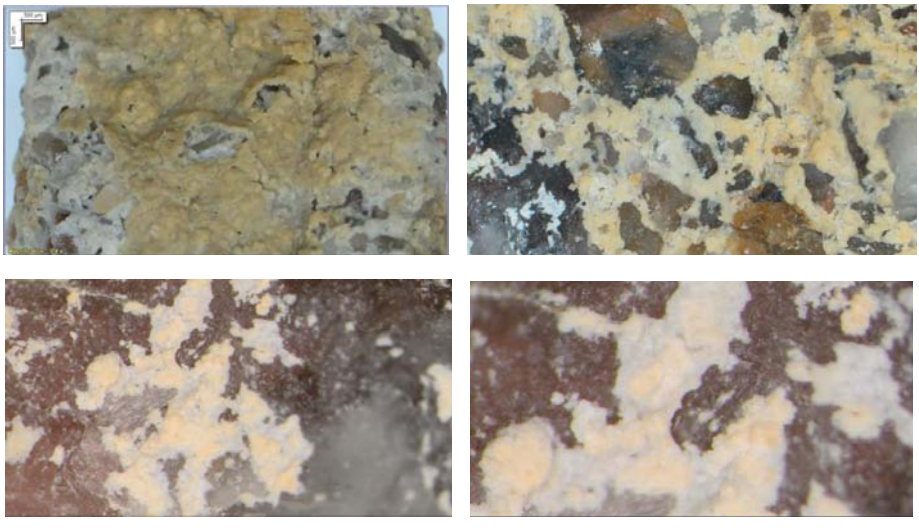

Figure 2: Samples after sulphate attack

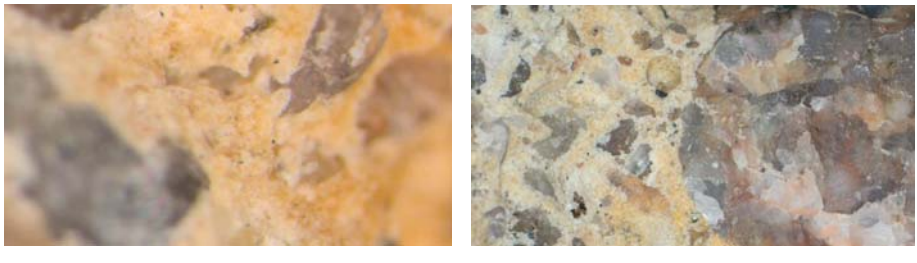

Figure 3: Samples after chloride attack

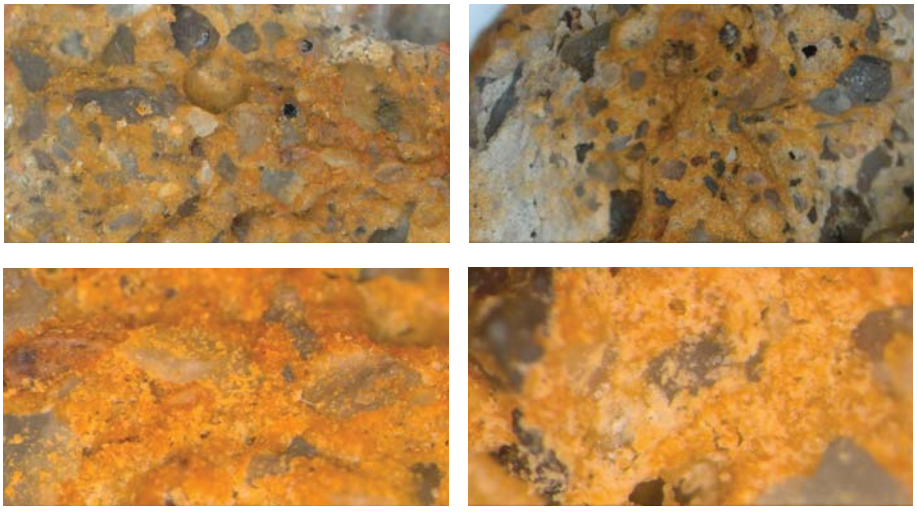

Figure 4: Samples after nitrate attack

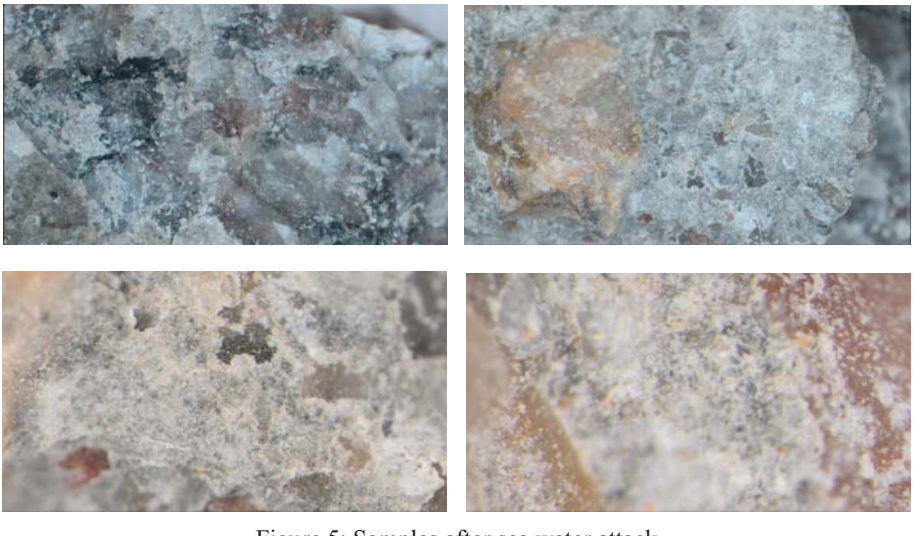

Figure 5: Samples after sea water attack

3.2 Assessment of change in strength of BDM due to aggressive chemicals

The following values of AIV were found after the samples were allowed to stay in the aggressive chemical solutions for 7 days (Table 1). The impact value test on the virgin BDM (max. size of 10 mm) resulted in the value of 35%. This is equal to the maximum permissible AIV for natural aggregates according to IS-2386: Part 3 (1963) for cement concrete pavements. Sulfuric acid and hydrochloric acid immersions did not affect much of its AIV (36.7% compared to 35% before the immersion). But as the limiting value is 35%, the use of BDM in sulfuric acid or sulfate-prone zones and in the presence of chlorides are discouraged. In case of nitric acid attack, the impact value is found to be 40% (relatively high in comparison to the prior value) much higher than the limiting value and thus this kind of attack results in adverse effects.

Table 1: Effect of chemical exposure on AIV of the BDM samples

Sl. No.	Prevailing condition	Aggregate Impact Value (%)
1	Before any chemical attack	33
2	After sea water attack	43.3
3	After sulphate attack	40.6
4	After chloride attack	43.3
5	After nitrate attack	40

3.3 Check for change in weight of BDM due to aggressive chemicals

It was observed that weight of the sample increased by 6.67% after sulphate attack. But, there was no notable weight gain or weight loss due to any other chemical attacks.

4 CONCLUSIONS

- From the aggregate impact values, and stereomicroscopy, it is clear that the BDM were strongly attacked by the chemicals present in the solutions. These reactions might have been primarily due to reactivity of the mortar stuck on aggregate surfaces.

- The reduction in AIV clearly made BDM unfit for their usage in soil subbase according to MoRTH specifications.

- Weight gain of the sample due to sulphate attack showed that the sample will show expansion if they are exposed to a soil containing sulphate in it. Thus, it can be concluded that they are highly susceptible to such aggressive environment.

- The observations from this study are based on locally acquired BDM and soil. Further studies need to be conducted on materials collected from other sources to formulate the initial steps for developing standard codes of practice for BDM in geotechnical applications.

REFERENCES

[1] USEPA, 'Sustainable Management of Construction and Demolition Materials', https://www.epa.gov/smm/sustainable-management-construction-and-demolition-materials (2017). Last accessed: 31. 03. 2017.

[2] Rao, A., Jha, K. N., and Misra, S. 'Use of aggregates from recycled construction and demolition waste in concrete' *Resources, conservation and Recycling* **50**(1) (2007) 71-81.

[3] Melton, J. S., 'Recycled Base Aggregates in Pavement Applications' in 'Sustainable Geotechnical Applications', Webinar hosted by ASCE, July 24, 2015, Part III of VI (AWI051611).
[4] Zuquan, J., Wei, S., Yunsheng, Z., Jinyang, J., and Jianzhong, L. 'Interaction between sulfate and chloride solution attack of concretes with and without fly ash' *Cement and Concrete Research* **37**(8) (2007) 1223-1232.
[5] Meyer, C., 'Concrete as a green building material' in 'Construction Materials Mindess Symposium', August, 2005.
[6] NEWMOA, 'Construction & Demolition Waste Management in the Northeast in 2006", Northeast Waste Management Officials' Association, 129 Portland Street, Suite 602 Boston, MA 02114, Report submitted June 30, 2009. Available at: http://www.newmoa.org/solidwaste/CDReport2006DataFinalJune302009.pdf. Last accessed on February 10, 2017.
[7] Kien, T.T., Thanh, L.T. and Lu, P.V., 'Recycling construction demolition waste in the world and in Vietnam'. In 'The International Conference on Sustainable Built Environment for Now and the Future', Hanoi, 2013, 27.
[8] Tam, V.W., 'Comparing the implementation of concrete recycling in the Australian and Japanese construction industries' *Journal of Cleaner Production* **17** (7) (2009) 688-702.
[9] Shrivastava, S. and Chini, A., 'Construction Materials and C&D waste in India' in 'Lifecycle Design of Buildings, Systems and Materials', Conference Proceedings of CIB W115 Construction Material Stewardship, Enschede, The Netherlands, June 2009, 72.
[10] Anagal, V., Nagarkar, G., Atnurkar, K. and Patel, A., 'Construction and Demolition Waste Management-A Case Study of Pune', on 'Role of Infrastructure for Sustainable Development', 28th National Convention of Civil Engineers, Roorkee, 2012 (Institution of Engineers (India), Roorkee Local Centre) *A-18*.
[11] CSE, 'Construction and Demolition Waste', Centre for Science and Environment 41, Tughlakabad Institutional Area, New Delhi 110 062, INDIA, Available at: http://www.cseindia.org/userfiles/Construction-and%20-demolition-waste.pdf. Last accessed on February 10, 2017.
[12] Corinaldesi, V., Monosi, S. and Moriconi, G., 'Effect of different recycled aggregates on mortar performance' in 'Proceedings of the Sustainable Construction Materials and Technologies', International Conference on Sustainable Construction Materials and Technologies, Coventry, United Kingdom, June, 2007, 5962.
[13] Arulrajah, A., Jegatheesan, P., Disfani, M. M., and Myint, W.B., 'Geotechnical and geoenvironmental properties of recycled construction and demolition materials in pavement subbase applications' *Journal of Materials in Civil Engineering* **25** (8) (2012) 1077-1088.
[14] Pani, L., Francesconi, L. and Concu, G., 'Influence of Replacement Percentage of Recycled Aggregates on Recycled Aggregate Concrete Properties' in 'Proceedings of the Fib Symposium', Prague, Czech Republic, June, 2011, 810.
[15] Melton, J., Clark, C. and Regis, P., 'Feasibility study on building-derived concrete debris for use in highway construction' in 'Testing and Specification of Recycled Materials for Sustainable Geotechnical Construction', ASTM International, 2012.
[16] Adams, M.P., Fu, T., Cabrera, A.G., Morales, M., Ideker, J.H. and Isgor, O.B., 'Cracking susceptibility of concrete made with coarse recycled concrete aggregates' *Construction and Building Materials* **102** (2016) 802-810.
[17] Silva, R.V., Neves, R., De Brito, J. and Dhir, R.K., 'Carbonation behaviour of recycled aggregate concrete' *Cement and Concrete Composites* **62** (2015) 22-32.
[18] Khoshkenari, A.G., Shafigh, P., Moghimi, M. and Mahmud, H.B., 'The role of 0–2mm fine recycled concrete aggregate on the compressive and splitting tensile strengths of recycled concrete aggregate concrete' *Materials & Design* **64** (2014) 345-354.
[19] Ghoddousi, P., Nikmehr, B., Hosseini, M.R., Chileshe, N. and Rameezdeen, R., 'Barriers to Construction and Demolition Waste Management in Developing Countries: Case of Iran'. in 'Unmaking Waste 2015 Conference', Adelaide, South Australia, (2015).

Nanosilica Coated Aggregates: Effects on Strength, Microstructure, and Transport Properties of Hydraulic Cement Mortars

Parth Panchmatia, Jan Olek, Ehsan Ghafari, Seyedali Ghahari and Lu Na

Lyles School of Civil Engineering, Purdue University, USA

ABSTRACT

The typical interface between aggregates and cement paste in unmodified concrete systems, referred to as the interfacial transition zone (ITZ), will often be more porous than the bulk paste and thus is believed to reduce the overall mechanical and durability properties of concrete. Techniques suggested to improve the ITZ often involve the use of pozzolanic cementitious materials to replace a portion of OPC in the bulk mixture. This work discusses targeted application of nano-silica thin films on aggregate surfaces to improve the ITZ and to evaluate the impact of this treatment on the development of mechanical, microstructural, transport, and mineralogical properties of mortar specimens. Preliminary testing has demonstrated that 28-day old mortar samples made with aggregate coated with 25 % (by weight) of colloidal nano-silica solution showed a 50 % increase in compressive strength and approximately three times lower $Ca(OH)_2$ content compared to mortars without nano-silica treatment. The ITZ of mortar made with nano-silica coated aggregate appeared denser than the ITZ of mortar prepared using virgin aggregate when observed using a SEM. The non-steady state chloride diffusion coefficient of mortar specimen made with nano-silica coated aggregates was approximately one order of magnitude lower than that of the reference mortar specimen.

Keywords: nano-silica, interfacial transition zone, portlandite, microstructure

1 INTRODUCTION

Concrete is a material made of aggregates and cement paste. Although (in most cases) the aggregate can be considered to be a non-reactive filler, it is also recognized that both, fresh and hardened properties of concrete are strongly influenced by its various characteristics, including absorption, gradation, shape, thermal expansion, mineralogy, and chemical composition [1,2]. The topic of the interface between the aggregate and the cement paste, referred to as the interfacial transition zone (ITZ), has been extensively studied ever since it was first observed in the 1960's. Scrivener et al. [3] found a strong gradient in the porosity as a function of the distance from the aggregate surface, with the maximum value of 30 % porosity reported in the innermost 5 μm thick layer. On the other hand, the image analysis investigation conducted by Diamond et al. [4] did not reveal the existence of such a strong gradient. Since concrete consists of approximately 70 % (by volume) of aggregate, the ITZ could influence the material's properties significantly.

Numerous researchers agree that the combined influence of 'wall effect' and 'microbleeding' during early stages of hydration results in the formation of the ITZ [5–7]. The packing of anhydrous cement grains is typically more loose around aggregate surfaces compared to their packing in the bulk paste region. This phenomenon is referred to as the

'wall effect'. Microbleeding and thin film formation around the aggregates results in a higher water in the region surrounding the aggregate [4,7]. As cement hydrates, both, the concentration of the calcium ions and the pH of the pore solution, increase. On reaching saturation limits, $Ca(OH)_2$ precipitates in the region occupied by water. Therefore, after completion of hydration process, the ITZ shows higher porosity and large $Ca(OH)_2$ deposits [7,8].

The high porosity of the ITZ makes it susceptible to crack formation under loading [9]. In addition, the high concentration of $Ca(OH)_2$ in the ITZ makes it a preferential zone for other type of distresses such as sulphate attack, chloride attack, and/or carbonation. High volume of aggregates in concrete/mortars can result in interconnected ITZ, which, according to Winslow et al. [10] and Garboczi et al. [11] can significantly increase the permeability and transport properties of concrete and mortars.

Traditional techniques employed to improve the ITZ include partial replacement of ordinary Portland cement (OPC) with pozzolanic supplementary cementitious materials (SCMs) such as fly ash, ground granulated blast furnace slag and silica fume. Pozzolans react with the $Ca(OH)_2$, generated during hydration of OPC, to form additional (to that resulting from the hydration of the OPC itself) calcium silica hydrate (CSH) which densifies the matrix and (to certain extend) the ITZ [12–14]. To enhance the efficiency of SCMs in improving the ITZ, Ping and Beaudoin [15] deposited silica fume on the surface of the aggregate which was used to produce concrete. They reported that the resulting ITZ was denser than the bulk paste due to the pozzolanic reaction. Similarly, Munoz et al. [1] showed that coating aggregates with nano-silica is more effective in improving of the ITZ than using nano-silica distributed within the bulk of the cement paste matrix. The aggregates can be coated with colloidal suspension of nano-silica using either the "dip" or "spray" methods.

However, a study on the influence of this coating method on the mechanical, microstructural, and transport properties of mortars and concrete is missing. Therefore, this paper attempts to quantify the influence of nano-silica coated aggregates on the strength, microstructural, and transport characteristics of mortar specimens.

2 EXPERIMENTAL PROGRAM

2.1 Materials

Table 1 summarizes the chemical composition of Type 1 OPC used in this study. Ottawa sand conforming to the specifications of graded sand in ASTM C778-13 [16] was used to prepare mortar samples. Prior to placement in the mortar mixer, the sand was coated with colloidal nano-silica, using four different concentrations (by weight) of nano-silica in the colloidal suspension: 25 %, 17.5 %, 10 %, and 1 %. The 25 % colloidal nano-silica (with an average particle size of 30 nm) was obtained from a commercial producer and diluted to prepare the remaining three concentrations.

2.2 Mixture design and sample conditioning

The mortar was prepared following the procedure described in ASTM C305-14 [17]. All samples were prepared with a water/cementitious ratio of 0.50. The volumetric mixture proportions of mortars used in the study are given in Table 2. The aggregate volume was maintained at 50 % of the total volume for all mixtures. Reference mortar was prepared using virgin aggregates. Prior to preparing mortar samples with coated aggregates, 10 %, 17.5 %, and 25 % solution of colloidal nano-silica was poured over the aggregate and drained three times. The aggregates were then allowed to dry at room temperature overnight. Aggregates coated with 10%, 17.5 %, and 25 % colloidal nano-silica showed an increase in the dry mass of, respectively, 2.73 %, 5.68 %, and 9.0 %. These values were used to estimate the quantity

of nano-silica in different mortar mixtures based on the amount of coated aggregate used to produce those mortars. The specific gravity values for virgin aggregate and aggregate coated with 10 %, 17.5 %, and 25 % colloidal nano-silica was measured following the procedure described in ASTM C 128 [18] and found to be 2.69, 2.67, 2.64, and 2.55 respectively. These values were used to develop the volumetric mixture design for the mortars.

Table 1: Chemical composition of cementitious materials used in the preparation of paste

Chemical Compound in Type 1 OPC	Content (% by mass)
Silicon Dioxide, Si_2O	18.94
Aluminium Oxide, Al_2O_3	5.65
Ferric Oxide, Fe_2O_3	3.29
Calcium Oxide, CaO	63.2
Magnesium Oxide, MgO	3.13
Sulphur Trioxide, SO_3	3.43
Loss of Ignition	1.13
Total alkali as Sodium Oxide, Na_2O_{eq}	0.86

Table 2: Mixture Design

Components		Amount (kg/m^3)				
		Reference (R)	Mortar with aggregate soaked in colloidal nano-silica of % by wt. of			
			10% (M2)	17.5% (M3)	25% (M4)	25% (M4-modified)
Type 1 OPC Cement		599	577	552	534	497
Ottawa Sand	Virgin	1344	0	0	0	0
	Coated	N.A.	1334	1319	1275	1275
Nano-silica*		0	36.4	77.3	105.9	105.9
water/cementitious		0.50	0.50	0.50	0.50	0.55
* Values estimated using the increase in the dry mass of coated aggregates,						
** Represents the mortar prepared using coated aggregates which were used to prepare the mortar mixtures immediately after completion of the coating process (without drying)						

Four 5 cm cube samples and one 101.6 mm x 203.2 mm cylindrical sample were prepared for each mixture. Specimens were demoulded after 24 hours of casting and cured in a 100 % RH chamber maintained at 23 °C before being tested.

2.3 Test methods

2.3.1 Compressive strength

Three 5 cm (2 in.) mortar cube samples (from each mortar mixture) were tested for compressive strength following the procedure described in ASTM C109-16 [19]. A displacement controlled testing machine was used to apply the compressive load at the rate of 517.107 kPa/s (75 psi/s).

2.3.2 SEM (Scanning electron microscopy) analysis

SEM analysis was conducted on fractured and polished surfaces. Fracture surface specimens were obtained from 5 cm x 5 cm x 5 cm cube samples after crushing them using displacement controlled testing machine. These specimens were soaked in isopropyl alcohol for 1 day to stop the hydration and vacuum dried at 65 °C for 2 days before being examined using a SEM. The polished SEM samples were prepared from specimens (~2.5 cm x 2.5 cm x

2.5 cm) which were extracted (using an oil cooled saw) from the middle of the mortar cylinder after 28 days of hydration. These specimens were dried at 65 °C for 2 days, epoxy impregnated, lapped and polished before being examined using a SEM equipped with energy dispersive X-ray (EDX) analyser.

2.3.3 Thermogravimetric Analysis (TGA)

3-day, 7-day, and 28-day hydrated samples were crushed and soaked in isopropyl alcohol for 1 day to stop hydration and vacuum dried at 65 °C. Dried specimen were crushed and sieved. Powdered samples passing through 200 μm sieve was analysed using TA instrument's Q50 thermogravimetric analyser. The change in weight of powdered samples was recorded as the temperature of samples was increased to 800 °C at the rate of 10 °C/min. Calcium hydroxide decomposes into calcium oxide and water at temperatures ranging between 380 – 470 °C. The calcium hydroxide content was estimated using the change in mass of the sample observed between 380 – 470 °C.

2.3.4 Transport properties

The mortar samples were vacuum saturated following the procedure described in AASHTO T357-15 [20]. The rapid migration procedure, described in AASHTO T357-15 [20], was used to determine the depth of chloride penetration of mortar samples made with virgin and nano-silica coated aggregates. Furthermore, equations described in NT BUILD 492 [21] were used to calculate the non-steady state diffusion coefficients of different mortar samples.

3 RESULTS AND DISCUSSION

3.1 Compressive Strength

Figure 1 presents the compressive strength results for different mortars after 1, 3, 7 and 28 days of hydration. Mortar samples prepared with aggregates coated with 10 % (by mass) colloidal nano-silica (M2) showed the highest strength for all hydration ages. After 1 day of hydration, the strength of reference mortar (R) was slightly higher than the compressive strength of mortars prepared using aggregates coated with 17.5 % (M3) and 25 % (M4) colloidal nano-silica. However, with age, M3 and M4 mortar samples showed higher strength compared to reference mortar samples.

The lower (compared to M2) compressive strength of M3 and M4 mortars can be attributed to the observed agglomeration of nano-silica particles (refer to section 3.2) observed in the microstructure of M3 and M4 mortar samples. The process of drying the coated aggregates (at 23 °C) prior to mixing might have exaggerated the potential of agglomeration of nano-silica particles for aggregates coated with high concentration (17.5 % and 25 %) of colloidal nano-silica. An exploratory study to validate the aforementioned hypothesis demonstrated that mortars prepared using aggregates coated with 25 % colloidal nano-silica (without drying) showed a compressive strength value which was 50 % higher than the reference after 7 days of hydration. This increase in the compressive strength was observed despite the fact that the water/cementitious ratio of the modified M-4 mixture was 0.55 (instead of 0.50).

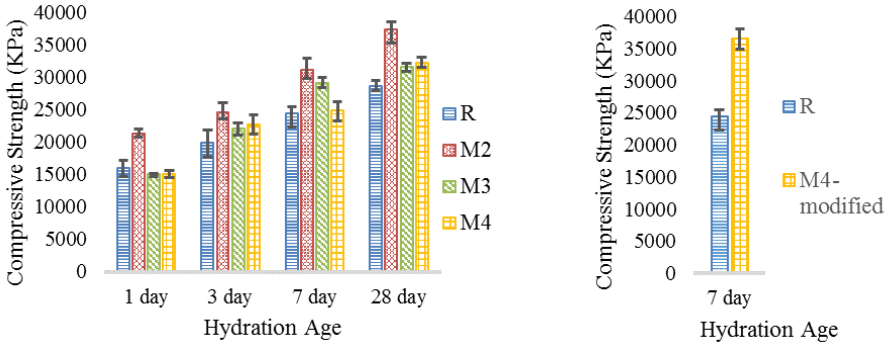

Figure 1: Compressive strength of mortar samples prepared a) using dried and coated aggregates and b) using wet and coated aggregates

3.2 SEM (scanning electron microscopy) analysis

SEM analysis was conducted to observe and to contrast the ITZ of mortar samples made with virgin aggregate and with aggregates coated with nano-silica. The ITZ of mortar samples prepared using aggregates coated with 10 % colloidal nano-silica (M2) [shown in Figure 2 (a)] is denser compared to the ITZ of mortar prepared using virgin aggregate (Reference) [shown in Figure 2 (b)]. The ITZ is not visible in Figure 2 (c) (obtained from M2 mortar) whereas it is clearly discernible in Figure 2 (d) (obtained from reference mortar). This increase in density of the ITZ could result in better mechanical and transport properties of the mortar prepared using coated aggregates. However, agglomeration was observed in mortar samples prepared using aggregates coated with 17.5 % (M3) and 25 % (M4) colloidal nano-silica solution [as shown in Figure 2 (e)]. This agglomeration could be the cause of the lower compressive strength of M3 and M4 mortars compared to M2 mortars.

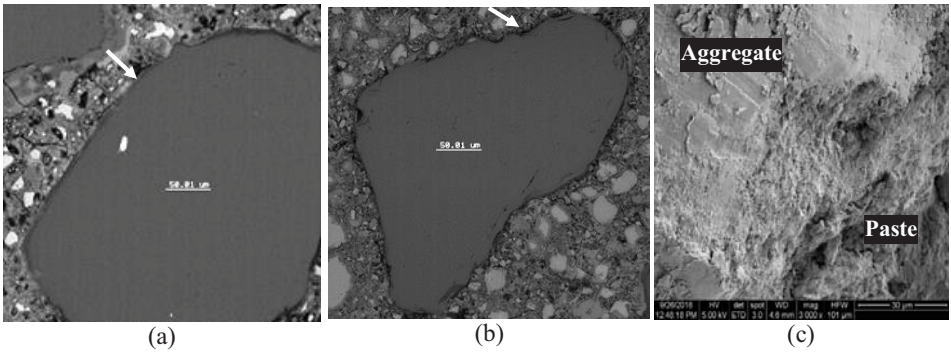

(a) (b) (c)

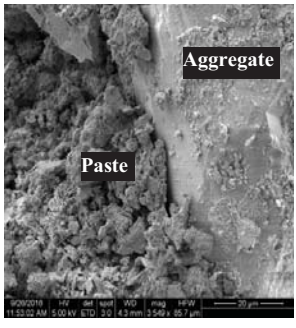

(d)

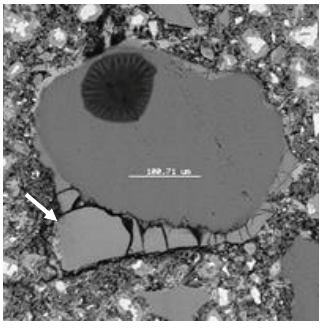

(e)

Figure 2: SEM images showing a) polished surface of the ITZ of M2 mortar, b) polished surface of ITZ of reference mortar, c) fractured surface of the ITZ of M2 mortar, d) fractured surface of the ITZ of reference mortar, and e) agglomeration of nano-silica particles around aggregate in M4 specimen

In addition to the ITZ being porous, $Ca(OH)_2$ deposits were also encountered more frequently in the ITZ of reference mortar as opposed to the ITZ of M2, M3 and M4 mortar samples. Figure 3 (a) and (b) show the chemical composition (determined using EDX) of the solid near the aggregate surface for reference mortar and M2 mortar sample respectively. For reference mortar samples the ITZ is filled with $Ca(OH)_2$ whereas for mortar prepared using coated aggregate (M2) the region around the aggregate has CSH deposits (the result of the reaction of nano-silica with $Ca(OH)_2$). Overall, the presence of nano-silica on the aggregate surface densifies the microstructure of the ITZ and reduces the $Ca(OH)_2$ content at that location.

To verify that pre-coating of aggregate surfaces with nano-silica is more effective with respect to the enhancement of the ITZ, the ITZ of M2 mortar samples was compared with the ITZ of mortar samples prepared by using nano-silica in the traditional way. Preliminary investigation revealed that the ITZ of mortar prepared using nano-silica coated aggregate is indeed denser [Figure 4 (a)] than that of mortar samples prepared by dispersing the same quantity of nano-silica in the cement paste [Figure 4 (b)]. However, more detailed analysis is required to determine whether the observed difference is statistically significant.

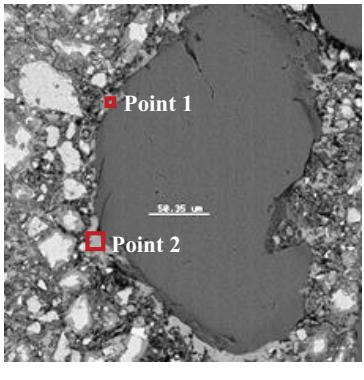

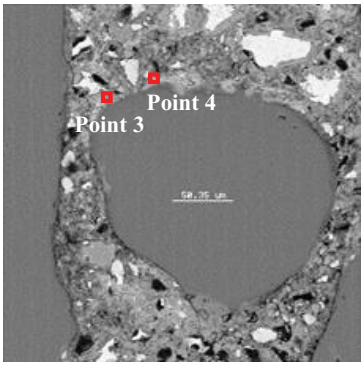

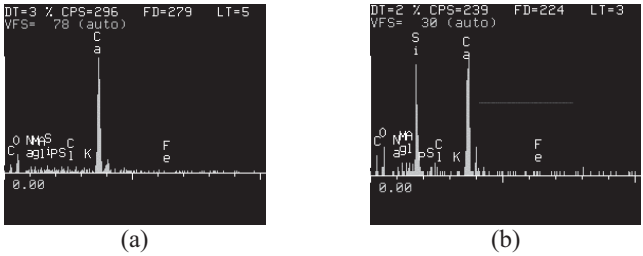

(a) (b)

Figure 3: SEM images showing the chemical composition of the ITZ for a) reference mortar sample (point 1 and 2) and b) M2 mortar sample (point 3 and 4)

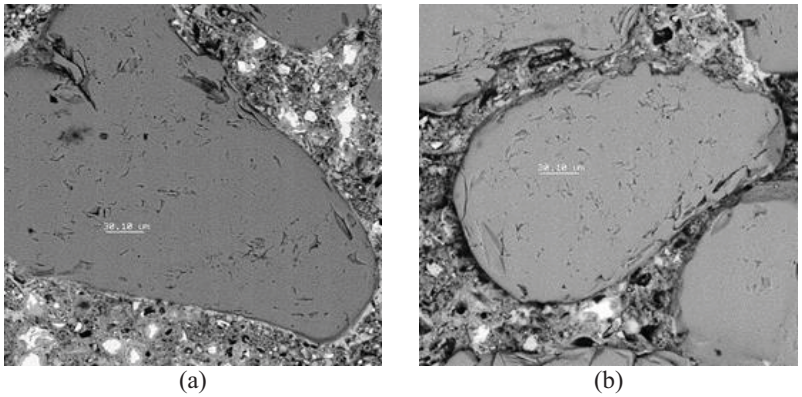

(a) (b)

Figure 4: SEM images showing the ITZ of mortar sample prepared using a) aggregates coated with nano-silica (M2) and b) nano-silica powder spread in the paste matrix

3.3 TGA (Thermogravimetric analysis)

Figure 5 (a) shows the TGA curves of 7-day hydrated mortars. The reference mortar had the highest slope (in the temperature range of 25 – 300 °C) whereas mortars prepared using coated aggregates (M2, M3, and M4) had overlapping curves. The highest slope for the reference mortar sample suggests that the mortar samples prepared using coated aggregates did not hydrate as much as the reference mortar sample. Although not shown, similar trends were observed for mortars hydrated for 3 days and 28 days.

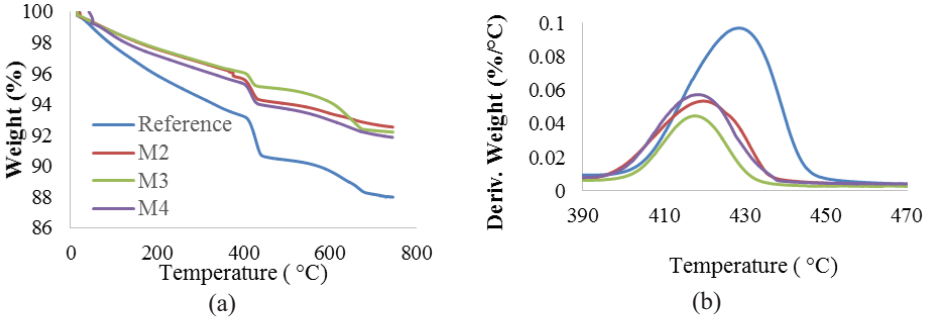

(a) (b)

Figure 5: a) TGA curve for 7-day hydrated mortars and b) DTG curve for 7-day hydrated mortars

Table 4: Percent mass change due to decomposition of portlandite for mortar samples

Mixture Type	Age (Days)		
	3 days	7 days	28 days
Reference	2.15%	2.39%	3.35%
M2	1.66%	1.29%	1.05%
M3	1.74%	0.83%	0.85%
M4	1.68%	1.16%	0.97%

Figure 5 (b) shows the plot of the derivative (with respect to temperature) of the weight of 7-day hydrated mortars in the temperature range from 390 °C to 470 °C (the temperature range in which $Ca(OH)_2$ decomposes). The area under the derivative curve provides a measure of the amount of $Ca(OH)_2$ in the sample. The reference mortar contained the highest amount of portlandite (i.e. $Ca(OH)_2$). No significant differences were observed in the portlandite content of three mortars prepared using coated aggregates (M2, M3, and M4). The lower portlandite content of M2, M3, and M4 mortars could be due to the combined effect of lower degree of hydration and pozzolanic reaction. The portlandite content of mortar samples after 3, 7, and 28 days of hydration was quantified and is presented in Table 4. As expected, the portlandite content of the reference mortar increased with age as hydration progressed. On the other hand, the portlandite content of mortars prepared using coated aggregates (M2, M3, and M4) reduced with age due to (presumably) pozzolanic effect of nano-silica. Since only 2 samples were tested for each mixture, a more detailed and statistically significant study needs to be conducted to provide further insights on the effect of this coating technique on the portlandite content.

3.4 Chloride ions penetration

As described in AASHTO T357 [20], silver nitrate solution was used to determine the depth of chloride ions penetration in mortar specimen. The depth of penetration for reference, M2, and M4-modified mortar sample is shown in Figure 6. As expected, the penetration depth was largest for the reference mortar sample. The chloride penetration depth for M4-modified mortar sample is half the chloride penetration depth of reference mortar sample. The non-steady state diffusion coefficients were 2.1 x 10^{-11} m^2/s, 9.3 x 10^{-12} m^2/s, and 3.23 x 10^{-12} m^2/s for reference, M2, and M4-modified mortar respectively. The reduction of almost one order of magnitude in chloride diffusion coefficient could increase the service life of concrete structures significantly [22].

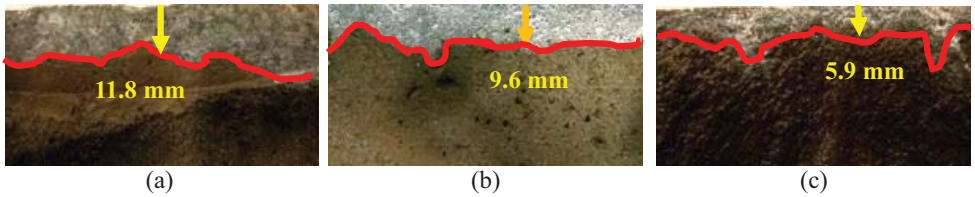

(a) (b) (c)

Figure 6: Depth of penetration of chloride in a) reference mortar sample, b) M2 mortar sample, and c) M4-modified mortar sample

4 CONCLUSION

Mortar prepared using aggregate coated with nano-silica showed higher compressive strength compared to mortar prepared using virgin aggregate. Mortars with aggregate coated

with 10 % (by weight) of colloidal nano-silica had compressive strength which was 30 % greater than the reference mortar samples after 28 days of hydration. However, allowing the coated aggregates to dry prior to mixing resulted in agglomeration of nano-silica, which was detrimental for strength development of M3 and M4 mortars (containing aggregate coated with 17.5 % and 25 % of colloidal nano-silica respectively). The detrimental effect of drying of the coat of nano-silica prior to mixing was confirmed by the results of the 7-day compressive strength of mortars prepared with aggregates used in the preparation of the mixture immediately after coating them with 25 % (by weight) of colloidal nano-silica (M4-modified). That strength was 50 % higher than the 7-day compressive strength of reference mortars and the 28-day compressive strength of mortar prepared using aggregates which were allowed to dry after coating them with 25 % (by mass) colloidal nano-silica (M4). The targeted application of nano-silica on surfaces of aggregate produced a denser ITZ for M2 and M4-modified mortar sample when compared to the ITZ of reference mortar and mortar prepared by dispersing the same amount of nano-silica powder throughout the entire paste matrix.

Using nano-silica coated aggregates reduced the portlandite content of 28-day hydrated mortar by a multiple of three. The reduction of portlandite content could be partially attributed to the lower degree of hydration observed in M2, M3, and M4 mortars as opposed to reference mortar samples.

The non-steady state diffusion coefficient for M4-modified mortar was approximately one order of magnitude lower than that the diffusion coefficient for reference mortar. However, further work is required to compare the diffusion coefficients of mortars prepared using targeted application of nano-silica on aggregate surface and mortars prepared by distributing the same amount of nano-silica throughout the paste matrix.

5 REFERENCES

[1] Muñoz, J.F., Meininger, R.C., and Youtcheff, J., 'New possibilities and future pathways of nanoporous thin film technology to improve concrete performance', *Transp. Res. Rec. J. Transp. Res. Board.* **2142** (2010) 34–41.
[2] Gonilho, C., Castro-gomes, J., and Oliveira, L.P.De., 'Influence of natural coarse aggregate size , mineralogy and water content on the permeability of structural concrete', *Constr. Build. Mater.* **23** (2009) 602–608.
[3] Scrivener, K.L., Bentur, A., and Pratt, P., 'Quantitative characterization of the transition zone in high strength concretes', *Adv. Cem. Res.* **1** (1988) 230–237.
[4] Diamond, S. and Huang, J., 'The ITZ in concrete - A different view based on image analysis and SEM observations', *Cem. Concr. Compos.* **23** (2001)179–188.
[5] Ollivier, J.P., Maso, J.C., and Bourdette, B., 'Interfacial transition zone in concrete', *Adv. Cem. Based Mater.* **2** (1995) 30–38.
[6] Leemann, A., Münch, B., Gasser, P., and Holzer, L., 'Influence of compaction on the interfacial transition zone and the permeability of concrete', *Cem. Concr. Res.* **36** (2006) 1425–1433.
[7] Diamond, S. and Kjellsen, K.O., 'Scanning electron microscopic investigations of fresh mortars: Well-defined water-filled layers adjacent to sand grains', *Cem. Concr. Res.* **38** (2008) 530–537.
[8] Scrivener, K.L., Crumbie, A.K., and Laugesen, P., 'The Interfacial Transition Zone (ITZ) Between Cement Paste and Aggregate', *Interface Sci.* **12** (2004) 411–421.
[9] Tokyay, M. and Tahir, C., 'Effect of coarse aggregate size on interfacial cracking under uniaxial compression', *Mater. Lett.* **57** (2002) 828–833.
[10] Winslow, D.N., Cohen, M.D., Bentz, D.P., Snyder, K.A., and Garboczi, E.J., 'Percolation and pore structure in mortars and concrete', *Cem. Concr. Res.* **24** (1994) 25–37.
[11] Garboczi, E.J. and Bentz, D.I., 'Modelling of the microstructure properties of concrete', *Constr. Build. Mater.* **10** (1996) 293–300.
[12] Jiang, L., 'The interfacial zone and bond strength between aggregates and cement pastes incorporating high volumes of fly ash', *Cem. Concr. Compos.* **21** (1999) 313–316.
[13] Wong, Y.L., Lam, L., Poon, C.S., Zhou, F.P., 'Properties of fly ash-modified cement mortar-aggregate interfaces', *Cem. Concr. Res.* **29** (2000) 1905–1913.
[14] Caliskan, S., 'Aggregate / mortar interface : influence of silica fume at the micro- and macro-level', *Cem. Concr. Compos.* **25** (2003) 557–564.

[15] Ping, X.I.E. and Beaudoin, J.J., 'Modification of transition zone microstructure - Silica fume coating of aggregate surfaces', *Cem. Concr. Res.* **22** (1992) 597–604.
[16] ASTM C778-13, 'Standard specification for standard sand', ASTM international , West Conshohocken, PA, 2013.
[17] ASTM C305-14, 'Standard practice for mechanical mixing of hydraulic cement pastes and mortars of plastic consistency', ASTM international, West Conshohocken, PA, 2014.,
[18] ASTM C128-15, 'Standard test method for relative density (specific gravity) and absorption of fine aggregate', ASTM international, West Conshohocken, PA, 2015.
[19] ASTM C109/C109M-16a, 'Standard test method for compressive strength of hydraulic cement mortars (using 2-in . or 50-mm cube specimens), ASTM international, West Conshohocken, PA, 2016,
[20] AASHTO T 357-15, 'Standard method of test for predicting chloride penetration of hydraulic cement concrete by the rapid migration procedure', American Association of State Highway and Transportation Officials, 444 North Capitol Street, suite 249, Washington D.C., 2015.
[21] NT BUILD 492, 'Concrete, mortar and cement-based repair materials: chloride migration coefficient from non-steady-state migration experiments', NORDTEST, P.O. Box 116, Espoo, Finland 02151, http://210.42.35.80/G2S/eWebEditor/uploadfile/20110819235419966.pdf
[22] Bentz, D.P., Snyder, K.A., Cass, L.C., and Peltz, M.A., 'Doubling the service life of concrete structures. I: reducing ion mobility using nanoscale viscosity modifier', *Cem. Concr. Compos.* **30** (2008) 674–678

Sensitivity of Reactivity Test Methods to the Fineness of Supplementry Cementitious Materials

Anuj Parashar, Vineet Shah and Shashank Bishnoi

Department of Civil Engineering, IIT Delhi, India

ABSTRACT

Reactivity of pozzolanic materials highly depends upon their fineness. Generally quality of calcined clay pozzolana is very fine and reacts faster than other pozzolanic materials. Reactivity test methods, which do not consider the fineness as an important factor can create the hindrance for their actual strength potential when used in mortar or concrete. This study compares the pozzolanic reactivity of different supplementary cementitious materials (SCMs) after changing fineness using different methods. For this purpose, one type of calcined clay, one fly ash and one slag was selected. The SCMs were ground to the higher fineness and their reactivity was compared with the original state. Different test methods such as lime reactivity, Chapelle's test and isothermal calorimetry was tried for the reactivity study before and after changing the fineness. A clear difference in the compressive strength of cement mortar cubes and lime reactivity cubes were observed. Similar trend was observed with the help of calorimeter. In the case of Chapelle's test, no variation on the calcium consumption was observed by altering the fineness of SCMs. This behaviour was also confirmed for fly ash sample with induction coupled plasma optical emission spectroscopy (ICP-OES). It was concluded that the methods which consider the factor of fineness while accounting the reactivity can be best suitable for the realistic reactivity potential of SCMs.

Keywords: Supplementary cementitious materials, fineness, reactivity methods.

1 INTRODUCTION

Reactivity of pozzolanic materials highly depends upon their fineness. Generally quality of calcined clay pozzolana is very fine and reacts faster than other pozzolanic materials. Reactivity test methods, which do not consider the fineness as an important factor can create the hindrance for their actual strength potential when used in mortar or concrete. This study compares the pozzolanic reactivity of different supplementary cementitious materials (SCMs) after changing fineness using different methods. For this purpose, one type of calcined clay, one fly ash and one slag was selected. The SCMs were ground to the higher fineness and their reactivity was compared with the original state. Different test methods such as lime reactivity, Chapelle's test and isothermal calorimetry was tried for the reactivity study before and after changing the fineness. A clear difference in the compressive strength of cement mortar cubes and lime reactivity cubes were observed. Similar trend was observed with the help of calorimeter. In the case of Chapelle's test, no variation on the calcium consumption was observed by altering the fineness of SCMs. This behaviour was also confirmed for fly ash sample with induction coupled plasma optical emission spectroscopy (ICP-OES). It was concluded that the methods which consider the factor of fineness while accounting the reactivity can be best suitable for the realistic reactivity potential of SCMs.

Reactivity of supplementary cementitious materials (SCMs) highly depends on their fineness and that is why improving the fineness is also considered as one of the promising

technique for accelerating their early age reaction [1]. Another advantage of improving the fineness of SCMs, that it helps in increasing the filler effect and thus causes the higher degree of reaction at the early age [2]. Higher the fineness of SCMs, higher will be the heat of hydration and this behaviour in most of the case is due to the filler effect except for the calcined clay in which reactive alumina increases the heat of hydration [3-4]. Improving the fineness may also cause higher water demand but overall it improves the various properties of concrete in different ways. Of course, these facts are widely known and studied by many researchers for different materials [1-4] but no one observed the effect of fineness on the sensitivity of the methods for testing their reactivity.

There are various different methods available today for the testing of pozzolanic behaviour of SCMs. The most widely used methods can be divided on the basis of their phenomenon for observing the reactivity. Few methods are based on the mechanical properties such as compressive strength [6] whereas some are chemistry-based methods and observes the consumption of calcium ion during the pozzolanic reaction [6]. There is no doubt about the fact that actual potential of any SCM can only be obtained in the presence of ordinary portland cement (OPC) because of the realistic conditions [5]. That is why it can be stated that almost every method predict the reactivity of SCMs only in the presence of favourable conditions which are close to the OPC but not the same.

In this study, an attempt was made to figure out the effect of fineness of SCMs on their pozzolanic reactivity with the help of different reactivity methods. Later the reactivity was compared with the actual potential of SCMs in the presence of OPC+SCMs mortar cubes cured at various stages. Different techniques were used for this purpose and finally, the sensitivity of reactivity test methods affected by the fineness of SCMs was discussed.

2 MATERIALS

For this study, one type of calcined clay having low kaolinite content and contains quartz (K) in it was procured from Bhuj, Gujarat region of India. One type of fly ash (FA) was selected from the thermal power plant near Delhi, India and one type of slag (S) was procured from Goa, India.

Total 3 different SCMs were ground to the higher fineness i.e. fine clay (K-F), fine fly ash (FA-F) and fine slag (S-F). Lab scale ball mill was used for the grinding. Raw materials were characterised for various physical and chemical properties with the help of X-Ray florescence, particle size distribution and reported in Table 1 and Table 2 respectively.

Table 1: Chemical and physical properties of SCMs

No.	Constituent %	K	FA	S
1	Loss on ignition	4.24	1.11	0.32
2	Silica SiO_2	52.70	58.82	32.26
3	Iron Fe_2O_3	4.00	6.19	1.93
4	Aluminium Al_2O_3	38.14	30.62	23.16
5	Calcium CaO	0.09	1.01	33.88
6	Magnesium MgO	0.02	0.41	7.01
7	Sulphate SO_3	0.10	0.12	Traces
8	Sodium Na_2O	0.18	0.19	0.34
9	Potassium K_2O	0.17	1.30	0.65
10	Combined H_2O	---	---	---
11	Reactive Silica (SiO_2)	---	29.42	31.58
12	Manganese Mn_2O_3	---	---	0.30
13	Specific Gravity	2.67	2.26	2.87

Table 2: Particle size distribution of SCMs

SCMs	Particle size volume		
	d(10) µm	*d(50)* µm	*d(90)* µm
FA	10.5	44.0	166.0
FA-F	1.54	11.9	42.0
K	3.46	18.7	95.0
K-F	1.76	4.97	31.9
S	3.28	12.47	31.90
S-F	1.21	3.96	24.95

3 METHODS

Total 4 different techniques were used for the study. One method, standardised as per IS 1727-1967 was adopted to observe the mechanical performance of lime mortar cubes [5]. Another standardised method as per French standard NF P18-513 for Chapelle's test was used due to its short period of testing and widespread knowledge [6-7]. Induction coupled plasma optical emission spectroscopy (ICP-OES) was also used to check the solubility of silica (Si) and alumina (Al) only for FA and FA-F for confirming the solubility behaviour at high temperature. One calorimetry-based technique was used to observe the difference in heat release from the paste of SCMs with calcium hydroxide (CH). Finally, the data obtained from different methods was compared with the actual strength potential of SCMs in cement mortar cubes. A brief description of all the methods is explained in the next section.

3.1 Lime reactivity

Observation of mechanical property such as compressive strength of mortar cubes containing SCMs seems to be more close to the realistic conditions. In lime reactivity test method, a similar approach was adopted. As per this method the mortar cubes with lime and SCMs need to cast as per the volume based mix design approach. The flow of mortar paste needs to be observed for obtaining the same workability of different SCMs. Finally, after casting the standard cubes of 5 cm in size, the moulds need to store in the room condition at 27 ± 2°C for 2 days. During this period the samples need to be covered with a glass plate and a wet piece of cloth over it. After two days the samples need to be demoud and then need to kept under accelerated conditions of 50° ± 2°C and 90 ± 5% humidity for another 8 days. Finally, in the end, the samples need to be tested at the age of 10 days under compression. A brief description of the procedure can be found in the literature [5].

3.2 Chapelle's Test

Need of a fast test method to check the reactive of any SCM, emphasise the need of accelerating the testing conditions. In this method, the reactivity of SCM is accelerated into two different ways. First, by providing excess of calcium in the presence of very high water/powder ratio causing fast dissolution. Secondly, by performing this test at 85± 5°C for 16 hrs. This test observes the ultimate reactivity of any SCM. Though it is only standardised technique for calcined clay but it is very well used for many different SCMs such as FA, S, natural pozzolana, etc. [7,9-10]. This method is also criticised by few authors due to high-temperature conditions [8]. Another major disadvantage is that, in such testing conditions, the crystalline quartz also becomes reactive and consumes calcium from the system [9-10]. That is why sometimes this method can overestimate the reactivity of SCMs. As per the method, 2 gram of calcium oxide with one gram of SCM need to stirrer with 250 ml of water for 16 hours at 85 ± 5°C. After this step, sugar solution need to be mixed before filtration of the solution under vacuum condition. The filtered solution need to be tested for the concentration

of Ca ions and thus indicates its consumption. A brief description of this method are also available in the literature [6-7].

3.3 Isothermal Calorimetry

This technique is quite flexible and can be applied in different fields. Some of the interesting applications of this technique are understanding the cement hydration (also for binary and ternary cement), gypsum adjustment in the cement mix, the pozzolanic reactivity of any SCMs in calcium hydroxide (CH) or cement system, observation of filler and nucleation during OPC hydration, etc. [1,3-4,7,10-11]. For this study, isothermal calorimeter having 8 channels was used. Paste samples were prepared with SCM and CH at 1:1 ratio. After dry mixing the powder for 2 minutes, double distilled water was added to maintain the *w/p* ratio of 0.6. After continuous mixing for 2 min with the help of vortex mixer, a total of 80 gm of paste was kept in each sample cell. Overall time required for the sample preparation was less than 5 min. Finally, the data was recorded at 27°C for 7 days.

3.4 ICP-OES

This technique is very well known for the characterisation of hydrated cement pore solution. In modern research sector, this is one of the powerful tool for understanding the solubility rate of different phases in SCMs while kept under alkaline condition. The rate of solubility of Si and Al can explain the phenomenon of reactivity of any SCM. Recently use of this study for observing the degree of reactivity of FA was reported in the literature [12]. The similar technique was adopted in this study. A high pH alkaline solution having 0.5 M concentration of sodium hydroxide was prepared with de-ionised ultra pure water having 18.2 Ω conductivity. Containers or any type of glassware used for this testing was intensively clean with the help of detergent, acid and pure water with 3 cycles for each. Finally, 0.1 gm of FA was added in a plastic container contains 100 ml of solution. The samples were stored at 60°C in an oven for testing at the age of 1,3, and 7 days. Higher temperature was selected to finish the complete dissolution in a shorter period and to observe the dissolution behaviour of SCMs.

3.5 Mortar strength

It is the only method, which monitors the effect of every physical and chemical factor of SCMs reactivity. That is why it is necessary of compare the reactivity date from other method with the compressive strength data of this method. The only disadvantage of this method is its time requirement. For a slow reactive pozzolana such as FA, it can take up to 90 or 120 days to achieve the equilibrium. However, this method is also modifies by accelerating the curing temperature. It is necessary to note that increasing temperature also changes the kinetics of chemistry and thus can provide higher values of reactivity [8]. Too high temperature can decrease the hydration of OPC resulting in the underestimation of SCMs reactivity. With this method the difference in strength of SCMs at two different fineness was observed. The standard mortar cubes of 7.06 cm as per IS were cast with 1:3 ratio of binder and standard sand with a fix w/b ratio of 0.45 for all the mix. The binder was used in a proportion of 70% OPC with 30% SCM. Three different grades of standard sand were added equally. Finally, the cubes were demoulded after one day of casting and water cured at 27°C for the testing at 3, 7 and 28 days age.

4 RESULTS AND DISCUSSION

4.1 Lime reactivity test

The compressive strength data of the cubes tested at the age of 10 days under compression loading rate of 0.6 kN/min. The ultimate failure load was recorded and is plotted in Figure 1. It can be clearly observed that the strength of finer SCMs was high in comparison with the original fineness. The maximum increase was observed in the case of FA that was approximately 238%. This high increase in strength explains the high solubility of reactive silica due to the higher surface area. The order of reactivity as per this method was S-F>S>K-F>K>FA-F>FA. These results clearly indicate the effect of fineness on the reactivity of different SCMs.

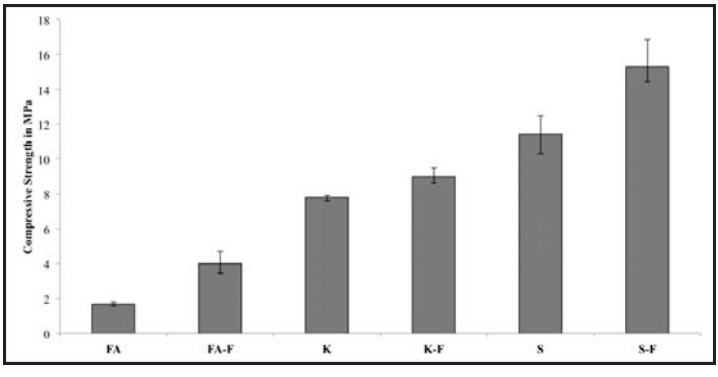

Figure 1: Compressive strength data of lime reactivity mortar cubes.

4.2 Chapelle's Test

The results of this test are reported in Table 3 as the amount of Ca consumed. Clay was found to be the most reactive SCM. The results were not similar to the lime reactivity data were S-F was observed to be the most reactive. This phenomenon can be explained due to the fact that slag does not requires much of CH for its reaction and thus showing the lower consumption of Ca in this test [11]. Other surprising fact observed about this method was the approximately same calcium consumption of an SCM having different fineness. In the case of K and K-F, the same amount of Ca consumption was observed even after improving *d(50)* from 18.7 μm to 4.9 μm. Similar observations were noticed for FA, FA-F and S, S-F. The reason of this fact could be the high solubility of SCMs in the presence of high amount of water and high temperature. Due to it, the solubility of reactive phases becomes independent to the surface area and consumes the same amount of Ca for different fineness levels. This can be considered as one of the shortcomings of this method as it was found to be non-sensitive to the surface are. This disadvantage can cause variation in the actual strength potential especially in the case of coarse SCMs. Another doubt created by this test was the consumption of Ca by FA. As it is very well reported in many different studies that this test gives positive reactivity for crystalline quartz [7,9-10], so in case of SCMs containing quartz such as FA, this test may be helpless for calculating the actual potential.

Table 3:Calcium consumed by SCMs in Chapelle's test

SCM	Quantity of CH consumed/gram of SCM (mg)
FA	306.73
FA-F	306.29
K	852.53
K-F	853.67
S	665.78
S-F	666.21

4.3 ICP-OES

The extracted samples at the age of 1,3 and 7 days were diluted with pure water in order to adjust the pH value for the analysis. Finally, the standard solution of Si, and Al were prepared with different concentration for cross checking the calibration of the instrument. The data obtained is plotted in Figure 2. From this analysis, two major observations came out. One was that the high temperature allows quick rate of dissolution of FA. The second fact was the rate of dissolution was not depended on of the fineness of FA. It was not surprising because similar results were obtained in Chapelle's test. This study also confirms the findings of Chapelle's test.

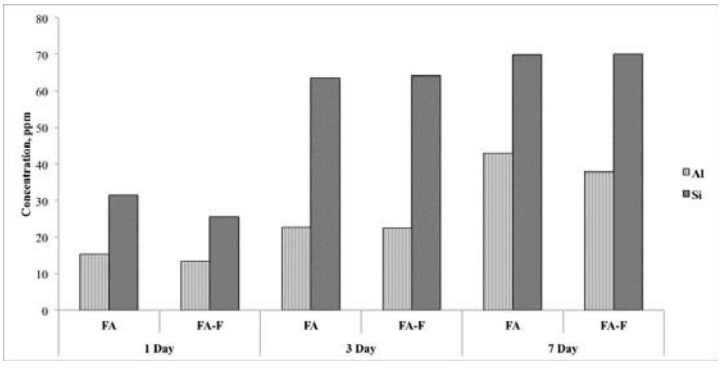

Figure 2: Concentration of Al and Si ions for FA and FA-F observed by ICE

4.4 Isothermal Calorimetry

The cumulative heat released by the reaction between CH and SCMs was calculated by differentiating the power data with respect to time. The final values are plotted in Figure 3. The heat release was maximum for S-F. The observation of this test was in the identical order of lime reactivity test. From this study, FA and FA-F are proved to be least reactive SCM among all. The final values of energy were in the order of S-F>S>K-F>K>FA-F>FA.

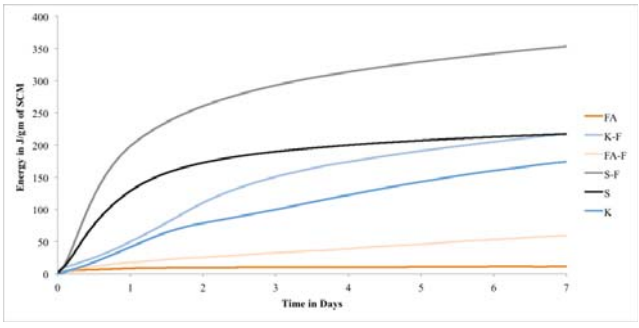

Figure 3: Cumulative energy data recorded calorimeter

4.5 Mortar Strength

Finally, to confirm the claim of reactivity by different test methods, the cement mortar cubes were tested for compressive strength at the age of 3, 7 and 28 days. The mean strength data of 3 cubes with error bars is plotted in Figure 4. It can be clearly observed from this test that the fineness of SCMs plays a major role in the cement hydration for strength development. The S-F gain maximum strength among all the SCMs and FA was minimum. A surprising change in the strength data was observed by increasing the fineness of SCMs, especially for S-F and FA-F. Interestingly FA-F gains more strength than K-F, which can also be due to the lower kaolinite content in the clay. The difference in the strength for K-F was barely noticeable when compaired with K. The reason of that could be the improper mixing. Overall, this data proves a significant change in cement mortar strength data due to the change in fineness of SCMs.

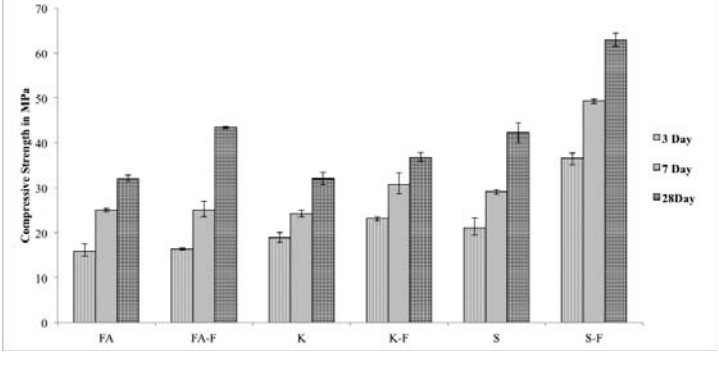

Figure 4: Compressive strength of cement mortar cubes

From the findings of compressive strength data, we can simply compare the trends of reactivity observed by other methods. The lime reactivity tetst gives the almost similar trend for the result observed by mortar strength except for FA-F. The reason of which could be the fact that FA is slow reactive pozzolana and at full hydrated stage can react equally or more than S. Lower kaolinite content of K clearly influences the strength data which Chapelle's test was not able to measure properly. As per Chapelle's test, the results are totally opposite in the case of clay. The reason of that could be due to the fact that clay was of low quality and contains quartz in it. The quartz content present in the clay may lead to significant increase in

the consumption of Ca ions in the Chapelle's test [7,9-10]. Moreover, the same solubility of FA having different fineness at higher temperature was also confirmed by ICP OES data.

Data from isothermal calorimetry shows high reactivity of clay that could be due to the reactive alumina present in it, which leads to the high heat release during its dissolution and reaction [3,4,7,10]. The very low reactivity of FA and FA-F was observed which is not in favour of mortar strength test.

5 CONCLUSIONS

The sensitivity of different reactivity test methods against the fineness of 3 different SCMs were studied using lime reactivity strength test, Chappelle's test, and isothermal calorimetry. ICP-OES was used just to check the solubility of Si and Al from FA and FA-F at 60° C. Finally the trends were compared with the actual cement mortar strength data made with 30% replacement of cement with SCMs. Following conclusions can be drawn based on the observation.

1) The lime reactivity test and isothermal calorimeter were found to be suitable for testing the reactivity of SCMs with different fineness.
2) Chapelle's test was found to be unsuitable due to its zero sensitivity for the different fineness of SCMs. This phenomenon was also proved by ICP-OES.
3) Reactivity of quartz in Chapelle's test can be an issue for predicting the actual potential of any low-grade SCMs, and especially in the case of low grade calcined clay.

REFERENCES

[1] Mounanga, P., Khokhar, M. I. A., Hachem, R. E., and Loukili, A., 'Improvement of the early-age reactivity of fly and blast furnace slag cementitious systems using limestone filler', *Materials and Structure*, **44** (2011) 437-453.

[2] Koop, Y., and Peled, A., 'Setting behaviour of blended cement with limestone: influence of particle size and content', *Materials and Structure*, **49** (2016) 439-452.

[3] Antoni, M., Rossen, J., Martirena, F., and Scrivener, K., 'Cement substitution by a combination of metakaolin and limestone', *Cement & Concrete Research*, **42** (2012) 1579-1589.

[4] Andres, L. M. V., Antoni, M. G., Diaz, A. D., Hernandez, J. F. M., and Scrivner, K. L., 'Effect of fineness in clinker-calcined clay-limestone cements', *Advances in Cement Research*, **27(9)** (2015) 546-556.

[5] IS: 1727-1967, 'Methods of test for pozzolanic materials', *Bureau of Indian Standards* 2004.

[6] NF P18-513, 'Additions pour beton hydraulique metakaolin' *AFNOR* 2012.

[7] Snellings, R., and Scrivener, K. L., 'Rapid screening test for supplementary cementitious materials: past and future', *Materials and Structure*, **49** (2016) 3265-3279.

[8] Aubert, J. E., Segui, P., Husson, B., and Measson, M., 'A method developed to quantify lime and gypsum consumed by mineral additions', *Cement & Concrete Composites*, **34** (2012) 847-880.

[9] Benezet, J. C., and Benhassaine, A., 'Grinding and pozzolanic reactivity of quartz powders', *Powder Technology*, **105** (1999) 167-171.

[10] Avet, F., Snellings, R., Diaz, A. A., Haha, B. M., and Scrivener, K., 'Development of new rapid, relevant and reliable (R^3) test method to evaluate the pozzolanic reactivity of calcined kaolinitic clays', *Cement & Concrete Research*, **85** (2016) 1-11.

[11] Kocaba, V., Gallucci, E., and Scrivener, K. L., 'Methods for determination of degree of reaction of slag in blended cement pastes', *Cement & Concrete Research*, **42** (2012) 511-525.

[12] Haha, M. B., Weerdt, K. D., and Lothenbach, B., 'Quantification of the degree of reaction of fly ash', *Cement & Concrete Research*, **40** (2010) 1620-1629.

A Review on Biofortified Self-Healing Concrete

Sachin Tiwari[1], Shilpa Pal[1], Rekha Puria[2] and Vikrant Nain[2]

[(1)]Department of Civil Engineering, School of Engineering, Gautam Buddha University, Greater Noida, U.P., India

[(2)]School of Biotechnology, Gautam Buddha University, Greater Noida, U.P., India

ABSTRACT

Concrete is widely used as construction material due to its low cost and high compressive strength. However, low tensile strength and susceptibility to chemical attack leads to the formation of cracks. This not only reduces the life of infrastructure but also burdens economy of any nation. Continuous efforts are made over the years for development of efficient repair methods. Physical and chemical methods aid in repair of cracks but their usage is limited. In recent years, the self-healing ability of concrete by bacteria is being extensively explored for development of sustainable concrete. This review focuses on the self-repair methods with special emphasis on the usage of bacteria in crack healing. Self-repair primarily means the ability to heal damages with available environmental resources. There are some challenges to make a durable biofortified concrete such as the viability of various types of bacterial cells and its effect on the mechanical properties. Evaluation of self-healed concrete can be done by destructive and non - destructive methods at macro, micro and nano level. The paper concludes with the future works which need to be done for making a sustainable biofortified concrete.

Key Words: Biofortified concrete, viability, mechanical properties, destructive and non-destructive methods

1 INTRODUCTION

Concrete is used for making durable and sustainable structures due to its high compressible strength, resilience, compatible behaviour with reinforcement bars, low price and desirable casting. However, attributes like low tensile strength and susceptibility to chemical attack reduces durability which results in the formation of different types of cracks such as thermal, mechanical and chemical. While thermal cracks are formed due to the temperature variation in the concrete, chemical cracks are formed due to the chemical reaction of acids with reinforcement bars [37]. Chemicals permeate cracks and react with reinforcement bars, causing initiation of corrosion which breaks the bond between the concrete and reinforcement [8]. Mechanical cracks are generated on the concrete surface due to impact loading and vibrations. Regular maintenance of concrete based structures is required to ensure their integrity and durability over a long time [30,14]. The expenses on maintenance

significantly affect national economy. As per the estimate of the Construction Industry Development Council (CIDC), New Delhi, 32,000 crores are required to rebuild India's damaged concrete structures [23]. Actually, there is a dearth of cost effective efficient methods of repair. The most commonly used ways to heal the cracks includes the application of paste of putty, mortar and adhesives on the cracked surfaces. This requires regular manual inspection of damages which is labour intensive, time-consuming and costly. Over the years, continuous efforts have been made for the development of effective methods of repair. The recent and most appealing is the development of autonomous methods of crack healing largely called as self-healing. Self-healing basically means the ability to detect own problem/damages and heal the damage partially or completely by chemical or biological based materials/cells without any manual activity [20,9]. There are three approaches and processes to develop self-healing concrete [54] (i) Natural based (ii) Chemical based, and (iii) Biological based (Figure 1).

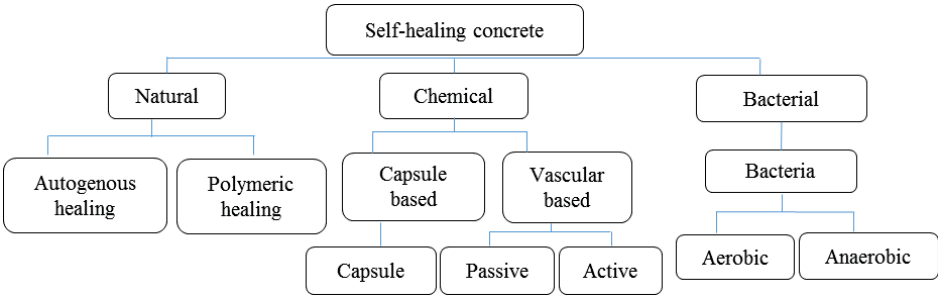

Figure 1: Concrete Self-healing approaches

Natural based or natural self-healing process, also known as "intrinsic self-healing", is further categorized as autogenous healing and polymeric healing. In autogenous healing, crack is filled by hydration of cement particles and dissolved calcium hydroxide in the presence of water. The formation of $CaCO_3$ and expansion of the cement particles mostly occur simultaneously [54]. The swelling of CSH helps to block the cracks [71]. Natural self-healing process heals the crack range of 0.1 mm to 0.3 mm [22,30]. Cracks are partially healed by impurities in the water and cementitious materials such as magnesium silicates and calcium [41]. In polymeric healing, polymer modified concrete (PMC) is used to fill the crack. It consists of homogenized polymer concrete matrix which is composed of cement, aggregates, polymers and binders which provide the adhesive property to form a monolithic network.

In the chemical based healing process, adhesive agent or binders are embedded into the concrete matrix for crack healing. This embedding is carried by two methods (i) capsule-based self-healing and (ii) vascular-based self-healing [54]. In the capsule based self-healing micro to nano size capsules are added to the concrete matrix which ranges in size from 5 to 300 µm. [47]. Microcapsules are filled in with glue (epoxy resin) and a hardener (acrylic resin) [38]. White et al. [66] used microencapsulation process with adhesive agent in self-healing concrete. They observed that when cracks are formed in the concrete due to loading or stresses, filled capsules with adhesive agents activates and heal the cracks.

In the vascular self-healing process, adhesive agents are released from hollow pipettes and vessel networks containing glue. The insertion of vessels and pipettes is done in concrete matrix by two ways active and passive. In active method, vessels arrangement is provided inside the concrete which associates with an exterior supply of adhesive agents. In passive method, hollow pipettes are provided in concrete specimens which contain adhesive agents inbuilt [13].

The third way is self-healing by bacteria, which is possible due to biomineralization wherein bacteria produce minerals like $CaCO_3$ using environmental resources via metabolic activities. This $CaCO_3$ can seal the cracks generated in concrete based infrastructures. This has been successfully employed in sand consolidation (ash) [11] and monument repair [40,56]. It's an economic approach with no bearing on the environment. The aspect of the use of bacteria in fortification of concrete is presented in the current review.

1.1 Biofortification: fortification of concrete by bacteria

Largely, bacteria pose the ability to generate minerals from the environmental samples. Numbers of these bacteria can biomineralize $CaCO_3$ from different sources as their metabolic activity e.g., Ureolytic bacteria can catalyze the conversion of Urea to ammonia and CO_2 [46]. The high pH in cement facilitates the conversion of CO_2 to bicarbonate and carbonate ions which precipitate with environmental calcium ions to calcium carbonate minerals. Though the production of ammonium ions increases the environmental load of nitrogen, fortified cement with decreased permeability is generated. Further certain bacteria can generate calcium carbonate by dissimilatory reduction of sulfates at high pH. Bacillus cohnii, Bacillus pseudofirmus and Bacillus alkalinitrilicus can induce precipitation of $CaCO_3$ by oxidation of organic compounds e.g., acetate and lactate [25,27,67]. Studies are still going on for the screening of bacteria with high metabolic ability for generation of $CaCO_3$ with high dependence on naturally available resources.

1.2 Bacteria based crack repair

The repair of cracks generated in concrete based infrastructures can be achieved by two methods using bacteria. One is direct method wherein, bacteria can be applied on the concrete surface by immersion, by spraying or coating with a layer of bacteria [26]. Though this approach is straightforward and easy, the successful application is hampered by various environmental factors e.g., temperature, pH [21,7]. High temperature significantly affects morphology of crystals, influence bacterial activity, enzymatic activity, solubility and reaction rate. Therefore, various optimizations are required to assure stability and durability of surface treatments.

Second method is self-healing of damages by bacterial growth inside concrete structure. The bacteria along with the required nutrient and other porous materials are impregnated in concrete at the time of mixing [65]. These bacteria are expected to seal/plug the freshly formed cracks wherever generated by their metabolic activities. Though approaches seem feasible and have been shown to seal the cracks, several concerns still need to be answered before their commercial application.

2 CHALLENGES IN DEVELOPMENT OF BIOFORTIFIED CONCRETE

2.1 Viability of bacteria

Table 1 gives an insight into the details of the bacteria encapsulated in mortar/concrete specimens which are able to heal the crack of variable width.

Table 1: Studies on healing of artificial cracks by Bacteria (*= days, *B. = Bacillus)*

Ref	Bacteria	Specimen	Crack Dimensions (mm)	Crack Development Techniques	Healing (width in mm)
57	*B.sphaericus*	Concrete Cubes Cylinders	10 or 20 depth and 0.3 mm width 0.05-0.87 width	0.3 mm Copper plate Split Tensile test	20 mm depth
67	*B.alkalinitrilicus*	Mortar prism	0.05-1mm	Zinc plated steel bar stretched by tensile loading	0.46 mm in bacterial concrete
62	*B.sphaericus*	Mortar Prism Cylinders	0.35 width 0.25mm	Three-point bending	N.A.
3	*B.sphaericus*	Mortar cubes	3mm wide 13.4,18.8 and 27.2 mm depth	N.A.	27.2 mm depth
60	*B.sphaericus*	Reinforced prisms Cylinders	N.A.	Uniaxial tensile test	970 μm in bacterial series
64	*B.sphaericus*	Mortar Prism Cylinders	N.A.	Tensile test	0.5 mm in bacterial hydro-gels. 0–0.3 mm in non-bio hydrogels
52	*B. pseudofirmus*	Concrete Prism	N.A.	3-point bending	0.08 and 0.22 mm
44	*B.mucilaginous*	Concrete Prism	0.1 – 1	3-point bending	0.4 mm width
35	Alkali-resistant bacteria	Concrete Prism	0.1 to 1	Compression testing machine	0.3 mm width
43	*B. mucilaginous*	Mortar Specimen	50–100 μm.	Bending test	Cracks upto (50–100 μm)
36	*Alkaliphilic bacteria*	Cement Paste	N.A.	Compression test	0.18mm healed after 28d* 0.26mm healed after 40d* 0.48 mm healed after 80d*
15	*Diaphorobacternitroreducens*	Mortar	0.1–0.6 mm	Tensile Load	Up to 0.5 mm crack widths heal.
28	*B.subtilis*	Concrete	1 mm	Compression testing machine	N.A.
58	*B.Alkaliphilic*	Reinforced Concrete	350 μm	3-point-bending test	N.A.
16	*Diaphorobacternitroreducens Pseudomonas aeruginosa*	Steel bar	N.A.	Uniaxial tensile load	370 ± 20 μm in 28 days 480 ± 16 μm in 56 days

Studies are going on to find suitable entrapment methods/materials for identifying the bacteria with high viability and metabolic activity in concrete structure. It has been observed that the initial concentration of Bacillus*megaterium* was 8.3×10^4 cfu/ml and 9.0×10^4 cfu/ml cells in mortar and concrete samples which decreased to 3.2×10^4 cfu/ml cells and 5.2×10^4 cfu/m respectively at 28 days [4]. There was no change in the concentration of bacteria cells after 7 days. Jonkers et al. [27] incorporated *Bacillus cohnii* spores into the concrete matrix which were completely viable up to 9 days, but survival rate decreased after 22 and 42 days. *Bacillus mucilaginous L3* had lost the repair effect and decrease the viability after 60 days due to high alkaline environments [44]. Diverse alternatives have been exploited to improve the survival of bacterial cells in concrete based structures. Entrapment of bacteria in different polymers and other porous materials has shown promising results. The bacteria are entrapped

in silica gel or polyurethane [57], melamine formaldehyde based microcapsules [60], modified-alginate based hydrogel [61] porous light weight aggregates [28, 67], expanded clay [67] and diatomaceous earth [63] which alters the overall survival of bacteria in the concrete matrix. Bacillus sphaericus encapsulated in melamine formaldehyde based microcapsules was viable upto 56 days [60]. *Bacillus sphaericus* encapsulated in hydro gel and their viability was checked under UV irradiation, grinding and drying process but the spores were still viable after that [64]. Entrapment prevents damage of bacteria during casting of concrete as the bacteria encapsulated in light weight aggregate have increased upto 28 days [28].

Further work has been done with the bacterial spores. Spores are metabolically inactive highly resistant forms of bacteria. These remain trapped in structures and activates only under favourable conditions e.g., cracks leading to seepage of water, air and other nutrients inside the structure. Metabolic activity leads to sealing of gaps generated by damages. In order to understand the contribution of bacteria in crack healing, artificial cracks of variable width are generated in labs by various approaches. Commonly used bacteria in labs are of Bacillus species as they can survive at high pH. Table 1 highlights that the best healing has been shown by *Bacillus sphaericus* where cracks generated by tensile loading has been healed upto 970 μm [60]. Cracks of width 0.1 – 1.6 mm developed in mortar using tensile loading have been healed upto 0.5 mm by nitro reducers bacteria using *Bacillus sphaericus* [15].

2.2 Effect on mechanical properties of biofortified concrete

Addition of large volume of bacterial cells or nutrients or additives alters the mechanical properties of the concrete mix. Earlier studies have shown that addition of nutrients affects the strength of concrete. Addition of *Bacillus sp. CT-5 type of bacterial cell* increased the compressive strength of cubes by 40% of that of the control specimen [3]. *B. megaterium*, *B. licheniformis and B. flexus type of bacterial cell* increased compressive strengths of biofortified concrete beam specimen upto 12.1, 10.6, and 6.1% respectively as compared to control concrete specimens [29]. Use of other material such as light weight aggregates (LWA), Porous clay and diatomaceous earth have also been used by many researchers to enhance the viability of bacteria in concrete mix. In the encapsulation methods, water permeability decreases using hydrogel-encapsulated carbonate spores [64]. Bacterial concrete incorporated with light weight aggregate (LWA) and graphite nanoplatelets (GNP) resulted in an increase of 12% & 9.8% respectively in compressive strength as compared to controlled concrete specimens [28]. Concrete using different percentages of rice husk ash increased compressive strength by 9% and 11.8% at the age of 28 and 56d at 10% *RHA* [50]. There is a need to understand the effect of other additives materials such as wood ash, wood chips etc. which support microbial growth without altering/enhancing the mechanical/physical properties of concrete.

3 EVALUATION OF BIOFORTIFIED CONCRETE

The quality and healing properties of concrete specimens are examined by various physical and chemical tests, destructive, non-destructive testing at macro, micro and nano level which are elaborated in Table 2. Apart from the commonly used methods, there is a need to focus on new techniques such as SEM with EDX, XRD, Image processing, Coda wave interferometry and other nano level based tests to give a better insight into the healed concrete matrix. The schematic illustration of the biofortified concrete is given in Figure 2.

Table 2: Evaluation of healing efficiency using various structural tests

Type of tests	Tests	References
Chemical Test	Sulphate, Chloride, RCPT	[10], [55], [50], [49], [52], [41], [3]
Physical Test	Water Permeability, water Absorption, Porosity, Air permeability, Capillary Sorptivity, Fluidity test	[35], [48], [34], [58], [49], [55], [50] [24], [43], [70], [42], [36], [45], [1], [5], [51], [12],[64], [68],[41],[62], [31],[2]
Destructive test	Compressive test, Flexural test, Tensile Test, Toughness, Stiffness	[28], [10], [33], [34], [58], [74], [49] [55], [50], [24], [45], [1], [54], [6], [39], [72], [53], [18], [52], [5], [3], [2]
Non Destructive Test	XRD, SEM, ESEM, FTIR, UPV, TGA, Acoustic emission, X-ray Computed Tomography, Pullout test	[35],[36],[28],[33],[74],[49],[50], [17], [73], [24], [70], [42], [60], [36], [45], [1], [15], [72], [32], [35], [19]
Nano Structural test	Nanoscale Measurement	[72]
Image Processing		[35], [69], [43], [59], [52]
Oxygen Consumption Measurements		[58], [19]
Coda wave Interferometry		[33]
Absorption of CO_2		[43]
Zeta Potential		[70]

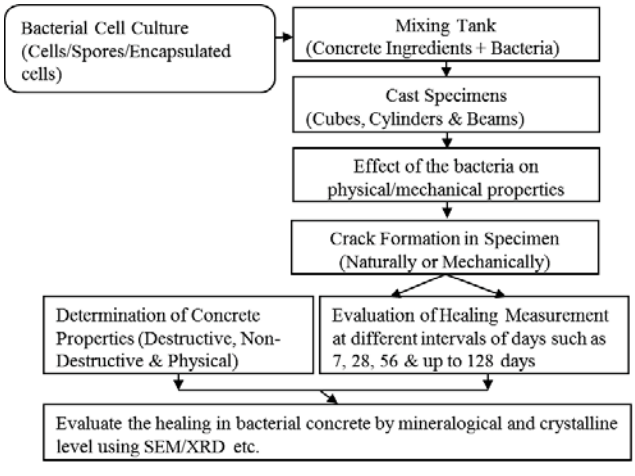

Figure 2: Schematic Illustration of Bio-fortified concrete

4 CONCLUSIONS

This review focuses on biofortification of concrete by bacteria. The ability of bacteria to generate minerals from the environment is exploited in the autonomous healing of concrete. Various species of Bacillus have been shown to repair the cracks to different extents. The crucial issue in usage of bacteria is unfavorable conditions prevalent in cement which drastically impacts the growth of bacteria. Continuous efforts are being made to improve the survival of bacteria in cement e.g., use of spores which are more resistant to harsh conditions and grow only under favorable conditions. Further entrapment of bacteria in polymers,

supplementation of additives e.g., porous clay and porous aggregate has been shown to improve the survival of bacteria and hence self-healing of cracks. The addition of growth factors improves the viability of bacterial cells but also impacts the mechanical properties of cement. Thereby optimization of growth media with insignificant impact on the sustainability of cement is highly desirable. We propose supplementation of bacteria with wood powder and ash as growth supporting material. These are expected to improve the viability of cells in concrete with better self-healing properties. Bacteria are highly diverse in nature with the ability to grow in wide range of environmental conditions. Most studies have been done with mixing of concrete with a single type of bacteria. We speculate that use of bacteria in combination should positively affect healing of damages in concrete e.g., use of bacteria with better biomineralization ability in combination with bacteria that can protect damages in reinforcements. Studies are presently going on establish the contribution of diverse additives and synergistic effect of different bacteria.

5 REFERENCES

[1] Abo-El-Enein, S.A., Ali, A.H., Talkhan, F.N. and Abdel-Gawwad, H.A., 'Application of microbial biocementation to improve the physico-mechanical properties of cement mortar', *H.B.R.C. J.* **9** (2012) 36–40.

[2] Achal, V., Mukerjee, A. and Reddy, M.S., 'Effect of calcifying bacteria on permeation properties of concrete structures', *J. Ind. Microbiol. Biotechnol*. **38** (9) (2011) 1229–1234.

[3] Achal, V., Mukerjee, A., and Reddy, M. S., 'Biogenic treatment improves the durability and remediates the cracks of concrete structures' *Constr Build. Mater*. **48** (2013) 1–5.

[4] Achal, V., Pan, X. and Özyurt, N., 'Improved strength and durability of fly ash-amended concrete by microbial calcite precipitation', *Eco. Eng.* 37 (2011) 554–559.

[5] Aldea, C.M., Song, W.J., Popovics, J.S. and Shah, S.P., 'Extent of healing of cracked normal strength concrete', *J. Mater. Civ. Eng.* **12** (1) (2000) 92–96.

[6] Bang, S.S., Galinat, J.K. and Ramakrishnan, V., 'Calcite precipitation induced by polyurethane-immobilized Bacillus pasteurii', *Enzyme Microb. Technol.* **28** (4 –5) (2001) 404–409.

[7] Barton, L. L. and Northup, D. E. 'Microbial Ecology', (Hoboken, John Wiley & Sons, Inc, 2011).

[8] Basheer, L., Kropp, J. and Cleland, D.J., 'Assessment of the durability of concrete from its permeation properties: a review', *Constr. Build. Mater*. **15** (2–3) (2001) 93–103.

[9] Bekas, D.G,Tsirka, K., Baltzis, D. and Paipetis A.S., 'Self-healing materials: a review of advances in materials, evaluation, characterization and monitoring techniques' *Compos. B Eng*. **87** (2015) 92–119.

[10] De Kostera, S.A.L., Morsb, R.M., Nugterena, H.W., Jonkers, H.M., Meestersa, G.M.H. and Van Ommen, J.R., 'Geopolymer coating of bacteria-containing granules for use in self-healing concrete' 7th World Congress on Particle Technology (WCPT7) Elsevier, Procedia Engineering **102** (2015) 475 – 484.

[11] Dhami, N.K, Reddy M.S., and Mukherjee, A., 'Improvement in strength properties of ash bricks by bacterial calcite', *Ecol. Eng.* **39** (2012) 31–35.

[12] Dong, B., Han, N., Zhang, M., Wang, X., Cui, H. and Xing, F., 'A microcapsule technology based self-healing system for concrete structures', *J. Earthquake Tsunami* **07** (3) (2013) 1350014.

[13] Dry, C., 'Three design for the internal release of sealants, adhesives and waterproofing chemical into concrete to release', *Cem. Concr. Res.* **30** (2000) 1969–77.

[14] DTI, Construction statistics annual report, London TSO, 2006.

[15] Ersan, Y.C., Gruyaert, E., Louis, G., Lors, C., Belie, N.D. and Boon, N., 'Self protected nitrate reducing culture for intrinsic repair of concrete cracks', *fmicb.* **6** (2015) 01228.

[16] Ersan, Y.C., Hernandez-Sanabria, E., Boon, N. and Belie, N.D., 'Enhanced crack closure performance of microbial mortar through nitrate reduction', *Cem. Concr. Compos.* **70** (2016a) 159-170.

[17] Erşan, Y.C., Verbruggen, H., De Graeve, I., Verstraete, W., Belie, N.D. and Boon, N., 'Nitrate reducing CaCO3 precipitating bacteria survive in mortar and inhibit steel corrosion', *Cem. Concr. Res.* **83** (2016b) 19–30.

[18] Granger, S. and Loukili, A., 'Mechanical behavior of self-healed ultra-high performance concrete: from experimental evidence to modeling', 3rd International Conference on Construction Materials' Performance, Innovations and Structural Implications (ConMat'05), Vancouver, Canada, August, 2005.

[19] Guadalupe Sierra-Beltran, M., Jonkers, H.M., Schlangen, E., 'Characterization of sustainable bio-based mortar for concrete repair' *Constr Build. Mater*. **67** (2014) 344–352.

[20] Hager M. D., Greil, P., Leyens, C., van der Zwaag, S. and Schubert, U.S., 'Self-healing materials' *Adv. Mater.* **22** (47) (2010) 5424–5430.

[21] Hammes, F., and Verstraete, W., 'Key roles of pH and calcium metabolismin microbial carbonate precipitation', *Rev Environ SciBiotechnol* 1 (2002) 3–7

[22] Hearn, N., 'Self-sealing, autogenous healing and continued hydration: what is the difference', *Mater. Struct.* **31** (1998) 563–567

[23] http://www.cidc.in

[24] Huaicheng, C., Chunxiang, Q. and Haoliang, H., 'Self-healing cementitious materials based on bacteria and nutrients immobilized respectively', *Constr. Build. Mater*.126 (2016) 297–303.

[25] Jonkers, H.M. and Schlangen, E., 'Development of a bacteria-based self-healing concrete', *Tailor Made Concrete Structures – Walraven&Stoelhorst (eds)*, (2008).

[26] Jonkers, H.M., 'Bacteria-based self-healing concrete', *Heron* **56** (2011) 1-12.

[27] Jonkers, H.M., Thijssen, A., Muyzer, G., Copuroglu, O. and Schlangen, E., 'Application of bacteria as self-healing agent for the development of sustainable concrete', *Ecol. Eng.* **36**(2) (2010) 230–235.

[28] Khaliq, W. and Ehsan, M.B., 'Crack healing in concrete using various bio influenced self-healing techniques', *Constr. Build. Mater.* **102** (2015) 349–357.

[29] Krishnapriyaa, S., Venkatesh Babub, D.L. and Arulraj G, P., 'Isolation and identification of bacteria to improve the strength of concrete', *Mic. Res.* **174** (2015) 48–55.

[30] Li, V.C., Yang, E.H. and Zwaag (e.d), S.V.D., 'Self-healing materials – an alternative approach to 20 centuries of materials science, self- healing in concrete materials', Springer, Netherlands. (2007) 161–194

[31] Li, W., Jiang, Z., Yang, Z., Zhao, N. and Yuan, W., 'Self-healing efficiency of cementitious materials containing microcapsules filled with healing adhesive: mechanical restoration and healing process monitored by water absorption', *PLoS One* **8** (11) (2013) 81616.

[32] Liu, B., Zhang, J.L., Ke, J.L., Deng, X., Dong, B.Q., Han, N.X. and Xing, F., 'Trigger of self-healing process induced by EC encapsulated mineralization bacterium and healing efficiency in cement paste specimens', 5th International Conference on Self-Healing Materials', Durham North Carolina, 2015, 1–4.

[33] Liu, S., Bundur, Z.B., Zhu, J. and Ferron, R.D., 'Evaluation of self-healing of internal cracks in biomimetic mortar using coda wave interferometry', *Cem. Concr. Res.* **83** (2016) 70–78.

[34] Luo, M. and Qian, C., 'Influences of bacteria-based self-healing agents on cementitious materials hydration kinetics and compressive strength' *Constr. Build. Mater*. 121 (2016) 659–663.

[35] Luo, M., Qian, C.X. and Li, R.Y., 'Factors Affecting Crack Repairing Capacity of bacteria-based self-healing concrete', *Constr. Build. Mater.* **87** (2015a) 1–7.

[36] Luo, M., Qian, C., Li, R. and Rong, H., 'Efficiency of concrete crack-healing based on biological carbonate precipitation', *J. Wuhan Univ. of Tech.-Mater. Sci. Ed.***30** (2015b) 1255–1259.

[37] Métayer-Levrel, G.L., Castanier, S., Orial, G., Loubière, J.F. and Perthuisot, J.P., 'Applications of bacterial carbonatogenesis to the protection and regeneration of limestones in buildings and historic patrimony', *Sediment Geol.* **126** (1999) 25–34.

[38] Nishiwaki, C., 'Fundamental study on development of intelligent concrete with self-healing capability'. Master's thesis, Department of Architecture and Building Science, Graduate School of Engineering, Tohoku University (1997).

[39] Nishiwaki, T., Kwon, S., Homma, D., Yamada, M. and Mihashi, H., 'Self-healing capability of fiber-reinforced cementitious composites for recovery of water tightness and mechanical properties', *Mat*. **7** (3) (2014).

[40] Orial, G. La biomineralisationappliquée à la conservation dupatrimoine: bilan de dix ansd'experimentation. *Restaurar la memoria* (2000), Valladolid, Spain.

[41] Parks, J., Edwards, M,Vikesland, P. and Dudi, A., 'Effects of bulk water chemistry on autogenous healing of concrete', *J. Mater. Civ. Eng.* **22** (5) (2010) 515–524

[42] Pei, R., Liu, J., Wang, S. and Yang, M., 'Use of bacterial cell walls to improve the mechanical performance of concrete', *Cem. Concr. Compos.* **39** (2013) 122–130.

[43] Qian, C., Ren, L., Xue, B. and Cao, T., 'Bio-mineralization on cement-based materials consuming CO_2 from atmosphere', *Constr. Build. Mater.* **106** (2015a) 126–132.

[44] Qian, C.X., Chen, H, Ren, L. and Luo, M.,'Self-healing of early age cracks in cement-based materials by mineralization of carbonic anhydrase microorganism', *f.micb* (2015b) 01225.

[45] Qureshi, T.S., Kanellopoulos, A. and Al-Tabbaa, A., 'Encapsulation of expansive powder minerals within a concentric glass capsule system for self-healing concrete', *Constr. Build. Mater* .**121** (2016) 629–643.

[46] Rivadeneyra, M. A., Parraga, J., Delgado, R., Ramos-Cormenzana, A., and Delgado, G. 'Biomineralization of carbonates by Halobacillustrueperi in solid and liquid media with different salinities',*FEMS Mi Eco*. **48** (2004) 39–46.

[47] Rodriguez-Navarro, C., Rodriguez-Gallego, M., Chekroun, K. B., & Gonzalez-Munoz, M. T., 'Conservation of ornamental stone by Myxococcusxanthus-induced carbonate biomineralization', *Appl. Environ. Microbiol.* **69**(4), (2003) 2182–2193.

[48] Roig-Flores, M., Pirritano, F., Serna, P. and Ferrara, L., 'Effect of crystalline admixtures on the self-healing capability of early-age concrete studied by means of permeability and crack closing tests', *Constr. Build. Mater.* **114** (2016) 447–457.

[49] Sahmara, M., Keskin, S.B., Ozerkan, G. and Yaman, I.O., 'Self-healing of mechanically-loaded self-consolidating concretes with high volumes of fly ash', *Cem. Concr. Compos.* **30** (2008) 872–879.

[50] Siddique, R., Singh, K., Kunal, Singh, M., Corinaldesi, V. and Rajor, A., 'Properties of bacterial rice husk ash concrete', *Constr. Build. Mater.* **121** (2016) 112–119.

[51] Snoeck, D., Van Tittelboom, K, Steuperaert, S, Dubruel, P. and De Belie, N., 'Self-healing cementitious materials by the combination of microfibres and superabsorbent polymers, *J. Intell. Mater. Syst. Struct.* **25** (1) (2014) 13–24.

[52] Stuckrath, C., Serpell, R., Valenzuela L. M., and Lopez M. 'Quantification of chemical and biological calcium carbonate precipitation: performance of self-healing in reinforced mortar containing chemical admixtures' *Cem. Concr. Compos.* **50** (2014) 10–15.

[53] Suji, D. and Gandhimathi, A., 'Studies on the development of eco-friendly self-healing concrete a green building concept', *Nat. Environ. Pollut. Technol.* **14** (3) (2015) 639–644.

[54] Talaiekhozan, A., Keyvanfar, A., Shafaghat, A., Andalib, R., Majid, M.Z.A., Fulazzaky, M. A., Zin, R.M., Lee, C.T., Hussin, M.W., Hamzah, N., Marwar, N.F. and Haidar, H.I., 'A review of self-healing concrete reaserch development', *J. Env. Treat. Tec.* **2** (2014) 1-11.

[55] Termkhajornkit, P., Nawa, T., Yamashiro, Y. and Saito, T., 'Self-healing ability of fly ash–cement systems' *Cem. Concr. Compos.* **31** (2009) 195–203.

[56] Tiano, P., Biagiotti, L., and Mastromei, G. 'Bacterial bio-mediated calcite precipitation for monumental stones conservation: methods of evaluation', *J. Micbio. Meth.* **36** (1999) 139–145.

[57] Tittelboom, K.V., Belie, N.D., Muynck, W.D. and Verstraete, W., 'Use of bacteria to repair cracks in concrete', *Cem. Concr. Res*. **40** (2010) 157–166.

[58] Tziviloglou, E., Wiktor, V., Jonkers, H.M. and Schlangen, E., 'Bacteria-based self-healing concrete to increase liquid tightness of cracks', *Constr. Build. Mater.* **122** (2016) 118–125.

[59] Wang, J., Dewanckele, J., Cnudde, V., Vlierberghe, S.V., Verstraete, W., and Belie, N.D., 'X-ray computed tomography proof of bacterial-based self-healing in concrete', *Cem. Concr. Compos.* 53 (2014) 289–304.

[60] Wang, J., H. Soens, W. Verstraete, and N. De Belie, 'Self-healing concrete by use of microencapsulated bacterial spores', *Cem.Concr. Res.*(2014a) **56** 139-152.

[61] Wang, J., Mignon, A., Snoeck, D., Wiktor, V., VanVliergerghe, S., Boon, N. and Belie, De N., 'Application of modified alginateen capsulated carbonate producing bacteria in concrete:a promising strategy for crack self-healing', **6** (2015) 1088.

[62] Wang, J., Tittelboom, K.V., Belie N.D., and Verstraete, W., 'Use of silica gel or polyurethane immobilized bacteria for self-healing concrete', *Constr. Build. Mater.* **26** (1) (2012) 532–540.

[63] Wang, J.Y., De Belie N., and Verstraete, W. 'Diatomaceous earth as a protective vehicle for bacteria applied for self-healing concrete', *J. Ind. Microbiol. Biot.* **39** (2012b):567–577.

[64] Wang, J.Y., Snoeck, D., Van Vlierberghe, S., Verstraete, W. and Belie, N.D., 'Application of hydrogel encapsulated carbonate precipitating bacteria for approaching a realistic self-healing in concrete', *Constr. Build. Mater.* **68** (2014b) 110–119.

[65] Wang, J.Y., Vlierberghe, S.V., Dubruel, P., Verstraete, W. and Belie, N.D., 'Hydrogel encapsulated bacterial spores for self-healing concrete: proof of concept', Proceedings of the 4th International Conference on Self-Healing Materials (ICSHM), Belgium, June, 2013 606-609.

[66] White, S.R., Sottos, N.R., Geubelle, P.H., Moore, J.S., Kessler, M.R., Sriram, S.R., Brown, E.N. and Viswanathan, S., 'Autonomic healing of polymer composites', *Nature*. 409 (6822) (2001) 794-797

[67] Wiktor, V. and Jonkers, H.M., 'Quantification of crack-healing in novel bacteria-based self-healing concrete', *cem. Con. comp*. **33** (2011) 763-770.

[68] Wiktor, V. andJonkers, H.M., 'Field performance of bacteria-based repair system: pilot study in a parking garage', *Case Stud. Constr. Mater.* **2** (2015) 11–17,

[69] Williams, J., Lawrence, M. and Walker, P., 'A method for the assessment of the internal structure of bio-aggregate concretes', *Constr. Build. Mater.* **116** (2016) 45–51.

[70] Williams, S.L., Kirisits, M.J. and Ferron, R.D., 'Influence of concrete-related environmental stressors on biomineralizing bacteria used in self-healing concrete', *Constr. Build. Mater.* (2016).

[71] Wu, M., Johannesson, B. and Geiker, M., 'A review: self-healing in cementitious materials and engineered cementitious composite as a self-healing material', *Constr. Build. Mater.* 28(1) (2012) 571–583

[72] Xu, J. and Yao, W., 'Multiscale mechanical quantification of self-healing concrete incorporating non-ureolytic bacteria-based healing agent', *Cem. Concr. Res.* **64** (2014) 1–10.

[73] Zhang, J.L., Wu, R.S., Li, Y.M., Zhong, J.Y., Deng, X., Liu, B., Han, N.X. and Xing, F., 'Screening of bacteria for self-healing of concrete cracks and optimization of the microbial calcium precipitation process', *Appl. Microbiol. Biotechnol*. **100** (15) (2016) 6661–6670.

[74] Zhong, W. and Yao, W., 'Influence of damage degree on self-healing of concrete', *Constr. Build. Mater.* **22** (6), (2008) 1137–1142.

Acceleration of GGBS Cements by Chloride, New Insights on Early Hydration

L. Steger(1), C. Patapy(1), B. Salesses(1), M. Chaouche(2) and M. Cyr(1)

(1)LMDC, Université de Toulouse, INSA, UPS, France

(2)LMT, ENS Cachan, France

ABSTRACT

The substitution of ordinary Portland cement (OPC) by large proportions of ground granulated blast furnace slag (GGBS) reduces the early hydration kinetics, causing a slower development of mechanical strengths. Chlorides are well known for their accelerating effect on ordinary Portland based cements but are mostly used for specific applications such as non-reinforced concretes, due to their detrimental effects regarding the corrosion of steel bars. However GGBS based concretes are known for their ability to resist chloride ingress because of their refined porosity and their capacity to fix more chlorides in hydrates, reducing the free chlorides available for corrosion. Some studies have shown the positive effects of chloride products for early strength development of high-GGBS-content concretes, without an investigation of the microstructure development, and several works studied the effects of chlorides on OPC hydration during the 1980's-90. From these studies, many hypotheses have been put forward, such as the impact of different anhydrous phases (C_3S, C_3A, GGBS, etc.) on dissolution kinetics and the nature of products, but the question has not been definitely settled. This experimental work brings new insights in to the interactions of chlorides/GGBS blends, including in-situ XRD monitoring of early age hydration for the crystalline phases (AFt, AFm, calcium sulphates, etc.). Scanning Electronic Microscope observations are used at early age of hydration to observe dissolution/precipitation phenomena at the surface of GGBS grains and in the fluid filled areas.

Keywords: GGBS, early hydration, chlorides, microstructure.

1 INTRODUCTION

Ground Granulated Blast furnace Slag (GGBS) is a by-product of the pig-iron industry. After being quenched and finely ground, it becomes a latent hydraulic powder, which has been used for decades in the cement and concrete industry as a supplementary cementitious material (SCM). OPC substitution by GGBS helps to reduce the environmental impact of concrete. However, GGBS is less reactive than OPC and, even though the long-term performance can exceed that of OPC, the early age strength of GGBS blends is usually lower. For some applications, such as in the precast industry, where the production rate of concrete components has to be kept at least as high as that permitted by OPC, the lack of early strength (typically before 24 h) can become an issue.

Multiple solutions exist to accelerate GGBS reaction, such as increasing its intrinsic reactivity by additional grinding, thermal activation or the use of chemical activators. Among the chemicals available, chloride salts, even at low contents, are commonly used to accelerate GGBS blended cements and show an interesting amount/effect ratio [1-3]. However, the

presence of chlorides has detrimental effects on reinforced concrete, specifically because of the risks of steel rebar corrosion. On the other hand, it has been demonstrated that GGBS cements have a finer microstructure, which decreases the ingress of chlorides through their porosity, and also a higher capacity to fix chlorides in their hydration products (mainly aluminate phases), thus reducing the amount of deleterious free chlorides and limiting corrosion [4-6].

This study aims to bring new insights into the first hours of hydration of high GGBS content blends and into the acceleration mechanisms of chloride salts. Early age hydration is followed by isothermal calorimetry and in-situ XRD monitoring. SEM observations coupled with EDS reveal the main features of their microstructural development.

2 MATERIALS AND METHODS

2.1 Materials

The GGBS used was NF EN 15 804 compliant, with an amorphous content of around 98%. The OPC was a CEM I 52.5R according to NF EN 197-1. The chemical compositions are given in Table 1. For the mortars, 0/2 mm siliceous sand in accordance with EN 196-1 was used and pastes and mortars were made with de-ionized water. The accelerator in this study was calcium chloride ($CaCl_2 \cdot 2H_2O$). The salt was first dissolved in the mixing water before being brought into contact with the dry mix.

Table 1: Chemical composition of the materials for this study

Chemical composition (% oxide)		
	OPC (CEM I 52.5R)	GGBS
CaO	64.5	41.1
SiO_2	20.1	35.4
Al_2O_3	4.8	12.7
MgO	1.0	7.3
Fe_2O_3	2.5	0.59
K_2O	0.17	0.39
Na_2O	0.14	0.51
SO_3	3.5	2.0
Cl^-	<0.1	<0.01

2.2 Methods

The binder blend for this study contained 70% GGBS and 30% OPC. For the accelerated samples, 1% $CaCl_2 \cdot 2H_2O$ (representing 0.5% Cl^-) was added during the preparation. For the compressive strength trials, mortar samples were prepared in compliance with EN 196-1. The sand/binder mass ratio was 3:1 and the water/binder mass ratio was 0.5. Each batch produced three specimens with dimensions 4 × 4 × 16 cm. The prisms were kept in their moulds for 24 h before being cured in water at 20°C until used. Pastes were prepared in 100 g batches, with a 0.4 water/binder ratio. The mixes were stirred for 2 mins with a mechanical stirrer set at 1500 rpm. For the isothermal calorimetric measurements, 15 g of fresh paste was sampled in glass ampoules and directly inserted into one of the chambers of a TAM AIR calorimeter from TA Instruments, stabilized at 20°C. De-ionized water was used as the inert reference.

The hydration kinetics was also monitored by XRD on hydrating paste encapsulated in a Kapton sheet with a D8 diffractometer from Bruker AXS under CuKα radiation, scanning from 8° to 45° 2θ with variable divergence slits set to maintain a constant irradiated surface

on the sample, 0.02° of step width and 0.31 s counting time per step, leading to a total scan time of around 10 mins. The time between 2 scans was set at 45 mins, to present a satisfactory overview of the hydration kinetics. Microstructural observations were made on 1 day aged pastes. For the hydration stoppage by solvent exchange method, 1-2mm thick slices were cut with a saw and immersed in isopropanol for 48h before being dried and stored under vacuum in a desiccator. Before the observation, the samples were polished with a JEOL IB-19510CP cross section polisher and prepared with a conductive coating. SEM observations were made on a JEOL FEG JSM7100 coupled with an EDS detector (SDD X-Max 80mm2 Oxford Instruments AZtecEnergy).

3 EXPERIMENTAL RESULTS AND DISCUSSION

3.1 Chloride accelerating effect on compressive strength

Figure 1 presents the compressive strength results for mortar bars. The accelerating effect of the chloride salt was most marked at early age, with an improvement of more than 61%, 55% and 30% at 1, 2 and 7 days, respectively. Later on, the efficiency decreased to around 5% at 28 days and, after 56 days, accelerated blends showed lower performance than blends without salts. This tendency for the enhancement effect to decrease over time can also be observed in the precast industry when acceleration is provided by thermal activation [7]. However, strength development continues in both systems. The following parts of this paper will focus on the first day of hydration and on the influence of chloride salts on the microstructural development and the specific activity of GGBS in blended cements.

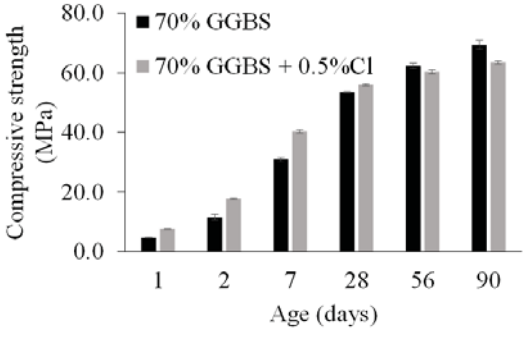

Figure 1: Compressive strength of samples containing 70% GGBS with or without activation by calcium chloride

3.2 Isothermal calorimetry

Figure 2 shows the heat flow and cumulative heat released during the hydration of systems with and without calcium chloride. The heat flow in the non-accelerated sample (a) presents the main features of plain OPC hydration. After a large initial heat release attributed to the initial dissolution upon contact with the mixing water and the rapid formation of ettringite ($C_3A.3C.32H$), an induction period precedes the main activity peaks, followed by a deceleration period [8]. The first shoulder of the main peak is attributed to the silicate reaction forming C-S-H, while the aluminate reaction forming ettringite usually comes slightly afterwards, as shown by the second shoulder on the figure. During the deceleration period, formation of C-S-H continues more slowly and ettringite formation stops due to lack of sulphates. During this period, additional aluminates react to form AFm (Aluminate-Ferrite mono), which combines with residual sulphates (AFm-SO_4), carbonates (AFm-CO_3) or

chlorides (AFm-Cl). In the sample containing chlorides, the induction period is shorter; the main activity phase starts 1h earlier and shows an important increase in heat flow. The AFm formation is observable through the apparition of a large peak during the deceleration period after 11h. The cumulative heat (b) clearly indicates that the accelerated mix undergoes a greater hydration reaction during the first 2 days. Later on, the slope of the plain mix tends to remain constant while the activity of the mix with calcium chloride starts to slow down.

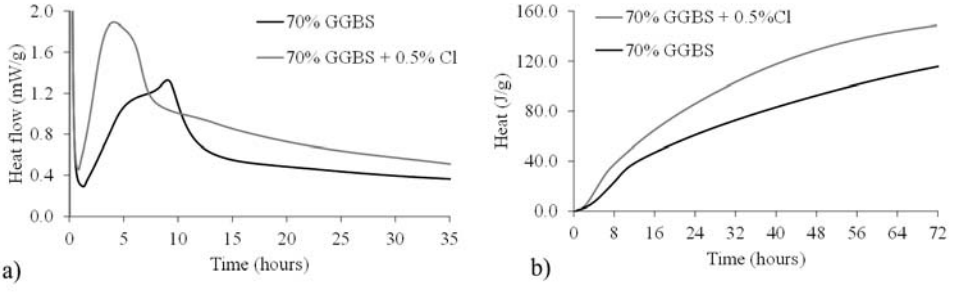

Figure 2: Heat flow and cumulative heat release in blended cements containing 70% GGBS accelerated with calcium chloride

3.3 In situ XRD/Calorimetry coupling

Following the hydration of the pastes by XRD gave very precise information on the formation kinetics of crystalline phases. It is interesting to consider XRD data with isothermal calorimetry measurements to identify the activity during the different time periods.

For this study, the XRD analysis focused on ettringite and AFm formation. The consumption of the calcium sulphates, as gypsum and anhydrite here, was also monitored. Figure 3 combines calorimetry results for both plain and accelerated systems and gives qualitative XRD information. However, the action of the chloride salt can be highlighted by the following observations:

- The calcium sulphates completely run out after 10 hours in the accelerated system whereas, in the plain cement, there is still residual anhydrite after 24 hours.
- Ettringite formation is greater from the very beginning of the hydration, and participates in the intensification of the first thermal peak. Addition of chloride seems to promote the formation of a larger amount of ettringite.
- The AFm phase is modified by the presence of chlorides and switches from a sulphate-carbonate AFm (identified at 10.7° 2θ in the plain mix) to a sulphate-chloride AFm (Kuzel's salt, identified at 10.95° 2θ in the accelerated mix) [9]. The chloride-rich AFm forms directly and no trace of other AFm is found, as shown in Figure 4. The formation starts 5 hours earlier than in the plain mix and the maximum intensity seems to indicate a higher amount of product formed, which is in agreement with the additional peak on the corresponding calorimetric curve. This could be explained by the lower consumption of sulphate for AFm formations due to the presence of Cl- in place of SO4- in their crystallographic structure. However, more aluminium will be required to maintain AFm-Cl formation.

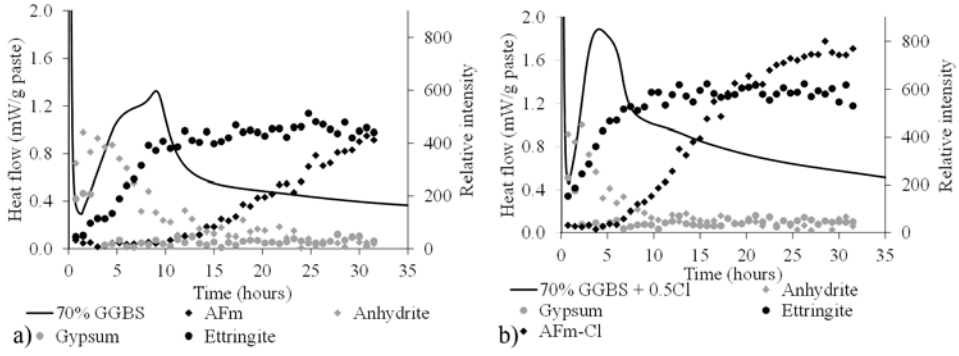

Figure 3: In-situ XRD monitoring of formation of ettringite (black dots) and AFm phases (black lozenges), and consumption of anhydrite (grey lozenges) and gypsum (grey dots) in plain 70% GGBS blend (a) and 70% GGBS accelerated with calcium chloride (b).The corresponding heat flow is shown by the black line

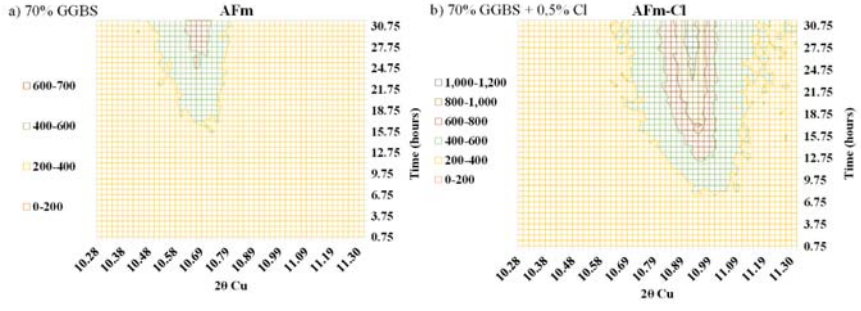

Figure 4: XRD results and identification of the formation of the different AFm phases in plain (a) and accelerated (b) samples

3.4 Microstructural characterisation

The previous part clearly shows the impact of the calcium salt on the global hydration kinetics but direct information on GGBS/chlorides interaction was difficult to isolate. SEM/EDS is a useful tool, allowing direct observation of selected and identified products.

Figure 5 presents an overview of the microstructure of the plain sample after 1 day of hydration. The cross section polishing method allowed raw samples to be observed without the need to impregnate them with resin. However, very porous samples such as this one can hardly be correctly coated to become conductive. Therefore, the low magnification view presented in Figure 5 was obtained under low vacuum conditions. In this sample, OPC is considered as the main activator for the hydration of GGBS, through the formation of calcium hydroxide (portlandite, $Ca(OH_2)$), increasing the local basicity of the solution and promoting the dissolution of slag grains. The OPC represents only 30% of the anhydrous blend here, creating notable variations of the microstructural features on a local scale. As shown in Figure 5, C_3S has already partially reacted and inner (Ip) and outer (Op) C-S-H are perceptible. A calcium hydroxide gel fills the space on the bottom right hand side of the picture, surrounding GGBS grains. C-S-H formation can also be observed at the GGBS surface, but is thinner than the Ip at the OPC surface. There seems to be very little sign of

GGBS reaction at this stage. C_3A and C_4AF are present in the bottom left part of the picture, and their hydration leads to the local formation of sulphate-carbonate AFm.

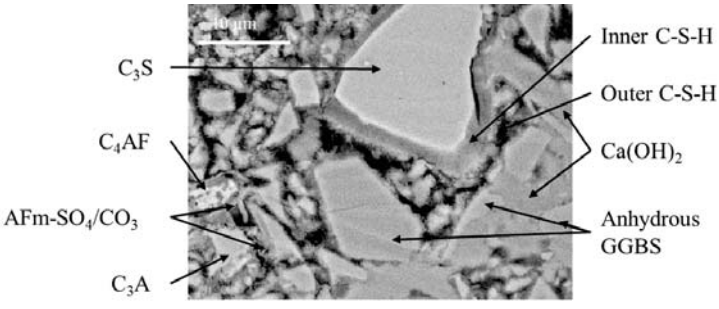

Figure 5: Low vacuum SEM picture of a 70% GGBS blend after 1 day of hydration

Figure 6 shows the two main environments of GGBS grains in the hydrated paste: surrounded by portlandite (1) or in a porous area (2). Needle like C-S-H formations mixed with ettringite can be observed around the anhydrous grains. The presence of C_3A promoted the precipitation of AFm as seen at the bottom of the picture (3), as well as in proximity with fine slag particles (4). The microstructure of the accelerated samples is presented in Figures 7 & 8, which show porous areas and portlandite filled areas, respectively. In the area without portlandite, the presence of aluminate OPC grains promoted the formation of AFm, and chemical analysis showed that chlorides were included (1). Complementary XRD information identified this phase as a Kuzel's salt phase. In this system, multiple GGBS grains show a dissolved surface, which is directly related to the local presence of chlorides, as in area (2). The C-S-H formed in the accelerated system also present a finer structure and are more developed than in the sample containing no accelerator. In the areas where the pore space has been filled by portlandite, as presented in Figure 8, C-S-H is difficult to distinguish morphologically. However, with the local presence of chlorides, a magnesium-rich product forms at the surface of slag grains (1). Chemical mapping showed that the area was rather poor in calcium but rich in silica and aluminium, indicating the probable formation of some M-S-H type phase coexisting with hydrotalcite and brucite[10], the latter two being in rather small amounts and so not detected by XRD. It should be noted that hydrotalcite generally shows good affinity for chloride binding [11], [12], which justifies its presence in this area.

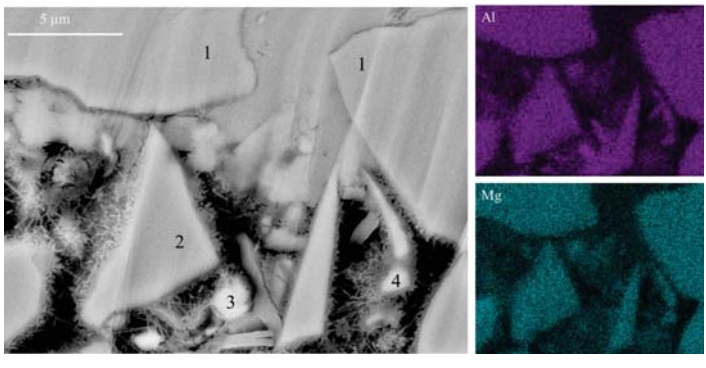

Figure 6: SEM picture and corresponding Al and Mg EDS mappings of a 70% GGBS paste after 1 day of hydration

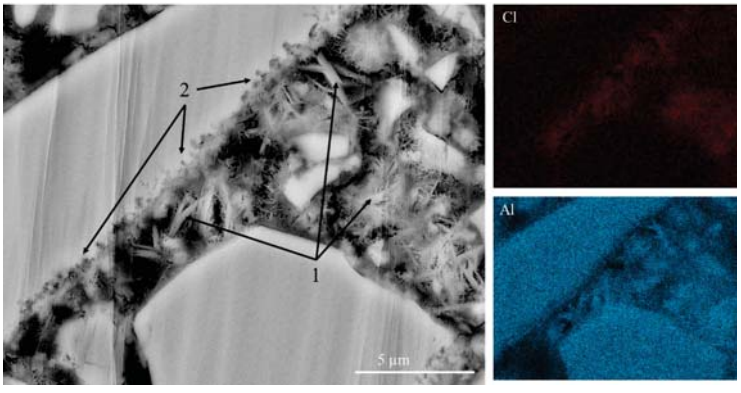

Figure 7: SEM picture of a 70% GGBS accelerated with calcium chloride after 1 day of hydration. Focus on aluminates

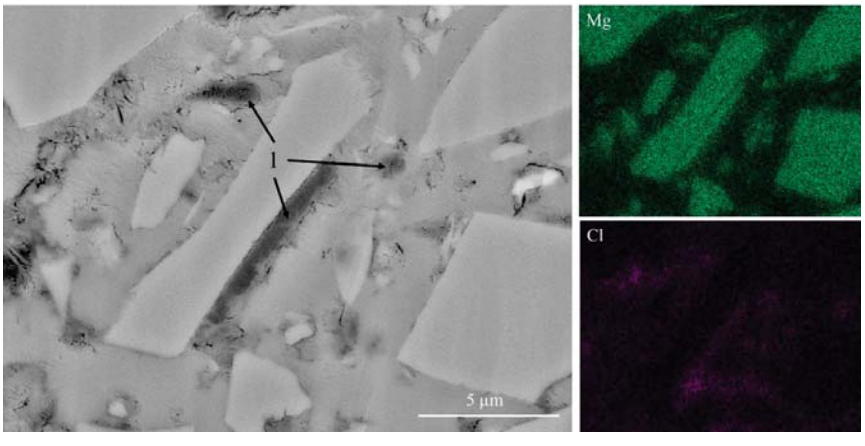

Figure 8: SEM picture of a 70% GGBS accelerated with calcium chloride after 1 day of hydration. Focus on GGBS surrounded by portlandite

4 CONCLUSIONS

This experimental investigation highlights the following observations:

- In situ XRD monitoring, in agreement with calorimetric measurement, shows the influence calcium chloride on the increase of the formation of ettringite and AFm phases in blended cements containing 70% GGBS.
- Electron Microscope Images provide information on a denser microstructure after 1 day of hydration in chloride-accelerated systems, partly due to the formation of additional aluminate phases, which might be directly related to the mechanical strength increase.
- SEM coupled with EDS shows evidence of a higher dissolution of GGBS grains in accelerated samples, and the formation of specific hydrates, such as Kuzel's salts and Mg based phases. The local presence of chloride in these features tends to indicate a direct action of the salt on the reaction kinetics of GGBS, in addition to the OPC activation, whose reaction is also accelerated by calcium chloride.

This study shows an increase of the early age strength (+55% at 2 days) of a 70% GGBS blended cement 0.5% of chloride is added, in the form of calcium chloride. This evolution is

related to a higher hydration rate, confirmed by calorimetric measurements and microstructural observation, which show, respectively, a higher hydration rate and a denser microstructure. In accelerated samples, GGBS presents specific features such as surface attack and formation of Mg phases. However, it remains unclear if this behaviour is related to the direct action of the chlorides or an indirect action from the OPC acceleration. Also, accelerating the mixes promotes the formation of AFm including chlorides in their structure and thus reduces the corrosion potential of the system.

ACKNOWLEDGEMENTS

The authors wish to express their gratitude and sincere appreciation to Ecocem Materials for financing this research work.

REFERENCES

[1] V. S. Ramachandran, *Concrete Admixtures Handbook, 2nd Ed.: Properties, Science and Technology*. William Andrew, 1996.

[2] F. Bellmann and J. Stark, "Activation of blast furnace slag by a new method," *Cem. Concr. Res.*, vol. 39, no. 8, pp. 644–650, Aug. 2009.

[3] G. Van Rompaey, "Etude de la réactivité des ciments riches en laitier, à basse température et à temps court, sans ajout chloruré," 2006.

[4] R. Luo, Y. Cai, C. Wang, and X. Huang, "Study of chloride binding and diffusion in GGBS concrete," *Cem. Concr. Res.*, vol. 33, no. 1, pp. 1–7, Jan. 2003.

[5] R. K. Dhir, M. A. K. El-Mohr, and T. D. Dyer, "Chloride binding in GGBS concrete," *Cem. Concr. Res.*, vol. 26, no. 12, pp. 1767–1773, Dec. 1996.

[6] J. S. Ryou and K. Y. Ann, "Variation in the chloride threshold level for steel corrosion in concrete arising from different chloride sources," *Mag. Concr. Res.*, vol. 60, no. 3, pp. 177–187, Apr. 2008.

[7] R. Derabla and M. L. Benmalek, "Characterization of heat-treated self-compacting concrete containing mineral admixtures at early age and in the long term," *Constr. Build. Mater.*, vol. 66, pp. 787–794, Sep. 2014.

[8] J. W. Bullard *et al.*, "Mechanisms of cement hydration," *Cem. Concr. Res.*, vol. 41, no. 12, pp. 1208–1223, Dec. 2011.

[9] A. Mesbah, C. Cau-dit-Coumes, G. Renaudin, F. Frizon, and F. Leroux, "Uptake of chloride and carbonate ions by calcium monosulfoaluminate hydrate," *Cem. Concr. Res.*, vol. 42, no. 8, pp. 1157–1165, Aug. 2012.

[10] D. R. M. Brew and F. P. Glasser, "Synthesis and characterisation of magnesium silicate hydrate gels," *Cem. Concr. Res.*, vol. 35, no. 1, pp. 85–98, Jan. 2005.

[11] O. Kayali, M. S. H. Khan, and M. Sharfuddin Ahmed, "The role of hydrotalcite in chloride binding and corrosion protection in concretes with ground granulated blast furnace slag," *Cem. Concr. Compos.*, vol. 34, no. 8, pp. 936–945, Sep. 2012.

[12] M. S. H. Khan, O. Kayali, and U. Troitzsch, "Chloride binding capacity of hydrotalcite and the competition with carbonates in ground granulated blast furnace slag concrete," *Mater. Struct.*, vol. 49, no. 11, pp. 4609–4619, Nov. 2016.

The Effect of Limestone on the Hydration and Workability of Ternary Blended Cement LC3: Limestone, Calcined Clays and Cement

Aurélie R. Favier and Karen L. Scrivener

Laboratory of Construction Materials, EPFL, Switzerland

ABSTRACT

Our study is based on the replacement of 45% of clinker by calcined clay and limestone; the cement is known as LC3 cement. It has been found that limestone accelerates hydration at early ages while calcined clay has pozzolanic properties, also the reaction between limestone and calcined clay contributes to strength development. The kinetics of these reactions are closely linked to the particle size distribution and the BET specific surface of the raw materials. It is widely accepted that the smaller the particle size and larger surface area, faster the reaction. However, if the cement is too fine, the water demand will increase drastically. Some previous work already showed that the calcined clays and the limestone are not 100% reacted. In this study, we propose to optimize the size distribution of limestone by mixing different grades of limestone (with different particle size). Finally, it will be found a compromise between the strength development and the workability.

Keywords: LC3, workability, limestone, calcined clay

1 INTRODUCTION

It is very common today to find cements whose part of the clinker is substituted by Supplementary Cementitious Materials (SCM) in order to reduce the ecological impact of the concrete [1]. For many years, much research has been done to demonstrate the feasibility of using limestone and calcined clays as SCMs [2–4]. The combined use of both allows greater clinker substitution and a marked improvement in properties [5–9]. In order to be able to use this cement in large quantities and in spite of demonstrations and publications proving the concept, certain limitations have to be lifted concerning workability in particular. There are several methods to tune the workability of a concrete, one consists to add water but this will affect the resistance. It is also possible to work with superplasticizers, but unless the design is adapted to use of clays [10], the commercial products do not allow a reasonable dosage from an economic point of view. The third method is to optimize the granular skeleton of concrete aggregates, which has been done for decades [11-12]. The idea of this work is to optimize the particle packing at the cement scale directly. In this paper, we are interested only

in the empirical approach of the improvement of the packing via the optimization of the distribution of the particles of limestone.

2 MATERIALS AND METHODS

The main objective was to define mixes using limestone with different particle size distribution to optimize the packing of the LC3 system.

We prepared different LC3 mixes with commercial limestones provided by OMYA, calcined clay from India and a commercial CEM I 42.5N. The designs are described Table 1. We always kept the minimum amount of fine limestone LS 5 to 5% corresponding to the high degree of reaction of limestone in LC3 system. LS5, LS 65, and LS 130 are the names of limestone based on the commercial grades; higher the number is, lower the fineness.

Table 1: Mix design of LC3-50 mixes

	Mean diameter (microns)	LC3 LS5	LC3 LS65	LC3 LS130	LC3 LS5-65	LC3 LS5-130	Plain cement (PC)
Calcined clay (50% calcined kaolinite)	11.5	30	30	30	30	30	
Limestone LS5	7.1	15			5	5	
Limestone LS65	27		15		10		
Limestone LS130	95.6			15		10	
Plain cement	16.3	52	52	52	52	52	100
Gypsum	-	3	3	3	3	3	

The particle size distribution measured by laser granulometry and the specific surface by N_2 adsorption following procedure given in [13] are given Figure 1.

Finally, cement pastes were cast with water to binder (W/B) ratio equal to 0.4 for mercury intrusion porosimetry (MIP) and isocalorimetry [13] and with W/B equal to 0.5 for mini cone test. This W/B ratio does not lead to any bleeding of the pastes in our systems. The mini-slump cone has a bottom diameter of 38 mm, a top diameter of 19 mm, and a height of 57 mm. Mortars were cast compressive strength is measured on a 4 cm cube following EU standard 196-1.

3 RESULTS AND DISCUSSION

3.1 Particle size distribution

After the raw materials were mixed using Turbula, particle size distribution and the specific surface were measured (Figure 2). An enlargement of the distribution curve for LC3 mixes is observable. For all blends, the specific surface remains similar but 4 times higher than that of a conventional cement.

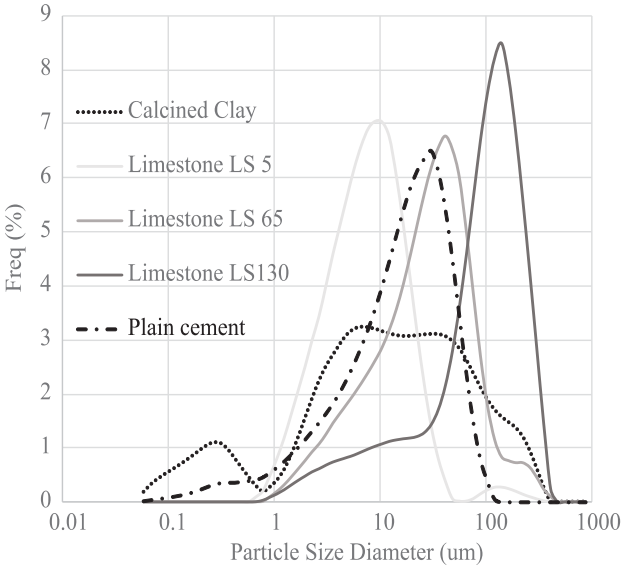

	BET (m^2/g)
Calcined Clay	7.41
LS 5	1.73
LS 65	0.13
LS 130	0.07
Plain cement	0.63

Figure 1: Particle size distribution and BET specific surface of raw materials

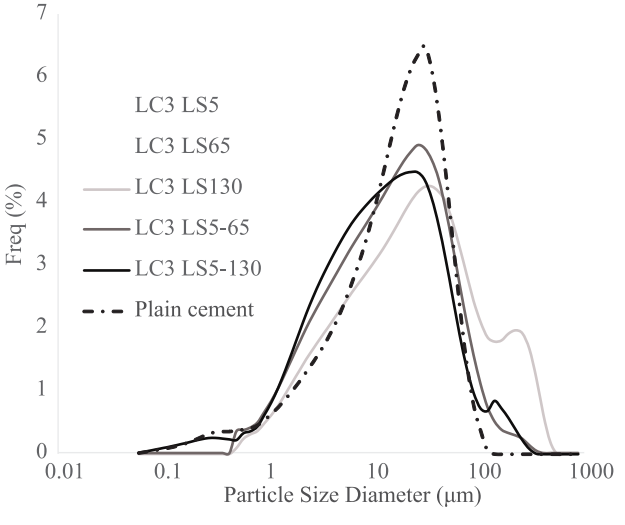

	BET (m^2/g)
LC3 LS5	2.7
LC3 LS65	2.44
LC3 LS130	2.47
LC3 LS5 65	2.64
LC3 LS5 130	2.65
Plain cement	0.63

Figure 2: Particle size distribution and BET specific surface of blended cements

3.2 Hydration by isocalorimetry

It can be observed in Figure 3 that the kinetic of hydration of our blends compared to plain cement. All LC3 systems presents the same heat evolution and the curves are superposed.

Obviously, the blends, which contained less clinker, present a lower heat release at 20°C. Unexpectedly, it cannot be detected important changes between the blends linked to size of limestone. It was expected that system LC3 LS130 containing only coarse limestone should less react. Small differences going in these direction can be observed on the second peak (aluminate reaction peak affected by limestone with alumina reaction) in Figure 3a. Obviously, it is impossible to conclude to a real effect. It is possible that the quantity of fine particles observable in LS 130 (Figure 1) are in enough quantity to participate to the limestone reaction. It is well known that the degree of reaction of limestone is low (less than 5% in Portland cement system) [14].

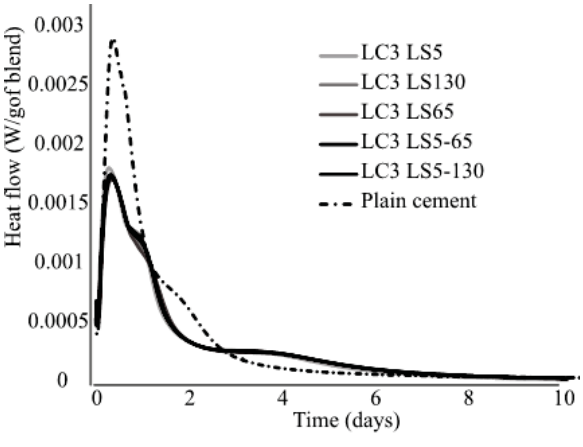

a)

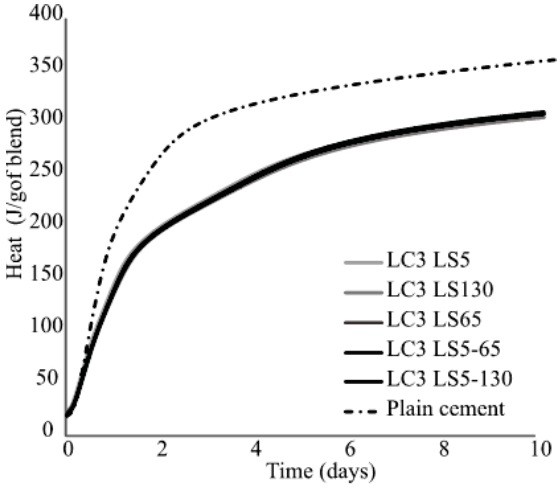

(b)

Figure 3: (a) Heat flow and (b) Heat of cement pastes by isocalorimetry at 20°C

3.3 Mechanical strength on mortar

Figure 4 shows the mechanical strength of mixes on mortar with a W/B ratio of 0.5. Unsurprisingly, plain cement presents the best result at 2 days. At 7 days, it is challenged by the blend LC3 LS5 containing the finest limestone and the LC3 LS 5-130 containing a mix of the finest limestone and the coarsest limestone (ratio between limestones= 1:2). However, at 28 days, all blends present a good mechanical performance. These results confirm that only a small quantity of really fine limestone is needed to improve the strength at early age.

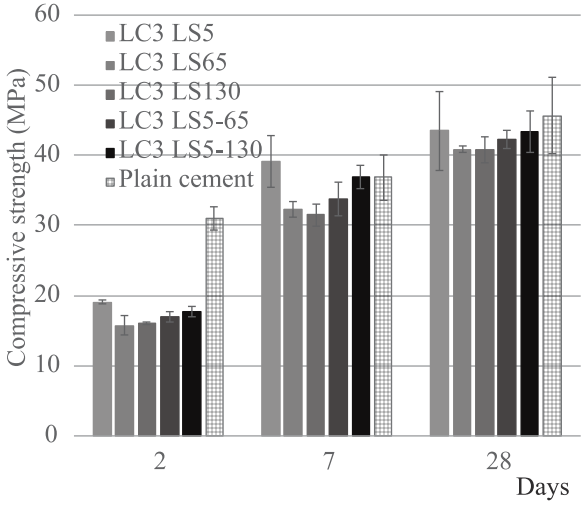

Figure 4: Compressive strength on mortars over time for all mixes

3.4 Workability using mini cone on paste

Based on the mechanical strength, we knew that the system with the finest limestone had the best mechanical performance but fine particles in big quantity are detrimental for workability. Calcined clays have a higher water demand as a conventional cement due to their adsorption capacity. Depending on the specific surface area of these calcined clays, workability of LC3 will be assess. The European standard EN 197 for resistance to compression sets the W/C ratio at 0.5 while the standard ASTM C109 sets the flow. In both cases, the difference in solid volume between the PC and the LC3 is not considered. The average density of LC3 in this study is 2.9. A commercial cement has an average density of 3.1. It means that in Figure 5, we should not compare systems with the same W/B ratios but the LC3 with W/B= 0.5 and the plain cement with W/B= 0.45 (red circle). It is shown that the LC3 LS130 has the best workability compared to other blends and it is not so far from plain cement paste. If now, we took in consideration the mechanical performance, we can conclude that it is very possible to use the LC3 LS5-130, which mixes to different limestone to get the best compromise between good workability and good compressive strength.

3.5 Mercury intrusion porosimetry

Finally, some experiments were carried out to measure the pore volume of these systems (Figure 6).

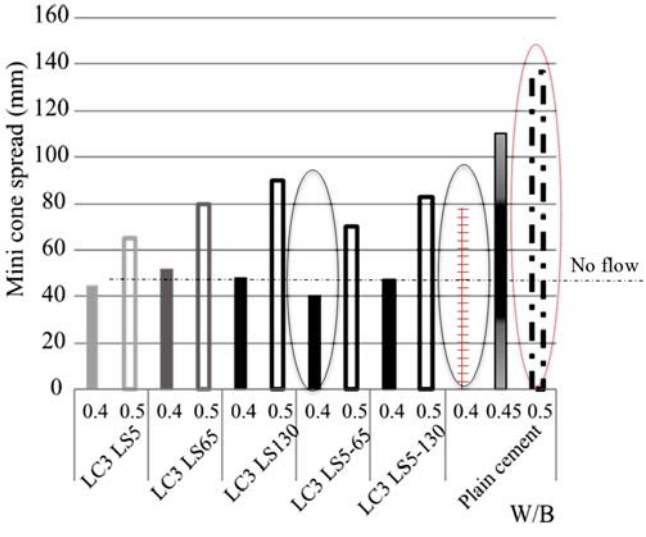

Figure 5: Spread measured by mini cone on paste prepared with all blends and different W/B ratios

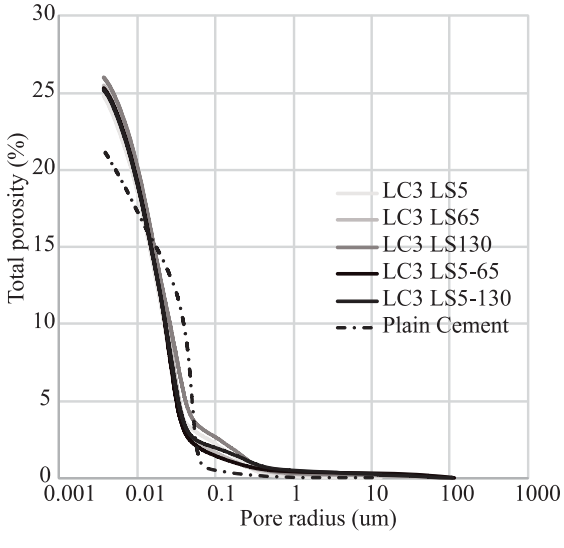

Figure 6: Total porosity measured by MIP on hydrated pastes at 28 days after stopping hydration by solvent exchange

As it was observed in different studies about SCM effect, the porosity is refined when compared to plain cement. However, the total porosity is slightly higher. The blend LC3 LS 130 containing the coarsest limestone presented also a higher volume of big pores (around 0.1 microns) than other blends. Generally, the effect of limestone particle size did not have any detrimental effect.

4 CONCLUSION AND PERSPECTIVE

To sum up:

- Fine limestone gave the best mechanical performance but the worst workability.
- Coarse limestone gave the best workability but an increase in the volume of big pores and a bad resistance at early age.
- The best compromise is to mix fine limestone in enough quantity (really small quantity as degree of reaction is really low) to allow good mechanical resistance and coarse limestone to obtain good workability.

All conclusions are empirical and the next step should to use packing model (such as Andersen-Andreassen model [15,16]) to design cement which can give the best compromise depending on the availability of the calcined clay and limestone without the need to test all systems.

5 ACKNOWLEDGEMENTS

The authors gratefully acknowledge financial support from the Swiss Agency for Development and Cooperation (Project number 7F08527).

6 REFERENCES

[1] B. Lothenbach, K. Scrivener, R.D. Hooton, Supplementary cementitious materials, Cem. Concr. Res. **41** (2011) 1244–1256. doi:10.1016/j.cemconres.2010.12.001.

[2] K. De Weerdt, E.J. Sellevold, K. Kjellsen, H. Justnes, Fly ash–limestone ternary cements: effect of component fineness, Adv. Cem. Res. **23** (2011) 203–211.

[3] B. Lothenbach, G. Le Saout, E. Gallucci, K. Scrivener, Influence of limestone on the hydration of Portland cements, Cem. Concr. Res. **38** (2008) 848–860. doi:10.1016/j.cemconres.2008.01.002.

[4] B.B. Sabir, S. Wild, J. Bai, Metakaolin and calcined clays as pozzolans for concrete: a review, Cem. Concr. Compos. **23** (2001) 441–454. doi:10.1016/S0958-9465(00)00092-5.

[5] M. Antoni, J. Rossen, F. Martirena, K. Scrivener, Cement substitution by a combination of metakaolin and limestone, Cem. Concr. Res. **42** (2012) 1579–1589. doi:10.1016/j.cemconres.2012.09.006.

[6] F. Avet, R. Snellings, A. Alujas, K. Scrivener, Development of a New Rapid, Relevant and Reliable (R3) Testing Method to Evaluate the Pozzolanic Reactivity of Calcined Clays, in: Calcined Clays Sustain. Concr., Springer, 2015: pp. 539–544.

[7] A. Favier, F. Avet, M. Antoni, K. Scrivener, Limestone Calcined Clays Cement for a sustainable development, in: Guillaume Habert, Arno Schlueter, Zurich, Switzerland, 2016. doi:10.3218/3774-6.

[8] K.L. Scrivener, J.D. Laffely, A. Favier, Limestone calcined clay cement, Cem. Plant Environ. Handb. 2nd Ed. (2014) 159.

[9] K. Scrivener, Options for the future of cement, Indian Concr. J. (2014).

[10] O. Akhlaghi, T. Aytas, B. Tatli, D. Sezer, A. Hodaei, A. Favier, K. Scrivener, Y. Menceloglu, O. Akbulut, Modified poly(carboxylate ether)-based superplasticizer for enhanced flowability of calcined clay-limestone-gypsum blended Portland cement, Cem. Concr. Res. (Submitted).
[11] F. de Larrard, T. Sedran, Mixture-proportioning of high-performance concrete, Cem. Concr. Res. **32** (2002) 1699–1704. doi:10.1016/S0008-8846(02)00861-X.
[12] N. Roussel, Understanding the Rheology of Concrete, Woodhead Pub Ltd, 2012.
[13] Scrivener Karen, Snellings Ruben, Lothenbach Barbara, A Practical Guide to Microstructural Analysis of Cementitious Materials, CRC Press. (2015). https://www.crcpress.com/A-Practical-Guide-to-Microstructural-Analysis-of-Cementitious-Materials/Scrivener-Snellings-Lothenbach/p/book/9781498738651 (accessed May 19, 2016).
[14] T. Matschei, B. Lothenbach, F.P. Glasser, The role of calcium carbonate in cement hydration, Cem. Concr. Res. **37** (2007) 551–558. doi:10.1016/j.cemconres.2006.10.013.
[15] A.H.M. Andreasen, Ueber die Beziehung zwischen Kornabstufung und Zwischenraum in Produkten aus losen Körnern (mit einigen Experimenten), Kolloid-Z. **50** (1930) 217–228. doi:10.1007/BF01422986.
[16] H.J.H. Brouwers, Particle-size distribution and packing fraction of geometric random packings, Phys. Rev. E. **74** (2006) 031309. doi:10.1103/PhysRevE.74.031309.

Micro-Physical Characterization of Buffalo Dung Ash

P. Jagadesh[(1)], A. Ramachandramurthy[(2)] and R. Murugesan[(2)]

[(1)]Department of Civil engineering, Coimbatore institute of Technology, Coimbatore, Tamil Nadu, India

[(2)]CSIR-Structural Engineering Research Centre, Chennai, Tamil Nadu, India

[(3)]Department of Civil Engineering, IRTT, Erode, Tamil Nadu, India

ABSTRACT

Ordinary Portland cement (OPC) is the second most consumable material next to water makes an immediate call to utilize other waste material to make sustainable environment. One such waste considered in this study is buffalo dung, an attempt to use it in construction field by converting into buffalo dung ash (BDA). Burning the dry buffalo dung in open atmospheric conditions the BDA is obtained. The aim of the present work is to determine pozzolanic compounds available in BDA using various techniques like X-ray diffraction (XRD), fourier transform infra-red spectroscopy (FTIR), thermo-gravimetric analysis (TGA), derivative thermo gram (DTG), scanning electron microscopy (SEM) and energy-dispersive X-ray spectrometer (EDAX) to investigate the usefulness of BDA for the construction sector. These techniques are used to indicate the type of mineral, state of nature of mineral, morphological aspects, elemental analysis, etc. From the results, it is confirmed that pozzolanic mineral profiles are found in BDA, so it can be used as cement replacement in concrete, which makes a greener environment in construction sector.

Keywords: Buffalo dung, buffalo dung ash, pozzolanic mineral, sustainable environment, cement replacement, greener environment

1 INTRODUCTION

The world major construction material is ordinary Portland cement (OPC) [1] which is the most expensive material in concrete. The 2014 annual production of cement is 3.57 billion metric tonnes [2]; therefore approximately, 3.57 billion ton of CO_2 [3-4] a greenhouse gas, is delivered into the atmosphere [5], which is second largest CO_2 behind power generation industry [6]. It also includes, 5.71 billion tonnes of natural resources [7-9] are consumed with energy consumption of approximately 14.28 GJ [10-11]. These makes, an urgency call of researchers for use of any available alternative material for OPC in concrete in order preserve our environment for future generation and also provides way for sustainable environment. The qualitatively and quantitative characterization of an alternative material used is BDA in order to find out the degree of activity. The state, presence and forms of pozzolanic minerals using various scientific techniques in BDA become main objective of this study. The studies start with the mineralogical identification of BDA is done with help of XRD and EDAX is used for elemental analysis. FTIR and SEM techniques are used for the confirmation of mineralogical and morphology. Thermal analysis is used to observe the mass changes of minerals with respect to temperature.

2 MATERIALS AND METHODS

Wet buffalo dung (Figure 1) is obtained from the domestic cobber gas waste pit located in Erode district, Tamil Nadu, India. The dry buffalo dung (Figure 2) is obtained by drying wet buffalo dung at room temperature and burned in open atmospheric condition at 100°C to convert into BDA (Figure 3). Although, the buffalo dung is used as fertilizer in agriculture, there is need of any alternative material, in order to preserve nature and encouraging the sustainability in construction sector. Sometimes, this buffalo dung is used to heat the boilers in agricultural sectors for various purposes, through which also BDA is obtained. About 43.9% of weight is lost to obtain dry buffalo dung from 3.0 kg of wet buffalo dung in open atmosphere where again 31% of weight loss is noticed when it is subjected to burning. The specific gravity of BDA is found to be as 1.95 [12]. The fineness modulus of BDA is 0.304 [13]. The particle size distribution curve for BDA [14] is shown in Figure 4.

Figure 1: Wet Buffalo Dung

Figure 2: Dry Buffalo Dung

Figure 3: Buffalo Dung Ash

2.1 X-Ray Diffractometer

The peak identification of spectrum was carried out with a Bruker D2-Phaser XRD-diffractometer, Germany that used as monochromatic Cu-Kα1 radiation at 30 kV and 10 mA is used for qualitative analysis of specimens. The samples were scanned in the range of 10° to 80°, 2θ at the rate of 1.5°/min. By comparing the intensities and positions of Bragg peak with JCPDS-ICDD data files, the crystalline phases are identified.

2.2 EDAX Spectrometer

Elemental analysis or concentrations of elements present in sample is measured using EDAX spectrometer, working is simple that voltage pulse is proportional to the energy of incoming x-ray photon. Hence, EDAX is an analytical technique used for quantitative purpose of chemical elements present in samples. In this investigation EDS, ZEISS EVO18 is used for finding elemental composition.

2.3 FTIR Spectrometer

The spectral resolution was 4 cm^{-1} and 256 scans were coded into the mid infrared region (4000 cm^{-1} - 400 cm^{-1}). Different wave length of light will be absorbed by different types of molecules or groups of atoms creating fingerprint spectrum representing molecular absorption and transmission. The qualitative analysis of material like surface of bonding, functional groups and nature of bond are determined by fingerprint spectra obtained from FTIR (Nicolet 6700, Thermo Scientifics, USA).

2.4 Scanning Electron Microscope

Scanning Electron Microscope (SEM), ZEISS EVO18 accelerate electrons which carries energy dissipated as variety of signals, which includes secondary electrons (produces SEM

micrographs), diffracted back scattered electrons (used for determination of crystal structure and orientation of minerals) and photons (used for elemental analysis). Before loading the dried sample in loading assembly, it should be coated with gold using sputter for 30 seconds and were placed on carbon tape.

2.5 Thermal Analysis

At controlled temperature and atmosphere, the change in mass of material is monitored as function of temperature or time can be analysed and quantified using characterization technique known as thermal analysis. The quantification includes loss of water, loss of solvent, thermal degradation, oxidation phase and loss in weight of sample. The phase transitions and decomposition rate of sample, which are loaded in alumina crucibles, were assessed for the temperature from 100°C to 1400°C. The quantifying the mass change with temperature (TGA) and derivative of mass changes with temperature (DTG) are measured using TGA/DTG, NETZCH STA 449F3 which is recorded as thermal graph.

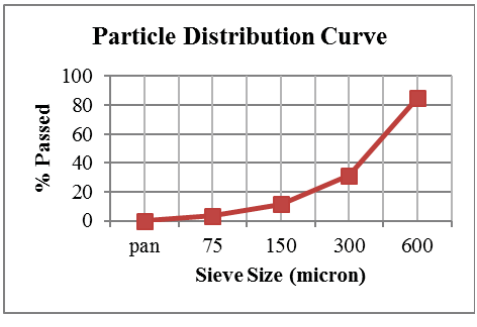

Figure 4. Particle Size Distribution curve for BDA

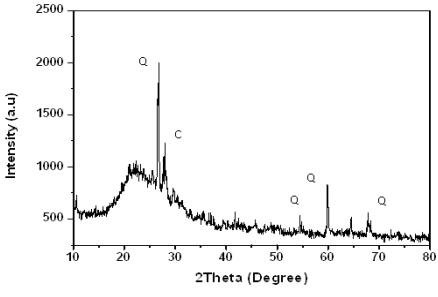

Figure 5. XRD analysis of BDA

3 RESULTS AND DISCUSION

3.1 X – Ray Diffractometer

Diffraction image is specific for every crystalline phase of minerals and the phase of the crystalline is identified [15] in BDA through diffraction peaks of constructive interferences are in a range of 2θ angles between 20º to 30° and the diffraction peaks upto 80°is possible. Quartz (Q) is obtained as amorphous form and Crystobalite (C) is obtained in crystalline form which is observed in silica as two different phases. The diffraction 2θ angle range for both the forms of silica is between 15º to 30º (2θ) as observed in BDA from Figure.5 and which is also observed by others all around the world [16-18]. BDA contain some reasonable sharp and intense peak starts to show up at amorphous background [19]. The peak intensities of BDA are observed between 25º to 30º, having highest diffraction angle for both forms are observed. The sharp intensities indicates that the silica is in the C form which is responsible for hydration process, which suggests it has pozzolanic activity and apart from it, the Q form is present rapidly in BDA sample shows that the crystallization of silica is not yet completed and it is just started. This is because of low burning temperature of sample [20-22] and it is burned in uncontrolled manner. The broad peak of BDA sample is observed between 20º to 30° indicates that the formation of silica gel [23] due to burning in uncontrolled manner.

Table 1: Diffraction angle for two different forms of silica in different types of ashes

Types of cementitious materials	Quartz (2θ)		Cristobalite (2θ)		References
	Minimum	Maximum	Minimum	Maximum	
Sugar Cane Bagasse Ash	22	74	26	32	37
Palm oil fuel ash	20	70	29	55	20
Rice husk ash	22	68	24	68	46
Fly ash	20	70	-	-	47
Municipal solid waste ash	22	70	24	40	48

Table.1 shows the supplementary cementitious materials (SCM) used in present days with *Q* and *C* content in it for (2θ) [6,24]. From Figure 5 it is observed that maximum *Q* is at 70° with minimum *Q* is at 23° and maximum *C* is at 68° with minimum *C* at 27°, which coincides with the SCM in table randomly, hence it is suggests that the BDA can be used as SCM after processing & burned in controlled temperature. The most predominant form of silica in the form of *Q* indicated that the recrystallization of BDA is not yet completed while burning in uncontrolled manner and in open atmosphere. During drying process of wet buffalo dung or burning process of dry buffalo dung or presence of *Q* in waste itself, result in presence of large amount of *Q* in it.

3.2 EDAX Spectrometer

EDAX analysis used for qualitative analysis which involves the identification of the lines in the spectrum and quantitative analysis which involves determination of the element concentrations by measuring line intensities for each element present in the sample and for the same elements in calibration Standards of known composition.

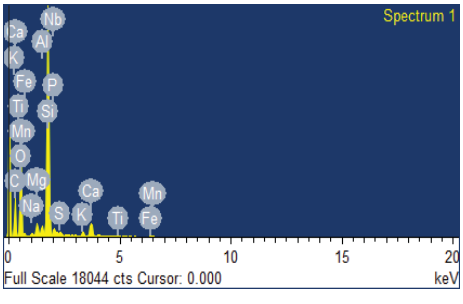

Figure 6: EDAX analysis of BDA

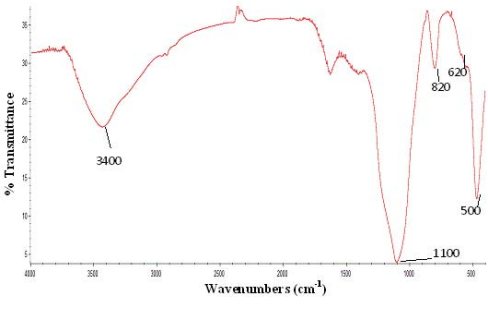

Figure 7: FTIR analysis of BDA

Below 4 keV, the most of elements are observed and all other elements are recorded below 7 keV. The concentrations of chemical elements are more when the peak of spectrum is higher; in BDA two peaks are observed. One peak (Ca, K, Fe, Ti, Mn & O) and other peak (Al, P & Si) are visible below 3 keV indicates K-series spectra having minerals of lower atomic numbers was observed with EDAX. These lower atomic number minerals absorb lower energy range below 3 keV for BDA. The presence of silica is confirmed by EDAX analysis shown in Figure.6, the presence of silica concentration about 16.34% in BDA sample. Apart from the silica, the concentration of other pozzolanic minerals observed in BDA is Al, Fe, Mn, K with O. Hence, BDA is classified as SCM due to presence of more concentrations of pozzolanic minerals.

3.3 FTIR

The crystallinity evolution progress of BDA can be conveniently monitored by FTIR. FTIR vibration graph of BDA from Figure 7 has two different stretching bands, one stretching is in strong band between 500 cm^{-1} to 1100 cm^{-1} and other is in broad band between 1400cm^{-1} to 3400cm^{-1}. The strong band and broad band absorption is due to presence of silica and stretching of O-H vibrations respectively. The bending and stretching of short range molecules like O-H molecules, the vibrations response are recorded in FTIR [25-26].

Table 2: Possibles vibrations bond to some of the peaks observed in Figure 3

Wave number [cm^{-1}]	Possible bond	Reference
500	Si-O	27
656–658	SiO_4	28, 29
714	CO_3	30, 29, 31, 6
847–848	Al–O, Al–OH	28, 31
877–878	CO_3	28, 29, 31, 6
1011–1080	Polymerized silica	32
1100–1200	SO_4	33, 30, 32, 29
1400–1500	CO_3	25, 32, 29, 31, 6
1620–1624	water in sulphates	33, 29, 34
1640–1650	H_2O	32, 35, 31
3398–3408	H_2O, capillary water	35
3457	H_2O	32,35
3554	H_2O	33, 31

As a result FTIR can be applied equally well to all forms of silica minerals, making it as ideal for observing different mineral forms phase transition. The presence of silicon bonds vibrations as symmetric stretching manner is indicated by strong band clearly. The stretching and bending of Si-O bonds in BDA are observed in FTIR wave numbers below 1400 cm^{-1} as sharp peaks [26]. The SiO_4 symmetric stretching vibrations are observed at wavenumbers 820 cm^{-1} and 620 cm^{-1}. The stretching and bending of silica-oxygen bonds are absorbed below the sharp absorption peaks in strong band [26]. The asymmetric and symmetric stretching vibrations of tetrahedral SiO_4, is assigned for the band at 1100 cm^{-1} and 820 cm^{-1} respectively. The crystalline C form of silica is assigned for the week vibration band of 620 cm^{-1}. The bending mode of Si-O is absorbed at vibration band at 500 cm^{-1} [27]. *C* form of silica is present in BDA is confirmed in FTIR, agreement to XRD analysis. Broad band vibration which is symmetric and asymmetric in nature is the result of hygroscopic nature of BDA particle. Broad band stretching at 3400 cm^{-1} is due to oxygen hydrogen bonded molecule in water [36,25] result in asymmetric vibration. The possible bond in minerals and related FTIR wave numbers absorbed by other researchers are listed in Table.2.

3.4 Scanning Electron Microscope

Figure 7 shows that the crystalline masses are present in the surface of BDA crystals. The smooth silky layer surrounds the tetrahedral shape of crystal is observed from Figure 7.a. The

surfaces of prismatic crystals looks like properly finished but the surface areas of it are seems to be less which makes it to be less reactive. Figure 7.b indicates that the columnar fibrous structures of crystals are surrounded by the elongated shape of precipitate upon which fibrous silky layer, which looks similar to prismatic tetrahedral systems shape of crystals covered by the cellulose sheet like pattern. The structure looks like precipitate, it is distributed unevenly on the surface of crystals show that improper burning of BDA. The cellulose sheet like pattern is due to crystalline formation of BDA is not yet completed [19] so that they are accumulated as sub-microcrystalline masses. The SEM image of BDA showing characteristics like tetrahedral shape (prismatic), fibrous nature, crystalline masses, silky layers, etc., which is similar to that of C mineral of silica.

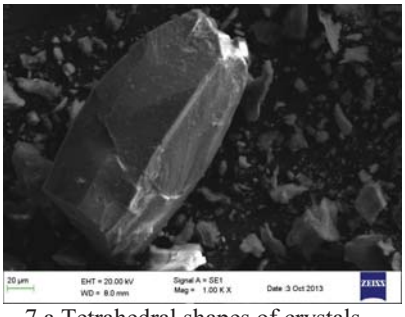

7.a Tetrahedral shapes of crystals

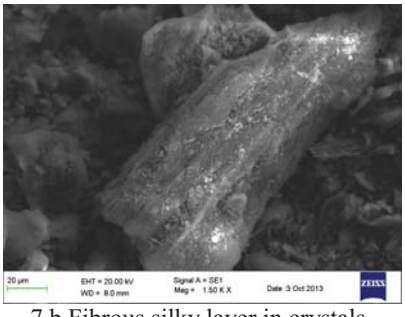

7.b Fibrous silky layer in crystals

Figure7: SEM analysis of BDA

The metastable *C* mineral and prismatic shape nature of BDA indicates that the temperature during burning of dry buffalo dung in open atmosphere is not sufficient to form stable C mineral and also they needed further temperature and controlled atmospheric conditions are required to form stable reactive pozzolanic mineral. Generally, C is formed at high temperature of 1470ºC and melts at 1713°C [38,39]. However, it may be formed at lower temperatures when silica is present in high concentrations [40-43] which show that conformation of results of SEM, XRD and EDAX. At the time of burning of dry buffalo dung in open atmosphere and uncontrolled condition, silica reacts with temperature and oxygen, it will changes the forms.

3.5 Thermal Analysis

Endothermic reactions of four decomposition characteristics were observed in TGA curve of BDA as shown in Figure 8. The first inflection point of BDA occurs at peak of 210°C which shows a mass change around -3.23% is due to hygroscopic nature of ash particles which will evolve surface water adsorbed at low temperature of 79.8°C, and there is change in mass per minute about -0.47% as observed in DTG curve at a temperature of 94.0°C, where the results were already recorded in FTIR. When the Q mineral is heated, there will be rearrangement of structure which increases the mass change upto -3.5% which is due to endothermic curve after 900.0 °C in next TGA curve. However, it is not completed up to approximately 1200°C, after that there is an abrupt change in the bonding arrangement of Si-O-Si indicated sharply by endothermic reaction on the third TGA curve having a mass change of -2.21%. The continue preferential rearrangement of silica mineral occurs, due to further increase in temperature, which result in newly developed tetrahedral structural framework to attain a more desired arrangement is observed by change in mass up-to 2.41% at a temperature above 1400°C as indicated by TGA curve.

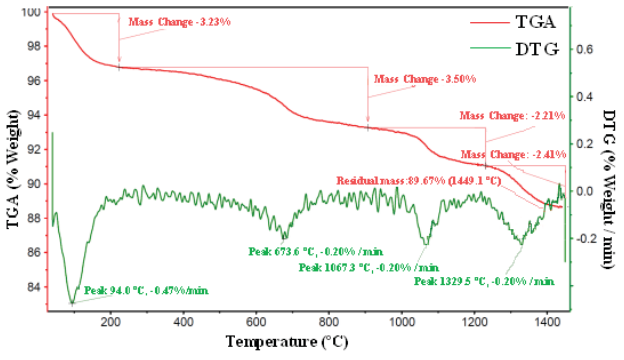

Figure 8: Thermal analysis of BDA

The degree of tetrahedral organization is a direct function of temperature and as temperature is increased, the rearrangement accomplished as observed in DTG curve at 1329.5°C, in each minute there is change in mass of -0.20 %. Until it reaches 1449.1°C, the materials dimensions will change with change in mass of -15.19%, which is recorded in TGA curve. Finally, 89.67% of total residue is obtained. There is no gradual change in mass per minute 0.20% in DTG curve after 673.6°C. As in dimension there is no additional change, between the 300°C to 800°C it is slow, due to Q minerals metastable in nature. If there is increase in crystallization temperature it becomes more stable. The presence of α- cristobalite mineral is indicated at 1200°C undergoes mass change and with C form silica as tetrahedral characterization is obtained. Above 800°C the tetrahedral reorganization occurs with only function of temperature indicates the pozzolanic activity of BDA. The high temperature silica phase is C which undergoes phase transformation from cubic to tetrahedral structure around 220°C and it is confirmed by SEM. C form of silica is found to be stable at temperatures below 268ºC.

4 SUMMARY AND CONCLUSIONS

An in-depth micro-analytical study of BDA indicates either mechanical method or physical method or chemical method or combination of these methods to form appropriate shape, size, particle surface area, nature of particle surface, etc. of pozzolanic mineral which is useful for improving the pozzolanic activity of BDA, so that it also used as SCM in concrete. The pozzolanic minerals in BDA (amorphous silica) are helpful for improving the pozzolanic activity [44-45] of concrete. The silica in the form of Q and C, the reaction between calcium and water to form calcium silicate hydrate directly which will improve the bond between hydrated cement matrix and sand in mix, hence increasing the strength [8]. Hence, the pozzolanic activitiy index is related to the presence of pozzolanic minerals which will contribute to its behaviour. The present scientific and technical studies on the BDA by using XRD, EDAX, FTIR, SEM and thermal analysis enabled the following conclusions:

- Sharp peaks of XRD indicate that the silica is in the form of C in Q background and it is present even after 30 degree (2θ).
- In XRD, silica is observed in the form of C and Q
- Most of minerals are in lower energy range which is observed in EDAX
- There are also some other pozzolanic minerals like Fe, Al, etc., which is observed along with oxides in EDAX
- The strong band observation in FTIR shows that the existences of silicon bonds
- The week band observation in FTIR indicates the presence of water molecules bonds

- Incomplete calcination of BDA is observed in XRD, SEM and EDAX
- Crystalline C form of silica mineral is observed in SEM
- Tetrahedral shape of mineral covered by cellulose like spongy layer in appearance is observed by SEM
- Endothermic reaction of BDA is noted in TGA indicating that the sufficient reactive minerals are formed above calcination temperature
- The pozzolanic activity of BDA is function of temperature

The need of incorporating BDA in concrete should be exploited by the construction industries in order to create a sustainable environment and cleaner production. The improved processes or techniques of BDA enable to use it as environmental friendlier material in construction sector.

5 ACKNOWLEDGEMENTS

The authors wish to thank the Agriculture farm of Mr. K. S. Palanisamy/ Mrs. P.Vijayalaksmi in Erode district, Tamil Nadu, India for providing the wet buffalo dung, which was dried in open atmospheric condition, burned in uncontrolled manner and converted to ash in their farm, are used in this investigation.

6 REFERENCES

[1] Altwair, N.M., Johari, M.A.M., Hashim, S.F.S., 'Influence of calcination temperature on characteristics and pozzolanic activity of palm oil waste ash'. *Australian journal of Basic and applied sciences*. **5**(11) (2011a) 1010-1018.

[2] U.S Department of Interior & U.S Geological Survey 2015. Mineral Commodity Summarizes 2015. January 30, 2015.

[3] Ogbeide, S. O., 'Developing an optimization model for CO_2 reduction in cement production process'. *JESTR Journal*, **3** (2010) 85-88.

[4] Worrell, E., Price, L., Martin, N., Hendriks, C., Meida, L.O., 'Carbon dioxide emissions from the global cement industry'. *Annual Review Energy Environment*. **26** (2001) 303-329.

[5] Fairbairn, E.M.R., Americano, B.B., Cordeiro, G.C., Paula, T.P., Filho, R.D.T., Silvoso, M.M., 'Cement replacement by sugar cane bagasse ash: CO_2 emissions reduction and potential for carbon credits'. *Journal of Environmental Management*, **91** (2010) 1864-1871.

[6] Yu, P., 'Structure of calcium silicate hydrate (C-S-H): near-, mid-, and far infrared spectroscopy' *Journal of American Ceramic Society*. **82**(3) (1999) 742–748.

[7] Alsop, P.A., Post, J.W., 1995, The Cement Plant Operations, Handbook (First edition). Tradeship Publications Ltd: Dorking, UK.

[8] Greer, W.L., Johnson, M.D., Morton, E.L., Raught, E.C., Steuch, H.E., Trusty, Jr C.B., 1992, Portland Cement in Air Pollution Engineering Manual. Anthony J. Buonicore and Waynte T. Davis (eds.). New York: Van Nostrand Reinhold.

[9] Jagadesh, P., Ramachandramurthy, A., Murugesan, R., 'Effect of water cementitious ratio on the strength development of Unary Blended Concrete – An Overview'. *International Journal of earth sciences and Engineering*. **8**(3), 2015c, 1493-1500.

[10] Muga, H., Betz, K., Walker, J., Pranger, C., Vidor, A., 'Development of appropriate and sustainable construction materials. Sustainable Futures Institute', Michigan Technological University, Michigan, USA; 2005.

[11] Malhotra, V.M., 'Fly Ash, Slag, Silica Fume, and Rice Husk Ash in concrete: A review'. *Concrete International*. **15**(4) (1993) 23-28

[12] Indian Standard 1727-1967. Method of test for pozzolanic materials. First revision, Bureau of Indian Standards, New Delhi; 1967.

[13] Indian Standard 4031 – 1996. Method of test for hydraulic cement, Part 1 - Determination of fineness by dry sieving. Second revision, Bureau of Indian Standards, New Delhi; 1996.

[14] Indian Standard 1607 – 2013. Methods of test sieving. Second revision, Bureau of Indian Standards, New Delhi; 2013.

[15] Wahal, F.M., Grim, R.E., Graf, R.B., 'Phase Transformation in silica as examined by continuous X ray diffraction'. *The American mineralogist*, **46** (1961) 196-208.

[16] Castaldelli, V.N., Akasaki, J.L., Melges, J.L.P., Tashima, M.M., Soriano, L., Borrachero, M.V., Monzo, J., Jordi Paya, 'Use of Slag/Sugar Cane Bagasse Ash (SCBA) Blends in the Production of Alkali-Activated Materials'. *Materials*. **6** (2013) 3108-3127.

[17] Martirena, J.F., Middendorf, B., Gehrke M, Budelmann, H., 'Use of wastes of sugar industry as pozzolana in lime-pozzolana binders: study of the reaction'. *Cement Concrete Research*. **28** (1998) 1525–1536.

[18] Ramirez, R.A., Garcia, P.M., Reyes, J.M., Juarez, D.C.A., Ponce, Y.G., 'The use of sugarcane bagasse ash and lime to improve the durability and mechanical properties of compacted soil blocks'. *Construction and Building Materials*. **34** (2012) 296–305.

[19] Parthipa Agarwal., Rahul, P.S., Yogesh, A., 'Use of nano-silica in cement based materials-A review', *Cogenet Engineering*. **2**(1) (2015) 1-11.

[20] Altwair, N.M., Johari, M.A.M., Hashim, S.F.S., 'Strength activity index and microstructural characteristics of treated palm oil fuel ash'. *International journal of Civil & Environmental Engineering.* **11**(5) (2011) 100-108.

[21] Cook, D.J., Rice husk ash. In: Swamy RN, editor. 'Concrete technology and design. Cement replacement materials', vol. 3. London: Surrey University Press, (1986) 171–96.

[22] James, J., Rao, M.S., 'Characterization of silica in rice husk ash'. *American Ceramic Society Bulletin*. *65*(8) (1986) 1177–80.

[23] Huang, C.Y., Feldman, R.F., 'Hydration reactions in Portland cement–silica fume blends. Cement and Concrete Research'. **15**(4) (1985) 585–592.

[24] Borilini, M.S., Vieira, C.M.F., Sanchez, R., Conte, R.A., Pinatti, D. G., Monterio., 'Characterization of Granulometric Fractions of Ash from Boiler Burnt Sugarcane Bagasse'. In: Proceedings of sixth international Latin-American Conference on powder technology, Rio de Janeiro, Brazil, (2007) 7-10.

[25] Kronenberg, A. K., 'Hydrogen speciation and chemical weakening of quartz. In: Heaney, P. J., Prewitt, C. T. & Gibbs, G. V. eds. Silica Physical Behaviour', *Geochemistry and Materials Applications*. (1994) 123–176.

[26] Langer, K., Florke, O.W., 'Near infrared absorption spectra (4000-9000cm^{-1}) of opals and the role of "water" in these SiO_2 nH_2O minerals'. *Fortschritte der Mineralogie*. **52**(1) (1974) 17–51.

[27] Jagadesh, P., Ramachandramurthy, A., Murugesan, R., Sugarcane bagasse ash – Material Characterization'. *International Journal of Applied Engineering and Research*. **10**(62) (2015b) 363-368.

[28] Mollah, M.Y.A., Kesmez, M., Cocke, D.L., 'An X-ray diffraction (XRD) and Fourier transform infrared spectroscopic (FT-IR) investigation of the long-term effect on the solidification/stabilization (S/S) of arsenic (V) in Portland cement type-V'. *Science of the Total Environment*. **325** (2003) 255–262.

[29] Pera, J., Husson, S., Guilhot, B., 'Influence of finely ground limestone on cement hydration'. *Cement and Concrete Composites*. **21** (1999) 99–105.

[30] Kloprogge, J.T., 'Vibrational spectroscopic study of syngenite formed during the treatment of liquid manure with sulphuric acid'. *Vibrational Spectroscopy*. **28** (2002) 209–221.

[31] Trezza, M.A., Lavat, A.E., 'Analysis of the system $3CaO{\cdot}Al_2O_3$–$CaSO_4{\cdot}2H_2O$–$CaCO_3$–H_2O by FT-IR spectroscopy'. *Cement and Concrete Research*. 31 (2001) 869–872.

[32] Mollah, M.Y.A., 'A Fourier transform infrared spectroscopic investigation of the early hydration of Portland cement and the influence of sodium lignosulfonate'. *Cement and Concrete Research.* **30** (2000) 267–273.

[33] Ghosh, S.N., Handoo, S.K., 'Infrared and Raman spectral studies in cement and concrete'. *Cement and Concrete Research*. **10** (1980) 771–778.

[34] Vazquez-Moreno, T., Blanco-Varela, M.T., 'Table of infrared frequencies and absorption spectra of compound related to cement chemistry'. *Materiales de Construction*, **182** (1981) 131–148.

[35] Richard, T., 'Diffuse reflectance infrared Fourier transform spectroscopy as a tool to characterise water in adsorption/confinement situations'. *Journal of Colloid and Interface Science,* **304** (2006) 125–136.

[36] Graetsch, H., Florke, O.W., Miehe, G., 'The Nature of Water in Chalcedony and Opal-C from Brazilian Agate Geodes'. *Physics Chemistry Minerals*, **12** (1985) 300–306.

[37] Jagadesh, P., Ramachandramurthy, A., Murugesan, R., and Saryu, K., 'Micro-analytical studies on sugarcane bagasse ash'. *Sadhana – academy proceedings in engineering science*. **40**(5) (2015a) 1693.

[38] Deer, W.A., Howie, R.A., Zussman., 1975, An Introduction to the Rock-Forming Mineral. Logman Group Ltd. London, pp.340-355.

[39] Torikai, D., Schinohara, A.H., Iwasaki, H., Suzuki, C.K., 'Estudo de Atenuação Ultrassônica em Quartzo'. *Ceramica*, **33**(211) (1987) 167.

[40] Amin, N., Ali, K., Shah, M.T., Alam, S., 'Chemical activation of bagasse ash in cement mortar'. *Advances in Cement Research*. **23**(2) (2011) 89-95.

[41] Cordeiro, G.C., Toledo Filho, R.D., Tavares, L.M., Fairbairn, E.M.R., 'Ultrafine grinding of sugar cane bagasse ash for application as pozzolanic admixture in concrete'. *Cement and Concrete Research*. **39** (2009) 110-115.

[42] Cordeiro, G.C., Toledo Filho, R.D., Fairbairn, E.M.R., 'Effect of calcination temperature on the pozzolanic activity of sugar cane bagasse ash'. *Construction and building materials*. **23** (2009) 3301-3303.

[43] Ganesan, K., Rajagopal, K., Thangavel, K., 'Evaluation of bagasse ash as supplementary cementitious material'. *Cement & Concrete Composites*. **29** (2007) 515-524.

[44] Erika, Y.N., Moises, F., Sagrario, M.R., Sergio, F., Santos, Michelle, S.R., Olga, R., Holmer, S., 'Characterization and properties of elephant grass ashes as supplementary cementing material in pozzolan/$Ca(OH)_2$ pastes'. *Construction and Building Materials*, **73** (2014) 391–398.

[45] Madruga F., 'Western opaline rocks of Spain. Applications with construction materials and evaluation of their pozzolanicity by conductometric techniques'. In: Junta de Castilla y León, Consejería de Fomento. Valladolid. (1991) 94.

[46] Farooque, K.N., Zaman, M., Halim, E., Islam, S., Hossain, M., Mollah, Y.A., Mahmood, A.J., 'Characterization and Utilization of Rice Husk Ash (RHA) from Rice Mill of Bangladesh'. *Bangladesh Journal of Science and Industrial Research*, **44**(2) (2009) 157-162.

[47] Rao, B.J., Narayanasamy, P., Siva, P., 'Thermal stability of nano structured fly ash synthesized by high energy ball milling'. *International Journal of Engineering Science and Technology.* **2**(5) (2010) 284-299.

[48] Thesipi, S.S., Dreizin, E.L., 'Metal Partitioning in products of incineration of municipal solid waste'. *Chromosphere*. **46**(6) (2002) 837-849.

Performance Evaluation of Concrete made of Recycled Fine Aggregates from Different Exposure Conditions

B. S. Dhanya, Anujith K. Babu, Jacob Sebastian, Varsha S. Kumar and Smruthi P. Nair

Department of Civil Engineering, RIT, Government Engineering College, Kottayam, Kerala, India

ABSTRACT

Concrete is the most widely used construction material. Over the years there has been an acute shortage of natural fine aggregates. The use of aggregates prepared by recycling construction and demolition waste is a promising solution in this regard. This paper discusses the fresh, mechanical and durability properties of concrete made with recycled fine aggregate (RFA), which are prepared from deteriorated concrete collected from different exposure conditions. The sites from where the deteriorated concrete collected belong to XS1 and XC1 as per the environmental exposure classification system suggested by BS 8500: 2006. In addition, fresh leftover hardened concrete from the laboratory which are least deteriorated are also used for making RFA. Each type of RFA were used in partial replacement of 10%, 20%, and 30% for fine aggregate in concrete mixes with a cement content of 380 kg/m^3 water cement ratio of 0.45. In addition, control mixes were also prepared. The concrete properties studied include workability, unit weight, compressive strength, split tensile strength, chloride ion penetrability (by ASTM C 1202) and water permeability (DIN 1048 part 5). The results show that, the concrete with RFA has comparable properties with that of conventional concrete irrespective of the source.

Keywords: RCA - recycled concrete aggregate, RFA - recycled fine aggregate, C&D waste - construction and demolition waste.

1 INTRODUCTION

The sources of natural aggregates required to manufacture concrete are depleting in a rapid pace. The excessive mining of river sand from riverbeds converted many perennial rivers into seasonal rivers and lead to the collapse of bridges. Hence, the government had put many regulations for mining river sand. Because of this, the demand of crushed stone sand, popularly known as manufactured sand or M-sand is increasing. The increased mining of rock for this purpose also lead to ecological imbalance and environmental degradation. Thus, it is high time to find a technologically sound alternative for natural fine aggregates. Recycled concrete aggregate is one of the options before the technologist. These are manufactured by crushing the concrete from construction and demolition (C&D) waste. Recycled aggregates conserve natural resources, save economy and avoid dumping of C&D waste to landfills. However, it is to be noted that the recycled aggregates might be a direct source of contaminant to the concrete, which can adversely affect the durability properties of concrete. Most of the concrete in C&D waste are deteriorated in one way or the other. Thus, a detailed study is required on fresh, mechanical and durability aspects of concretes made with recycled fine aggregates obtained from the C&D wastes collected from different

exposure conditions. The present study focuses only on the performance evaluation of recycled concrete aggregates as fine fractions alone and the same as coarse fractions is in progress, which is out of the scope of this paper.

The use of recycled fine aggregate (RFA) is limited owing to its increased water demand, effect on compressive strength and shrinkage. The hardened cement paste contained in RFA increases porosity and water demand thereby affecting the workability and strength parameter of concrete made out of it [1-2]. The microstructure of recycled aggregate concrete is much more complicated than that of the conventional concrete. These aggregates have two types of interstitial transition zones, one between the aggregate and new mortar matrix (new ITZ) and the other between aggregate and old mortar attached (old ITZ). The structural behavior of concrete made with recycled aggregate is generally slightly weaker in comparison to that of concrete made with natural aggregates [3]. As the replacement level of recycled aggregates increases, the relative compressive strength decreases when compared with conventional concrete made of natural aggregates. The detrimental effects are reported to be dominant after a replacement level of 30% [4].

This paper discusses the fresh, mechanical and durability properties of concrete made with recycled fine aggregate (RFA), which are prepared from deteriorated concrete collected from different exposure conditions. For the present study, the C&D wastes were collected from zones XS1 and XC1 as per the environmental exposure classification system suggested by BS 8500: 2006 [5]. In addition, fresh leftover hardened concrete from the laboratory which were least deteriorated were also used for making RFA.

2 EXPERIMENTAL PROGRAMME

The first phase of the study involves collection of C&D waste from different exposure conditions and preparation of RFA. The concrete samples from C&D waste were crushed using hammer to size of 40 to 50 mm. The steel reinforcements present, if any, were removed. Further, the samples were crushed into the size of fine aggregate with the help of a jaw crusher. RFA produced from concretes collected from zones XS1, XC1 and laboratory are named R1, R2 and R3 respectively. The sample collected from XS1 was approximately 20 years old and that from XC1 was 25 years old.

In this experimental programme, all the three categories of RFA were used in partial replacement levels of 0 %, 10 %, 20 % and 30 % in concrete mixes with a cement content of 380 kg/m^3 and a water cement ratio of 0.45. The replacement level beyond 30 % is not studied as it is reported that replacement level beyond 30 % is detrimental to the properties of concrete [4]. The concrete properties studied include workability, unit weight, compressive strength, split tensile strength, chloride ion penetrability and water permeability.

2.1 Materials

The materials used for this study in addition to RFA include Portland pozzolana cement, crushed stone sand or M sand, crushed stone aggregate (10 mm and 20 mm nominal size) and SNF based chemical admixture. The properties of the materials used are compiled in Table 1.

Table 1: Material properties

I	**Cement**				
a.	Standard consistency (%)	33			
b.	Initial setting time (minutes)	270			
c.	Final setting time (minutes)	485			
d.	Fineness (%)	1			
e.	Specific gravity	3.15			
f.	Compressive strength at 3 days (N/mm^2)	17			
g.	Compressive strength at 7 days (N/mm^2)	28			
h.	Compressive strength at 28 days (N/mm^2)	33			
II	**Coarse Aggregates**	**10mm nominal Size**		**20mm nominal Size**	
a.	Water absorption (%)	0.2		0.1	
b.	Specific gravity	2.71		2.78	
III	**Fine Aggregates**	**M-sand**	**R1**	**R2**	**R3**
a.	Water absorption (%)	1.2	1.5	3.9	3
b.	Specific gravity	2.77	2.51	2.38	2.61
c.	Loosely packed bulk density(kg/m^3)	1816	1371	1214	1379
d.	Void content (%)	34.4	45.4	49.0	47.3
e.	Zone(*From Sieve Analysis*)	I	I	I	I
f.	Fineness modulus	3.46	3.11	3.94	4.02

2.2 Mix design

A total of ten concrete mixtures are studied in the work. The cement content and water - cement ratio in all the concrete mixes was 380 kg/m^3 and 0.45. Concrete mix proportioning was done as per IS 10262 : 2009 [6]. The mixes were designed to get a slump between 50 to 100 mm by the use of SNF based superplasticizer. The concrete mixtures are designated as given in Table 2.

Table 2: Description of concrete mix proportions

Sl. No.	Designation	Description
1	**M-sand – 100%**	Control mix with 100 % M-sand
2	**R1-10%**	10% replacement of M-sand by R1
3	**R1-20%**	20% replacement of M-sand by R1
4	**R1-30%**	30% replacement of M-sand by R1
5	**R2-10%**	10% replacement of M-sand by R2
6	**R2-20%**	20% replacement of M-sand by R2
7	**R2-30%**	30% replacement of M-sand by R2
8	**R3-10%**	10% replacement of M-sand by R3
9	**R3-20%**	20% replacement of M-sand by R3
10	**R3-30%**	30% replacement of M-sand by R3

2.3 Test Methods

The fresh, mechanical and durability properties of different concretes were assessed by the following tests described below.

2.3.1 Test methods to assess fresh properties of concrete

The fresh properties studied include workability and fresh unit weight. Workability is assessed by slump test. The slump test was conducted as per IS 1199:1959 [7]. The unit weight of concrete in its fresh state is an important parameter. Unit weight is used to calculate yield of concrete**.** Unit weight of concrete in fresh state in each mix is determined as per ASTM C138 [8].

2.3.2 Test methods to assess mechanical properties of concrete

The mechanical properties studied are compressive strength and split tensile strength. Compressive strength is determined as per IS 516 – 1959 [9] using 150mm size standard concrete cube specimens. This test was conducted at the age of 7 and 28 days. Split tensile strength test is an indirect method to determine the tensile strength of concrete. This test is done in accordance with IS 5816:1999 [10] on cylindrical concrete specimens with a diameter of 150mm and height of 300 mm, at the age of 90 days.

2.3.3 Test methods to assess durability properties of concrete

The durability of concretes was assessed by two test methods – rapid chloride permeability test (RCPT) and water permeability test (WPT). RCPT is used to assess the chloride ion penetrability of concrete whereas WPT is used to assess water penetrability of concrete. Following are the brief description of these two test methods.

Rapid chloride permeability test (RCPT) determines the electrical conductance of concrete to provide a rapid indication of its resistance to penetration of chloride ions. This test method is standardized as ASTM C1202 [11]. In this method, a potential of 60 Volts is applied on a vacuum saturated cylindrical concrete specimen. One side of the specimen is exposed to 3% NaCl solution and the opposite side to 0.3 M NaOH solution. The resulting current is measured at an interval of 30 minutes, for a total period of 6 hours. From the current measurements, the total charge passed (in Coulombs) is calculated using trapezoidal rule. The total charge passed is an index of durability. As the total charge passed is more, the chloride ion penetrability is more, and the concrete is less durable. For the present study, the RCPT was conducted at the age of 90 days. Table 3 shows the classification criteria suggested by ASTM C 1202 for concretes based on the total charge passed.

Table 3: Chloride ion penetrability based on total charge passed [11]

Total charge passed (Coulombs)	Chloride ion penetrability
> 4000	High
2000 - 4000	Moderate
1000 - 2000	Low
100 - 1000	Very Low
< 100	Negligible

The resistance to water penetration is assessed using water permeability test done as per the German standard DIN 1048 Part 5 [12]. The test is performed on 150 mm size cubes. In this test, concrete cube specimen of size 150 mm is subjected to a 5 bar water pressure on its top surface in a permeability cell. The pressure is kept constant for a period of three days with the help of air compressor. After three days, the pressure is released and the specimens are removed from the permeability cell. Immediately after removing, the specimens are split into two halves and the depth of water penetration is noted. The smaller the depth of penetration, higher is the resistance to water penetration under hydrostatic pressure and the concrete is more durable. For the present study, the WPT was conducted at an age of 90 days. The typical results reported by the Concrete Society, 1998 [13] are as given in Table 4.

Table 4: Typical depth of water penetration results for different concretes

Concrete type	Depth of water penetration (mm)
Dense concrete with slag and superplasticizer	5
Concrete to be used in aggressive environment	< 30
Concrete to be used in water retaining structures	< 50

3 RESULTS AND DISCUSSION

3.1 Comparison of material properties of different fine aggregates

The material properties of the fine aggregates used in the study are given in Table 1. It is evident from Table 1 that all the fine aggregates are in the same gradation (all the aggregates fall in zone I). This is because the recycled aggregates are produced in the laboratory itself using a jaw crusher. The similar particle gradation is obtained by adjusting the jaw opening size. However, it can be seen that the specific gravities of RFA are lower and the water absorption of RFA are higher than that of manufactured sand. It is to be noted that the parent concrete sample of R1 (XS1) was about 20 years old, and R2 (XC1) was about 25 years old. Further, R1 was collected soon after the demolition whereas R2 was collected after one year of demolition. The deterioration happened to the parent concrete may attribute to the high water absorption and low specific gravity shown by R2. The high water absorption and lower specific gravity in RFA may also be due to the porosity attributed by the hardened cement mortar present.

3.2 Comparison of the fresh properties of concretes

All the concretes were designed to get a slump value between 50 and 100 mm by adjusting the superplasticizer dosage. Figure 1 shows the amount of chemical admixture added to get the specified workability range.

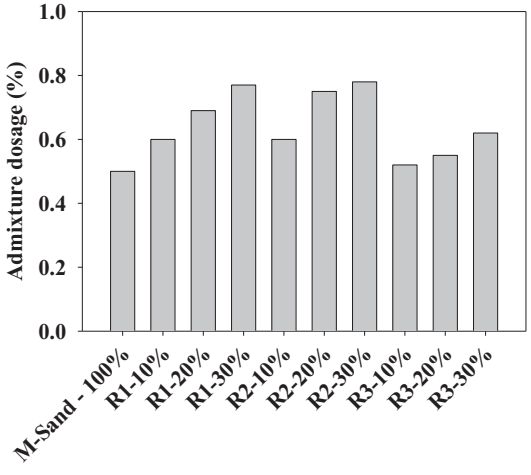

Figure 1: Chemical admixture dosage to different concrete mixes

Figure 1 depicts that as the replacement level increases, the dosage of superplasticizer required is more to get the same level of workability. This implies that, workability decrease with increase in RFA content. It can again be attributed to the presence of old, hardened mortar in RFA. This increases porosity and water demand, affecting the workability of concrete [1-2]. Figure 2 indicates the unit weight of different concrete mixes.

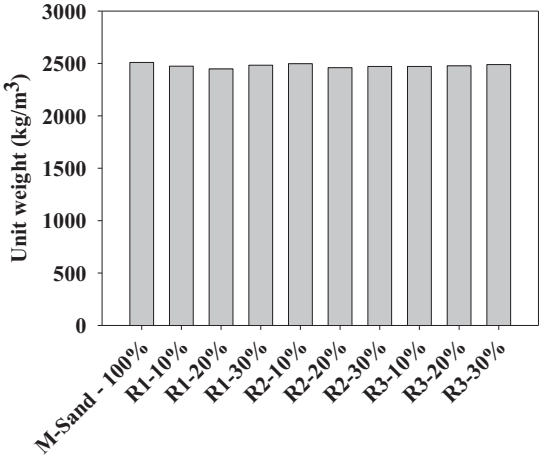

Figure 2: Unit weight of different concrete mixes

Figure 2 shows that there is no significant change in the unit weight of RFA concrete compared with that made of natural fine aggregate [12]. This indicates that use of RFA in concrete does not lead to under-yield or over-yield of concrete mixes.

3.3 Comparison of the mechanical properties of concretes

Figure 3 shows the compressive strength at 7 day and 28 day of the concrete made with RFA comparable to that of conventional concrete made with natural fine aggregate. Figure 4 indicates the split tensile strength of concrete at 90 days.

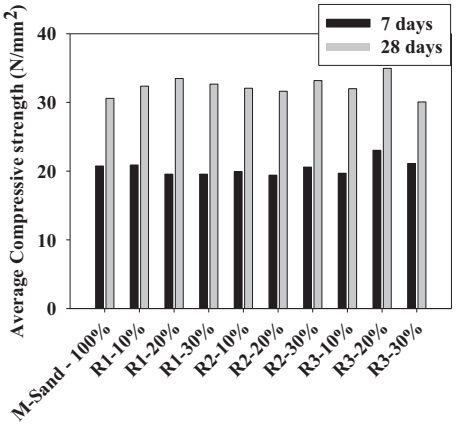

Figure 3: Average compressive strength of different concrete mixes

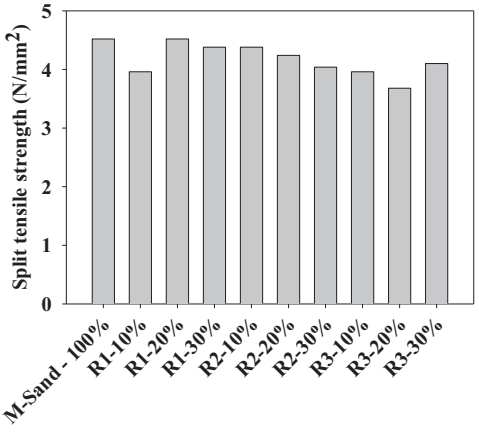

Figure 4: Split tensile strength of different concrete mixes

From Figures 3 and 4, it is clear that replacement level of up to 30%, does not affect the mechanical properties of concrete. Both compressive strength and split tensile strength test

results indicate that the properties obtained from RFA mixes are comparable to that with normal concretes.

3.4 Comparison of the durability properties of concretes

The results of rapid chloride permeability test and water permeability test are presented in Figures 5 and 6 respectively.

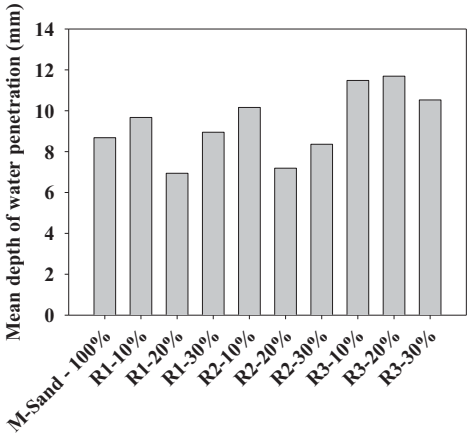

Figure 5: Mean depth of water penetration of different concrete mixes

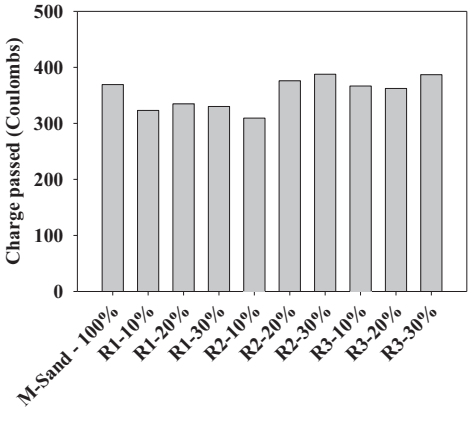

Figure 6: Cumulative charge passed of different concrete mixes

Figure 5 shows that the mean depth of water penetration for all samples used in this study is well within the limits set by Concrete Society. Figure 6 shows that all the concrete are falling in the same chloride ion penetrability category (very low) as indicated Table 3. Hence

it is clear that the durability of concretes made with RFA is similar to that with conventional concrete when assessed in terms of chloride ion penetrability and water permeability.

The observations made by studying the fresh, mechanical and durability aspects of concrete made using different RFA collected from different exposure conditions indicate that the source of the recycled aggregate does not have much significance in determining the properties of the resulting concrete.

4 CONCLUSIONS

In the present study, the fresh, mechanical and durability properties of concrete made with RFA produced from deteriorated concrete with different exposure conditions are studied. The samples studied were deteriorated concretes collected from XS1 and XC1 exposure conditions as well as fresh leftover hardened concrete which are least deteriorated. Each type of RFA were used in partial replacement of 0%, 10%, 20%, and 30% for M-sand in concrete mixes with a cement content of 380 kg/m^3 and water cement ratio of 0.45. Following are the major conclusions from the study.

- RFA has higher water absorption and lower specific gravity than M-sand.
- Workability of concrete made with RFA is less than that of the concrete made with conventional aggregates. The reduction in workability can be managed by adjusting the dosage of chemical admixtures.
- Unit weight of concrete in its fresh state, made with RFA is almost same as that of conventional concrete. Use of RFA in concrete does not contribute to under-yield or over-yield of concrete mixes**.**
- Upto a replacement level of 30%, use of RFA does not affect the compressive strength ad split tensile strength of concrete substantially.
- The durability behaviour of concrete made from RFA is similar to that of conventional concrete assessed in terms of chloride ion penetrability and water penetrability. The RFA used in this study was produced from C&D wastes collected from XS1 and XC1 exposure conditions as well as from lab-rejected samples. Irrespective of the source, the concrete produced from all the three types of RFA showed similar results, in terms of mechanical and durability properties.
- It is concluded from the present study that the source of the recycled aggregate (especially XS1 and XC1) does not have much significance in determining the properties of the resulting concrete.

ACKNOWLEDGEMENTS

Authors thank TEQIP Phase II, RIT, Kottayam for the financial assistance under its research seed money grant scheme. The authors are grateful to the staff and fellow students of Department of Civil Engineering, RIT, Kottayam for their support in various capacities.

REFERENCES

[1] 'Guidelines on Recycling, Use and Management of C&D Wastes', Technical committee report, Indian Concrete Institute (2015)

[2] 'Best Practice Guide for the use of Recycled Aggregates', New Concrete Cement & Concrete Association of New Zealand, (2011)

[3] Xiao, J., Li, W., Fan, Y. and Huang, X. 'An overview of study on recycled aggregate concrete in China (1996–2011)', *Construction and Building Materials*, **31** (2012) 364–383

[4] Evangelista, L., and de Brito, J., 'Mechanical behaviour of concrete made with fine recycled concrete aggregates', *Cement and Concrete Composites*, **29** (5) (2007) 397–401

[5] BS 8500-1:2006, Concrete –Complementary British Standard to BS EN 206-1 – Part 1: Method of specifying and guidance for the specifier (2006)

[6] IS 10262 :1982 Recommended guidelines for concrete mix design, Bureau of Indian Standards (1982)
[7] IS 1199 :1959 Methods of sampling and analysis of concrete, Bureau of Indian Standards (1959)
[8] ASTM C138, Standard Test Method for Density (Unit Weight), Yield, and Air Content (Gravimetric) of Concrete, Annual book of ASTM standards,West Conshohocken, United States, (2001)
[9] IS 516 :1959, Method of Tests for Strength of Concrete, Bureau of Indian Standards (1959)
[10] IS 5816 :1999 Method of Test Splitting Tensile Strength of Concrete, Bureau of Indian Standards (1999)
[11] ASTM C1202, Standard test method for electrical indication of concrete's ability to resist chloride penetration, Annual book of ASTM standards, West Conshohocken, United States (2010)
[12] DIN 1048-Part 5, Testing concrete water permeability, German Standard (1991)
[13] IS 875(Part 1):1987,Code of practice for design loads (other than earthquake) for buildings and structures part 1 dead loads-unit weights of building materials and stored materials, Bureau Of Indian Standards (1987)
[14] Basheer, P. A. M. 'Permeation analysis'.*In* V. S. Ramachandran, and J. J. Beaudoin (eds.) 'Handbook of analytical techniques in concrete science and technology Principles, Techniques, and Applications', Noyes Publications, Park Ridge, New Jersey, USA (2001) 658 -737

Feasible Use of Recycled Concrete Aggregates in Self-Compacting Concrete: A Review

Tung-Chai Ling, Yuxuan Liu and K. Senthil Kumar

College of Civil Engineering, Hunan University, Changsha, Hunan, China.

ABSTRACT

Globally, large volumes of recycled concrete aggregate (RCA) are produced from construction and demolition works and are increasing over time. To overcome this issue, sustainable use of resources and finding better ways to manage construction and demolition (C&D) waste have been studied and explored. One of the most promising strategies is to introduce RCA into the production of new concrete. Unlike normal vibrated concrete, RCA used in making self-compacting concrete (SCC) has only been focused on and developed in the past 10 years. This paper presents an overview of the current research works published on the use of coarse and/or fine RCA in the production of SCC. The benefits and challenges of using RCA as natural coarse and fine aggregate replacement for SCC are presented. Accordingly, the high water absorption and porous structure of RCA have been particular challenges for its use in producing SCC with high fluidity and good mechanical strength. However, some studies have demonstrated that a proper water compensative method as well as the use of supplementary cementitious materials could help enhance the overall properties of SCC prepared with RCA.

Keywords: Self-compacting concrete, C&D waste, Recycled concrete aggregate (RCA), properties, durability

1 INTRODUCTION

Concrete is the most widely used material in construction and second-most used material after water on Earth. In 2015, it was estimated that the concrete consumption in Europe was greater than 800 Mt/year [1]. In the US alone, the amount of generated C&D waste was more than 150 Mt/year for the whole of the last decade [2]. As for China, about 200 Mt of waste concrete is produced annually from C&D activities [3]. It should be highlighted that in some countries natural aggregate is a scarce commodity, and each year a huge amount of natural aggregate (~50 billion tonnes) are extracted worldwide [4]. To minimize the destruction of landscape and upsetting of the biological balance, recycled concrete aggregate (RCA) derived from C&D debris could be a great potential source of aggregate to guarantee concrete production, as well as to preserve the environment without generating piles of waste all over the world.

Self-compacting concrete (SCC) is a special concrete invented in Japan in the 1980s. Its special features are that SCC can flow under its own weight and fill formwork easily even in the presence of a high density of reinforcement bars, without mechanical vibration or undergoing any excessive segregation [5]. According to Gaimster and Dixon [6], high powder content and viscosity modifying agents are the key to achieving such self-compacting features, including the filling ability, passing ability, and resistance to segregation. However, the reduction of coarse aggregate content in the concrete system has caused a negative impact

on creep strain and drying shrinkage [7]. In general, aggregate used in SCC accounts for 62% of its total volume, of which 26% and 36% are fine and coarse aggregates respectively (Figure 1).

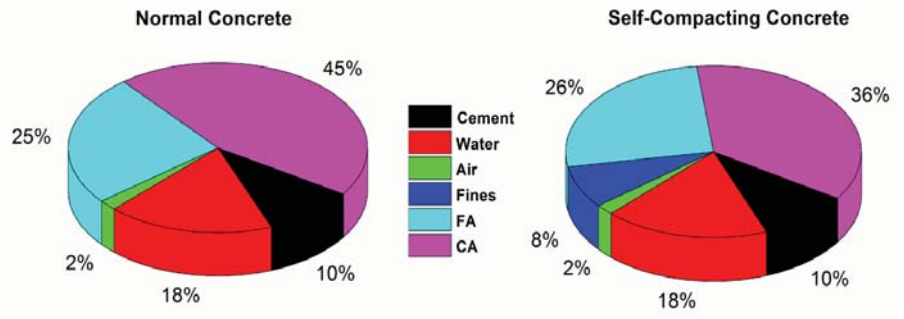

Figure 1: Constitution differences of normal concrete and self-compacting concrete [modified from reference 7]

The use of RCA in SCC is relatively new if compared to traditional vibrated concrete, and this particular research topic has only been widely explored in the past 10 years [3, 4, 8-12]. Based on the recently sourced literature published, an overview of the feasible use of coarse and fine RCA in SCC is presented in this paper. The effect of RCA used as coarse and fine aggregate replacement on SCC properties including fresh, hardened (compressive strength, flexural strength, splitting tensile strength, bond strength, thermal conductivity), durability and microstructural changes are also discussed.

2 EFFECT OF RECYCLED COARSE CONCRETE AGGREGATE (RCCA) ON SCC

Incorporation of RCA in SCC has been examined over the last decade. Most of the studies focused on the effects of the percentage use of recycled coarse concrete aggregate (RCCA) on SCC properties. The microstructural examination and ways to improve the performance of SCC containing RCCA are detailed and summarized below.

2.1 Fresh properties

One of the major key drawbacks of using RCCA is the high water absorption characteristic associated with the adhered old mortar (Figure 2). Therefore, it is important to control the high water absorption and maintain sufficient fluidity in the SCC mixture when incorporating RCCA. Many attempts have been reported in the literature and can be classified into a few methods: (i) Immersion of RCCA in water for a certain period of time [13, 14], (ii) Adjustment of the mix proportion to meet the required workability criteria [15, 16], (iii) Introducing special admixtures [13, 17-19], (iv) Correction through experimental mixing procedures [20], and (v) Adding a certain amount of compensative water [1, 21]. As reported in the previous literature, with a proper water compensation method and mix proportion design, the feasibility of RCCA adoption to meet the required workability criteria has been validated [13-16, 19, 21, 22]. Generally, the usage of RCCA causes a marginal reduction in filling ability (slump flow test, T_{500} test, V-funnel test). However, the passing ability is not significantly affected by the use of RCCA. Khan et al. [22] demonstrated that passing ability mainly depends on the concrete mix proportion, although density reduction has a slight effect on the change. Tuyan et al. [13] indicated that passing ability is more likely to be dominated by the usage of a superplasticizer than the RCCA content.

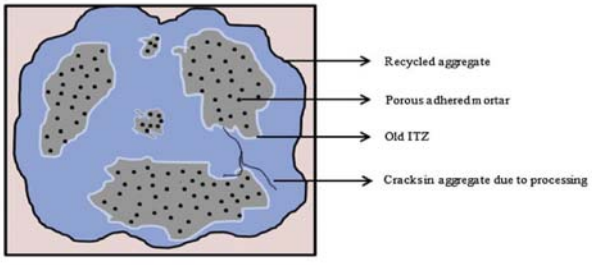

Figure 2: General structure of recycled concrete aggregate [10]

2.2 Hardened properties

Hardened properties are an important parameter for the employment of RCA in SCC. In general, RCCA affects the properties of concrete in many aspects [10]. Compressive strength decreases with an increase of RCCA substitution, which could be due to its lower intrinsic strength, poor interfacial ability and micro cracks. Also, the RCCA replacement adversely affects the split tensile strength and flexural strength [10]. They also found that the concrete creep of RCCA samples is higher, probably due to the higher mortar content. An approximate 45% reduction in elastic modulus was observed at 100% RCCA content [10]. The significant reduction of the modulus of elasticity could result in a high drying shrinkage ratio.

Several published papers [12-20, 22] have reported some aspects of utilization of RCCA in SCC. The effect of RCCA on the fresh and hardened properties of SCC are discussed below and summarized in Table 1,

- Compressive strength: Compressive strength decreases with an increase of RCCA replacement, and it was noticed that commonly the strength loss is within 20% regardless of the replacement content. Although different parameters could affect the compressive strength, generally it was noticed that the extent of strength loss in self-compacting concrete is relatively lower than that found in normal recycled concrete.
- Split tensile and flexural strength: Tensile strength decreases with increased use of RCCA. The variation of strength loss varies in the literature. Some is relatively low (~18%) [13, 15], while as high as 58% reduction of tensile strength was also reported in a study by Revathi et al. [16]. Modani and Mohitkar [14] suggest that the failure pattern of concrete is due to an interfacial bond and aggregate failures. As for flexural strength, Panda and Bal [17] indicated that their experimental flexural test results were lower than the theoretical value calculated based on compressive strength.
- Bond strength: Wang [23] conducted a pull out test with two different types of RCCA: pre-treated aggregate and untreated recycled aggregate. It was reported that although the reinforcement steel bar profile dominates the bond strength, the quality and content of RCA slightly affects their bonding behaviour. Several bond strength prediction models have been introduced in [23], showing that the experimental bond strength results are always higher than the predicted values.
- Thermal conductivity: Fenollera et al. [24] performed a test to investigate the thermal conductivity of SCC with incorporated RCCA. Generally, a linear decrease of thermal conductivity was observed with increasing RCCA content used.

Table 1: Summary of works using RCCA on the fresh and mechanical properties of SCC

Ref.	Source of RCCA	Compensative method	Effect on fresh properties and hardened properties
[13]	Laboratory concrete waste	Using saturated surface dried RCCA and a superplasticizer	**Fresh properties**: more superplasticizer was needed with higher RCCA. Passing ability was not significantly affected by RCCA. **Compressive strength:** slight increase for replacement < 40%, and no significant effect was observed up to 60% of RCCA. **Split tensile strength:** 8.8-16% reduction with 60% RCCA replacement.
[14]	Laboratory concrete waste	Immersed in water for 24 hours and the RCA was dried before use	**Fresh properties:** satisfy the requirements. **Compressive strength**: 28 days, reduction of 3.7% (20% ratio), 5.8% (40% ratio), lower strength development. **Tensile strength:** similar to compressive; interfacial bond failure and aggregate failure were indicated
[15]	40 year old bridge	Experimentally adding water to achieve the required consistency	**Fresh Properties:** slightly difference, but satisfied all the requirements. **Compressive strength:** decreased by 3.88% and 8.55% for 50% and 100% replacement content. **Tensile strength:** decreasing range of 2.49-13.05%
[16]	35 year old building	A few trials were conducted first to determine the mix proportion	**Fresh properties:** slight decrease, but satisfied all the requirements. **Compressive strength:** slight decrease (for 50% ratio), and 10~20% strength reduction for 75% and 100% RCCA replacement ratios. **Tensile strength:** up to 58% of reduction
[17]	25 year old building	Adjusted by using an admixture	**Compressive strength:** decrease with an increase of RCCA content. **Flexural strength:** 28 days' flexural strength was less than the theoretical value for all RCCA content. **Tensile strength:** decrease with an increase of RCCA content.
[18]	Commercial supply	Oven dried aggregate with use of a superplasticizer	**Compressive strength:** only 3.3% loss was observed for 100% replacement. **Modulus of elasticity:** reduced about 8%.
[19]	Laboratory concrete waste	Use of a superplasticizer	**Fresh properties:** satisfy workability criteria. **Compressive strength:** 8.5-17.3% loss in 28 days and 19.9% loss in 56 days was observed for 100% replacement.
[20]	6 months tested concrete cubes	Corrected by the mix procedure	**Fresh properties:** slightly improved with 30% and 50% replacement, and decreased at a higher dosage. Not likely to satisfy the filling ability requirement at >50% dosage. Higher segregation ratio for 70% and 100% replacement.
[22]	Building	Not specified	**Fresh properties**: decrease of workability, while maintaining the passing ability (L-box value). **Compressive strength:** reduced 15-20% with 100% replacement.

2.3 Durability properties

Durability of concrete is also an important aspect in SCC, in particular for structure and marine applications. Some research works have been performed in regard to this topic.

Kapoor et al. [25] reported that the initial rate of surface absorption was found to be 40% higher in SCC prepared with RCCA than that of natural aggregate SCC. A similar increasing trend of permeability was also observed in a study by Modani and Mohitkar [14] in that the water absorption increased by about 40% with 100% RCCA replacement, and a higher number of permeable voids was retained in the RCCA concrete sample. Oliveira et al. [18] report that the capillary suction capacity mainly depends on the superficial layer of the concrete; therefore, there is no close correlation between RCCA and capillary suction capacity. Moreover, it was revealed that employing silica fume (SF) and metakaolin (MK) can greatly compensate the durability inferior properties. Tuyan et al. [13] performed a freeze thaw test with 300 cycles on concrete with 0%, 20%, 40% and 60% RCCA replacement, and the results (Figure 3) indicated that the use of RCCA caused severe damage and cracks, thus decreasing the freeze-thaw resistance.

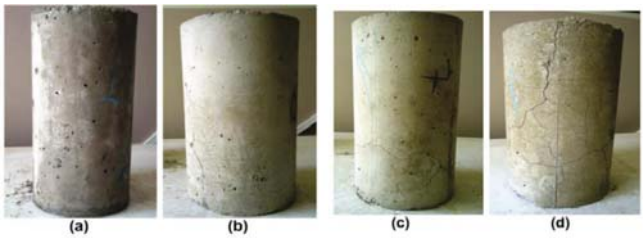

Figure 3: Images of concrete samples after 300 freeze-thaw cycles [13]

Singh et al. [19] conducted accelerated carbonation tests, and an increase of carbonation depth was observed with increasing RCCA replacement content. There was approximately a 63% increment of carbonation depth when coarse aggregate was fully replaced by RCCA. Also, a good linear correlation of carbonation depth and compressive strength was observed. Modani and Mohitkar [14] found that the presence of RCCA in SCC causes a reduction of resistance to acid attack and chloride penetration. It was observed that the mass loss of the RCCA SCC sample was 2.8 times higher than natural aggregate SCC samples after exposure to sulphuric acid solution attack. However, strength loss (after acid exposure) of SCC samples prepared with 20% of RCCA was only slightly lower than samples prepared with natural aggregate. But, more than 17% strength loss was observed when RCCA replacement exceeded 60%.

2.4 Microstructure

As pointed out by Behera et al. [10], the existence of an old interfacial transition zone and the porous nature of adhered mortar are two distinct properties of recycled aggregate, which results in the reduction of both mechanical and durability performance. A typical microstructure of SCC incorporating RCCA is shown in Figure 4, indicating its porous nature with micro and macro pores of old mortar. It is generally agreed that the mechanical and durability properties mainly depend on the microstructural development. The presence of old ITZ and a weak microstructure not only cause weak mechanical strength but also results in an increase of concrete permeability [19].

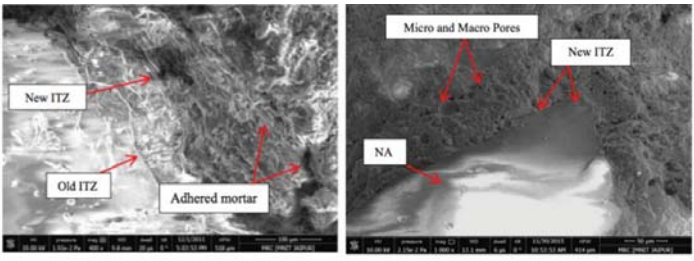

Figure 4: SEM image showing ITZ and the porous nature of adhered mortar of recycled SCC [19]

2.5 Roles of mineral admixtures in SCC with RCCA

As discussed earlier, there are some drawbacks to RCCA incorporation, such as strength loss, higher water absorption and air permeability, inferior resistance to carbonation, freeze-thaw, and chloride attack. Mineral admixtures have been introduced and found to be effective in improving the detrimental properties of SCC prepared with RCCA. Khan et al. [22] indicate that the use of 10% fly ash and 15% silica fume results in an increase of compressive strength. Moreover, Gesoglu et al. [29] pointed out that incorporating SF improves the compressive strength, splitting tensile strength, flexural strength and modulus of elasticity. Kapoor et al. [25] found that 10% replacement of silica fume (SF) and metakaolin (MK) compensated for the strength loss of concrete prepared with 50% of RCCA. It shows that SF and MK are effective in microstructure refinement and reduce the chloride ion penetration and water absorption. As for fresh properties, it was pointed out by Senthamilselvi and Revathi [27] that the replacement of mineral admixtures like SF and GGBS increases the filling ability and benefits the segregation resistance. Singh et al. [26] used a SEM to examine the effect of fly ash and MK particles on the microstructural change of concrete containing 50% and 100% of RCCA. It was observed that fly ash and MK particles effectively fill the pores, refine the microstructure and thus can improve the properties of SCC in many aspects.

3 EFFECT OF RECYCLED FINE CONCRETE AGGREGATE (RFCA) ON SCC

Fine fractions of recycled concrete aggregate (<5 mm) are also gaining interest for use in SCC. Compared to RCCA, experiments on the use of RFCA in SCC are still limited. The following sections briefly describe the fresh and hardened properties of SCC containing RFCA.

3.1 Fresh properties

Kou and Poon [21] conducted an experiment to investigate the feasibility of using fine recycled aggregate in SCC (0%, 25%, 50%, 75%, 100% of fine aggregate by volume) with three different W/B ratios (0.44, 0.40, 0.35). To ensure that the mix achieved the designed W/B, compensative water was added to the concrete mix based on the 24h water absorption value of RCA. It was noticed that the concrete properties with RFCA were slightly different from those prepared with natural river sand. In terms of fresh properties, an increase in slump was observed with an increase of RFCA content. This was due to the additional water (initially used for saturating the RFCA) that remained in the concrete mixture and thus contributed to the increase of slump flow. Also, Güneyisi et al. [28] demonstrated that pre-soaked recycled coarse and fine aggregate has a positive effect on the fresh properties of SCC. Similarly, Lopez et al. [1] performed an experiment in which less adjusted water was used to pre-soak the recycled aggregate to prevent the risk of segregation. The results show

that the amount of RFCA replacement has a great impact on the flowability and workability of SCC. Generally, a decrease in filling ability and passing ability have been observed with increased use of RFCA, and concrete with more than 20% of RFCA fails to meet the workability requirements of SCC. This is partly due to the increase of yield stress, according to the rheology tests by Lopez et al. [1]: the incorporation of recycled fine aggregate causes a higher yield stress, thereby requiring higher stress to initiate and maintain concrete flow. This also indicates that the shear thickening behaviour of SCC noticeably declines with increasing use of RFCA, which essentially explains the noticed improvement of fresh properties to a certain extent [28].

3.2 Mechanical and durability properties

According to Kou and Poon [21], compressive and tensile split strengths decrease with an increase of RFCA content. A similar increase was observed for drying shrinkage. A study of Carro-López et al. [1] reported a 8% and 47% decrease of compressive strength when 20% and 100% of RFCA were used in SCC. Gesoglu et al. [29] also demonstrated a 30.9% strength loss at 56 days when both coarse and fine recycled aggregates were used in SCC. However, a different result was found in [30] which indicated a marginal increase of compressive strength at 28 days with the use of recycled aggregate. About 11%, 5%, and 8% increases of strength were reported for respective SCC samples prepared with 20% of RFCA, 20% of RCCA, and a 20% combination of both RCA. As for durability, Kou and Poon [21] reported that good chloride resistance of SCC was observed when incorporating RCFA, probably attributed to the content of finer particles (<0.3 mm) acting as an “effective filler” to produce a denser microstructure. The inferior properties of RFCA can also be enhanced by adopting supplementary cementitious materials (SCM).

4 SUMMARY AND CONCLUSION

This paper presents a comprehensive review of the effect of adopting coarse and fine recycled concrete aggregate (RCA) in self-compacting concrete (SCC). In general, RCA can be suitably used as coarse and fine aggregate in SCC manufacturing. The effects of using recycled aggregate on the properties of SCC are:

- The use of RCCA significantly affects the fresh properties of SCC mixture, in particular the filling ability. However, with proper water compensative methods and mix designs, it is feasible to utilize RCCA up to 100% and meet all the required workability criteria of SCC.
- SCC with RCCA exhibits lower mechanical properties and poor durability as compared to natural aggregate SCC associated with the porous nature and weak bonding of old interfacial transition zones of RCCA. However, most of the published data suggest that the reduction of compressive strength is within 20% regardless of the RCCA content used.
- It is promising to use mineral admixtures such as silica fume or metakaolin to enhance the overall properties of SCC prepared with RCCA. Moreover, the microstructure and adhesion between the RA and cement paste can be improved with the presence of these very fine materials as filler and pozzolanic materials.
- As for the incorporation of RFCA, the effects on the fresh and hardened properties are found to be similar to that of RCCA used in SCC. To date, there is still very little information reported in regard to the microstructure and long-term durability performance of SCC with RFCA, and thus more studies are needed.

5 ACKNOWLEDGEMENTS

Research funding from the Hunan University (531109020061) and the Thousand Young Talent Expert Program (733201005) and are gratefully acknowledged.

6 REFERENCES

[1] Carro-López. D, González-Fonteboa. B, De Brito. J, Martínez-Abella. F, González-Taboada .I, and Silva.P, 'Study of the rheology of self-compacting concrete with fine recycled concrete aggregates',*Constr. build. mater.* **96** (2015) 491-501.

[2] Ding.T and Xiao.J., 'Estimation of building-related construction and demolition waste in Shanghai', *Waste. manage.* **34**(11) (2014) 2327-2334.

[3] Xiao.J, Li.W, Fan.F, and Huang.X, 'An overview of study on recycled aggregate concrete in China (1996–2011)', *Constr. build. mater.***31** (2012) 364-383.

[4] De Brito. J, Ferreira.J, Pacheco.J, Soares.D, and Guerreiro.M, 'Structural, material, mechanical and durability properties and behaviour of recycled aggregates concrete', *Journal of Building Engineerin.* **6** (2016) 1-16.

[5] Geiker.M, "9 - Self-compacting concrete (SCC) A2 - Mindess, Sidney," in Developments in the Formulation and Reinforcement of Concrete, ed: Woodhead Publishing, (2008),187-207.

[6] Gaimster.R and Dixon.N, "9 - Self-compacting concrete," in Advanced Concrete Technology: Processes, J. Newman and B. S. Choo, Eds., ed United Kindom: Butterworth-Heinemann, 2003.

[7] Nayak. N.V and Jain A.K, Handbook on Advanced Concrete Technology, Alpha Science International, 2012.

[8] Li.X, 'Recycling and reuse of waste concrete in China: Part I. Material behaviour of recycled aggregate concrete', R*esour.Conserv. Recy.* **53** (1-2) (2008) 36-44.

[9] Li.X, 'Recycling and reuse of waste concrete in China: Part II. Structural behaviour of recycled aggregate concrete and engineering applications', *Resour.Conserv. Recy.* 53 (1-2) (2008) 107-112.

[10] Behera.M, Bhattacharyya.S.K, Minocha.A.K, Deoliya.R, and Maiti.S, 'Recycled aggregate from C&D waste & its use in concrete – A breakthrough towards sustainability in construction sector: A review', *Constr. build. mater.* **68** (2014) 501-516.

[11] Fan C.C, Huang.R, Hwang.H, and Chao.S.J, 'Properties of concrete incorporating fine recycled aggregates from crushed concrete wastes', *Constr. build. mater.* **112** (2016) 708-715.

[12] Poon.C.S, Shui.Z.H, and Lam.L, 'Effect of microstructure of ITZ on compressive strength of concrete prepared with recycled aggregates', *Constr. build. mater.* **18**(6) (2004) 461-468.

[13] Tuyan.M, Mardani-Aghabaglou.A, and Ramyar.K, 'Freeze–thaw resistance, mechanical and transport properties of self-consolidating concrete incorporating coarse recycled concrete aggregate', M*ater. Design.* **53** (2014) 983-991.

[14] Modani.P.O and Mohitkar.V.M, 'Self-compacting concrete with recycled aggregate: A solution for sustainable development', *International Journal of Civil & Structural Engineering,* **4**(3) (2014) 430-440.

[15] Grdic.Z.J, Toplicic-Curcic.G.A, Despotovic.I.M, and Ristic.N.S, 'Properties of self-compacting concrete prepared with coarse recycled concrete aggregate', *Constr. build. mater.* **24**(7) (2010) 1129-1133.

[16] Revathi.P, Selvi.R.S, and Velin.S.S, 'Investigations on Fresh and Hardened Properties of Recycled Aggregate Self Compacting Concrete', *J. Inst. Eng. India Ser. A.* **94** (2013) 179-185.

[17] Panda.K.C and Bal.P.K, 'Properties of Self Compacting Concrete Using Recycled Coarse Aggregate', *Procedia Eng.* **51** (2013) 159-164.

[18] Pereira-de-Oliveira.L.A, Nepomuceno.M.C.S, Castro-Gomes.J.P, and Vila.M.F.C, 'Permeability properties of self-compacting concrete with coarse recycled aggregates', *Constr. build. mater.* **51** (2014) 113–120.

[19] Singh.N and Singh. S.P, 'Carbonation and electrical resistance of self compacting concrete made with recycled concrete aggregates and metakaolin', *Constr. build. mater.* **121** (2016) 400-409.

[20] Safiuddin.M.D, Salam.M.A, and Jumaat.M.Z, 'Effects of recycled concrete aggregate on the fresh properties of self-consolidating concrete', A*rch Civ Mech Eng.* **11**(4) (2011) 1023-1041.

[21] Kou.S.C and Poon.C.S, 'Properties of self-compacting concrete prepared with coarse and fine recycled concrete aggregates', *cement concrete comp.* 31(9) (2009) 622-627.

[22] Khan.R.M, Amin.F, and Ahmad.M, 'Comparison of self compacting concrete using recycled aggregates & normal aggregates', *International Journal of Advance Research in Science and Engineering,***4** (2015) 75-83.

[23] Wang.H.L, 'Steel–concrete bond behaviour of self-compacting concrete with recycled aggregates', *Mag. concrete res.* **68**(13) (2016) 678-691.

[24] Fenollera.M, Míguez.J, Goicoechea.I, and Lorenzo.J, 'Experimental Study on Thermal Conductivity of Self-Compacting Concrete with Recycled Aggregate' *Materials,* **8**(7) (2015) 4457-4478.

[25] Kapoor.K, Singh.S.P, and Singh.B, 'Durability of self-compacting concrete made with Recycled Concrete Aggregates and mineral admixtures', *Constr. build. mater.* **128**, (2016), 67-76.

[26] Singh.N and Singh.S.P, 'Carbonation resistance and microstructural analysis of Low and High Volume Fly Ash Self Compacting Concrete containing Recycled Concrete Aggregates', *Constr. build. mater.* **127** (2016) 828-842.

[27] Senthamilselvi.R and Revathi.P, 'Effect of mineral admixtures of the fresh properties of self compacting concrete produced with recycled aggregate', *International Journal of Research in Engineering and Technology,* **5**(20) (2016) 194-200.

[28] Guneyisi.E, Gesoglu.M, Algın.Z, and Yazıcı.H, 'Rheological and fresh properties of self-compacting concretes containing coarse and fine recycled concrete aggregates', *Constr. build. mater.* **113** (2016) 622-630.

[29] Gesoglu.M, GUneyisi.E, Oz.H.O, Taha.I, and Yasemin.M.T, 'Failure characteristics of self-compacting concretes made with recycled aggregates', *Constr. build. mater.* **98** (2015) 334-344.

[30] Vinay Kumar.B.M, Ananthan.H, and Balaji.K.V.A, 'Experimental studies on utilization of coarse and finer fractions of recycled concrete aggregates in self compacting concrete mixes', *Journal of Building Engineering,* **9** (2017) 100-108.

Chloride Induced Corrosion of Steel in Alkali-activated Cements : A Review

Shishir Mundra[(1)], Susan A. Bernal[(1,2)] and John L. Provis[(1)]

[(1)]Department of Materials Science and Engineering, The University of Sheffield, Sir Robert Hadfield Building, Sheffield, S1 3JD, United Kingdom

[(2)]Department of Civil and Structural Engineering, The University of Sheffield, Sir Frederick Mappin Building, Sheffield, S1 3JD, United Kingdom

ABSTRACT

Alkali-activated materials (AAMs) have significantly different hydration products and pore solution compositions, when compared to Portland cement based concretes. The alkaline nature of the pore solution in both types of cements allows the embedded steel rebar to be protected by a passive film, composed of a complex solid assemblage of iron oxides and hydroxides. The corrosion of the steel rebar is one of the primary reasons for the premature failure of reinforced concrete structures, and corrosion of the rebar is primarily driven either by the lowering of pH of the pore solution (leaching of alkalis, carbonation) or by the presence of chlorides above a threshold concentration at the steel-concrete interface. This paper presents an overview of the factors that influence the service life of mild steel reinforced AAMs in chloride rich environments: the hydration product chemistry, type of precursor, alkali-activator, the pore structure, and pore solution chemistry, the effect of chloride binding, and the corrosion of the steel reinforcement.

Keywords: Alkali-activatedcements, Chloride, Corrosion, Steelrebar,

1 INTRODUCTION

The alkaline environment in reinforced concrete structures allows the embedded steel reinforcement to be passivated by a thin film, composed of a complex solid assemblage of iron oxides and hydroxides [1]. When in service, the alkalinity of the pore solution in mild steel reinforced concretes needs to be sufficiently high (pH > 9-10) to ensure the stability of the passive film [2]. Corrosion of the embedded steel reinforcement has been identified as one of the primary causes of premature degradation of reinforced concrete structures. Corrosion of steel in concrete environments is primarily driven by either the lowering of the pH of the pore solution (leaching of alkalis, or carbonation) which can lead to uniform corrosion; or due to the ingress of chloride in significant concentrations resulting in localised breakdown of the passive film [3].

In developed parts of the world, where the use of de-icing salts and marine sprays (in coastal regions) are frequent, chloride ingress is one of the major causes of premature failure of reinforced concrete structures. Therefore, the durability or the service life of a structure is often described by the rate of chloride ingress, or the time required for chloride ions to achieve a threshold concentration at the steel-concrete interface. This threshold concentration has been defined as the minimum chloride concentration required for the breakdown of steel passivity, and is often referred to as the ‘critical chloride level’ or ‘chloride threshold value’ [1].

Alkali-activated materials (AAMs) have witnessed rapidly increasing research and commercial attention over the past few decades, due to their potential to achieve reduced greenhouse emissions and performance advantages, in some applications, when compared to Portland cement (PC)-based concrete [3–5]. AAMs are produced through the chemical reaction between a powdered aluminosilicate source (usually an industrial by-product such as slag, fly ash) and an alkaline solution (generally a solution of sodium hydroxide, sodium silicate) [4]. AAMs can be broadly categorised into systems with high Ca content such as alkali-activated slags where the phase assemblage is dominated by a calcium-aluminosilicate hydrate (C-A-S-H) type gel; and low-Ca systems such as alkali-activated fly ashes, where the main reaction product is a three-dimensional hydrous alkali-aluminosilicate (N-A-S-H) type gel [4]. The pore structure and pore solution chemistry of AAMs have been found to be significantly different from those of PC-based concretes; and within the class of materials that can be described as AAMs, the composition of the pore solution and the pore network vary due to the differences in the precursor chemistry. The ingress of chloride into alkali-activated cement matrices has also been found to differ from the behaviour of PC-based concretes [2].

Therefore, an understanding of the movement of chloride through such matrices, the interaction of the steel reinforcement with the pore solution at the steel-concrete interface, and the initiation of chloride induced corrosion are important to assess the durability of steel-reinforced AAMs. This paper presents an overview of the factors that can influence the service life of steel reinforced AAMs in the presence of chlorides.

2 FACTORS INFLUENCING CHLORIDE INGRESS IN AAMS

The ingress of chloride into concrete in structural contexts has been studied extensively for the case of PC based systems [6-7]. The transport of chloride from the external environment toward the steel-concrete interface has been shown to be influenced by a number of factors such as the external environment, quality of concrete cover, the binder chemistry, and its capacity to bind chloride, the pore structure, and the pore solution chemistry [8]. Unlike PC based concretes where the reaction of chloride with hydration products results in structural modification, AAMs do not show significant transformation of layered calcium sulfoaluminate hydrates to chloroaluminates such as Friedel's salt [2]. Therefore, the permeation of chloride through AAM depends primarily on the resistance of the binder to chloride transport, and potentially binding in other disordered reaction products without such marked structural changes, as discussed below. Only a limited number of studies have reported the ingress of chloride into AAMs. When compared to PC/blended systems under the same conditions, AAMs have in several cases been reported to possess a lower chloride permeability [2].

The nature of the binder gel and the secondary hydration products in AAMs has been demonstrated to have an impact on the chloride permeability. In high-Ca AAMs such as alkali-activated slags (AAS), where a C-A-S-H type gel is the major reaction product, chloride ions have the potential to be chemisorbed and chemically bound to the C-A-S-H gel [9]. Kayali et al. [10] demonstrated the capability of layered double hydroxides (LDH), formed in in PC/slag blended systems, to adsorb chloride, and related the decrease in corrosion rate of the steel reinforcement to the degree of chloride binding. Secondary reaction products in AAS such as LDH-structured phases (including hydrotalcite-like and AF_m/strätlingite components) also have the capability to bind chloride through adsorption and ion-exchange. On studying the chloride binding capacity of individual solid phases in AAS, Ke et al. [11] reported surface adsorption to be the dominant binding mechanism for chloride uptake in hydrotalcite-like phases, and lattice substitution to be the major binding mechanism in the case of strätlingite. The higher porosity and the higher surface area exhibited by the N-

A-S-H type gels provide a greater potential for the surface adsorption of chloride in low Ca AAMs, when compared to high-Ca AAMs with the C-A-S-H gel [9]. In alkali-activated fly ashes, the presence of halite (NaCl) in the X-ray diffraction analysis of dried specimens of chloride-penetrated regions could possibly suggest the N-A-S-H gel hosting a chloride rich pore solution [9].

The concentration of alkalis and hydroxides in neat PC hydrates have been observed to be up to approximately 0.70 M [12]. The concentration of Ca^{2+} and SO_4^{2-} are around 2 mM and 7 mM respectively, while Si and Al are present at levels of less than 1 mM [12]. However, these concentrations would change as a function of time and composition of the cement, particularly if pozzolanic additives are used. As mentioned earlier, the pore solution chemistries of AAMs and PC differ significantly due to the differences in the hydration products and the bulk composition of binders. A general consensus exists in the literature that the concentration of alkalis and hydroxides in AAMs is much higher (> 1 M even at later stages of curing) than in PC, and the alkalinity of the pore solution is dependent on the concentration of the alkali-activator [13–17]. The higher alkalinity and the greater ionic strength of the pore solutions in AAMs when compared to the pore solutions of PC could create a potential gradient leading to retardation of the transport of chloride. The concentrations of Al and Si in the pore solution were found to be relatively low (between 0.3 to 3 mM) in both highCa and lowCa AAMs as they are incorporated into the respective gel frameworks [13–17]. In the case of AAS, the sulfide from the slag exists mainly in S2- state in the pore solution, with the potential to be oxidised to complex sulfur species. Gruskovnjak et al. [16] reported the total concentration in pore solutions of AAS to be around 0.45 M. The influence of S^{2-} on the corrosion behaviour of the steel reinforcement is discussed in Section 3 below.

The pore structure of a cementitious binder material plays an important role in the movement of ions from the external environment towards the steel-concrete interface. The pore structure of AAMs at a particular curing age depends strongly on a number of factors, such as the type of activator (for e.g. alkali hydroxide, silicate, and carbonate), the water/binder (w/b) ratio, the binder type, and curing conditions [2, 18]. In general, the pores in alkali hydroxide activated AAMs have been reported to be much larger than in alkali silicate activated AAMs [18]. Puertas et al. [19] using MIP showed that the total porosity in mortars of slags activated using waterglass was half that of NaOH activated slags after 28 days of curing. Similar to PC, the porosity in AAMs has been found to have a direct correlation to the w/b ratio [18] and a higher w/b ratio leads to a higher volume of connected pores. AAS have been found to possess a more refined pore structure than alkali-activated fly ashes. Provis et al. [20], through X-ray microtomography measurements, presented an inverse relationship between the segmented porosity and the diffusion tortuosity for slag-rich and fly-rich binders. A lower segmented porosity and a higher diffusion tortuosity were observed for AAS when compared to alkali-activated fly ashes. Ismail et al. [9] reported that the volume of permeable voids in AAS was lower than in alkali-activated fly ashes and suggested that greater amounts of bound water in AAS than alkali-activated fly ashes lead to higher pore-filling capabilities of the C-A-S-H gel (in high-Ca AAMs) than the N-A-S-H type gels (characteristic of low-Ca AAMs). In comparison to PC based concretes, the total porosities of AAS based concretes have been found to be either comparable or lower [21]. Bernal et al. [22], Ismail et al. [9] and Puertas et al. [19] each reported a lower volume of permeable voids for AAS when compared to PC, however the total porosity was much higher for alkali-activated fly ashes. Provis et al. [20] found comparable diffusion tortuosity and lower porosity values for AAS when compared to theoretical values for porosity and tortuosity of PC. In both low-Ca and high-Ca AAMs, it is very important to note that unlike in PC based concretes, there exists no detectable quantity of portlandite that can act as a buffering agent,

therefore the durability of the embedded reinforcement in AAMs are highly dependent on the quality of curing [14].

Some authors have used the salt ponding test (ASTM C1543) and the NordTest NT Build methods 492 and 443 to quantify the chloride diffusion coefficient and the migration coefficient. Ismail et al. [9] observed the chloride diffusion coefficient of alkali-activated fly ash mortars to be much higher than those of AAS, primarily due to the higher porosity in alkali-activated fly ashes. Ma et al. [23] and Ismail et al. [9] also reported the non-steady state diffusion coefficient of AAS concretes to be much lower than that of PC concretes. They related the lower diffusion coefficient to the refined pore structure and its high tortuosity.

3 CORROSION OF STEEL REINFORCEMENT

As stated earlier, corrosion of the embedded reinforcement is highly dependent on the local environment of the steel-concrete interface, and is initiated either due to the lowering of pH (leaching of alkalis or carbonation of the concrete cover) or by the ingress of chloride. In the case of chloride ingress, the concentration of chloride at the steel-concrete interface needs to be above a threshold level to initiate localised corrosion of the steel reinforcement. This threshold concentration has been reported to be dependent on several parameters such as the hydration products, the pore solution chemistry and alkalinity, and local microstructural features such as air voids [1]. In the case of PC based systems, there exist a plethora of reported chloride threshold values and methods for their determination, primarily due to the number of variables and parameters which can be important [1]. However, there exist limited data for both high Ca and low Ca AAMs.

Given the higher alkalinity of the pore solution in AAMs in comparison to PC, the degree of passivation of the steel reinforcement may also vary and lead to differences in the critical chloride content. However, Bastidas et al. [24] and Miranda et al. [25] observed very similar passivation behaviours for alkali-activated fly ashes and PC mortars, and reported an increased degree of reinforcement corrosion upon the addition of chloride (2 wt. % of binder) in the former. Babaee and Castel [26] reported comparable polarisation resistances for steels embedded in low-Ca fly ash geopolymers and PC concretes. Monticelli et al. [27], on the other hand, obtained chloride threshold values for alkali-activated fly ash mortars (1-1.7 wt. % of binder) which were 2-3 times higher than PC mortars (0.5 wt. % of binder). A lower degree of corrosion for alkali-activated fly ashes in comparison to PC mortars was also reported by Kupwade-Patil and Allouche [28]. The variation in the corrosion behaviour/chloride threshold values for steel embedded in alkali-activated fly ashes (or low-Ca AAMs) when compared to PC based systems, can be attributed primarily to the differences in the chemistry of the binder, the curing times and the differences in the manner in which chloride is introduced. In a previous study by the authors [29], it was found that higher the alkalinity of the pore solution at the steel-concrete interface, the higher would be the degree of passivation and consequentially the chloride threshold concentration (shown in Figure 1). The onset of pitting due to chloride in highly alkaline solutions was proposed to be related to the dissolution of the outer layer of the passive film and the concentration of chloride, and the onset of pitting in these highly alkaline conditions appeared at $[Cl^-]/[OH^-]^3 = 1.25$ [29] rather than being a direct ratio between these concentrations as is often used in the literature.

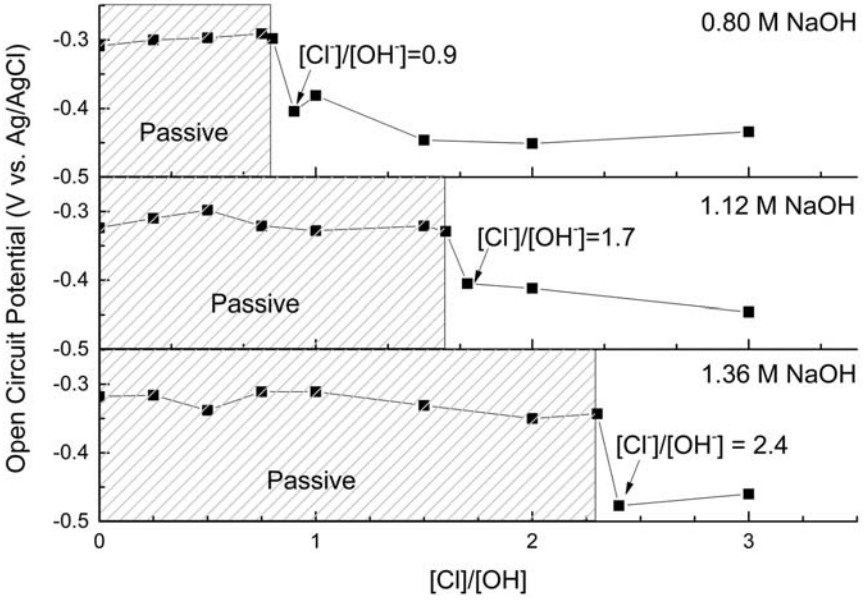

Figure 1: The chloride threshold values determined using open circuit potential.

Measurements for steel immersed in simulated pore solutions representative of low-Ca AAMs (0.80 M, 1.12 M and 1.36 M NaOH solutions) (adapted from [29]). The dashed grey regions indicate the concentration of chloride for which the steel remains in its passive state. The sudden decrease in the open circuit potential is indicative of the active state, characterised by the formation of pits. An increased alkalinity of the pore solutions provides a higher degree of passivation to the steel reinforcement, resulting in a higher chloride threshold concentration.

In highCa AAMs such as AAS, it can be presumed that the presence of significant quantities of S^{2-} would change the nature of the passive film as well as the mechanism of depassivation in chloride rich environments. The influence of S^{2-} on the behaviour of steel corrosion is also of significant importance in PC/slag blended systems [30]. The presence of S^{2-} would reduce the amount of available oxygen at the steel surface as it readily oxidises. The presence of sufficient amounts of oxygen is essential for the development of the passive film. It is also well known that the presence of S^{2-} species would create a reducing environment around the steel surface and therefore, the existence of Fe^{2+} species would be more favourable than the more usual Fe^{3+} present in passivating oxide films [30]. Shoesmith et al. [31,32] studied the passivation of steel in highly alkaline solutions with varying quantities of sulfide and found that the presence of sulfide could lead to the formation of a black iron sulfide film, possibly a $Fe_{1-x}S$ mackinawite layer. According to Myers et al. [17] and other authors [13,15,16] mentioned in Section 2, the concentration of sulfide in the pore solution of AAS is around 0.45 M. Therefore, steel embedded in AAS, it could be hypothesised that the formation of a hydrated iron oxide passivating film would be hindered by the high concentration of sulfide and the oxide layer on the steel surface (which exists prior to embedding in the concrete) would be reduced to a non-stoichiometric FeS layer through a dissolution mechanism. Therefore, the critical chloride level in AAS based concretes can plausibly be assumed to be dependent on the chemistry of the passive layer. Holloway and Sykes [33], in a study characterising chloride induced corrosion of steel in AAS mortars using the galvanostatic pulse method, suggested that the oxidation of S2-

toelemental sulfur with time plays a crucial role in the resistance to chloride induced pitting. Some authors have suggested that sulfide in low concentrations could possibly inhibit pitting due to chlorides for PC/slag blended systems. Scott and Alexander [30] studied the influence of sulfide and other sulfur species such as thiosulfates and sulfate in simulated pore solutions of PC/slag blended systems on the chloride threshold value and found that the reinforcement exposed to sulfide containing solutions had a lower chloride threshold value than those immersed in sulfide free-solutions. They reported that the redox potential to be inversely related to the amount of reduced sulfur species in the pore solution. Criado et al. [34] studied the corrosion behaviour of steel in AAS mortars immersed in alkaline medium with and without chlorides and found the redox potential to be around -600 mV. Similar potentials were found when steel was immersed in simulated pore solutions of AAS. Conventionally, the steel would be considered to be corroding at such low potentials, however, analysis upon removal of the steel from the mortar revealed no corrosion products/pits; and no chloride-induced pitting was observed for steel immersed in simulated pore solutions of AAS even with $[Cl^-]/[OH^-]$ ratios as high as 4 when tested with shorter durations of exposure [35]. Such an observation indicates the role of sulfide in creating a reducing environment and inhibiting the development of the passive Fe^{3+} oxide film. The role of sulfide in passivation and its breakdown are still unclear, and therefore, further research is required to conclusively comment on the corrosion behaviour of steel in AAS.

4. CONCLUSIONS

The service life of a reinforced concrete structure based on AAMs can be said to strongly depend on the nanoand micro-structural features of the reaction products that are governed by the type of precursor and alkali activator used, the age of the material and the environment it is exposed to. In the case of chloride induced corrosion of the steel reinforcement, it is also important to take into account the chloride binding capacity of the different hydration products (such as C-A-S-H, N-A-S-H, LDH), the effect of high ionic strength of the pore solution and the pore solution chemistry to determine the effective diffusion coefficient. At the steel-concrete interface, the effect of different ions in the pore solution, the passivation chemistry and the chloride threshold level are important parameters. These parameters differ significantly from PC-based concretes and therefore, the consideration of each factor in significant detail is essential for the commercial advancement of AAMs.

ACKNOWLEDGEMENTS

The research leading to these results received funding from the European Research Council under the European Union's Seventh Framework Programme (FP/2007-2013) / ERC Grant Agreement #335928. The authors would like to acknowledge the technical support provided by Dr Oday Hussein.

REFERENCES

[1] U. Angst, B. Elsener, C.K. Larsen, Ø. Vennesland, Critical chloride content in reinforced concrete - A review, Cem. Concr. Res. 39 (2009) 1122–1138.

[2] S.A. Bernal, J.L. Provis, Durability of alkali-activated materials: progress and perspectives, J. Am. Ceram. Soc. 97 (2014) 997–1008.

[3] J.S.J. Van Deventer, J.L. Provis, P. Duxson, Technical and commercial progress in the adoption of geopolymer cement, Miner. Eng. 29 (2012) 89–104.

[4] J.L. Provis, Geopolymers and other alkali activated materials: why, how, and what?, Mater. Struct. 47 (2013) 11–25.

[5] J.L. Provis, S.A. Bernal, Geopolymers and related alkali-activated materials, Annu. Rev. Mater. Res. 44 (2014) 299–327.

[6] T. Luping, L.O. Nilsson, Chloride binding capacity and binding isotherms of OPC pastes and mortars, Cem. Concr. Res. 23 (1993) 247–253.
[7] C. Andrade, Calculation of chloride diffusion coefficients in concrete from ionic migration measurements, Cem. Concr. Res. 23 (1993) 724–742.
[8] L. Tang, L.-O. Nilsson, P.A.M. Basheer, Resistance of Concrete to Chloride Ingress: Testing and Modeling, Taylor and Francis, (2012).
[9] I. Ismail, S.A. Bernal, J.L. Provis, R. San Nicolas, D.G. Brice, A.R. Kilcullen, S. Hamdan, J.S.J. van Deventer, Influence of fly ash on the water and chloride permeability of alkali-activated slag mortars and concretes, Constr. Build. Mater. 48 (2013) 1187–1201.
[10] O. Kayali, M.S.H. Khan, M. Sharfuddin Ahmed, The role of hydrotalcite in chloride binding and corrosion protection in concretes with ground granulated blast furnace slag, Cem. Concr. Compos. 34 (2012) 936–945.
[11] X. Ke, S.A. Bernal, J.L. Provis, Uptake of chloride and carbonate by Mg-Al and Ca-Al layered double hydroxides in simulated pore solutions of alkali-activated slag cement, Cem. Concr. Res. Submitted (2016).
[12] A. Vollpracht, B. Lothenbach, R. Snellings, J. Haufe, The pore solution of blended cements: a review, Mater. Struct. 49 (2016) 3341–3367.
[13] F. Puertas, A. Fernández-Jiménez, M.. Blanco-Varela, Pore solution in alkali-activated slag cement pastes. Relation to the composition and structure of calcium silicate hydrate, Cem. Concr. Res. 34 (2004) 139–148.
[14] R.R. Lloyd, J.L. Provis, J.S.J. van Deventer, Pore solution composition and alkali diffusion in inorganic polymer cement, Cem. Concr. Res. 40 (2010) 1386–1392.
[15] S. Song, H. Jennings, Pore solution chemistry of alkali-activated ground granulated blast-furnace slag, Cem. Concr. Res. 29 (1999) 159–170.
[16] A. Gruskovnjak, B. Lothenbach, L. Holzer, R. Figi, F. Winnefeld, Hydration of alkali-activated slag: Comparison with ordinary Portland cement, Adv. Cem. Res. 18 (2006) 119–128.
[17] R.J. Myers, S.A. Bernal, J.L. Provis, A thermodynamic model for C-(N-)A-S-H gel: CNASH_ss. Derivation and validation, Cem. Concr. Res. 66 (2014) 27–47.
[18] Z. Zhang, H. Wang, Analysing the relation between pore structure and permeability of alkali-activated concrete binders, Woodhead Publishing Limited, (2015).
[19] F. Puertas, M. Palacios, T. Vázquez, Carbonation process of alkali-activated slag mortars, J. Mater. Sci. 41 (2005) 3071–3082.
[20] J.L. Provis, R.J. Myers, C.E. White, V. Rose, J.S.J. Van Deventer, X-ray microtomography shows pore structure and tortuosity in alkali-activated binders, Cem. Concr. Res. 42 (2012) 855–864.
[21] C. Shi, Strength, pore structure and permeability of alkali-activated slag mortars, Cem. Concr. Res. 26 (1996) 1789–1799.
[22] S.A. Bernal, R. Mejía de Gutiérrez, A.L. Pedraza, J.L. Provis, E.D. Rodriguez, S. Delvasto, Effect of binder content on the performance of alkali-activated slag concretes, Cem. Concr. Res. 41 (2011) 1–8. doi:10.1016/j.cemconres.2010.08.017.
[23] Q. Ma, S. V. Nanukuttan, P.A.M. Basheer, Y. Bai, C. Yang, Chloride transport and the resulting corrosion of steel bars in alkali activated slag concretes, Mater. Struct. 49 (2015) 3663–3677.
[24] D.M. Bastidas, A. Fernández-Jiménez, A. Palomo, J.A. González, A study on the passive state stability of steel embedded in activated fly ash mortars, Corros. Sci. 50 (2008) 1058–1065.
[25] J.M. Miranda, A. Fernández-Jiménez, J.A. González, A. Palomo, Corrosion resistance in activated fly ash mortars, Cem. Concr. Res. 35 (2005) 1210–1217.
[26] M. Babaee, A. Castel, Chloride-induced corrosion of reinforcement in low-calcium fly ash-based geopolymer concrete, Cem. Concr. Res. 88 (2016) 96–107.
[27] C. Monticelli, M.E. Natali, A. Balbo, C. Chiavari, F. Zanotto, S. Manzi, M.C. Bignozzi, Corrosion behavior of steel in alkali-activated fly ash mortars in the light of their microstructural, mechanical and chemical characterization, Cem. Concr. Res. 80 (2016) 60–68.
[28] K. Kupwade-Patil, E.N. Allouche, Examination of chloride-induced corrosion in reinforced geopolymer concretes, J. Mater. Civ. Eng. 25 (2013) 1465–1476.

[29] S. Mundra, M. Criado, S.A. Bernal, J.L. Provis, Chloride-induced corrosion of steel rebars in simulated pore solutions of alkali-activated concretes, Cem. Concr. Res. (2016) Submitted.
[30] A. Scott, M.G. Alexander, Effect of supplementary cementitious materials (binder type) on the pore solution chemistry and the corrosion of steel in alkaline environments, Cem. Concr. Res. 89 (2016) 45–55.
[31] D.W. Shoesmith, P. Taylor, M.G. Bailey, B. Ikeda, Electrochemical behaviour of iron in alkaline sulphide solutions, Electrochim. Acta. 23 (1978) 903–916.
[32] D.W. Shoesmith, M.G. Bailey, B. Ikeda, Electrochemical formation of mackinawite in alkaline sulphide solutions, Electrochim. Acta. 23 (1978) 1329–1339.
[33] M. Holloway, J.M. Sykes, Studies of the corrosion of mild steel in alkali-activated slag cement mortars with sodium chloride admixtures by a galvanostatic pulse method, Corros. Sci. 47 (2005) 3097–3110.
[34] M. Criado, S. Mundra, S.A. Bernal, J.L. Provis, A study on the passive state stability of steel embedded in alkali activated slag mortars, in: XIV DBMC - 14th Int. Conf. Durab. Build. Mater. Components., Ghent, Belgium, (2017).
[35] S. Mundra, M. Criado, S.A. Bernal, J.L. Provis, Breakdown of the passivity of steel in simulated alkali-activated concrete pore solutions, in: 36th Cem. Concr. Sci. Conf., Cardiff, Wales, (2016).

Reactivity and Performance of Limestone Calcined-Clay Cements (LC^3) Cured at Low Temperature

Franco Zunino and Karen Scrivener

Laboratory of Construction Materials, EPFL STI IMX LMC Station 12, CH-1015 Lausanne, Switzerland

ABSTRACT

Limestone calcined-clay cements (LC^3) take advantage of the synergetic effects of calcium carbonate reaction with the additional alumina provided by the calcined clay. As temperature decreases, calcium carbonate solubility increases, therefore, the early-age hydration kinetics are modified. This study explored the reactivity and mechanical performance of different LC^3 systems cured at 10 and 20°C. Mixtures containing PC, PC-limestone and LC^3 blends with 50 or 65 % clinker factors and 0.5:1, 1:1 and 2:1 clay-to-limestone ratio were cast and compared. The hydration kinetics were assessed using isothermal calorimetry at each temperature. Compressive strength was monitored over time on cement paste samples. The phase assemblage was monitored using XRD. Results showed that LC^3 systems are more resilient to low temperature curing conditions than traditional PC systems with enhanced early-age performance due to modifications of the phase assemblage. The increased solubility of limestone allows the same performance to be obtained at lower clay-to-limestone ratios.

Keywords: Calcined clay, temperature, hydration, aluminates, limestone, sustainability.

1 INTRODUCTION

Environmental concerns, such as energy consumption and CO_2 emission reductions, have become of increasing concern in the construction industry during the last decades [1]. Therefore, the use of supplementary cementitious materials (SCMs) as a means to reduce the cement content in concrete mixes [2–5] and enhance the durability of the material to increase the service life of concrete structures [6] have become of increasing interest among researchers.

Mineral additions, commonly referred as supplementary cementitious materials (SCMs), are widely used either in blended cements or added to concrete separately in the mixer. The use of SCMs leads to a significant reduction of CO_2 emissions per unit volume of concrete, and significant potential for use of wastes and by-products [3,7].

Some SCMs will react with calcium hydroxide (CH) at ambient temperature to form hydration products such as calcium silicate hydrates (C–S–H) [8]. However, as replacement rate increases, the mechanical properties of concrete are negatively affected, particularly at early age, mainly due to the limited amount of CH available to react with excess SCMs. In addition, some SCMs also negatively affect the setting and early strength gain rate of

concrete, imposing restrictions to construction pace [9]. Furthermore, the available amounts of commonly used SCMs, such as fly ash, blast furnace slags and natural pozzolans, are much lower than the worldwide demand of ordinary Portland cement (OPC). Consequently, research interest has shifted towards alternative and more abundant sources of SCM's such as calcined clays.

Clays are unique among the supplementary cementitious materials because of their worldwide availability since they are widely distributed throughout in the earth crust. Heat treatment of kaolinitic clays between 600 and 800°C leads to the dehydroxylation of its crystalline structure to give a state of more structural disorder known as metakaolin [10-11].

Fine limestone is also commonly used in OPC-based materials. Additions of fine limestone powder can interact with cement hydration and bring setting times back to normal range when using high OPC-by-fly ash replacement levels [9]. It has been also established that limestone additions up to around 5 % can react with OPC, particularly with aluminum rich phases such as calcium aluminates [12–14], leading to the formation of mono and hemicarbonate (AF_m) phases. The increased solubility of limestone at lower temperatures can lead to enhanced precipitation of carbonate-AF_m phases, leading to a decrease in porosity [15].

The combination of metakaolin and limestone in OPC-based systems can give synergetic benefits from both well-known systems. The additional reactive alumina supplied by metakaolin can enhance limestone reaction and allow higher replacement levels with improved performance [16-17]. For this reason, so called, LC^3 (limestone calcined clay cements) have become of great interest. This study focus on understanding the effect of lower curing temperature on the hydration and strength development of LC^3 systems. In particular, the effect of the increased solubility of limestone in the presence of aluminates from clay is explored.

2 MATERIALS AND METHODS

Portland cement classified as CEMI 42.5R from Holcim was used for the preparation of blended cement pastes. A kaolinitic clay from Chile with 60.3% kaolinite content as quantified by thermogravimetric analysis (TGA) was also used. The raw clay was grounded in a steel ball mill for 3 hours in batches of approximately 4 kg. Subsequently, it was calcined in alumina crucibles at 800ºC for 1 hour in a high temperature furnace (Borel FP1100). After calcination, the complete dehydroxylation of kaolinite was confirmed by TGA. For the limestone fraction, Durcal 5 from OMYA (D_{50} = 5 μm) was used. The mineralogical composition of the limestone was confirmed to be 100% calcite by X-ray diffraction (XRD) analysis.

Blended LC^3 cement samples were prepared with different clay-to-limestone ratios (*c/l*), in order to assess the effect on hydration of increased amounts of limestone at low temperature. As consequently the amount of aluminates sourced from clays varied in the different mixtures, different levels of gypsum content adjustment were made, based on trial isothermal calorimetry tests. A volumetric water-to-solids ratio (*w/s*) of 1.234 (equivalent to a w/c ratio 0.4 by weight on the OPC system) was used for all of the mixtures. The volumetric approach was intended to provide a fair comparison basis with different blending proportions, by keeping the initial porosity (i.e. water volume) constant [12-18]. The powder materials were blended for 30 minutes using a Turbula blender. Water and raw materials were preconditioned at the curing temperature (10 or 20ºC) 24 h prior to mixing. Mixing was performed on plastic

containers using a high shear mixer operating at 1600 rpm for 2 minutes. The detailed mixture design is given in Table 1.

Table 1: Mixture proportioning for LC^3 systems

Mixture ID	Clinker+Gypsum (% wt. binder)	Limestone (% wt. binder)	Calcined Clay (% wt. binder)	*c/l* ratio	*w/b*
Control	100	0	0	-	0.40
LS225	77.5	22.5	0	-	0.41
$LC^3$50- 2/1	55	15	30	2	0.43
$LC^3$50 – 1/1	55	22.5	22.5	1	0.43
LC^3 50 – 1/2	55	30	15	0.5	0.43
LC^3 65 – 2/1	70	20	10	2	0.42

2.1 Compressive strength

After mixing, 2 cm cubes were cast for compressive strength measurements. Samples were stored in sealed containers at temperature controlled rooms (10 or 20°C) during the first 24 hours, and then placed in limewater until time of testing. Compressive strength tests were performed at 1, 7, and 28 days, using 0.4 kN/sec load speed, measuring 3 samples at each age.

2.2 Isothermal calorimetry

Isothermal calorimetry tests were carried out to assess the hydration kinetics and compare the results with compressive strength measurements. A TAM air isothermal calorimeter, calibrated at 10 or 20°C was used in this study. Approximately 10 g of cement paste mixture was placed in each glass ampule, and distilled water references with an equivalent heat capacity were used. Tests were conducted from the moment of mixing up to 28 days.

2.3 X-ray diffraction (XRD)

X-ray diffraction (XRD) was used to monitor the crystalline phases formed upon hydration. Measurements were carried out on freshly cut cement paste slices at 1, 7, and 28 days. The slices were mounted on an XRD sample holder and measured in Bragg–Brentano mode using a X'Pert PANalytical diffractometer with CuKα source operated at 45 kV and 40 mA. Samples were scanned from 7 to 70 degrees 2θ with a step size of 0.0167 2θ, using a X'Celerator detector, resulting in an equivalent time per step of 30 s.

3 RESULTS AND DISCUSSION

Compressive strength results at 1, 7 and 28 days are shown in Figure 1 a, b and c, respectively. It can be observed that at 1 day, the strength at 10°C is significantly lower compared to 20°C curing temperature, mainly due to the slowest cement hydration and the significantly reduced rate of reaction of kaolinite at low temperature, reflecting its high apparent activation energy. This is further supported with results at 7 days (Figure 1 b), where no significant differences in strength are observed between LC^3-50 systems with different *c/l* ratios, as it is the case for samples cured at 20°C (higher strength as the clay proportion increases). Therefore, the mechanical behaviour of the systems cured at low temperature seems to be dominated by the Portland cement and limestone fraction. It is also observed that

at 7 days, the strength of the system with limestone (LS225) is higher for the samples cured at 10°C compared to the same mixture cured at 20°C.

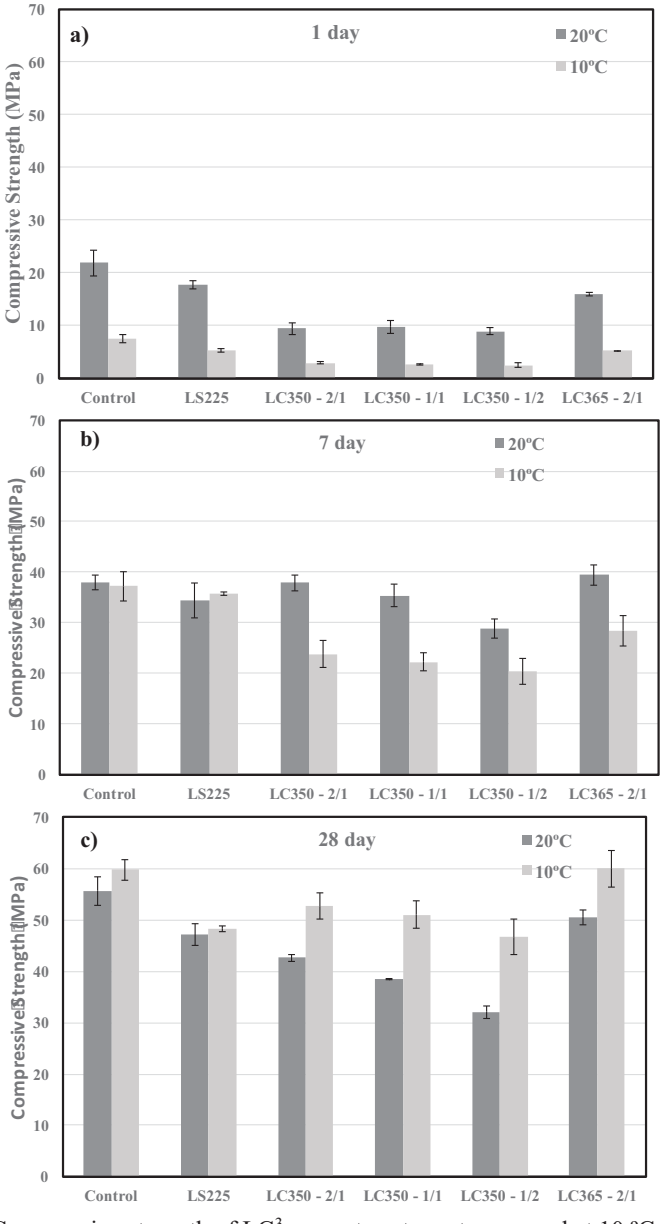

Figure 1: Compressive strength of LC^3 cement paste systems cured at 10 ºC and 20 ºC

At 28 days, the strength of the LC^3 systems cured at 10°C is higher than the same systems cured at normal temperature (20°C). However, no significant difference is observed between the systems with 2:1 and 1:1 *c/l* ratios, suggesting that the effect of additional clay fraction is less significant at lower temperature compared to 20°C, where the difference between both systems is more evident. On the other hand, the strength of the control system is also higher for the samples cured at 10°C at this age. This result may be attributed to the coupled effect of precipitation of C-S-H with lower porosity [19] combined with the reaction of limestone present in the cement (1.7 % as measured by TGA). Thus, the good results observed for the LC^3 systems at low temperature should be considered as a combination of these effects. The LC^3-65 system reaches the same strength as the control mixture at 28 days.

When comparing the compressive strength results at 1, 7, and 28 days with the heat release per mL of water, a strong linear correlation is observed (Figure 2). This parameter has proved in previous studies to accurately reflect strength development, even in systems with slightly different w/b ratios, as is the case of this study due to the volumetric proportioning approach [20]. It is observed that the trend points to higher strength levels for the low curing temperature systems for the same amount of heat release, supporting the supposition that the nature and quality of the hydration products changed compared to normal curing conditions. LC^3 systems seem to deviate from the linear correlation at 20°C curing condition, probably due to the overlapping of the clay reaction which further contributes to strength with a different heat release footprint associated.

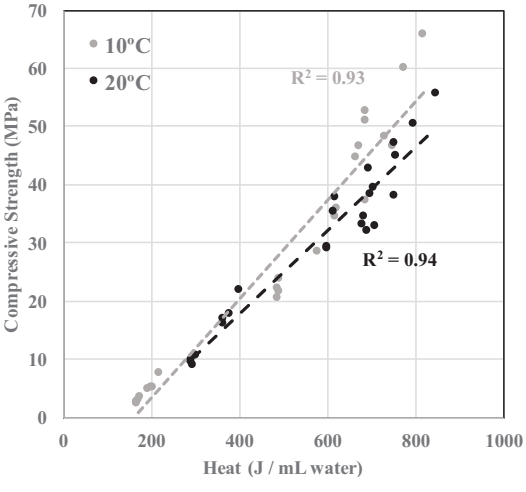

Figure 2: Heat release versus strength plot (1, 7, and 28-day strength) for systems cured at 10°C and 20°C

XRD measurements confirmed the increased amount of hemicarbonate precipitation at low temperature. As expected, the amount of monocarbonate is lower at 10°C since this phase is less stable at low temperature. However, considering both phases together, the amount of carbonated AF_m phases formed is higher at low temperature. Furthermore, an increased

amount of ettringite was observed in the low temperature systems at 7 and 28 days, as seen as example in Figure 3 for the LC^3-50 2:1 system.

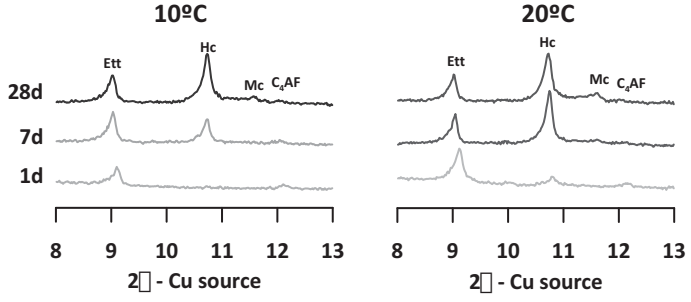

Figure 3: XRD patterns of LC^3-50 2:1 system at different ages, cured at 10°C and 20°C. Ett: ettringite (AFt) H_c: hemicarbonate M_c: monocarbonate C_4AF: ferrite

4 CONCLUSIONS

From the results presented in this study, it is observed that the LC^3 system can take advantage of the enhanced limestone reaction in low temperature curing conditions. However, the reactivity of clay is also significantly reduced, which leads to the opportunity of further proportioning optimization for these specific conditions. The increased solubility of limestone at low temperature leads to an increased formation of hemicarbonate phase. It was observed that at 28 days, the strength of the LC^3 systems cured at low temperature is higher compared to their respective counterparts cured at 20°C. Isothermal calorimetry results also suggest that the nature of the hydration products formed at low temperature is different. Therefore, the observed enhancements are attributed to the coupled effect of low porosity (higher quality) C-S-H formation at low temperature, enhanced AFt phase formation and higher hemicarbonate precipitation.

5 FUTURE RESEARCH PROSPECTS

This study is part of a long term research plan focused on understanding the behaviour of LC^3 under realistic application conditions. Regarding, in particular, this low temperature study, strength measurements will be conducted up to 1-year age. XRD phase assemblage will be contrasted with thermodynamic simulations in order to better understand the effect of temperature on phase assemblage. Porosity is being monitored by mercury intrusion porosimetry (MIP) and SEM observations, which also will allow to determine compositional changes in the hydration products at different temperatures by EDS analysis. The LC^3-65 system will be studied in more depth, as it seems to offer the best compromise between low clinker factor and good performance at early age when cured at low temperature.

6 ACKNOWLEDGEMENTS

Authors acknowledge funding provided by the Swiss commission for scholarships for foreign students (FCS), through their Ph.D. scholarship program.

7 REFERENCES

[1] M. Schneider, M. Romer, M. Tschudin, H. Bolio, Sustainable cement production—present and future, Cem. Concr. Res. 41 (2011) 642–650. doi:10.1016/j.cemconres.2011.03.019.

[2] R.C. Lara, M. Antoni, A.A. Díaz, K. Scrivener, J. Fernando, M. Hernández, Estudio de la adición de arcillas calcinadas en la durabilidad de hormigones, Rev. Ing. Construcción. 26 (2011) 25–40.

[3] B. Lothenbach, K. Scrivener, R.D. Hooton, Supplementary cementitious materials, Cem. Concr. Res. 41 (2011) 1244–1256. doi:10.1016/j.cemconres.2010.12.001.

[4] N. Jain, Effect of nonpozzolanic and pozzolanic mineral admixtures on the hydration behavior of ordinary Portland cement, Constr. Build. Mater. 27 (2012) 39–44. doi:10.1016/j.conbuildmat.2011.08.006.

[5] E. Karim, K. El-Hadj, B. Abdelkader, B. Rachid, Analysis of Mortar Long-Term Strength with Supplementary Cementitious Materials Cured at Different Temperatures, ACI Mater. J. (2010) 323–331.

[6] P. Mehta, Durability - Critical Issues for the Future, Concr. Int. 19 (1997) 69–76.

[7] M. Schneider, M. Romer, M. Tschudin, H. Bolio, Sustainable cement production—present and future, Cem. Concr. Res. 41 (2011) 642–650. doi:10.1016/j.cemconres.2011.03.019.

[8] H.F.W. Taylor, Cement Chemistry, 2nd ed., Thomas Telford, London, 1997.

[9] D.P. Bentz, T. Sato, I. De La Varga, W.J. Weiss, Fine limestone additions to regulate setting in high volume fly ash mixtures, Cem. Concr. Compos. 34 (2012) 11–17. doi:10.1016/j.cemconcomp.2011.09.004.

[10] A. Tironi, M. a. Trezza, A.N. Scian, E.F. Irassar, Assessment of pozzolanic activity of different calcined clays, Cem. Concr. Compos. 37 (2013) 319–327. doi:10.1016/j.cemconcomp.2013.01.002.

[11] R. Fernandez, F. Martirena, K.L. Scrivener, The origin of the pozzolanic activity of calcined clay minerals: A comparison between kaolinite, illite and montmorillonite, Cem. Concr. Res. 41 (2011) 113–122. doi:10.1016/j.cemconres.2010.09.013.

[12] D.P. Bentz, C.F. Ferraris, S.Z. Jones, D. Lootens, F. Zunino, Limestone and Silica Powder Replacements for Cement: Early-Age Performance, Cem. Concr. Compos. 78 (2017) 43–56. doi:10.1016/j.cemconcomp.2017.01.001.

[13] T. Matschei, B. Lothenbach, F.P. Glasser, The AFm phase in Portland cement, Cem. Concr. Res. 37 (2007) 118–130. doi:10.1016/j.cemconres.2006.10.010.

[14] O. Chowaniec, Limestone Addition in Cement, 2012. https://infoscience.epfl.ch/record/174700.

[15] D.P. Bentz, P.E. Stutzman, F. Zunino, Low-Temperature Curing Strength Enhancement in Cement-Based Materials Containing Limestone Powder, Mater. Struct. (2016) Under review.

[16] F. Avet, R. Snellings, A. Alujas Diaz, M. Ben Haha, K. Scrivener, Development of a new rapid, relevant and reliable (R3) test method to evaluate the pozzolanic reactivity of calcined kaolinitic clays, Cem. Concr. Res. 85 (2016) 1–11. doi:10.1016/j.cemconres.2016.02.015.

[17] M. Antoni, J. Rossen, F. Martirena, K. Scrivener, Cement substitution by a combination of metakaolin and limestone, Cem. Concr. Res. 42 (2012) 1579–1589. doi:10.1016/j.cemconres.2012.09.006.

[18] D.P. Bentz, Activation energies of high-volume fly ash ternary blends: Hydration and setting, Cem. Concr. Compos. 53 (2014) 214–223. doi:10.1016/j.cemconcomp.2014.06.018.

[19] E. Gallucci, X. Zhang, K.L. Scrivener, Effect of temperature on the microstructure of calcium silicate hydrate (C-S-H), Cem. Concr. Res. 53 (2013) 185–195. doi:10.1016/j.cemconres.2013.06.008.

[20] D.P. Bentz, T. Barrett, I. De la Varga, W.J. Weiss, Relating Compressive Strength to Heat Release in Mortars, Adv. Civ. Eng. Mater. 1 (2012) 1–16. doi:10.1520/ACEM20120002.

Effects of Crystalline Admixtures on the Repeatability of Self Healing in Fiber Reinforced Concrete

Estefanía Cuenca [(1)] and Liberato Ferrara[(2)]

[(1)] Postdoctoral Fellow, Department of Civil and Environmental Engineering, Politecnico di Milano, Italy

[(2)] Associate professor, Department of Civil and Environmental Engineering, Politecnico di Milano, Italy

ABSTRACT

This paper analyzes the repeatability of autogenous and engineered self-healing in fiber reinforced concrete (FRC) with and without crystalline admixtures. To this purpose, the tensile response of two different mixes, differing by the presence of the crystalline admixture, was investigated, after a series of pre-cracking and conditioning cycles. An indirect testing methodology was employed to the aforementioned purpose, i.e. Double edge wedge splitting (DEWS) test. Specimens were healed under three different exposure conditions: open air exposure, water immersion, and wet/dry cycles. Specimens were pre-cracked up to a crack width of 0.25 mm (pre-crack cycle) and then healed for one month, three or six months, tested again up to a crack width of 0.25 mm (cycle after 1st healing) and re-healed for one or two further months. Comparison with specimens pre-cracked up to 0.25 mm and continuously healed for three months was also performed to assess the interaction between the presence of the crystalline admixture and the cracking/healing cycles. Investigation is still on-going, repeating healing/cracking cycles according to the scheme above.

Keywords: Self-healing, "cracking-healing" fatigue, FRC, crystalline admixtures.

1 INTRODUCTION

The increasing concern for a wise use of material resources and the need to guarantee for longer times higher and tailored level of material and structural performance in engineering applications has promoted a huge amount of research on self-healing cement-based construction materials. The main goal of providing such a functionality would be to close the entry path (cracks) to external aggressive agents, so that the onset of material degradations is delayed or prevented at all.

It is well known that, by itself, concrete has some moderate self-healing capabilities (autogenous healing) because, in most concretes, approximately 20-30% of the cement particles remain anhydrous. When a crack appears, such anhydrous particles come into contact with water or moisture and react with it, creating thus hydration products that contribute to the closure of the crack [1-4]. "Autogenous healing" occurs when cracks are healed with materials formed by materials that are not specifically added to the same matrix for self-healing purposes. On the other hand, the healing process is called "engineered healing" when tailored additions designed to promote self-healing are added to the concrete matrix [5-7].

Tailored additions such as crystalline admixtures [8-12] and super absorbent polymers (SAPs) have been also recently used to enhance the self-healing capability of fiber reinforced concrete mixtures [13-16].

It is also well-known that fibers added into a concrete mix, can effectively control crack propagation. In fact, FRC is characterized by enhanced toughness due to the crack-bridging effects provided by fibers [17-21]; fibers provide substantial post-peak resistance and ductility [22-26] and restrict maximum crack width, average crack width and average crack spacing are reduced [19,20].

Synergy between fiber reinforced concrete cementitious composites (FRCCs) and self-healing techniques may result into promising solutions [6]. Fibers can improve the self-healing process due to their capacity to restrict crack widths and enhance multiple crack formation [3, 8, 11, 27-30]. It has been shown that cracks smaller than 30 μm healed completely [16] and, in some cases even 50 μm [4, 31]. Once known the advantages of the combination between self-healing and FRCCs, the next step would be to analyze if the repair mechanism is maintained over time after several cycles of loading and unloading. Compared to the large number of investigations on self-healing [6, 8-10, 12, 28-30], studies on the repeatability of self-healing FRCC are very limited [14, 32, 33].

The main objective of this paper is to analyze the repeatability of self-healing in FRCC and the effect on it of a crystalline admixture with the purpose of engineering the healing capacity. The mechanical behavior, before and after several healing cycles of the two investigated FRCs (with and without the crystalline admixture) will be compared. The evolution of the crack opening will be analyzed by means of a digital microscope and correlated to the recovery, if any, of the residual post-cracking/post-healing strength. For the same purpose, an ordinary fiber reinforced concrete (FRC) mix was produced, according to the mix proportions shown in Table 1.

Table 1: Mix composition of investigated FRCs.

Constituent [kg/m3]	Mix w/out crystalline admix	Mix with crystalline admix
Cement type II 42.5	360	360
Crystalline admixture	0	2.9
Water	180	180
Superplasticizer	3.5	3.5
Fine aggregate 0-4 mm	814	811
Coarse aggregate 4-16 mm	1077	1077
Steel fibers,5D 65/60BG	40	40

2 EXPERIMENTAL PROGRAMME: MATERIALS AND TEST METHODOLOGY

Besides the reference mixes as shown in Table 1, a further mix containing 0.8% by cement weight of a crystalline admixture used as healing promoter was also produced, leaving the mix proportions substantially unaltered. The employed crystalline admixture (Penetron admix ®) consists of a blend of cement, sand, and micro-silica. SEM magnified particles are shown in Figures 1a-c: they have irregular shape and size in the range of about 1-20 μm and their morphology is similar to that of cement grains; EDS analysis confirmed the presence of calcium, oxygen, silicon, magnesium, aluminum and potassium. This

spectrum is comparable with that of an ordinary portland cement, except for the slightly higher peak of sulfur.

Both mixes contained 40 kg/m^3 hooked-end steel fibers 60 mm long and 0.9 mm in diameter (aspect ratio equal to 65).

Nine 150 × 150 × 650 mm prisms were cast with each mix and tested according to EN 14651 to characterize the FRC performance. Once tested, the prisms were cut into slices as shown in Figure 2a. Because of the high flowability of concretes, casting of prismatic specimens was accomplished through a free flow parallel to the longer side of the formworks (Figure 2b). This allowed to achieve preferential orientation of the fibers along the same direction. Due to the suitably conceived notched specimen geometry [34] (Figure 2c), it was possible to predetermine the fracture plane, in such a way that it resulted parallel or orthogonal to the flow direction and hence to the obtained preferential alignment of the fibers. In this way, for the specimens labelled as H1 and H3 the preferential alignment of fibers was orthogonal to the fracture plane, on the other hand, in the specimens labelled as H2, V1, V2 and V3, the fibers did not cross the fracture plane orthogonally.

After 4 months curing in a humidity chamber at 20ºC and 95% relative humidity, the DEWS specimens obtained as above were pre-cracked according to the DEWS test methodology [34]. Tests were performed controlling and measuring the crack opening displacement (COD) across the ligament on both the front and rear faces of each specimen as shown in Figure 3.

Pre-crack tests were carried out up to a crack opening value equal to 0.25 mm; specimens were then subjected to different exposure conditions: immersion in tap water, open air exposure, and a combination of both, wet/dry cycles (4 days in water and 3 days exposed to open air). As for the open air exposure, the climate characteristics in Milan during the healing period consisted of temperatures between 15 and 29ºC and relative humidity at an average value of 71%.

After one month exposure to the different conditioning environments, specimens were tested again up to or further a crack opening of 0.25 mm, and, after that, subjected again to the same exposure conditions for two further months and finally, they were re-tested again and pre-cracked up to further 0.25 mm.

For the sake of comparison the following cases were also considered:

- Specimens continuously healed for three months after pre-cracking at 0.25 mm, re-cracked up to further 0.25 mm, further healed for one month and then re-cracked up to further 0.25 mm;
- Specimens continuously healed for six months after pre-cracking at 0.25 mm and then re-cracked up to further 0.25 mm;

Reference specimens were monotonically tested as well up to a crack opening width equal to 2.5 mm.

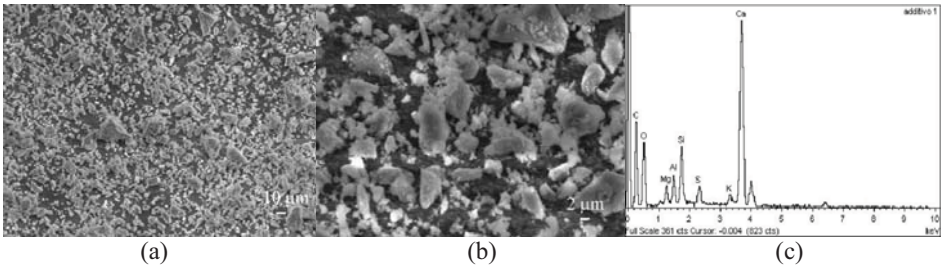

(a) (b) (c)

Figure 1: SEM magnification (a, b) and EDS analysis (c) of admixture particles.

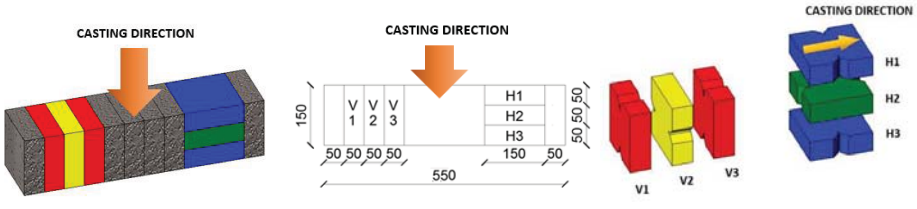

(a) (b) (c)

Figure 2: Casting and cutting scheme to obtain specimens for DEWS tests from prisms.

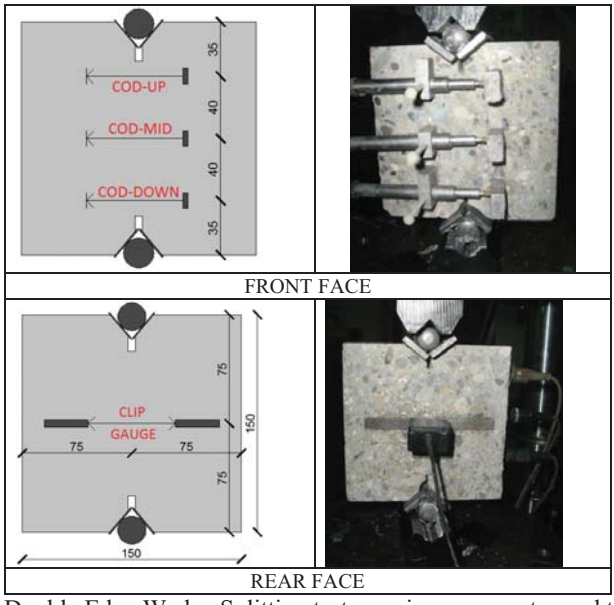

Figure 3: Double Edge Wedge Splitting test: specimen geometry and test set-up (dim. in mm).

3 EXPERIMENTAL RESULTS

3.1 Monotonic reference tests

As explained above, DEWS specimens were obtained by cutting longer prismatic specimens along two orthogonal directions. In this way, two specimen groups with clearly different preferential fiber alignment were obtained: H1 and H3 specimens had favourable fiber orientations, that is, the fracture plane was designed to be orthogonal to the main "supposed" alignment of fibers. On the contrary, the other type of specimens (H2, V1, V2, V3) featured unfavorable fiber orientations.

To quantify this effect, on the monotonically tested DEWS specimens the fibers which crossed the fracture plane were counted and, the fiber density per unit area of fracture surface was calculated. The relationship between the residual tensile stress at different crack openings (CMOD= 0.25, 0.5, 1.25 and 1.5mm) and the fiber density is shown in Figure 4. In all cases a very good fitting was obtained, with moderate differences between the residual

stresses at progressively increasing crack opening, as expectable because of the fiber pull-out nature of such stresses.

This result will be exploited in guessing the reference performance of specimens subjected to repeated cracking/healing cycles to evaluate the effects of healing on the residual post-cracking tensile strength, as it will be here after explained.

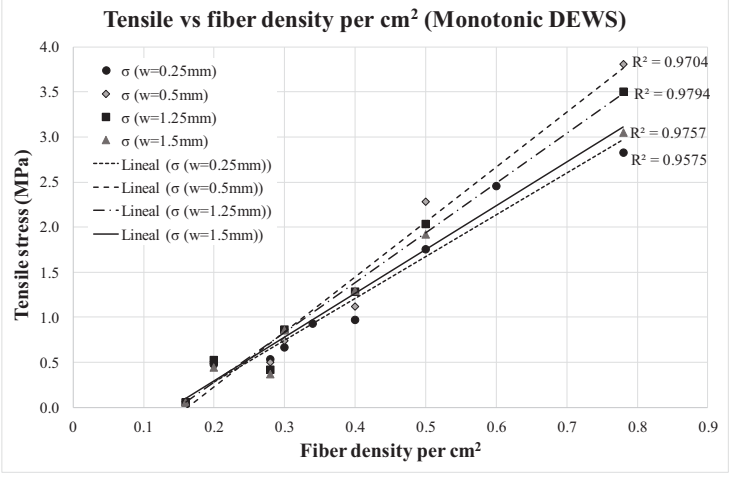

Figure 4: Residual tensile stresses at different crack openings vs. fiber density - monotonic tests.

3.2 Optical microscopy observation of crack closure

As a first proof of the occurred healing, the maximum crack opening was measured before and after each healing period with a digital optical microscope at different locations along the crack for both concretes. The percentage of crack closure was hence calculated as follows:

$$\% \text{ crack closure} = \left(\frac{w_0 - w_1}{w_0}\right)\% \quad (1)$$

where: w_0 = crack width at pre-cracking
w_1 = crack width after healing

The results are shown in Figures 5 a-c, first comparing the effect of a one cycle healing duration (1, 3 and 6 months) and then comparing the performance after the repetition of cracking-healing cycles (1+2 months vs. 3 months and 1+2 months vs. 3+1 months).

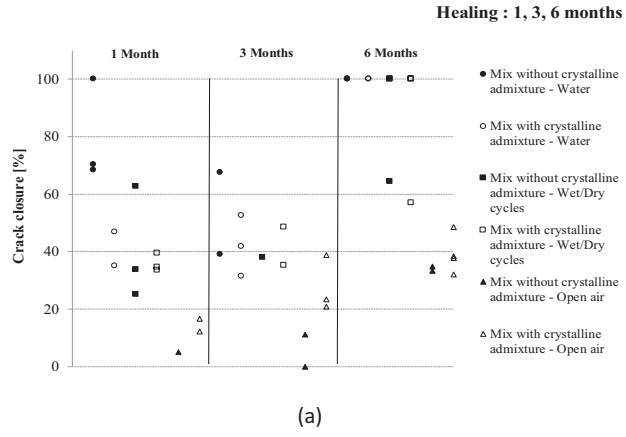

(a)

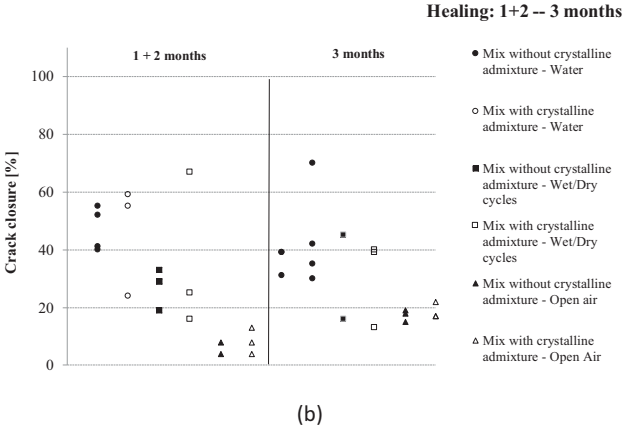

(b)

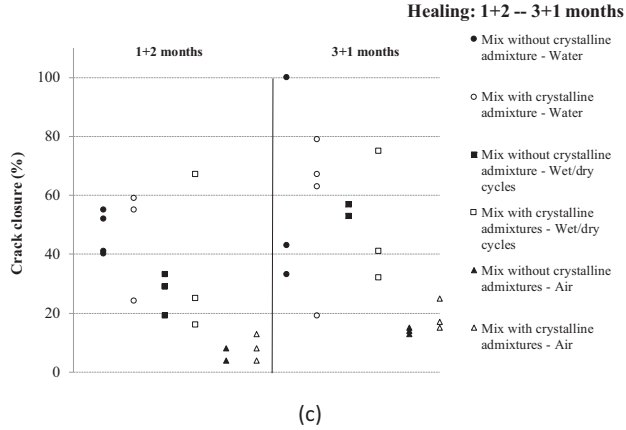

(c)

Figure 5: Crack closure (%) after different healing and cracking/healing exposures

The following statements hold:

- Prolonged exposure to all healing conditions results in an improved crack healing; the presence of crystalline admixture results in a faster crack sealing, mostly under less favourable exposure conditions (wet/dry cycles and open air) (Figure 5a);
- The performance after the second cracking/healing cycle, is generally comparable with that after the corresponding first cracking-healing cycle, and somewhat better when a crystalline admixture is added to the mix; the longer the duration of the first healing period (3 vs. 1 month), the better the performance after the second cracking/healing cycle (Figure 5 b-c);
- For the same cumulative healing period, an intermediate cracking/healing cycles (1+2 months vs. 3 months continuing exposure) results in a slightly worse healing performance (Figure 5 b-c).

3.3 Mechanical regain after cracking/healing cycles

The healing efficiency was evaluated by comparing the crack-cycling curves with the monotone curve for a similar reference specimen (Figure 6). This was obtained by adapting the average post-cracking stress vs. crack opening curve of monotonically tested specimens to the level of residual post-cracking stress featured by each single specimen subjected to cracking/healing cycles upon the first pre-cracking stage. The correlation between post-cracking residual stresses and fiber orientation number legitimates this procedure.

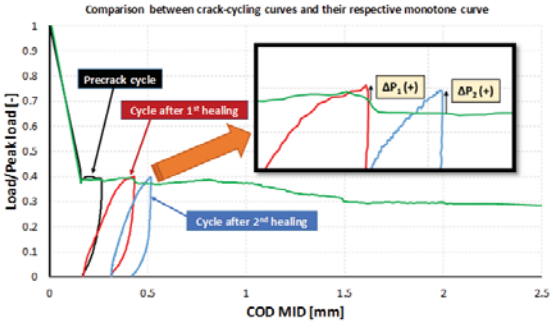

Figure 6: Example of load-COD cycling curves and evaluation of the residual load recovery.

With reference to the sample curve and notation shown in Figure 6, two values of residual stress recovery were calculated (load ratio recovery): the increase of the dimensionless value of the (Load/Peak load) ratio after the 1st healing (ΔP_1) and after the 2nd healing (ΔP_2) respectively. A positive load recovery ratio indicates that the healing reactions have not only closed the cracks but also provided a recovery of the post-cracking residual strength, which, in this case, is likely attributable to an improvement of the fiber matrix bond.

The results in Figure 7 confirm the aforesaid statements as far as the effects are concerned of the healing duration, repeated cracking/healing cycle and crystalline admixture.

The limited values of the measured load recovery should not be deceptive about the true significance of the occurred healing. As a matter of fact, an effective crack healing aims in this case at preserving the level of post-cracking strength over time even against any trend of degradation which the fibers and the fiber/matrix interface could undergo upon exposure to external environment at crack locations.

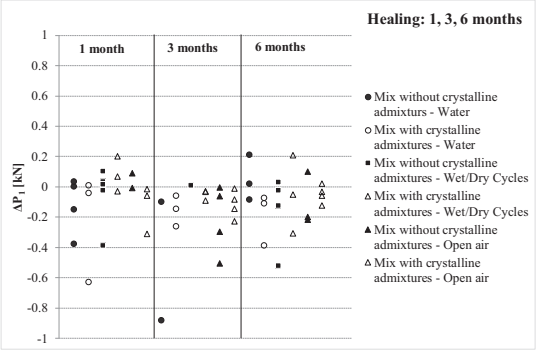

(a)

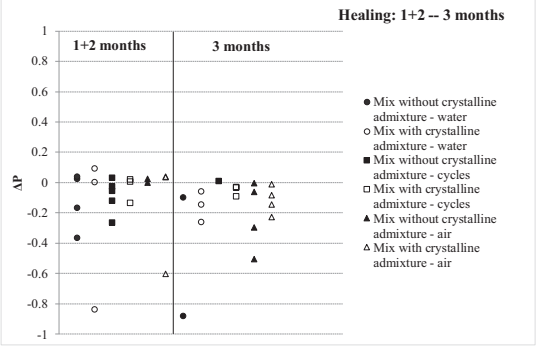

(b)

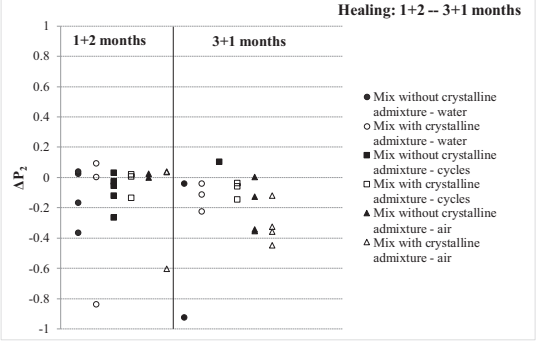

(c)

Figure 7: Recovery of residual load bearing after different healing and cracking/healing exposures

4. CONCLUDING REMARKS

In this paper, the repeatability of self-healing on fiber reinforced concrete after repeated cracking/healing cycles and the effectiveness of a crystalline admixture as self-healing promoter have been investigated under three different exposure conditions. The evolution of

the crack opening and of the mechanical behaviour after one or two cracking/healing cycles for different durations of the first healing period have been analyzed. From the obtained results, the following conclusions can be drawn:

- The highest healing rate was reached for specimens immersed in water, followed by those subjected to dry/wet cycles and by those exposed to open air.
- For FRC with crystalline admixtures a general trend was found for all exposure healing conditions in which the crack sealing and healing effectiveness after the 2nd healing was is higher than after the 1st. It can be reasonably assumed that the crystalline admixture is able to provide a reservoir for delayed hydration reactions over time.

The investigation is on-going to provide a stronger support to the statements above.

5. ACKNOWLEDGEMENTS

The authors acknowledge the financial support of the PoliMi International Fellowships 2015 (PIF), Politecnico di Milano, Italy and of Penetron Italia srl (MArch E. GastaldoBrac).

6. REFERENCES

[1] Edvarsen, C., "Water Permeability and Autogenous Healing of Cracks in Concrete," ACI Materials Journal, 96(4), 1999, pp. 448-454.
[2] Homma, D., Mihashi, H. and Nishiwaki, T., "Self-healing capability of fibre reinforced cementitious composites", Journal of Advanced Concrete Technology, 7(2), 2009, pp. 217-228.
[3] van Tittelboom, K., Gruyaert, E. et al., "Influence of mix composition on the extent of autogenous crack healing by continued hydration or calcium carbonate formation", Construction and Building Materials, 37, 2012, pp. 349-359.
[4] Yang, Y., Lepech, M. et al., "Autogenous healing of engineered cementitious composties under wet-dry cycles", Cement and Concrete Research, 39, 2009, pp. 382–390.
[5] vanTittelboom, K., Snoeck, D. et al., "Most recent advances in the field of self-healing cementitious materials," Proceedings, 4th ICSHM, Ghent, Belgium, 2013.
[6] Cuenca E. and Ferrara, L., "Self-healing capacity of fiber reinforced cementitious composites. State of the art and perspectives", KSCE Journal of Civil Engineering, accepted, 2017.
[7] Nishiwaki, T., Sasaki, S. et al., "Experimental study on self-healing effect of FRCC with PVA fibers and additives against freeze/thaw cycles," Proceedings, 5th ICSHM, Raileigh, USA, 2015.
[8] Ferrara, L., Ferreira, S.R., et al., "Natural fibers as promoters of autogenous healing in HPFRCCs: Results from on-going Brazil-Italy cooperation," ACI SP 305, 2015, pp. 11.1-11.10.
[9] Ferrara, L., Krelani V. and Carsana, M., "A "fracture testing" based approach to assess crack healing of concrete with and without crystalline admixtures", Construction and Building Materials, 68, 2014, pp. 535–551.
[10] Ferrara, L., Krelani, V. and Moretti, F., "On the use of crystalline admixtures as promoters of self-healing in cement based construction materials", Smart Materials and Structures, 25(8), 2016, pp. 1-17.
[11] Roig-Flores, M., Moscato, S et al., "Self-healing capability of concrete with crystalline admixtures in different environments", Construction and Building Materials, 86, 2015, pp. 1-11.
[12] Roig-Flores, M., Pirritano, F. et al., "Effect of crystalline admixtures on the self-healing capability of early-age concrete studied by means of permeability and crack closing tests," Construction and Building Materials, 114, 2016, pp. 447-457.
[13] Snoeck, D., "Self-healing and microstructure of cementitious materials with microfibres and superabsorbent polymers", PhD Thesis, Ghent University, 2015.
[14] Snoeck D. and De Belie, N., "Repeated autogenous healing in strain-hardening cementitious composites by using superabsorbent polymers", ASCE Journal of Materials in Civil Engineering, 28 (1), 2015, pp. 1-11.

[15] Snoeck, D., Dewanckele, J. et al., "X-ray computed microtomography to study autogenous healing of cementitious materials promoted by superabsorbent polymers", Cement and Concrete Composites, 65, 2016, pp. 83-93.
[16] Snoeck, D., van Tittelboom, K. et al., "Self-healing cementitious materials by the combination of microfibers and superabsorbent polymers", Journal of Intelligent Material Systems and Structures, 25(1), 2014, pp. 13-24.
[17] Cuenca E. and Serna, P. "Shear behavior of Self-Compacting concrete and Fiber-Reinforced concrete push-off specimens", Proceesings, SCC2010, Montreal, Canada, 2010, pp. 429-438.
[18] diPrisco, M., Plizzari, G. and Vandewalle, L., "MC2010: Overview on the shear provisions for FRC," in fib Bulletin 57, 2010, pp. 61-76.
[19] Susetyo J. and Vecchio, F., "Effectiveness of the steel fiber as minimum shear reinforcement: panel test," in fib bulletin 57, 2010, pp. 227-241.
[20] Cuenca E. and Serna, P., "Shear behavior of prestressed precast beams made of Self Compacting Fiber Reinforced Concrete," Construction and Building Materials, 45, 2013, pp. 145-156.
[21] Conforti, A., Tiberti G. and Plizzari, G., "Splitting and crushing failure in FRC elements subjected to a high concentrated load", Composites Part B: Engineering, 105, 2016, pp. 82-92.
[22] Kim, K., Lee, D. et al., "Shear behavior model for steel fiber-reinforced concrete members without transverse reinforcements", Composites Part B: Engineering, 43(5), 2012, pp. 2324-2334.
[23] Cuenca E. and Serna, P. "Failure modes and shear design of prestressed hollow core slabs made of fiber-reinforced concrete", Composites Part B: Engineering, 45(1), 2013, pp. 952-964.
[24] Bencardino, F., Rizzuti, L. et al., "Experimental evaluation of fiber reinforced concrete fracture properties", Composites Part B: Engineering, 41(1), 2010, pp. 17-24.
[25] Minelli, F., Conforti, A. et al., "Are steel fibres able to mitigate or eliminate size effect in shear?", Materials and Structures, 47(3), 2014, pp. 459-473.
[26] Cuenca, E., Echegaray-Oviedo J. and P. Serna, "Influence of concrete matrix and type of fiber on the shear behavior of Self Compacting Fiber Reinforced Concrete beams", Composites Part B: Engineering, 75, 2015, pp. 135-147.
[27] Wu, M., Johannesson B. and Geiker, M., "A review: Self-healing in cementitious materials and engineered cementitious composite as a self-healing material", Construction and Building Materials, 28, 2012, pp. 571-583.
[28] Ferrara, L., Krelani, V. et al., "Effects of autogenous healing on the recovery of mechanical performance of HPFRCCs: part 1", Cement and Concrete Composites -Submitted-, 2016.
[29] Snoeck D. and De Belie, N., "From straw in bricks to modern use of microfibers in cementitious composites for improved autogenous healing - A review," Construction and Building Materials, 95, 2015, pp. 774-787.
[30] Ferrara, L., Krelani V. and Moretti, F., "Autogenous healing on the recovery of mechanical performance of HPFRCCs: part 2", Cement and Concrete Composites, 73, 2016, pp. 299-315.
[31] Li, V., Wang S. and Wu, C., "Tensile strain-hardening behavior of polyvinyl alcohol engineered cementitious composites (PVA-ECC)", ACI Materials Journal, 98(4), 1997, pp. 483-492.
[32] Sahmaran, M., Yildirim, G. et al., "Repeatability and pervasiveness of Self-Healing in Engineered Cementitious Composites", ACI Materials Journal, 112(4), pp. 513-522.
[33] Li, M. and Fan, S., "Designing repeatable Self-healing into cementitious materials", Proceedings, 5th International Conference on Durability of Concrete Structures, China, 2016.
[34] diPrisco, M., Ferrara, L. and Lamperti, M.G.L., "Double edge wedge splitting (DEWS): an indirect tension test to identify post-cracking behaviour of fibre reinforced cementitious composites", Materials and Structures, 46(11), 2013, pp. 1893-1918.

Diffusion And Interactions of Chloride Ions with Ternary Blends of Portland Cement-Limestone-Calcined Clay Binders

Hamed Maraghechi, Fancois Avet and Karen Scrivener

Ecole Polytechnique Fédérale de Lausanne (EPFL), LMC, Lausanne, Switzerland

ABSTRACT

Ingress of chloride ions through concrete is known to be the most important durability concern. Development of new cementitious materials is rapidly evolving, which is due to environmental and economic motivations. One of the promising blended cements is composed of ternary mixture of Portland cement with calcined clay and limestone (known as LC^3). Calcined clay in LC^3 systems are kaolinitic, which are abundant on the earth's crust with variable kaolinite content. While most of the past research has focused on high purity clays, the durability performance of LC^3 systems made using intermediate grade clays are evaluated in this study. The rate of chloride diffusion, as well as the interaction of chloride ions with the solid phases are quantified. The interactions are assessed using XRD-Rietveld analysis and measurement of chloride binding isotherms.

Keywords: Calcined clay, limestone, durability, chloride transport.

1 INTRODUCTION

Utilization of supplementary cementitious materials (SCM) in concrete is known to significantly reduce CO_2 emissions associated with cement and concrete production. Conventional SCM's include blast furnace slag, fly ash, waste glass, calcined clay, etc. Considering the global demand for cement due to the population growth, the only viable option to significantly reduce greenhouse gas emissions is the use of calcined clays, as elaborated in [1]. Calcined clays that are based on kaolinite has been of a great interest due to the global availability and price. It is also concluded that addition of limestone to Portland cement- calcined clay can provide further economic, environmental and technical benefits. This ternary blend is known as LC^3. Limestone can further react with aluminate from clay and form more AF_m phase of hemicarboaluminate and monocarboaluminate, hence not being an inert phase [2]. Currently, LC^3 cements have been started to be produced in few countries. For example, in Cuba, concrete blocks are made using LC^3 cement and are exposed to the corrosive environment of the ocean to assess chloride ingress. Preliminary examinations have demonstrated superior performance of LC^3 concrete in comparison to the current OPC based concrete mixtures being used in the region [3]. Reactivity of a clay source, and the mechanical performance, is mainly related to the kaolinite content [4]. In this paper, durability of LC^3 mortars and binders with different kaolinite content against chloride transport is discussed.

2 MATERIALS AND METHODS

The oxide composition and properties of the cementitious materials used in this study is presented in Table 1. The clays were either calcined at around 800 °C for 1 h in a high temperature furnace (Borel FP1100), or received as calcined. The values of d_{v50} were

obtained using laser diffractometer analysis. One of the clays contains high kaolinite content (95%), and is considered as a high grade clay (Clay H) in this study. The other two contain intermediate kaolinite contents of 50% and 42%, shown as Clay I-1 and Clay I-2 respectively. These are more abundant globally and can be obtained with much lower costs.

Table 1: Properties of the cementitious components used in this study

	Cement (CEM-I 42.5R)	Limestone	Clay H High grade	Clay I-1 Intermediate grade	Clay I-2 Intermediate grade
Kaolinite [wt.%]	–	–	95	50.3	41.9
Dv_{50} [μm]	8.4	7.2	5.1	10.9	7.8
BET surface [m^2/g]	0.9	1.8	9.6	45.7	9.2
SiO_2	19.3	0.1	52.0	44.9	53.5
Al_2O_3	5.7	–	43.8	32.3	34.8
Fe_2O_3	3.6	–	0.3	15.4	3.3
CaO	63.6	55	–	1.3	0.1
MgO	1.6	0.2	–	0.8	0.1
SO_3	3.2	–	0.1	0.1	0.03
Na_2O	0.2	0.1	0.3	0.4	0.2
K_2O	1.2	–	0.1	0.2	0.2
TiO_2	0.3	–	1.5	2.4	2.3
P_2O_5	0.2	–	0.2	0.4	0.2
MnO	0.1	–	–	0.1	0.01
Others	0.3	–	0.1	0.2	0.02
LOI	0.8	42.6	1.5	1.7	4.7

Ternary blends of OPC-calcined clay-limestone (LC^3), were prepared with 50 wt.% clinker, 5 wt.% gypsum, 30 wt.% calcined clay and 15 wt.% limestone. The gypsum content includes the initial gypsum of the cement and the amount added to avoid under-sulfated condition. As described above, addition of limestone not only provides economic benefits, but can also contribute to formation of further AF_m phases and provide a good surface for nucleation of hydrates, yet diluting the systems with regards to OPC.

Paste samples were prepared using water/solid ratio of 0.5 (solid is OPC + calcined clay + limestone) and cured in sealed containers for 28 days. After that, they were dried under vacuum for 4 weeks and then exposed to NaCl solutions of 0.1, 0.3, 0.5, 1.0 and 2.0 M for 60 days in accordance with the procedure explained in [5]. For that, dried paste samples were crushed into small pieces (1-3 mm), and placed in sealed plastic containers with NaCl solution added to obtain solution volume/sample mass ratio of 4.00 cm^3/g. After stabilization, chloride concentration of solution in each container was measured to obtain the amount of bound chloride. In parallel, one thin paste slide was also exposed to the same solutions for XRD analysis to quantify existing and forming phases in the pastes. Quantification was accomplished using Rietveld analysis. A PANalytical X'Pert Pro MPD diffractometer in a θ–

θ configuration using CuKα source (λ=1.54 Å) with a fixed divergence slit size of 0.5° was employed.

In addition, mortar cylinders (11 cm Diameter - 14 cm Height) were prepared in accordance with EN 196-1 procedure, cured for 28 days in fog room (RH > 95%), and after that coated with epoxy on the sides and exposed to 3% NaCl solution for 1D diffusion of chlorides. After 1 year of exposure, the samples were removed from the solution, and chloride ion profiles with depth were measured according to ASTM C1152 procedure.

3 RESULTS AND DISCUSSIONS

Figure 1 shows the binding isotherm curves for the three LC^3 and the control OPC pastes. The measured data points were fitted according to Freundlich isotherm equation $C_b = a.\ C_f^b$ to find the parameters "a" and "b" (shown in Figure 1), where C_b and C_f are bound and free chloride concentrations, respectively.

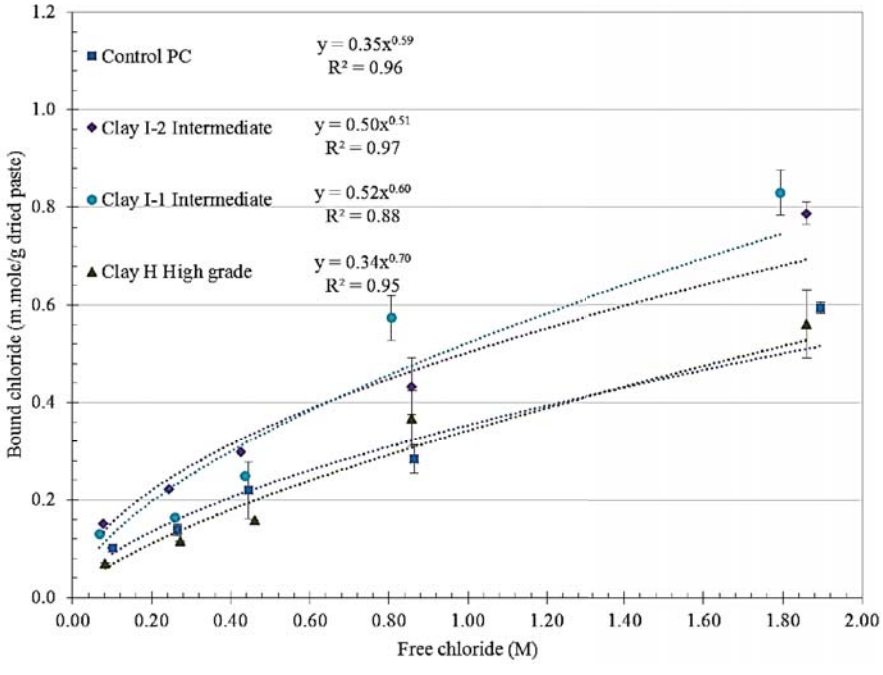

Figure 1: Chloride binding isotherm curves for three LC^3 and OPC pastes

Exposure of pastes to NaCl solutions result in transformation of AF_m phases into Friedel's salt. This is confirmed and quantified through XRD Rietveld analysis. Figure 2 shows the Friedel's salt peaks of XRD patterns. It is seen that the intermediate clays form more Friedel's salt. This is in fact due to the higher amount of AF_m phases that form in these binders and is mainly attributed to the higher degree of reaction of clinker in LC^3 with intermediate grade clays.

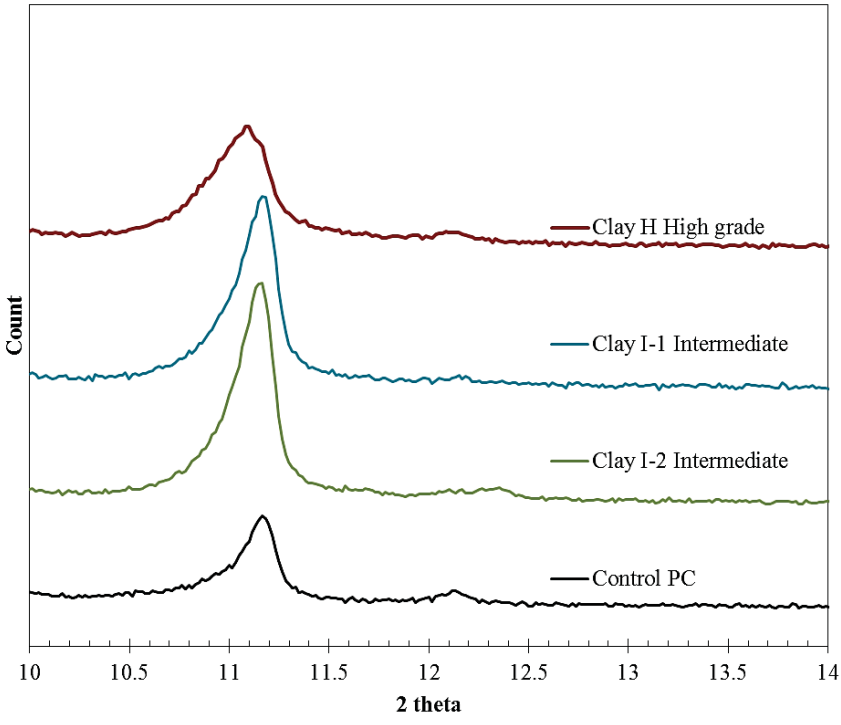

Figure 2: Friedel's salt peak in XRD analysis for OPC and LC^3 pastes prepared using high or intermediate grade clays after exposure to 1 M NaCl solution

Figure 3 shows the amount of bound chloride in LC^3 and OPC pastes, Friedel's salt and its corresponding chloride content, generated from binding isotherm experiments, as well as XRD analyses. It can be observed that in LC^3 pastes with intermediate grade clays, the amount of total bound chloride is higher than LC^3 paste with high grade clay. It is also interesting to observe that most of the bound chloride is in fact chemically bound into Friedel's salt. The rest would be physically bound into C-A-S-H.

Figure 4 shows the chloride profiles of OPC and two of the LC^3 mortars, after 1 year of exposure to NaCl solution. The profile for the intermediate clay I-2 is currently not available. Resistance of LC^3 mortars against chloride transport is significantly superior to that of OPC mortar. This is mainly due to the refined porosity of these binders as it has already been confirmed by porosity analysis [6]. Having higher amount of AF_m phases, and therefore higher binding capacity in LC^3 binders can also be an extra benefit.

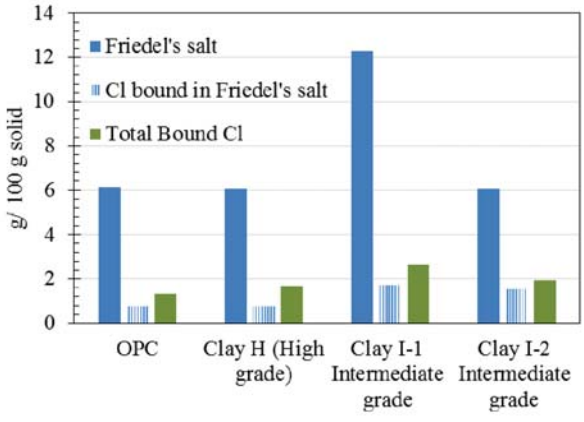

Figure 3: Amount of bound chloride and Friedel's salt formed after exposure of the pastes to 1 M NaCl solution. Paste samples were prepared with 100 g cementitious materials (solid) and 50 g water

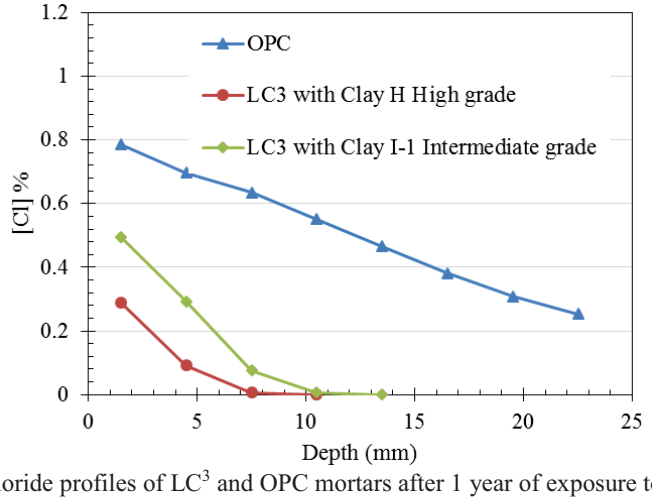

Figure 4: Chloride profiles of LC^3 and OPC mortars after 1 year of exposure to 3% NaCl solution

4 CONCLUSIONS

Chloride binding of OPC-limestone-calcined clay pastes, prepared with high and intermediate grade clays were analysed and compared to OPC. It is found that LC^3 binders have higher binding capacity. This is alongside with higher Friedel's salt formation, which was confirmed using XRD analysis. Most of the bound chloride is chemically bound into AF_m phase, specifically hemi and mono carboaluminates. Depth of chloride penetration in OPC and LC^3 mortars, after 1 year of exposure to NaCl solution was measured and the significant resistivity improvement in LC^3 mortars was highlighted.

REFERENCES

[1] Scrivener K., John V. M, Gartner E.M., Eco-efficient cements: Potential economically viable solutions for a low-CO_2 cement-based materials industry. UNEP (United Nations Environment Program, Dec (2016).

[2] Antoni, M., Rossen, J., Martirena, F., Scrivener K., Cement substitution by a combination of metakaolin and limestone, Cement and Concrete Research, **42** (2012) 1579-1589.

[3] Martirena F. Ribalta J., Maraghechi H., Rocha D. Alujas A., Scrivener K., Performance of concrete made with calcined clays, limestone and Portland cement under natural aggressive condition, XIV International Conference on Durability of Building Materials and Components, DBMC, Ghent (2017).

[4] Avet, F., Snellings, R., Alujas Diaz, A., Ben Haha, M., Scrivener, K. Development of a new rapid, relevant and reliable (R3) test method to evaluate the pozzolanic reactivity of calcined kaolinitic clays, Cement and Concrete Research, **85** (2016) 1-11.

[5] Thomas M.D.A., Hooton R.D., Scott A., Zibara H., The effect of supplementary cementitious materials on chloride binding in hardened cement paste, Cement and Concrete Research, **42** (2012) 1–7.

[6] Avet F., Maraghechi H., and Scrivener K., Analysis of chloride transport and binding in limestone-calcined clay binders with various kaolinite content, 14th International Conference on Durability of Building Materials and Components, Ghent (fex2017), (2017).

Mix Proportioning for Structural Concrete Containing Recycled Concrete Aggregates

Marco Pepe[(1)], Romildo Dias Toledo Filho[(2)], Eduardus A. B. Koenders[(3)] and Enzo Martinelli[(1)]

[(1)] Department of Civil Engineering, University of Salerno, Italy.

[(2)] Department of Civil Engineering, COPPE, Federal University of Rio de Janeiro, Brazil.

[(3)] Institute of Construction and Building Materials, Technical University of Darmstadt, Germany.

ABSTRACT

This study proposes a conceptual formulation for predicting and controlling the key mechanical properties of structural concrete produced with coarse Recycled Concrete Aggregates (RCAs). As a matter of principle, due to the presence of attached mortar, RCAs are significantly more porous than corresponding natural aggregates, and, consequently, affects the mixture proportioning rules commonly adopted for ordinary concretes. In general, common rules cannot be applied for cement-based mixtures produced with RCAs to create Recycled Aggregate Concrete (RAC). Therefore, the approach proposed herein is intended at generalizing the aforementioned rules by explicitly taking into account the specific features of RCAs. The proposed methodology is supported by a wide set of experimental results which unveil the influence of several aspects and parameters, such as source and processing procedures of RCAs, aggregate replacement ratio, water-to-cement ratio, water absorption capacity and initial moisture condition of aggregates, on the resulting performance of RAC. The proposed methodology demonstrates that the mechanical behavior of RAC can be easily predicted by considering only one unique parameter, i.e., the water absorption capacity, to identifying the "quality" of RCAs, and with this, the quality of the produced RAC.

Keywords: Concrete mix design, recycled concrete aggregates, recycled aggregate concrete, compressive strength, water absorption, porosity.

1 INTRODUCTION

In the last decades, several industrial sectors have been committed to improve their environmental impact by reducing and controlling, for example, their carbon footprint emissions and, among them, the construction sector is, certainly, one the most relevant [1]. As a matter of the fact, it is responsible of both the natural resources depletion (e.g., natural rocks) and the landfill disposal of construction and demolition waste [2]. On the other hand, in the last years, several studies highlighted as the concrete industry is responsible of almost 7% of CO_2 worldwide emissions [1]. For these reasons, in the last years, several research groups have been investigating the feasibility of various eco-friendly solutions for greening the concrete industry [3]. Moreover, one of the most promising solution for the production of structural concrete is based on employing recycled aggregates derived from crushed concrete members (i.e., Recycled Concrete Aggregates, RCAs) for the partial-to-total replacement of natural aggregates (leading to the so-called Recycled Aggregate Concretes, RACs) [4]-[5].

It is worth to highlight that several efforts have been made in literature for this purpose, but the use of RCAs in structural concrete is not generally allowed without restriction due to their intrinsic peculiarities [6]. In fact, being a two-phase raw material [namely, composed of Attached Mortar (AM) and natural stones] RCAs present a higher porosity (i.e., higher water absorption capacity) in comparison with the corresponding ordinary aggregates derived from the crushing processes of natural rocks. This leads to significant impact on the resulting RACs properties at both fresh (e.g., reducing workability) and hardened state (e.g., affecting the mechanical performance) [7]. Thus, in order to minimize the performance gap between ordinary and recycled aggregate concrete mixtures, some authors proposed several methodologies for improving the physical properties of RCAs (i.e., removing the AM and reducing their water absorption capacity) [3].

In this context, the present study proposes a conceptual formulation for proportioning (based on achieving the required compressive strength) structural concrete mixtures produced with coarse RCAs [8]. In fact, it is well-known that the common rules and procedures adopted for the mixtures proportioning of ordinary concretes cannot be applied as such in the case of RACs. Therefore, the approach proposed herein is intended at extending the aforementioned rules by explicitly taking into account the specific characteristics of RCAs. The proposed methodology is supported by a wide set of results derived from several experimental tests performed on both RCAs and RACs produced with them [7].

Section 2 describes the materials employed, the methods (experimental and theoretical) adopted for both analyzing the key RCAs properties and understanding the influence of RCAs on the produced concrete performance [7-8] and summarizes the key experimental evidences. Then, based on the analysis of the experimental results, a mixture proportion method for RACs is proposed and validated (with several data available in literature) in Section 3.

2 EXPERIMENTAL CHARACTERIZATION OF RCAS AND RACS

2.1 Recycled Concrete Aggregates

In this study, several coarse Recycled Concrete Aggregates (RCAs), derived from crushed debris of both concrete elements already tested in laboratories and the demolition of old existing concrete structures were employed. Specifically, different size fractions were adopted for RCA particles characterized by a nominal diameter: lower than 9.5 mm and higher than 4.75 mm (size 1); lower than 19 mm and higher than 9.5 mm (size 2); and lower than 31 mm and higher than 19 mm (size 3).

In addition, on some of the employed RCA particles derived from the demolition process of an existing concrete structure, an *autogenously cleaning process* was executed with the aim of understating the influence of the processing procedures on the resulting physical properties (i.e., density, porosity and AM content) of coarse RCAs [9]. On the RCA particles considered in this study, several tests were performed:

i. Computed Tomography scans and image analysis [10] aimed at measuring the Attached Mortar content within the RCA;
ii. Mercury Intrusion Porosimetry [11] for evaluating the open porosity of RCAs;
iii. Particles density;
iv. Time evolution of the water absorption capacity up to the 24 hours.

Figure 1 summarizes the main experimental results obtained for RCAs: it highlights that the higher porosity (and, consequently, the lower particle density) characterizing RCAs, in comparison with ordinary natural aggregates is mainly due to the presence of Attached Mortar.

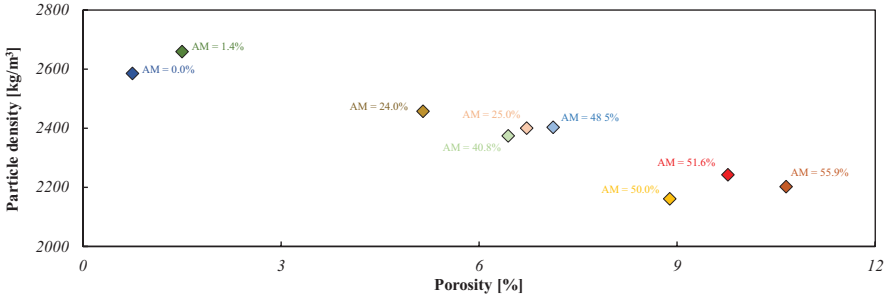

Figure 1: Porosity, particle density and AM content for RCAs: experimental evidences.

2.2 Recycled Aggregate Concrete

Once characterized the coarse RCAs employed herein, several concrete mixtures including them were produced. As aforementioned, the RCAs are characterized by a significant high water absorption capacity and, for this reason; the experimental tests performed on RACs are mainly intended at investigating the role played by relevant parameters for RCAs:

- Initial moisture condition of aggregates: oven dried (OD) or saturated with dry surface (SSD) obtained by submerging the aggregates in water for 24 hours;
- Aggregate replacement ratio;
- Nominal water-to-cement ratio;
- processing procedures (i.e. with and without performing the autogenous cleaning [9]).

Table 1 summarizes the results for one of the experimental program performed on RACs [8]: compressive strength tests (on cubic samples) were executed at 1, 3 and 28 days of water curing (under controlled isothermal conditions at a temperature 20±2°C).

Table 1: Experimental campaign for RAC.

Mix [#]	w/c	RAC [%]	Moisture condition	w/ceff	Rcm,28 [MPa]
1	0.50	0	OD	0.50	49.12
2			SSD	0.50	47.00
3		50	OD	0.46	47.55
4			SSD	0.50	40.88
5		100	OD	0.39	38.57
6			SSD	0.50	31.66
7	0.40		OD	0.32	42.39
8			SSD	0.40	41.15
9	0.60		OD	0.47	36.60
10	0.60		SSD	0.60	22.59

The compressive strength results highlight that the presence of RCAs in concrete tends to reduce the mechanical resistance and the same effect occurs when (for a fixed replacement ratio) SSD aggregates are employed. This can be attributed to the higher porosity characterising RCAs that affect the water transportation phenomena and, consequently, the free water available for the mixtures (e.g., when OD RCAs are used, they tend to absorb part of the mixing water). Based on these considerations and a more comprehensive analysis of the results performed by the authors in previous studies [7-8], an effective water-to-cement ratio (considering both the initial moisture condition and the aggregates porosity) can be defined as follows:

$$\left(\frac{w}{c}\right)_{eff} = \frac{w}{c} + \frac{w_{add}}{c} - \delta \cdot \left(\sum_{i=1}^{n} \frac{p_i \cdot P_i}{c}\right) \quad (1)$$

where, *w/c* represents the nominal water-to-cement ratio, w_{add} takes into account of the additional water that is, generally, considered for the partial-to-total saturation of the aggregates. Then, p_i and P_i represent, respectively, the water absorption capacity and the weight in the mixture of the i-th aggregate fraction. Finally, the parameter δ takes into account of the initial moisture condition of the aggregates: its value (calibrated on the experimental results above presented) is equal to zero for SSD conditions and is equal to 0.5 for dried ones [7-8].

Moreover, these results demonstrate that the presence of RCAs in concrete as well as their initial moisture condition can affect the hydration and, consequently, the time evolution of the concrete compressive strength. Therefore, in order to have an indirect estimation of the hydration process, for all the concrete mixtures, the time evolution of the temperature was measured in the centre of the cubes with a continuous system of measurements (up to 28 days) by using thermocouples when the concrete samples were cured in semi-adiabatic conditions [12]. These experimental data were employed for evaluating the time evolution of the degree of hydration by using a numerical procedure recently proposed by the authors [12]-[13]. Then, the degree of hydration (α) has been correlated to the experimental data obtained in terms of compressive strength (R_c) and, as also well demonstrated in literature [14], their correlation is almost linear:

$$R_c = R_{c,max} \frac{\alpha - \alpha_0}{1 - \alpha_0} \quad (2)$$

In the adopted formula (2) the parameter α_0 represents the minimum degree of hydration (i.e. end of setting phase) meanwhile $R_{c,max}$ represents the maximum compressive strength (theoretically, corresponding to the maximum degree of hydration equal to 1). This linear correlation between the compressive strength and the degree of hydration is able to highlight the influence of the presence of RCAs in concrete. In fact, their porosity and initial moisture conditions, as well as the presence of attached mortar define and control the formation of the concrete microstructure and the corresponding strength.

3 MIXTURE PROPORTIONG FOR STRUCTURAL RACS

Based on the analysis of the experimental results achieved in this study, a conceptual mixture proportioning method is proposed for structural concrete mixtures incorporating Recycled Concrete Aggregates. The methodology, described in this section, can be mainly divided in two parts: "*Physical properties of RCAs*" in which some correlations between the key physical properties of RCAs (including the AM content) are proposed, then, in the second part "*Mechanical properties of RACs*" some mix-design abaci, optimized for achieving the required time evolution of the compressive strength, are formulated.

3.1 Physical properties of RCAs: the role of AM

The first formula proposed for the mixture proportioning of RACs correlates the open porosity (p) of the RCAs and the corresponding Attached Mortar content:

$$p = \left[p_{NA} \cdot (1 - AM) + p_{AM}(AM)\right] \cdot \frac{d_0}{d} \quad (3)$$

In equation (3) d represents the nominal diameter of the aggregates (in mm), p_{NA} and p_{AM} are the porosity of a natural aggregate and the attached mortar inside RCA, respectively. As a matter of the fact, since the RCA is composed by natural aggregates and AM its porosity can be calculated by a linear combination of these two phases: the results obtained with MIP and CT scans (see section 2) lead to the calibration of the p_{NA} and p_{AM} parameters equal to 0.45% and 15%, respectively. Moreover, it is worth to highlight that this formula is conceived for a reference diameter equal to 20 mm (i.e., d_0). Then, a possible linear correlation can be also proposed between the open porosity (p) of the recycled aggregate particles and their density (γ): as highlighted in Figure 1 the γ tends to decreases when the p increases. Based on this consideration the following formula is proposed:

$$\gamma = \gamma_0 \cdot (1 - \beta \cdot p) \qquad (4)$$

in which γ_0 (equal to 2700 kg/m^3) represents a fictive particle density of a an aggregate characterized by an open porosity equal to zero meanwhile the parameter β is a constant value equal to 2.

Finally, an analytical expression is proposed for taking into account of the possible processing procedures performed on RCA particles for reducing its AM content. Particularly, based on the results achieved with the *autogenous cleaning process* [9] the following equation is formulated:

$$p(t) = \left(1 - \frac{a \cdot t}{b + t}\right) \cdot p_{t=0} \qquad (5)$$

where, the open porosity (p) is correlated to the "autogenous cleaning process time" (t in minutes): $p_{t=0}$ is the open porosity before the cleaning process and a (equal to 0.6 for RCAs of size 1 and 0.2 for RCAs of size 2) and b (equal to 2 in all the cases) are constant parameters.

3.2 Mechanical properties of RACs

Once defined the physical and geometrical properties of RCAs, in order to propose the mixture proportioning methodology for the design of structural RAC mixtures, the possible influence of the mixture composition and the physical parameters characterising RCAs on the time evolution of the compressive strength of RACs should be unveiled.

First of all, a possible correlation can be proposed by analysing the values obtained for α_0 and $R_{c,max}$ (calibrated for each mixture as already described in section 2 [12]) and the effective water-to-cement ratio [see equation (1)]: this unveils the role of the free mixing water on the time evolution of the concrete compressive strength. Then, since the concrete strength is also influenced by the aggregates typology (i.e., the aggregates' strength), another important parameter is the aggregate replacement ratio. This can be considered by introducing a further parameter (A_{MIX}) calculated as the average open porosity of the coarse fraction of the aggregates included within the mixture and representing an estimation of the void amount characterizing the aggregates phase:

$$A_{MIX} = \sum_{i=1}^{n} p_i \cdot V_i \qquad (6)$$

where, p_i and V_i are the open porosity and the relative volume (express in %) of the i-th coarse aggregates fraction.

As a matter of the principle, these parameters (i.e., effective water-to-cement ratio, α_0 and $R_{c,max}$ and A_{MIX}) can unveil the role of RCA on the resulting compressive strength of RACs.

From the physical point of view, the values of α_0 and $R_{c,max}$ (characterizing the time evolution of the compressive strength of RACs) can be compared with some reference values $\alpha_{0,NAT}$ and $R_{c,max,NAT}$, describing the time evolution of the compressive strength of an ordinary

reference concrete produced with natural aggregates. This can be done by introducing the r^* and α^* ratios for expressing the reduction in the time evolution of the compressive strength:

$$r^* = \frac{R_{c,max}}{R_{c,max,NAT}} = \frac{a_R \cdot \frac{A_{NAT}}{A_{MIX}}}{b_R + \frac{A_{NAT}}{A_{MIX}}} \quad (7) \qquad \alpha^* = \frac{\alpha_0}{\alpha_{0,NAT}} = \frac{a_\alpha \cdot \frac{A_{NAT}}{A_{MIX}}}{b_\alpha + \frac{A_{NAT}}{A_{MIX}}} \quad (8)$$

In equation (7) and (8) A_{NAT} is the $_{MIX}$ value for an ordinary concrete mixture produced with natural aggregates. Then, a_R, b_R, a_α and b_α are constants that can be, in principle, be calibrated on experimental results (in this study the values of a_R and b_R have been assumed equal to 1.06 and 0.06, respectively, meanwhile a_α and b_α are equal to 1.05 and 0.05).

Then, if the individual pairs of $R_{c,max}$ and α_0 are divided by the corresponding values of r^* and α^* and correlated to the effective water-to-cement ratio [7-8] all the points (w/c_{eff}-$R_{c,max}/r^*$) can be aligned on a curve that can be analytically expressed by the well know Abram´s (see expression (9)). Similarly, a possible linear correlation existing between w/c_{eff} and α_0/α^* can be described by the proposed analytical formula (10):

$$R_{c,max} = \frac{A_R}{B_R^{w/c_{eff}}} \cdot r^* \quad (9) \qquad \alpha_0 = A_\alpha \cdot \left(\frac{w}{c_{eff}} - B_\alpha \right) \cdot \alpha^* \quad (10)$$

The constants A_R, B_R, A_α, and B_α were calibrated on the experimental results proposed in section 2 and are assumed equal to 265, 9.5, 1.62 and 0.28, respectively.

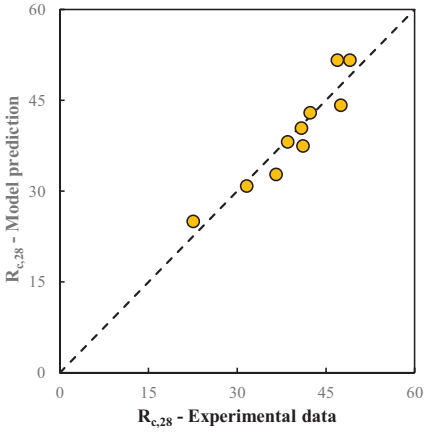

Figure 2: Mixture proportioning methodology calibration.

The accuracy of the proposed methodology can be estimated by analysing Figure 2 where both the experimental data and the model prediction results are reported in terms of cubic compressive strength of RACs at 28 days. Design abaci and model flow chart

The mixture proportioning methodology proposed herein is based on the definition of the parameter A_{MIX} representing the average porosity of the RAC that can be easily calculated by applying the equation (6). Then, by using the equations (9) and (10) some design abaci can be extrapolated as reported in Figure 3 in terms of $R_{c,max}$ and α_0 values related to both the A_{NAT}/A_{MIX} parameter and the effective water to cement ratio.

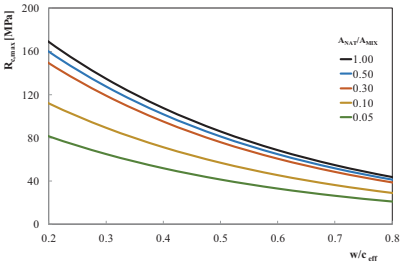

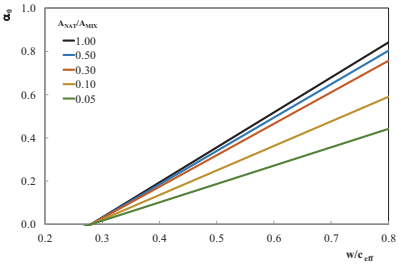

$R_{c,max} - (w/c)_{eff}$ (a) $a_0 - (w/c)_{eff}$ (b)

Figure 3: Influence of A_{NAT}/A_{MIX} on $R_{c,max}$ and α_0.

With the graphs reported in Figure 3 it is possible to evaluate the $R_{c,max}$ and α_0 parameters and hence the time evolution of the compressive strength can be easily determined by applying the numerical model recently proposed by the authors for estimating the time evolution of the degree of hydration[12-13].

3.3 Model flow chart

A flow charts (i.e., step by step calculation) summarizing the proposed methodology can be schematized as follow:

- the physical properties of RCAs (i.e., p, γ and AM) can be evaluated for each aggregates fraction;
- the composition of a reference mixture (i.e., produced with only natural aggregates) and the corresponding A_{NAT} value can be defined.
- once the replacement ratio is fixed, the value A_{MIX} can be determined (see eq. (6));
- the parameters r^* and α^* can be determined (eq. (7) and (8)) as well as the values of $R_{c,max}$ and α_0 can be obtained (Equation (9) and (10));
- the value of compressive strength at 28 days can be estimated (eq. (2)), once the corresponding value of α is determined (e.g., following the numerical procedure proposed by the authors [12]) or, alternatively, in the absence of more accurate determinations, the following analytical relationship can be applied [15]:

$$\alpha_{max} = \frac{1.031 \cdot \frac{w}{c_{eff}}}{0.194 + \frac{w}{c_{eff}}} \quad (11)$$

Finally, it is worth highlighting that the above procedure may also be inverted and used as a mixture proportioning methodology.

3.4 Model potential and validation

The proposed mixture proportioning method was applied to some experimental results available in literature [16-19]. The comparison of this analysis is reported in Figure 4 and shows that even if the proposed formulation should be better calibrated with further experimental data, the introduction of the parameter A_{MIX} is able to explain the changes of the mechanical performance of RACs compared with ordinary mixtures.

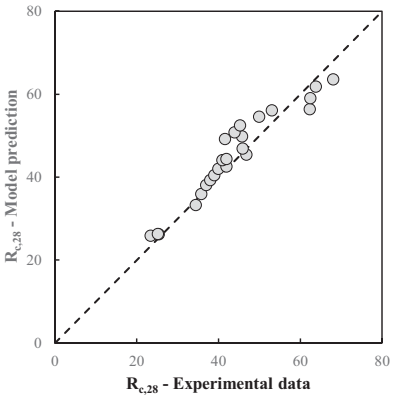

Figure 4: Model validation.

4 CONCLUSION

This study proposed a mixture proportioning methodology for assessing the compressive strength development of concrete mixtures produced with RCAs for structural purposes. Based on the analysis of the results proposed herein, the following conclusions can be drawn:

The presence of the AM in RCAs can affect their physical properties (increasing their porosity) leading to a higher water absorption capacity and particle density;

Due to the presence of AM, the mechanical performance of RACs is governed by the effective water-to-cement ratio and the aggregates replacement ratio. In fact, the nature of the attached mortar influences the strength of resulting concrete and this is taken "implicitly" into account within the water absorption capacity of RCAs;

Introducing the parameter A_{MIX} leads to estimating the concrete compressive strength.

5 ACKNOWLEDGEMENTS

The present study is part of the activities carried out by the Authors within the "EnCoRe" Project (FP7-PEOPLE-2011-IRSES n° 295283; www.encore-fp7.unisa.it) funded by the European Union within the Seventh Framework Programme.

6 REFERENCES

[1] Meyer C. 'The greening of the concrete industry', *Cement and Concrete Composit*es **31**(8) (2009) 601-605.

[2] McNeil K. and Kang T.H.K. 'Recycled concrete aggregates: A review', *International Journal of Concrete Structures and Materials* **7**(1) (2013) 61-9.

[3] Behera M., Bhattacharyya S.K., Minocha A.K., Deoliya R. and Maiti S. 'Recycled aggregate from C&D waste & its use in concrete–A breakthrough towards sustainability in construction sector: A review', *Constr Build Mater* **68** (2014) 501-16.

[4] de Brito J. and Saikia N. 'Recycled aggregate in concrete: use of industrial, construction and demolition waste', Springer Science & Business Media (2012).

[5] González-Taboada I., González-Fonteboa B., Martínez-Abella F. and Pérez-Ordóñez J.L., 'Prediction of the mechanical properties of structural recycled concrete using multivariable regression and genetic programming', *Constr Build Mater* **106** (2016) 480-499.

[6] Belin P., Habert G., Thiery M. and Roussel N. 'Cement paste content and water absorption of recycled concrete coarse aggregates', *Materials and Structures* **47** (2014) 1451-1465.

[7] Pepe, M. 'A Conceptual Model for Designing Recycled Aggregate Concrete for Structural Applications', *Springer Theses* (2015) Springer.
[8] Pepe M., Toledo Filho R.D., Koenders E.A. and Martinelli E. 'A novel mix design methodology for Recycled Aggregate Concrete, *Constr Build Mater*, **122** (2016) 362-372.
[9] Pepe M., Toledo Filho R.D., Koenders E.A.B. and Martinelli E., 'Alternative processing procedures for recycled aggregates in structural concrete', *Constr Build Mater* **69** (2014) 124-32.
[10] ASTM E1570, Standard Practice for Computed Tomographic (CT) Examination. American Society for Testing and Materials, USA (2011).
[11] ASTM D4404, Standard Test Method for Determination of Pore and Pore Distribution of Soil and Rock by Mercury Intrusion Porosimetry, American Society for Testing and Materials, USA (2010).
[12] Martinelli E., Koenders E.A.B. and Caggiano A., 'A numerical recipe for modelling hydration and heat flow in hardening concrete', *Cement and Concrete Composites* **40** (2013) 48-58.
[13] Koenders E.A., Pepe M. and Martinelli, E. 'Compressive strength and hydration processes of concrete with recycled aggregates', *Cement and Concrete Research* **56** (2014) 203-212.
[14] Lokhorst S.J., 'Deformation behaviour of concrete influenced by hydration related changes of the microstructure' Internal Report nr. 5-99-05, Delft University of Technology, Netherland (1999) pp.178.
[15] Hansen T.C., 'Physical structure of hardened cement paste. A classical approach', *Mater Struct* **19** (6) (1986) 423-36.
[16] Gómez-Soberón J.M. 'Porosity of recycled concrete with substitution of recycled concrete aggregate: an experimental study', *Cement and concrete research* **32**(8) (2002) 1301-1311.
[17] Etxeberria M., Mari A.R. and Vazquez E. 'Recycled aggregate concrete as structural material', *Mater Struct* **40**(5) (2007) 529-541.
[18] Younis K.H. and Pilakoutas K., 'Strength prediction model and methods for improving recycled aggregate concrete', *Constr Build Mater* **49** (2013) 688-701.
[19] Amario M. 'Dosagem cientifica de concretos estruturais contendo agregado de residuo de concreto (ARC)', Master Thesis (in Portuguese), Federal University of Rio de Janeiro, COPPE/UFRJ, Brazil, (2015).

Compressive Strength and Surface Morphology of Hydrated Cement Paste Containing Micro- and Nano- Cement Additives

S. Al-Bahar, J. Chakkamalayath and A. Joseph

Construction and Building Materials Program, Energy and Building Research Centre, Kuwait Institute for Scientific Research, Kuwait

ABSTRACT

The scarcity of raw materials and increased awareness towards environmental protection has resulted in the use of alternative supplementary cementitious materials (SCM) in concrete construction. The deterioration of concrete structures in the marine environment is a growing problem in the construction industry in Gulf countries. Therefore, the challenge before the engineering community is to achieve a durable high-performance concrete having adequate strength, which is cost-effective, environment-friendly, and therefore sustainable. With the abundance of volcanic ash (VA) reserves in the Arabian Gulf region, it became a suitable natural pozzolanic material for the production of green cement and more economical concrete. This paper presents the experimental results, describing the effects of the partial replacement of ordinary Portland cement (OPC) with regionally available VA, microsilica (MS), or nanosilica (NS), in binary and ternary blends, on the surface morphology and mechanical properties of the cement matrices. Scanning electron microscopy (SEM) analysis showed denser C-S-H gel structure when the OPC was replaced with a combination of VA and MS, and this structure became much denser when the MS was replaced with NS. The compressive strength results support the microstructural analysis in which NS performs better than MS when combined with VA due to better particle size gradation.

Keywords: Microsilica, mechanical properties, microstructure, nanosilica, volcanic ash.

1 INTRODUCTION

The use of pozzolanic materials as a partial replacement for ordinary Portland cement (OPC) has become an unavoidable practice in concrete construction because of their economic, environmental, and durability advantages. The construction sector in Kuwait and other Gulf countries always demand the use of innovative materials and methods due to the extreme climatic conditions together with the marine environment of the region, which have an adverse effect on the life of concrete structures. In the recent years, the increased cost of imported cementitious materials such as fly ash, slag, and silica fume has resulted in diverting the attention of researchers towards the use of regionally available volcanic ash (VA) for the sustainable concrete construction in the Gulf region. Most of the studies related to blended cements with VA are generally limited to the specific properties such as the hydration behaviour of cement paste, mortar, and concrete with the addition of VA [1-7]. These results cannot be adopted for VA obtained from a different region, as VA is a natural material and its properties vary with origin and mode of formation [8]. Further to this, significant improvements in the durability and mechanical properties of cementitious materials by the incorporation of VA, nanosilica (NS), and microsilica (MS) in binary blended system are reported through previous research works [9-10]. The use of VA along with commercially available MS and NS causes a reduction in heat evolution, decrease of permeability, and

improvement of durability properties. The objective of this study was to understand the effect of replacing OPC with VA, MS, or NS in different percentages on the mechanical properties as well as on the microstructural modifications. Accordingly, a systematic study on the effect of incorporating micro- and nano- additives on the compressive strength and surface morphology was conducted, and the results are presented in this paper.

2 EXPERIMENTAL DETAILS

2.1 Materials

Major deposits of VA are abundant in Yemen and Saudi Arabia. The VA sample used in the present study was collected from Saudi Arabia, the neighbouring country of Kuwait in the Gulf region. Locally available Type 1 OPC complying to ASTM C150/150M-16 and VA samples of the average size of 21.34 μm were used in this study. The characterization of VA was carried out according to ASTM C 618-12a and ASTM C 311-13 to check its suitability to use as a pozzolan. Commercially available MS and NS of the average particle size of 21.84 μm and 9.30 μm, respectively, were also used as the micro- and nano-cement additive in the present study.

3 SAMPLE PREPARATION AND TESTING

The experimental study was conducted on the control cement paste prepared with OPC, VA, and different percentages of MS or NS. The OPC was replaced with 20 % and 50 % VA in the binary system, whereas the MS content was 10% and NS was used in two different dosages of 2 % and 6 % in the ternary system. This experimental investigation included the scanning electron microscopy (SEM) analysis and the compression test in microscale and macroscale, respectively. Cubes of 50 mm side were prepared from the cement paste mix for determining the compressive strength with OPC, VA, and various percentages of MS or NS. Microstructural development was studied by SEM combined with energy-dispersive X-ray spectroscopy (EDX). The microscope was operated in the secondary electron detection mode with high vacuum and an acceleration voltage of 15-20 kV. Cement paste samples of size 20 × 20 × 10 mm were placed on carbon tape attached to the sample holder with gold coating.

4 RESULTS AND DISCUSSIONS

4.1 Comparison of physical and chemical properties of OPC and VA

The comparison of the physical properties of OPC and VA is given in Table 1. It was observed from the test results that the density of VA is comparable with that of conventional mineral admixtures such as fly ash and silica fume. The strength activity index was 87% for the cement paste with VA, which was more than the minimum required value of 75% specified by the standard, ASTM C 618-12 (2012). This confirms that the available VA has good pozzolanicity and can be used as a micro-cement additive to concrete.

A comparative analysis of the chemical composition of OPC and VA was conducted using X-ray fluorescence (XRF) spectrometer and the major oxides are given in Table 2. The major compounds present were CaO, SiO_2, and Al_2O_3,and the results confirmed the low quantity of CaO and the higher quantity of SiO_2 for VA as in the case of other mineral admixtures. The SO_3 content was lower in VA than in OPC, whereas MgO, Fe_2O_3, and alkali contents were higher in VA than in OPC.

Table 1: Physical properties of OPC and VA

Property	OPC	VA
Air content (%)	6.6	6.5
Density (g/ cm^3)	3.15	2.75
Fineness (m^2/kg)	367	396
Consistency (%)	22.5	23.4
Initial setting time (Minutes)	105	132*
Final setting time (minutes)	175	202*
Strength Activity Index		87%

*Cement paste prepared with 20 % VA

Table 2: Chemical composition of OPC and VA

Property (%)	OPC	VA-20 micron
SiO_2	16.63	38.89
Al_2O_3	3.63	13.00
Fe_2O_3	3.28	12.41
CaO	62.27	9.09
MgO	1.22	6.16
Na_2O	0.34	3.12
K_2O	0.61	1.31
SO_3	3.91	0.14
TiO_2	0.24	2.44

4.2 Microstructural analysis

The SEM analysis was conducted to understand the effect of the replacement of OPC with different percentages of VA on the microstructural development of hydrated cement paste. Figure 1 shows the SEM images of samples at 0.35 water to cement (w/c) ratio with varying VA content after 28 days of curing. Various hydration products like C-S-H, C-H, and ettringite were identified as given in the previous reports [11-12]. C-H crystals with longer needles of ettringite were formed during the hydration process in the control mix as shown in Figure 1. Figure 1(b) and 1(c) shows less C-H crystals, indicating the pozzolanic reaction due to the addition of VA. Ettringite was formed separately in the control mix, whereas embedded ettringite was formed after adding VA.

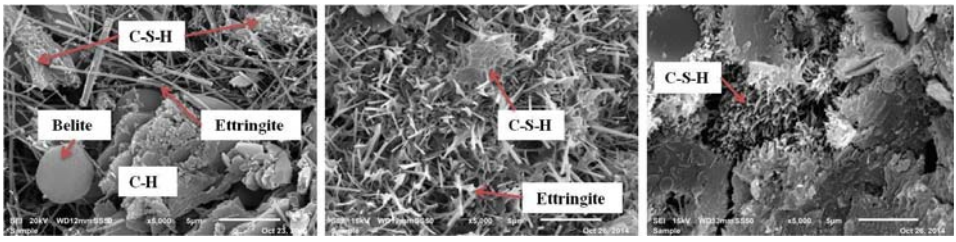

(a) (b) (c)

Figure 1: SEM images of hardened cement paste (a) 0% VA, (b) 20% VA, and (c) 50% VA (chipped sample) at 0.35 w/c ratio after 28 days of curing

Figure 2 shows the SEM images of samples with micro-and nano- additives at 0.35 w/c ratio after 28 days of curing. The comparison of Figure 1 and Figure 2 show that the surface morphology was different in the case of binary and ternary blended systems. Much denser morphology was observed in the case of ternary blended cements with varying OPC, VA, and NS/MS at a w/c ratio of 0.35 after 28 days of curing. In most of the cases, a gel type C-S-H morphology was observed. Very few CH crystals were noticed and ettringite needles were not observed in any of the samples.

The progress of the hydration reactions can be clearly seen on the surface of the samples with MS as shown in Figure 2a. The C-S-H gel structures were interconnected to each other on the surface. A much denser gel structure was observed for samples with optimal NS replacement of 6% (Figure 2b) than those with MS (Figure 2b).

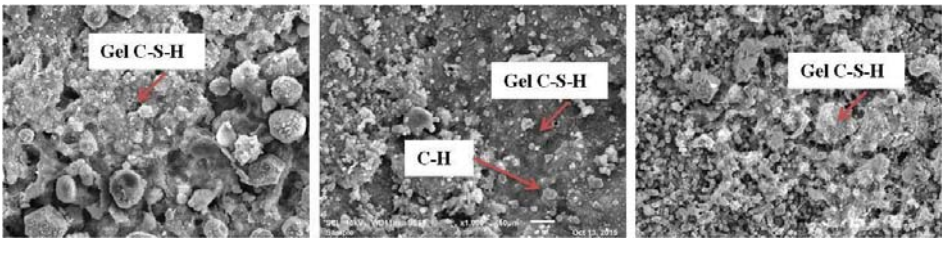

(a) (b) (c)

Figure 2: SEM images of (a) OP40VA50MS10, (b) OP44VA50NS6 and (c) OP80VA18NS2 (w/c = 0.35) after 28 days of curing

The chemical compositions of C-S-H, C-H, and other hydration products were determined by SEM based EDX analysis to validate the phases identified through SEM as shown in Figure 3.

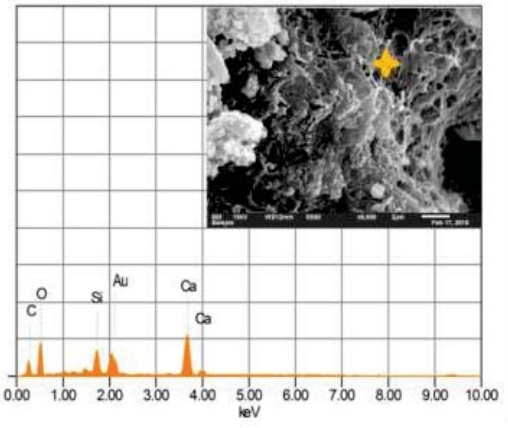

Figure 3: SEM-EDX analysis of C-S-H

4.3 Compressive strength

In order to understand the effect of micro- and nano- additives on the mechanical properties of hydrated cement paste, the compressive strength of both binary and ternary blended cement pastes with VA, MS, and NS was determined after 28 days of water curing. The compressive strength results showed that, compared to control the mix, the compressive strength of hydrated cement paste decreased with the incorporation of VA, MS, and/ NS at different percentages. The compressive strength results support the microstructural analysis in which NS gives higher strength than MS when combined with VA, as shown in Figure 4.

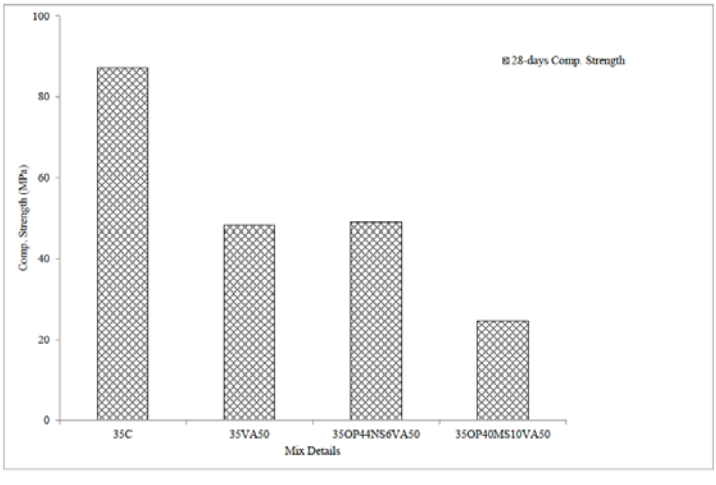

Figure 4: Compressive strength of mixes with micro- and nano- cement additives

5 CONCLUSIONS AND RECOMMENDATIONS

The effect of the partial replacement of OPC with VA, MS, or NS on the properties of hydrated cement paste was analysed in the microscale and macroscale. The addition of micro-

and nano- additives resulted in the modification of the microstructure as well as the densification of the cement matrix. Microstrucural studies using SEM shows that the binary blended cement system with different percentages of VA replacement of OPC shows a less denser morphology after 28 days of curing. A much denser gel morphological structure was observed for ternary blended cement samples containing NS than MS. This is clear evidence that the additional material, either NS or MS, not only enhances the early pozzolanic reactions but also acts as a filler material to form a much denser microstructure. The compressive strength results correlate with the microstructural analysis in which the performance of NS is better than MS when combined with VA in a ternary blended system due to better particle size gradation and pozzolanic action. The studies conclude that understanding the properties of cementitious materials in the multi scale can ensure their optimal use for improving the performance of concrete.

6 ACKNOWLEDGEMENTS

The authors are grateful to the Kuwait Foundation for the Advancement of Sciences (KFAS) and the Kuwait MIT Office (KUMIT) for funding this joint project between the Kuwait Institute for Scientific Research (KISR), Kuwait University (KU), and Massachusetts Institute of Technology (MIT). Gratitude is extended to KISR for providing the facilities and approval for carrying out this project.

7 REFERENCES

[1] Hossain, K.M.A., 'Blended cement using volcanic ash and pumice', Cem. and Conc. Res.33(10) (2003)1601–1605.

[2] Hossain, K.M.A. and Lachemi, M., 'Corrosion resistance and chloride diffusivity of volcanic ash blended cement mortar', Cem. and Conc. Res.34(4) (2004) 695–702.

[3] Hossain, K.M.A., 'Volcanic ash and pumice as cement additives: pozzolanic, alkali-silica reaction and autoclave expansion characteristics', Cem. and Conc. Res.35(6) (2005) 1141–1144.

[4] Hossain, K.M.A. and Lachemi, M. ,'Performance of volcanic ash and pumice based blended cement concrete in mixed sulfate environment', Cem. and Conc. Res.36(6) (2006) 1123–1133.

[5] Hossain, K.M.A. and Lachemi, M., 'Fresh, mechanical, and durability characteristics of self-consolidating concrete incorporating volcanic ash', J. of Mat. in Civil Eng. 22 (2010)651–657.

[6] Siddique, R.,'Effect of volcanic ash on the properties of cement paste and mortar', Resour.Conser. and Recycl.56(1) (2011) 66–70.

[7] Siddique, R.,'Review–properties of concrete made with volcanic ash', Resour. Conser. and Recycl.66 (2012) 40– 44.

[8] Pekmezci, B.Y. and Akyu¨z, S., 'Optimum usage of a natural pozzolan for the maximum compressive strength of concrete' ,Cem. and Conc. Res.34(12) (2004) 2175–2179.

[9] Barbhuiya, S., Chow, P. and Das, A., 'Nanomechanical Properties of Cement Paste Containing Silica Fume', Proceedings of International Conference on Architecture and Civil Engineering (ICAACE'14), Dubai, 25-26 December 2014. DOI: 10.17758/UR.U1214325.

[10] Singh, L.P.,Karade, S.R., Bhattacharyya, S.K., Yousuf, M.M. and Ahalawat, S.,'Beneficial role of nanosilica in cement based materials – A review', Const. and Build. Mat.47 (2013)1069–1077.

[11] Jumate, E. and Manea, D.L.,'X-ray Diffraction (XRD) study of hydration processes in the Portland Cement', J. of Appl. Eng. Sci.1(1) (2011) 79–86.

[12] Jumate, E. and Manea, D.L., 'Application of X-ray diffraction (XRD) and scanning electron microscopy (SEM) methods to the portland cement hydration processes' ,J. of Appl. Eng. Sci.2 (1) (2012) 35–42.

Effect of Hydraulic Retention Time on the Filtration Performance of Porous Concrete

Murugan Muthu[(1)], Manu Santhanam[(1)] and Mathava Kumar[(2)]

[(1)] Building Technology and Construction Management Division, Department of Civil Engineering, Indian Institute of Technology Madras, Chennai 600 036, Tamil Nadu, India

[(2)] Environmental and Water Resources Engineering Division, Department of Civil Engineering, Indian Institute of Technology Madras, Chennai 600 036, Tamil Nadu, India

ABSTRACT

This study investigates the effect of hydraulic retention time on the filtration performance of porous concrete for removal of lead. Porous concrete, which is made of cement, gap-graded coarse aggregates and water, can present a way forward for slow filtration, as it allows the water to percolate through its interconnected voids. Cylindrical porous concrete specimens of size 100 × 150 mm (ø × H) having flow rate of 626 ± 301 mL/min were prepared and then cured in tap water for a period of 7 days. Up to 86% and 98% of Pb were chemically trapped in the porous concrete specimens after passage of dilute solution containing 8 mg/L Pb through such specimens maintained with 30 cm constant head and trickling head respectively. This suggests that the increase in residence time increased the filtration of heavy metal by the porous concrete.

Keywords: Porous concrete, hydraulic retention time, chemical precipitation, trickling head, X-ray tomography

1. INTRODUCTION

Porous concrete is a special type of concrete composed of cement, water, gap graded or blended coarse aggregates, and additives, with little or no fine aggregates [1-3]. Porous concrete pavement system helps in groundwater recharge by providing channels for infiltration of storm water through the inter-linked voids that prevail over the entire depth [4-6]. Porous concrete is used for various functions in the form of pavements, walls, and tile drains for the purpose of water infiltration, thermal insulation, and noise control activities [1, 7-9].

The general applications of porous concrete are parking lots, green house floors, tennis courts, zoo areas, low volume roads, patios, shoulders, noise barriers, slope stabilization, drains, swimming pool decks and friction course for pavements [9]. Porous concrete pavements are eco-friendly in terms of groundwater recharge by allowing the storm water to runoff through the coarse pore structure [10, 11]. Furthermore, the acoustic properties of porous concrete help to reduce the noise generated by vehicles on the road pavements [9]. However, only a few studies have reported on the characteristics of storm water percolated through the porous concrete, which is generally a composite of rich cementitious matrix interlaced with coarse aggregates.

Groundwater contamination is reduced when the dissolved heavy metals present in storm water are adsorbed on the inner pore walls of porous concrete pavements [12-14]. Fresh and clean water is essential for the survival of living beings. Biological, organic, inorganic and

toxic pollutants heavily contaminate ground and surface water reserves. These render the water unsafe for human consumption, irrigation and industrial needs [15]. In the future, people belonging to economically weaker sections and rural communities will find it difficult to afford clean water [16]. This problem can be overcome by developing economically affordable solutions to filter the polluted water [17]. Haselbach et al. [12] have reported that porous concrete maintained with a trickling head was able to chemically trap 90 % Cu and 87 % Zn from the dilute solutions containing 0.02 mg/L Cu and 0.10 mg/L Zn after passage.

This paper attempts to develop a concrete-based water filtration system to address the problem of removing the toxic heavy metals, especially Pb from industrial effluents. This system is based on porous concrete. Although the characteristics of water percolated through the flow channels of porous concrete have been studied, the use of such concrete for water filtration is still a challenge due to various factors like control over pore size distribution, filtrate characteristics, lime leaching and sediment blockage [12, 18-22]. The hydraulic conductivity of porous concrete is found to influence the characteristics of water after passage. In this paper, the effect of hydraulic retention time on the filtration performance of porous concrete was studied. Lead containing solution having Pb concentration of 8 mg/L was passed through the cylindrical porous concrete specimens mounted on the permeability set up maintained with 30 cm constant head and trickling head respectively. The experimental findings are discussed in this paper.

2. MATERIALS AND METHODS

53 Grade ordinary Portland cement (OPC) and crushed granite coarse aggregates conforming to IS 12269 and IS 383, respectively, and 0.5 wt% polycarboxylic ether (PCE)-based superplasticizer were used in the preparation of porous concrete mixture. This mixture was designed to have an aggregate to cement ratio (a/c) and water to cement ratio (w/c) of 4 and 0.32. Table 1 lists the gradation of aggregates that were used in this study.

Table 1: Gradation of aggregates that were used in this study

Aggregate size fraction	6.30 to 4.75 mm	4.75 to 2.36 mm	2.36 to 1.18 mm	1.18 mm to 300 μm	≤ 300 μm
% by weight	45	25	20	5	5

Cylindrical porous concrete specimens of size 100 × 200 mm (ø × H) were prepared using iron moulds. A Marshall hammer having a foot diameter of 98.4 mm was the tool used to have uniform compaction. The compaction was achieved by dividing the concrete into three layers. The fresh concrete required for each equal layer was weighed, poured into the mould, and compacted with 26 blows; after the top layer was compacted, the top surface of fresh concrete was finished using a trowel. The cylindrical specimens were demoulded after 24 hours and then cured in tap water for a period of 7 days. At the time of finishing the concrete surfaces using trowel, the bleed water containing cement slurry was noticed to occupy the coarser voids at the top of the specimen. Furthermore, some cement slurry had also settled on the bottom part of the cylinder. To obtain a uniform sample of the porous concrete, slices from the top and bottom of the cured specimens of about 25 mm thickness were removed using a diamond-tipped saw. The sliced specimens were used to analyse the filtration characteristics.

Dilute solution containing 8 mg/L Pb was prepared using lead (II) nitrate salts and then stored in a reservoir having flow control arrangement. This solution was passed under gravity through the concrete specimens mounted in the permeability set up for a period of 60

minutes. A head of 30 cm, as well as a trickling head was maintained constantly over two different concrete specimens for the whole testing period by precisely regulating the flow control valve of the solution reservoir, as schematically illustrated in Figure 1.

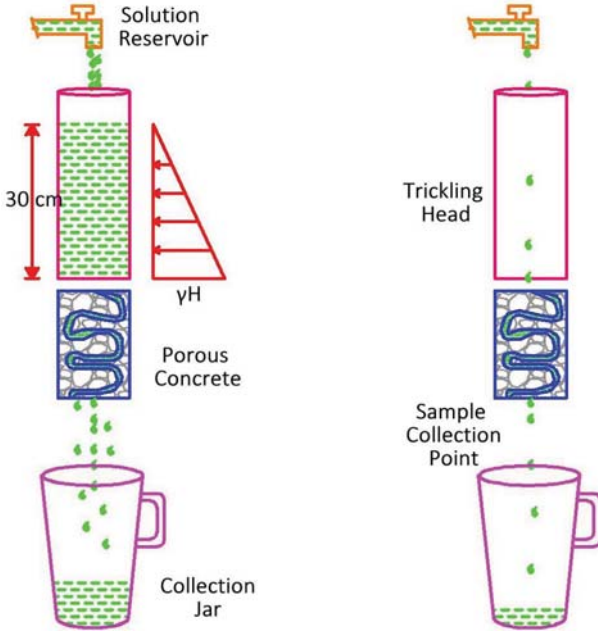

Figure 1: Permeability testing of porous concrete maintained with a 30 cm constant head and a trickling head

A small amount of filtrate, approximately 15 mL, was collected at every 15 minutes and the remaining solution was collected in the plastic jar that was kept below the concrete specimen. The amount of Pb remaining in the collected filtrate was analysed using inductively coupled plasma mass spectrometry (ICP-MS).

In this study, the void structure inside the porous concrete was imaged using 3-dimensional X-ray tomography. Concrete specimens of size 40 × 100 mm (ø × H) were cored and sliced from the 100 × 200 mm concrete specimens using core cutting machine and diamond-tipped saw respectively. These specimens (in dried condition) were then scanned using X-rays generated at a voltage and current of 120 kV and 70 µA respectively. The scanning rate was maintained around 4 milliseconds per image. The GE phoenix v|tome|xs 3-D X-ray Computed Tomography (CT) machine, used for this study, was fitted with a Caesium Iodide flat panel based detector. The resultant 2-dimensional radiographs were extracted from the acquisition software named Phoenix datos|x CT. Next, their 3-dimensional reconstruction was performed using the software VGStudio MAX version 2.2.

3. RESULTS AND DISCUSSION

3.1 X-ray tomography images

Figure 2 illustrates the 3-dimensional tomography images of porous concrete that was used in this study.

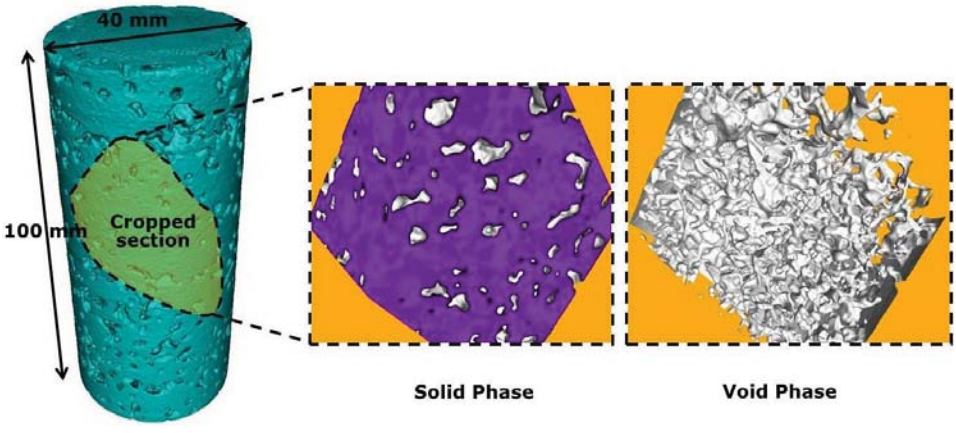

Figure 2: 3D X-ray CT image illustrating the presence of void structure inside the porous concrete specimen that was used in this study

Firstly, the 3D CT image of porous concrete specimen was sectioned into multiple shapes to clearly visualise the interconnected voids inside the material. This was also done to remove the noise created by the exterior surface of the CT image, which was in direct contact with air (low density phase).

The connected voids were noticed to be irregular and highly tortuous, which suggests that the porous system could be highly prone to sediment blockage. The reconstructed software named VGStudio Max 2.2 has in-built algorithms and modes, which can locate the pores or voids with high contrast inside the material. These algorithms control the grey scale histogram of the CT image. By performing sequential image analysis operations on the void structure, the void size ranges and the porosity of the concrete were determined to be 0.1 – 14.8 mm and 14.7% (± 4.2%) respectively.

3.2 Constant head permeability test results

Permeability set up, as suggested by Sonebi and Bassuoni [23] was fabricated for this study and thereby the flow rate of porous concrete was determined as 626 ± 301 mL/min. This flow rate was found to be similar to the sand filters that are used in water treatment plants. Figure 3 illustrates the lead ions remaining in the filtrate after passage of dilute solution containing 8 mg/L Pb through the porous concrete specimens maintained with 30 cm constant head and trickling head.

It may be noticed from the results that the porous concrete was able to trap Pb significantly from aqueous solutions. Up to 86% and 98% of Pb were chemically trapped in the porous concrete specimens after passage of dilute solution containing 8 mg/L Pb through such specimens mounted on the permeability set up maintained with 30 cm constant head and trickling head respectively.

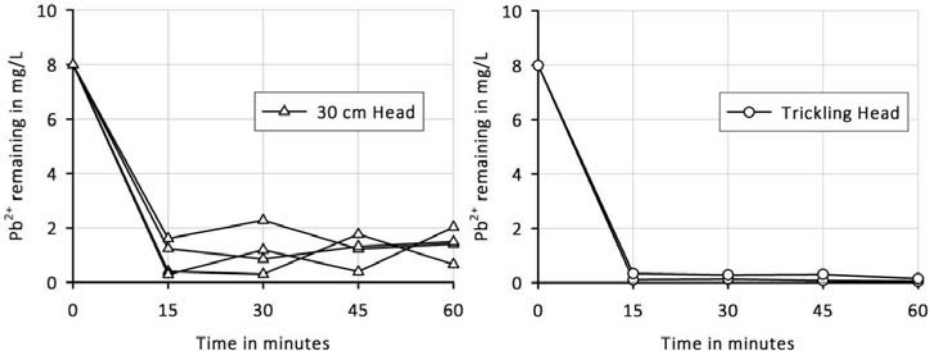

Figure 3: Lead ions remaining in the filtrate after passage of Pb containing solution (8 mg/L) through the porous concrete maintained with 30 cm constant head (left) and trickling head (right)

The presence of hydroxyl and carbonate ions in the flow channel of porous concrete had interacted with the Pb ions and thereby got precipitated as lead hydroxide and lead carbonates. This effect suggests that the heavy metal was removed because of co-precipitation. Apart from this, the decrease in flow rate in the case of the trickling head had increased the residence time and thereby the filtration performance of porous concrete was enhanced.

4. CONCLUSIONS

The key findings from this study are listed as below:

- The tortuous interconnected voids inside the porous concrete system were visualised using 3-D X-ray CT images. The porous concrete filtration system designed in this study had void sizes in the range of 0.1 – 14.8 mm and the overall porosity was 14.7 ± 4.2%.
- Porous concretes maintained with 30 cm constant head, trickling head was able to trap the Pb ions from the aqueous solution by up to 86%, and 98%, which suggests that the hydraulic retention time influences the concentration of heavy metals that are required to be filtered using porous concrete.
- Porous concrete based filtration systems are effective in removing lead from industrial effluents, and can present a low cost alternative for this process.

1 REFERENCES

[1] N. Neithalath, J. Weiss, J. Olek, Characterizing enhanced porosity concrete using electrical impedance to predict acoustic and hydraulic performance, Cement and Concrete Research 36(11) (2006) 2074-2085.

[2] N. Neithalath, M.S. Sumanasooriya, O. Deo, Characterizing pore volume, sizes, and connectivity in pervious concretes for permeability prediction, Materials Characterization 61(8) (2010) 802-813.

[3] M.S. Sumanasooriya, N. Neithalath, Pore structure features of pervious concretes proportioned for desired porosities and their performance prediction, Cement and Concrete Composites 33(8) (2011) 778-787.

[4] B.O. Brattebo, D.B. Booth, Long-term stormwater quantity and quality performance of permeable pavement systems, Water Research 37(18) (2003) 4369-4376.

[5] N. Ghafoori, S. Dutta, Building and Nonpavement Applications of No-Fines Concrete, Journal of Materials in Civil Engineering 7(4) (1995) 286-289.

[6] A. Golroo, S.L. Tighe, Pervious Concrete Pavement Performance Modeling Using the Bayesian Statistical Technique, Journal of Transportation Engineering 138(5) (2012) 603-609.
[7] J. Yang, G. Jiang, Experimental study on properties of pervious concrete pavement materials, Cement and Concrete Research 33(3) (2003) 381-386.
[8] N. Neithalath, Extracting the performance predictors of Enhanced Porosity Concretes from electrical conductivity spectra, Cement and Concrete Research 37(5) (2007) 796-804.
[9] ACI.522R, Report on Pervious Concrete, American Concrete Institute (2010).
[10] M. Scholz, P. Grabowiecki, Review of permeable pavement systems, Building and Environment 42(11) (2007) 3830-3836.
[11] W. Schlüter, C. Jefferies, Modelling the outflow from a porous pavement, Urban Water 4(3) (2002) 245-253.
[12] L. Haselbach, C. Poor, J. Tilson, Dissolved zinc and copper retention from stormwater runoff in ordinary portland cement pervious concrete, Construction and Building Materials 53 (2014) 652-657.
[13] J.D. Luck, S.R. Workman, M.S. Coyne, S.F. Higgins, Solid material retention and nutrient reduction properties of pervious concrete mixtures, Biosystems Engineering 100(3) (2008) 401-408.
[14] J.D. Luck, S.R. Workman, M.S. Coyne, S.F. Higgins, Consequences of manure filtration through pervious concrete during simulated rainfall events, Biosystems Engineering 102(4) (2009) 417-423.
[15] A. Zaporozec, Ground-Water Pollution and its Sources, GeoJournal 5(5) (1981) 457-471.
[16] M.R. Riley, C.P. Gerba, M. Elimelech, Biological approaches for addressing the grand challenge of providing access to clean drinking water, Journal of Biological Engineering 5 (2011) 2-2.
[17] A.C. Twort, F. Law, F. Crowley, D. Ratnayaka, Water supply, Edward Arnold (Publisher) Ltd.1994.
[18] J.G. Jang, Y.B. Ahn, H. Souri, H.K. Lee, A novel eco-friendly porous concrete fabricated with coal ash and geopolymeric binder: Heavy metal leaching characteristics and compressive strength, Construction and Building Materials 79 (2015) 173-181.
[19] S.-B. Park, M. Tia, An experimental study on the water-purification properties of porous concrete, Cement and Concrete Research 34(2) (2004) 177-184.
[20] M.E. Vancura, K. MacDonald, L. Khazanovich, Location and Depth of Pervious Concrete Clogging Material before and after Void Maintenance with Common Municipal Utility Vehicles, Journal of Transportation Engineering 138(3) (2012) 332-338.
[21] U. Solpuker, J. Sheets, Y. Kim, F.W. Schwartz, Leaching potential of pervious concrete and immobilization of Cu, Pb and Zn using pervious concrete, Journal of Contaminant Hydrology 161 (2014) 35-48.
[22] J. Sansalone, X. Kuang, G. Ying, V. Ranieri, Filtration and clogging of permeable pavement loaded by urban drainage, Water Research 46(20) (2012) 6763-6774.
[23] M. Sonebi, M. Bassuoni, Investigating the effect of mixture design parameters on pervious concrete by statistical modelling, Construction and Building Materials 38 (2013) 147-154.

Initial Study on Determining the Design Values of Macro Synthetic FRC for Floors-on-Grade

William P Boshoff(1), Hermanus L Bester(1) and Celeste Viljoen(2)

[1]Unit for Construction Materials, Stellenbosch University, South Africa

[2]Department of Civil Engineering, StellenboschUniversity, South Africa

ABSTRACT

Fibre reinforced concrete has been used for some time in concrete floors-on-grade and is probably the most successful application of FRC other than shotcreting in tunnels and mines. The most important material property of FRC is the post peak resistance which is typically measured using notched- or unnotched flexural beam tests. The number of fibres bridging the small scale test cracks are small, thus geometric variation of fibre distribution adds variability that will not be found in larger scale implementations where geometric variations are averaged out over a larger crack area. In the derivation of characteristic- and design values this scale effect need to be properly accounted for to achieve appropriate reliability without over conservatism. This paper presents a large set of flexural tests of macro synthetic FRC to firstly evaluate the effect of scatter. Current guidelines on calculating the characteristic and design values are also reviewed and suggestions are made on how to determine design values for macro synthetic FRC for concrete floors-on-grade

Keywords: Fibre reinforced concrete; reliability design, characteristic values, scatter, residual tensile stress

1 INTRODUCTION

Fibre reinforced concrete (FRC) is becoming more predominantly used in floors-on-grade and shotcrete with numerous codes and guidelines available, e.g. TR34, 2013 [1] for floors-on- grade and EFNARC, 1999 [2] for shotcrete. For these applications, both steel, and macro synthetic fibres are appropriate. For the fibres to make a difference of design, a plastic approach (e.g. yield line design) has to be used as the fibres are only activated after the concrete has cracked [3]. Other design codes exist which incorporates fibres, for example beams and suspended slabs [4]. Many countries have also their own guideline for FRC, e.g. in Sweden [5] and Germany [6]. Guidelines however still do not include the effect of creep for cracked fibres reinforced concrete and should be taken into account when using FRC, especially synthetic FRC [7].

There is however one aspect that still need to be properly addressed, namely the large scatter in post-peak resistance measurements found in the characterising tests. The number of fibres bridging the small scale test cracks are small, thus geometric variation of fibre distribution adds variability that will not be found in larger scale implementations where the geometric variations are averaged out over a larger crack area. This scale effect has been mentioned before [4–9], but the proposals to approach the problem differ significantly.

Design values for resistance must be appropriately conservative to account for inherent variability [10], statistical- and model uncertainty [11]. Modern design standards achieve this through a limit state approach where partial factors are calibrated to achieve the target reliability β_t, which is in turn based on principles of economic optimisation [12]. Resistance and load effect are decoupled based on the relative uncertainty of each; typical sensitivity factors are 0.7 and 0.8 respectively [13]. The resistance design value then corresponds to a low probability fractile of $0.8\beta_t$ standard deviations below the mean value [14]. To limit the influence of statistical uncertainty it is common practice to estimate the characteristic fractile based on measurement data (for material resistance this would typically be a 5% fractile) and to derive the design value based on an assumed probability distribution [10] that is further informed by wider sources of data and engineering judgement.

Sources of uncertainty or variability for FRC yield line capacity will include the inherent variability of parameters that contribute to post-peak plastic bending capacity, such as concrete mix parameters, fibre properties, bond properties and the scale effect already mentioned. Statistical uncertainty relates to the limited number of samples available for determination of characteristic values and sample statistics. Model uncertainty include uncertainty in the relation between bending capacity and gauge displacement resulting in differences between predicted- and actual capacity, experimental uncertainty, uncertainty in the definition of failure etc.

In this paper, a large set of EN 14651 [15] flexural tests results of macro synthetic FRC are presented. Numerous mix variations were made deliberately in order to identify parameters that affect the post peak resistance. These results are then further analysed to determine characteristic values according to different published approaches. Finally design values are derived using these approaches together with a new approach.

2 EXPERIMENTAL WORK

A large number of EN 14651 [15] flexural tests were done on a number of variations of a standard FRC mix design. The volume of the fibres in all the mixture was however kept constant. The reader is referred to Manus (2017) [16] for tests where the volume of the fibres was also varied.

2.1 Tests setup and procedure

The test samples were manufactured and tested according to EN 14651 [15]. The 150 ×150 × 700 mm^3 samples were demoulded around 24 hours after casting and were then submerged in water until the testing age of 28 days. Not later than 3 days before testing, a 25 mm deep notch were cut in the centre on a cast face adjacent to the top casting surface of the beam after which the beams were submerged again. A gauge was installed for measuring the crack opening displacement, COD, during the test. The gauge is manufactured by Instron and has a 4 mm measuring range. Two knife edges were glued to the bottom of the beam across the notch to which the COD gauge was affixed. The beams were tested in a three point bending setup as shown in Figure 1. The load cell used has a capacity of 250 kN. The test were controlled by the crack mouth opening displacement as measured and were 0.05 mm/min for the first 0.1 mm and then 0.2 mm/min until the test was stopped at a crack opening of 4 mm.The residual values can be calculated using the following equation for values f_{R1} to f_{R4}:

$$f_{Ri} = \frac{3}{2}\frac{F_i L}{b d^2}$$

with F_i the force at CODs of 0.5 mm, 1.5 mm, 2.5 mm and 3.5 mm respectively for *i = 1 to 4*, *L* the span, b the width of the beam and *d* the height of the beam excluding the notch.

2.2 Materials

A conventional concrete mix was designed using water, cement, aggregates, and admixtures. The potable water used was supplied by the local municipality and the cement was locally manufactured by Pretoria Portland Cement. Two types of cement were used, namely CEM III/A 42.5 N and CEM II/A-L 52.5 N. The coarse aggregate used is crushed greywacke stone, graded according to SANS 1083 [16] to nominal sizes of 19 mm, 26.5 mm, and 37.5 mm. The relative density of the stone is 2.7. The fine aggregate is a mix between 60% dune sand and 40% greywacke crusher sand with a combined relative density of 2.65. An admixture, Plast Omega 134 supplied by CHRYSO, was used to ensure the appropriate workability.

Lastly, the fibre is an experimental fibre supplied by CHRYSO. The length is 50 mm with an equivalent diameter of 1.3 mm and it is twisted in form. The Young's Modulus of the fibre is 5 GPa and the tensile strength 600 MPa. A bundle of the fibres together with a single fibre and a pen can be seen in Figure 1. The dosage of the fibre was kept constant at 4 kg/m3.

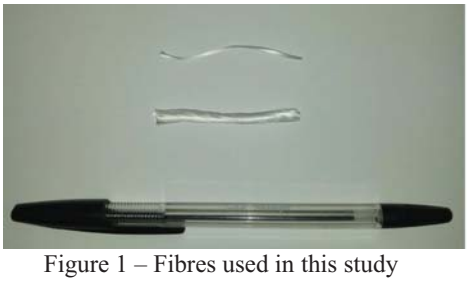

Figure 1 – Fibres used in this study

2.3 Test programme

A total of 156 beams were cast, allowing combinations of different stone size, stone volume, w/c ratio, and type of cement. Six beams were cast per test set to ensure a sufficient sample size for each combination. The control mix design is shown in Table 1 together with the other combinations. The w/c ratio combinations were done for both cement types, but only for the standard stone size, and content. The coarse aggregates volume and size were adjusted together to create all the possible permutations, but this was only done for the reference w/c and cement. These combinations replicate the typical variations found with large scale mixing.

2.4 Test results

The results of all tests are shown in this section. A linear trend line is used to group each set of data points, i.e. f_{R1} to f_{R4}. A positive or negative gradient does not necessarily imply statistical significance. The results of the statistical analyses are presented in Section 3.

Table 1. Mix design parameters. The control (reference) is the combination shown as bold

Mix design parameter	Low	Middle-low	Middle	Middle high	High
Nominal coarse aggregate size (mm)	19		26.5		37.5
Coarse aggregate volume (l/m^3)	350		400		450
W/C ratio	0.4	0.5	0.6	0.7	0.8
Cement type and class	52.5 N CEM II& 42.5 N CEM III				
Water content (l/m^3)	170				
Fine aggregate	Adjusted to complete 1 m^3				
Admixtures (plasticiser)	Dosage adjusted to control workability				

Figure 2 shows the effect of the compressive strength on the f_{R1} to f_{R4} values, for both the cement types. There is a negligible trend of decreasing f_{R2} to f_{R4} values with increasing compressive strength, but f_{R1} shows a slight positive trend.

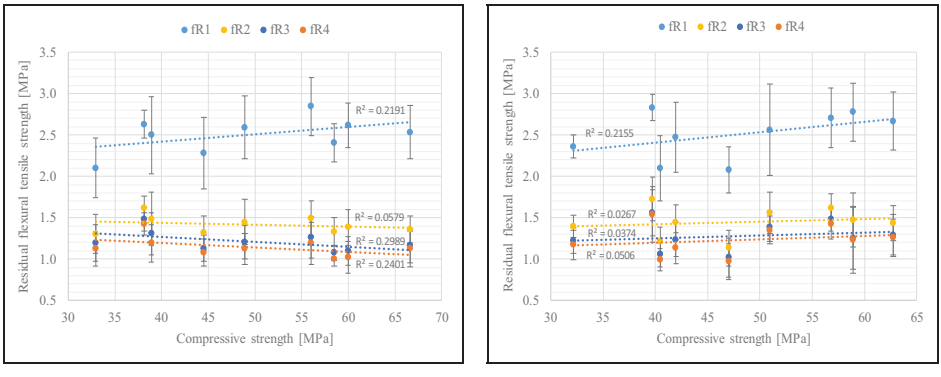

a) 52.5 N CEM II **b) 42.5 N CEM III**

Figure 2.The effect of the compressive strength and type of cement on the fibre performance.

The results of the aggregate variations are shown in Figures 3 and 4. Figure 3 shows that aggregate size does not influence the f_{R2} to f_{R4} values, but a slight decrease in f_{R1} is observed with increasing aggregate size. Figure 4, the results of the volume of the stone for three different nominal stone sizes, show similar trends, with, once again, f_{R1} most affected. In the following sections the statistical significance of these possible correlations are determined.

3 STATISTICAL ANALYSIS OF RESULTS

In this section the large database of test results are used to firstly do statistical significance test in order to determine if any of the independent variables has an effect on the fibre performance. Secondly, characteristic values are determined using different approaches.

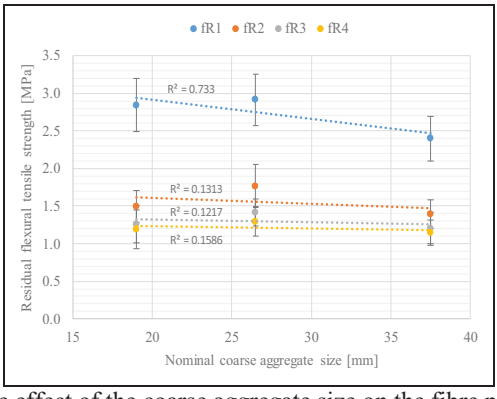

Figure 3.The effect of the coarse aggregate size on the fibre performance.

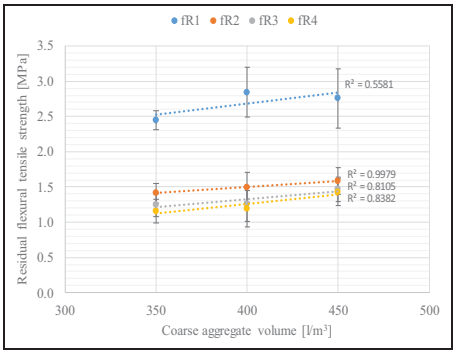

a) 19 mm

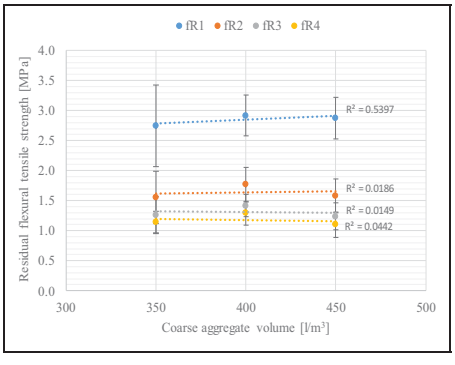

b) 26.5 mm

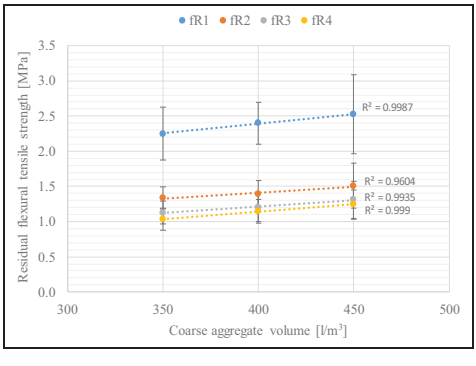

c) 37.5 mm

Figure 4.The effect of the aggregate volume on the fibre performance for different coarse aggregate sizes.

3.1 Significance test using linear regression

The first step of the multiple linear regression analyses is to perform a univariate test of significance for each dependent variable. The univariate test of significance takes account of the effect of all independent variables and identifies the independent variable(s) with the most significant effect. In this case the independent variables are the concrete compressive strength, and the stone volume, and size. Note the w/c ratios and two different cement types were combined into one independent variable, namely the compressive strength. The dependant variables are f_{R1} to f_{R4}.

The multiple linear regression analyses are based on the average values from the sets of six beams each of the observed data. Note that this analyses was performed elsewhere based on the individual 156 test results and the outcome was similar [16].

Table 2 indicates the significance of each independent variable on the dependent variables according to the univariate tests of significance, implementing a significance threshold of p=0.05. From the data presented it can be concluded not one of the independent variables has any significant effect on the fibre performance. The closest dependant variable to having an effect is f_{R3} influenced by the compressive strength with a p value of 0.065. It is important to note that the outcome of the various multiple linear regression analyses is based on a primary interaction between all the independent variables. Secondary affects, i.e. the secondary interactions between independent variables, are excluded from the analyses due to limitations on the number of tests that could be done.

Table 2.The results of the significance analyses on the effect of the independent variables.

Independent variable	*P*-values			
	f_{R1}	f_{R2}	f_{R3}	f_{R4}
Compressive strength	0.164	0.837	0.065	0.164
Nominal coarse aggregate size	0.914	0.743	0.416	0.275
Coarse aggregate volume	0.194	0.405	0.165	0.262

3.2 Characteristic strengths

Based on the significance tests it can be concluded that even large variations on the w/c ratio, aggregate content (therefore also the sand content) and aggregate size has negligible influence on the post-peak resistance of the tested FRC. The water content was never varied, but it is believed the different combinations of w/c ratio and aggregate content simulates the effect of a water content variation. It can therefore be concluded that on-site mixing is not expected to introduce bias (adjusted mean values) or add uncertainty (variability) to the post-peak resistance parameters estimated through laboratory testing.

The specific fibre content and fibre type used in this paper should be considered an example. It is believed that the approach will be valid for any reasonable fibre content and other synthetic macro fibre. As long as the correct amount of fibres are dosed on site (it can easily be checked with the number of empty bags), the mean is expected be the same as found in a laboratory study with a sufficient number beams (at least 6, preferable 12).

The characteristic strength corresponds to a 95% exceedance probability, estimated here by assuming a normal or lognormal distribution respectively. The test results from all 156 beams are used, therefore the student t distribution approaches a normal distribution.

The standard deviation is calculated in two ways. The first way is to use the average and standard deviation of the whole sample, i.e. all 156 beams. The second way is using the means of the sets of six beams as data points. The results of both methods are shown in Table 3 with the standard deviation, CoV (coefficient of variation), and the characteristic strength. The two ways actually presents test results from two sizes of specimens. Using all the data points is of course representing a test crack area of 150 × 125 mm^2 which is a single beam test. On the other hand, the average of a set of six samples represents a crack area six times larger, with a comparatively lower standard deviation, which is expected since some of the geometric variation in fibre distribution is averaged out. It can be seen from Table 4 that the reduced variation leads to characteristic strengths that are between 15% and 20% higher as the reduced uncertainty reduces the required safety margin.

Table 3.The calculated characteristic strengths using two different approaches.

[MPa, except CoV]	f_{R1}	f_{R2}	f_{R3}	f_{R4}
Average of all beams	2.537	1.456	1.258	1.189
Standard deviation of all beams	0.417	0.262	0.240	0.241
CoV	0.164	0.180	0.191	0.202
skewness	0.245	0.476	0.419	0.745
Characteristic strength (f_{Ri} ~ N)	1.851	1.026	0.862	0.793
Characteristic strength (f_{Ri} ~ LN2)	1.937	1.083	0.919	0.853
Average of set of 6 averages	2.537	1.456	1.258	1.189
standard deviation of set of 6 averages	0.243	0.147	0.141	0.149
CoV	0.096	0.101	0.112	0.125
Characteristic strength (f_{Ri} ~ N)	2.137	1.214	1.026	0.944
Characteristic strength (f_{Ri} ~ LN2)	2.166	1.233	1.046	0.968

The analyses were also repeated using a two parameter lognormal distribution (LN2) as its zero value lower bound is appropriate for characterising material strength parameters and the data showed significant skewness. The assumption of a normal distribution (N) is conservative as it leads to lower estimates of the characteristic values. Assuming a normal distribution may however be overly conservative for determining partial resistance factors.

4 FRC DESIGN VALUES

The inherent problem with calculation FRC design values is that it is based on the test result of a very small cross section, most commonly only 150 × 125 mm^2 in size. As the number of fibres crossing this section is on average relatively small, significant scatter is found in the results as the fibre distribution plays a significant role in the result. This would be representative if the real structure also would experience such a high scatter of results, but this is not the case. Using the scatter of the small beam test is in fact conservative as the scatter would not be so great in real structures.

To the authors' knowledge there is only two guidelines published which takes this effect of scatter in FRC into account. They are the German Guideline [6] and the Swedish Codes [5]. In the following section the design values will be calculated using the TR34 [1] and the two mentioned guideline/codes and also a new proposed approach.

4.1 Published guidelines

The basic approach to determine the design values are as follows:

$$\sigma_{r1} = \frac{0.45\, f_{R1k}}{\gamma_m} K \quad (2)$$

$$\sigma_{r4} = \frac{0.37\, f_{R4k}}{\gamma_m} K \quad (3)$$

With σ_{ri} the design values and γ_m the material partial factors, f_{R1k} and f_{R4k} are the characteristic values of f_{R1} and f_{R4}, and K any additional factors used by the different guidelines/standards. The 0.45 and 0.37 is factors to convert the values to design (uni-axial tension) values. This is because the f_{R1k} and f_{R4k} values are derived from using Equation 1 which assumes linear elastic behaviour with the neutral axis in the centre of the test beams. This is not the case, therefore the values are adjusted using an inverse analysis. The reader is referred to the Model Code 2010 [4] and Vanderwalle et al. 2003 [18] for more on this inverse analyses approach.

The first approach shown is TR34 [1], an approach that is specifically published for the use of fibres for floors-on-grade and includes the use of synthetic fibres. None of the other approaches presented here include the use of synthetic fibres, but they are nevertheless used here. The TR 34 [1] specifies a partial material factor of 1.5, the same of concrete in compression. The calculated design values according to TR34 [1] is shown in Table 4. Note that only f_{R1k} and f_{R4k} are shown as they are used in floor-on-grade design according to TR34 [1]. This approach was done for both the characteristic value based on all the results and also based on the mean of sets of six beams.

Table 4. The calculated design values using the different approaches [1,5-6]

	Characteristic Values				Design values	
	f_{R1k} [MPa]	f_{R4k} [MPa]	Additional Factor K	Resistance Partial Factor γ_m	σ_{R1} [MPa]	σ_{R4} [MPa]
TR34	1.851	0.793	1	1.5	0.555	0.196
TR34 using cov from sets of 6 beams averages	2.137	0.944	1	1.5	0.641	0.233
Swedish Code	1.851	0.793	2	1.5	1.111	0.391
German Guidelines	1.294	0.606	1.7	1.25	0.704	0.305
Proposed Approach: Using cov from sets of 6 beams averages and assuming f_{Ri}~LN2	2.166	0.968	1	1.20	0.812	0.301

The Swedish Code [5] for FRC used an approach by increasing the design value by a factor based on the level of in determination of a structure. The higher the level, the more the design value will be increased. This method is further explained in [9]. For floors-on-grade they derived a value of η_{det} of 2. This value is just multiplied to the design values shown in Equations 2 and 3, i.e the factor K. They also have a factor for fibre orientation, but for "horizontally cast members (width > 5 x thickness)", this factor is 1. The rest of the calculation is the same as Equations 2 and 3. The partial material factor is specified as 1.5. The design values using this approach are shown in Table 4.

The approach by die German Guideline [6] is more complex, but the link to reliability based design is clear. There are however a few significant differences. Their prescribed test methods has a cross section of 150 × 150 mm^2 compared to 150 ×125 mm^2 of EN 14651 [15], so inherently they will have less scatter in their test results. This means applying this method to the test results presented here will be conservative. Also, the characteristic value is limited to no more than 51% of the mean value. This is based on the assumption that the scatter in a set of tests should never be less than a CoV of 0.25. Therefor the shown characteristic values in Table 4 for this approach is less than the rest of the approaches. The calculation of σ_{r1} uses a factor of 0.40 instead of the 0.45 of Equation 2 which makes it even more conservative.

This approach also adds two factors to the calculation of the design value, one for the fibre orientation and one for the actual cracked section area in the structure. The factor for taking the actual crack section area into account, κ^f_G, is

$$\kappa^f_G = 1.0 + 0.5\, A^f_{ct} \quad \leq 1.7 \qquad (4)$$

With A^f_{ct} the real crack cross section in m^2. This is a good approach, but not so easy to apply for a floor-on-grade calculation using a yield-line approach. There are many different yield lines that can occur for different types of loading expected on one floor, and the number of, for example, positive radial yield lines forming under a point load is also not clear. For the purpose of this paper the maximum allowable κ^f_G value of 1.7 is used. This corresponds to a crack area of 1.4 m^2, equating to a total yield crack length of 7 m in a 200 mm thick slab.

The last approach presented here is the TR34 approach using the sets of six beams as data points. The lower CoVwill result in a smaller partial resistance factor, $\gamma_{m,}$, which may be determined using reliability principles and assuming a lognormal distribution as:

$$\gamma_m = \frac{f_k}{f_d} = \frac{\mu e^{(u_{0.05} w)}}{\mu e^{(\alpha \beta_t w)}} = e^{(\alpha\beta + u_{0.05})w}$$

with γ_{ct} the partial resistance factor for post-peak resistance, f_k and f_d the characteristic and -design strengths respectively, $u_{0.05} = -1.645$, $\alpha = 0.8$ for resistance, $\beta_t = 3.8$ for typical ULS design. The equation is accurate for coefficients of variation, $w < 0.2$. The estimated partial factors are $\gamma_{ct} = 1.15$ for $w = 0.1$ and $\gamma_{ct} = 1.32$for $w = 0.2$.

5 CONCLUSIONS

This paper presents published and a new proposed approach to determine the fibre reinforced concrete design values to be used for floors-on-grade. There are still a number of shortfalls in this study; however, the following conclusions can be made:

A statistical analyses on a large set (156) EN 14651 [15] beam tests with a single type of macro synthetic fibre concluded that the following variables do not have a significant effect on the fibre performance

- The water / cement ratio
- The type of cement
- The volume of coarse aggregates
- The size of the coarse aggregates

FRC design values were calculated using five methods and the results, in order starting with the most conservative, are as follows:

- The TR34 approach using each individual beam test results
- The TR34 approach where sets of six beams were seen as a single data point
- The German guideline

- The method proposed in this paper
- The Swedish Standards approach which is the least conservative

This work shows the discrepancies in current methods used and shows that this requires further attention.

6 REFERENCES

[1] TR34: Concrete Society, Technical Report 34, Concrete Industrial Ground Floors, 4th ed., Surrey, United Kingdom, 2013.

[2] EFNARC, European specifications for sprayed concrete, guidelines for specifiers and contractors, Surrey, United Kingdom, 1999.

[3] G. Vitt, Steel fibre concrete industrial floors, Bochum, Germany, 2003.

[4] CEB FIP, Model Code 2010 Parts 1 & 2, Lausanne, Switzerland, 2012.

[5] Swedish Standard 812310, Fibre concrete – Design of fibre concrete structures, Stockholm, Sweden, 2014.

[6] German Committee for Structural Concrete, Commentary on the DAfStb Guideline "Steel Fibre reinforced concrete", Germany, 2015.

[7] AJ Babafemi, WP Boshoff, Testing and modelling the creep of cracked macro-synthetic fibre reinforced concrete (MSFRC) under flexural loading, Material and Structures, Vol 49, pp 4389-4400, 2016.

[8] B. Parmentier, E. De Grove, L. Vandewalle, F. Van Rickstal, Dispersion of the mechanical properties of FRC investigated by different bending tests, Tailor Made Concrete Structures, London, Taylor & Francis Group, 2008.

[9] J.. Silfwer Brand, How to deal with scatter in steel fibre concrete structures, a Swedish Proposal, Cape Town, South Africa, 2016.

[10] J.C. of S. Safety, JCSS Probabilistic Model Code, (2001).

[11] M. Holicky, J.. Retief, M. Sykora, Assessment of model uncertainties for structural resistance, Probabilistic Eng. Mech. 45, 188 – 197, 2016.

[12] R. Rackwitz, Optimization — the basis of code-making and reliability verification, Struct. Saf. 22, 27–60, 2000.

[13] EN 1990, Basis of structural design, 2002.

[14] M. Holicky, Reliability analysis for structural design, 2009.

[15] 2012 EN 14651, Test method for testing metallic fibre concrete – measuring the flexural tensile strength (limit of proportionality, residual strength, United Kingdom, 2012.

[16] H.. Bester, Generic Model for Predicting the Performance of Macro-Synthetic Fibre Reinforced Concrete for Industrial Flooring Applications, Stellenbosch University, South Africa, 2017.

[17] SANS 1083:2006, Aggregates from natural sources : aggregates for concrete, 2.1., Pretoria: Standards South Africa, n.d, 2006.

[18] Vanderwalle L, σ-ε Design Method, final recommendation, Mater. Struct. 36, 560–567, 2003.

Research on the Chloride-free and Alkali-free Liquid Set Accelerator for Sprayed Concrete

Ling WANG(1), Jiezhong GAN(2), Xia ZHAO(1), Ping ZHANG(1), Yading Xu(1)

(1) State Key Laboratory of Green Building Materials, China Building Materials Academy, China

(2) Jiangsu China Railway ARIT New Materials Co., LTD, China

ABSTRACT

Sprayed concrete is used for the construction of tunnel and mine. The recent trend in accelerator development is the chloride-free and alkali-free liquid accelerator in response to the demand for durable, high-quality sprayed concrete that minimizes environmental risk. A kind of liquid accelerator characterized of environmental friendly, chloride-free and alkali-free (named ASA) is developed through orthogonal experiments. Relevant properties and action mechanism of the accelerator were studied. When the dosage of ASA accelerator is 7%, the initial and final setting time of cement paste were decreased to 2min40s and 4min40s respectively. The 1d compressive strength and 28d compressive strength of concrete with ASA increased by 43.5% and 10.2% respectively. XRD, ESEM and MIP were used to analysis the hydration products and microstructure of hardened cement paste with ASA. It shows that the fast setting and high early compressive strength of cement paste with ASA are due to Al^{3+} and SO_4^{2-} in ASA reacted with dissolved Ca^{2+} in the liquid phase instantly forming a large amount of ettringites. The consumption of Ca^{2+} in liquid phase promoted the hydration of C_3S, the generated C-S-H gel filled in the pore, making the microstructure denser and increasing the 28d compressive strength.

Keywords: Alkali-free set accelerator; setting time; compressive strength; sprayed concrete

1 INTRODUCTION

Constructions of railway and highway in mid-west and southwest of China have been in a rapid development in recent years. By 2020, it is expected that about 8000 railway tunnels and more than 155 kilometer of highway tunnels will be constructed. Shotcrete technology is widely used in tunnel support system construction.

The 'dry process' technique for shotcrete was used in early days. A dry mix of sand, cement and powder set accelerator is placed into the pressurized chamber. The mix is then conducted from the chamber to a nozzle where water is added. Then admixed materials set in a very short period as strengthening of tunnels [1]. Problems of dry process technique were found in site, such as large rebound, unhealthy environment condition for workers in the confined space of a tunnel, unstable W/C ratio and poor quality of shotcrete [2]. Meanwhile, in the 'wet process' technique, sand and cement have to be fully mixed with water before being pumped through a machine, which is able to apply wet-mix spray concrete robotically in tunnelling projects. The mix is pumped to nozzle by compressed air; the liquid set accelerator is admixed in nozzle and sprayed onto work surface. The 'wet process' makes

shotcrete high efficiency, low rebound, much safer and healthier working environment. So far, the 'wet process' is accepted and used worldwide [3]. As the raising of awareness of environmental protection in China, the wet-mix sprayed concrete will replace the dry-mix sprayed concrete and leads the trend of shotcrete.

As the essential raw material of wet-mix sprayed concrete, there will be huge demand for liquid set accelerator in China. The main constituent of the earliest liquid set accelerator is sodium aluminate or potassium aluminate. Its alkali content is higher than 10%, so it is also called high alkali set accelerator. The 28d compressive strength retention of the concrete with the high alkali set accelerator is smaller than 80% of the plain concrete [4-5]. In order to reduce the later strength loss, sulfate and silicate are used to modify the previous sodium aluminate or potassium aluminate [6-8]. Then liquid set accelerator with medium alkali content of 4% and 28d compressive strength ratio of 90% was developed [9].

Aluminum sulfate [10-11], amorphous $Al(OH)_3$ [12-13] and magnesium fluoride are utilized to replace alkali metal salt [14] to produce liquid alkali-free set accelerator (L-AFA) with alkali content lower than 1%. L-AFA solves the AAR problems caused by high alkali content. The 28d compressive strength ratio of concrete with L-AFA improves a lot. So using L-AFA to replace traditional alkali set accelerator is a general trend in China now.

There are some issues that need to be solved on the L-AFA, (1) Stability: Aluminate salt is the main constitute of liquid alkali-free set accelerator. It has a low solubility and is reactive to a hydrolysis-aggregation-precipitation reaction. So L-AFA is unstable and easy to flocculate, precipitate and crystalize with the extension of storage time. Stable period of liquid alkali-free set accelerator is usually less than 3 months [15-16]. Trying to inhibit the crystallization and hydrolysis of highly saturated aluminum solution in the L-AFA is one important task. (2) Lower 28d compressive strength ratio: Compared to high alkali and medium alkali set accelerator, later compressive strength of concrete with L-AFA increases to some extent. But the 28d compressive strength ratio is still lower, which is around 80% ~ 90% of the plain concrete [17-18].Trying to increase the 28d compressive strength ratio is another important task. (3) Safety of raw materials: Fluorine ion promotes formation of hydrates, reduce final setting time, increase strength and increase stability of aluminum ion in aqueous solution by forming stable complex compound with aluminum sulfate. Hydrofluoric acid [19], sodium fluoride [20], aluminum fluoride [14] and magnesium fluoride [21] were often used as raw materials of liquid alkali-free set accelerator. For field workers, excess fluorine storage in body is a great threat to their health. Excess fluorine storage in human body may cause fluorosis. Slight fluorine poisoning causes dental fluorosis, severe fluorine poisoning cause skeletal fluorosis which leads to a complete loss of harbor ability and self-care ability. Trying to use non-fluorine raw material to prepare the L-AFA is the third important task.

Aiming to three tasks above, a new kind of alkali-free set accelerator (named ASA) was prepared and the action mechanism of ASA was studied.

2 MATERIALS

2.1 Materials for liquid alkali-free accelerator preparation

All materials for the preparation of L-AFA are commercial chemical reagent: polyaluminium sulfate, magnesium sulfate, alkanolamine, inorganic acid and stabilizer.

2.2 Materials for test the setting time and compressive strength

P.I 42.5 cement and ISO Standard sand are used to test the properties of L-AFA. Chemical composition and physical properties of the cement are list in Tab. 1 and Tab. 2.

Table 1: Chemical composition of the cement

SiO_2 /%	Al_2O_3 /%	Fe_2O_3 /%	CaO /%	MgO /%	SO_3 /%	f-CaO /%
21.18	4.73	3.41	62.49	2.53	2.83	0.72

Table 2: Physical properties of reference cement

Residue (80μm) /%	Density /g·cm^{-3}	Blain fineness /m^2·kg^{-1}	Setting time /min		Strength/MPa			
					Flexural		Compressive	
			initial	final	3d	28d	3d	28d
0.3	3.14	350	172	222	5.6	8.7	28.3	51.6

3 TEST METHOD

3.1 Setting time of the cement paste

Mixed 400 g cement with 160 g water (including water in L-AFA) in the agitating pan first, added the L-AFA into it at a recommended dosage, and then quickly stirred the paste for 30 s. Then transferred the paste into Vicat moulds, slightly vibrated several times. Removed the excess paste by gently sawing motion until the upper surface smooth. Determined setting times according to ISO 9597.

Setting time recording was started as soon as L-AFA was added. Every sample was tested twice and the mean value of the two tests was the result. For cement paste with L-AFA, the initial setting time ≤ 3 min and the final setting time ≤ 8 min are the objectives in this research.

3.2 Compressive strength of cement mortar

Added 450 g water (including water in L-AFA) into 900 g cement and mixed first, then added 1350 g ISO Standard sand and mixed till enough distribution. After that added L-AFA into the panat a recommended dosage and quickly stirred it for 40 s~50 s. Casted the mortar into moulds (40 mm × 40 mm × 160 mm) and vibrated for 30 s, removed the excess mortar and smooth the upper surface of mortar.

Control samples (without L-AFA) and test samples (with L-AFA) were prepared at the same time. All samples were cured at standard condition. 1d and 28d compressive strength were determined. 28d compressive strength ratio (ratio of the 28d compressive strength of the test samples to that of the control samples) was calculated. For the test samples, 1d compressive strength ≥7.0 MPa and 28d compressive strength ratio ≥ 100 % are the objectives in this research.

3.3 Stability of liquid set accelerator

Put L-AFA into transparent and clean plastic bottles, sealed and stored at (20±2) ℃. Observed the appearance of the stratification, precipitation or crystallization, recorded the appearance time. 6 months is the objective stability period in this research.

3.4 Microstructure analysis

W/C of the specimen for microstructure analysis is 0.4. Mixed the cement and water evenly, then added L-AFA at the dosage of 7%. Stirred the cement paste for 30 s, and then put the cement paste into a mould with the dimension 30 mm × 30 mm × 30 mm. Cured the specimen at standard condition till the given age 10 min, 1h,1d and 28d. Then broke the specimens into powder or small particles with the size of 2 mm～5 mm for XRD, ESEM and MIP analysis.

4 TEST RESULTS AND ANALYSIS

4.1 Preparation of the new kind of liquid set accelerator

The raw materials for the L-AFA developed in this paper include polyaluminium sulfate (A), magnesium sulfate (B), alkanolamine (C), inorganic acid (D) and stabilizer (E). The influences of each single raw material on the set accelerating are shown in Fig.1.

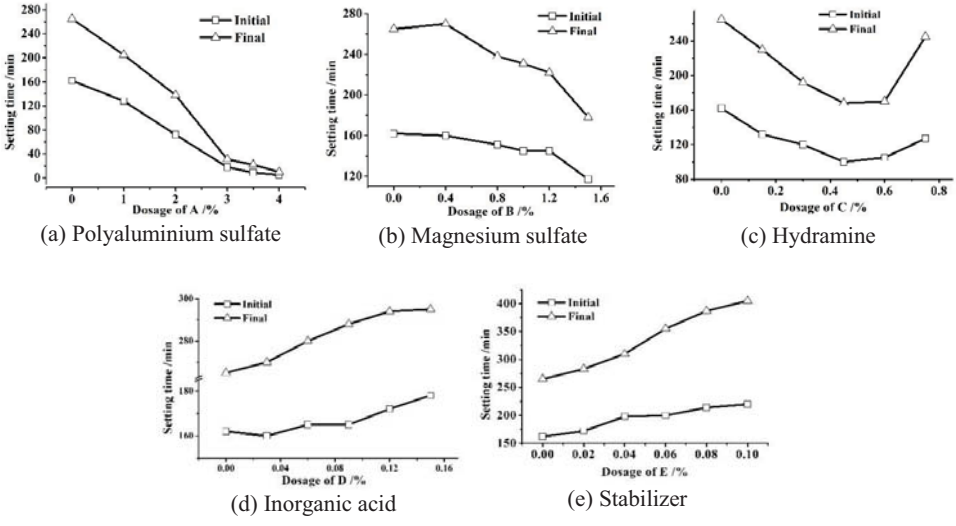

(a) Polyaluminium sulfate (b) Magnesium sulfate (c) Hydramine

(d) Inorganic acid (e) Stabilizer

Fig.1 Influence of each single raw materials on the setting time of cement

The process chart of the L-AFA using the above five kinds of raw materials in this research is shown in Fig.2.

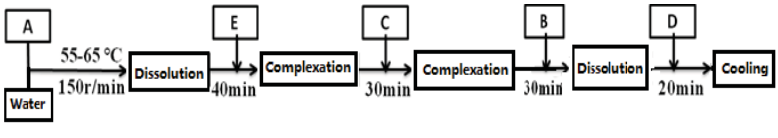

Fig.2 Preparation process flow of the L-AFA

The initial setting time and final setting time were used as assessment indexes in orthogonal experiment. Considering the properties of set accelerator, stability and cost, the best mass ratio is determined as polyaluminium sulfate: magnesium sulfate: hydramine: inorganic acid: stabilizer: water = 48: 14: 10: 1.5: 1.0: 25.5. The L-AFA is named ASA due

to the main constitutes -- Aluminum Sulfate. The characters of the ASA is listed in Tab. 3. Its color is light green to brown yellow.

Table 3: Properties of ASA liquid alkali-free accelerator

Alkali content /%	Chloride ion /%	Density /g·m^{-3}	Solid content /%	pH
0.037	0.014	1.41	51%	3.0

4.2 Influence of ASA dosage on setting time and the compressive strength

The influence of ASA dosage on the properties of ASA is shown in Fig.3.

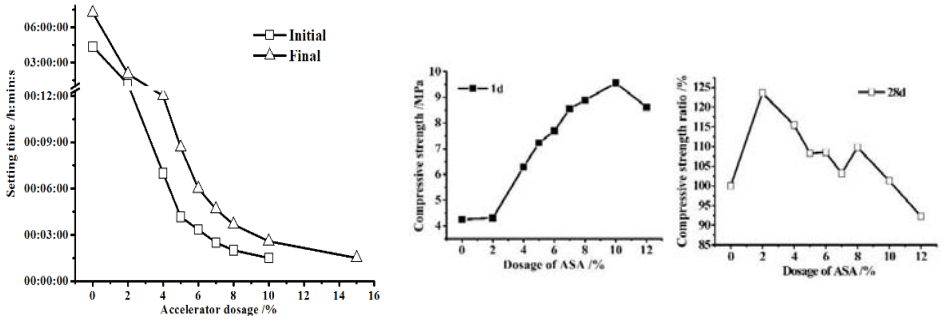

(a) the setting time (b) 1d compressive strength (c) 28d compressive strength ratio

Fig.3 The effect of ASA dosage on of cement paste

From Fig.3, it can be seen the setting time shortens with the increase of ASA dosage, while the 1d compressive strength increases with the increase of ASA dosage until it reaches 10%, then decreases a lot when the dosage exceeds 10%. The 1d compressive strength is larger than 6 MPa when the dosage of ASA is more than 4%. The 28d compressive strength ratio is bigger than 100% which the dosage is between 2% ~ 10%. This gives important information that ASA can enhance the later compressive strength in a wide dosage range.

When the dosage of ASA is 5%, the initial and final setting time of cement paste are 4 min 10 s and 8 min 40 s respectively, while the 1d compressive strength and 28d compressive strength ratio of mortar are 7.23 MPa and 108.3%. While the dosage of ASA is 7%, the initial and final setting time of cement paste decrease to 2 min 40 s and 4 min 40 s respectively. The 1d compressive strength of mortar is 8.56 MPa, increasing by 99% compared with control sample, and the 28d compressive strength ratio of mortar is 103% at this time.

So it can be clearly found all properties meet the research targets scheduled, and the recommended dosage of ASA is 5% ~ 7%.

Usually, cement paste or mortar dosed with accelerator sets very fast, pores are unable to be filled, a porous micro-structure generates as a result and it leads to a low early age compressive strength. In order to understand the action mechanism of ASA, several analysis such as XRD, EMSA and MIP are carried out to study the microstructure of cement paste samples dosed with ASA.

XRD analysis of test samples (AF) and control samples (Ref) at the same age are compared in figure 4 and figure 5. Microstructure of sample AF and Ref at different ages are observed using ESEM, results are showed in figure 6.

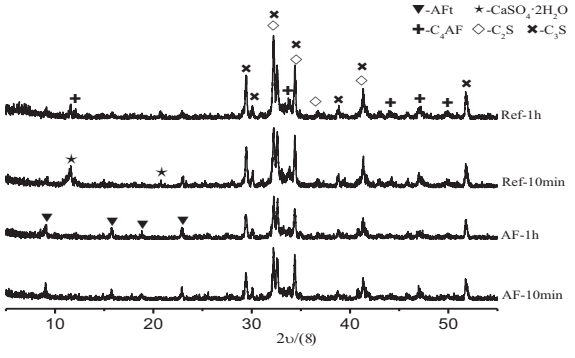

Fig. 4 XRD pattern of samples at 10mins and 1h

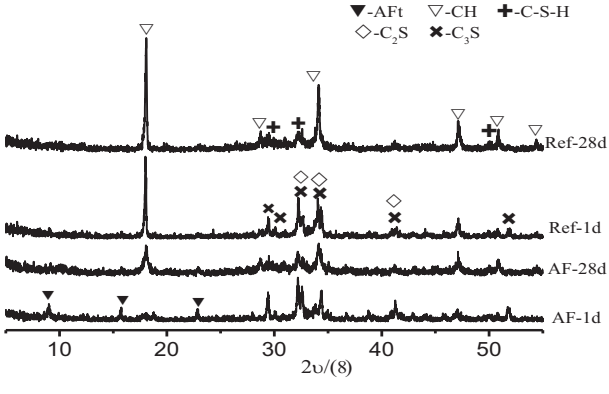

Fig. 5 XRD pattern of samples at 1d and 28d

In the control sample Ref, there are no ettringite and CH after 10 min and 1h of hydration. The hydration products are mainly C-S-H gel (the C-S-H gel could be associated with the tobermorite), CH and a few ettringite after 28d of hydration (see Fig. 4 ~ 5). On the contrary, many rod-like ettringites are found in the test sample AF only after 10 min of hydration which formed on the surface of cement particles and liquid phase. After 1h of hydration, the AFt grow rapidly and overlapp, gel C-S-H cover on the ettringites and fill the pores, there is no CH. After 1d of hydration, a great deal of AFt form, less CH form compared to the control sample. After 28d of hydration, needle-like and rod-like ettringite overlap and insert into C-S-H, forming a dense matrix (see Fig. 4 ~ 6).

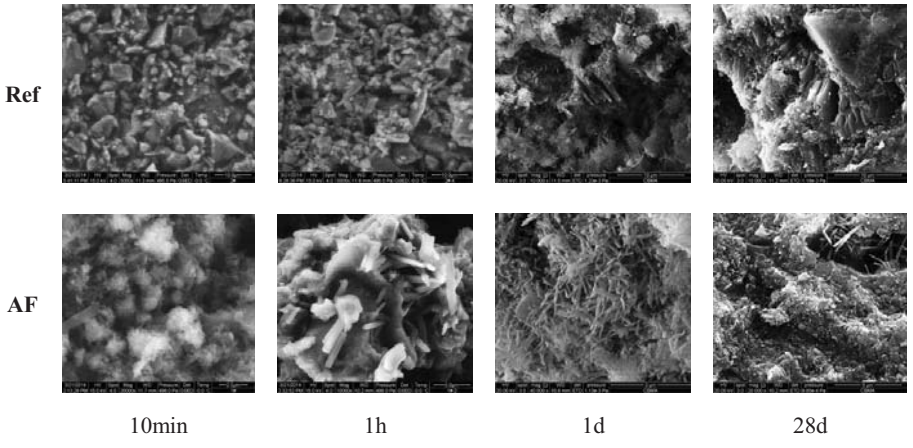

Fig.6 The ESEM pictures of samples at different hydration time

In order to promote strength development of cement paste, multicomponents are designed for ASA in this research. Polyaluminium sulfate as raw material provides massive Al3+ and SO42- which hydrate rapidly with Ca^{2+} in C_3A and liquid phase, forming a large amount of ettringite. C-S-H formed by C_3S hydration covers on the ettringite and promotes paste setting, and thus increases 1d strength. Magnesium sulfate as raw material introduces in the Mg^{2+}.Solubility of $Mg(OH)_2$ is 6 order of magnitude smaller than that of $Ca(OH)_2$, Mg^{2+} bonds prior with OH-, forming $Mg(OH)_2$ as crystal nucleus, promoting generating of C-S-H hydrated from C_3S thus filling voids and increasing strength. Alkanolamineas raw material is miscible with water. Complexation of alkanolamine with ions such as $Al^{3+}$and Fe^{3+} forms many soluble domains during the hydration process, increasing diffusing of hydration products, promoting the hydration and increasing the early strength.

Comparison of pore structure of hardened cement paste between the test sample AF and the control sample Ref at the age of 1d and 28d are showed in Table 4.

Table 4: Pore structure of hardened cement paste

No.	Total porosity /%	<10nm	10～50nm	50～100nm	>100nm
Ref-1d	45.08	8.62	16.63	20.06	54.69
AF-1d	37.68	9.5	21.45	18.77	50.28
Ref-28d	22.60	31.10	50.65	11.35	6.90
AF-28d	22.29	19.70	65.25	8.21	6.84

After 1d of hydration, total porosity of AF is 37.68% which is 7.4% smaller than Ref, pores diameters bigger than 100nm in AF is 50.28% which is 4.41% smaller than that in Ref. After 28d of hydration, total porosity and pores with diameters bigger than 100 nm of hardened sample AF and Ref are almost the same. But in AF, there are more capillary pores and obviously less gel pores smaller than 10 nm. This is the reason why 28d compressive strength of AF mortar is higher than tant of the control sample.

4.3 Stability of the ASA liquid set accelerator

Stability comparison experiments between ASA and an international brand liquid alkali-free accelerator S-5 (41% solid content) are carried out. The two set accelerators are stored at (20±2)℃for 180d. Naked eye observations on the stratification and crystallization in the liquid accelerator at different storage time have been done (see Fig. 7).

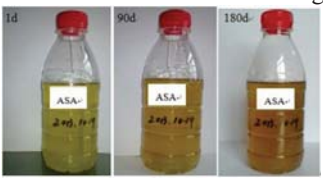

4.3.1.1.1.1.1.1.1 (a) ASA

4.3.1.1.1.1.1.1.2 (b) S-5

Fig. 7 The stability test of two kinds of liquid set accelerator

The liquid set accelerator ASA is homogeneous and transparent liquid. After 6 months of storage, it is still homogeneous and transparent; there is no precipitation, crystallization and stratification except for a slight color change. The reason of color change is that Fe2+ introduced by raw materials oxidized to Fe^{3+} by O^2 in the bottle, causing the color changes from light green to light brown. The liquid set accelerator S-5 obviously stratifies after 30d, flocculation occurs and flowability gets worse after 60d. The stability of ASA is much better than that of S-5.

Liquid set accelerator whose mainly components is aluminum sulfate is a colloidal system. The stability of the liquid accelerator is determined by stability of this colloidal system which means the ability of particles of keeping dispersed suspension state in a period. Many factors influence stability of the colloidal system such as Brownian movement, electrostatic repulsion, hydration of particle surface, steric hindrance between colloids. As storage time extends, colloidal particles aggregate and adhere on each other, causing the increasing of particle size and then the coagulation occurs which leads to a stratification of supernatant and sediment.

Crystallization of highly saturated aluminum sulfate is the reason of instability. Aluminum ions are easy to hydrolyze-polymerize-precipitate in aqueous solution, transforming the solution to irreversible gel. The key to improve the stability of ASA is inhibiting crystallization and hydrolysis of highly saturated aluminum solution. Stabilizers such as inorganic salt, organic surface active agent, organic carboxylic acid have been used to try to solve this problem abroad and domestic. These stabilizers can neither reduce Al3+ concentration in solution effectively nor inhibit hydrolysis of Al^{3+}, so none of them is satisfactory.

Based on the analysis of stability mechanism, the following three measures are taken trying to solve the poor stability of liquid set accelerator effectively in the preparation of ASA.

First, using polyaluminium sulfate as one kind of raw material. Its molecule formula is [Al2(OH)n(SO4)3-n/2]m(m≤10, 1≤n≤5), and its most arresting feature is high Al_2O_3 / SO_3 ratio. Domestic enterprises often use industrial aluminum sulfate as raw material in preparation process of L-AFA. Al_2O_3 content of industrial aluminum sulfate is usually 14%~15%, more aluminum sulfate has to be used in order to get an acceptable accelerating efficiency, forming a highly saturated aluminum solution which is extremely unstable. Al_2O_3 content in polyaluminium sulfate used in this research is higher than 18%. Ionization of polyaluminum sulfate in aqueous solution generates more Al^{3+} and less SO_4^{2-}, which means

less polyaluminium sulfate is needed to get an acceptable accelerating efficiency. Less polyaluminum sulfate means the solution saturation level decreases and the stable period of accelerator effectively increases.

Second, powdery organic carboxylic acid is used as the stabilizer. It is soluble in water and can react with Al^{3+} forming a soluble complex ion. Molecule of the stabilizer contains coo^{2-} in which O as coordination atom provides electrons and coordinates with Al^{3+}, forming stable complex, effectively decreasing free Al^{3+} concentration, increasing the stability of ASA.

Third, inorganic acid in the raw materials is used to adjust pH of ASA, which inhibits the hydrolysis of Al^{3+}, increasing the stability of ASA.

Experiments above show that these measures are very effective, the stability period of ASA is longer than 6 months, while precipitation and crystallization occurs in the comparison sample in some extend after 1~2 months.

5 CONCLUSIONS

- A liquid set accelerator (ASA)is developed which accelerates setting of cement and increases compressive strength of hardened paste. ASA is safe to human body and harmless to concrete durability due to alkali metal ion free, chloride ion free and fluoride ion free.
- The stability period of ASA are increased to more than 6 month by using polyaluminium sulfate which has a high Al_2O_3 / SO_3 ratio as raw material, using powdery organic carboxylic acid as stabilizer, and using inorganic acid to adjust pH value. These measures inhibit the hydrolysis of Al^{3+}effectively.
- Test results of XRD, ESEM and MIP show that Al^{3+} and SO_4^{2-} provided by ASA react with dissolved Ca^{2+} in the liquid phase instantly forming a large amount of ettringites, those ettringites netted to each other leading fast setting of cement paste. The precipitated ettringites in the liquid phase didn't cover the surface of C_3A wholly, resulting in the continued hydration of C_3A. The consumption of Ca^{2+} in liquid phase promoted the hydration of C_3S, the generated C-S-H gel filled in the pore, making the microstructure denser and increasing the early and later compressive strength of hardened paste.

6 ACKNOWLEDGEMENTS

The financial support from National Key Science and Development Project of China (YS2017YFGX010029) is gratefully acknowledged.

7 REFERENCES

[1] W. Hochmuth, A. Krischke, J. Weber. Subway construction in Munich, developments in tunneling with shotcrete support [J]. Rock Mechanics and Rock Engineering, 1987 (20):1-38.
[2] K. Kalmana. History of the sprayed concrete lining method, part I: milestones up to the 1960s[J]. Tunnelling and Underground Space Technology, 2003, 18(1):57-69.
[3] K. Ono. Health and safety in shotcrete: ITA Working Group on shotcrete use in tunnelling [J].Tunnelling and Underground Space Technology, 1996,11 (4) :391-409.
[4] R.C. Snyder, P. F. Snyder. Liquid concrete accelerator mixtures and methods for use thereof: US, 4046584[P]. 1977-9-6.
[5] K. Allemann, K. Deneke, H. Hass. Liquid accelerator for the setting of concrete mixture: US, 4504315[P]. 1985-3-12.
[6] T. Hidenhiro, T. Tamaki, W. Toshiyuki. Liquid set-accelerator agent and raid-setting cement concrete and its manufacture: JP, 2002047048 A2 [P]. 2002-2-12.

[7] C. Schutz, J. Raymond. Rapid set accelerator for cementitious compositions: US, 317008[P]. 1983-11-9.
[8] O. Helmboldt, I. Potenvsil, J. Breker, et al. Use of basic aluminium sulphates as set accelerators for cement: US, 5660625A[P]. 1997-8-26.
[9] LianQin,Xiong Zhang,Yongjuan Zhang.Environment friendly liquid alkali free set accelerator for shotcrete and preparation method:China,01423356[P].2009-5-6. (in Chinese)
[10] T. Mlye. Sprayed concrete for rock support [M]. 9th ed. Switzerland: MBT international underground construction group, 2001:55.
[11] J. Höfler, J. Schlumpf. Shotcrete in tunnel construction [M]. 3rd ed. Zürich: Putzmeister AG, 2004:21-23.
[12] H. Thomas. Preparation of Concrete Accelerator: US, 2002195026A1 [P]. 2002-12-26.
[13] E. Kolomiets, M. Alfonso, W. Albis, et al. Accelerator Mixture and Method of Use: US, 20120085266A1[P]. 2012-4-12.
[14] Zhimin Zhang, WeilongJia, JunpingLi,etc.Set accelerator for concrete and its preparation method:China,102424541A[P].2012-04-25. (in Chinese)
[15] E. Kolomiets, M. Alfonso, W. Albis, et al. Accelerator Mixture and Method of Use: US, 20120085266A1 [P]. 2012-4-12.
[16] A. Terje. Set accelerator For Sprayed Concrete: US, 8118930 B2 [P]. 2010-02-21.
[17] YonghuiGao. Alkali free and chlorine free of liquid set accelerator: China, 102745937A [P].2012-10-24.(in Chinese)
[18] Changwen Miao, Jiangang Zhang, Qianping Ran,etc. Alkali free liquid set accelerator: China, 101648785A [P].2010-02-17. (in Chinese)
[19] M. Sommer, F. Wombacher, T. A. Burge. Sulfate-free and alkali-free setting and hardening accelerator: US, 6540826B2 [P]. 2003-4-1.
[20] Kemin Liang.A liquid alkali free set accelerator for shotcrete:China, 102079642 A[P].2011-06-01.
[21] T. Hidenhiro, T. Tamaki. Liquid set-accelerator agent and rapid-setting cement concrete and its manufacture: JP, 2002047048 A2 [P]. 2002-2-12.

Enhancement of Mechanical Properties and Corrosion Behaviour of Concrete due to Addition of Ultrafine GGBS

M. Pradeep Kumar[(1)], Murali Rangarajan [(2,3)] and K. M. Mini[(1)]

[(1)]Department of Civil Engineering, Amrita School of Engineering, Amrita University, Coimbatore, India

[(2)]Center of Excellence in Advanced Materials and Green Technologies, Amrita School of Engineering, Amrita University, Coimbatore, India

[(3)]Department of Chemical Engineering and Materials Science, Amrita School of Engineering, Amrita University, Coimbatore, India

ABSTRACT

The effects of introducing ultrafine ground granulated blast furnace slag (GGBS) on the mechanical properties and the corrosion prevention properties of concrete are examined in this preliminary study. Introducing ultrafine GGBS reduces the workability of concrete, increases the compression strength, and surface bond stress. The ability of ultrafine GGBS to reduce corrosion of the steel rebar in concrete was studied using measurements of half-cell potential, open circuit potential, linear polarization resistance, and Tafel polarization in an accelerated environment 3.5% NaCl and 1 M H_2SO_4. For 10% addition of ultrafine GGBS, both the half cell and open circuit potentials shifted by about −20 mV, indicating enhanced cathodic protection of the steel rebar. The linear polarization resistance increased by about 50% from 50 KΩ to 100 KΩ by the addition of 10% ultrafine GGBS, while the corrosion current in Tafel polarization measurements reduced by 42%.

1 INTRODUCTION

Developing and introducing environmentally friendly materials that enhance the properties and performance of reinforced concrete structures is an area of research that has attracted significant interest. Of specific interest are the improvements in mechanical properties and enhanced resistance to the rebar corrosion. In highly alkaline pH environments such as concrete, iron surface is typically in a passivated oxide state, which provides a natural protection for corrosion, in addition to the resistance arising from the solid structure that resists diffusion of corroding species. However, due to either carbonation or chloride penetration, local corrosion phenomena initiate on the steel surface, leading to significant debonding, loss of strength and potential structural failure [1]. This preliminary work studies the effect of the mineral admixture ultrafine GGBS on the mechanical properties and corrosion behaviour of reinforced concrete.

Sharmila and Dhinakaran have studied the compressive strength of readymade GGBS on compressive strength, porosity and sorptivity of high strength concrete [2, 3]. They have found that the slag fills micro-voids, and observed that ground slag performed better than the readymade commercially available slag. Increasing the quantity of the slag resulted in aggregation of particles, densified the microstructure and reduced the mechanical strength. Teng et al., have suggested that increased surface area enhanced the rates of hydration and

pozzolanic reactions, resulting in lower permeability and better durability [4]. Introducing nanosilica of various particle sizes ranging from 12 to 40 nm enhances the compressive strength of cement mortar, though larger nano particles show better improvement, possibly because of lesser agglomeration effects and better dispersion. These studies indicate significant promise in the use of ultrafine mineral additives to cement for enhancing its material properties. However, no studies have so far examined the effects of GGBS on the corrosion behaviour of the reinforced concrete.

Montemor et al., have studied the effects of fly ash on the corrosion of reinforced concrete in sodium chloride solution using electrochemical impedance spectroscopy, and have observed that resistivity of concrete increased with addition of fly ash, resulting in delay of corrosion initiation as well as a decrease in the rate of corrosion [5]. The effect of introducing zeolite and diatomite on corrosion of reinforcement steel in 1M HCl has been studied by Gerengi et al., using electrochemical impedance spectroscopy [6]. They observe that the resistance to corrosion offered by concrete matrix is higher for zeolite than for diatomite, though this resistance increases with time for both the samples. Thus, continuous protection of the concrete is enabled even after six months.

In this work, the corrosion properties of Alccofine-1203, a commercially available ultrafine GGBS material, when used as a partial replacement to ordinary Portland cement is reported. After examining the mechanical properties of the resultant modified concrete, corrosion behaviour is studied using open-circuit potential measurements, half-cell potential measurements, linear polarization resistance measurements, and Tafel polarization studies. These studies are carried out in an accelerated corrosion environment containing 3.5 wt% sodium chloride and 1 M sulphuric acid.

2 MATERIALS AND METHODS

Ordinary Portland Cement (OPC) (53 grade) was used in this study [7]. Some of the physical properties of OPC and the additive ultrafine GGBS are given in Table 1. Locally available aggregates of size greater than 4.75 mm and less than 20 mm as per IS 456:2000 [8], with specific gravity of 2.45 and water absorption of 0.75% were chosen as graded coarse aggregates. River sand, as per grading zone II, with specific gravity of 2.5 and water absorption of 2%, conforming to IS 383:1970 [9], was chosen as graded fine aggregate. Cubic and cylindrical specimens were prepared with a mix design of 1:1.47:2.45 (Cement: Fine aggregate: Coarse aggregate), with a water to cement ratio of 0.45. Thermo-mechanically treated (TMT) rebars of Fe 415 grade, of 10 mm diameter and 450 mm height, with density 7850 kg/m^3, elastic modulus 200 GPa and Poisson ratio 0.28 were used. The cast specimens were demoulded after 24 hours and cured in normal tap water for 28 days. Workability of the concrete was studied with a slump test as per IS 1199:1959 [10], and compression strength was measured in a compressive testing machine as per IS 516:1959 [11]. Cubes of size 100 mm × 100 mm × 100 mm were prepared and an average of three results were taken. Bond strength between the steel rebar and the concrete was measured using a pull-out test as specified in IS 2770: 1967 (Part – 1) [12]. Water absorption studies were carried out on concrete cubes as per ASTM C642-06 [13].

Table 1: Physical properties of OPC and the additive Ultrafine GGBS

Property	Unit	Cement (OPC 53 GRADE)	Ultrafine GGBS
Average particle size	Microns	10 to 100	4 to 6
Fineness	cm^2/gm	2250	12000
Specific Gravity	-	2.98	2.86±0.02
Bulk density	kg/m^3	830 to 1650	600 to 700

For determining the corrosion behaviour of the concrete, half-cell potentials were measured based on ASTM C876-91 [14]. All electrochemical measurements were carried out on an electrochemical analyser (CHI604E, CH Instruments, Inc.). A cylindrical reinforced concrete sample was used as the working electrode, a concentric stainless steel (SS304) mesh was used as a counter electrode, and Ag/AgCl electrode served as a reference electrode. Once open circuit potentials were established, linear polarization studies were carried out in a small window (± 10 mV) around the open circuit potential at the rate of 1 mV/s. Tafel polarization experiments were carried out at a scan rate of 10 mV/s, approximately in a window of ± 500 mV from the open circuit potential.

3 RESULTS AND DISCUSSION

Introducing ultrafine GGBS into the concrete decreased its slump, thereby its workability. Water absorption also decreased with addition of ultrafine GGBS, but at 15% ultrafine GGBS, more water got absorbed. Compression strength, on the other hand, showed an opposite trend (Table 2). The highest compression strength of 42 MPa was observed for the addition of 10% ultrafine GGBS. It is likely that the ultra-fine particles of the additive fill the micro-pores of the concrete, thereby reducing the amount of water absorbed, and increasing the compression strength. However, the particles tend to agglomerate at high concentrations, resulting in the formation of larger voids, increased water absorption and reduced compression strength. Thus, it was determined that addition of 10% ultrafine GGBS to concrete was an optimum level of modification, and further studies were carried out with this modified concrete.

Whenever external load is applied on concrete, the reinforcing bar receives part of the load through load transfer mechanisms to generate steel stress, which acts parallel to the surface bond stress developed. Higher bond stress implies better load transfer to the steel rod, thereby better performance of the reinforced concrete. It is observed that the introduction of 10% ultrafine GGBS increases the bond stress by more than 31% from 0.707 MPa to 1.03 MPa.

To examine the corrosion properties of the concrete, electrochemical measurements were carried out. The half-cell potential or open-circuit potential determines the energetic state of the steel-concrete interface in the absence of an external driving force for corrosion. A large value of the potential implies high surface free energy, indicating a strong propensity for corrosion. This open circuit potential for the half-cell comprising the steel surface and its neighbouring concrete was measured by both an Elcometer as well as a Potentiostat with reference to a Silver-Silver chloride (Ag-AgCl) electrode for 600 seconds. Both measurements were consistent with each other, with –0.650 V from Elcometer and –0.651V from the CHI604E potentiostat for the unmodified concrete and –0.670 V from Elcometer and –0.672 V from the CHI604E potentiostat for the concrete modified with 10% Ultrafine GGBS. Negative potentials indicate a cathodic state of the electrode (steel). Therefore, as the potential becomes more negative, the steel is protected cathodically, leading to less corrosion. However, this protection is only for uniform corrosion, and localized corrosion can still take place. Thus, the open circuit potential measurements indicated that the steel bar in the concrete is prone to corrosion.

Table 2: Mechanical properties and water absorption of concrete samples

Sl. No.	Mixture	Workability (mm)	Compressive Strength (MPa)	Water Absorption (%)
1	OPC (100%)	80	35.6	4.82
2	OPC (95%) + ultrafine GGBS (5%)	75	38	4.42
3	OPC (90%) +ultrafine GGBS (10%)	70	42	4.16
4	OPC (85%) +ultrafine GGBS (15%)	65	28	4.86

While open circuit measurements provide a thermodynamic assessment of propensity of a concrete to induce corrosion in the steel, they do not provide any information either on the resistance offered by the concrete to corrosion or on the rate of corrosion. Therefore, linear polarization resistance measurements were made around ± 10 mV of the open circuit potential, as shown in Figure 1. These measurements were carried out in a solution of 3.5% NaCl and 1 M H_2SO_4. The studies showed that the ultrafine GGBS-modified concrete had a substantial 50% increase in corrosion resistance, from 50 KΩ to 100 KΩ, over unmodified concrete, even upon exposure to strong corroding agents such as chloride and sulphuric acid. Thus, the modified concrete is highly resistant to corrosion for small perturbations from the equilibrium (open circuit) conditions, which may arise during the course of application of the concrete in construction applications.

In order to determine the performance of the concrete under accelerated corrosion environments, Tafel polarization studies were carried out and the results are shown in Figure 2. Over a wide range of potentials, i.e., around ± 500 mV, neither concrete samples showed any signatures of localized corrosion behaviour. The values of E_{corr} were found to be –0.600 V for both the unmodified and the modified concrete. On the other hand, the corrosion current density (i_{corr}) decreased for the ultrafine GGBS-modified concrete by 42% from 10.59 nA/cm^2 to 6.14 nA/cm^2. Due to reduced water absorption, it is expected that chloride ingress in the ultrafine GGBS-modified concrete would be reduced, thereby leading to the reduction in corrosion. These initial results are promising, and further studies of long-term corrosion measurements are being carried out currently.

4 CONCLUSIONS

Concrete based on OPC grade 53 was modified by an ultrafine GGBS, found that 10% composition of ultrafine GGBS gave the highest compression strength and least water absorption, while further increase in ultrafine GGBS decreased the strength due to possible aggregation of the particles. This modification also increased the bond strength between the concrete and steel rebar. A significant 50% increase in corrosion resistance was observed in a solution containing 3.5% NaCl and 1 M H_2SO_4. Tafel polarization studies showed no features of localized corrosion over a range of around ±500 mV from the open circuit potential, and a reduction in the corrosion current by 42% due to the addition of ultrafine GGBS.

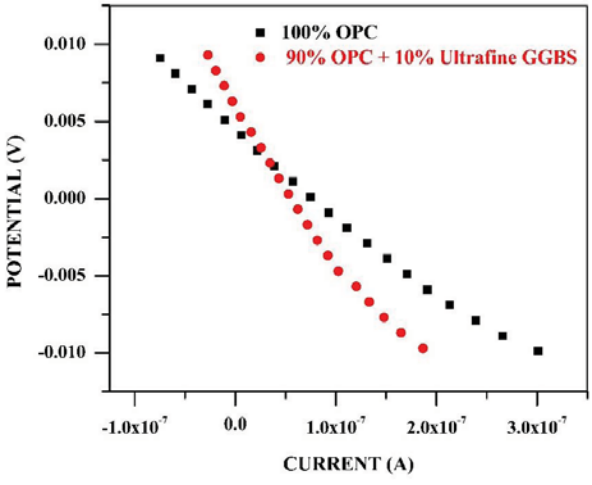

Figure 1: Linear polarization results for unmodified and ultrafine GGBS-modified concrete in 3.5% NaCl and 1 M H_2SO_4 solution

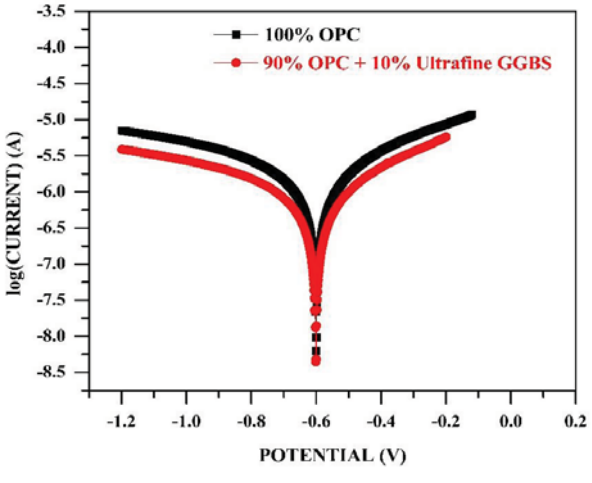

Figure 2: Tafel polarization results for unmodified and ultrafine GGBS-modified concrete in 3.5% NaCl and 1 M H_2SO_4 solution

5 ACKNOWLEDGEMENTS

The authors acknowledge the financial support of Amrita Vishwa Vidyapeetham. One of the authors (M.R.) acknowledges funds from the Ministry of Human Resource Development (FAST Scheme; F. No. 5-6/2013-TS.VII).

6 REFERENCES

[1] Andrade, C. and Buják, R., 'Effects of some mineral additions to Portland cement on reinforcement corrosion', *Cement Concrete Res.***53** (2013) 59-67.

[2] Sharmila, P. and Dhinakaran, G.,'Compression strength, porosity and sorptivity of ultra-fine slag based on high strength concrete', *Constr Build Mater*. **120** (2016) 48-53.

[3] Sharmila, P. and Dhinakaran, G., 'Strength and durability of ultra-fine slag based on high strength concrete', *Struct Eng Mech*. **55**(3) (2015) 675-686.

[4] Teng, S., Lim, T. Y. D. and Divsholi, B. S., 'Durability and mechanical properties of high strength concrete incorporating ultra-fine Ground Granulated Blast-furnace Slag', *Constr Build Mater*. **40** (2013) 875-881.

[5] Montemor, M. F., Simões, A.M. P. and Salta, M.M., 'Effect of fly ash on concrete reinforcement corrosion studied by EIS', *Cement Concrete Comp.* **22** (2000) 175-185.

[6] Geregi, H., Kurtay, M., and Durgun, H., 'The effect of zeolite and diatomite on the corrosion of reinforcement steel in 1 M HCl solution', *Res Phys.* **5** (2015) 14-153.

[7] Bureau of Indian Standards (BIS), Specification for 53 grade ordinary Portland cement (fourth revision), IS 12269:1989, New Delhi, 1989.

[8] Bureau of Indian Standards (BIS), Plain and reinforced concrete-code of practice (fourth revision), IS 456:2000, New Delhi, 2000.

[9] Bureau of Indian Standards (BIS), Specification for coarse and fine aggregates from natural sources for concrete (second revision), IS 383:1970, New Delhi, 1971.

[10] Bureau of Indian Standards (BIS), Methods of sampling and analysis of concrete (eleventh revision), IS 1199:1959, New Delhi, 1959.

[11] Bureau of Indian Standards (BIS), Methods of tests for strength of concrete (Eighteenth revision), IS 516:1959, New Delhi, 1959.

[12] Bureau of Indian Standards (BIS), Methods of testing bond in reinforced concrete (Part-1 Pull-out test) (Sixth revision), IS 2770 (PART-1):1967, New Delhi, 1968.

[13] American Society for Testing and Materials (ASTM), Standard test method for density, absorption and voids hardened concrete, ASTM C642-06, United States, 1969.

[14] American Society for Testing and Materials (ASTM), Standard test method for half-cell potentials of uncoated reinforcing steel in concrete, ASTM C876-91 United States, 1999.

Innovative Manufacturing Methods of Drapable Textile Reinforcements for Folded/Double Curved Concrete Facade Elements

Gözdem Dittel, Andreas Koch and Thomas Gries

Institut fuer Textiltechnik (ITA) of RWTH Aachen University, Germany

ABSTRACT

Textile reinforcements made of materials such as carbon and glass fibres meet the growing requirements for corrosion-free and high-strength lightweight structures in the building industry. One of the most sustainable developments is textile reinforced concrete (TRC). The high formability is one of the challenging advantages of TRC structures compared to steel reinforced concrete. The inherent drapability of textile reinforcements allows the production of folded and/or double curved TRC elements with a high-quality finish. The minimum radius of the curve decides the required drapability level of the textile. The textile manufacturing process of warp knitting allows substituting single threads and changing of the stitch type during production. This makes warp knitting suitable to achieve the goal of locally adapted reinforcing textiles. This paper will present the results of a completed public funded project "Concrete Fold" in which possible combinations of stitching patterns were classified to determine their influence on the drapability of the textiles on basis of a cantilever test. Furthermore, the paper will give an overview about the scope of another public funded project "CurveTex" as a follow-up research where the manufacturing of double curved TRC elements through a combination of elastic and high modulus fibres is pursued.

1 INTRODUCTION

TRC has numerous technical and ecological advantages compared to conventional steel reinforced concrete. A higher durability due to corrosion-resistant textile reinforcement, high CO_2 savings due to filigree and concrete-saving design (up to 80 %), a reduction of transport and assembly costs due to the high weight and volume savings are some of the major advantages of TRC [1]. Furthermore, TRC allows the realizing of very thin and structurally strong elements (5-50 mm) with a high surface quality due to using a fine grain concrete matrix [2-3].

A further advantage can be used for the design of structural elements which relates to the low bending stiffness of not impregnated reinforcing structures and the good formability respectively drapability of these structures. Thin-walled free-formed (folded or double curved) TRC elements can be easily produced by a suitable casing. However, depending on the design of a free-formed TRC facade, a corresponding casing needs to be produced for each mould. This is technically possible, but with increasing complexity regarding the design not economic.

The textile design enables a desired textile drapability behaviour on predefined textile parts. Therefore, ITA researched the possibility of locally adapted textiles for folded TRC

elements. The promising results started a new research project to manufacture elastically adapted textiles for double curved TRC elements.

2 TEXTILE DEVELOPMENT FOR FOLDED TRC FACADE ELEMENTS

The ITA developed textile reinforcements for folded TRC facade elements and examined their behaviour in the folding point. A reinforcement of an open-meshed biaxial warp knitted textile structure was used which usually consists of AR glass (alkali-resistant glass fibre) or carbon rovings in the warp and weft direction.

The drapability of these textile structures is influenced in particular by the parameters which are listed in Table 1.

Table 1: Textile drapability influencing parameters

Parameter	**Specification**
Yarn material	carbon or AR-glass (warp and weft)
Yarn titer	800 - 3300 tex
Mesh size	5 - 30 mm
Stitching pattern	pillar, tricot, plain

The stitching pattern looms large in the textile production as an influencing parameter since it is the only parameter that can be changed during the production of the biaxial warp knitted textiles. All other parameters are defined before production and cannot be changed during production. Thus, the ITA pursued the approach of changing the stitching modification in the production direction to change the bending stiffness of the warp knitted structure locally, i.e. only at a predefined point (the folding point) for a predetermined length.

During the research project three different textile biaxial types were developed and tested. AR glass fibres and three different types of stitching pattern (pillar, tricot and plain) were used. The relatively flexural rigid pillar stitching pattern was combined with a relatively bend-relaxed plain binding by varying the type of binding from pillar to plain in a range of approximately 50 mm. The properties of all developed textile types are listed in Table 2.

Table 2: Properties of the developed textile types

Textile Type	**Material**	**Stitching pattern**	**Bending stiffness**
1	AR-Glass 2400 tex	pillar	high
2	AR-Glass 2400 tex	plain	low
3	AR-Glass 1200 tex	tricot	low
4	AR-Glass 2400 tex	pillar-plain	locally adapted

The bending stiffness of textile structures was tested with a cantilever test according to DIN 53362 at the ITA.

With the cantilever test stand, the flexural stiffness of textile types 1 and 2 has been investigated. It turned out that the textile type 2 (plain) has only one fifth of the bending stiffness of the textile type 1 (pillar). For further tests, the plain binding and the textile type 3 (tricot) was used. Due to the relatively high bending stiffness, as shown in Figure 1, the pillar binding is not suitable for folded or simply curved textile concrete components.

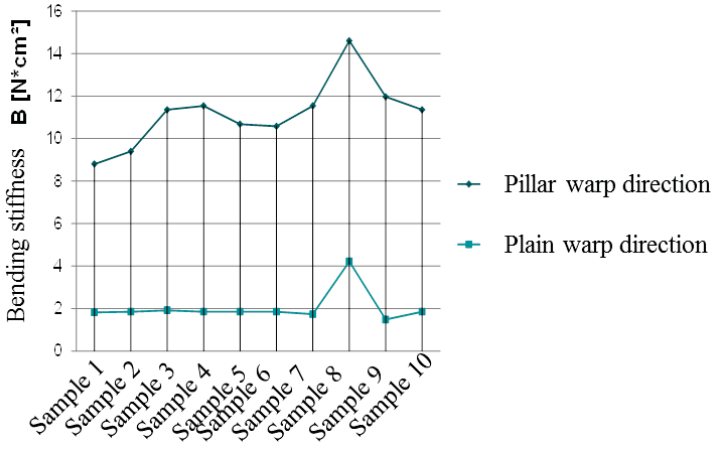

Figure 1: Test results of bending stiffness textile 1 (pillar) and textile 2 (plain) at the ITA

Locally adapted textiles which combine two different levels of drapability in one single fabric were realized and the possibility to manufacture adapted textiles for special folded elements is generated (Figure 2).

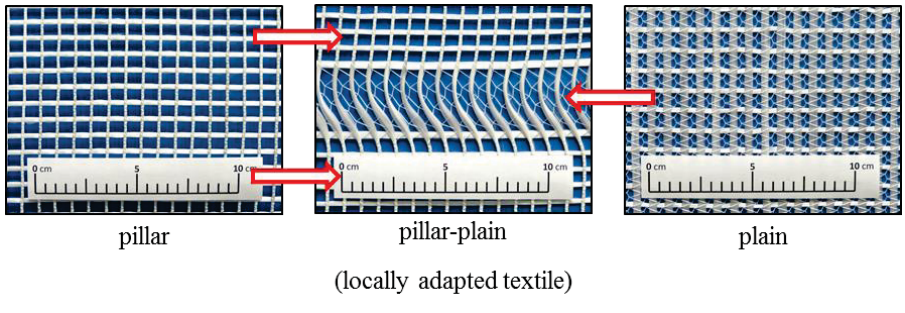

Figure 2: Combination of different drapability levels First demonstrator of a locally adapted biaxial warp knitted textile

For the research project intended at production of folding structures, these locally adapted warp knitted structures were used to develop a kind of textile joint that offers the greatest degree of moldability, especially at the folding point. In order to visualize this idea, a handling and shaping test was carried out using this locally adapted warp knitted structure. These tests are shown in the Figure 3 (manual handling test above, mould test below).

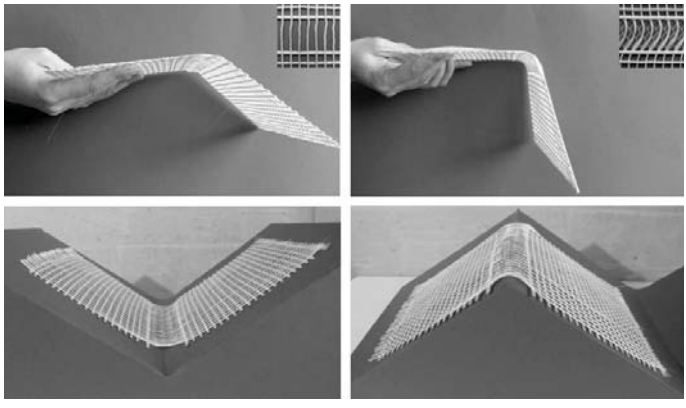

Figure 3: Bending and shaping behaviour of the adapted local section

In the upper figures (Figure 3), the weft roving with a production length of approximately 50 mm was removed and only the stitch type was changed (pillar/left, plain/right). The locally used plain binding allows a larger bend angle at the desired folding point than the pillar binding in comparison. The lower figure (Figure 3) shows that the locally adapted warp knitted structure optimally adapts to a folded structure.

3 THE FOLLOW-UP RESEARCH

As a follow-up project to "ConcreteFold", within another research project ("CurveTex"), a new elastically adapted reinforcement structure for the crease-free reinforcement of double-curved components is being developed.

The research objectives are the development of a drapable textile reinforcement for concrete and the development of the related production processes for double-curved textile concrete elements (concrete injection and concrete casting methods) with continuous fibre reinforcement.

Figure 4 shows the development steps involved in connection with the current state of the art.

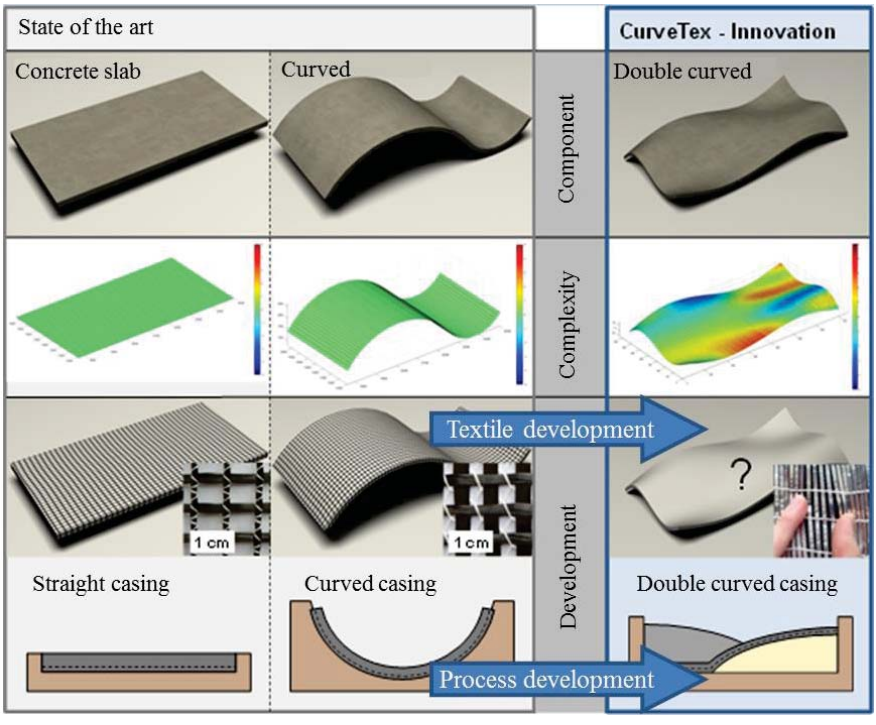

Figure 4: Development steps of double curved TRC facade element

4 CONCLUSIONS

Through realizing the locally adapted textile structures an industrial production technology for folded TRC facade elements, as well as a demonstration facade at RWTH Aachen University was developed. Folded and simply curved geometries were defined for the application area "curtain facade" and a method for concrete shaping in the green belt was developed. With a new folding tool and an innovative manufacturing process, facade elements could be realized that exceed conventional concrete facades in terms of technical functionality and aesthetics. The development steps of the folded TRC facade are shown in Figure 5.

Through the production of the demonstration facade the practicability could be demonstrated. A quick and flexible adaptation of the folding tool for different folding geometries is possible. Folded TRC elements can be produced in a cost-effective process.

All current research approaches in the area of three-dimensional textile concrete elements are limited to a simple curvature (simply curved or folded structures). This is due to the low draping capability of the textile reinforcement structures currently in use. The main target of the ongoing research project “CurveTex” is to disestablish this limitation.

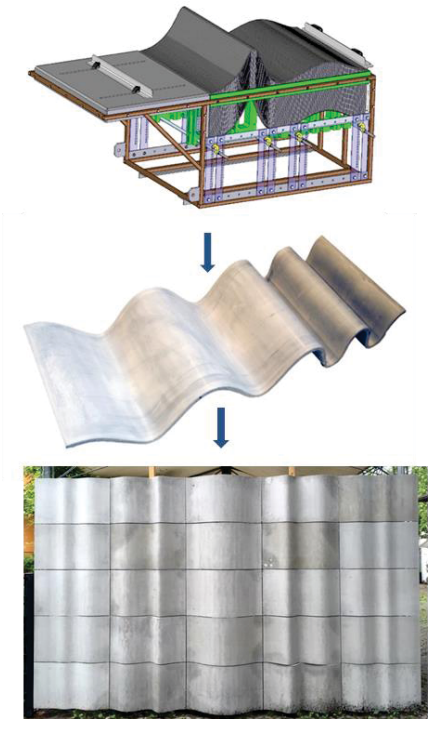

Folding tool

- Tool development

Focus: Construction/realisability

- Textile development

Focus: Bending stiffness/formability

Component

- Component tests

Focus: Prototype construction

- Concrete developement

Focus: Beton characteristics green stage

Facade

- Anchoring elements

Focus: Facade connection

- Creative possibilities

Focus: Geometry analysis

Figure 5: Development steps of folded TRC facade

5 ACKNOWLEDGEMENTS

The authors would like to acknowledge the financial support from the “ConcreteFold”-project and the “CurveTex”-project funded by the BMWi for carrying out the projects.

The authors would like to thank the partners of the “ConcreteFold”-project: Florack Bauunternehmung GmbH, Germany, ingema t+h ingenieurgesellschaft mbH, Germany, W+S bau-instandsetzung GmbH, Germany, Institut für Bauforschung (ibac) der RWTH Aachen University and Lehrstuhl für Plastik (LfP) der RWTH Aachen University for the good cooperation.

The authors would like to thank the partners of the “CurveTex”-project: Penn Textile Solutions GmbH, Germany and Stanecker Betonfertigteilwerk GmbH, Germany for the good cooperation.

6 REFERENCES

[1] Gries, T., Tomoscheit, S., EU Life06 Insu-Shell: Environmentally Friendly Facade Elements made of thermal insulated Textile reinforced concrete, Bund Deutscher Architekten, Ortsverein Aachen, Aachen 30.10.2009.

[2] Janetzko, S., Methodik zur Gestaltung von Bewehrungssystemen für textilbewehrten Beton, Ph. D. Thesis, Institut für Textiltechnik (ITA) der RWTH Aachen University, Germany, 2013.

[3] Arbeits- und Ergebnisbericht / Sonderforschungsbereich 532 "Textilbewehrter Beton - Grundlagen für die Entwicklung einer neuartigen Technologie", Aachen, 2002.

High Performance Concrete for Hydraulic Engineering Projects with Aggregates Presenting an AAR Hazard

Falikman V.R.(1), Safarov K.B.(2) and Stepanova V.F.(3)

(1)Moscow State University of Civil Engineering, Moscow, Russia

(2)Central Building Laboratory of the Rogun Hydropower Plant, Tajikistan

(3)Scientific Research Institute for Concrete and Reinforced Concrete after A.A. Gvozdev, Moscow, Russia

ABSTRACT

Rogun Dam is an embankment dam in the preliminary stages of construction on the Vakhsh River in southern Tajikistan. Rogun was listed as the highest dam in the world. When constructed, it expected to produce 17.1 TWh of electrical power per year. Integrated studies of a wide range of local aggregates were conducted according to GOST 8269.0. It was established that crushed stone from local quarries all contained alkali-soluble silica in concentrations of much more than 50 mmol/l. The aggregates comprise sandstones, granite, limestones, amphibolite, shale, siltstone etc. Local sulphate resistant Portland cement is used for concrete mixes because groundwater in the construction area contains sulfates in high concentration (more than 34000 mg/l). The use of cement with mineral additives precludes development of hazardous damage to concrete with the above-specified aggregates. Additions of silica fume, metakaolin and siliceous fly ash as constituents of mortars and high-performance concrete were studied. The samples were tested for long-term alkali-silica reaction expansion (up to 20 months) in accordance with the GOST 8269.0 specification. It was showed that considerable increasing of concrete durability could be attained using active mineral additives and a polycarboxylate-based superplasticizer.

Keywords: Alkali-aggregate reaction, high performance concrete, hydraulic structures, mineral additives and sulfate resistance.

1 INTRODUCTION

The Rogun Hydro on the Vakhsh River in Tajikistan (under construction now) is comprised by the Vakhsh cascade being its upper development. According to the design it is the reservoir power station with a high (335 m) rock-fill dam. The Hydro design capacity is 3600 MW, the annual average generation is 17.1 billion kW-h. Six radial flow hydraulic units with 600 MW capacity each will be installed in the powerhouse. The Hydro dam shall form the large Rogun water reservoir with total storage of 13.3 km^3 and effective capacity of 10.3 km^3. The water reservoir is planned to be used both for the power generation and irrigation purposes on arid lands over 300 thousand hectares in area. Upon completion of the project the Hydro dam will be the world highest.

As is intrinsic for the most hydraulic structures, the concrete elements of the Rogun Hydro are simultaneously affected by several forms of corrosion. For example, under the

river bottom where there is the most vantage place for the dam, the rock salt $NaCl^-$ filled fracture occurs. The groundwater has high sulfate content (over 34000 mg/l). In addition, the dam site is at high seismicity zone with weak earthquakes occurring every month.

In construction of the Rogun Hydro the local rock aggregate is used to make concrete mixes. These aggregates comprise 40 % of sandstone, 20 % of granite, 20 % of limestone and 20 % of amphobolite, shale rock, siltstone and other potentially reactive minerals [1]. The total volume of concrete and reinforced concrete on the site is over 2 million (mln) m^3 including that in hydraulic structures – over 1 mln m^3.

All the above said predetermines the necessity to set up and conduct studies aimed at ensuring the life cycle of this unique hydraulic structure. The search for new efficient ways to simultaneously control the aggregate reactivity and to increase the concrete sulfate resistance becomes one of the post important scientific research and practical problems to be solved to improve durability of concrete and reinforced concrete structures.

2 STATE OF STRUCTURES OF THE ROGUN HYDRO WATERWORKS

The Hydro construction preparatory period was started in 1976. The upstream cofferdam and the Vakhsh river closing was started in 1987. By 1993 the upstream cofferdam height reached 40 m, and by this time 21 km of tunnels had been driven, and the spaces of the powerhouse hall (70 %) and the transformer station (80 %) had been mined. After collapse of the Soviet Union the Hydro construction was suspended.

Resumption of construction with the World Bank participation required expert investigations including condition analyses of the earlier built structures.

In underground hydraulic structures of the Rogun Hydro many reinforced concrete components were damaged, e.g. water and traffic tunnel walls (Figure 1). The phase and element composition of concrete core specimens was studied in the Central building laboratory of the Rogun Hydro using XFS spectrometer and X-ray diffractometer. The analysis data have shown that the structure of sample cores comprises chalcomorphite and thaumasite that gives evidence of the sulfate corrosion process.

Figure 1: View of underground reinforced concrete structures with damages associated with several types of corrosion actions

At the same time, thin and polished sections were studied that had been prepared from concrete cores sampled from underground reinforced concrete structures of the Rogun Hydro built in the period from 1985 to 1990.

Photomicrographs obtained using optical and electron scanning microscopes show signs of AAR (Alkali aggregate reaction). In interaction of the pore grout alkaline medium and

siliceous aggregates the reaction products (alkali-silica hydrogel) were formed that are capable to significantly increase in volume and to create internal stresses leading to concrete failure. The alkali-silica reactions are also evidenced by the presence of typical cracks directed radially from aggregate grains deep into the mortar matrix as well as the cracks penetrating the aggregate particle itself. The cracks are filled with the gel-like reaction product (Figure 2).

Figure 2: Propagation of alkali-silica hydrogel along the crack in the aggregate and the matrix (photo in the polarized light)

Presence of a typical hem from the reaction product [C-(N+K)-S-H hydrogel] around the grains indicates high activity of the reactive aggregate. In this case the pore liquid attack occurs locally on the aggregate particle region of imperfections and on its contact zone with the paste matrix. The pore fluid enters the imperfections through microcracks, meanwhile the walls are eroded and the crack itself is filled with the alkali-silica gel. By means of cracks and pores the gel penetrates deep into a particle, creating stresses in its internal zones that lead to formation of new cracks and particle destruction. The external signs of the alkali-silica reaction (ASR) in this case can be found in several years since the moment of the reaction start.

In the gross volume, one observes few signs of alkaline corrosion expressed by the presence of typical cracks. Not all aggregates were affected by ASR, but coarse inclusions with a high degree of the structure amorphism and, consequently, with higher reactivity (solubility) in relation to alkalis.

It is obvious that one requires constant and long-term monitoring of structures and the concrete composition itself with the aim to determine dynamics of ASR and kinetics of the paste matrix phase composition. Petrographic and mineralogical studies should be conducted with extensive (representative) sampling of specimens of a certain age.

3 MATERIALS AND METHODS

The aggregate reactivity was assessed in conformance with GOST 8269.0. Sulfate resistance of mortar and concrete specimens was assessed by ASTM C1012. For the tests the sulfate-resistant Portland cement SRC M400 (CEM I SR 32,5N), $C_3A<3.5$ %, produced by Tajik Cement Plant was used as envisaged by the construction project (Table 1).

Table 1: Cement mineral composition by Bogue.

Cement	C_3S	C_2S	C_3A	C_4AF	R_2O
SRC PC400 D0 (CEM I 32,5N)	52.82	22.7	3.33	14.62	0,83

Sand and crushed stone prepared by local rock breaking and grading were taken from the Rogun Hydro site stores according to the origin certificates. Technical characteristics of the mineral additives used are given in Table 2.

Table 2: Characteristics of mineral additives

Indicator	High-active metakaolin (HMK)	Ultra-fine silica fume (USF)	Fly ash (FA)
True specific gravity, g/cm^3	0.83	0.43	0.77
Bulk density, g/cm^3	4.1	2.1	2.04
Specific surface area, g/cm^3	18000	12000	9500
Chemical composition, %			
SiO_2	52.5	97.12	53,82
Al_2O_3	44.5	0.01	22.56
Fe_2O_3	0.9	0.05	4,48
TiO_2	1.7	0.02	0.01
CaO	0	0.37	2.0
MgO	0	0.28	2.45
Na_2O	0	0.04	0
K_2O	0	0.58	0
SO_3	0	0.04	0
П.п.п.	0.7	1.36	0.9

Fly ash is delivered to the site from the Varzob thermal power plant, Dushanbe, and is a siliceous fly ash (CaO<10%) product (SFA). The ultra-fine silica fume used in the tests is delivered from the Islamic Republic of Iran, while the high-active metakaolin – from the Russian Federation. Polycarboxylate superplasticizer (PCE) used in the tests is a commercial product.

Flowability of mixtures was tested according to GOST 310.4 (cone test). For the first 24 hours after casting the specimens were stored in a normal hardening chamber, then after demolding and throughout the test – in air-dry conditions (20-25 ^oC, 60-70 % relative humidity). Concrete mixtures were prepared in accordance with GOST 10181.0.

Fresh mortars (fine-grained concretes) were tested according to GOST 10181, and hardened mortars (concretes) – according to GOST 12730.0 – 12730.5. Compressive strength

of hardened samples was measured in accordance with GOST 10180. Impermeability to water for series of concrete samples was estimated according to GOST 12730.5 by maximal water pressure, at which on four of six cylindrical samples the water percolation was not observed.

Shrinkage deformations of each specimen were measured using a length comparator, sensitivity of 1 μm, and gage studs on the end sections of the mortar prisms starting from the 1-day age (zero reading). A reference invar bar was used to check stability of the length comparator. Each result presented is the average value of three measurements.

4 ESTIMATION OF THE AGGREGATE REACTIVITY

The analysis of locally available inert materials (fine and coarse aggregate) has shown that they are represented mainly by sandstones, dolomitic limestones, tuffs, granites and amphibolites (Table 3).

Table 3: Characteristics of rock for aggregate preparation

Quarry	Name of rock in aggregates and quantity, % mass	Soluble silica (SiO_2) content, mol/l
Quarry «15B»	Sandstone - 40 Limestone– 20 Granite – 20 Shales– 6 Amphibolite– 4 Red argillite – 5	55.3
Labidara quarry	Sandstone - 35 Limestone– 18 Granite– 20 Shales– 2,5 Siltstone– 2,5 Amphibolite– 22	66.3
Quarry «2B»	Sandstone -100	77.3

All aggregates comprise silicic rocks, calcite and its modifications, microcrystals of quartzite and chloritic minerals. By their mineralogical composition the aggregates may be reactive with cement alkalis. In this connection, the studies were conducted according to GOST 8269.0-97 to determine the aggregate reactivity with cement alkalis. The results obtained have shown that by the soluble silica content practically all aggregates are potentially reactive; the soluble SiO_2 content is in the range of 55.33 to 77.33 mol/l.

However, assessment of possible internal concrete corrosion only by the aggregate chemical analysis and the soluble SiO_2 content is far from ambiguous [2]. The aggregate reactivity is defined by a set of methods according to GOST 8269.0-97. Petrographic and chemical methods are used, as a rule, at the stage of exploration and periodically in field developments. The accelerated method with strain measurement is used with mortar and concrete specimens at a stated time (not more than 1 month), the concrete specimen tests by the basic procedure are conducted for one year, if the previous tests have shown that the aggregates are reactive.

The accelerated tests of aggregate reactivity with strain measurement using mortar specimens have shown that the specimen expansion deformation value in the sodium hydroxide solution is over 0.1%, and the eleventh test result differs from the three preceding results by 16.23%, i.e. more than by 15%. It shows that according to GOST 8269.0-97 the

aggregate is considered potentially reactive in relation to cement alkalis. The results of determining the aggregate reactivity by the basic procedure of concrete prism strain measurement have confirmed the potential reactivity of the Rogun aggregates [3, 4].

5 ASSESSMENT OF FLY ASH EFFICIENCY AND ITS ACTIVATION

The drawback of siliceous fly ash (SFA) is that its use governs reduction of concrete strength due to low hydraulic activity. Therefore, to activate SFA it is often used along with additives having high pozzolanic activity [5, 6]. Following the standard methods specified by the regulatory documents (SP 28.13330.2012, GOST 25818 and NIIZhB recommendations on concrete protection against corrosion caused by interaction of silicium dioxide in aggregates and alkalis in cement [7]) as well as the accumulated experience in construction of other hydraulic structures [8], the siliceous fly ash (SFA) fly ash and silica fume were used as active mineral additives to prevent reactivity of inert materials from the Rogun deposits.

The fly ash used in construction is supplied to the Rogun Hydro site from the Varzob thermal power plant located near Dushanbe. By its chemical composition it refers to the siliceous fly ash (SFA) category (CaO < 10) and does not have high hydraulic activity. The fly ash mechanical activation was performed in the laboratory disc mill RetschRS200 that mills solid particles by the abrasion method and reduces the milled particle size from 100 to 0.1 mkm. The fly ash particle size determination prior to and after milling was performed by the laser granulometer (Analyzette-22NanoTech).

To determine the effect of fly ash activation after milling on concrete strength the fine-grained concrete specimens were made having the same W/B and degree of cement substitution 20 and 30 %. From each batch 9 prism specimens were made, 3 specimens for each test period – 3, 7 and 28 days. The compression strength test results are given in Table 4.

Table 4: Compression strength of mortars

No.	Consumption of materials, g					Test results			
	Cement	Water	Sand	Fly ash	Milled fly ash	Slump, mm	Compression strength, MPa		
							3 days	7 days	28 days
1	500	190	1500	-	-	114	23,0	31,0	49,8
2	400	190	1500	100	-	112	21,7	30,1	48,7
3	400	190	1500	-	100	114	27,0	34,0	58,9
4	350	190	1500	150	-	113	22,6	29,9	48,8
5	350	190	1500	-	150	114	26,3	34,9	55,1

By the test results the specimen strength with 20 % of milled fly ash exceeds that of specimens without fly ash and the specimens with 20 % of initial ash by 18 % and 21 %, respectively. The specimen strength with 30 % of milled fly ash exceeds that of specimens without ash and specimens with 30 % of initial ash by 11 % and 13 %, respectively.

6 SULFATE RESISTANCE OF MORTAR SPECIMENS WITH COMPOUND BINDERS

The effect of the mineral additive complex on concrete sulfate resistance was determined by the accelerated method according to ASTM C 1012. The specimens were made from 3 cement-sand mortars, in two of which a part of cement was replaced by fly ash and silica fume and fly ash and metakaolin (Table 5). The test results are presented in Figure 3.

Deformations in reference specimens and specimens with ash and silica fume exceed allowable value limits 0.1%, while deformations in specimens with ash and metakaolin develop within allowable limits.

The effect of milled fly ash on concrete sulfate resistance was determined by the accelerated method according to ASTM C1012. The specimens were made from 3 cement-sand mortars, in two of which 20% and 30% of cement was replaced by milled fly ash. The mortar compositions and strain measurements are given in Table 6 and Figure 4.

Table 5: Mortar specimen compositions

Materials, g	Reference	FA + SF	FA + MK
Cement	500	375	375
Sand	1375	1375	1375
Water	230	230	230
Fly ash	---------	100 (20%)	100 (20%)
Silica fume	---------	25 (5%)	----------
Metakaolin	---------	---------	25(5%)

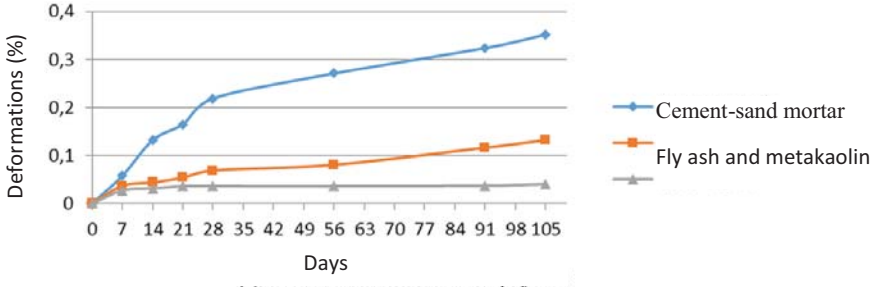

Figure 3: Mortar specimen deformations in the sulfate environment

Table 6: Mortar specimen compositions

Materials, g	Compositions		
	Reference	20 % of milled fly ash	30 % of milled fly ash
Cement	500	400	350
Sand	1375	1375	1375
Water	230	230	230
Fly ash	------	100 (20 %)	150 (30 %)

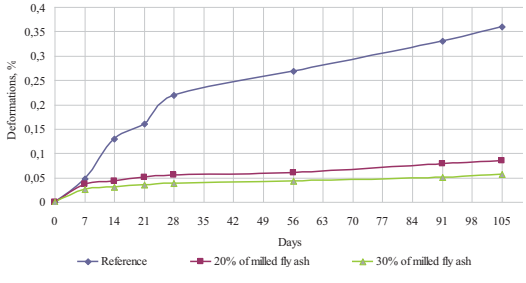

Figure 4: Effect of milled fly ash on concrete sulfate resistance

Table 7: Concrete compositions and laboratory test results

Material	Designation	Material consumption, kg/m^3
Cement	SRC 400 D0	400
Additive	Ash	152
	Metakaolin	24
Sand	natural	412
	pit	413
Crushed stone	5 - 20 mm	804
Admixture	PCE	5,2
Water		172
Concrete and mix properties		
Concrete mix density, kg/m^3	designed	2382
	actual	2380
Slump, cm	15 min	72
	120 min	69
Concrete strength, MPa	3 days	18
	7 days	32
	28 days	53

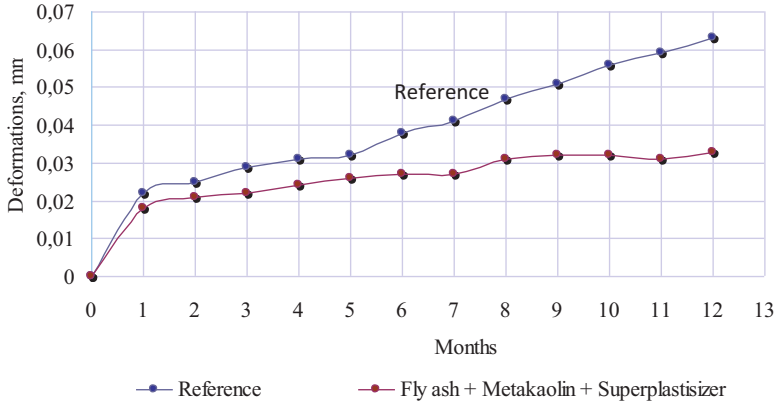

Figure 5: Relative deformations of concrete specimens

The quantitative value of concrete corrosion resistance is a resistance coefficient (RC), i.e. the ratio of resistance of concrete specimens in corrosive solution and the strength of specimens in fresh water. Variation of compression strength and bending tensile strength of concrete specimens immersed in 5 % sodium sulfate solution and in drinking water for the length of 12 months had been studied (Table 8).

As is seen from the data obtained, the resistance coefficients by the values of compression and bending tensile strengths of concrete specimens made from "fly ash + metakaolin + superplasticizer" complex in the corrosive sulfate environment and neutral water are close to unity. Consequently, the expected phase of concrete specimen strength development in the sulfate environment owing to compaction in pores with chalcomorphite formation has not happened for the 12-month test period, this testifying of high sulfate resistance of the concrete obtained.

Table 8: Variation of compression and bending tensile strengths of concrete specimens in different environments

Time	Compression strength, MPA		RC	Bending tensile strength, MPa		RC
	Water	5% Na_2SO_4 solution		Water	5% Na_2SO_4 solution	
1 month	51,9	52,1	1.00	6,6	6,6	1.00
2 months	53,2	52,8	0.99	6,8	6,7	0.99
3 months	54,7	55,5	1.01	7,0	7,2	1.03
6 months	55,1	56,0	1.02	7,0	7,3	1.04
9 months	56,3	56,5	1.00	7,3	7,4	1.01
12 months	57,1	55,8	0.98	6,6	6,6	1.00

The test of concrete specimen corrosion resistance with account of the aggregate reactivity was performed by the basic procedure according to GOST 8269.0-2004. Two types of concrete specimens (70 × 70 × 280) were made: the reference specimens without active mineral additives and specimens of concrete with "fly ash + metakaolin + superplasticizer" complex with bringing the cement alkali sum ($Na_2O+0,658*K_2O$) to 1.5 %. Relative deformations of concrete specimens were measured monthly for 12 months and did not exceed the allowable limit of 0.04 %.

7 DISCUSSION

- The studies were conducted with thin sections made from concrete cores taken from the visually corroded reinforced concrete structures of the Rogun Hydro. Micrographs show signs of alkaline corrosion. The alkali-silica reaction process is evidenced by the presence of typical cracks directed radially from the aggregate grains deep into the matrix as well as the cracks piercing the aggregate particle itself. The cracks are filled with a reaction gel-like product.
- Substitution of 15 % of cement by fly ash and 5 % of silica fume ensures an effective way to reduce reactivity of inert materials from the Rogun Hydro local quarries. High-active metakaolin activates siliceous fly ash (SFA), this being proved by the results obtained in specimen strength tests.
- It is shown that substitution of 25 % of cement by the complex additive comprising 20 % of siliceous fly ash (SFA) and 5 % of high-active metakaolin also allows controlling the aggregate reactivity. The same additive increases sulfate resistance of cement-sand specimens.
- It is proved that the use of "fly ash + metakaolin + superplasticizer" complex allows obtaining high-workability self-compacting concrete mixes with low W/C. It is found that physic mechanical properties of concretes with "fly ash + metakaolin + superplasticizer" complex meet all requirements necessary for manufacture underground reinforced concrete hydraulic structures.
- The use of "fly ash + metakaolin + superplasticizer" complex allows obtaining the concrete with high corrosion resistance in high-corrosive sulfate environments with SO_4^2

ion concentration over 34000 mg/l as well as allows controlling internal alkaline corrosion of concrete in relation to the aggregate reactivity. The test of concrete specimen corrosion resistance with account of the aggregate reactivity using "fly ash + metakaolin + superplasticizer" complex has shown that relative deformations do not exceed the standard limit of 0.04 % for the 12-month period.

- It has been found that with siliceous fly ash milling its activation takes place owing to increasing the particle specific surface area, and its use in the amount of 30 % of the cement mass improves concrete strength by 20 % compared to the initial ash.
- By measuring deformations of mortar bars it has been established that substitution of 30 % of cement by the milled fly ash controls the aggregate reactivity and concrete sulfate corrosion.

8 CONCLUSION

With consideration of the results obtained the commercial concrete compositions will be adjusted and studied. This is one of the most important scientific and technical problems to be solved to improve concrete corrosion resistance and, consequently, to increase durability of hydraulic reinforced concrete structures of the Rogun Hydro.

REFERENCES

1. Zolotykh, H.B. (ed.) (1990) Typification of potentially reactive minerals from nonmetallic building material deposits". State-of-the Art Report. Scientific-research and design prospecting Institute for mining, transportation and processing of mineral raw materials in the building materials industry - FSUE "VNIIPIstromsyrye". 90p.
2. Rosental, N.K., Lyubarskaya, G.V., & Rosental A.N. (2014) Test of concrete with reactive aggregates. *Beton i zhelezobeton (Concrete and reinforced concrete)*, No. 5, pp. 24–29.
3. Safarov K. B. (2015). Use of reactive aggregates in production of concrete resistant to aggressive media. *Building materials*. No. 7. Pp. 17-21.
4. Safarov K. B., Stepanova V.F. (2016). Regulation of the aggregates reactivity and increase of the sulphate-resistance of concrete by the joint application of low-calcium fly ash and highly reactive metakaolin. *Building materials*, No. 5, p. 70 – 73.
5. Thomas, M.D.A. (2011). The effect of supplementary cementing materials on alkali–silica reaction. *Cement and Concrete Research*. №41. pp. 1224–1231.
6. Pan, J.W., Feng, Y.T., Wang, J.T., Sun, Q.C., Zhang, C.H., Owen, D. R. J. (2012). Modeling of alkali–silica reaction in concrete: *Frontier of Structural Civil Engineering*. №6. pp. 1–18.
7. STO 36554501-002-2010 (2010) Concrete protection against corrosion caused by the reaction of aggregate SiO_2 with cement alkalis. NITs "Stroitel'stvo" JSC.
8. Viktorov, A.M. & Lozhkin, A.N. (1992) Problems of alkali corrosion of concrete dams. *Hydraulic Engineering*, 116, No. 11. pp. 52–53.

Role of Reactive Alumina and Reactive Oxide Ratios on Strength Development in Alakaline Activation of Low-Calcium Fly Ash

G.V.P. Bhagath Singh and Kolluru V.L. Subramaniam

Indian Institute of Technology Hyderabad, Hyderabad, India.

ABSTRACT

The role of reactive alumina and process variables such as sodium content and molarity on alkaline activation of different low calcium fly ashes are explored. Reactive alumina content of a fly ash is the key parameter which determines the maximum compressive strength achieved from the alkaline activation. The oxide ratios in the activated system, based on the total silica in the system consisting of the reactive silica contributed by fly ash and the reactive alumina in fly ash are shown to provide consistent results for achieving the highest strength. A method called XRD-based direct decomposition is used to determine the unreacted glassy content and amorphous reaction product in the system. The strength gain in the system is directly related to a decrease in the unreacted fly ash glassy content and an increase in the reaction product content in the system.

Keywords: Alkaline activation, Reactive Alumina, Reactive Silica, Molarity, Unreacted glassy content, geopolymer

1 INTRODUCTION

Geopolymers are alumino-silicate binders made using materials that are rich in alumina and silica. The typical aluminosilicate source materials used to develop the geopolymers such as blast-furnace slag, metakaolin, rice husk ash, Al-rich waste, red mud, and fly ash [1-7]. In the Asian sub-continent, fly ash, which is an industrial waste product is the most attractive source material due to its ready availability in large quantities. The quality of fly ash which is typically available is however, of low grade with little reactive content [8].

Several factors such as reactive oxide contents, particle size, NaOH concentration, temperature, alkali activator to binder ratio and oxide ratios of SiO_2, Al_2O_3, and Na_2O influence the microstructure and mechanical properties of fly ash-based geopolymers [6,9-10]. SiO_2/Al_2O_3, SiO_2/Na_2O ratios are the dominant factors in strength prediction of geopolymers. Compressive strength increases with increasing concentration of NaOH in the activating solution [11]. The quantity of NaOH required depends on the type of fly ash [12]. Geopolymers tends to be less stable at low SiO_2/Na_2O than at high SiO_2/Na_2O [9]. The highest compressive strength is obtained at the ratio of SiO_2/Na_2O is 0.69 [13]. Increasing the Al_2O_3/Na_2O and SiO_2/Na_2O weight ratios in the activating solution influence the compressive strength [11,14] and the optimum values of 8.01 and 1.94 for SiO_2/Na_2O and Al_2O_3/Na_2O ratios to provide highest compressive strength in class F fly ash based geopolymers [11]. The strength of the geopolymers depends on the vitreous portion of SiO_2/Al_2O_3 ratio [15].

Fly ash contributes Al and Si to the reaction product, which is supplemented by the activators. Reactive oxide components especially the reactive Al_2O_3 and SiO_2 are key oxide contents which are involved the during the geopolymerisation process. Most commonly used activators are combinations of sodium hydroxide (NaOH) and sodium silicate ($NaSiO_3$),

which are mixed in varying proportions. Most researchers did not consider the contribution from fly ash and hence the ratios reported in the literature are applicable for the particular fly ash used in the study. The solution ratios derived from results of a fly ash with high reactive silica content would not require additional $NaSiO_3$ for achieving high strength. Few researchers considered a vitreous portion of the SiO_2 and Al_2O_3 [15].

Activator solutions would have to be developed considering the composition and the reactive silica and alumina contents of fly ash. Current paper explores the role of reactive Al_2O_3 content, the total reactive oxide ratios including a contribution from fly ash and the molarity of NaOH on strength development in alkali activated low calcium fly ash. An experimental study is conducted using two different low calcium siliceous fly ashes. The influence of reactive alumina content is evaluated. The total silica in the activated system used for evaluation consists of the reactive silica contributed by fly ash and the activator solution. XRD based direct decomposition method was used to determine the glassy content and reaction product content in reacted systems.

2 MATERIALS AND METHODS

The fly ashes used in this study were directly collected from thermal power plants and labeled as A and B. A Microtrac S3500 laser particle size analyzer was used to determine the particle size distribution of the fly ashes. Mineralogical phases and reaction products were determined using D2 PHASER (BRUKER) benchtop automated X-ray diffractometer equipped with LYNXEYE super speed position sensitive detector. Cu-Kα-radiation was used. Scans were collected between 10 and 70^{o}and the scan rate was 0.6 step per second with the step rate of 0.02^o. The X-ray tube generator was operated at 30 kV and 10 mA. Quantitative phase analysis was performed using TOPAS 4.2 software with the NIST SRM 676a α-Al_2O_3 external standard. Crystal structure of known phases was taken from the inorganic crystal structure database.

The oxide composition of fly ashes was determined using Energy Dispersive X-Ray Fluorescence (ED XRF) and the values are listed in Table 1. Oxides in trace quantities are not reported. Based on the oxide compositions, the fly ashes conform to the requirements of siliceous fly ash as per the Indian Code of practice, IS 3812 [16]and Class F fly ash as per ASTM C 618 [17].The particle size distributions of the fly ashes are shown in Figure 1. There is a small difference in the particle size distribution of both the fly ashes.

Table 1: Oxide composition of the fly ashes (% mass).

Composition (%mass) / Label	A	B
Al_2O_3	26.06	31.40
SiO_2	58.14	48.81
Fe_2O_3	7.32	7.85
CaO	2.75	3.80
TiO_2	2.02	2.93
K_2O	2.17	1.52
MgO	1.12	0.70

The total glassy content and individual reactive oxide content of fly ashes were determined using the procedure outlined by the authors [8]. The reactive components of SiO_2

and Al_2O_3 were determined by subtracting the crystalline forms of SiO_2 and Al_2O_3 in the form of Quartz and Mullite (obtained from Rietveld refinement) from the total oxide contents (obtained from XRF). The total glassy content determined by subtracting the sum of the weight fractions of crystalline phases from unity. The obtained values are listed in Table 2. It can be seen that the fly ashes had very low reactive SiO_2 content. Fly ash A had higher in the reactive Al_2O_3 and SiO_2 Content than the fly ash B. These are the typical available fly ashes in India with very low lime and glassy content.

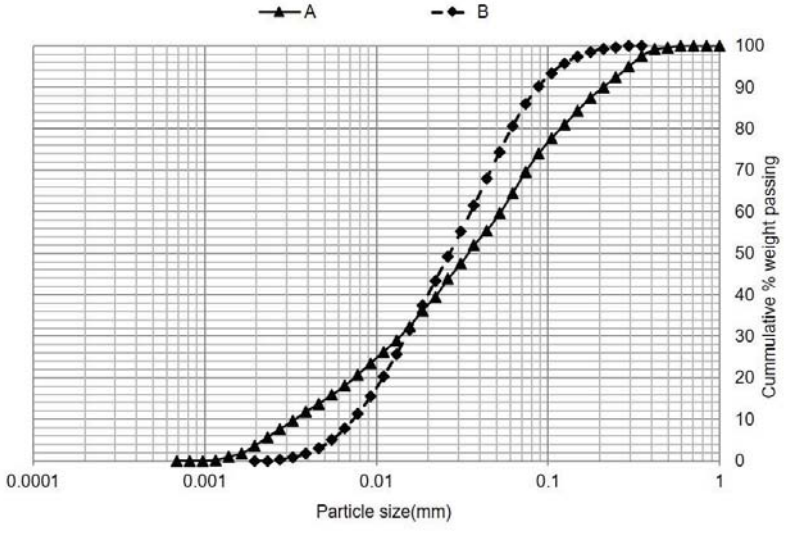

Figure 1: Particle size distribution of fly ashes.

Table 2: Reactive SiO_2 and Al_2O_3 contents and total amorphous content (% mass) of fly ashes.

Composition (% mass)	Al_2O_3	SiO_2	Total amorphous content
A	15.72	18.28	48.16
B	7.89	13.45	35.11

Due to the very low reactive SiO_2 content of fly ashes, additional silicates are required to produce a stable binder. Here, sodium silicate solution was used to increase the soluble SiO_2 content in the system. Along with the SiO_2content, sodium silicate will contribute Na_2O content to the system. The molarity and Sodium content in the system was adjusted using sodium hydroxide pellets.

The total reactive oxide ratios in the activated system were calculated using the reactive Al_2O_3 and the total reactive SiO_2 (total SiO_2) consisting of reactive SiO_2 from fly ash and SiO_2 obtained from sodium silicate solution. The SiO_2/Na_2O ratio was varied without affecting the Al_2O_3/ SiO_2 ratio. The total Na_2O content was calculated as the Na_2O content from sodium silicate solution and Na_2O obtained from NaOH. For a given fly ash, the total

reactive Al_2O_3 content contributed by fly ash is fixed. The molarity of NaOH was determined using its concentration in water. The increase in the sodium content is achieved decrease in the SiO_2/Na_2O ratio, which leads to the increasing the molarity of NaOH. The detailed experimental matrix is listed in Table 3. The two fly ashes have different reactive Al_2O_3, which allows or evaluating the role of reactive Al_2O_3 content.

Table 3: The Activated Solution and Total reactive oxide mix ratios of alkali activated fly ashes.

Mix label	Activated solution ratios		Total reactive oxide ratios	
	SiO_2/Na_2O	Molarity (M)	SiO_2/Na_2O	SiO_2/Al_2O_3
A-5.80	1.85	1.90	5.80	1.70
A-4.72	1.51	3.20	4.72	1.70
A-2.66	0.85	10.50	2.66	1.70
B-5.80	1.87	1.40	5.80	2.50
B-2.66	0.86	6.20	2.66	2.50

Sodium Hydroxide and Sodium silicates were used as an alkali activator to activate the fly ash. Solutions were prepared using 99% reagent grade sodium hydroxide pellets and Sodium silicate with the composition of 10.8% Na_2O, 30.5% SiO_2, and 41.3% H_2O. NaOH Solution was prepared with the required concentration of Na_2O content. After 24 hours, solution was mixed with the sodium silicate solution. The activator (the total mass of activating solution) to fly ash mass ratio was kept equal to 0.40. Fly ash was mixed with alkali solution using pan mixer till a uniform consistency of the paste was obtained. 7 cm cube specimens were prepared. All the samples were prepared at room temperature. Immediately after casting, all specimens were cured in a sealed condition for 24 hours at room temperature before being subjected to further curing at 60^{o}C with the relative humidity 95%. Compressive strength was measured from the cube samples at 3, 7, 14, and 28 days of age. After the completion of compression test, small samples were collected from the failed cube and ground to a smaller size (<60 μm) using mortar and pestle. To stop the further reaction, samples was washed with isopropanol. The isopropanol was then evaporated at 40^{o}C. The samples were then stored in a desiccator over silica gel in a Nitrogen atmosphere until testing.

3 RESULTS AND DISCUSSION

The compressive strength of alkali activated both the fly ash mixes cured at 60^{o}Cwith the age are shown in Figure 2. Results clearly indicate that the there is higher early strength and higher strength with increasing the sodium content. The A-2.66 mix achieved maximum strength at the age of 3 days after which there is little improvement in strength. The A-4.72 mix showed increment in strength till 7 days, after which there is a marginal increase. The strength of the A-4.72 mix is comparable to the strength of the A-2.66 mix. The A-5.80 mix showed steady increment in compressive strength till 28 days and showed a lower strength than the A-4.72 and the A-2.66 mixes. Based on these results, the optimum ratio of the SiO_2/Na_2O is in the range 4.72 to 2.66, since increasing the sodium content within this range does not appear to improve the ultimate strength. Considering the molar oxide ratios in the working solution and the total reactive oxide composition ratios (given in Table 3), results

indicate that the reactive oxide composition ratios are higher than the working solution ratios. The results here confirm the results of previous studies which indicate that the oxide ratios derived considering the reactive oxide contents from fly ash are important for the strength of the geopolymer than the ratio of oxides in the working solution [18]. The ratio of (total SiO_2)/Na_2O ratio in the range 4.72 to 2.66 and (total SiO_2)/Al_2O_3near to 1.70 along with the sufficient reactive Alumina content in the system produce stable geopolymer with the required compressive strength. Comparing the A-4.72 and A-2.66 mixes, beyond certain limit sodium content does not influence on the compressive strength.

Fly ash B mixes showed a lower compressive strength than the fly ash A mixes at any age. The B-5.80 showed lower in strength than the B-2.66 mix. Comparing both the fly ash mixes, the total reactive SiO_2 and Na_2O contents and the total reactive oxide ratios are almost same but the individual reactive Al_2O_3 content is different. Fly ash B had very low reactive Al_2O_3 content, which was almost half of the reactive Al_2O_3 in fly ash A. Due to this effect, fly ash B mixes developed lesser strength than the fly ash A mixes at identical oxide ratios. Reactive Al_2O_3 content which defines the ultimate compressive strength of the paste. Results clearly indicate that the reactive Al_2O_3 content is very important parameter along with the total reactive ratios on strength development of alkali activated fly ashes.

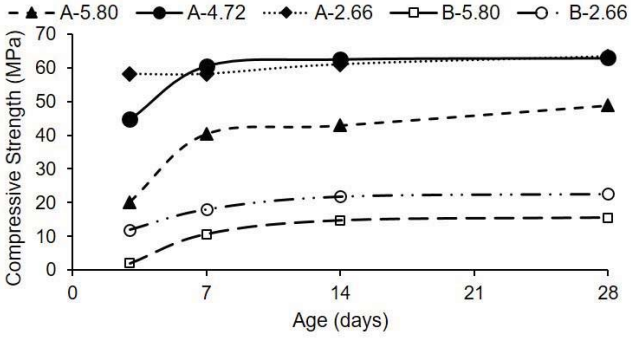

Figure 2: Compressive strength of alkali activated fly ash mixes cured at 60ºC with the age.

The X-ray spectrum of fly ash B and alkali activated fly ash B shown in Figure 3. There is a distinctive shift in the shape of the hump between the fly ash and alkali activated fly ash along with the different crystalline phases. The broad hump in the pattern is produced by diffuse scattering of the amorphous material in activated fly ash. The hump associated with the glassy content of fly ash is centered on lower 2θ angle (between 15-25º). After alkali activation the hump is shifted to higher 2θ angles (between 25-38º). XRD based direct decomposition method was used to quantify the unreacted glassy content and reaction product content alkali activated fly ashes as described by the authors [19]. The intensity contribution of individual amorphous components to the total intensity pattern of the amorphous phase is obtained by decomposition of the total intensity signature as a sum of fundamental underlying PV peak shapes using the unconstrained non-linear peak fit algorithm, as shown in the same Figure. Results of decomposition of the total amorphous phase into component PV peaks clearly indicate two distinct peaks; a peak at lower 2θ angle identified as PV fit-1 and the second peak at higher 2θ angles identified as PV fit-2. The use of additional peaks did not result in any improvement to the overall fit. The peak position PV fit-1 is centered on 2θ angle near to 22ºand PV fit-2 is centered on 2θ angle near 28º. Two

distinct peaks, a peak at lower 2θ angle associated with unreacted glassy content of fly ash and the second peak at higher 2θ angles produced by X-ray amorphous reaction products of alkali activated fly ash are clearly identified in the diffraction pattern of the total amorphous phase. The percentage of unreacted glassy content is determined as the proportion of the area under the intensity profile obtained from PV fit-1 to the area under the total intensity profile. The reaction product content is determined from the proportion of the area under the intensity profile obtained from PV fit-2 to the area under the total intensity profile.

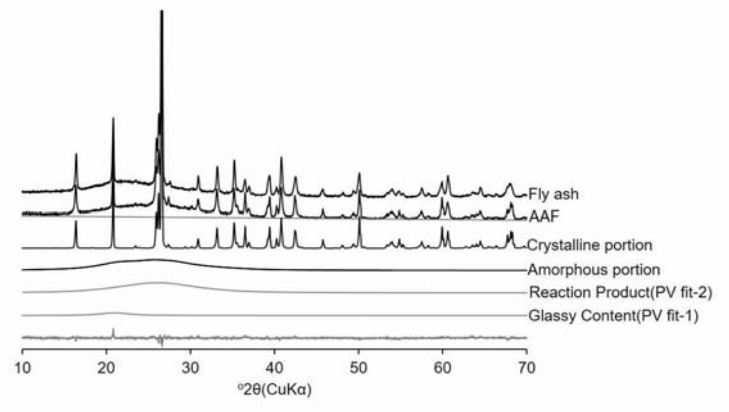

Figure 3: X-ray diffraction patterns of fly ash B and Alkali activated B-2.66 mix cured at 60°C at the age of 14 days. The total crystalline and the total amorphous content obtained after direct decomposition and the PV fits for the amorphous phase in each material shown in the figure. The difference curve is shown at the bottom of the plot.

The unreacted glassy content of the alkali activated fly ash mixes cured at 60°C with age shown in Figure 4. The unreacted glassy content is the amorphous content of fly ash associated with the glassy phase, which has not dissolved. There is a decrease in the unreacted glassy content of fly ash at any age with an increase in the sodium content. At 1 day, higher the molarity mixes (A-2.66 and B-2.66) showed lower glassy content than the other mixes. A-4.72 mix showed higher in the glassy content at 1 day than the A-2.66 mix and the glassy content steadily decreasing till 7 days. After 7 days of age A-4.72, A-2.66 mixes showed almost similar glassy contents. There is a considerable depletion of glassy phase observed till 14 days and there is a little change in the glassy content after 14 days. Almost total glassy content has been dissolved at the age of 28 days. The mixes with lower the molarity (A-5.80, B-5.80) exhibit a significant undissolved glassy content at the age of 28 days.

The one-day values of unreacted glassy content show a clear decrease with a decrease in the SiO_2/Na_2O ratio. In the activating solutions, a lower SiO_2/Na_2O ratio was achieved at the expense of higher molarity of NaOH. The results from the dissolution at 1 day indicates that on increasing the molarity of NaOH there is a very rapid early dissolution of glassy phase. The results from the dissolution at 3 days indicates that on increasing the molarity of NaOH there is a very rapid early dissolution of the glassy phase.AS per these results, it does not require higher molarity to dissolves glassy from fly ash. Molarity level depends on the total glassy content of the fly ash.

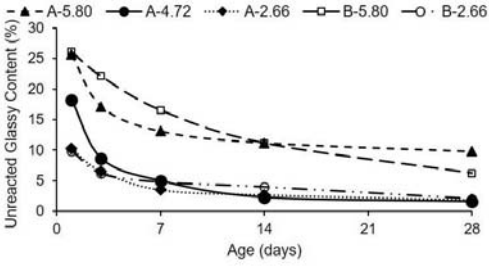

Figure 4: Unreacted Glassy Content of alkali activated fly ash mixes cured at 60°C with age

The reaction product content of the alkali activated fly ash mixes cured at 60°C with the age shown in Figure 5. Fly ash B mixes, which had lower the reactive Al_2O_3 content showed a smaller reaction product content than the fly ash A mixes. A-4.72 mix showed smaller reaction product content than the A-2.66 mix at the age of 3 days. After 7 days, the reaction product content in these two mixes is identical. A-5.80 mix showed smaller reaction product content than the A-4.72 mix and the A-2.66 mix. Comparing the both the fly ash mixes, the reaction product content depends on the reactive alumina content in the system since the other reactive contents and ratios are the same in both the mixes. The experimental results clearly show that the mixes with higher reaction product content and higher reacted glassy content exhibited higher compressive strength. Mixes with lower the strength had smaller reaction product content and higher unreacted glassy content. The quantity of the reaction product formed is therefore directly related to the extent of glassy phase dissolution.

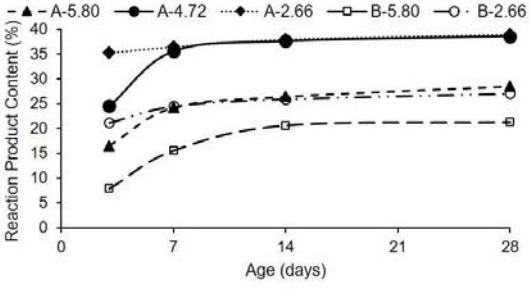

Figure 5: Amorphous reaction product content of alkali activated mixes cured at 60°C with age

4 FINDINGS AND CONCLUSIONS

In this study, the alkaline activation of low calcium fly ash is investigated. The influence of total reactive oxide ratios SiO_2/Na_2O and Al_2O_3/SiO_2 on the compressive strength of the activated fly ashes were evaluated. In calculating oxide ratios, the reactive Alumina and reactive silica obtained from fly ash were used. The reactive Al_2O_3 content of the fly ash has a direct bearing on the ultimate strength achieved from a given fly ash. The sodium content in the solution does not influence the development of compressive strength of paste beyond a certain dosage. The strength of the paste increases with the decreasing ratio of the SiO_2/Na_2O

ratio and the highest ultimate compressive strength is achieved for the ratio close to 2.66. Higher molarity of NaOH dissolves the glassy phases from fly ash very rapidly. The required molarity is therefore dependent on the total reactive Glassy present in that particular fly ash.

5 REFERENCES

[1] Cheng, T.W. and Chiu, J.P., 'Fire-resistant geopolymer produced by granulated blast furnace slag', Miner. Eng. 16 (2003) 205-10.

[2] Gao, K., Lin, K.L., Wang, D.Y., Hwang, C.L., Shiu, H.S. and Chang, Y.M. 'Effects SiO_2/Na_2O molar ratio on mechanical properties and the microstructure of nano-SiO_2 metakaolin-based geopolymers', Constr. Build. Mater. 53 (2014) 503-510.

[3] Hwang, C.L. and Huynh, T.P. 'Effect of alkali-activator and rice husk ash content on strength development of fly ash and residual rice husk ash-based geopolymers', Constr. Build. Mater.101 (2015) 1-9.

[4] Chindaprasirt, P., Rattanasak, U., Vongvoradit, P. and Jenjirapanya, S., 'Thermal treatment and utilization of Al-rich waste in high calcium fly ash geopolymeric materials', Int. J. Miner. Metall. Mater. 19 (2012) 872-878.

[5] He, J., Jie, Y., Zhang, J., Yu, Y. and Zhang, G., 'Synthesis and characterization of red mud and rice husk ash-based geopolymer composites', Cem. Concr. Compos. 37 (2013) 108-118.

[6] Fernandez-Jimenez, A and Palomo, A. 'Composition and microstructure of alkali activated fly ash binder: effect of the activator', Cem. Concr. Res. 35 (2005) 1984-92.

[7] Van Jaarsveld, J.G.S., Van Deventer, J.S.J. and Lukey, G.C., 'The characterisation of source materials in fly ash-based geopolymers', Mater. Lett. 57 (2003) 1272-80.

[8] Bhagath Singh, G.V.P. and Subramaniam, K.V.L., 'Quantitative XRD Analysis of Binary Blends of Siliceous Fly ash and Hydrated Cement', J. Mater. Civil Engineering (ASCE). 28 (8) (2016) 04016042 (1-7).

[9] Duxson, P., Fernandez-Jimenez, A., Provis, J.L., Lukey, G.C., Palomo, A. and Van Deventer, J.S.J., 'Geopolymer technology: the current state of the art', J. Mater. Sci. 42 (2007) 2917-33.

[10] Van Deventer, J.S.J., Provis, J.L., Duxon, P. and Lukey, G.C., 'Reaction mechanisms in the geopolymeric conversion of inorganic waste to useful products', J. Hazard. Mater. A 139 (2007) 506-513.

[11] Ryu, G.S., Lee, Y.B., Koh, K.T. and Chung, Y.S., 'The mechanical properties of fly ash-based geoploymer concrete with alkaline activators', Constr. Build. Mater. 47 (2013) 409-18.

[12] Alvarez-Ayuso, E., Querol, X., Plana, F., Alastuey, A., Moreno, N., Izquierdo, M., Fonta, O., Morenoa, T., Dieza, S., Vázquezb, E. and Barrab, M., 'Environmental, physical and structural characterisation of geoploymer matrixes synthesised from coal (co-) combustion fly ashes', J. Hazard Mater. 154(1) (2008) 175-83.

[13] Criado, M., Fernandez-Jimenez, A., De la Torre, A.G., Aranda, M.A.G. and Palomo, A. 'An XRD study of the effect of the SiO_2/Na_2O ratio on the alkali activation of fly ash', Cem. Concr. Res. 37 (2007) 671-679.

[14] Songpiriyakij, S., Kubprasit, T., Jaturapitakkul, C. and Chindaprasirt, P., 'Compressive strength and degree of reaction of biomass and fly ash-based geopolymer', Constr. Build. Mater. 24 (2010) 236-240.

[15] Jang, J.G. and Lee, H.K., 'Effect of fly ash characteristics on delayed high-strength development of geopolymers', Constr. Build. Mater. 102 (2016) 260-69.

[16] Bureau of Indian Standards, IS 3812-part 1, Pulverized Fuel Ash-Specification, 2003.

[17] ASTM, Standard C 618: Standard Specification for Coal Fly Ash and Raw or Calcined Natural Pozzolan for Use in Concrete, 2015.

[18] Bhagath Singh, G.V.P. and Subramaniam, K.V.L., 'Evaluation of Sodium content and Sodium Hydroxide Molarity on compressive strength of Alkali Activated low calcium fly ash', Cem. Concr. Comp. (2017) (Revision Submitted)

[19] Bhagath Singh, G.V.P. and Subramaniam, K.V.L., 'Quantitative XRD study of amorphous phase in alkali activated low calcium siliceous fly ash', Constr. Build. Mater. 124, (2016b) 139-147.

Application of Waste-Derived Lightweight Aggregates for Internal Curing of Concrete

Pietro Lura[1,2], Mateusz Wyrzykowski[2], Sadegh Ghourchian[1,2], Sakprayut Sinthupinyo[3], Clarence Tang[3], Natechanok Chitvoranund[3], Tipwimol Chintana[3] and Kritsada Sisomphon[3]

[1] Empa, Swiss Federal Laboratories for Materials Science and Technology, Switzerland

[2] Institute for Building Materials (IfB), ETH Zürich, Switzerland

[3] Siam Research and Innovation, SCG Cement–Building Materials, Saraburi, Thailand

Abstract

One of the common methods for reduction of early-age shrinkage of concrete is replacement of part of the aggregates with lightweight aggregates saturated with water, also called internal curing. In this work, different types of industrial waste (ashes) are employed as internal curing agents. The experimental study consisted of measurements of pore structure of aggregates, autogenous shrinkage and mechanical properties of mortars and concretes. Our results show that the waste-derived lightweight aggregates can considerably limit autogenous shrinkage of concrete. At the same time, even though the lightweight aggregates are porous materials that replace normal-weight sand, they do not lead to a considerable reduction of mechanical properties; on the contrary, even a strength improvement has been observed for some mixtures. Moreover, some types of lightweight aggregate can be added to concrete in the dry state without the need of prior water saturation.

1 INTRODUCTION

In high performance concrete (HPC), self-desiccation of the cement paste results in high capillary stresses that cause autogenous shrinkage. Restrained shrinkage may result in cracking and loss of durability of concrete structures even in the absence of external drying. For HPC with low water-to-cement ratio (w/c), resulting in low porosity and permeability, external curing is not sufficient to limit self-desiccation because the curing water is only able to penetrate several mm into the concrete. Instead of external curing, internal curing may be used, which consists in distributing small water reservoirs into the concrete mixture [1- 2]. The small, well distributed water pockets are able to release the water they contain locally and are thereby efficient in limiting self-desiccation. Water reservoirs that have been used in research and in field applications are porous lightweight aggregates (LWA) [3] and, to a lesser extent, superabsorbent polymers (SAP) [4].

The efficiency of LWA as internal curing agents depends on the water absorption and desorption. The LWA should ideally take up water rapidly when they are stored underwater before concrete mixing and release the water rapidly during concrete hardening. Most porous aggregates absorb significant amounts of water (about 10–30% by mass) thanks to their high porosity and well-connected pores [5]. However, not all LWA release the absorbed water rapidly and in sufficient amount to limit or avoid self-desiccation of HPC (see also [6]). Although recent work has shown that water has high mobility in hydrating cement paste in the first few hours to days [7-8], the water needs first to be rapidly released by the LWA while the internal RH is still high. The desorption behavior of LWA is a direct consequence

of their pore structure. It has been shown that LWA with coarse pore structure are better internal curing agents [9].

In this paper, the internal curing performance of different LWA, all based on industrial or agricultural wastes (ashes), is evaluated in terms of impact on the internal relative humidity, autogenous shrinkage and mechanical properties of high-performance mortars. In particular, the examined LWA are bottom ash and LWA produced from biomass-derived waste. The results presented in this paper derive from published [10-11] research by the authors.

2 MATERIALS AND METHODS

2.1 Materials

Internal curing agents

LWA produced from pelletization of sugar cane bagasse fly ash (bio-LWA) had particle sizes between 0.25 and 0.71 mm [10]. Bottom ash (BTA-P) derived from a stoker burning process had particle sizes between 63 μm and 0.71 mm [11].

Mortars

An ordinary Portland cement CEM I 42.5N was used. A polycarboxylate-based superplasticizer (SIKA Viscocrete 1S) replaced part of the mixing water (deionized water) in an amount allowing for obtaining similar spread (~170 mm after 15 shocks of the table) for all analyzed mixtures. The mixture composition is shown in Table 1. Different amounts of either bio-LWA or BTA-P were used based on their absorption (see Table 1) in order to introduce into the mixture the same amount of water. In one additional mixture, the BTA-P were also added in the dry state together with additional mixing water corresponding to their absorption potential.

The bio-LWA or the BTA-P replaced part of the NWA and the total aggregate volume was fixed at 40%. The NWA was alluvial sand composed of (by weight): sandstone 37%, limestone 37%, dolomite 18% and metamorphic rocks 8% with grain sizes 0.25 – 1.0 mm.

Table 1 Mix compositions of mortars.

Material	Mass [kg/m^3]			
	REF w/c 0.30	REF w/c 0.35	bio-LWA	BTA-P[a]
Cement	973.4	899.7	973.0	974.07
NWA (sand)	1063.8	1063.6	555.9	526.1
LWA	-	-	324.3	374.8
Mixing water	281.3	310.4	286.1	269.9
Water in LWA	-	-	48.6	48.7
Superplasticizer	10.7	4.5	5.8	22.4
w/c basic	0.30	0.35	0.30	0.30
w/c entrained	-	-	0.05	0.05
w/c total	0.30	0.35	0.35	0.35

[a] Both with BA added as presaturated and dry.

2.2 Methods

Density and water absorption

Density and water absorption in saturated surface dry (SSD) conditions was determined according to the standard ASTM C1761/C1761M–12. In this method, LWA are immersed in water for 72 h before the SSD condition is determined using a cone. The water absorption is referenced to dry state obtained after 24 h oven drying at 110°C.

Pore structure – MIP

In order to relate the desorption properties with the microstructure of the aggregates, Mercury Intrusion Porosimetry (MIP) was performed, which allows determining the equivalent size distribution of the pores [12]. The dry aggregates were inserted into the sample holder, which was first filled with mercury at pressures up to 200 kPa in a low pressure porosimeter (Pascal 140). At this pressure range, mainly the intergranular spaces were filled by the mercury. The sample was then moved to a high pressure porosimeter (Pascal 440) which reached intrusion pressures up to 200 MPa.

Desorption isotherms

The water desorption isotherms were determined with a VTI+ Dynamic Vapor Sorption (DVS) analyzer. Before performing the desorption tests, the samples were saturated with water for 24 ± 2 h. 30-100 mg of saturated LWA were placed in a sample holder and changes of mass due to water desorption were monitored continuously at different RH steps. At the end of each test, the sample was dried to constant mass at 105°C and 0% RH in order to obtain the reference mass for water-content calculations. The equilibrium condition for proceeding to the next RH step was set as 0.001% of the initial mass per 5 min.

Internal relative humidity

Measurements of internal RH in reference mortars and mortars with BTA-P and bio-LWA were performed using water activity HC2-AW sensors by Rotronic. Each mortar obtained from a single mixing was measured at two stations in parallel. The nominal accuracy of the sensors was ±0.8% RH. The sensors were calibrated at the beginning and at the end of each measurement with three saturated salt solutions with equilibrium RH in the range 98–85%. This procedure allowed reducing the difference between two sensors measuring the same mortar to below 0.5% RH. The temperature of the sample and the sensor was maintained at 20 ± 0.02 °C by means of tempered water circulating in the casings of the measuring chambers.

Right after mixing, the mortars were cast in sealed plastic containers. At the age of approximately 24 h the mortars were crushed into pieces of 2–5 mm. About 8 g of crushed mortar were inserted into sealed measuring chambers. The measurement continued until the age of 7 days.

Linear autogenous shrinkage

The linear autogenous shrinkage of mortars was measured using the corrugated tube method [13, 14]. The length change was measured on a stainless steel bench, which can accommodate three specimens in parallel, with two linear variable differential transformers (LVDTs) for each specimen. The measuring bench was placed in a tempered silicone oil bath at 20±0.1 °C. Duplicate samples from independent mixings were measured for each mixture; average results are presented in the graphs. Automatic measurements allowed recording the deformation starting approximately 1 h after mixing. Nevertheless, the results were zeroed at final set [13]. The setting times were estimated by Vicat needle on corresponding cement pastes (same composition as the mortars, but without aggregates).

Mechanical properties

The mechanical properties of the mortars were determined on 25×25×100 mm^3 prisms. The moulds were filled during 3 min vibration on a vibrating table. After casting, the samples were kept at >95%RH and 20 ± 0.3 °C for 1 d. At the age of 1 d, the samples were demolded and sealed by wrapping them in three layers of plastic wrap and closed into a tight plastic box. The sealed samples were stored at 90 ± 3% RH and 20 ± 0.3 °C. Compressive strength and Young modulus were determined at the ages of 1, 3 and 28 d. For the elastic modulus

measurements, 2 samples were tested at each age, while for strength 2 samples were tested at 1 d and 3 samples at 3 and 28 d.

As mentioned above, the strength was measured on two miniature samples for each mixture and age; the small number of samples and their reduced dimension were a consequence of the small volume of the mixing batch in the vacuum mixer. While the bending strength (reported in [11]) was measured on two prismatic samples, the compressive strength was measured on the four half-prisms that resulted from the bending tests. The procedure for strength measurements was based on the European standard EN 196-1, however using smaller samples (the standard prescribes 40×40×160 mm^3) and loading rate reduced in compressive strength tests to 0.5 kN/s (from the standard 2.4 kN/s). The static elastic Young modulus in compression was determined using a procedure based on the Swiss standard SIA 262-1 (similar to the European EN 12390-13 standard), with the compressive load equal to 25% of compressive strength and using smaller samples, suitable for mortars with fine aggregates.

The presented values are the average from the tested samples and the error bars represent 95% confidence intervals (normal distribution).

3 RESULTS AND DISCUSSION

3.1 Density and water absorption

The density and the water absorption of the LWA determined at SSD conditions are presented in Table 2. The BTA-P had slightly higher density and lower absorption than the bio-LWA. In [11], the kinetics of the water absorption of BTA-P were measured and it was noticed that more than 60% of all water absorbed within 24 h is absorbed already during the first 10 min. This rapid absorption suggested the possibility of employing dry BTA-P for internal curing. The BTA-P could be added to the mixture together with the surplus internal curing water that they are expected to absorb during concrete mixing, using a similar principle as employed with SAP [2, 4].

Table 2 Density and water absorption of LWA

LWA type	Dry density [kg/m^3]	Absorption at 24 h [g/g]
bio-LWA	1700	0.15
BTA-P	1868	0.13

3.2 Pore structure and desorption isotherms

The pore size distributions and the desorption isotherms of the LWA are shown in Fig. 1. The BTA-P had higher porosity and larger pores than the bio-LWA (Fig. 1a). It should be noted that the 200 MPa used as maximum intrusion pressure allowed accessing pores of equivalent radii larger than approximately 4 nm. For the BTA, this pressure may have not allowed to intrude the whole pore volume, which is supported by the fact that the pore size distribution did not reach a plateau at the highest intrusion pressures, (Fig. 1 a). In the BTA, a substantial amount of pores had equivalent entrance radii larger than 100 nm. The bio-LWA had slightly finer pores, with a majority between 100 and 30 nm. A further analysis based on multi-cycle MIP [12] (results shown in [10, 11]) reveals that most of the pores in the bio-LWA were ink-bottle pores, accessed only through pores with smaller radius. Also the BTA had a majority (about 70%, against the 90% of e.g. bio-LWA) of ink-bottle pores. It is expected that only the pore volume accessed through larger pores (larger than about 50-100 nm) might be useful for storing internal curing water. In fact, smaller pores would not be able to release the water at the high RH levels needed to avoid or limit autogenous shrinkage.

The results of the desorption isotherms presented in Fig. 1b appear to support this hypothesis. Both bio-LWA and BTA released a substantial amount of water already at 97-98% RH. Moreover, while the bio-LWA were almost empty by 97% RH, the BTA retained a part of the absorbed water down to 70% RH and below. This could be explained by the presence of both large and small pores in the BTA, as suggested by MIP.

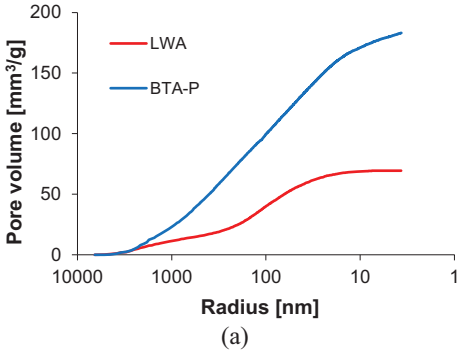

(a)

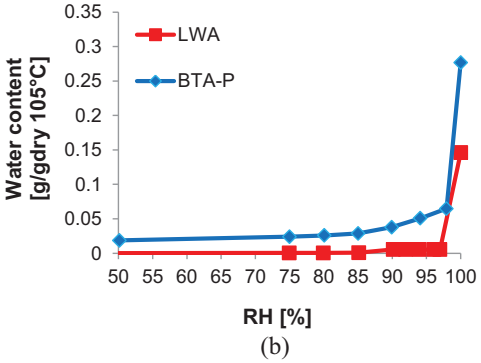

(b)

Figure 1 a) MIP equivalent pore size distributions (cumulative curves); b) desorption isotherms.

3.3 Internal relative humidity and autogenous shrinkage

In Fig. 2a, the internal RH evolution in the mortars is presented, while the deformation in autogenous conditions, referred to the length at final set determined with the Vicat needle, is shown in Fig. 2b. The addition of both BTA-P and bio-LWA is keeping the internal RH considerably higher (especially in the first few days) compared to the reference mortar with w/c 0.30 (Fig. 2a). The RH is also higher than in the mortar with the same total amount of water, which supports the correctness of the principles at the basis of internal curing [1, 2]. The autogenous shrinkage is strongly reduced in both mortars with BTA-P and with bio-LWA (Fig. 2b). It is noticeable that the two reference mortars differ only in the first day but have similar shrinkage rate afterwards, while the mortars with internal curing both show an initial expansion and a subsequent lower long-term shrinkage rate. The addition in the dry state of the BTA-P resulted in keeping the internal RH slightly higher, while the autogenous shrinkage was almost the same. Based on these results and others shown in [10, 11], it is possible to conclude that both BTA and bio-LWA are both efficient internal curing agents.

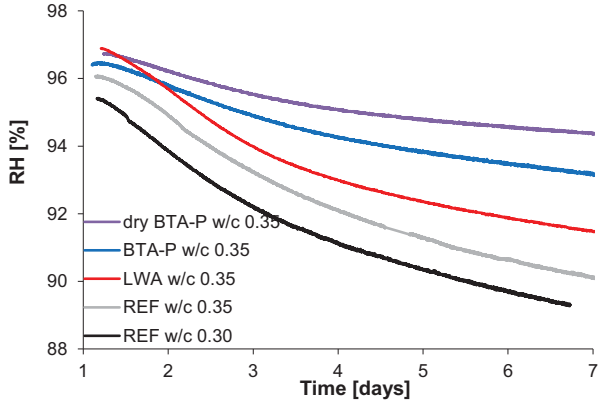

(a)

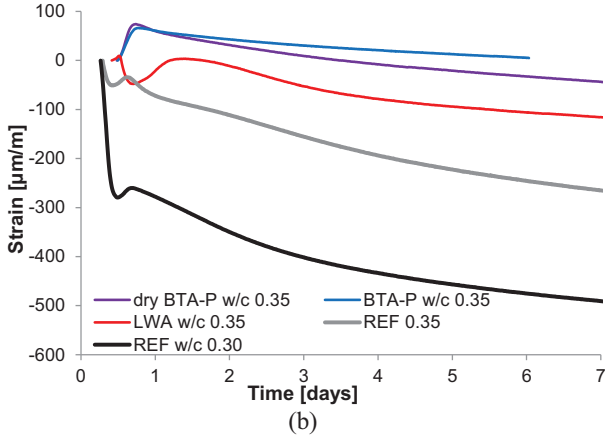

(b)

Figure 2 a) Evolution of internal RH in reference mortars and mortars with BTA and bio-LWA. b) autogenous deformation of mortars with BTA and bio-LWA.

3.4 Mechanical properties

Fig. 3 displays the mechanical properties of the mortars prepared with addition of either presaturated or dry BTA-P. A partial replacement of NWA by BTA-P does not lead to any significant compressive strength reduction (Fig. 3a) compared to mortar REF w/c 0.30 with the same basic w/c as the tested mortars (thus excluding the water introduced within the BTA-P), while the strength of the REF w/c 0.35 mortar with the same total w/c (basic w/c resulting from mixing water plus entrained w/c resulting from water absorbed by the BTA) is generally lower. The elastic modulus (Fig. 5b) is lower in the mortars with BTA, since they replace a part of the NWA with substantially higher modulus.

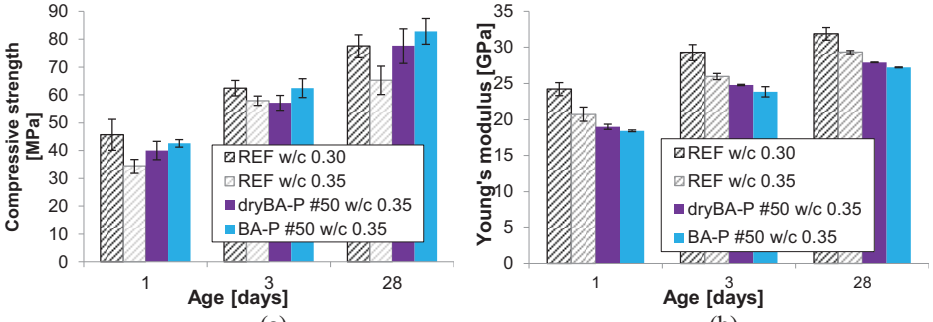

Figure 3 Mechanical properties of mortars with BTA-P: a) compressive strength, b) elastic Young modulus. Error bars indicate 95% confidence intervals (normal distribution).

4 CONCLUSIONS

In this study, the porosity, the absorption and desorption of two different LWA types, a LWA produced from pelletization of sugar cane bagasse fly ash (bio-LWA) and a bottom ash from burning of wastes in the paper industry, obtained in a stoker burning process (BTA-P) were characterized. Both types of LWA show high open porosity and high water absorption (13-15% by mass). Both had a steep desorption curve at high RH, losing most of the water already above 97-98% RH. The pore structure of these LWA makes them particularly useful for delivering water into hydrating high-performance concrete by means of so-called internal curing.

Internal RH measurements in high-performance mortars show that the RH decrease due to self-desiccation can be considerably reduced if these types of LWA are added, which leads to almost eliminating autogenous shrinkage in the first week of hydration. In the case of the BTA-P, the internal curing performance was almost unaltered when the LWA were added dry, with extra water to compensate for their absorption. This is a very useful solution in practice, since it eliminates the need for lengthy and costly presaturation of the LWA.

The compressive strength of mortars with BTA-P was very similar to the reference mortar without LWA, while the elastic modulus was only slightly reduced.

This study demonstrates that LWA derived from waste materials can be efficient for internal curing, if they are appropriately selected based on high absorption and coarse porosity.

5 ACKNOWLEDGEMENTS

This research was funded by Siam Research and Innovation and by Empa.

6 REFERENCES

[1] D. P. Bentz, K. A. Snyder, Protected paste volume in concrete: extension to internal curing using saturated lightweight fine aggregate, Cem. Concr. Res. 29 (11) (1999)1863-1867.

[2] O. M. Jensen, P. F. Hansen,Water-entrained cement-based materials: I. Principles and theoretical background, Cem. Concr. Res. 31 (4) (2001) 647-654.

[3] A. Bentur, S. I. Igarashi, K. Kovler, Prevention of autogenous shrinkage in high-strength concrete by internal curing using wet lightweight aggregates, Cem. Concr. Res. 31 (11) (2001) 1587-1591.

[4] O. M. Jensen, P. F. Hansen, Water-entrained cement-based materials: II. Experimental observations, Cem. Concr. Res. 32 (6) (2002) 973-978.

[5] J. Castro, L. Keiser, M. Golias, J. Weiss, Absorption and desorption properties of fine lightweight aggregate for application to internally cured concrete mixtures, Cem. Concr. Compos. 33 (10) (2011) 1001-1008.
[6] O. M. Jensen, P. Lura, Techniques and materials for internal water curing of concrete, Mater. Struct. 39 (9) (2006) 817-825.
[7] P. Trtik, B. Münch, W. J. Weiss, A. Kaestner, I. Jerjen, L. Josic, E. Lehmann, P. Lura, Release of internal curing water from lightweight aggregates in cement paste investigated by neutron and X-ray tomography, Nucl. Instrum. Methods Phys. Res. A 651 (1) (2011) 244-249.
[8] M. Wyrzykowski, P. Lura, F. Pesavento, D. Gawin, Modeling of water migration during internal curing with superabsorbent polymers, J. Mater. Civ. Eng. 24 (8) (2012) 1006-1016.
[9] S. Ghourchian, M. Wyrzykowski, P. Lura, M. Shekarchi, B. Ahmadi, An investigation on the use of zeolite aggregates for internal curing of concrete, Constr. Build. Mater. 40 (2013) 135-144.
[10] P. Lura, M. Wyrzykowski, C. Tang, E. Lehmann, Internal curing with LWA produced from biomass-derived waste, Cem. Concr. Res. 59 (2014) 24-33.
[11] M. Wyrzykowski, S. Ghourchian, S. Sinthupinyo, N. Chitvoranund, T. Chintana, P. Lura, Internal curing of high-performance mortars with bottom ash, Cem. Concr. Comp. 71 (2016) 1-9.
[12] J. Kaufmann, R. Loser, A. Leemann, Analysis of cement-bonded materials by multi-cycle mercury intrusion and nitrogen sorption, J. Colloid Interface Sci. 336 (2009) 730-737.
[13] ASTM, ASTM C1698-09 Standard test method for autogenous strain of cement paste and mortar, ASTM International, West Conshohocken, PA, 2009.
[14] O. M. Jensen, P. F. Hansen, A dilatometer for measuring autogenous deformation in hardening portland cement paste, Mater. Struct. 28 (1995) 406-409.

Sustainability Study on Self-Compacting Concrete in-built with Raphanussativus as an Efficient Internal Curing Agent

Rampradheep G. S(1), Sivaraja M(2), Geetha M(3), Raghupathy S(4), Ragasudha P(4)

(1)Department of civil engineering, Kongu engineering college, Erode, Tamil Nadu

(2)N.S.N. College of Engineering and Technology, Karur, Tamil Nadu, India-639603.

(3)CSI polytechnic college, Salem, Tamil Nadu, India- 636007.

(4)Department of civil engineering, Kongu engineering College, Erode, Tamil Nadu

ABSTRACT

Compaction and curing is found to be the most essential role in construction to achieve better sustainability. An attempt has been made on natural compound from the ground called Radish also termed as Raphanussativus, as a self-curing agent in self-compacting concrete. The main genesis beyond the intention of radish as a self-curing agent is the presence of bond water and its effectual existence of hydroxyl and ether group in a chemical structure of radish family. The design grade of concrete was affixed as M40 and its conceived procedure for such modernistic concrete was merely based on trial and error and its final upshots were verified with the EFNARC specifications. The agent used for robotic curing at the start was inspected to probe its water retention capacity. Expository study was retrieved using Fourier transform infrared (FTIR) spectrum analyser. Various tests were composed to scrutinize the workability properties, mechanical properties and durability properties of the concrete. Footprints proved that alike poly-ethylene glycol (PEG) and other curing agents, extract from radish is also a powerful curing agent and upswing the cement hydration, minimizes shrinkage and tweaks the durability of concrete whereas the conventional methods necessitates improvement.
Keywords: Radish, compaction, curing, poly-ethylene glycol, durability, shrinkage

1 INTRODUCTION

Over the last few decades, a great deal of interest has been shown in the study of making concrete better by the process of incorporating specifically engineered ingredients and simulating the methods of batching and mixing. Compared to traditional concrete, modern types of concrete are highly advantageous in as much as they provide good workability in the fresh state, possess high strength and low permeability. However, these types of concrete have also shown to be more sensitive to early age cracking than traditional concrete. High performance concrete, falling into the category of the so-called modern concrete, is essentially characterized by a cement matrix with low water/cement ratio (w/c), often including mineral additions like silica fume and the use of admixtures as super plasticizers [1]. One of the major problems with these mixtures is their tendency to undergo early age cracking. While this cracking may or may not compromise the compressive strengths of these concretes, it likely does compromise their long-term durability. Concrete with internal curing may also have evolved from the concept of self-curing concrete, which is based on the introduction of a chemical admixture that is able to reduce water evaporation by a retaining

function. The addition of a self-cure chemical based on a water-soluble polymeric glycol lead to improved durability of concrete cured in air [2]. However, the performance of such admixture does not attain the efficiency of the water film curing [3]. In high performance concrete, capillary discontinuity may significantly delay and even limit the water movement throughout the system. This makes the use of water ponding or other external curing methods inefficient in assuring the continuous internal moisture of the material. In this case, the use of internal curing methods may be required to counteract autogenous deformation. As there is only little experience on the practical use of internal curing methods to improve early-age properties of high performance concrete, the subject constitutes great challenge to technicians and industrialists of the modern age [4].

2 EXPERIMENTAL INVESTIGATION

2.1 Materials used

Concrete was cast with basic ingredients of OPC 53 grade that confirms to IS: 12269-2013 [5], Class F Fly ash based on ASTM C 618 [6] and aggregates that confirm to IS: 383-1970 [7]. Potable water free from salts was adopted to mix the concrete ingredients for the design mix. Radish extract (SO) was used as a natural curing agent and the outcomes were compared with poly-ethylene glycol (PEG), the existing curing agent and the conventional cured concrete which involves full / immersion curing (FC) and sprinkler curing (SPRC). Figure 1 shows the presence of hydroxyl ion for PEG and SO under FTIR. The presence of OH ions can be viewed from the molecular structure of SO as shown in Figure 2. Extract from radish is shown in Figure 3.

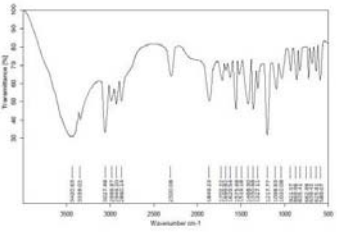

Figure1: Presence of OH – SO

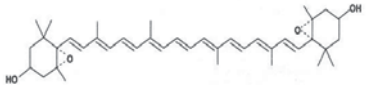

Figure 2: Molecular structure of SO

Figure 3: Radish extract

2.2 Mix Proportion

The mix was designed to convince the performance norms of the both fresh and hardened concrete. Here, as per EFNARC identification [8] to gain medium strength self-compacting concrete of grade M40, with 2% of MGS were used. Specimens with optimised content of poly-ethylene glycol (PEG), super absorbent polymers (SAP), external coating Paint (ECP), Potable Water Treatment Plant Sludge (PWTS), light weight aggegate (LWA - Vermiculite), radish extract (SO), liquid paraffin wax (LPW) were added and its individual effect has been observed with conventional concrete under full/immersion cured and sprinkler cured concrete.

2.3 Curing and Testing of Specimens

The optimized percentage of internal curing agents used in cement paste were analysed for DSC & TGA analysis and diffusion co-efficient. Similarly, the concrete under various internal curing agents and control / conventional concrete were tested for long term properties like RCPT, Accelerated corrosion test and autogenous shrinkage test in order to analyze the sustainability behaviour.

2.4 Self – Desiccation Analysis

The fresh condition of cement paste was analyzed with respect to ages to examine the water holding capacity for the optimized percentage of mix with various self-curing agents.

2.5 DSC & TGA Analysis

The DSC and TGA analysis stands for Differential Scanning Calorimeter and Thermo-gravimetric Analysis as shown in Figure 4. It is the technique meant to evaluate the mass loss behaviour of the cement paste sample in-built with and without self-curing admixtures. This test also helps to compute the water retention capacity (or) resistance to self-desiccation of the sample with self-curing agents and in order to make the analysis, the cement pastes with and without internal curing admixtures is made. The self-curing agent is prepared at a concentration of 0.1 M and it is well mixed with cement paste having designed water. In controlled mix, only the plain cement paste is tested without the addition of any internal curing agents but with the well addition of stabilized and constant made self-compacting admixture. Ten sets of beakers 56 mm diameter and 70 mm height are taken and are well segregated into two sets, five for designed/target concrete and the remaining for control concrete. A small quantity of cement, say 100 gm well mixed with designed water and prepared internal curing agent with 0.1 M, was poured into the beaker. The test was carried out under constant room temperature and humidity say between 32°C and 90%. A pinch of

freshly made paste with and without agent is taken and placed in the calorimeter to make the thermo-gravimetric analysis of the sample. It is performed under consistent increment of 10°C / minute upto the designed temperature of 1000°C in sequenced refreshed nitrogen. The values of bound and evaporable water could be obtained from the calorimetric analysis at the ages of temperature. Temperature vs mass loss analysis is made and the output delivers the residual mass percentage of the material. In respect to that analysis, the diffusion co-efficient has been calculated as per Dhir et al. (1998) method [3] of analysis given in Equation 1,

$$D^* \times 106 = 218.7 \left(\frac{db^*}{Mew}\right) \text{ in } m^2/s \quad (1)$$

where, d is the thickness of specimen, b* is the slope of the line produced by plotting mass loss vs. time, and M_{ew} is the mass of evaporable water.

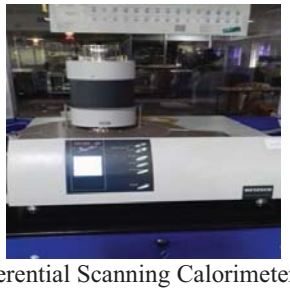

(a) Differential Scanning Calorimeter

(b) Sample under analysis

Figure 4: DSC & TGA Analysis

2.6 Rapid Chloride Penetration Test

RCPT is a non-destructive technique used to examine the chloride permeability of in-place concrete. Researchers developed the test procedures that are currently specified in AASHTO T277 [9] and ASTM C1202 [10]. A 50 mm specimen cut from the sample of 100 mm diameter core was tested. The side of the cylindrical specimen was coated with epoxy, and after the drying of epoxy, the specimen was placed in a vacuum chamber for 3 hours and vacuum saturated for 1 hour and allowed to soak for 18 hours. It was then placed in the test device called acrylic cell. The left-hand side (–ve) of the test cell is filled with a 3% NaCl solution. The right-hand side (+ve) of the test cell is filled with 0.3M NaOH solution. A 60 V potential was applied for 6 hours. Readings tabulated at intervals of 30 minutes for 6 hours. The amount of coulombs passed through the specimen is calculated after the removal of the specimen. Figure 5 shows the measurement of permeation of chloride ions. The total charge Q passed in 6 hrs is calculated as per the Equation 2,

$$Q \text{ (in Coulombs)} = 900 \times (I0 + 2\times I30 + 2\times I60 + 2\times I120 \text{ .....} + I360) \quad (2)$$

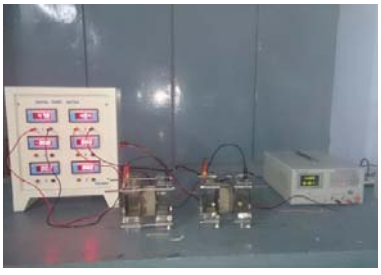

Figure 5: RCPT Analysis

2.7 Accelerated Corrosion Test

The corrosion test is the phenomenon of assessing the gradual deterioration of steel under the application of external current as per ASTM C 876 specifications [11]. Steel rod of specific diameter under the study was embedded into the concrete cube of size 100 mm with 20 mm as a cover thickness. The specimen then immersed into the container with 5% of NaCl diluted well into one litre of water with a steel sheet of very fine thickness perfectly surrounding the RCC specimen. The positive end of the supply was connected to the steel sheet and negative one to the steel in concrete with external supply of 12V. The behaviour analyzed for six days. The corrosion in embedded steel was measured using Half-Cell potential meter. The corrosion test on concrete and its interpolation analysis are shown in Figure 6.

(a) Corrosion cell connected to meter

(b) Half-Cell Potential analysis

Figure 6: Accelerated Corrosion Test

2.8 Autogenous Shrinkage Test

A specimen which deforms in a fresh state under self condition with respect to the atmospheric condition is called autogenous shrinkage. It is effectively computed by ASTM C 1698-09 code of practice [12]. A specimen of freshly mixed paste or mortar was prepared using a corrugated mould that offers little resistance to length change of the specimen. The mould is sealed to prevent moisture loss and the specimen is stored at constant temperature.

The change in length is recorded at regular time intervals until the designated age using a dilatometer and the autogenous strain calculated using the changes in length and original length. The set up accessories and test progress are shown in Figure 7.

Figure 7 : Autogenous Shrinkage Test

3 RESULTS AND DISCUSSION

3.1 Self-desiccation Analysis

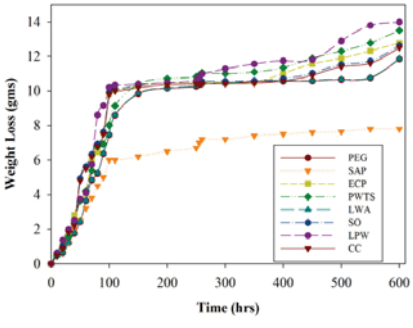

Figure 8 : Weight loss Vs Time

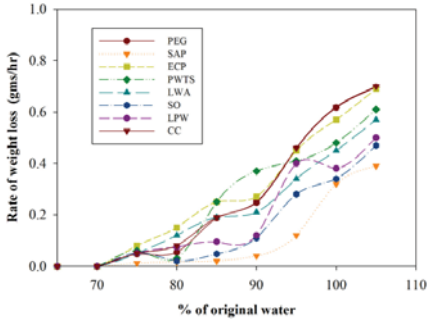

Figure 9 : Rate of weight loss vs. % of original water

Figure 8 indicates the compiled weight loss vs. time graph which analyzed for 28 days in terms of hours. Weight loss was found to be 5.28% for SAP, 7.35% for ECP, 12.29% for PWTS, 0.25% for LWA, 6.25% for SO, 15.30% for LPW. It is found that there is an increase in mass loss of 0.5% for PEG with respect to SAP. The reduction in loss for SAP is due to quite efficient hydration as there is a considerable evolution of heat under various time intervals. The reason for slight increase in weight loss for other curing agents with respect to SAP is due to slender variation effect under heat evolution and the binding of water by chemical mode during hydration.

The rate of weight loss with respect to quantity of original water added is depicted in Figure 9. It clearly indicates there is a fluctuation in turnout, as ultimate the matrix with curing agents shows lesser release rate under various percentage of mix water than the paste without any curing agent. The reduction in percentage of weight loss with respect to original water present are 12.5% with SAP, 50.87% with ECP, 46.66% with PWTS, 37.77% with LWA, 17.64% with SO, 26.31% with LPW and 54.83% for PEG. It is found that there is a reverse phenomenon between the cement paste with PEG and SAP, as the quantity of weight loss is considerably higher for PEG with SAP at a lower rate but the degree of loss when

compared for PEG is small with SAP, because of capillary pore reduction as effectively filled by the perfect humidity. But in overall, the CC behaves the increase in rate of weight loss compared to the mix with curing agents.

3.2 Diffusion Co-efficient Analysis

From Figure 10 (a), it is clear that the decrease in diffusion co-efficient is observed with increase in time period and the proportional decrement is noticed for paste without curing agent than the paste with curing agent. In detail, it is found that the increase in diffusivity for conventional mix was 75% with PEG, 61.11% with SAP, 56.94% with ECP, 43.06% with PWTS, 38.88% with LWA, 73.61% with SO and 19.44% with LPW. The above condition is reversed for the co-efficient analysis with respect to moisture content as found from Figure 10 (b). It is clear that the increase in moisture content leads to increase in diffusion co-efficient but the paste with curing agent posses less diffusion co-efficient than paste without curing agent. In addition, the increase in percentage of conventional mix is found to be 83.33% with PEG, 35.26% with SAP, 69.55% with ECP, 10.89% with PWTS, 7.6% with LWA, 67.31% with SO and 67.63% with LPW respectively. This condition attributes to perfect homogeneity in the mix comparable to the ordinary mix.

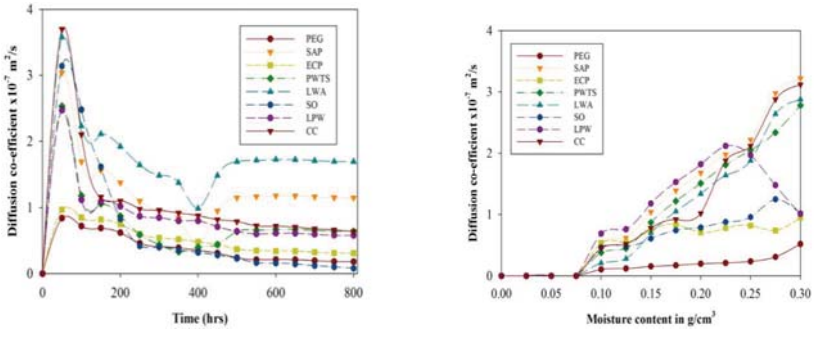

(a) Time vs. Diffusion co-efficient (b) Moisture content vs. Diffusion co-efficient

Figure10: Diffusion co-efficient Analysis

3.3 Rapid Chloride Permeability Test

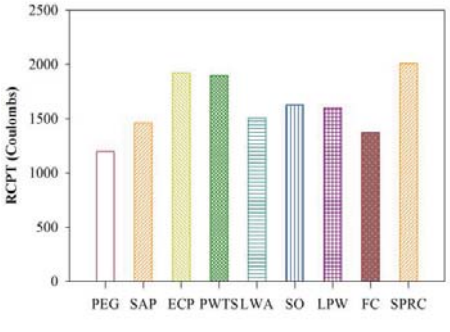

Figure 11: Curing agents vs. Charge passed

From Figure 11, it is noticed that the values under RCPT under different curing agents including FC is subjected to 'Low' permeability condition as the condition falls between 1,000 to 2,000 as per ASTM C 1202. The presence of very slight pores in negligible percentage of low heat of evolution resulted in better hydration for the hardened specimen irrespective of type of curing agents. For the concrete under SPC, since the output falls between 2,000 to 4,000, it is categorized as 'Moderate' because the presence of micro pores is found to be slightly higher. So, it is not advisable for sprinkler curing technique during the construction activities.

3.4 Accelerated corrosion test

From Figure 12, it is estimated that the average corrosion rate for all specimens is less than 200 mV, nil corrosion was observed. The reduction in corrosion rate is due to the high resistance effect of pores to the harmful agencies as it results by the closure of pore mouth by C-S-H under subsidiary age of concrete.

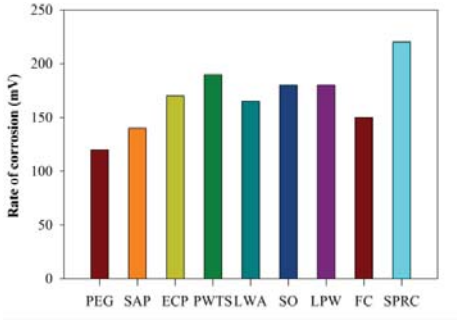

Figure 12: Curing agents vs. Rate of Corrosion

3.5 Autogenous shrinkage of cement paste

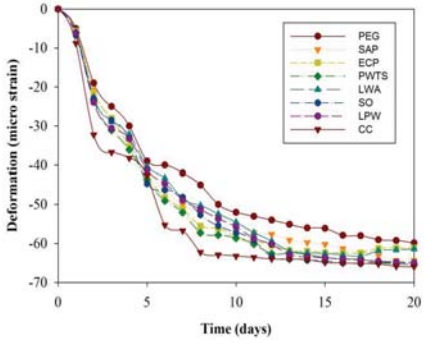

Figure 13 : Curing agents vs. Linear Deformation in Concrete

From Figure 13, it is found that the specimens with curing agents and immersion curing are experienced from very slight differential shrinkage. In ultimate, the effect due to autogenous shrinkage strain is found to be very negligible, as it does not affect the characteristics of concrete. The reason in reduction in overall effect of shrinkage is due to perfect interior bonding of elements inside the mix, thus prevented the elongation of element with respect to age.

3.6 Micro-structural Properties

The broken specimens from compression test under various modes and optimized percentage of curing is taken in an air and water proof cover and it is well sealed. A small quantity of the broken sample from SCSCC (Self-Compacting Self-Curing Concrete) and CC (Conventional Concrete), coated with gold was left free for half-an-hour to enhance complete bonding with the grain in order to achieve perfect out pack during the test. Closing the outer box of the machine, interior nature of the sample was examined through system connected interface. Figure 14 (a) shows the hydrated products by the reaction with basic ingredients. This may attribute to arrest of pores and thereby prevent the ultimate deterioration.

From Figure 14 (b), clearly indicates the unhydrated products due to free water deficiency. It results in formation of fault plane and debonding effect, as it leads to the further development of hair cracks in Interfacial Transition Zone (ITZ). Over evaporation condition of mix water followed by drying of core structure inside the concrete, provided a path for ingress of external agencies.

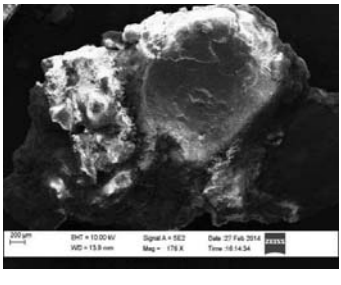

(a) SCSCC

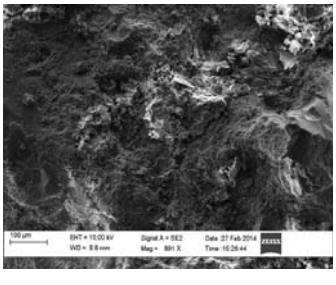

(b) CC

Figure 14: SEM Image for Concrete

4 CONCLUSIONS

From the various tests on water retention and durability properties in cement paste and concrete, the following conclusions are drawn.

The concrete with self-curing agents show reliable performance with immersion curing and superior behaviour to sprinkler curing. The humidity profile for SCSCC is better compared to conventional cement paste mix and negligible bleed water was experienced. All the specimens experienced very negligible chloride permeability. The percentage of porosity and permeability is inconsiderable for SCSCC than normal concrete. Plastic shrinkage values

are very negligible for cement paste with various curing regimes than values obtained for conventional mix. The presence of gel formation in SCSCC indicates efficient matrix than the observation from conventional concrete.

5 REFERENCES

[1] Bentz, D.P. and Snyder., K A., 'Protected paste volume in concrete: extension to internal curing using saturated lightweight fine aggregate', Cement and Concrete Research, 29 (11)(1999)1863-1867.

[2] Dhir, R K, Hewlett, P C & Tom Dyer, 'Durability of self-cure concrete', Cement and Concrete Research, 25(6) (1995) 1153-1158.

[3] Hewlett, P C, Tom Dyer & Dhir, R K, 'Mechanisms of water retention in cement paste containing self-curing agent', Magazine of Concrete Research, 50 (1) (1998) 85-90.

[4] Lee, H K, Lee, K M &Kim B G, 'Autogenous shrinkage of high-performance concrete containing fly ash', ICE Virtual Library – Magazine of Cement Research, 55(6) (2003) 507-515.

[5] IS: 12269-2013, 'Indian Standard for Ordinary Portland Cement, 53 Grade - Specification ', Bureau of Indian Standards, New Delhi – 110 002.

[6] ASTM C 618: 1997 'Standard Specification for Coal Fly Ash and Raw or Calcinated Natural Pozzolan for Use in Concrete', PA: American Society for Testing and Materials, Philadelphia.

[7] IS: 383-1970, 'Indian Standard Specification for Coarse and Fine aggregates from Natural Sources for Concrete', Reaffirmed 2002, Bureau of Indian Standards, New Delhi –110 002.

[8] EFNARC 2002, 'Specifications and Guidelines for Self-Compacting Concrete', EFNARC, Association House, 99 West Street, Farnham, Surrey GU9 7EN, UK.

[9] AASHTO T277 / 83, 'Standard Method of Test for Rapid Determination of the Chloride Permeability of Concrete', American Association of States Highway and Transportation Officials, Standard Specifications - Part II Tests, Washington, D. C., 1990.

[10]ASTM C 1202, 'Electrical Indication of Concrete's Ability to Resist Chloride Ion Penetration', Annual Book of American Society for Testing Materials Standards, West Conshohocken.

[11]ASTM C 876, 'Standard Test Method for Half-Cell Potentials of Uncoated Reinforcing Steel in Concrete', ASTM International, West Conshohocken.

[12]ASTM C 1698-09, 'Standard Test Method for Autogenous Strain of Cement Paste and Mortar', ASTM International, West Conshohocken.

Latest Technologies for Industrial Concrete Floors; an International Overview

C. Cortinovis[(1)], M. Velikettil[(2)] and Lee Brockway[(3)]

[(1)]RCR Industrial Flooring sàrl, Spain

[(2)]Monofloor India Pvt Ltd, India

[(3)]Permaban Ltd, ACIFC, UK

Abstract

The evolution of logistics, boosted by e-commerce and the raising requirements of industries (JIT, total quality) are changing the flooring industry. The flooring companies have to move from subcontracting labour for general contractors and become responsible contracting experts. In order to adapt, this industry needs to build faster and cheaper technical floors with higher durability. These concrete slabs will need to resist abrasion generated by intense traffic, to be flatter to allow higher storage, to minimize exposed joints and last but not least to look good. This article is demonstrating new ways to deal with the needs of modern logistics and of several demanding industries:

- Load transfer and impact reduction of construction joints
- Volumetric restrained shrinkage of concrete
- Special surface coatings for abrasion resistance and aesthetics of concrete slabs

It describes latest innovations of the industry which are not only products but different approaches from conception to execution techniques, QC and surveys. The presentation will be done by experts with international experience and based on real projects executed in various continents (Europe, Latin America, Africa and Asia).

Keywords: Industrial floor, concrete reinforcement, shrinkage compensated concrete, jointless slabs, surface hardeners, logistics.

1 INTRODUCTION

The industrial floors have always been considered of minor interest by the academic world and in general by the construction industry. Very few specific courses have been developed in universities and by engineering schools. The explanation of this lack of focus is that in most cases floors on grade (FOG) are not structural elements of the structure. Therefore, defects or failures during conception or execution will never have structural consequences and will not threaten the integrity of the building and of the people working inside.

This purely constructive approach disregards the economic consequences of defects for the final user. The interaction between the process of the logistics operators or the production manager and the industrial floor is constant. The main solicitations from the user's processes and the building are with the floor. Any defect due to a lack of consideration of those interactions will result in severe problems in efficiency:

- Reduction of the productivity
- Downtimes
- Direct and indirect costs of maintenance and repairs

Several initiatives have brought significant technological developments for the conception and execution of concrete floors.

The evolution of equipment is reducing the human factor and helping to shift from heavy burden manual art craft to mechanized specialist industry. The productivity and quality delivered by reduced teams is dramatically increased. Finished surfaces like 2000 to 3000 m^2/day can be reached by a reduced team, provided the supply of ready-mix concrete is consistent. We can refer to the wide offer of flooring dedicated machines like laser guided levellers (Laserscreed) (Figure. 1), Topping-spreaders (Figure. 2) for surface hardeners, double or triple trowels ride-on finishing machine

Figure.1: Laserscreed, Spain ®RCRIF

Figure.2: Topping Spreader, RSA ®RCRIF

The contribution of the steel fibres' producers has brought more science in the approach of flooring design through tight cooperation with universities. These researches have led to a better understanding of the effects of static and dynamic loads for floors on grade and allowed to build design codes and specific standards. After three decades of intensive use, steel fibre reinforced concrete (SFRC) is not any more an innovation for concrete floors on ground and is considered as standard practise. The design approach is well known and ultimately validated by an international approach with FIB Model Code [1]. SFRC is also taking an important role in technical floors, including structural slabs like floors on piles or foundations of clad racks [2].

The flooring companies themselves have taken their responsibilities, and via national associations have launched various initiatives to regulate and to implement, via technical recommendations and standards, the evolution of products and techniques leading to a better satisfaction of the final user.

For instance, the British Concrete Society, with a decisive contribution of the Association of the Concrete Industrial Flooring Contractors (ACIFC), created the internationally recognized document TR34 [3], which is covering major technical aspects for concrete slabs. This document is considered as a reference for the specification and the survey of floor flatness.

Warehouses are not considered for their surface (m^2) but for the volume of product that can be stored (m^3). The effect is to store every time higher, up to 10 to 16 m instead of 5 to 8 meters in the past, and to limit the area for traffic in the aisles, changing from "free movement" to "defined movement" in very narrow aisles (VNA) (Figure. 3 and Figure. 4).

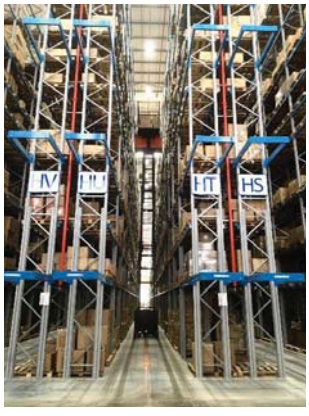

Figure 3: VNA (detail)

Figure 4: VNA South Africa ®PC Floors

The material handling equipment (MHE) follow and accelerate this trend with new generations of forklifts which are faster and able to lift pallets very high while moving. Modern logistics, driven by massive investments of e-commerce define new challenges for the ultimate generation of logistic buildings. They are not any more defined by their surface or by the volume of products they can shelter, but by the throughput which can be obtained, 24/7. The main indicator is becoming the number of seconds to load or unload a truck.

These evolutions lead to higher requirements in terms of flatness, and also bring new durability challenges for joints and abrasion resistance of the floors. This paper will develop the technical solutions applied to address those new objectives.

2 ULTIMATE SOLUTIONS TO LIMIT JOINTS PROBLEMS

It is widely acknowledged that joints provide the greatest source of problems in industrial floors. The joints are always seen as a weak spot creating nuisance in the operations and a need for frequent repairs or corrections.

2.1 Contraction joints

Contraction joints are saw cut joints which are made generally one day after casting the panels to release tensions generated by the shrinkage of concrete and avoid random cracks. Typically, the contraction joints are cut to create sub-panels of 4 x 4 m (up to 6 x 6 m when steel fibres are used). In reality, we have to admit that those cuts initiate cracks which will become weak points in the slabs. The load transfer is difficult to insure and mostly depends on aggregates interlocks. Mesh or steel fibres mostly ensure that the joint opening is not too important. Special dowels pre-positioned under the saw cuts are seldom used for internal floors. They create extra hassle and additional costs and therefore are mostly used in external pavements for unidirectional traffic [4].

The second problem generated by formed joints is the important need for maintenance. After few weeks, the joints have to be filled with elastic joint sealants with capacity to follow the drying shrinkage of the concrete. After one year, they have to be replaced by semi-rigid sealant fillers, which have a lifetime of one to two years.

The arris of the saw cut joints is fragile and very likely to break under intense traffic. This will generate dust, vibrations of the MHE and accelerated wear of the wheels. The general trend in modern logistics is to eliminate these induced joints when high intensity free movement traffic, particularly where motorised pallet trucks are used and to develop solutions without saw cut control joints, called “jointless floors” (Refer section 2.2).

2.2 Construction joints

Armoured joints are considered as a must in modern logistics for the conception and execution of floors. They are used to create a leave in place form with integrated functions of load transfer via continuous or discrete dowels and edge protection by a steel section on top of the joint.

These engineered joints extend the life of a joint. However, the straight edges of the joints allow wheel impact which may cause damages for the MHE or long term to the joint. The steel reinforcement is not absorbing impact but transferring it to the concrete which can fail after a high number of cycles. This phenomenon is even amplified in jointless floors as the concrete shrinkage of the poured panel is not spread between induced joints and construction joints but concentrated in construction joints which can open up to 20 mm or more in large panels.

To overcome this problem, the industry has developed a new generation of joints with disruptive face. The arris is formed in such a way that the wheels are not causing any impact when crossing the joint. Several solutions are available. For instance, plate type joints cover the gap in the joint and open with a sinusoidal shape. These joints may develop new joints on each side of the plate which would be again acting as straight joints. The most efficient products are full depth joints offering a **discontinuous arris** (sinusoidal semi hexagonal (Hex) shaped) (Figure .5).

Figure. 5: Disruptive face joint – UK ®Permaban

The lower part is equipped of load transfer devices typically made of discrete dowels as recommended in TR34 [3].When incorporating these joints into design, the load transfer capacity should be checked using existing design standards (TR34 3rd and 4th edition) and making sure that for structural use, the joint is compliant with Construction Products Regulation [6-7]. The load transfer capacity can be enhanced up to 50% by the use of steel fibres which will increase the shear strength of concrete and the burst capacity of the concrete slab. [8]

With impact free disruptive face joints, the speed of MHE can be maximum, with no vibration and therefore limited maintenance on the floor and on the forklifts and improved health and safety conditions for the drivers.

3 JOINTLESS FLOORS

The evolution in logistics buildings of concrete slabs towards jointless solutions is becoming global in all continents, but with different techniques. The most obvious option is a heavily reinforced slab with double mesh which is technically giving good results but not used in practice as it makes difficult the use of laser guided screeding equipment and economically not viable. Another solution is post-tensioned slabs which allow casting large rectangular panels with no saw cut joints. The economics of this high-end technique restrains the use to special conditions (fixed layout, fluid tight floors and bonded overlays) [9]. In Europe, steel fibre reinforced floors is the main option to get rid of contraction joints [10] (Fig. 6).

Figure .6: SFRC jointless floor, France ®Placeo

The fibre dosage is increased from a rate of 15-25 kg/m^3 to a dosage between 30 and 45 kg/m^3, depending on the intrinsic performance of the selected fibre and of the size of panels (20 × 20 m, up to 40 × 40 m, even larger in some special projects). The additional fibres are taking the stresses caused by drying shrinkage of concrete and the joint opening is localised in the construction joints. This is a proven technique which is performing well and only has few limitations:

- Important joint openings
- Necessity to define square panels when defining the pouring sequence
- Subject to curling which can be limited with careful optimization of mix design

In USA, the steel fibres are not widely used and shrinkage compensating concrete reinforced with mesh is the main way to achieve large panels without any saw cut joints. The advantages are the more freedom with the shapes and less curling. Nevertheless, this technique is not as reliable as SFRC solutions regarding crack control. After a significant expansion phase, which needs mesh or high fibre dosage to control it, the contraction phase is delayed, still active during months and may induce cracks at a later stage, several months after casting.

A new technique, volumetric retraction stability (VRS), using an innovative concrete additive, including a calcium compound reacting with cement, is combining the advantages of SFRC and shrinkage compensated concrete (Figure. 7).

Figure. 7: VRS jointless floor, Peru ®Pavimenta

The additive, added in the concrete mix with a dosage between 15 and 30 kg/m^3, absorbs free water during plastic phase. It becomes a gel, avoiding water evaporation during this phase. The dynamic of the chemical reaction of this additive is stable and controlled. The product reacts and increases the volume of concrete at the final stage of plastic phase. During this period, it does not produce internal stresses into the matrix. A minimum reinforcement with steel fibres is sufficient to avoid plastic cracks during hardening phase. After the initial volume expansion of the concrete matrix, begins a slight contraction process (50-150 microns/meter) which is taking place slowly and progressively in the first three months. This limited contraction occurs when the most of resistance of concrete has been met. Under those circumstances it is possible to reduce the amount of reinforcing steel fibres to control shrinkage cracks during drying phase. The quantity necessary to undertake the static and dynamic loads is therefore sufficient. The end result is the behaviour of a SFRC slab on grade with almost no joint opening and limited curling. This technique is also allowing to take freedom with the conventional square shape (Length < 1.4 width) and to allow irregular or rectangular shapes (Length = 5 times width). This technique has been validated through laboratory tests and real size projects in 8 countries and more than 2,000,000 ft^2 realized in the past two years [11].

It is also important to mention the possibility to design and execute seamless floors with no joints at all. In this technique, even the construction joints are eliminated, creating a continuous slab. The technology is a combination of mesh and special steel fibres with a high ductility at small deformations. The value of these seamless slabs is enhanced when there is a need for fluid tight floors (chemical industry) [12].

4 SURFACE PROTECTION

After achieving flat jointless floors without curling and with impact free construction joints or no joint at all, the forklifts can operate at maximum speed. The types of wheels used in recent forklifts are also becoming harder, generating more frictions at the surface of the concrete slabs. Rubber is replaced by neoprene, hard nylon, polyamide, not even mentioning steel. The last issue to treat is the abrasion resistance of these floors and eventually the aesthetics aspects. In many standards or technical recommendations, the specification for wear protection used to consider dozens or hundreds of cycles per day. In modern logistics, operating 24/7, the number of cycles can reach thousands of cycles by day. The abrasion suffered by the slab is such condition in one year is equivalent to ten years of use in a

warehouse designed in the past century. The surface of the slab must be covered with a protective skin which is hard enough to resist to the intensity and speed of forklifts and thick enough to endure 5 to 10 years without being worn out. Economic techniques to improve the concrete surface like "burnish" polishing or application of liquid densifiers do not bring enough resistance and durability in case of intense traffic. Even standard cementitious based surface hardeners with quartz do not show sufficient abrasion resistance to warrantee reasonable durability. It is important to come back to the roots and to check both the quality of surface protection and the quantity. The performance of surface hardeners is guided by the cement content, the quality and sieve curve of aggregates, the type and content of extra hard components with high Mohs hardness (Table 1) (quartz, emery, corundum etc.).

Table 1 : Mohs Hardness Scale

Mineral Name	Scale Number	Common Object
Diamond	10	
Corundum	9	
Emery	8,5	Mason drill
Quartz	7	
	6,5	Steel nail
Silica sand	6	
	5,5	Knife / Glass plate
Fluorite	4	
	3,5	Copper Penny
Calcite	3	
	2,5	Finger nail
Talc	1	

The abrasion resistance of surface hardeners is measured according to different methods, in laboratory on the product (Böhme, Taber tests) or directly on the slab (AR tests) [13]. The split between mineral and metallic products does not make sense when dealing with abrasion resistance. Steel is showing lower results in abrasion than mineral or synthetic emeris or corundum and mainly bringing high impact resistance. For some industrial processes, impact will be a dominant factor to consider, before any consideration on abrasion (Figure. 8).

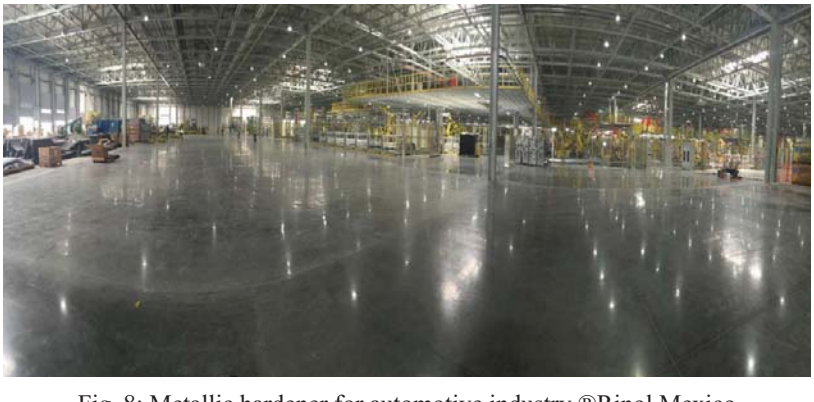

Fig. 8: Metallic hardener for automotive industry ®Rinol Mexico

The homogeneity and the quantity of applied hardeners is the second parameter to consider for long durability. Mechanized topping-spreaders allow to apply evenly significant quantities of hardeners ranging from 4 to 7 kg/m^2. This is called a dry on fresh technique as the surface hardener will be moistened by the freshly levelled concrete and will bond to create a monolitics lab. If high performance hardeners are selected, high dosages will give a lifetime of 10 years even in case of intense traffic. The use of higher dosages is implying an addition of anti-shrinkage agents in the surface hardeners to avoid microcracking in surface (Figure. 9).

Figure. 9: 8-year-old light grey coloured surface hardener, Spain ®Rocland

In absence of topping-spreader (smaller projects, difficulty to operate mechanised spreader) or to increase the life time to 15-20 years, the traditional technique wet-on-wet can be used. The dry shake is mixed with water to create a slurry which can be applied with high dosage (12 to 30 kg/m^2) on fresh concrete after levelling (Figure. 10).

Figure. 10: Application of coloured wet on wet slurry, Spain ®Suesco

The German DIN is giving a useful guidance to define the dosage according to the intensity of traffic and the category of hardener selected [13]. The use of this technology with cementitious based surface hardeners is also offering new possibilities to obtain exceptional aesthetical results with a high density of colour. Pigments are added in the composition of the surface hardeners to create light reflective floors (white, light grey) or to respond to marketing or design requirements from the architect, or for branding purposes.

5 CONCLUSION

The new challenges brought by the evolution of logistics and industries can be technically addressed with innovative products and techniques which have been developed and proven in the past years. But this require also an evolution of the flooring companies which need to be acting as specialist contractors and no more as subcontractors. They have to act as experts with the sufficient knowledge and structure to identify the real needs of final users, to develop comprehensive solutions with design, selection of products and master the execution of various techniques with controlled processes. The floors can be certified, warranted and delivered with a maintenance guide to ensure an optimum use of the floor during at least a decade. The floor is no longer an underestimated piece of construction but the first capacity investment for the final user. It should be treated accordingly.

6 REFERENCES

[1] Fib Model Code 2010, Final draft, Volume 1 and 2.
[2] New applications for steel fibre concrete and combined reinforcement – P. Guirguis – Fibre Concrete Conference – Sep 2013 – Prague, Czech Republic.
[3] Concrete Society. Concrete industrial ground floors – A guide to design and construction. Technical Report 34 fourth edition, The Concrete Society, Camberley 2013.
[4] Guide for Concrete Floor and Slab Construction – Chapter 3 Design considerations – Reported by ACI Committee 302 pp. R-7/R-12.
[5] Disruptive face joints: a review – T. Hancock - Concrete Journal -UK - Sep 2016 pp. 33-34.
[6] European Union. Regulation (EU) Nº 305/2011 of the European Parliament and of the Council of 9 March 2011 laying down harmonised conditions for the marketing of construction products.
[7] Repeal Council Directive 89/106/EEC (1) Official Journal of the European Union, Vol.54, 4 April 2011, Brussels, Belgium.
[8] Jointing Systems In Concrete Structures – D. Underwood, Y.C. Wong, R. Arnold in collaboration with School of Engineering Queensland University of Technology, May 2002, pp. 23-24.
[9] Innovative Industrial Floor Initiatives for Jointless Floors: A bonded post tensioned solution - F J Le Roux, S Humpries and S Van Huyssteen- Abstracts of the 31st Southern African Transport Conference (SATC 2012) - 12 July 2012, Proceedings ISBN Number: 978-1-920017-53-8, Pretoria, South Africa.
[10] Steel Fibre Reinforced Concrete Floors – N. Williamson – Concrete – UK - April 2011, pp. 20-22.
[11] New volumetric stability additive – J. de Jorge - Concrete Engineering International - January 2017, pp. 46-48.
[12] Neubau der Paulaner Brauerei in München-Langwied – A. Meyer, A. Haus - Industrie und Gewerbebauten (Ernst &Sohn) Feb 2016, pp. 23-27.

[13] Abrasion resistance of industrial floors – M Sadegzadeh, V. Vassou, R. Kettle – Concrete Journal - Sep 2012, pp. 30-33.
[14] Floor screeds in building constructions – Heavy duty floor screeds (industrial floor screeds) - DIN 18560-7.

Stress-Crack Separation Relationship for Macrosynthetic, Steel and Hybrid Fiber Reinforced Concrete

Chiranjeevi Reddy Kamasani[(1)], Jayakrishnan R[(2)], Kolluru V L Subramaniam[(3)]

[(1)]Research Scholar, Department of Civil Engineering, Indian Institute of Technology Hyderabad, Hyderabad, India.

[(2)]Post Graduate Engineering Trainee, Kirby Building Systems, Hyderabad, India.

[(3)]Professor, Department of Civil Engineering, Indian Institute of Technology Hyderabad, Hyderabad, India.

ABSTRACT

An experimental evaluation of the crack propagation and post-cracking response of macro fiber reinforced concrete in flexure is conducted. Two types of structural fibers, hooked end steel fibers and continuously embossed macro-synthetic fibers are used in this study. A fiber blend of the two fibers is evaluated for specific improvements in the post peak residual load carrying response. At 0.5% volume fraction, both steel and macrosynthetic fiber reinforced concrete exhibits load recovery at large crack opening. The blend of 0.2% macrosynthetic fibers and 0.3% steel fibers shows a significant improvement in the immediate post peak load response with a significantly smaller load drop and a constant residual load carrying capacity equal to 80% of the peak load. An analytical formulation to predict flexure load-displacement behaviour considering a multi-linear stress-crack separation (σ-w) relationship is developed. An inverse analysis is developed for obtaining the multi-linear σ-w relation, from the experimental response. The σ-w curves of the steel and macrosynthetic fiber reinforced concrete exhibit a stress recovery after a significant drop with increasing crack opening. Significant residual load carrying capacity is attained only at large crack separation. The fiber blend exhibits a constant residual stress with increasing crack separation following an initial decrease. The constant residual stress is attained at a small crack separation.

Keywords: Cohesive crack, hinge, macrosynthetic fibers, cohesive stress-crack opening relationship, toughness.

1 INTRODUCTION

Concrete is a quasi-brittle material and it exhibits an increase in brittleness with increasing strength. Plain concrete has low tensile strength and toughness. Failure in concrete under applied tensile loading is associated with cracking. A crack is produced at low tensile stress and once formed it grows rapidly in the material. Adding short and randomly distributed fibers to concrete has been shown to increase the tensile strength, ductility and toughness [1-5] of the material. Fibers bridge cracks and suppress the propagation of the crack which imparts post cracking ductility. Inclusion of fibers increases the energy absorption property of the composite, thereby increasing the toughness. Today a variety of fibers are available for use in concrete for different applications. Most widely used fibers are

made of steel, synthetic (polypropylene and polyethylene), glass and carbon. Synthetic fibers are typically softer and used in small volume fractions to control shrinkage cracking. Synthetic fibers provide limited potential for use in structural applications. Steel fibers are used in a wide range of structural applications, in general, when the control of concrete cracking is important such as industrial pavements [6-8] precast structural elements [8] and tunnel linings [9]. Steel fibers have high elastic modulus and stiffness and produce increase in toughness and improvements in tensile strength and toughness of concrete [10-11].

The improvement in the material performance obtained from a single type of fiber is usually within a limited range. Incorporation of two or different types of fibers provide superior properties and is known as hybrid fiber reinforced concrete. The main reason for hybridization is to control the cracks at different opening levels of the concrete during different loading stages. Hybrid combination of steel and micro polypropylene fiber have been shown to increase the ultimate compressive strain of the composite [12]. Combination of steel and micro polypropylene fibers showed that the stronger and stiffer steel fiber improved the ultimate strength, while the more flexible and ductile polypropylene fibers improved toughness and strain [13]. The steel macro-fibers with highly deformed geometry produce better hybrids than those with a less deformed geometry. Banthia and Soleimani (2005) [14], reported a positive synergy of hooked end steel fibers with cellulose fibers. On comparing with double deformed fibers, hooked end fibers provided better synergy [15]. Lawler et al. (2002) [16], reported hybridization showed a reduction in permeability of cracked hybrid fiber reinforced mortar under load containing steel and polypropylene.

2 OBJECTIVES

- The broad objective of the work is to investigate the influence of hybridization of hooked end steel and macro-synthetic fibers on the mechanical behavior of fiber reinforced concrete.
- To study the influence of crack bridging on the flexural response of hybrid fiber reinforced concrete and to provide an interpretation for the observed tension response of hybrid fiber reinforced concrete in flexure in terms of crack propagation and toughening mechanisms in the composite.
- To determine the crack bridging stresses contributed by hybrid macro-synthetic fibers.

3 MATERIALS AND METHODS

3.1 Materials

This section presents the details of materials and experimental methods used in the study. Commercially available 53 Grade ordinary Portland cement supplied by ACC conforming to IS 12269 (2013) [17] was used for all concrete mixtures. Fly ash conforming to the requirements of IS 3812-1 (2003) [18] and IS 1727 (1967) [19] was used as supplementary cementitious material in concrete mixtures. Crushed sand was used as fine aggregate and crushed granite coarse aggregate were used. Two different coarse aggregate fractions with maximum aggregate sizes in the ranges 10-4.75 mm and 20-10 mm were blendedtogether in equal proportions.

Two types of fibers which are specifically engineered with specific surface improvements to provide enhanced performance for use as discrete reinforcement in concrete were used in the study. FibreTuff^{TM} monofilament structural polypropylene fibers of 60 mm length manufactured by Bajaj Reinforcements were used in this study. The fibers are made of a modified polyolefin and have a modulus of elasticity between 6 GPa to 10 GPa and tensile strength between 550 and 640 MPa. 3D Dramix Hooked End Steel fibers of 60 mm length, 0.75 mm diameter and of aspect ratio 80 manufactured by Baekart Pvt Ltd were used in this

study. These fibers have Young's modulus of 210 GPa and tensile strength of 1225 MPa. Photographs of the fibers used in this study are shown in Figure 1.

(a) (b)

Figure 1: Types of fibers used in this study (a) Polypropylene fibers; (b)Steel fibers

Concrete mix proportions as per guidelines of IS 10262 (2009) [20] for achieving a characteristic compressive strength of 35 MPa are given in Table 1. The water/cement ratio was equal to 0.48. Three mixes were prepared. First two mixes with fiber volume fractions equal to 0.5% of steel and 0.5% of macrosynthetic fibers were prepared. The third mix is a hybrid mix which consists of a blend of steel and macrosynthetic fibers at 0.3% and 0.2% volume fractions, respectively.

Table 1.Summary of weight proportion of the various mixes in kg/m^3

Fine Aggregate	20 mm - Coarse Aggregate	10 mm - Coarse Aggregate	Water	Cement	Fly ash
823	508	508	163	200	140

3.2 Flexure testing

Flexural testing was conducted on notched beams using a test procedure, which was consistent with the guidelines given by EN 14651:2005 [21]. Beams of size 150 × 150 × 500 mm were tested in the three-point bending configuration. A notch of 25 mm depth was introduced at the mid-span using a circular saw as per the guidelines given in EN 14651. The flexure test was conducted in crack mouth opening displacement (CMOD) control by increasing the CMOD at a rate of 0.05 mm/min. The corresponding deflection of the beam was measured using a reference bar attached to the specimen at mid-depth directly over the supports. During the test, the crack tip opening displacement (CTOD) was measured using a clip gauge mounted at the tip of the notch. A photograph of the test setup is shown in Figure 2.

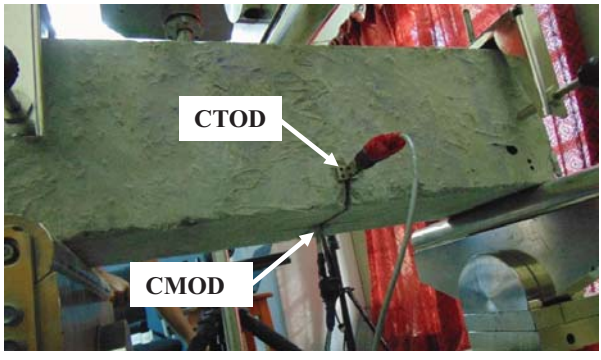

Figure 2: Experimental setup for Notched specimens

3.3 Analytical formulation

A fictitious crack hinge model was used to predict the flexural behavior of fiber reinforced beams. The model was introduced by Ulfkjaer et al (1995) [22] which was further improved by Olesen (2001) [23]. In this model a fictitious crack is considered in an elastic layer with a thickness proportional to the beam depth. A part of the beam close to the propagating crack is modelled as a layer of independent spring elements formed by incremental horizontal strips, and are attached at each end to a rigid boundary which can translate and rotate. In this way the disturbance of the strain field, caused by the presence of the crack, is confined to take place between the rigid boundaries. In the elastic beams, stresses obtained from the classical beam theory represent the far-field stresses away from the crack.

A multi-linear cohesive σ-w relationship was assumed in the cracked portion of the beam. A procedure for obtaining the moment-rotation relationship using force equilibrium of beam section was developed by Chiranjeevi and Subramaniam (2017) [24] and final equations are presented here in Equations 1 to 3.The equations were given for the two cases. Case I describes pre-cracked state of beam whereas case II describes post cracked state which further includes cases without (Figure 3-II (a)) and with traction free crack (Figure 3-II (b)).

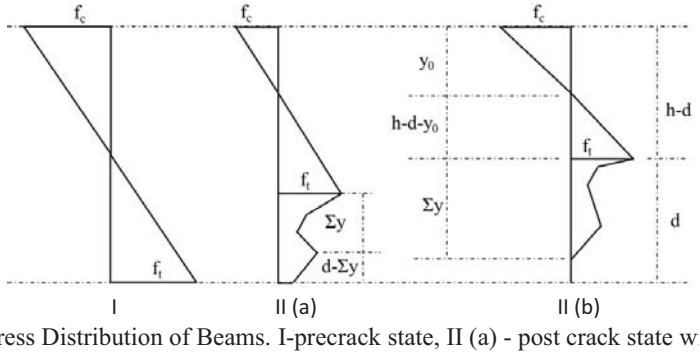

Figure 3: Stress Distribution of Beams. I-precrack state, II (a) - post crack state without traction free crack, II (b) - post crack state with bottom traction free crack

Pre-crack state (θ<=1): Case I

$$\mu(\theta) = \theta \tag{1}$$

Post crack state (θ>1): Case II(a)

$$\mu(\theta) = \left(1-\alpha-\frac{1}{2\theta}\right)^2.(1+(2-2\alpha)2\theta) + \frac{1}{4\theta^2}\left[\left\{\sum_{z=1}^{i-1} 3k_z.(b_z+b_{z+1}).\left(\sum_{v=1}^{z-1}k_v.\right)\right\}+\left\{\sum_{z=1}^{i-1}\left(k_z^2.(b_z+2b_{z+1})\right)\right\} + \left\{\left(2\alpha\theta-\sum_{z=1}^{i-1}k_z\right).\left(\left(3.(b_i+2b_b).\sum_{z=1}^{i-1}k_z\right)+\left(2\alpha\theta-\sum_{z=1}^{i-1}k_z\right).(b_i+2b_b)\right)\right\}-1\right] \tag{2}$$

Post crack state (θ>1): Case II(b)

$$\mu(\theta) = \left(1-\alpha-\frac{1}{2\theta}\right)^2.(1+(2-2\alpha)2\theta) + \frac{1}{4\theta^2}\left[\left\{\sum_{z=1}^{i} 3k_z.(b_z+b_{z+1}).\left(\sum_{v=1}^{z-1}k_v.\right)\right\}+\left\{\sum_{z=1}^{i}\left(k_z^2.(b_z+2b_{z+1})\right)\right\}-1\right] \tag{3}$$

Where μ, θ and α represents normalized moment, normalized rotation and normalized crack depth respectively. A load CTOD relation was then developed from the known moment rotation relationship.

3.4 Inverse analysis

In order to extract the cohesive stress-crack separation parameters an inverse algorithm was developed which basically optimizes the crack opening parameters to match analytical load-CTOD with experimental load-CTOD response. The parameters of the cohesive relationship were optimized using a two-step analysis to minimize the least square residual. The initial part of load deflection response is highly dependent on matrix properties and it was found to be highly sensitive to flexural strength and initial slope of σ-w relation. Hence early part of the load response was optimized separately by considering load-CTOD response up to a CTOD of 0.3 mm using the objective function given by Equation 4.

$$Norm = \left|\left(P_u^{exp} - P_u^{theorotical}\right)\right| + \frac{1}{n}\sqrt{\sum_{i=1}^{n}\left(P_i^{exp} - P_i^{theorotical}\right)^2} \tag{4}$$

where P_u^{exp} and $P_u^{theoretical}$ and the peak loads obtained from the experiment and from the numerical model, respectively and P_i^{exp} and $P_i^{theoretical}$ are the i^{th} loads in the experimental and numerically predicted load responses at corresponding predefined values of CTOD, respectively and 'n' corresponds to number of input load-CTOD points up to 0.3 mm

In the second stage, flexural strength and ordinate of initial line obtained in the previous step were fixed, and the other cohesive stress values at predefined crack openings were optimized considering displacements up to CTOD value equal to 3 mm using objective function given by Equation 5.

$$Norm = \frac{1}{n}\sqrt{\sum_{i=1}^{n}\left(P_i^{exp} - P_i^{theorotical}\right)^2} \tag{5}$$

4 RESULTS AND DISCUSSION

The load-CMOD response for polypropylene, steel and hybrid FRC are shown in Figure 4. while the macrosynthetic FRC exhibited a slightly lower average peak load when compared with steel and blended FRC, the variations in the peak load are within the range of experimental scatter for each type of fiber. The load-CTOD response exhibits a load recovery following a load drop in the immediate post-peak for FRC specimens with steel, polypropylene and hybrid fibers. The hybrid blend exhibits a higher residual load carrying capacity than the steel FRC at smaller crack opening up to 0.6 mm and steel FRC shows improved performance compared with the hybrid FRC at larger crack opening. The macrosynthetic FRC exhibits a rapid decrease in the load carrying capacity with increasing CTOD following the peak load and the load carrying capacity is lower than the steel FRC and the hybrid FRC.

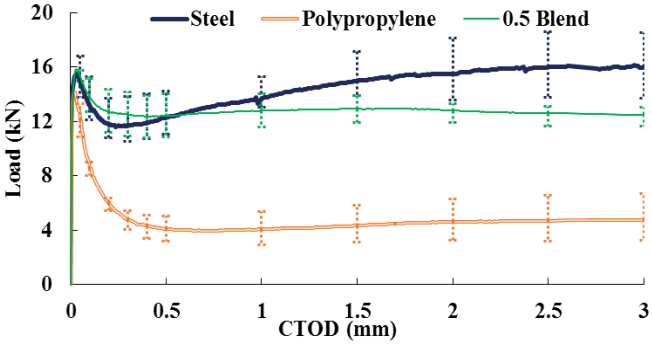

Figure 4: Load-CTOD response of FRC with 0.5% volume fraction

The parameters of the σ-w relationship were obtained using constrained minimization based on the interior point algorithm method, which was implemented numerically in Matlab®. Constraints were applied on crack opening parameters and tensile strength of concrete. Eleven transition points were used in determining the cohesive relationship. The normalized stress with crack separation are plotted in Figure 5. In all FRC, there is a decrease in the stress initially, which is followed by stress recovery at larger values of crack separation. Steel FRC gives a higher crack bridging stress at large values of crack opening. There is very little stress recovery in polypropylene FRC at 0.5% volume fraction. The hybrid FRC shows a superior response for small values of crack opening. The crack bridging stress provided by the hybrid blend is higher than the steel FRC for crack openings up to 0.5 mm.

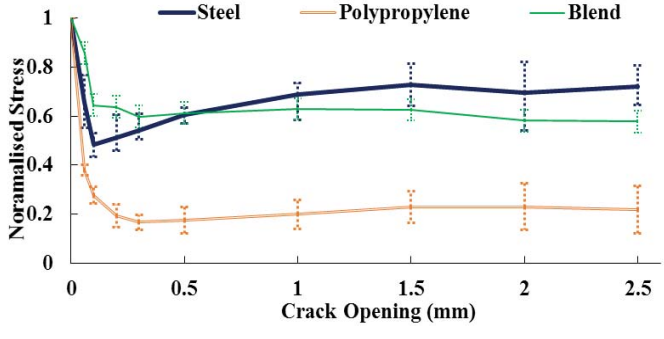

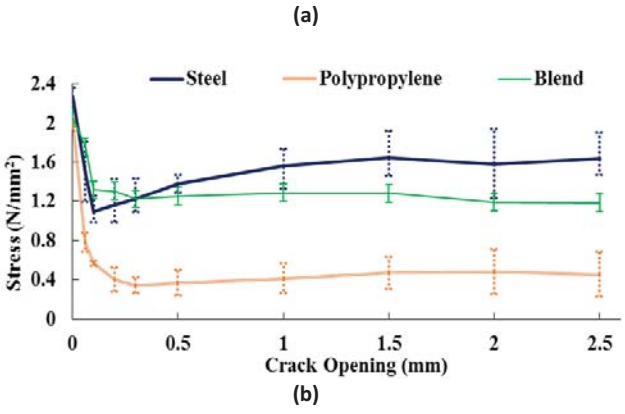

Figure 5.Stress vs. crack separation of FRC with 0.5% volume fraction

a) Stress normalized with cracking stress b) Absolute stress

The values of flexural stress at the peak load based on strength of materials approach are compared with the f_t values from inverse analysis in Table 2. It is clear that the values computed by considering peak moment and section modulus are significantly higher compared to the f_t values from the cracked hinge model, which accounts for pre-peak crack growth.

Table 2 .Flexural stress value based on strength-based apprach and cracked hinge model

	Strength of materials (MPa)	f_t from cracked hinge model (MPa)
Polypropylene	4.12 (0.310)	2.07 (0.182)
Steel	4.55 (0.240)	2.27 (0.071)
Hybrid	4.58 (0.095)	2.05 (0.045)

5 FINDINGS AND CONCLUSIONS

The load CTOD response indicates an initial softening after attaining initial peak and subsequent hardening. Analytical load response using cracked hinge model with a multi linear cohesive stress crack opening relation is shown to capture the initial softening and the subsequent load recovery in the flexural response of a notched beam. The σ-w relationship obtained by matching the analytically predicted load response of the notched beam specimen obtained from the cracked hinge model with the experimental response exhibits an initial softening with increasing crack opening, which is followed by a stress recovery phase. Hybrid FRC engages early in providing crack opening resistance and steel FRC provides better response at small crack openings.

6 REFERENCES

[1] Kar, J. N., and Anil K. P. "Strength of fiber-reinforced concrete." *Journal of the Structural* Division, 98(5) (1972) 1053-1068.

[2] Johnston, C. D. "Definition and measurement of flexural toughness parameters for fiber reinforced concrete." *Cement, Concrete and Aggregates* 4(2) (1982): 53-60.
[3] Shah, S. P., and Chengsheng O. "Mechanical Behavior of Fiber-Reinforced Cement-Based Composites." *Journal of the American Ceramic Society* 74(11) (1991): 2727-2953.
[4] Gopalaratnam, V. S., and Gettu, R. "On the characterization of flexural toughness in fiber reinforced concretes." *Cement and concrete composites* 17(3) (1995): 239-254.
[5] Soutsos, M. N., Le, T. T., and Lampropoulos, A. P. "Flexural performance of fibre reinforced concrete made with steel and synthetic fibres." *Construction and building materials* 36 (2012): 704-710.
[6] Belletti, B., Cerioni, R., Meda, A. and Plizzari, G., "Design aspects on steel fiber-reinforced concrete pavements." *Journal of Materials in Civil Engineering* 20(9) (2008): 599-607.
[7] Sorelli, L. G., Alberto, M., and Giovanni, A.P. "Steel fiber concrete slabs on ground: a structural matter." *ACI Structural Journal* 103(4) (2006): 551-558.
[8] Ferrara, L. and Alberto, M. "Relationships between fibre distribution, workability and the mechanical properties of SFRC applied to precast roof elements." *Materials and Structures* 39(4) (2006): 411-420.
[9] Gettu, R., Barragan, B., Garcia, T., Ortiz, J. and Justa, R. "Fiber concrete tunnel lining". *Concrete international*, 28(08) (2006): 63-69.
[10] Taerwe, L, and Van Gysel, A. "Influence of steel fibers on design stress-strain curve for high-strength concrete." *Journal of engineering mechanics* 122(8) (1996): 695-704.
[11] ACI (American Concrete Institute) ACI 544.1R: State-of-the-art report on fiber reinforced concrete. ACI (1996), Farmington Hills,MI, USA.
[12] Glavind, M, and Tine A."High-strength concrete with increased fracture-toughness." M*aterials Research Society Proceedings*. Vol. 211. Cambridge University Press, (1990): 39-46.
[13] Feldman, D. and Zhihong Z. "Synthetic fibres for fibre concrete composites." *Materials Research Society Proceedings*. Vol. 305. Cambridge University Press, (1993):123.
[14] Banthia, N. and Sayed, M. S. "Flexural response of hybrid fiber-reinforced cementitious composites." *ACI Materials journal* 102(6) (2005): 382.
[15] Banthia, N., Majdzadeh, F., Wu, J. and Bindiganavile, V. "Fiber synergy in Hybrid Fiber Reinforced Concrete (HyFRC) in flexure and direct shear." *Cement and Concrete Composites* 48 (2014): 91-97.
[16] Lawler, J., Zampini, D., Shah, SP., "Permeability of cracked hybrid fiber reinforced mortar under load."*ACI Mater Journal*, 99(4) (2002):.379–85.
[17] IS 12269: Ordinary Portland Cement, 53 Grade – Specification, [CED 2: Cement and Concrete (2013)], *Bureau of Indian Standards*, New Delhi, India
[18] IS 3812-1: Specification for Pulverized Fuel Ash, Part 1: For Use as Pozzolana in Cement, Cement Mortar and Concrete [CED 2: Cement and Concrete (2003)], *Bureau of Indian Standards*, New Delhi, India
[19] IS 1727: Methods of test for pozzolanic materials [CED 2: Civil Engineering (1967)], *Bureau of Indian Standards*, New Delhi, India.
[20] IS 10262:Concrete Mix Proportioning- Guidelines, [CED 2: Cement and Concrete (2009)], *Bureau of Indian Standards*, New Delhi, India.
[21] CEN (European Committee for Standardization) EN 14651: Test method for metallic fibre concrete. Measuring the flexural tensile strength (limit of proportionality (LOP), residual). *CEN (*2005), Brussels, Belgium.
[22] Ulfkjær, J. P., Steen, K. and Rune, B. "Analytical model for fictitious crack propagation in concrete beams." *Journal of Engineering Mechanics* 121(1) (1995): 7-15.
[23] Olesen, J. F. "Fictitious crack propagation in fiber-reinforced concrete beams." *Journal of Engineering Mechanics* 127(3) (2001): 272-280.
[24] Reddy, K. C., and Subramaniam, K. V. L. "Analysis for multi-linear stress-crack opening cohesive relationship: Application to macro-synthetic fiber reinforced concrete." *Engineering Fracture Mechanics* 169 (2017): 128-145.

Prestress Load Influence on Pull-out Behaviour of Post- installed Torque- controlled Expansion Anchors

N. Rouane[(1)], P. Salomon[(1)], B. Pallud[(2)] and F. Delhomme[(1)]

[(1)]Univ Lyon, INSA-Lyon, SMS-ID, F-69621, France

[(2)]Hilti France, Magny-les-Hameaux, France

ABSTRACT

Post-installed anchors in reinforced concrete structures are increasingly important in current constructions especially in repair or upgrading works. A research program was completed to determine the tightening torque and anchorage depth influence on the pull-out performances of torque-controlled expansion anchors. The anchor diameter d was 10 mm. Six configurations were tested on 18 concrete blocks. Three pre-tension loads and two anchorage depths were considered. The results show the fastening torque has no influence on the load-bearing capacity of anchors far away from the concrete edge. However, an increase of the torque leads to a decrease of the anchor's slipping during pull-out tests. Nevertheless, applying an excessive fastening torque may lead to a steel-rupture of the anchor during the fastening phase and premature splitting in case of anchors close to an edge. An embedment increase leads to a better anchor load capacity and reduces the concrete cone rupture risk. Finally, a simplified model of the anchor tension response with a bilinear load-displacement relationship was suggested.

Keywords: Concrete, anchor, pullout, prestress

1 INTRODUCTION

Post-installed anchors are, for the time being, increasingly useful in construction and civil engineering especially in repair or upgrading works. Torque-controlled expansion anchor pull-out strength is mainly due to the friction at the interface between the concrete and the expansion sleeve of the anchor. Tensile strength is function of several parameters such as concrete compressive strength, reinforced concrete or not, hole diameter, free-edge distance or setup process. During the fastening phase, the body of the anchor is pulled up, so that the surrounding steel sleeve is more and more compressed against the internal face of the hole. The tightening can be settled by using a torque wrench. Few studies report experiments carried out for describing fastening torque influence on the pull-out behaviour. The aim the study is the analysis of this influence. Three pre-tension loads and two embedment depths are tested with normal strength concrete-made blocks. Because it was a need for carrying out an analysis of the prestress load influence, a previous study of pre-tension loss phenomenon, happening after fastening phase and before pulling-out, was also realised. After analysis of the results, a comparison to the guidelines values is made, and a simplified modelling of the pull-out behaviour has been given.

2 MATERIALS AND METHODS

European guidelines [1] give standard test benches, geometries and processes for carrying out regulatory pull-out tests. The Ghobarah A. et al. [2] study precisely describes the setup and protocol applied on series of pull-out tests, according to Canadian and international standards [3]. Here, the blocks were $2h_{ef}$ high. The other dimensions for anchors between M8 and M12 were the following: 533 mm × 305 mm. Concrete blocks and samples were stored in wet conditions during seven days. Among the numerous studies [5-9] dealing with the rupture modes of anchors in concrete, one gives the description of several modes [2]. Ghobarah observed these ruptures during pull-out tests on post-installed anchors. Six diameters were tested (M8, M10, M12, M16, M20 and M24), which were installed following the manufacturer's instructions. Four main rupture modes have been observed: anchor steel rupture, extraction/sliding of the anchor, extraction of the anchor followed by concrete block splitting, and concrete cone breakout. Similar rupture modes were identified in another study, realised in UHPFRC [10]. The mechanical interpretation, based on several numerical modelling is given in case of concrete cone breakout in the document [5]. The regulatory formula for determining the characteristic pull-out strength of a system to concrete cone breakout is given by Eq. 1 [1]:

$$N_{rk,c}=N^{0}_{rk,c}\frac{A_{cN}}{A^{0}_{cN}}\psi_{sN}\psi_{reN}\psi_{ecN}\psi_{ucrN} \quad (1)$$

$$N^{0}_{rk,c}=k\sqrt{f_{ck,cube}}h_{ef}^{1,5} \quad (2)$$

where $N^{0}_{rk,c}$ is the initial characteristic resistance of an anchor in cracked concrete, $f_{ck,cube}$ the concrete characteristic compressive strength (MPa), h_{ef} the effective embedment depth (mm). The k value depends on the concrete cracked state of the block. Moreover, the proportional relation between $N^{0}_{rk,c}$ and $\sqrt{f_{ck,cube}}h_{ef}^{1,5}$ is proved by many other authors [11-13]. A^{0}_{cN} is the theoretical concrete cone area, ψ_{sN}, ψ_{reN}, ψ_{ecN} and ψ_{ucrN} are coefficients respectively taking into account the the load layout in concrete due to edge effect, the block surface chipping off, the group effect and the concrete cracked state.

Concerning the splitting mode, a numerical study [9] was carried out with two anchor diameters (12.7 and 15.9 mm) and anchorage depth between 4, 5 and 9 times the diameter (4.5d and 9d) in normal strength concrete. A typical splitting mechanism has been deduced from these results: radial cracking under the expansion sleeve as the anchor is fastened; growth of the conical cracks from the sleeve/concrete interface, horizontally and vertically, towards the surface of the block; superficial cracking of the concrete block before reaching the maximal load; growth of vertical cracks until they reach conical cracks at the concrete/sleeve interface after having exceeded the maximal load, in the same time, El Sharnouby [9] observed superficial cracks growing towards the edges of the concrete block. According to this study, splitting failure has only been observed for embedment depths between 4, 5d and 6d. The crack surface regularly increases until 95% of the maximal load is reached, and shows an important acceleration in a second time. The anchor's sliding after maximal load leads to a widening of the cracks and to a fast growth until block rupture. Until the prestress load is reached, anchors have a very high stiffness (minimal displacement). A repetitive process follows: the anchor slides and stops until rupture [9]. The regulatory characteristic pull-out strength in case of splitting failure is given [1] by Eq.3:

$$N_{rksp}=N_{rk,c}\Psi_{hsp} \quad (3)$$

Where Ψ_{hsp} is a factor taking the real block height h influence into account.

According to Eligehausen et al. [5], if the anchor expansion sleeve is too thin/small, the concrete in hydrostatic stress condition fails because of compression, leading to an extraction of the anchor. Another study [9] observes that extraction only happens with embedment depths between 7.5d and 9d. A combined rupture mode extraction/splitting with embedment depths between 6d and 7.5d. It finally seems that the embedment depth has no influence on the expansion anchor pull-out behaviour above 7.5d. The standard characteristic pull-out strength N in case of extraction is only given for highest embedment depths (above 9d) because of being a non-decisive value for other depths [14]. Steel rupture of the anchor is the fourth identified failure mode [2]. The characteristic tensile strength N of the anchor is given in ATE 11-0374[14]. The numerical modelling of El Sharnouby et al. [9] for 12.7 mm diameter anchors and a 6d embedment depth shows no influence of the prestress load on the load-bearing capacity of the anchor. Moreover, the post prestress removal stiffness is the same whatever the value of the prestress load. However, increasing prestress load leads to a decrease of the anchor displacement at the maximal external load. The study of K. Jin-Sup et al. [7] leads to similar conclusions for M10 and M12 anchors with embedment depths at 50 mm and 100 mm. According to the results, it is difficult to get a correct overview of the link between prestress load and pull-out behaviour of post-installed expansion anchors. With M10 anchors, increasing the fastening torque leads to the anchor displacement decrease at rupture. An important phenomenon to be taken into account to evaluate the influence of fastening torque is the prestress losses after fastening phase. R. Eligehausen et al. [5] shows that, for expansion anchors, the higher the prestress load (the torque) is, the more important the losses are. Most of the losses happen during the first hours after fastening.

3 TEST SETUP AND PROTOCOLS

The tested parameters during experiments are the following: 2 embedment depths: 50 mm (5 times the anchor diameter d) and 60 mm (6d) which are two given values in the technical specifications of the used anchors; 3 prestress loads F at approximately 50%, 100% and 180% of the prestress deduced from the manufacturer's recommended torques T using the Kellermann and Klein formula [15], so respectively: 5.70, 11.4 and 20.5 kN (Eq. (4)).

$$F = T\left(0.159P + 0.578\mu_t d_2 + \mu_h \frac{D_h}{2}\right)^{-1} \quad (4)$$

where μ_t and μ_h coefficients of friction respectively between threads and between bearing surfaces under nut or bolt head; d_2 the basic pitch diameter of thread, D_h mean diameter under the bold head.

The tested anchors are HSA M10 50/40/10 Hilti post-installed torque-controlled expansion anchors [16]. The main mechanical characteristics of the anchors were a 650 MPa nominal thread tensile strength and a 520 MPa thread yield limit. A single anchor was installed in each concrete block (340 x 340 mm and 150 mm high). Blocks were large enough to avoid splitting during anchor setting at the centre of it ($\geq$ 2). The concrete used is a standard C25/30 graded concrete. The mean compressive and splitting tensile strengths of the concrete are given for each configuration in Table 1. Concrete compressive and splitting tensile strengths were tested on 220 mm high and 110 mm diameter cylindrical samples just before or after the pull-out tests. The blocks were cast into wood forms, 340 mm square shaped and 150 mm high. Blocks were turned out one day after cast and protected against desiccation by plastic sheets. The anchors were tested at least 28 days after casting. The anchors were installed on the lower faces of the blocks because of their high level of regularity and flatness due to contact with the form. Settling was carried out respecting the manufacturer protocol [14,16]. The fastening phase occurred at the beginning of the pull-out tests. Before starting pull-out tests, an analysis of the prestress loss phenomenon was carried

out on three additional blocks. So as to reproduce the predicted configuration of pull-out tests, a load sensor was installed. Then, the anchor was fastened at approximately 180% of the recommended torque because it was the most unfavourable configuration. Measurements were carried out over 24 hours for each block, at an acquisition rate of 2 Hz over the first 20 min and 1/30 Hz after. Pull-out tests were carried out on a 250 kN capacity hydraulic press, blocks were fixed in order to put a pure tensile strain around the anchor (Figure 1). The quasi-static tensile loading was displacement controlled with a loading rate of 1 mm.min^{-1}. The load was applied until failure or a 10 mm anchor displacement was reached. This choice was due to the disorders that may have been caused by a 10 mm anchor displacement in real use situation. 3 identical samples of each configuration were tested. Fastening with direct prestress load control was chosen because of preliminary tests with wrench torque controlled fastening which showed too much deviation in prestress values (35-40% scattering for the configurations at 50% of the theoretical pre-tension). Prestress load was controlled during fastening phase with the load sensor. The recorded data, at acquisition rate of 10 Hz, were the prestress load with the load sensor, the displacement between the anchor and the upper surface of the block with a LVDT and the external applied pull-out load. The main characteristics and parameters of the realized pull-out tests are given in Table 1.

Table 1: Main testing parameters of pull-out tests (3 tests for each configuration).

Configuration	Mean depth (mm)	Mean pre-stress load (kN)	Mean concrete compressive strength (MPa)	Mean concrete tensile strength (MPa)
L50C50	50.3 ± 0.7	5.78 ± 0.04	40.9	3.7
L50C100	50.2 ± 0.5	11.57 ± 0.31	45.8	3.8
L50C180	50.3 ± 0.4	20.98 ± 0.71	45.8	3.8
L60C50	59.9 ± 0.2	5.77 ± 0.06	46.1	3.2
L60C100	60.0 ± 0.3	11.75 ± 0.10	46.1	3.2
L60C180	60.7 ± 0.6	19.86 ± 0.24	40.9	3.7

Note: Lx = means embedment depth x (mm), Cy = means prestressing at y (%) of the recommended torque value

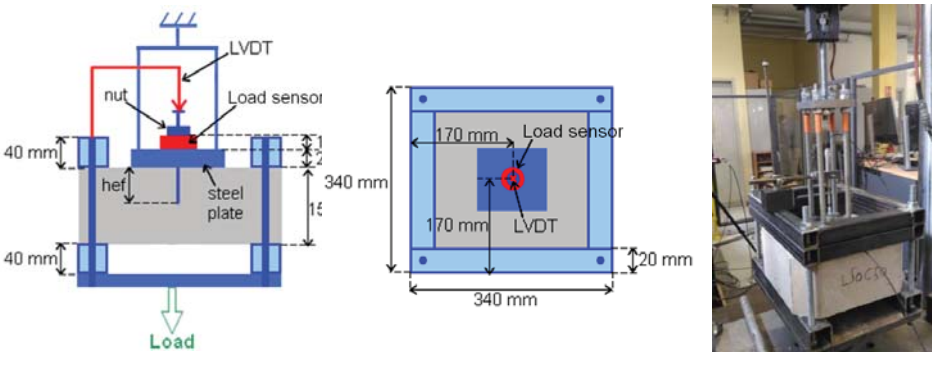

Figure 1: Setup and instrumentation for pull-out tests

4 PRESTRESS LOSS TESTS RESULTS

Prestress load evolution over 24 hours after fastening for the three additional tested blocks is given in figure 2. The mean measured loss at 24 h is 48.0 ± 3.7% of the initial prestress load. The stabilization of the creep, according to these results, starts around 7.5 hours after fastening. Most of the losses happen during the first minutes after fastening. In fact, 58% of the 24 h losses are reached after 10 minutes. It is possible to identify two different steps in the prestress loss process. In a first time, a period of fast instantaneous losses and in a second time, after approximatively 7.5 hours, a progressive stabilization of the creep. The test bench installation time was approximately 30 min. Thus, the pre-tension loss at the starting of the pull-out test was at least 30% of the initial prestress load, applied during the fastening phase.

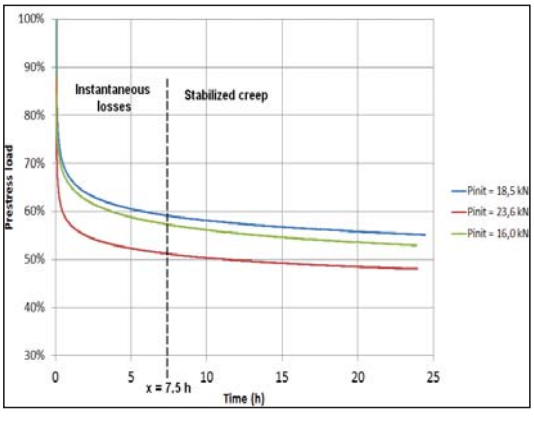

Figure 2: Anchor pre-tension load evolution

5 PULL OUT TESTS RESULTS

The main results of the tests are given in Table 2. The uncertainty on the mean values is given by the standard deviation on the three tests of each configuration.

Table 2: Results of the pull-out tests (*E= extraction, C= concrete cone, S= splitting*)

Configuration	Rupture mode	Mean maximal external load F_{extmax} (kN)	Mean stiffness k2 (kN/mm)	Anchor displacement at F_{extmax} (mm)
L50C50	2xC; 1xE	19,05 ± 1,45	2,85 ± 0,23	5,16 ± 0,40
L50C100	2xC; 1xS	19,52 ± 1,11	2,85 ± 0,23	4,11 ± 0,27
L50C180	2xC; 1xS	20,55 ± 0,77	2,07 ± 0,82	1,89 ± 0,75
L60C50	3xE	22,00 ± 1,44	3,09 ± 0,31	6,28 ± 0,42
L60C100	2xS;1xE	22,54 ± 1,61	2,72 ± 0,03	5,30 ± 0,23
L60C180	3xS	21,93 ± 1,03	2,19 ± 0,60	2,97 ± 0,47

5.1 Rupture modes

An identical behaviour was identified for each rupture mode, each embedment depth and each prestress load (Figure 3). This behaviour is divided into three main steps: concrete decompression until prestress is removed and perfect anchor/concrete adhesion; anchor sliding of several millimetres that may be combined to an anchor sleeve/body sliding; a final

brittle rupture mode in case of splitting or pure concrete cone, progressive in case of extraction or concrete cone combined to extraction (a high load level even after peak load).

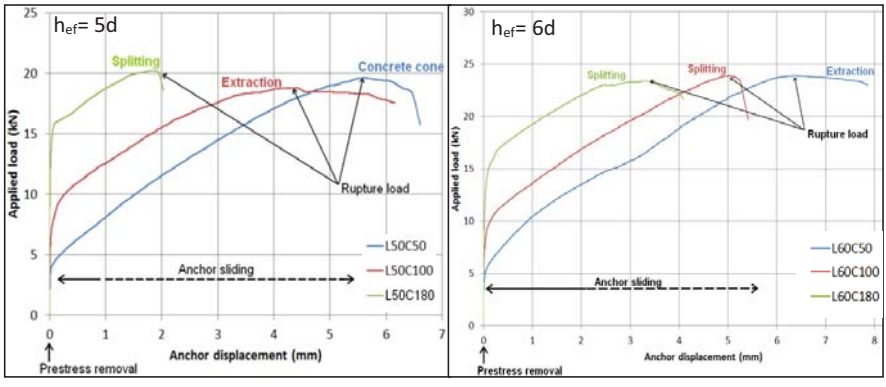

Figure 3: Typical load-displacement curves

Consequently, for all the tests, an important sliding of the anchor occurs which can be considered as the design failure mode. The final rupture mode which depends of the random variations of test conditions can be: a concrete cone breakout, an anchor extraction and a concrete splitting. Signs of several rupture modes are present on each block of each configuration. The concrete cone breakout was only observed on L50C50 and L50C180 configurations. The mean inclination angle of the cone with the horizontal direction was 26°. Conical cracks were identified even though another mode occurred. Anchor extraction failure criterion was an anchor displacement reaching 10 mm before any steel or concrete failure. The failure phase was progressive, and radial cracks appeared on the block surface during the rupture in addition to internal conical microcracks. This rupture mode was identified for all the configurations except those with the maximal prestress load. Two mechanisms were identified: anchor body/expansion sleeve sliding, and concrete/expansion sleeve sliding. Moreover, after cutting the tested blocks, a sliding of the anchor was systematically observed, whatever the predominant rupture mode. Concrete block splitting was characterised by a brittle behaviour. At the rupture, the load drastically falls down, without previous signs or visual damages. Splitting was observed on all the configurations except those with the minimal prestress load. Steel rupture was observed twice during fastening phase at 180 % of the recommended load, once with 5d embedment depth, and once with 6d. Thanks to the load sensor, it was observed that, getting closer to the rupture, the prestress load fell faster and faster between fastening times. This phenomenon is due to the steel plastic deformation. The rupture happened around 190 % of the recommended load and systematically took place where the sleeve was situated, at the minor resisting area. The anchor body, contrary to the threaded part, is only 7 mm diameter under the sleeve. The steel rupture load was reached because of the weak precision when fastening at the highest loads.

5.2 Embedment depth influence

Embedment depth appears to have no influence on anchor extraction occurring probabilities (3 extractions with 5d embedment depth and 4 with 6d embedment depth). However, concrete cone breakouts only occurred for configurations with 5d embedment depths (Table 2). The increase of the embedment depth leads to increasing the conical

resisting area because it systematically starts at the concrete/expansion sleeve interface. Table 2 shows splitting becoming predominant compared to concrete cone breakout when passing from a 5d to a 6d embedment depth. Mean pull-out maximal load for configurations with 5d embedment depths was 19.7 ± 1.4 kN when it is 22.4 ± 1.4 kN for 6d embedment depths. Then, a 10 mm increasing of embedment depth implied a pull-out strength 14% rising by. Embedment depth seems to have no influence on the post-prestress removal stiffness. In fact, no tendency has been identified on the present study field. Moreover, because of the important dispersion in results, an identical mean stiffness can be found around 2.6 kN.mm^{-1}.

5.3 Prestress load influence

According to Table 2, it appears that prestress load has no influence on concrete cone breakout occurring probabilities. This rupture mode appears to be only due to a too small embedment depth. Moreover, whatever the embedment depth can be, a prestress load increasing from 5d to 6d implies moving the rupture mode from anchor extraction to concrete block splitting. This phenomenon is explained by the anchor displacement decrease due to an increase of the concrete/expansion sleeve friction when prestress load is increased. Thus, the splitting has more possibilities to happen in case of high pre-tension loads. Results for configurations with embedment depths at 5d and 6d show that the prestress load has no significant influence on the pull-out strength (over the studied value field). Experimental results confirm and are similar to those of El Sharnouby et al. Anchor displacement at maximal pull-out load decreases when prestress load increases. This is proved by results at a 5d embedment depth (5.16 ± 0.4 mm at 50% of the recommended prestress load, 4.11 ± 0.27 mm at 100% and 1.89 ± 0.75 mm at 180%) and at 6d (6.28 ± 0.42 mm at 50% of the recommended prestress load, 5.30 ± 0.23 mm at 100% and 2.97 ± 0.47 mm at 180%). Moreover, a linear link is observed between the displacement at ultimate load and the prestress load. The mean slope of the recorded curves, which is around 4.35 kN.mm^{-1}, gives the proportionality coefficient that links the initial prestress load to the anchor displacement at the ultimate load. Pre-tension load appears to finally have no influence on the post prestress-removal stiffness. In fact, results (Table 2) do not allow any conclusion about any influence on post prestress-removal stiffness, results that fit with those of El Sharnouby et al [9].

6 COMPARISON TO EUROPEAN STANDARDS

The experimental and theoretical characteristic values of pull-out strength, taking into account the mean compressive concrete strength, are gathered in Table 4. Theoretical rupture loads (Table 2) for tested configurations implied systematic concrete cone breakout, whatever the embedment depth or the prestress load.

Table 3: Comparison to the European standards

Configuration	Theoretical characteristic failure load (kN)				Main rupture mode	Mean rupture load (kN)
	Steel rupture	Extraction	Concrete cone	Splitting		
L50C50	28.0	-	17.0	22.2	Cone	19.0 ± 1,5
L50C100	28.0	-	17.0	22.2	Extraction	19.5 ± 1,1
L50C180	28.0	-	17.0	22.2	Cone	20.6 ± 0,8
L60C50	28.0	-	22.3	25.9	Extraction	22.0 ± 1,4
L60C100	28.0	-	22.3	25.9	Splitting	23.7 ± 0,2
L60C180	28.0	-	22.3	25.9	Splitting	21.9 ± 1,0

In fact, the concrete cone breakout was not systematically observed, but only for the L50C50 and L50C180 configurations after an important sliding of the anchor. The inclination angle with the horizontal direction of the cone was 29° for L50C50 and 23° for L50C180, for a mean value around 26°. Theoretical value of this angle, deduced from ETAG 001, Annex C, is 34°. That implies, for identical embedment depths, a higher resisting conical area in experiments than regulatory predicted. Nevertheless, concrete cone breakout failure mode can appear at the end of the anchor sliding phase (Figure 3) due to the decrease of the concrete cone height by a mean value of 26±4% in comparison to h_{ef}, on the tested embedment depths. Concerning the other configurations, the higher resisting conical area let the possibility to other modes to occur as a complete anchor extraction or a concrete block splitting.

7 BILINEAR MODELLING

The recorded load-displacement curves show a bilinear behaviour. During the prestress removal phase (Figure 3), the stiffness (k1) is very high with a mean value, over all the configurations, of 1137 kN.mm^{-1}. After the prestress removal, the second stiffness (k2) is subsequently lower than k1, with a mean value of 2.6 kN.mm^{-1}, so well that k1 can be considered as infinite compared to k2. These results are the basis of the suggested bilinear modelling of anchor tensile behaviour. This spring type model has a bilinear behaviour law (Figure 4) with infinite stiffness during prestress removal phase and a 2.6 kN.mm^{-1} stiffness k after removal. Rupture load can be assimilated to the Guidelines one. Only valuable for configurations fitting with those tested here, this curve can easily be built for first approach studies. First, the load increases with an infinite stiffness of the system. After having reached the prestress load, displacement of the anchor with a constant stiffness around 2.6 kN.mm^{-1} until the rupture is reached (ultimate load or displacement). This simplified modelling can be use in order to model the local behaviour of anchors in a finite element model of a complete structure.

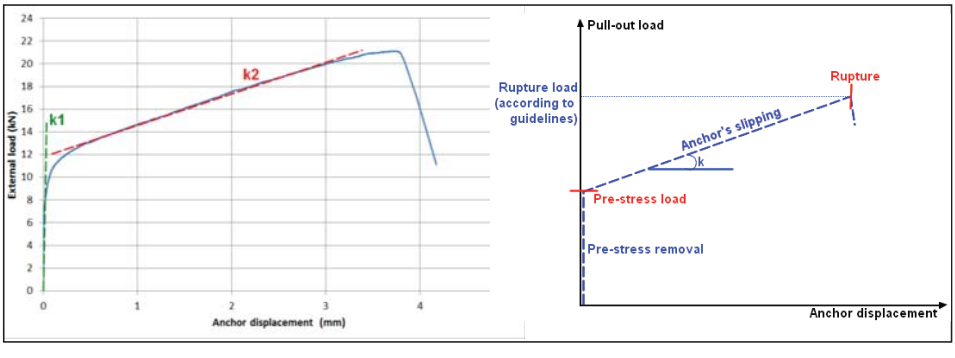

Figure 4: Simplified modelling of the anchorage pull-out behaviour

8 CONCLUSION

Concerning the creeping after the fastening phase, experiments showed that the major part of the prestress losses happened in the first minutes, hours after applying pre-tension load on the anchor. About 44% of the initial load is lost at the end of the instantaneous losses phase, around 7.5 hours after fastening. A stabilized creep phase follows, and approximately 52% of the initial load is lost over 24 hours. 18 pull-out tests composed of six combinations of embedment depth and prestress load led to the following conclusions, confirming and completing those of the previous studies:

- The pre-tension load has no influence on the pull-out strength, in case of single post-installed torque-controlled expansion anchors installed far away from the concrete edges. This conclusion is true over the tested prestress values. However, it is obvious that in real service conditions, under-torqueing may lead to an incorrect setting, and consequently, as well as to smaller pull-out strength (although it was not observed during the tests). Under-torqueing may also lead to a potentially non-satisfactory behaviour under serviceability loads.
- The more important the prestress load is, the smaller the anchor displacement at rupture load will be. On the tested anchors, the proportionality coefficient linking initial prestress load to ultimate anchor displacement is around 4.35 kN.mm-1. However, applying a too high pre-tension load may lead to a steel rupture of the anchor during the fastening phase.
- A higher embedment depth implies higher pull-out strengths for expansion anchors. A 14% higher resistance was recorded when moving the embedment depth from 5d to 6d.
- The embedment depth also affects the concrete cone breakout probabilities. The depth above which no concrete cone can occur is situated between 50 mm and 60 mm for a 10 mm diameter anchor, i.e. between 5d and 6d, with d the anchor diameter.
- Increasing the pre-tension load will favour the block splitting instead of the extraction
- Both prestress load and embedment depth have no significant influence on the anchor post prestress removal behaviour before failure

The pull-out behaviour of HSA M10 anchors can be modelled by bilinear load-displacement curves that can be divided into two consecutive steps: infinite stiffness until complete removal of pre-tension load and displacement of the anchor with a 2.6 kN.mm-1 stiffness up to the rupture.Even if the tested configurations are some of the most used ones in nowadays buildings, these results and conclusions are valid only over the chosen parameters field. Further studies could be considered to complete these results. First, tests in cracked concrete and tests with edge effect could be carried out. In a second time, other types of stresses could be tested and particularly cyclic ones. In fact, in case of such stresses, the pre-tension load influence may be significant on the anchor behaviour.

9 ACKNOWLEDGEMENT

The writers wish to thank P. Chaudet, J. Gioratto, M. Masappolo, E. Bruyere, V Sao-Vicente and R. Trunfio for their help in carrying out this study. We wish to thank the Hilti Company, and particularly M. Meunier, for the means they invested in this research program.

10 REFERENCES

[1] European Organisation for Technical Approvals (EOTA). Guideline for European technical approval of metal anchors for use in concrete. ETAG 001. Bruxelles: EOTA, April 2013, 52 p.
[2] Ghobarag A, Aziz T. Seismic qualification of expansion anchors to Canadian nuclear standards. Nuclear Engineering and Design, March 2004, vol. 228, 377-392.
[3] CSA N287.2. Material Requirements for Concrete Containment Structures for CANDU Nuclear Power Plants, 1998, Canadian Standards Association, Rexdale, Ont.
[4] ASTM E 488. Standard Test Methods for Strength of Anchors in Concrete and Masonry Elements. American Society for Testing and Materials, 1996, West Conshohochen, PA.
[5] Eligehausen R, Mallee R, Solva JF. Anchorage in Concrete Construction. Ernst &Sohn. 2006, 391 p. ISBN: 978-3-433-01143-0.
[6] Fushs W, Eligehausen R, Breen JE, Concrete capacity design (CCD) approach for fastening to concrete. ACI Structural Journal, Detroit, MI, USA. Volume 92, Issue 1, January 1995. 73 – 94.
[7] Jin-Sup K, Woo Young J., Minho K, Bu-Seog J. Performance evaluation of the post-installed anchor for sign structure in South Korea. Construction and Building Materials, July 2013, vol. 44, pp. 496-506.

[8] Al-Taan S, Al-Jaffal A, Mohammed AA. Breakout Capacity of Headed Anchors in Steel Fibre Normal and High Strength Concrete. Asian Journal of Applied Sciences, 2012, 485-496.
[9] El Sharnouby MM, El Naggar MH, Numerical investigation of the response of expansion anchors used to attach helical pile connectors to concrete foundations. Revue canadienne de génie civil, 2010, 866-877.
[10] Delhomme F, Giorrata J, ChaudetP. Tensile behaviour of post-installed bonded anchors in ultra-high performance fiber reinforced concrete. 9th RILEM international symposium on fiber reinforced concrete, 2016. 320 – 329.
[11] Bode H, Hanenkamp W, Strength of headed bolts subjected to tensile loads, Bauingenieur Berlin, Volume 60, Issue 9, September 1985. 361 – 367.
[12] EligehausenR, Sawade G, A fracture mechanics based description of the pull-out behaviour of headed studs embedded in concrete. Stuttgart University, 1989 [online]. Available on: http://elib.uni-stuttgart.de/bitstream/11682/7947/1/eli52.pdf (visited on 04/10/2016).
[13] Elihegausen R, Bouska P, Cervenka V, Pukl R. Size effect of the concrete cone failure load of anchor bolts. Stuttgart University, 1992 [online]. Available on: http://elib.uni-stuttgart.de/bitstream/11682/7911/1/eli81.pdf (visited on 04/10/2016).
[14] European Organisation for Technical Certification. Chevilles de fixation Hilti HSA. ATE-11/0374. Berlin :DeutschesinstitutfürBautechnik, July 19, 2012, 19 p.
[15] Kellermann, R.; Klein, H. (1955): Untersuchungenüber den Einfluß der Reibung auf Corspannung und AnzugsmomentbeiSchrau-benverbindungen (Investigation of the influence of friction on the tightening torque of screws). Konstruktion, 1955, No. 7, pp.54–68 (in German).
[16] Hilti. Technical specifications sheet for HSA anchors, éd. 2014 [online]. 2014. Available on: https://www.hilti.fr/medias/sys_master/documents/h89/9118010343454/Fiche_technique_du_goujon_HSA_Fiche_technique_ASSET_DOC_LOC_1917353.pdf (visited on 06/01/2016).

Role of Steel Fibers in Shear Resistance of Beams in Arch Action

Sahith Gali and Kolluru V. L. Subramaniam

Indian Institute of Technology Hyderabad, Hyderabad, TS 502285, India.

ABSTRACT

Reinforced concrete beams with discrete hooked-end steel fibers were tested with a shear span to depth ratio equal to 1.8. Digital image correlation (DIC) technique was used to obtain the full-field displacements from the beam during the load response. The formation and propagation of a shear crack which directly influences the load response and peak load in the load response of the beam is monitored using the displacement from the DIC measurements. There is a continuous slip across the crack faces of the shear crack with increasing load carrying capacity up to the peak load. The shear crack exhibits a dilatant behavior with increasing slip. Failure in control beams is brittle which was by the opening of dominant shear crack in shear span at a small value of crack opening. At the peak load, the shear crack pattern in fiber reinforced concrete was identical to the crack pattern in the control beam. The dilatant behavior from the measured crack opening and crack slip displacements obtained from the control and the SFRC beams is identical. The fiber reinforced concrete beams exhibit a ductile response with a post peak load carrying capacity even after the continued opening of the dominant shear crack.

Keywords: Hooked-end steel fibers, ductility, crack propagation, shear-dilatant behaviour, shear span to effective depth ratio.

1 INTRODUCTION

Often in shear critical members, the requirement of shear reinforcement leads to close spacing of stirrups. This problem is compounded while considering the ductile detailing requirements to meet the concerns of seismic design, which requires provision of extra stirrup. The extra stirrups, often lead to heavy congestion of steel. Methods of reducing steel congestion, which provide the required capacity and ductility have often involved the use of fiber reinforcement in concrete. A survey of literature indicates that there is an increase in the load carrying capacity and ductility with the addition of steel fibers [1-12]. ACI 318 (2008) [13] allows the usage of steel fibers as minimum shear reinforcement. Most of the data in the literature has been obtained for slender beams with shear span to depth (a/d) ratios greater than 2.5 in which beam action governs the failure. There is very limited data available from beams with low a/d ratio i.e., short beams for which arch action governs the failure. The role of fibers in beams with low a/d ratio is still not clear. An a/d ratio less than 2.0 was selected to contribute additional data to the limited available data set. Further, for small a/d ratio, failure is shown to be produced by a shear crack within a small region [2, 3, 9], which allows for studying the behavior of the shear crack.

Many researchers have proposed empirical equations for the shear strength of fiber reinforced concrete by modifying the existent equations available for the reinforced concrete beams. In all the codes the shear strength equation for reinforced concrete is given as two separate components those are the contribution coming for concrete and stirrup contribution [14-16]. Researchers have modified the concrete contribution term to propose the shear

strength expression for fiber reinforced concrete. These proposed equations takes into account major factors responsible for shear behavior which includes shear span to depth ratio, percentage of longitudinal reinforcement, and other factors include volume of fibers, fibers aspect ratio, fiber geometry, fiber tensile behavior and also concrete matrix properties [1-12] [17]. All the proposed equations are empirical relations estimated from the experiments on steel fiber reinforced concrete beams and few on other types of fibers. The major effect of fiber parameters is in improving stress transfer across the crack due to the bridging action which in turn effects the post cracking behavior of concrete beam.

Addition of fibers increases the post cracking stress transfer ability in concrete, which primarily contributes to improving the ductility [18-19]. To assess the true potential of fibers the post cracking stress transfer across crack has to be accounted for. This is accounted for by including an additional term contributed by steel fibers to the total shear resistance. The post cracking stress transfer is particularly important for shear where shear transfer by aggregate interlock provides significantly to shear capacity of RC elements [20]. The slip displacement along rough cracks also results in dilatancy under shear and torsion [21-24]. The crack bridging provided by fibers can potentially provide for increased mobilization of aggregate interlock, thereby providing shear load capacity. An understanding of the influence of fibers on the post-cracking shear stress transfer across rough cracks surface and its influence on the shear capacity of reinforced concrete beams needs to be understood to develop design provisions which consider the influence of fibers on shear capacity.

Motivation for the study comes from the need to understand the role of discrete steel fiber reinforcement in contributing to the shear behavior of reinforced concrete beams. The overall objective of this study is to investigate the influence of steel fibers on the shear response of reinforced concrete. In particular, it is proposed to investigate the influence of fibers on shear behavior of beams with potential arch action. Beams with shear span to depth ratio of 1.8 was considered in the present study. The influence of the steel fibers on the shear transfer across rough cracks in concrete and its influence on the shear behavior of reinforced concrete is investigated. An approach which combines experimental and digital image analysis is presented to develop an understanding of shear response of reinforced concrete with steel fibers.

2 EXPERIMENTAL PROGRAM

Reinforced concrete beams of dimensions 125 mm width, 250 mm depth and 1500 mm length were used in the test program. In the test program, both control and fiber reinforced concrete beams were cast for testing. These beams include three beams each of control and fiber reinforced concrete with fiber volume fractions (v_f=0.5%). Dramix^{RM} 3D hooked end and glued non-balling steel fibers of aspect ratio 80 (length 60 mm and diameter of 0.75 mm) manufactured by Bekaert industries were used in this study. The fibers have a modulus of elasticity of 210 GPa and tensile strength equal to 1225 MPa. Table 1 describes the details of the beam and the major test variables.

Table 1: Test beam details

Identification of beams	Volume of fibers (%)	Compressive strength (MPa)
SFRC_0	0	38.2
SFRC_0.5	0.5	38.8

All beams were reinforced with two reinforcing bars of 16 mm diameter placed with a clear cover of 20 mm as shown in Figure 1. The reinforcing bars confirmed to the

requirements of IS 1786 (2008) [25] and had a prescribed yield stress defined at 0.2% offset strain equal to 500 MPa, Elastic modulus equal to 200 GPa and an ultimate strain equal to 0.16. One half of the beam was reinforced with 8 mm closed shear stirrups at a spacing of 150 mm. The stirrups were provided in one half of the beam to reinforce it against shear failure and to ensure that shear failure occurred only on one side of the beam. The part of the beam without shear reinforcement allowed for a closer examination of the shear crack patterns and to evaluate the mechanisms contributing to shear resistance. Closely placed stirrups with a spacing equal to 100 mm were also provided at the supports of beam to avoid possible anchorage failure.

All the beams were tested with a shear span to depth ratio equal to 1.8. The testing was performed using a servo-controlled test machine where the net deflection of the center of the beam was measured using LVDT. The test was performed in displacement control where the deflection of the beam was increased in a controlled manner. The loading arrangement used in this study confirmed to the requirements of ASTM 1609, which ensured that no torsion is generated in the beam due to eccentricity. The loads were applied using hardened steel rollers, which ensured perfect line loading at precisely marked locations of the beam. Each roller was attached to the actuator through individual swivel head which allowed for reducing the influence of torsion in the loading arrangement.

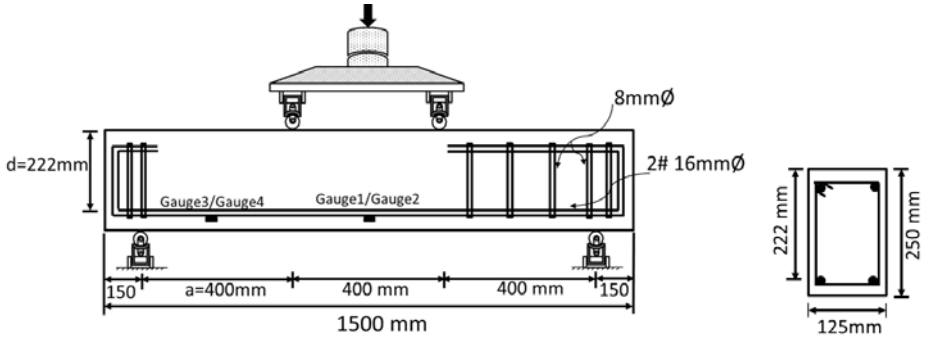

Figure1: Details of the test beam

The surface displacements, strains and development of cracks during the entire load response were determined using a digital image analysis procedure called digital image correlation. Digital image correlation (DIC) is a full-field optical technique which provides spatially continuous measurement of displacements across the surface of the specimen. DIC relies on correlation of the random pattern of speckles between images of the deformed and reference (undeformed) configurations of the specimen within small neighborhoods called subsets [27-28]. A sprayed-on speckle pattern was created on the surface of the beam without the shear stirrups. A uniform coat of white paint and after the white paint dried, the sprayed-on speckle was created by spraying a black mist.

During a test, digital images of the specimen were captured for use in digital image correlation using a high resolution camera (5 mega pixel), which was controlled by a computer. Uniform light intensity was ensured across the surface of the beam using normal white light. The camera was fitted with a 50 mm lens and was placed at a distance of 1 m from the specimen surface. Calibration for the pixel size was performed using a graduated rule placed in front of the specimen. From this measurement, the physical calibration was established. Typical calibration was in the range of 7-10 pixels per mm. A reference image was captured in the undeformed state prior to the initiation of loading program. Images of the

specimen were captured at regular intervals during the test. A photograph of the test setup is shown in Figure 2(a) and a schematic figure of the DIC test setup is shown in Figure 2(b). For the setup used in this study, the random error in the measured displacement is in the range of 0.02 pixels and a conservative estimate of the resolution in strain obtained from the digital correlation was 17μm [29-30]

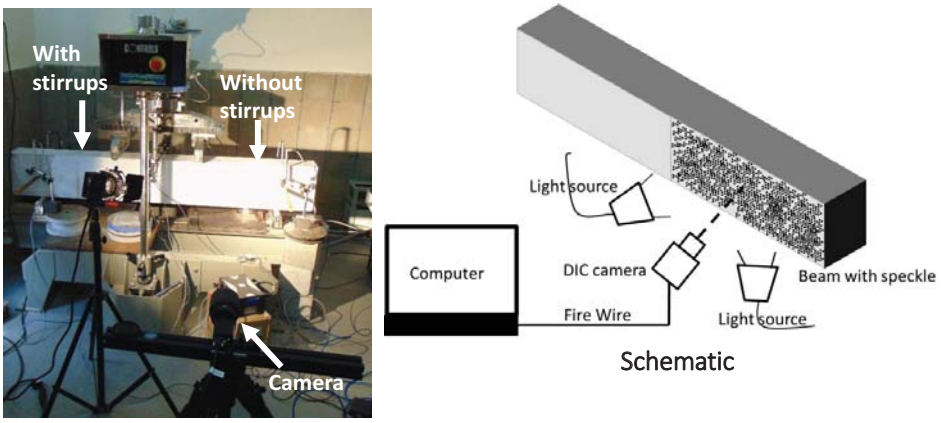

Figure 2: Test setup

3 EXPERIMENTAL RESULTS

The load-deflection responses of the control and hooked end steel fiber reinforced concrete (SFRC) beams are shown in Figure 3. Failure in control specimens was sudden, immediately after attaining the peak load and could not be controlled even in displacement control. The load response of the SFRC beams is nominally similar to the load response obtained from the control specimens up to the peak load of the control beams. In the 0.5% SFRC beams (containing 0.5% volume fraction steel fibers), there is a small increase in the peak load when compared to the control beams. After the peak load there is a continuous decrease in the load carrying capacity with increasing deflection following which, the load carrying capacity essentially levels to a constant value with increasing deflection.

During the loading process, digital images were taken at regular intervals of load. These images were processed using the VIC 2D^{TM} software to obtain the full-field surface displacements. Contours of strain in X-direction in SFRC_0_1 and SFRC_0.5_1 at different points of load response are shown in Figures 4 & 5, respectively. The progression of cracks and the crack patterns are clearly identified from the contour plots. With the application of load, initially, flexural cracks were formed in the constant moment region. In control beam (labelled SFRC_0_1), at an applied load of 95 kN a shear crack emanating from the flexural crack located approximately 215 mm from the support up to the mid-height of the beam can be identified. The crack angle is formed at an angle approximately equal to 45 degrees with respect to the horizontal. The crack was located at a distance approximately equal to the depth of the beam, in the range of 230-250 mm from the support at mid-height level. With increasing load, this shear crack continued to propagate up to the top of the beam. Ultimate failure was by a crack which propagated along the rebar towards support producing splitting along the rebar (shown in Figure 4(b)).

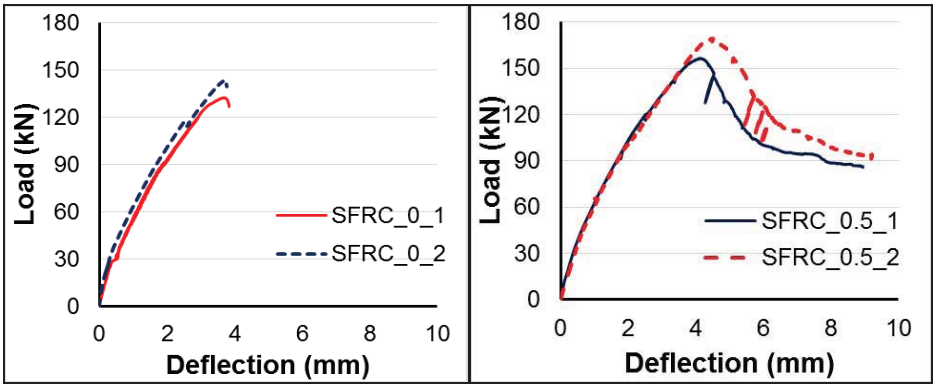

Figure 3: Load-Deflection Response of Control and SFRC beams

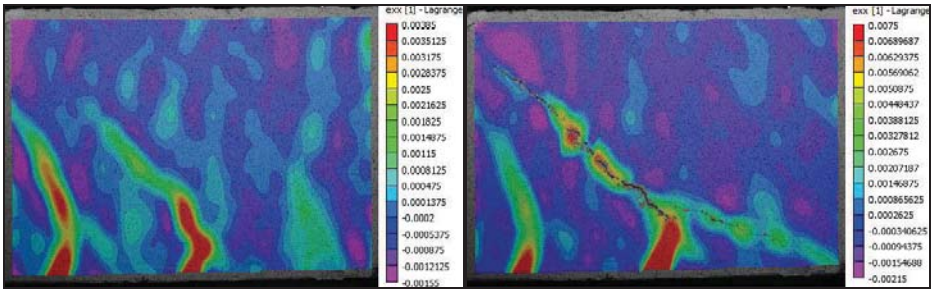

(a) (b)

Figure 4: Contours of strain in X-direction of SFRC_0_1 at (a) initiation of the diagonal crack (at 95 kN) (b) Peak load (at 132 kN).

In the FRC specimen (labelled SFRC_0.5_1), a shear crack was also initiated from a flexural crack located approximately 210 mm from the support at a comparable load in the range of 100 kN. The location of the shear crack and the angle of the crack were also nominally similar to those observed in the control beams. At loads corresponding to the peak load in the control beams, the shear crack was fully established between the level of the flexural reinforcement and the compression region close to the top of the beam (Figure 5(b)). The sudden failure by splitting along the flexural reinforcement was not observed. There was a noticeable decrease in the flexural crack spacing in SFRC beams compared to the control beams. At the peak load the shear crack is fully established, extending from the load point to the bottom of the beam (Figure 5(c)). The shear crack continued to open with increasing deflection after the peak load (Figure 5(d)).

In all beams, the shear crack was formed at distance of 250 mm from the support at the mid-height location of the beam. The crack angle within the shear region extending over the middle third of the beam is also nominally similar in all specimens, approximately equal to 45 degrees with respect to the horizontal. The load responses of the SFRC beams are nominally similar to the load responses obtained from the control specimens, up to peak load of the control. The shear crack extends across the full depth of the beam at the peak load. At corresponding loads, the crack opening in SFRC specimens are significantly smaller when

compared with the control beams. The shear crack continued to open in a controlled manner in the 0.5% SFRC past peak load.

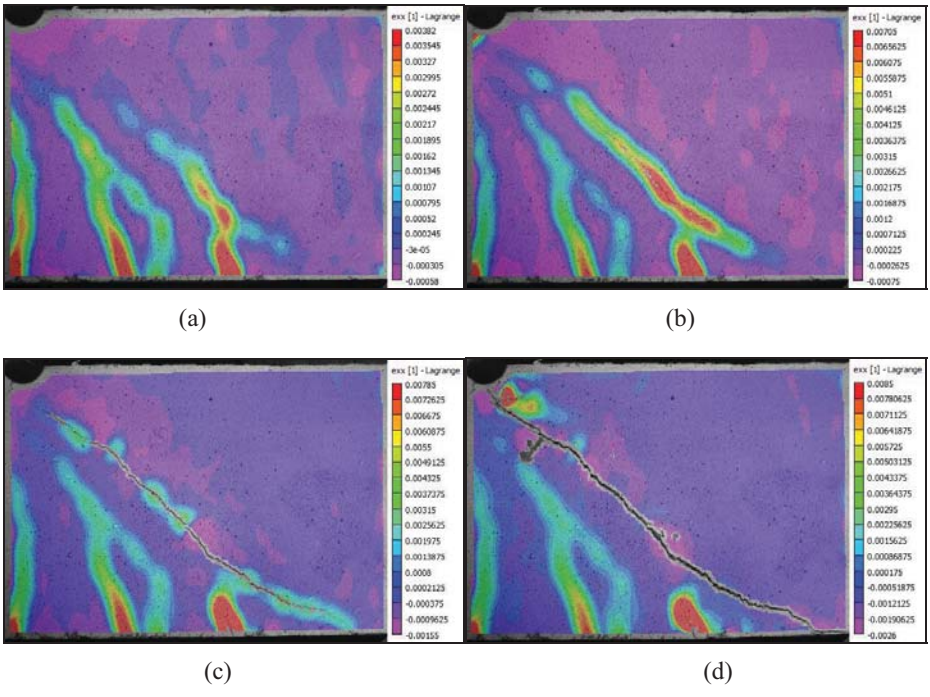

(a) (b)

(c) (d)

Figure 5: Contours of strain in X-direction of SFRC_0.5_1 at (a) initiation of the diagonal crack (at 100 kN), (b) SFRC_0_1 beam peak load (at 132 kN), (c) Peak load (168 kN) (d) load in post peak (146 kN) of load response.

4 DIGITAL IMAGE ANALYSIS OF SHEAR CRACKS

The use of DIC allows for accurate identification of cracks, which may not be delineated visually. The use of DIC allows for tracking changes in the material response across a crack after the shear crack is identified. From a record of images, the location of the crack can be identified and the opening and shear displacements across the shear crack can be studied from a load point before the initiation of the crack. To understand the shear crack opening behavior in the beams, gauge points identified with two sets of boxes (labelled G1 through G6) about 80 × 80 pixels were considered at locations on either side of the crack such that the line joining their centers is perpendicular to the crack direction as shown in the Figure 6. The exact location of the gauge points was decided considering the load points close to failure, where the shear crack was fully established. The gauge points are identified with the center of the box and were located in the shear region within the middle third portion of the beam. The location of the gauge points were kept fixed in all images for analysis. The average values of displacements were obtained from within the area of each box from each location; the average horizontal and vertical displacements were obtained from the values of displacements of all the pixels within each box.

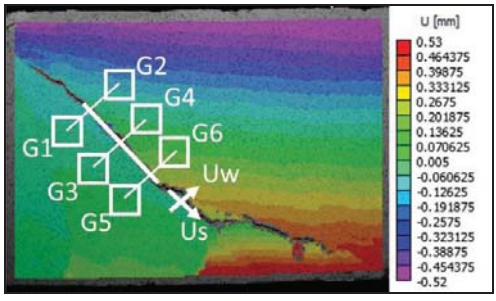

Figure 6: Contour plot of displacement in x-direction from the SFRC_0_1 beam at at 132 kN.

Typical horizontal and vertical displacements from two pairs of points across the shear crack, located within the shear region (middle third of the beam) of the beam, were used to calculate the components of relative displacements in the directions which are perpendicular and parallel to the crack. The component of relative displacement which is parallel to the crack gives the slip across the crack (U_s) and the component which is perpendicular to the crack gives the crack opening displacement across the crack (U_w). The U_w and U_s obtained from the two points located at the mid-height of the beam, G3 and G4 are shown in Figure 7. The U_w and U_s of the two gauge points are initially identical with increasing load. The formation of the shear crack can be identified by the divergence of the displacements measured from the two gauge points. With increasing load there is an increasing divergence in the displacements of the pair of gauge points. The average slip and average crack opening displacement across the crack was determined as the average of the difference in the relative displacement from pairs of points G1 and G2, G3 and G4, G5 and G6.

The average crack slip as a function of the average crack opening across the primary shear crack formed in the pre-peak load response obtained from both control and SFRC beams is shown in Figure 8. The resulting behavior obtained from the shear region indicates a dilatant behavior. There is an increase in crack opening associated with an increase in slip between the rough crack surfaces. With the application of load, after the onset of the shear crack, the crack opening increases nominally in linear manner with an increase in the average slip. The dilatant behavior (crack opening – slip response) exhibited by both control and the SFRC beams is identical. This suggests that the relationship between slip and crack opening is of the same origin. In the 0.5% SFRC beams, the crack slip and the crack opening continue to increase past the peak load of the control specimens.

A comparative analysis of the control and 0.5% SFRC beams is performed using the measured responses from each. The shear dilatant behaviors recorded from a control specimen (SFRC_0_1) and a 0.5% SFRC beam (SFRC_0.5_1) are shown in Figure 9(b) and Figure 9(c) respectively. The load responses of the two beams are plotted in Figure 9(a) for reference. The crack opening and the crack slip measurements at a load corresponding to the peak load in the control beam is marked in the dilatant behavior. At the peak load of the control specimen, both the crack opening and the crack slip in the SFRC beam are smaller than the corresponding values in the control specimen. The crack opening and the crack slip values recorded at the peak load in the response of the SFRC beam are comparable to the values obtained from the control specimen at peak load. The dilatant behavior, the general trend in the crack opening and crack slip relationship is not altered after the peak load.

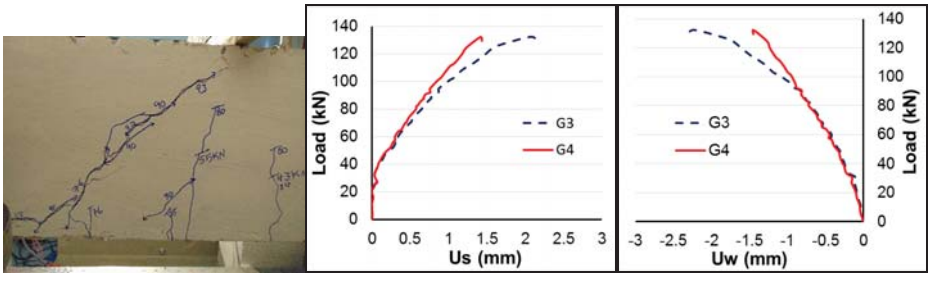

(a) (b) (c)

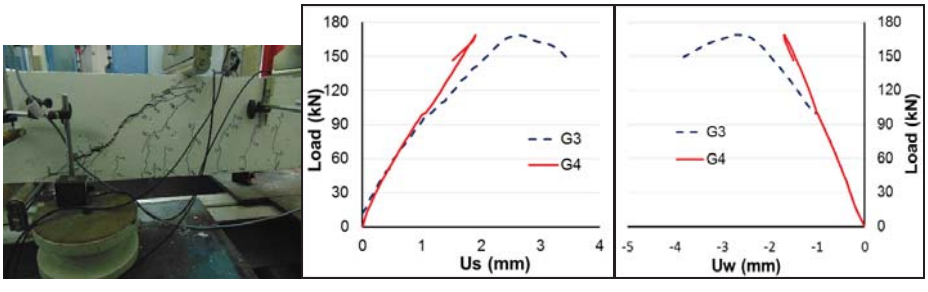

(d) (e) (f)

Figure 7: A photograph showing crack pattern of (a) SFRC_0_1 (d) SFRC_0.5_1 beams; At G3 and G4, the variation of vertical displacement of (b) SFRC_0_1 (e) SFRC_0.5_1; horizontal displacements of (c) SFRC_0_1 (f) SFRC_0.5_1 beams.

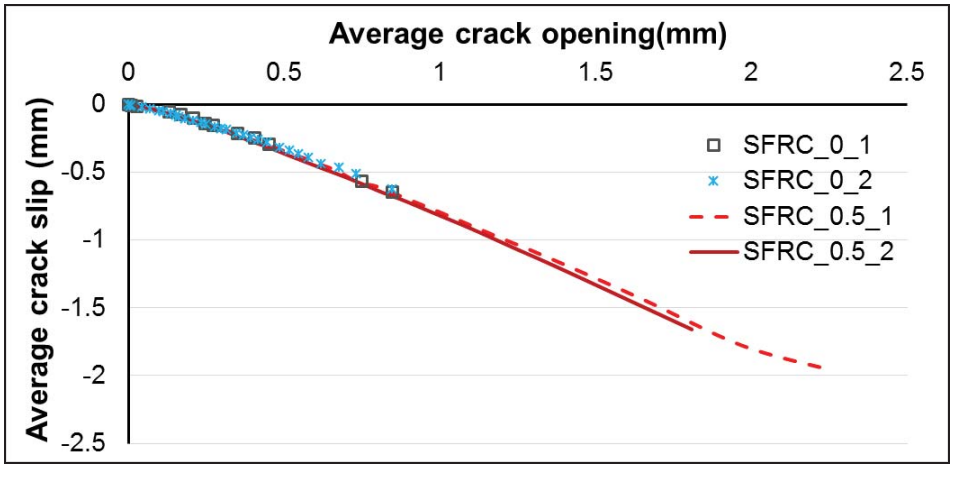

Figure 8: Crack opening-slip response of control and SFRC beams

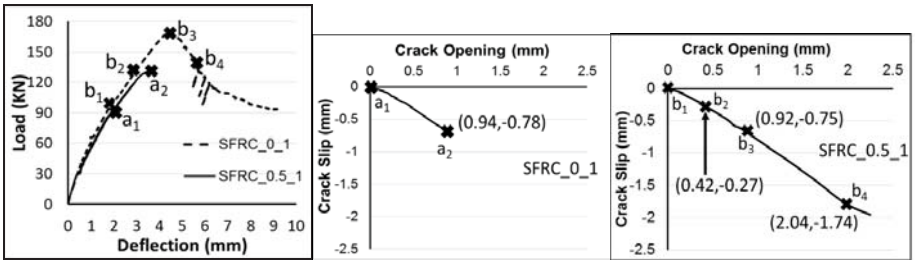

(a) (b) (c)

Figure 9: (a) Load-response; Crack opening-slip response of (b) SFRC_0_1 and (c)SFRC_0.5_1 beams

5 SUMMARY AND CONCLUSIONS

From the experimental results, in control beams when the shear crack reaches the rebar level it goes along the rebar till the support point and finally fails by splitting along this crack as the resistance coming from the aggregate interlock is lost with increased crack width. Addition of fibers do not influence shear cracking load or direction. Shear slip to crack opening relationship of a rough shear crack upto peak is not altered by the fibers. Fibers are effective after the formation of crack and help sustain the shear transfer ability across the rough crack. This helps sustain shear load carrying capacity of the beam. Sudden splitting along the shear crack is suppressed due to the presence of fibers bridging the crack leading to a continuous resistance to load for a larger deflection of the beams. With the addition of steel fibers failure mode changed from brittle to ductile failure.

6 REFERENCES

[1] Mansur, M. A., K. C. G. Ong, and P. Paramasivam. "Shear strength of fibrous concrete beams without stirrups." *Journal of structural engineering* 112.9 (1986): 2066-2079.

[2] Sharma, A. K. "Shear strength of steel fiber reinforced concrete beams." *Journal Proceedings*. Vol. 83. No. 4. 1986.

[3] Narayanan, R., and I. Y. S. Darwish. "Use of steel fibers as shear reinforcement." *Structural Journal* 84.3 (1987): 216-227.

[4] Ashour, Samir A., GhaziI S. Hasanain, and Faisal F. Wafa. "Shear behavior of high-strength fiber reinforced concrete beams." *Structural Journal* 89.2 (1992): 176-184.

[5] Li, Victor C., Robert Ward, and Ali M. Hmaza. "Steel and synthetic fibers as shear reinforcement." *Materials Journal* 89.5 (1992): 499-508.

[6] Tan, K. H., K. Murugappan, and P. Paramasivam. "Shear behavior of steel fiber reinforced concrete beams." *Structural Journal* 90.1 (1993): 3-11.

[7] Imam, M., et al. "Shear domain of fibre-reinforced high-strength concrete beams." *Engineering structures* 19.9 (1997): 738-747.

[8] Kwak, Yoon-Keun, et al. "Shear strength of steel fiber-reinforced concrete beams without stirrups." *ACI Structural Journal* 99.4 (2002): 530-538.

[9] Cho, Soon-Ho, and Yoon-IL Kim. "Effects of steel fibers on short beams loaded in shear." *Structural Journal* 100.6 (2003): 765-774.

[10] Cucchiara, Calogero, Lidia La Mendola, and Maurizio Papia. "Effectiveness of stirrups and steel fibres as shear reinforcement." *Cement and concrete composites* 26.7 (2004): 777-786.

[11] Sahoo, DiptiRanjan, and Nitin Kumar. "Monotonic behavior of large-scale SFRC beams without stirrups." *Engineering Structures* 92 (2015): 46-54.

[12] Sahoo, DiptiRanjan, SauravBhagat, and T. ChanakyaVishwanath Reddy. "Experimental study on shear-span to effective-depth ratio of steel fiber reinforced concrete T-beams." *Materials and Structures* 49.9 (2016): 3815-3830.

[13] ACI Committee, American Concrete Institute, and International Organization for Standardization. "Building code requirements for structural concrete (ACI 318-08) and commentary." American Concrete Institute, 2008.
[14] Park, Robert, and Thomas Paulay. *Reinforced concrete structures*. John Wiley & Sons, 1975.
[15] Wright, James K., and J. G. MacGregor. "Reinforced concrete: Mechanics and design." *Pearson Education International, Upper Saddle River (NJ)* (2009): 61-72.
[16] Winter, G., and Nilson, A. "Design of concrete structure."*9th ed*., McGraw Hill, New York, 1986
[17] Khuntia, Madhusudan, BozidarStojadinovic, and Subhash C. Goel. "Shear strength of normal and high-strength fiber reinforced concrete beams without stirrups." *Structural Journal* 96.2 (1999): 282-289.
[18] Vandewalle, Lucie. "Design method for steel fiber reinforced concrete proposed by RILEM TC 162-TDF." *Fifth International RILEM Symposium on Fibre-Reinforced Concrete (FRC)*. Eds. P. Rossi, and G. Chanvillard. RILEM Publications SARL, 2000.
[19] Vandewalle, Lucie. "RILEM TC162-TDF: Test and Design methods for Steel Fibre Reinforced Concrete: Bending test (final recommendation)." *Materials and Structures* 35 (2002): 579-582.
[20] Collins, Michael P., Evan C. Bentz, and Edward G. Sherwood. "Where is shear reinforcement required? Review of research results and design procedures." *ACI Structural Journal* 105.5 (2008): 590.
[21] Walraven, JoostCornelis. *Aggregate interlock: a theoretical and experimental analysis*. Diss. TU Delft, Delft University of Technology, 1980.
[22] Walraven, J. C., and H. W. Reinhardt. "Concrete mechanics. Part A: Theory and experiments on the mechanical behavior of cracks in plain and reinforced concrete subjected to shear loading." *NASA STI/Recon Technical Report N* 82 (1981).
[23] Walraven, Joost C. "Fundamental analysis of aggregate interlock." *Journal of the Structural Division* 107.11 (1981): 2245-2270.
[24] Subramaniam, Kolluru V., John S. Popovics, and Surendra P. Shah. "Testing concrete in torsion: Instability analysis and experiments." *Journal of engineering mechanics* 124.11 (1998): 1258-1268.
[25] IS 1786, "High strength deformed steel bars and wires for concrete reinforcement,"*Bureau of Indian Standards*. New Delhi, 2008.
[26] ASTM, C. "1609/C 1609M Standard Test Method for Flexural Performance of Fiber-Reinforced Concrete (Using Beam With Third-Point Loading)." *Replaces ASTM C* 1018 (2009).
[27] Sutton, M. A., et al. "Determination of displacements using an improved digital correlation method." *Image and vision computing* 1.3 (1983): 133-139.
[28] Sutton, Michael A., et al. "Effects of subpixel image restoration on digital correlation error estimates." *Optical Engineering* 27.10 (1988): 271070-271070.
[29] Carloni, Christian, and Kolluru V. Subramaniam. "Direct determination of cohesive stress transfer during debonding of FRP from concrete." *Composite Structures* 93.1 (2010): 184-192.
[30] Reddy, K.C., and Subramaniam, K.V., "Post cracking Hinge-type Behavior in Flexure Response of Macro-synthetic Fiber Reinforced Concrete," accepted for publication in Magazine of Concrete Research, 2017.

An Analysis of Steel Fiber Efficiency on Reinforced Concrete Beams and Slabs Subjected to Static and Cyclic Loads

Buttignol, T. E. T.(1), Fernandes, J. F.(1), Sousa, J. L. A. O.(2) Bittencourt, T.(1)

(1)Polytechnic School, University of São Paulo, Brazil

(2)FEC, University of Campinas, Brazil

ABSTRACT

This paper investigates the efficiency of steel fiber incorporation in reinforced concrete (RC) elements submitted to static and cyclic loads. An extensive experimental campaign was carried out on RC slabs and RC beams without and with the addition of different amounts (20 kg/m^3 and 60 kg/m^3) of steel fibers. The results of four-point bending (4PB) static tests demonstrated that fiber's contribution was much more apparent on the RC slabs in relation to RC beams, especially regarding the improvement obtained in the material toughness. This aspect is important for structural design optimization since it is an indication that fiber effectiveness can be higher in RC slabs compared to RC beams. Static tests on RC beams have shown a small increment of the total deformation due to the incorporation of fibers. In contrast, the addition of steel fibers in RC slabs has significantly improved the ductility, highlighting fiber efficiency. In both cases, an increment in the flexural strength was noticed. Cyclic tests on RC slabs evidenced the positive effect of the fibers (crack bridging due to the pull-out effect) to reduce the maximum vertical displacement and postpone steel bars yielding point.

Keywords: Cyclic load, static test, fiber reinforced concrete, flexural behaviour, toughness.

1 INTRODUCTION

The main advantage of the incorporation of fibers in the bulk concrete is the ductile behaviour obtained in quasi-brittle cementitious materials, as is the case of fiber reinforced concrete (FRC). In this case, after cracking, fibers are progressively engaged until the pull out mechanism is fully activated. As a result, failure could occur due to a progressive propagation of the crack through the matrix, characterizing a softening behaviour with crack localization and crack opening control due to fibers debonding. Otherwise, a multicracking pattern (hardening behaviour) can be developed before crack localization and collapse.

FRC structural response (softening or hardening behaviour) depends on the type and quantity of fibers and the kind of test performed. The type of fiber (straight, hooked-end, twisted) influences the post-peak response. Experimental tests carried out by [1] show that improving fiber bond behaviour (by increasing matrix density, fiber and matrix strengths and fiber mechanical bond by adding twisted or hooked end fibers) can lead to a higher

performance of the material. In relation to the quantity of fibers, experimental tests on RC beams reinforced with steel fibers carried out by [2] have shown a small improvement both in the flexural strength capacity and toughness due to the increase in the quantity of fibers from 30 kg/m^3 to 60 kg/m^3. A large-scale experimental campaign performed by [3] on SFRC beams demonstrated that the influence of fibers on the flexural capacity is small.

The type of test has an effect on the post-peak behaviour. A material tested in uniaxial tension could show a single crack (softening behaviour) before failure, while the same material in bending could be subjected to a multicracking state and a hardening response, as is described in the fib Model Code 2010 [4].

Slabs exhibit a higher redistributing capacity, which is related to the failure mechanism (number of plastic hinges and yield lines) [5]. Experimental tests carried out by [6] on two-way FRC slabs with 35 kg/m^3 of hooked-end steel fibers have shown a strain softening response. In contrast, RC slabs reinforced with steel fibers tested by [6] have shown an increase in the redistribution capacity after cracking. In this case, more load was transferred to the supports in the weaker direction after cracking due to the positive effect of steel fibers to the load redistribution capacity of RC slabs. In the tests performed by [6], no additional load was transferred to the supports in the weak direction after cracking in RC slabs without fibers.

Fibers dispersion (distribution, alignment and orientation) in the bulk concrete contribute to increase the variability (scattering) of the results in nominally identical tests (with the same material, casting process and test procedures). A significant scatter in the flexural capacity of FRC beams without reinforcing bars was found in [3]. In the case of reinforced concrete (RC) beams with steel fibers, the variability of the results was smaller since the rebars took most of the load after concrete cracking [3].

The scattering of the results can be attributed to the heterogeneity of the material. The coefficient of variation (CoV) calculated by [7] from 3PB tests varied up to 38 %. According to [8], a CoV larger than 20 % is commonly observed in flexural tests. Test results from [9] found CoV values of the FRC residual strengths f_{R1} (SLS, CMOD = 0.5 mm) and f_{R3} (ULS, CMOD = 2.5 mm) from 3PB tests ranging between 10 % and 33 %. The CoV seems not to decrease with FRC long-term aging effects, as was observed in [10] experimental campaign with 10-years-old specimens. In this case, the CoV of the flexural residual strengths (f_{R1} and f_{R3}) from 3PB and 4PB tests carried out at 10 years-age varied between 11.53 % and 26.23 %.

Moreover, the incorporation of fibers in the concrete mix is important to guarantee a better response of the structure under cyclic and seismic loads. The energy absorption capacity (toughness) and the ductile behaviour of FRC structures can prevent an abrupt failure by guaranteeing large deformations and stress redistributions (multicracking pattern). Besides, fibers are responsible for the crack opening control (fiber bridging), reducing the damage and increasing the durability of structures. This is particularly important in the case of bridge deck and girders. Cyclic tests performed by [11], considering 4PB tests and a step-by-step displacement-controlled loading and reloading up to failure, have shown that the cyclic flexural behaviour and ductility of FRC beams are greatly improved by the amount of fibers. The increase in the performance was more apparent on self-consolidating concrete (SCC) and high strength concrete (HSC) reinforced with steel fibers in relation to ordinary fiber reinforced concrete. Fatigue tests performed by [12] on ordinary concrete (OC) beams demonstrated that fatigue energy was not improved in the case of specimens with FRC overlay until a thickness ratio above 0.5, even with high fiber volume fractions. In contrast,

specimens with FRC underlay were able to improve the fatigue energy even at a lower FRC thickness ratio.

2 RESEARCH SIGNIFICANCE

This paper is aimed to investigate the effectiveness of steel fiber incorporation in RC beams and one-way slabs subjected to static and cyclic loads. Fiber contribution in different structural elements is related to the heterogeneity (fiber distribution and orientation) and the redistribution capacity of the member, the cracking pattern and the failure mechanism. Moreover, the durability of the structure is directly related to the capacity of the fiber to provide enough ductility and toughness (energy absorption capacity) to the structure subjected to static and cyclic loads.

The heterogeneity is an inherent property of FRC. It is a result of fiber distribution, alignment and orientation in the bulk matrix. It significantly penalizes the material, reducing the efficiency of the mechanical response in tension. Due to the heterogeneity, a higher scattering is observed in FRC post-peak mechanical behaviour. The scattering is reduced in the case of RC elements reinforced with fibers. In this case, the steel bars increase the redistribution capacity of the material, resisting to most of the tensile stresses after concrete cracking. However, the influence of fibers in different structural elements (1D-beams and 2D-slabs) is not the same. It is important to have a clear understanding of the benefits of the fibers in different structural elements in order to have more accurate design procedures and also to incorporate fibers in structures which can give a better response, increasing its cost-benefit and its utilization by design engineers and constructors.

A better understanding of fibers benefits in structures subjected to cyclic loads is important to the construction of safer and more durable structures. This is particularly important in the case of bridge design. In this case, the improvement in the mechanical properties (ductility, toughness, flexural capacity) and structural behaviour (deflection, crack opening and distribution, strain hardening/softening response) can lead to the reduction of the maintenance costs during the service life.

3 DESCRIPTION OF THE EXPERIMENTAL CAMPAIGN

The experimental campaign consisted of four-point bending (4PB) static and cyclic tests carried out on RC beams and slabs with different amounts of fiber (20 kg/m^3 and 60 kg/m^3). Static tests were performed in 9 slabs and 3 beams, while cyclic tests were performed in 6 slabs and 3 beams, as is shown in Table 1.

Table 1: Experimental test programme

	Static tests			Cyclic tests		
	RC	FRC 20 kg/m^3	FRC 60 kg/m^3	RC	FRC 20 kg/m^3	FRC 60 kg/m^3
Beams	1	1	1	1	1	1
Slabs	3	3	3	1	3	2

3.1 Material properties

The concrete mix design is shown in Table 2. Three different mixes, respectively with no fiber, 20 kg/m^3 and 60 kg/m^3 of hooked-end steel fibers, were prepared. Dramix 65/35, with 35 mm long and an aspect ratio (l_f/d_f) of 65 was utilized. The mean compressive strength, obtained from 8 nominally identical tests on cylindrical specimens, was equal to 75 MPa.

Table 2: FRC mix design

Material	Quantity (kg/m^3)
Cement	404.00
Coarse aggregates (2.36 – 12.7 mm)	86.00
Quartzite sand	569.00
Artificial sand	410.00
Water	182.00
Polyfunctional	2.45
Hyper-plasticizer	4.55
Total mass	2436.00

The specimens were cast in the same day, in two consecutive batches, using self-compacting concrete (SCC). The steel fibers were incorporated directly in the concrete mixer truck before casting. A moist curing of fourteen days was adopted.

The flexural reinforcement of the beams comprised two bottom steel bars with 16 mm diameter and two top 6.3 mm rebars. The shear reinforcement consisted of 8 mm stirrups spaced respectively with 8 cm between the load point and the support and with 20 cm between the two load points, as shown in Figure 1.

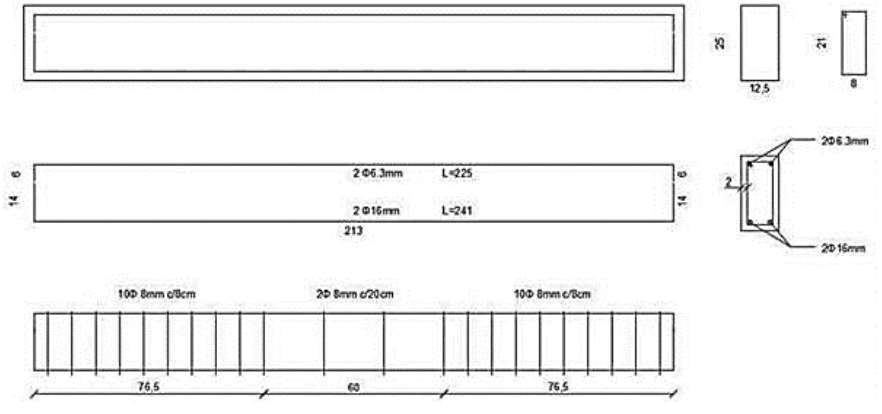

Figure 1: Layout of the reinforcement in beams

The reinforcement of the slabs comprised 7 nos of 16 mm ϕ steel bars in the principal direction and 10 nos. of 8 mm ϕ in the transversal direction, corresponding to a reinforcement ratio of 0.0093, as shown in Figure 2.

The reinforcement of respectively one RC beam and one RC slab, both without fibers, was instrumented with strain gages. The strain gages of the beam were installed on the two bottom longitudinal steel bars, while the ones of the slab were installed on four steel bars, as shown in Figure 3.

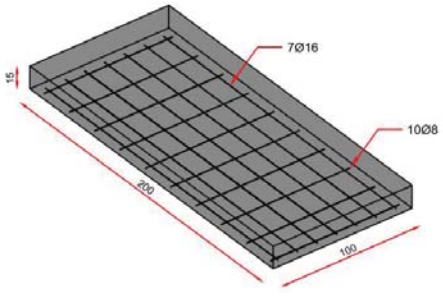

Figure 2: Reinforcement layout of the slabs

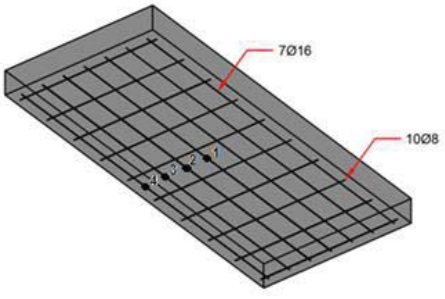

Figure 3: Instrumentation of the steel bars on the slabs

3.2 Experimental tests procedures

The experimental tests were carried out in the Technological Hall of the University of São Paulo. Both the beams and the slabs were subjected to 4PB tests considering a span of 1.80 m and a distance between the two load-knives of 0.60 m, as is shown in Figure 4. The load was applied by means of a servo-hydraulic static and dynamic actuator with a loading capacity of 100 kN.

Deformation controlled static tests, for both the beams and slabs, were carried out considering a constant rate of 0.025 mm/s. Cyclic tests were performed assuming a sinusoidal load variation with a frequency of 4 Hz and a number of cycles limited to 2 million.

Two load variable differential transformers (LVDTs) were used to measure the vertical displacement of the beams and slabs. The LVDTs were installed over the mid-height of the specimens by means of two yokes fixed on the samples (Figure 5).

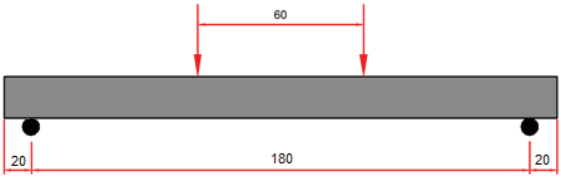

Figure 4. 4PB test scheme for the beams and the slabs

Figure 5. Test on the beam

4 STATIC TESTS RESULTS

4.1 Four-point bending tests on beams

The incorporation of steel fibers led to an increase up to 14.65% of the load bearing capacity of the beams, as is shown in Table 3. In contrast, the vertical displacement had a small improvement due to fibers addition (Table 3).

Table 3: Load carrying capacity (P_{max}) and maximum vertical displacement (δ) of the beams

	P_{max} (kN)	ΔP (%)	δ_{max} (mm)
RC beam with no fibers	157	-	26.68
RC beam with 20 kg/m^3 of steel fibers	169	764	31.02
RC beam with 60 kg/m^3 of steel fibers	180	1465	30.71

4.2 Four-point bending tests on slabs

The three RC slabs demonstrated a ductile behaviour, with steel bars yielding and a maximum deflection beyond the deformation limit capacity (SLS). The RC slabs reinforced with steel bars developed closely spaced cracks in relation to the RC slabs.

The incorporation of steel fibers in the RC slabs led to increased load bearing capacity higher ductility. The results are in agreement with the test results of [6], which have demonstrated an increase of the ultimate load-carrying capacity by approximately 20% due to the incorporation of 35 kg/m^3 hooked-end steel fibers in the concrete mix.

The values of the vertical displacements of the slabs with steel fibers reached two times the ones of the RC slabs (Table 4) and were approximately three times higher than the ones of the RC beams (Table 3).

4.3 Discussion of the results

The static tests have shown that steel fiber incorporation was more efficient in RC slabs in comparison with RC beams, especially regarding ductility and tenacity. The slabs demonstrated a much higher energy absorption capacity and developed higher deformations in relation to the beams due to the addition of fibers. This is patent from the observation of Figure 6.

Table 4: Load carrying capacity (P_{max}) and maximum vertical displacement (δ) of the slabs

	Specimen	P_{max} (kN)	Mean (kN)	ΔP (%)	δ_{max} (mm)
RC slab with no fibers	1	317	286	-	42.60
	2	276			26.46
	3	264			50.00
RC slab with 20 kg/m^3 of steel fibers	1	315	336	17,48	89.11
	2	357			92.56
	3	336			83.52
RC slab with 60 kg/m^3 of steel fibers	1	393	375	31,11	97.77
	2	357			80.00

The higher flexural strength of the RC beams is related, among others, to its higher stiffness in relation to the RC slabs: the first moment of area (W) of the beams is 3 times higher than the one of the slabs (Table 5). Despite the difference in stiffness, the reinforcement ratio ($\rho = A_s/A_c$) was similar in both cases, as is shown in Table 5.

The higher ductility of the RC slabs can be attributed to the biaxial stress state. The internal stresses of the RC slabs are partially absorbed by the reinforcement (before and after cracking) oriented in the transversal direction.

An important increase of the vertical displacement (about two times the one of the RC slab) due to fibers addition was noticed. This phenomenon was not observed in the RC beams, which had a marginal increase of the vertical displacement due to fibers incorporation. Further analyses will be carried out to investigate the contribution of the fibers to the slab ductility.

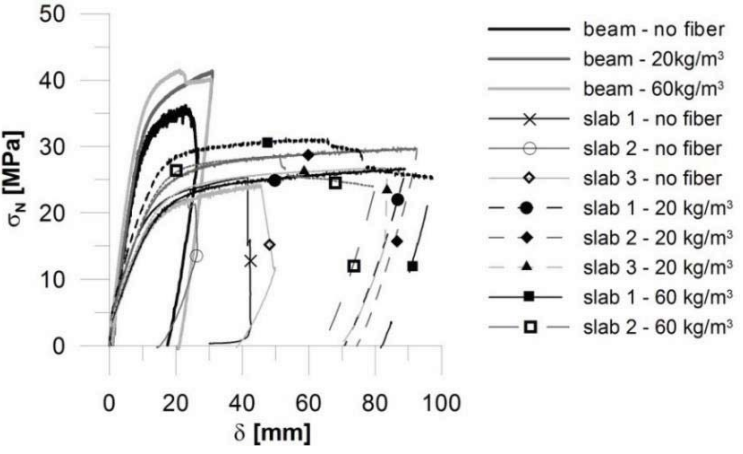

Figure 6: Nominal stress (σ_N) versus vertical displacement (δ) of beams and slabs

Table 5: First moment area (W) and reinforcement ratio (ρ)

	W (cm^3)	ρ (-)
RC beams	0.0013	0.013
RC slabs	0.00375	0.0094

5 CYCLIC TESTS RESULTS

The specimens were submitted to a cyclic load up to 30% of their maximum load carrying capacity in order to represent the likely behaviour of real bridge structures. The amplitude of the load level is shown in Table 6.

Before the beginning of the cyclic tests, the structural elements were submitted to a static loading up to the appearance of the first cracking. After that, the specimens were loaded up to the maximum load level (Table 6) in order to measure the crack width and delineate the crack length. This procedure was repeated three times. The tests were performed assuming a load frequency of 4 Hz and were limited to 2 million cycles.

Table 6: Load levels of the cyclic tests

	Fiber amount (kg/m^3)	Minimum load level (MPa)	Load variation (MPa)	Maximum load level (MPa)
Slabs	no fiber	50	40	90
	20	50	40	90
	60	50	40	90
Beams	no fiber	10	40	50
	20	10	40	50
	60	10	40	50

5.1 Cyclic tests on beams

The first crack appeared at a load level of 22 kN (σ_N = 5 MPa). The load variation (amplitude) during the tests was within the range of 10 kN ($\cong$ 0.06 P_{max}) and 50 kN ($\cong$ 0.30 P_{max}), above the cracking stress. One of the beams has failed at the beginning of the test due to an electrical instability, which led to the lack of control of the actuator.

The results of the tests are shown in Figure 7. In this case, no benefit of fiber incorporation in the RC beams was noticed. It is important to mention that these results cannot be generalized and more tests should be carried out in order to confirm the experimental values. A deeper investigation, including numerical analyses, is still needed to better understand the variability of the results.

5.2 Cyclic tests on slabs

The first crack appears at a load equal to 50 kN (σ_N = 4 MPa), which was defined as the minimum load level. The load variation during the tests was within the range of 50 kN (0.16 P_{max}) and 90 kN (0.30 P_{max}).

The results of the tests are shown in Figure 8. The incorporation of steel fibers in the RC slabs contributed positively to restrain the crack opening due to fiber crack-bridging. As a result, the vertical displacement of the specimens with steel fibers has shown lower values and also a lower variability in comparison with the specimens without fibers. This behaviour was enhanced in the specimen with higher amount of fibers (60 kg/m^3).

5.3 Discussion of the results

The incorporation of steel fibers in the RC slabs led to a reduction of the deflections in time due to the effect of the cyclic load. A greater reduction of the vertical displacements was obtained in the specimen with higher amount of steel fibers (60 kg/m^3). In contrast, no benefit of fiber addition was noticed in the case of the RC beams. A deeper analysis, including numerical simulations, is in progress in order to better understand the differences found in the behaviour of RC beams and slabs.

It is worth mentioning that deflection control (fiber crack-bridging), as was the case of the RC slabs with steel fibers, can guarantee the serviceability limit states (maximum displacements and crack openings) during the structure service life and, as a result, improve the structural durability and increase fatigue service life. This is important, for example, in bridge decks and girders, to control the crack openings due to cyclic loads and, consequently, reduce the permeability (ingress of chlorides and sulfates in water solution) and steel bars

corrosion. Moreover, structural oscillations are decreased due to the reduction of the variability of the vertical displacement (user's comfort).

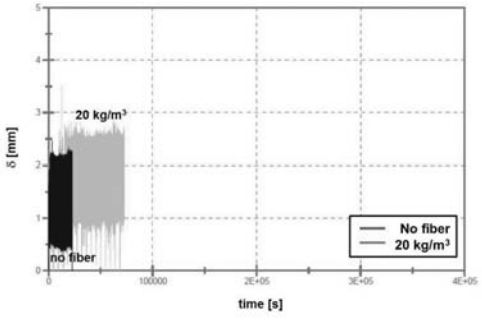

Figure 7: Cyclic tests results of RC beams

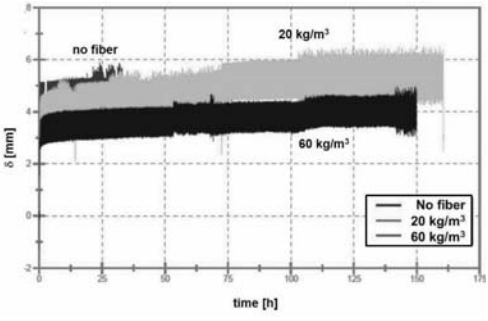

Figure 8: Cyclic tests result of RC slabs

6 CONCLUSIONS

- The static tests have shown that steel fibers incorporation was more efficient in RC slabs in comparison to RC beams, especially regarding ductility and tenacity. The slabs had a much higher energy absorption capacity and developed higher deformations in relation to the beams due to the addition of fibers. The vertical displacement of the RC slabs with steel fibers was approximately three times higher than the ones of the RC beams.
- The flexural capacity of both the RC beams and slabs increased with the addition of steel fibers. Nonetheless, the load carrying capacity of the slabs increased two times more than the beams.
- The cyclic tests demonstrated that fiber incorporation did not result in lower deflections in the case of the beams. In contrast, the RC slabs with steel fibers developed lower deflections compared to their companions with no fibers. The reduction of the vertical displacements was greater in specimens with higher amouts of steel fibers. As a result, the fibers were efficient to control the deflection (crack bridging) in one-way RC slabs, demonstrating their capacity to improve fatigue service life and guarantee the serviceability limit states (lower oscillations and reduction of crack openings).

7 ACKNOWLEDGEMENTS

The authors would like to acknowledge the support of CNPq through a post-doctoral scholarship granted to the first author. This research is part of a large investigation of fiber reinforced concrete structural behaviour developed with the financial support of the hydropower Furnas Centrais Elétricas in Brazil, which is greatly acknowledged.

8 REFERENCES

[1] Wille, K., Kim, D.-J. and Naaman, A. E., 'Strain-hardening UHP-FRC with low fiber contents', *Materials and Structures*, vol. **44**, (2011), pp. 583–598.

[2] Altun, F., Haktanir, T. and Ari, K., 'Effects of steel fiber addition on mechanical properties of concrete and RC beams', *Construction and Building Materials*, vol. **21**, (2007), pp. 654–661.

[3] Dupont, D. and Vandewalle, L., '*Bending capacity of steel fibre reinforced concrete (SFRC) beams*', Proceedings of the International congress on challenges of concrete construction, Dundee; 2002. pp. 81–90.

[4] Berlin, Ernst, V and Sohn, fib - International Federation for Concrete Structures, 'Fib Model Code for Concrete Structures 2010', 92013).

[5] Hognestad, E., 'Yield-Line Theory for the Ultimate Flexural Strength of Reinforced Concrete Slabs', ACI Journal Proceedings, vol. **49** (3), (1953), pp. 637–656.

[6] Fall, D., Shu, J., Rempling, R., Lundgren, K. and Zandi, K., 'Two-Way Slabs: Experimental Investigation of Load Redistributions in Steel Fibre Reinforced Concrete', *Engineering Structures* **80**, (2014), pp. 61–74, http://dx.doi.org/10.1016/j.engstruct.2014.08.033.

[7] Logfren, I., Stang, H. and Olesen, J. S., 'The WST method, a fracture mechanics test method for FRC', *Materials and Structures* **41**, (2008), pp. 197-211.

[8] Laranjeira, F., Grunewald, S., Walraven, J., Blom, C., Molins, C. and Aguado, A., 'Characterization of the orientation profile of steel fiber reinforced concrete'. *Materials and Structures* **44**, (2011), pp. 1093–1111.

[9] Soetens, T. and Matthys, S., 'Different methods to model the post-cracking behaviour of hooked-end steel fibre reinforced concrete', *Construction and Building Materials* **73**, (2014), pp. 458–471.

[10] Teixeira Buttignol, T. E., Colombo, M. and di Prisco, M., 'Long-term aging effects on tensile characterization of steel fibre reinforced concrete', *Structural Concrete* **149**, (2016), pp. 12.

[11] Boulekbache, B., Hamrat, M., Chemrouk, M. and Amziane, S., 'Flexural behaviour of steel fibre-reinforced concrete under cyclic loading', *Construction and Building Materials* 126, (2016), pp. 253–262.

[12] Matsumoto, T., 'Fatigue analysis of fiber reinforced concrete overlaid/underlaid beams', *Fracture Mechanics of Concrete Structures*, de Borst et al (eds), Swets & Zeitlinger, Usse, (2001), pp. 1007-1012.

[13] Kang, S.-T., Lee, Y., Park, Y.-D. and Kim, J.-K., 'Tensile fracture properties of an Ultra High Performance Fiber Reinforced Concrete (UHPFRC) with steel fiber', *Composite Structures* **92**, (2010), pp. 61–71.

[14] Naaman, A. E., 'A statistical theory of strength for fiber reinforced concrete', PhD thesis, Massachusetts Institute of Technology, 1972.

[15] ABNT NBR 8522:2008, "Concrete - Determination of the elasticity modulus by compression", 2008. (in Portuguese)

[16] ABNT NBR 6118, "Design of concrete structures — Procedure", 2014. (in Portuguese)

[17] Logfren, I., Stang, H. and Olesen, J. S., 'The WST method, a fracture mechanics test method for FRC', *Materials and Structures* **41**, (2008), pp. 197-211.

[18] Laranjeira, F., Grunewald, S., Walraven, J., Blom, C., Molins, C. and Aguado, A., 'Characterization of the orientation profile of steel fiber reinforced concrete', *Materials and Structures* **44**, (2011), pp. 1093–1111.

[19] Soetens, T. and Matthys, S., 'Different methods to model the post-cracking behaviour of hooked-end steel fibre reinforced concrete', *Construction and Building Materials* **73**, (2014), pp. 458–471.

[20] Teixeira Buttignol, T. E., Colombo, M. and di Prisco, M., 'Long-term aging effects on tensile characterization of steel fibre reinforced concrete', *Structural Concrete* **149**, (2016), pp. 12.

On the Tensile Characterization of Fiber Reinforced Concrete according to Fib Model Code 2010

Buttignol, T. E. T. [(1)], Fernandes, J. F. [(1)] , Bittencourt, T. [(1)], Sousa, J. L. A. O. [(2)]

[(1)] Polytechnic School, University of São Paulo, Brazil

[(2)] FEC, University of Campinas, Brazil

ABSTRACT

The primary objective of this paper is to investigate the reliability of the new fib Model Code 2010 (MC 2010) to classify and characterize a fiber reinforced concrete (FRC) mix design developed for the hydropower company Furnas Centrais Elétricas in Brazil. One of the most important aspects of FRC regards its heterogeneity, which is directly related to the amount, alignment and distribution of fibers in the bulk concrete. The lack of design codes imposes a barrier to the development of the full potential of this material for structural applications, which remains mostly used for concrete crack control and durability purposes. The introduction of design rules for FRC characterization and classification in the new fib Model Code represents a significant step forward in the rationalization of its applications. In this project, three-point bending tests were carried out to obtain the material class. From the latter, FRC constitutive law in tension was determined. To verify MC 2010 reliability, indirect tensile Double Edge Wedge Splitting (DEWS) tests were performed and compared with the FRC constitutive law. The comparison of the results demonstrated that the design procedures described in MC 2010 are reasonable and are on the safe side.

Keywords: Fiber reinforced concrete, material classification, design procedure, constitutive law, bending test, Double edge wedge splitting (DEWS).

1 INTRODUCTION

During the last decades, a large effort was made in order to characterize fiber reinforced cementitious composites (FRCC). The incorporation of fibers to concrete was a milestone for concrete structural design and construction. The main innovation introduced by this new cementitious composite is the ductile response after concrete cracking obtained by the fiber pull-out effect of dispersed fibers immersed in concrete. In this system, the matrix is responsible to carry the compressive load and the fibers are responsible to carry the tensile forces alone or in companion with steel bars. After concrete cracking, fibers are continuously engaged until crack localization, when fiber pull-out mechanism is fully activated and a progressive debonding takes place (crack bridging). The higher energy absorption capacity (toughness) and ductility of FRC allowed a better response of structures to seismic actions, severe loads and fatigue. Fiber reinforced concrete (FRC) is currently largely utilized in pavements and tunnelling applications for crack control due to drying-shrinkage and permanent deformations (plastic and creep strains). FRC lower permeability reduces water penetration and, as a result, steel bars corrosion, guaranteeing a larger durability of the structural element.

One of the main problems of FRC, together with the cost of production (especially in developing countries) and the lack of design codes, is related to the heterogeneity of the material (fibers distribution and orientation), which restricts its applications as a structural material, limiting it to improve the durability of concrete elements. Fibers distribution has been studied for a long time and new casting techniques were created to induce fiber orientation in predefined directions.

Fibers distribution is also affected by the lower workability of FRC. The problem of flow ability affects especially structures with dense reinforcement. The development of new super and hyper-plasticizers ensure very high slump values and contributed to the development of new types of materials, such as self-compacting concrete (SCC), which guarantee a better alignment of the fibers in the bulk concrete.

Besides that, FRC structural response (softening or hardening behavior) largely depends on the type and quantity of fibers and on the type of test performed. For example, a material tested in uniaxial tension could develop a single crack and a softening behavior in terms of nominal stress versus crack opening displacement (σ_N-COD). The same material in bending could be subjected to a multiple crack pattern, resulting in a hardening response in terms of load-deflection (P-δ) curve. As a result, [1] and [2] proposed to classify and explain FRC structural behavior according to the different test methodologies (bending tests, panel tests or uniaxial tensile tests) and the material response (softening or hardening). In spite of that, a very important issue regards the procedures adopted in order to obtain the post-cracking response. Different test procedures were developed to characterize the mechanical behavior of FRC, for example, round panel test ASTM C1150 [3], flexural tests on notched and unnotched beams (RILEM TC 162-TDF [4] and EN 14651 [5]), uniaxial direct and indirect tensile tests (Barcelona (BCN) [6], Wedge Splitting Test (WST) [7] and Double Edge Wedge Splitting (DEWS) [8]).

The DEWS [8] test is an indirect tensile test, as WST [7], in which a compressive load is applied to induce the development of splitting forces on the ligament. The advantage of DEWS methodology is that it does not need an inverse analysis to determine the σ_N-COD curve. In this case, a double notch both at the top and at the bottom of the specimen is created, generating a pure mode I fracture behavior and allowing the complete uncoupling of the stress field, which results in the development of an arch of compression and the concentration of tensile stresses on the ligament.

Since concrete post-peak behavior is the most important characteristic of FRCC, the experimental test should be able to capture fibers pull-out response. The fib Model Code 2010 [9] (MC 2010) recommends bending tests on notched beams and an inverse analysis, as described in [2], to obtain the tensile constitutive law of the material.

One important question treated in the MC 2010 [9] is FRC classification and characterization. The classification takes into account the characteristic residual post-cracking strength, determined from bending tests on notched beams according to standard procedures. The characteristic values can be calculated based on Eurocode [10]. The tensile characterization, for design purposes, can be determined from the material class, as described in the MC 2010 [9].

In this paper, FRC tensile characterization is carried out by means of 3PB tests according to EN 14651 [5]. The material classification is determined following MC 2010 [9] recommendations, by means of the characteristic values of the flexural residual strengths. The constitutive law of the material is obtained according to the MC 2010 [9]. It is compared with the results of the DEWS tests in order to verify the reliability of the MC 2010 procedures.

2 RESEARCH SIGNIFICANCE

The introduction of a chapter regarding FRC in the MC 2010 [9] offers a great opportunity to expand fibers utilization for structural applications and not only for serviceability conditions (crack control) and durability purposes. This is especially important in developing countries, where the lack of a more profound understanding of the benefits and properties of the material both by design engineers and constructors, together with the higher cost of production and the lack of national codes, imposes a barrier to the expansion of FRC to different areas, such as bridges (girders and deck), buildings (slabs and beams) and wind towers (precast elements). New design codes are in development worldwide, taking the MC 2010 [9] as the main reference, as is the case of the new Brazilian code.

Taking that in mind, this paper is aimed to verify MC 2010 [9] reliability by means of a comparison between the FRC constitutive law and indirect tensile DEWS [8] tests. The constitutive law was obtained from the material class, which was defined based on the residual post-cracking strength of 3PB tests on notched beams. These tests are part of a larger project developed for the hydropower company Furnas Centrais Elétricas in Brazil.

3 DESCRIPTION OF THE EXPERIMENTAL CAMPAIGN

The experimental tests, including three-point bending tests and indirect tensile DEWS tests, were carried out in the Technological Hall of the University of São Paulo using an electromechanical press INSTRON 8802, with a loading capacity of 250 kN.

The flexural tests were carried out using twelve prisms 150 × 150 × 600 mm, divided in two groups of six beams, respectively with 20 kg/m^3 and 60 kg/m^3 of hooked-end steel fibers. The specimens were cast in the same day using self-compacting concrete (SCC). The steel fibers were incorporated insite directly in the concrete mixer truck before casting.

DEWS tests were performed on fifteen cubes sawed from two rectangular plates with 750 × 750 mm and a depth of 150 mm. The plates were cast respectively from the center and from the border, as is shown in Figure 1, with the same concrete batch.

A moist curing of fourteen days was adopted. After this period, the elements were demolded and prepared to the tests (sawing and notching procedures).

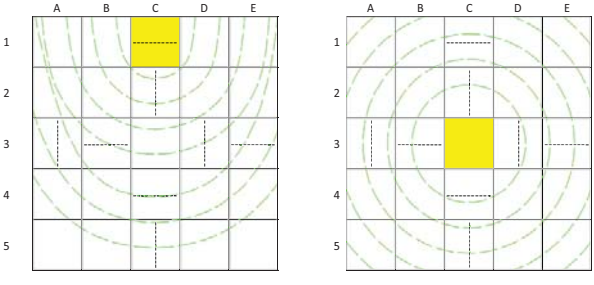

Figure 1. Casting procedures of FRC plates (circular and concentric dashed lines) and notch orientation (straight dashed lines) of DEWS samples.

3.1 Material properties

The concrete mix design is shown in Table 1. Two different mixes, respectively with 20 kg/m^3 and 60 kg/m^3 of hooked-end steel fibers, were prepared. In this case, Dramix 65/35, with 35 mm long and an aspect ratio (l_f/d_f) of 65 was utilized.

Table 1: FRC mix design

Material	Quantity (kg/m^3)
Cement	404
Coarse aggregates (2.36 – 12.7 mm)	864
Quartzite sand	569
Artifitial sand	410
Water	182
Polyfunctional	2.45
Hyper-plasticizer	4.55
Total mass	2436

The compressive strength and the Young modulus were measured on cylindrical specimens. The Young modulus, determined experimentally, was slightly higher in FRC specimens compared to plain concrete. The average values of the experimental results, together with the estimated values of the characteristic compressive strength and Young modulus, are shown in Table 2, where: PC is the plain concrete; F20 is the concrete specimens with 20 kg/m^3 of steel fibers; F60 is the concrete specimens with 60 kg/m^3 of steel fibers.

Table 2: Experimental and estimated values of the compressive strength and Young modulus

Properties	PC	F20	F60
No. of specimens:	8	5	5
$f_{cm\ (exp)}$ (MPa)	74.73	74.45	75.65
$^{**}f_{ck\ (estimated)}$ (MPa)	67.0	67.0	67.00
$^{*}E_{c(exp)}$ (MPa)	37.45	41.97	39.87
$^{**}E_{cm\ (estimated)}$ (MPa)	42.91	42.91	42.91

* According to the Brazilian National Code NBR 8522:2008 [11].
** According to the Brazilian National Code NBR 6118:2014 [12].

3.2 Flexural tests procedure

The three-point bending tests were performed according to EN 14651 [5], as is shown in Figure 2.

The crack-mouth opening displacement (CMOD) was measured with a clip gage installed in the center of the mouth of the beam notch.

Twelve tests were carried out, divided in two groups of six beams, respectively with 20 kg/m^3 and 60 kg/m^3 of steel fibers. The tests of each group were nominally identical, considering the same material, experimental procedure, casting method and specimen dimension.

3.3 Double Edge Wedge Splitting (DEWS) tests procedure

Fifteen cubic specimens with 150 × 150 × 150 mm and 20 kg/m^3 of steel fibers were tested. The samples were sawed from two plates cast respectively from the center and from the border. In the first case, eight specimens were tested, while in the second case, seven tests were performed.

The DEWS tests were carried out according to di Prisco et al [8] procedure. The crack opening displacement (COD) was measured with two LVDTs installed on the center of the front and rear surfaces of the specimen.

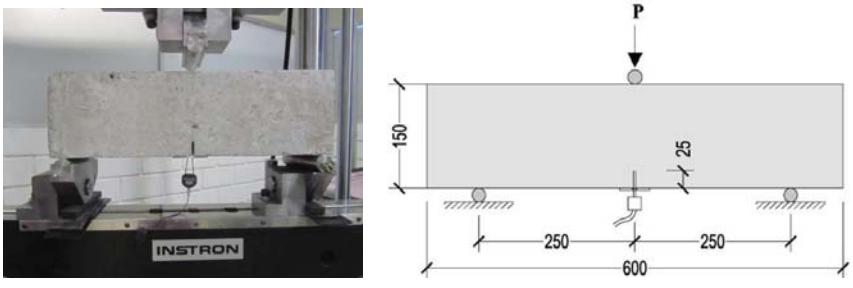

Figure 2. Three-point bending tests according to EN 14561 [5].

4 EXPERIMENTAL RESULTS

4.1 Three-point bending tests

The experimental results of the 3PB tests, considering the first crack strength (f_{LOP}) and the residual strengths at 0.5 mm (f_{R1}), 1.5 mm (f_{R2}), 2.5 (f_{R3}) and 3.5 mm (f_{R4}), together with the mean values and the coefficient of variance (CV), are shown in Table 3.

The experimental results in terms of σ_N - CMOD curves are shown in Figure 3.

Table 3. Experimental results of three-point bending tests

Fiber amount (kg/m³)	Parameters	Samples						Mean	CV (%)	Standard Deviation
		1	2	3	4	5	6			
20	f_{LOP}	4,63	6,51	6,88	6,98	6,62	5,70	6,22	14,47	0,90
	f_1	2,36	1,63	2,60	1,91	1,97	1,99	2,08	16,67	0,35
	f_2	1,66	1,61	2,16	1,64	1,97	1,76	1,80	12,17	0,22
	f_3	1,14	0,99	1,35	1,27	1,09	1,02	1,14	12,27	0,14
	f_4	0,93	0,77	1,00	0,90	0,89	0,64	0,86	15,07	0,13
60	f_{LOP}	5,80	9,45	7,87	7,05	8,81	7,63	7,77	16,61	1,29
	f_1	8,87	15,75	15,76	10,26	15,19	10,78	12,77	24,56	3,14
	f_2	7,91	16,30	12,68	9,79	14,76	9,42	11,81	27,99	3,31
	f_3	7,48	15,30	9,35	8,30	13,75	7,26	10,24	33,53	3,43
	f_4	6,27	13,43	7,30	7,32	12,73	5,74	8,80	38,37	3,38

From the results, it is possible to notice that the CV was higher in the tests considering specimens with 60 kg/m³ of steel fibers. This can be attributed to the higher variation of the amount of fibers in these specimens. The fibers counting after the tests indicated a value between 70 kg/m³ to 135 kg/m³. In contrast, the specimens with 20 kg/m³ have shown a small variation in the quantity of fibers, ranging from 16.5 kg/m³ to 21.5 kg/m³.

The variation of the CV values is in agreement with the ones described in literature. The CV calculated by [13] from 3PB tests varied up to 38%. According to [14], a CV larger than 20% is commonly observed in flexural tests. In turn, [15] found CV values of f_{R1} (SLS, CMOD=0.5 mm) and f_{R3} (ULS, CMOD=2.5 mm) from 3PB tests ranging between 10% and 33%.

These results highlight the high heterogeneity of fiber reinforced cementitious materials. They are an important reminder of the importance of a highly controlled casting procedure, which should be in agreement with design recommendations. Poor insite control can lead to fiber segregation during casting, high variability in the amount of fibers and a random orientation of the fibers, which can lead to a high variability in the flexural response among the structural elements.

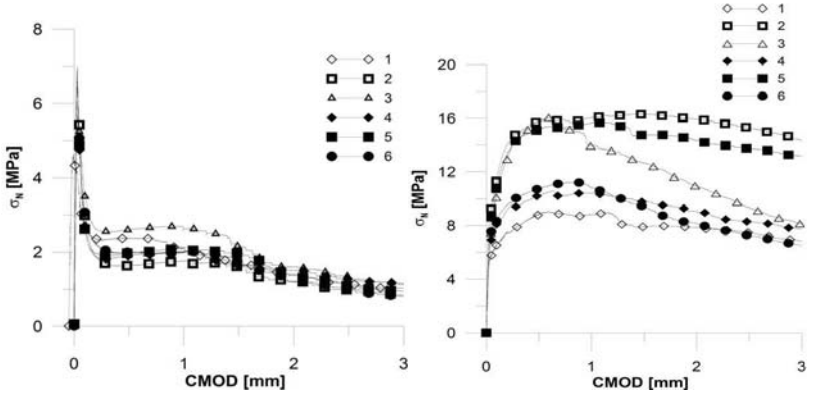

(a) (b)

Figure 3. Experimental results of 3PB tests in terms of σ_N-CMOD curves: a) specimens with 20 kg/m^3 of fibers; (b) specimens with 60 kg/m^3 of fibers.

4.2 Double Edge Wedge Splitting (DEWS) tests

The experimental results in terms of σ_N-COD curves are shown in Figure 4.

The scattering of the test results obtained in this case is directly associated with the position of the notch cutting in relation to the fiber alignment and the casting flow (Figure 1). Casting from the border is more effective to obtain a better alignment of the fibers in one preferential direction. In this case, the wall effect is reduced to the opposite side of the casting place and a preferential alignment is induced in the direction of the concrete flow. When casting from the center, the wall effect acts on the four sides of the concrete mold. In this case, for the same notch cutting, the specimens sawed from the plate cast from the center (Figure 4b) have shown a slightly higher scattering of the results in comparison to the ones sawed from the plate cast from the border (Figure 4a). Despite that, the difference in the DEWS test results can be attributed mainly to the notch position in relation to the fiber preferential alignment (perpendicular or parallel) and the quantity of fibers in the ligament (crack bridging).

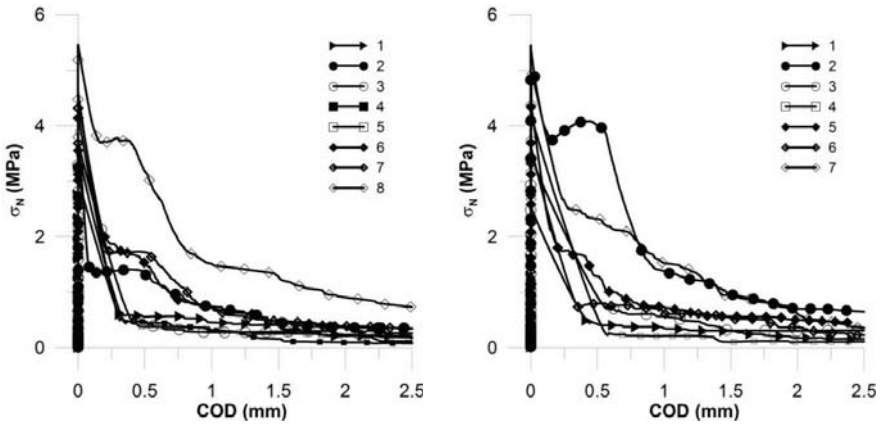

Figure 4. Experimental results of DEWS tests in terms of σ_N-COD curves: a) specimens sawed from the FRC plate cast from the border; b) specimens sawed from the FRC plate cast from the center.

5 FRC CLASSIFICATION AND CHARACTERIZATION ACCORDING TO MC 2010

5.1 Characteristic values

The characteristic values were calculated according to Eurocode [10] as is shown in Equation 1, where: X_m is the average stress value and V_x is the coefficient of variation.

The coefficient of variation (CV) is defined according to Equation 2, where σ_x is the standard deviation and K_m is a parameter that depends on the number of specimens tested and the previously knowledge of V_x. In this case, to define the value of K_m (Table 5), the coefficient of variation (V_x) was supposed to be unknown. Eurocode [10] states that "V_x known" should be used only when the coefficient of variation or a realistic upper limit is known from prior knowledge. In this case, no prior data or an upper limit value exists for this material. As a result, the value of K_m was defined as equal to 2.18.

The characteristic values of the 3PB tests, considering the first crack strength (f_{LOP}) and the residual strengths at 0.5 mm (f_{R1}) and 2.5 mm (f_{R3}) are shown in Table 4.

$$X_k = X_m \cdot (1 - K_m \cdot V_x) \quad (1)$$

$$V_x = \sigma_x / X_m \quad (2)$$

Table 4: Characteristic values of the three-point bending tests

Quantity of fibers	$f_{LOP,k}$ (MPa)	$f_{R1,k}$ (MPa)	$f_{R3,k}$ (MPa)
20 kg/m^3	4.26	1.32	0.84
60 kg/m^3	4.95	5.93	2.75

Table 5: Values of K_m for the 5% characteristic value (Eurocode [10])

n	1	2	3	4	5	6	8	10	20	30	∞
V_x known	2.31	2.01	1.89	1.83	1.80	1.77	1.74	1.72	1.68	1.67	1.64
V_x unknown	-	-	3.37	2.63	2.33	2.18	2.00	1.92	1.76	1.73	1.64

5.2 Material classification

The classification of the material was carried out according to MC 2010 [9]. The post-cracking strength is defined according to the value of $f_{R1,k}$ within the range 1,0 to 8,0 MPa. The ratio $f_{R3,k}/f_{R1,k}$ defines the material behavior (softening or hardening) according to the alphabet letters "a" to "e", as is shown in Table 6. For structural applications: $f_{R3,k}/f_{R1,k} > 0.5$.

The material class, for the two types of specimens (containing 20 kg/m^3 and 60 kg/m^3 of steel fibers) is shown in Table 7. For classification purposes, one has to define a value of $f_{R1,k}$ that is equal or lower than the characteristic one obtained from the experimental tests(Table 4). Moreover, the ratio of $f_{R3,k}/f_{R1,k}$ should be equal or higher than 0.5. The values of $f_{R1,k}$ and $f_{R3,k}$ adopted are shown in Table 7.

Table 6: FRC classification according to the material response

Class	f_{R3k}/f_{R1k}	material response
A	0.5	Softening
B	0.7	
C	0.9	
D	1.1	Hardening
E	1.3	

Table 7: Material class according to MC 2010

Quantity of fibers:	20 kg/m^3	60 kg/m^3
Class:	1b	5a

One interesting aspect of the results is that the amount of fibers was inversely proportional to the material response: the specimens with a lower quantity of fibers (20 kg/m^3) demonstrated a better post-peak behaviour (higher value of $f_{R3,k}/f_{R1,k}$). This is an indication of the difference in the levels of heterogeneity between the two types of materials.

In contrast, the amount of fibers was directly proportional to the peak strength, which was improved for the specimens with 60 kg/m^3 of steel fibers. The results demonstrate the benefits of fiber incorporation in the concrete mix.

5.3 FRC tensile constitutive law

The tensile constitutive law (simplified post-peak nominal stress-crack opening relationship) of the material was obtained from the 3PB tests and the material class, considering the specimens with 20 kg/m^3 of fibers. The MC 2010 model is based on the residual strengths both at Serviceability Limit State (f_{Fts}; COD = 0 mm; SLS), as is shown in Equation 3, and Ultimate Limit State (f_{Ftu}; COD = 2.5 mm; ULS), as described in Equation 4. The values of f_{R1} and f_{R3}were obtained from the material classification.

$$f_{Fts} = 0.45 \cdot f_{R1}\text{b} \quad (3)$$

$$f_{fTU} = 0.50 \cdot f_{R3} - 0.2 \cdot f_{R1} \quad (4)$$

6 COMPARISON BETWEEN FRC TENSILE CONSTITUTIVE LAW AND DEWS RESULTS

A comparison between the indirect tensile DEWS tests and the tensile constitutive law, considering the characteristic $(\sigma\text{-}w)_k$ and design values$(\sigma\text{-}w)_d$, is shown in Figure 5. In this case: $X_d = X_k/\gamma_d$; $\gamma_d = 1$.

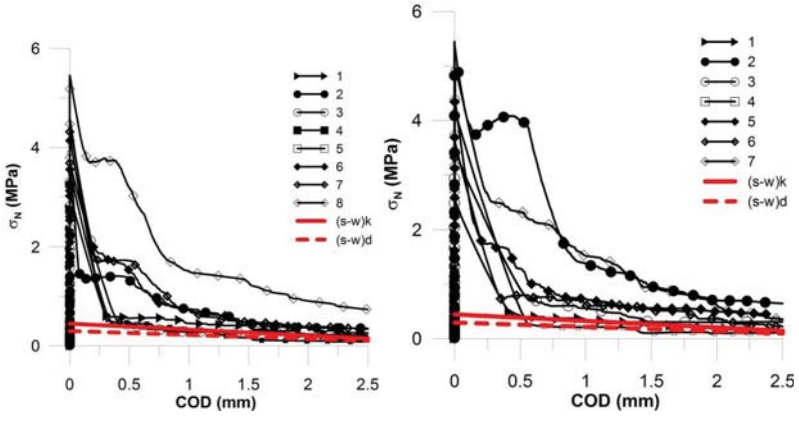

Figure 5. Comparison between DEWS results and the tensile constitutive law: a) specimens cast from the border; b) specimens cast from the center.

The results are in agreement with the ones obtained by [16], demonstrating that the procedures adopted to determine the tensile design constitutive law, as is described in MC 2010, are on the safe side.

- It is worth mentioning that FRC heterogeneity, related to fibers amount, alignment and distribution, has a major impact on the classification and characterization of the material. It can lead to a non-negligible difference between the mean and the characteristic residual flexural strength values. In the case investigated, considering the beams with 60 kg/m^3 of fibers, the f_{R1}mean value was equal to 12.77 MPa, while the characteristic value was equal to 5.93 MPa (-115%) and the material was classified as 5a (-155%). These results had a direct effect on the back identified constitutive relationship. They led to low residual tensile strength values and also to an underestimation of the true tensile response, which is expected for design purposes.

7 CONCLUSIONS

- The classification and characterization of FRC from three-point bending tests were carried out in accordance with fib Model Code 2010 [9]. The tensile constitutive law of the material, determined from the simplified procedure described in MC 2010, was compared with indirect tensile DEWS tests. The main conclusions are described below.
- The heterogeneity of FRC leads to a high scattering of the results. In the experimental tests, the coefficient of variation (CV) ranged from 14% to 38%.
- A high variability in the amount of fibers, together with a random orientation and poor dispersion (segregation), can lead to a high variation in the flexural response (peak strength and slope of the post-peak curve) of nominally identical tests. In the case

analysed, the specimens with a lower amount of fibers (20 kg/m^3) demonstrated a better post-peak behaviour (f_{R3k}/f_{R1k} = 0.70) in relation to the ones with 60 kg/m^3 (f_{R3k}/f_{R1k} = 0.50).

- FRC heterogeneity led to a non-negligible difference between the mean and the characteristic values, with a direct effect on the characteristic flexural strength values and, hence, on the classification and characterization of the material.
- The comparison between the tensile constitutive law and the DEWS results demonstrated that the procedure adopted to determine the tensile constitutive law, based on the material classification described in the MC 2010, is on the safe side. The results are in agreement with BUTTIGNOL et al. [16].

8 ACKNOWLEDGEMENTS

The authors would like to acknowledge the support of CNPq through a post-doctoral scholarship granted to the first author. This research is part of a large investigation of fiber reinforced concrete structural behaviour developed with the financial support of the hydropower Furnas Centrais Elétricas in Brazil, which is greatly acknowledged.

9 REFERENCES

[1] Naaman, A. E., Reinhardt, H. W., Proposed classification of HPFRC composites based on their tensile response. *Materials and Structures*, 39 (2006) 547–555.

[2] diPrisco, M., Colombo; M., Dozio, D., Fibre-reinforced concrete in fib Model Code 2010: principles, models and test validation, *Structural Concrete*,14 (2013) 342–361.

[3] ASTM C1150, Standard Test Method for Flexural Toughness of Fiber Reinforced Concrete (Using Centrally Loaded Round Panel) (2008).

[4] RILEM TC 162-TDF, Recommendations of RILEM TC 162-TDF: Test and design methods for steel fibre reinforced concrete, *Materials and Structures* 33(225) (2000) 3-5.

[5] EN 14651, Test method for metallic fibered concrete - Measuring the flexural tensile strength (limit of proportionality (LOP), residual), European Committee for Standardization (2005).

[6] Carmona, S., Aguado, A., Molins, C., Characterization of the properties of steel fiber reinforced concrete by means of the generalized Barcelona test, *Construction and Building Materials*,48, (2013), 592–600.

[7] Logfren, I., Stang, H., Olesen, J. S., The WST method, a fracture mechanics test method for FRC, Materials and Structures 41 (2008), 197-211.

[8] Di Prisco, M., Ferrara, L., Lamperti, M. G. L., Double edge wedge splitting (DEWS): an indirect tension test to identify post-cracking behaviour of fibre reinforced cementitious composites, *Materials and Structures*, 28 (2013).

[9] *fib* - International Federation for Concrete Structures, Fib Model Code for Concrete Structures, (2010), Berlin, Verlag Ernst and Sohn, (2013).

[10] EN 1990, Eurocode: Basis of Structural Design, (2002).

[11] ABNT NBR 8522:2008, Concrete - Determination of the elasticity modulus by compression, (in Portuguese) (2008).

[12] ABNT NBR 6118, Design of concrete structures — Procedure, (in Portuguese) (2014).

[13] Logfren, I., Stang, H., Olesen, J. S., The WST method, a fracture mechanics test method for FRC, *Materials and Structures* 41 (2008) 197-211.

[14] fLaranjeira, F., Grunewald, S., Walraven, J., Blom, C., Molins, C., Aguado, A., Characterization of the orientation profile of steel fiber reinforced concrete *Materials and Structures* 44 (2011) 1093–1111.

[15] Soetens, T., Matthys, S., Different methods to model the post-cracking behaviour of hooked-end steel fibre reinforced concrete, *Construction and Building Materials* (73) (2014) 458–471.

[16] Teixeira Buttignol, T. E., Colombo, M., di Prisco, M., Long-term aging effects on tensile characterization of steel fibre reinforced concrete, *Structural Concrete* (149) (2016) 12.

Application of Digital Image Correlation (DIC) and Fracture Mechanics to Monitor and Measure Complex Mechanisms of Damage and Fracture in Reinforced Concrete structures

Luis Saucedo-Mora and M. Carmen Andrade Perdrix

Institute Eduardo Torroja for Construction Sciences (CSIC), Madrid, Spain

ABSTRACT

The reinforced concrete structures need to be monitored to ensure their structural integrity, but sometimes those measurements are very local and the instrument is complex to locate physically in the structure and may interfere in it. Digital image correlation, DIC, is a non-contact and non-destructive experimental technique capable to measure the displacement field in a big region of a structure with a great accuracy. This allows extracting valuable information from the fracture processes of reinforced concrete structures critical for the evaluation of the structural integrity. The identification of the energy dissipated by the structure is essential for the identification of the strength mechanisms that are failing in the structure, and to identify a proper repair. In this work using fracture mechanics valuable information is extracted from the fracture processes of the reinforced concrete beam, such as the Mode I and Mode II fracture energy released at each loading step, which is essential to evaluate the elastic energy that the structure can accumulate before collapse. The examples enable to anticipate the importance of DIC for future studies at large scale of fracture in reinforced concrete and other materials related to construction.

Keywords: Digital Image Correlation, structural integrity, fracture mechanics.

1 INTRODUCTION

For any solicitation the structure always behaves following the energetic balance where the external work is mainly transformed into kinetic, elastic, plastic and fracture energies [1]. This is altered in a damaged structure, which has a lack of capacity to store elastic energy, releasing part of the external work as fracture energy and allowing the cracks to grow influenced by the local material and geometry [2]. Through the identification of the cracks tips and measuring the full field displacement, the stress intensity factors can be calculated as well as the energy release rate of each crack [3] in shear and tension [4]. This information is valuable to determine the integrity of a structure. Showing that the strain state along the structure, and especially around each crack tip can predict the microstructural mechanisms failing in the material [5]. Identifying the repairs required, and the safety of the structure through its total energy release rate, with independence of the loading history, our results demonstrate how a contactless and affordable technique can tackle this highly demanded problem.

Digital Image Correlation (DIC) is a robust, non-destructive and non-contact experimental technique widely used in the last decades for micromechanical characterization of materials [6]. It uses images of a surface to measure its local displacements, being the input of DIC a pair of images (i.e. the reference and deformed), which are divided in

windows to correlate them and measure its displacements [7]. This technique is well-known, although is still very scarcely employed in real size concrete structures with successful results. The great complexity and size of the concrete elements were a drawback for the use of DIC, but the information that can be extracted with it is essential for the full characterization of the fracture processes of concrete, which has encouraged its application. Thus, among others, in 2006 Küntz et al. [8] applied DIC to measure the stability of a shear crack in a reinforced concrete bridge during loading. In 2012 Lee et al. [9] compared the measurements done with DIC in a reinforced concrete structure with foil and vibrating wire strain gauges. They concluded that DIC is more versatile and as accurate as the others. In 2013, Dutton et al. [10] used DIC to measure the curvature of a reinforced concrete beam of 3.8m long. They did it imaging 2 regions of 600 × 400 mm where the deflection was calculated. And in 2014, Fayyad and Lees [11] used it to measure the opening of a crack in a notched beam of 0.8 m long.

This paper will focus on exploring the possibilities of application of DIC as a health monitoring technique for civil structures, mainly motivated by its non-contacting and non-destructive nature.

2 EXPERIMENTS

2.1 Fracture test of a pre-stress beam

In this case the DIC method was applied to a three point bending test in a concrete beam with 4 rebars and a span of 700 mm with a 250 × 200 mm section. The concrete has a compressive strength of 75 MPa, and the beam has 4 longitudinal rebars of a 1670 C steel with a diameter of 7.5 mm located 2 at 50 mm from the top of the beam, and other 2 at 40 mm from the bottom without any shear reinforcement. The imaged area was 390 × 260 mm located beneath the loading point in the centre of the beam front. The images were taken with a camera Nikon D7200, with a size of 6000 × 4000 pixels (i.e. 24 Megapixels) resulting in a pixel size of 0.065 mm. The images are treated with the softwares Moire Analysis V0.956b [12] and Image J 1.46r [13], using a windows size of 160 × 160 pixels and an overlap of the 50% with a single pass, and corrected with the algorithm of Saucedo-Mora [14]. This gives an error of 5 μm, measured with an undeformed image displaced with a rigid body movement. After the calculation with the deformed images, the displacement field was corrected for rigid body movements, rotation and out of plane movements.

During the different loading steps, the cracks tips were located manually through the DIC information, and the K_I and K_{II} were fitted through the stress intensity factor formulation, then the energies G_{fI} and G_{fII} were obtained from the values of the strain intensity factors. With this procedure, the energies shown in Figure 1 were calculated.

3 RESULTS

Figure 1 shows the strain energy release rate of 2 cracks located in the center of the beam and in one side. These were measured in load/unload cycles, taking the reference pictures on the unloaded and the deformed ones after the reload ensuring the independency of the measurements. Crack 1 is located in the center of the beam and Crack 2 at one side. The Crack 1 appeared at 215 kN (A of Figure 1) and started releasing energy in Mode I until it crossed the pre-stressed bars, when the crack release energy in Mode II combined with Mode I. The strain energy release rate of this crack continues growing until the failure in point B. At 400 kN, the Crack 2 starts to grow, but perhaps it's inclined, the energy is released in Mode I, decreasing its strain energy release rate, which means that the internal mechanism of the material were capable to resist it. Globally, looking at any point of the full test, the energy is mainly released in Mode I, so if we want to repair it, we should act in the Mode I

mechanisms, such as the reinforcement at the bottom of the beam. Also, thanks to the DIC strain field, the damaged region can be identified, making the repairs local.

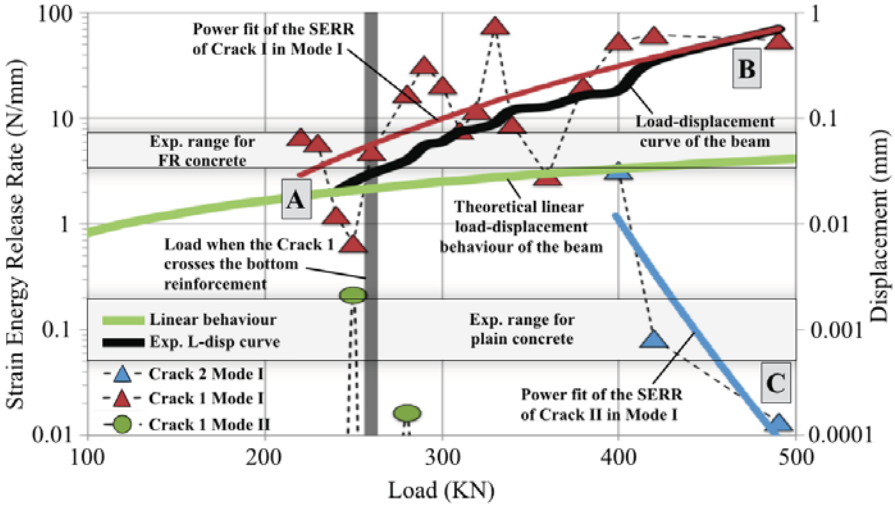

Figure 1. Relationship between the load-displacement behaviour of the beam, measured with the load cell and the displacement of the actuator, and the energy release rate of the 2 cracks at each point, in Mode I and Mode II

4 CONCLUSIONS

The contactless nature of this methodology and the reduced cost of its experimental equipment also pave the way for the application of this technique in the structural integrity evaluation of key buildings and infrastructures, where the safety after an earthquake or an accident needs to be ensured. Further investigation needs to be done to accurately relate the value of the strain energy release rate with the structural integrity and to identify the most suitable repairs to stop the energy release rate in Mode I and Mode II.

ACKNOWLEDGEMENT

Luis Saucedo-Mora wants to acknowledge the financial support given by the Secretariat of State for Research, Development and Innovation of the Spanish government under the grant IJCI-2014-19362 associated to a Juan de la Cierva Incorporation Fellowship. The authors want to acknowledge Jesús Rodríguez Santiago for the design and preparation of experiments of the reinforced concrete beams, which were done as part of the Master SEDUREC in the CSIC. The company Hijos De Gregorio Del Pliego S.L generously supplied the beams at no cost. The authors want to acknowledge as well Rogelio Sánchez Verdasdo for his support during the test with the manipulation and setup of the cameras.

REFERENCES

[1] Z. P. Bažant, L. Cedolin. Stability of Structures: Elastic, Inelastic, Fracture and Damage Theories, 2010, World Scientific Publishing Co. Pte.Lfd., ISBN-13:978-981-4317-02-3.

[2] A. Carpinteri, N. Pugno. Are scaling laws on strength of solids related to mechanics or to geometry?. Nature Materials, 2005, 4: 421-423.

[3] S.P. Shah, S.E. Swartz, C. Ouyang. Fracture Mechanics of Concrete: Applications of Fracture Mechanics to Concrete, Rock and Other Quasi-Brittle Materials. Wiley, 1995, ISBN: 978-0-471-30311-4.
[4] J.M. Ramsey, F.M. Chester. Hybrid fracture and the transition from extension fracture to shear fracture. Nature, 2004, 428: 63-66.
[5] R. O. Ritchie. The conflicts between strength and toughness. Nature Materials, 2011, 10: 817-822.
[6] T. C. Chu, W. F. Ranson, M. A. Sutton. Applications of digital-image-correlation techniques to experimental mechanics. Experimental Mechanics. 1985. 25(3): pp. 232-244. doi: 10.1007/BF02325092
[7] B. Pan, K. Qian, H. Xie and A. Asundi. Two-dimensional digital image correlation for in-plane displacement and strain measurement: a review. Measurement Science and Technology. 2009. 20: 062001. doi: http://dx.doi.org/10.1088/0957-0233/20/6/062001
[8] M. Küntz, M. Jolin, J. Bastien, F. Perez, F. Hild. Digital image correlation analysis of crack behavior in a reinforced concrete beam during a load test. Canadian Journal of Civil Engineering, 2006, 33:1418-1425, doi: 10.1139/l06-106
[9] C. Lee, W.A. Take, N. A. Hoult, M. ASCE. Optimum Accuracy of Two-Dimensional Strain Measurements Using Digital Image Correlation. Journal of Computing in Civil Engineering, 2012, 26(6): 795-803. doi: 10.1061/(ASCE)CP.1943-5487.0000182
[10] M. Dutton, W. Take, N. Hoult. Curvature Monitoring of Beams Using Digital Image Correlation. Journal of Bridge Engineering, 2014, 19(3). doi: 10.1061/(ASCE)BE.1943-5592.0000538, 05013001.
[11] T.M. Fayyad, J.M. Lees. Application of Digital Image Correlation to reinforced concretefracture. Procedia Materials Science, 2014, 3: 1585 – 1590. doi: 10.1016/j.mspro.2014.06.256
[12] B. Pan, Z. Wang, Z. Lu, Genuine full-field deformation measurement of an object with complex shape using reliability-guided digital image correlation, Optics Express, 2010, 18(2): 1011-1023. doi: 10.1364/OE.18.001011
[13] W.S. Rasband. ImageJ, U. S. National Institutes of Health, Bethesda, Maryland, USA, http://imagej.nih.gov/ij/, 1997-2015.
[14] L. Saucedo-Mora. Correction of the spurious strains and displacements caused by out of plane movements in Digital Image Correlation (DIC) with a single camera. 2016. Journal of Non destructive Evaluation, under review.

Finite Element Analyses of Pinned Precast Beam Column Connections

Jaya Prakash Vemuri, Sahith Gali and Subramaniam Kolluru

Department of Civil Engineering, IIT Hyderabad, India

ABSTRACT

Precast concrete structures are rapidly being adopted as an alternative to traditional cast-in-situ concrete buildings. In low rise precast structures, pinned connections using steel dowels have been traditionally used, especially to connect beams to columns. Recent earthquakes have exposed the vulnerability of such connections which experienced significant damage. Experimental tests on pinned connections are limited and consequently closed form codal equations to estimate pinned connection strength are lacking. In this paper, monotonic and cyclic behaviour of pinned beam column connections are examined using finite element analyses. Key failure modes such as breaking of the dowel, spalling of concrete in both the beam and column are observed. The yield strength of steel and compressive strength of concrete are the key parameters affecting strength. The cyclic hysteresis loops are observed to be asymmetric and exhibit significant pinching behaviour. There is a progressive loss in stiffness and a degradation of strength. Reverse cyclic loading causes significant decrease in the load carrying capacity when compared to the monotonic response.

Keywords: Cyclic loading, dowel connection, finite element analyses, precast joint, shear loading.

1 INTRODUCTION

Precast concrete structures have inherent advantages over traditional cast-in-situ concrete buildings. They offer higher quality control at precasting plants, faster pace of construction and an option to choose from standardized cross section shapes. Two common structural systems are prevalent in precast structures: wall panel system and structural frame system. The wall panel system consists of solid wall panels and floor slabs, and is widely adopted in schools and hotels. Structural frame system consist of beams, columns and slabs and is mainly used for offices and car parks. Well detailed precast structures, especially those with rigid connections, are reported to have performed well in many earthquakes [1-3]. However, visible damage has been often observed in precast concrete structures with simple dry pinned connections. In the 2001 Bhuj, Gujarat earthquake, around 4,000 newly built precast schools were damaged due to connection degradation [4]. Structural elements in these school buildings were joined using pinned dowel connections. Similar damage to precast structures with hinged connections was observed in the 2009 L'Aquila, Italy earthquake [5]. The seismic performance of precast structures is highly dependent on the performance of connections, particularly, the beam to column connections. There is an absence of codal provisions for the design of pinned connections. The poor earthquake performance of pinned precast structures makes it imperative to study the behaviour of pinned beam-column connections.

In this paper, finite element analyses are performed on a model of a pinned beam column connection. The numerical model was developed to simulate an actual shear dowel connection tested [6]. Simulations were performed on the FEM model to match test results. Results from monotonic loading of the model are calibrated against experimental monotonic curves. Damage patterns observed in the FEM analyses are matched against actual damage observed in experiments. A cyclic loading protocol is implemented on the validated model to get insights into the failure behavior of a connection under reversed cyclic loading. The damage pattern consisting of distributed and localized cracking in concrete was simulated.

2 SHEAR RESISTANCE OF PINNED CONNECTIONS

Pinned beam-column connections usually have dowels protruding from the top of a column. These dowels fit into sleeves inserted in the beam. The sleeves are filled with grout to ensure a good anchorage of dowels by bond. Figure 1 shows a dowel jointed beam column connection.

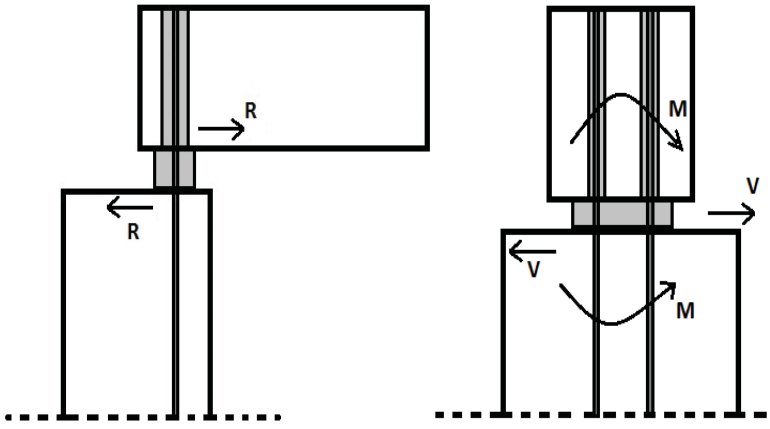

Fig. 1: Precast Beam-Column Connections with Dowels

In Figure 1, R is the horizontal shear force in longitudinal direction of the beam. In the transverse direction, V and M are the shear resistance of the dowels and the corresponding flexure, respectively. It has been observed from experimental tests on dowels embedded in concrete that significant strength and stiffness degradation occurs under cyclic loading [7]. An expression to estimate shear resistance of a dowel was also proposed [7], with the assumption that dowels are covered only by concrete, without any transverse reinforcement:

$$R_d = \delta . {d_b}^2 . \sqrt{f_{ck} . f_{yk}} \quad \text{(for monotonic loading)} \quad [1]$$

$$R_{dc} = 0.5\, R_d \quad \text{(for cyclic loading)} \quad [2]$$

where R_d is the resistance of the dowel under monotonic loading, R_{dc} is the dowel's resistance for cyclic loading, δ is a coefficient depending on the position of the dowel from the edges of the column, d_b is the diameter of the dowel, f_{ck} is the characteristic strength of concrete and f_{yk} is the characteristic yield strength of steel. These formulae are valid for concentric dowels under certain limits of concrete cover. Since these early experimental

studies in the 1980s, very little investigation has been reported on precast dowel connections. However, recent experimental investigations [8] show that these analytical expressions underestimate the strength of the single eccentric dowel connection and overestimate the capacity of the connections with one eccentric and two eccentric dowels. Indeed, estimating the shear strength of dowel connections is complex. Under small joint rotations, failure depends on the spacing between anchors, the edge spacing of anchors, the concrete strength, the steel strength, the embedment depth and the flexural stiffness on the anchor. Under large rotations, there may be axial forces induced in the dowels and failure may be due to any of the following mechanisms: yielding of anchor, pull out of anchor, concrete breakout, splitting of concrete splitting and side-face blowout. While limited guidance is available on general design of anchors [9], a detailed study is necessitated to estimate strength of precast dowel connections.

3 NUMERICAL MODEL

In this study, a numerical model was developed for the actual shear dowel connection tested [6]. The ABAQUS Dynamic/Explicit program [10] was used for modelling and analyses. The model consisted of the following parts: beam, column, dowels, bearing pad and a steel plate. Nodes at the base of the column were fully restrained against any movement. Nodes at the edge at the back end of the beam were constrained against vertical movement by introducing a roller support. Load is applied to the steel plate fixed to the back end of the beam. Figure 2 shows details of the FEM model.

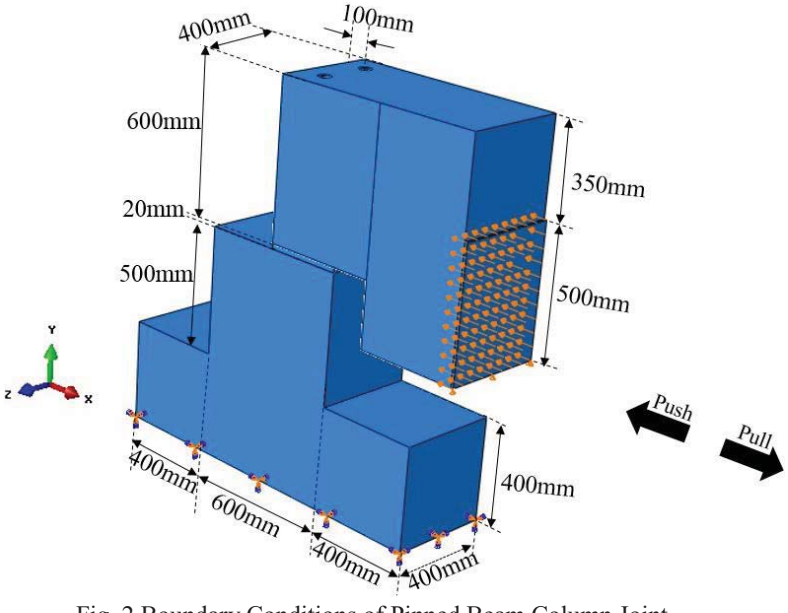

Fig. 2 Boundary Conditions of Pinned Beam Column Joint

For meshing of the connection, *C3D8R* and *C3D4* elements were used. The *C3D8R* element is a general purpose linear brick element, with reduced integration (1 integration point). The *C3D4* is a general purpose tetrahedral element with one integration point. To model dowel-grout interaction (in beam) and dowel-concrete interaction (in column), contact properties were assigned in two orthogonal directions. Hard contact in the

longitudinal direction and friction coefficient of 0.6 was assigned in the tangential direction. The nonlinear behavior of concrete was simulated by using the Concrete Damaged Plasticity (CDP) Model. The CDP model considers degradation of stiffness induced by plastic straining in compression and tension. The compressive behavior is elastic until initial yielding, followed by stress hardening and later, strain softening after the ultimate stress. Material and geometric properties were obtained from experimental tests [6]. Model for confined concrete proposed by [11] was used. The tensile stress of concrete was assumed to be one-tenth of the compressive stress.

Figure 3a illustrates the stress strain behaviour of unconfined concrete. For concrete in the beam and column, the unconfined compressive strength was 34 MPa, the Young's modulus was 32 GPa and the Poisson's ratio was assumed to be 0.20. The same unconfined concrete model, but with lower strengths, was used to model the grout material. For grout, the unconfined compressive strength was 23 MPa, the young's modulus was 26 GPa and the poisson's ratio was assumed to be 0.20. Figure 3b illustrates the stress strain behaviour of grout. Steel dowels were of diameter of 25 mm and were assigned the plastic model of ABAQUS, with yield strength and ultimate strength values. The yield strength was 580 MPa and the ultimate strength was 700 MPa. The Poisson's ratio was 0.15 and the young's modulus was 200 GPa. The bearing pad is 20 mm thick and assumed to be an elastic material with young's modulus of 1.7 MPa and Poisson's ratio was 0.20. The steel plate was also assumed to be elastic with Poisson's ratio of 0.15 and young's modulus of 200 GPa.

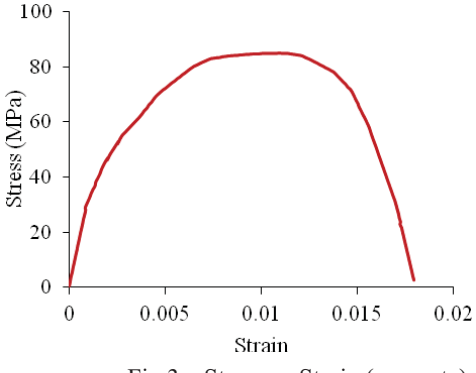

Fig 3a: Stress vs Strain (concrete)

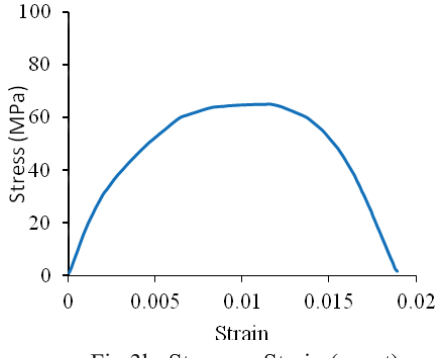

Fig 3b: Stress vs Strain (grout)

Figure 4 shows the cyclic displacement protocol adopted in this study. One cycle at small displacement level of 2.5 mm and 5 mm is applied to the connection through the steel plate. Next, three cycles at 7.5 mm are applied, followed by two final cycles at 10 mm displacement. In Figure 5a, tensile damage distribution in the connection is plotted where damage to concrete side cover in the beam is clearly observed. The concrete in the column, normal to the direction of loading, is also observed to be damaged. The crack pattern observed in the FEM analyses is similar to the test behaviour [6]. In Figure 5b, Von-Mises stress distribution in dowel bars is shown. Tensile stresses develop in the bars under large rotations causing them to deform. The deformation in the dowels was around the joint level and dowel bars yield inside the beam to form plastic hinges.

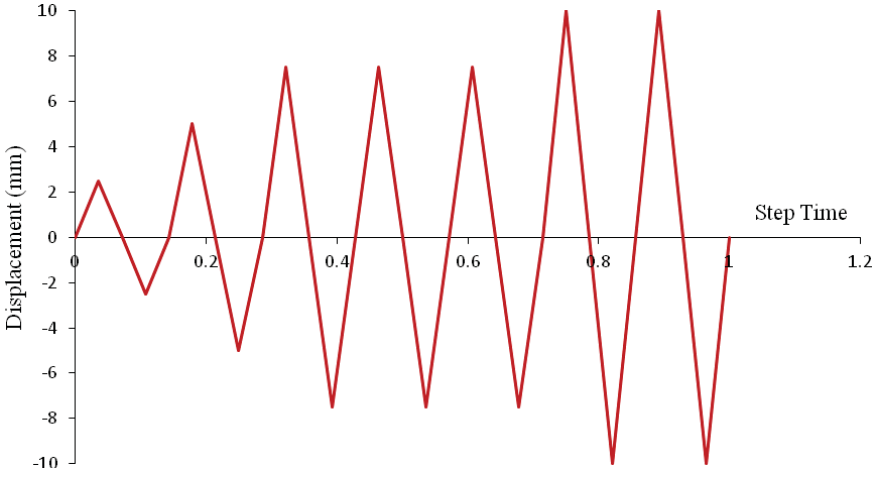

Fig 4 Cyclic Displacement Protocol

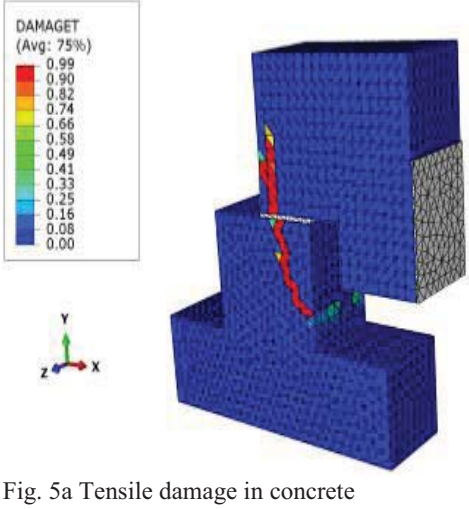

Fig. 5a Tensile damage in concrete

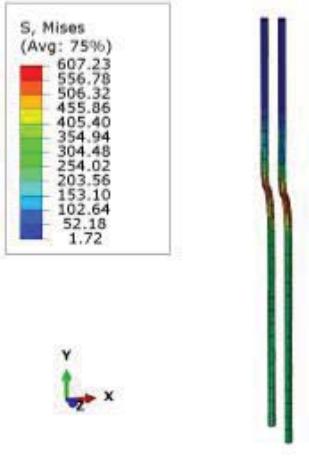

Fig 5b Von Mises Stress in Steel dowels

Figure 6 shows the response of the connection under monotonic pull loading. Experimental obtained monotonic curve is also plotted. It is observed that the numerical results compare favourably with experiments. In pull loading, the concrete cover is damaged near the bottom edge of the beam. Concrete around the dowels splits followed by fracture of dowels. The damage in the concrete causes a loss of stiffness and the force displacement graph is observed to plateau. In monotonic push loading, damage occurs by spalling of concrete around the dowels and splitting of concrete normal to the loading direction in the beam and column parts. There is no fracture of dowels and the interaction between the beam and column parts leads to further increase in shear resistance after initial yield.

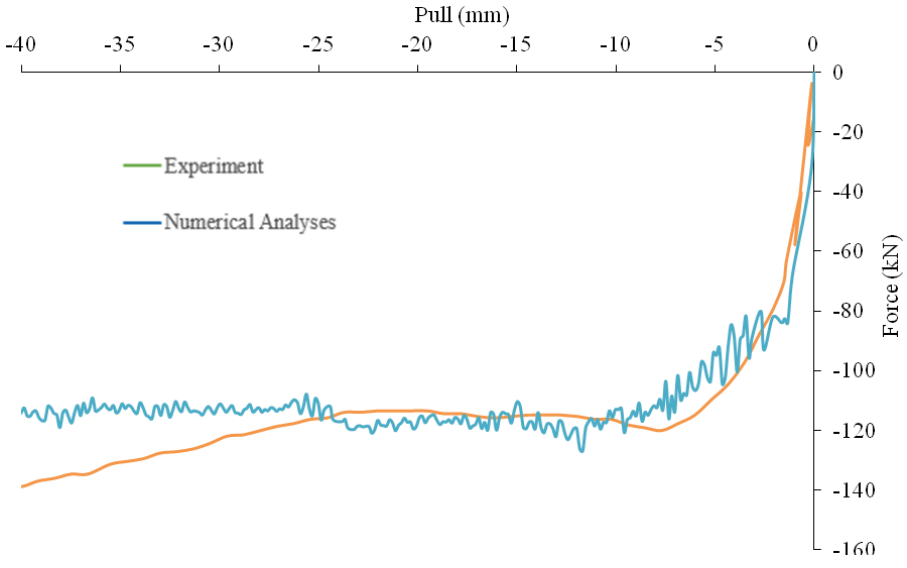

Fig.6 Monotonic loading in the pull direction

The response of the connection under reversed cyclic loading is observed in Figure 7. The backbone curve obtained from monotonic push and pull loadings, are also plotted. It is observed that the cyclic hysteresis loops lie below the backbone curves. Under reversed cyclic loading, the damage pattern is: spalling of the concrete cover, crushing of the concrete/grout around the dowels followed by fracture of dowels. Load response under reversed cyclic loading exhibits asymmetry, pinching and strength and stiffness degradation. There is significant strength degradation under reversed cyclic loading and the achieved loads are lower than the monotonic envelope. Considering the directionality of the test response, the use of the monotonic envelope in static analyses based procedures, such as the pushover analyses, would lead to a unconservative response. The hysteresis loops in reversed cyclic loading are asymmetric due to the interaction between the beam and column parts. Significant pinching is exhibited in unloading produced by closure of cracks in the beam and column parts. There is progressive loss of stiffness in each loading cycle. Further, it may be observed that under reversed cyclic loading, there is a significant degradation of strength when the specimen is loaded to the same displacement level.

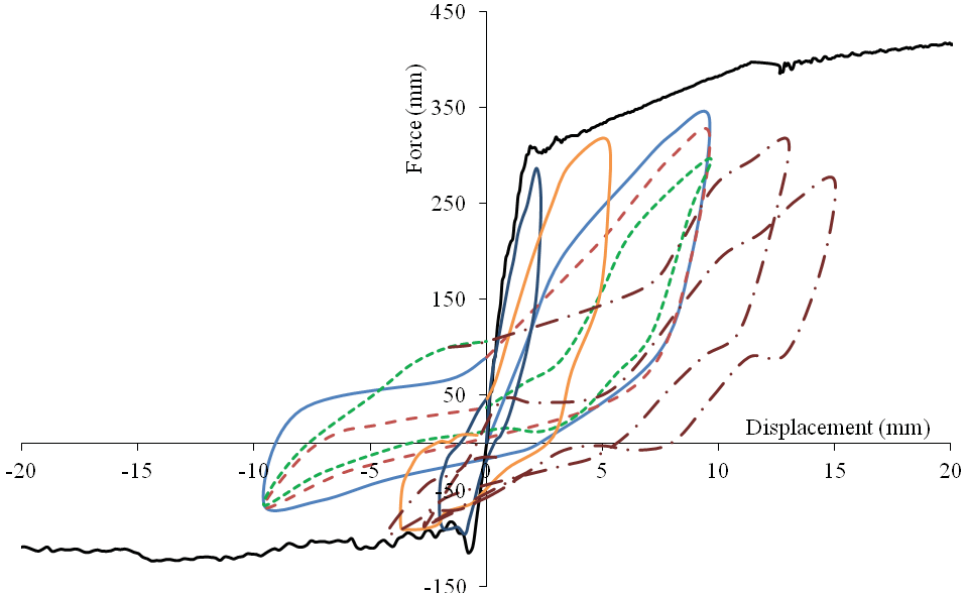

Fig. 7 Backbone curve and cyclic hysteresis loops

4 CONCLUSIONS

In this study, pinned precast beam to column connections were subjected to monotonic and cyclic loading. For each loading pattern, the force-displacement curve was plotted. When the connection was analysed under loading in the push direction, the observed damage was spalling of concrete at the top of the beam around the dowels and spalling of concrete cover normal to the loading direction at the column. There is no fracture of dowels and the interaction between the beam and column parts leads to further increase in shear resistance after initial yield. When loaded in the pull direction, there is spalling of the concrete cover, splitting of concrete around the dowels and fracture of dowels. It is observed that shear resistance in the push direction is much higher as compared to the pull direction. Under reversed cyclic loading, spalling of the concrete cover followed by crushing of the concrete/grout around the dowels is observed. Flexural yielding of dowels and simultaneous crushing of the surrounding grout causes loss of shear resistance and leads to the failure of the connection.

Typical precast shear connection exhibits highly asymmetric load response in the push and pull direction, which is due to different mechanisms of damage. Reverse cyclic loading leads to a significant decrease in the load carrying capacity when compared to the monotonic response. Considering the directionality of the response, the use of the monotonic envelope in static analyses based procedures would be unconservative.

3 REFERENCES

[1] Moguruma, H., M. Nishiyama, and F. Watanabe. "Lessons learned from the Kobe earthquake – A Japanese perspective.", *PCI Journal.* 40 (4) (1995) 28-42

[2] Saatcioglu, M. 2001. "The August 17, 1999 Kocaeli (Turkey) earthquake – Damage to structures.", *Canadian Journal of Civil Engineering*. 28 (4) (2001) 715-737

[3] Earthquake Engineering Research Institute. "Kocaeli, Turkey, earthquake of August 17, 1999 reconnaissance report.", *Earthquake Spectra*, Supplement to Vol.16, 2000

[4] Rai D C, Prasad A M, and Jain S K, "Hospitals and Schools" in "2001 Bhuj, India Earthquake Reconnaissance Report", *Earthquake Spectra*. 18 (2002) 265-277

[5] Toniolo,G. and Colombo,A. "Precast concrete structures: the lessons learned from the L'Aquila earthquake", *Structural Concrete.* 13 (2) (2012) 73-84

[6] Psycharis, I.N., and H.P . Mouzakis. "Shear resistance of pinned connections of precast members to monotonic and cyclic loading.", *Engineering Structures*. 41 (2012), 413-427

[7] Vintzeleou, E.N., and T.P. Tassios. "Behavior of dowels under cyclic deformations.", *ACI Structural Journal.* 84 (1) (1987) 18-30

[8] Apostolska, R., Necevska-Cvetanovska, G., Bojadziev, J., Fischinger, M., Isakovic, T. and Kramar, M. "Analytical investigations of beam-column connections in precast buildings under seismic loads." *Proceedings of the 15th World Conference on Earthquake Engineering*, Lisboa, Portugal. 2012

[9] ACI Committee 318 "Building Code Requirements for Structural Concrete (ACI 318-11) and Commentary"*, American Concrete Institute*, Farmington Hills, Michigan. (2011)

[10] ABAQUS "ABAQUS Standard 6.11 Users Manual ", *Dassault Systems*. (2011)

[11] Chang, G.A., and Mander, J.B. "Seismic Energy Based Fatigue Damage Ananlysis of Bridge Columns: Part 1 – Evaluation of Seismic Capacity," *NCEER Technical Report No. NCEER-94-0006*, State University of New York, Buffalo, N.Y. (1994)

Investigation of Compression Failure in Brick Masonry Assemblies made with Soft Brick

Mehar Babu Ravula and Kolluru V. L. Subramaniam

Department of Civil Engineering, IIT Hyderabad, India

ABSTRACT

An experimental investigation of compressive failure in masonry made of soft clay bricks is presented. Damage evolution associated with the formation and propagation of vertical splitting cracks during the compressive load response of masonry assemblies in the stack bonded arrangement is evaluated. Full-field surface displacements during the compression load response of the masonry are obtained using digital image correlation (DIC). A clear evidence of the crack forming in the mortar and propagating into the brick is established. In mortar with lower strength than the brick unit, failure is produced by spalling associated with multiple vertical cracks, which result in loss of load bearing area. For mortar with a higher strength than the brick, cracking occurs when the level of compression is a significant proportion of the compressive strength of the brick. Failure is a result of global instability produced by the localized crushing of the brick.

Keywords: Masonry, dilatancy, failure, mortar, brick, soft.

1 INTRODUCTION

Masonry is a composite material, constructed using brick units and mortar. The composite response of the masonry is determined by the relative stiffness's of the two components and the interaction between the components at different stress levels. Typically most studies are on masonry consisting of stiffer bricks and relatively softer mortar, which is applicable to the case of hard-fired bricks or stone [1-3]. However, the use of soft clay bricks coupled with steady improvements in cements, have resulted in mortars having higher stiffness and higher compressive strength than the bricks. In most of India, mortar has comparable or higher compressive strength than the brick [4, 5]. The relationship between constituent properties, the compressive stress-strain relationship and the compressive strength of masonry made with such bricks have been investigated [6-8]. Most of these studies however did not explicitly study the failure in the masonry as it relates to the state of stress in the constituent materials.

In this paper, an experimental investigation of the compressive behaviour of masonry assemblies made with soft clay fired brick is reported. Two different mortars, one with compressive strength higher than the brick strength and another with compressive strength lower than the strength of the brick unit are used in the experimental program. Masonry assemblies in the stack bonded arrangement are tested to evaluate the influence of the relative strength of mortar on the observed damage evolution and compressive failure. The stack bonded layout was used since the stress field in the constituent materials is simpler to interpret, and the complexities arising from the head joint are avoided. Further, the stack bonded test configuration is also recommended in the codes of practice for evaluating the strength of masonry [9-11]. In the test program, the evolution of damage in the brick and the mortar is investigated using the surface displacements measured using the DIC technique.

2 BACKGROUND

The compressive strength of masonry depends on characteristics of the brick unit and the mortar. During compression of masonry prisms with stiff bricks and soft mortar, the mortar is in a state of triaxial compression and the brick is subjected to in-plane biaxial tension coupled with axial compression. This state of stress results in vertical splitting cracks in bricks, which ultimately leads to the failure of the masonry prisms [1-3].

Very few investigations on the compressive behaviour of low-strength clay brick masonry have been reported in the literature [12-15]. In masonry made of low strength brick, the compressive strength of the masonry strength is lower than the compressive strengths of both the brick unit and the mortar [8,13,15]. Typically, low strength bricks have lower elastic modulus than the mortar. For an applied axial stress on the masonry, a triaxial compression state of stress is produced in the bricks while the mortar joints are under a biaxial tension stress state with superimposed axial compression (shown in Figure 1). The major form of distress in the masonry is associated with splitting of bricks, which ultimately produces failure [8,15,16]. An understanding of the failure in masonry as it relates to the stress state resulting from composite material behaviour of brick units and mortar is still not available.

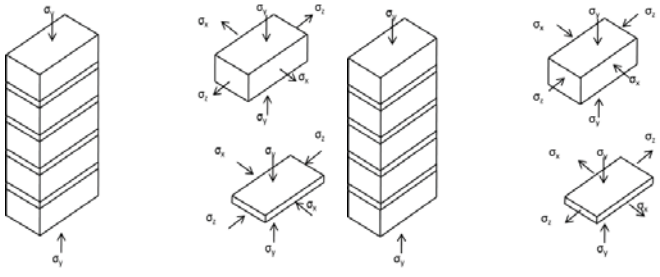

Figure 1: Stress states in masonry under compression for (a) stiff brick (b) soft brick.

3 EXPERIMENTAL PROGRAM

In the experimental program, the compressive response of wire cut bricks, mortar and stack bonded masonry was evaluated. Extruded, wire cut bricks were used in this study. The nominal dimensions of the bricks are 220 mm (length), 70 mm (height) and 100 mm (thickness). The water absorption of the bricks determined as per the requirements of IS 3495 (part2): 1992 was 9 percent [17].

In the study, two different mortar compositions given by volumetric proportions of cement: sand equal to 1:3 and 1:6 were used. The mortar with cement: sand equal to 1:3/1:6 is referred to as the strong/weak mortar. Mortar cylinders of 100 mm diameter and height equal to 200 mm were prepared from the same mortar mix used for preparing masonry specimens. Specimens were covered with wet burlap immediately after casting. The specimens were demoulded after one day and kept in curing tank for 28 days.

Stack bonded masonry specimens consisting of five bricks and four mortar joints were prepared. Following the procedure reported by Sarangapani et al. (2005), the brick units used in preparing the masonry assemblage were first submerged in water for two hours before laying, to allow better brick-mortar bond development. After casting, the masonry specimens were kept wrapped in moist burlap up to testing.

4 COMPRESSIVE BEHAVIOR OF BRICK

Compression tests were performed on brick blocks with cross-sectional dimensions equal to 35 mm x 35 mm and height equal to 70 mm, which were cut from the brick unit. The top and bottom square cross-sectional surfaces of the specimens were capped with a thin layer of plaster-of-Paris (gypsum plaster) to provide a uniform, level contact surface with the platens of the test machine. Initially, the load was cycled and the deformation over a gage length of 35 mm was measured using a surface mounted clip gage. After load cycles, the clip gage was removed and the specimens were tested in load control, up to failure. The Young's modulus measured from the brick blocks using the surface mounted gage was 1.09 GPa (standard deviation of 230 MPa). The compressive strength obtained from blocks was 7.4 MPa (coefficient of variation 0.16).

The compressive stress-strain response of the entire brick unit was obtained from a displacement controlled test. The deformation of the brick was recorded using a pair surface mounted linear variable displacement transformers (LVDT) mounted on opposite faces of the brick over a gage length of 35 mm. Additionally, the lateral expansion of the brick was measured using two LVDTs which were reacted off of the brick at the mid-height location. During the test, the rate of displacement measured between the two platens was increased at the rate of 0.6 mm per minute. Typical stress-strain response of the brick unit is shown in Figure 2(a). The lateral expansion of the brick is also plotted in the figure for comparison. A photograph of the failed specimen of the brick unit is shown in Figure 2(b). The failure of the specimen was observed to be produced by vertical cracks. The cracks were observed to form in the pre-peak part of the load response associated with the onset of significant non-linear response. In the non-linear pre-peak load response, the formation of the vertical cracks contributed to the increase in the lateral strain. The crack opening displacement produced by cracks, resulted in very large values of lateral strain. Calculation of continuum measure of Poisson's ratio is therefore misleading after the formation of the vertical cracks. The average compressive strength obtained from ten brick units was 13.98 MPa (coefficient of variation was equal to 0.178). The Poisson's ratio of the bricks determined in the early part of the load response was 0.25 (standard deviation was 0.15).

The compressive strength obtained from the brick unit is significantly higher than the strength obtained from blocks of smaller size cut from the brick. This suggests the influence of end constraints from platens [18]. Both specimens had the same height but different cross-sectional areas. The compressive response obtained from blocks cut from the brick units are representative of the unconfined behavior of the material. There is a significant influence of self-confinement on the compressive response obtained from the brick unit. Under an applied compression, the level of confinement would be the highest at the geometric center of the brick unit. Considering the confinement of the material, higher compressive strength is obtained from the brick unit. The unconfined compressive strength of the material obtained from the brick block is smaller than the strength of the brick unit. This factor is acknowledged in Eurocode for structural masonry and block strengths are normalized by applying an empirically derived shape factor to account for aspect ratio effects [19, 20] The aspect ratio (height/least width) for the brick unit is 2.0, and the correction factors for obtaining the unconfined compressive strength from the compressive strengths of the brick unit is 0.6. The unconfined compressive strength of the brick predicted using the correction factor is equal to 8.4 MPa, which is close, but higher than the value obtained from the blocks.

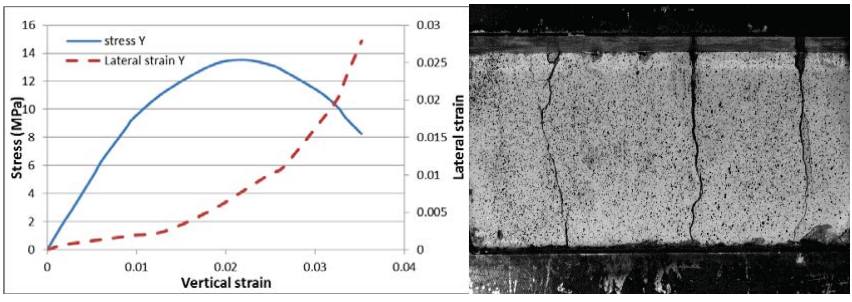

(a) (b)

Figure 2: (a) Stress-strain response of brick unit tested in compression; (b) Typical failed specimen of brick unit.

5 COMPRESSIVE BEHAVIOR OF MORTAR

Mortar cylinder specimens were capped using a capping compound prior to testing. The axial deformation of the specimen was recorded using LVDTs attached to surface mounted rings over a gage length of 60 mm. The lateral expansion of the specimen was recorded using two LVDTs which were reacted off of the specimen at the mid-height location. During the test, the rate of displacement measured between the two platens was increased at the rate of 0.6 mm per minute. Typical stress-strain behaviour of mortar specimens is shown in Figures 3 (a) and (b) for the weak and the strong mortars, respectively. The onset of non-linearity in the compressive response is associated with an increase in the rate of lateral expansion. Comparing the two mortars, it can be seen that there is a significantly larger lateral strain at peak load in the weak mortar when compared with the strong mortar. This corresponds with the larger extent of cracking observed in the weak mortar when compared with the strong mortar. Significant dilatancy is observed in the post-peak part of the load response, where there is significant increase in the lateral strain. A comparison of the stress-strain curves of the two mortars are plotted on non-dimensional axes in Figure 3(c). The values of stress have been normalized with respect to the peak stress and the values of strain have been normalized with respect to the strain corresponding to the peak. The pre-peak responses of the strong and weak mortars are nominally similar. The strong mortar however exhibits a more brittle post-peak response. The results from the mortar are summarized in Table 1.

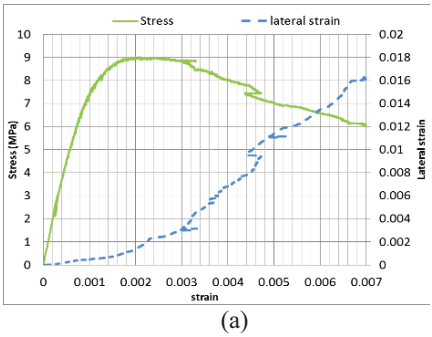

(a)

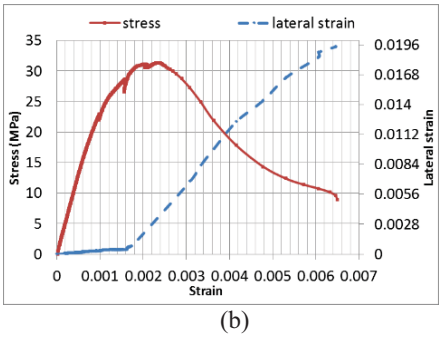

(b)

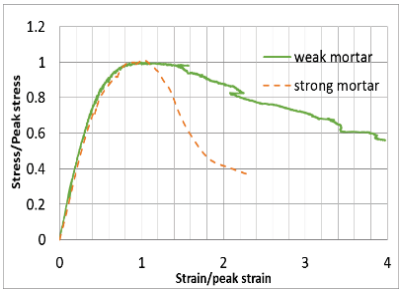

(c)

Figure 3: Stress-strain response of mortar (a) weak mortar; (b) strong mortar; and (c) compression responses of strong and weak mortars in a non-dimensional plot.

6 COMPRESSIVE BEHAVIOR OF MASONRY

The top and bottom surfaces of the masonry specimens were capped with a thin layer of gypsum to ensure uniform contact with the platens of the test machine. The front face of the masonry specimen was prepared for digital image correlation by creating a sprayed-on speckle pattern [21]. Local measurement of vertical strains are obtained from the average of two LVDTs fixed on the side surfaces between the 2nd brick and 4th over a gauge length of 160 mm. In a typical compression test, the rate of displacement measured between the two platens of the test machine was increased at a constant rate of 0.6 mm/minute. During the compression test, images of the specimen were captured for correlation using a high resolution camera (5 mega pixel). The camera was fitted with a 50 mm lens and was placed at a distance of 1 m from the specimen surface. Uniform light intensity was ensured across the surface of the masonry using normal white light. A schematic diagram of the test setup is shown in Figure 5. A reference image was captured in the undeformed state prior to the initiation of loading program.

The typical stress-strain curves obtained from the surface mounted LVDTs are shown in Figure 4(a) and Figure 4(b) for the specimens made with the weak and the strong mortars, respectively. Specimens made with both mortars exhibited strengths which are lower than the compressive strengths of both the constituent materials. The results of the mechanical characteristics masonry are summarized in Table 1.

Table 1: Characteristics of mortar and masonry

Material	Specimen size mm	Strength (Std. Dev.) MPa	E (Std. Dev.) GPa	Peak strain (Std. Dev.)
Strong Mortar	100 mm cylinder	30 (1.75)	26.5 (0.442)	0.0025 (0.00043)
Weak Mortar	100mmcylinder	9.36 (1.77)	8.0 (0.176)	0.00203 (0.00024)
Masonry with strong mortar	220 × 100 × 380 (l × b ×h)	7.95 (0.2)	0.96 (0.056)	0.0083 (0.00084)
Masonry with weak mortar	220 ×100 × 380 (l × b × h)	5.8 (0.34)	0.88 (0.041)	0.0082 (0.0015)

While the peak loads are not significantly different, there are considerable differences in the load responses and modes of failure in the masonry specimens made from the two mortars.

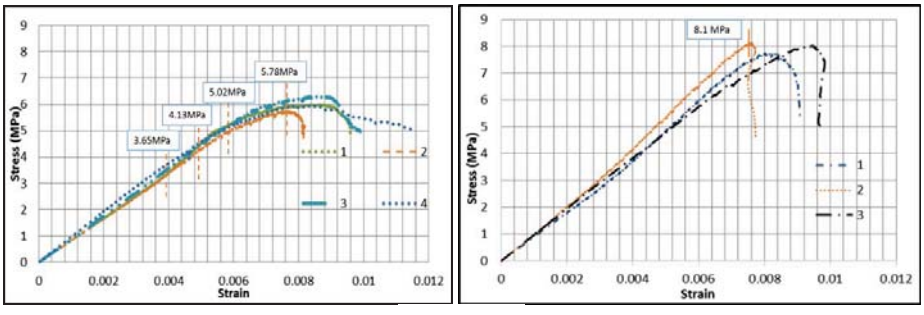

(a) (b)

Figure 4: Load response of the stack bonded masonry prism with (a) weak mortar and (b) strong mortar.

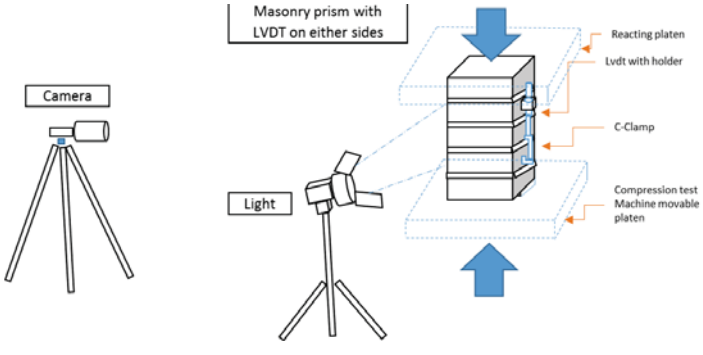

Figure 5 : Schematic test setup for masonry prism test

Specimens with the weak mortar exhibit a significantly higher level of pre-peak non-linearity. The response of specimens made with the strong mortar exhibit an almost linear response up to the peak load. The failure of specimens with the strong mortar was significantly more brittle with a very rapid decrease in load in the post-peak.

7 ANALYSIS OF COMPRESSION RESPONSE

A two-dimensional displacement field on the surface of the masonry specimen was obtained from cross-correlation of images the undeformed specimen with the image in the deformed state [22,23]. A subset size equal to 32x32 pixels was used for the correlation. A Quintic B-spline interpolation of the grey values was used to achieve sub-pixel accuracy. The cross correlation analysis of the digital images was performed using the VIC-2D^{TM}software, which maximizes the correlation coefficient between grey levels in the subsets in the reference and deformed images. Surface displacements and displacement gradients at each loading stage were calculated at each subset center, by evaluating the shape functions and their partial derivatives at the subset center. For the setup used in this study, the random error in the measured displacement is in the range of 0.002 pixels. Strains were computed from the

gradients of the displacements. A conservative estimate of the resolution in strain obtained from the digital correlation was 10 με [24, 25].

In masonry specimen with weak mortar, the crack initiation from the brick-mortar interface is shown in Figure 6(a).The load point at crack initiation is shown marked on the load response of the specimen in Figure 4(a). The formation of the crack coincides with the onset of non-linearity in the load response at an applied axial stress of 4.13MPa. The sharp profile of the crack is identified by closed contours with very high strain gradient in a small region. The displacement contours coalesce at the crack. On increasing the axial stress, the vertical splitting crack increased in length and the crack opening at the brick-mortar interface continued to increase. Subsequently, additional cracks were formed across the width of the specimens. Cracks in the specimen at an applied axial stress equal to 5.78 MPa are shown in Figure 6(b), where ε_{xx} is plotted over an area spanning three bricks and including two mortar joints. The corresponding ε_{yy} are plotted in Figure 6(c). Tensile splitting of the brick is driven by the differential lateral expansion of the brick and mortar at the interface, which results in the crack being the widest at the brick-mortar interface. In the contour plots of ε_{yy}, some strain localization is evident at the interface between brick and mortar at these load levels. Very high strains occur in a small region located at the interface. The local strains in compression in the interface region indicate some localized crushing in the material. The splitting cracks are initiated at different locations along different brick-mortar interfaces. These cracks eventually grow vertically across multiple joints. Failure occurred when several cracks joined causing spalling of a piece of the masonry reducing the load carrying area.

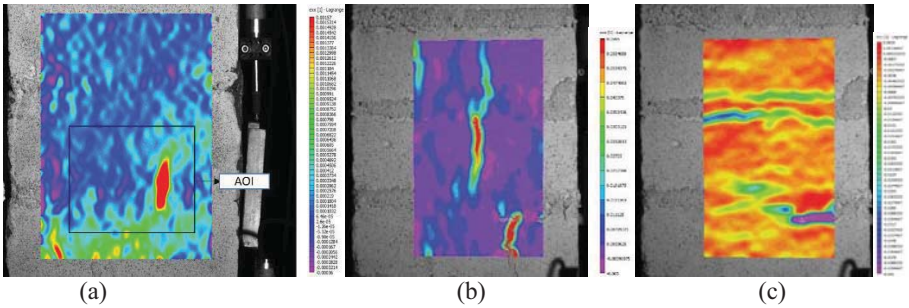

(a) (b) (c)

Figure 6 (a) Contour plot of ε_{xx} over the surface of the masonry specimen with weak mortar at applied axial stress equal to 4.13 MPa; (b) Contours of ε_{xx} at applied axial stress equal to 5.78 MPa (b) Contours of ε_{yy} at applied axial stress equal to 5.78 MPa

In masonry specimen made with the strong mortar, cracking was observed at a higher load level when compared with the masonry made with weak mortar. As the strong mortar tensile strength is higher compared with the weak mortar, cracking occurs later in the load response. The strain contours in the masonry specimen at an applied compressive stress equal to 8.1 MPa (shown marked on the load response in Figure 4) are shown in Figure 7. From the strain contours of ε_{xx} in Figure 7(b), the crack can be identified as starting from the mortar and it propagates into the brick. The corresponding vertical strain in the specimen is shown in Figure 7(c). Significant strain localization in ε_{yy} occurs in the brick-mortar interface region. Therefore while the global strain in the brick is not high, the localization increases the magnitude of strain in a small region. The localization is likely attributed to the large difference in stiffness of brick and mortar. The brick is much softer compared to the mortar and hence cause axial strain accumulation at interface. The formation of the crack in the brick leads to a release of stress and loss of confinement from the mortar. The failure strength

therefore approaches to that of unconfined brick strength. The ultimate failure was produced by global instability caused by the localized crushing and spalling of material from a small region.

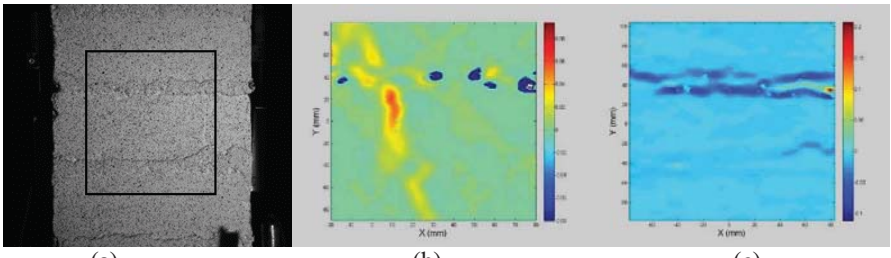

(a) (b) (c)

Figure 7: Strain contour plot at mortar joint in prism specimen with 1:3 mortar at axial compressive stress equal to 8.1 MPa: (a) Area Of Interest used for correlation; (b) ε_{xx} contour showing crack initiation from the mortar joint; c) ε_{yy} contour showing strain localization at the mortar brick interface.

8 CONCLUSIONS

The results of the experimental program indicate that the compressive strength of the masonry made with soft brick is lower than the compressive strength of both brick and mortar irrespective of mortar strength. For a large increase in mortar strength, a small increase in masonry strength will be obtained. Compressive strength of masonry is insensitive to the mortar strength but the failure mode is directly influenced by the mortar strength relative to that of brick. For soft bricks, where the elastic modulus of brick is lower than the elastic modulus of the mortar, failure in both low and high-strength mortars is associated with cracking in bricks, which is initiated in the mortar.

Failure in low strength mortar is produced by spalling associated with vertical cracking in bricks. Failure in masonry with high-strength mortar is more brittle and is produced by localized crushing of bricks near the brick-mortar interface. Severe localized crushing of brick close to the interface at a value of stress close to the unconfined compressive strength of the brick material is produced. Failure is produced by the local crushing of the material leading to global instability

9 REFERENCES

1. McNary WS, Abrams DP (1985) Mechanics of masonry in compression. J Struct Eng 111(4):857–870
2. Atkinson RH and Noland JL. (1983) A proposed failure theory for brick masonry in compression. Proc., 3rd Canadian Masonry Symp., Edmonton, pp5.1–5.17.
3. Drysdale RG, Hamid AA., and Baker LR. (1994) Masonry structures: Behaviour and design. Prentice-Hall, Englewood Cliffs NJ.
4. Dayaratnam P (1987) Brick and reinforced brick structures. Oxford and IBH, New Delhi, India.
5. Sarangapani G, Venkatarama Reddy BV, and Jagadish KS (2002) Structural characteristics of bricks, mortar and masonry. J. Struct. Eng. (India), 29(2), 101–107.
6. Deodhar SV. (2000) Strength of Brick Masonry Prisms in Compression. JInstitution of Eng (India), 81(3):133-137.
7. Gumaste KS, Venkatarama Reddy BV, Nanjunda Rao KS, Jagadish KS (2004) Properties of burnt bricks and mortars in India. Masonry Int 17(2):45–52.

8. Kaushik HB, Rai Durgesh C, Jain Sudhir K(2007) Stress-strain characteristics of clay brick masonry under uniaxial compression. J of Mater Civil Eng, 19(9):728-739.
9. IS 1905-1987 Code of practice for structural use of unreinforced masonry. Bureau of Indian Standard, New Delhi.
10. SP20 (1991)Handbook on masonry design and construction. Bureau of Indian standard.
11. ASTM (2003) Standard test method for compressive strength of masonry prisms. C1314-03b, ASTM International, West Conshohocken
12. Matthana MHS (1996) Strength of brick masonry and masonry walls with openings. Ph.D thesis, Department of Civil Engineering, Indian Institute of Science, Bangalore, India.
13. Sarangapani G, Venkatarama Reddy BV, Jagadish KS (2005) Brick–mortar bond and masonry compressive strength. J Mater Civil Eng (ASCE), 17(2):229–237.
14. Raghunath S, JagadishKS (1998)Strength and elasticity of bricks in India. Workshop on Recent Advances in Masonry Construction, WRAMC-98, Roorkee, pp 141–150.
15. GumasteKS,Rao KSN, Reddy BVV,JagadishKS (2007) Strength and elasticity of brick masonry prisms and wallettes under compression. Mater and Struct40:241–253.
16. Venkatarama Reddy BV, Uday Vyas ChV (2008)Influence of shear bond strength on compressive strength and stress–strain characteristics of masonry. Mater Struct 41:1697–1712.
17. IS3495 Part-2 (1992) Code of practice for Methods of test of burnt clay building bricks. Bureau of Indian Standard, New Delhi, India.
18. Morel JC,Pkla A, Walker P (2007) Compressive strength testing of compressed earth blocks. Constr and Building mater, 21(2):303-309.
19. EN (2005) Eurocode 6-design of masonry structures Part 1-1: general rules for reinforced and unreinforced masonry structures. European Committee for Standardization, Brussels, Belgium.
20. Krefeld WJ. (1983) Effect of shape of specimen on the apparent compressive strength of brick masonry. Proceedings of American Society of Materials, 363-369.
21. Ravula MB, and Subramaniam KVL (2017) Experimental Investigation of compressive failure in masonry brick assemblages made with soft brick. Mater Struct, 50:19. Doi: 10.1617/s11527-016-0926-1.
22. Sutton MA, Wolters WJ, Peters WH, Ranson WF and McNeil SR (1983) Determination of displacements using an improved digital correlation method. Image and Vision Comput 1(3): 133-139.
23. Sutton MA, McNeill SR, Jang J. and Babai M(1988) Effects of sub-pixel image restoration on digital correlation error. J Opt Eng, 27(10):870-877.
24. Bruck HA, McNeil SR, Sutton MA and Peters WH (1989) Digital image correlation using newton-raphson method of partial differential correction. Exp Mech 29(3):261-267.
25. Schreier HW, Garcia D, Sutton MA (2002) Systematic errors in digital image correlation due to under-matched subset shape functions. Exp Mech 42(3):303-310.

Longitudinal Reinforcement Limits in RC Vertical Elemets Based on Creep and Shrinkage Prediction Models

Najeeb Shariff and Devdas Menon

Dept. of Civil Engineering, Indian Institute of Technology Madras, Chennai, India

Abstract
International codes of practice specify limits on reinforcement percentage in Reinforced Concrete (RC) columns and walls. The upper limit to reinforcement is usually attributed to congestion of rebars. However, an additional check on tensile stress in concrete, as a consequence of restrained shrinkage due to high steel ratio, is necessary. Similarly, the lower limit to reinforcement is generally attributed to accidental loading and crack control. However, passive yielding of steel on account of excessive compressive stress due to creep and shrinkage in concrete must also be checked. This paper compares the creep and shrinkage strains predicted using four models, viz. ACI 209, EC2, CEB-FIP MC10 and GL2000, for different cross-sections, grades of concrete and humidity ranges, in addition to different ages of concrete. These strains are used in computing the reinforcement limits for RC columns and walls based on analytical method suggested by Lin and Furlong, 1995. Based on the design life of the structure, geometry, material properties and environmental conditions, reinforcement limits are proposed. Finally, the reinforcement ratios are checked against codal provisions, and it is established that the additional checks proposed are required in some cases for maximum steel ratio. However, the minimum steel ratio in columns can be lower than the values specified in codes, provided accidental loads and crack-widths are taken care of.

Keywords: Concrete; creep; shrinkage; reinforcement limits; prediction models.

1 INTRODUCTION

Vertical elements in buildings such as columns and structural walls are critical elements, as distress in these elements may have serious implications on the structural integrity. Careful assessment of strains (both instantaneous and long-term) is important. Concrete exhibits long-term strains due to dimensional instability under ambient conditions, mainly due to loss of adsorbed water from the hydrated cement paste. Presence of reinforcement in RC members alters their time-dependent response. International codes of practice recommend maximum and minimum reinforcement percentage limits for columns and structural walls [1-5]. The limit on maximum reinforcement percentage is provided to avoid congestion of rebars, which would otherwise lead to improper concreting. Additionally, the maximum reinforcement percentage limit ensures that the tensile stress developed in concrete due to restrained shrinkage (caused by the high steel percentage) does exceed its capacity. Similarly, although the main intent behind specifying minimum reinforcement percentage is to cater to the accidental loads, in addition to keeping a check on the crack widths, minimum steel is also necessary to prevent passive yielding of reinforcement [6]. Maximum and minimum reinforcement percentage limits specified by different international codes for columns and structural walls are tabulated in Table 1 and 2 respectively.

Table 1: Comparison of maximum reinforcement percentage limits for columns and structural walls with respect to different international codes

Code	Columns	Structural Walls
ACI – 318 (2014)	4.0%	4.0%
AS 3600-2009	4.0%	4.0%
CAN/CSA-A-23.3-04	8.0%	8.0%
EN 1992-1-1-2004	4.0%	4.0%
IS 456-2000	6.0%	6.0%

Table 2: Comparison of minimum reinforcement percentage limits for columns and structural walls with respect to different international codes

Code	Columns	Structural Walls
ACI – 318 (2014)	1.0%	0.12% < 16ϕ bar 0.15% otherwise
AS 3600-2009	1.0%	0.15%
CAN/CSA-A-23.3-04	1.0%	0.15%
EN 1992-1-1-2004	Max (0.1N/f_{yd}, 0.2%) where N – axial load; f_{yd} - design yield strength of steel	0.20%
IS 456-2000	0.8%	0.12% < 16ϕ bar 0.15% otherwise

In the present study, rigorous analysis based on the creep and shrinkage prediction models for plain concrete, available in literature (ACI 209, EC2, CEB-FIB MC10 and GL2000) is carried out [4,6,7,8]. The time dependent strains have been worked out for three classes of structures: (i) temporary or low importance structures having a design life of 10 years, (ii) normal structures having a design life of 50 years, and (iii) important structures having a design life of 100 years. Further, normal strength concrete (M30) and high strength concrete (M60) are parameters used to predict the strains. Studies have shown that ambient relative humidity (RH) is one of the most important parameters in long-term strain development and hence, in the present study two conditions viz. (i) dry – 50% RH and (ii) wet – 80% RH, are used. The analytical method proposed by Lin and Furlong is used to calculate the time-dependent strains of RC members along with the longitudinal reinforcement limits [8].

2 PREDICTION MODELS FOR PLAIN CONCRETE

Accurate prediction of time-dependent strains in concrete is complex. However, simplified models have been developed, which are used in practical design. Four popular models have been chosen in the present study.

i. The ACI 209 model was first proposed in 1971 and was developed by Branson and Christiason (1971). This was later modified and improved in ACI 209R-82, ACI 209R-92 and ACI 209.2R-08. This model is simple to use, as it requires minimal input. However, since it is empirically derived, it has inherent uncertainties and limitations on the range of applicability. The ACI 209.2R-08 model is popularly used in the design of concrete structures [10].

ii. The International Federation for Structural Concrete (*fib*), in association with CEB, proposed a Model Code for Concrete Structures in 1978. A subsequent edition of this code (MC90) was proposed in 1990. Recently, a more improved version of the Model Code (MC10) was released in 2010. The creep and shrinkage model proposed in this code is mainly derived from the work of Müller and Hilsdorf (1990).

iii. Eurocode 2 has also proposed a model to predict creep and shrinkage strains in concrete. This model is very similar to the CEB *fib* model; however, there are slight variations in the equations proposed to predict shrinkage strains.

iv. Gardner and Lockman (2001) proposed the GL2000 model which was basically intended for design office use. The proposed model is simple and requires minimal input parameters. The main advantage of this method is its applicability to any chemical or mineral admixture.

3 INFLUENCE OF REINFORCEMENT ON TIME DEPENDENT STRAINS

Creep and shrinkage strains in steel are only marginal when compared to that in concrete. This results in lesser creep (ε_{cr}) and shrinkage strains (ε_{sh}) in reinforced concrete than in plain concrete. Due to the unequal strains in concrete and steel, there is an interaction between the two. As concrete undergoes time-dependent deformation, the compressive load is transferred to the steel reinforcement. In addition to the elastic strain due to loading, the steel reinforcement is now subjected to time-dependent strains as well. When this strain value exceeds the yield strain in compression, passive yielding of reinforcement occurs. This necessitates a lower limit on the steel reinforcement. A schematic representation of the time-dependent deformation in RC column of height (l) is shown in Figure 1.

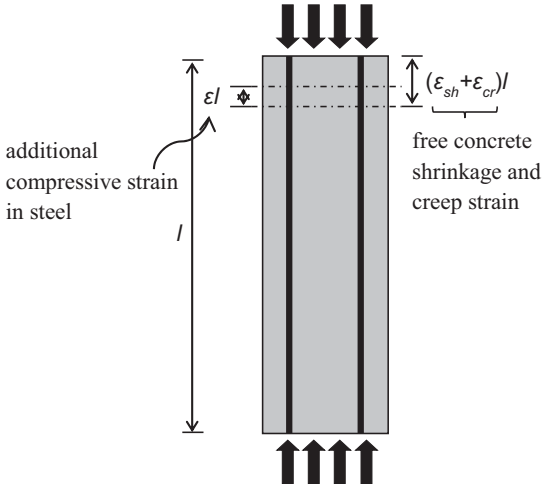

Figure 1: Schematic representation of time-dependent deformation in an RC column

Here εl is the time-dependent deformation resisted by the steel reinforcement.

Due to the effect of shrinkage in concrete, compressive force is transferred to the longitudinal steel reinforcement. Since the reinforcement resists this compressive force, an equilibrating tensile stress is developed in the concrete. When this tensile stress exceeds the direct tensile capacity of concrete, cracking occurs. This calls for a limit on the maximum steel reinforcement allowed in the column or wall,although sustained axial load on the vertical element reduces the possibility of cracking.

4 REINFORCEMENT PERCENTAGE LIMITS

4.1 Maximum Steel Ratio

Shrinkage strain (ε_{sh}) for different cases can be computed from the models available in literature. The force resisted by the steel due to time-dependent deformation (P_{res}) is given in Eq (1).

$$P_{res} = \varepsilon_{sh} E_s A_g \rho_g \tag{1}$$

where, E_s – modulus of elasticity of steel

A_g – gross cross-sectional area of the RC member

ρ_g – ratio of area of steel to area of concrete

When P_{res} is applied to the transformed area of the column, a tensile strain ε is developed in concrete. Eq (2) describes the tensile stress in concrete f_{ct}.

$$f_{ct} = \frac{\varepsilon_{sh} E_s A_g \rho_g}{\left[A_g \left(1-\rho_g\right) + m\rho_g A_g \right]} = E_c \varepsilon \tag{2}$$

where m is the modular ratio and E_c is modulus of elasticity of concrete.

As the reinforcement ratio increases, the tensile strain in concrete increases. However, presence of axial compressive load on the member minimizes the possibility of cracking and hence the elastic stress (f_e) needs to be subtracted from the tensile stress in concrete.

$$f_e = E_c \varepsilon_e \tag{3}$$

Here, ε_e is defined as the strain under compressive loading. The following procedure is used to obtain the value of εe.

$$1.5DL + 1.5LL = P_{ur} \tag{4}$$

$$1.5DL + \alpha 1.5DL = P_{ur}; \qquad \text{where } \alpha = \frac{LL}{DL} \tag{5}$$

$$DL = \frac{P_{ur}}{\left(1.5+\alpha 1.5\right)} \tag{6}$$

$$\varepsilon_e = \frac{P_{ur}}{\left(1.5+\alpha 1.5\right) A_g E_c} = \frac{0.4 f_{ck}}{\left(1.5+\alpha 1.5\right) E_c} \tag{7}$$

Tensile cracking in concrete due to restrained shrinkage from the reinforcement occurs when

$$\left[f_{ct} - E_c \varepsilon_e \right] > f_t; \qquad \text{where } f_t = 0.33\sqrt{f_{ck}} \tag{8}$$

On substitution we get,

$$\rho_{g\max} = \frac{f_{ct}}{\varepsilon_{sh} E_s - f_{ct}(m-1)} \tag{9}$$

where,

DL – dead load

LL – live load

P_{ur} – capacity of the column/wall

f_t – allowable direct tensile stress in concrete

$\rho_{g\max}$ – maximum steel ratio

For different live load to dead load ratios (α) and different volume to surface area ratios (V/S), the maximum steel ratio is calculated using the ε_{sh} obtained from prediction models.

ρg_{max} values for different cases of live load to dead load ratio, grades of concrete, ambient humidity and volume to surface ratios (V/S) are calculated. Higher V/S represents a

wall and lower V/S represents a column, i.e. for the same volume, a wall has higher surface area as against a column. Tables 3 to 5 show the ρ_{gmax} values for three ages: 10 years, 50 years and 100 years respectively.

It can be seen that for all three ages GL2000 model shows that ρg_{max} value can be less than code recommended 4%, when the live load to dead load ratio is high (in this case $\alpha = 3$), grade of concrete is lesser (f_{ck} = 30MPa) and dry condition (RH = 50%). In all other models, ρ_{gmax} value was found to be higher than code recommendation. This is because GL2000 model over estimates the creep and shrinkage strains of plain concrete.

4.2 Minimum Steel Ratio

Lower limit on steel ratio is a function of both creep and shrinkage strains. The stress in longitudinal reinforcement due to creep and shrinkage is expressed in Eq (10).

$$f_{st} = E_s\left(\varepsilon_{sh} + \varphi\varepsilon_e - \varepsilon\right) \tag{10}$$

where φ is the creep coefficient.

Total stress in steel including dead load and live load is expressed as:

$$f_s = E_s\left(\varepsilon_{sh} + \varphi\varepsilon_e - \varepsilon\right) + mE_c\varepsilon_e\left(1+\alpha\right) \tag{11}$$

The maximum allowable stress allowed in steel is taken as:

$$f_s = Rf_y \tag{12}$$

Here R is taken as 0.87.

ε in Eq (11) can be computed using the following expression:

$$\varepsilon = \frac{m\rho_{g\min}\left(\varepsilon_{sh} + \varphi\varepsilon_e\right)}{1 + \rho_{g\min} + m\rho_{g\min}} \tag{13}$$

On re-arranging, we get the minimum steel ratio (ρ_{gmin})

$$\rho_{g\min} = \frac{\varepsilon}{m\left(\varepsilon_{sh} + \varphi\varepsilon_e - \varepsilon\right) + \varepsilon} \tag{14}$$

The present study is conducted using steel of yield strength 415 MPa and 500 MPa. However, the analysis revealed that there was no minimum limit on steel ratio for columns and walls for all conditions where were considered with respect to creep and shrinkage effects.

Table 3: Maximum steel ratios for 10 years life structure

f_{ck}	RH(%)	V/S	Live load to Dead load ratio (α)							
			0.5				3			
			ACI	MC 10	EC2	GL2000	ACI	MC 10	EC2	GL2000
30	50	75	0.152649	0.10757	0.111132	0.066252	0.054908	0.045918	0.044655	0.030059
		135	0.333556	0.136781	0.151601	0.08521	0.086589	0.055387	0.0559	0.037079
30	80	75	0.45234	0.275776	0.348856	0.169077	0.099282	0.089734	0.091793	0.062297
		135	-	0.397	0.654949	0.247448	0.17921	0.110285	0.119309	0.079752
60	50	75	0.370405	0.342887	0.328493	0.239934	0.099857	0.101441	0.096396	0.079952
		135	1.280398	0.456513	0.461698	0.351981	0.162747	0.119134	0.116245	0.101712
60	80	75	2.810163	1.185931	1.24658	1.847743	0.189142	0.176161	0.17088	0.19256
		135	-	2.281147	3.201422	-	0.373391	0.205756	0.205586	0.270229

Table 4: Maximum steel ratios for 50 years life structure

f_{ck}	RH(%)	V/S	Live load to Dead load ratio (α)							
			0.5				3			
			ACI	MC 10	EC2	GL2000	ACI	MC 10	EC2	GL2000
30	50	75	0.14766	0.096849	0.108427	0.059279	0.053684	0.04218	0.043831	0.027324
		135	0.296178	0.102835	0.142008	0.063174	0.081577	0.044285	0.053405	0.028863
30	80	75	0.423741	0.238091	0.334257	0.144824	0.096599	0.08183	0.089856	0.055836
		135	14.17927	0.258742	0.563263	0.15811	0.16506	0.086268	0.113024	0.059448
60	50	75	0.354702	0.303702	0.319868	0.205367	0.09751	0.09419	0.094882	0.071827
		135	1.014887	0.325422	0.429394	0.224298	0.152518	0.098293	0.111968	0.076374
60	80	75	2.291335	0.949592	1.179274	1.072369	0.183502	0.163937	0.168225	0.167157
		135	-	1.07467	2.479893	1.421922	0.338298	0.170861	0.19812	0.181158

Table 5: Maximum steel ratios for 100 years life structure

f_{ck}	$RH(\%)$	V/S	Live load to Dead load ratio (α)							
			0.5				3			
			ACI	MC 10	EC2	GL2000	ACI	MC 10	EC2	GL2000
30	50	75	0.147053	0.0955	0.108094	0.0584	0.053534	0.041699	0.043729	0.026973
		135	0.291939	0.098511	0.140853	0.06036	0.08097	0.042769	0.053098	0.027754
30	80	75	0.42038	0.233569	0.332499	0.141915	0.096269	0.080821	0.089617	0.05502
		135	9.654904	0.243728	0.553227	0.14845	0.163388	0.083068	0.112257	0.05684
60	50	75	0.35281	0.298863	0.31881	0.201225	0.097221	0.093245	0.094694	0.070799
		135	0.988332	0.309691	0.425536	0.210532	0.151286	0.095343	0.111436	0.073092
60	80	75	2.239058	0.923517	1.171282	1.011704	0.182812	0.162341	0.167896	0.164064
		135	-	0.982734	2.409529	1.154887	0.334228	0.165885	0.197192	0.170998

5 CONCLUSIONS

Maximum and minimum steel ratios are governed by creep and shrinkage strains in reinforced concrete columns and walls. International codes of practise have arrived at the reinforcement limits by considering these effects. However, the present study shows that creep and shrinkage in concrete has no effect on the minimum limit of steel ratio. With high yield strength bars available in market (with $f_y > 415$MPa), the possibility of passive yielding of steel is completely eliminated. $\rho_{g\min}$ is governed by accidental loading and crack width criteria. Further, using an appropriate model to predict the creep and shrinkage strain in concrete, rather than adopting a constant conservative value (commonly done in practice) will eliminate the constraint of maximum steel ratio limit in columns and walls with respect to creep and shrinkage. Congestion of reinforcement governs the $\rho_{g\max}$ value.

6 REFERENCES

[1] ACI Committee 318. Building Code Requirements for Structural Concrete: (ACI 318-14) ; and Commentary (ACI 318R-14). Farmington Hills, MI:American Concrete Institute, 2014.
[2] Australian Standard, Concrete Structures, (Sydney 2009)
[3] Canadian Standards Association. A-23.3-04 Design of Concrete Structures, (Ontario, Canada, 2004).
[4] Eurocode 2: Design of Concrete Structures – Part 1-1: General rules and rules for buildings,*CEB*, (Brussels, 2004).
[5] IS 456-2000. Indian Standard. Plain and Reinforced Concrete – Code of Practice, *Bureau of Indian Standards*, New Delhi, India (2000).
[6] ACI Committee 209. Guide for Modeling and Calculating Shrinkage and Creep in Hardened Concrete, (ACI 209.2R-08). Farmington Hills, MI:American Concrete Institute, 2008.
[7] Ziehl, P.H., Cloyd, J.E., and Kreger, M.E., 'Evaluation of Minimum Longitudinal Requirements for Reinforced Concrete Columns', Research Report 1473-S (University of Texas at Austin, 1998).
[8] Model Code 2010, Volume 1, (CEB-FIB MC 10). Lausanne, Switzerland, 2010.
[9] Lin, C-H., and Furlong, R.W., 'Longitudinal Steel Limits for Concrete Columns', *ACI Structural Journal.***92-S26** (1995) 282-287.

Study on Concrete-Steel Sandwich Panel with Composite Skin

Smriti Raj[1], B. H Bharatkumar[2] and V. Ramesh Kumar[3]

[1]Advance Materials Laboratory, Academy of Scientific and Innovative Research, CSIR-SERC, Taramani, Chennai-600113, Tamilnadu, India

[2]Advance Materials Laboratory, CSIR- SERC, Taramani, Chennai-600113, Tamilnadu, India

[3]Computational Structural Mechanics Group, Academy of Scientific and Innovative Research, CSIR- SERC, Taramani, Chennai-600113, Tamilnadu, India

ABSTRACT

The general advantage of sandwich concept over monolithic concept is to increase the inertia of the member by keeping skin faces apart, resulting into increase in flexural rigidity. In this study, the sandwich panel was designed such that skins are made up of self-flowing-concrete & steel composite and are kept apart through connector provided in the form of web of profile sheet. Since concrete is weak in tension, a non –uniform cross section of profile sheet was used such that tensile flange area was more than compressive flange area. The used concrete along with steel in bottom skin will increase the flexural rigidity and provide cover to steel. Sandwich panel was designed aiming at complete failure should not happen either in compression, tension and core should be strong in shear till strain limit of 3500 micron strain. For the same dimension of sandwich panel (850 x 1800 x 150) mm, monolithic slab was designed and the performance of sandwich panel in terms of strength to cost and strength to weight ratio over monolithic slab have been investigated both theoretically and experimentally. The designed sandwich panel will aim to substitute flexural member slab, considering more strength for less weight and less cost.

Keywords: Sandwich panel, self-flowing concrete, skin, core, failure

1 INTRODUCTION

Sandwich panel is a composite structure element which means that two skins/faces and core are made up of distinct part or materials but are bound together to form an integral unit. The structure of sandwich panel follows a typical basic pattern that comprises of a relatively thin, stiff and strong skin enclosing a relatively thick and light core [1]. Sandwich panels are preferred in construction sector due to its numerous advantages enabling it as suitable structural component which can be customised to exhibit better axial or flexural performance based on the requirement to act as wall, slab or beam. Sandwich panels can also be used as service comfort element by providing perfect insulation against heat, cold and sound. In construction, where the cost increases with time, the sandwich panels can reduce time when prefabricated in mass in industries which will also help in maintaining better quality. Various studies have been reported where sandwich panel is constructed by using different types of skin and core such as i) textile reinforced concrete (TRC), ii) ultra-high performance reinforced concrete (UHPRC) , iii) carbon fibre reinforced polymer (CFRP) composites skin and autoclaved aerated concrete core, iv) Ferro cement encased aerated concrete sandwich

wall element, v) textile reinforced concrete facing and polyurethane foam core with discrete metallic connectors and stiffeners, vi) two concrete layers and internal insulation layer made up of expanded and extruded polystyrene with rigid polyurethane foam, vii) Polyurethane core, outer layer of glass fibre reinforced cement and steel laminates, viii) lightweight pre-casting steel fibre reinforced self-compacting concrete (SFRSCC) panel [2-9].

Generally, in most of the cases, the skin of the sandwich panel is kept thin; hence, in combination of concrete and steel, steel is preferred as outer skin material [10-13]. Some studies were conducted where, steel has been used as core and concrete with enhanced strength have been used as skin [14-16]. In the present study, a sandwich panel is evolved with thin concrete steel composite skin and profile sheet core. The skin of the panel is the flange of profile sheet encased in self-flowing concrete to exhibit steel concrete composite behaviour and the web of the profile sheet act as core as shown in Fig 1.

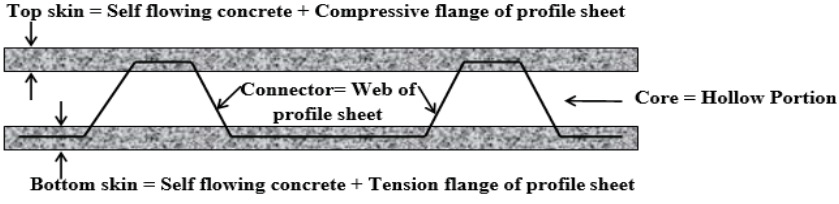

Fig. 1. Sandwich panel C/S

2 DESIGNING OF SANDWICH PANEL

As such, there is no effective guidelines available for the designing of sandwich panel. Allen has suggested that using simple mechanics formulae, load for different failure mode can be calculated and lowest of these failure modes would govern the design of sandwich panel [17]. It was found that most common failure mode of the sandwich panel under flexural are: (i) compressive/ tensile failure of the skin (ii) shear failure of the core (iii) compressive/tensile failure of the core. In the present study, top skin, bottom skin and core are designed based on trial and error such that both materials used in construction of sandwich panel i.e. concrete and steel should be utilised to evolve the sandwich concept.

In the present study, unsupported breadth to thickness ratio is maintained to be less 20, in order to prevent local buckling of plates. Hence for the 3 mm thick profile sheet, any unsupported portion of the top flange of profile sheet is limited to a width of 60 mm (IS 801 clause 5.2.1.2). The profile sheet is fabricated with 2 numbers of 60 mm width compression flange as shown in Fig 2. Thickness of top skin 't' was arrived based on trial and error such that strain across thickness lies in between 2000 to 3500 micron strain as shown in Fig 2. For t = 25mm, and total depth of sandwich panel D = 150 mm, the neutral axis depth x_u was computed to be 68.75 mm using Eqn1 assuming the cross section of sandwich panel as balanced section.

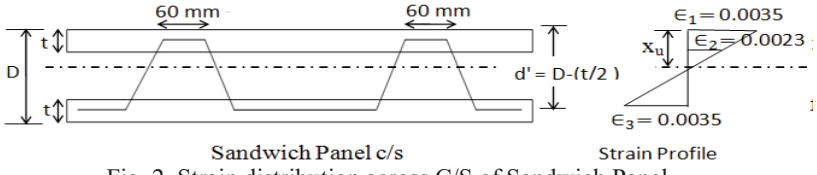

Fig. 2. Strain distribution across C/S of Sandwich Panel

$$\frac{\epsilon_1}{x_u} = \frac{\epsilon_3}{d' - x_u} \tag{1}$$

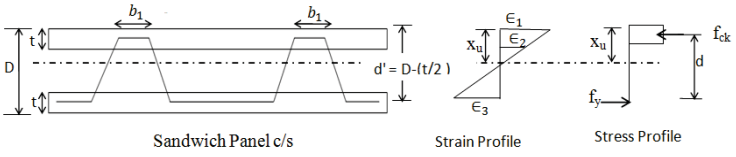

Fig. 3. Force Distribution across c/s of Sandwich Panel

With computed x_u, strain ϵ_2 at level of t = 25 mm was computed to be 2300 micron strain so that the assumed thickness of top skin will not govern the failure of the sandwich panel due to compressive failure of top skin before the global failure of the sandwich panel. The stress –strain profile used in computing the capacity of sandwich panel is shown in Fig 3. Again, to have ductile mode of failure, tensile flanges of profile sheet was designed based on trial and error such that it should be designed as under reinforced section. The grade of concrete was taken as 55 MPa and the flexural strength was taken as 5.6 MPa. Total steel area provided in compressive side is 360 mm^2 as mentioned in Eqn 2. For balanced failure, the amount of steel required in tension side is 4925 mm^2 as mentioned in Eqn 3. For ductile mode of failure, 1650 mm^2 steel area was provided as shown in Fig 4. Web of the profile sheet was designed based on shear load of 265.75 kN calculated as per two pint load as shown in Fig 6 and mentioned in Eqn 6, which was calculated based on minimum moment carrying capacity of sandwich panel under compression 'M_1' and under tension 'M_2' using strain and stress profile of concrete and steel as shown in Fig 5 and given in Eqn 4 & Eqn 5 i.e. M = min (M_1, M_2) = 66.43 kNm. For full composite action in sandwich panel, the top skin should not deform individually, so the thickness was cross checked using flexural formula as computed using Eqn 8.

$$A_{sc} = n \times b_1 \times t = 2 \times 60 \times 3 = 360\ mm^2 \tag{2}$$

$$A_{st} = \frac{(f_{ck} \times b \times t) + (f_y \times A_{sc})}{f_y} = \frac{(55 \times 850 \times 25) + (256 \times 360)}{256} = 4925.42\ mm^2 \tag{3}$$

where f_{ck} = Concrete compressive strength = 55 MPa

b = width of panel = 850 mm, t = thickness of top skin = 25 mm

f_y = steel yield strength = 256 MPa

A_{sc} = Area of steel in compression = 360 mm^2

A_{st} = Area of steel in tension = 1650 mm^2

Using trial and error, area of steel in tension side is provided as under reinforced section.

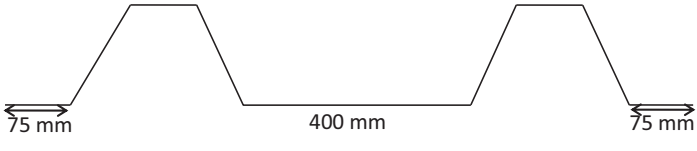

Fig. 4. Cross section of Profile sheet

Area of steel provided in tension side, (75 + 400 + 75) x 3 = 1650 mm^2< 4925.42

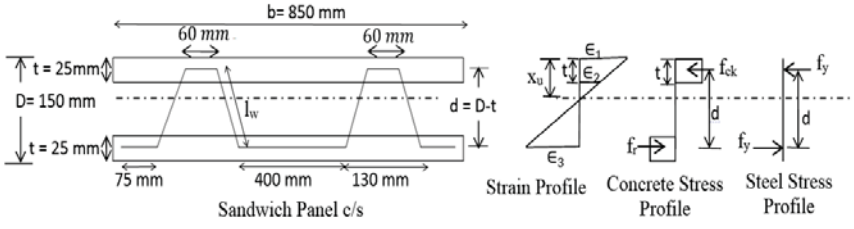

Fig. 5. Force distribution across sandwich panel c/s

Moment carrying capacity of sandwich panel under compression 'M_1'

$$M_1 = (f_{ck} \times b \times t \times d) + (f_y \times A_{sc} \times d) = (55\times 850 \times 25 \times 125) + (250\times 360 \times 125) \quad (4)$$

= 157.34 × 10^6 N mm

Moment carrying capacity under tension 'M_2'

$$M_2 = (f_r \times b \times t \times d) + (f_y \times A_{st} \times d) = (5.6 \times 850 \times 25 \times 125) + (250 \times 1650 \times 125) \quad (5)$$

= 66.43 × 10^6 N mm

Taking Moment carrying capacity of sandwich panel as M = min (M_1, M_2) = 66.43 kNm

For two point loading under flexural load as shown in Fig 6, shear load can be calculated as :

$$M = \frac{P\times L}{6} = 66.43 \times 10^6 = \frac{P\times 1500}{6}; P = 265.75\ kN \quad (6)$$

Web area required = $\frac{265.75\times 1000}{250} = 1063\ mm^2$

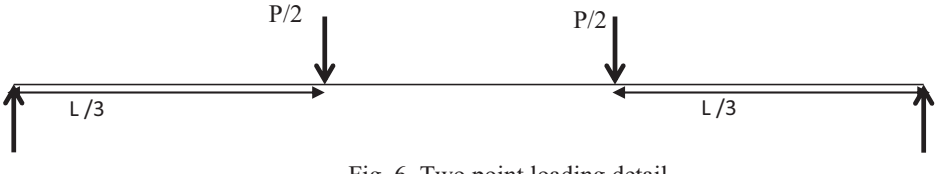

Fig. 6. Two point loading detail

Web area provided = $n \times l_w \times t$ = 4 × 130 × 3 = 1560 mm^2>1063 mm^2

So, web of profile-sheet is safe under shear.

Udl load w = $\frac{P\times 1000}{850} = \frac{265.75\times 1000}{850} = 312.64\ N/mm$ (7)

External moment due to load M = $\frac{w\times l^2}{8} = \frac{312.64\times 400^2}{8} = 6.25 \times 10^6 kNm$

The thickness of section to be provided for taking external moment of M kNm is calculated through flexural formula.

$$t = \sqrt{\frac{6\times M}{\text{fck}\times \text{b}}} = \sqrt{\frac{6\times 6.25\times 10^6}{55\times 1000}} = 26\ mm \quad (8)$$

Sandwich panel was designed aiming at top skin should be strong in compression, bottom skin should be strong in tension and core should be strong in shear. Sandwich panel, where both top and bottom skin comprises of steel – self flowing concrete composite and connected by web of profile sheet. Since in tension side, more steel is needed in compare to compression side, so non uniform cross section was designed. Continuous profile sheet was designed where the single profile sheet will act as composite in both top and bottom skin and it will resist shear by connecting both top and bottom skin. Using the continuous sheet to be used as in top and bottom skin, the web of profile sheet will serve dual purpose, act like connector as well as shear carrying member. Generally thin steel sheet are prone to buckling in compression region, but due to embedding the steel sheet in compression region inside self-flowing concrete, the concrete will provide lateral restraint to steel to prevent it from local buckling too. The designed sandwich panel will aim to use as substitute to flexural member slab where sandwich panel will aim to have high strength to weight ratio and less cost effectiveness in compare to slab. Other than that, the sandwich panel can also be preferred to use where extra construction is required for providing extra service like pipe, wire etc. in the slab since the core of the panel is hollow and it can also be filled with fire insulation or sound proof insulation material as per the requirement.

3 DESIGNING OF SLAB

Slab of dimension (850 x 150 x 1500) mm was designed using stress-strain profile as shown in Fig 7 as per IS-456 as given below.

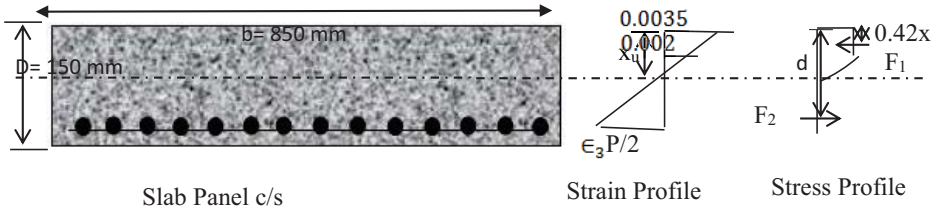

Fig. 7. Force distribution across slab c/s

Taking 10 mm Ø Fe-415 @ 100 mm c/c for 2 layer as main reinforcement

No. of bar in each layer = $\frac{0.85\times 1000}{100} = 8.5 \approx 9$

Area of main reinforcement provided $A_{st} = \frac{2\times 9\times \pi\times 100}{4} = 1413\ mm^2$

$F_1 = (f_{ck}\times b\times 0.43x_u) + (0.66\times f_{ck}\times b\times 0.57x_u) = 0.81\times f_{ck}\times b\times x_u$

$F_1 = 0.81\times 55\times 850\times x_u = 37867.5\,x_u$

$F_2 = (f_y\times A_{st})$

For balanced section, $F_1 = F_2$

$x_u = \frac{f_y\times A_{st}}{0.81\times f_{ck}\times b} = \frac{586395}{37867.5} = 15.48$ mm

F_1 = (37867.5 x 15.48)/1000 kN = 586.18 kN

d = (100-15-5-5) = 75 mm

Moment carrying capacity of section = 'M'= F_1 × (d- 0.42 x_u) =

= (586.18 × 1000 × (75-(0.42 ×15.48)))/1000000 kNm = 40.15 kNm

$$M = \frac{P \times L}{6}$$

$40.15\times 10^6 = \frac{P\times 1500}{6}$

$$M = \frac{P \times L}{6}$$

$40.15\times 10^6 = \frac{P\times 1500}{6}$

P = 160.6 kN

Where

F_1 = Total Compressive Force

F_2 = Total Tensile Force

f_{ck} = Concrete compressive strength

b = Width of slab

x_u = Depth of neutral axis

f_y = Yield strength of steel

A_{st} = Area of steel

4 COST ANALYSIS OF SLAB AND SANDWICH PANEL

Density of concrete ϱ_c = 2350 kg/m^3

Density of steel ϱ_s = 7850 kg/m^3

Cost of concrete = 4 Rs/kg

Cost of Steel = 55 Rs/kg

4.1 Sandwich Panel

Total weight of concrete = $2350 \times 0.85 \times 1.5 \times 0.025 \times 2 = 149.8\ kg$

Total weight of steel =

$(7850 \times ((360 \times 1500) + (1650 \times 1500) + (1560 \times 1500)))/10^9 = 42\ kg$

Cost of concrete = 150 x 4 = 600 Rs

Cost of steel = 42 x 55 = 2310 Rs

Total cost = 2910 Rs

4.2 Slab

Total weight of concrete = $2350 \times 0.85 \times 1.5 \times 0.150 = 449.43\ kg$

Total weight of steel =

$((1413 + 502.4) \times 1500 \times 7850))/10^9 = 22.5\ kg$

Cost of concrete = 450 x 4 = 1800 Rs

Cost of steel = 22.5 x 55 = 1237.5 Rs

Total cost =3037.5 Rs

5 EXPERIMENTAL STUDY ON SANDWICH PANEL & SLAB

The static flexural test was performed on slab and sandwich panel using universal hydraulic monotonic testing machine (capacity 50 tonne) in accordance with ASTM C393 [18]. The load was applied at one third locations at a loading rate of 0.1 mm/min for both, sandwich panel and slab of dimension (B= 850 mm, D = 150 mm, L=1800 mm, L_{eff} = 1500 mm), under simply supported condition. The width plate used at hinge and roller support location were 350 x 875 x 50 mm. The loading roller and support has diameter of 50 mm. The test was discontinued after the 40 % degradation in post peak region for safety purpose. The load and its corresponding deflection at mid span was studied experimentally. From the experimental study, the peak load for the Sandwich panel was 140 kN at deflection of 11.81 mm and for the slab was 180 kN at deflection of 34.24 mm as shown in Fig 8.

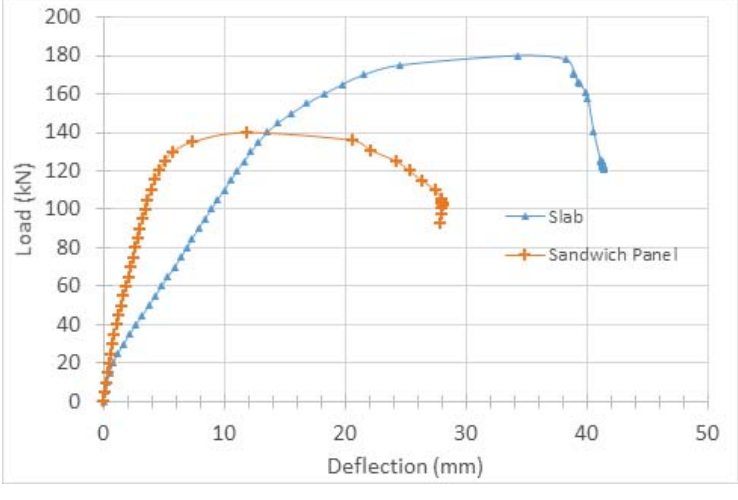

Fig. 8. Experimental studies on Slab & Sandwich panel

6 CONCLUSION

From the experimental studies as shown in the load deflection behaviour of Fig 8, both sandwich panel and slab showed ductile mode of failure for which it was designed also. The

same mode of failure in the sandwich panel as slab shows the compositeness in the sandwich panel. The maximum strength of the sandwich panel was 140 kN against theoretical calculated load of 265.75 kN. For the slab, the maximum strength was 180 kN against theoretical calculated load of 160.6 kN. Although the strength of sandwich panel was not to the full for which it was designed but the strength to weight ratio of sandwich panel was 0.7 and that of slab was 0.4 i.e. the sandwich panel was found to have strength to weigh ratio twice in compare to slab. The sandwich panel was cost effective also in compare to slab as strength to cost ratio for sandwich panel was 20% less in compare to slab.

ACKNOWLEDGEMENT

The author's thank the support rendered by the staff of Group, Advanced Material Lab and Fatigue & Fracture Laboratory in doing the experimental studies.

REFERENCES:

[1] Davies, J. Michael. "Design criteria for sandwich panels for building construction."ASME-PUBLICATIONS-AD55 (1997): 273-284.

[2] Shams, Ali, Alexander Stark, Florian Hoogen, Josef Hegger, and Hartwig Schneider. "Innovative sandwich structures made of high performance concrete and foamed polyurethane." Composite Structures121 (2015): 271-279.

[3] Mousa, Mohammed A., and Nasim Uddin “Experimental and analytical study of carbon fiber-reinforced polymer (FRP)/autoclaved aerated concrete (AAC) sandwich panels”. Engineering Structures 31, no. 10 (2009): 2337-2344.

[4] Sumadi, SalihuddinRadin, and MahyuddinRamli. "Development of lightweight ferrocement sandwich panels for modular housing and industrialized building system." UTM, Research Vote73311 (2008).

[5] Junes, A., and A. Si Larbi. "An experimental and theoretical study of sandwich panels with TRC facings: Use of metallic connectors and TRC stiffeners." Engineering Structures113 (2016): 174-185.

[6] Gara, Fabrizio, Laura Ragni, DavideRoia, and LuiginoDezi. "Experimental tests and numerical modelling of wall sandwich panels." Engineering Structures37 (2012): 193-204

[7] Abeysinghe, Chanaka M., David P. Thambiratnam, and Nimal J. Perera. "Flexural performance of an innovative hybrid composite floor plate system comprising glass–fibre reinforced cement, polyurethane and steel laminate." Composite Structures95 (2013): 179-190.

[8] Barros, Joaquim, Eduardo Pereira, and Simão Santos. "Lightweight panels of steel fiber-reinforced self-compacting concrete." Journal of Materials in Civil Engineering19, no. 4 (2007): 295-304.

[9] Lameiras, Rodrigo Melo, Isabel Valente, Joaquim AO Barros, Miguel Azenha, and Patrícia Isabel da Silva Ferreira. "Fibre reinforced polymer (FRP) connectors for steel fibre reinforced self-compacting concrete (SFRSCC) sandwich panels." InCICE 2012 6th International Conference on FRP Composites in Civil Engineering, pp. 1-8. CICE 2012 6th International Conference on FRP Composites in Civil Engineering, 2012

[10] Anandavalli, N., N. Lakshmanan, GM Samuel Knight, Nagesh R. Iyer, and J. Rajasankar. "Performance of Laced Steel–Concrete Composite (LSCC) beams under monotonic loading." Engineering Structures41 (2012): 177-185.

[11] Mydin, MdAzreeOthuman, and Y. C. Wang. "Structural performance of lightweight steel-foamed concrete–steel composite walling system under compression." Thin-walled structures49, no. 1 (2011): 66-76.

[12] Flores-Johnson, E. A., and Q. M. Li. "Structural behaviour of composite sandwich panels with plain and fibre-reinforced foamed concrete cores and corrugated steel faces." Composite Structures 94, no. 5 (2012): 1555-1563.

[13] Prabha, P., V. Marimuthu, M. Saravanan, G. S. Palani, N. Lakshmanan, and R. Senthil. "Effect of confinement on steel-concrete composite light-weight load-bearing wall panels under compression." Journal of Constructional Steel Research81 (2013): 11-19.
[14] Gopinath, Smitha, V. Ramesh Kumar, HarishkumarSheth, A. Ramachandra Murthy, and Nagesh R. Iyer. "Pre-fabricated sandwich panels using cold-formed steel and textile reinforced concrete."Construction and Building Materials64 (2014): 54-59.
[15] Raj, Smriti, V. Ramesh Kumar, BH Bharath Kumar, SmithaGopinath, and Nagesh R. Iyer. "Flexural studies on basalt fiber reinforced composite sandwich panel with profile sheet as core." Construction and Building Materials82 (2015): 391-400.
[16] Murthy, A. Ramachandra, V. Ramesh Kumar, SmithaGopinath, PrabhatRanjanPrem, Nagesh R. Iyer, and ReshmiBalakrishnan. "Structural Performance of Precast and Cast-in-situ Ultra High Strength Concrete Sandwich Panel." International Journal of Computers, Materials, & Continua44, no. 1 (2014): 59-72.
[17] Allen, Howard G.Analysis and Design of Structural Sandwich Panels: The Commonwealth and International Library: Structures and Solid Body Mechanics Division. Elsevier, 2013
[18] ASTM C393 - 00, “Standard Test Method for Flexural Properties of Sandwich Constructions”

Pull-out Phenomenon of Synthetic Macro Fibres from a Cementitious Matrix

Adewumi J. Babafemi and William P. Boshoff

Unit for Construction Materials, Department Civil Engineering, Stellenbosch University, South Africa

ABSTRACT

Studies to quantify the creep of cracked fibre reinforced concrete have seen a marked increase in recent times. Even though it is known that one of the mechanisms responsible for the crack widening of cracked macro-synthetic fibre reinforced concrete under sustained loading is fibre pull-out, this phenomenon is yet to be fully understood. It is uncertain whether fibre pull-out and lengthening are co-occurring within the matrix during sustained loading or if only the pulled out portion lengthens due to creep. This study, therefore, investigates the phenomenon occurring during the pull-out of synthetic macro fibres tested under sustained loadings. Three types of synthetic macro fibres were partially embedded in 50 mm cube mortar specimens and were subjected to a 55% load of the average maximum pull-out load obtained from single fibre pull-out tests. The time-dependent pull-out displacement was studied in a controlled climate room. X-ray computer tomography (CT) images of specimens were taken at different pull-out stages to study the mechanisms during the fibre pull-out. The results have shown that fibre lengthening and pull-out co-occurring within the cement matrix are the phenomena occurring during increased crack widening of cracked macro synthetic fibre reinforced concrete. However, fibre lengthening is prominent.

Keywords: Time-dependent fibre pull-out, pull-out creep, synthetic macro fibre, sustained loading, fibre creep.

1 INTRODUCTION

Since the advent of synthetic macro fibres over two decades ago, it has seen a marked increase in usage in the construction industry as they are now being used to replace steel reinforcement and steel fibres in certain applications. Some areas of the application of synthetic macro fibres are precast structural elements, slabs on grade, industrial pavements, tunnelling, foot bridges, and concrete pipes [1-4]. Similar to their counterpart, steel fibres, significant improvement in the mechanical properties of concrete has been recorded with the use of synthetic macro fibres. Improvement in post cracking residual strength of the material, toughness, energy absorption capacity and impact resistance have been reported for macro-synthetic fibre reinforced concrete (MSFRC) [1, 5]. The enhancement of these properties by the fibre relates to its bridging activity of cracked planes, hence controlling crack opening and propagation. In aggressive environments, MSFRC is however considered to perform better than steel fibre reinforced concrete (SFRC) due to the resistance of the synthetic macro fibres to alkali and acids [6].

One critical issue with synthetic macro fibres is its significant low stiffness (4 –10 GPa) compared to steel fibres (210 GPa). This implies that during its bridging activity, deformation of the fibre could be expected. An earlier study by Babafemi & Boshoff [7] had revealed that fibre creep and pull-out are the mechanisms responsible for the time-dependent deformation

of MSFRC under sustained loadings. However, it is still uncertain if these mechanisms of fibre pull-out and lengthening are co-occurring within the matrix during sustained loading or if only the pulled out portion lengthens due to creep. This study, therefore, investigated the phenomenon occurring during the pull-out of synthetic macro fibres tested under a sustained load.

2 MATERIALS AND TEST PROGRAMMES

2.1 Concrete mix

The composition of the mix design is shown in Table 1. The coarse aggregate had a size ranging from 4.75 to 6 mm. A well-graded locally available sand passing through a sieve of 4.75 mm was used. The making and curing of test specimens were in accordance with EN 12390–2 [8]. After casting, specimens were left in the moulds for 24 h, demoulded and cured in water tanks at a temperature of 25 ˚C until immediately before testing.

Table 1. Composition of concrete mix

Material type	Volume (kg/m^3)
Cement (CEM I 52.5)	395
Stone (Greywacke, 6 mm max.)	800
Sand (Malmesbury)	990
Water	190
Superplasticiser (0.4% by wt. of binder)	1.58

100 mm cube specimens tested following the procedure outlined in EN 12390–3 [9] had average 7- and 28-d compressive strengths of 43.8 and 55.1 MPa, respectively. Fibres were not added to the mix in the preparation of test specimens at the single fibre level (single fibre pull-out and pull-out creep tests).

2.2 Synthetic macro fibres

Three types of synthetic macro fibres were used in this research – embossed, flat and crimped. The properties of the fibres are presented Table 2.

Table 2: Properties of synthetic macro fibre

Fibre type	Fibre designation	Fibre length (mm)	Fibre material	Specific gravity	Tensile strength (MPa)	Modulus of elasticity (MPa)	Cross-section	Deformation
EPC BarChip 54	Fibre 1	54	Modified Olefin	0.91	640	10	Irregular	Embossed
Geotex 600 Series	Fibre 2	50	Poly-propylene	0.91	450	1.8 – 3.0	Flat	Corrugated
Geotex 500 Series	Fibre 3	50	Poly-propylene	0.91	405	1.62 – 2.7	Round	Crimped

2.3 Pre-damaging of fibres

During mixing, the properties of the fibres are altered [10]. To simulate the actual state of fibres in a cement-based composites, a handful of the three fibre types were added to the

concrete mix shown in Table 1 during the mixing process. The fibres were added at the same time to ensure uniform mixing condition and time. After that, the fibres were picked out, washed cleaned and then used for the single fibre tests. The effect of mixing was visible on the pre-damaged fibres compared to virgin fibres. Fibres showed rough surfaces after the mixing operation.

Due to the fibrillating nature of the flat fibre (Fibre 1), after mixing, the fibre showed different geometrical properties compared to the virgin fibre. It is expected that these differences in the geometrical properties would introduce large variability in the pull-out response of the flat fibres.

2.4 Single fibre pull-out test

The instantaneous pull-out test was undertaken in a monotonic test for the purpose of determining the maximum pull-out load from the load – slip relationship.

2.4.1 Specimen preparation

Before the casting of test specimens, the stones in the concrete were sieved out to obtain only the cement-sand paste. The cement-sand paste was cast into moulds already prepared as shown in Figure 1a.

The specimen size for the instantaneous pull-out test ($40 \times 40 \times 100$ mm^3) was obtained by using a wooden separator in a 100 mm cube size mould (Figure 1a). The specimens were cast in two layers with each layer vibrated. The pre-damaged fibres, which had already been marked to half their lengths, were then carefully and manually inserted into the midpoint of the surface area of each specimen. Thereafter, each mould, with 8 test specimens, were gently vibrated again to ensure the closure of voids created during the insertion of the fibres. Also, care was taken to ensure each fibre remains vertical (perpendicular to the inserted area) after the gentle vibration. Cast specimens are shown in Figure 1b. All test specimens were demoulded after 24 h and then cured in water at a temperature of 23 ºC until testing. Since the intent of the study is to understand the pull-out phenomenon of synthetic fibres, specimens were cured and tested on the 7-d.

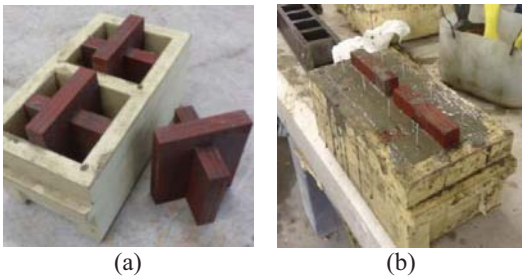

(a) (b)

Figure 1: (a) Specimens' moulds (b) Cast specimens showing inserted fibres

2.4.2 Test programme

The test specimens were taken out of the curing tank, and the test was performed in a climate controlled room at a temperature of 23±1 ºC and relative humidity of 65±5%. The instantaneous single fibre pull-out test was performed in a Zwick Z250 Universal Testing Machine (Figure 2) with a capacity of 250 kN. However, due to relatively much lower pull-out loads expected, a load cell with a capacity of 2 kN was interposed between the upper and lower clamps for accurate measurement of loads.

To effectively grip the fibre without any slippage, a clamp with two steel plates (40×40 mm^2) was fabricated and attached to the 2 kN load cell as shown in Figure 2. It was ensured that the fibre clamp gripped the fibre as close as possible to the specimen's surface.

This simulates a pre-cracked fibre reinforced concrete (FRC) specimen. It was ensured that no load was applied to the fibre prior to the commencement of the test. It should be noted that the test specimen was clamped well below the maximum fibre embedment length to prevent any confinement pressure. The pull-out slip was measured using two 50 mm linear variable displacement transducers (LVDT) attached to a polyvinyl chloride strip which was in turn held in position by connection to the test arrangement. All tests were initially pre-loaded to 10 N, thereafter, controlled at a displacement rate of 0.2 mm/s.

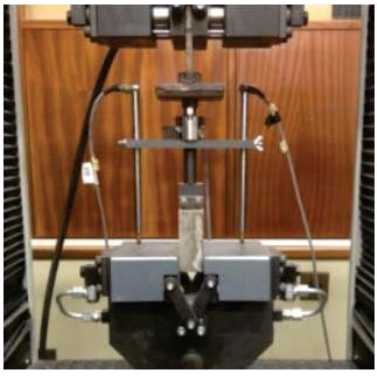

Figure 2: Test setup for single fibre pull-out test

2.5 Time-dependent single fibre pull-out test

The pull-out creep tests were conducted to study the response of each fibre type to sustained load. The sustained load was 55% of the mean instantaneous single fibre pull-out load for each fibre type.

2.5.1 Specimen preparation

The specimens for the pull-out creep test were prepared using the same mix and procedure described in Section 2.4.1. However, specimen sizes for this test were 50 mm cubes produced using cement-sand mortar.

2.5.2 Test programme

The 50 mm cube specimens with the single embedded fibres were held in position by a hollow 100 mm cube square steel section shown in Figure 3a. The steel section was cut open at the centre, 25 mm width by 75 mm length (on one of the sides), Figure 3b. Perpendicular to this centre groove, an opening was created to allow for the placement of the test specimen.

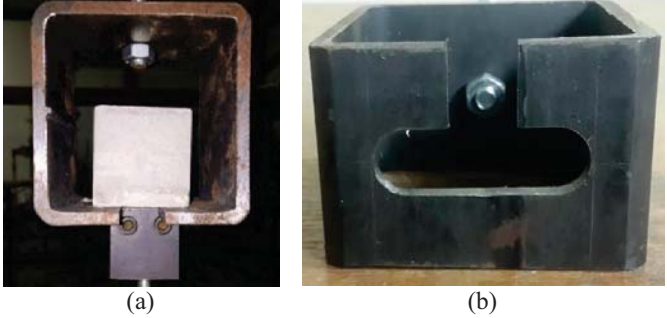

(a) (b)

Figure 3: Specimen position on offcut of square steel section for the pull-out creep test

On the opposite side of the opening, the steel section was drilled to accommodate a 10 mm threaded steel bar that connected the section supporting the test specimen to the creep frame as shown in Figure 4.

The creep loads were applied using free hanging weights. The sustained load of 55% of the mean peak pull-out load obtained from the instantaneous pull-out test for each fibre type was applied after due calibration. The measurement of the time-dependent pull-out displacement for each fibre was started immediately after the weights were applied to each fibre.

The time-dependent pull-out displacement was measured optically using a microscope with an attached 3.1 mega-pixel Leica EC3 camera. A reference photo was initially taken before the creep load was applied and other photos taken as defined periods throughout the test. The internal diameter of the nut on the fibre clamp was used as the scale reference for the determination of the pull-out displacement of each fibre over time.

Figure 4: Time-dependent pull-out creep test setup

2.6 Computer tomography (CT) scan test

The pull-out creep test specimens were subjected to CT scans to understand the pull-out phenomenon of synthetic macro fibre from the cementitious matrix. Three specimens were scanned at a time, one for each fibre type. At such times, the specimens were unloaded, taken for CT scans and reloaded again. The scanned images were studied and correlated with the measured pull-out displacement to deduce if fibre pull-out and lengthening were occurring at the same time or if the fibre lengthening only occurred on the pulled out portion of the fibre.

3 RESULTS AND DISCUSSION

3.1 Single fibre pull-out test result

Four test specimens were used for each fibre type to investigate the pull-out response under monotonic loading. The time-dependent sustained pull-out load was also based on a percentage of the mean maximum pull-out load obtained from the instantaneous pull-out test.

3.1.1 Pull-out response of Fibre 1

The result of the pull-out response of Fibre 1 is presented in Figure 5a. The result shows a mean ultimate pull-out load of 261 N with a coefficient of variation of 8%. This indicates a good consistent ultimate pull-out load for all the fibre samples.

However, beyond the ultimate pull-out load, two forms of responses can be observed. While fibres for Specimens 2 to 4 fractured beyond their ultimate pull-out load, showing a sudden drop in load, Specimen 1 shows significant energy absorption capacity until complete pull-out from the matrix. Figure 5b shows each fibre after the pull-out test, specimens 1 to 4 from left to right, respectively. The peak load and the post peak response are governed by the bond strength between the fibre and matrix. The bond strength is in turn influenced by the stiffness of the fibre and its surface geometry. While some previous works have reported complete fibre pull-out [7, 11], the embossed surface configuration and somewhat high stiffness of the Fibre 1 synthetic macro fibre is believed to have increased the bond between the fibre and matrix. Hence the rupture observed.

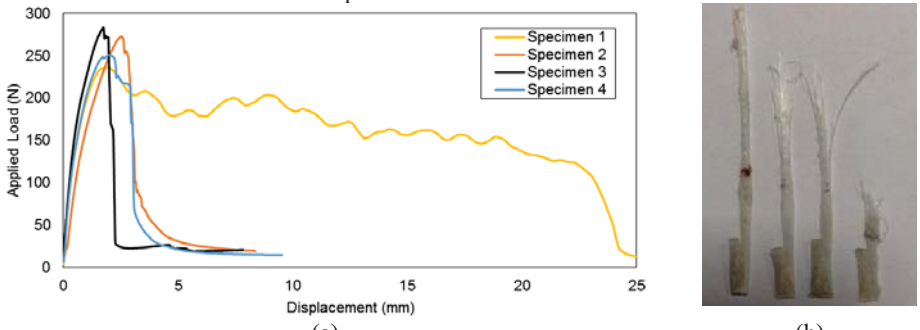

(a) (b)

Figure 5: Single fibre pull-out result for Fibre 1

3.1.2 Pull-out response of Fibre 2

Figure 6a presents the monotonic pull-out response of the flat fibre (Fibre 2). Evidently, the result shows a significant variation in the peak loads of the four specimens with a maximum and minimum of 61 N and 9.4 N, respectively. This variation in the peak loads is expected as previously explained in Section 2.3 In fact, some virgin fibres were already splitting on delivery. Figure 6b shows the corresponding fibres pulled out from the matrix for Specimens 1 to 4. The low pull-out load also attests that flat fibres with smooth surface have a very poor bond with cement matrix as also reported by Singh *et al.* [12].

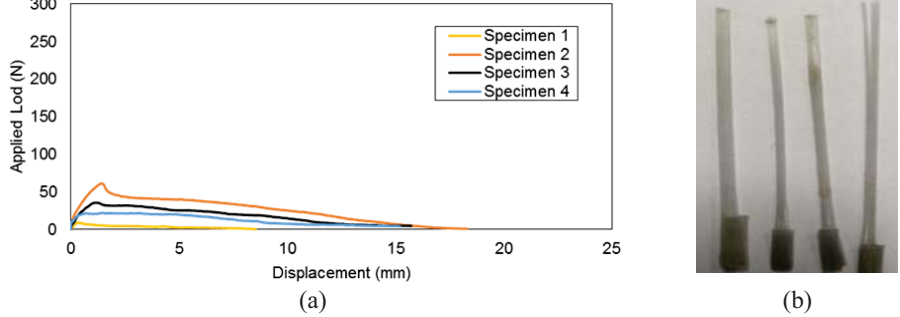

(a) (b)

Figure 6: Single fibre pull-out result for Fibre 2

3.1.3 Pull-out response of Fibre 3

The result of the fibre pull-out response of the crimped Fibre 3 is shown in Figure 7a. The mean peak load of the four specimens is 81 N with a coefficient of variation of 4%. Three of

the fibres pulled out completely while one fractured at peak load. It should be noted, however, that the fracture of the fibre occurred at the clamp and therefore believed to be caused by the clamping force. The effect of the crimped configuration can be seen in the post-peak region with a considerable energy absorption capacity and toughness compared to Fibre 2. Figure 7b shows that the fibre lost their crimped configuration due to lengthening after been pulled out with a wool-like hair around the embedment length.

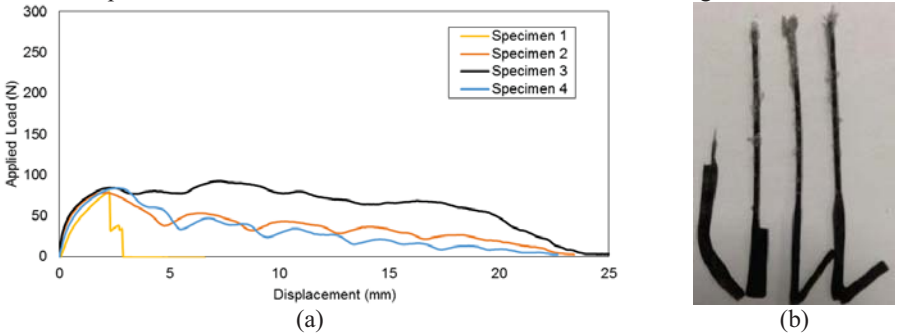

(a) (b)

Figure 7: Single fibre pull-out result for Fibre 3

3.2 Time-dependent single fibre pull-out creep test result

3.2.1 Pull-out creep response of Fibre 1

The result of the pull-out creep of the two specimens with Fibre 1 tested under a sustained load of 143.6 N (55% of the mean monotonic pull-out load) is shown in Figure 8. Significant instantaneous displacement is observed in both specimens after the application of loads. It should be noted that Specimen 1 used for the CT scan, hence, it was unloaded and reloaded a number of times. While Specimen 1 sustained load up to 22 d, Specimen 2 pulled out from the matrix after 26 mins. Evidently, deformation is larger after the initial period of loading (instantaneous deformation), but the rate soon decreases as loading time increases. The complete pull-out of the fibres is believed to be due to bond loss between the fibre and the matrix as a result of fibre lengthening during pull-out.

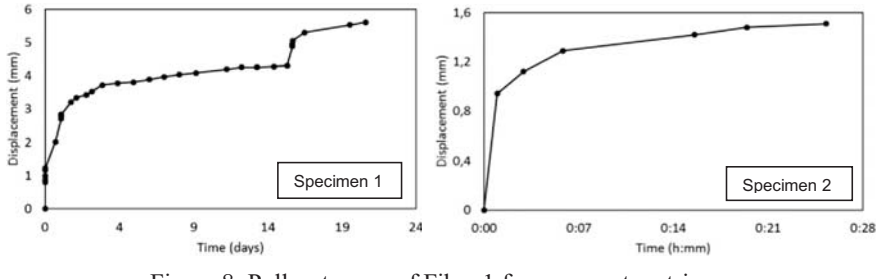

Figure 8: Pull-out creep of Fibre 1 from cement matrix

3.2.2 Pull-out creep response of Fibre 2

Figure 9 presents the result of the pull-out creep of Fibre 2. Creep load was initially at 50% of the maximum load (61 N) obtained from the pull-out test but was later increased to 55%. Specimen 2 was used for the CT scan to study the pull-out phenomenon. The fibres failed by complete pull-out from the matrix after the last measurements were taken.

Earlier days of testing showed more creep than the latter ages. Compared to the performance of Fibre 1 (Specimen 1), Fibre 2 showed lesser time-dependent pull-out creep. The fibres failed by complete pull-out from the matrix.

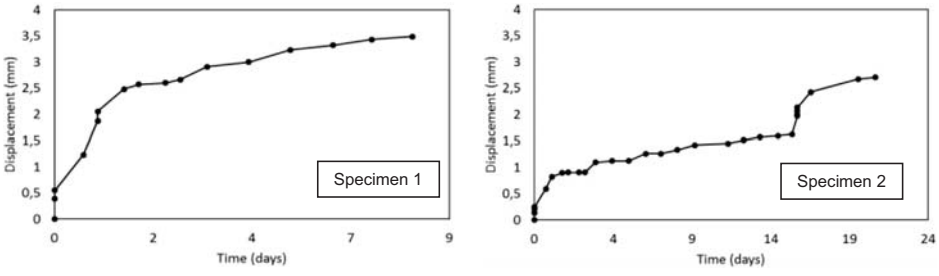

Figure 9: Pull-out creep of Fibre 2 from cement matrix.

3.2.3 Pull-out response of Fibre 3

Here (Figure 10), specimens failed by complete pull-out from the matrix on the application of 55% of the mean maximum load obtained in the single pull-out test. Specimens 1 was unloaded and reloaded at intervals for performing CT scans on the specimen. Displacement rate was also higher at earlier ages and then decreased with time, and the crimped configuration straightened out after fibres pulled out from the matrix.

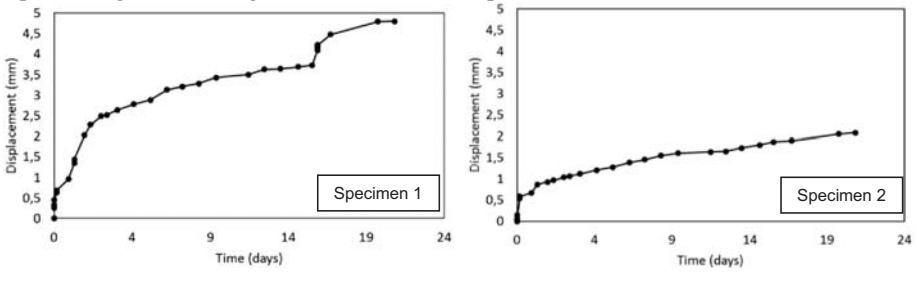

Figure 10: Pull-out creep of Fibre 3 from cement matrix

3.3 CT scan results of single fibre pull-out creep test

The results of the CT scans are shown in Figure 11. For each specimen, CT scans were done 24 h and 15 d after loading. At 24 h of loading, significant pull-out displacements have been recorded using the optical measurement. However, CT scans taken after unloading test specimens at 24 h show that the fibre ends (within the matrix) did not experience any displacement. This is an indication of fibre lengthening proportionally to the matrix displacement without pulling out. This displacement relaxes soon as the specimens were unloaded. After reloading, a slight displacement is observed at the end of each fibre type in the second images, 15 d after test commenced. This shows the fibre pulling out from the cement matrix. Optically compared to the scaled displacements, the pull-out displacements measured was typically 20 times more than the pull-out at the end of the fibre (inside the matrix).

This is an indication that fibre lengthening, leading to loss of bond at the fibre/matrix interface, and thereafter, pull-out occurring are the phenomena responsible for the pull-out of synthetic macro fibres in a cement matrix. These phenomena occurred simultaneously in the matrix. However, the fibre lengthening is much more prominent than the fibre pulling out from the surface of the matrix.

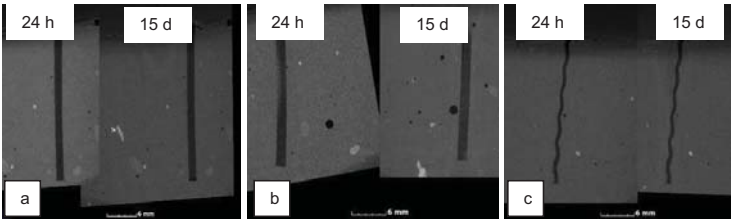

Figure 11: CT scans of fibres embedded in cement matrix (a) Fibre 1 (b) Fibre 2 (c) Fibre 3

4 CONCLUSIONS

The results of the pull-out phenomenon of synthetic macro fibre from cement matrix have shown that the failure mechanisms of cracked macro synthetic fibre reinforced concrete are fibre lengthening (fibre creep) and time-dependent pull-out, both co-occurring. However, this study has revealed that fibre lengthening is prominent.

5 ACKNOWLEDGEMENT

The assistance given by Mr N. D. Muller during the laboratory experiment is well appreciated.

6 REFERENCES

[1] Buratti, N., Mazzotti, C. & Savoia, M., 'Post-cracking behaviour of steel and macro-synthetic fibre-reinforced concretes', *Constr. & Build. Mats.* **25**(5) (2011) 2713-2722.

[2] Alani, A.M. & Beckett, D., 'Mechanical properties of a large scale synthetic fibre reinforced concrete ground slab, *Const. & Build. Mats.* **41** (2013) 335-344.

[3] Peyvandi, A., Soroushian, P. & Jahangirnejad, S., 'Enhancement of the structural efficiency and performance of concrete pipes through fiber reinforcement', *Const. & Build. Mats.* **45** (2013) 36-44.

[4] de la Fuente, A., Escariz, R.C., de Figueiredo, A.D. & Aguado, A., 'Design of macro-synthetic fibre reinforced concrete pipes', *Construction and Building Materials*, **43** (2013) 523-532.

[5] Deng, Z. & Li, J., 'Mechanical behaviors of concrete combined with steel and synthetic macro-fibers', *Int. J. Phy. Sci.* **1**(2) (2006) 57-66.

[6] Wang, Y., Backer, S., & Li, V.C., 'An experimental study of synthetic fibre reinforced cementitious composites', *J. Mats. Sci.* **22**(12) (1987) 4281-4291.

[7] Babafemi, A.J. & Boshoff, W.P., 'Tensile creep of macro-synthetic fibre reinforced concrete (MSFRC) under uni-axial tensile loading', *Cem. & Conc. Comp.* **55** (2015) 62-69.

[8] British Standard Institution, 'Testing hardened concrete. Making and curing specimens for strength tests (EN 12390-2)', BSI, 2009, London.

[9] British Standard Institution, 'Testing hardened concrete - compressive strength of test specimens (EN 12390-3)', BSI, 2002, London.

[10] Lerch, J.O., van Rooyen, A.S. & Boshoff, W.P., 'The influence of mixing on the single-fibre performance of macro synthetic fibre reinforced concrete', in Proceedings of 9th RILEM International Symposium on Fiber Reinforced Concrete (BEFIB 2016), Vancouver, BC, Canada, September 19-21, 2016, 264-277.

[11] Richardson, A.E., Coventry, K. & Landless, S., 'Synthetic and steel fibres in concrete with regard to equal toughness', *Struct. Surv.* **28**(5) (2010) 355-369.

[12] Singh, S., Shukla, A. & Brown, R., 'Pull-out behavior of polypropylene fibers from cementitious matrix', *Cem. & Conc. Res.* **34**(10) (2004) 1919-1925.

Impact of C_3A Content on the Chloride Diffusivity of Concrete

Q. H. Vu, G. Pham, A. Chonier, A. Bauland, G. Pommier and F. Moro

LafargeHolcim Research Center (LCR), France

ABSTRACT

The tri-calcium aluminate (C_3A) content in cement has been known to impact significantly on the chloride binding capacity of concrete. However, little has been done on how this impact would affect the chloride diffusivity of concrete measured with a migration test. Some data collected from the literature and from LCR internal research projects have shown that concretes with low C_3A content cement have systematically higher chloride diffusivity than those with high C_3A content cement. In adding pure synthesized cubic C_3A into ordinary Portland cement (OPC) at 5% by mass, it was found that the chloride diffusivity of concrete can be significantly reduced for low water to binders ratio (W/B=0.4). For high water to binders ratio (W/B=0.66), the impact is lesser.

Keywords: Chloride diffusivity, migration test, C_3A content

1 INTRODUCTION

One of the main causes of deterioration of buildings exposed to marine environments or de-icing salts is the corrosion of steel rebar due to chloride attack. In order to prevent buildings from damages, construction standards require the use of chloride resistant concrete in case of risk, according mainly to the so-called "Prescriptive Approach". The principle of this approach is to fix a minimum compressive strength class and a threshold for several parameters in the mix-design of concrete, e.g. the W/B ratio, the minimum cement content, the maximum additions content, etc., depending on the risk classification [1]. However, this approach has shown its limitations and during the last decades, another approach considered more scientific has been being implemented. This new approach, called "Performance-Based Approach", consists in evaluating the durability performance of concrete based on a set of appropriate durability indicators but no longer on its mix-design and its compressive strength [2-3]. For the case of chloride attack, the most important indicator is the chloride diffusivity (apparent diffusion coefficient). This indicator allows classifying the resistance of concrete to chloride ingress. Additionally, together with the environmental exposure conditions, it can be used as input for estimating the service life of structures [4-5].

According to many of actual standards, the chloride diffusivity of concrete is measured using an accelerated chloride migration test which can last from 24 h to several days. Several authors have highlighted the impact of the chemical composition of the cement used, especially the amount of alumina, on the chloride binding capacity of concrete [6-13]. However, little has been done on how this impact would affect the chloride diffusivity measured with a migration test, given the short duration of this latter. Spiesz et al. [14], in calibrating their transport model on experimental data, have demonstrated that an important amount of chloride could be bound during migration test even for a very short duration of 6 h.

In this study, the impact of C_3A content on the chloride diffusivity of concrete was considered only for OPC systems. In the first step, a bibliographic search was performed to collect data on concretes with low and high C_3A content cement from the literature and from different internal research projects at LCR. In the second step, pure synthesized cubic C_3A was added into OPC at 5% by mass. Concretes with two water to binders ratios (W/B=0.4 and W/B=0.66) were produced using both plain OPC and C_3A added cement and the impact of C_3A added was highlighted.

2 ANALYSIS OF EXISTING DATA

In this section, some data collected from the literature and from different internal projects at LCR were analysed.

2.1 Data in the literature

Saillio [15] has investigated the impact of the mineralogical composition of OPC on the chloride diffusivity. Two cements with 9.91% and 2.38% C_3A content (following Bogue's calculation) were used to produce concretes with the same mix-design. The W/C ratio was 0.53 and the mass of cement was 300 kg/m^3 of concrete.

The chloride diffusivity (D_{app}) was measured following a protocol similar to NT Build 492 [17] but using different equipment.

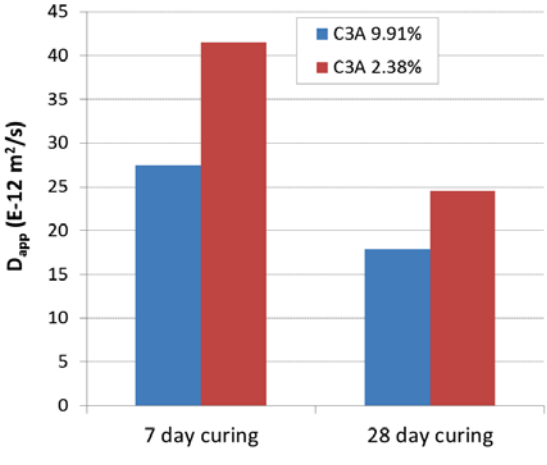

Figure 1 : Chloride diffusivity of concretes with low and high C_3A content cements, Saillio [15]

The result is presented in the Figure 1. It was observed that the chloride diffusivity is significantly higher for concrete with low C_3A content cement.

Maes et al. [16] have shown similar trend (Figure 2) in using two OPCs with 7.92% and 2.5% C_3A content (following Bogue's calculation). Concretes were produced using both cement with the same mix-design (W/C=0.45, 350 kg of cement per m^3 of concrete). The chloride diffusivity was measured following NTBuild 492 [17].

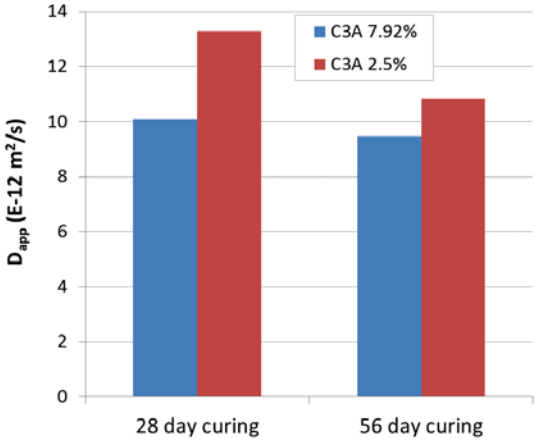

Figure 2 : Chloride diffusivity of concretes with low and high C_3A content cements, Maes [16]

2.2 LCR internal data

Several data have been collected from different projects realized at LCR. The C_3A content was about 7% for OPCs with high C_3A content and about 2.5% for OPCs with low C_3A content (following Bogue's calculation).

The chloride diffusivity was measured after 90 days of moist curing following the French standard XP P18-462 [18]. The cylindrical concrete sample is fixed between two cells containing 0.1M NaOH and 0.1M NaOH + 0.5M NaCl solutions. A 20-25V voltage is applied between two opposite faces of the sample. The test duration can vary from 2 to 7 days in general and is estimated based on the electrical current measured at the beginning of the test.

Two concretes using high and low C_3A content cements with the same mix-design (W/C=0.45, 400 kg of cement per m^3 of concrete) are considered first (Figure 3). It is also clear that the chloride diffusivity of concrete is significantly higher with low C_3A content OPC.

Other results are presented in the Figure 4.

It is found that for concretes with high C_3A content, there exists a good correlation between the chloride diffusivity and the W/C ratio. When putting data obtained with low C_3A content concretes, an important gap can be observed. Concretes with low C_3A content cement tend to have sensitively higher chloride diffusivity.

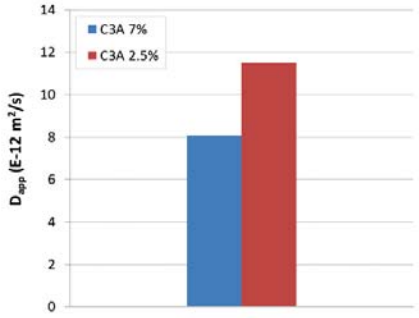

Figure 3 : Chloride diffusivity of concretes produced at LCR using low and high C_3A content cements (same mix-design)

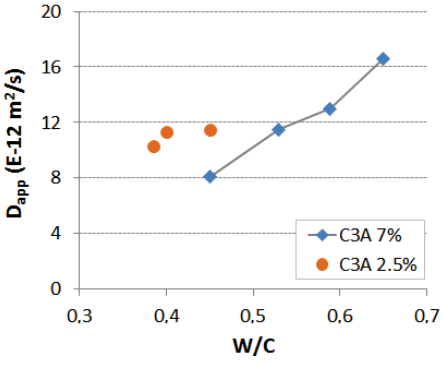

Figure 4 : Chloride diffusivity of concretes produced at LCR using low and high C_3A content cements with different mix-designs

Together with data collected from the literature, it can be concluded that high C_3A content OPC (C_3A content from 7%) is in general sensitively more chloride resistant than low C_3A content OPC (C_3A content lower than 3%). However, it is not obvious to conclude if this behaviour is directly related to the C_3A content because other mineral phases also vary with this latter, which results in other differences as the global hydration degree, the amount and types of hydrates formed.

3 IMPACT OF PURE C_3A

As illustrated above, high C_3A content OPC is in general significantly more chloride resistant than low C_3A content OPC. However, the C_3A content may not be the only cause of difference because the whole mineral composition varies also. In order to decouple the impact of C_3A from other factors, it was decided to add pure synthesized cubic C_3A at 5% by mass into OPC to artificially increase the total C_3A content. The content of other mineral phases in the new binder can be considered as unchanging given the small amount of pure C_3A added.

The mineral composition of plain OPC analysed by Rietveld X-ray diffraction and the main oxide composition of synthesized C_3A analysed by X-ray fluorescence are given in the Table 1.

Table 1 : Composition of OPC and synthesized cubic C_3A (in % by mass)

OPC		C_3A	
C_3S	60.6	CaO	63.48
C_2S	16.3	Al_2O_3	35.80
C_3A	6.5	SiO_2	0.08
C_4AF	9.8		

Concretes were produced using plain OPC and C_3A added OPC with two water to binder ratios (W/B=0.4 and W/B=0.66). The mass of binder was 380 kg and 280 kg per m^3 of concrete for W/B=0.4 and W/B=0.66, respectively.

The chloride diffusivity was measured after 90 days of moist curing following the French standard XP P18-462 [18].

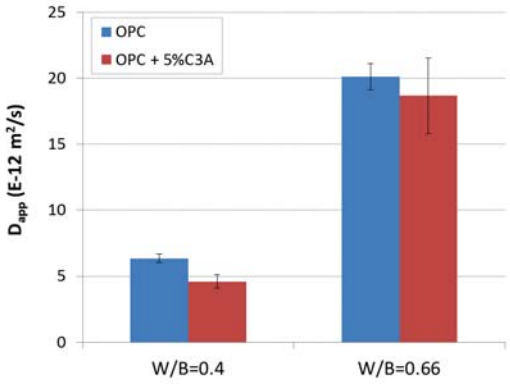

Figure 5: Chloride diffusivity of concretes produced with plain OPC and C_3A added OPC

The comparison result is shown in the Figure 5. For W/B=0.4, it is clear that adding pure C_3A reduces significantly the chloride diffusivity of concrete. The effect seems to be lesser for W/B=0.66. This may be explained by two reasons. Firstly, for high W/B ratios, the porous network is strongly open so that chloride ions can migrate easily and the migration part becomes dominant compared to the binding part related to the added C_3A. It can be seen for plain OPC that the chloride diffusivity is nearly quadrupled by passing from W/B=0.4 to W/B=0.66. Secondly, since the C_3A adding rate was always 5%, the mass of added C_3A was smaller for W/B=0.66 than it was for W/B=0.4 (i.e. 14 kg against 19 kg per m^3 of concrete). Therefore, the binding effect of added C_3A could be lesser for W/B=0.66.

It is also noted that pure C_3A was added into an OPC whose C_3A content was already quite high (6.5%). In using a low C_3A content OPC as reference (C_3A content < 3%), the impact of added C_3A would be expected to be more significant.

4 CONCLUSIONS AND PERSPECTIVES

In this study, the impact of the C_3A content in OPC on the chloride diffusivity of concrete measured with migration test was highlighted.

Data collected from the literature and from different internal projects at LCR showed that high C_3A content OPC (C_3A content from 7%) confers to concrete sensitively lower chloride diffusivity than low C_3A content OPC (C_3A content lower than 3%) does.

The impact of the C_3A content was equally decoupled from that of other mineral phases in OPC in adding pure C_3A into a reference OPC containing 6.5% C_3A. The impact of added C_3A was sensitively seen for low W/B ratio (W/B=0.4) while it was lesser for high W/B ratio (W/B=0.66).

It is recommended from this study that the C_3A content of cement must be seriously taken into account in formulating chloride resistant concrete. In the case that the use of low C_3A content cements is required, it is necessary to raise the awareness of the detrimental effect on the chloride resistance of concrete.

Following this study, some future works should be envisioned:

- Impact of pure C_3A added into low C_3A content OPC (C_3A content < 3%)

- Impact of the quantity of pure C_3A added into OPC
- Impact of reactive alumina content in pozzolanic additions (fly ash, pozzolan, metakaolin)

5 REFERENCES

[1] EuroCode 2 – Design of concrete structures, 1992

[2] Alexander, M. G., J. R. Mackechnie, and Y. Ballim. Guide to the use of durability indexes for achieving durability in concrete structures. *Research monograph* (1999).

[3] Baroghel-Bouny, V., et al. Which toolkit for durability evaluation as regards chloride ingress into concrete? Part I: Comparison between various methods for assessing the chloride diffusion coefficient of concrete in saturated conditions. Andrade et J. Kropp, éditeurs: Third International RILEM Workshop on Testing and Modelling Chloride Ingress into Concrete (2004)

[4] DuraCrete – Final technical report, General Guidelines for Durability Design and Redesign, Brite EuRam III project, (2000) 138.

[5] FIB, Model code for service life design. International federation for structural concrete (FIB). Switzerland (2006) 110.

[6] Baroghel-Bouny, V., et al. Prediction of chloride binding isotherms of cementitious materials by analytical model or numerical inverse analysis. *Cement and concrete research* (2012): 1207-1224.

[7] Florea, M. V. A., and H. J. H. Brouwers. Chloride binding related to hydration products: Part I: Ordinary Portland Cement. *Cement and Concrete Research* 42 (2012) 282-290.

[8] Arya, C., and Y. Xu. Effect of cement type on chloride binding and corrosion of steel in concrete. *Cement and Concrete Research* 25(4) (1995) 893-902.

[9] Justnes, Harald. A Review of chloride binding in cementitious systems. Nordic Concrete Research-Publications 21 (1998) 48-63.

[10] Arya, C., N. R. Buenfeld, and J. B. Newman. Factors influencing chloride-binding in concrete. *Cement and Concrete research* 20(2) (1990) 291-300.

[11] Suryavanshi, A. K., J. D. Scantlebury, and S. B. Lyon. Mechanism of Friedel's salt formation in cements rich in tri-calcium aluminate. *Cement and concrete research* 26(5) (1996) 717-727

[12] Patel, R A., et al., Diffusivity of saturated ordinary Portland cement-based materials: A critical review of experimental and analytical modelling approaches. *Cement and Concrete Research* 90 (2016): 52-72.

[13] Ampadu, K. O., K. Torii, and M. Kawamura. Beneficial effect of fly ash on chloride diffusivity of hardened cement paste. *Cement and concrete research* 29(4) (1999) 585-590.

[14] Spiesz, P., and H. J. H. Brouwers. The apparent and effective chloride migration coefficients obtained in migration tests. *Cement and concrete Research* 48 (2013): 116-127.

[15] M. Saillio, Interactions physico-chimiques ions-matrice dans les bétons sains ou carbonatés : influence sur le transport ionique, PHD Thesis, Université Paris-Est, 2012

[16] Maes, Mathias, and Nele De Belie. Resistance of cracked concrete to chloride attack. 3rd international conference on sustainable construction materials and technologies. Kyoto Research Park. 2013.

[17] NTBuild 492, Chloride migration coefficient fromnon-steady-state migration experiments, Nordtest method, 1999

[18] XP P18-462, Test on hardened concrete – Chloride migration accelerated test in non-steady state – Determination of the apparent chloride diffusion coefficient (in french), French standard, 2012

[19] Talero, R., et al. "Comparative and semi-quantitative XRD analysis of Friedel's salt originating from pozzolan and Portland cement." *Construction and building materials* 25(5) (2011) 2370-2380.

Easy Evaluation of Air-Void Systems in Concrete as Spatial Point Processes

Tkakuma Murotani [(1)], Hidefumi Koto [(2)] and Shin-ichi Igarashi [(3)]

[(1)] Taisei Corporation, Japan
[(2)] Asanuma Corporation, Japan
[(3)] Kanazawa University, Japan

ABSTRACT

Air-void systems in concretes were treated as spatial point processes. The spacing between air voids in concrete was evaluated by the statistics functions for the process. The R software was used to calculate the functions. Air voids in real concretes look clustered since aggregate particles prevent their random arrangement. However, comparison of the air-void systems in real concrete and the simulated systems confirms that air voids can be regarded as random points dispersed within a cement paste matrix. This means that any air-void systems in concretes can be simply represented by random point patterns. A characteristic distance of the random distribution of air voids was defined by the nearest-neighbour distance function. The characteristic distances in real concretes were almost comparable to the spacing factors defined in ASTM C457. Furthermore, the characteristic distances in the simulated point patterns were also almost the same as the spacing factors. The characteristic distance can be used as a new parameter to evaluate air-void systems in concretes. Otherwise, the proposed method using the point process statistics can be an alternative way to obtain the spacing factor of ASTM easily.

Keywords: Air voids, point process, spatial statistics, spacing factor, R software, simulation

1 INTRODUCTION

Frost resistance is an important performance required for concrete in cold climates. The most effective and common means to provide the frost resistance with concrete is to entrain a proper amount of air in concrete. To entrain the air, various types of air-entraining (AE) agents have been widely used. Taking account of the mechanism by which concrete is protected from the frost action, the spacing between air voids must be less than a certain distance. In this regard, the spacing factor is considered as a more important parameter than the absolute amount of air. To examine whether a proper air-void system is present or not in concrete, the number of air voids should be counted under a microscope, following the procedure specified by ASTM C457[1]. However, this procedure is quite time-consuming and needs skills and experiences in petrographic examination of concrete. Therefore, for the sake of simplicity, the total air content is generally used for judging whether or not the concrete is properly designed to have required frost resistance. However, it should be noted that an air content in fresh concrete is not necessarily the same as that in hardened concrete.

It is more than half a century since the basic concept of the spacing factor was proposed by Powers [2]. The spacing factor has been still considered as a useful parameter to evaluate air-void systems in concrete. However, it should be also noted that the air-void structure in which the spacing factor is defined is a virtual system in which mono-sized air bubbles are

regularly arranged in a cement paste matrix. If there is a reliable technique available for evaluating real air-void systems as they are, we should use it. This is the strong motivation of this study.

These days, IT has made a remarkable progress in various techniques to examine concrete. Sophisticated equipment combined with personal computers are commonly used in routine examination of concrete properties. Observation of air bubbles in concrete is no exception. It is easy to obtain high resolution digital images with various types of microscopes and digital cameras. Furthermore, theories for spatial data analysis or modelling have been developed with powerful numerical analysis techniques [3]. Not only the amount of air bubbles but also their spatial arrangement are directly evaluated from the digital images. Real distribution of air bubbles in concrete can be evaluated with a spatial statistical background. It is not necessary to change a real air-void system into a virtual regular arrangement as in the definition for the spacing factor. In addition, a free software package of R that can analyse a spatial data set can be downloaded [4]. If the package is used for analysing air voids as spatial data, any sophisticated programming or numerical analysis techniques are not required for concrete practitioners to calculate statistical functions of air-void distribution in concrete. The authors have pointed out that the treatment of air-void systems as spatial point processes is quite useful for evaluating air-void systems in cement pastes and mortars [5]. Once digital images of air voids are acquired by any procedures, a characteristic distance which is comparable to the spacing factor is immediately evaluated without following the time-consuming procedure specified by ASTM.

In this study, the easy technique mentioned above is applied to air-void systems in concretes containing different amounts of air. Images of air voids acquired with a commercial flatbed scanner are analysed as a spatial data set. The characteristic distance determined by the point process function is compared with the spacing factor defined in ASTM. Furthermore, using the R package, air-void systems in concretes are simulated as random processes. Characteristics of the simulated spatial structure of air voids are also compared with the real structure. The treatment as a 2D point process is proposed as an easy and reliable method to examine air-void systems and estimate the spacing factor in concrete.

2 EXPERIMENTAL

2.1 Materials and specimens

The cement used was an ordinary Portland cement. River sand and gravel (maximum size=25 mm) were used as fine and coarse aggregates, respectively. The water/cement ratios of concrete were 0.40 and 0.55. Air contents of the concretes were changed by the amounts of AE and AE-water reducing agents. Mix proportions of the concretes are shown in Table 1. Prism specimens of 100×100×400 mm were produced in accordance with JIS R5201. They were demolded at 24h after casting. They were then cured in water at 20ºC for 7 days.

Table 1: Mix proportions of the concretes

W/C	0.40			0.55		
Mix	C1-1	C1-2	C1-3	C2-1	C2-2	C2-3
Point density (/mm^2)	1.00	1.36	2.30	0.58	1.10	1.55
Average air void diameter (μm)	124	131	133	131	156	171
Air (hardened) (%)	2.0	3.0	5.2	1.6	3.9	7.8

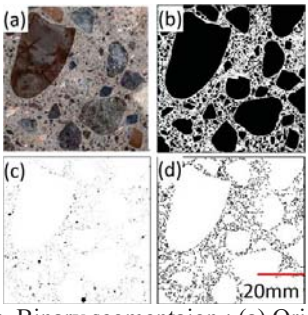

Figure 1: Binary segmentaion : (a) Original image (b) aggregate (c) air voids (d) point process

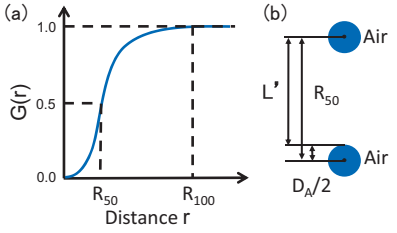

Figure 2: Schematic drawings : (a) nearest-neighbour distance function and definition of R_{50} (b) relationship between R_{50} and L'

2.2 Image acquisition

At the age of 7 days, slices about 15 mm thick were cut from the concrete prisms. They were finely polished with abrasive SiC papers. To distinguish aggregate particles from the surrounding cement paste matrix, the polished surfaces were treated with a solution of phenolphthalein. Ten images of each concrete specimen were acquired with a conventional flatbed scanner [6]. Then the treated surfaces with the phenolphthalein solution were dyed with a black ink. Air voids on the surfaces were filled with a white powder of calcium carbonate (mean diameter = 12-13 μm). Then the surfaces were scanned again to obtain images of air voids. The resolution of the images obtained by the scanner was about 30 μm/pixel.

2.3 Image analysis

Images used in the analysis are shown in Fig. 1. All the relevant information as spatial data was extracted from an original scanned image (Fig. 1(a)). Aggregate particles were segmented on the basis of brightness and chromaticity (Fig. 1(b)). Air voids were directly segmented from the scanned images of the black-coloured cross sections (Fig. 1(c)). Considering a common range of air-void diameters, small isolated voids of one pixel were deleted as noises or other defects in the images. The residual voids were regarded as air bubbles. The area fraction of them was simply obtained by image analysis. Centroids of each air void $\boldsymbol{x}_i$ $(\mathrm{i} = 1, \cdots \mathrm{n})$ were also obtained by the image analysis procedure. Then all the air voids were converted to a set of spatial points of which positions agreed with the centroids of original air voids (Fig. 1(d)). The set of those points was regarded as a spatial point process$\mathrm{X}_c = \{\boldsymbol{x}_i : \mathrm{i} = 1, \cdots \mathrm{n}\}$. Air void characteristics evaluated by the image analysis are given in Table 2.

Table 2: Air void characteristics in scanned images of concretes

Mix	W/C (%)	Sand/total aggregate ratio (%vol.)	Slump (cm)	Air (%)	Unit Content (kg/m^3) W	C	S	G	AE water reducing admixture (%wt./C)	AE admixture (%wt./C)	Measured Slump (cm)	Measured Air (%)
C1-1				2.5±0.5			686	1033		0.001	13.0	2.8
C1-2	40	39.9	15±2	4.5±0.5	175	438	665	1002	0.25	0.002	17.0	5.0
C1-3				7.0±0.5			639	963		0.012	16.0	7.4
C2-1				2.0±0.5			785	1045		-	17.0	1.7
C2-2	55	42.9	15±2	4.5±0.5	175	318	754	1008	0.25	0.002	16.5	4.0
C2-3				9.0±0.5			707	941		0.010	17.0	9.0

2.4 Calculation of spatial point process statistics

2.4.1 Point intensity

The point intensity λ_A of the point process X_c was determined by the following equation.

$$\lambda_A = \frac{N(W)}{A(W)} \tag{1}$$

where N(W) is the total number of points in an observation window W. A(W) is the area of the whole observation window.

2.4.2 K-function and nearest-neighbour distance distribution function

The K-function and the nearest neighbour distance function (G-function) of a point pattern were calculated using Eqs.(2) and (3) [7]. The calculated K-function was converted to the L-function (Eq.(4)). All of those functions were calculated using a package "spatstat" of the R language [4].

$$K(r)=\frac{1}{{\lambda_A}^2}\sum_{i\neq j}\frac{\mathbf{1}(|x_i - x_j|\leq r)}{s(x)} \tag{2}$$

$$G(r)=\frac{\sum_{i=1}^{N(W)}\mathbf{1}(s_i\leq r)\cdot\mathbf{1}(s_i\leq b_i)\cdot w(s_i)}{\sum_{i=1}^{N(W)}\mathbf{1}(s_i\leq b_i)\cdot w(s_i)} \tag{3}$$

$$L(r)=\sqrt{\frac{K(r)}{\pi}} \tag{4}$$

Where $x = |x_i - x_j|$, $s(x)$ and $w(s_i)$ are the functions for edge correction. $\mathbf{1}(\cdot)$ is the indicator function, i.e. equal to one if its argument is true and zero otherwise. r is distance. b_i is the shortest distance from each point x_i to the edges of the window W. The variable s_i is the distance to the nearest other point in the point process. A schematic drawing of the nearest neighbour distance function is shown in Fig. 2. It is a probability distribution function of distance from a point x_i to the nearest neighbour $x_j (x_i, x_j \in X_c \; ; i \neq j)$. The function is expressed as a cumulative probability function. A median distance R_{50} is defined as a parameter corresponding to the cumulative probability of 50% (Fig.2 (a)). In this procedure to determine the median distance as a characteristic for a given air-void system, the sizes of air bubbles are ignored. On the other hand, the spacing factor of ASTM considers the mean size of air bubbles. Therefore, a characteristic distance L' which considers the sizes of air voids is defined by Eq.(5) (Fig.2(b)). Where D_A is the mean diameter of air voids, and discussed later.

$$L' = R_{50} - \frac{D_A}{2} \tag{5}$$

2.4.3 Spacing factor of air voids

Using the images acquired in 2.2, the spacing factor L of ASTM C457 was calculated by Eqs. (6) and (7).

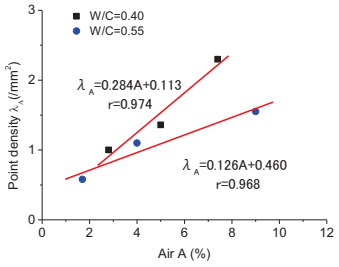

Figure 3: Correlation between point density and air content in concrete

$$L=\frac{3}{\alpha}\left[1.4\sqrt[3]{\frac{P}{A}+1}-1\right] \qquad (P/A>4.342) \tag{6}$$

$$L=\frac{P}{A\alpha} \qquad (P/A\leq 4.342) \tag{7}$$

$$\alpha=\sqrt{\frac{6\pi}{\bar{a}}} \tag{8}$$

where P is the volume fraction of cement paste. A is the volume fraction of air in concrete. α is the specific surface area of air bubbles. It is calculated from Eq.(8) . $\bar{a}$ is the mean area of air bubbles. It should be mentioned that all the parameters in Eqs.(6)-(8) including $\bar{a}$ are calculated using the image analysis software. The procedure such as the linear traverse specified in ASTM C457 is not used in this study at all.

2.4.4 Simulation of air-void distribution

Using the package "spatstat" mentioned above, random points of which density is equal to λ_A are generated as a binomial point process. The simulated process is considered as a completely random point process X_R. The L-function and G-function of X_R were also obtained, following the same procedure as for X_c. The simulation as a binomial point process was repeated 20 times for each scanned image. Then the 95% confidence intervals of the L-function and G-function were determined from the simulations of 200 times.

3 RESULTS AND DISCUSSION

3.1 Simulation of air-void systems

Fig.3 shows the relationship between the point density and the air content in the concretes. There is a good correlation between them. The point density increases with the increase in the amount of air volume. If the plot against the extreme air content of 9% is ignored, the relationship seems to be expressed with one regression line regardless of *w/c*. From the viewpoint of stereology, generally speaking, the point density cannot be directly related to the number of points as 3D objects (i.e. air bubbles). However, air bubbles in concrete are convex with sphere shapes. Therefore, we can assume that one air bubble does not produce two cross sections in a 2D plane. Thus the point density can be regarded as a parameter of the air content in concrete. If the air content is increased extremely, coalescence of air bubbles occurs in the limited volume of cement paste matrix. Thus the point density did not greatly increase in spite of entraining air by the high volume of 9%.

An example of comparison between real ($\mathbf{X_C}$) and simulated ($\mathbf{X_R}$) processes is shown in Fig.4. The process $\mathbf{X_R}$ was produced by generating the same number of points as $\mathbf{X_C}$ in the

compliment area of aggregate particles. Exact locations of each point in the simulated process are clearly different than those in the real process $\mathbf{X}_C$. However, at first glance, there is no difference in an impression between the two processes. In the real process, the regions of a high point density and the ones of sparse points coexist in the whole cement paste matrix. These features are also seen in the point process generated by a simple random simulation technique.

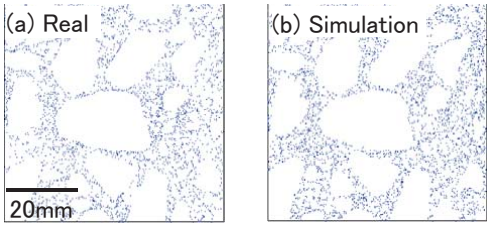

Figure 4: Distribution of air voids : (a)real concrete (b)simulation as a binomial process with the same point intensity

Fig.5 shows the L-functions of air voids in real concretes and the confidence interval that was determined from 200 simulations as a binomial process [8]. The L-functions of the real processes are greater than those of the Poisson point process ($\mathbf{L(r) = r}$). As expected, air voids in concrete make a clustered pattern if the whole observation field is taken as a reference area. In other words, effects of aggregate particles on interrupted arrangement of air voids are properly evaluated by the L-function. If air voids are simulated as a point pattern in a limited area of cement paste matrix, the nearest neighbour points of air voids happen to be very close each other. This results from ignoring the size of air voids in the simulation. On the other hand, the nearest neighbour point in a real air-void system must be a certain distance away from its neighbour points since two voids have their own sizes. Therefore, the L-functions of the simulated patterns are plotted above the Poisson point process while the functions of the real processes are always smaller than the Poisson process in a range of short distances. In other words, the functions of the real processes have x-intercepts. Therefore, strictly speaking, the air-void systems in the concretes are not completely random in terms of point process statistics. However, in view of the functions in the distance range greater than about 100 μm, all the L-functions are plotted within the confidence intervals. Therefore, the air voids can be regarded as a random point process if they are present at certain distance away. Then we can assume that those points are dispersed independently without any influence from other points. This suggests that the air-void systems in the concretes can be represented by generating random points in the cement paste matrix.

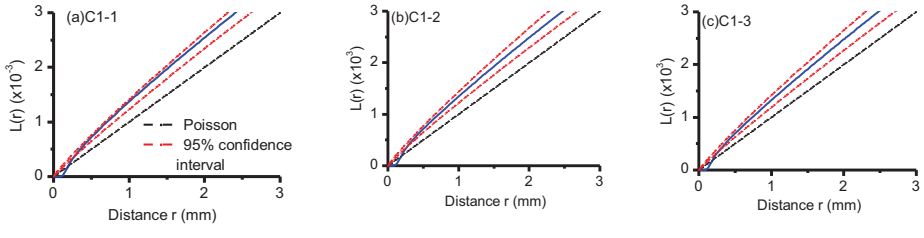

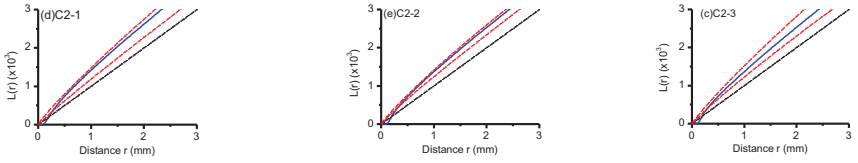

Figure 5: L-functions of air voids in concretes

Fig.6 shows the nearest neighbour distance functions of the point processes $\mathbf{X_C}$ of real air voids. Like the L-functions in Fig.5, the nearest neighbour distance functions show that air voids cannot be regarded as random processes in the range of short distances. However, the functions are again plotted within the confidence intervals at the median distances corresponding to the probability of 50%. This means that the real distributions of air voids are included in the population set that has the same point density as the original pattern in real concrete. Therefore, the median distance that specifies the spatial distribution of air voids may be also estimated from the random simulation without observing or analysing real air voids in concrete. This would be beneficial to evaluation of air-void systems in concrete.

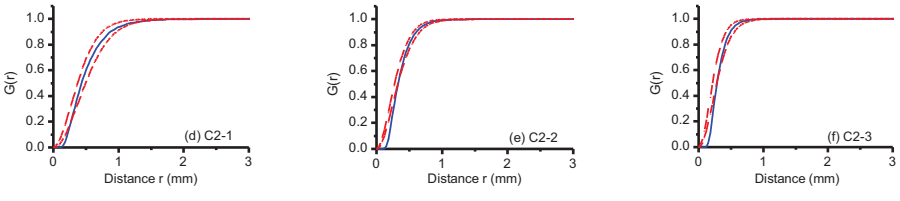

Figure 6: G-functions of air voids in concretes

Fig.7 shows the relationship between the median distances $\mathbf{R_{50}}$ of the real air-void systems and the ranges of confidence intervals that are determined from 200 binomial simulations. The median distance decreases with the increase in the point density, as expected. Further, the median distances are inside the confidence intervals at the low point densities. They approach to the upper limits of the intervals as the point density increases. This also results from ignoring the size of air voids. However, the differences in distance from the intervals are quite small even at the greatest point density. It is at most a distance of one pixel (i.e. 30 μm). Thus a simple simulation that generates random points in the cement paste matrix gives approximate values of the median distance between air voids in real concrete. In other words, real distances between air voids in concrete can be estimated from the simulated point patterns.

3.2 Characteristic distance L' as spacing between air voids

Both the median distance $\mathbf{R_{50}}$ and the characteristic distance $\mathbf{L'}$ are defined for a 2D point process (Fig.2). On the other hand, the spacing factor $\mathbf{L}$ defined in ASTM C457 is the mean value of the longest distance from an arbitrary location in the cement paste matrix to the nearest surface of air voids in concrete. To calculate the spacing factor L, a real air-void system is converted to a virtual 3D regular arrangement of mono-sized air bubbles. Therefore, those characteristic values of $\mathbf{L'}$ and $\mathbf{L}$ are defined for different spatial arrangements of air voids, respectively. It may be irrelevant to discuss equivalence between the 2D real distance $\mathbf{L'}$ and the 3D virtual distance $\mathbf{L}$ in detail. However, this is of interest since the 2D real distance could be used as a parameter instead of the spacing factor L.

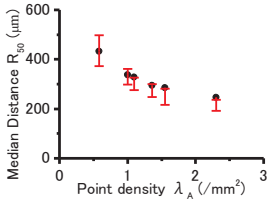

Figure 7: Median distances in the process X_c and confidence intervals in X_R

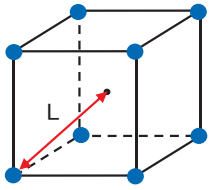

Figure 8: Regular arrangement of air voids and a spacing factor defined in the cubic corresponding to the point intensity of N_V

If the shape and size of air bubbles are assumed, the number of points observed in a 2D unit area can be related to the number of points in a 3D unit volume. Then the characteristic distance L' in the 2D area can be compared with the distances in the 3D regular arrangement of voids in which the spacing factor L is derived. Here the particle size distribution of air voids appeared in a 2D plane is assumed the same as that of air bubble spheres in 3D space. Then the mean diameter D_V of the spheres in 3D space is obtained as the mean diameter D_A of the voids appeared in the images. The 3D number density N_V of spherical particles can be estimated from 2D section, using the DeHoff-Rhines relation (Eq. (9)) [9].

$$N_A = E[H]N_V \tag{9}$$

where N_A is the number of particles per unit area (= the point density λ_A). $E[H]$ is the mean diameter of air bubble spheres in 3D space (=D_A). N_V is the number of spheres per unit volume (= the point densityλ_V). Taking account of the fact that air bubbles are present in the cement paste matrix phase in concrete, the number of air bubbles per unit volume of the cement paste matrix N_V is given by Eq.(10).

$$N_V = \frac{\lambda_A}{pD_A} \tag{10}$$

where p is the volume fraction of cement paste in concrete. The reciprocal of N_V is the volume of a cubic which is provided for one point (i.e. one air bubble). Half the diagonal length of the cubic $R_c/2$ is given by Eq.(11). The spacing factor L is equal to the half of the length subtracting the mean diameter from the diagonal length. Thus the spacing L_D in a point process assuming the DeHoff-Rhines relation is given by Eq.(12). It should be noted that the value of L_D has the same physical meaning as the spacing factor L of ASTM C457 (Fig.8).

$$\frac{R_c}{2} = \frac{\sqrt{3}}{2} \times \sqrt[3]{\frac{1}{N_V}} = \frac{\sqrt{3}}{2} \times \sqrt[3]{\frac{pD_A}{\lambda_A}} \tag{11}$$

$$L_D = \frac{R_c - D_A}{2} = \frac{\sqrt{3}}{2} \times \sqrt[3]{\frac{pD_A}{\lambda_A}} - \frac{D_A}{2} \tag{12}$$

Fig.9 shows the relationship between L_D derived from the 2D point patterns and the conventional spacing factor L of ASTM. The distance L_D is almost the same as the spacing factor L. It is well known that the measurement of the spacing factor L is quite time-consuming, and requires experiences in petrographic examination of concrete. On the

contrary, it is quite easy to obtain L_D once the images of air voids are converted to 2D point processes. As mentioned above, it should be noted that L_D is analogous to L in its geometrical meaning. Therefore, it seems that L_D may be used as a parameter to characterize the distance between air voids instead of the spacing factor L.

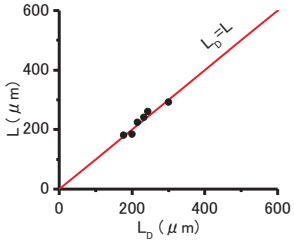

Figure 9: Relationship between the spacing factor L and the distance L_D

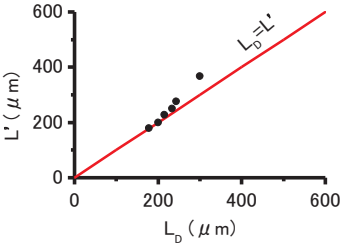

Figure 10: Relationship between the characteristic distance L' and the distance L_D

Fig.10 shows the relationship between L_D and L', which is a characteristic distance of real point distribution. Difference between the two distances decreases with the increase in point density. This means more homogenous distribution of air voids takes place at high point densities in 3D space so that local variation in terms of spatial statistics is decreased. In other words, as the point density increases, the mean distance between air voids gets close to the half of the diagonal length of the cubic from which the spacing factor is derived. To confirm this behaviour, the simulation in which the point density was gradually increased was carried out. The characteristic distance R_{50} was obtained from the nearest neighbour distance function at each point density. The simulation was executed for the concrete mixture of C2-2 since its air content was within a range in ordinary concrete. Simulation of binomial point process was repeated 200 times. Then the mean value of the median distance R_{50} from the simulation and the half of the diagonal length ($R_C/2$) of the cubic are plotted against the point density (Fig.11). When the point density is small (i.e. a little air content), there is an appreciable difference between the two distances (i.e. R_{50} and $R_C/2$). However, there is little difference at greater point densities. For example, the point density ranging from about 0.8 to 2.2/mm^2 corresponds to the concretes that have an air content of 3 to 7%. In this range, the difference between the median distance R_{50} and $R_C/2$ is at most 30μm (i.e. one pixel). Therefore, it is found from Fig.11 that almost the same distance as the spacing factor can be easily estimated from R_{50}, without following the procedure of ASTM C457. Again it should be noted that the median distance R_{50} was easy to obtain if the R package was used. In conclusion, if point process statistics is applied to air-void systems in images, a distance parameter is easily obtained by combining the data of image analysis and the R calculation. The parameter of point process statistics is quite comparable to the spacing factor which has been used as a unique parameter for air-void systems in concrete. Therefore, instead of following the procedure of ASTM to measure the spacing factor, it would be much easier to evaluate L from R_{50}.

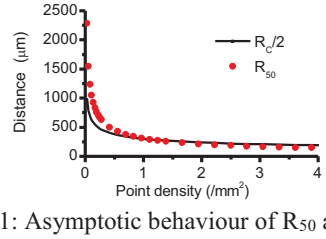

Figure 11: Asymptotic behaviour of R_{50} and $R_c/2$

4 CONCLUSIONS

A simple procedure to analyze spatial distribution of air voids in concrete was proposed. The method is based on second-order statistics of spatial point processes. A software package to calculate the relevant statistics on air voids can be downloaded from the R site. Therefore, it could be easy for practitioners to introduce the technique into routine works for examining air-void systems in concrete. The characteristic distance as a parameter for the air-void system was also proposed. The major results obtained in this study are summarized as follows;

(1) There is a good correlation between the air contents in fresh concretes and the point densities of air voids observed in hardened concretes.
(2) Air voids are dispersed randomly in the cement paste matrix in concrete except a range of short distances between them. The characteristic distance of real air-void system was defined by the nearest neighbor distance function. It is easy to obtain the characteristic distance with R. Furthermore, the distance can be also estimated from the simulation in which the point density is the same as in real concrete. The R package is also used for the simulation.
(3) The characteristic distance estimated from the point process statistics agreed quite well with the conventional spacing factor.
(4) The median distance R_{50} of air-void systems approaches to the length corresponding to the spacing factor as the air content increases.
(5) The median distance and the resultant characteristic distance can be regarded as parameters for air-void systems. They can be also used as an alternative for estimating the conventional spacing factor.

5 REFERENCES

[1] ASTM C457/C457M-12 : Standard Test Method for Microstructural Determination of Parameters of the Air-Void System in Hardened Concrete, (2012).
[2] Powers, T.C., 'The air requirement of frost-resistance concrete', *Proc. Highway. Research. Board.* **29,** (1949)184-211.
[3] Pleau, R. and Pigeon, M., 'The use of the flow length concept to assess the efficiency of air entrainment with regards to frost durability: Part 1- description of the test method', *Cement, Concrete and Aggregates.* **18**(1), (1996) 19-29.
[4] Baddeley, A.J. and Turner, R., 'Spatstat: an R package for analyzing spatial point patterns', *J. Statistical Software*, **12**(6), (2005) 1-42.
[5] Koto, H., Murotani, T. and Igarashi, S., 'Correlation between characteristics distances of air voids as point porocesses and spacing factors in mortars', Proc. Intl. RILEM Conf. on Materials, Systems and Structures in Civil Engineering 2016 ;Segment on Frost Action in Concrete, (2016) 81-90.
[6] Zalocha, D. and Kasperkiewicz, J., 'Estimation of structure of air entrained concrete using a flatbed scanner', *Cement and Concrete research.* **35** (10), (2005) 2041-2046.
[7] Stoyan, D., Kendall, W.S. and Mecke, J., 'Stochastic Geometry and its Applications', 2nd Edn. (WILEY, 2008).
[8] Ripley, B.D., 'Spatial statistics', (WILEY, 1981)
[9] DeHoff, R.T. and Rhines, F.N., 'Determination of number of particles per unit volume from measurements made on random plane sections; the general cylinder and the ellipsoid', Transactions AIME, **221,** (1961) 975-82.

A Bayesian Approach to Assess the Influence of Coarse Aggregate on the Chloride Test Outcome

Naga Pavan Vaddey, Mahmoud Shakouri and David Trejo

Oregon State University, Corvallis, OR, 97331, USA.

Abstract

Chlorides in concrete can result in premature corrosion of the reinforcement steel and can reduce the service life of reinforced concrete structures. Correctly assessing the initial chloride content requires information on the variation of the chloride concentration distribution throughout the procured samples. Because concrete is a heterogeneous material, understanding how mixture proportions can affect the chloride concentration is important. The present study takes a Bayesian approach to determine how the unbalanced distribution of coarse aggregates in concrete can result in variability in chloride measurements. Concrete specimens were cast with 0.25% admixed chlorides by the weight of cement with coarse aggregates meeting ASTM C33 grade No.67. After curing, specimens were cut at different depths, and the proportions of the coarse aggregates for each layer were determined using quantitative image analysis. Two hierarchical Bayesian models were developed by relating the measured acid-soluble chloride concentration as the response variable to different coarse aggregate size ranges. Results show that the total proportion of coarse aggregate is an influential factor. Increase in coarse aggregate content leads to a reduction in the measured chloride content. The proposed model can be used as a quality control tool for making more informed decisions regarding the expected initial chloride content in fresh concrete. It can also be used to determine the number of samples that are required for a reliable test program.
Keywords: Initial chloride, coarse aggregate, variability, Bayesian

1 INTRODUCTION

Corrosion of reinforcing steel can reduce the service life of concrete structures. A study by the U.S. Federal Highway Administration estimates that the annual corrosion costs for the infrastructure sector to be more than $22.6 billion [1]. Chlorides in concrete are one of several major factors responsible for the initiation of reinforcement corrosion.

Chlorides can be introduced into concrete systems in various ways. Constituent materials of the concrete such as cement, water, aggregates,and admixtures can contain chlorides. These are referred to here as initial chlorides (C_i). Exposure of concrete structures to chloride-laden environments, including seawater and de-icers, can also introduce chlorides into the hardened concrete through various transport mechanisms. These are referred to here as penetrated chlorides (C_{pen}). Regardless of how chlorides enter the concrete, reinforcement corrosion initiates when the chloride concentration at the steel-concrete reaches some level, commonly referred as critical chloride threshold (C_T).

Due to the deleterious nature of chlorides in concrete, U.S. organizations, including the American Concrete Institute (ACI) and many state highway agencies (SHAs), specify allowable admixed chloride limits (C_A) for concrete. The objective of these limits is to lower the risk of corrosion caused by the initial chlorides (i.e., $C_i \leq C_A$). Standard documents that specify CA limits direct the users to follow the test methods developed by the American

Society of Testing and Materials (ASTM) or by the American Association of State Highway and Transportation Officials (AASHTO). However, neither the ASTM nor the AASHTO test standards provide information regarding the number of samples required to test C_i. Different sample sizes can result in significantly different mean chloride test results (Ctest). The variability of C_{test}, if not considered, could lead to unrepresentative results and variability. That is, a result could indicate that the concrete has a chloride concentration greater than the allowable chloride when in fact it doesn't ($C_i<C_A<C_{test}$; i.e., a false-positive). False-negative could also occur with insufficient data since the C_i can influence the corrosion and long-term performance of reinforced concrete structures, it is essential that the measurement of C_i be representative of the actual value. A C_{test} value that is over the C_A limit can lead to significant testing costs, confusion, and litigation. Ensuring that the C_{test} value represents the true value of C_i is essential. This requires a better understanding of the variability of chloride test results.

The mean and variability of the chloride test results may be influenced by various factors including the heterogeneity of concrete caused by the presence of different sizes and proportions of aggregates. For instance, consider the two concrete cross sections "*A*" and "*B*" shown in Figure 1. Section "*A*" has smaller sizes and lower proportions of aggregate when compared to section "*B*."Assume that both cross sections belong to the same concrete system containing overall 65% aggregates and 35% cement paste by volume of concrete. Also, assume that the initial chloride concentration of the concrete is 0.2% by weight of cement paste proportion in the mixture and the amount of chlorides in the aggregates is zero. Now consider that the concrete samples from sections "*A*" and "*B*" contain cement paste and aggregate proportions as shown in Table 1. If samples from "*A*" and "*B*" are tested for chlorides, the total chloride values expressed as the percent by weight of cement paste would be 0.29% and 0.11%, respectively. These values differ significantly from the overall initial chloride content of 0.2%. This is a result of the different volume of the coarse aggregate in the test sample. This level of variability in test results may expose contractors and designers to a great deal of financial risk and therefore, there is a need to account for such variability.

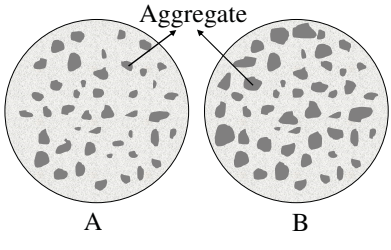

Figure 1: Illustrative concrete cross sections with different aggregate profiles

Table 1: Material proportions and chloride concentrations of different cases

	Cement paste (% total volume)	Aggregate (% total volume)	Chlorides (% wt. cement paste)
Original	35	65	0.2
Section A	50	50	0.29
Section B	20	80	0.11

This paper presents a Bayesian statistical approach to assess the influence of the different proportions of coarse aggregates on the chloride test results. Aggregates having a size greater than 4.75 mm (0.19 in) are considered as coarse aggregates in this study. Quantitative image

analysis is performed on the images of several concrete discs to obtain distributions of the different size ranges of the coarse aggregates. Chloride concentration of samples from each disc is then estimated using acid-soluble chloride testing. A hypothesis is developed to investigate whether the proportion of total coarse aggregate in a disk influences the measured acid-soluble chloride concentrations. Based on the significance of the hypothesis testing, a hierarchical Bayesian linear model is developed by relating the acid-soluble chloride concentration as the response variable to different coarse aggregate size ranges. Furthermore, the performance of the model is tested and compared with a single variable model using the total coarse aggregate proportion.

2 EXPERIMENTAL PROGRAM

2.1 Materials

An ASTM Type I/II cement was used in this study. No supplementary cementitious materials were used. River sand complying with the fine aggregate grading requirements of ASTM C33was used for all mixtures [2]. Coarse aggregate met ASTM C33 grade 67 requirements. Figure 2 shows the estimated size distribution of the coarse aggregates along with lower and the upper limits of different aggregate sizes. ACS grade NaCl was used for adding the initial chlorides to the concrete, and the amount of chlorides was determined through molar mass conversions.

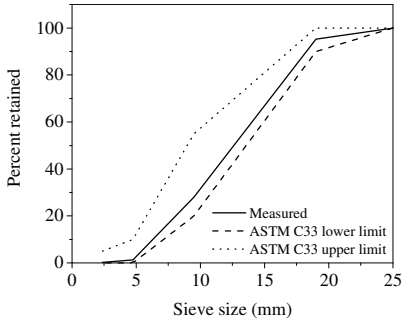

Figure 2: Sieve analysis for coarse aggregate

2.2 Specimen preparation and testing

A concrete mixture with a cement content of 449 kg/m^3 (756 lb/yd^3), a water content of 202 kg/m^3 (340 lb/yd^3), a coarse aggregate content of 929 kg/m^3(1566 lb/yd^3) and, a fine aggregate content of 697 kg/m^3(1175 lb/yd^3)was used in this study. Triplicate 150 mm (6 in) diameter by 150 mm (6 in)tall specimens were prepared with 0 and 0.25% admixed chlorides by weight of cement. Specimens containing admixed chlorides (0.25%) were cast by thoroughly dissolving the salt in water before mixing. Specimens with no admixed chlorides exhibited little variation in test results and were used to estimate the mean background chloride content (C_{bg}) of the concrete. All specimens were subjected to moist curing for 28 days before testing.

Twenty 20 mm (0.79 in) thick discs were procured from three specimens containing admixed chlorides. All cut surfaces were air dried after cutting. Before grinding, a high-quality picture of the cut surface was obtained for quantitative image analysis. Figure 3 shows a sample image taken from a disk. Before processing the images, they were converted to 8-bit greyscale images. Then using Photoshop, the aggregates visible with the naked eye were colored black. This process was used to reduce the error in the image analysis of

aggregates. After this, the colored aggregates for each sample were isolated by bi-level thresholding using the brightness histogram in ImageJ software [3]. Finally, the areas and the proportions of aggregates with area greater than 17.72 mm^2 (this is the area for a circle of 4.75 mm diameter) were estimated.

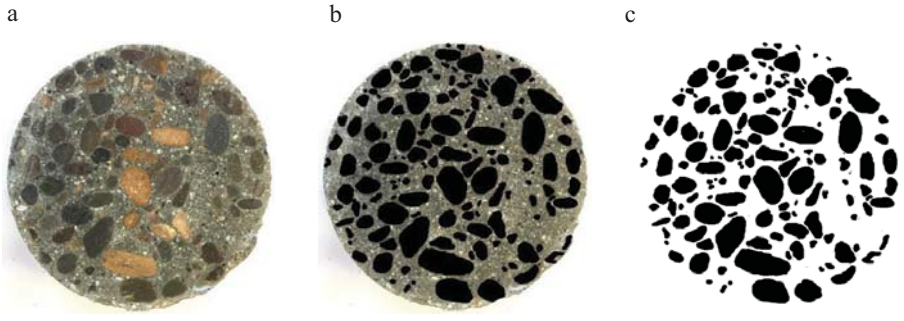

Figure 3: Image analysis for determining shape and distribution of coarse aggregates (a) original image; (b) enhanced image; (c) bi-level thresholding

After image processing, an 1.5 mm (0.06 in) thick concrete section was ground from each surface using a profile grinder to obtain ~50 gm (1.76 oz) of powder material. The chloride contents of these samples were determined by performing the acid-soluble test as specified by ASTM C1152 [4].

[1] TEST RESULTS

Figure 4 shows the distribution of coarse aggregates and the measured chloride content for all sections.

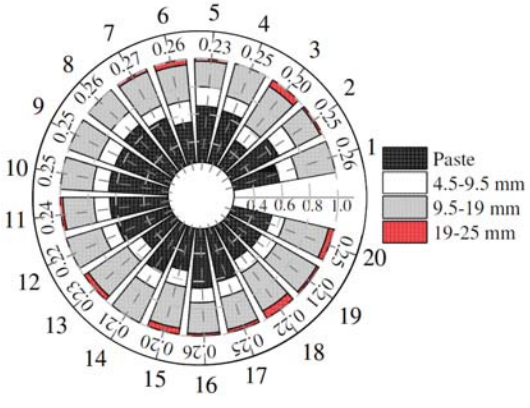

Figure 4: Distribution of coarse aggregates and measured chloride contents

The numbers outside the radial plot represent the sample numbers, and those just inside the outer ring represent the chloride concentration of the respective sample expressed as percent by weight of cement. The coarse aggregates were divided into three groups: 4.75 to 9.5 mm (0.19 to 0.37 in), 9.5 to19 mm (0.37 to 0.75 in), and 19 to 25 mm (0.75 to 0.98 in).

The proportion of coarse aggregates relative to the section area ranged from 0.09 to 0.16 for the coarse aggregate falling in 4.75 to 9.5 mm group, 0.19 to 0.34 for the coarse aggregate falling in 9.5 to 19 mm group, and 0 to 0.06 for the coarse aggregate falling in 19 to 25 mm group.

[2] BAYESIAN ANALYSIS

The application of Bayesian models in the engineering fields have become increasingly popular among researchers in the recent years. Frequentists' methods of data analysis are often accurate if the data meet a certain number of assumptions (e.g., normality and homogeneity of variance). In reality the collected data often do not meet such assumptions and the analysis is performed based on making approximations. Bayesian models, on the other hand are free from such restrictions and they provide a robust and coherent framework for data analysis. This section provides an overview of Bayesian model development to assess the influence of coarse aggregate size and proportion on chloride measurements.

Let y_i represents the measured chloride content of the i^{th} sample. Also assume that y_i follows a normal distribution such that $y_i \sim \mathcal{N}(\theta,\tau)$, where θ is the mean and τ is the precision that is the inverse of the variance. Using the Bayes theorem, the conditional probability distribution for θ and τ given the data is given by:

$$p(\theta,\tau|\mathbf{Y}) = \frac{p(\theta,\tau)\,p(\mathbf{Y}|\theta,\tau)}{p(\mathbf{Y})} \propto p(\theta,\tau)\,p(\mathbf{Y}|\theta,\tau) \tag{1}$$

where $\mathbf{Y}$ is a vector of measured chloride contents, $p(\theta,\tau|\mathbf{Y})$ is known as the posterior distribution, $p(\theta,\tau)$ is the prior distribution, and $p(\mathbf{Y}|\theta,\tau)$ is the likelihood. By choosing a Gaussian prior for θ such that $\theta \sim \mathcal{N}(\mu_0, n_0\tau)$, and an inverse Gamma function as a prior on τ such that $\tau \sim Gamma\ (\alpha,\beta)$ where $\tau=1/\sigma^2$, the posterior for θ and τ can be obtained by using Eqs. 2 and 3.

$$\mu|\tau, y \sim N\left(\frac{n\tau}{n\tau+n_0\tau}\bar{y}+\frac{n_0\tau}{n\tau+n_0\tau}\mu_0, n\tau+n_0\tau\right) \tag{2}$$

$$\tau|\mathbf{Y} \sim Gamma\left(\alpha+\frac{n}{2}, \beta+\frac{1}{2}\sum\left(y_i-\bar{y}\right)^2+\frac{nn_0}{2(n+n_0)}\left(\bar{y}-\mu_0\right)^2\right) \tag{3}$$

When new data are available, the posterior distribution can be updated using Eq.1. However, it is often the case that the proportionality constant in Eq.1 makes the evaluation of the posterior distribution difficult. One solution to this challenge is to apply the Markov Chain Monte Carlo (MCMC) simulation technique using the Metropolis-Hastings algorithm [5]. In this study, a parametrized model consisting of the likelihood, priors, and data were developed in Jags and used for MCMC simulation [6-7]. The model was defined using diffuse priors for θ (i.e., $\theta \sim \mathcal{N}(\bar{y}, 10\tau)$), and τ (i.e., $\tau \sim Gamma$ (0.01, 0.01)). MCMC was performed with four chains and 25,000 iterations for each chain [8]. Figure 5 shows the sampled MCMC chains and their corresponding diagnostic plots.

Results show that the model performance is acceptable. No signs of orphaned chains are observed in Figures 5-a, and 5-e. The autocorrelation plots indicate that the model has no autocorrelation with a large effect size. The Gelman-Rubin convergence statistics (shrinkage factor) for the model parameters are very close to 1.0, and the superimposed density plots for different chains confirm that the model has converged. The value of the Monte Carlo standard error (MCSE) that represents the standard deviation of the sample mean in the chain is very low, indicating a stable parameter estimation.

Figure 6 provides information regarding the posterior distributions of the model parameters. Figure 6-a shows the histogram of the actual data with the superimposed posterior normal distribution for the chloride content concentration. The posterior distribution on θ has a 95% highest density interval (HDI) extending from 0.229 to 0.249 percent by weight of cement. The 95% HDI for the mean excludes the actual value of the initial chlorides (0.265 % wt. cement). The posterior on the effect size, that is amount of change in chloride concentration relative to the standard deviation, has a large effect size mode with a 95% HDI that excludes zero [9]. Therefore, it can be concluded that the measured chloride concentration in the samples is significantly lower than the true C_i. The posterior distribution of the standard deviation has a mode of 0.022 with a 95% HDI that extends from 0.016 to 0.032 suggesting low variability in standard deviation (σ).

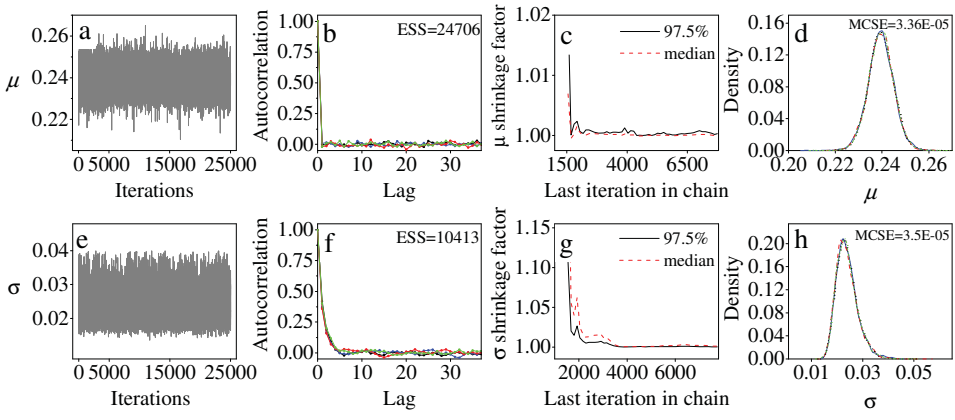

Figure 5: Convergence diagnostics for model parameters

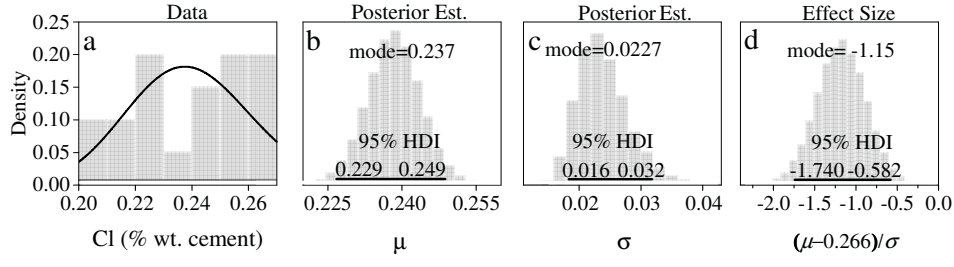

Figure 6: Posterior distribution of chloride content

By hypothesizing that the proportion of coarse aggregates can be one of the factors contributing to the difference between the initial chloride level and the measured chloride concentration, two hierarchical Bayesian linear models were developed. The first model aims at modeling the relationship between measured chloride concentration, denoted as ***Y,*** and the proportion of three groups of aggregate with sizes ranging from 4.75 to 9.5 mm (0.19 to 0.37 in), 9.5 to19 mm (0.37 to 0.75 in), and 19 to 25 mm (0.75 to 0.98 in). These three groups are denoted by X_1, X_2, and X_3 respectively, and the normal linear model that relates Y to X_1, X_2, and X_3 is given by:

$$Y = X\theta + \sigma\varepsilon \quad (4)$$

where X is a $n \times p$ matrix of regressors, θ is a $p \times 1$ vector of the coefficient of the regressors, σ is the model standard deviation, and $\boldsymbol{\varepsilon}$ is an $n \times 1$vector of Gaussian white noise with the expected value of zero and variance of unity. If $\boldsymbol{\Theta} = (\theta, \sigma)$, then the posterior distribution of the unknown model parameters Θ can be written as:

$$p(\boldsymbol{\Theta}|\mathbf{Y}) \propto L(\boldsymbol{\Theta}|\mathbf{Y})\, p(\boldsymbol{\Theta}) \tag{5}$$

where $L(\boldsymbol{\Theta}|\boldsymbol{Y})$ is the likelihood function of $\boldsymbol{\Theta}$ for the given data and $p(\boldsymbol{\Theta})$is the prior.

To create a predictive model (hereafter referred to as aggregate range model), the experimental data were divided randomly into two groups. Sixteen data points were used as an in-sample training dataset, and the remaining four data points were used as an out-of-sample dataset to assess the accuracy of the developed model, as follows:

$$y_i = \theta_0.1 + \theta_1.X_{9.5mm} + \theta_2.X_{19mm} + \theta_3.X_{25mm} + \sigma\varepsilon_i \qquad i = 1, 2, \cdots, 16 \tag{6}$$

The second model (hereafter referred to as total coarse aggregate model) was considered with the total proportion of coarse aggregate as the only independent variable given by:

$$y_i = \theta_0.1 + \theta_1 X_{total} + \sigma\varepsilon_i \quad i = 1, 2, \cdots, 16 \tag{7}$$

The directed acyclic graph (DAG) for the model along with the selected priors for the modelare shown in Figure 7. The only difference between two models is that in the total coarse aggregate model only one set of priors are defined for θ_0 and θ_1, whereas in the aggregate range model a set of priors must be defined for each independent variable (i.e., X_1, X_2, and X_3).

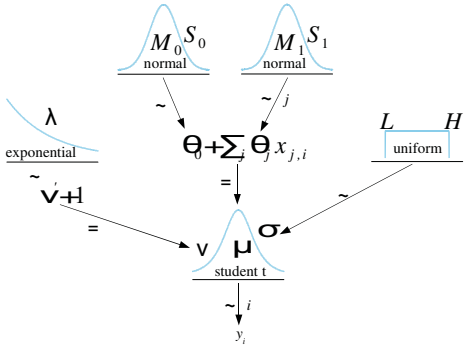

Figure 7: DAG model for multiple linear regression

To accommodate outliers, a heavy-tailed t distribution is used such that $y \sim t$ ($\sum_j \beta_j x_{j,i}$, σ, υ). A diffuse uniform prior is used for the scale parameter such that σ ~ *Uniform* (1E-5, 1E+1). This choice of a vague prior covers a broad range of values and because it is large relative to the data, it has minimal influence on the posterior. The normality factor υ is set to have an exponential prior such that $\upsilon \sim$ *exponential* (1/30). It should be noted that when υ exceed 30, the shape of the t-distribution becomes approximately normal. Two broad normal priors with the mean of zero and variance of four were used for the intercept and slopes of the linear model.

Table 2 presents the summary of MCMC results for the aggregate range model. The negative mean values of the parameters in the mean column suggest that increasing the proportion of the coarse aggregates in the concrete mixture while holding other variables constant would result in the reduction of the chloride concentration. However, the 95% HDI

for the mean includes positive values which make it impossible to draw a definite conclusion. It is expected that with a larger sample size the range of the HDI is reduced and becomes closer to the estimate of the mean parameter.

Comparing the parameters suggests that the coarse aggregates falling within the range of 19 to 25 mm (0.75 to 0.98 in), followed by aggregates within the range of 9.5 to19 mm (0.37 to 0.75 in) are the most influential parameter in this model. This is because aggregates are inert here and with the increase in the size of aggregates, less space is available for the paste, resulting in the reduction of chlorides in the section. The coefficient of determination for the aggregate range model shows that 0.5% of the variation in the chloride measurements can be explained by the proportion of the coarse aggregates in the mixture. Other sources of variability such as chloride binding, sampling technique, and test environments can contribute to the remaining variation.

Table 2: Posterior Statistics of $\boldsymbol{\Theta}$ for aggregate range model (R^2=0.305)

					HDI	HDI	Correlation coefficient					
	Mean	SD	Mode	ESS	low	high	θ_0	θ_1	θ_2	θ_3	σ	ν
θ_0	0.308	0.07	0.31	12935	0.16	0.45	1					
θ_1	-0.091	0.46	-0.12	3741	-1.02	0.818	-0.85	1				
θ_2	-0.202	0.17	-0.16	1728	-0.54	0.142	-0.68	0.21	1			
θ_3	-0.299	0.45	-0.32	2331	-1.17	0.621	0.52	-0.35	-0.60	1		
σ	0.023	0.00	0.02	12661	0.013	0.034	0.01	-0.01	-0.01	0.05	1	
ν	34.33	30.45	9.81	11498	0.876	95.20	0.05	-0.03	-0.04	-0.01	0.19	1

Table 3 shows the summary of the results for the total coarse aggregate model. Results show that the 95% HDI for the total aggregate proportion does not include zero. Therefore, it can be concluded that total aggregate proportion is an influential factor in determining the chloride content of concrete specimen.

Table 3: Posterior Statistics of $\boldsymbol{\Theta}$ for total coarse aggregate model (R^2=0.31)

	Mean	SD	Mode	ESS	HDIlow	HDIhigh
θ_0	0.326	0.04	0.32	15000	0.25	0.40
θ_1	-0.216	0.10	-0.20	15000	-0.41	-0.03
σ	0.021	0.01	0.02	13386	0.01	0.03
ν	35.89	31.05	11.22	11925	1.35	96.99

To evaluate the prediction performance of the models, four data points that were not included in the initial model were used for making an out-of-sample prediction. The performance of the created models is assessed using mean square error (MSE), and their prediction performance is measuredby using the mean absolute percent error (MAPE) which is the average relative error of the predicted values from the observed values. Furthermore, the performance of competing models can be compared by using Akaike information criterion (AIC_c) [10] and the Bayesian information criterion (BIC) [11]. These two criteria determine how well the model fit the data. Thus, the model with the lowest values of AIC_c and BIC is preferred. AIC_c and BIC can be determined using Eq.7 and Eq.8, respectively.

$$AIC_C = n\ln\left(\frac{RSS}{n}\right) + 2k \times \frac{\left(2k \times (k+1)\right)}{n-k-1} \tag{8}$$

where n is the number of data points, RSS is the residual sum of squares, and k is the number of parameters in the model, including the intercept and error term.

$$BIC = n\ln\left(\frac{RSS}{n}\right) + k\ln(n) \tag{9}$$

The accuracy of the models regarding MAPE, AICc, and BIC values are shown in Table 4. Per Table 4, the total coarse aggregate model, with respect to all the metrics, performs better than the aggregate range model in predicting the chloride content of a concrete section.

Table 4: MSE, MAPE, AICc, and BIC values of the models

Model	MSE	MAPE (%)	AIC_c	BIC
Aggregate range model	3.91E-04	5.16	-53.75	-26.81
Total coarse aggregate model	3.95E-04	3.97	-55.26	-28.33

Figure 8 shows the predicted values of chloride content versus the measured values for the aggregate range model and total coarse aggregate model. The 1:1 line is used as a reference to check how close the predicted chloride contents are to the measured chlorides.

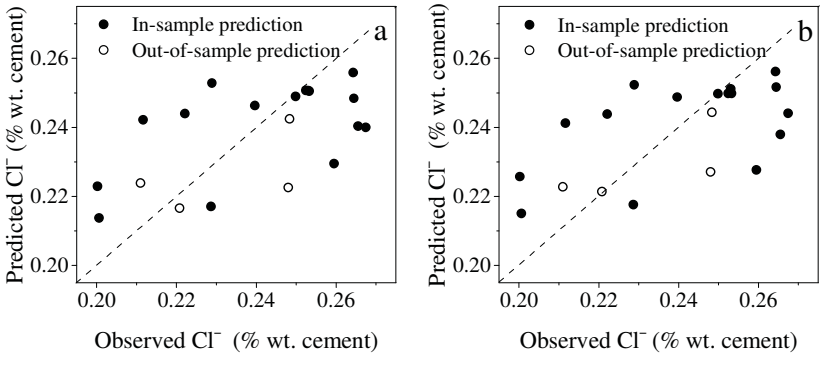

Figure 8: Predicted versus observed value of chloride content based on (a) aggregate range model, and (b) total coarse aggregate model

3 CONCLUSION

An understanding of the expected variation in chloride test measurements is essential to reliably assess the corrosion risk of initial chlorides in reinforced concrete structures. Several factors influence the variability of chloride test measurements. The objective of this study was to test the hypothesis if the proportion of coarse aggregates affects chloride measurements using Bayesian methodology. Results showed that the proportion of the overall coarse aggregate is an influential factor and an increase in the total coarse aggregate proportion leads to the reduction of chloride test result. Based on this finding, two Bayesian regression models were developed to fit the measured chloride test results against the proportions of coarse aggregates. One model considered the total proportion of coarse aggregates as an explanatory variable while the other considered the proportions of different coarse aggregate size ranges as the explanatory variables. The Akaike information criteria and Bayesian information criteria showed that using the total proportion of aggregates as opposed to the proportion of individual sizes of aggregates results in a more efficient predictive model. The proposed model can assist engineers and researchers to verify chloride

measurement results and reduce the error caused by non-uniform distribution of coarse aggregates in the concrete samples.

4 REFERENCES

[1] NACE International. Highways and Bridges. 2016 [cited 2016 Feb 2]; Available from: https://www.nace.org/Corrosion-Central/Industries/Highways-and-Bridges/

[2] ASTM C33/C33M – 16e1, "Standard Specification for Coarse Aggregates,"ASTM International (Philadelphia, PA, (2016).

[3] Rasband, W., (1997)"ImageJ software," National Institutes of Health,(Bethesda, MD, USA, (2012).

[4] ASTM C1152/C1152M-04(2012) e1, "Standard Test Method for Acid-Soluble Chloride in Mortar and Concrete," ASTM International (Philadelphia, PA, (2012).

[5] Chib, S., and Greenberg, E., "Understanding the metropolis-hastings algorithm. The americanstatistician," 49(4) (1995) 327-335.

[6] Plummer, M., "JAGS: A program for analysis of Bayesian graphical models using Gibbs sampling," *Proceedings of the 3rd international workshop on distributed statistical computing,* 124 (2003).

[7] Kruschke, J., "Doing Bayesian data analysis: A tutorial with R," JAGS and Stan Academic Press (2014).

[8] Hastings, W.K., "Monte Carlo sampling methods using Markov chains and their applications," *Biometrika*, 57(1) (1970) 97-109.

[9] Cohen, J.,"Statistical power analysis for the behavioural sciences," Lawrence Earlbaum Associates (Hillsdale, NJ, (1988) 20-26.

[10] Akaike, H.,"A new look at the statistical model identification," IEEE transactions on automatic control, 19(6) (1974)716-723.

[11] Schwarz, G., "Estimating the dimension of a model," The annals of statistics, 6(2) (1978) 461-464.

Relationship between Concrete Resistivity and the Indication of Chloride Penetration by ASTM C1202 in Concrete made with OPC, and Admixed with Slag and/or Limestone Powder

Yury A. Villagrán Zaccardi[1,2], Natalia M. Alderete[1,2] and Ángel A. Di Maio[1]

[1]LEMIT and CONICET, 52 entre 121 y 122 s/n, 1900 La Plata, Argentina

[2]Labo Magnel, Ghent University, Tech Lane Ghent Science Park, Campus A, Technologiepark Zwijnaarde 904, B-9052 Gent, Belgium

ABSTRACT

One of the most widespread methods to assess concrete ability to resist chloride penetration is the one described in ASTM C1202. This method consists in the determination of the amount of electrical charge that passes through a concrete sample in a 6 h period, whereas an electrical potential is applied. This highly empirical method has received some criticism due to its lack of representativeness of the actual process of chloride ingress into concrete. Moreover, the result of the test is a qualitative value that cannot be used for service life design based on performance. In this sense, even more practical methods can be considered with the same aim. This paper shows experimental results from the application of the method in ASTM C1202 and the measurement of resistivity in both conventional concrete and concrete admixed with slag and/or limestone powder, as these constituents significantly affect conductivity. A correlation between results from both methods is made, and some considerations are presented regarding the practicality of applying one method or the other in relation with the information they provide. The results reveal that the correlation between resistivity and results from ASTM C1202 is independent from the composition of the concrete.

Keywords: Chloride migration, resistivity, slag, limestone powder.

1 INTRODUCTION

Corrosion due to chlorides is a major issue regarding the durability of reinforced concrete structures in the marine environment. The ingress of chlorides into concrete leads to reinforcement pitting. In the marine environment, the presence of chloride in the surrounding atmosphere is inevitable, and chlorides eventually ingress into concrete. When certain chloride content is reached at the level of reinforcement, namely chloride threshold content, a localized rupture of the passive layer on reinforcement occurs. Then, the main factors that determine the time required for reinforcement depassivation in concrete in the marine environment are the porosity, the pore size distribution and the thickness of cover concrete.

The chloride ingress profile (chloride content as a function of depth) in concrete in the marine environment depends on time [1, 2], environmental conditions, material properties, and the design and construction practices [3]. Transport mechanisms for the chloride ingress

into concrete are complex and combined with other interfering processes; its theoretical description is then not easy to complete.

From a regulatory point of view, the quantification of the rate of chloride ingress into concrete is highly significant, not only as a way of establishing prescriptive criteria but also, and perhaps more importantly, to provide design tools for durability. An appropriate evaluation method shall be reliable, repeatable, representative, and practical and economical at the same time.

Chloride diffusion tests require long-term evaluations, and they are then unsuitable for control procedures during construction. Several accelerated methods have been developed with the aim of assessing rapidly the rate of chloride transport in concrete. These experiments are based on an electric field imposed across the material that speeds up the ingress of chlorides. This electric field affects ions so that they migrate towards the oppositely charged electrode. The value of electrical potential gradient should be limited as high gradients in the electrical potential involve the development of heat that increases the temperature of the sample. However, even when transport indexes from diffusion and migration tests differ from each other, from the theoretical and the numerical points of view, a comparison is still possible for practical purposes [4].

One of the most widespread chloride migration tests is the so-called Rapid Chloride Permeability Test, described by ASTM C1202 [5]. Early since its implementation, this method has received some criticisms due to its lack of representativeness of the actual process of chloride penetration into concrete [6-9]. However, this criticism has not impeded that it is still one of the most used methods to assess the resistance of concrete against chloride penetration, probably due to the absence of a more simple procedure for the same purpose.

In this sense, resistivity can also be proposed as a durability index in relation with chloride ingress. A correlation between concrete resistivity and chloride ingress has been indicated by both theoretical and experimental studies [10-12]. This relationship between the chloride diffusion coefficient and concrete resistivity has been suggested as inversely proportional, in relation to the fact that, for a particular pore structure, larger pore connectivity will lead to a comparatively lower resistivity and faster chloride penetration rate. Despite this, the method according to ASTM C1202 is still more widespread than resistivity regarding the evaluation chloride ingress rate. This is based on the assumption that it provides additional information than resistivity, as it includes a chloride solution in the procedure. However, it is unclear what additional information is provided, whereas any additional information is in any case only qualitatively included. Resistivity, on the other hand, shows the advantage of being much simpler and cheaper than any migration method.

In this paper, results of chloride migration tests according to the ASTM C1202 method applied to concrete made with ordinary Portland cement, slag and limestone powder are presented and compared with the resistivity of saturated concrete. The proposed objective is to establish a basis for judging the suitability of ASTM C1202 method depending on its complexity in relation to the qualitative information it provides. The comparison includes not only conventional concrete but also concrete containing slag (as this constituent significantly affects the conductivity of concrete).

2 ON THE ASTM C1202 METHOD

The basis for the ASTM C1202 [5] method was developed by the Federal Highway Administration (FHWA) of the United States in 1981. This method had a great diffusion initially, but it can currently be put into question in terms of its representativeness of the rate of chloride ingress and its qualitative nature. This is the reason for which it is restricted to the application of prescriptive design for durability.

A major issue regarding the representativeness of the method arises from the high electrical gradient that it is applied (60 V). This value results in significant heat development (depending on the electrical resistance of the sample) and a consequential increase in the temperature of the specimen. Thus, high conductivity concretes will increase temperature to a great extent, and therefore, the chloride penetration rate will increase as well. On the other hand, the resulting current through the sample is a result of the sum of all ions moving in the pore solution, not only chloride. This is one of the main reasons for which there are significant differences in cases in which mineral admixtures are used (especially slag), as they show a lowering action of the ionic strength of the pore solution.

For practical applications, Berke and Hicks [13] proposed an empirical relationship between chloride permeability according to ASTM C1202, defined by the total electrical charge being transported (Q_e), and the effective chloride diffusion coefficient (D_s) (Eq. 1).

$$D_s = 0.0103 \cdot 10^{-8} \cdot (Q_e)^{0.84} \ [cm^2/s] \quad (1)$$

However, Q_e must be considered as a merely qualitative factor. It is also very doubtful whether or not the chloride binding capacity of concrete can be fully developed in the short period during which the migration method is applied [14]. The recommended interpretation of results is made according to criteria in Table 1. Broad ranges of variation for the results are specified in the standard [5], 12,3% (1σ) and 42% (2σ) of variation between results from the same operator, increasing to 18% (1σ) and 51% (2σ) for inter laboratory results. These quite high variation ranges indicate a limited precision for a quantitative description of concrete properties.

Table 1: Interpretation criteria for results from ASTM C1202 method [5]

Charge passing (C)	Penetrability of chlorides
>4000	High
2000 – 4000	Moderate
1000 – 2000	Low
100 – 1000	Very Low
<100	Despicable

Some studies have previously shown a direct relationship between the initial current and the charge passed during the 6 h that the test lasts, Qe [15-18]. Therefore, the results of this same method indicate that even with the experimental setup specified in the standard it might be unnecessary to conduct the test for 6 h considering that the initial measurement of the current might be sufficient, especially when Qe <1000 C. In addition, there are no reasons to believe that a different setup would lead to different results between the assessment of the initial current in the migration method and the measurement of the conventional bulk resistivity.

3 MATERIALS AND METHODS

The studied concretes included the use of ordinary Portland cement (OPC), blended Portland cement (BPC, containing slag and limestone), blast furnace slag and limestone powder. Slag is the mineral addition that affects concrete resistivity the most and it is frequently used in ternary blends together with limestone powder. The aggregates used were two siliceous river sands, fine (FSS) and coarse (CSS), and granitic crushed stone with

19 mm of nominal maximum size (GCS). The proportions of studied concretes are presented in Table 2. The naming corresponds to the type of binder (N: pure OPC; E: OPC+slag; F: OPC+limestone; EF: OPC+slag+limestone; C: BPC), followed by the water to cementitious materials ratio (w/cm) multiplied by 100. For example, N35 refers to concrete made with OPC and w/cm = 0.35.

Table 2: Proportions of concrete mixes.

Series	N35	N40	N41	N45	N50	N60	E40	F40	EF40	C40	C60
w/cm	0.35	0.40	0.40	0.45	0.50	0.60	0.40	0.40	0.40	0.40	0.60
Materials (kg/m^3)											
Water	133	140	140	144	150	164	140	140	140	140	168
OPC	380	350	350	320	300	274	227	262	227	-	-
BPC	-	-	-	-	-	-	-	-	-	350	280
Slag	-	-	-	-	-	-	123	-	88	-	-
Limestone powder	-	-	-	-	-	-	-	88	35	-	-
FSS	189	190	190	193	193	242	190	190	190	190	187
CSS	749	754	754	766	767	726	755	755	755	754	742
GCS 6-20	980	980	980	980	980	959	980	980	980	980	980
Water reducer (l)	6.2	5.9	5.25	6.0	3.6	2.74	4.9	4.2	4.1	5.25	2.80
Entrained air (%)	3.0	3.1	3.0	3.0	3.1	3.0	3.2	3.5	3.4	3.0	3.0
Properties											
Unit weight (kg/m^3)	2404	2417	2404	2392	2404	2354	2392	2354	2385	2392	2354
Slump (cm)	8.0	10.0	8.0	6.0	6.0	10.0	10.0	9.0	7.0	10.0	10.0
Bleeding (%)	<0.01	<0.01	n/d	3.03	0.40	n/d	<0.01	<0.01	<0.01	n/d	n/d
Porosity (%)	8.03	8.68	8.56	8.90	8.85	10.19	9.83	9.99	9.79	10.53	13.17
Compressive strength 28d (MPa)	60.2	53.8	51.2	48.3	44.3	36.7	52.6	42.2	51.1	40.3	25.3

With the manufactured concretes, 10 cm × 20 cm cylindrical specimens were cast and cured in a humid chamber for 28 days. Methods based on resistivity or other electrical properties allow describing porous properties of concrete largely. A method for measuring resistivity is straightforward and economical, with little influence of the operator excepting for potential variations in the pressure applied to put the electrodes in contact with the sample [19]. Conventional resistivity measurements were performed on concrete samples in the saturated surface dry condition. Here, a potential of 13 ± 1V AC 50 Hz is applied by electrodes consisting in perforated stainless discs on each side of the cylindrical specimen of 10cm x 5cm in diameter and thickness. These samples were obtained by cutting the section between 3 and 8cm from the base of the 10 cm × 20 cm specimens. The electrical contact between electrodes and concrete surface was ensured by interleaving wet natural fiber clothes. The ensemble was joined by pressure exerted by a sergeant screw. The applied

pressure on the electrodes on the surface of the samples was approximately 0.2 kg/cm^2. Determinations on six samples for each series were performed.

On these same samples, also the resistance to chloride penetration according to ASTM C1202 method was tested. This method determines the amount of electric charge passing through the sample, Qe, in a period of 6 hours. The test is performed using a two-compartment cell separated by the concrete sample. An electrical potential is applied between the anodic and cathodic compartments, causing a chloride flow from the cathodic compartment containing chloride to the anodic compartment, which is filled with a chloride-free alkaline solution. The potential gradient is 60 V, and the current passing through the saturated cylindrical sample is measured at regular time intervals (every 30 min in this work).

4 RESULTS AND DISCUSSION

Resistivity values are presented in Figure 1. The series Nxx includes concrete mixes N35, N40, N41, N45, N50, and N60. The electrical resistivity of saturated concrete is directly related to the accessible pore volume and connectivity, since the electrical conductivity in concrete is due to the relative volume of pore solution, the ions it contains, and the structure of the pore system. Then, this inverse variation of the resistivity of saturated concrete with the w/cm ratio is to be expected.

A very significant increase of resistivity values with the use of slag can be observed. Differently, the use of limestone powder does not significantly alter the value of resistivity. The concrete ability for conducting electric current increases significantly with increasing w/cm ratio, but this relationship is very dependent on the type of binder used in the mixture, as the action of mineral additions involves a significant alteration of the pore solution chemistry and the connectivity of the pore structure.

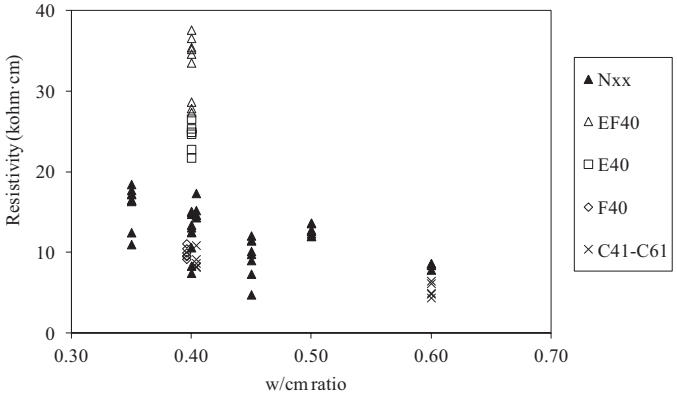

Figure 1: Resistivity values for concrete in saturated surface dry condition.

In Figure 2, results of resistance to chloride penetration are presented. These values show, as expected, an increasing trend with w/c. Still, the influence of slag on Qe is less evident than on resistivity.

Figure 3 presents the relationship between resistivity and Qe determined according to ASTM C1202. A particular common aspect of these two methods is that neither of them can consider the influence of chloride binding capacity of concrete, which is widely influenced by the use of supplementary cementitious materials. Indeed, these are some of the limitations for their application for durability assessment in the marine environment. Regarding resistivity,

chloride binding capacity is not reflected as the electrical current transported through the pore solution is the result of the sum of all dissolved ionic species. For the case of ASTM C1202 method, even when it exposes concrete to a 30 g/l NaCl solution and there is chloride ingress into the concrete sample, the test is so fast that it does not allow sufficient time for the retention capacity to develop fully. In this sense, migration tests involving lower electrical potential and lasting around one week have shown results more representative of reality [20]. Moreover, as in the case of resistivity, there are other ions that also carry charge and relativize the net effect of chloride ions on the result of the test.

In Figure 3, a clear relationship between Qe and concrete resistivity arises. This means that ASTM C1202 method is a clear reflection of the concrete electrical conductivity. Thus, this evaluation method does not offer major advantages than the assessment of conductivity in saturated surface dry condition (applying alternating current). This lack of added value implies that the ASTM C 1202 method, which has to be performed for 6 hours, is too laborious and expensive for the information it provides. Then, it is equivalent to measuring resistivity, which requires less than 5 minutes to be performed. In this sense, for all the studied concretes, the qualification based of Qe according to ASTM C1202 can be transferred to the respective resistivity values. The relationship found here (Figure 3) is similar to the one presented in [18], but different from the relationships reported in [21-23] where the surface resistivity was used for the comparison. Being that the case, the pressure exerted on the electrodes when assessing resistivity seems to be of major importance, where manual pressure will always result in higher resistivity values.

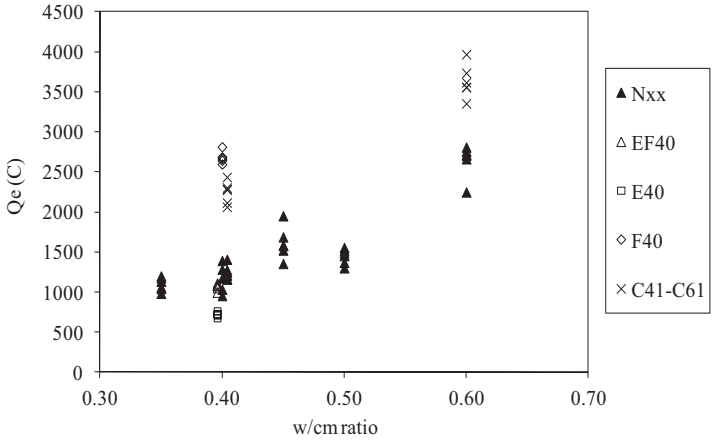

Figure 2: Results from ASTM C1202 test

In Figure 4, the relationship between standard bulk resistivity and the initial resistivity of concrete in the ASTM C1202 test configuration is presented. This comparison must include a differentiation between the variables for each of the two methods: the electrical potential and current type (60 V DC vs. 13 V CA), the type of contacting between electrodes and the sample (chloride solution and alkaline solution vs. pressed wet clothes), and test period (6 h vs. 5 min). Even with all these differences, the trend shows fairly equal values. From the comparison between Figures 3 and 4, it can be seen that the more porous concretes increase Qe more than initial conductivity.

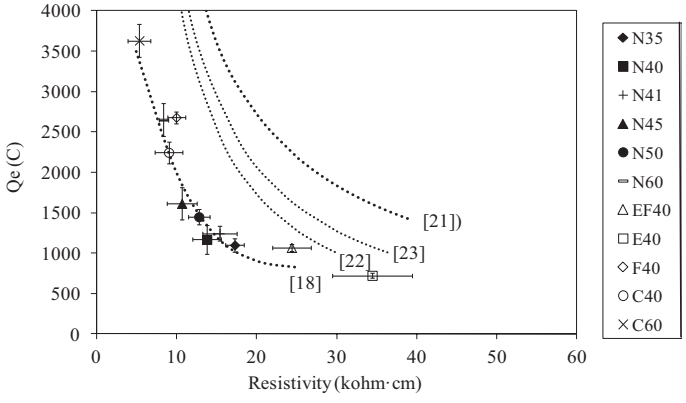

Figure 3: Relationship between resistivity and Qe according to ASTM C1202.

This is very likely connected to the heat produced due to the high electrical potential of 60 V that is applied. A significant temperature increase is caused, which in turns fastens the transport mechanism. This issue brings some doubts concerning the comparison by means of ASTM C1202 method among concretes with significantly different w/cm ratio, as they are ultimately tested at different temperatures.

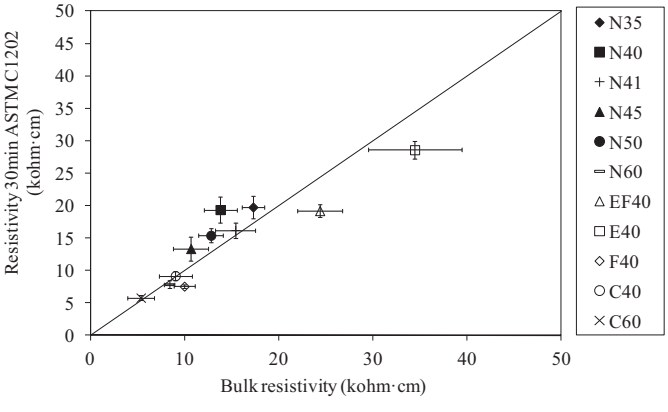

Figure 4: Relationship between resistivity after 30 min with ASTM C1202 configuration and conventional resistivity.

Naturally, the effect of active mineral admixtures on concrete conductivity is also reflected for the charge passing during the ASTM C1202 test. This is also a clear indication of this technique being an electrical conductivity method rather than providing an index of the chloride penetration rate. Additionally, it would be difficult to correct the temperature influence as it varies from one concrete to the other according to the porosity of each one.

Finally, a consideration to be made is that both resistivity and ASTM C1202 methods do not reflect on their results the chloride binding capacity. They are therefore useful in the description of porous properties of concrete but incomplete for the description of the resistance of concrete to chloride ingress. They can be applied as prescriptive indexes, but for

performance based design complementary evaluation methods should be considered. This is particularly of interest in concretes containing blast furnace slag, as they usually show a much higher chloride binding capacity.

5 CONCLUSIONS

The results and analyses presented indicate the inadvisability for the application of the ASTM C1202 method. The same description of concrete can be obtained with the aid of the much simpler assessment of resistivity in the saturated surface dry condition, independently of concrete containing only OPC, OPC+slag or OPC+slag+limestone powder. Moreover, this assessment of resistivity does not imply any change in the temperature of the sample, as it occurs in the ASTM C1202 method.

Therefore, it is derived that the ASTM C 1202 method is essentially an electrical conductivity method rather than a method of assessing the resistance to chloride penetration. In fact, any migration method would be related to concrete conductivity, but the ASTM C1202 method is beyond all the rest of techniques, as it only analyzes the value for the charge passed. This is a significant limitation for the applicability of the method. The obtained results show that the information offered by the ASTM C1202 method is the same as that provided by the resistivity of concrete to alternating current. It should be mentioned that different correlations with the bulk resistivity and the four-point resistivity might be expected. In addition, the assessment of resistivity is less laborious, faster and more economical than the evaluation of the concrete's ability to resist the penetration of chloride ion, as defined by ASTM C1202. Moreover, the measured flowing charge show a linear relationship with the electrical current at the beginning of the test, making reasonable to consider a proposal to reduce the time length of the method, with a corresponding adaptation of the qualitative parameters to whether current, conductivity, electrical resistance or resistivity for interpreting the results.

Concrete resistivity shows great potential as a durability index. Besides its application for a qualitative approach, its usefulness would be increased with the characterization of the conductivity of the pore liquid. Then, this would allow to study concrete as a composite material and to infer the relationship between phases. From a pragmatic point of view, the implementation of concrete resistivity as a durability index is equivalent in utility to the ASTM C1202 method, but with a much more practical procedure.

6 REFERENCES

[1] Poulsen, E., Mejlbro, L, "Diffusion of Chloride in Concrete: Theory and Application", Spon Press, 2005, London, United Kingdom.

[2] Villagrán Zaccardi, Y.A., Di Maio, A.A., Traversa, L.P., "Time evolution of chloride diffusivity in concrete" (in Spanish), Proceedings, 16ª Reunión Técnica de Tecnología del Hormigón, Mendoza, Argentina AATH, pp 187-194.

[3] Traversa, L.P., Villagrán, Y.A., Di Maio, A.A., Zicarelli, S.S., "Methods for evaluation and diagnosis of the remanent service life of reinforced concrete structures in the marine environment" (in Spanish), Proceedings, XIX Jornadas Argentinas de Ingeniería Estructural, Mar del Plata, Argentina, 112.

[4] Castellote, M., Andrade, C., Alonso C., "Measurement of the steady and non-steady-state chloride diffusion coefficients in a migration test by means of monitoring the conductivity in the anolyte chamber. Comparison with natural diffusion tests", Cement and Concrete Research, 31, 2001, pp 1411-1420.

[5] ASTM International, "ASTM C 1202 Standard Test Method for Electrical Indication of Concrete's Ability to Resist Chloride Ion Penetration", West Conshohocken, USA, 2010.

[6] C. Andrade, Calculation of chloride diffusion coefficients in concrete from ionic migration measurement, Cement and Concrete Research, 23 (5), 1993, pp. 724–742.

[7] R.F. Feldman, G.W. Chan, R.J. Brousseau, P.J. Tumidajski, Investigation of the rapid chloride permeability test, ACI Materials Journal, 91 (3), 1994, pp 246–255.
[8] P.E. Streicher, M.G. Alexander, "A critical evaluation of chloride diffusion test methods for concrete", Proceedings, Third CANMET/ACI International Conference on Durability of Concrete, Supplementary Papers, Nice, France, ACI, MI, USA, 1994, pp. 517–530
[9] C. Shi, J.A. Stegemann, R. Caldwell, Effect of supplementary cementing materials on the rapid chloride permeability test (AASHTO T 277 and ASTM C1202) results, ACI Materials Journal, 95(4), 1998, pp. 389–394
[10] Andrade, C., Sanjuan, M.A., Alonso, M.C. "Measurement of chloride diffusion coefficient from migration tests", Proceedings, NACE Corrosion'93, Houston, USA, 319.
[11] Polder R.B., "Chloride diffusion and resistivity testing of five concrete mixes for marine environment", Proceedings, RILEM International Workshop on Chloride Penetration into Concrete, St-Remy-les-Chevreuses, France, pp. 225-233.
[12] Gulikers J., "Theoretical considerations on the supposed linear relationship between concrete resistivity and corrosion rate of steel reinforcement", Materials and Corrosion, 56(6), 2005, pp 393–403
[13] Berke, N.S., Hicks, M.C., "Estimating the life cycle of reinforced concrete decks and marine piles using laboratory diffusion and corrosion data", in: "Corrosion Forms and Control for Infrastructure", ASTM STP 1137, ASTM, 1992, Philadelphia, USA.
[14] Castellote, M., Andrade, C., Alonso, C., "Chloride-binding isotherms in concrete submitted to non-steady-state migration experiments", Cement and Concrete Research, 29(11), 1999, pp 1799-1806.
[15] Berke, N.S., Hicks, M.C., "Predicting times for corrosion from field and laboratory chloride data", in: "Techniques to assess the corrosion activity of steel reinforced concrete structures", STP 1276, ASTM, 1996, West Conshohocken, USA.
[16] Riding, K.A., Poole, J.L., Schindler , A.K., Juenger, M.C.G., Folliard, K.J., "Simplified concrete resistivity and rapid chloride permeability test method", ACI Materials Journal, 105(4), 2008, pp 390-394.
[17] Villagrán Zaccardi, Y.A., Zega, C.J., Di Maio, A.A., Migrational methods for evaluating chloride ingress rate into concrete" (in Spanish), Proceedings, IV Congreso Internacional de la AATH, Mar del Plata, Argentina, 8p.
[18] Feldman, R., Prudencio, L.R. Jr., Chan, G., Rapid chloride permeability test on blended cement and other concretes: correlations between charge, initial current and conductivity, Construction and Building Materials, 13(3), 1999, pp 149–154.
[19] Newlands, M.D., Jones M.R., Kandasami, S., Harrison, T.A., Sensitivity of electrode contact solutions and contact pressure in assessing electrical resistivity of concrete, Materials and Structures, 41, 2008, pp. 621-632.
[20] Castellote, M., Andrade, C., Alonso, C., Chloride-binding isotherms in concrete submitted to non-steady-state migration experiments, Cement and Concrete Research, 29, 1999, pp. 1799–1806.
[21] Ramezanianpour, A.A., Pilvar, A., Mahdikhani, M., Moodi, F., Practical evaluation of relationship between concrete resistivity, water penetration, rapid chloride penetration and compressive strength, Construction and Building Materials, 25(5), 2011, pp 2472–2479.
[22] Ardani, A., Surface Resistivity Test Evaluation as an Indicator of the Chloride Permeability of Concrete, FHWA-HRT-13-024, Federal Highway Administration, McLean (VA), USA.
[23] Chini, A.R., Muszynski, L.R., Hicks, J., Determination of acceptance permeability characteristics for performance-related specifications for portland cement concrete, University of Florida, 2003, Gainesville (FL), USA.

Importance of the Curing Period Length on the Chloride Transport through Concrete containing SCMs

F.J. Luna Molina, Á. Fernández Pérez and M.C. Alonso Alonso

Instituto de Ciencias de la Construcción Eduardo Torroja, CSIC, Spain

ABSTRACT

The fabrication of concretes containing supplementary cementitious materials (SCMs) is gaining force with the aim of reducing the production of Ordinary Portland Cement (OPC), the largest component of energy consumption and CO2 emissions generated during cement manufacturing. Concretes containing SCMs have the concern of the slower rate of strength development as consequence of the higher hydration times needed for the SCMs respect to plain OPC. Less work has been done on the effect of this slowdown in hydration on the durability performance of blended concretes. The present research studies the influence of the curing length on the diffusion of chlorides through concrete by means of ponding tests after 28 and 90 days of curing. Two types of concrete have been considered to know also the influence of the presence of SCMs, (1) 100% OPC and (2) 64% OPC + 30% Blast furnace slags (BFS) + 6% Limestone filler (LF). Results show that the extension of curing period from 28 to 90 days scarcely produces variations in the accumulation of chlorides on the concrete surface and in the chloride transport regardless the concrete tested. However, and in spite of the intrinsic scatter of the tests, a slightly decreasing tendency of the apparent chloride diffusion coefficient and a slightly increasing tendency of the surface chloride concentration were found when OPC concrete was used.

Keywords: Concrete, chlorides, slags, curing, diffusion.

1 INTRODUCTION

The penetration of chloride ions into the concrete of structures placed in marine environments or exposed to de-icing salts usually spread in cold locations is a major cause of reinforcement corrosion and therefore a threat for the service life of these reinforced concrete (RC) structures [1]. In consequence, great efforts are continually done [2] in the search of the most suitable cements to be used in RC structures intended to be placed in chloride contaminated environments.

It can be easily found in literature that the employment of certain blended cements decreases the transport of chlorides through concrete if compared with which happens in plain OPC concrete [3]. Among the most employed supplementary cementitious materials (SCMs) in concrete, blast furnace slags (BFS) represent one of the most efficient SCM to delay the chloride transport through concrete [3, 4]. An example can be found in [4], where is compared the resistance to chloride transport of OPC concretes and concretes containing BFS with different compressive strength and apparent chloride diffusion coefficients three times lower for the blended concretes were revealed in all cases.

This protection against the chloride entrance of the concretes containing BFS is essentially due to two different phenomena associated to this SCM. BFS have the ability to bind

chlorides ions, which causes a significant reduction of the ions chloride ingress in concretes containing this SCM [5-8]. Furthermore, the BFS inclusion in cements leads to a higher refinement of the pore structure of concrete from the early ages [9], which brings with it a decrease in the water permeability [10] and as consequence a delay on the chloride transport through concrete.

It must be highlighted at this point that the refinement of the concrete pore structure associated to the incorporation of BFS as SCMs continue at long term [9, 11-13] due to the higher densification of the paste due to the additional C-S-H gel formation with respect to a plain OPC. However, no special attention has been paid to the curing effect of concrete containing BFS on its resistance to chloride entrance. Most studies only consider one age of hydration, usually 28 days [4]. Other works tackle the curing effect on the chloride penetration into concretes fabricated with cements containing BFS but only consider curing periods until 28 days. Tumidajski [14] studied the curing effect in concretes with different replacement of BFS and revealed better protection against chloride entrance for the specimens cured for 28 days than for those only cured for 3 days. Gastaldini [15] investigated the curing effect on the resistance to chloride entrance of concretes with 50% replacement of BFS and wet cured for 3, 7 and 28 days, reporting the lower values of charge passed through the specimens for the longer curing period tested. However, it can be observed that a lack of studies dealing with curing ages longer than 28 days.

Furthermore, most research has been done with concretes containing binary cements made of OPC and BFS [16] and few works can be found in literature considering ternary blended cements. Environmental and economic reasons, as the reduction of CO_2 emissions and energy consumption in the cement fabrication, leads to the need to contemplate the use of ternary concretes [17] also in chloride contaminated environments.

The present research studies the resistance to chloride penetration of two concretes, a plain concrete and a concrete containing a ternary cement composed of OPC, BFS and limestone filler (LF), focusing the interest of the research on the effect of curing.

2 EXPERIMENTAL PROCEDURE

2.1 Materials and samples characterization

100% OPC CEM I 42.5 R-SR has been employed as the reference binder. The mineralogical composition of the OPC, from Bogue [18] calculation after the correction of the 4% of $CaCO_3$ present in its composition, shows a 4% content of C_3A, resulting in cement with low chloride binding capacity [19]. The sum of 64% OPC + 30% BFS + 6% LF was used for the ternary blended cement. The chemical composition of the three components is included in Table 1.

Table 1. Chemical composition of the raw materials

%	Na_2O	K_2O	CaO	SiO_2	Al_2O_3	Fe_2O_3	MgO	SO_3	LoI
OPC	0.18	0.34	60.3	17.4	4.68	5.08	1.78	3.17	4.2
BFS	0.42	0.49	45.5	36.57	10.39	0.29	7.46	0.05	NA
LF	0.55	2.65	26.09	21.39	7.75	2.57	5.8	0.05	30.1

LoI: Lost of Ignition; NA: Not Analyzed

The OPC and the blended cement were employed to fabricate mortar and concrete specimens, identified as OPC and SL attending to the binder. Concrete specimens were fabricated for the chloride penetration tests. In addition to the described binders, round siliceous aggregates of two different sizes (0-4 and 4-12 mm) were employed. The nominal

composition of concretes is indicated in Table 2. The water/binder ratio was slightly varied to obtain the same soft consistency (6-9 cm) in both concretes. The fabrication of the concrete specimens for further arrangement of chlorides transport was made according to the prescriptions of [20]. For the present study, cubic samples of 10 × 10 × 10 cm were fabricated. Two identical specimens were fabricated from the same batch to have a duplicate for condition studied (type of cement -OPC and SL- and a curing period length -28 and 90 days) and to allow observing variability. The specimens were cured in a chamber at 21±2ºC and 98±2% RH for 28 or 90 days.

Table 2. Nominal composition of concretes

Component	OPC	SL
OPC (kg/m^3)	385	247
BFS (kg/m^3)	-	116
LF (kg/m^3)	-	23
Water (kg/m^3)	235	227
water/binder	0.61	0.59
Coarse aggregate 4-12 mm (kg/m^3)	802	802
Sand 0-4 mm (kg/m^3)	842	842

Standard mortar specimens were also fabricated with OPC and SL binder to know the mechanical performance and the porosity of these materials after the two curing periods evaluated, in order to establish possible relationship with the resistance to chloride entrance into concrete. The flexural strength was determined in two specimens of 40 × 40 × 160 mm per condition following the indications of in [22]. The compressive strength was determined in the pieces of concrete resulting from the flexural tests, also according to [22]. The porosity was determined on a sample of around 1 cm^3 extracted from a central region of an identical 40 × 40 × 160 mm mortar specimen through the application of the mercury intrusion porosimetry (MIP) technique with the equipment AutoPore IV 9500 V1.05. Variations of total porosity and pore size distribution have been followed. Tests in mortar allow the use of MIP for porosity characterisation without the interference of the coarse aggregate size respect to the dimension of the sample but follow the advance of hydration and cement paste formation during curing. The same curing conditions followed for the concrete specimens were applied for the mortars.

2.2 Arrangement of the chloride penetration tests on concrete specimens

The lateral and bottom surface of the specimens were painted with epoxy resin in order to limit the chloride ingress to occur only through the exposed surface. A ponding with 3% wt. NaCl was maintained during 3 months, the reference period of chloride exposure prescribed in [20].

At the end of the exposition time, a cylinder of 50 mm diameter and 100 mm height was drilled in the center of each concrete cube, therefore respecting the minimum distance of 10 mm from the border of the pond and the concrete cube sides as it is prescribed in [20]. From the cylindrical core, successive concrete layers were taken for the determination of their chloride content and the representation of the chloride profile to assess the entrance of these ions into concrete. The first 2 cm were grounded in depth intervals of 2 mm. Then, slices of 1 cm were cut until completing the total height of the core of concrete. The concrete slices were grounded to obtain also powder size. The chlorides were dissolved with nitric acid of 0.5 mol/l. The total chloride determination was made according to the potentiometric titration

method prescribed in [21], employing 0.1 M silver nitrate and an automatic titrator 702SM Titrino (Metrohm) controlled by the software Tinet 2.5.

Furthermore, the concentration of chlorides at the concrete surface (also named surface chloride concentration, CS) and the chloride diffusion coefficient at a non-steady state (also named apparent chloride diffusion coefficient, Dapp), were calculated from the non-linear curve fitting through minimum squares of the chloride profiles to the solution of Fick's second law of diffusion. The initial chloride content was supposed to be zero and therefore all layers from the second layer to the first layer with a concentration lower than 0.015% by weight of concrete were considered for the fitting, as prescribed in [20].

3 RESULTS AND DISCUSSION

The effect of SCMs on the chloride ingress into concrete has been first assessed through the interpretation of the chloride concentration profiles and the values of apparent chloride diffusion coefficient and surface chloride content. Results were first assessed separately for the two concretes employed, focusing the discussion on the effect of the curing on the chloride penetration and transport. The influence of the porosity on the chloride transport was also addressed. Finally, a comparison of the behavior of the two concretes fabricated was made to understand the effect of the partial replacement of OPC by BFS and LF.

3.1 Effect of the curing period on the chloride penetration and transport through concrete

3.1.1 OPC concrete

The results of the extension of the curing period from 28 to 90 days for OPC concrete are presented in the next figures. Fig. 1a shows the chloride profile of the two specimens fabricated with OPC concrete for the two curing periods (28 and 90 days).

Similar distribution of the chloride concentration can be appreciated in Fig. 1a for all specimens, regardless the curing period length. However, higher clarification of this effect of curing time can be appreciated from the average values of the apparent chloride diffusion coefficient and the surface chloride concentration (see Fig. 1b and c respectively). It has to be highlighted the variability associated to these two parameters. As example, it can be noted that Ferreira et al. [23] found, for a type of concrete containing CEM I 42.5, similar cement content and identical w/b ratio, higher resistance to chloride penetration and transport than that conferred by the OPC concrete of the present research. In particular, a value of 1,2·E-11 m^2/s and a value of 4.2% by mass of binder were reported for D_{app} and C_s respectively from specimens exposed for 90 days to the chloride solution. However, it must to be clarified that crushed granite coarse aggregates were employed in [23] and that the age of curing was not reported.

In present paper, the results of chloride entrance resistance with the age of curing will be analyzed with regard binding ability and porosity. This OPC concrete is expected to present a limited chloride binding capacity [19], due to the low content in C_3A and the hydration is almost complete after 28 days of curing as found by Geiseler et al. (1995). According to this fact, possible differences in the resistance to chloride penetration and transport should be attributed to changes in porosity with curing time. Fig. 2a shows a negligible decrease of the total porosity with curing (Fig. 2a). Furthermore, although a certain pore refinement can be observed in Fig. 2b with the extension of curing, the increase of the porosity associated to the capillary pores (< 1μm), typical ways for the chloride transport, was not significant (less than 10%). This similarity in porosity together the low binding capacity and the almost complete hydration after 28 days of curing are the responsible of the similar values of D_{app} and C_S obtained for the two curing periods tested.

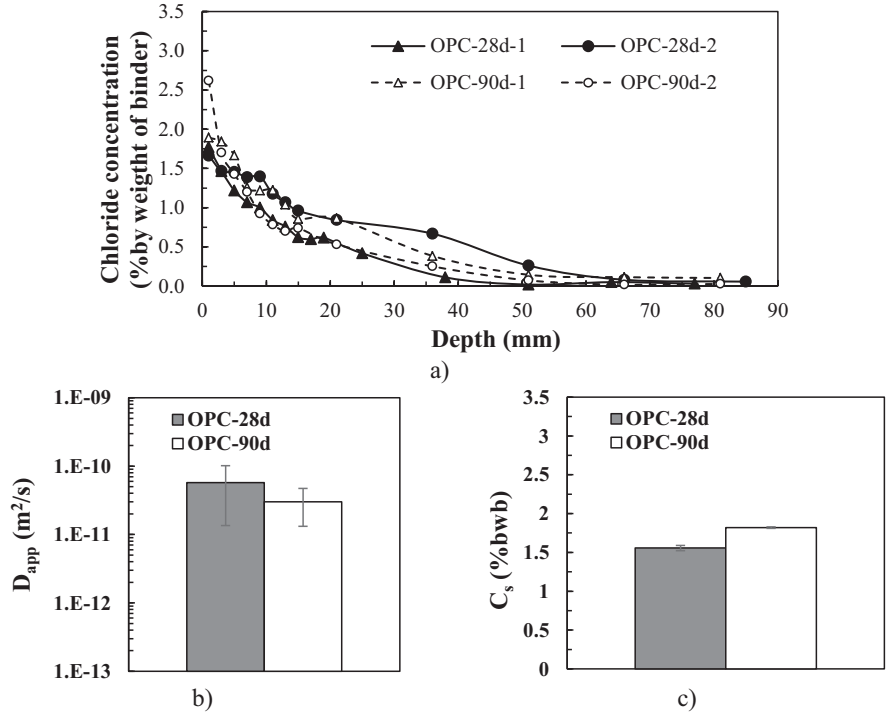

Fig. 1. Effect of curing period on OPC concrete: a) chloride profiles, b) D_{app}, c) C_s

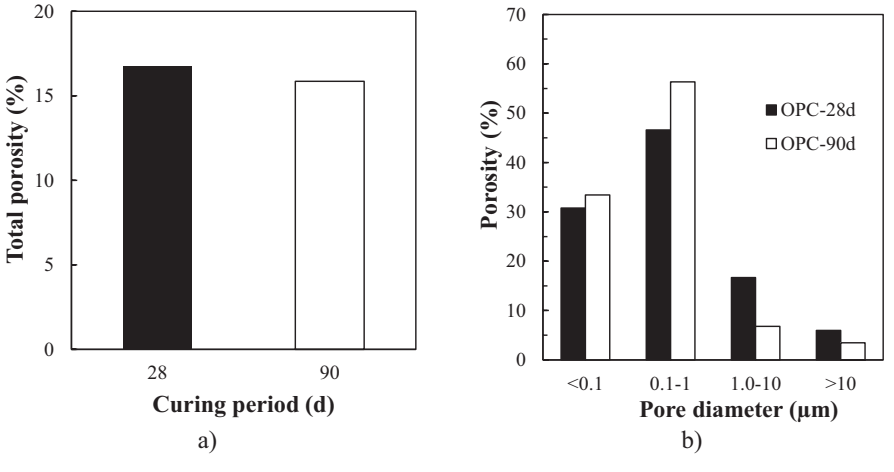

Fig. 2. Evolution of OPC mortar porosity with curing time: a) total porosity, b) porosity size distribution

3.1.2 Concrete containing blast furnace slag and limestone filler (SL)

Fig. 3 shows the chloride profile determined in the SL concrete specimens and the average value of D_{app} and C_s per curing period considered (28 and 90 days).

As happened with OPC concrete, no clear differences are appreciated (Fig. 3a) from the observation of the chloride profiles of the SL concrete specimens tested. Furthermore, the observation of D_{app} and C_s (see Fig. 3b and c respectively) also revealed no differences between the specimens cured 28 and 90 days. However, the D_{app} was between twice and thrice lower in SL, and the values of C_s up to 30% higher than those measured for OPC.

This result might be understood with the observation of the porosity and binding ability evolution within this blended concrete. It can be observed in Fig. 4b that, although porosity size distribution in SL concrete slightly changes when the curing period is extended to 90 days, the total porosity is some lower, being not enough to affect the chloride transport. The reason for this could be attributed to that BFS have not hydrated in sufficient proportion even after 90 days of curing, as also postulated in the literature [24] giving not effect in chloride transport. However, similar resistance to chloride entrance is observed for the two curing periods considered. It has to be considered that the concrete specimens are saturated during the chloride penetration tests so that the hydration of BFS evolves with time in specimens cured both 28 and 90 days, leading to similar porosity and similar binding capacity.

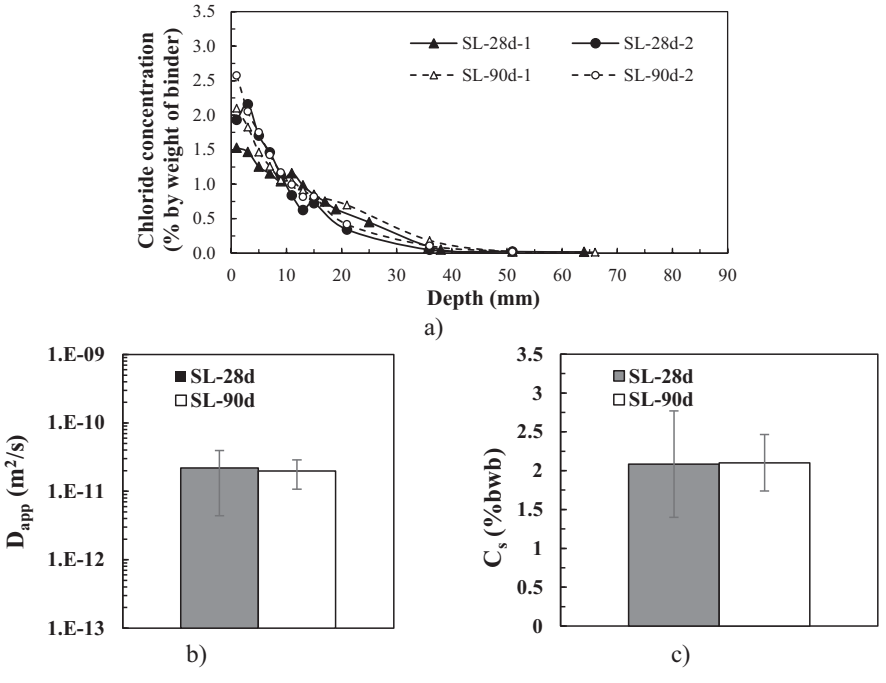

Fig. 3. Effect of curing period on SL concrete: a) chloride profiles, b) D_{app}, c) C_s

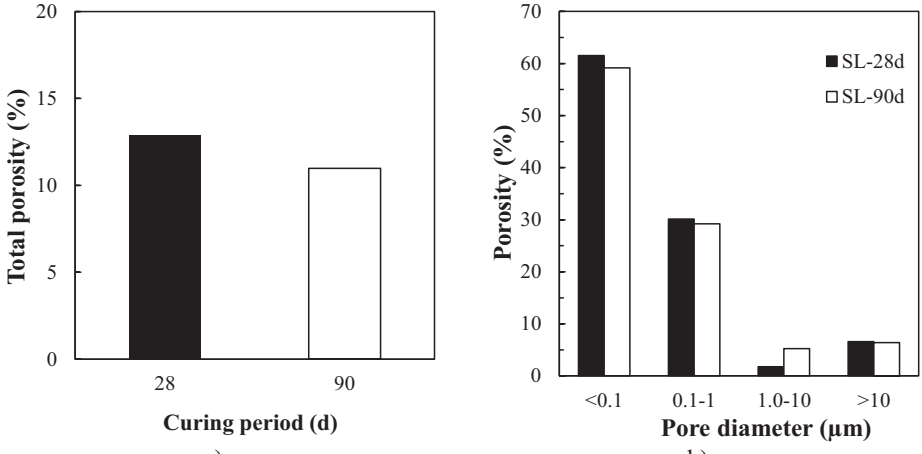

Fig. 4. Evolution of SL mortar porosity with curing time: a) total porosity, b) porosity size distribution

3.2 Importance of the concrete mix design on the chloride penetration and transport through concrete

3.2.1 Influence of the porosity

In addition to the curing time, the influence of the porosity on the chloride penetration and transport has been also studied. A relationship between of the results of chloride penetration and transport and porosity has been established in Fig. 5.

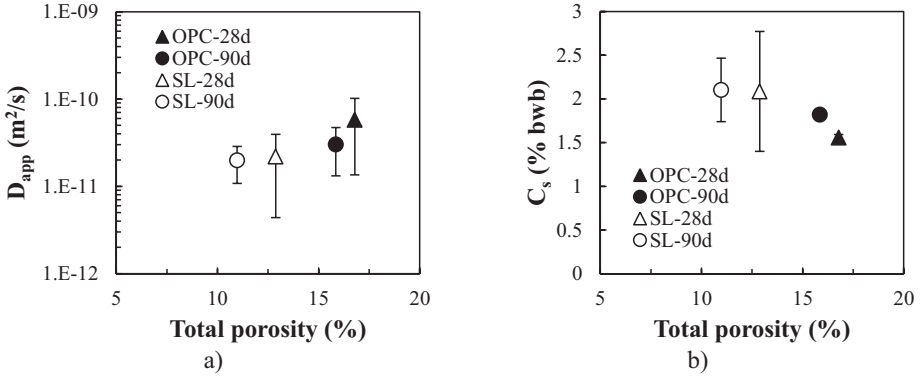

Fig. 5. Influence of the total porosity on: a) D_{app}, b) C_s

It can be observed in Fig. 5 that higher values of total porosity lead to lower D_{app} (see Fig. 5a) and higher C_s (see Fig. 5b) and therefore lower protection against the chloride entrance into concrete.

3.2.2 Influence of the binder type

The effect of the partial replacement of OPC by BFS and LF on the delay of chloride ions transport has been also evaluated for the two ages of curing considered. For this aim, the D_{app} and C_s values of the two specimens fabricated per concrete and curing period tested were plotted in Fig. 6.

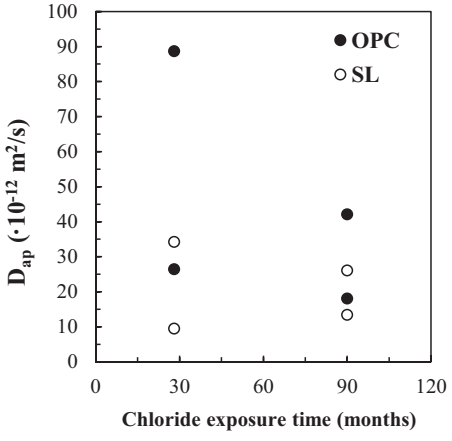

Fig. 6. Influence of binder type on D_{app}

The first to notice in Fig. 6 is the large deviation of values, so that exponential trend lines were drawn to better assess the binder type on chloride penetration. As it can be observed in Fig. 6, SL concrete attained in general lower values of D_{app} than OPC concrete for the two ages of curing considered, similar to found in literature [16]. In line with the results of D_{ap}, higher values of C_s were observed in SL concrete than those measured for OPC. This result evidences the major protective effect of SL concrete against the chloride penetration and transport of these ions when BFS and LF are used in the proportions specified.

This fact is clearly consequence of the effect of BFS and LF on the chloride ingress into concrete. While LF decreases the capacity of chloride binding [19, 23, 25], BFS do the contrary effect [5-8]. Furthermore, BFS are in higher proportion than LF in the mix (30% versus 6%, respectively). Therefore, higher binding capacity is expected in SL concrete than in OPC and hence the higher D_{app} and lower C_s found in the blended concrete, as for the two curing ages.

4 CONCLUSIONS

An experimental investigation of the resistance of OPC and SL concrete to the chloride penetration through natural chloride diffusion tests was conducted. Ponding tests of 3 months duration were carried out on specimens cured for two different periods (28 and 90 days). The following conclusions can be drawn from this research:

- The extension of the curing time from 28 to 90 days has not significantly reduced the chloride penetration into concrete with SCMs. In OPC concrete, a slightly decreasing tendency of the chloride diffusion coefficient with curing time was noticed.
- The partial substitution of OPC by BFS and LF in the proportions specified in the present research has led to the fabrication of a type of concrete slightly more resistant to the entrance of chlorides.
- It is confirmed that lower porosities result in higher resistance to chloride entrance.

ACKNOWLEDGEMENTS

The authors would like to thank Ministerio de Economía y Competitividad for financing the research project IMCORPRO BIA2011-22670 and especially Javier Luna for the funds BES-2012-061300. The authors would also like to thank the suppliers of the raw materials. In addition, the authors would like to thank the technician Virtudes Flor-Laguna for her contribution to the acid-soluble chloride analysis.

REFERENCES

[1] Tang, S.W., Yao, Y., Andrade, C., Li, Z.J. "Recent durability studies on concrete structure", Cement and Concrete Research 78 (2015) 143–154.

[2] Wu, K., Shi, H., Xu, L. Ye, G., De Schutter,G. "Microstructural characterization of ITZ in blended cement concretes and its relation to transport properties", Cement and Concrete Research 79 (2016) 243–256

[3] McPolin, D., Basheer, P.A.M., Long, A.E., Grattan, K.T.V., Sun, T. "Obtaining progressive chloride profiles in cementitious materials", Construction and Building Materials 19 (2005) 666–673.

[4] Chen, H.J., Huang, S.S., Tang, C.W., Malek, M.A., Ean, L.W., "Effect of curing environments on strength, porosity and chloride ingress resistance of blast furnace slag cement concretes: A construction site study", Construction and Building Materials 35 (2012) 1063–1070.

[5] Leng, F., Feng, N., Lu, X., "An experimental study on the properties of resistance to diffusion of chloride ions of fly ash and blast furnace slag concrete". Cement and Concrete Research, 30 (2000) 989-992.

[6] Detwiler, R.J., Fapohunda, C.A., Natale, J., "Use of supplementary cementing materials to increase the resistance to chloride ion penetration of concretes cured at elevated temperaturas". *ACI Materials Journal*, 91 (1994) 63-66.

[7] Moon, H.Y., Kim, H.S., Choi, D.S., "Relationship between average pore diameter and chloride diffusivity in various concretes, *Construction and Building Materials*, 20 (2006) 725-732.

[8] Song, H-W., Saraswathy, V., "Studies on the corrosion resistance of reinforced steel in concrete with ground granulated blast-furnace slag-An overview". *Journal of Hazardous Materials*, 138 (2006) 226-233.

[9] Bijen, J., "Benefits of slag and fly ash". *Construction and Building Materials*, 10 (1996) 309-314.

[10] Geiseler, J., Kollo, H., Lang, E., "Influence of blast furnace cements on durability of concrete structures". *ACI Materials Journal*, 92 (1995) 252-257.

[11] Manhoman, D., Metha, P.K., "Influence of pozzolanic, slag and chemical admixtures on pore size distribution and permeability of hardened cement pastes", *Cement, Concrete and Aggregates*, 3 (1981) 63-67.

[12] Ortega, J M., Ferrándiz, V., Antón, C., Climent, M.Á., Sánchez, I., "Influence of curing conditions on the mechanical properties and durability of cement mortars", en: Mammoli, A. A., Brebbia, C. A., (Eds.), Materials Characterisation IV. Computional Methods and Experiments, Witpress, Ashurst Lodge (UK), 2009.

[13] Schiessl, P., Wiends, U., "Rapid determination of chloride diffusivity in concrete with blending agents". RILEM International Workshop on Chloride Penetration into Concrete, RILEM publications, 1995.

[14] Tumidajski, P.J., Chan, G.W. "Durability of high performance concrete in magnesium brine, *Cement and Concrete Research*, Vol. 26, No. 4, pp. 557-565, 1996.

[15] Gastaldini, A.L.G., Isaia, G.C., Saciloto, A.P., Missau, F., Hoppe, T.F. Influence of curing time on the chloride penetration resistance of concrete containing rice husk ash: A technical and economical feasibility study, *Cement & Concrete Composites,* 32 (2010) 783–793.

[16] Sung-Won, Y., Seung-Jun, K. Effects of cold joint and loading conditions on chloride diffusion in concrete containing GGBFS, i 115 (2016) 247–255.

[17] Menéndez, G., Bonavetti, V., Irassar, E.F., "Strength development of ternary blended cement with limestone filler and blast-furnace slag". *Cement and Concrete Composites*, 25 (2003) 61-67.

[18] Bogue, R.H. "Calculation of the compounds in Portland cement". *Industrial and Engineering Chemistry* (1929) 1:192-197.
[19] Suryavanshi, A.K., Scantlebury, J.D., Lyon, S.B., "The binding of chloride ions by sulphate resistant Portland cement". *Cement and Concrete Research*, 25 (1995) 581-592.
[20] CEN 2015. Testing hardened concrete - Determination of the chloride resistance of concrete, unidirectional diffusion. EN 12390-11:2015.
[21] CEN 2007. Products and systems for the protection and repair of concrete structures. Test methods. Determination of chloride content in hardened concrete. EN 14629.
[22] CEN 2005. Methods of testing cement. Part 1: Determination of strength. EN 196-1:2005.
[23] Ferreira, R. M., Castro-Gomes, J. P., Costa, P. and Malheiro, R. Effect of Metakaolin on the Chloride Ingress Properties of Concrete, *KSCE Journal of Civil Engineering* (2016) 20(4):1375-1384.
[24] Kocaba, V., Gallucci, E., Scrivener, K.L., "Methods for determination od degree of reaction of slag in blended cement pastes". *Cement and Concrete Research*, 42 (2012) 511-525.
[25] Rasheeduzzafar, Al-Saadoun, S.S., Al-Gahtani, A.S., Dakhil, F.H., "Effect of ticalcium aluminate content of cement on corrosion of reinforcing steel in concrete". *Cement and Concrete Research*, 20 (1990) 723-738.

Physical Model of the Capillary Absorption in Cementitious Materials, New Approach to Calculate Analytically the Pore Size Distribution from the Gravimetric Test

Luis Saucedo-Mora[(1)], Carmen Andrade[(1)], Sandra Cabeza[(2)] and Dietmar Meinel[(2)]

[(1)]Institute eduardo torroja for construction sciences (CSIC), Madrid, Spain

[(2)]Federal institute for materials research and testing (BAM), Berlin, Germany

ABSTRACT

The capillary absorption experiment on cement and concrete is very simplistic and widely accepted by the scientific community. Nowadays it is mainly used for the determination of the capillary porosity of a material, and from theoretical models to extract information about the average pore size. This, with the permeability and pore size distribution obtained with the water permeameters and mercury intrusion porosimeters, respectively, can characterize the behavior of the material regarding to the water penetration. In this work, we propose a model capable to interpret physically the wetting part of the absorption test in order to extract solely from this experiment valuable information such as the permeability, porosity and pore size distribution. Computer tomography is used to validate the physical model, and three examples of cement pastes with different water/cement ratios are shown to validate and demonstrate the potentiality of this new technique.

Keywords: Capillary absorption, pore size distribution, X-ray CT, gravimetry, MIP

1 INTRODUCTION

Capillary water absorption in concrete has been studied during decades [1, 2]. Due to the presence of moisture it is a crucial factor for numerous degradation processes in concrete, being the capillary absorption one of the most common mechanisms of water transport in concrete. Another advantage of capillary water absorption tests is its simplicity because it is not necessary more instruments than a balance. The test consists in placing the only one face of the concrete specimen in contact with few mm height of water and weight the specimen periodically.

Mention has to be also made in this subject to the work of RILEM TC -116 [3] "Performance criteria for Concrete Durability" chaired first by H.K. Hilsdorf and then by J. Kropp. This TC studied the different transport mechanisms of liquids, gases and ions through concrete and their interrelation. Although the main initial aim of the committee was to explore the relationships from permeability and durability, soon it appeared a very complex subject due to the different degradation mechanisms, different fluids moving (water, vapour, ions) and the different rates of evolution depending on cement nature and concrete porosity. However, the committee clarified the interrelation between several of these aspects and identified the needs of research. Regarding absorption, it was found in the inter-laboratory round-robin testing that it was not very sensitive to the different concrete qualities and sometimes the term sorptivity gave contradictory results, but the very low scatter of the results allows to distinguish between different concrete qualities.

Water transport modelling is a crucial aspect related to very long prediction, as needed in nuclear installations of radioactive wastes where hundreds or thousands of years are the horizon of service life for concrete as engineering barrier. In these cases, the penetration of water in the concrete, either by capillary absorption or permeation, is the main factor taken into account due to the possible leakage of radio nuclides if the water percolates and is released to the surrounding lands.

2 METHODLOGY

The model used in this paper is the one developed by Saucedo-Mora et al. [4] that through an energetic balance and considering the kinetics of the water and its dynamic loss of energy, can formulate the velocity of absorption for each pore. And through an approximation of the integral of the velocities and areas of the pores along the statistical distribution of the pore size, the model can calculate the weight-time behaviour of the material. Also the pore size distribution and the permeability of the material can be obtained through the measurement of the weight and time when the weight-time graph loses its linearity. The model of Saucedo-Mora et al. [4] is applied to the results of Andrade at al. [5] in the validation section.

3 EXPERIMENTS

As mentioned before the gravimetric test is very simplistic and cheap; it consists in a piece of cement paste left in contact with water at its bottom face, which is weighted in intervals of time during the first 24 or 48 h. But perhaps because of its simplicity, it is completely determined by the pore network of the material. In order to characterize the phenomenon in a first approach, six gravimetric measurements where done in a cement paste with 3 different water/cement (w/c) ratio (0.4, 0.5 and 0.6). Measuring the evolution of the weight in samples of 0.01×0.01×0.1 m in intervals of 30 minutes during the first 8 hours of test, and then at 12 h and 24 h. The samples were placed with the largest side in the vertical direction as shown in Figure 1.

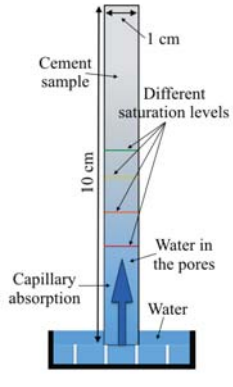

Figure 1: Gravimetric test of the water absorption, the sample was always covered by the water in its first 5 mm.

The recipient under the sample was always filled with water, and the bottom of the sample was completely in contact with the water.

CT X-Ray scans were also performed in the same samples that were used for the gravimetric test during the first 4 hours of the absorption process, as well as after 24 h. Those

test were done at the federal institute for materials research and testing (BAM) CT laboratories with a 225 kV X-ray micro focus tube with an energy set to 180 kV, current 160 μA, a pre-filter of 1 mm Cu for hardening the X-ray spectra, and a detector size of 2048 × 2048 pixel with a detector pixel pitch of 0.2 mm. For the fast measurements, 900 radiographic projections in 360° rotation of the sample in equidistant angle steps were taken with 1s acquisition time (total time of 15 min), achieving 89 μm pixel resolution. The slow measurements comprised 2000 projections (total of 30 min), giving a resolution of 45 μm. A cone-beam algorithm of Feldkamp was then applied to reconstruct the 3D volume of the sample. Three cement paste samples with the different w/c ratios were investigated. From this data, the saturation levels shown in Andrade et al. [5] were calculated with image contrast, as shown in Figure 2. And will be crossed with the model of Saucedo-Mora et al. [4] for the full validation of the phenomena.

Also Mercury intrusion porosimetry (MIP) tests were done for the 3 w/c ratios at the Institute Eduardo Torroja for construction science (CSIC), obtaining the permeability and pore size distribution of the 3 samples.

4 RESULTS

The gravimetric and MIP results are shown in the validation section. In this section we show in Figure 2 the result of a sample of 0.04x0.04x0.16 m and a w/c ratio of 0.5. The different colours represent the variation of the saturation level, and the grey dots the large porosity of the sample. The temporal evolution of the saturation defines the phenomenon and the different pore sizes saturated as the different heights [4]. The curvature of the water front in the first centimetre is due to the border effect, but the central absorption was found representative [5].

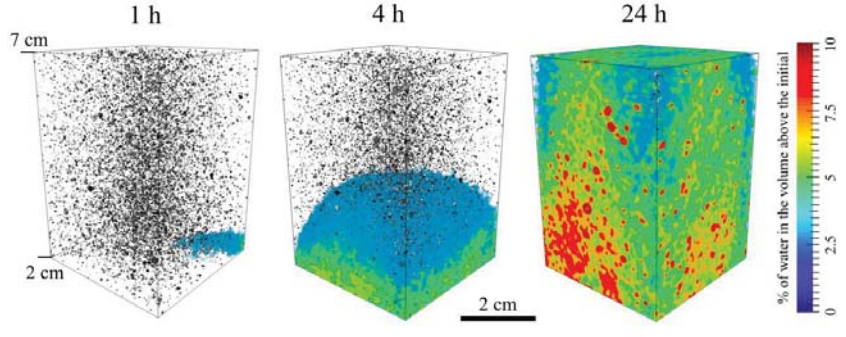

Figure 2: different saturation levels of a cement paste sample with a w/c ratio of 0.5

5 VALIDATION

The model is validated with the gravimetric data and the MIP measurements of the 3 samples with different w/c ratios (0.4, 0.5 and 0.6). The only input parameter of the model was the measurement of the points where the non-linearity starts in the weight-time graph (Figure 3a), in the model this non-linearity is reproduced by the pores that reach the top of the sample and can't gain more weight. With this information measured in the gravimetric test, the geometry of the sample and the physical variables of water (e.g. density, capillary tension), the model [4] can reproduce the behaviour with simple equations and without fitted parameters. As shown in Figure 3 there is a good agreement and the full behaviour (i.e. linearity and non-linearity) of the phenomenon is reproduced, as well the pore size distribution obtained is representative.

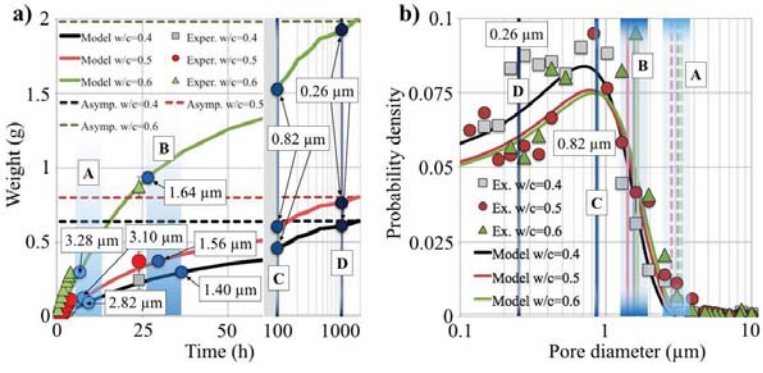

Figure 3: Model and experimental data of the weight-time behaviour (a) and the pore size distribution (b) showing the pore size that is reaching the top of the sample at each time.

The different regions of Figure 3 marked with points and lines are: A the points when the non-linearity starts, which is different for each w/c ratio, B is the time when the prolongation of the straight line of the initial behaviour intersects the horizontal final asymptote which is an input parameter of the model and C and D are 2 points at the end of the saturation process used to show the size of the pores that fills the sample at the end of the test. Those points are also shown in Figure 3b as well as their relationship with the pore-size distribution.

6 CONCLUSIONS

The gravimetric test is very simple and cheap, but the filling behaviour of the pores is complex and involves the kinetics and energetic loss of the water penetration through the pores. The example presented shows the capability of the model to calculate the pore size distribution and reproduce the full weight-time behaviour only with the experimental measurement of the weight and time when the non-linearity starts in the gravimetric test.

7 ACKNOWLEDGEMENTS

Luis Saucedo-Mora wants to acknowledge the financial support given by the Secretariat of State for Research, development and innovation of the Spanish government under the grant IJCI-2014-19362 associated to a juan de la cierva incorporation fellowship. The authors want to acknowledge the federal institute for materials research and testing (BAM) CT laboratories for allowing us to do the experiments in their facility. We also want to acknowledge the institute eduardo torroja for construction sciences (CSIC) for the MIP measurements.

8 REFERENCES

[1] Fagerlund G., 'The long term water absorption in the air-pore structure of concrete'. *Report TVBM*. Vol. 3051. Division of Building Materials, LTH, Lund University.
[2] Hall, C. and Hoff, W.D., 'Rising damp: capillary rise dynamics in walls', *Proc. R. Soc. A.* 463 (2007) 1871-1884.
[3] RILEM TC 116-PCD, 'TC 116-PCD: Permeability of concrete as a criterion of its durability', *RILEM Publications SARL* 32 (217) (1999) 163-173.
[4] Saucedo-Mora, L., Andrade Perdrix, M.C., Cabeza, S. and Meinel, D., 'Physical model of the capillary absorption in cementitious materials ', Under preparation
[5] Andrade Perdrix, M.C., Saucedo-Mora, L., Cabeza, S. and Meinel, D., 'Water absorption test through XR tomography', Under preparation

Effect of Calcium Nitrite Inhibitor on Mechanical and Durability Parameters of Concrete

Bhaskar Sangoju[(1)], B. H. Bharatkumar[(1)] and Ravindra Gettu[(2)]

[(1)]CSIR- Structural Engineering Research Centre, Chennai

[(2)]Indian Institute of Technology Madras, Chennai, India

ABSTRACT

This paper discusses the results of laboratory studies on the effect of calcium nitrite inhibitor (CNI) with different dosages (10, 20 and 30 l/m^3) on the mechanical and durability parameters of fly ash based Portland pozzolana cement concrete. A water-to-cement ratio of 0.47 was used and different specimens such as cubes, cylinders and prisms as per ASTM G 109 were cast. For determining the effects of chemical admixtures on corrosion of embedded steel in concrete exposed to chloride environments, G 109 test was believed to be more representative of field conditions compared to other accelerated tests. Therefore, G 109 test specimens with different dosages of CNI were cast and exposed to continuous wetting and drying cycles for a period of more than 2 years. Half-cell potential measurements indicate the concrete with CNI did not show any inhibition effect on the occurrence of proneness of corrosion. The current in specimens of concrete with 10 l/m^3 of CNI showed large variation whereas the average integrated macrocell current in control specimens is about 4.08 C indicating the test to be continued for still more longer periods to reach the integrated macrocell currents equal to or greater than 150 C. The 28 day compressive strength and RCPT results of concrete with CNI indicate lower compressive strengths (about 11 to 20%) and higher charge passed (about 4 to 42%) when compared to that of control concrete.

Keywords: Concrete durability, corrosion inhibitor, dosage, half-cell potential.

1 INTRODUCTION

Corrosion of the reinforcement bar (rebar) in concrete is a general phenomenon and needs to be controlled. Some of the commonly used corrosion control measures are: (i) good quality concrete with low water-to-cement ratio (w/c) and use of superplasticizers, (ii) provision of adequate concrete cover, (iii) use of epoxy coated and galvanized steel, (iv) concrete surface coatings, (v) use of pozzolans (fly ash, silica fume, slag), (vi) use of corrosion inhibitors, (vi) use of electrochemical techniques such as cathodic protection, chloride extraction, etc. [1,2]. In the recent past, chemical admixtures such as superplasticizers and calcium nitrite corrosion inhibitors are commonly used in the reinforced concrete (RC) construction [3]. Berke and Rosenberg [4] carried out pioneering research on corrosion inhibitors and stated that calcium nitrite inhibitor (CNI) performs well even in cracked concrete. However, some research indicated detrimental effects of CNI on the properties of concrete as well as in preventing corrosion of rebars. Nmai and MacDonald [5] found that CNI seems to be ineffective at reducing corrosion, unless a large amount is added to the mixture. Berke [6] observed an increase in the chloride ion permeability due to the presence of CNI. Some researchers [7] reported that the addition of calcium nitrite influences the hydration process

of cement paste by accelerating and stabilising the formation of the crystal phase of calcium hydroxide, which leads to an increase in the micropore diameter in the hardened cement paste, and thus an increase in chloride ion permeability compared to concrete without inhibitor. Li et al. [8] observed a decrease in compressive strength of concrete with the addition of CNI and also observed that the addition of CNI changes the microstructure. Amara et al. [9] performed extensive studies on rapid chloride ion permeability (RCPT) of four different concretes with and without nitrite based inhibitor, and observed higher permeability at early ages in concretes with nitrite based inhibitor. Berke et al. [10] also reported an increase in RCPT values due to the presence of calcium nitrite. Bhaskar [11] carried out accelerated impressed current tests and observed that CNI did not show any inhibition effect emphasizing the need for detailed investigation before arriving at general conclusions. There is a difference in opinion among researchers about the effect of CNI on strength and durability of concrete [8-11]. Some researchers report that accelerated tests such as RCPT and impressed current are not appropriate tests to evaluate the performance of CNI [11-13]. Also, some literature support the long term tests such as ASTM G 109 could be a suitable one to assess the effect of CNI on the corrosion inhibition in RC [14-15]. This is because the ASTM G 109 test method possesses moderate conditions and slow corrosion response of the test specimens is believed to be more representative of field conditions compared to other accelerated tests. Hence, the objective of the present study is to investigate the effects of different dosages of CNI on the mechanical and durability parameters of concretes.

2 EXPERIMENTAL PROGRAM

Fly ash based Portland pozzolana cement (PPC) and commercially available calcium nitrite inhibitor (CNI) is used in the present study. A water-to-cement ratio (w/c) of 0.47 is used for making the concrete and water available in the CNI (650 ml/l) is accounted during the mix preparation. ACI 211 [16] guidelines are followed in the mix design and the mix details are presented in Table 1. As per manufacturer's specification, the inhibitor contains about 30% calcium nitrite by mass and meets the ASTM C 494 [17]. TMT bars of 12 mm are used as the reinforcement.

Table 1: Quantities per cubic meter (kg/m^3)

w/c	Cement	Sand	Coarse aggregate	Water
0.47	362	815	1056	170

Three concrete prisms (280×150×115mm) were cast for each set of concrete mix (without CNI, control and with three dosages of CNI). The recommended dosage of CNI by the manufacturer is 5 l/m^3 to 30 l/m^3. However, it is reported in literature that the dosage of CNI depend on the severity of corrosion environment and the anticipated chloride loading of the structure. In the previous study, where accelerated corrosion was simulated, three dosages (10 l/m^3, 20 l/m^3 and 30 l/m^3) within the upper and lower limits recommended by the manufacturer were used [12]. Hence, in the present study also, same dosages are used for easy understanding. Each prism specimen is provided with three steel bars of 12 mm diameter. One rebar is placed at 25 mm from the top surface (close to the top of the specimen) and is used as the anode of the circuit. Two rebars are placed at the bottom with 25 mm clear cover from bottom and are used as the cathode of the circuit. The top rebar with only middle 200 mm is embedded with the concrete (only 200 mm is exposed and the remaining is sealed with insulating tape and epoxy). The concrete without CNI (control concrete) is used for comparison purposes. Total four sets of specimens are cast and the

details are presented in Table 2. In addition, 150 mm cubes and 100 mm diameter and 200 mm height cylinders are also cast for compressive strength, ultrasonic pulse velocity (UPV) and RCP tests. After 28 days of water curing, top and bottom rebars of prism specimen is connected electrically with 100 Ω resistors. A plastic dam is created on the top of each specimen with dimensions of 150 × 75 × 75mm (line sketch is shown in Figure 1). The dam is filled with 3% NaCl solution for two weeks and then emptied for the next two weeks and the cycle of wetting and drying is continued for a period of 2 years. Figure 2 shows the photograph of ASTM G 109 test setup.

Table 2: Details of sets

Set	Details
Set 1 (S1)	Control concrete
Set 2 (S2)	Concrete with 10 l/m^3 of CNI (2.76 % by weight of cement)
Set 3 (S3)	Concrete with 20 l/m^3 of CNI (5.52 % by weight of cement)
Set 4 (S4)	Concrete with 30 l/m^3 of CNI (8.28 % by weight of cement)

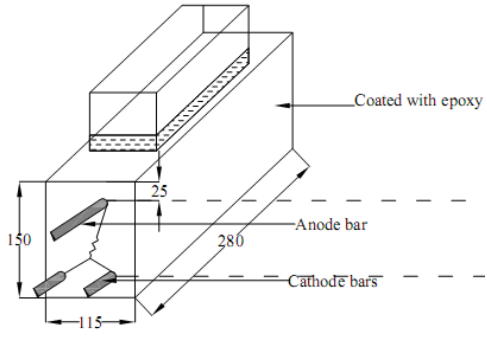

Figure1: Details of ASTM G 109 test specimen with dam on the top surface

Figure 2: ASTM G 109 test specimens under continuous wetting and drying cycles

3 RESULTS AND DISCUSSION

3.1 Compressive strength and UPV

Concrete compressive strength and ultrasonic pulse velocity has been evaluated on cube specimens. Three specimens are tested after 7, 28 and 56 days of water curing and their average is presented in Table 3. It can be seen that the compressive strength increases as the curing period increases, as expected. However, it has been observed that there is a reduction in compressive strength of concretes with CNI when compared to that of the control concrete and is about 11 to 20%. The results obtained agree with previous work, where the reduction in compressive strength has been attributed to the change in pore ratio and diameter [8]. The UPV values are in the range of 4.7 km/s to 5 km/s.

Table 3: Compressive strength and UPV test results

Description	Compressive strength (MPa)		
	7 days	28 days	56 days
S1	26	44	50
S2	22	41	46
S3	21	35	45
S4	22	38	45

No significant difference is observed and the UPV values are more or less same for concretes with and without the presence of CNI.

3.2 Rapid Chloride Penetration and Water absorption Test

Rapid chloride ion penetration test (RCPT) is carried out on concrete discs as per ASTM C 1202 [13]. Cylinders of 100 mm diameter and 200 mm height are cut into discs of 50 mm thickness. The specimens were kept in water for 24 hours for full saturation and then subjected to RCPT by impressing a 60 V current. For this, two sides of the disc are sealed in Plexiglas containers. One side of the container is filled with 3% NaCl solution (cell connected to the negative terminal) and the other side is filled with 0.3 N NaOH solution (cell connected to the positive terminal). Current is measured at every 30 minutes for a period up to 6 hours. At the end of 6 hours, the total charge passed is calculated.

Table 4 presents the RCPT and water absorption results of control concrete and concrete with different dosages of CNI at different ages. It is observed that the RCPT values of concretes with CNI are higher (about 4 to 42%) than that of control concrete. The higher value of RCPT for concretes with CNI can be attributed to the high ionic nature of CNI, which causes more negative charge to pass through the concrete. Similar results were reported by other researchers [8, 18-19]. Berke et al. [10] studied the effect of various combinations of admixtures and reported that there was an increase in charge passed due to the presence of calcium nitrite. However, Ma et al. [7] reported that the addition of calcium nitrite influences the hydration process of cement paste, which leads to an increase in the micropore diameter in the hardened cement paste. The larger pores could lead to an increase in chloride permeability when compared to the concrete without inhibitor [8]. Loulizi et al. [20] performed RCPT studies on four different concretes with and without nitrite based inhibitor and observed higher RCPT values at early ages in concretes with nitrite based inhibitor. Also, in the present study, it is observed that the RCPT values are decreasing as the

dosage increases. However, the exact reason is not known. Further, microstructural studies are needed.

Table 4: RCPT and water absorption values

Description	RCPT Values (Coulombs)			
	28 days	56 days	90 days	120 days
S1	2219	1388	785	610
S2	3151	1805	1399	940
S3	2500	1780	1057	826
S4	2312	1701	848	756

3.3 Half-cell potentials results

Half-cell potential measurements using copper/copper sulphate (CSE) electrode have been recorded at every fortnight during mid-wetting and mid-drying cycles for a period of nearly 700 days. The half-cell potential values (Figure 3) for mid-wetting cycles are in the range of -52 to -150 mV; -72 to -180 mV; -100 to -275 mV and -120 to -230 mV, respectively for control concrete (S1); concrete with 10 l/m^3 of CNI (S2); concrete with 20 l/m^3 of CNI (S3); and concrete with 30 l/m^3 of CNI (S4). The trend of half-cell potential values indicates that the control concrete (without CNI) showed lower negative potentials when compared to that of concrete with CNI.

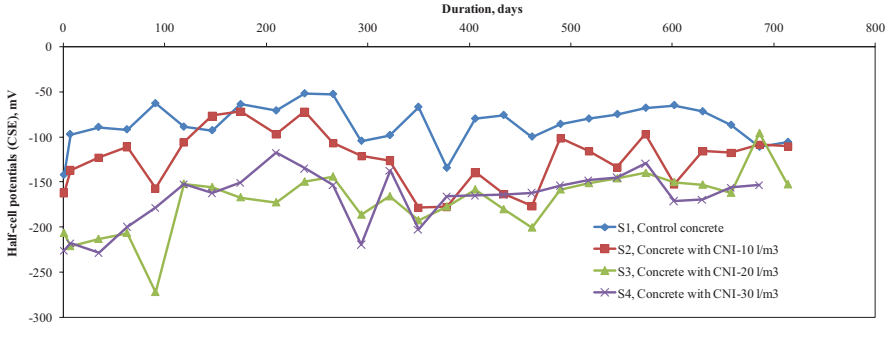

Figure 3: Half-cell potentials of control and concretes with different dosages of CNI

3.4 Corrosion Current

As per ASTM G 109, the voltage across 100 Ω resistor is to be measured and the corresponding corrosion current is to be calculated. In the present study, the voltage and the corresponding current is measured at regular intervals using Solartron 7151 high impedance multimeter for a period of about 2 years. The total integrated current can be computed as in Eqn 1:

$$TC_j = TC_{j-1} + \left[\left(t_j - t_{j-1}\right) \times \left(\mathrm{i}_j + i_{j-1}\right)/2\right] \quad (1)$$

where,

TC = Total corrosion (coulombs),

t_j = Time (seconds) at which measurement of the macrocell current is carried out, and

i_j = macrocell current (amps) at time,t_j

As per ASTM G 109, the test is to be continued until the average integrated macrocell current of the control specimens reach 150 Coulombs (C) or greater, and at least half of the specimens show integrated macrocell current equal to 150 Coulombs or greater. ASTM G 109 states that this limit will be reached in about six months. In the present study, at about two years, except S2, none of the three series (S1, S3 and S4) reached that level. However, during measurements at regular intervals, it has been observed that the voltage and the corresponding current in S2 series alone are abnormally high (large variations) and hence, it was decided to stop the test for S2 series specimens and break open the rebar. Figure 4 shows average total integrated current, TC, (C) Vs time for all series. The average integrated macrocell current in S1, S2, S3 and S4 series are about 4 C, 5776 C, 11 C and 3 C, respectively. The specimens of S2 series are cut around the perimeter of specimen at the level of the top reinforcement split apart. Figure 5 shows the two faces of the cut specimen with rebar. Figure 6 shows the autopsied rebars before cleaning and can be observed some brownish colour locally at one or two places.

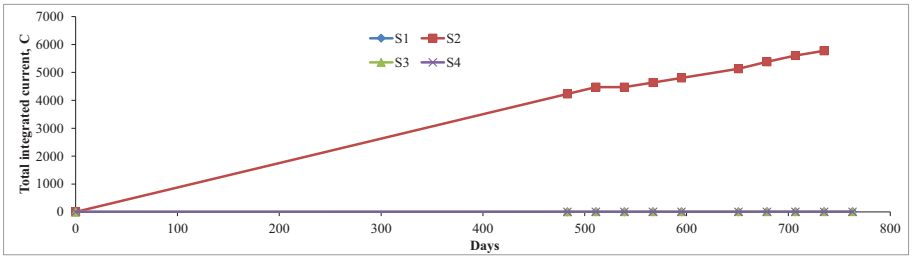

Figure 4: Integrated current Vs Time for control and concretes with different dosages of CNI

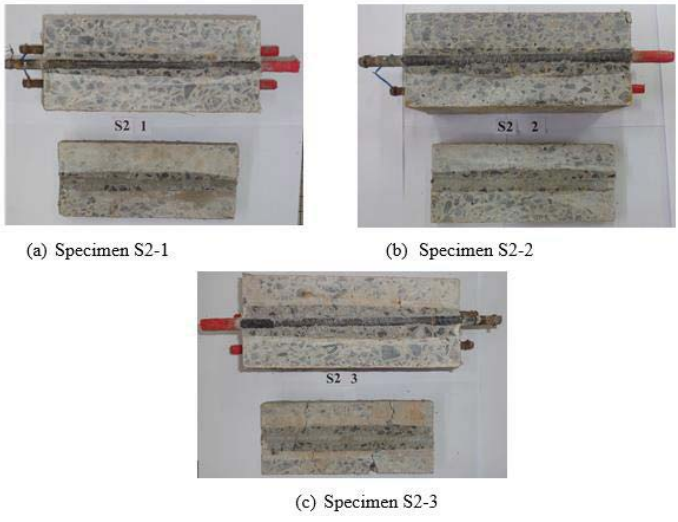

(a) Specimen S2-1 (b) Specimen S2-2

(c) Specimen S2-3

Figure 5: Cut-open (at anode bar) specimens of S2 series

The rebar is cleaned as per ASTM G 1 [21] to remove the rust and Figure 6 also shows the autopsied bars after cleaning.0.1 N Silver nitrate solution ($AgNO_3$) is sprayed on freshly split concrete specimen. Measured the chloride penetration depth, when the white silver chloride precipitation on the split surface is clearly visible (nearly about 15 min.).Table 5 shows the chloride penetration depths of S2 series specimens. The average chloride penetration depth of S2 series is 12.21 mm. However, at one or two places the chloride profile reached 25mm touching the rebar. The gravimetric weight loss of the rebar due to macrocell corrosion is measured as the relative loss in weight over the 200mm contact length, and represents the average weight loss over the length considered. The weight loss is negligible/very marginal and the average weight loss is about 0.30 g. Since, the HCP potentials for S2 are in the range of -45 to -180mV and the average chloride penetration depths did not reach the rebar, the abnormal values observed in current measurement could be due to local rusting of rebar on the outer exposed area or improper measurement. Also, there is no consistency in the current observations, therefore, the results of S2 series is discarded.

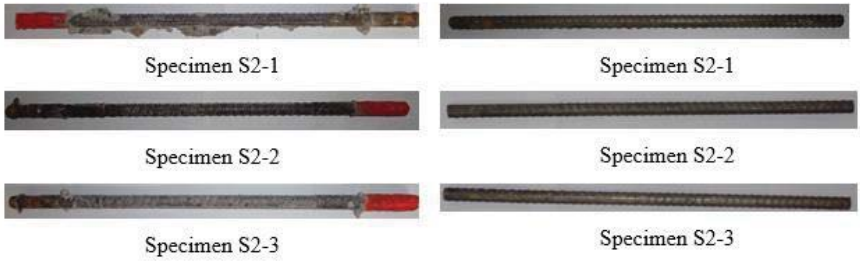

Figure 6: Rebars taken out from autopsied specimens of S2 series

Table 5: Chloride penetration depths of S2 series

Specimen No.	Chloride penetration depth, mm	Average, mm	SD, mm
1	11, 25, 16, 6, 15, 17, 10, 5, 12, 7, 15, 6, 12, 15, 9	12.07	5.32
2	10, 9, 25, 15, 26, 8, 13, 18, 10, 11, 14	14.45	6.18
3	11, 11, 16, 13, 10, 11, 14, 6, 10, 8, 10, 8, 12, 6, 3, 6, 11, 12,14	10.11	3.28

From the total integrated current results of S1, S3 and S4 series and also from the results of autopsy and weight loss measurements of S2 series it can be said that the alternative wetting and drying cycles (ASTM G 109 test) to be continued for still some more years. So that the total integrated macrocell currents shall be equal to or greater than 150 C in control concrete. Barke and Hicks [18] tested G 109 specimens and observed the time to reach the total integrated macrocell current (150 C as per ASTM G 109) for control specimens was over 2 years and for specimens with epoxy coated bars was over 4.5 years. The same study also reported specimens containing CNI did not exhibit until after 8 years of testing. Hansson et al. [22] studied the effect of high performance concrete on chloride induced corrosion of rebar and reported that even after 3.5 years, none of the specimens exhibited corrosion. In the present study, fly ash based PPC concrete with w/c of 0.47 is used which may take still some more time since the resistivity of fly ash based PPC concrete is generally higher than that of OPC concrete [12]. Halmen and Trejo [15] proposed a modified test by increasing the temperature and humidity of the environment to reduce the test duration. However, for systems with more corrosion resistance, the time to reach 150C will be still long and the G 109 test is not recommended for evaluating these systems. Overall, it can be said that ASTM G 109 test method is not effective for fly ash based concrete with w/c = 0.47 and cover thickness 25 mm in reaching the time for 150 C even after two years. New tests are needed to quickly assess the corrosion resistance of rebar concrete systems.

CONCLUSIONS

Based on the experimental results obtained from this study, following conclusions can be drawn:

- There is a reduction in compressive strength for concretes with CNI when compared to that of the control concrete and the reduction is in between 11 to 20% for the selected dosages of CNI.
- RCPT values of concretes with CNI are higher (about 4 to 42%) than that of control concrete.
- Half-cell potential measurements indicate the concrete with CNI did not show any inhibition effect on the occurrence of proneness of corrosion.
- ASTM G 109 test method is not effective for fly ash based concrete with w/c = 0.47 in reaching the total integrated macrocell current of 150 C even after two years. New tests are needed to quickly assess the corrosion resistance of rebar concrete systems.

REFERENCES

[1] Andrade, C. and Alonso, C.,'Progress on design and residual life calculation with regard to rebar corrosion of reinforced concrete', in 'Techniques to assess the corrosion activity of steel reinforced concrete structures', ASTM STP 1276, West Conshohocken PA, USA,(1996)152-164.

[2] USDT-Publication No. 00-081, 'Materials and methods for corrosion control of reinforced and prestressed concrete structures in new construction', U. S. Department of Transportation, 2000.
[3] Rixom, R. and Mailvaganam, N., 'Chemical admixtures for concrete', Third edition, E &FN SPON, Ltd. London, 1999.
[4] Berke, N. S., and Rosenberg, A, 'Calcium nitrite corrosion inhibitor in concrete', in 'Admixtures for concrete; Improvement of properties', Proceedings of International RILEM Symposium, Champman & Hall, London, 1990, 297-315.
[5] Nmai C. K. and McDonald, D. 'Long-term effectiveness of corrosion inhibiting admixtures and implications on the design of durable reinforced concrete structures: a laboratory investigation' in'The Role of Admixtures in High Performance Concrete'. Proceedings of RILEM International Symposium,Monterey, Mexico, 1999,1-17.
[6] Berke, N. S.,'Effect of calcium nitrite and mix design on the corrosion resistance of steel in concrete (part 2 long-term results)', in'Corrosion of Metals in Concrete'NACE, Proceedings of the Corrosion-87,Houston, (1987) 134-144.
[7] Ma, B., Li, Z., Peng, J., 'Effect of calcium nitrite on high performance concrete containing fly ash', Proceedings of Six CANMETInternational Conference-Supple Papers, ACI,Bangkok, Thailand, 1998, 113–124.
[8] Li, Z., Ma, B., Peng, J., and Qi, M., 'The microstructure and sulfate resistance mechanism of high-performance concrete containing CNI', *Cem.Concr. Comp.***22** (2000) 369-377.
[9] Amara, L., Al-Qadi and Diefenderfer, B. K, 'Effects of nitrite based corrosion inhibitor on concrete's rapid chloride permeability values and its dielectric properties'. *ACI Mater. J.*, **97** (4), (2000) 465-471.
[10] Berke, N. S. Hicks, M. C., Malone, J.J., and Rieder, K.A. 'Holistic approach to corrosion of steel in concrete', in'Concrete: Material science to application', ACI-SP-206, Detroit, 2002, 137-155.
[11] Bhaskar, S., Ravindra Gettu and Bharatkumar, B.H., 'Influence of chemical admixtures on corrosion of rebars in cracked concrete', in 'Microstructural related Durability of Cementitious Composites','Second international Conference,11-13 April 2012, Amsterdam, The Netherlands.
[12] Bhaskar, S.,'Study of chloride induced corrosion of reinforcement steel in cracked concrete', PhD Thesis, Indian Institute of Technology Madras, Chennai, India, 2013.
[13] ASTM C 1202-97,'Standard Test Method for electrical indication of concrete's ability to resist chloride penetration', Annual book of ASTM standards, American Society of Testing and Materials, USA, 2009.
[14] ASTM G 109-07,'Standard test method for determining effects of chemical admixtures on corrosion of embedded steel reinforcement in concrete exposed to chloride environments', Annual book of ASTM standards, ASTM, USA, 2010.
[15] Halmen and Trejo,' Accelerating strandard test method for assessing corrosion of steel in concrete', *ACI Mat. J.*, 2012, 421-430.
[16] ACI 211.1-91,'Standard practice for selecting proportions for normal, heavyweight and mass concrete', ACI Publication, USA, 2015.
[17] ASTM C 494-10a, 'Standard Specification for Chemical Admixtures for Concrete. Annual book of ASTM standards', *American Society of Testing and Materials*, USA, 2015.
[18] Berke, N. S. and Hicks, M. C.,'Predicting times to corrosion from field and laboratory chloride data', in'Techniques to assess the corrosion activity of steel reinforced concrete structures', ASTM STP 1276, USA, 1996, 41-57.
[19] Issa, M. A., Khalil, A.A., Islam, S. and Krauss, P.D., 'Mechanical properties and durability of high performance concrete for bridge decks', *PCI J.,***53**(4), 2008, 108-130.
[20] Loulizi, A., Al-Qadi I. L., and Diefenderfer, B. K., 'Effects of nitrite based corrosion inhibitor on concrete's rapid chloride permeability values and its dielectric properties',*ACI Mat. J.*, **97** (4),2000, 465-471.
[21] ASTM G 1,'Standard practice for preparing, cleaning, and evaluating corrosion test specimens. Annual book of ASTM standards', American Society of Testing and Materials, USA, 2015.
[22] Hansson, C. M., Poursaee, A. and Laurent, A. 'Macrocell and microcell corrosion of steel in ordinary Portland cement and high performance concretes', *Cem. Con. Res.,*36, 2006, 2098-2102.

Durability Performance of Concretes Made with Different Cement Types

Fabrizio Moro[(1)] and Roberto Torrent[(2)]

[(1)] LafargeHolcim, Lyon, France

[(2)] Materials Advanced Services Ltd., C1425ABV Buenos Aires, Argentina

ABSTRACT

18 concrete mixes with w/c ratios 0.40 (380 kg/m³ binder) and 0.65 (280 kg/m³ binder) were prepared changing only the cement type. The cements covered EN 197 Types I, II/A, II/B, III/A, III/B, IV/A, and IV/B. The potential durability of those concretes was assessed by several short term tests (mass transport of water, gases and ions and accelerated carbonation). All tests but one (O_2 diffusivity) are covered by national or international standards. The paper presents the results obtained and discusses the influence of w/c ratio and cement type on the performance of the concretes. The correlation between different tests is also discussed, in view of developing performance based specifications.

Keyword: Durability, performance based specifications, accelerated carbonation, mass transport, O2 diffusivity

1 INTRODUCTION

Today's most important concrete standards and codes (ACI 318 [1], Eurocode 2 [2], EN 206-1 [3], AASHTO [4]) follow a prescriptive approach to care for the durability of concrete structures. All those standards establish maximum limits to the w/c (or w/cm) ratio of the mixes, as function of the severity of the environments to which the concrete structures will be exposed. In some cases [3,4], a minimum amount of cement (binder) is also specified for each exposure class. For concretes exposed to frost, a range of entrained air content is also specified. This means that, to a large extent, the composition of the concrete mix is already fixed by the specifications.

Regarding the cement types that can be used, most standards specify sulphate-resisting cements (binders) for concrete exposed to sulphate-bearing soils or water. For other deterioration mechanisms, in particular to chloride- or carbonation- induced corrosion, no specific cement types are specified in standards [1-4]. In the case of EN 206-1, national annexes put some limits to the types of cement that can be used for certain exposure classes [5,6], with criteria that are very different for each country (from very restrictive, like in Germany, to very permissive, like in Italy).

Prescriptive standards consist of the "Deemed-to-satisfy" approach [5] to specify durability requirements. In it, based on the accumulated experience in many countries, a set of primarily prescriptive rules has been established which, when rigorously observed, should result in a service life typically of 50 years (Eurocode 2).

This prescriptive approach assumes that all concrete constituents are "commodities" that can be used indifferently, and that an identical performance would be achieved with any set of them. Anyone that has been involved in concrete mix design knows that, at least for strength, this is not true and that the materials, especially the cement type and characteristics, play an important role on the performance of a concrete of given proportions.

There is no reason to believe that the above does not apply to durability, although here there is an extra complication in that the performance of the concrete has been, traditionally, evaluated in the long term.

In recent years, a series of 'short-term durability tests' have been developed (with several standardized), capable of giving an indication of the potential durability of a concrete mix by measuring its resistance to the transport of matter. A special case is the accelerated carbonation test, in which the rate of carbonation is measured under 'optimal' conditions (temperature, moisture, CO_2 concentration) for the reaction to progress fast.

The above mentioned tests measure properties that can be regarded as 'Durability Indicators' [5].

The objective of this paper is to present results of 'Durability Indicators' obtained on 18 concrete mixes of fixed compositions, made with 9 widely different industrial cements. These results shall give a good indication on whether the prescriptive standards premise (same composition same performance) holds and, if not, how the different systems behave under such tests.

2 EXPERIMENTAL PROGRAMME

2.1 Concrete Mixes

A total of 18 concrete mixes, 9 with w/c=0.40 and 380 kg/m³ of binder and 9 with w/c=0.65 and 280 kg/m³ of binder, were prepared.

Standard aggregates used in Holcim's Concrete Lab were proportioned to achieve overall gradings following DIN B for mixes with w/c=0.40 and one, slightly finer, falling in between DIN B and Fuller, for mixes with w/c=0.65. Maximum size was 20 mm. Most mixes had a consistency within "plastic" range F3 of EN 206-1.

A conventional WR, Sikament 210 S was added to most mixes with 0.65 w/c ratio, in the dosage required to achieve the desired consistency of the concrete. A HRWR, Glenium C327 was added to the mixes with 0.40 w/c ratio in the dosage required to achieve the desired consistency of the concrete.

2.2 Binders

Each pair of mixes (w/c=0.40 and 0.65) was prepared with a different binder, covering a wide range of compositions, as described in Table 1.

The first letter of the code indicates the clinker used to produce the cements (H: Höver, Germany; M: Merone, Italy). The values in brackets indicate the content and type of mineral additions originally included in the cement (MIC). When a mineral addition was added separately as SCM into the concrete mix, the content and type is indicated in italics.

Table 1: Binders used in the Concrete Mixes

Code	Brand (MIC) + *SCM*	EN Class
H0	Holcim Pur-5N	CEM I 52.5 N
H8M	92 % Holcim Pur-5N + *8% Silica Fume*	CEM II/A-D
H22S	Holcim Ferro 4 (22% GBFS)	CEM II/B-S 42.5R
H41S	Holcim Duo 4 (41% GBFS)	CEM III/A 42.5 N
H68S	Holcim Aqua 4 (68% GBFS)	CEM III/B 42.5 L
M0	I 52,5 R	CEM I 52.5 R
M26L	II/B-LL 32.5R (26% Limestone)	CEM II/B-LL 32.5 R
M31FL	IV/A 32,5 R (27% Fly Ash + 4% Limestone)	CEM IV/A 32.5 R
M40FL	87% IV/A 32,5 R +*13% Fly Ash*	CEM IV/B 32.5

2.3 Properties Measured and Test Procedures

Table 2 presents a summary of the relevant properties measured, the test methods (and relevant standard) applied and the specimen type and preconditioning employed. All specimens were cured under water (20°C) for 28 days (except for Test #10). All the mixes were prepared and specimens cast and water cured at EMPA concrete laboratory.

Out of the 10 tests, #2 to #9 measure some transport property of the concrete:

- #2 and #3 water transport
- #4 to #6 gas transport
- #7 to #9 ions transport

The results of all transport tests reported indicate the relative easiness with which matter is transported through the concrete. This is why electrical conductivity instead of its reciprocal (resistivity) has been chosen as durability indicator.

All applied transport tests are relatively fast, ranging from seconds (#7) and few minutes (#5) to few days (#3, #6 and #9). Hence all of them, in principle, provide durability indicators suitable for performance specifications.

The coefficient of oxygen diffusion D_O was measured by exposing one flat face of the sample to a stream of oxygen and the opposite face to a stream of nitrogen at equal pressure and temperature. The rate of diffusion of oxygen is determined by measuring the oxygen concentration in the nitrogen stream.

The coefficient of capillary suction a_{24} was calculated as:

$$a_{24} = m / (A \cdot t^{1/2}) \quad (1)$$

where: a_{24} = coefficient of capillary suction (g/m²/s$^{1/2}$); m= mass of water absorbed in 24 h (g); A = cross section of the specimen (m²); t = absorption time (s).

Table 2: Properties Measured and Test Procedures

Test #	Symbol (Unit)	Property(Standard)	Specimens, Preconditioning
1	f'_c (MPa)	Cube Compressive strength (SN EN 12390-3 [9])[@]	3# 150 mm cubes
2	WP (mm)	Water Penetrationunder Pressure (EN 12390-8 [10]) [#]	3# 150 mm cubes tested after removal from curing bath. Value reported is the maximum water penetration of the specimen.
3	a_{24} (g/m²/s^{½})	CapillarySuction (SIA 262/1-A [11]) [#§]	3# Ø50×50 mm discs drill+cut of a cast 150mm cube. Prior to testing, 2 d. oven-drying at 50°C
4	kO (m²)	"Cembureau" OxygenPermeability(RILEM PCD 116 [12]) [§]	3# Ø150x50 mm discs cut of a cast Ø 150×300 cylinder. Prior to testing, 6 d. oven-drying at 50°C.
5	kT (m²)	"Torrent" AirPermeability (SIA 262/1-E [11])[§]	
6	D_O (m²/s)	Oxygen Diffusion (EMPA Method) [@]	3# Ø150×50 mm discs cut of a cast Ø 150×300 cylinder. Prior to testing, 7 d. in dry room (20°C, 35%) + 7 days oven-drying at 50°C
7	σ (S/m)	"Wenner" Electrical Conductivity (AASHTO TP95 [13]) [§]	120×120×360 mm water cured prism, using 4-point AC-resistivity setup with four stainless steel electrodes positioned unidirectional.
8	RCPT (Coulomb)	ChloridePenetration (ASTM C1202 [14])[§]	3# Ø50×50 mm discs drilled+cut of a cast 150mm cube
9	M_{Cl} (m²/s)	"Tang-Nilsson" Chloride Migration (NT Build 492 / SIA 262/1-B [11]) [#]	3# Ø100×50 mm discs were drilled+cut from 150 mm cubes and water saturated
10	K_N (mm/y^{½})	'Equivalent Natural' Carbonation Rate from accelerated carbonation test (SIA 262/1-I [11])[§]	120×120×360 mm prism, 3 d. water curing + 25 d. at 20±2°C, 57±3% RHand ≤ 0.15 vol.% CO_2. Then, exposed to accelerated carbonation conditions (20±2°C, 57±3% RH and4.0±0.1 vol% CO2). Carbonation depth measured after 0d, 7d,28d and 63d on freshly broken surfaces. Equivalent natural carbonation rate K_N is converted from measured accelerated carbonation rate K_S with K_N (mm/y^{½}) = 2.6 K_S (mm/d^{½})

Tests were conducted in the following Swiss laboratories: [#] SUPSI, Lugano; [§] Holcim, Holderbank; [@] EMPA, Dübendorf.

3 TEST RESULTS

3.1 Presentation of Test Results

Figures 1 to 10 present the test results for each binder in stacked bars format showing the values for the two mixes with different w/c ratios. The gas transport tests results, given their wide range, are plotted in log scale.

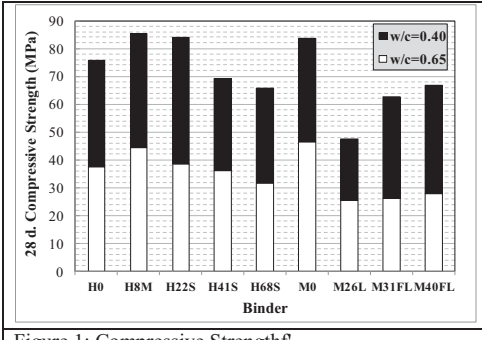

Figure 1: Compressive Strength f'_c

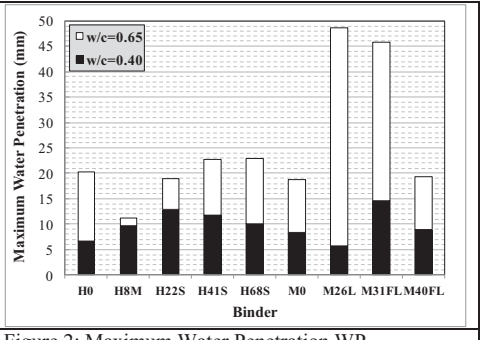

Figure 2: Maximum Water Penetration WP

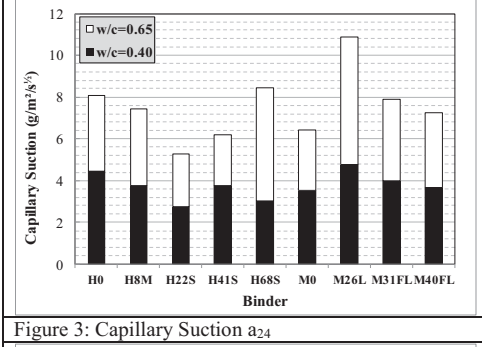

Figure 3: Capillary Suction a_{24}

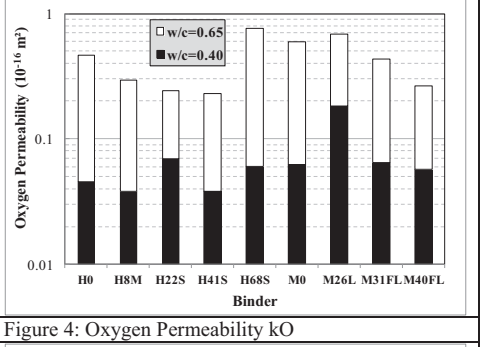

Figure 4: Oxygen Permeability kO

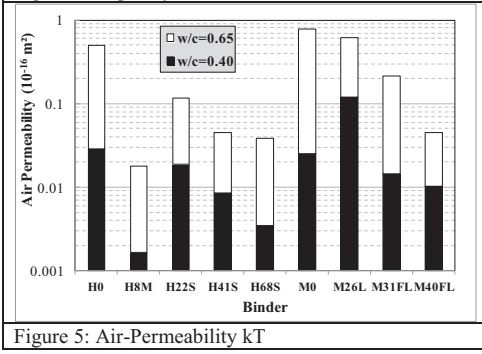

Figure 5: Air-Permeability kT

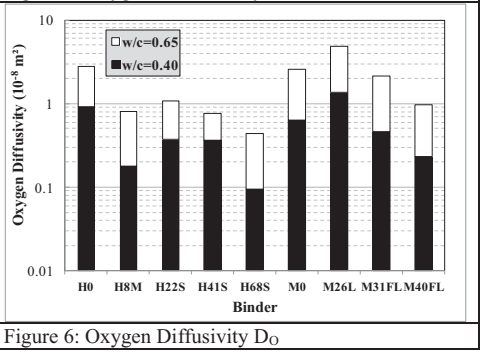

Figure 6: Oxygen Diffusivity D_O

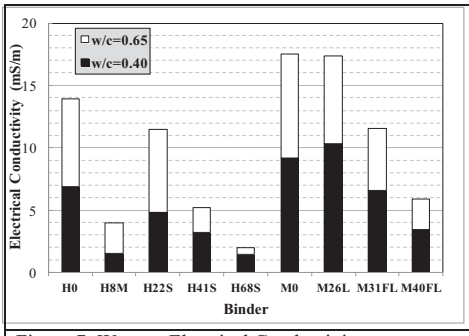

Figure 7: Wenner Electrical Conductivity σ

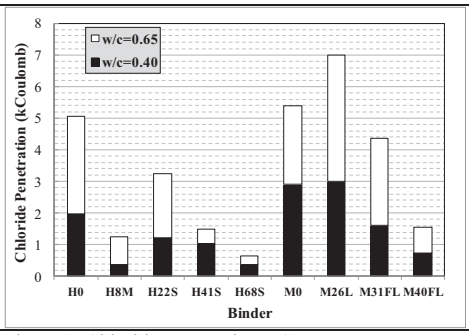

Figure 8: Chloride Penetration RCPT

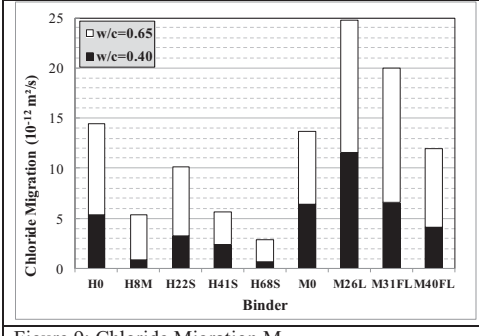

Figure 9: Chloride Migration M_{Cl}

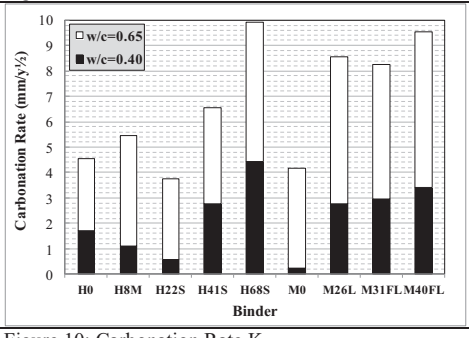

Figure 10: Carbonation Rate K_N

Table 3 presents the ranking of the different binders in terms of performance of the 0.40 w/c ratio mixes. Number 1 indicates best performance and number 9 worst performance. The w/c = 0.40 was chosen for the analysis, because w/c = 0.65 is not compatible with durable concretes.

Table 3: Ranking of binders performance (w/c=0.4 concrete) under the different tests applied

Transport of		Water		Gas			Ions			Overall Transport	
Binder	f'_c	WP	a_{24}	kO	kT	D_O	σ	M_{Cl}	RCPT		K_N
H0	4	2	8	3	8	8	7	6	7	**6**	4
H8M	1	5	6	1	1	2	2	2	1	**1**	3
H22S	2	8	1	8	6	5	5	4	5	**5**	2
H41S	5	7	5	2	3	4	3	3	4	**3**	6
H68S	7	6	2	5	2	1	1	1	2	**1**	9
M0	3	3	3	6	7	7	8	7	8	**6**	1
M26L	9	1	9	9	9	9	9	9	9	**9**	5
M31FL	8	9	7	7	5	6	6	8	6	**8**	7
M40FL	6	4	4	4	4	3	4	5	3	**3**	8

The column before the last one indicates overall rating taking into consideration exclusively the transport tests.

3.2 Analysis of Test Results

The fallacy of prescriptive standards' assumption that w/c alone is a universal durability indicator becomes obvious from Figures 2 to 10. It is evident that the binder type plays as important role as w/c ratio in the performance of the concretes. Indeed, only for a 24 and kO tests was the maximum value for the concrete with w/c=0.40 below the minimum for w/c=0.65 (longest black bar below shortest top bar in Figure 3 and 4). In all the rest of the durability tests, it was possible to find concretes of w/c=0.65, made with certain binders, performing better than concretes of w/c=0.40, made with different binders.

Regarding the transport test results, there is a very good agreement in the results of kT, σ, M_{Cl} and RCPT in judging the performance of the different binders (for w/c=0.40). This is reflected in Figure 11, extracted from Table 3; it can be seen that the four tests rank the binders within a range of ± 1 (except for binder M31FL).

It is interesting to notice that the four tests showed in Figure 11 not only provide similar rankings but also correlate quite well with each other. Table 4 shows the correlation coefficient R between the results obtained by them using 18 concrete mixes.

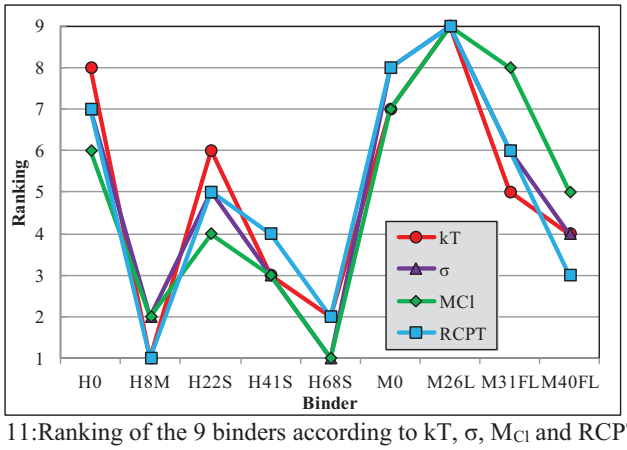

Figure 11:Ranking of the 9 binders according to kT, σ, M_{Cl} and RCPT tests

Table 4: Correlation Coefficients R between kT, σ, M_{Cl} and RCPT tests

R	σ	M_{Cl}	RCPT
kT	0.915	0.862	0.902
σ	---	0.872	0.977
M_{Cl}	---	---	0.914

As shown in Table 3 and Figure 10, the binders showing the best performance in mass transport tests are H8M (8% silica fume) and H68S (68% slag). On the other extreme the worst performance was shown by binder M26L (26% limestone). It is worth mentioning the improvement in performance (compared with the corresponding OPCs H0 and M0) of the binders containing 22% slag (H22S) and about 40% slag or fly-ash (H41S and M40FL).

Figure 9 shows that concretes of w/c=0.40, made with binders H8M, H41S and H68S, reach values of M_{Cl} below 2.5 10-12 m²/s which, according to [6], correspond to "Extremely high resistance to chloride ingress" and are suitable for structures exposed to chlorides for extended periods (provided that a sufficiently thick concrete cover is also provided). For instance a mean value of M_{Cl} = 3.0 10-12 m²/s was adopted for marine tidal and splash zones in the probabilistic service life design (120 years) of the Hong Kong-Zhuhai-Macao link [7].

Canadian standard A23.1-04/A23.2-04 "Concrete materials and methods of concrete construction/Methods of test and standard practices for concrete" specifies for severe chloride exposure a limiting value of 1500 Coulomb (for RCPT test) and of 1000 Coulomb in case of "higher durability performance expectations". Figure 8 shows that concretes with w/c ratio of 0.40, made with binders H8M, H22S, H41S, H68S, and M40FL comply with the limiting value of 1500 Coulomb. For the more demanding limit of 1000 Coulombs, only binders H8M, H41S1, and H68S comply. The test results for carbonation require a separate analysis. In the accelerated test applied, the carbonation depth measured (by the phenolphthalein method) is the result, on the one hand of the easiness with which CO_2 penetrates (diffuses) into concrete and, on the other, on the rate at which $Ca(OH)_2$ is converted into $CaCO_3$ in the carbonation reaction. The first element is considered by the transport tests (especially gas-transport tests), whilst the second depends strongly on the composition of the binder, in a first approximation on its clinker content.

This is best reflected by the case of binder H68S (68% slag) which, being one of the best performing with respect to transport tests, is the worst performing in terms of resistance to carbonation, obviously due to its low clinker content (and, possibly, to the short moist curing time prescribed by the test method). Actually, the best performing binder in terms of carbonation resistance is M0, which is among the worse in terms of mass transport performance. An interesting case is binder H8M (8% silica fume) that shows top performance in transport tests and also a very good performance.

In order to put the carbonation results in perspective, the K_N values (expressed in mm/y½) presented can be interpreted as 1/10 of the carbonation depth reached after 100 years of service. This means that the carbonation depth after 100 years is expected to be less than 20 mm for w/c=0.40 concretes made with binders H0, H8M, H22S, and M0, a very safe level. It is clear from the analysis above that any prescriptive specification must take into consideration the type of binder involved; the same applies if durability indicators based on mass transport are applied. The accelerated carbonation test adopted by Swiss standard 261/1:2013 Annex I seems an interesting tool to design concretes for service life against carbonation-induced corrosion [8].

3 CONCLUSIONS

A series of "Durability Indicators" tests has been applied on a wide range of concretes, both in terms of composition (w/c ratio) and type of binders involved. The main conclusions that can be derived from the results are the following:

1. The water/cement ratio, used by most standards as main "Durability indicator" is not suitable as such because the performance of concretes of same w/c ratio varies enormously with the type of binder involved
2. The best performing binders, in terms of mass transport tests, are H8M (8% silica fume) and H68S (68% slag), followed by H41S (41% slag) and M40FL (40% fly-ash)

[1]In fact, the result at 28 days was 1043 Coulombs, but just 575 at 91 days (not reported here). Since the Canadian Standard accepts test up to 56 days of age, clearly binder H41S complies with the 1000 Coulomb limit.

3. Concretes of w/c=0.40 made with binders H8M, H41S, and H68S showed extremely high resistance to chloride ingress in terms of M_{Cl} and RCPT tests and are suitable for structures exposed to chlorides for extended periods (say 100-120 years)
4. Four standard tests showed great potential to provide suitable "Durability indicators" in view of performance specifications, namely: kT "Torrent" air permeability, $\rho=1/\sigma$ "Wenner" electrical resistivity, M_{Cl} "Tang-Nilsson" chloride migration and RCPT (Coulomb test)
5. The fact that the above-mentioned tests showed coherence and good correlations with each other indicate that kT "Torrent" air permeability and $\rho=1/\sigma$ "Wenner" electrical resistivity tests may be suitable for quality control, given their short duration, with ρ more appropriate for quality control on specimens and kT for site testing of the end-product
6. Transport tests do not give a true picture of the performance of concrete exposed to carbonation, since the chemistry of the cement has a great influence on the carbonation rate. The accelerated test included as Swiss standard constitute an interesting tool for service life design against carbonation-induced corrosion
7. The scenario for introducing performance specification for durability of concrete structures is mature enough. What is needed is courage and vision from the standards committees to move from a clearly unsatisfactory situation (prescriptive specifications) to a more realistic one, based on performance specifications

4 REFERENCES

[1] ACI 318, " Building Code Requirements for Structural Concrete and Commentary", 2014.
[2] EN 1992-1, "Eurocode 2: Design of concrete structures - Part 1-1 : General rules and rules for buildings", 2004
[3] EN 206-1, " Concrete – Part 1: Specification, performance, production and conformity", 2014
[4] AASHTO LRFD Bridge Design Specification. Customary U.S. Units. Sixth edition, 2012.
[5] Andrade, C., "Multilevel (four) methodology for durability design", RILEM Proceedings PRO 47, 2006, 101-108.
[6] Nilsson, L., Ngo, M.H. and Gjørv, O.E., "High Performance Repair Materials for Concrete Structures in the Port of Gothenburg", *Proc. 2nd Intern. Conference of Concrete under Severe Conditions - Environment and Loading*", v.2, ed. O.E. Gjørv, K. Sakai and N. Banthia, E & FN Spon, London, 1998
[7] Li, Q., Li K. F., Zhou X., Zhang, Q. and Fan, Z., "Model-based durability design of concrete structures in Hong Kong-Zhuhai-Macao sea link project", *Struct. Safety*, v.53, 2015, 1-12.
[8] Leemann, A. and Moro, F., "Carbonation of concrete: the role of CO2 concentration, relative humidity and CO2 buffer capacity", *Materials and Structures*,(2017) 50:30
[9] SN EN 12390-3:2009; SIA 262.253:2009,"Prüfung von Festbeton - Teil 3: Druckfestigkeit von Probekörpern"
[10] EN 12390-8:2009, "Testing hardened concrete. Depth of penetration of water under pressure"
[11] SIA 262/1:2013, "Construction en béton - Spécifications complémentaires":
Annex A: "Perméabilité à l'eau"
Annex B: "Résistance aux clorures"
Annex E: " Perméabilité à l'air dans les structures"
Annex I: "Résistance à la carbonatation"
[12] RILEM TC 116-PCD, "Measurement of the Gas permeability of Concrete by the Rilem-Cembureau Method", *Materials and Structures*, v.32, April 1999, 174-179
[13] AASHTO TP 95, "Standard Method of Test for Surface Resistivity Indication of Concrete's Ability to Resist Chloride Ion Penetration", 2014
[14] ASTM C1202, "Standard Test Method for Electrical Indication of Concrete's Ability to Resist Chloride Ion Penetration", 2012.

Prediction of Carbonation-Induced Corrosion Initiation of Steel in RC Structures Exposed to Natural Inland Environment of South Africa

Jacob O. Ikotun, Mike B. Otieno and Yunus Ballim

School of Civil and Environmental Engineering, University of the Witwatersrand, Johannesburg, South Africa

ABSTRACT

While there are many empirical and analytical models to predict carbonation-induced corrosion initiation period in concrete with extensive data presented in literature, most do not capture the necessary parameters to allow their application to steel RC structures exposed to the natural inland environment. In this paper, an empirical model to predict time to carbonation-induced corrosion initiation in concrete is developed based on the 28-day oxygen permeability index (OPI) and the 2-year natural carbonation data of concretes containing 100% PC, 35% fly ash (FA), 50% ground granulated blast-furnace slag (BS), 10% silica fume (SF) and (30% BS + 10% SF) exposed to the Johannesburg natural weather. The concretes were made using 0.40, 0.60 and 0.95 water/binder ratios and initially cured in water for 7 and 28 days. The 28-day OPI was used to characterise and quantify the quality of the concretes. Multiple linear regression analysis using the least squares method is used to develop a model that can be used to predict time to carbonation-induced corrosion initiation in concrete exposed to inland weather conditions. The proposed model showed the combined influence of concrete quality, cover depth and exposure conditions on the predicted carbonation-induced steel corrosion initiation time of the different concretes.

Keywords: Carbonation; corrosion initiation; service life prediction; inland environment

1 INTRODUCTION

Carbonation is one of the leading causes of steel reinforcement corrosion in inland environments. It is a chemical reaction that takes place in concrete when gaseous carbon dioxide (CO_2) dissolves in the concrete pore water to form carbonic acid (H_2CO_3) which then reacts with the calcium hydroxide to precipitate mainly as calcium carbonate as shown in Equations 1 and 2 [1].

$$H_2O + CO_2 \rightarrow HCO_3 + H^+ \quad (1)$$

$$Ca(OH)_2 + 2H^+ + CO_3^{2-} \rightarrow CaCO_3 + 2H_2O \quad (2)$$

Carbonic acid can also penetrate into the pore structure of hardened cement paste through CO_2 dissolved in rainwater. Carbonation reaction causes the depletion of hydroxyl ions in the concrete pore solution and lowers the concrete pH from above 12 to below 9. [2-3]. At this pH, the passive layer of gamma ferric oxide on the surface of the reinforcing steel becomes unstable setting a stage for corrosion to occur in the presence of sufficient oxygen and moisture [4]. The time taken for the carbonation front to reach the reinforcing steel and destroy its passive layer is known as the time to corrosion initiation. The time to corrosion

initiation depends on the rate at which the carbonation front advances in concrete and thickness of the concrete cover. Carbonation rate is defined as the advancement of carbonation front with time in concrete. It is influenced by the exposure conditions (relative humidity-RH, temperature, and atmospheric CO_2 concentration) and quality of concrete. Assuming that the ingress of carbon dioxide inside concrete is constant the dependence of the carbonation depth on time can be expressed using the square root of time law shown in Equation 3 [5].

$$d = Kt^{0.5} \tag{3}$$

where t (years) represents the time at which carbonation front reaches a particular depth in the concrete, d *(mm)* is the carbonation depth, and K (mm/years$^{0.5}$) is the carbonation rate. Previous research by Alexander [6] established the adequacy of the square root of exposure time law for expressing carbonation rate for the Johannesburg locality. This was based on the relative uniform exposure conditions of Johannesburg throughout the year [6]. Equation 4 expresses the time required for the carbonation front to reach the level of the reinforcing steel to initiate its corrosion. At this point of time, the depth of the carbonation front becomes the concrete cover depth as illustrated in Equation 4.

$$t_i = \left[\frac{c}{K}\right]^2 \tag{4}$$

where t_i (years) is time to corrosion initiation of steel and c (mm) is concrete cover depth.

Numerous attempts have been made to predict the time to corrosion initiation of steel in concrete with extensive data presented in the literature. Most of these attempts do not capture the necessary parameters to allow their application to RC structures exposed to the natural inland environment. Some of the existing models that have similar input parameters with this proposed model cannot be suited to predict the time to corrosion initiation in RC structure exposed to the natural inland environment because their exposure coefficients were derived using a particular climate different from the natural inland environment. Concrete material variations as well do not favour the application of these models in the inland environment.

In this paper an empirical model is developed based on carbonation data of concretes containing 100% PC, 35% fly ash (FA), 50% ground granulated blast-furnace slag (BS), 10% silica fume (SF) and (40% BS + 10% SF) exposed to Johannesburg natural weather for a period of 2 years. The concretes were made using 0.40, 0.60 and 0.95 water/binder ratios and 28-day oxygen permeability index (OPI) was used to characterise and quantify their quality. Multiple linear regression analysis (least squares method) was used to establish a relationship between the carbonation rate and the investigated influencing variables. Square root of time law was used to obtain a generalised equation that can be used to estimate the time to initiate carbonation-induced corrosion in concrete.

2 MATERIALS AND METHOD

The various proportions of the mix constituents and the 28-day average compressive strength of the mixtures used are shown in Table 1. The binder materials conform to SANS 50197 Part 1-2: 2000; and SANS 1491-Part 1-3:2005 requirements.The aggregates used were crushed coarse granite (maximum size of 19 mm) and fine granite sand (nominal size of 4.75 mm) that meet the requirements of SANS 1083 (2006) [8]. Concrete (100 × 100 × 100 mm) cube samples were made using water/binder ratios (w/b) of 0.95, 0.60 and 0.40 representing concrete strength grades of < 25 MPa, 25-50 MPa and > 50 MPa respectively for each binder type. Concrete strength grade of < 25 MPa was included to represent the case of unsatisfactory site practices in concrete production [9] while 25-50 MPa and > 50 MPa strength grades are common in concrete applications. Moreover, the decision to use the three

w/b ratios for each of the binder type was to enable comparision of the concretes regarding their investigated properties.

Batching and mixing of the concrete materials were done as described in SANS 10100:2-2000 [10]. To study the effect of early-age moist curing duration on predicted carbonation resistance of the concrete samples, they were cured in water for 7 and 28 days at a temperature of 22±1°C. The concrete samples used for the OPI test were moist cured for 28 days as specified in SANS-3001-CO3-2: 2015 [11].

Table1: Mix proportions and 28-day average compressive strength of the concretes

Mix label	Binders (kg/m^3)				Aggregates (kg/m^3)		Water (kg/m^3)	w/b	Compressive strength (MPa)
	PC	FA	BS	SF	Sand	Granite stone			
PC	255	–	–	–	910	1002	242	0.95	22.6
	350	–	–	–	849	1015	210	0.60	48.7
	450	–	–	–	800	990	180	0.40	70.6
PC-FA	178	77	–	–	910	1002	242	0.95	23.1
	245	105	–	–	849	1015	210	0.60	49.1
	315	135	–	–	800	990	180	0.40	72.2
PC-BS	127	–	128	–	910	1002	242	0.95	14.4
	175	–	175	–	849	1015	210	0.60	33.4
	225	–	225	–	800	990	180	0.40	75.8
PC-SF	230	–	–	25	910	1002	242	0.95	24.2
	315	–	–	35	849	1015	210	0.60	54.6
	405	–	–	45	800	990	180	0.40	87.7
PC-BS-SF	153	–	77	25	910	1002	242	0.95	23.5
	210	–	105	35	849	1015	210	0.60	49.5
	270	–	135	45	800	990	180	0.40	76.2

3 TEST PROCEDURES

3.1 Oxygen permeability index (OPI) test

South African Oxygen Permeability index (OPI) test was used to measure the concretes' permeability. The test is used to assess the overall micro and macrostructure of the near surface of the cast concrete [12]. The test is useful in studying the variation in concrete w/b ratio and binder type. Therefore, OPI test method as specified in SANS-3001-CO3-2: 2015 [11] was followed in this study. This involved passing oxygen gas through a concrete disc sample of size 70 ± 2 mm diameter and 30 ± 2 mm thickness at an initial pressure of 100 ± 5 kPa. As permeation occurred with time, the decrease in pressure with time was measured and converted to the OPI as described in SANS-3001-CO3-2: 2015 [11]. An average OPI measurement of 4 identical concrete disc samples represents the OPI of that particular concrete mix. For a given concrete, a higher OPI represents a less permeable

concrete (high quality) while a lower OPI represents a more permeable concrete (low quality).

3.2 Carbonation test

After curing the concrete cube samples in water for 7 and 28 days respectively, they were exposed to the natural inland environments (indoor, outdoor sheltered and unsheltered from rain) and carbonation depths were measured at 6, 12, 18 and 24 months. The exposure conditions were chosen based on classification specified in BS EN 206-1 2006 [13] as XC1, XC3 and XC4 representing moderate, less-severe and severe carbonation-induced corrosion exposures. Phenolphthalein indicator test was used to determine the carbonation resistance of the concrete samples at 6, 12, 18 and 24 months of exposure. For each sample 12 measurements (3 measurements on each side face) were taken and an average of 36 readings on 3 identical specimens was reported as the carbonation depth of that particular concrete mixture at a testing period.

4 RESULTS AND DISCUSSION

4.1 Oxygen permeability index

The results of the 28-day oxygen permeability test conducted on the different concrete disc specimens are presented in Figures 1. As shown in Figure 1, there are significant differences in the mean OPI values for the same concrete at different w/b ratios; concrete becomes more permeable as w/b ratio increases. This trend is common to all the concrete types and can be attributed to the increased capillary porosity of their cement paste and interconnectivity of the pores which increases along with an increase in the w/b ratio [14–16]. The increased capillary porosity at higher w/b ratio can be attributed to its lower binder content which causes inefficient packing of the cement particles with the aggregates [17].

A discernible trend between the OPI and binder type is also noted but not as much as that between the OPI and w/b ratio. At the same w/b ratio, the SCM blended concretes are less permeable than the PC concretes. This can be attributed to the effect of pozzolanic reaction and complex products of hydration reaction of the SCM (forming new CSH phase) [18]. These products tend to block the capillary pores resulting in a denser microstructure with a finer pore structure [18]. The SCM particle sizes are noted to be smaller than PC particles; such a feature is beneficial in controlling the width of cement packing with aggregates. However, the BS blended concretes behaved differently and are more permeable compared to the other SCM concretes at all the w/b ratios considered. This can be attributed to the inability of the BS blend at the early age (28 days) to attain its full reactivity potential in refining its pore structure which is also evident in their compressive strength results as shown in Table 1. The inability of the BS blend to attain its full reactivity potential at 28 days of moist curing may be due to the lower PC content of the BS blended concrete mixture compared to the other SCM blended concretes.

The improved performance of the SF blended concretes compared to the other concretes can be attributed to its early reactivity and a higher degree of its particle fineness as noted by various researchers [19–22]. The results of the permeability test obtained in this study clearly reflect the influence of w/b ratio and binder type on the overall pore structure of the concretes and therefore can be used as part of the input parameters in an empirical model that can reasonably predict carbonation rate in concretes.

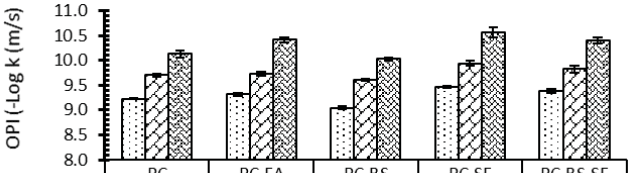

	PC	PC-FA	PC-BS	PC-SF	PC-BS-SF
0,95 w/b	9.23	9.32	9.04	9.47	9.39
0,60 w/b	9.70	9.73	9.60	9.94	9.82
0,40 w/b	10.13	10.41	10.03	10.56	10.40

Figure 1: 28-day OPI results (error bars represents $\mu \pm (\sigma / n^{0.5})$)

4.2 Carbonation rate

A typical plot of carbonation depth against the square root of the exposure time is shown in Figure 2. A linear regression line was fitted to the carbonation data (Note that carbonation depth was assumed to be zero at the beginning of the exposure, this was based on a research finding by Ikotun [23] where concretes tested for accelerated carbonation at 7 days exposure showed no sign of carbonation. The slope of the regression line defines the carbonation rate of the concretes. The measured carbonation rates (K) of the concretes are presented in Figures 3 and 4 where variability in the carbonation rate results is evident. The variability can be attributed to the influences of the exposure conditions at the respective concrete locations, the permeability of the concretes as evident in Figure 1 and duration of the initial moist curing conditions.

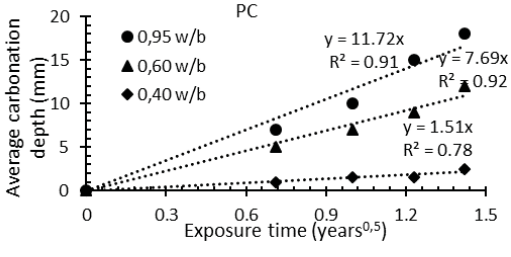

Figure 2: Carbonation depth vs square root of the exposure time – PC concrete

As shown in Figures 3 and 4, the ranking of the carbonation rate (maximum to minimum) regarding their exposure conditions is given as indoor → outdoor sheltered → outdoor unsheltered. The order of carbonation rate (maximum to minimum) regarding the binder type is given as: PC-SF → PC-BS-SF → PC→PC-FA → PC-BS, while increasing the early-age moist curing duration increased the carbonation rate of the concretes as shown in Figures 3 and 4.

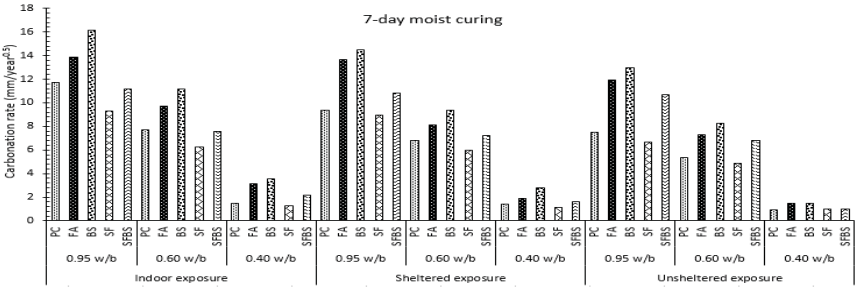

Figure 3: Carbonation rate of the concretes initially moist cured for 7 days

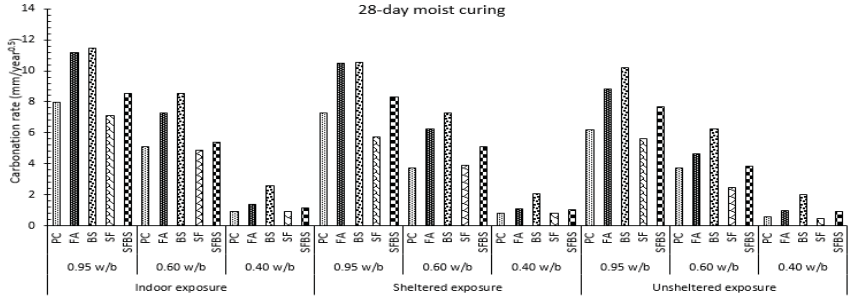

Figure 4: Carbonation rate of the concretes initially moist cured for 28 days

4.3 Carbonation rate prediction model

Concrete deterioration starts from its exposed surface; hence a knowledge of its surface properties is important to predict its performance against carbonation (Ballim & Alexander 2005). The fact that the reinforcing steel is close to the near surface makes the cover concrete an important factor in concrete deterioration. This means that prescription of rate-controlling factors of concrete deterioration, that is the operating environmental conditions and quality of concrete in terms of gaseous transport properties become important parameters in the carbonation rate prediction model. Therefore, a general carbonation rate model is developed as shown in Equation 5 using multiple regression analysis (least squares method). The outputs of the regression analysis are presented in Table 2.

$$K_{c,j} = \beta_3 - \beta_4(OPI) + \beta_5 I_{Indoor} + \beta_6 I_{Sheltered} + \beta_7 I_{Unsheltered} + \beta_8 I_{C7} + \beta_9 I_{C28} \quad (5)$$

where $K_{c,j}$ (mm/year$^{0.5}$) represents carbonation rate of a particular concrete. Carbonation rate is further expressed in terms of binder type, j (PC, PC-FA, PC-BS, PC-SF and PC-BS-SF) as shown in Table 2. For example, K_{cPC} means the estimated carbonation rate of the PC concrete. The *OPI* represents 28-day oxygen permeability index and subscripts C7 and C28 represent 7 and 28 days moist curing conditions. The coefficients associated with the input variables are also given in Table 2. The possible value of I shown in Equation 5 is 1 or 0. The value of I is 0 if its subscript does not apply to the concrete in question and 1 if it does apply to the concrete in question.

Table 2: Regression slopes, coefficients and adjusted R^2 for Equation 5

Carbonation rate, $K_{c,j}$ (mm/year$^{0.5}$)	Regression slope	Regression coefficients						R^2
	β_3	β_4	β_5	β_6	β_7	β_8	β_9	
$K_{c,pc}$	81.50	8.08	1.77	0.88	0	1.75	0	0.9381
$K_{c,PC\text{-}FA}$	93.97	9.08	1.91	1.05	0	2.11	0	0.9787
$K_{c,PC\text{-}BS}$	103.90	10.00	2.18	1.01	0	2.23	0	0.9439
$K_{c,PC\text{-}SF}$	60.70	5.80	1.43	0.87	0	1.51	0	0.9547
$K_{c,PC\text{-}BS\text{-}SF}$	84.60	8.14	0.83	0.51	0	1.91	0	0.9787

Table 2 also shows the adequacy of the regression model, the R^2 (usually used for testing the adequacy of multiple regression model [25]) is greater than 0.93 at 95% confidence level in all the concretes. The analysis of the regression results shows that more than 93% of the variability in the carbonation rate can be explained by the three input variables used (concrete permeability, exposure conditions, and duration of initial moist curing conditions) while less than 7% is due to other causes that were not investigated in this study. It is therefore concluded that the model has a strong correlation between the output and input variables for all the concretes. Therefore, the proposed model demonstrates that the input variables are capable of describing the carbonation rate.

4.4 Time to corrosion initiation model

The model used to predict the time to corrosion initiation is expressed as shown in Equation 7. The Equation 6 is obtained by using the square root of time law expressed in Equation 4. The resulting equation represents the carbonation-induced corrosion initiation model for the concretes. The model can be used to estimate the time to initiate corrosion in RC structure exposed to the inland environment when the concrete cover depth is known, assuming that corrosion is immediately initiated carbonation reaches the steel reinforcement.

$$t_{i,j} = \left[\frac{c}{K_{c,j}}\right]^2 \tag{6}$$

where $t_{i,j}$ (mm/year$^{0.5}$) represents the time to corrosion initiation of a particular concrete which is further expressed in terms of its binder type, j (PC, PC-FA, PC-BS, PC-SF and PC-BS-SF).

Figures 5a, 5b, 6a, and 6b show the graphical representation of the time to corrosion initiation prediction model. The model parameters were arbitrarily selected to demonstrate the potential of using the empirical corrosion initiation time model to objectively compare potential durability performance of a concrete with different permeability, exposure conditions, early-age curing duration, binder type and cover depth. The analysis was done by varying a particular input parameter while other input parameters were kept constant.

(i) Effects of cover depth and exposures on the predicted time to corrosion initiation

It is evident from the results presented in Figure 5a that the predicted time to corrosion initiation increases when concrete cover depth is increased from 10 mm through to 100 mm for a given concrete and exposure conditions. This may be attributed to the fact that the

proportion of carbonating material in a larger cover is greater compared to a smaller cover depth. It is understood that the greater the amount of carbonating material in concrete the longer time it takes carbonation reaction to being completed.

It is also observed in Figure 5a that the variation in the predicted corrosion initiation time is quite distinct at some greater cover depths compared to the lower cover depths. This may be attributed to the early drying of the concrete surface immediately after wetting of the outdoor concretes which allows early resumption of carbonation in a lower cover depth. This shows that at some lower cover depths, variation in inland exposure conditions may not have any significant effect on natural carbonation process in concrete.

Figures 5a and 5b also show the influence of the exposure conditions on the predicted time to corrosion initiation. It can be observed that the predicted initiation times are delayed for the concretes exposed to outdoor environments compared to indoor exposed concretes. Considering the outdoor exposed concretes, the predicted time to corrosion initiation is greater for the outdoor unsheltered concrete compared to the sheltered concrete. This can be attributed to the frequent wetting of the outdoor unsheltered concrete by rain which hinders the flow of CO_2 when concrete pores are saturated with water. In the case of indoor concretes, their shorter initiation time can be attributed to the relatively higher concentration of CO_2 usually found within the indoor environment (due to its lower degree of ventilation) compared to the outdoor exposures [6,15].

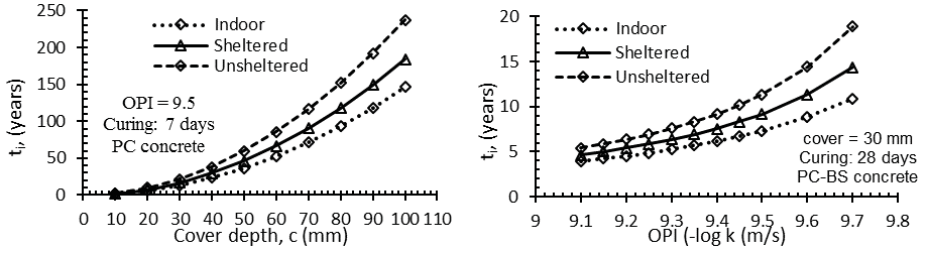

(a) (b)

Figure 5: Effect of (a) cover depth and (b) permeability on predicted corrosion initiation time

(ii) Effect of concrete quality on the predicted corrosion initiation time

Figure 5b shows the relationship between the predicted corrosion initiation time and the concrete quality. It is found that at a constant cover depth and exposure condition the predicted corrosion initiation time increases with increasing concrete quality. A more permeable concrete (low quality) is characterised by many and large interconnected capillary pores, which can easily allow the penetration of CO_2 and moisture into concrete leading to a higher carbonation rate. This reduces the corrosion initiation time compared to a lesser permeable concrete which is characterised by smaller pore spaces and lower degree of pore interconnectivity. In addition, the amount of carbonating material is smaller and can be quickly consumed by the carbonation reaction in a lower quality concrete compared to a higher quality concrete.

The variation in the predicted time to corrosion initiation of the concretes in terms of their binder type is shown in Figure 6a. The order of ranking (longest to shortest initiation time) is given as PC-SF → PC → PC-BS-SF → PC-FA → PC-BS. This order of ranking shows the dominating influence of permeability and pozzolanic activities of the concretes blended with the SCM on the predicted time of corrosion initiation. The proposed model also reflects the importance of early moist curing period on the concretes. A concrete initially moist cured for

28 days can be seen with an extended predicted corrosion initiation time compared with a similar concrete moist cured for 7 days as shown in Figure 6b. This can be attributed to the higher degree of hydration experienced by the concretes cured in water for a longer duration compared to the same concretes cured in water for a shorter period.

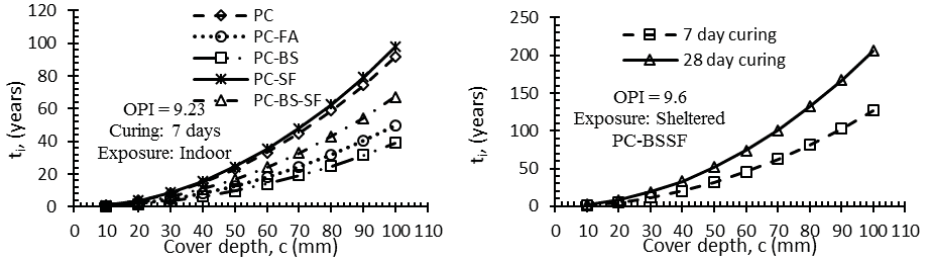

(a) (b)

Figure 6: Effects of (a) binder type (b) duration of moist curing on time to corrosion initiation

5 CONCLUSION

- The results of the permeability test clearly reflect the influence of w/b ratio and binder type on the overall pore structure of the concretes.
- Increasing the cover depth delayed the predicted time to corrosion initiation of the reinforcing steel in all the concretes.
- The order of predicted time to corrosion initiation (maximum to minimum) in terms of the exposure conditions is given as: indoor → outdoor sheltered → outdoor unsheltered.
- The order of predicted time to corrosion initiation (maximum to minimum) regarding the binder type is given as: PC-SF → PC-BS-SF → PC→PC-FA → PC-BS.
- Increasing the early-age moist curing duration increased the predicted time to corrosion initiation of the concretes.

6 REFERENCES

[1] Visser J. H. M. Accelerated carbonation testing of mortar with supplementary cementing materials - Limitation of the acceleration due to drying. HERON 2012; (2012), 57p.

[2] Zhou Y, Gencturk B, Willam K, Attar A. Carbonation-Induced and Chloride-Induced Corrosion in Reinforced Concrete Structures. J Mater Civ Eng 2014. [3] Loo YH, Chin MS, Tam CT, Ong KCG. A carbonation prediction model for accelerated carbonation testing of concrete. Mag Concr Res 1994:191–200.

[4] Ballim Y, Lampacher BJ. Long-term carbonation of concrete structures in the Johannesburg environment. SAICE 1996:5–9.

[5] Schiessl P. Corrosion of Steel in Concrete, Report of Technical Committee 60-CSC. Chapman and Hall, London, New York, 1988: 1988.

[6] Alexander MG, Mackechnie JR, Yam W. Carbonation of concrete bridge structures in three South African localities. Cem Concr Compos 2007;29:750–9.

[7] SANS 50197-2 : 2000. South African National Standard Cement Part 2 : Conformity evaluation. 2000.

[8] SANS 1083. South African Standard: Aggregates from natural sources-Aggregates for concrete. 2006.

[9] Adewole KK, Ajagbe WO, Arasi IA. Determination of appropriate mix ratios for

concrete grades using Nigerian. Leonardo Electron J Pract Technol 2015:79–88.
[10] SANS 10100:2-2000. South African Standard:The structural use of concrete Part 2: Materials and execution of work. Pretoria: 1992.
[11] SANS 3001-CO3-2. South African Natioanl Standard Civil engineering test methods Part CO3-2 : Concrete durability index testing — Oxygen permeability test. Pretoria: 2015.
[12] Salvoldi BG, Beushausen H, Alexander MG. Oxygen permeability of concrete and its relation to carbonation. Constr Build Mater 2015;85:30–7.
[13] BS EN 206-1. Part 1: Method of specifying and guidiance for specifier. Johannesburg: 2006.
[14] Salvoldi BG. Modeling the carbonation of concrete using early age oxygen permeability index tests. University of Cape Town, 2010.
[15] Alhassan AY. Effects of materials and micro-climate variations on predictions of carbonation rate in reinforced concrete in inland environment. PhD Thesis, University of the Witwatersrand, 2014.
[16] Ananmalay N. Characterising the strength and durability performance of South African Silica fume concretes. MSc thesis. University of the Witwatersrand, 1996.
[17] Garboczi EJ. Microstructure and transport properties of concrete. In: Kropp J, Hilsdorf H., editors. Perform. Criteria Concr. Durab., London: E & FN SPON; 1995, p. 198–212.
[18] Mehta PK. Pozzolanic and Cementitious By-Products as Mineral Admixtures for Concrete - A critical Review. Proc First ACI/CANMET Int Conf Use Fly Ash, Silica Fume, Slag, Other Miner By-Products Concr Montebello, Canada,Vol 1, ACI SP-79 1987;1:1–46.
[19] Terence CH. Silica Fume User's Manual. Lovettsville, VA: 2005.
[20] King D. The Effect of Silica Fume on the Properties of Concrete as Defined in Concrete Society Report 74, Cementitious Materials. 37th Conf. Our World Concr. Struct. 29 - 31 August 2012, Singapore: 2012.
[21] Arum C, Moya D. Effect of packing densities of aggregates on the workability and compressive strength. 4th West Africa Built Environ. Res., 2012, p. 301–14.
[22] Buss K. Ternary combination concretes using GGBS , fly ash & limestone. university of Dundee, 2013.
[23] Ikotun JO. Benefits of utilising oil drill cuttings as filler replacement in cement and ternary cement concretes. MSc. thesis. University of Dundee, UK, 2010.
[24] Ballim Y, Alexander MG. Towards a performance based specification for concrete durability. African Concr. Code Symp., 2005, p. 206–18.
[25] Montgomery DC, Runger GC. Applied statistics and probability for Engineers. Fifth. Danvers: John Wiley & Sons, Inc.; 2011.

Suitability of Accelerated Test Methods as a Tool for Service Life Prediction for RC Structures Made of Ordinary Portland and Blended Cement

V.V Arora and Puneet Kaura

National Council for Cement and Building Materials, India

ABSTRACT

During the last two decades, concrete had encountered with the problem associated to its destruction through the attack by external agents like chlorides, carbon dioxide and other deleterious substances. In order to solve this problem, extensive research had been carried out in the field of SCM's as a part replacement of cement whose purpose is to serve as a durability enhancer for concrete to ensure longer service life. In our research study thrust has been laid to discover a suitable accelerated testing technique which would serve as a tool for service life prediction for RCC consisting of SCM's exposed to chloride environment. Present study deals with three varieties of cement, one non-blended cement (OPC) and other two cements blended with slag and fly ash. Generalized curves are drawn in order to rationalize the behavior of different varieties of cements against the various accelerated test methods for six w/c ratios. The results of accelerated tests are compared with conventional chloride diffusion test done by immersion method. The purpose of formulating these generalized curves is to develop a performance based service life design guidelines and quality control measures for evaluating concrete durability in the field made with these binders.

Keywords: RCPT, NT build 492, Electrical Resistivity and Air permeability

1 INTRODUCTION

Concrete and steel are commonly used together in reinforced concrete structures. Such type of materials matrix exhibit desirable engineering properties, the most important of which is strength. However, corrosion of the steel reinforcement which is governed by the durability aspect of concrete is a serious problem for structures exposed to a chemically aggressive environment. Corrosion of reinforcement not only affects the performance and serviceability of the RCC structure as a whole but also reduces the ductility of the load carrying members [1].

Use of supplementary cementitious material like fly ash, slag and silica fume in different proportions as a part replacement to Ordinary Portland cement have shown improved behavior compared to Ordinary Portland cement in aggressive environment especially chloride rich atmosphere[2-3]. In certain Nordic countries use of 3 to 5 % of silica fume is mandatory under the severe environment. Polder (1996) and Maochieh Chi (2012) in their respective study with the help of different durability test methods like RCPT, NT build 492, electrical resistivity etc clearly depicts positive semblance of supplementary cementitious materials under chloride environment [4-6]. But cautions of doubt always exist over the

acceptability of accelerated durability test methods as the process of chloride ion transportation is implicit in nature.

Ingress of chlorides into the concrete is generally quantified in terms of chloride diffusion coefficient. In order to determine chloride diffusion coefficient in concrete a number of test methods are available but reliability is the major concern. Most of the conventional chloride diffusion test methods are laborious and time consuming in nature [7-10]. During past, in order to obtain quick/instant information regarding chloride ion penetration, numerous attempts had been made to develop conventional test methods/techniques based upon the concept of steady state and non-steady state ion migration. Accordingly tests like rapid chloride penetrability test method (RCPT) and NT build 492 (non-steady state chloride migration test) were developed. These test methods does not requires much time and less expensive in comparison to conventional chloride diffusion test methods. The advancement in technology has seen non- destructive techniques like air permeability and electrical resistivity come into existence and could be seen as a partial replacement to destructive techniques for the prediction of service life of reinforced concrete structures.

But certainly a check is needed in order to certify the suitability of developed accelerated test methods/techniques. The win ability factor for such test methods could be explored only on the basis of relationship that could be developed between natural process of chloride diffusion and accelerated migration processes involving steady and non-steady state chloride ion transportation. In the last few decades, various studies in this regard had been conducted where researchers had tried to develop correlation between the two processes of chloride ion mobility. Yang et.al (2004, 2005) and Sugiyama et.al (2001) studies had clearly indicated the use of steady state migration technique as a replacement to conventional long term method of chloride ion diffusion [12-14]. But the non-steady state migration method (RCPT) studied by Andrade et.al (2001) and Yang (2004) were not able to generate satisfactory relationship between the charged passed and chloride migration coefficient [11,13].

In general steady state migration test methods are time consuming and test runs for months. In order to save time, the need of the present system is accelerated test methods. The test methods like RCPT, NT build 492 and electrical resistivity which are accelerated in nature are deployed/ utilized during the study. McNally et.al (2005) had conducted series of chloride penetration test over concrete composed of supplementary cementitious material (SCM) like flyash and GGBS and it was seen that rapid migration non- steady state test method i.e. NT build 492 carried out at an age of 28 days was not able to give satisfactory result as desired when comparison had been made with the chloride diffusion coefficients so obtained from immersion test and ponding test [15]. Similar type of concrete composition was studied by Claisse et.al (2010) using NT build 492 at an age of 100 days which shows promising results when comparison was done [16]. Early age accelerated testing should be avoided as the presence of fly ash and GGBS requires greater duration of hydration, so care and experience is required while applying the accelerated migration test in case of concrete substituted with SCM's.

The present research study was conducted at maturity age of 56 days. Early age testing in case of accelerated test methods/techniques was avoided because presence of SCM's would affect the results whereas the chloride diffusion test through immersion had been conducted on 28 days matured concrete samples followed by 90 days exposure to 3 % NaCl solution.

This research paper deals with the behavior of blended cement containing fly ash and slag under chloride aggressive environment and persistence efforts have been made to develop relationship between accelerated test methods with long term durability test method in conjunction to the cement type, so as to predict service life of concrete structures. The generalized curves so developed could be helpful in the formulation of performance based design guidelines for durable structures.

2 EXPERIMENTAL PROGRAM

2.1 Cement

The cements used were Ordinary Portland cement (OPC-43, confirming to IS 269:2015), Portland Pozzolana cement (PPC, confirming to IS 1489 Part-1:2015 with fly ash content up to 30 %) and Portland Slag cement (PSC, confirming to IS 455:2015 with slag content up to 45 %). Its physical and chemical properties are given in Table 1.

2.2 Aggregates

The coarse aggregates (20 mm and 10 mm) and the sand (Zone II), confirming to IS 383 were used in all the concrete mixes. Some of the physical properties of aggregates so used are mentioned in Table 2.

2.3 Admixture

Super plasticizer normal type confirming to IS 9103 was used in concrete mix design.

2.4 Concrete mix composition

The research was primarily conducted on six water/cement ratios (0.36, 0.40, 0.45, 0.50, 0.55, and 0.60) with three different varieties of cement i.e. OPC-43, PPC, and PSC correspondingly resulting into 18 concrete mixes. The concrete mix proportion for all the six w/c ratio's had been described in Table 3 whereas the 28 days compressive strength of the concrete mixes was mentioned in Table 4.

2.5 Specimen preparation and conditioning

For each concrete mix, number of cylindrical specimens (dia =100 mm, height= 200 mm) and concrete slabs (300 x 300 x 100mm) were cast. After 24 hours, the concrete specimens were demoulded and water cured for 28 days. After 28 days of water curing, all the concrete specimens either cylinder or slabs were shifted to controlled laboratory environment of RH= 65 ± 5 % and temp = 27 ± 2 °C till the age of testing. Specific conditioning regime and sample size had been indicated in details for each test.

Table 1: Physical & chemical properties of cement

Sl. No.	Properties	OPC -43	PPC	PSC
(A) Physical Analysis:				
1	Blain's fineness, m^2/kg	285	379	346
	Setting time, minutes			
	Initial	240	135	140
2	Final	295	205	220
	Compressive strength, N/mm^2			
	3 days	34.5	30	26.5
	7 days	42.5	41.5	34.5
3	28 days	57.5	55.5	49
(B) Chemical analysis, % :				
1	Loss of Ignition (LOI)	5.42	1.85	1.89
2	Silica(SiO_2)	19.94	32.20	27.37
3	Iron Oxide (Fe_2O_3)	3.87	3.57	12.01
4	Aluminium oxide (Al_2O_3)	4.16	10.84	1.12
5	Calcium oxide (CaO)	58.56	43.42	47.68
6	Magnesium oxide (MgO)	4.16	4.05	6.60
7	Sulphate (SO_3)	2.21	2.21	1.95

8	Total Alkalies as Na_2O equivalent:	0.792	1.239	1.040
9	Chlorides	0.048	0.001	0.005
10	Insoluble Residue	2.84	26.64	3.50

Table 2: Physical properties of aggregates

Property	**Sand**	**Coarse Aggregate**	
	(Natural)	**20 mm**	**10 mm**
Specific gravity	2.61	2.83	2.83
Water absorption (%)	0.8	0.40	0.40

3 TEST CONDUCTED

3.1 NT Build 492

This is a non-steady state chloride migration test which requires cylindrical concrete specimens of 100 mm diameter and a thickness of 50 mm. An external electrical potential was applied across the sample in order to force the chloride ions to migrate into the concrete. The solutions used in the cathode and anode are a 10% NaCl and a 0.3 N NaOH respectively. This test was initiated by applying a 30 V potential difference across the concrete specimen and thereby measuring the amount of current generated. Then, the applied voltage was adjusted and the test duration is determined. After the test, the sample was split and a silver nitrate solution was sprayed on the concrete surface. The penetration depth was measured from the chloride precipitation, and the migration coefficient was determined through Nernst Planck Equation.

3.1.1 Curing and Conditioning

The test was conducted on concrete specimen at an age of 56 days which includes 28 days water followed by 28 days air curing under controlled laboratory environment.

Table 3: Concrete mix proportion

Sr no	**w/c ratio**	**Type of cement**	**Mix Constituents**					**Air content (%)**
			Cement (kg/m^3)	**Sand (kg/m^3)**	**Coarse aggregate (kg/m^3)**	**Water (kg/m^3)**	**Dose of admixture(% by wt of cement)**	
1	0.36	OPC-43	444	736	1161	160	0.5	1.2
2		PPC	444	701	1152	160	1	3
3		PSC	444	728	1147	160	1	1.2
4	0.4	OPC-43	400	770	1165	160	0.4	1.5
5		PPC	400	727	1170	160	1	2.9
6		PSC	400	762	1153	160	1	1.1
7	0.45	OPC-43	356	805	1169	160	0.4	2
8		PPC	356	764	1170	160	1	2.1
9		PSC	356	799	1160	160	0.6	1.2
10	0.5	OPC-43	320	837	1167	160	0.35	1.8
11		PPC	320	803	1179	160	1	2
12		PSC	320	831	1158	160	0.6	1.1
13	0.55	OPC-43	300	849	1160	165	0.2	1.7
14		PPC	300	788	1178	165	0.8	2
15		PSC	300	863	1131	165	0.55	1.2
16	0.6	OPC-43	280	863	1155	168	0	2.2
17		PPC	300	801	1130	180	0.4	2
18		PSC	280	877	1127	168	0	1.4

Table 4: Compressive strength (in MPa) at 28 days

Type of cement \ w/c	0.36	0.4	0.45	0.5	0.55	0.6
OPC-43	52.63	45.97	42.33	38.26	33.65	28.06
PPC	59.02	53.65	43.72	37.79	35.16	33.7
PSC	48.64	47.57	34.71	33.48	30.67	28.48

3.2 Rapid chloride penetration test (ASTM C1202)

In this test method, a steady external electrical potential of 60 volts D.C potential was applied to the concrete specimen of 50 mm thick and 100 mm diameter for period of 6 hours. The anode and cathode were filled with 0.30 N sodium hydroxide and 3.0% sodium chloride solutions respectively. The total charge passed during the 6 hour test was recorded and used as a measure to chloride ion penetration in concrete.

3.2.1 Curing and Conditioning

The test was conducted on concrete specimen at an age of 56 days which includes 28 days water followed by 28 days air curing under controlled laboratory environment.

3.3 Chloride immersion test, unidirectional diffusion (ISO 1920 Part 11)

In this method, cylindrical specimens (dia. = 100 mm and length =75 mm) were immersed into the 3 % NaCl solution for 90 days and the chloride profile was measured immediately after the exposure by grinding off material into at least eight depth intervals parallel to the exposed surface followed by titration analysis in order to determine acid soluble chloride content in each concrete powder. Through non-linear regression analysis by least squares curve fitting, the non-steady state chloride diffusion coefficients (*Cd*) were determined by the following equation which is also known as Fick's second law of diffusion.

$$C(x,t) = C_s - (C_s - C_i) \times erf\left(\frac{x}{2 \times \sqrt{Cd \times t}}\right)$$

Similarly, chloride diffusion coefficients *(Cd)* were obtained for other w/c ratios

$Cd(t) = Cd(to)\left(\frac{to}{t}\right)^{a}$ Where α represents ageing factor and *Cd(t)* represents a constant equivalent diffusion coefficient giving a similar chloride profile to the measured one for a structure exposed to the chloride environment over a period *t*.

3.3.1 Curing and Conditioning

The test was conducted on 28 days water cured concrete specimen.

3.4 Electrical Resistivity (Four point Wenner Probe method)

The electrical resistivity, inverse of conductivity, is the property of the material that reflects the ability to transport electrical charge [17].In this method four equally spaced probes were applied to the concrete slabs (300x300x100 mm) in a line.

3.4.1 Curing and Conditioning

The test was conducted on concrete specimen at an age of 56 days which includes 28 days water followed by 28 days air curing under controlled laboratory environment. Prior to testing concrete specimen was water saturated for 48 hours.

3.5 Air permeability

This test was conducted on the concrete slabs (300x300x100 mm) which were water cured for 28 days followed by 28 days conditioning in laboratory environment which includes pre-conditioning for 3 days in an environmental chamber under a controlled temperature and RH of 50 °C and 80 %, respectively followed by 10 days storage in sealed container at 27 ± 2 ºC. The concrete slabs were tested at the age of 56 days.

4 RESULTS AND DISCUSSION

4.1 Effect of w/c on conventional/long term durability test method

Figure 1 shows the relationship between chloride diffusion coefficients Cd obtained from immersion test with w/c. Figure 1, shows a very good correlation between w/c ratio and chloride diffusion coefficient value Cd for PPC concrete, PSC concrete and OPC concrete.

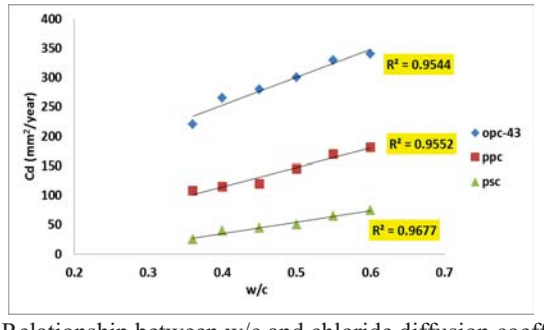

Figure 1- Relationship between w/c and chloride diffusion coefficient *C*d

4.2 *Cd* (chloride immersion test) vs RCPT

The values of chloride coefficient obtained from immersion test is shown in figure 2 and compared with charge passed obtained from RCPT test for the concrete mixes of different w/c ratios. From Figure 2, it was seen that the individual behavior of OPC, PPC and PSC concrete chloride diffusion values with RCPT value resulting in poor correlation whereas figure a fair correlation, not so good correlation between *Cd* with RCPT (coulombs) values was observed when combined together. Figure 2 could be utilized in service life prediction of RC structures on the basis of different category of chloride ion penetrability range as mentioned in ASTM C1202.

4.3 *Cd* (chloride immersion test) vs Cd (NT build 492)

In *Figure* 3, the values of chloride diffusion coefficient obtained from accelerated migration tests NT build 492 (Cd (NT)) is graphically correlated with Chloride diffusion coefficient obtained from chloride immersion (Cd). From Figure 3, Cd values of three types of concrete i.e. OPC, PPC, and PSC when plotted individually against Cd (NT), a good correlation could be seen in case of OPC concrete and a fair correlation in case of PPC concrete whereas in case of PSC concrete, poor correlation was worked out whereas a fair correlation was seen when all three types of concrete matrix.

4.4 *Cd* (chloride immersion test) vs KT (Air permeability coefficient)

The air permeability coefficient value reflects the pore geometry of the concrete specimen which is one of the crucial element in determining durability of cover concrete. Figure 4 shows a very good correlation between *Cd* (chloride diffusion coefficient) and *KT* (coefficient of air permeability value) when plotted individually for different types of concrete as well as universally (on combination) when tested at the age of 56 days.

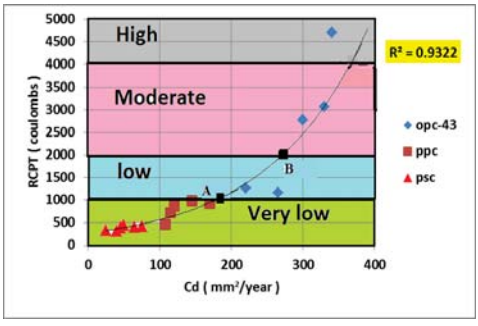

Figure 2- Combined relationship of concrete types between chloride diffusion coefficient Cd and RCPT values - Good correlation

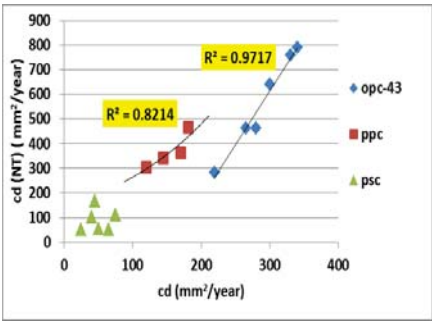

Figure 3- Individual relationship of concrete types between Cd (NT) and Cd values- Fair correlation

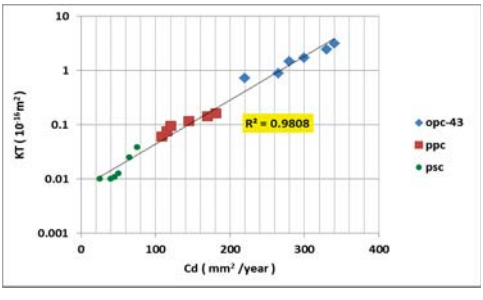

Figure 4- Combined relationship of concrete types between Graph between chloride diffusion coefficient Cd and KT values- Good correlation

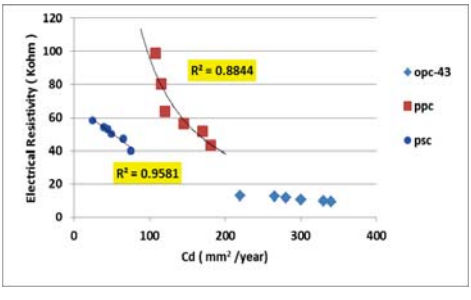

Figure 5- Individual relationship of concrete types between Cd and Electrical Resistivity values – Fair Correlation

In Torrent permeability tester, air permeability coefficients for concrete specimen depend upon the quantum of vacuum so developed. So, in order to achieve a good relationship between chloride diffusion coefficient and air permeability coefficient values, the concrete specimens should be sufficiently dry so as to get pores within the concrete matrix at most free from water [18]. In NCB laboratory, air permeability coefficient values were generated from the concrete specimens which were water cured for 28 days followed by 28 days air curing at controlled temperature and relative humidity conditions. It was found that keeping the concrete specimens into air for time duration of 28 days under controlled environment also had led to the generation of intermediate moisture conditions with the opening of pores which were earlier occupied by the water. This had led to the generation of condition that actually prevails during the service of concrete structure.

4.5 *Cd* (chloride immersion test) vs Electrical resistivity

In Figure 5, the chloride diffusion coefficient values obtained from chloride immersion test is correlated graphically with the electrical resistivity values obtained from concrete specimens at the age of 56 days which includes 28 days of water curing followed by 28 days of air curing. Electrical resistivity of concrete containing blended cement increases with the increase in age. Therefore, correlation curve so generated between Cd and electrical resistivity at later age was more suitable rather than generating the correlation curve at 28

days or earlier ages. Their exist a fair correlation between Cd and electrical resistivity values in case of blended concrete (PPC and PSC concrete) when plotted individually as shown in Figure 5 whereas a poor correlation was seen when all three types of concrete matrix i.e. OPC concrete, PPC concrete and PSC concrete are combined together. Therefore, individual curves should be used in case of blended concrete system rather than a combined curve when generalization is required to predict service life of RC structures on the basis of electrical resistivity test values.

4.6 Service life prediction based upon accelerated / short term durability test methods.

It can be seen that single accelerated/short term durability test method cannot be used for the prediction of service life of RC structures because of variability in the test data. On perusal of results achieved, in case of concrete made from Ordinary Portland Cement, for the determination of chloride diffusion coefficient, chloride diffusion coefficient value obtained from the correlation developed from any of the three tests i.e. RCPT, electrical resistivity and Air permeability can be taken for the service life prediction. However for better results so as to reduce variability two out of three tests can be performed and average value of chloride diffusion coefficient obtained can be used in the model for the service life prediction of RC structures. In case of concrete made from blended Cement, average chloride diffusion coefficient value obtained from the correlation developed from the two test i.e. electrical resistivity and Air permeability value can be taken as a input for the service life design model for concrete structures located in marine environment. Based on the correlation developed, required test values for different tests for the predicted service life of 50 years for RC structures in tidal zone and away from shoreline have been calculated in Table 5 using Fick's second law of diffusion considering ageing factor α as 0.5

Table 5: Required test values for different tests for the predicted service life of 50 years for RC structures made with Portland pozzolana cement (fly ash based)

Sr no	Parameters	Exposure Conditions			RCPT values (coulombs)	Air permeability Coefficient KT ($x10^{-16}$ m^2)	Electrical Resistivity (kohm-cm)
		Tidal Zone	Near Shore Line (Dock yard) [19]	About 0.5 km Away from Shore Line			
1	Threshold value of chloride content (% by weight of concrete)	0.067	0.067	0.067			
2	Surface value of chloride content (% by weight of concrete)	1.5	1	0.5			
3	Required Cover depth for predicted 50 years service life for RC Structures for the following Chloride diffusion coefficient value taken from Fig 6						
3.1	Point A (Cd = 180mm^2/year)	75mm	70mm	55mm	<1000	<0.2	>44
3.2	Point B (Cd =280mm^2/year)	90mm	85mm	70mm	<2000	<1.2	>24

5 CONCLUSIONS

1. Water-cement ratio has considerable effect on the long term durability test and accelerated /short term test methods. The chloride diffusion coefficients values obtained either from chloride immersion test (*Cd*) shows an increasing trend with increase in w/c ratio which is ideal in case of OPC concrete and PPC concrete. But dependency of chloride diffusion coefficient values on w/c is much smaller in case of PSC concrete.
2. Non steady state migration test RCPT shows a good trend with chloride diffusion coefficient generated from immersion test when plotted universally whereas fair correlation was found between chloride diffusion coefficient obtained from chloride immersion test (*Cd*) and NT build 492 (*Cd* (NT)).
3. Electrical Resistivity test and air permeability test correlate well with chloride diffusion coefficient. These tests can be used for the determination of chloride ingress in concrete but such tests are affected by the conditioning of specimen. Therefore due attention is required while using electrical resistivity test and air permeability as a substitute for chloride ingression. For OPC concrete air permeability test shows better relationship in comparison to electrical resistivity test because data range for OPC concrete in electrical resistivity test is narrow.
4. For quality control purposes at construction site, air permeability test and electrical resistivity could be used where durability design of RC structure is done on the basis of chloride diffusion coefficient.
5. In case of concrete made from ordinary portland Cement ,for the determination of chloride diffusion coefficient, average chloride diffusion coefficient value obtained from the correlation developed any of the two test i.e. RCPT, electrical resistivity and air permeability can be taken for the service life prediction and in case of concrete made from blended cement, average chloride diffusion coefficient value obtained from correlation developed from the two test i.e., electrical resistivity and air permeability value can be taken as a input for the service life design model for concrete structures located in marine environment.
6. The correlations developed are valid for the specific curing and conditioning regime adopted under different test conducted in research study
7. Further research work has to be done to obtain more data in order to further enhance the correlations so developed.
8. Time of accelerated tests can be further reduced by adopting accelerating curing techniques (developed for blended cement specifically). Work in this direction is in progress at NCB.

REFERENCES

[1] ISO/FDIS 16204 ‘Durability — Service life design of concrete structures’.

[2] R E Melchers & C Q Li., ‘Reinforcement Corrosion initiation and activation times in concrete structures exposed to severe marine environments’, *Cement and Concrete Research* 39 (2009) 1068-1076.

[3] Faguang Leng, Naiqian, Xinying Lu., ‘An experimental study on the properties of resistance to diffusion of chloride ions of fly ash and blast furnace slag concrete’, *Cement and Concrete Research* 30 (2000) 989-992.

[4] Rob B Polder., ‘The influence of blast furnace slag, flyash and silica fume on corrosion of reinforced concrete in marine environment’, *HERON,* Vol. 41, No. 4 (1996) ISSN 0046-7316.

[5] Rob B. Polder., 'Effects of slag and fly ash in concrete in chloride environment – research from the Netherlands'.

[6] Maochieh chi., 'Durability of concrete containing supplementary cementitious materials', *Journal of WuFeng University*, Vol20.

[7] Eluozo S.N., 'Predictive model to monitor the rate of diffusion chloride ions transport in homogenous concrete structure', *World journal of Science and Technology Research*, Vol1 No.4, June 2013.

[8] A Delagrave, J Marchand and E Samson., 'Prediction of diffusion coefficients in cement-based materials on the basis of migration experiments', *Cement and Concrete Research,* Vol 26 (1996).

[9] Stanish K.D, Hooton R.D and Thomas M.D.A., 'Testing the Chloride Penetration Resistance of Concrete: A Literature Review.' FHWA Contract DTFH61-97-R-00022.

[10] Ahmad Altaf, Kumar Anil., 'Chloride ion migration/diffusion through concrete and test methods'. *International Journal of Advanced Scientific and Technical Research,* Issue 3 Volume 6, Nov.-Dec. 2013.

[11] Castellote M, Andrade C and Alonso C., 'Measurement of the steady and non-steady state chloride diffusion coefficients in a migration test by means of monitoring the conductivity in the anolyte chamber with natural diffusion tests'. *Cement and Concrete Research* 31 pp.1411-1420, 2001.

[12] Yang C.C, Lin S.S and Cho S.W., 'Relation between migration coefficient from accelerated chloride migration test and diffusion coefficient from ponding test', *Kuwait Journal Science. Eng.* 32(2) pp.165-186, 2005.

[13] Yang C.C., 'The relationship between migration coefficient of chloride ions for concrete and charge passed in steady state using accelerated chloride migration test.,' *ACI Materials Journal* 101 pp124-130, 2004.

[14] T.Sugiyama, T.Tsuji and T.W Bremner., 'Relationship between coulomb and migration coefficient of chloride ions for concrete in a steady state chloride migration test', *Magazine of concrete Research*, 2001, Feb, 13-24.

[15] McNally, Ciaran, Richardso, Mark G, Evans, Conor, Callanan & Thomas., 'Chloride diffusion coefficient determination for specification', *Proceedings of the 6th international Congress on global construction* (2005).

[16] P.Claisse and J Lizarazo., 'Determination of the transport properties of a blended concrete from its electrical properties measured during a migration test', *Magazine of Concrete research*, 2010, 62, No3, March, 163-175.

[17] RELIM Recommendation., 'Test method for on-site measurement of resistivity of concrete, Materials and structures', Vol*, 33* December 2000.

[18] VV Arora and Puneet Kaura., 'Durability Testing of blended cement- Relationship between accelerated tests and long term tests' in 2nd ICDC, New Delhi.

[19] A. Costa and J.Appleton., 'Chloride penetration into concrete in marine environment-Part II: Prediction of long term Chloride penetration', *Materials and Structures*. Vol 32, June 1999, PP.354-359.

Comparative Study of Models for Porosity of Cement Paste

Shatabdi Mallick[(1)], M. B. Anoop [(2)] and K. Balaji Rao [(2)]

[(1)] Engineering of Structures, AcSIR, CSIR-SERC, Chennai, India

[(2)] Risk & Reliability of Structures, CSIR-SERC, Chennai, India

ABSTRACT

The complex microstructure of hydrating cement paste, comprises of the solid hydration products (primarily calcium silicate hydrate, CSH), unhydrated clinkers and the pore structure of cement paste. Studies on porosity in cement paste are fundamental in understanding the microstructural development and in understanding mechanical and durability properties of concrete. In the present study, a detailed review of existing models for pore structure characterization in cement paste has been carried out. The predictions of capillary porosity and gel porosity using different models are compared with the experimental data on porosity of cement paste reported in literature, and the values of modelling error associated with the models are determined. A sensitivity analysis study is carried out to identify the parameters that have the largest influence on porosity. Finally, an attempt is made to understand the implications of the pore structure on the creep of concrete.

Keywords: Cement paste, porosity, models, sensitivity analysis, creep.

1 INTRODUCTION

The development of pore structure with time and its influence on properties of concrete has been an important area of research. However, despite decades of research on the complex microstructure development in the cement-based materials upon chemical reaction with water, a complete understanding about it is yet to be achieved and agreed upon. Understanding the porosity in cement paste is a fundamental study which needs to be stressed upon [1].

In this paper, an attempt is made to review some of the existing models on pore structure characterization. The models considered for the study are those by Powers and Brownyard (1947), van Breugel (1997), Tennis and Jennings (2000) and Maekawa et al. (2009). Experimental data reported in literature is used to study the predictive capability of the models considered. Deterministic sensitivity analysis has been carried out to understand the sensitivity of the response variable in the models. As a way forward, the implications of porosity on creep of cement paste is discussed.

2 PORE STRUCTURE IN CEMENT PASTE

Classification of porosity based on size is attributed to studies carried out by Powers and Brownyard (1947). Pore structure is classified into two, viz, capillary pores, which are the water filled spaces, and gel pores i.e, pores in the solid hydration product (CSH). The classification of pores based on the size is not mutually exclusive; instead there is a visible overlap between the subsystems.

Capillary Pores: The water-filled spaces, formed initially at the instant of mixing are called capillary pores, water of which takes part in the hydration reaction to form the solid hydration products. These pores are connected at the beginning of hydration reaction, however as the hydration proceeds and the solid hydration products get deposited in the water filled spaces, the sizes of capillary pores reduce and becomes more disconnected.

Gel Pores: Gel pores are formed within the interstitial spaces of the CSH gel, and are filled with gel water. The size of gel pores are of order of few nanometers. Gel water is also adsorbed on the solid hydration products. This water is evaporable; however, it is not available for hydration. As hydration proceeds, the capillary pore space is occupied by the CSH gel, causing increase in gel porosity.

Interlayer Pores: Pores within the layered structure of CSH is called interlayer pores, which are filled with the interlayer water. Interlayer water forms a structural part of CSH and is also known as chemically combined or non-evaporable water. Like gel water, interlayer water also is not available for hydration.

3 MODELS FOR PORE STRUCTURE OF CEMENT PASTE

In the present study, four prediction models for pore structure of cement paste have been reviewed, viz, Powers and Brownyard model, van Breugel model, Tennis and Jennings model and Maekawa et al. model. The basis for consideration of these models is their strong physics and mechanics based approach in development of the model, rather than an empirical one.

3.1 Powers and Brownyard Model

Powers and Brownyard (1947) carried out water adsorption experiments to study the internal porosity of C-S-H, based on which a model for pore structure of cement paste was proposed. The significant features of the Powers and Brownyard model are the distinction between gel porosity and capillary porosity and classification of three different water in cement paste viz, capillary water, gel water and combined/non-evaporable water. The parameters of the model on which porosity depends are water-cement ratio and degree of hydration. One of the basic assumption of Powers and Brownyard (1947) work was that of a constant specific volume of the hydration product C-S-H. However, investigations by Tennis and Jennings (2000) and Constantinides and Ulm (2004) have shown the presence of two different packing densities of C-S-H, that is low and high density. According to Powers and Brownyard (1947), capillary porosity and gel porosity of the cement paste are given by Equation 1,

$$\Phi_{cp} = \frac{\frac{w}{c} - h\frac{w_n}{c}\left(v_n + \frac{w_g}{w_n}v_g\right)/v_w}{0.317 + w/c}; \qquad \Phi_{gp} = \frac{h\frac{w_n}{c}\frac{w_g}{w_n}\frac{v_g}{v_w}}{0.317 + w/c} \tag{1}$$

where,

$$\left.\begin{aligned} \frac{w_n}{c} &= 0.187\chi_{C_3S} + 0.158\chi_{C_2S} + 0.665\chi_{C_3A} + 0.213\chi_{C_4AF} \\ \frac{w_g}{w_n} &= 4 * \left(\frac{V_m}{w_n}\right) = 4 * \left(0.230\chi_{C_3S} + 0.320\chi_{C_2S} + 0.317\chi_{C_3A} + 0.368\chi_{C_4AF}\right) \end{aligned}\right\} \tag{2}$$

v_n =0.72 cm^3/g, v_g=0.9 cm^3/g, $v_w = 1$ cm^3/g, Φ_{cp} is the capillary porosity, Φ_{gp} is the gel porosity, V_{cp} is the total capillary pore volume, V_t is the total volume of water and cement, V_w is the volume of pore water, V_s is the total solid phase, h is the degree of hydration, $v_n$is the specific volume of the non-evaporable water, v_g is the specific volume of gel water, v_w is the specific volume of free water, $w_g$is the gel water mass, w_n is the non-

the specific volume of free water, w_g is the gel water mass, w_n is the non-evaporable water mass, V_m is the mass of water necessary to cover the hydration cement with a monolayer.

One of the basic assumption of Powers and Brownyard model was that of a constant specific volume of the hydration product (C-S-H). However, investigations by Tennis and Jennings (2000) and Constantinides and Ulm (2004) have shown the presence of two different packing densities of C-S-H, that is low and high density. Even though, Powers and Brownyard (1947) distinguished between capillary and gel porosity, the distinction was not clear. Also, Powers and Brownyard (1947) assumed same fractional rate of hydration for the Portland cement constituents (alite and belite), which is not appropriate.

3.2 van Breugel Model

This model divides the pore system into narrow gel pores and wide capillary pores [3]. As hydration progresses, the volume of the wide capillary pores reduces and the volume of the narrow gel pores increase, resulting in a net decrease in the overall pore volume. The parameters of the porosity model are water-cement ratio (w/c) and the degree of hydration h. This model assumes that gel porosity, that is pores of 20 Å or less are excluded from the total pore volume and they constantly remain water-filled. The gradual reduction in volume of the capillary pores is until a thermodynamic equilibrium is reached. At an intermediate equilibrium stage, the capillary pore is filled partly with water and partly with water vapour. The porosity at any arbitrary degree of hydration is given by Equation 3,

$$V_{por(h)} = V_{cap(h)} + V_{chsh(h)} \tag{3}$$

where $V_{por(h)}$ is the porosity at any degree of hydration, $V_{cap(h)}$ is the capillary porosity and $V_{chsh(h)}$ is the porosity caused due to chemical shrinkage. The porosity caused due to chemical shrinkage is assumed to be 25% of the volume of the chemically combined water, which is 25% of the weight of the reacted cement. Equations 4-5 give the expression for capillary porosity and porosity due to chemical shrinkage.

$$V_{cap(h)} = \frac{\rho_{ce}}{1 + \rho_{ce} w/c}[w/c - 0.4h] = \frac{w/c - 0.4h}{0.317 + w/c} \tag{4}$$

$$V_{chsh(h)} = 0.25 * 0.25 * h * \frac{\rho_{ce}}{1 + \rho_{ce} w_o} \tag{5}$$

where ρ_{ce} is specific mass of cement (gm/cm^3) =3.15, w_o is the water-cement ratio.

3.3 Tennis and Jennings Model

Tennis and Jennings (2000) proposed the presence of two different densities of CSH in the cement paste, viz, high density (HD) CSH and low density (LD) CSH. The model is based on simple stoichiometric reactions of the compounds of cement paste. The porosity is a function of water-cement ratio and degree of hydration of the compounds and not the overall degree of hydration. Tennis and Jennings model is based on nitrogen sorption experiments, and since nitrogen cannot penetrate into the gel pores in HD CSH, the model under predicts gel porosity. The capillary porosity is given by Equation 6 given below.

$$V_{cp} = V_w - \sum_i (V_p - V_r) = \frac{w/c - \sum_i (V_p - V_r) 0.317 + w/c}{0.317 + w/c} \tag{6}$$

The volume of CSH is inclusive of the volume of gel pores. The gel porosity is given by Equation 7.

$$V_{pCSH} = (V_{LD} - V_{SLD}) + (V_{HD} - V_{SHD}) = 0.2M_t + 0.13M_rM_t \quad (7)$$

where, $M_t = 0.4402\alpha_{C_3S} + 0.191\alpha_{C_2S}$, $M_r = 3.017w/c\,h - 1.347h + 0.538$, V_{cp} is the volume percentage of capillary pores, V_w is the initial volume percentage of water, V_p is the volume percentage of hydration products, V_r is the volume percentage of reactants, i is the reactions, V_{pCSH} is the volume percentage of pores in CSH which includes the gel pores, V_{LD} and V_{HD} are volume percentage of LD and HD CSH respectively, V_{SLD} and V_{SHD} are the volume percentage d-dried LD and HD CSH respectively. M_t is the total mass of CSH and M_r is the ratio of mass of LD CSH to the total mass of CSH.

The existence of two types CSH has been questioned by different researchers [20-21]. Also, Tennis and Jennings model assumes that the CSH globules undergo restructuring leading to a more densely packed system, which has been questioned.

3.4 Maekawa et al. Model

Maekawa et al. (2009) developed an analytical microstructure model, considering the fundamental physical processes occurring during the reaction of cement and water. The model assumes a layered structure for CSH. The pore space is broadly classified into three categories, viz, interlayer porosity, gel porosity and capillary porosity. The parameters on which the porosity depends are degree of hydration (h) and the water cement ratio. The characteristic porosity associated with the gel products is assumed to be a constant (i.e., 0.28) throughout the hydration. The capillary, gel and interlayer porosities as per the model are given by Equations 8 - 10.

$$\phi_{cp} = 1 - V_s - (1-h)\frac{w_p}{\rho_p} \quad (8)$$

$$\phi_{gl} = V_s\phi_{ch} - \phi_l \quad (9)$$

$$\phi_l = \frac{t_w S_l \rho_g V_s}{2} \quad (10)$$

where ϕ_{cp} is the capillary porosity, V_s Volume of the gel products in a unit volume of paste, $V_s = \frac{\alpha w_p}{1-\phi_{ch}}\left[\frac{1}{\rho_p} + \frac{\beta}{\rho_w}\right]$, $w_p$is weight of powder materials per unit paste volume, $w_p = \frac{1}{\frac{1}{\rho_p} + \frac{w}{c}}$, h is degree of hydration, $h = \frac{amount\ of\ heat\ liberated}{maximum\ possible\ heat\ of\ hydration}$, $\phi_{ch}$is the characteristic porosity (0.28 for ordinary cements), $\rho_p$is average specific gravity of powder material, β is the amount of chemically combined water per unit weight of powdered material (=0.25), ρ_w density of chemically combined water=1.25g/cm3, ϕ_{gl} is the gel porosity, ϕ_l is the interlayer porosity, t_w is the Interlayer thickness (2.8 Å), S_l is the specific surface area of interlayer, $S_l = 510f_{pc} + 1500f_{sg} + 3100f_{fa}$, where f_{pc}, f_{sg}, f_{fa} are the weight fractions of Portland cement, slag and flyash respectively, ρ_g is the dry density of gel products, $\rho_g = \frac{\rho_p\rho_w(1+\beta)(1-\phi_{ch})}{(\rho_w + \rho_p\beta)}$

The characteristic porosity associated with the gel products is assumed to be a constant (i.e., 0.28) throughout the hydration. However, as shown by the investigations of Tennis and Jennings (2000) and Constantinides and Ulm (2004), the hydration of cement gives rise to high density inner product (HD CSH) and low density outer product (LD CSH). As hydration proceeds, the fraction of LD CSH reduces and the fraction of HD CSH increases. Hence the

assumption of a constant characteristic porosity for the gel products throughout the hydration is not proper.

3.5 Comparison

Table 2 shows the simplified equations of porosity for the models considered in the study. These simplified equations were obtained by substituting the relevant values in the model equations to obtain the porosities of all the models in terms of degree of hydration and water-cement ratio.

Following are the observations made from the comparison of the models:

- Porosity is a function of water-cement ratio and overall degree of hydration in all the models except Tennis and Jennings model. In Tennis and Jennings model, porosity is a function of water-cement ratio and degree of hydration of the individual Portland cement compounds (C_3S and C_2S).
- It is noted that capillary porosity predictions by Maekawa et al. (2009) and van Breugel (1997) are the same.
- The capillary porosity predictions by Powers and Brownyard model is higher in comparison to models by Maekawa et al. (2009) and van Breugel (1997).
- Gel porosity predictions made by Powers and Brownyard model is almost same as that of combine gel and interlayer porosity prediction made using Maekawa et al. model. This is because Powers and Brownyard model do not make any distinction between gel porosity and interlayer porosity.

Table 2: Simplified equations of porosity obtained by substituting relevant values in the model equation for porosity

Model	Capillary Porosity	Gel Porosity	Interlayer Porosity
Powers and Brownyard*	$\frac{w/c - 0.36h}{0.317 + w/c}$	$\frac{0.19h}{0.317 + w/c}$	-
van Breugal	$\frac{w/c - 0.4h}{0.317 + w/c}$	-	-
Tennis and Jennings	$\frac{\frac{w}{c} - \sum_i (V_p - V_r)0.317 + w/c}{0.317 + w/c}$	$0.2M_t + 0.13M_rM_t$	-
Maekawa et al.	$\frac{w/c - 0.4h}{0.317 + w/c}$	$\frac{0.11\,h}{0.317 + w/c}$	$\frac{0.089\,h}{0.317 + w/c}$

(Note: * - from Neville [7])

Figure 1(a) and (b) shows the variation of porosity with *h*, typically for Powers and Brownyard model and Tennis and Jennings model, respectively. From these figures, it is seen that, as *h* increases, capillary porosity reduces. With progress in hydration the water in the capillary pores reacts with the unhydrated cement to produce solid hydration products. The solid hydration products partly occupy the capillary pore space thus reducing the capillary pore volume.

From Figure 1(a) and 1(b), it is also seen that gel porosity increases with *h*. This is because, with increase in solid hydration products, the gel pore volume increases. For Powers and Brownyard model, the gel porosity at w/c of 0.3 is greater than that at 0.5, for the same *h*. While a similar trend is seen in case of van Breugel and Maekawa et al. models, there is a reverse trend in case of Tennis and Jennings model. This is because Tennis and Jennings model considers the presence of LD CSH and HD CSH. The LD CSH is more porous than

the HD CSH, and volume fraction of LD CSH increases with increase in *w/c*. Therefore, for Tennis and Jennings model, the gel porosity at *w/c* of 0.5 is more than that at *w/c* of 0.3 for same *h*. The other models do not differentiate between the morphologies of CSH and consider it to be single hydration product.

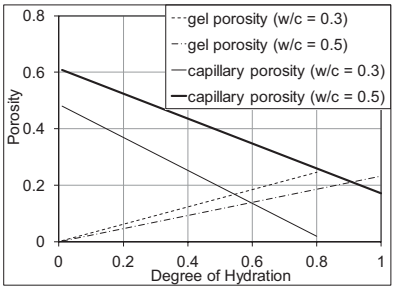

(a) Powers & Brownyard Model

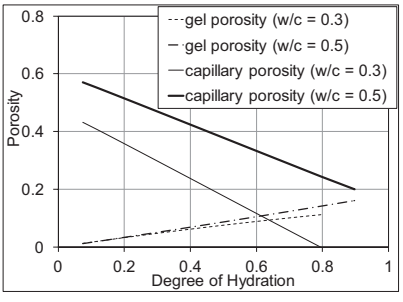

(b) Tennis & Jennings Model

Fig 1: Variation in capillary and gel porosity with respect to degree of hydration

In Tennis and Jennings model, it is seen that, at constant degree of hydration, gel porosity at *w/c* of 0.3 is lower than *w/c* of 0.5. This is because, at lower *w/c*, the amount of LD CSH is less and hence gel porosity is less [8].

4 COMPARISON OF MODELS USING EXPERIMENTAL DATA

The model predictions are compared with experimental values reported in the literature. The details of the experiment considered for comparison of the model predictions are given in the Table 3.

Table 3: Details of experimental investigations considered in the comparison study

Investigator	Type of test	*w/c*	*h*
Pang *et al.* [9]	MIP	0.30-0.70	0.345-0.818
Ma and Li [10]	MIP	0.30-0.50	0.28 - 0.81
Goran Fagerlund [11]	Water Adsorption	0.32-0.80	0.26-0.72
Powers and Brownyard [2]	Water Adsorption	0.44-0.489	0.71-0.94

Figure 2 shows the scatter plot of comparison of the model predictions of porosity with experimental results. From the figure, it is seen that capillary porosity predictions by the models are more or less in satisfactory agreement with the experimental values. However, the gel porosity predictions show visible dispersion. To quantitatively make conclusive statements, the mean and coefficient of variation (COV) of modelling error, ψ, associated with models are computed. Modelling error is given by Equation 11.

$$\psi = \frac{Porosity\ from\ the\ experiment}{Porosity\ predicted\ using\ the\ model} \tag{11}$$

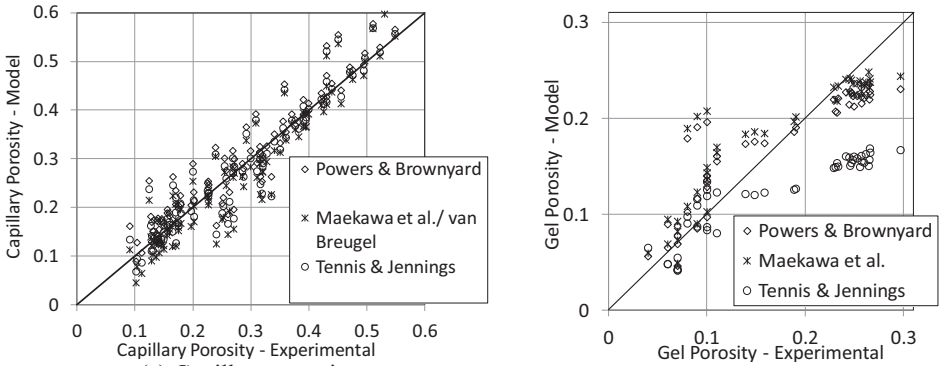

(a) Capillary porosity (b) Gel porosity

Figure 2: Comparison of model predictions of porosity with experimental results

The values of mean and COV of the modelling error for capillary and gel porosity for all the models are given in Table 4. From the results obtained, following observations are made:

- *Capillary Porosity*: R^2 values for all the models is 0.90 suggesting a high correlation of the model predictions with the experimental values. Considering mean and COV values of modelling error, predictions of capillary porosity using Tennis and Jennings model are closer to the experimental values.
- *Gel Porosity*: R^2 values for all the models are in the range 0.81-0.82 showing that gel porosity predictions are not as good as the capillary porosity predictions. This is because the experimental methods (water adsorption and MIP) have their own limitations with respect to obtaining the information about the gel pores. Considering mean and COV of modelling error, gel porosity predictions by Powers and Brownyard model are closer to that of experimental values. It is also noted that Tennis and Jennings model under predicts the gel porosity. This is because Tennis and Jennings model is developed based on results of nitrogen sorption experiments on cement paste, and nitrogen cannot penetrate into the gel pores in HD CSH [4].

Table 4: Values of R^2, and mean and COV of modelling error

Model	*Capillary porosity*			*Gel porosity*		
	R^2	Modelling Error		R^2	Modelling Error	
		mean	COV		mean	COV
Powers & Brownyard	0.90	0.93	0.17	0.81	0.97	0.24
van Breugel	0.90	1.11	0.23	-	-	-
Tennis & Jennings	0.90	1.02	0.18	0.82	1.36	0.25
Maekawa *et al.*	0.90	1.11	0.23	0.81	0.92	0.24

5 SENSITIVITY ANALYSIS

In order to study the influence of the input variables on the porosity of cement paste, a sensitivity analysis is carried out. The sensitivity is characterised in terms of the relative sensitivity coefficient, defined as fractional sensitivity of response variable with fractional change in the input variable. Let R be the response variable and X_i (i=1,2,..n) be the input

variables, where R is a function of vector X, and X_o is the reference value of X. The relative sensitivity coefficient with respect to X_i is given by [12]

$$\zeta_{Ri}^{D} = \frac{\partial R}{\partial X_i}\left(\frac{X_i}{R}\right) \; at \; X = X_o \tag{12}$$

Figures 3(a) and (b) show the variation in sensitivities of capillary porosity estimated using different models with respect to h and w/c. It is seen that capillary porosity is more sensitive with respect to w/c than h. This is because, capillary porosity is the water-filled spaces, formed initially at the instant of mixing, and, hence is more influenced by the water content. It is also seen that capillary porosity estimated using Maekawa et al. and van Breugel models are more sensitive with respect to h and w/c, when compared to other models. Figures 4 (a) and (b) shows the variation in sensitivities of gel porosity with respect to h and w/c. It is seen that gel porosity is more sensitive with respect to h than w/c. This is expected because gel porosity is part of the hydration product (CSH), amount of which depends on the degree of hydration. It is also seen from Figure 4 (a) that the sensitivity of gel porosity with respect to h or w/c does not change with degree of hydration for Powers and Brownyard and Maekawa et al. models. However, from Figure 4 (b), it is seen that sensitivity of gel porosity with respect to w/c increases with increase in water-cement ratio for these two models. Gel porosity estimated using Tennis and Jennings model is sensitive to changes in h or w/c, and the sensitivity increases with increase in degree of hydration or water-cement ratio.

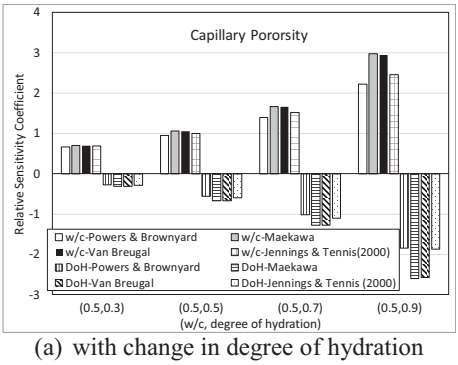

(a) with change in degree of hydration

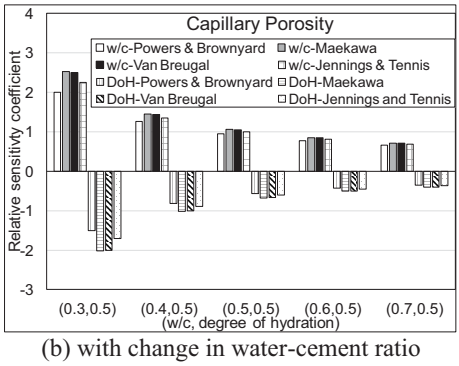

(b) with change in water-cement ratio

Figure 3: Variation in sensitivities of capillary porosity with respect to water-cement ratio (*w/c*) and degree of hydration (DoH)

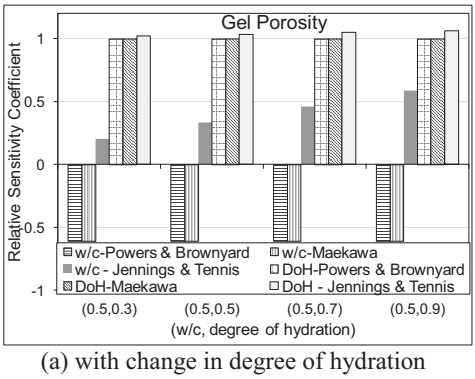

(a) with change in degree of hydration

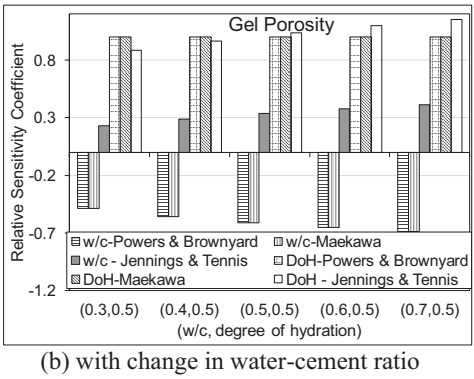

(b) with change in water-cement ratio

Figure 4: Variation in sensitivities of gel porosity with respect to h and w/c

6 IMPLICATIONS OF POROSITY ON CREEP OF CONCRETE

Porosity studies in cement paste are fundamental in understanding the micro structural development and subsequently understanding the mechanical and durability properties of concrete. In this section, the link between pore structure in cement paste and creep is discussed. The role of pore fluid movement on creep of cement paste has been an area of research for a while. Creep rates determined from experimental investigations distinguishingly show presence of two creep kinetics viz, a short term kinetics lasting for a few days after loading and a long term kinetics without an asymptote for at least three years. The two different kinetics or creep mechanisms are associated with two different pore spaces in cement paste [17]. The short term creep (which is also the reversible component of creep) is associated with the relatively easy movement of the capillary water under application of load. A long term creep is associated with slow movement of gel water in the gel pores formed within the interstitial space of the CSH [4]. Recent studies by Shatabdi Mallick et al. (2016) show a bimodal retardation spectrum for basic creep of concrete, which is in agreement with the observation of two creep kinetics that might be related to the two different pore spaces in the cement paste [18-19].

While the origin of creep of concrete has been attributed to CSH [8], there is no conclusive agreement on the site at which it occurs [13]. Also, there is disagreement also on the microstructural arrangement under sustained loading and its subsequent evolution. For example, Feldman and Sereda (1970) observed that reversible creep is due to the decomposition and liberation of the interlayer water under application of load. Bazant et al. (1997) have proposed that a sliding mechanism governs the long term creep. Hindered adsorption of water molecules in the micropores leading to unstable bonds and shear slips causes creep. The unavailability of these overstressed sites over a period causes creep rate to decline. Rossi et al. (2012) conducted studies on basic creep of concrete through acoustic emission techniques and attributed the short term creep to the fluid transport within the concrete sample. With advancement in technology, many of these theories are partially verified with experimental investigations and many new theories are being postulated, but a definite correlation between porosity and creep mechanism is still an active area of research being pursued world over.

7 SUMMARY

From the review of models for pore structure of cement paste, it is found that in all the models, porosity is a function of water-cement ratio and degree of hydration. It is also noted that the model proposed by Tennis and Jennings (2000) predicts values of capillary porosity which are in satisfactory agreement with the experimental observations. For gel porosity, Powers and Brownyard model gives predictions closer to that of the experimental values. From a sensitivity analysis, it is noted that capillary porosity is more sensitive to water-cement ratio while gel porosity is more sensitive to degree of hydration. The importance of pore structure in understanding the phenomenon of creep in concrete is brought out.

ACKNOWLEDGEMENTS

The authors are thankful to Mr. Vijaya Bhaskara G.S., Scientist, CSIR- Structural Engineering Research Centre, Chennai, for the useful discussions.

REFERENCES

[1] Jennings, H. M., Bullard, J. W.,Thomas, J.J., Andrade, J.E., Chen, J.J. and Scherer, G.W., 'Characterization and modeling of pores and surfaces in cement paste: correlations to processing and properties', *Jl. Adv. Concr. Tech*., **6** (2008) 5-29.

[2] Powers, T.C. and Brownyard, T.L., 'Studies of the physical properties of hardened Portland cement paste', Bull. 22, Res. Lab. of Portland Cement Association, Skokie, IL, U.S.A., reprinted from *J. Am. Concr. Inst. (Proc.)*, **43** (1947), 101-132, 249-336, 469-505, 549-602, 669-712, 845-880, 933-992.

[3] van Breugel, K. *Simulation of Hydration and Formation of Structure in Hardening Cement-based Materials*. PhD thesis, Delft University of Technology, (1997)

[4] Tennis, P.D. and Jennings, H.M., 'A model for two types of calcium silicate hydrate in microstructure of Portland cement paste', *Cem. Concr. Res.*,**30** (2000) 855-863.

[5] Maekawa, K., Ishida, T.and Kishi, T., *Multi-scale Modeling of Structural Concrete*, Taylor and Francis, (2009).

[6] Constantinides, G. and Ulm F.-J., 'The effect of two types of C-S-H on the elasticity of cement-based materials: results from nanoindentation and micromechanical modeling', *Cem. Concr. Res.*,**34**(1) (2004), 67–80.

[7] Neville, A.M., *Creep of Concrete: Plain, Reinforced, and Prestressed*, North-Holland Pub. Co., (1970).

[8] Vandamme, M. and Ulm, F.-J., 'The nanogranular origin of concrete creep', *P Natl Acad Sci*, **106** (2009) 10552-10557.

[9] Pang, Gi-S., Chae, S.-T., and Chang, S.-P., 'Predicting model for pore structure of concrete includinginterface transition zone between aggregate and cement paste', *Int. Jl. of Concr. Struct. and Mater.* **3**(2) (2009) 81-90.

[10] Ma, H. and Li, Z.,'Realistic pore structure of Portland cement paste: experimental study and numerical simulation', *Comp. and Concr.*, **11**(4) (2013) 317-336.

[11] Fagerlund, G., *Porosity and Specific Surface of Portland Cement Paste*, LUND University of Technology, (2006).

[12] Anoop, M.B., Prabhu, G. and Balaji Rao, K., 'Probabilistic analysis of shear fatigue life of steel plate girders using a fracture mechanics approach', *Proc. Inst. Mech. Eng.rs, Part O: Jl. Risk and Reliability,* (2011) 225-389.

[13] Ye, H., 'Creep mechanisms of calcium-silicate-hydrate: an overview of recent advances and challenges', *Int. Jl. of Concr. Struct. and Mater.***9** (4) (2015) 453-462.

[14] Feldman, R.F. and Sereda, P.J., 'A new model for hydrated portland cement and its practical implications', *National Research Council of Canada, reprinted from Eng. Jl.* **53** (1970) 53-59.

[15] Bazant, Z.P., Hauggard, A.B., Baweja, S. and Ulm, F-J., 'Microprestress-solidification theory for concrete creep. I: aging and drying effects', *Jl. of Eng. Mech., ASCE*, **123** (1997) 1188-1194.

[16] Rossi, P., Tailhan, J.-L., Le Maou, F., Gaillet, L.and Martin, E., 'Basic creep behavior of concretes investigation of the physical mechanisms by using acoustic emission', *Cem. and Concr. Res.*, **42**(1) (2012) 61-73.

[17] Ulm, F.-J., Le Maou, F. and Boulay, C., 'Creep and shrinkage of concrete - kinetics approach', *Adam Neville Symposium: Creep and Shrinkage - Structural Design Effects*, *ACI SP-194 (*2000) 135-154.

[18] Shatabdi Mallick, Anoop, M.B. and Balaji Rao, K., 'Prediction of basic creep of concrete - semi-empirical model based on adaptive link mechanism', *ACI Mater. Jl*., **114**(1) (2017) 29-39.

[19] Shatabdi Mallick, Anoop, M.B. and Balaji Rao, K., 'Continuous retardation spectrum for basic creep of concrete', *Jl. Struct. Eng*. **43**(3) (2016) 297-302.

[20] González-Teresa, R., Morales-Florez, Víctor, Manzano, Hegoi and Dolado Jorge S., 'Structural models of randomly packed Tobermorite-like spherical particles: A simple computational approach', *Materiales de Construcción*, 60 (2010) 7-15.

[21] Nguyen,D.-T., Alizadeh,R., Beaudoin, J.J., Pourbeik, P., and Laila Raki, L., 'Microindentation creep of monophasic calcium–silicate–hydrates, *Cem. & Concr. Comp.*, 48 (2014) 118-126.

Influence of 2D Chloride Ingress on Corrosion Initiation and Propagation in Cracked and Uncracked Concrete: A Critical Literature Review

Authors: Ze G. Zakka[1, 2] and Mike B. Otieno[1]

[1]School of Civil and Environmental Engineering, University of the Witwatersrand, Johannesburg, South Africa.

[2]Abubakar Tafawa Balewa University, Bauchi. Nigeria

ABSTRACT

Many studies undertaken on chloride-induced corrosion in steel reinforced concrete (RC) corrosion have focused on one-dimensional (1D) chloride penetration; where the RC is exposed to penetration of chlorides from only one face. The findings of 1D chloride penetration studies though useful, may not rightly depict the deterioration of steel reinforcement bars located at corners of rectangular shaped RC elements in-service condition as they are mostly exposed to two-dimension (2D) chloride penetration. This paper presents a review of findings on the effect of chloride ingress paths (1D and 2D) on chloride penetration rate, binder type, time-to-corrosion initiation, cover cracks, and corrosion damage in relation to diameter and cover depth of steel reinforcement. The review also brings the need for determining the effect of 2D chloride ingress on the corrosion rate of corner located steel reinforcement bars in cracked and uncracked concrete using various binders (FA and GGBS). The determination of the corrosion rate is explored due to its influence on the service life of steel RC components after corrosion initiation. Areas of further research are highlighted along with a brief outline of the experimental setup for this research work.

Keywords: Chloride-induced corrosion, steel reinforcement corrosion, 1D chloride penetration, 2D chloride ingress, corrosion rate.

1 INTRODUCTION

Most RC corrosion research has assumed chloride penetration to occur in one-dimension (1D) [1–4]. However, RC concrete elements may be subject to two-dimensional (2D) chloride penetration at rectangular corners thereby making the reinforcements placed at the corners more vulnerable to faster deterioration than those on faces that are away from corners [5-6]. Hence, the use of 1D chloride-induced corrosion models to predict chloride penetration, corrosion free life and corrosion damage in 2D scenarios has been disputed by some researchers [5, 7–13]. This paper is a review of the studies conducted by researchers on the effect of 2D chloride penetration on RC steel corrosion initiation and propagation.

2 CHLORIDE PENETRATION DIMENSIONS

Chlorides can penetrate RC elements in 1D (walls and slabs) [Fig. 1a], 2D (along corners of rectangular beams and columns) [Fig. 1b] or three-dimension (3D) (at beam and column ends) [Fig. 1c] with diffusion being the dominant means of chloride penetration [14–16]. Though the diffusion process consists of random molecular motions, it can be assumed

to occur in a three-dimensional (3D) space (x, y, and z) depending on the diffusing mediums shape, exposure and presence of a chloride gradient in the space being considered [8,17]. 1D and 2D chloride penetration have been identified as most critical as they affect reinforcements on the plane face and along corners of RC element while 3D chloride penetration affects the ends of the reinforcement bars [10].

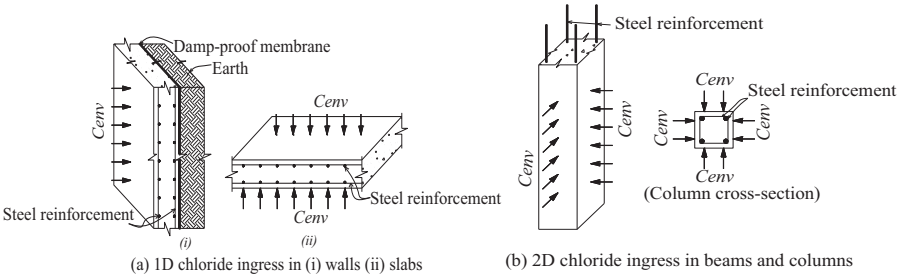

(a) 1D chloride ingress in (i) walls (ii) slabs

(b) 2D chloride ingress in beams and columns

Figure 1: Illustration of (a) 1D, (b) 2D, and (c) 3D chloride penetration modes where C_{env} is chloride penetration from the environment.

3 CORROSION INITIATION

The time-to-corrosion initiation in RC is strongly related to the penetration rate of corrosion causing agents through the cover concrete and build-up of chloride ions to a critical concentration at the surface of the steel reinforcement bar to cause its depassivation [5,16, 18]. 1D analytical solution to Fick's second law (using the first term of Equation 1) have been used to find the diffusion coefficient, chloride penetration and concentration at depth (x) from the concrete surface. Unlike the 1D scenario, few 2D analytical solutions to Fick's second law provide reliable diffusion coefficient values, chloride penetration depth and shape exist [8,13].

$$\frac{\partial C}{\partial t} = D\left(\frac{\partial^2 C}{\partial x^2} + \frac{\partial^2 C}{\partial y^2} + \frac{\partial^2 C}{\partial z^2}\right) \quad (1)$$

where C (kg/m^3) is the concentration of the diffusing substance, x, y and z (m) are spatial coordinates, D (m^2/s) is the diffusion coefficient, and t is time.

2D analytical solutions to Fick's second law were provided by Crank [19] and Edwards and Penney [20] respectively by using; (i) product solution of two 1D solutions and (ii) series solution by separation of variables method. Numerical methods such as random field, random variable, and finite and boundary element methods (FEM and BEM) have also be used to estimate 2D chloride penetration and time-to-corrosion initiation [21].

Using the random field approach, parameters which affect the diffusion process are taken as both spatial in time and temporally thereby capturing possible field variations; this is considered adequate in predicting the chloride penetration as compared to the random variable method which assumes the parameters to be constant. The probability of corrosion due to 1D and 2D chloride penetration was assessed using these methods by Frier and Sørensen [22] (see Fig. 2).

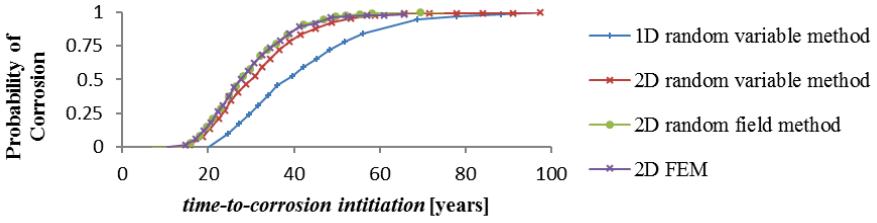

Figure 2: Probability distributions for the time-to-corrosion initiation of corner rebar using random variable, random field and finite element methods [22].

Probabilistic and stochastic methods have also been used to predict 2D chloride penetration; however, various limitations such as increasing complexity with the addition of variables which affect the corrosion process have been cited in the use of probabilistic and stochastic methods to evaluate the corrosion phenomenon [10]. Inadequate data on 2D chloride penetration studies in literature also serve as a limit to the use of these methods since they require a large amount of data.

Kang and Shim [8] conducted an empirical study of the effect of 2D chloride penetration at the corner of a bridge pier and compared the results with a numerical (FEM) prediction model (Fig. 3).

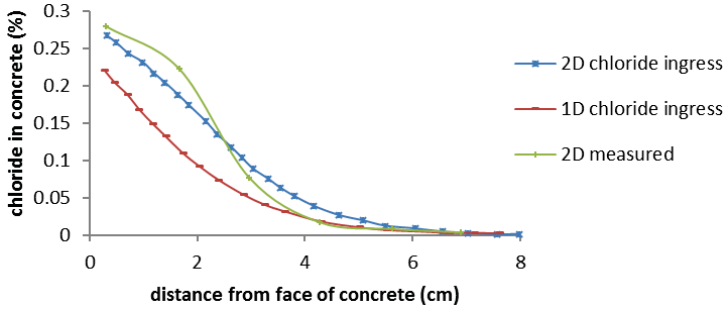

Figure 3: Numerically determined and measured chloride profile from concrete bridge pier [8].

The result of 1D and 2D chloride penetration studies by Frier and Sørensen [22] and Kang and Shim [8] shows that chloride penetration is underestimated when considered as a 1D case at concrete corners.

3.1 Chloride penetration

A comparison of 1D and 2D chloride penetration studies from various researchers shows a variance in 1D and 2D chloride penetration rates [7–12]. While, 1D chloride penetration is assumed to occur parallel to the concrete surface, 2D chloride penetration is influenced by chloride penetration from adjacent RC faces that are joined. This is known as dimensional interaction.

i) **Dimensional interaction:** Frier and Sørensen [22] used both 1D and 2D analytical and numerical solutions to assess the effect of 2D chloride penetration of two concrete elements of cross sectional dimension; 100 mm × 100 mm and 400 mm × 400 mm. The chloride penetration from adjoining concrete faces results in a higher chloride penetration

rate; concretes with thin and small sections (Fig. 4a) being most affected compared to those with large sections (Fig. 4b). In both instances, 2D solutions provided a better interpretation of chloride penetration at the concrete corners in comparison to the 1D solution.

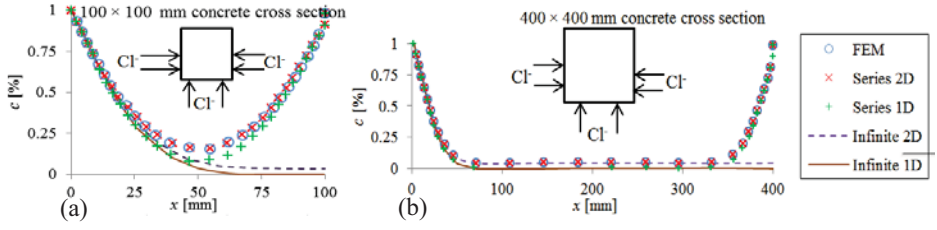

Figure 4: Distribution of chloride within a quadratic domain after 30 years of exposure, 50 mm from the surface with sides of: (a) 100 × 100 mm and (b) 400 × 400 mm cross sections [22].

Zhang et al., [11] assessed the effect of dimensional interaction on the chloride penetration rate by exposing fly ash (FA) blended concrete to 2D and 3D chloride penetration. They proposed a chloride acceleration factor (K_{nD}); defined as the chloride acceleration rate exceeding 1D diffusion;

$$K_{nD} = \frac{D_E}{D_T} \quad (2)$$

where n is the dimension of chloride ingress (n= 2, or 3), D_E and D_T are the experimental and theoretical diffusion coefficients respectively. Using least square regression, the chloride interaction coefficient (K_{nD}) was determined in relation to immersion age (t = 12 months of immersion);

$$K_{2D}= 2.01 \text{ and } K_{3D}= 2.27$$

The chloride ion penetration rate at the corners exceeded an initial theoretical chloride concentration estimate of √2 = 1.4 and √3 = 1.73 for 2D and 3D chloride ingress.

ii) Stress accelerating factor: With stress applied in relation to the concrete flexural stress on beam specimens (70 × 70 × 250 mm), Zhang et al. [12] reported higher diffusion coefficients in the stressed beams exposed to 2D chloride penetration compared to specimens exposed to 1D chloride penetration (Table 1) [11, 12]. They proposed a stress acceleration factor ($K_{\delta s}$) in concrete as a ratio of chloride ion diffusion coefficient in the loaded state ($D_{\delta s}$) at flexural stress (δs) and chloride diffusion coefficient (D_o) in the unloaded state.

$$K_{\delta s} = \frac{D_{\delta s}}{D_o} \quad (3)$$

The diffusion coefficient of the stressed samples varied with the FA proportion; an increase in FA content (40 to 60%) resulted in an increase in the diffusion coefficient (7.5 to 23.5). However, a reduction in w/b ratio (0.35 to 0.30) caused a reduction of stress diffusion coefficient (7.5 to 6.8).

An estimate of the chloride acceleration factor in stressed and non-stressed conditions provides an understanding of stress effect on chloride penetration at square corners of RC elements. The size of the specimens used could have an effect on the results as proposed by Frier and Sørensen [22].

Table 1: 1D and 2D Chloride ion diffusion coefficients of PC and FA concrete [11-12].

Batch	w/c ratio	Apparent Cl^- diffusion coefficient ($\times 10^{-8} cm^2/s$) *Non-stressed		Effective Cl^- diffusion coefficient ($\times 10^{-8} cm^2/s$) **Stressed (flexural stress ratio=0.35)	
		1D	2D	1D	2D
PC(100)	0.35	1.7	4.2	7.1	13.9
PC(80)/FA(20)	0.35	0.88	2.9	3.0	12.3
PC(60)/FA(40)	0.35	1.8	2.8	3.9	7.5
PC(40)/FA(60)	0.35	2.4	6.7	12.0	23.5
PC(60)/FA(40)	0.30	1.7	3.1	3.4	6.8
PC(60)/FA(40)	0.40	1.1	4.6	4.7	9.2

*12 months immersion **6 months immersion in 3.5% chloride solution

The dimensional interaction factors and stress acceleration factors can be used to transform 1D chloride penetration rates to that of 2D or 3D. However, to adapt to changing scenarios, the diffusion interaction and stress acceleration factor equations may need to reflect other factors which influence chloride penetration; concrete quality, binder type, w/b ratio, temperature, relative humidity, moisture content, concrete age, stress, C_3A content of cement etc.

Considering that the result of this research bothers on uncracked concrete, the effect of cover cracks on chloride ingress in concrete needs to be taken into account. Though the effect of cover cracks is still being debated, it is worth noting that the transport properties of fluids and gases can be affected by the cracks [13,23–26]. An assessment of the influence of cover cracks may yield an understanding of their influence on time-to-corrosion initiation, corrosion rate and corrosion damage characteristics of steel reinforcement bars placed at RC corners that are subjected to 2D chloride penetration.

3.2 Chloride threshold level

Chloride threshold level (CTL) is the chloride concentration required in concrete to cause depassivation of steel reinforcement. It is presented as a percentage mass of either acid soluble (bound) or water soluble (free) chlorides in cement, or as a ratio of $[Cl^-]:[OH^-]$. It is widely agreed that free chlorides are responsible for steel corrosion; however, it has also been reported that bound chlorides can be released to take part in the corrosion process when the concrete is carbonated or intruded by sulphates [27]. Though literature reports a wide range of CTL values (0.07-2.2) [1,28–31] for mortar, in-service and laboratory concrete specimens, higher chloride concentrations have been recorded at concrete corners exposed to 2D chloride penetration. Though the CTL may not vary for corner located reinforcement bars, corrosion initiation has been reported to commence earlier due to chloride build up from 2D, increased chloride penetration rate and concentration as compared to 1D chloride penetration.

4 CORROSION PROPAGATION

After corrosion initiation, the build-up of corrosion products in the steel concrete interface (SCI) results in damage to both the concrete and steel [32–34]; corrosion-induced

cracks, concrete spalling, loss of reinforcement diameter, strength and ductility, loss of bond and delamination between the concrete and steel reinforcement bar.

The surface area of reinforcing steel prone to depassivation due to 1D and 2D chloride penetration has been reported to vary. In comparison to 1D chloride penetration, a larger perimeter of the steel reinforcing bar is depassivated due to 2D chloride penetration, hence the corroding area is larger [35-37]. The chloride concentration at the level of the reinforcement bar closest to the exposed concrete face was also assessed to be higher in 2D chloride penetration scenarios with larger diameter bars having higher chloride concentrations due to an increased area resisting chloride flow into the concrete [9]. As in 1D chloride penetration, 2D chloride penetration results in non-uniform corrosion of reinforcement bars located at RC element corners. There is a need for more research on 2D chloride-induced corrosion damage in relation to parameters such as chloride concentration and concrete durability properties.

A new paradigm in service-life prediction has been proposed with corrosion rate being identified as an important parameter in the determination of the service-life of RC structures after corrosion initiation [9,38-39]. A critical review of existing corrosion rate models has been presented by Otieno et al. [39]. The 2D penetration of chlorides and other corrosion causing agents is likely to vary the corrosion rate of corner located reinforcement bars phenomenally. Hence, there is a need to further explore the available corrosion rate models with a view of adapting them to the 2D chloride penetration scenario. The corrosion rate can also be affected when a reinforcement bar is connected to other bars that are either not corroding or are corroding at different rates (galvanic corrosion). Hence, in the experimental setup, a cathode bar (stainless steel) is used to assess its effect on the corrosion rate of reinforcement bar that is placed on the near face exposed to chlorides.

5 EXPERIMENTAL DESIGN

RC beams (72#) specimens of size, 150 × 150 × 625 mm will be cast using binder blends; PC(70)/FA(30) and PC(50)/GGBS(50) with a w/b ratio of 0.40 and moist cured for 28 days. Concrete cover to reinforcement of 20 mm will be used. The RC beams will be epoxy coated on some of its faces (4 or 5) so as to allow 1D or 2D chloride penetration (see Fig. 5). Half of the beam specimens (36#) will be mechanically cracked using the 3 point loading method to induce cracks (0.2 mm width) while the other half will be left uncracked. The cracked samples will be loaded onto 3 point loading rigs to keep the cracks open during the experiment. The cracked and uncracked beams will be subjected to a 2 week wetting (by immersion) and drying regime in 5% NaCl solution in the laboratory. Corrosion data (corrosion potential, corrosion rate and concrete resistivity) will be collected at the end of each wetting and drying cycle [15]. The data will be used to assess the influence of 1D and 2D chloride penetration on the corrosion initiation and propagation of the steel reinforcement bars in the concrete beams.

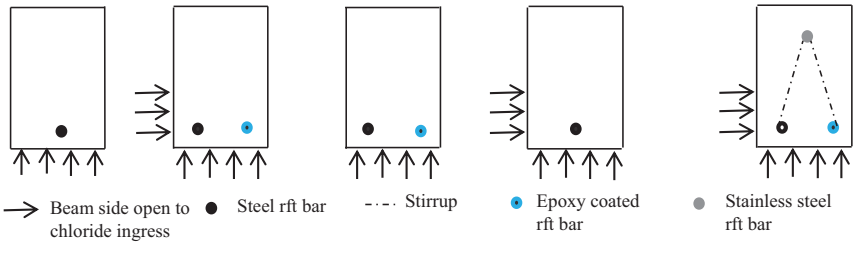

Figure 5: RC beam specimen reinforcement (rft) details and chloride penetration

6 CLOSING REMARKS

Most research in chloride-induced corrosion has been conducted assuming a 1D chloride penetration scenario. This has been disputed by some researchers who have considered the time-to-corrosion initiation and corrosion damage of RC steel reinforcement bars located at rectangular corners of beam and column elements which are subject to 2D chloride penetration. Most literature available on 2D chloride penetration has focused on time-to-corrosion initiation as it relates to chloride penetration and corrosion damage of the corner located bars. This review brings to fore the need for consideration of corrosion rate of the corner located bars as it relates to the variables; binder type, concrete quality and cover cracks.

7 REFERENCES

[1] A. Michel, A. O. S. Solgaard, B. J. Pease, M. R. Geiker, H. Stang, and J. F. Olesen, "Experimental investigation of the relation between damage at the concrete-steel interface and initiation of reinforcement corrosion in plain and fibre reinforced concrete," *Corros. Sci.*, vol. 77, pp. 308–321, (2013).

[2] B. Richard, F. Ragueneau, C. Cremona, L. Adelaide, and J. L. Tailhan, "A three-dimensional steel/concrete interface model including corrosion effects," *Eng. Fract. Mech.*, vol. 77, no. 6, pp. 951–973, (2010).

[3] A. N. Scott, "The Influence of Binder Type and Cracking on Reinforcing Steel Corrosion in Concrete," University of Cape Town, (2004).

[4] A. K. Suryavanshi and R. N. Swamy, "Stability of Fridel's Salt in Carbonated Concrete Structural Elements," *Cem. Concr. Res.*, vol. 26, no. 5, pp. 729–741, (1996).

[5] K. Tuutti, "Corrosion of steel in concrete," Royal Institute of Technology, Stockholm, Stockholm, (1982).

[6] BS 8110-1, "Structural Use of Concrete," p. 168, (1997).

[7] C. Frier and J. D. Sørensen, "Stochastic Simulation of Chloride Ingress into Reinforced Concrete Structures by Means of Multi-Dimensional Gaussian Random Fields," in *9th International Conference on Structural Safety and Reliability, ICOSSAR 2005*, pp. 617–624, (2005)..

[8] B. Kang and H. Shim, "Two Dimensional Chloride Ion Diffusion in Reinforced Concrete Structures for Railway," *Int. J. Railw.*, vol. 4, no. 4, pp. 86–92, (2011).

[9] S. Muthulingam and B. N. Rao, "Numerical assessment of non-uniform corrosion scenarios of rebar in concrete exposed to natural chloride environment," *Indian Acad. Sci.*, vol. 40, no. June, pp. 1313–1341, (2015).

[10] D. V. Val and P. A. Trapper, "Probabilistic evaluation of time to corrosion initiation in RC elements exposed to chlorides: 2-D modelling," in *3rd International Conference on Bridge Maintenance, Safety and Management - Bridge Maintenance, Safety, Management, Life-Cycle Performance and Cost*, pp. 527–528, (2006).

[11] Y. Zhang, W. Sun, S. Chen, and F. Guo, "Two- and three-dimensional chloride ingress into fly ash concrete," *J. Wuhan Univ. Technol. Sci. Ed.*, vol. 26, no. 5, pp. 978–982, (2011).

[12] Y. Zhang, W. Sun, Z. Liu, and S. Chen, "One and two dimensional chloride ion diffusion of fly ash concrete under flexural stress," *J. Zhejiang Univ. - Sci. A (Applied Phys. Eng.*, vol. 12, no. 9, pp. 692–701, (2011).

[13] O. G. Rodríguez and R. D. Hooton, "Influence of cracks on chloride ingress into concrete," *Am. Concr. Inst.*, vol. 100, no. 2, pp. 120–126, (2003).

[14] Š. Branko, *Experimental And Numerical Investigation Of Chloride Ingress In Cracked Concrete*. (2014).

[15] G. Golden, "The Effect of Cyclic Wetting and Drying on the Corrosion Rate of Steel in Reinforced Concrete," University of Cape Town, South Africa, (2015).

[16] E. Poulsen and L. Mejlbro, *Diffusion of Chloride in Concrete: Theory and Application*. London and New York: Taylor & Francis Group, (2006).

[17] P. Arora, B. N. Popov, B. Haran, M. Ramasubramanian, S. Popova, and R. E. White,

"Corrosion initiation time of steel reinforcement in a chloride environment - A one dimensional solution," *Corros. Sci.*, vol. 39, no. 4, pp. 739–759, (1997).
[18] A. Neville, "Chloride attack of reinforced concrete: an overview," *Mater. Struct.*, vol. 28, no. 2, pp. 63–70, (1995).
[19] J. Crank, *The Mathematics of Diffusion*, 2nd Editio. Oxford: Clarendon Press, 1975.
[20] C. Edwards and D. Penney, "Elementary differential equations with boundary value problems." (1993).
[21] L. F. Yang, Z. Chen, Q. Gao, and J. W. Ju, "Compensation length of two-dimensional chloride diffusion in concrete using a boundary element model," *Acta Mech.*, vol. 224, no. 1, pp. 123–137, (2012).
[22] C. Frier and J. D. Sørensen, "Stochastic analysis of the multi-dimensional effect of chloride ingress into reinforced concrete," in *Proceedings of the 10th International Conference, 31 July - 3 August 2007,* pp. 191–200, (2007).
[23] M. B. Otieno, "Transport mechanisms in concrete. Corrosion of steel in concrete (initiation, propagation & factors affecting)," University of Cape Town, (2010).
[24] M. Otieno, "Corrosion Propagation in Cracked and Un-cracked Concrete," Univeristy of Cape Town., (2008).
[25] A. Djerbi, S. Bonnet, A. Khelidj, and V. Baroghel-bouny, "Influence of traversing crack on chloride diffusion into concrete," *Cem. Concr. Res.*, vol. 38, no. 6, pp. 877–883, (2008).
[26] J. Carmeliet, J.-F. Delerue, K. Vandersteen, and S. Roels, "Three-dimensional liquid transport in concrete cracks," *Int. J. Numer. Anal. Methods Geomech.*, vol. 28, no. 78, pp. 671–687, (2004).
[27] J. Harald, "A Review Of Chloride Binding In Cementitious Systems," *Nord. Concr. Res.*, vol. 21, p. 48–63., (1998).
[28] G. K. Glass and N. R. Buenfeld, "The presentation of the chloride threshold level for corrosion of steel in concrete," *Corros. Sci.*, vol. 39, no. 5, pp. 1001–1013, (1997).
[29] K. Y. Ann and H.-W. Song, "Chloride Threshold Level for Corrosion of Steel in Concrete," *Corros. Sci.*, vol. 49, no. 11, pp. 4113–4133, (2007).
[30] S. L. Poulsen and H. E. Sørensen, "Chloride Threshold Values - State of the art," *Danish Expert Cent. Infrastruct. Constr.*, pp. 0–33, (2012).
[31] J. M. Frederiksen, "Chloride threshold values for service life design," no. September, 2000.
[32] C. Andrade, C. Alonso, and F. J. Molina, "Cover cracking as a function of bar corrosion: Part I-Experimental test," *Mater. Struct.*, vol. 26, no. 8, pp. 453–464, (1993).
[33] F. J. Molina, C. Alonso, and C. Andrade, "Cover cracking as a function of rebar corrosion: Part 2—Numerical model," *Mater. Struct.*, vol. 26, no. 9, pp. 532–548, (1993).
[34] T. D. Marcotte, "Characterization of Chloride-Induced Corrosion Products that form in Steel-Reinforced Cementitious Materials," University of Waterloo, (2001).
[35] S. Muthulingam and B. N. Rao, "Non-uniform time-to-corrosion initiation in steel reinforced concrete under chloride environment," *Corros. Sci.*, vol. 82, pp. 304–315, (2014).
[36] Y. Zhao, A. R. Karimi, H. S. Wong, B. Hu, N. R. Buenfeld, and W. Jin, "Comparison of uniform and non-uniform corrosion induced damage in reinforced concrete based on a Gaussian description of the corrosion layer," *Corros. Sci.*, vol. 53, no. 9, pp. 2803–2814, (20110.
[37] C. Cao and M. M. S. Cheung, "Non-uniform rust expansion for chloride-induced pitting corrosion in RC structures," *Constr. Build. Mater.*, vol. 51, pp. 75–81, (2014).
[38] C. M. Hansson, A. Poursaee, and A. Laurent, "Macrocell and microcell corrosion of steel in ordinary Portland cement and high performance concretes," *Cem. Concr. Res.*, vol. 36, no. 11, pp. 2098–2102, (2006).
[39] M. Otieno, H. Beushausen, and M. Alexander, "Prediction of corrosion rate in RC structures - A critical review," *RILEM Bookseries*, vol. 5, no. 9, pp. 15–37, (2011).

A Study of Concrete Deterioration Faced by Distillery Industry

Ramaswamy K. P.[1, 2], Padmanabhan K.[3] and Manu Santhanam[1]

[1]Dept. of Civil Engineering, Indian Institute of Technology Madras, Chennai – 600036, India

[2]Dept. of Civil Engineering, TKM College of Engineering, Kollam – 691005, India

[3]Dept. of Civil Engineering, Bannari Amman Institute of Technology, Erode – 638401, India

ABSTRACT

Distillery spent wash is a highly polluting effluent generated from molasses based distillery industry. The high toxicity and large quantity of effluents generated demand the storage of these effluents in concrete tanks for treatment processes. Owing to its acidic nature, the effluent could react with cementitious materials resulting in degradation due to acid attack. The paper presents a case study in which concrete tanks used to store distillery spent wash in a molasses based distillery plant experienced premature deterioration. The nature of degradation was investigated by using characterisation techniques such as X-ray diffraction, scanning electron microscopy with energy dispersive spectroscopy and X-ray microtomography. The test results show that the deterioration could be due to the combined action of sulphuric and other organic acids present in the spent wash. The deterioration mainly results in the dissolution of crystalline hydrates to form an amorphous silica gel. Gypsum and calcite were found to be the secondary reaction products when sulphuric acid reacted with hydrates. Organic acids could also react with hydrates leading to the formation of soluble salts which leach out leaving the matrix highly porous as evident from the tomography images.

Keywords: Concrete, deterioration, distillery, spent wash, acid attack, and characterization.

1 INTRODUCTION

Distillery spent wash is a highly polluting effluent from distillery industry and is generated from the fermentation of sugarcane based molasses to produce alcohol. Molasses based distilleries have a very high BOD and COD, rich in organic contents. The wastewater (effluent) generated from the distillation of fermented mash is known as spent wash. The spent wash has a temperature range of 70–80 °C, and is deep brown in color and acidic in nature (low pH about 4-5) with a high concentration of organic materials and solids [1]. On an average, 8–15 litres of spent wash effluent are generated for every litre of alcohol produced [2]. India has about 620 sugar mills and about 400 molasses based distilleries with an installed capacity of 400 billion litres of alcohol and a potential to generate, on an average, 40 billion litres of spent wash annually. If disposed untreated on land and in an uncontrolled manner, this toxic effluent may also be hazardous to vegetation and affect the ground water quality due to dissolved leachates and colour. The enormous quantity of effluents generated necessitates the storage for further treatment processes before its safe disposal as per the pollution control board regulations [3-4]. Often, these effluents are stored in large silos made with concrete. Concrete being highly alkaline due to the nature of its pore solution and chemical composition, is prone to damage by these chemically aggressive effluents.

Anaerobic bacteria that thrive in these effluents consume the organic matter and produce a mixture of organic acids whose action on concrete can be highly detrimental [5]. The concrete deterioration due to acid attack in these aggressive environments is not well understood and needs further investigation.

The paper presents a case study of concrete deterioration due to spent wash in a molasses based distillery in Tamil Nadu, India. The concrete tank which is used to store spent wash was seen to be experiencing premature deterioration; the resultant frequent repairs had huge cost implications for the plant. The objective of this study is to understand the nature of concrete deterioration caused by these effluents by employing a set of micro-analytical characterisation techniques. Concrete samples were collected from the deteriorated locations, just below the water level where the spent wash is stored and characterisation techniques were used to investigate the deterioration further.

2 PRODUCTION OF SPENT WASH AND ITS CHARACTERISTICS

Sugar is produced in the sugar mills from sugarcane. This process generates a viscous liquid by-product named molasses and leaves sugarcane based bagasse (residue after crushing of sugarcane) as an industrial waste. Molasses from sugar industry is taken to distillery industry for alcohol production. The production of alcohol involves the process of fermentation, which is followed by distillation, leaving the residual liquid waste as spent wash.

According to Mohana et al. (2009), the production and the characteristics of the spent wash are highly variable [2]. It depends upon the raw material properties and various aspects related to the production of ethanol. The spent wash is acidic, recalcitrant in nature, has an unpleasant obnoxious odour of burnt sugar, and has very high BOD and COD. It is also found to be rich in inorganic substances such as nitrogen, potassium, phosphates, calcium, and sulphates. The typical composition of distillery spent wash is shown in Table 1. The dark brown colour of spent wash is attributed to the thermal degradation of the reducing sugars and the presence of amino compounds. This is due to the formation of melanoidins and polyphenolic compounds/complexes. The formation of melanoidin is also largely responsible for the very high COD of the effluent.

Table 1: Typical composition of distillery spent wash [2, 6-7]

Parameters	Values	Parameters	Values
pH	3.0–4.5	Total dissolved solids (mg/L)	90,000–150,000
BOD (mg/L)	50,000–60,000	Chlorides (mg/L)	8000–8500
COD (mg/L)	110,000–190,000	Phenols (mg/L)	8000–10,000
Total solids (mg/L)	110,000–190,000	Sulphate (mg/L)	7500–9000
Total volatile solids (mg/L)	80,000–120,000	Phosphate (mg/L)	2500–2700
Total suspended solids (mg/L)	13,000–15,000	Total nitrogen (mg/L)	5000–7000

3 SAMPLE COLLECTION AND TEST METHODS

The objective of the study is to understand the nature of concrete deterioration caused by the distillery spent wash generated in a molasses based distillery in Tamil Nadu, India. A large quantity of spent wash is generated by the plant and stored in considerably large sized open tanks lined with concrete. Fig. 1 shows the tank in which the spent wash in large quantity is stored for further treatment processes before its disposal to meet the environmental regulations. Concrete samples were collected using chisel and hammer from the severely deteriorated locations, just below the water level where the spent wash is stored.

The aggressiveness of spent wash resulted in premature deterioration of concrete inside, demanding frequent maintenance and repair works. Samples for testing were collected before the repair work in the inside of the tanks was carried out. The aspect of the samples collected is shown in Fig. 2. The samples appeared dark brown in colour due to the attack by spent wash and had pungent smell due to the ingress of spent wash into the concrete. The samples were found to be weak and it was relatively easy to chisel out the samples. A set of micro-analytical characterisation techniques was then used to investigate the deterioration in detail.

Fig. 1: Tank for storing spent wash

Fig. 2: Deteriorated concrete samples

4 TEST METHODS

The concrete deterioration due to the attack by aggressive chemicals present in spent wash resulted in serious alteration in microstructure primarily due to decalcification and associated lixiviation of hydrated cementitious phases. Tests such as X-ray diffraction, scanning electron microscopy with energy dispersive spectroscopy and X-ray computed micro-tomography were used to investigate the deterioration in detail.

4.1 X-ray diffraction

X-ray diffraction test was carried out on powdered samples passing 75 μm sieve so as to understand the mineralogical alterations in phases that occurs due to degradation of the cement matrix. The concrete samples were immersed in iso-propanol for 3 days and dried. In order to prepare the sample for testing, mortar chunks were separated from the concrete sample. The mortar samples so collected were crushed gently using a ceramic mortar and pestle and sand grains were separated as much as possible using coarser sieves. X-ray diffractograms were obtained using X'Pert Pro PANalytical diffractometer. The scanning range adopted was over the 2θ range from 5-65° at a step size of 0.02°. A Cu K_α radiation was used to generate X-rays with voltage of 45 kV and current of 30 mA. The identification of phases was done using the software, X'Pert HighScore Plus with ICSD database.

4.2 Scanning electron microscopy

Scanning electron microscopy coupled with energy dispersive spectroscopy was used to study the morphological changes of phases and to understand the mechanism of alteration. Flat samples were cut using a diamond tipped saw. The samples were then immersed in isopropanol for 3 days followed by drying. The dried samples were sputter coated with gold for imaging. A scanning electron microscope named Inspect F, which has a field emission gun with high vacuum, was used in secondary electron imaging mode. As the cut sample cross-section was relatively flat, energy dispersive spectroscopy was used directly on the samples to determine the elemental composition of various phases observed.

4.3 X-ray tomography

X-ray Computed Tomography (CT) is a non-invasive technique for visualizing the microstructural features within the solid objects, and for obtaining the digital information on their 3-D geometries and properties. Tomography has been successfully used by researchers to characterize the microstructure evolution and deterioration associated with calcium leaching in cement-based materials [8-10]. The tomography test set up at IIT Madras used for imaging, v|tome|x s is a versatile high resolution system consisting of both micro and nano focus X-ray tubes. Cubical samples of size approximately 10 mm were cut from the samples collected using a diamond tipped saw. Solvent exchange process using iso-propanol (3 days immersion of samples) was used for the specimen conditioning followed by drying in desiccator. The dried specimens were then taken for the CT imaging. A voltage of 70 kV and current of 200 μA was maintained during the test. Microfocus X-ray tube was used for generating the X-rays. The specimen was rotated 360° and a total of 900 images were captured during the complete rotation of specimen in the stage, to reconstruct the three dimensional image. The 3-D image was then processed to get the desired 2-D slice images.

5 RESULTS AND DISCUSSION

5.1 X-ray diffraction

Two types of concrete samples were collected from the deteriorated locations of the tank wall. The sample collected from 0-5 mm from the surface was highly deteriorated, and is named as P_1 outer. Another sample was collected from approximately 5-10 mm from the surface and is named as P_1 inner. The X-ray diffractogram of the P_1 outer sample is shown in Fig. 3. It can be seen from the diffractogram that the outer zone (0-5 mm) is mostly amorphous with a prominent amorphous silica band centered at 2θ of about 27°. The low pH of the spent wash resulted in severe decalcification of cementitious materials resulting in leaching and dissolution of crystalline hydrate phases in the outer zone. In the process, CSH and other hydrates containing Si and Al got converted to an amorphous gel rich in silica and alumina. Formation of silica gel and decalcification of Ca from hydrates increased the porosity of the matrix, thus having impact also in the transport and mechanical properties. As the spent wash is rich in sulphate and also contains sulphuric acid (added to the fermentation broth to adjust the pH), there could be additional phases formed due to its reaction with hydrates also. The reaction of calcium bearing cement hydrates such as portlandite, ettringite, CSH etc. with sulphuric acid led to formation of substantial quantity of gypsum. However, it was found only in 0-5 mm from the surface due to the limited penetration of sulphuric acid and lower concentration of acid present in spent wash. Quartz peak was prominent in the diffractogram and this is mostly due to the unavoidable crushing of fine aggregates which might be present during the preparation of sample for XRD analysis. Small quantity of calcite and hematite was also formed as secondary reaction product. Formation of calcite on the surface could be due to diffusion of carbon dioxide and subsequent reaction with portlandite during the dry cycle when the tank was not in operation. It is interesting to note that hydrates such as ettringite, portlandite and anhydrous phases such as alite and belite were totally absent in the outer zone. This confirms the aggressiveness of acids present in spent wash as the hydrates and anhydrous phases are finally converted to silica gel. The reaction of most of the organic acids (such as acetic acid) with the hydrates form calcium and aluminum salts which are soluble and leach to the outside solution, and are hence not detected in the diffractogram of the outer zone.

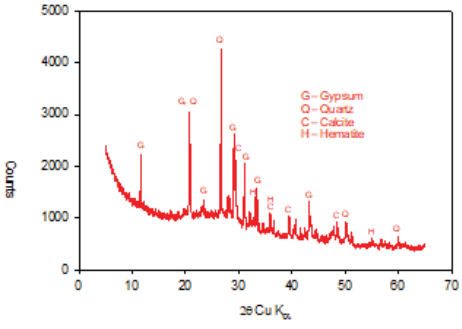

Fig. 3: XRD pattern of P_1 outer

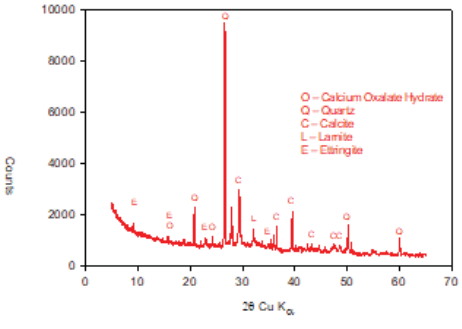

Fig. 4: XRD pattern of P_1 inner

The diffractogram of the sample P_1 inner is shown in Fig. 4. Unlike the outer 5 mm, ettringite in small quantity is found to be stable in 5-10 mm zone. This could be due to the relatively higher pH at which ettringite is stable. Ettringite formation may be attributed to the combined sulphate and acid attack in which tricalcium aluminates are converted to ettringite. As the formation of gypsum was limited to the external surface, it was not observed in the 5-10 mm zone. The presence of quartz to some extent may be attributed to the crushing of fine aggregates at the time of sample preparation. It was noted that the inner zone was less amorphous compared to the outer zone indicating lesser decalcification and degradation. Calcite was identified with its primary peak at 29.5°. A small quantity of anhydrous larnite (dicalcium silicate) was also observed in this zone. Oxalic acid present in spent wash could have reacted with various hydrates to form the salt, calcium oxalate hydrate also known as Whewellite ($Ca(C_2O_4)H_2O$) which is less soluble and hence, traces of it were detected in the XRD pattern of P_1 inner sample. The precipitation of this salt could have a protective effect in limiting the progress of the reaction front as it could seal the porosity of the matrix to some extent, similar to gypsum in the case of lower concentrations of sulphuric acid. The other acids (primarily acetic acid) in the spent wash form soluble salts. Such salts leach into the solution and hence were not detected in the diffractogram. Overall, X-ray diffractograms suggest the fact that the deterioration is mainly due to combined action of a mixture of organic acids and sulphuric acid. The deterioration results in lixiviation of cementitious phases forming ettringite and gypsum in addition to a gel skeleton rich in silica and alumina, depending upon the depth from the surface.

5.2 Scanning electron microscopy

The degradation of concrete due to the action of various acids results in alteration in microstructure mainly due to the decalcification of calcium and aluminum bearing phases of hydrates. Electron micrographs were collected from the deteriorated regions in secondary electron mode. Fig. 5 shows the morphology of the attacked surface at a magnification of 250x. The morphology presented in Fig. 5 is typical of cementitious matrix that is decalcified by the action of acids. Loosely held particles along with aggregate phases (mainly quartz) were observed. In order to obtain more information about the reaction products formed, a magnified image (1000x) is taken in a void near to aggregate phase and is shown in Fig. 6. The major reaction products as confirmed by EDS results were observed to be gypsum and an amorphous gel rich in silica. These results were in line with the X-ray diffractograms obtained. Fig. 7 show the morphology of gypsum bound with silica gel. The cement hydrates such as Portlandite, CSH, CASH, ettringite and calcium aluminates decalcify to form gypsum and a gel rich in alumina and silica on reaction with sulphuric acid present in spent wash. It is

also observed that magnesium is also present in substantial quantities on attacked surface. Presence of magnesium points out the possibility that the concrete being tested may have had a binder admixed with slag at the time of construction because of its enhanced chemical resistance.

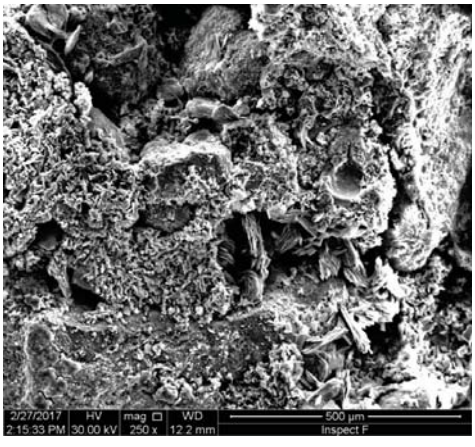

Fig. 5: Morphology of acid interacted surface exhibits degradation

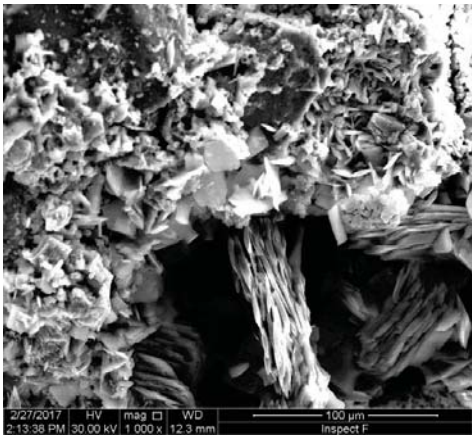

Fig. 6: A close look at the acid interacted surface showing reaction products

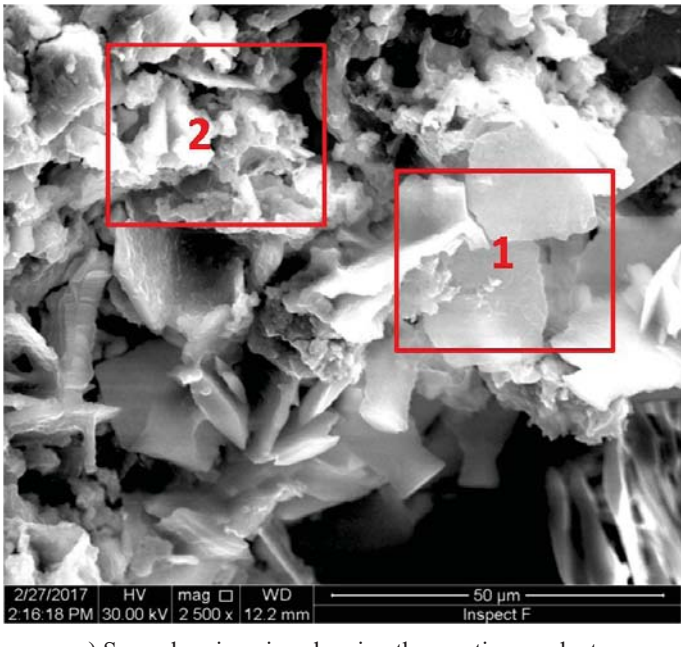

a) Secondary imaging showing the reaction products

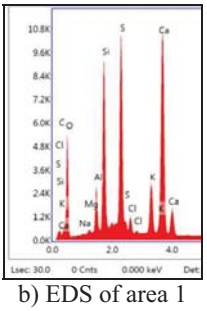

b) EDS of area 1

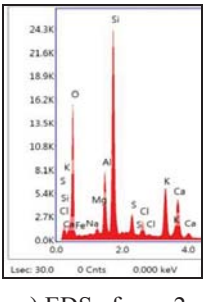

c) EDS of area 2

Figure 7: A close look at the morphology of reaction products showing gypsum and silica gel

5.3 X-ray tomography

Fig. 8(a) shows the 3D rendered image of the sample collected from 0–5 mm from the surface (P_1 outer). The sample was found to be highly porous and weak. This was evident at the time of sample preparation for CT imaging. Mechanical and binding properties being lower, cubical shape was not obtained for the sample despite the use of high precision diamond saw cutting blade. The action of various organic acids on concrete resulted in dissolution of hydrates, especially portlandite, on the surface and this led to the rough texture of the surfaces of specimens that is quite evident from the 3D rendered image. Fig. 8(b) is obtained by performing suitable thresholding operation on the 3D reconstructed image using the software Volume Graphics (by moving the isobar line to the right) so that only high dense particles in the matrix such as aggregates are visible in the 3D image. Siliceous aggregates are generally considered to be stable and inert to the attack by mild concentrations of various acids. From Fig. 8(b), it can be inferred that the matrix is richer in aggregates. The 3D reconstructed image is processed further to get Fig. 8(c), to highlight the various phases including the porosity. Coarse and fine aggregates appear light grey in colour due to its higher density while porosity (voids) is seen as black in colour. The deteriorated paste phase appears as darker due to the decalcification of cement hydrates and associated reduction in density of the phases. It is seen only as a very thin layer around the aggregate phase. The high porosity of the samples is also clearly evident from Fig. 8(c).

A stack of 2D slice images (top view and front view) were generated from the 3D reconstructed image. Fig. 9(a) shows the top view slice image of the sample cut from 0-5 mm from the external surface (P_1 outer). It is evident that the deterioration is more pronounced at the exterior surface. The outer zone as depicted in Fig. 9(a) appears very dark and this could be attributed to the severe decalcification of paste due to the attack of various acids forming silica gel, resulting in lower grayscale values of pixels in the 2D slice images. Sulphuric acid present in spent wash react with hydrates to form gypsum and is embedded in a gel skeleton rich in silica and alumina. Organic acids also react with hydrates to form calcium salts along with silica alumina gel. The formation of silica alumina gel results in dark appearance of paste in images. The specimen loses the binding ability due to the formation of this amorphous gel. Three mineralogical zones could be identified from the slice images; an outer zone which is severely degraded (zone 1), middle zone which has been decalcified (zone 2) and inner zone (zone 3) which is decalcified to a lesser extent (decalcification ongoing).

Conversion of hydrates to silica alumina gel results in reduction of volume and leads to formation of decalcification-related shrinkage cracks. These cracks around the aggregates are prominent in the slice images and this could have led to increased rate of deterioration due to further acid ingress towards inside. Some organic acids such as acetic acid present in spent wash form soluble salts on reaction with cement hydrates, which get leached away to the spent wash solution. This may be one of the reasons for the increased porosity of the specimen. The highly dense particles which appear white in colour in slice images could be ascribed to the possible use of aggregates containing limestone. The presence of limestone is concluded from the calcite phase that is identified from the XRD analysis. The front view image of the specimen as shown in Fig. 9(b) also confirms the very high porosity and cracking in the interfacial transition zones (ITZ) which could have led to the increased rate of degradation. It appears from the slice images that most of the pores are large in size and this could be possibly due to improper compaction done during the construction. Action of various acids along with the increased porosity has led to the rapid rate of degradation of the structure being investigated.

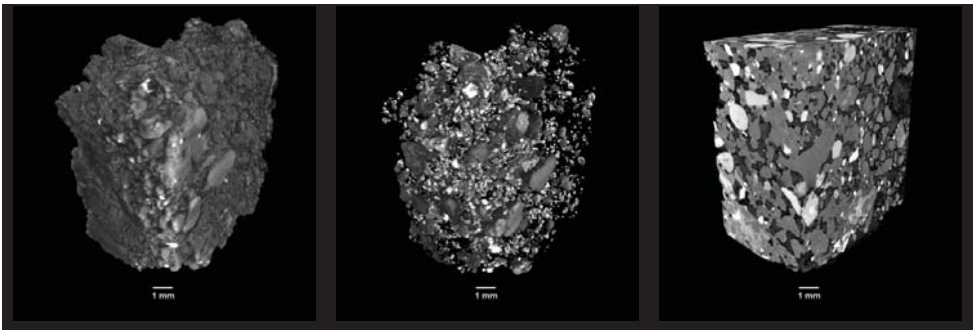

Fig. 8: X-ray CT images of P_1 outer sample

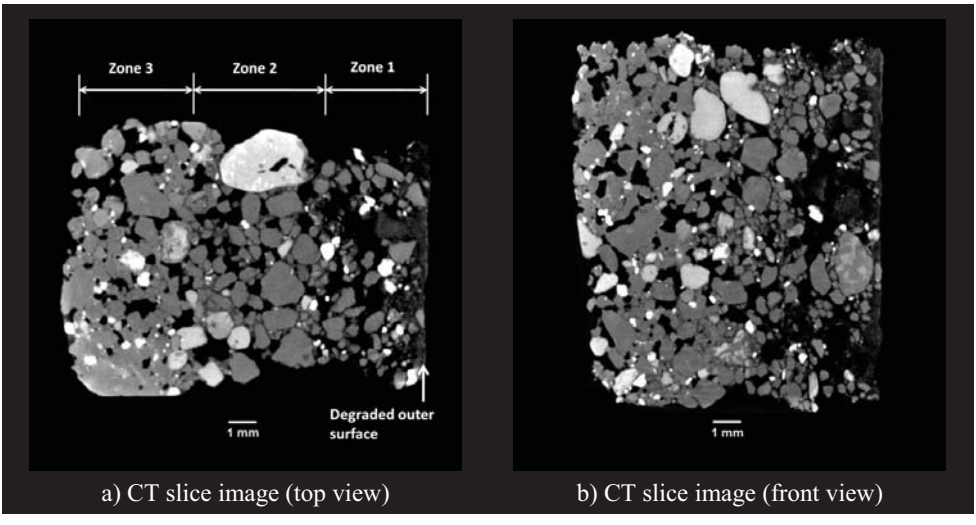

Fig. 9: CT images of P_1 outer sample showing deterioration

6 CONCLUSIONS

The concrete deterioration due to the spent wash in molasses based distillery industry is investigated using micro-analytical characterisation techniques such as X-ray diffraction, scanning electron microscopy coupled with energy dispersive spectroscopy and X-ray computed micro-tomography. Distillery spent wash is a highly polluting effluent, rich in organic matter and the organic acids produced by anaerobic microorganisms thriving in these effluents along with sulphuric acid are highly detrimental to the cementitious matrix as it results in the deterioration due to decalcification of hydrated products because of acid attack.

The alteration in microstructure due to decalcification results in mineralogical zonation. XRD results reveal that the outer zone (0-5 mm) has turned out to be mostly amorphous with a prominent amorphous silica band centered at 2θ of about 27°. The reaction of hydrates with sulphuric acid present in the spent wash led to gypsum formation in the 0-5 mm zone. A very small quantity of calcite and hematite was also formed as reaction products. It is observed that cement hydrates such as ettringite, portlandite and anhydrous phases such as alite and

belite are totally absent in the outer zone, which confirms the aggressiveness of the effluent. Unlike the outer 5 mm, ettringite in small quantity was found to be stable in 5-10 mm zone. This inner zone was found to be less amorphous compared to the outer zone indicating lesser decalcification and degradation. Calcite was also identified with its primary peak at 29.5°. Traces of the less soluble salt, calcium oxalate hydrate ($Ca(C_2O_4)H_2O$) which is formed due to the reaction of oxalic acid with various hydrates were also detected in the diffractograms of the sample collected from 5-10 mm from the surface.

SEM and EDS results were found to be in line with the analysis results obtained based on XRD. The morphology of the acid interacted surface showed severe degradation. Loosely held particles comprising of silica gel along with aggregate phases (mainly quartz) are observed. The morphology of the attacked surface was typical of slag admixed concrete. Presence of magnesium in EDS results validates this conclusion that the concrete being tested might have been admixed with slag owing to its enhanced resistance to chemical attack. X-ray tomography images also revealed serious deterioration. The deteriorated paste appeared darker due to the decalcification of cement hydrates and associated reduction in density of the phases. Sulphuric acid present in spent wash reacts with hydrates to form gypsum and is embedded in a gel skeleton rich in silica and alumina. Organic acids also react with hydrates to form calcium salts along with silica alumina gel. The formation of silica alumina gel results in dark appearance of paste in images. The specimen loses the binding ability due to the formation of this amorphous gel. Three mineralogical zones could be identified from the CT slice images; an outer zone which is severely degraded, middle zone which has been decalcified and inner zone which is decalcified to a lesser extent (decalcification ongoing). Some organic acids present in spent wash form soluble salts on reaction with cement hydrates that get leached away to the spent wash solution. This may be one of the reasons for the increased porosity of the specimens.

It is concluded that the severe and premature deterioration of concrete tanks in the sugar molasses based distillery industry is primarily due to the attack by various acids (sulphuric acid and organic acids) that are present in the spent wash. Calcium bearing hydrate phases are relatively not stable in these low pH aggressive acidic environments. The effectiveness of inclusion of supplementary cementing materials and special cements such as high alumina cements in enhancing the acid resistance of concrete needs to be explored further to combat these aggressive conditions.

7 REFERENCES

[1] Mohana, S., Acharya, B. K., Madamwar, D., 'Distillery spent wash: Treatment technologies and potential applications', *Journal of Hazardous Materials*, 163 (2009), 12-25.

[2] Saha, N. K., Balakrishnan, M., Batra, V. S., 'Improving industrial water use: Case study for an Indian distillery', *Resources, Conservation and Recycling*, 43 (2005) 163-174.

[3] Tewari, P. K., Batra, V. S., Balakrishnan, M., 'Water management initiatives in sugarcane molasses based distilleries in India', *Resources, Conservation and Recycling*, 52 (2007)351-367.

[4] Pant, D., Adholeya, A., 'Biological approaches for treatment of distillery wastewater: A review', *Bioresource Technology*, 98 (2007) 2321-2334.

[5] Larreur-Cayol, S., Bertron, A., Escadeillas, G., 'Degradation of cement-based materials by various organic acids in agro-industrial waste-waters', *Cement and Concrete Research*, 41 (8) (2011) 882-892.

[6] Mohana, S., Desai, C., Madamwar, D., 'Biodegradation and decolorization of anaerobically treated distillery spent wash by a novel bacterial consortium', *Bioresource Technology*, 98 (2007) 333-339.

[7] Acharya, B. K., Mohana, S., Madamwar, D., 'Anaerobic treatment of distillery spent wash: A study on upflow anaerobic fixed film bioreactor', *Bioresource Technology*, 99 (2008) 4621-4626.
[8] Koenig, A., Dehn, F., 'Main considerations for the determination and evaluation of the acid resistance of cementitious materials', *Materials and Structures*, 49 (5) (2016). 1693 – 1703.
[9] Dyer, T., 'Influence of cement type on resistance to organic acids', *Magazine of Concrete Research*, 69 (4) (2016) 175-200.
[10] Ramaswamy, K. P., Santhanam, M., 'Degradation kinetics of cement-based materials in citric acid', *10th Structural Engineering Convention*, (2016) 1690-1695.

Changes in Pore Structure Properties of Cement Paste and Concrete on Carbonation

Vineet Shah, Anuj Parashar and Shashank Bishnoi

Indian Institute of Technology Delhi, India

ABSTRACT

Carbonation is one of the major factors affecting the performance of concrete. Calcium hydroxide (CH) and calcium silicate hydrate (C-S-H) which constitutes the major part of the hydration products, aids in maintaining the alkaline environment in concrete. The hydration products get transformed to calcium carbonate (CC) on exposure to carbon dioxide. Because of difference in molar solid volume of the hydrated and carbonated products, overall porosity and pore structure of the concrete system is altered. In this study effect of carbonation on the microstructure of cement paste and concrete cast with ordinary Portland cement, binary and ternary cement have been investigated. Carbonation study was carried out at 3% carbon dioxide concentration, 60% relative humidity and 27°C. Coarsening of pore structure was observed on carbonation in general. For blended cement, the total porosity increased on carbonation.

Keywords: Accelerated carbonation, porosity, pore Structure, molar volume

1 INTRODUCTION

The hydration reaction of Portland cement produces calcium hydroxide (CH) and calcium silicate hydrate (C-S-H) as the main hydration phases. The hydration products of cement form a highly alkaline pore solution in concrete. In the alkaline environment, the compounds of iron form a thin protective oxide film around reinforced steel embedded in concrete. This layer does not stop the corrosion reaction but reduces the rate of corrosion to an insignificant level [1]. Carbon dioxide from atmosphere diffuses into capillary pores of concrete and dissolves in pore water forming carbonic acid, which reacts with the dissolved ions of hydration products available in pore solution, resulting in reduced pH of the system. At reduced pH, the oxide layer protecting reinforcement is destroyed, making steel in concrete susceptible for corrosion. In blended cements due to dilution effect and pozzolanic reaction of supplementary cementitious materials (SCMs) the overall alkalinity of the system is lower and thus making it more prone to corrosion due to carbonation [2].

Carbonation leads to change in the microstructure of concrete due to the difference in molar solid volume of the hydrated and carbonated phases. Several studies have reported a reduction in porosity of concrete on carbonation of CH. The molar solid volume of ($C\bar{C}$) formed is 11-14% more as compared to that of CH depending upon the type of polymorph precipitated [2-3]. Various studies have reported decrease in porosity and critical pore diameter on carbonation of concrete cast using ordinary Portland cement (OPC) [4-6]. Cement containing SCMs have lower amount of calcium hydroxide as compared to OPC due

to the pozzolanic reaction of SCMs. In absence of CH, C-S-H carbonates extensively. The volume change due to carbonation of C-S-H is not yet established because of the absence of exact stoichiometric calculations [3]. Carbonation results in decalcification of C-S-H leading to formation of Si-OH groups because of the presence of excess negative charges. The Si-OH groups condense with neighbouring groups to form Si-O-Si linkages, resulting in the polymerization of silicate chains and release of water which might lead to reduction in solid volume and coarsening of pore structure [7-8]. Lack of knowledge and discrepancies in evaluating change in solid volume on carbonation makes it difficult to accurately quantify the change in porosity due to carbonation in cement.

This study aims at examining change in microstructure properties of concrete and cement paste cast using blended cements. Ordinary Portland cement (OPC), Portland pozzolana cement (PPC), Portland slag cement (PSC) and limestone calcined clay cement (LC^3) were used in the study. Effect of carbonation on water absorption and rate of water absorption on concrete was measured whereas mercury intrusion porosimetry (MIP) was used to study the changes occurring in the pore structure characteristics on carbonation.

2 METHODOLOGY AND EXPERIMENTS

2.1 Materials

OPC was produced in laboratory by grinding clinker in a laboratory scale ball mill. PPC was produced by interblending 70 % OPC and 30 % fly ash in a ball mill. LC^3 was produced having composition of 50% clinker, 31% calcined clay, 15% limestone and 4% gypsum. PSC was produced by interblending 50% OPC and 50% slag in a ball mill. All the above materials were ground individually and thereafter intermixed in a ball mill to produce the blend. The chemical properties of the raw materials measured using X-ray fluoresce spectroscopy (XRF) is shown in Table 1.

Table 1: Chemical analysis of raw materials

	Clinker	**Limestone**	**Gypsum**	**Clay**	**Fly-Ash**	**Slag**
SiO_2	21.07	11.02	2.77	51.67	58.82	32.26
Fe_2O_3	4.32	1.55	0.36	4.93	6.19	1.93
Al_2O_3	4.65	2.53	0.62	27.69	30.62	23.16
CaO	65.16	44.24	32.62	0.06	1.01	33.88
MgO	2.13	1.96	1.20	0.13	0.41	7.01
SO_3	0.77	---	38.75	0.10	0.12	---
Na_2O	0.38	0.50	0.06	0.12	0.19	0.010
K_2O	0.20	0.28	0.037	0.25	1.30	0.37
LOI Ignition	0.96	36.96	23.02	10.28	1.11	1.08
Specific Gravity		2.62	2.57	2.64	2.17	2.80
D50(μm)		20.2	20.1	5.86	17.5	14.1

2.2 Casting and Exposure Conditions

Concrete was cast using four different types of cement at a water to cement ratio of 0.35. Cylinder specimens having diameter of 10 cm and height of 20 cm were cast. After 24 hours of casting, the specimens were demolded. Thereafter, the concrete samples were cured under lime saturated water for 120 days. Prolonged curing period was selected to ensure maximum hydration of cement. Cement paste samples were cast in a cylindrical mold having a diameter

of 2 cm and a height of 10 cm at a water to cement ratio of 0.35. Curing conditions similar to concrete was adopted for curing cement paste samples.

After the curing regime, the cylinders were cut into disc specimens having height of 5±0.2 cm. Epoxy was applied on the circumference of the cylinders, leaving only top and the bottom face exposed. Thereafter, the specimens were kept in a conditioning room having temperature of 27°C and relative humidity of 60% for 15 days. Thin discs of 3-5 mm were cut from cement paste and were exposed to carbon dioxide straightaway without any preconditioning. All the specimens were kept in carbonation chamber having carbon dioxide concentration of 3%, 27°C and 60% relative humidity.

2.3 Methodology

The porosity was measured according to the guidelines described in ASTM C642, whereas rate of water absorption was measured according to the guidelines mentioned in ASTM C1585. The initial properties of concrete i.e. non-carbonated concrete were measured on specimens after the end of the preconditioning period. Tests on carbonated specimens were done at the end of 28 days of exposure to carbon dioxide. MIP was performed on fully carbonated cement paste samples. Prior to MIP analysis, the disc samples were dried by solvent exchange method [9]. At the time of analysis, the dried disc samples were broken into smaller fragments having dimensions of approximately 3×3×3 mm. A total of 5 such pieces with the cumulative mass of 1.5-1.8 g were used for the analysis.

3 RESULTS

3.1 Water absorption and rate of water absorption

Porosity of non-carbonated and carbonated concrete was determined through water absorbed by concrete. Figure 1 shows the result of change in porosity of concrete on carbonation. Sorptivity test was conducted to observe change in rate of water absorption due to carbonation. Figure 2 shows the sorption index of non-carbonated and carbonated concrete. Only the primary rate of absorption of concrete was measured in this study

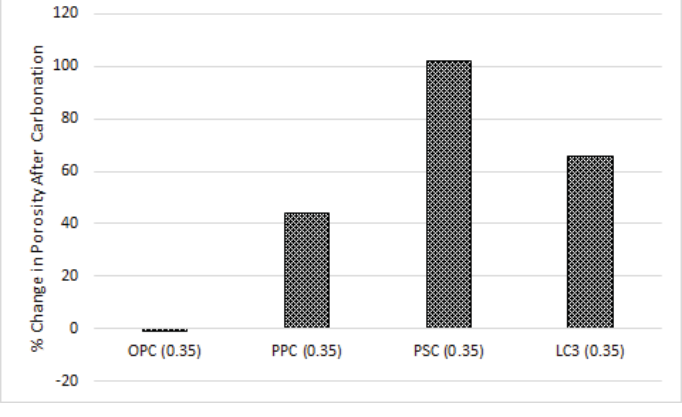

Figure 1: Change in porosity of concrete on carbonation after 28 days of exposure to carbon dioxide

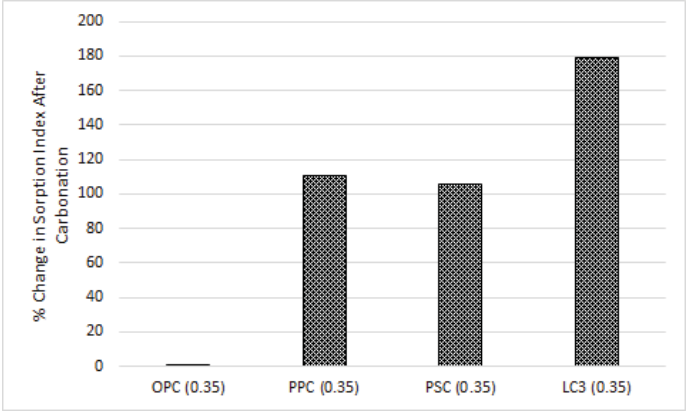

Figure 2: Water absorption index (sorption index) of concrete on carbonation after 28 days of exposure to carbon dioxide

3.2 Pore structure

The MIP results of non-carbonated (NC) and carbonated (C) samples are shown in figure 3 and 4 respectively. The critical pore diameter of the blended cements is smaller than OPC in non-carbonated samples. The pozzolanic reaction of SCMs helps in refinement of pore structure. However, volume of mercury intruded in OPC is lowest. On carbonation, coarsening of pore structure is observed in all the blends. Also, volume of mercury intruded is increased on carbonation in blended cements whereas small reduction in intruded volume is observed for OPC sample. The MIP curves of OPC, PPC and LC^3 are part of results published elsewhere [11] and are used here for completeness of this study.

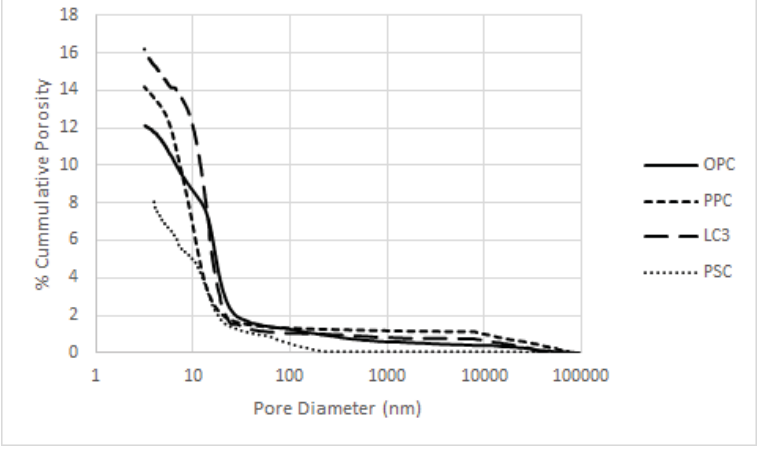

Figure 3: Mercury intrusion porosimetry curves of non-carbonated samples

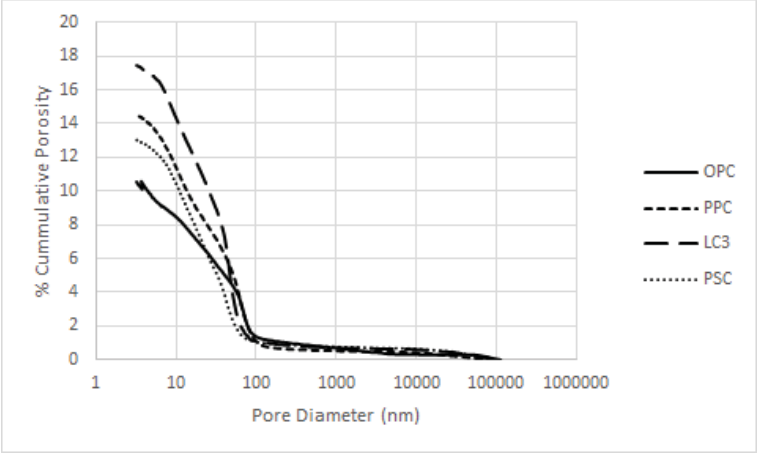

Figure 4: Mercury intrusion porosimetry curves of carbonated samples

4 DISCUSSION

All the phases formed on hydration of cement have the tendency to carbonate [12-13]. Calcium hydroxide is the major phase responsible for maintaining pH in concrete which results in stabilization of other hydration phases. The change in volume caused by carbonation of phases other than calcium hydroxide is not as straightforward. For an instance, carbonation of C-S-H leads to the formation of calcium carbonate and silica gel. The removal of calcium ions from C-S-H leads to formation of Si-OH groups. These silica chains condense with each other and polymerize. The volume of the silica gel produced depends upon the extent of polymerization, whether the carbonation of C-S-H produces any free water similar to reaction of CH or some/all the water molecules are attached with the silica gel formed is not clear [3]. This makes it difficult to establish an exact stoichiometry for the carbonation of C-S-H. Similarly, phases comprising of alumina form calcium carbonate and aluminum hydroxide on carbonation. The total solid volume of the products formed will vary depending upon polymorph of calcium carbonate formed and type of aluminum hydroxide formed i.e. as gibbsite or amorphous alumina gel. The total solid volume of ettringite reduces by approximately 35% after carbonation whereas solid volume of carbonated C-S-H may reduce or increase by 20% depending upon extent of polymerization and amount of water associated with decalcified C-S-H [10-11]. Therefore, depending upon the age of testing, type of cement and phases getting carbonated varying results can be obtained.

The change in pore structure measured on cement paste by MIP shows shifting and coarsening of pores on carbonation. Coarsening of pores is allied with increase in total number of capillary/permeable pores. The porosity measured by boiling water test is mainly due to capillary pores, MIP results indicate the increase in the volume of capillary pores on carbonation, hence confirming the higher porosity in carbonated system. The sorption index which primarily measures the absorption because of capillary pores also increases on carbonation which further validates the above observation of coarsening of pores on carbonation. The change in porosity of concrete made using OPC is minor, this can be due to precipitation and clogging of pores by calcium carbonate formed from carbonation of calcium hydroxide. The increase in porosity and coarsening of pore structure is more pronounced in systems having lower clinker factor.

5 CONCLUSIONS

Carbonation study was carried out on blended cements, in accelerated carbonation condition, to understand the effect of carbonation on pore structure characteristics of concrete.

- MIP results depict restructuring of pores on carbonation. Coarsening of pore structure and increased critical pore diameter is observed on carbonation in all the cements.
- Increase in water permeable porosity of concrete is observed on carbonation, irrespective of type of blended cement used for casting. Minor reduction in porosity of concrete cast using OPC was observed.
- The rate of water absorption of the concrete is increased on carbonation due to increase in fraction of capillary pores. Increased capillary pores may escalate the susceptibility of concrete for deterioration due to faster diffusion of water and other ions through the pores.
- The increase in porosity on carbonation can be attributed to carbonation of hydrated phases other than calcium hydroxide which has lower molar solid volume as compared to original hydration products on carbonation.

REFERENCES

[1] Richardson, M.G., 'Fundamentals of durable reinforced concrete', (London, 2002)

[2] Lagerblad, B., 'Carbon dioxide uptake during concrete life cycle – State of the Art Report', Cement & Concrete Research, Vol. CBI 2005:2

[3] A. Morandeau, M. Thiery, P. Dangla, Investigation of the carbonation mechanism of CH and C-S-H in terms of kinetics, microstructure changes and moisture properties, Cement and Concrete Research, 56 (2014) 153-170

[4] Phung T.Q., Maes N., Jacques D., Bruneel E., Driessche V.I., Ye G. and Schutter D.G., 'Effect of limestone fillers on microstructure and permeability due to carbonation of cement pastes under controlled CO_2 pressure conditions', Construction and Building Materials 82 (2015) 376-390

[5] FrÍas M. and GoñI S., 'Accelerated carbonation effect on behavior of ternary Portland cements', Composites: Part B, 48 (2013) 122-128

[6] Ngala T.V. and Page C.L., 'Effects of carbonation on pore structure and diffusional properties of hydrated cement pastes', Cement & Concrete Research, 27(7) (1997) 995-1007

[7] Borges R.H.P, Costa O.J., Milestone B.N., Lynsdale J. C. and Streatfield E. R., 'Carbonation of CH and C-S-H in composite cement pastes containing high amounts of BFS', Cement and Concrete Research, 40 (2010) 284-292

[8] Gruyaert E., Heede D.V.P. and Beile D.N., 'Carbonation of slag concrete: Effect of the cement replacement level and curing on the carbonation coefficient – Effect of carbonation on the pore structure', Cement and Concrete Research, 35 (2013) 39-48

[9] Durdzinski T.P., 'Hydration of multi-component cements containing cement clinker, slag calcareous fly ash and limestone', PhD Thesis, Ecole Polytechnique Federale De Lausanne, 6834 (2016)

[10] Lamberet S., 'Durability of ternary binders based on Portland cement, calcium aluminate cement and calcium sulfate', PhD Thesis, Ecole Polytechnique Federale De Lausanne, 3151 (2005)

[11] Shah V, Bishnoi S. and Bhattacharjee B., 'Pore structure characteristics of carbonated concrete', submitted to Construction and Building Materials (2017)

[12] Papadakis V.G., Vayenas C.G. and Fardis M.N., 'Fundamental modeling and experimental investigation of concrete carbonation', ACI Materials Journal, 88(4) (1991) 363-373

[13] Glasser F.P. and Matschei T., 'Interactions between Portland cement and carbon dioxide', Proceedings 12th International congress on the chemistry of cement, Canada (Monteral) (2007)

Bond Enhancement of Repair Mortar via Biodeposition

Didier Snoeck[(1)], Jianyun Wang[(1)], Dale P. Bentz[(2)] and Nele De Belie[(1)]

[(1)]Magnel Laboratory for Concrete Research, Faculty of Engineering and Architecture, Ghent University, Technologiepark Zwijnaarde 904, B-9052 Ghent,Belgium

[(2)]Engineering Laboratory, National Institute of Standards and Technology, 100 Bureau Drive, Stop 8615, Gaithersburg, MD 20899, USA

ABSTRACT

The bond between repair mortars and existing concrete substrates is critical for the long-term performance and durability of the repaired structure. The carbonation state of the substrate is one of the parameters that may affect this bond strength. The type of calcium carbonate polymorph (calcite, aragonite or vaterite) affects the nucleation and growth of cement hydration products. In this study, carbonation of the mortar substrate is promoted via the biodeposition of calcium carbonate by aureolytic bacteria strain previously employed in bioconsolidation. X-ray diffraction and scanning electron microscopy were used to examine the interfaces between the repair material and the substrate, as well as the polymorph of the deposited calcium carbonate. It appeared that the approximately 50 µm thick biodeposition film on the mortar surface mostly consisted of calcite and vaterite. The deposited crystals were full of bacterial imprints. Both the repair material and the substrate tended to show a good adherence to that layer. The bond, as assessed in this study by slant shear specimen testing, was improved by the presence of the biodeposition layer.

Keywords: Calcium carbonate, bond strength, slant shear, biodeposition.

1 INTRODUCTION

Concrete is one of the most widely used construction materials on Earth. It is an ideal material to resist compressive forces, but when sufficient tensile forces are present, the restrained concrete may crack. And, without repair of the cracks, the durability can be critically compromised. One can decide to use a self-healing concrete during the design phase of construction [1-3], but repair of existing concrete structures will still often be needed. This manual repair should be made with care and precautions should be taken to assure that the repair is long-lasting, durable and efficient. If the bond between repair product and concrete substrate is not sufficient, delamination or spalling may occur. Therefore, one needs to make sure that the surface treatment of the substrate is properly executed.

One way of increasing and controlling the bond between the repair material and the concrete substrate could be the use of a biodeposition layer. One of the first patented applications on biodeposition was the protection of ornamental stone by a microbially deposited carbonate layer [4,5]. This calcium carbonate precipitation can be biologically induced by bacteria. These bacteria synthesize the minerals in a unique form, characteristic of the specific species of bacteria. This biodeposition technique has also been applied on cementitious materials resulting in an increased resistance of mortar specimens towards chloride penetration, freeze/thawing and carbonation [4,6-8]. It should merely be considered as a coating system as carbonate precipitation is mainly a surface-controlled phenomenon due

to the limited penetration of bacteria into the porous cementitious matrix. Thin-section analysis revealed that the thickness of the bacterial layer was typically within the range of 10 to 40 μm; in which larger crystals up to 110 μm could be found [4]. This layer can be a promising route to engineer for optimal bond strength characteristics.

In this paper, the bond strength was assessed by slant shear testing. Specimens with and without biodeposition layer were studied and the crystal formation composition and morphology were examined.

2 MATERIALS AND METHODS

2.1 Bacterial strain and cultivation condition

Bacillus sphaericus LMG 22257 (Belgian coordinated collection of microorganisms, Ghent) was used in this study. The bacteria were grown aseptically in the growth medium (400 mL per batch) which consisted of a blend of yeast extract (20 g/L) and urea (20 g/L). The culture was incubated at 28°C on a shaker at 100 rpm [10.5 rad/s] for 24h. Subsequently, the bacterial cells were harvested by centrifugation (7000 rpm [733.0 rad/s], 7 min) of the 24h old grown culture and were resuspended in sterile saline solution (NaCl, 8.5 g/L). The concentration of the bacteria in the suspension was $1.5 \cdot 10^9$ cells/mL to $2 \cdot 10^9$ cells/mL. The obtained bacterial suspension was stored in a 4°C refrigerator for further experimental use.

2.2 Mortar specimens

The standard used to make the mortar substrates was ASTM C882/C882M-13 on 'Bond strength of epoxy-resin systems used with concrete by slant shear'. Six Portland-cement mortar cylinders with a standard mixture composition according to EN 196-1 were cast (510 kg/m³ CEM I 52.5 N, 1530 kg/m³ silica sand 0/2, and 255 kg/m³ water). The specimens' diameter and height were 75 mm and 150 mm respectively, and each had a diagonally cast bonding area at a 30° angle from the vertical, as per the ASTM standard.

The specimens were manually ground (bonded surface) by means of a sand paper until the desired roughness was reached. The International Concrete Repair Institute (ICRI) has a set of "roughness" surface profile chips (http://www.jdtechnical.com/Surface_Prep-JD.htm). An intermediate profile, similar to the CSP-5 chip, was targeted at an age of 28d. All prepared surfaces were visually similar.

2.3 Biodeposition treatment

Mortar specimens (BAC) were partially immersed in a precipitation medium which consisted of urea (30 g/L), calcium nitrate (118 g/L) and yeast extract (5 g/L) for 24h. The medium level was approximately 10 mm above the immersed surface (elliptical surface for applying repair material) of the mortar specimens. After that, the specimens were taken out from the precipitation medium and put upside down until surface dry. Subsequently, bacterial suspension was sprayed (approximately 0.5 mL/cm²) all over each elliptical surface every 6h for 4 times.

2.4 Repair material application and slant shear testing at 28d

All mortar substrate specimens were soaked in tap water for 24 h. The face of the mortar section was put on an absorbent material for 10 min and was subsequently dried in air for 15 min. The repair material (Sika MonoTop-124 N[1]) was mixed for 3 min. The prepared

[1] Certain commercial products are identified in this paper to specify the materials used and the procedures employed. In no case does such identification imply endorsement or recommendation by Ghent University or

bonding surface was put horizontal and 2 mm of repair material was applied, followed by the application of a second mortar specimen. The entire cylinder (especially the sides) was(/were) covered with plastic foil and tape to exclude movement during hardening of the repair material. The specimens were kept horizontal for 48h. Afterwards they were put in a moist room at 95±5% RH and 20±2°C until the repair product achieved an age of 28d. Prior to testing, the loading surfaces of each cylinder were ground to produce a smooth testing surface. The composite specimen was loaded in compression and its strength was recorded. The bond strength was determined by dividing the load carried by the specimen at failure by the area of the bonded surface. The area of the bonded surface was reduced by that of any voids found in the bond layer on inspection after the test. Only voids larger than 3 mm in diameter were taken into account.

2.5 Characterization of the interface between mortar substrate and repair material

The mineral phases in the mortar-biodeposition layer-repair material interface were investigated by use of X-ray diffraction (XRD), Scanning Electron Microscopy (SEM), and thin section analysis. After the slant shear test, shards from the mortar surface, repair material surface, and biodeposition layer were manually collected using a spatula.

A copper X-ray tube was used for the XRD analysis. The samples were manually trimmed into about 1 cm in diameter and 2 to 3 mm thick pieces to fit the sample holder. Scanning was performed from 10° to 70° two-theta with a step size of 0.039°

Samples for SEM analysis were first subjected to a gold coating process. SEM analysis was performed on an instrument equipped with an EDX detector operating at an acceleration voltage of 20 kV.

To study the formed crystals near the interface between the mortar substrate and the repair material, thin sections (40 mm × 25 mm × 25 µm) were prepared from the tested slant shear specimens, perpendicular to the interface and along the height of the cylindrical specimen (Figure 1). First, the specimens were cut to expose 40 mm × 25 mm faces, which were then glued on a glass slide with a thickness of 2.9 mm. The combined sample was cut and polished until a height of the specimen and glass of 10.1 mm was reached. Next, the specimens were impregnated under vacuum with a fluorescent epoxy. The excess epoxy was polished away and an object glass was glued on the smooth surface. Finally, the glass slides were cut off and the remaining part was polished until a thin section with 25 µm thickness was achieved. A cover glass was glued on top to protect the thin section. The thin sections were then analysed under normal and fluorescent light.

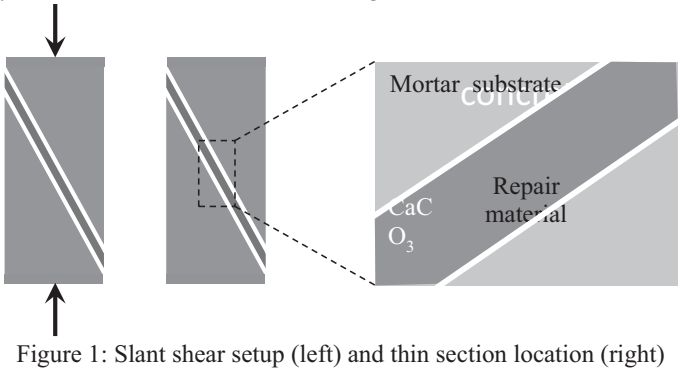

Figure 1: Slant shear setup (left) and thin section location (right)

the National Institute of Standards and Technology, nor does it indicate that the products are necessarily the best available for the purpose.

3 RESULTS

3.1 Slant shear test

The results obtained when performing a compression test on the slant shear specimens, are shown in Table 1. The elliptical surface area was measured after the test. Possible defects at the edges and larger air voids were subtracted from the complete area. No distinct differences in elliptical surfaces were found on the studied samples series and the results thus could be compared. The bond strength results were characterized by an average and standard deviation of 12.6 MPa ± 1.6 MPa and 14.3 MPa ± 1.0 MPa for the REF and BAC specimens, respectively. The average results for the bacterially treated specimens are 13% higher than the un-treated specimens. The bacterial treatment thus seems to improve the overall bonding strength, but this preliminary result is only significantly different at a significance level of 0.18 (t-test). The BAC III specimen showed a lower force when performing the slant shear test for unknown reason. Additional future tests will elucidate this assumption and an improved treatment will be proposed.

Table 1: Force, elliptical surface area and bond strength results

	Force [kN]	Elliptical surface area [cm²]	Bond strength [MPa]
REF I	99.15	9120.6	10.9
REF II	117.04	9131.6	12.8
REF III	126.78	9040.3	14.0
BAC I	135.7	9148.5	14.8
BAC II	136.21	9143.8	14.9
BAC III	119.99	9079.6	13.2

Figure 2 shows the elliptical surface after performing the slant shear test. The surface of the reference samples is smooth and debonding of the repair material layer from the mortar surface occurred. Conversely, a clear whitish layer was observed on the bacterially treated specimens. This is from the calcium carbonate biodeposition due to the bacterial treatment. Partial debonding of the calcite layer deposited by the bacteria was seen by comparing the bonding surfaces after compression (Figure 2). This rougher surface is thus possibly primarily responsible for the increase in slant shear bond strength.

REF BAC

Figure 2: Bonding surfaces after performing the slant shear test

3.2 XRD analysis of the carbonates

The XRD spectra are shown in Figure 3 and the EDX spectra in Figure 4. The biodeposition film on the mortar surface mostly consisted of calcite and vaterite. The amount of both was quite significant, which is indicated by the sharp and strong dominant diffraction

peaks in the spectrum (green lines). The compositions of the mortar substrate and repair material surfaces were quite similar, as they are both cementitious materials. They both contained calcite, vaterite and quartz. The detailed percentage of each mineral is unknown from this qualitative analysis. Yet it can still be seen that calcite was the main mineral, while the amount of vaterite was much less than that of calcite on the mortar substrate and repair material surfaces. This can be judged by the fact that the dominant diffraction peaks of vaterite were very weak in the spectra of the samples from mortar substrate and repair material surfaces (blue and red lines). No calcium hydroxide (CH) or calcium silicate hydrate gel (C-S-H) was found on the surfaces, suggesting that they were highly carbonated. Nor was aragonite indicated in any of the XRD spectra.

Vaterite is the major product in the pH-range between 8.5 and 10. Conversely, aragonite preferably forms at pH 11, while calcite is the dominant product when the pH is higher than 12 [9]. Vaterite is a metastable polymorph of calcium carbonate and is rare in natural environments [10]. It is unstable and transforms to calcite (or aragonite) at room temperature in an aqueous solution [11]. However, vaterite can be synthesized in chemical processes and often forms in the presence of microorganisms [12]. This gives an indication that bacteria and their secretion (mainly organic compounds) may facilitate the formation of vaterite.

The three kinds of surfaces had completely different morphologies. No obvious crystals were observed on the mortar surface. While on the repair material surface, particles of a size ranging from 2 to 5 μm were seen. Based on the EDX spectrum, these particles might be Ca-Mg-carbonates.

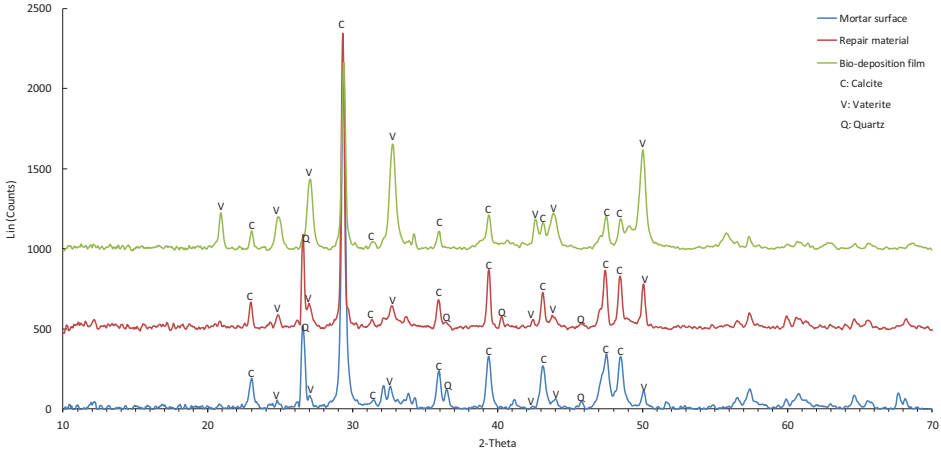

Figure 3: XRD spectra from mortar substrate, repair material and bio-deposition surfaces

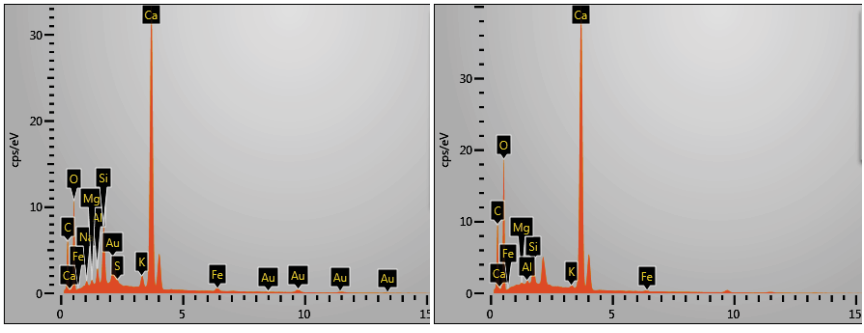

Figure 4: EDX spectra from the mortar substrate (left) and the repair material (right) surfaces

The biodeposition film was full of bacterial imprints. These imprints could be seen as long elliptical shaped spots with a length of approximately 2 µm. The EDX spectra indicated that the film was mainly composed of calcium carbonate. The film was not flat; instead, it was rough with a lot of pits. This could be due to roughening of the mortar surface with sand paper.

3.3 Thin-section analysis

Thin-section analysis is useful in viewing the interlayers between the mortar and the repair product in case of the reference samples and the interlayers between the mortar, calcium carbonate (biodeposition) layer, and the repair material respectively, for the bacterially treated specimens. In the case of the reference sample, the crack propagated through the interface of the mortar substrate and the repair material. This seems to be the weakest link when applying the repair material.

In the case of the bacterial treated specimens, it could be seen that debonding takes place in the repair material near the vicinity of the $CaCO_3$ layer or in the interface between the layer and the substrate. Both the bonding with the mortar substrate and the repair material seems to be sufficient to increase the bond strength.

The complete system in the bacterially treated specimens is shown in Figure 5. A clear whitish layer can be seen in between the mortar substrate and the repair material.

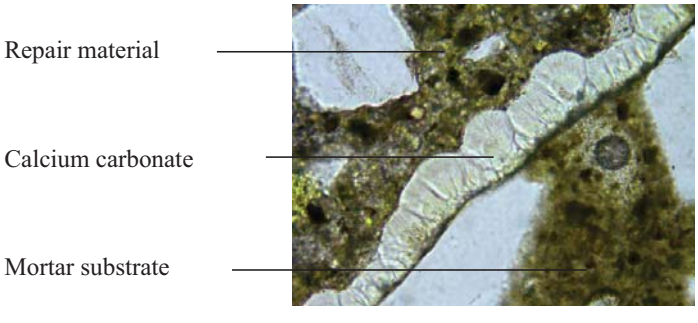

Figure 5: Formed $CaCO_3$ layer attributed to bacterial activity near the interface. The figure width corresponds to 800 µm

The whitish $CaCO_3$ layer in the bacterial specimens has an average thickness of 52±14 µm (n = 250). No corresponding white layer can be found in the reference specimens.

The formed $CaCO_3$ layer has a rough surface due to the formation of irregular crystals. Both the repair material and the mortar substrate tend to show a good adherence to that layer. This roughness could also partially lead to the increase in observed bond strength. Future tests will elucidate this assumption.

4 CONCLUSIONS

Based on this preliminary study of applying a biodeposition layer for bond enhancement of repair materials, the following conclusions can be drawn:

- A bacterial treatment has been shown to enhance the bonding of a repair product to a mortar substrate. Further research will focus on how to further optimize the bacterial layer to obtain a significantly higher bonding strength.
- The biodeposition film on the mortar surface mostly consisted of calcite and vaterite.
- Both the mortar substrate and the repair material exhibited a good bonding with the calcium carbonate crystals precipitated by the bacteria.

Ongoing studies are focusing on further enhancing the bond strength of the composite system by further engineering of the biodeposition layer.

5 ACKNOWLEDGEMENTS

As Postdoctoral Research Assistants of the Research Foundation-Flanders (FWO-Vlaanderen), Didier Snoeck and Jianyun Wang want to thank the foundation for its financial support.

6 REFERENCES

[1] Snoeck, D. and N. De Belie, 'From straw in bricks to modern use of microfibres in cementitious composites for improved autogenous healing – a review', *Constr.Build. Mater.***95** (2015) 774-787.
[2] Van Tittelboom, K. and N. De Belie, 'Self-Healing in Cementitious Materials - A Review', *Materials***6**(6) (2013) 2182-2217.
[3] Wang, J., D. Snoeck, S. Van Vlierberghe, W. Verstraete, and N. De Belie, 'Application of hydrogel encapsulated carbonate precipitating bacteria for approaching a realistic self-healing in concrete', *Constr.Build. Mater.***68** (2014) 110-119.
[4] De Muynck, W., N. De Belie, and W. Verstraete, 'Microbial carbonate precipitation in construction materials: A review', *Ecol. Eng.***36** (2) (2010) 118-136.
[5] Adolphe, J.P., J.F. Loubière, J. Paradas, and F. Soleilhavoup, 'Procédé de traitement biologique d'une surface artificielle', E. patent 90400G97.0 (1990).
[6] De Muynck, W., K. Cox, N. De Belie, and W. Verstraete, 'Bacterial carbonate precipitation as an alternative surface treatment', *Constr. Build. Mater.***22**(5) (2008) 875-885.
[7] De Muynck, W., D. Debrouwer, N. De Belie, and W. Verstraete, 'Bacterial carbonate precipitation improves the durability of cementitious materials', *Cem. Con. Res.***38**(7) (2008) 1005-1014.
[8] De Muynck, W., S. Leuridan, D. Van Loo, K. Verbeken, V. Cnudde, N. De Belie, and W. Verstraete, 'Influence of pore structure on the effectiveness of a biogenic carbonate surface treatment for limestone conservation', *Appl. Environ.Microbiol.***77**(19) (2011) 6808-6820.
[9] Watanabe, J. and M. Akashi, 'Formation of various polymorphs of calcium carbonate on porous membrane by electrochemical approach', *J. Cryst. Growth***311**(14) (2009) 3697-3701.
[10] Lippmann, F., 'Sedimentary Carbonate Minerals', (Springer, UK, 1973).
[11] Spanos, N. and P.G. Koutsoukos, 'The transformation of vaterite to calcite: effect of the conditions of the solutions in contact with the mineral phase', *J. Cryst. Growth***191**(4) (1998) 783-790.
[12] Giralt, S., R. Julia, and J. Klerkx, 'Microbial biscuits of vaterite in Lake Issyk-Kul (Republic of Kyrgyzstan)', *J. Sediment. Res.***71** (3) (2001) 430-435.

Performance of RC Walls with Openings Strengthened by Fiber Reinforced Polymers: An Experimental and Theoretical Investigation

Cosmin Popescu[1,2], Gabriel Sa[1,2], Thomas Blanksvärd[2] and Björn Täljsten[2]

[1] Northern Research Institute—NORUT, Rombaksveien E6-47, N-8517 Narvik, Norway.

[2] Luleå University of Technology, Department of Civil, Environmental and Natural Resources Engineering, SE-971 87 Luleå, Sweden.

ABSTRACT

Redesigning buildings to improve their space efficiency and allow changes in use is often essential during their service lives to comply with shifts in living standards and functional demands. This may require the introduction of new openings in elements e.g. walls, which inevitably reduces their structural performance, and hence necessitates repair or strengthening. Here the authors report an experimental investigation of the effectiveness of fibre-reinforced polymer (FRP)-based strengthening for restoring the axial capacity of a solid reinforced concrete wall after cutting openings. Nine half-scale specimens, designed to represent typical wall panels in residential buildings with and without door-type openings, were tested to failure. FRP-confinement and mechanical anchorages increased the axial capacity of walls with small and large openings (which had 25% and 50% reductions in cross-sectional area, respectively) by 34-50% and 13-27%, to 85-94.8% and 56.5-63.4% of their pre-cutting capacity, respectively. Current design models are assessed against experimentally obtained capacities.

Keywords: Concrete walls, openings, strengthening, CFRP, digital-image correlation.

1 INTRODUCTION

At present, one of the most significant discussion points relating to sustainable development of our society is that such development must always be supported by a safe, functional and durable built environment. It is widely acknowledged that our building stock requirements (e.g. maintenance) are enormous, due to the ever-increasing demands of society, with continual wear and degradation on structures potentially leading to large monetary and social losses. For example, the need for repair and refurbishment in the house building sector increases annually (FIEC 2014); figures indicate an estimated 270 billion Euros were spent in 2014 in the E.U.

The majority of structures around the world are made of reinforced concrete (RC), most of which were built between 1946 and 1980 [1]. A high proportion of these buildings are multi-dwelling buildings made of prefabricated sandwich panels. The system (see Figure 1a), called large panel building, was developed in the West and used for the first time in Denmark, England and France [2], later expanding across the whole of Europe. This type of structure consists of an integral wall system in which load-bearing walls run along both longitudinal and transversal directions of the building. This makes the floor layout rather rigid in terms of space utilisation. In recent years, there has been a growing interest in

enlarging spaces by connecting adjacent rooms using openings created in existing solid walls. Thus, greater flexibility and better use of spaces can be achieved. However, such modifications may involve cutting openings into structural walls to allow for new windows, doors or ventilation systems (Figure 1b). The effects of such openings are stiffness and load-bearing capacity reduction.

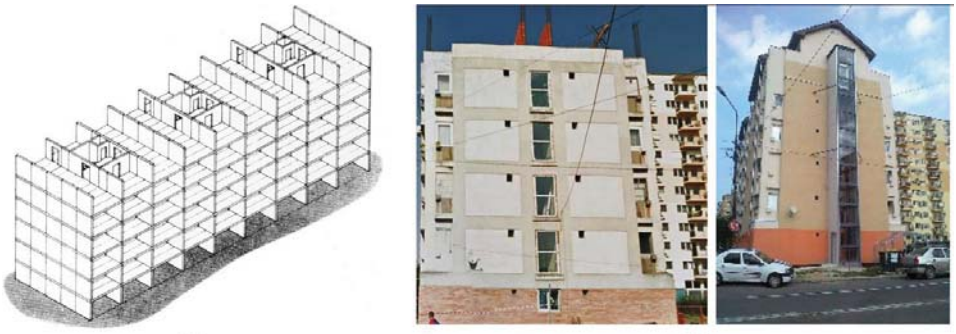

(a) (b)

Figure 1: (a) Typical large panel building [3] and (b) example of structural modifications in buildings

Two methods have, traditionally, been employed to strengthen RC walls with openings. One is to create a frame using RC/steel members around the opening, the other is to increase the cross-sectional thickness. An alternative is to use externally bonded fiber-reinforced polymers (FRPs), a technique successfully tested by a number of authors in seismic retrofitting scenarios [4-7]. However, the contexts of these tests were seismic retrofits, and thus, they may not be applicable for repairing gravitationally-loaded walls. Literature on the behaviour of axially loaded walls has been recently reviewed by Popescu et al. [8]. It was concluded that research studies investigating walls with cut-out openings strengthened by FRP is scarce. For non-seismically designed walls with openings, Mohammed et al. [9] was the first who investigated performances of one-way walls (supported only on top and bottom edges of the wall) when FRP-strengthened. Hence, in the current study the effectiveness of FRP-repaired two-way walls (restrained along all four edges) for increasing the axial strength weakened by cut-out openings was investigated.

2 EXPERIMENTAL PROGRAMME

2.1 Design of experiments and test matrix

The specimens were designed to represent typical wall panels in residential buildings. In total, nine half-scale specimens were tested to failure. The walls were 1800 mm long, 1350 mm high and 60 mm thick. The size of opening and structural condition of the wall were selected as the two most influential parameters.

For the first parameter, namely size opening, small (450 × 1050 mm) and large openings (900 × 1050 mm) were set as the minimum and maximum levels. The minimum level represents the width of a typical door opening in a residential building whereas the maximum level corresponds to a double-door opening. Note that the terms small and large carry no meaning other than being a useful way of labelling the opening sizes.

For the second parameter, pre-cracked and uncracked conditions were established as the minimum and maximum levels. The minimum level represents the wall in a pre-cracked state

(loaded until 75% of the peak load) whereas the maximum level corresponds to the uncracked condition. The 75% level was obtained based on nonlinear FE analyses [10] and observations of when the reference specimens developed a significant crack width.

The designed test matrix is shown in Figure 2 and divided into stages I, II and III, relating to reference specimens, pre-cracked and uncracked specimens strengthened with CFRP, respectively. For convenience, the naming system adopted consists of the test stage described above (I, II or III) and the type of wall C, S, L (where C refers to a solid wall, S and L refers to a wall with a small and large opening, respectively). In addition, the tests from the third stage were repeated and thus, the specimen's name contains a serial number. For example, II-S refers to a pre-cracked wall with a small opening, strengthened with CFRP.

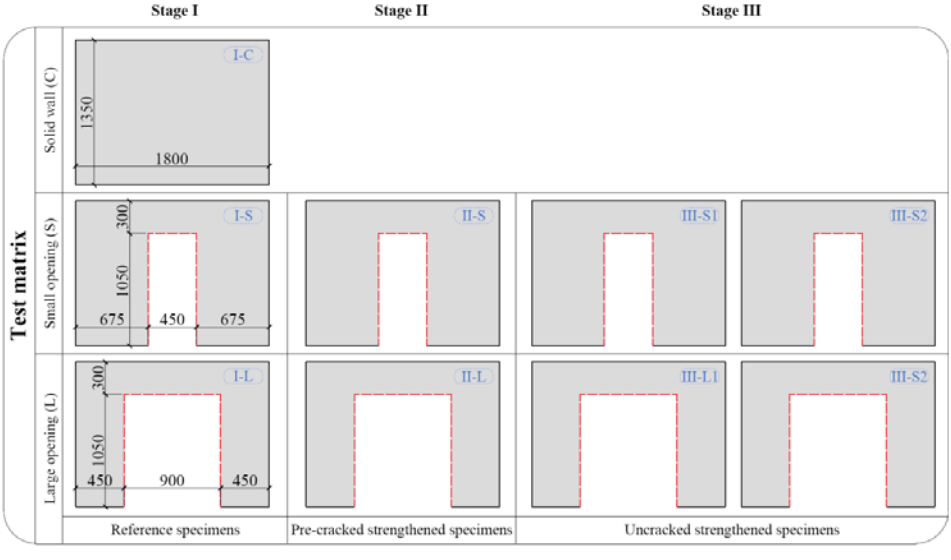

Figure 2: Test matrix

2.2 Specimen preparation

The specimens were solid panels (i.e. constant thickness) with no voids or insulating layers. They were reinforced with a single, centrally placed, welded wire mesh. The welded fabric consisted of 5 mm diameter deformed bars, spaced at 100 mm in both orthogonal directions (see Figure 3). Before casting, electrical resistance strain gauges with pre-attached wires were bonded to the reinforcement. The walls were long-line cast, laid down on a steel platform. A batch line can accommodate up to five specimens.

Two methods were available to restore the capacity to that of a solid wall. One was to increase the specimen's thickness (e.g. RC jacketing, textile-reinforced mortars), the other was to increase the concrete compressive strength through confinement. The latter was the focus of interest for the work presented here. Confinement has proved to be a viable solution where ductility and/or axial strength are concerned. The method is highly dependent on the cross-section geometry: a uniform confinement effect is obtained for circular cross-sections whereas only part of the cross-section is effectively confined for rectangular cross-sections [11-12]. The transverse fibre sheets were fixed using steel bolts so as to create virtual cross-sections with an aspect ratio limited to 2 (60 × 120 mm) starting from the opening edge.

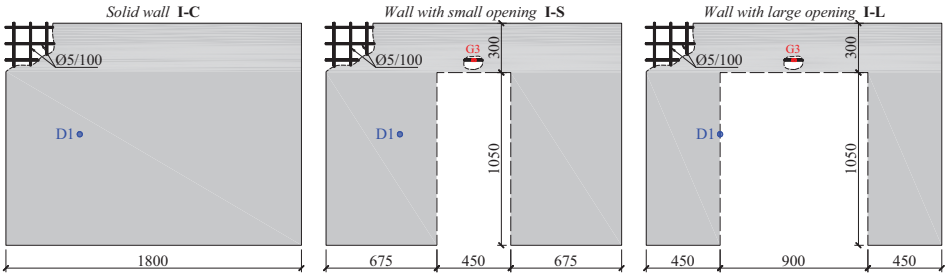

Figure 3: Configuration and details of the tested wall

Prior to the application of the CFRP strengthening, 8 mm holes were drilled through the wall at positions marked on the concrete surface to help the installation of the mechanical anchorages. The concrete surfaces were then prepared by grinding – to remove the irregularities and cement paste layer, and thus, exposing the aggregates – and cleaning with compressed air. The CFRP sheets were applied using the wet lay-up procedure. First, a two-component epoxy primer (StoPox 452 EP) was applied to the specimens, followed by the application of the impregnated fibres on the concrete surface after approximately 6 hours. They were wrapped around the piers in a U-shape; full wrapping was not possible due to the existing boundary conditions. High-strength CFRP sheets (two and three 0.17 mm thick layers for the specimens with small and large openings, respectively) were used to strengthen the walls. When the epoxy had cured, the anchorage bolts were inserted into predrilled holes and prestressed with a torque estimated from the clamp load (i.e. 8.7 kN).

2.3 Material properties

The average cubic compressive strength of the concrete was 62.8 MPa and 64.4 MPa for the first and second concrete batch. Coupons were taken from the reinforcing steel meshes and tested to determine their stress-strain properties. Their mean yield strength was 632 MPa at mean strain of 0.28%. No material tests were carried out on the CFRP system (fibres + epoxy) and their nominal properties are given here according to the tests undertaken by the supplier. The fibres of the CFRP sheets were unidirectional with tensile strength of 5500 MPa and elastic modulus of 290 GPa. The epoxy resin had an elastic modulus of about 2 GPa.

2.4 Test set-up and instrumentation

The walls were tested in two-way action and subjected to axial loading with low eccentricity along the weak axis ($1/6^{th}$ of the wall's thickness) to represent imperfections due to thickness variation and misalignment of the panels during the construction process. The specimens were tested in a test-rig specifically designed to simulate as-built conditions: side restraints permitted rotation and prevented translation while top/bottom restraints allowed full free rotation.

Four hydraulic jacks were networked together to apply a uniformly distributed load along the wall length. The load was incrementally increased at 30 kN/min with breaks every 250 kN to allow stress distribution and to monitor the cracks in the specimens. All reactions were transmitted to a reaction frame fixed in a strong floor. A general view of the test setup is shown in Figure 4.

An extensive instrumentation scheme was devised in order to monitor the behaviour of the walls during the loading cycles. Linear displacement sensors were used to measure out-of-plane and in-plane displacements, with strain gauges placed on steel reinforcement and on

the compression side of the concrete surface. These measurements were supplemented by measuring full-field strain distributions using the three-dimensional digital image correlation (3D-DIC) technique. Due to space limitations, however, only selected measurements are presented herein. The location of the sensors is shown in Figure 3.

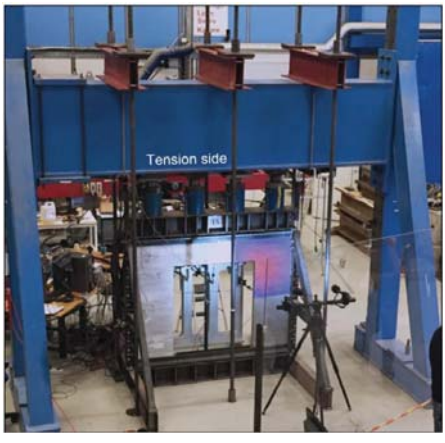

Figure 4: General overview of the test set-up. Reprinted from Popescu et al. [13] with permission from ASCE

3 EXPERIMENTAL RESULTS

In order to investigate the effect of the cut-out on the axial strength, three specimens were loaded to failure in stage I: one was a solid panel, one had a symmetric half-scaled single door-type opening and the third had a symmetric half-scaled double door-type opening. The small and large openings represented a 25% and 50%, respectively, reduction in the cross-sectional area of the solid wall. The damage level was evaluated in terms of ultimate load, crack pattern, displacement profiles, strains in concrete and steel reinforcement and ductility and energy release at failure. Only selected results are given here and the reader is referred to Popescu et al. [13].

The effectiveness of the selected strengthening method was investigated in two scenarios: Stages II and III. The performance of the strengthening method was evaluated in terms of axial strength increase, ductility and energy release at failure, and steel reinforcement and CFRP strain utilisation. Only selected results are given here and the reader is referred to Popescu et al. [14] for more detailed results and analysis.

3.1 Reference specimens

The first stage comprises the reference specimens (i.e. a solid wall, a wall with small and large opening, respectively) that were loaded until failure. In this way a first analysis would be possible to evaluate the effect of introducing new openings in a solid wall. The walls behaved as predicted by the numerical analysis, showing a TW behaviour by deflecting in both vertical and horizontal directions. This aspect was also captured by the ARAMIS system in addition to strain development and distribution around the openings during loading cycles, as shown in the images in Figure 5.

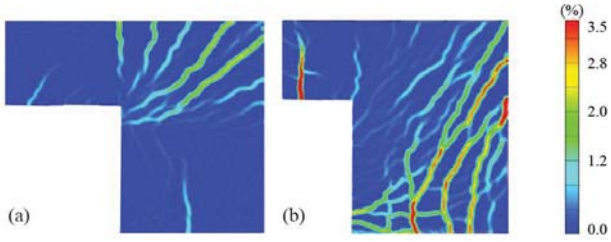

Figure 5: Principal strain development on the tension side of the specimens at peak load: (a) specimen I-S; (b) specimen I-L. Reprinted from Popescu et al. [13]with permission from ASCE

Cracks opened late in the loading of the solid wall (at 85% of the peak load), and earlier in the loading of specimens with both small and large openings (at 50% and 20% of peak load, respectively). The tensile and compressive strains that developed in the reinforcement were significant at higher loads, with yielding of some bars occurring at failure. All specimens failed by concrete crushing with spalling and reinforcement buckling showing no forewarning prior to failure. Effects of opening size are shown in Figure 6, in which load-displacement curves of all three specimens (recorded at the same position on both piers – D1 as indicated in Figure 3) are plotted on the same graph. The crack pattern captured at failure is shown in Figure 7.

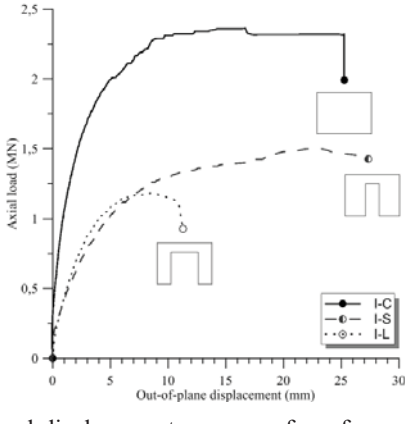

Figure 6: Load-displacement responses for reference specimens

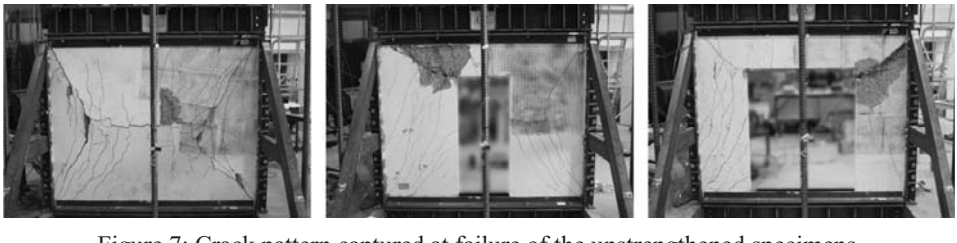

Figure 7: Crack pattern captured at failure of the unstrengthened specimens

3.2 Strengthened specimens

The strengthened walls failed due to crushing of concrete followed by debonding of the CFRP. The failure was concentrated in smaller regions compared to reference specimens i.e. at the bottom of one of the piers as seen in Figure 88. The strengthened specimens had lower deformations (thus increasing the stiffness) and higher capacity when compared with the unstrengthened ones, as can be seen in Figure 99. The increase in capacity was in the range of 34 – 50% and 13 – 27% for specimens with small and large openings, respectively.

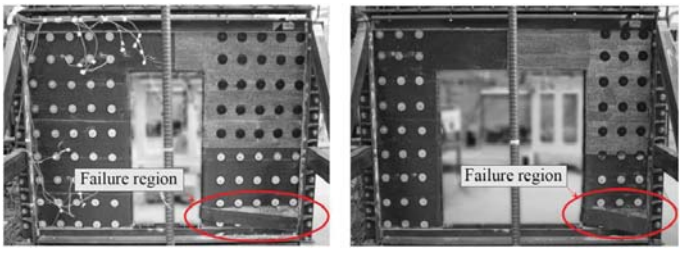

Figure 8: Typical failure mode of strengthened walls

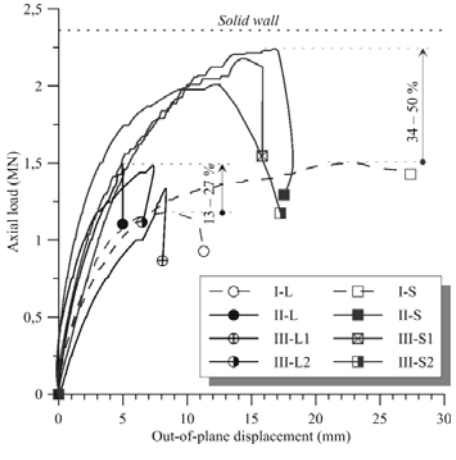

Figure 9: Strengthening effect on the walls with small and large openings

4 ANALYSIS OF RESULTS AND DISCUSSION

Practical design of axially-loaded concrete walls is generally based on column theory that accounts for the equilibrium of forces over their cross-sections, and stress-strain compatibilities. A simplified procedure is described in design codes such as [15-18] and research literature [19-21], just to mention a few. A complete description of the performance of current design models for axially-loaded walls with and without openings was published by the authors in [8]. Here, only the results obtained using the European [18] design model are presented. The equation used to predict the axial capacity of a solid wall was:

$$N_u = f_c \cdot L \cdot t \cdot \Phi \tag{1}$$

$$\Phi = 1.14\left(1 - 2\frac{e + e_a}{t}\right) - 0.02 \cdot \frac{H_{eff}}{t} \le \left(1 - 2\frac{e + e_a}{t}\right) \tag{2}$$

Here, f_c is the concrete compressive strength, L is the length of the wall, t is the wall thickness, e is initial eccentricity, equal to $t/6$ and e_a is the additional eccentricity due to lateral deflection of the wall; $e_a=H_{eff}/400$. The effective height $H_{eff,}$ is obtained by amending the wall height with the effective height factor, β. For walls with $L < H$ and restrained along all their sides, $\beta=L/2H$.

Currently there are no design philosophies or reliable theoretical guidelines for calculating the capacity of strengthened walls in the literature. The only design model [9] found in the literature only considered top and bottom restrained walls, and so the associated design model is only valid for such walls. For the current research, the authors used the European design model [20] in combination with Lam and Teng [22] design model to predict the increase in axial capacity.

The predictions using the European design model [18] for the unstrengthened walls were in good agreement with the test results; an average ratio between theoretically and experimentally determined capacity of 1.02 was obtained. The same cannot be said for the strengthened walls; the inability of the design model to capture the loading eccentricity seem to have produced inaccurate predictions. The average ratio between theoretically and experimentally determined capacities of 1.37 was obtained.

6. CONCLUSIONS

In this study, the authors report on an experimental investigation of the effectiveness of CFRP–based strengthening for restoring the axial capacity of a solid reinforced concrete wall after cutting openings. The following conclusions can be drawn from this investigation:

- Reducing the cross-sectional area with 25% (small opening) and 50% (large opening) of a solid wall the capacity decreases with nearly 36% and 50%, respectively.
- The failure progression can successfully be monitored during specimen loading using 3D-DIC measurements.
- Confining the walls with CFRP increases the capacity up to 95% of that of a solid wall.
- Design methods for predicting the axial capacity increase due to CFRP strengthening should be revisited. A design model capable of capturing complex effects such as load eccentricity and large aspect ratios of elements' cross-sections is currently developed by the authors and will be published upon completion of the study.

5 ACKNOWLEDGEMENTS

The authors would like to acknowledge The Research Council of Norway (RFF), Development Fund of the Swedish Construction Industry (SBUF) and Skanska for financing the presented work. Financial support provided by ÅForsk Foundation is gratefully acknowledged, as it offered the opportunity for the first author to present the work performed during his PhD studies – Popescu [23] – at 71st RILEM Week & ICACMS 2017 Conference.

6 REFERENCES

[1] Dol, K. and Haffner M. 'Housing Statistics in the European Union', Delft University of Technology, Netherlands: OTB Research Institute for the Built Environment (2010).

[2] Csoknyai, T., Hrabovszky-Horváth S., Georgiev Z., Jovanovic-Popovic M., Stankovic B., Villatoro O. et al. 'Building stock characteristics and energy performance of residential buildings in Eastern-European countries', Energ. Buildings. (2016) *In Press.*

[3] Eriksson, A. Structural behaviour of vertical joints in large panel buildings [PhD Thesis]. Göteborg, Sweden: Chalmers Tekniska Högskola; 1978.

[4] Demeter, I. Seismic retrofit of precast RC walls by externally bonded CFRP composites. Timisoara, Romania: Politehnica University of Timisoara; 2011.

[5] Li, B., Kai Qian and Tran C.T.N. 'Retrofitting earthquake-damaged RC structural walls with openings by externally bonded FRP strips and sheets', J. Compos. Constr.**17** (2) (2013) 259-70.
[6] Todut, C., Dan D. and Stoian V. 'Numerical and experimental investigation on seismically damaged reinforced concrete wall panels retrofitted with FRP composites', Compos. Struct.**119** (2015) 648-65.
[7] Mosallam, A.S. and Nasr A. 'Structural performance of RC shear walls with post-construction openings strengthened with FRP composite laminates', Compos. Part B: Eng. (2016) *In Press*.
[8] Popescu, C., Sas G., Blanksvärd T. and Täljsten B. 'Concrete walls weakened by openings as compression members: A review', Eng. Struct.**89** (2015) 172-90.
[9] Mohammed, B., Ean L.W. and Malek M.A. 'One way RC wall panels with openings strengthened with CFRP', Constr. Build. Mater.**40** (2013) 575-83.
[10] Popescu, C. and Sas G. 'The development of an experimental program through design of experiments and FEM Analysis: A preliminary study', Nord. Concrete Res.**51** (2014) 14.
[11] Wu, Y.-F. and Wei Y.-Y. 'Effect of cross-sectional aspect ratio on the strength of CFRP-confined rectangular concrete columns', Eng. Struct.**32** (1) (2010) 32-45.
[12] Liu, H.-X., Liu G.-J., Wang X.-Z. and Kong X.-Q. 'Effect of cross-sectional aspect ratio and basalt fiber-reinforced polymer-confined number on axial compression behavior of short columns', J. Reinf. Plast. Comp.**34** (10) (2015) 782-94.
[13] Popescu, C., Sas G., Sabău C. and Blanksvärd T. 'Effect of cut-out openings on the axial strength of concrete walls', J. Struct. Eng.**142** (11) (2016) 4016100.
[14] Popescu, C., Sas G., Blanksvärd T. and Täljsten B. 'Concrete walls with cut-out openings strengthened by FRP-confinement', J. Compos. Constr. (2016) *In press*.
[15] ACI 318. Building code requirements for structural concrete and commentary Farmington Hills, MI: American Concrete Institute (ACI); 2011.
[16] AS3600. Concrete structures. Sydney, Australia: Standards Australia; 2009.
[17 CAN/CSA-A23.3. Design of concrete structures. Mississauga, Ontario: Canadian Standards Association; 2004.
[18] EN1992-1-1. Design of concrete structures – Part 1–1: General rules and rules for buildings. Brussels, Belgium: CEN (European Committee for Standardization); 2004.
[19] Saheb, M. and Desayi P. 'Ultimate strength of RC wall panels with openings', J. Struct. Eng.**116** (6) (1990) 1565-78.
[20] Doh, J.H. and Fragomeni S. 'Ultimate load formula for reinforced concrete wall panels with openings', Adv. Struct. Eng.**9** (1) (2006) 103-15.
[21] Ganesan, N., Indira P.V. and Santhakumar A. 'Prediction of ultimate strength of reinforced geopolymer concrete wall panels in one-way action', Constr. Build. Mater.**48** (2013) 91-7
[22] Lam, L. and Teng J.G. 'Design-Oriented Stress-Strain Model for FRP-Confined Concrete in Rectangular Columns', J. Reinf. Plast. Comp.**22** (13) (2003) 1149-86.
[23] Popescu, C. CFRP Strengthening of Cut-Out Openings in Concrete Walls – Analysis and Laboratory Tests [PhD Thesis]. Luleå, Sweden: Luleå University of Technology; 2017].

Behavior of Hybrid NSM Reinforced and Externally Confined Reinforced Concrete Columns under Eccentric Compression – Experimental and Numerical Studies

Chellapandian M. and Suriya Prakash S.

Department of Civil Engineering, Indian Institute of Technology, Hyderabad, India

ABSTRACT

The effectiveness of hybrid combination of near surface mounted (NSM) and externally confined (EC) FRP strengthening on the performance of RC column elements under uniaxial eccentric compression is investigated. In total, ten short RC column elements were cast. Carbon FRP is used for strengthening due to its inherent stiffness and strength properties on par with other FRP materials. The columns were strengthened using NSM CFRP laminates, EC using CFRP fabrics and their hybrid combinations. A non-linear finite element model is developed using ABAQUS and the numerical model is calibrated using the experimental results to improve the accuracy of the predictions. Experimental results revealed that hybrid strengthening of RC columns was able to show a better performance in terms of stiffness, strength, ultimate displacement ductility when compared to other FRP strengthening techniques. The numerical predictions obtained were able to better capture the initial stiffness, peak load and post-peak behavior. Thus, the proposed hybrid strengthening technique for RC columns possess the capability of restoring the loss in stiffness, strength and ductility due to additional bending moment induced by the eccentric compression loading.

Keywords: CFRP, eccentric compression, hybrid strengthening, NSM, finite element modeling, RC column

1 INTRODUCTION

Reinforced Concrete (RC) columns are the pivotal load bearing elements in a structure that often requires strengthening due to various reasons like (i) decrease in load carrying capacity of the structure (ii) additional service requirements (iii) change in the type of load (iv) natural / man-made disasters. Moreover, RC columns were normally designed to resist compression due to its predominance over the other type of load acting on it. Nevertheless, the presence of significant amount of bending due to eccentricity can lead to a reduction in strength, stiffness, ductility and sudden brittle failure. In such cases, strengthening of columns is essential to meet the design requirements. Conventional methods of strengthening the concrete members like steel jacketing, concrete enlargement has been out-dated due to various issues tackled during its implementations [1]. FRP strengthening of concrete structures become conspicuous over the past few years due to (i) ease in application, (ii) distinctive strength and stiffness (iii) bond to the parent member (iv) negligible corrosion and environmental impact and (v) light weight.

Based on the method of application and type of retrofitting required, a different type of FRP technique is employed. Several researchers have investigated the improvement of the

axial capacity of RC columns using external confinement (EC) technique with FRP fabric. Widiarsa and Hadi [2] investigated the performance of square columns under eccentric loading and concluded that the strength and ductility can be improved significantly when compared to unwrapped specimens. Parvin and Wang [3] studied the efficiency of FRP confining technique under eccentric compression and concluded that the retrofit efficiency of FRP is affected due to strain gradient induced by eccentricity. Maddawy [4] studied the effect of different e/d ratio in the performance of FRP confined square columns and concluded that the strength improvement given by confinement decreases as the e/d ratio increases. This signifies that only FRP confinement technique cannot improve the capacity of RC columns by more than 20% when there is a reasonable amount of bending present. Past studies by different researchers have also found that NSM strengthening is very much efficient in retrofitting the concrete members that are deficit in bending [5 - 7]. Olivova and Bilcik [7] concluded from their experimental studies on NSM strengthening of RC columns that, FRP rods provides a significant improvement in strength. However, they also noted that NSM FRP bars are prone to buckling failure at very low strain levels when the amount of bending present in columns is low.

2 MOTIVATION AND OBJECTIVES

A unique strengthening technique named hybrid FRP strengthening scheme is proposed for retrofitting of RC columns under eccentric compression. In this approach, NSM FRP laminates act as external reinforcement and contribute significantly in improving the stiffness and ductility whereas the confined FRP fabric helps in improving the strength and delaying the failure of FRP laminates. As a result, the column will possess excellent improvement in stiffness, strength, ductility and energy dissipation capacity. Moreover, by this hybrid strengthening, the brittle failure mode can be converted into the ductile mode.

3 PROPERTIES OF TEST MATERIALS

3.1 Concrete and Steel Reinforcements

All the test specimens were cast in the materials laboratory at IIT Hyderabad. The materials used were locally available. The concrete is designed for the M40 grade to have a target cubic compressive strength of 48.25 N/mm^2 as per IS 10262-2009 [8]. The mix ratio obtained was 1: 2.1: 3.32. The specimens were water cured for a period of 28 days. The average cubic compressive strength of test specimen was found to be 52 N/mm^2 at 28 days. Steel reinforcements procured for the test were local obtained and the yield strength from tension test was found to be 512 MPa with ultimate rupture strain of 7.8%. The schematics of the test specimen with the cross-sectional details were provided in Figure 1. The length of the test specimen was limited to 450 mm due to constraints in the testing equipment.

3.2 FRP Materials

Pultruded CFRP laminates were used for strengthening the RC columns using NSM technique. Coupon specimens were prepared as per ASTM specifications [9] and tested using 100 kN servo controlled MTS universal testing machine. The values of elastic modulus and tensile strength were found to be 150 GPa and 2300 MPa respectively with the rupture strain of 1.3%. Unidirectional CFRP fabric is used for EC strengthening of columns. Coupon specimens prepared using hand layup process is tested in the servo controlled UTM. The values of elastic modulus and tensile strength were found to be 81.3 GPa and 1300 MPa respectively with the rupture strain of 1.4%.

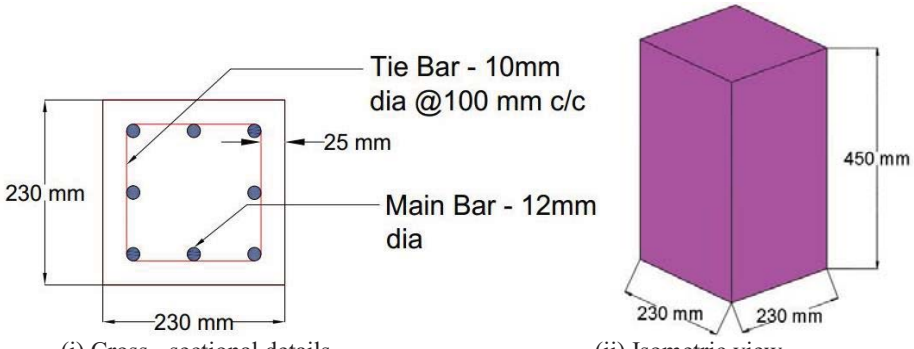

(i) Cross - sectional details (ii) Isometric view

Figure 1: Schematic representation of test specimen

4 FRP STRENGTHENING PROCEDURE

The schematic representation of different FRP strengthening techniques is represented in Figure 2. The procedure for the hybrid strengthening of RC columns is carried out as per ACI 440.2R provisions [10]. CFRP laminates of size 12.5 mm × 1.4 mm is made into 4.2 mm thickness. NSM strengthening is done prior after which external confinement using FRP fabric is carried out. Grooving of columns is carried out for the dimensions not lesser than 1.5 times the dimensions of the specimen. Primer (base: hardener= 2:1) is applied to obtain a good bond efficiency and to remove all the dust materials. After 24 hours of curing, epoxy resin (base: hardener= 2.6: 1) is applied and the CFRP laminates are pressed against the epoxy. After 48 hours of air curing, the specimens are confined using CFRP fabric. CFRP fabric of size 450 mm × 0.2 mm is used for EC strengthening. Firstly, the corners are ground to a minimum radius of 15 mm [10] to avoid edge failure. Epoxy resin is applied after 24 hours of primer application and the CFRP fabric is rolled over the surface with the hand roller to remove the air bubbles present. Two numbers of plies are applied. After two days of air curing, the specimens are tested under eccentric compression loading. The systematic procedure for hybrid strengthening is given in Figure 3.

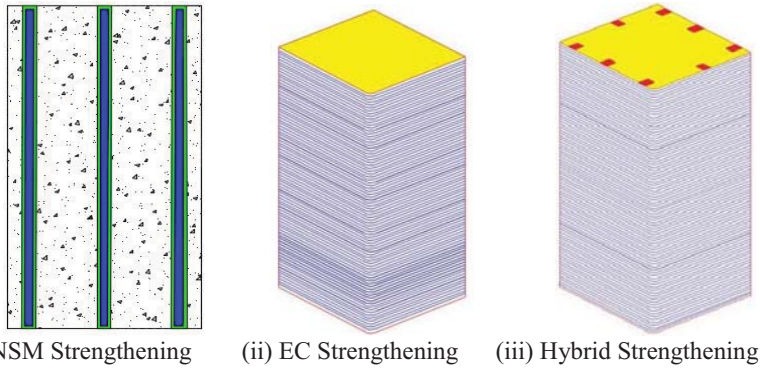

(i) NSM Strengthening (ii) EC Strengthening (iii) Hybrid Strengthening

Figure 2: Schematic Representation of different FRP Strengthening Techniques

(a) Grooving of specimen (b) Primer application (c) Application of epoxy

(d) NSM strengthened (e) Epoxy resin application (f) CFRP wrapping

Figure 3: Systematic strengthening procedure for hybrid strengthening of RC column

5 EXPERIMENTAL SETUP

The experimental setup and the instrumentation details for the testing of RC column stubs were illustrated in Figure 4. The column specimens were capped using high strength cement mortar at top and bottom to ensure uniform load transfer during testing. The specimens were tested in a servo controlled Compression Testing Machine (CTM) of 5000 kN capacity. The testing was carried out in a displacement-controlled mode to have better post peak predictions. The columns were subjected to a low eccentricity of 35 mm (e/h=0.15). The loading protocol is controlled with the help of two linear variable displacement transducers (LVDTs) of 10 mm stroke and an LVDT of 50 mm stroke. There were four LVDTs of 20 mm stroke length attached to the surface of the columns to measure the surface displacement and strain gradient effect. The surface LVDTs are connected to the HBM Data Acquisition System (DAQ) MX-840-A to collect the corresponding data. The strain gauges instrumented in the steel rebar of specimens during the casting process were connected to HBM DAQ MX-1615 to acquire the corresponding strain data during testing.

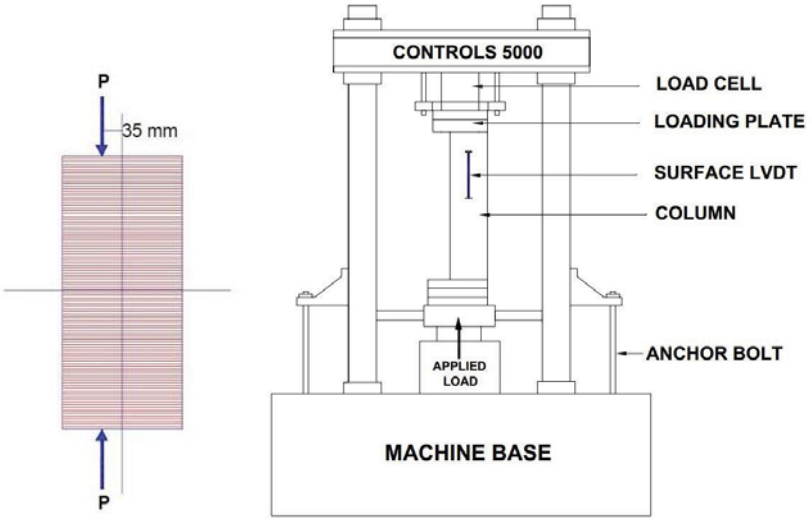

Figure 4: Schematics of test setup and instrumentation details

6 RESULTS AND FAILURE PROGRESSION

The results obtained from the experiments were tabulated and illustrated in Table 1 and Figure 5 respectively. The plain concrete specimen (S-EC-PCC) had an average peak load of 1606 kN corresponding to the displacement of 0.21 mm. After peak load, the specimen had rapid crack progression and failure was highly brittle under compression mode. The columns with conventional steel reinforcement (S-EC-CP) had an average peak load of 1998 kN. The specimen also had severe spalling after peak load and failed at an ultimate load of 1492 kN. The column specimen strengthened using NSM technique had a peak load of 2303 kN. The crack formation occurred between the strengthened FRP laminates and progressed towards the corners of the specimen. The improvement in strength and ultimate displacement was 15.3% and 12.4%, which is due to the efficiency of NSM technique to delay the failure induced by additional bending moment under eccentric compression. In the case of externally confined columns, the improvement in peak load and ultimate displacement was found to be 26.6% and 3.4%. The failure was highly brittle due to rupture and debonding of FRP fabric from concrete. Hybrid strengthened specimens were able to show improvement in terms of both strength and ultimate displacement by 46.4% and 50.6% respectively when compared to control specimens. In addition, the combination of NSM technique and EB technique is effectively utilized preventing premature failure of FRP.

Table 1: Summarized test results for RC columns under eccentric compression

Specimen ID	Load (kN)		Displacement (mm)		% Improvement	
	Peak	Ultimate	Peak	Ultimate	Peak Load (kN)	Ultimate Displ. (mm)
S-EC-PCC	1606	1263	0.21	0.24	--	--
S-EC-CP	1998	1492	0.78	0.89	0	0
S-EC-NSM	2303	1750	0.32	1.00	15.3	12.4
S-EC-EC	2530	1962	0.66	0.92	26.6	3.4
S-EC-HYBRID	2925	2120	0.46	1.34	46.4	50.6

***Note:** The load and displacement values mentioned refer to the average value obtained by testing two specimens of each series to improve the accuracy of results.

The percentage improvement for FRP strengthened specimens were calculated with respect to the control specimens (S-EC-CP).

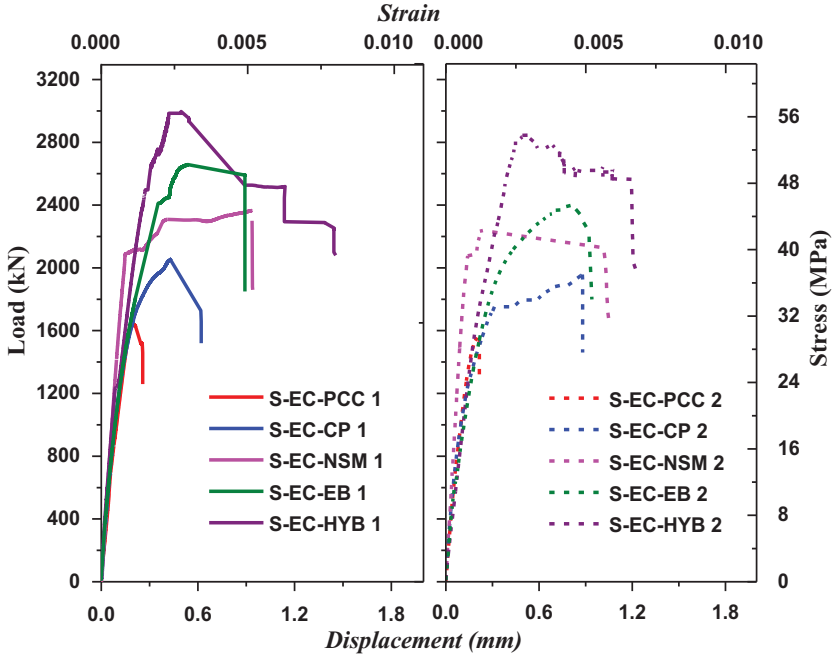

Figure 5: Overall load-displacement behavior of RC columns under eccentric compression

7 NUMERICAL PREDICTIONS

In order to validate the experimental results and to develop a nonlinear finite element model that is capable of representing the behavior of columns under eccentric loading, numerical modeling of FRP strengthened columns was carried out. The non-linear model is developed using the commercial finite element package ABAQUS. The modeling is carried out in order to predict the initial stiffness, peak strength, and post peak behavior and failure modes of RC columns with different FRP strengthening techniques under eccentric compression. The modeling procedure of columns is detailed in the following sequences.

7.1 Material Parameters

7.1.1 Concrete

Concrete damage plasticity (CDP) approach is used to model the nonlinear behavior of concrete. CDP has been preferred ahead of smeared cracking approach due to its capability to match the simulations with the experimental results. The properties of concrete in both compression and tension are considered and the damage parameters are provided. Concrete is modelled using C3D8R element i.e., three-dimensional eight noded brick element with three translational degrees of freedom at each node.

7.1.2 Steel reinforcement and FRP

Steel reinforcements used in this study were modelled as truss element using the elasto-plastic approach with the input values obtained from the tension testing of coupons. The yield stress and ultimate strain of steel were also plugged in to model the hardening behavior of steel. T3D2 (truss three dimensional two noded) element is used to model the steel reinforcements. CFRP laminates were also modelled as T3D2 truss elements exhibiting a linear elastic behavior. CFRP fabric is modelled as linear elastic material. Hasin's damage criterion is used to describe the stress parameters so as to model the FRP failure criterion. The S4R element is used to describe the behavior of CFRP fabric.

7.2 Interface Property

Due to high non-linearity of concrete behavior, the dynamic explicit scheme is used to model this quasi-static problem. The interface between concrete and steel is modelled using embedded region. The bond slip between the concrete and steel is neglected since the difference was minimal. The interface between the concrete and FRP is modelled using surface-to-surface contact (explicit) where the normal and tangential stiffness properties of the epoxy are defined. A steel plate of high stiffness is modelled and tied to the concrete surface on top and bottom to ensure uniform loading and means of applying eccentricity.

7.3 Boundary Conditions and Meshing

The bottom end of the column is given fixed condition (encastre). The top end of the column is applied with eccentric compression loading in a displacement-controlled mode. The amplitude of loading is calibrated as per the experimental results. Mesh converge study is carried out to find out the optimum mesh size. A mesh of size 25 mm is fixed. The experimental and numerical load –displacement comparisons and failure progression for the columns under uniaxial eccentric compression is illustrated in Figure 6.

7.4 Results and Failure Criterion

The predictions obtained from the FE analysis had a good correlation with the experimental results. The predictions in peak load had variation less than 10% when

compared to the experimental results. However, there was some variation in the trend followed by confined concrete at post-cracking behavior. The predictions can be further improved by calibrating the bond behavior of concrete and FRP. The damage progression of columns with and without FRP strengthening is shown in Figure 7.

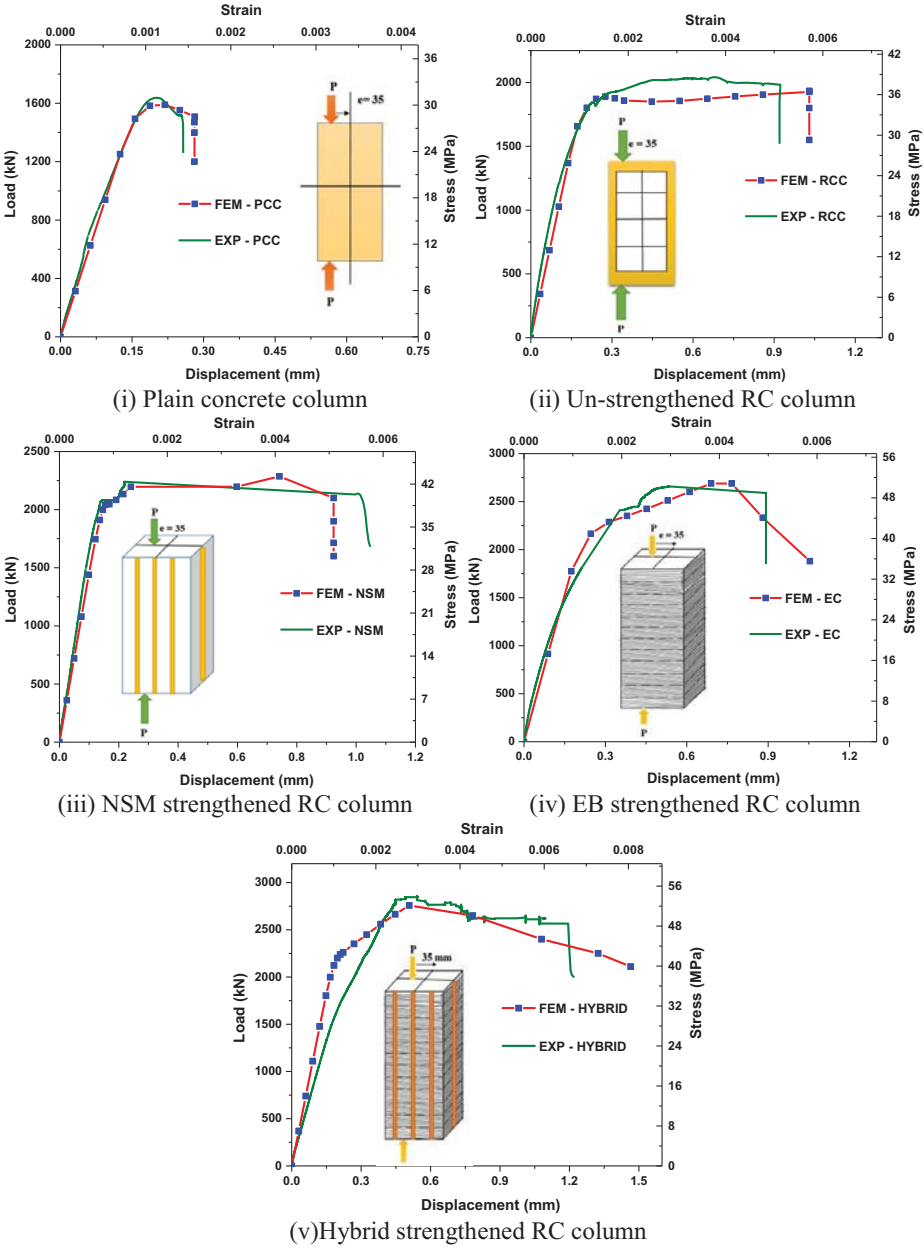

(i) Plain concrete column

(ii) Un-strengthened RC column

(iii) NSM strengthened RC column

(iv) EB strengthened RC column

(v)Hybrid strengthened RC column

Figure 6: Experimental- numerical comparison of RC columns with and without FRP strengthening under eccentric compression.

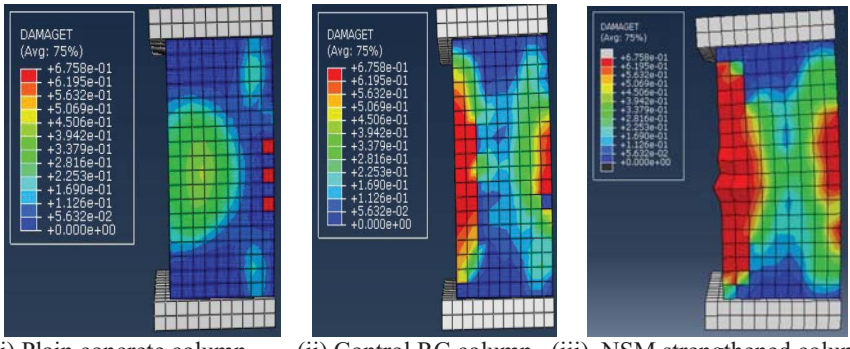

(i) Plain concrete column (ii) Control RC column (iii) NSM strengthened column

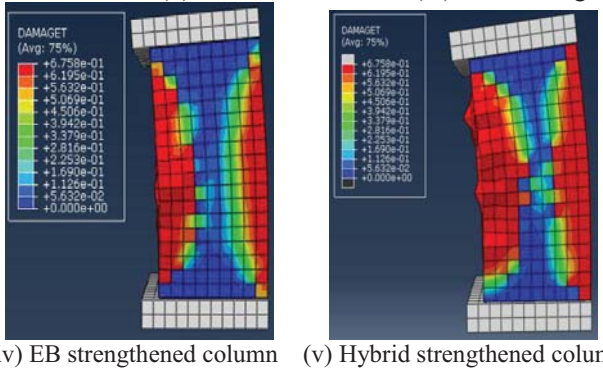

(iv) EB strengthened column (v) Hybrid strengthened column

Figure 7: Damage progression of RC columns under eccentric compression

8 CONCLUSIONS

Ten square reinforced concrete column elements were cast, strengthened using different FRP strengthening techniques and tested under uniaxial eccentric compression. A non-linear finite element model is developed using ABAQUS and the predictions are compared with the experimental results. The following are the major conclusions drawn from the study.

- Un-strengthened RC columns had a reduced strength and ultimate displacement due to the effect of additional bending moment developed due to eccentric compression.
- Column strengthened using only NSM strengthening technique had improvement in strength and ultimate displacement of about 15.3% and 12.4% respectively when compared to control specimens. The cracks initiated between the NSM CFRP laminates and propagated towards the top of the specimen.
- Column strengthened using only EC strengthening technique was able to restore the strength with reduced ultimate strain. The improvement in strength and ultimate displacement was about 26.6% and 3.4% respectively when compared to control specimens.
- Columns strengthened using hybrid strengthening technique had improvement in terms of initial and post peak stiffness, peak load and ultimate displacement. The improvement in strength and ultimate displacement was 46.4% and 50.6% with respect to the control specimen.
- The numerical model developed is able to match the initial stiffness, peak strength, damage progression and post peak degradation of confined and unconfined RC columns

under eccentric compression. Nevertheless, the accuracy of the predictions should be improved for confined specimens to better predict the post cracking stiffness and ultimate strain level.

9 ACKNOWLEDGEMENT

This research work was sponsored through "FAST- Center for Sustainable Development" at IIT Hyderabad, funded by Ministry of Human Resource Development, India. The authors gratefully acknowledge their generous support.

10 REFERENCES

[1] Chai, Y.H., Priestley, M.J.N., Seible, F (1994), Analytical model for steel jacketed RC circular bridge columns. J. Struct, ASCE, Vol.120(8), pp.2358-2376.

[2] Widiarsa, IBR., Hadi, MHS (2013), Performance of CFRP wrapped square reinforced concrete columns subjected to eccentric loading. Procedia Engineering, 54, pp.365-376.

[3] Parvin, A., Wang, Wei (2001), Behavior of FRP jacketed concrete columns under eccentric loading. J. Compos. Constr, Vol.5 (3), pp.146-152.

[4] Maddawy, ET (2009), Strengthening of eccentrically loaded reinforced concrete columns with fiber reinforced polymer wrapping system – experimental investigation and analytical modeling, J.Compos.Constr.Vol.13(1), pp.146-152.

[5] Parvin, A., Brighton, D (2014), FRP Composites strengthening of concrete columns under various loading conditions, Polymers,Vol.6, pp.1040-1056.

[6] Danesh, F., Baradaran, NB (2010), Flexural Strengthening of Concrete Columns Reinforced with Near Surface Mounted Fiber Reinforced Polymer Bars,14ECE2010, Ohrid, Macedonia.

[7] Olivova, K., Bilcik, J (2009), Strengthening of concrete columns with CFRP., Slovak Journal of Civil Engineering, pp. 1-9.

[8] Indian Standards 10262 (2009), Recommended Guidelines for Concrete Mix Design, Bureau of Indian Standards, New Delhi.

[9] ASTM D3039 (2000), Standard Test Method for Tensile Properties of Polymer Matrix Composite Materials, ASTM, West Conshohocken, PA.

[10] ACI 440.2R (2008), Guide for the design and construction of externally bonded FRP system for strengthening concrete structures. ACI committee 440. Farmington Hills (MI): American Concrete Institute.

[11] Chellapandian M, Prakash SS (2016), Behavior of FRP strengthened RC columns under pure Compression – experimental and numerical Studies. Proceedings of Structural Engineering Convention SERC; 1730-1735.

[12] Chellapandian, M., Prakash, SS., Sharma, A (2017), Strength and Ductility of Innovative Hybrid NSM Reinforced and FRP Confined Short Reinforced Concrete Columns under Axial Compression, Composite Structures, Elsevier (Accepted) DOI: 10.1016/j.compstruct.2017.05.033.

[13] Chellapandian, M., Jain, S., Prakash, SS., Sharma, A., An Experimental Study on the Behavior of Hybrid CFRP Strengthened Short RC Column Elements under Eccentric Compression, ACI Structural Journal (Under Review).

Application of a Self-Healing Mechanism in Concrete to Reduce Chloride Ingress Through Cracks

Bjorn Van Belleghem[1,2], Philip Van den Heede[1,2], Kim Van Tittelboom[1] and Nele De Belie[1]

[1] Magnel Laboratory for Concrete Research, Department of Structural Engineering, Faculty of Engineering and Architecture, Ghent University, Belgium

[2] Strategic Initiative Materials (SIM vzw), project ISHECO within the program 'SHE', Technologiepark Zwijnaarde 935, B-9052 Ghent, Belgium

ABSTRACT

Chloride induced corrosion of reinforcing steel is one of the most important damage mechanisms of reinforced concrete structures. The appearance of cracks in reinforced concrete structures will accelerate the ingress of chlorides and therefore cause a higher risk for corrosion and its propagation. In this research, autonomous healing of cracks by encapsulated polyurethane was investigated as a possible method to reduce chloride ingress through cracks. Therefore, uncracked, cracked, and healed concrete specimens were subjected to a high concentration NaCl solution for exposure periods of 7, 19, and 52 weeks. Chloride profiles were determined in the crack region after each exposure period. The resulting chloride profiles showed that the autonomous crack healing mechanism formed a partial barrier which prevented the immediate ingress of chlorides through cracks. At depths below the surface larger than 12 mm, a self-healing efficiency of at least 70% was found for all exposure periods. Due to this big reduction in chloride concentration, a much lower amount of chlorides will reach the steel reinforcement through the cracks. This will postpone the time to corrosion initiation and reduce the corrosion rate of the steel reinforcement. Consequently, the use of self-healing concrete will have important benefits for the durability of reinforced concrete structures in marine environments.

Keywords: Autonomous self-healing, chloride diffusion, concrete cracking, encapsulated polyurethane

1 INTRODUCTION

Concrete is categorized as one of the world's most widely used construction materials [1]. One of the main reasons for that is the large degree of freedom in construction design combined with a high compressive strength. However, most of the construction designs require materials that can both take compressive and tensile stresses. Therefore, steel reinforcement is used in almost every concrete structure. Reinforced concrete is without doubt an excellent construction material and it is categorized as one of the five longest lasting building materials [2]. Throughout the 20th century, the use of reinforced concrete as a building material has been growing a lot. However, nowadays a lot of structures that were built in the mid-20th century show deterioration due to durability problems before they reach their designed lifetime. One of the main causes of the durability problems in reinforced

concrete structures is the appearance of cracks in the concrete. Even though the steel reinforcement is well designed to take up the tensile stresses, cracks will appear in the concrete in the tensile zone. Consequently, aggressive substances can enter the concrete through the cracks and rapidly reach the steel reinforcement.

Thus, the main danger for the durability of reinforced concrete structures is the formation of cracks in combination with the presence of aggressive substances in the environment. For that reason, a lot of damage is reported for constructions in marine environments. Sea water contains a high concentration of chlorides which is one of the aforementioned aggressive agents that can enter the concrete. Reinforced concrete structures in marine environments are thus very susceptible to rapid chloride ingress through cracks. Several studies have already been done to investigate the chloride penetration through cracks in concrete [3-8]. All of these studies agree that the presence of cracks accelerates the rate of chloride ingress in concrete. When the cracks reach the reinforcing steel, a high chloride concentration can then cause very severe reinforcement corrosion. If no repair actions are undertaken, the corrosion of the steel will continue and can endanger the structural integrity of the construction.

In order to prevent deterioration of the structures, actions need to be taken to repair cracks and thus prevent rapid ingress of chlorides towards the steel reinforcement. Manual repair of cracks, however, is expensive and in some cases even impossible due to inaccessibility. Moreover, manual crack repair is mostly done when there is already some deterioration of the structure. It would be interesting if the cracks could be sealed at the moment of their appearance to prevent any further damage immediately. Therefore, the idea of giving the concrete matrix the property of restoring the cracks itself, also known as self-healing, grew during the last two decades [9-10]. A promising approach is modifying the concrete elements in order to obtain autonomous repair of cracks. This can for example, be obtained through the embedment of brittle capsules which are filled with a polymer based healing agent in the concrete matrix [11]. Acoustic emission analysis already proved that the brittle capsules are able to rupture upon crack formation [12]. Also, computed tomography was used to prove that the polymeric healing agent was released from the capsules and flew into the crack [11]. It was also already shown that an autonomous healing mechanism has a beneficial influence on the resistance against chloride penetration [13-14]. In this study, the autonomous crack healing mechanism was further investigated to evaluate the resistance against chloride penetration at different exposure times.

2 MATERIALS AND METHODS

2.1 Concrete

A fly ash containing concrete mix with a water-to-binder (W/B) ratio of 0.41 was used in this research. A fly ash-to-binder (F/B) ratio of 15% was used, according to the k-value concept [15]. This mixture composition is appropriate for use in a marine environment since an increased resistance against chloride penetration was found for concrete mixtures where cement is partially replaced by fly ash [16-18]. The mix composition and properties of the concrete are given in Table 1.

2.2 Self-healing mechanism

The autonomous healing mechanism that was used in this study consisted of embedding capsules filled with a polyurethane healing agent in the concrete matrix. The cylindrical capsules were made of borosilicate glass and had a length of 35 mm, an internal diameter of 3 ± 0.05 mm and a wall thickness of 0.175 ± 0.03 mm. In practice, the use of a very brittle material for encapsulation is only feasible when the capsules are placed in the mold of a

prefabricated element. The advantage of placing the capsules in the molds before pouring the concrete is that the healing mechanism can be placed at locations where the concrete is most vulnerable to cracking.

One end of the capsule was sealed by a methyl methacrylate (MMA) based glue. When the glue was hard, the polyurethane precursor was carefully injected in the capsules by means of a syringe with a needle. After that, the other end of the capsules was sealed with the same MMA based glue.

The polymer based healing agent used for this research is a one component polyurethane precursor. The precursor is a non-commercial product which was developed in the framework of another project (SHEcon). It has a viscosity of 6700 mPas at 25°C. It essentially consists of methylene diphenyl diisocyanate (MDI) and a polyether polyol. When the precursor comes into contact with moisture, it starts to polymerize and forms solid flexible foam within 24 to 48 hours.

Table 1. Concrete mix composition and properties

Sand 0/4 (kg/m³)	696
Aggregates 2/8 (kg/m³)	502
Aggregates 8/16 (kg/m³)	654
CEM I 52.5 N (kg/m³)	317.6
Fly Ash (kg/m³)	56
Water (kg/m³)	153
Superplasticizer (ml/kg binder)	3.0
W/B (-)	0.41
F/B (%)	15
Slump	S3
Strength class	C40/50

2.3 Concrete specimens with (out) self-healing properties

Cylindrical concrete specimens with a diameter of 100 mm and a height of 50 mm were cast using plastic PVC molds. Cracks were introduced in the specimens in an artificial way by means of thin brass plates. The plates had a thickness of 300 µm and a length of 60 mm. They were placed in the center of the PVC molds up to a depth of 25 mm by fixing them onto iron rods (see Figure 1(a)). In the self-healing concrete specimens, cracks were also produced using the thin brass plates. In order to trigger the autonomous crack healing mechanism at the moment of crack creation, the method described by Belleghem et al. [19] was used. Hereby, holes are drilled in the thin brass plate and the capsules are put through those holes. In this study, three capsules were put through the thin brass plate with an intermediate distance of 20 mm. Their position was fixed at half the depth of the crack (12.5 mm from the surface) by gluing the ends of the capsules on nylon wires (Figure 1b).

When the molds were prepared, concrete was cast and the samples were compacted on a vibrating table. After casting, the specimens were put in an air-conditioned room with a temperature of 20 ± 2 °C and a relative humidity of at least 95%. After 24 hours all specimens were demoulded and stored in the same environment for 27 days. A total of 27 specimens were prepared: 9 specimens without a crack (UNCR), 9 specimens containing an artificial crack (CR) and 9 specimens containing an artificial crack with the aforementioned autonomous crack healing mechanism (HEAL).

(a) (b)

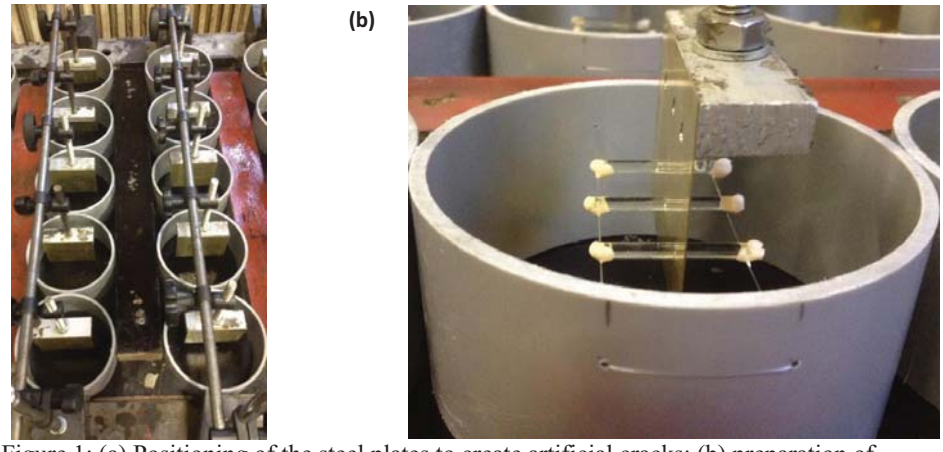

Figure 1: (a) Positioning of the steel plates to create artificial cracks; (b) preparation of specimens with an autonomous crack healing mechanism.

2.4 Crack creation and healing

At the age of 28 days, the specimens were removed from the air-conditioned room and the brass plates of the series CR and HEAL were removed from the specimens. The removal of these brass plates created standardized cracks in the concrete cylinders with a length of 60 mm, a depth of 25 mm and a width of 300 µm. For the specimens with the autonomous crack healing mechanism, the capsules broke due to the removal of the plates and the polyurethane precursor was released in the crack. The precursor then reacted with the moisture of the concrete matrix and solidified in the crack. All specimens were then left for 48 hours at a temperature of 20°C and a relative humidity of 60%. In this way, the polyurethane in the self-healing concrete samples was given the time to harden completely.

2.5 Specimen preparation

Due to the described crack creation method, the test surface of the specimens, containing the crack, was a troweled surface. Therefore, a layer of approximately 1 mm was cut off by water-cooled sawing in order to obtain a flat test surface. In order to ensure unidirectional chloride ingress through the test face of the sample, all sides of the specimens except the test surface were coated with an epoxy coating. The coating was applied in two layers to make sure that the coated sides were really watertight.

2.6 Accelerated chloride diffusion test

Accelerated chloride diffusion tests were performed on all specimens according to NT Build 443, though without pre-saturation of the specimens in saturated calcium hydroxide solution. The exposure solution for the accelerated diffusion test was an aqueous NaCl solution with a concentration of 165 g NaCl per liter of solution. The specimens were immersed in the prepared solution in closed containers. The containers were then placed in a temperature controlled room at 20°C.

The influence of cracks on chloride penetration and the efficiency of the proposed self-healing mechanism to limit the chloride ingress through cracks was investigated at different exposure times of 7, 19 and 52 weeks. At these respective times, three specimens of each series (UNCR, CR and HEAL) were removed from the exposure solution. Subsequently, layers with a thickness of 2 mm were ground from each cylinder parallel to the exposed

surface up to a depth of 20 mm. Since only the chloride ingress in the crack zone was important in this study, material was ground away in a zone of 16 × 78 mm around the crack. All collected powders were then dried in an oven at 105°C for a minimum of 7 days. When the powders were dry, the total chloride content of each powder was determined by an acid-soluble extraction in a nitric acid solution followed by a potentiometric titration against silver nitrate [20].

2.7 Chloride profile fitting

Fitting of the obtained chloride profiles of all specimens was performed according to the well-known formula suggested by Collepardi et al. [21]:

$$C(x,t) = C_s - (C_s - C_i) \cdot \mathrm{erf}\left(\frac{x}{\sqrt{4 \cdot D_e \cdot t}}\right) \quad (1)$$

where C(x, t) is the chloride concentration measured at depth x and time t (m%/binder), C_i is the initial chloride concentration (m%/binder), C_s is the constant surface concentration (m%/binder), erf(.) is the error function and D_e is the apparent diffusion coefficient (m^2/s). The first point of the profile (layer 0-2 mm) was omitted in this regression analysis, according to NT Build 443.

3 RESULTS AND DISCUSSION

The experimentally obtained chloride profiles and corresponding profile fittings according to Eq.(1) for all uncracked, cracked and healed specimens at the exposure periods of 7, 19 and 52 weeks are shown in Figure 2. The experimental results of the three replicate specimens of each series are indicated by separate dots and the corresponding fitting is denoted by a continuous line.

3.1 Influence of cracks on chloride penetration

As already mentioned in Section 1, it has been experimentally and numerically proven in several studies that the presence of cracks in concrete enhances the ingress of chlorides. It is thus not surprising that in this study a big increase in chloride ingress was found due to the presence of a 300 µm wide crack. As can be seen in Figure 2, the influence of the crack is small close to the exposed concrete surface since the (cracked) surface is directly exposed to chlorides. However, deeper inside the concrete the difference in chloride content between the uncracked and cracked specimens becomes much larger. To show this more clearly, the increase in chloride content due to the presence of a crack is plotted in function of the distance from the exposed surface in Figure 3.

At all exposure times, the increase in chloride content due to the presence of a crack rises nearly exponentially with depth. The influence of the crack is largest at the shortest exposure period (7 weeks). This can be explained by the fact that in the very early stage the ingress of chlorides in cracked concrete is governed by capillary suction. This is a very fast process and consequently the chlorides enter through the crack very fast, causing a high chloride content at a large depth below the surface. For longer exposure periods (19 or 52 weeks), there is still a big influence of the crack on the ingress of chlorides, but less pronounced than at 7 weeks. The reason for this is that at longer periods of immersion, diffusion becomes the dominating ingress mechanism. The diffusion rate of chlorides in cracked concrete is smaller compared to uncracked concrete, because a lot of chlorides were already present in the cracked concrete near the crack surface due to early capillary absorption.

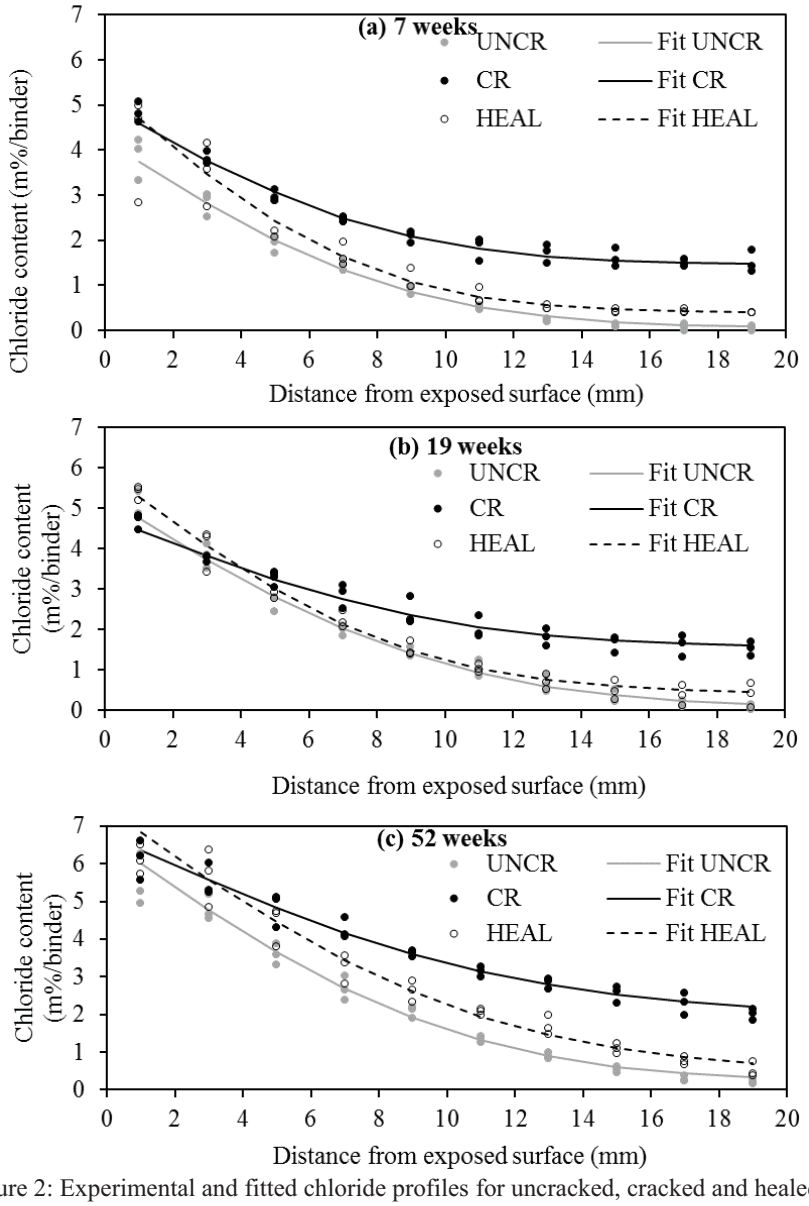

Figure 2: Experimental and fitted chloride profiles for uncracked, cracked and healed concrete after an exposure time of (a) 7 weeks, (b) 19 weeks and (c) 52 weeks to 165 g/l NaCl solution. (Partly redrafted after Van Belleghem et al. [22])

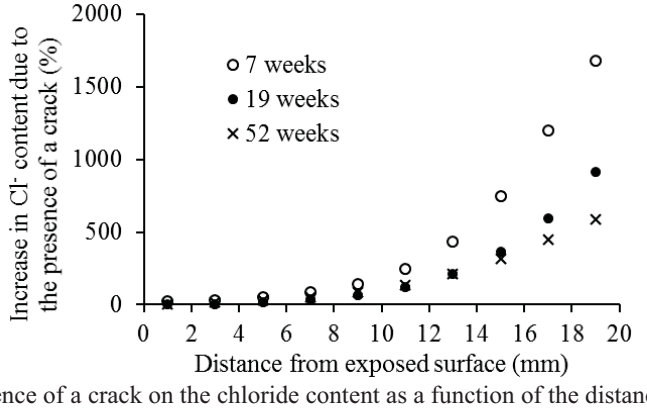

Figure 3: Influence of a crack on the chloride content as a function of the distance from the exposed concrete surface.

3.2 Efficiency of autonomous crack healing to limit chloride ingress through cracks

The previous section clearly shows that cracks can cause durability problems in concrete elements due to the higher chloride penetration. The main topic of this research was to investigate to what extent the proposed autonomous crack healing mechanism is able to reduce the ingress of chlorides through cracks. The chloride profiles in Figure 2 clearly show that autonomous crack healing is able to reduce the chloride content in the concrete to a large extent at all tested exposure times. It can be seen that the fitted chloride profile of the healed specimens lies in between the fitted chloride profiles of the cracked and uncracked specimens with exception of the first two layers (0-4 mm). This indicates that the autonomous crack healing is able to reduce the ingress of chlorides through a crack, but it does not make the concrete behave as it would be uncracked.

To give a quantitative idea about the performance of the healing mechanism, the self-healing efficiency (SHE) at every depth i below the exposed surface was defined according to equation 2 [22]:

$$SHE_i = \left(\frac{Cl^-_{CR,i} - Cl^-_{HEAL,i}}{Cl^-_{CR,i} - Cl^-_{UNCR,i}} \right) \cdot 100 \qquad (2)$$

where $Cl^-_{CR,i}$ represents the chloride content of the cracked specimen at depth i (m%/binder), $Cl^-_{HEAL,i}$ is the chloride content of the healed specimen at depth i (m%/binder) and $Cl^-_{UNCR,i}$ is the chloride content of the uncracked specimen at depth i (m%/binder).

The SHE was calculated for every depth at the three different exposure times. The results are shown in Figure 4. No SHE was calculated at a depth of 0-2 mm for an exposure time of 7 weeks and at a depth of 0-4 mm for an exposure time of 19 and 52 weeks. This is because the fitted profile of the healed specimens is located above the fitted profile of the cracked specimens at these respective depths. Consequently, a negative SHE would be found according to the definition given in Eq.(2).

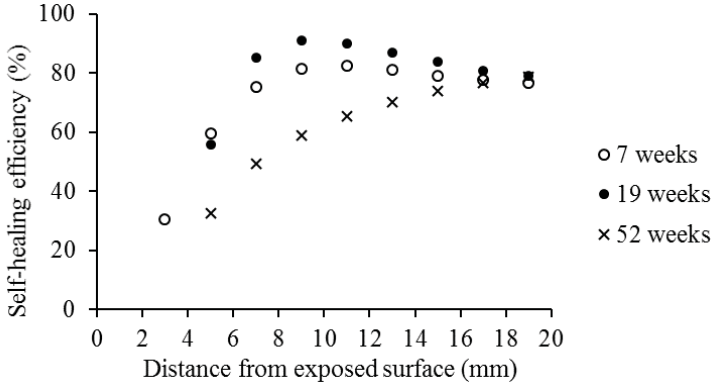

Figure 4: Self-healing efficiency in function of the distance from the exposed surface.

At exposure times of 7 and 19 weeks the SHE generally shows the same trend. A low healing efficiency is found close to the exposed surface, a maximum healing efficiency is found at depths below the surface of 8 to 12 mm and at larger depths the SHE decreases a little and has a tendency to go towards a stable value. The main reason for the location of the maximum SHE is the fact that the capsules are located at this depth. Although there is a slight decrease in the SHE from a depth of 12 mm onwards, still a healing efficiency of 75% or higher is found. It can also be noticed that the SHE is always a little higher at an exposure time of 19 weeks compared to 7 weeks. This is caused by the fact that the crack healing is never exactly the same for every crack. There is always a small variability in crack healing, so it is possible that the 3 healed specimens which were taken out of the solution at an exposure time of 19 weeks were slightly better healed than the ones that were taken out at 7 weeks. The evolution of the SHE in function of the depth below the surface at an exposure time of 52 weeks is different from the previous mentioned ones. In this case there is no maximum found at the location of the capsules. Instead, the SHE increases nearly logarithmically in depth (see Figure 4).

In the layers from 4 to 14 mm below the surface, the SHE at 52 weeks of exposure is up to 27% less than at 7 weeks and up to 36% less than at 19 weeks. A possible reason for this reduction can be that there is a degradation in the polyurethane after long term exposure to the high concentration chloride solution. However, this is still uncertain and should be further investigated. At depths below the surface larger than 14 mm, the SHE reaches values that are similar to the values at the other exposure times. At the deepest investigated layer (18-20 mm) the SHE after 52 weeks is still 79%.

The results show that the autonomous crack healing mechanism is able to form a partial barrier against immediate chloride ingress through cracks. For the longest exposure time of 52 weeks the SHE was generally less than for the shorter exposure periods, but at a depth of 18-20 mm a similar SHE of 77 to 79% was found for all exposure times. This means that the self-healing mechanism is effective in reducing the chloride concentration at a depth of 20 mm and probably also at higher depths. Since the concrete cover on the reinforcing steel of most reinforced concrete structures is larger than 20 mm, application of self-healing concrete will be effective in reducing the chloride concentration at the level of the steel reinforcement. For very high concrete covers and thus large crack depths it might be possible that two layers of capsules are needed to achieve a good self-healing efficiency.

4 CONCLUSIONS

Based on the accelerated diffusion tests done in this research, it was found that the presence of an artificial 300 µm wide crack has a large effect on the chloride ingress. The influence of a crack was small close to the exposed concrete surface, but increased exponentially with depth. At an exposure time of 7 weeks the chloride content at a depth of 20 mm was 18 times higher in cracked than in uncracked concrete. For longer exposure periods (19 or 52 weeks), there is still a big influence of the crack on the ingress of chlorides, but a little less pronounced than at 7 weeks. This shows that cracks in marine concrete structures can impair their durability because they act as preferential pathways for chlorides to penetrate the concrete. In this way high chloride concentrations can occur at the level of the reinforcement, which will lead to a fast onset of corrosion.

Clearly, crack closure could be very valuable to prevent the fast ingress of chlorides towards the steel reinforcement. Therefore, autonomous crack healing by means of encapsulated polyurethane was investigated in this research as a possible method to prevent fast ingress of chlorides through cracks. The results of the accelerated diffusion tests showed that healing of the cracks was able to reduce the penetration of chlorides to a large extent. For 7 and 19 weeks exposure to a concentrated chloride solution, at least 75% self-healing efficiency was found at a depth below the exposure surface of 6 mm and onwards. At the longest exposure time of 52 weeks the self-healing efficiency was generally less, but increased with depth and still reached 79% at the largest investigated depth of 18-20 mm. This big reduction in chloride concentration due to the proposed self-healing mechanism will have important benefits for the durability of reinforced concrete in marine environments since a much lower amount of chlorides will reach the steel reinforcement through the cracks. Consequently, an extension of the service life of the concrete elements is possible. It was already found by Van Belleghem et al. [22] that, using this approach, the service life of reinforced concrete elements could be increased by a factor of 10.

5 ACKNOWLEDGEMENTS

This research under the program SHE (Engineered Self-Healing materials), project ISHECO (Impact of Self-Healing Engineered materials on steel COrrosion of reinforced concrete) was funded by SIM (Strategic Initiative Materials in Flanders) and VLAIO (Flanders Innovation & Entrepreneurship). The financial support from the foundations for this study is gratefully appreciated. Kim Van Tittelboom is a postdoctoral fellow of the Research Foundation—Flanders (FWO) (project number 12A3314N) and acknowledges its support.

6 REFERENCES

[1] Crow, J.M., 'The concrete conundrum', *Chem. World.* **5** (2008) 62-66.
[2] Green Diary. Available online: 'http://www.greendiary.com/building-materials-long-lasting-buildings.html' (accessed on 3 November 2016).
[3] Djerbi, A., Bonnet, S., Khelidj, A. and Baroghel-bouny, V., 'Influence of traversing crack on chloride diffusion into concrete', *Cem. Concr. Res*. **38** (6) (2008) 877-883.
[4] Jacobsen, S., Marchand, J. and Boisvert, L., 'Effect of cracking and healing on chloride transport in OPC concrete', *Cem. Concr. Res*., **26** (6) (1996) 869-881.
[5] Jang, S.Y., Kim, B.S. and Oh, B.H., 'Effect of crack width on chloride diffusion coefficients of concrete by steady-state migration tests', *Cem. Concr. Res*., **41** (1) (2011) 9-19.
[6] Maes, M. and De Belie, N., 'Resistance of cracked concrete to chloride attack', Proceedings of 3rd International Conference on Sustainable Construction Materials & Technologies, Kyoto, August, 2013, 1-10.

[7] Gu, C., Ye, G. and Sun, W., 'A review of the chloride transport properties of cracked concrete: experiments and simulations', *J Zhejiang Univ Sci A.* **16** (2) (2015) 81-92.
[8] Audenaert, K., De Schutter, G. and Marsavina, L., 'Influence of cracks and crack width on penetration depth of chlorides in concrete', *Eur. J. Environ. Civ. En.* **13** (5) (2009) 561-572.
[9] Li, V.C., Lim, Y.M. and Chan, Y.-W., 'Feasibility Study of a Passive Smart Self-healing Cementitious Composite', *Compos. Part B.* **29** (6) (1998) 819-827.
[10] Mihashi, H., Nishiwaki, T., 'Development of engineered self-healing and self-repairing concrete – State-of-the-art report', *J.Adv. Concr. Technol.* **10** (5) (2012) 170-184.
[11] Van Tittelboom, K., De Belie, N., Van Loo, D., Jacobs, P., 'Self-healing efficiency of cementitious materials containing tubular capsules filled with healing agent', *Cem. Concr. Comp.* **33** (4) (2011) 497-505.
[12] Van Tittelboom, K., De Belie, N., Lehmann, F., and Grosse, C.U., 'Acoustic emission analysis for the quantification of autonomous crack healing in concrete', *Constr. Build. Mater.* **28** (1) (2012) 333-341.
[13] Maes, M., Van Tittelboom, K. and De Belie, N., 'The efficiency of self-healing cementitious materials by means of encapsulated polyurethane in chloride containing environments', *Constr. Build. Mater.* **71** (2014) 528-537.
[14] Van Belleghem, B., Van den Heede, P. and De Belie, N., 'Resistance to chloride penetration of self-healing concrete with encapsulated polyurethane', Proceedings of the 4th International Conference on Sustainable Construction Materials & Technologies, Las Vegas, August, 2016, 10p.
[15] NBN B15-001, 'Supplement to NBN EN 206–1: Concrete—Specification, Performance, Production and Conformity', BIN, Brussels, Belgium, 2004.
[16] Chalee, W., Jaturapitakkul, C. and Chindaprasirt, P., 'Predicting the chloride penetration of fly ash concrete in seawater', *Mat. Struct.* **22** (3) (2009) 341-353.
[17] Boğa, A.R. and Topçu, İ.B., 'Influence of fly ash on corrosion resistance and chloride ion permeability of concrete', *Constr. Build. Mater.* **31** (2012) 258-264.
[18] Yu, Z. and Ye, G., 'Chloride penetration and microstructure development of fly ash concrete', Proceedings of the 2nd International Conference on Microstructural-Related Durability of Cementitious Composites, Amsterdam, April, 2012, 586-594.
[19] Van Belleghem, B., Dewanckele, J., De Belie, N. and Cnudde, V., 'Analysis and visualization of water uptake in cracked and healed mortar by water absorption tests and X-ray radiography', Proceedings of the 4th International Conference on Concrete Repair, Rehabilitation and Retrofitting, Leipzig, October, 2015, 45-53.
[20] Mu, S., 'Chloride penetration and service life prediction of cracked self-compacting concrete', PhD thesis, Ghent University, Faculty of Engineering and Architecture. Ghent, 2012.
[21] Collepardi, M., Marcialis, A. and Turriziani, R., 'Penetration of chloride ions in cement pastes and in concretes', *J. Am. Ceram. Soc.* **55** (10) (1972) 534-535.
[22] Van Belleghem, B., Van den Heede, P., Van Tittelboom, K. and De Belie, N., 'Quantification of the Service Life Extension and Environmental Benefit of Chloride Exposed Self-Healing Concrete', *Materials* **10** (5), 22p.

GFRP Wrapped Concrete Filled Double Skin Tubular Beam-Columns subjected to Reversed Lateral Loading

Parvati T.S. and Dr. P.S. Joanna

Department of Civil Engineering, Hindustan Institute of Technology and Science, Chennai, India

ABSTRACT

Concrete Filled Double Skin Tubular (CFDST) members have found wide spread acceptance in the construction industry due to their greater ductility, lighter weight and greater speed of construction. Glass Fibre Reinforced Polymer (GFRP) sheets are gaining much popularity as a confinement material along with retrofitting application. This paper presents a study on the behaviour of GFRP wrapped CFDST beam-columns subjected to reversed lateral loading. Comparison between the behaviour of the CFDST beam-column member with a Concrete Filled Steel Tubular (CFST) beam-column member is also presented. Tests were conducted on two CFDST specimens and two CFST specimens were subjected to reversed lateral loading under constant axial load. The CFDST column members were connected with CFST beam member by angle plates and bolts. M30 concrete with 40% cement replacement with fly ash was used to fill the space between the two concentric tubes. The lateral load-lateral displacement behaviour, ductility, energy dissipation, stiffness degradation and the peak load behaviour of the specimens are illustrated.

Keywords: CFST, CFDST, GFRP sheet, reversed lateral loading and cold-formed steel.

1 INTRODUCTION

Concrete filled double skin tubular (CFDST) members are a type of composite construction which consists of two concentric steel tubes with concrete filled in between them. Due to the interaction between the steel and the concrete, these members have better load carrying capacity, greater ductility, less weight and better construction ability [1]. The steel tube confines the concrete thus increasing its strength and the concrete filled in between the two tubes aids in reducing the local buckling of the outer tube [2].

Large numbers of experimental works have been carried out to understand the response of the CFDST members to different loading conditions. Compression and bending tests were carried out by Zhao and Grezbieta on cold formed steel CFDST sections [3]. The study concluded that the CFDST sections have increased ductility both in compression and bending compared to empty steel tubes. Experimental investigations on CFDST short columns and beam-columns by Tao *et al*. and Han *et al*. revealed the ductile nature of the CFDST sections[4,5]. This enhanced behavior can be attributed to the 'composite action' between the steel and the concrete. Axial compression studies on composite short columns with CHS outer and SHS inner tubes also revealed increased strength ,ductility and energy absorption

capacity of CFDST sections when compared to empty steel tubes [6]. Han *et al*. conducted cyclic bending studies on CFDST beam-column sections [7]. The results also reinforced the high levels of energy dissipation and ductility of the CFDST sections. Enhanced strength and ductility was observed for CFDST beam-column sections with rectangular hollow section inner and outer tubes[8].The studies reveal that the concrete filled in between the two tubes eliminate the inward buckling of the outer tube thus increasing the section capacity of the members.

CFDST sections have found applications as electrical poles and bridge piers [1, 5, 9]. But steel, being susceptible to the chemical and electro chemical materials in the environment undergo corrosion. This results in loss of strength for members having very small thickness.

Due to the advantages offered by the FRP materials like high strength and resistance to corrosion they are used as retrofitting materials to strengthen the existing components. Investigations carried out by Fam and Rizkalla. CFST sections made of outer FRP tubes revealed increased flexural strength [10]. Axial compression studies revealed increased strength and ductility for the CFST sections confined with GFRP. By providing wrapping the local buckling in the stub columns were also delayed [11]. Axial compression behaviour of circular CFDST stub columns wrapped with GFRP was investigated by Wang *et al*. [12]. The test results also proved that the GFRP wrapping provides confinement and thus increases the load carrying capacity of the section. Literature survey reveals the lack of experimental investigations on wrapped beam-column members with bolted connections and subjected to reversed lateral loading.

In this context, this paper presents an experimental study on beam-column members subjected to constant axial load and reversed lateral loading which simulates earthquake force. The specimens consist of CFDST columns with GFRP wrapped outer square tube, an inner circular section and the space between them filled with fly ash concrete having 40% cement replacement with fly ash and CFST beam connected together by angle plates and bolts. The load – displacement hysteretic behaviour, energy dissipation, stiffness degradation and the displacement ductility of the specimens are illustrated.

2 EXPERIMENTAL PROGRAMME

2.1 Test Specimen Details

Experiments were conducted on four beam-column specimens which were subjected to reverse lateral loading and constant axial load. The beam-column specimens had a CFST beam of 1.5 m length and wrapped column of 1.1 m height connected together using through bolts and angle plates. Figure 1 shows the schematic diagram of the beam-column specimen. Two beam-column specimens had CFDST columns wrapped with GFRP wrapping (WCFDST) and CFST beams and the other two specimens had CFST columns wrapped with GFRP wrapping (WCFST) and CFST beam. Table 1 gives the details of the test specimens. The specimens were all fabricated from cold formed steel tubes of 3 mm thickness with yield strength of 479 N/mm^2. The CFDST members consist of an outer square tube of 100 x 100 mm cross section and an inner circular tube of 50 mm diameter and the space between them filled with M30 grade fly ash concrete while the CFST member consist of a square tube of 100 x100 mm completely filled with M30 grade fly ash concrete. The mix proportions of the concrete were cement: 370 kg/m^3, sand: 690 kg/m^3, course aggregate: 1084 kg/m^3; with a water cement ratio of 0.45 and 40% cement replacement with fly ash [13]. Master sky Glenium B233 super plasticizer was added to increase the workability of the mix and a curing compound (poly ethylene glycol) was added to facilitate self-curing of the concrete. The concrete used for the specimens were cured for 56 days as the fly ash concrete gain the 28

day strength of the normal concrete on 56th day. Three cubes were tested and average cube strength of 36.6 N/mm^2 was obtained. The connection between the beam and the column was achieved by angle plates of size (120×100× 6) mm and twelve numbers of 10 mm diameter high strength bolts.

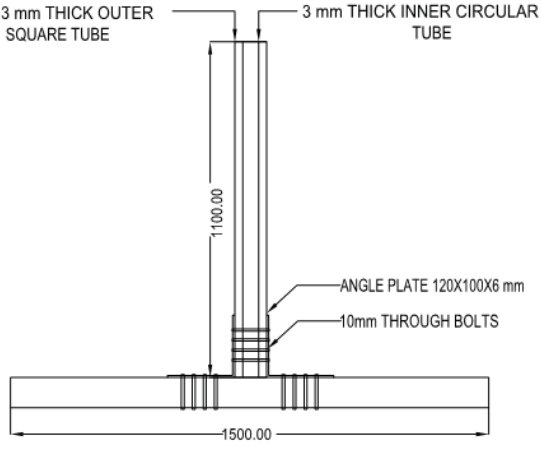

Figure 1: Schematic diagram of the beam-column specimen

Table 1: Details of test specimen

Sr. No.	Specimens	Description
1	WCFST1	Beam-column specimens with CFST beam and GFRP wrapped CFST column
2	WCFST2	
3	WCFDST1	Beam-Column with CFST beam and GFRP wrapped CFDST column.
4	WCFDST2	

The material properties of the GFRP sheets were studied by carrying out coupon tests on three flat specimens prepared as per ASTM D638 - 02a [14]. The GFRP specimens exhibited a tensile strength of 109.96 N/mm^2. The GFRP wrapping provided for the specimens had a thickness of 3 mm. The specimen surfaces were first rubbed with sand paper to remove the dirt. An initial layer of chopped strand mat of 0.1 mm thickness was placed on the cleaned surface of the cold formed steel tube followed by a layer of woven roving mat of 2.5 GSM (grams per square metre). Then two layers of shredded GFRP sheets and the finishing layer was placed. Isophthalic resin was used along with the GFRP sheets to prepare the wrapping. It was ensured that there was no airlock while the resin was applied to the sheet. Once the resin was dry, the ends were finished by drilling of the excess length. The circular steel tubes were placed at the centre of the GFRP wrapped square hollow sections and held in position by small steel pieces attached to the inner side of the outer tube. The beams and the GFRP

wrapped columns were connected by angle plates and through bolts. The beams and the columns were then filled with concrete with proper compaction.

2.2 Test setup

The test arrangement consist of a reaction frame which supports the actuator (200kN capacity) providing the lateral load and a hydraulic jack of 200 kN capacity which provides the constant axial load. The actuator which has a stroke length of ±100 mm was used to apply the lateral load to the column in both forward and reverse direction. The loading was applied in the form of displacements and the load was measured using the load cell attached to the actuator. The lateral displacement provided to the column was measured using a linear variable displacement transducer (LVDT) attached to the top of the column. The load and displacements readings were obtained from the data logger connected to a computer which captured the values till the completion of the test. The beam-column specimens were subjected to both forward and reversed loading and a constant axial load of 20% of the axial capacity of the column was applied to the column head using a hydraulic jack. Steel rollers placed in between two steel plates were provided for the proper transfer of the axial load. The testing was stopped when the load reduced below 85% of the peak lateral load. The test arrangement is illustrated in Figure 3.

Figure 3: Test setup

3 RESULTS

3.1 Lateral load (P)-lateral displacement (Δ) hysteretic curves

The load versus displacement curves for all the four specimens are shown in Figure 4 and Figure 5. The control specimens (WCFST) recorded an average load of 35.18 kN with an average displacement of 35.37 mm while the wrapped CFDST specimens (WCFDST1 and WCFDST2) exhibited an average load carrying capacity of 35.88 kN with an average displacement of 35.2 mm. Table 2 presents the load and the displacement recorded both in the forward and in the reverse direction.

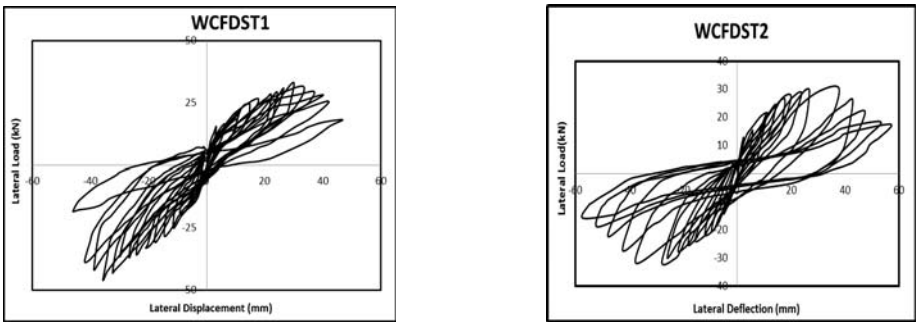

Figure 4: Lateral load – lateral displacement curves for WCFDST specimens

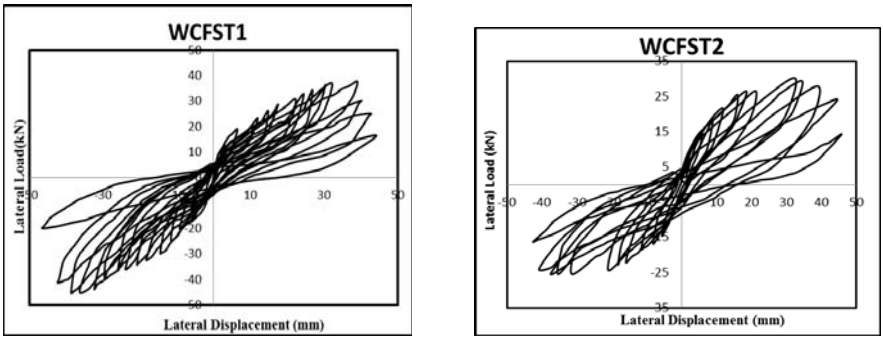

Figure 5: Lateral load –lateral displacement curves for WCFST specimens

The strength of the WCFDST and the WCFST specimens are nearly equal with reduction in self weight due to the hollow inner portion. This can be attributed to the confinement provided by the inner steel tube to the in filled concrete.

Table 2: Measured load and Displacements

Specimen	Yield values				Peak values				0.85Pmax=Pu			
	P_y (kN)		Δy(mm)		Pmax(kN)		Δmax(mm)		Pu(kN)		Δu(mm)	
	+ve	-ve	+ve	-ve	+ve	-ve	+ve	-ve	+ve	-ve	+ve	-ve
WCFST1	20.5	24.8	8.9	11.6	38.7	-45.3	39.0	-38.7	32.9	38.5	39.7	42.9
WCFST2	20.2	17.8	11.4	10.4	30.2	-26.5	32.4	-31.4	25.6	22.5	42.2	41.2
WCFDST1	19.6	26.8	7.0	13.3	33.2	-45.9	30.0	-35.7	28.2	37.4	39.6	42.2
WCFDST2	16.8	21.4	7.2	11.2	32.5	-31.9	37.7	-37.4	27.6	27.1	41.3	40.8

3.2 P-Δ envelope curves

The P-Δ envelope curves for all the specimens were obtained by connecting the peak points of all the cycles, both in the positive and negative direction. The WCFST1 specimen

recorded a maximum load of 42 kN at a displacement of 38.85 mm while the WCFST2 specimen at a displacement of 31.9 mm recorded a maximum load of 28.35 kN. The wrapped CFDST specimens (WCFDST1 and WCFDST2) recorded maximum load of 39.55 kN and 32.2kN at a displacement of 32.85 mm and 37.55 mm respectively. It was observed that the wrapped CFDST specimens exhibit nearly the same load capacity as the WCFST specimens. The P-Δ curves for all the specimens are shown in Figure 6.

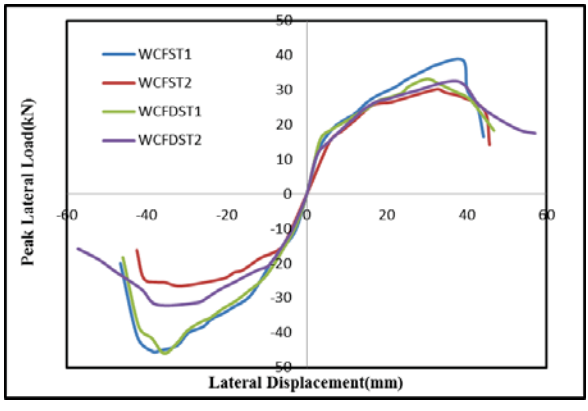

Figure 6: Peak Lateral Load vs Lateral Displacement

3.3 Stiffness or rigidity degradation

Figure 7 (a) and Figure 7(b) shows the rigidity degradation of the GFRP wrapped beam-column specimens as a function of relative displacement (Δ/Δ_y). Rigidity degradation with increasing displacement was observed during the testing in all the beam-column specimens. The rigidity degradation co-efficient defined with reference to JGJ 101-96 [15] is expressed as

$$K_j = \frac{\sum_{i=1}^{n} P_j^i}{\sum_{i=1}^{n} u_j^i} \quad (1)$$

where, P_j^i is the maximum load and u_j^i is the corresponding displacement in the i^{th} cycle. The parameter K_j expresses the rigidity degradation due to two factors, (a) decreasing rigidity with increasing displacement and (b) rigidity degradation due to repeated cycles under the same displacement [4]. The WCFDST specimens' exhibit increased initial stiffness as can be observed from Figure 7 (b) when compared to the control specimens.

WCFDST specimens exhibited an average initial stiffness of 4634.47 N/mm while the WCFST specimens had an initial stiffness of 3454.40 N/mm. The specimen WCFST1 reached 50% of its initial stiffness in the fifth cycle at $\Delta/\Delta_y = 1.4$ whereas the specimen WCFST2 reached 50% of its initial stiffness in the fourth cycle (at $\Delta/\Delta_y = 1.7$). The WCFDST1 and WCFDST2 specimens reached its 50% initial stiffness in the fourth cycle at$\Delta/\Delta_y = 1.14$ and at $\Delta/\Delta_y = 1.29$ respectively.

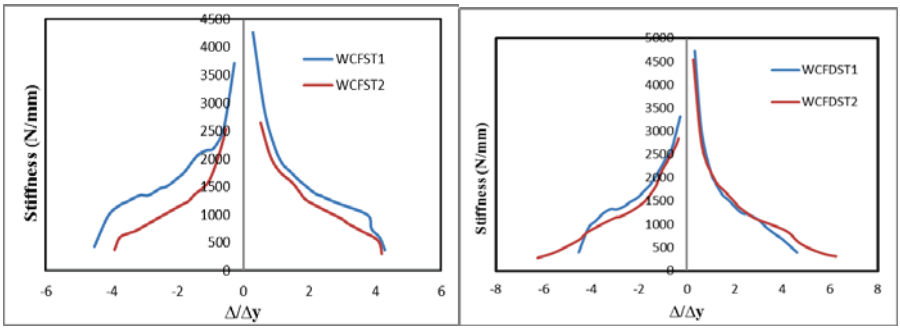

(a) Wrapped CFST specimens (b) Wrapped CFDST specimens

Figure 7: Stiffness Degradation of Beam-Column Specimens

3.4 Energy dissipation

The dissipated energy in each cycle is calculated as the area enclosed by the P-Δ hysteretic loop of that cycle. The cumulative dissipated energy (E_a) versus the relative displacement of each cycle (Δ/Δ_y) is illustrated in Figure 8. It can be observed that the E_a value increases with the increasing displacement. Table 4 gives the cumulative energy dissipation of the various specimens. The wrapped CFDST specimens have an average energy dissipation value of 5424.25 kNmm while the GFRP wrapped CFST specimens exhibit an energy dissipation of 5231.0 kNmm.

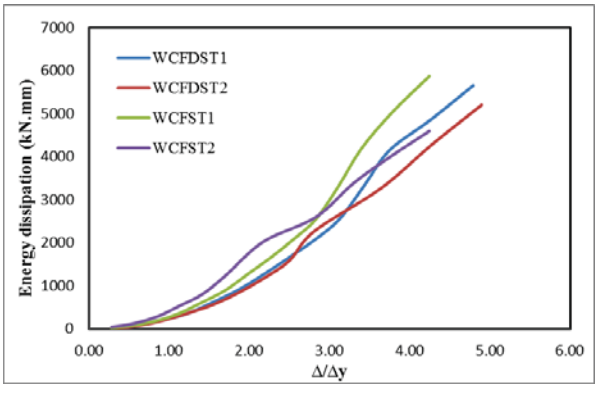

Figure 8: Energy Dissipation of the specimens

3.5 Ductility

Ductility is a significant index in evaluating the seismic performance of the structures. Ductility refers to the ability of the member to undergo large deformation without reduction in strength. The displacement ductility co-efficient (μ) is defined as

$$\mu = \frac{\Delta_u}{\Delta_y} \quad (2)$$

where, Δ_y is the displacement at yield and Δ_u is the displacement when the load is 85% of the peak load. Table 3 gives the measured values of the yield (Δ_y) and the ultimate

displacement(Δ_u). The displacement ductility co-efficient (μ) of all the specimens are presented in Table 4. The wrapped CFDST specimens exhibit 16% more ductility than the control specimens.

Table 4: Energy Dissipation and displacement ductility

Specimen	Displacement Ductility(μ)		Average displacement ductility ($\bar{\mu}$)	E_{total}(kN.mm)
	+	-		
WCFST1	4.4	3.7	4.1	5868.2
WCFST2	3.7	3.7	3.7	4593.9
WCFDST1	5.6	3.2	4.4	5651.9
WCFDST2	5.8	3.7	4.8	5196.6

4 CONCLUSIONS

The paper presents the experimental investigation on beam-column specimens with GFRP wrapped CFDST columns subjected to reversed lateral loading and constant axial load. Beam-column specimens with wrapped CFST sections were also tested. Based on the experimental investigation the following conclusions were drawn.

- The wrapped CFDST sections and CFST sections exhibited nearly the same load carrying capacity.
- Energy dissipation capacity was also nearly the same for both CFST and CFDST beam-columns.
- The wrapped CFDST specimens exhibited high initial stiffness compared to the wrapped CFST sections.
- The stiffness degradation of all the specimens followed the same pattern. The wrapped CFDST sections exhibited 16% more ductility that the wrapped CFST sections.

It can be observed that the beam-columns specimens with GFRP wrapped CFDST columns exhibit nearly the same load capacity as the specimens with wrapped CFST columns. But the CFDST specimens have greater initial stiffness, better ductility and more energy dissipation capacity, these being the properties required for a member to be adopted in regions of seismicity. Also CFDST specimens have lesser self-weight than the CFST section.

The CFDST sections exhibit better or nearly equivalent performance as the CFST section with lesser self-weight which makes it a better choice as structural member in regions of seismic risk.

REFERENCES

[1] W. Li, L.-H. Han, and T.-M. Chan, 'Tensile behaviour of concrete-filled double-skin steel tubular members,' *J. Constr. Steel Res.* **99** (2014) 35–46.

[2] W. Yuan and J. Yang, 'Experimental and numerical studies of short concrete-filled double skin composite tube columns under axially compressive loads,' *J. Constr. Steel Res.***80** (2013) 23–31.

[3] X.-L. Zhao and R. Grzebieta, 'Strength and ductility of concrete filled double skin SHS inner and SHS outer) tubes,' *Thin-Walled Struct.***40** (2) (2002) 199–213.

[4] Z. Tao, L.-H. Han and X.-L. Zhao, 'Behaviour of concrete-filled double skin (CHS inner and CHS outer) steel tubular stub columns and beam-columns,' *J. Constr. Steel Res.***60** (8) (2004) 1129–1158.

[5] L.-H. Han, Z. Tao, H. Huang, and X.-L. Zhao, 'Concrete-filled double skin (SHS outer and CHS inner) steel tubular beam-columns, '*Thin-Walled Struct.***42** (9) (2004) 1329–1355.

[6] M. Elchalakani, X.-L. Zhao, and R. Grzebieta, 'Tests on concrete filled double-skin (CHS outer and SHS inner) composite short columns under axial compression,' *Thin-Walled Struct.***40** (5) (2002) 415–4412.

[7] L.-H. Han, H. Huang, Z. Tao, and X.-L. Zhao, 'Concrete-filled double skin steel tubular (CFDST) beam–columns subjected to cyclic bending,' *Eng. Struct.* **28** (12) (2006) 1698–1714.

[8] Z. Tao and L.-H. Han, 'Behaviour of concrete-filled double skin rectangular steel tubular beam–columns,' *J. Constr. Steel Res.* **62** (7) (2006) 631–646.

[9] W. Li, L.-H. Han, Q.-X. Ren, and X.-L. Zhao, 'Behavior and calculation of tapered CFDST columns under eccentric compression,'*J. Constr. Steel Res.* **83** (2013) 127–136.

[10] A. Z. Fam and S. H. Rizkalla, 'Flexural Behavior of Concrete-Filled Fiber-Reinforced Polymer Circular Tubes,' *J. Compos. Constr.* **6** (2) (2002) 123–132.

[11] Y. M. Hu, T. Yu, and J. G. Teng, 'FRP-Confined Circular Concrete-Filled Thin Steel Tubes under Axial Compression,' *J. Compos. Constr.* **15**(5) (2011) 850–860.

[12] J. Wang, W. Liu, D. Zhou, L. Zhu, and H. Fang, 'Mechanical behaviour of concrete filled double skin steel tubular stub columns confined by FRP under axial compression,' *Steel Compos. Struct.* **17**(4) (2014) 431–452.

[13] Joanna P.S, Jessy Rooby, R.Preetha, G.Elumalai, C.SivathanuPillai, 'Performance of Reinforced Concrete Beams with 40% Fly Ash,' *Eur. J. Sci. Res.* **96** (4) (2013) 620–632.

[14] "ASTM D638-02a Standard Test Method for Tensile Properties of Plastics ASTM International." ASTM International, 2002.

[15] "JGJ101-96.Specification for test methods of seismic buildings. Beijing: China Architecture and Building Press." 2010.

Elastomeric Polyurethane for Retrofitting Application of Concrete Structures under Dynamic Loadings

Sudharshan N. Raman [(1)], H. M. Chandima C. Somarathna [(2)], Azrul A. Mutalib [(3)], and Khairiah H. Badri [(4)]

[(1)]Senior Lecturer, Department of Architecture, Universiti Kebangsaan Malaysia, 43600 UKM Bangi, Selangor, Malaysia,

[(2)]PhD Candidate, Department of Civil and Structural Engineering, Universiti Kebangsaan Malaysia, 43600 UKM Bangi, Selangor, Malaysia

[(3)]Senior Lecturer, Department of Civil and Structural Engineering, Universiti Kebangsaan Malaysia, 43600 UKM Bangi, Selangor, Malaysia

[(4)]Professor, School of Chemical Sciences and Food Technology, Universiti Kebangsaan Malaysia, 43600 UKM Bangi, Selangor, Malaysia

ABSTRACT

This research was formulated to establish a feasible technique to improve the dynamic resistance and enhance the energy absorption capability of concrete structures, through an innovative approach of providing elastomeric polyurethane (PU) coating on the structural elements. This paper reports the findings of the experimental investigation conducted using scaled concrete specimens, to evaluate the contribution of PU coatings in enhancing the dynamic mechanical response of the specimens. Concrete specimens with dimensions of 160 mm × 40 mm × 40 mm were prepared, and a total of four different coating configurations were developed by coating PU on both tension and compression faces of the concrete specimen with the thicknesses of 2.5% and 5% to the specimen's depth. Dynamic loading condition was simulated by conducting three-point bending test at an enhanced strain rate of 0.067 s^{-1}, in comparison to quasi-static strain rate (0.00033 s^{-1}). Findings indicated that the failure strain and strain energy density were enhanced by factors of 2.9-4.6, and 3.0-5.1 respectively with a marginal enhancement in the maximum flexural stress under dynamic conditions compared to un-coated specimens. In addition, it was noted that the response of concrete specimens was improved when the thickness of the PU coating was increased.

Keywords: Concrete, dynamic loadings, polyurethane (PU), retrofitting, strain rate.

1 INTRODUCTION

Interruptions or failure of critical infrastructure would highly impact and spread to the other sectors due to their interdependent nature of the services and industries. The protection of these infrastructure has therefore become a global challenge that needs to be addressed, which leads to the need for continual review and improvement of infrastructure protection strategies. The subjection of extreme dynamic loads of impact and blast onto these critical infrastructures can cause catastrophic damage to the buildings external and internal structural frames because these loads act within a short time duration with few or more cycles while transmitting very high energy. Loss of life and injuries can be caused by many reasons, such

as the direct effect of the loadings, collapse of structures, and due to the impact of debris [1-3]. To mitigate such incidents by providing adequate protection to buildings and critical infrastructure, and consequently, to their occupants, exploring and identifying novel and effective means to reduce the impulsive effects of dynamic loads on structures is necessary. Several advanced engineering solutions have been investigated as an active protective feature for structural elements and they have demonstrated both positive and negative results [4,5].

Application of materials which possess high stiffness together with high strain capacity is a highly effective way to enhance energy absorption capacity of structural elements [1,2]. One of the novel approaches to mitigate the effects of dynamic loads is the application of the elastomeric coatings to the structures. Significant amount of research have been conducted to investigate the possibility applying these protective coatings for structural strengthening because they appear to have potential in enhancing the dynamic resistance of structures [1,2,6]. In addition, this technique provides better solutions for limitations of conventional and other advanced techniques, by making it cost-effective, and applicable for the existing structures [8-12].

In consideration of the outstanding mechanical behaviour and the positive effect of the elastomeric polymers on other types of structural materials, the research and application of this technique on concrete structures are progressing extensively [6-12]. Polyurethane (PU) and its variance have been taking the attention among the researchers and engineers, because of their myriad of physical and mechanical characteristics including high flexibility, elastic, and resistance to impact, abrasion, and weather. It can be easily applied with simple techniques such as spraying, brushing, bar coating and pouring, and readily adheres to most of the surfaces and cure fast [6-7, 13-14]. In the present experimental study, the flexural behaviour of elastomeric PU coated scaled concrete specimens were investigated at laboratory-scale by simulating different load conditions.

2 EXPERIMENTAL PROGRAM

2.1 Materials

2.1.2 Concrete

Commercially available ordinary Portland cement (CEM-I) of 42.5 N/mm^2 strength class was used, and the density was 3160 kg/m^3. The fine aggregate used in this study was locally sourced from 5 mm downgraded river sand. Locally available crushed stones with a maximum size of 9.5 mm was used as coarse aggregate. One of the key objective of the current study is the application of the proposed technique to existing concrete structures. Since most of the existing RC structures are designed and constructed using medium-range normal-strength concrete of 25 to 40 MPa, the concrete grade considered in the present study was 30 MPa in cylinders. The cylinder strength values for 7th, 14th and 28th day compressive strengths were 24.4 MPa, 28.9 MPa and 32.1 MPa respectively.

2.1.2 PU

Literature and subsequent studies indicated that mechanical properties of PUs are highly dependent on its composition and synthesis technique. One type of PU namely PU6 has been selected under investigation of quasi-static and dynamic properties, out of eight of PUs from a previous study [6]. For the synthesis of this polymer, the palm-based polyol (PKO-p) was supplied by the Polymer Research Centre (PORCE) of Universiti Kebangsaan Malaysia. 4,4-diphenylmethane diisocyanate (MDI) was obtained from Cosmopolyurethane Sdn. Bhd., Malaysia. Acetone (industrial grade) and polyethylene glycol (PEG: Mw 200 Da) were

purchased from Sigma Aldrich (M) Sdn. Bhd., Malaysia. The PU resins were prepared from the rapid reaction between PKO-p and MDI in the presence of PEG as the chain extender via solution casting technique; acetone was used as a solvent in the pre-polymerization technique [6].

2.2 PU coated concrete test specimens

The concrete specimens were prepared with dimensions of 160 (L) × 40 (W) × 40 (T) mm using pre-designed moulds. In this paper, discussion of five different types of coating configurations, albeit with variations in coating thickness and location (Top and bottom faces of the test specimens) is provided. Table 1 presents the details of the coating configurations of the test specimens and their designations used in this study. In this discussion, 1 mm and 2 mm thick PU coatings were used, which are 2.5%, and 5% layer thickness compared to the thickness of the uncoated concrete specimen. PU coatings were applied on the dry surfaces of the concrete specimens and were cured for 14 days before testing (Figure 1).

Table 1: Details of the test specimens with coating configurations

Specimen designation	Thickness of PU coating (mm)	
	Top surface	Bottom surface
CON	-	-
T1	1	-
T2	2	-
B1	-	1
B2	-	2

(a) (b)

Figure 1: Bare concrete specimens (CON) (b) PU coated concrete specimen (T2)

2.3 Dynamic flexural test

Three-point bending test was conducted using Zwick 100 kN Proline Materials Testing Machine (Zwick Roell AG, Ulm, Germany), model no. Z100, according to ASTM C 78

standard. Crosshead speeds of 200 mm/min and 1 mm/min were used to obtain 0.067 s^{-1} and 0.00033 s^{-1} strain rate conditions, which corresponded to dynamic and quasi-static conditions, respectively. In the specimen designations, the two strain rates were represented with abbreviations of L and H, which denote lower strain rate and higher strain rate, respectively, that corresponded to quasi-static and dynamic conditions. Crosshead displacement was controlled using a computer with the testing software test Xpert II (Zwick Roell AG, Ulm, Germany). The test was continued until the ultimate failure of the specimens occurred. The time, load, and mid-span deflection of the testing system were obtained using the same computer program. Three specimens were tested for each case that was studied.

3 RESULTS AND DISCUSSION

The effectiveness of the proposed retrofitting technique was evaluated by focusing on strength, strain energy, deformation, and failure modes of the uncoated and PU-coated concrete specimens to different strain rate conditions. The effect of the thickness of the PU coatings on the dynamic resistance of concrete samples was investigated by testing concrete specimens with two PU layer thicknesses, which are 1 mm and 2 mm corresponding to 2.5 % and 5 % of the thickness of the concrete specimen. Coating position also plays a major role in the effectiveness of this technique. When PU layer is applied onto the impact face (load receiving face with respect to the impact), the loads and pressure would have to pass through the PU layer prior to impacting the concrete element, and a part of energy will be absorbed and dissipated through the elastic-plastic deformation of the PU before being transferred to the concrete element. Since the coating was applied on the compression side of the specimen, the stiffness of PU increases more than under tension, and subsequently increasing the amount of the energy absorbed. When the PU layer is on the rear face, the mechanism of dynamic resistance is considerably different. The loads and pressure would have to pass through the concrete element prior to PU coating, therefore part of the energy will be transferred to the PU layer. The concrete element is compressed more and thereby increasing its stiffness, and subsequently enhancing the energy absorption capacity. Subsequently, loads and pressure, which passes to the PU layer reflect off its free-face as tensile release wave, which results in a significant decrease in the PU's shear stiffness and concurrently substantial enhancement in its dissipative ability due to its viscoelasticity [15]. Therefore, the effect of PU coating position on the dynamic enhancement was evaluated by comparing the results of specimens with coatings on the top and bottom faces.

The stress-strain response of the specimens is shown in Figure 2. The mechanical response of the uncoated concrete samples is different under both quasi-static and dynamic conditions. Significantly higher stiffness and slightly higher ultimate flexural stress are shown under dynamic conditions in comparison to quasi-static conditions, with lower maximum deflection. This rate sensitive behaviour is a common occurrence for many materials where the strength values increase while strain values decrease when subjected to higher strain rate condition. The enhancement of the strength is due to two phenomena: viscous (free water) effect, cross-aggregate cracks, and structural (inertia forces and confinement) [16-17]. Past experimental investigation on PU by the authors showed that PU is a high strain-rate-sensitive elastomer, where a dramatic transition in behaviour from rubbery to leathery was observed in response to increasing strain rates [7]. These findings clearly state that the response of the coating configurations will be very different under the quasi-static and dynamic condition, and it is established with the findings shown in Figure 2.

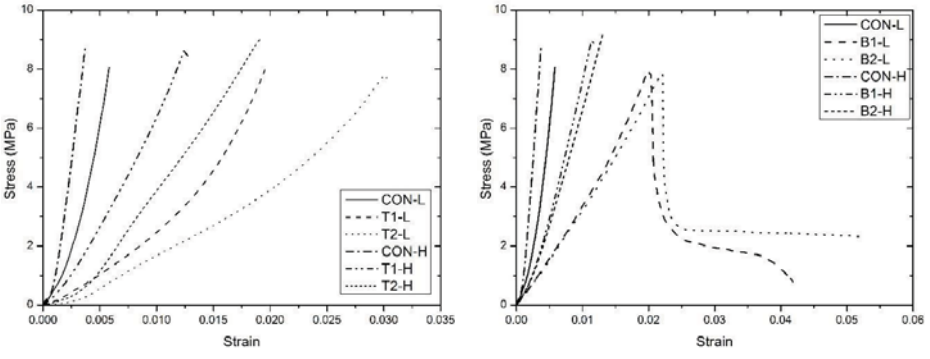

(a) (b)

Figure 2: The comparison of the stress-strain responses of the specimens (a) top coating (b) bottom coating: [T2-L, (T) coating face, (2) coating thickness, (L) strain rate condition]

As shown in Figure 2, the ductility of the PU-coated specimens increases with the coating thickness under both quasi-static and dynamic conditions. Figure 3 plots the variations in the cumulative strain energy with strain. A detailed comparison and the discussion on the ultimate flexural stress, failure strain and strain energy density are provided in the next sections.

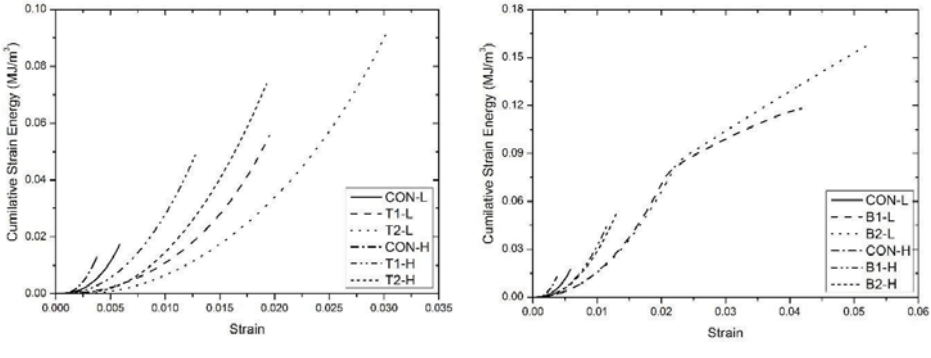

(a) (b)

Figure 3: The comparison of cumulative strain energy-strain responses of the test specimens (a) top coating (b) bottom coating: [T2-L, (T) coating face, (2) coating thickness, (L) strain rate condition]

3.1 Maximum Flexural Stress

The uncoated specimen attained its maximum flexural stress just before failure under both conditions. When the coating was applied on the impact face, the maximum flexural stress was recorded just before failure under both quasi-static and dynamic conditions. When the PU layer was applied on the rear face, under the quasi-static condition, the ultimate flexural strength of the PU-coated specimens was recorded before their ultimate failure, where the

ultimate flexural stress was attained just before the concrete specimen cracked. Though the concrete specimen cracked, the un-cracked PU layer was able to resist additional load and pressure up to a significant strain level until the PU layer cracked. However, under the dynamic condition, all specimens recorded the maximum flexural stress just before failure. Figure 4 (a) shows the plots of the average maximum flexural stress of the specimens tested. It can be observed that in all cases, the maximum flexural stress under dynamic condition was higher than those under quasi-static condition. Under the quasi-static condition, a significant difference was not observed in the maximum flexural stress when the coating thickness on any face is increased up to 5% of the thickness of the concrete specimen. However, under dynamic conditions, 4.4% stress enhancement was shown when 2 mm thick PU coating was applied on rear face, while only marginal deviation was observed when the coating thickness on the impact face was increased.

3.2 Failure Strain

The strengthened concrete specimens showed higher failure strain due to the elastomeric PU layer providing enhancement to the strain capacity of the concrete specimens due to the additional confinement effect provided by the PU matrix. Figure 4 (b) plots the comparison of the average failure strains, and it shows that the failure strains was increased remarkably with the thickness of the PU layer when the coating was applied one either side of the concrete specimen. In both cases, the lower enhancement was recorded under dynamic condition than under quasi-static condition due to the strain rate dependency of both concrete and PU. Both cases showed that the failure strain was increased with coating thickness. Under quasi-static conditions, higher strain enhancement was observed when the coating was applied on the rear face. However, strain enhancement under dynamic condition was higher with a coating on impact face than a coating on rear face.

3.3 Strain Energy Density

The strain energy was calculated by integrating the area underneath the stress-strain curve. Figure 3 plots the variation of cumulative strain energy against strain under both conditions. Meanwhile, Figure 4 (c) plots the variation of the ultimate strain energy density and, it shows clear enhancement in the strain energy density under both loading conditions. As the thickness of the PU layer increases, the strain energy density increases linearly with the PU layer thickness that is formed due to enhanced strain work. This enhancement to the strain energy density was observed under both loading conditions when the coating was applied on either side. All PU coated concrete specimens failed at higher strain energy density values, because of the enhancement in the strain capacity along with the coating thickness. This clearly shows that the presence of a PU layer on either face of the specimen improves the structural capacity and impact resistance of the concrete significantly. Similar to failure strain, strain energy density was increased with the increase in the coating thickness on either side. Under the quasi-strain condition, higher strain energy density was recorded when PU was coated on the bottom face, while under the dynamic condition, strain energy density was higher when the coating was applied on the impact face. Therefore, the application of PU coating on the impact face contributed positively in enhancing the strain energy in the coated concrete specimens under dynamic conditions. It is evident that the energy dissipation was shared between the concrete and PU coating, and the specimens were able to deflect more, which demonstrate the beneficial contribution of the PU layer in terms of energy absorption. Therefore, it can be concluded that the ductility of the concrete specimens was improved remarkably with the PU coating and subsequent increase in the PU layer thickness.

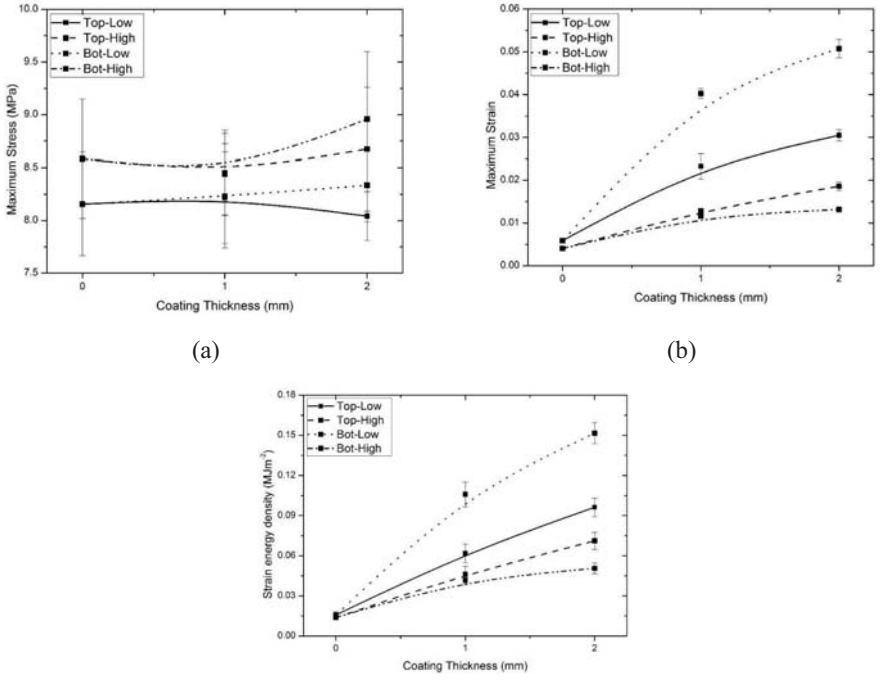

Figure 4: The comparison of flexural properties of the test specimens; (a) maximum flexural stress, (b) failure strain, and (c) strain energy density

4 CONCLUSIONS

The effectiveness of the proposed retrofitting technique was assessed, and the influence of the main parameters of PU coating, such as thickness and the location was evaluated in terms of maximum flexural stress, failure strain and strain energy density. Findings clearly showed that the dynamic resistance of the concrete specimens was increased significantly when the PU coating was applied on either side of the face with respect to loading. Specifically, failure strain and strain energy density were enhanced by factors of 2.9-4.6, and 3.0-5.1 respectively with a marginal enhancement in the maximum flexural stress under dynamic conditions compared to the dynamic response of un-coated concrete specimens. In addition, it was noted that the response of concrete specimens was improved when the thickness of the PU coating was increased and when the coating was applied on impact face rather than the rear face. No de-bonding of PU layer was observed in any of the specimens, indicating the superior bond properties between PU and concrete.

5 ACKNOWLEDGEMENT

The authors would like to express their gratitude to the Ministry of Higher Studies of Malaysia and Universiti Kebangsaan Malaysia for providing the necessary funding for this research and supporting this publication through the FRGS Grant (FRGS/1/2015/ TK01/UKM/02/1) and the UKM Top-Down Grant (TD-2016-008). Gratitude is also extended

to the Polymer Research Centre of UKM for the generous supply of palm-based polyol through the ETP-2013-026 grant.

6 REFERENCES

[1] Somarathna, H.M.C.C., Raman, S.N., Mutalib, A.A. and Badri, K.H. 'Elastomeric polymers for blast and ballistic retrofitting of structures', *Jurnal Teknologi (Sciences & Engineering)* 76 (2015) 1-13.

[2] Raman, S.N., Ngo, T. and Mendis, P. 'A review on the use of polymeric coatings for retrofitting of structural elements against blast effects,' *Electronic Journal of Structural Engineering*, 11 (2011) 69-80.

[3] Ngo, T., Mendis, P., Gupta, A. and Ramsay. J. 'Blast loading and blast effects on structures – An overview'. *Electronic Journal on Structural Engineering. Special Issue: Loading on Structures* (2007) 76-91.

[4] Malvar, L. J., Crawford, J. E. and Morrill, K. B. 'The use of composites to resist blast'. *ASCE Journal of Composites for Construction* 11(6) (2007) 601-610.

[5] Buchan, P. A., and Chen, J. F. Blast resistance of FRP composites and polymer strengthened concrete and masonry structures - A state-of-the-art review. *Composites Part B: Engineering* 38(5-6) (2007) 509-522.

[6] Somarathna, H.M.C.C., Raman, S.N. Badri, K.H., Mutalib, A.A., Mohotti, D. and Ravana, S.D. 2016. 'Quasi-static behavior of palm-based elastomeric polyurethane: for strengthening application of structures under impulsive loadings'. *Polymers* 8(5) (2016) 202, 23 pgs.

[7] Somarathna, H.M.C.C., Raman, S.N., Badri, K.H., Mutalib, A.A. 'Analysis of strain rate dependent tensile behaviour of polyurethanes'. Proceedings of 6th International Conference on Structural Engineering and Construction Management 2015, ICSECM 2015. Kandy, Sri Lanka, 11-13 December 2015. 7 pgs.

[8] Bahei-El-Din, Y. A. and Dvorak, G. J. 'Behavior of sandwich plates reinforced with polyurethane/polyurea interlayers under blast loads'. *Journal of Sandwich Structures and Materials* 9(3) (2007) 261-281

[9] Amini, M. R., Isaacs, J. and Nemat-Nasser, S. 'Investigation of effect of polyurea on response of steel plates to impulsive loads in direct pressure-pulse experiments'. *Mechanics of Materials* 42(6) (2010) 628-639.

[10] Grujicic, M., Pandurangan, B., He, T., Cheeseman, B. A., Yen, C. -F. and Randow, C. L. 2010. 'Computational investigation of impact energy absorption capability of polyurea coatings via deformation-induced glass transition'. Materials Science and Engineering: A 527(29-30) (2010) 7741-7751.

[11] Mohotti, D., Ali, M., Ngo, T., Lu, J., Mendis, P. and Ruan, D. 'Out-of-plane impact resistance of aluminium plates subjected to low velocity impact'. *Materials and Design* 50 (2013) 413-426.

[12] Mohotti, D., Ngo, T., Mendis, P. and Raman, S. N. 'Polyurea coated composite aluminium plates subjected to high velocity projectile impact'. *Materials and Design* 52 (2013) 1-16.

[13] Pztrovic, Z.S. & Ferguson, J. 1991. Polyurethane elastomers. *Progress in Polymer Science* 16(5) (1991)695-836.

[14] Badri, K.H. Chapter 20, 'Biobased Polyurethane from Palm Kernel Oil-Based Polyol'. In Polyurethane, pp. 447–470. Zafar, F., Sharmin, E. (eds.). (INTECH, Rijeka, Croatia, 2012).

[15] Raman, S. N. 'Polymeric Coatings for Enhanced Protection of Reinforced Concrete Structures from the Effects of Blast'. PhD Thesis. 308 pgs. Department of Infrastructure Engineering, The University of Melbourne, Australia, 2011.

[16] Johansson, M. Structural behaviour of concrete frame corners of civil defence shelters, non-linear Finite Element analyses and experiments. Doctoral Thesis, Department of structural engineering, Chalmers University of Technology, Goteborg, Sweden, 2000.

[17] Eibl, J. and Schmidt-Hurtienne, B. 'Strain-rate-sensitive constitutive law for concrete'. *ASCE Journal of Engineering Mechanics* 125(12) (1999) 1411-1420

Monitoring of Early-Age Characteristics of Concrete using EMI based Embedded PZT Transducers on Varying Plate Thickness

Jothi Saravanan T(1), Gopalakrishnan N(2) and Bharathi Priya C(3)

(1)Department of Civil Engineering, The University of Tokyo, Japan

(2)CSIR- Central Building Research Institute, Roorkee, India

(3)CSIR- Structural Engineering Research Centre, Chennai, India

ABSTRACT

Changes in admittance signatures measured using Electro-Mechanical Impedance (EMI) technique with a lead zirconate titanate (PZT) transducer, embedded in concrete is an indirect estimate of the localized changes in dynamic stiffness of the concrete in the proximity of the sensor. Experiments and observations on the EMI signatures obtained from PZT patches bonded onto identical plates of various thickness and embedded in concrete cubes with two sets of differential curing have been presented. Also, experiments are conducted on a concrete beam embedded with six PZT patches bonded on carrier plates of differing thickness by subjecting the beam to differential curing. Frequency shifts for these ultrasonic modes during the initial phase of four to five hours are comparatively less, but substantial damping enhancement is witnessed at this stage. The contribution of the present work is the application of serial/parallel connected sensors embedded in concrete (in a multi input single output, MISO mode), that can be typically deployed in a large scale structural health monitoring (SHM) scenario. Mandatory separation of resonant peaks in the admittance signature is a pre-requisite for tracking and observing the changes, which is achieved through plates of different thickness and hence different ultrasonic resonant (USR) modes.

Keywords: Multi-Sensing technique, serial/parallel connectivity, electro-mechanical impedance, strength gain, piezoelectric sensor, impedance based monitoring.

1 INTRODUCTION

Wave propagation based concrete early age monitoring using conventional techniques has been well established [1]. To ensure structural integrity and safety, these structures have to be equipped with tools, instruments, and techniques of structural health monitoring (SHM), which aims to develop automated systems for the continuous monitoring and damage detection of structures with minimum human involvement. SHM using Electro-Mechanical Impedance (EMI) technique is one of the cost-effective and reliable method for non-destructive evaluation (NDE) of a variety of engineering problems [2-6]. Monitoring of early age concrete and cracking in concrete structures using various embedded smart aggregates have been examined and its comparative performance is reported [7]. The motivation of this study is from the pioneering work where they have used multiplexed PZT sensors to monitor the health of aluminium plates [8,9]. They have arrived at the interference region and studied the mass influence of adjacent sensors in the composite EMI signature [10]. NDE of metallic structures is carried out using a multi-sensing EMI method [11]. Methods suggested by them, have provided good results for aluminium which is homogenous in nature. But concrete being heterogeneous, capturing the changes in the EMI signals are more challenging.

In this paper, an attempt has been made to capture the changes in the rheological properties of concrete, at various stages of setting: during fluid state, semi-solid state, and solid state, which are correlated with changes happening in the EMI signatures. An experimental study is reported on five concrete cubes embedded with PZT sensors bonded to steel plates of identical thickness and size, and the evolution of the EMI signatures with time is discussed. Due to the evolution of the concrete microstructure, the peaks which are initially evident due to the metallic resonances of the PZT and steel plate gives rise to fewer damped peaks. The curing patterns of the cubes are also differentiated and the EMI signature patterns are observed to reflect this differential curing. To further study the effects of curing pattern in a structural member of different aspect ratio a reinforced concrete beam with embedded packaged PZT is cast and differentially cured. One portion of the beam is subjected to proper curing by covering it with water-soaked jute wrappings and the other portion is left to atmospheric moisture curing. Conductance signatures from different patches are periodically acquired and statistical metrics are utilized to observe the changes, during various stages of strength development and during the curing process of the surrounding concrete. The other major contribution of the paper is in a large scale sensor deployment scenario, where it is difficult to interrogate each sensor individually and a convenient way is to electrically couple them in a series or parallel fashion such that the resulting conductance signature (termed as composite conductance) represents all the connected patches. This can be conveniently carried out, provided that the peaks from different sensors are distinguishable which is achieved by incorporating different thickness of the steel plates to which the PZT patches are bonded. The localized changes on the composite admittance signature, as captured by the individual peaks may indirectly indicate the strength development in that region or the deterioration associated with that region.

2 SERIAL/PARALLEL ELECTRICAL CONNECTIVITY OF PIEZO-ELECTRIC SENSORS

Interrogation time of feature extraction from signals of individual piezo elements can be substantially reduced by connecting them in series/parallel mode. A small group of two to three sensors can be connected and the composite signature can be acquired. In this research work, the electrical connectivity in serial/parallel mode and the mechanical de-coupling of the group of sensors by spacing them apart are carried out. As it is important to differentiate the peaks in the composite signature and attribute them to individual sensors, PZT sensors have been bonded to carrier plates of varying geometry and thickness. Both serial and parallel interfaced sensors are of multi-input single output (MISO) type, where multiple PZT patches are simultaneously excited, but a single output is obtained from the signature.

For the purpose of estimating the effect of mechanical coupling in the serial/parallel interfacing, the following methodology is adopted:

- Obtain the admittance signatures individually, for each of the piezo sensors in the cluster in a single input single output (SISO) mode.
- Obtain the admittance signature for the cluster in serial or parallel interfacing as the composite signature (i.e. MISO) mode.
- Obtain the electrically evaluated series/parallel signatures making use of the individual signatures, obtained in step-1 and through relevant expressions.
- Compare the signatures obtained in step-2 and step-3. The signatures obtained in step-3 is purely an electrical coupling while from step-2 is a combination of both electrical and mechanical coupling. The difference between these signatures is the mechanical interference coupling between the sensors, which is a function of the wavelength, frequency of excitation, wave velocity, mode of wave propagation etc.,

3 EXPERIMENTAL INVESTIGATION OF THE EVOLUTION OF EMI SIGNATURE FROM IDENTICAL SENSORS EMBEDDED IN CONCRETE CUBES

Five concrete cubes of dimensions 0.15 × 0.15 × 0.15) m have been cast with identical mix-proportions. Initially, PZT patches PIC-151 of size, (0.01 × 0.01 × 0.0003) m, are bonded onto mild steel plates of size (0.02 × 0.02 × 0.006) m using RS epoxy based resin. They are covered with the same epoxy at the top to prevent abrasion of the sensor by the flowing mix. Initial EMI signatures have been collected from PZT patch for free-free mode and immediately after patches are bonded onto the plate (Figure 1 (a)). This is referred to as the free-free conductance as the boundary conditions of the patch are unconstrained and free to move around all the edges. Then the plate-bonded PZT sensors are embedded and position-fixed in the cube mould. M40 grade concrete mix is prepared following the design mix. After the concrete is poured and surface finishing done, EMI signatures are acquired in LCR meter at every one-hour interval for the first ten hours and on days-2, signals are recorded twice a day and afterwards once in a day. This measurement process have been carried out for 28 days. The experimental setup is shown in Figure 1 (B). Two cubes with patch-1 (P1) and patch-2 (P2) are air cured and the rest of the cubes with patch-3 to patch-5 (P3, P4, and P5) have been immersed in water and cured, thus simulating two curing regimes.

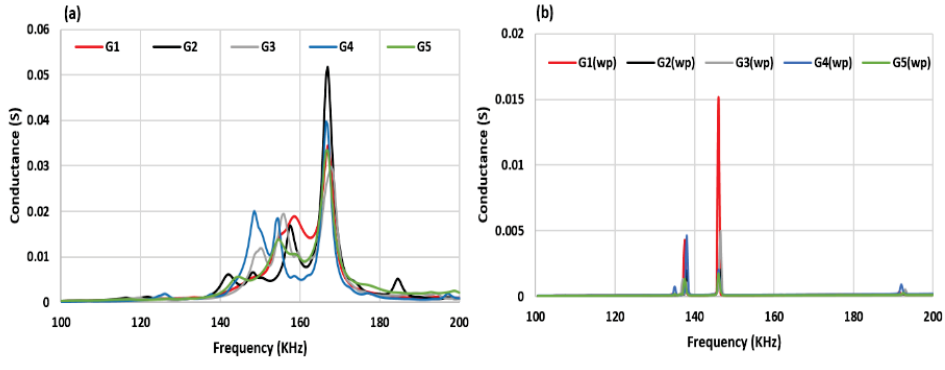

(A) EMI signatures for PZT patches : (a) free-free mode ; (b) fixed with steel plate

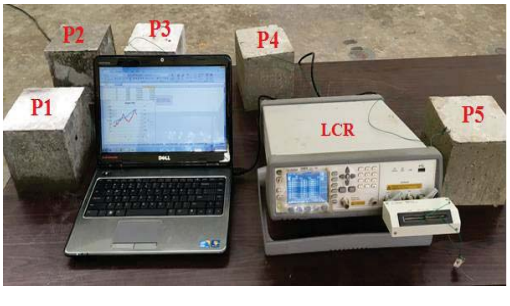

(B) PZT patch embedded in concrete cubes

Figure 1: Experimental investigation for identical sensors embedded in concrete cubes

Figure 2 (A and B) show the typical conductance signatures from day-0 to days-3, for patches 1-5 (patches 1-2 and patches 4-5 are shown for each set of curing). It can be seen that the general trend of the conductance plots are same for all the patches during the initial stages (for the first 24 hours) and slowly the trend of the conductance signatures deviate as the day's progress and the difference in curing are noticeable. The shift in the frequency of the resonant peaks is due to the addition of mass and stiffness whereas, the change in the damping results in the amplitude change. However, at levels of critical damping, the change in damping may cause a reduction in the resonant frequency. Following points could be summarized from the Figures 2 (A-B). Being pasted on identical plates (6 mm thickness), with almost constant adhesive thickness, all the five patches show a similar trend with similar resonant frequencies in the initial stages of concrete setting (at least for the first 4-5 days). The rheology change in the concrete due to transition from the fluid to the solid state causes a remarkable increase in the damping which has resulted in the amplitude reduction of the responses (Figure 2-(A)). 5th hour to 24th hour of concrete setting is accompanied by an abrupt change in the dynamic characteristics of the embedded system. As the concrete around the patches starts to solidify, it causes an increase in the mass, stiffness, and damping which has caused the peaks to undergo a frequency shift along with the reduction in the amplitude. After 24 hours of setting (Figure 2(B)) peaks observed near 150 kHz in the 4 hours signal (Figure 2(A)) tends to combine together.

From 72 hours onwards (Days-4), there is a growing noise in the system signature, either due to wave scattering or due to the appearance of many localized modes. From Days-5 onwards till Days-28, the resonant peaks in the frequency range 10 to 200 kHz, which are characteristics of the metal-bonded PZT patches, nearly vanish giving rise to a noisy trend. There is a very small change in the conductance signatures for patches embedded in uncured concrete. All the signatures are twined together for the patches in an uncured concrete cubes, whereas these are well separated and show the difference for patches in cured concrete cubes. Effect of curing slowly manifests in the signatures from the latter stages and not much in the first 72 hours (Days-3) of setting.

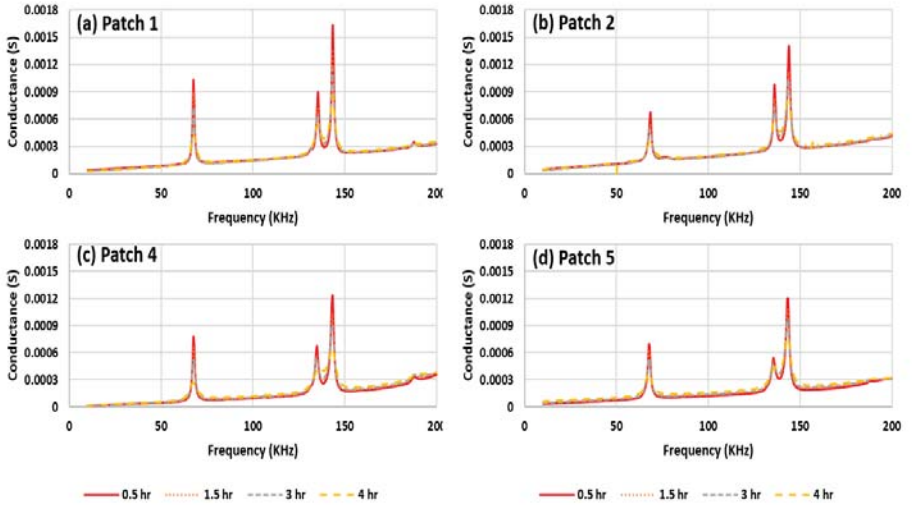

(A) First four hours of initial concreting (a-d)

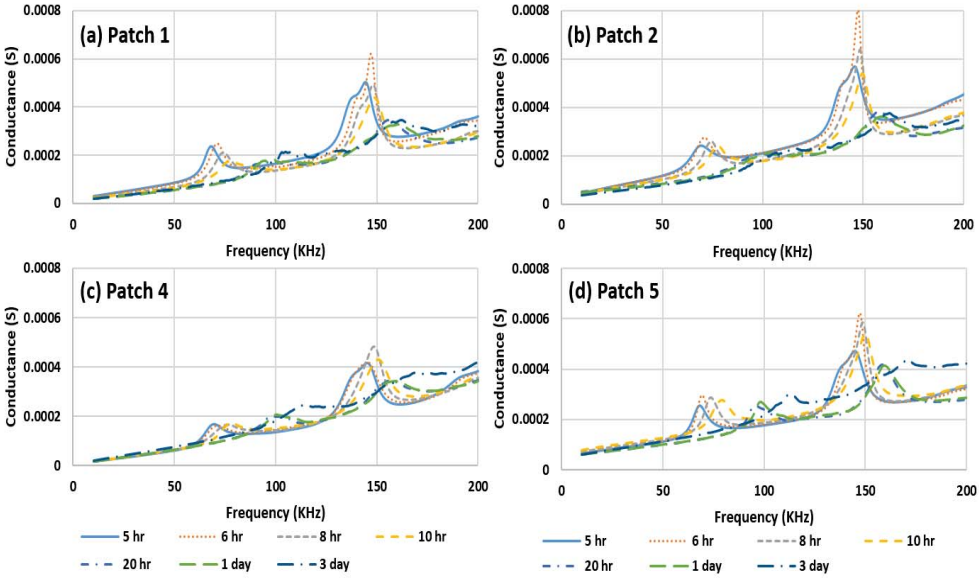

(B) 'Fifth hours to Days 3' after concreting (a-d)

Figure 2: Evolution of EMI signature from identical sensors embedded in concrete cubes for Day 0 to Days 3 (A and B)

4 EXPERIMENTAL INVESTIGATION OF THE EVOLUTION OF EMI SIGNATURE FROM VARIABLE SIZE SENSORS EMBEDDED IN CONCRETE BEAM

Unlike the experiment described earlier, where PZT patches bonded on identical steel plates are used for monitoring the setting and curing process in concrete, in this experimental investigation, PZT patches bonded on steel plates (size: 0.025 × 0.025) m of differing thicknesses are used. The significance of using the different thickness of plates assumes importance in serial and parallel connected sensors under MISO mode. This has been explained in a subsequent section. Table 1 illustrates the various thicknesses of mild steel plates measured using digital vernier calipers and Figure 3 shows the placement of steel-PZT sensors in the beam and experimental setup. The aim is to differentiate the resonant peaks in the composite signature, when multiplexed serial/parallel interfacing is used, connecting two or more sensors. Plates of higher thickness show higher modal density (number of sharp resonance peaks in a band of frequency) with less damped sharp peak proliferating the entire frequency band. This observation is very well defined in the frequency band of 100 to 300 kHz. As the thickness of the plates decreases, there are less number of these ultrasonic modes in the above-mentioned frequency band. Damping of these modes slowly increase to 100% of critical damping during the period from casting to final setting time and these peaks eventually vanish giving rise to reduced modal density with peaks of significant damping. PZT patches of nomenclature P2 to P7 are bonded to steel plates of variable thickness have been prepared and kept normal to the axis of the beam. The dimensions of the reinforced concrete beam are (0.15 × 0.10 × 1.50) m. M40 grade concrete is used and the mix design is as per suitable standards and trial mix. PZT embedded plates are set and position fixed in a

direction normal to the axis of the beam. Then the final compacted layer of concrete mix is laid. P2 to P7 are placed in a non-sequential order so that peaks due to them can be differentiated easily from each other as given in Figure 3. One-half of this beam is subjected to proper curing (P2, P5, and P3) by covering with water soaked gunny bags and the other half is left with atmospheric curing (P6, P4, and P7). Patches are placed at 0.24 m center to center with 0.15 m as edge distance. Continuous monitoring of the beam is carried out by obtaining the admittance signatures for different frequency ranges on all days, namely, pristine state, and one hour after casting and from days-2 to days-28. All the tests are conducted at room temperature.

Table. 1: Various thickness of mild steel plate

Patch	P2	P3	P4	P5	P6	P7
Thickness (mm)	1	0.75	0.9	1.5	3	6

Figure 4 (a-f) shows the conductance variation of different PZT packaged sensors. The legend 'G2_WP' stands for conductance signature obtained for 'Patch 2 with plate' condition and 'G2_1hr' stands for conductance signature obtained for 'Patch 2 with plate embedded in concrete for the first hour (1 Hr)' and it is equivalent for other patches as mentioned. The two curves correspond to the dynamic characteristics of the combined PZT and carrier plate before placing concrete and after one hour of concrete placement. Though the curves are obtained till 1 MHz, these figures show a typical variation from 100 to 300 kHz. The ultra-sonic resonances (USR) which are predominant of the carrier plates and are characterized by sharp resonances, with smaller damping values and higher modal density are seen in the curves before concrete is placed on the mould.

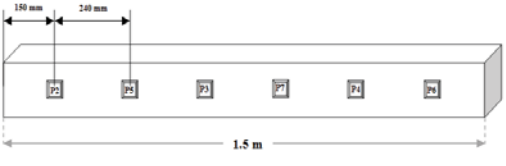

(a) Placement of PZT patch

(b) Experimental setup on concrete beam

Figure 3: PZT patches in concrete beam specimen

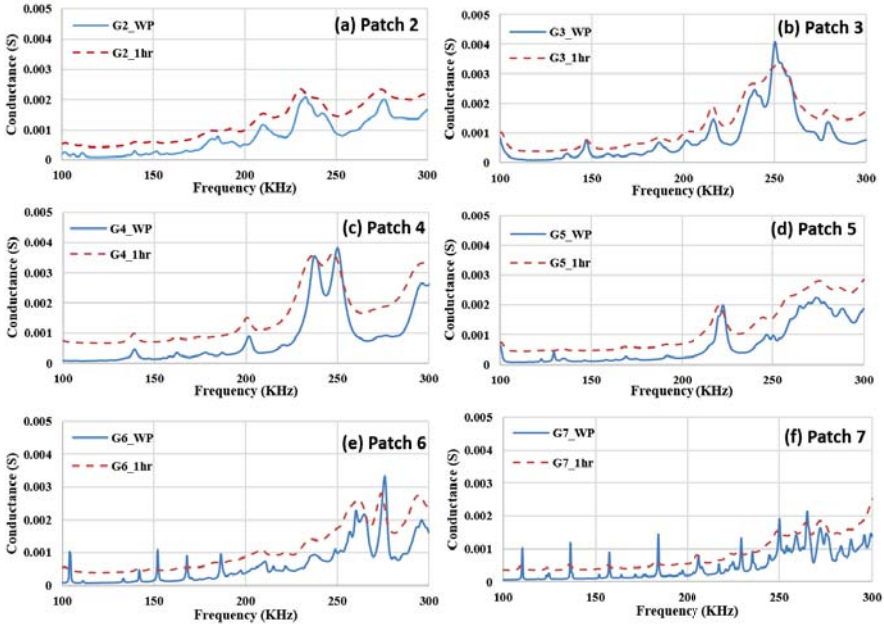

Figure 4: Conductance change for different patches of the embedded PZT sensors for pristine state and after one-hour concrete placement (Stage-1)

Although, concrete gains in strength and modulus, there is a shift in the peak frequency and mostly the results are well consistent. It can be seen that the entire behavior could be split into three different blocks of similarity namely, (1) pristine state of packaged PZT to the initial 4 to 5 hours of setting time; (2) first 4 hours to the initial three days of concrete curing; and (3) days 3 to days 28 after casting. It can be seen that these three blocks of data have large similarity and peaks, though the transition is very fast in the first two stages. Though, ideally, three stages of strength and stiffness evolution of concrete are worth studying, in the reported experimental investigation involving the concrete beam, only two stages are covered, Stage-1: Two measurements, one at the pristine stage of packaged PZT with the carrier plate and the other, after one hour of concrete casting, constitute this stage. Stage-2: It is covered between days-2 to days-28 of concrete microstructure evolution.

5 SERIAL/PARALLEL ADMITTANCE RESPONSE

During each of the measurement stage, individual responses are collected from each of the patches. After this, selected couplets and triplets of PZT patches are electrically joined together in a particular electrical connectivity and responses are taken again. Though many combinations of serial/parallel conductance responses are taken, the following couplets and triplets are shown for illustration. Figure 5 (a-d) show the combined P2-P6 responses during the pristine stage and after 1-day (2nd day) of casting. It may be seen that the serial response is a lower bound to both the individual patches and the parallel response is an upper bound to these patches. It is also seen that the peaks in the composite response come from the peaks of the individual patches. For example, the low damped, metallic ringing peaks of patch-6 (Figure 5a) are clearly distinguishable in both the serial and parallel responses. The peaks

corresponding to patch-6 in the days-2 (Figure 5c) composite response are difficult to separate out, though not entirely impossible. Figures 5 (c-d) shows the combined responses of the P2-P6 pair, from the pristine state to days-28, with both serial and parallel electrical connectivity respectively. The legends 'GS' and 'GP' stands for conductance signatures connected serially and parallel respectively.

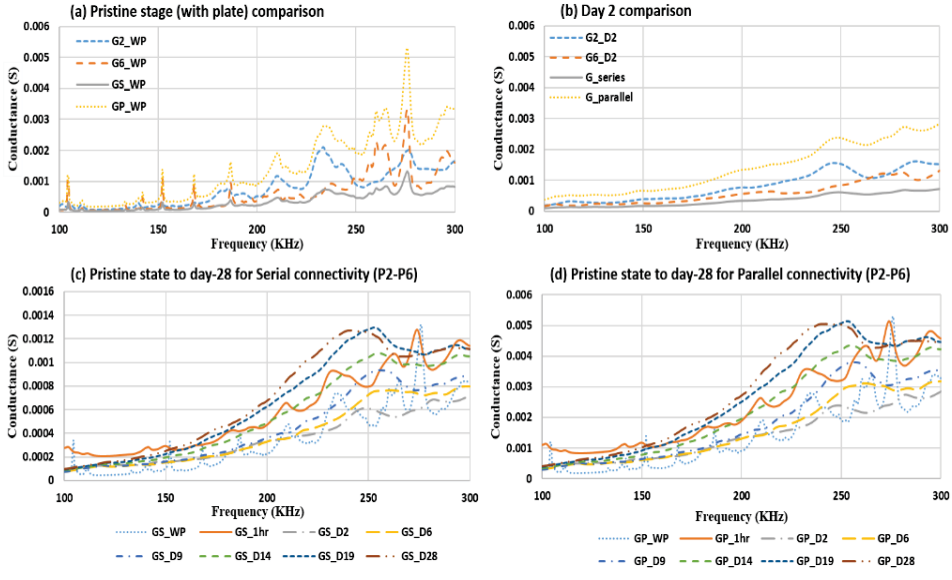

Figure 5: Composite responses of Patch 2 and Patch 6 for serial/parallel electrical connectivity

6 SIGNIFICANCE OF USING DIFFERENT THICKNESS PLATES

It is stated that using different thickness of plates is essential to distinguish the peaks due to different patches while using a series or parallel method of data acquisition. In order to understand the purpose, the conductance data of cube specimen in which all the five cubes (Figure 1) had patches attached to same thickness of plates (6 mm) and the beam specimen (Figure 2) in which the patches are attached to different plate thickness (Table 1) are considered. The patch 3 and 4 of cube specimen are normally cured and similarly the P2 and P5 of the concrete beam specimen and normally cured. For these patches of cube specimen and beam specimen, composite series and parallel responses are obtained by connecting the respective patches. From Figure 6, it can be seen that the parallel connection is an upper bound to the individual values and series is a lower bound. In the composite signature of the cube specimen (Figure 6b) where same steel plate thicknesses are used, it is difficult to clearly distinguish the peaks due to the Patch 3 and 4 as they tend to merge. Whereas, in the beam specimen where the steel plates of different sizes are used, the peaks due to the P2 and P5 can be clearly distinguished. Thus it is essential to vary the thickness of the steel plates in order to identify the performance of individual patches in a composite signature.

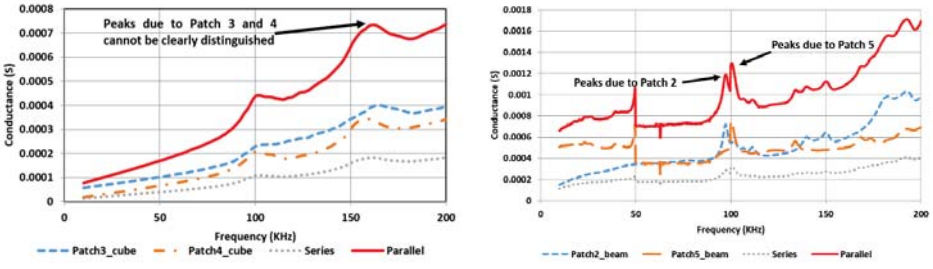

(a) Patches 3 and 4 of cube specimen having same steel plate thickness

(b) P2 and P5 of beam specimen having different steel plate thickness

Figure 6: Conductance signature for patches having identical and different steel plate thickness

7 CONCLUSIONS

The paper reports the result of two sets of experiments: (1) On concrete cubes with embedded piezo patches bonded onto identical carrier plates, where the modal peaks are identical and (2) On a concrete beam with carrier plates of varying thickness and geometry, where the modal peaks are different. Electrically coupled series or parallel conductance signature (termed as composite conductance) are obtained for RC beam experiment. Effects of differential curing on the development of conductance signature are also studied. From the study undertaken to investigate the variation of EMI signature for a packaged PZT patch on a metallic carrier, embedded in concrete, the following conclusions are drawn:

It is interesting to observe the changes in the ultrasonic modes as exhibited by the PZT patches pasted on metallic plates. Frequency shifts for these ultrasonic modes during the initial phase of four to five hours are comparatively less, but substantial damping enhancement is witnessed at this stage. Setting period from 4 to 96 hours show a dramatic shift in the right-ward direction of peaks, also associated with increased damping. A novel methodology on a serial/parallel based electrically connected multiple sensors to minimize the time of individual interrogation of EMI sensors is considered as a contribution. Multiplexed sensor arrangement for a quasi-brittle crystalline solid like concrete is attempted for the first time. Electrical inter-connectivity of selected pairs (or triplets) of PZT patches (MISO mode), may result in significant reduction of the collected and interrogated data. After obtaining the data using individual patches, serial/parallel data, with a pure electrical connectivity could be generated. For two cubes with no physical connection, mechanical coupling will be obviously absent for the sensors in these cubes. This cannot be extended when these patches are embedded in a beam. However, an essential pre-requisite is the well separated distinct peaks for each patch, around which, changes are monitored. From the reported investigation, it is much easier to distinguish the peaks at the initial setting period of concrete, as many of the metallic resonances are intact and are different from the other patches. Plates are intentionally made thicker to make these peaks clearly distinguishable. The same point, cannot be said of the latter-day curing change. Conductance signatures for the parallelly connected PZTs are upper bounds of the individual values and this result in larger amplitudes and better resolution. Serially acquired conductance signatures are the lower bound of the individual signatures. Patches, which are interconnected in serial and

parallel mode show identical trends as that of the individual patches when the changes are monitored around those peaks, which are characteristic of each patch.

8 REFERENCES

[1] Kwong, K.Z., Liew, W.Y.H. and Soh, C.K., 'Non-destructive concrete strength evaluation using smart piezoelectric transducer - a comparative study', *Smart Mat. Struct.* **25** (8) (2016) 085021.

[2] Liang, C., Sun, F.P. and Rogers, C.A., 'An impedance method for dynamic analysis of active material systems', *J. Vib. Acoust.* **116** (1) (1994) 120–128.

[3] Bhalla, S. and Soh, C.K., 'Electro-mechanical impedance modeling for adhesively bonded piezo-transducers', *J. Int. Mat. Syst. Struct.* **15** (12) (2004) 955–972.

[4] Soh, C.K. and Bhalla, S., 'Calibration of piezo-impedance transducers for strength prediction and damage assessment of concrete', *Smart Mat. Struct.* **14** (4) (2005) 671-684.

[5] Gu, H., Song, G., Dhonde, H., Mo, Y.L. and Yan, S., 'Concrete early-age strength monitoring using embedded piezoelectric transducers', *Smart Mat. Struct.* **15** (6) (2006) 1837–1845.

[6] Kong, Q., Hou, S., Ji, Q., Mo, Y.L. and Song, G., 'Very early age concrete hydration characterization monitoring using piezo-ceramic based smart aggregates', *Smart Mat. Struct.* **22** (8) (2013) 085025.

[7] Saravanan, T.J., Balamonica, K., Priya, C.B., Reddy, A.L. and Gopalakrishnan, N., 'Comparative performance of various smart aggregates during strength gain and damage states of concrete', *Smart Mat. Struct.* **24** (8) (2015) 085016.

[8] Annamdas, V.G.M. and Soh, C.K., 'Uniplexing and multiplexing of PZT transducers for structural health monitoring', *J. Int. Mat. Syst. Struct.* **19** (4) (2007) 457-467.

[9] Annamdas, V.G.M. and Soh, C.K., 'Three-dimensional electromechanical impedance model for multiple piezoelectric transducers-structure interactions', *J. Aero. Eng.* **21** (1) (2008) 35–44.

[10] Yang, Y., Liu, H. and Annamdas, V.G.M., 'Parallel and individual interrogations of piezo impedance transducers for damage detection', *Mat. Manuf. Proc.* **25** (4) (2010) 249-254.

[11] Na, S. and Lee, H.K., 'A multi-sensing electromechanical impedance method for non-destructive evaluation of metallic structures', *Smart Mat. Struct.* 22 (9) (2013) 095011.

Condition Assessment and Rehabilitation Measures for Fire Damaged Reinforced Concrete Supporting Structure of a Furnace

Bhaskar Sangoju, Ramanjaneyulu, K. A. Kanchanadevi and S. Saibabu

CSIR- Structural Engineering Research Centre, Chennai, India

ABSTRACT

This paper presents the details of condition assessment of a fire damaged reinforced concrete (RC) supporting structure of an arc furnace. The arc furnace was placed over a thick RC slab which was supported by RC columns. During the process of operation, the bottom slab portion of arc furnace steel plate got punctured locally and the liquid hot metal at about 1400˚C came out through the hole provided in the slab and spread all over the floor. The condition assessment was carried out by using non-destructive and partially destructive testing such as visual inspection, rebound hammer (RH), ultrasonic pulse velocity (UPV), concrete core and rebar sampling. Low UPV values were recorded in some of the fire affected columns, which indicate delamination of cover concrete. Compressive strength of concrete and yield strength of reinforcement steel were evaluated. Analysis was carried out to check the structural adequacy and found that the RC supporting structure is structurally adequate for the given loading and existing strength. Necessary rehabilitaion measures were suggested.

Keywords: Condition assessment, furnace supporting structure, NDT, rehabilitation

1 INTRODUCTION

When concrete is subjected to high temperatures, different physical processes and chemical reactions occur, which are highly dependent on the (i) material composition, (ii) loading and (iii) environmental conditions. The temperature rise causes temperature gradients and water migration leads to significant changes in the micro-and macro-structure of concrete [1]. Temperature attained during mild fire accidents (exceeding 300˚ C) can cause the loss of concrete strength. Number of on-site and laboratory techniques such as visual inspection, non-destructive testing (NDT) and partial destructive testing (PDT) are available for the condition assessment of reinforced concrete (RC) structures. This paper presents the details of investigation carried out for the condition assessment of fire affected arc furnace supporting RC structure, which experienced a fire accident [2]. The submerged arc furnace supporting RC structure consists of nine columns of size 600 mm × 600 mm, which support a circular RC slab of 11.06 m diameter and 1000 mm thick. The bottom steel plate of arc furnace with grid of rails was resting over the RC thick slab. M35 grade concrete was used in the construction of the supporting structure. It was reported that during the process operation the bottom steel plate of arc furnace got punctured locally and liquid hot metal at temperature of around 1400˚C came out through the hole provided in the slab for thermocouple insertion. The hot metal fallen through the hole and spread all over the floor. Fig. 1 shows photograph of fire affected submerged arc furnace supporting structure.

Figure 1: Photograph of furnace supporting structure

2 IN-SITU INVESTIGATION

The in-situ investigation work consists of (i) visual observation and documentation, (ii) rebound hammer and ultrasonic pulse velocity testing on columns and slab portions for assessing the quality and integrity of concrete, and (iii) concrete core and rebar sampling for estimating the compressive strength of concrete and yield strength of steel [3-4].

2.1 Visual Observation

All the columns were numbered for easy identification. Fig. 2 shows the plan of supporting structure with column numbers. A thorough inspection was carried out for visible defects, such as delamination, colour change, cracking, spalling of cover concrete, etc. [5]. It is observed that the bottom portion of slab and the columns (Column C5, C6, C7 and C9 (4 Nos.)) surrounding the punctured hole got severely damaged due to the flow-off of liquid hot metal. The damage was observed in the form of delamination, spalling, cracking and exposure of rebars (refer Fig. 3).

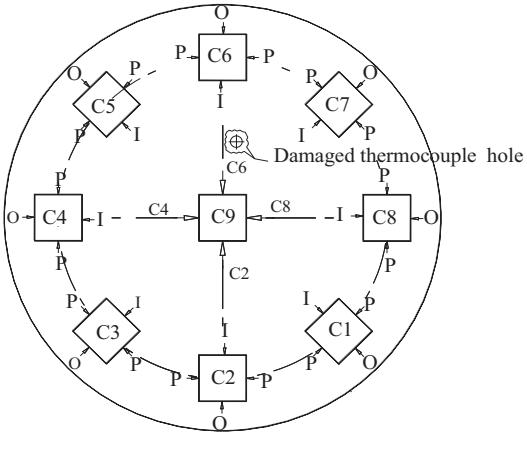

Figure 2: Plan of supporting structure with column numbers

In the severely damaged columns, nearly 75 to 100 mm thick cover concrete got damaged/affected and cracking was also noticed. Voids, honeycombing and delamination was also observed in other columns and slab portions away from the punctured hole, which could be due to poor quality of construction. Patch repair works carried out earlier on some columns were also noticed.

Figure 3: Spalling of cover concrete and exposure of rebars in the bottom of slab

2.2 Rebound Hammer (RH) test

Rebound hammer (RH) test was conducted on fire affected and unaffected columns. RH test procedure, principle, limitation and interpretation of test data is described in IS:13311 (Part-II) [6]. It should be noted that the RH values reflect the surface concrete quality. Nevertheless, the RH values provide a quick means of checking the delamination of cover concrete, uniformity of concrete and comparing a given concrete with a specified requirement. For testing, grid points were marked systematically on the columns and slab portions. Figure 4 shows the photograph of typical RH testing on a column. Table 1 presents the summary of RH data. Figures 5(a) and 5(b) present the contour plots of RH data for column 1 and column 9 (towards punctured hole). Low range of RH values in column 9 indicating loss in surface hardness of concrete due to fire damage.

Figure 4: Rebound hammer test on a typical column

Table 1: Summary of RH test data

Column No. (face)	No. of grid points	Max.	Min.	Avg.	SD.	CoV.
Column C1 (Outer)	27.0	63.0	22.3	43.4	10.8	24.8
Column C2 (Outer)	27.0	65.0	44.3	52.9	5.3	10.0
Column C3 (Outer)	26.0	61.3	22.3	48.1	8.4	17.4
Column C4 (Inner)	27.0	64.0	19.7	50.2	9.7	19.4
Column C4 (Outer)	27.0	54.7	29.0	43.2	8.3	19.3
Column C5 (Inner)	24.0	57.7	34.7	46.7	6.5	14.0
Column C5 (Outer)	21.0	54.0	29.0	46.2	6.4	13.8
Column C6 (Inner)	27.0	46.7	17.3	29.8	8.5	28.5
Column C6 (Outer)	16.0	58.3	38.3	50.0	5.3	10.6
Column C7 (Inner)	19.0	61.0	17.0	38.2	12.3	32.1
Column C7 (Outer)	24.0	63.7	24.0	43.9	11.2	25.6
Column C8 (Inner)	27.0	59.3	30.0	42.6	7.9	18.4
Column C8 (Outer)	27.0	61.3	36.0	49.5	7.1	14.4
Column C9 (C6 side)	19.0	53.7	21.7	36.2	9.1	25.2
Column C9 (C2 side)	27.0	56.3	13.0	39.9	10.0	24.9

Note: SD. Standard deviation; CoV. Coefficient of variation

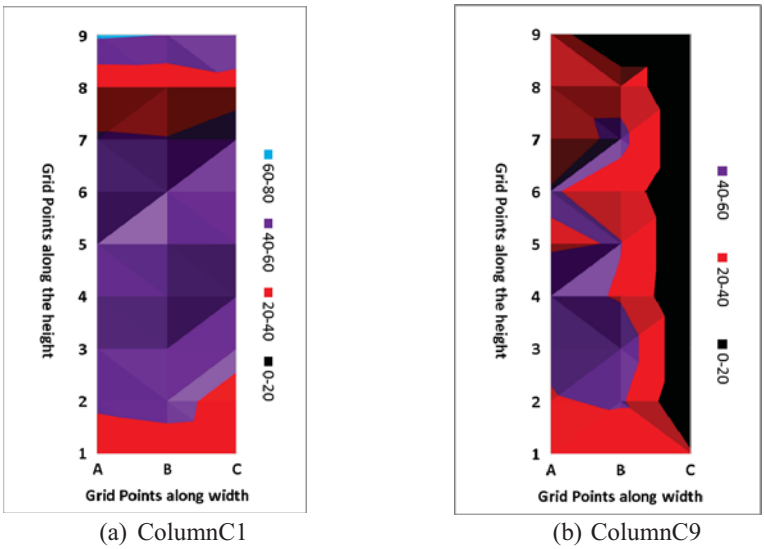

(a) ColumnC1 (b) ColumnC9

Figure 5 Contours of RH test results

2.3 Ultrasonic Pulse Velocity (UPV) Test

The UPV testing was carried out in a systematic way on the affected and unaffected columns and slab portions. The grid points were marked at every 300 mm along the height on two opposite faces and in two directions. The qualitative assessment of concrete based on UPV test results are described in IS 13311 Part I [7]. In general, any value less than 3.0 km/sec indicate either a poor quality concrete possessing excessive voids or delamination of cover concrete due to fire exposure. Tables 2 (a) and 2 (b) present the summary of UPV data of columns scanning (i) along inner and outer faces and (ii) along periphery. Figures 6 (a) and 6 (b) present the contour plots of UPV data for Column 1 and Column 9 (scanning along C8-C4). Low range of UPV values in Column 9 indicating loss in integrity of concrete due to fire damage.

Table 2 (a): Summary and statistical values of UPV data (km/sec) - Scanning along inner and outer faces

Column No.	No. of grid points	Max.	Min.	Avg.	SD.	CoV.
C1	27	4.05	1.63	3.26	0.711	21.80
C2	21	3.92	2.03	3.19	0.498	15.57
C3	24	3.95	1.85	2.97	0.725	24.42
C4	27	4.00	0.73	2.49	1.040	41.83
C5	18	4.14	0.67	2.62	1.122	42.85
C6	11	2.33	0.67	1.58	0.498	31.46
C7	15	3.37	0.80	2.05	0.682	33.23
C8	16	4.00	0.99	2.36	1.103	46.68
C9 (along C8-C4)	14	3.33	0.77	1.56	0.621	39.93

Table 2 (b):Summary and statistical values of UPV data (km/sec) - Scanning along periphery

Column No.	No. of grid points	Max.	Min.	Avg.	SD.	Cov.
C1	21	4.03	1.50	3.44	0.748	21.74
C2	27	3.92	1.54	3.35	0.565	16.84
C3	27	3.90	0.92	2.89	0.960	33.20
C4	26	4.00	0.82	3.06	0.702	22.96
C5	21	4.14	0.67	2.88	0.967	33.55
C6	21	3.95	1.15	2.00	0.655	32.71
C7	22	3.80	1.46	2.34	0.593	25.39
C8	20	4.03	1.67	3.36	0.788	23.47
C9 (along C2-C6)	11	1.80	0.82	1.49	0.349	23.36

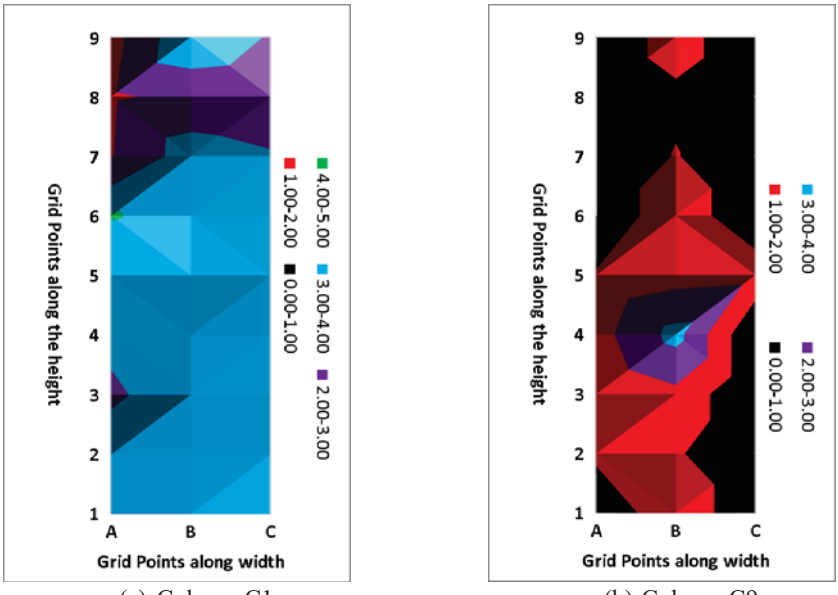

(a) Column C1 (b) Column C9

Figure 6 Contours of UPV test results

2.4 Core Sampling and Testing

Core test is a partial destructive test and is one of the best methods to assess the strength of the fire affected concrete. Core samples of 68 mm and 93 mm diameter with sufficient length were collected from the columns and slab, respectively. For petrographic examination of concrete, full length cores were collected in slab portion (1000 mm thick slab). Core samples were dressed in the laboratory using the concrete cutting machine. After dressing, the core samples are properly capped and tested in compression testing machine.

2.5 Rebar Sampling and Testing

The strength and deformability of steel are strongly influenced by temperature. Therefore, in the present study, three rebar samples were collected from the fire affected slab portions. The mechanical properties have been evaluated as per IS 1786 [8].

3 DISCUSSION OF TEST RESULTS

Based on visual observation, it was noticed that the bottom portion of slab and the columns surrounding the punctured hole got severely damaged due to the flow-off of liquid hot metal. The average RH values of most of columns are close to 40 indicating no significant difference from affected and unaffected columns. However, the inner face of fire affected columns (towards punctured hole) indicate lower RH values compared to that of the outer face. That means, the inner face towards fire was damaged more than that of outer face. In most of the fire affected columns, low UPV (average UPV is less than 3.0 km/sec) values were recorded, which indicate delamination and micro-cracking of concrete. For column C9 (central column), the UPV value is in between 1.49 and 1.56 km/sec (lowest among all), indicating severe loss of integrity due to its exposure to high temperature. Low UPV values were also recorded in the unaffected columns, which could be due to poor quality and

integrity of concrete. Around the slab periphery, direct scanning was carried out and the average UPV is 2.94 km/sec. In this portion, the low UPV was mainly due to the uneven surface of the top portion of the slab. In other portions of slab, indirect scanning was carried out. Lower UPV values were recorded in the fire affected areas indicating loss of integrity in the bottom surface region of slab.

The concrete compressive strength was evaluated in the columns and slab portions from the collected core samples [9]. The compressive strength is varying widely for (i) columns in the (a) affected area from 7.6 to 20.5 MPa (b) unaffected area from 7.5 to 18. MPa;(ii) for slab portions in the (a) affected area from 8.6 to 28.0 MPa and (b) unaffected area from 10.8 to 22.4 MPa. It is to be noted here that the compressive strength of concrete does not qualify for M35 grade in the fire affected as well as unaffected portions [2,10,11]. For the high yield strength deformed rebar samples, the yield strength obtained for one of the three samples is only 340 MPa (< 415 MPa; nearly 80% of YS = 415×0.8 = 332 MPa) and the percent elongation was about 30 (> 14.5%). Since, the compressive strength and the yield strength does not qualify the design reports, it was decided to check the structural adequacy of the supporting system for the specified load carrying capacity and existing core compressive and yield strengths [2].

4 ANALYSIS OF FURNACE SUPPORTING STRUCTURE

The supporting slab and the columns are modelled for analysis and the structural adequacy is checked for the specified loads and the available compressive strength of concrete and yield strength of steel. Analysis showed that the strength of the column is found to be adequate even for the estimated minimum core compressive strength (around 7.5 MPa) and yield strength of steel (340 MPa) to carry the factored loads coming on to the columns from the arc furnace and the slab. From the analysis, the maximum compressive stress on the column due to factored loads is found to be 6.9 MPa. This stress is lower than the estimated minimum compressive strength of core samples (i.e., 7.5 MPa) taken from columns. Hence, the strength of columns as such is adequate to carry the specified loads. However, the integrity and the quality of concrete in columns need to be improved for long term durability and hence, the same is recommended.

Also, based on the analysis results, the effective depth of slab required to carry the specified loads for the estimated minimum core compressive strength (around 8.6 MPa) and yield strength of steel (340 MPa) is 382.5 mm. However, the depth of slab provided is 1000 mm. The reinforcement required is 685 mm^2/m, which is less than the minimum reinforcement of 0.12 %. The provided reinforcement (16 mm @ 150 mm c/c) is based on the minimum reinforcement criteria. Hence, the strength of slab (of 1m thick) as such is adequate to carry the specified loads. However, the integrity and the quality of concrete in the slab need to be improved for long term durability and hence, the same is recommended.

5 REHABILITATION MEASURES

Before taking up the rehabiliation work, proper support system should be provided at the surroundings of the member to be repaired in order to relieve the stresses due to load coming over it. Typical repair procedure for columns is given below.

1. All the cover/loose (unsound) concrete shall be removed/chipped-off. The thickness of removal shall depend on the extent of damage (i.e. up to the sound concrete).
2. Clean the exposed surface by either compressed air or water jetting.
3. If the core concrete quality appears to be poor showing cracks, voids, honeycombing, etc., it shall be improved by means of epoxy grouting.

4. If snapping of the main reinforcement or ties is found, it shall be properly welded by providing additional reinforcement or replaced by a new one. Column ties shall be properly tied to the main rebars.
5. Shear connectors of 10 mm diameter 'L' shaped rods with sufficient anchorage length shall be provided by drilling and fixing into the core concrete.
6. Apply suitable epoxy bond coat to the surface of the parent concrete before applying the repair material.
7. Weld mesh of spacing 50 mm × 50 mm and 3 mm diameter shall be wrapped around the columns, tied to the original rebars and properly anchored to the concrete using U-hooks.
8. Shuttering shall be erected for columns to have a minimum cover thickness of 50mm all-round.
9. Free flowing concrete or micro-concrete shall be placed in stages of 1.5 m height. The grade of concrete shall not be less than M35. The concrete shall be properly cured after demoulding.

Similar procedure is suggested for the rehabilitation of damaged slab also. Grouting is suggested for improving the quality and integrity of concrete where voids and honeycombing is observed. Also, suggested to coat the entire exposed surface with a heat resistant protective coating.

6 CONCLUSIONS

The following conclusions can be drawn based on the field and analytical investigations:

- Visual observation indicated that the bottom portion of slab and the columns surrounding the punctured hole (Nos. C5, C6, C7 and C9) got severely damaged due to the flow-off of liquid hot metal.
- The average values of Rebound hammer test results did not show any significant difference between affected and unaffected columns. However, inner face of fire affected columns (towards punctured hole) showed lower RH values compared to that of the outer face.
- In most of the fire affected columns, low UPV values (average values less than 3 km/s) were recorded, which indicate delamination and micro-cracking of concrete. Low UPV values were also recorded in the unaffected columns, which could be due to poor quality and integrity of concrete.
- The evaluated compressive strength of concrete and yield strength of steel were lower than the specified grades. Nevertheless, the existing core compressive strength and yield strengths are adequate to carry the specified loads. However, the integrity and the quality of concrete need to be improved for long term durability and hence, the rehabilitation measures were recommended.

ACKNOWLEDGEMENTS

The CSIR-SERC team wish to acknowledge the technicians of CSIR-SERC team and the officials of M/s. Sarda Metals & Alloys Ltd., Vizianagaram for their cooperation during the field investigation.

REFERENCES

[1] Recommendation of RILEM TC 200-HTC: 'Mechanical concrete properties at high temperatures-modelling and applications', RILEM Technical committee, *Mat. and Struct.***40** (2007) 841-853.
[2] Bhaskar, S., Saibabu, S., Ramanjaneyulu, K., Prabakar, J. and Kanchana Devi, A. "Condition assessment of fire affected furnace supporting concrete structure", Report No. R&D 02-CNP6481-CR-01, (2016).
[3] Llanos, M D., Velasco, V S., and Preysler C I, Fires during nuclear power plant construction, Evaluation and repair of fire damage to concrete, SP-92, American Concrete Institute Michigan, U. S., (1986), pp. 15-23.
[4] Krampf, L. and Haksever, A., 'Possibilities of assessing the temperatures reached by concrete building elements during a fire', *Evaluation and repair of fire damage to concrete*, SP-92, ACI (American Concrete Institute), Michigan, U.S.A., (1986) 115-142.
[5] Narendra, K G, Ray, F. D. and Dilip, C. (1986), 'Evaluation and repair of fire damaged buildings', *Struct. Mag.* (2008) 18-22.
[6] IS 13311 (Part I1):1992, Indian standard Non-Destructive Testing of Concrete-Methods of Test, Part 2 Rebound Hammer, BIS, New Delhi (2004).
[7] IS 13311 (Part 1):1992 Indian standard Non-Destructive Testing of Concrete-Methods of Test, Part 1 Ultrasonic Pulse Velocity, BIS, New Delhi (2004).
[8] IS 1786:2008 "High strength deformed steel bars and wires for concrete reinforcement – Specification", BIS, New Delhi (2008).
[9] IS 516:1959 Indian standard Methods of Tests for Strength of Concrete, BIS, New Delhi (1999).
[10] IS 456:2000 (2005), Code of practice for Plain and Reinforced Concrete, BIS, New Delhi (2002).
[11] SP24-1983, Explanatory Handbook on Indian StandardCode of practice for Plain and Reinforced Concrete (IS 456:1978).

Acoustic Emission Behavior of Synthetic Fiber Reinforced Concrete under Flexure

Abdur Rasheed. M[(1)], Yuma Kawasaki[(2)], Suriya Prakash. S[(1)] and Naoki Ogawa[(3)]

[(1)]Department of civil engineering, IIT-Hyderabad, Telangana, India

[(2)]Department of civil engineering, Ritsumeikan University, Shiga, Japan

[(3)]Graduate school of science and engineering, Ritsumeikan University, Shiga, Japan

ABSTRACT

This paper presents the effect of synthetic structural fiber reinforcement on acoustic emission behavior of notched fiber reinforced concrete beams subjected to flexure. Influence of synthetic polypropylene fiber reinforcement on fracture process and acoustic activity is investigated by testing concrete beams under flexure. Different acoustic emission parameters are correlated with the crack propagation and damage accumulation. Notched beams are used to simulate and study the single crack opening characteristics. The results showed that the AE location was consistent with the actual crack development. Information from the acoustic emission signal analysis reveals that in bending, the matrix cracking produces signals with less number of hits that lie in the notched plane, whereas the post peak signals corresponds to more number of hits which tend to be scattered around the plane of notch due to the fiber pull out.

Keywords: Acoustic emission, non-destructive testing, poly propylene fibers, fracture, crack propagation

1 INTRODUCTION

The concept of fiber reinforcement in construction materials have been in use from ancient time. Historically horse hair was used as reinforcement in lime mortar and mud bricks. Usage of macro-synthetic fiber as a reinforcement in concrete has increased in the recent years due to its various advantages. The fiber reinforced concrete (FRC) thus obtained tends to have enhanced toughness, durability and impact resistance compared to that of their unreinforced counterpart. Better bonding characteristics is now possible by the virtue of surface improvement on the fiber. Lesser density, better corrosion resistance, chemical inertness etc., set these fibers apart from the steel fibers. However, their low modulus of elasticity restricts them to be used as primary reinforcement. These fibers can nevertheless be used for slab on-grade and in tunnel linings. Flexure remains the predominant loading mode in the applications of fiber reinforced concrete.

2 OBJECTIVE

There have been attempts in the past to qualitatively define the damage accumulation in concrete [1] using acoustic emission (AE) activity. Increase in the AE activity with increase in the amount of steel fiber reinforcement has been confirmed by recent studies [2]. Improvement of mechanical properties of high performance concrete by addition of synthetic

fiber reinforcement has been confirmed by various research outcomes [3,4]. Cracking due to corrosion has been detected and located [5] using AE technique. However, the crack source location in synthetic fiber reinforced concrete has not been adequately investigated in the past. This study aims at the following objectives: (i) locating crack source in synthetic fiber reinforced concrete using notched beams under flexure. (ii) validation of source location results using the defined path of crack opening through notch. (iii) differentiate between different modes of failures to understand the failure mechanism in plain and fiber concrete. Apart from the above mention objectives the study will help in laying the foundation for quantitatively assessing the damage in FRC by correlating AE parameters with crack width opening.

3 EXPERIMENTAL PROGRAM

3.1 Materials

The material ingredients used for casting concrete consisted of ordinary Portland cement, potable water, aggregates and super plasticizers (Table 1). Concrete mix proportions used for achieving a characteristic compressive strength of 40 MPa are given in Table 1. One control mixture and three different mixtures with different dosage of macro-synthetic polypropylene fibers were prepared from one batch of ingredients. Super plasticizer SP8SV Master Gelenium was used to increase the workability of freshly prepared fiber reinforced concrete. The plain concrete mix contained no fiber. Fiber reinforced concrete mixture contained macro polypropylene fiber contents equal to 6 kg/m^3. Fresh concrete properties were measured as soon as concrete was mixed. Special care was taken to attain the specified amount of air content. Any deviation from the specified amount of air content could lead to erroneous AE results.

Table 1: List of proportions(kg/m^3) in design mix

Water	Cement	Fine Aggregate	Coarse Aggregate	Fibers	Superplasticizer
170	340	715	1034	6.0	1.02

Table 2: Characteristics of the fibers

Specification	Value
Length (mm)	30
Diameter (mm)	1.2
Density (g/cm^3)	0.91
Tensile Strength (N/mm^2)	500
Tensile Modulus (kN/mm^2)	10
Aspect ratio	23
Shape	Rectangle
Surface finishing	Embossed

(a) group of fibers

(b) close-up view

Figure 1: Poly propylene macro-fiber

3.2 Test Setup

Flexural testing was conducted on notched beams using a test procedure, which was consistent with the guidelines given by EN 14651:2005. Beams of size 400 × 100 × 100 mm were tested in the three-point bending configuration. A notch of 30 mm depth was introduced at the mid-span using a circular saw as per the guidelines given in EN 14651. The flexure test was conducted in downward displacement control by LVDT operated at a rate of 0.05 mm/min. The corresponding crack mouth opening displacement of the notch was measured using two CMODs placed on the either side of the notch. Average of the two CMODs was considered in plotting the results. A photograph of the test setup is shown in Figure 2.

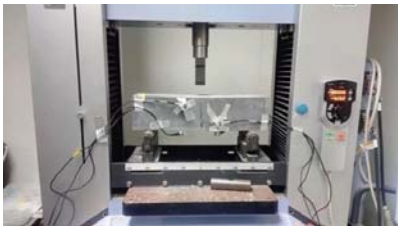

Figure 2: Three-point loading setup for notched specimen

3.3 Acoustic Emission Monitoring

During the fracture test on notched specimens, six narrow bandwidth AE sensors of resonance at 150 kHz (R15α, Physical Acoustics Corp., PAC) were attached to the beams at location defined by the coordinates given in the Table 2. Test set-up along with the AE equipment is shown in the Figure 3, while a schematic of sensor placement is depicted in Figure 4. The use of one or two sensors is typical for monitoring the AE hit rate and other major parameters in laboratory conditions where event location is not attempted. In this study, three dimensional event location is attempted. The preamplifier gain was set to 40 dB. After performing a pilot test, the threshold was also set to 40 dB in order to avoid the possibility of electronic/environmental noise. Calibration of sensors using lead-pencil break test was performed before each test to ensure that sensors have been properly bonded to the surface and signals are picked up by all the sensors. The signals were recorded in a six-channel monitoring board by PAC. AE hits (including waveforms) were recorded with a sampling rate of 5 MHz.

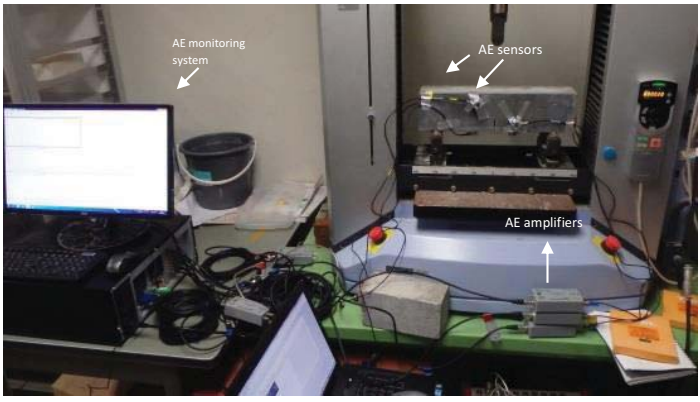

Figure 3: Setup for monitoring acoustic emission activity of notched specimen

Table 2: Co-ordinates of the AE sensors

Sensor number	X-co-ordinate(mm)	Y-coordinate(mm)	Z-coordinate(mm)
1.	160	100	30
2.	220	100	50
3.	160	0	50
4.	220	0	30
5.	160	50	100
6.	220	50	0

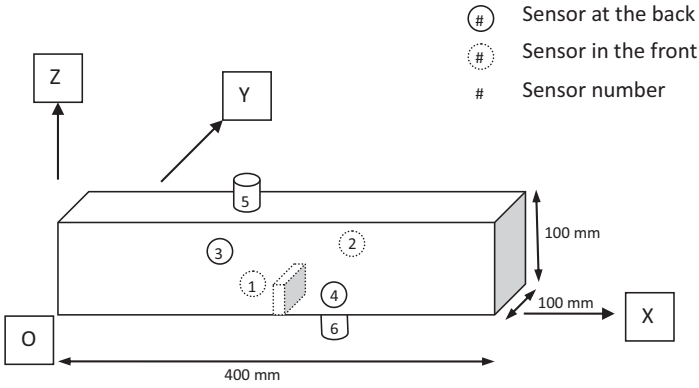

Figure 4: Schematic sketch for acoustic emission sensor placement on notched specimen

4 RESULTS AND DISCUSSION

4.1 Slump and Air content

The fresh concrete properties were measured as soon as concrete was mixed. Special care was taken to attain the specified amount of air content. Any deviation from the specified amount of air content could lead to erroneous AE results. Slump test results indicate that the workability of synthetic fiber reinforced concrete was decreased within tolerable limits. Table 3 shows that the slump decreased by 1.6 mm by addition of fiber. Addition of appropriate amount of superplasticizer causes the workability to remain largely unaffected. It is worth mentioning that it is typical to use 6 kg/m^3 of fiber reinforcement in synthetic fiber reinforced concrete.

Table 3: Properties of fresh concrete

	Slump (mm)	Air Content (%)
Plain concrete	13.8	5.5
Fiber reinforced concrete	12.2	4.9

4.2 Compressive strength and Modulus of Elasticity

The complete stress-strain response of plain concrete and fiber reinforced concrete casted is shown in figure 5 and figure 6 respectively.

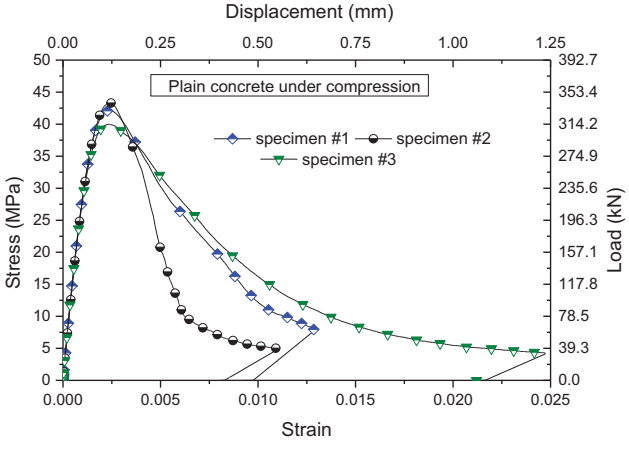

Figure 5: Stress-strain behavior of plain concrete cylinders under compression

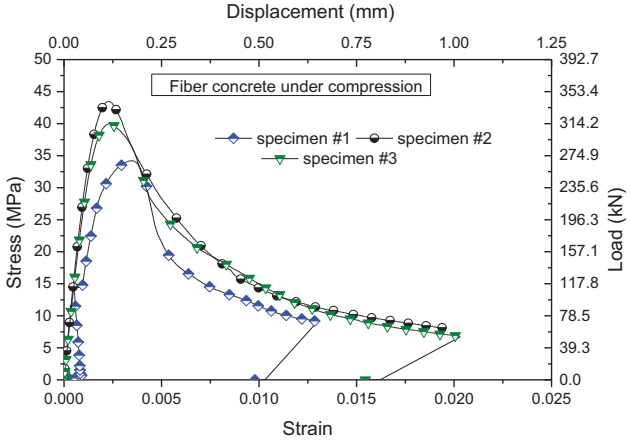

Figure 6: Stress-strain behavior of fiber concrete cylinders under compression

4.3 Flexure Test

Figure 7 and Figure 8 shows the load displacement response of notched plain concrete and fiber concrete beams respectively. Upto the cracking of concrete matrix, there is little difference between plain and fiber concrete. Soon after the cracking the plain concrete exhibits sharp decline in the load displacement response, whereas fiber reinforced concrete performs better in terms of ductility and post-peak toughness. There is clear improvement in post-peak flexural performance by incorporation of synthetic fiber. However, the focus of study is to study and correlate acoustic parameters with that of mechanical behavior rather than the improvement of mechanical performance by fiber addition.

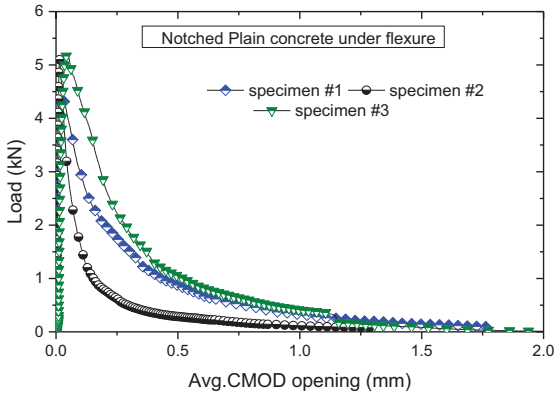

Figure 7: Load vs avg. CMOD opening of plain concrete under flexure

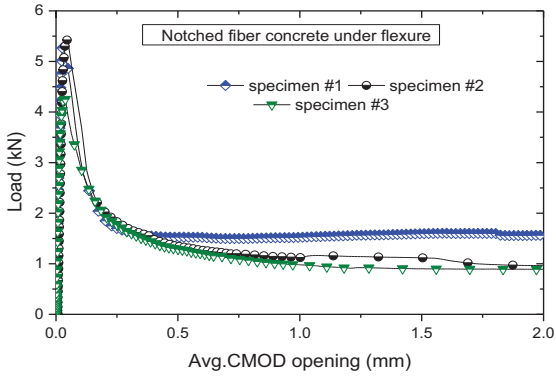

Figure 8: Load vs avg. CMOD opening of fiber concrete under flexure

4.4 Acoustic hits and Energy dissipated

Figure 9-11 shows the acoustic energy dissipated plotted against the load applied in the temporal frame. The maximum increase in the energy dissipated and the acoustic activities are recorded at the peak load. The region prior to matrix cracking records lesser number of acoustic hits and subsequently less energy is dissipated in this region. The increase in number of hits and energy in the post peak region can be attributed to the fiber pull out and breaking of fibers.

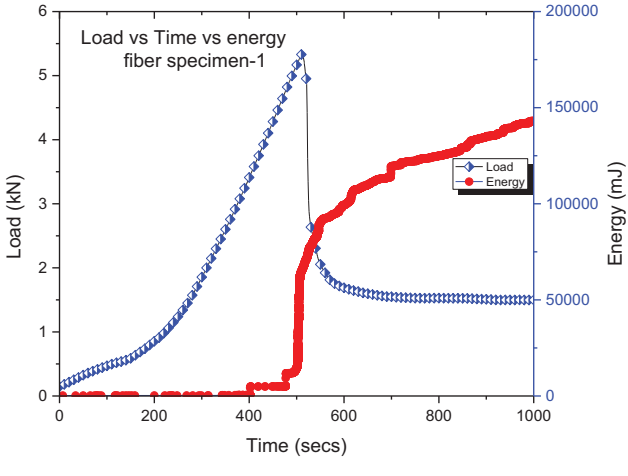

Figure 9: Load vs time vs energy of fiber concrete under flexure

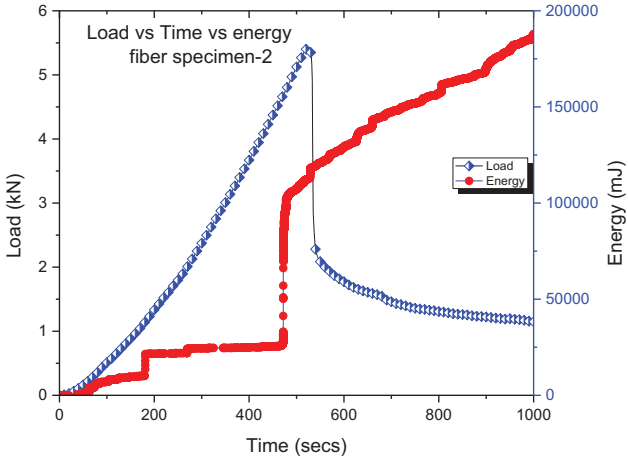

Figure 10: Load vs time vs energy of fiber concrete under flexure

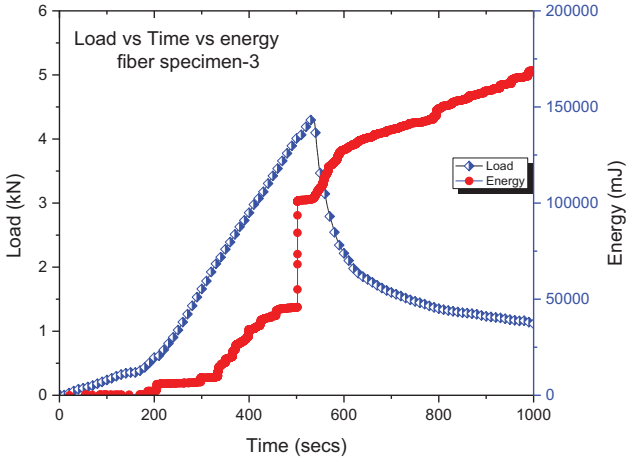

Figure 11: Load vs time vs energy of fiber concrete under flexure

5 IDENTIFICATION OF 3D-CRACK LOCATION

Identification of cracking location is of prime importance in structural health monitoring and retrofitting. This helps in rendering of proper retrofitting technique to the monitored structure. Furthermore, the mode of failure has to be properly distinguished in order to understand the global failure mechanism in the structure. Figure 12 and Figure 13 shows the crack location in three dimensional space for plain concrete and fiber reinforced concrete respectively.

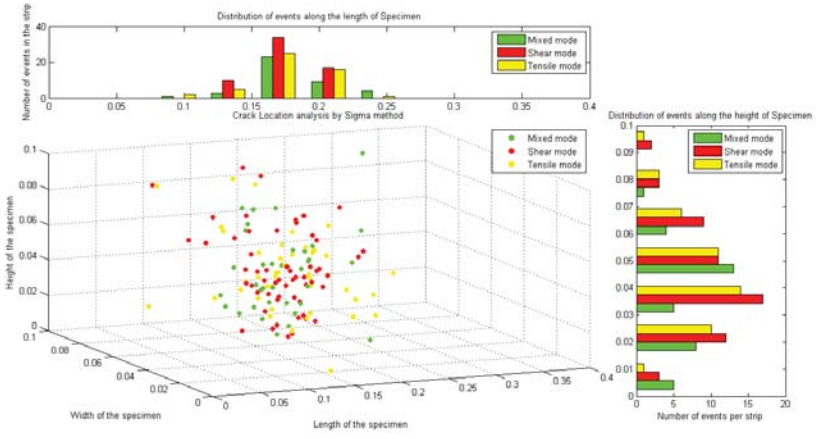

Figure 12: Hit source location of plain using AE sensors under flexure

The events that were recorded during the testing were differentiated as three modes of failure viz., shear, tensile and mixed mode. Plain concrete failure has well distributed pattern of all the modes of failure, where as fiber concrete shows a predominant shear mode of failure. This can be observed from the histograms that are plotted along side the hits.

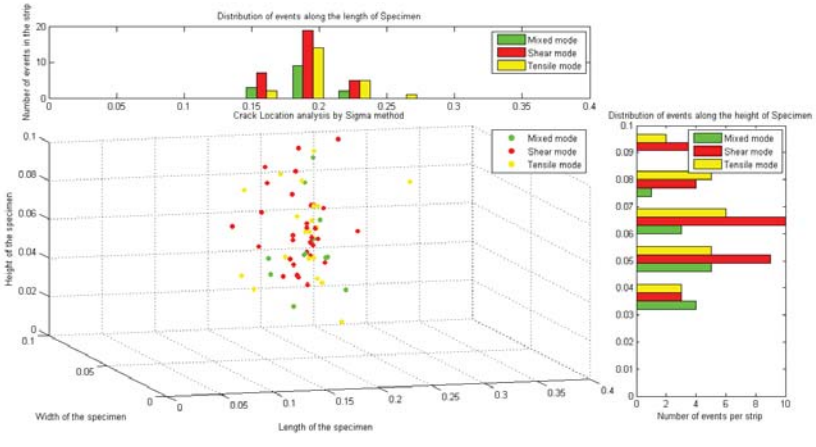

Figure 13: Hit source location of FRC using AE sensors under flexure

6 CONCLUSIONS

Notched fiber reinforced concrete beams were tested under three-point loading in flexure. Acoustic emission technique was applied to study the fracture behavior and its correlation to AE parameters. Acoustic parameters have been applied to distinguish the mode of fracture in synthetic fiber reinforced concrete. The following conclusions can be made from the limited results presented in this work:

- The study of shear ratios reveals that tensile mode of failure is predominant in the fracture process of plain concrete. Whereas, a shift towards shear mode of failure is observed for fiber reinforced concrete.

- Acoustic emission sensors were deployed in the fracture process zone. Source location analysis have been done and plotted in a three dimensional plane.
- Normal distribution of hits is observed in the horizontal plane with mean at the notch. A skewed normal distribution of hits is observed in the vertical plane

7 ACKNOWLEDGEMENTS

This work has been done as a part of joint-research collaboration between IIT-Hyderabad and Ritsumeikan University. Flexure tests were carried out in infrastructure lab at Ritsumeikan University. The help rendered by Mr. Matsumoto Akira, Mr. Sakurai Hirotaka and Mr. Abe Ryosuke is duly acknowledged here.

8 REFERENCES

[1] Ohtsu, M. and Watanabe, H. 'Quantitative damage estimation of concrete by acoustic emission', *Constr Build Mater*. **15** (2001) 217–224.

[2] Soulitoi, D., Barkoula, N.M. and Paipetis, A., 'Acoustic emission behavior of steel fibre reinforced concrete under bending', *Constr Build Mater.* **23** (2009) 3532–3536

[3] Abdur Rasheed, M. and Suriya Prakash, S. 'Mechanical behavior of sustainable hybrid-synthetic fiber reinforced cellular light weight concrete for structural applications of masonry', *Constr Build Mater.* **98** (2015) 631–640.

[4] Saumitra, J., Suriya Prakash, S. and Subramaniam, K.V.L., 'Monitoring of Concrete Cylinders With and Without Steel Fibers Under Compression Using Piezo-Ceramic Smart Aggregates', *Journal of Nondestructive Evaluation.* **4** (2016) 35-59.

[5] Kawasaki, Y., Kobarai, T. and Ohtsu, M.H., 'Kinematics of Corrosion Damage Monitored by Acoustic Emission Techniques and Based on a Phenomenological Model', *Journal of Advanced Concrete Technology*. **10** (4) (2012) 160-169.

Influence of Aggregate Modelling on Ultrasonic Wave Propagation in Concrete

Anand Kumar R[(1)], Pardeep K[(1)], Moorthi P V P[(2)], Bahurudeen A[(3)], Subair M[(4)] and Nikhil S[(3)]

[(1)]Department of Civil Engineering, National Institute of Technology Hamirpur, India

[(2)]Department of Civil Engineering, Indian Institute of Technology Bombay, India

[(3)]Department of Civil Engineering, Birla Institute of Technology and Science, Pilani, India

[(4)]Department of Mechanical Engineering, Indian Institute of Technology Madras, India

ABSTRACT

Infrastructure development is considered as a backbone for the development of any nation. Evaluation, maintenance, and repair of existing infrastructures need meticulous attention as well as substantial funds. Non-destructive techniques are extensively used for assessment of concrete structures to get accurate scientific insight on damages in less time. Ultrasonic pulse velocity test is one of the Non-destructive tests which are commonly used in the evaluation of concrete structures. A comprehensive study on modelling of ultrasonic waves, its propagation in concrete and behaviour on interfacial transition zone (ITZ) is not reported in the existing literature. As numerical models and simulation are in advance in the present computerised era, as a result, the study will act as a robust method for the design engineers to precisely simulate the UPV and compare with field assessment. In the study, concrete with different size of coarse aggregate ranging from 20 mm to 4.75 mm was modelled using ABAQUS with ITZ and voids. In addition, propagation of ultrasonic waves and resultant velocity were measured and compared with a concrete model which has only two sized coarse aggregates without interfacial transition zone. Results from the study show appropriate correlation with experimental observations.

Keywords: Ultrasonic pulse velocity, non-destructive testing, interfacial transition zone, concrete, aggregate.

1. INTRODUCTION

Non-destructive testing (NDT) of concrete structures has full-fledged from simple rebound hammer technique for surface hardness to impedance based sensor propagation technique that characterise precisely the delamination and voids present inside the concrete. Ultrasonic pulse waves that operate based on wave propagation has been utilised extensively in the construction sector for facility maintenance and assessment [1]. Experimental investigation of ultrasonic test needs support from other NDT methods to reach proper evaluation. In order to make these techniques more efficient and cost-effective, there is a need in extending it more towards virtual reality by extended modelling capacities that can achieve robustness by inhibiting potential weakness during inspection technique.

Wave propagation can be effectively modelled using numerical tools and virtual realisation can be successfully used as a means for complex domain analysis. A well-known tool that effectively models wave propagation boundary value problems is finite element method. Ample literature, that describes the utilisation of wave propagation technique for the

identification of cracks, corrosions and discontinuities in structural features especially using discrete approach for modelling [2].

Commercially available finite element codes are increasingly used for simulating wave propagation and scattering studies [3]. Although this novel technique can provide higher accuracy in prediction of defects and micro cracks, still they are underutilised in civil engineering field especially due to highly complex interfacial boundaries and interactions to be modelled which are highly under development. Considering concrete as a two layer or three layer material, a number of rationalised models with significant assumptions has been created [4-13].

One of the most rational assumptions considering concrete as a three-layered material, with mortar and aggregates as two separate layers and interfacial transition zone (ITZ) as an additional layer that establishes an interaction between mortar and aggregate layers [14,15]. Placing of these aggregates with ITZ layers inside the mortar layer based on random distribution requires certain valid assumptions such a way that the created model satisfies and reaches same as that of rationalised concrete made in practice. In order to address the validity of model as a concrete used in practice certain placing approaches have been developed such as take and place process, divide and fill method, stochastic heuristic algorithm, random particle drop method, discrete element method etc. [16-19].

Further development of this model and their analysis are subjected to different types of techniques such as finite element method, finite difference method etc. developing the models by above numerical approaches requires discretization of larger layers into finite elements for a proper spatial virtualization and for an appropriate analysis. Type of mesh and element adopted completely depends upon the type of analysis. Further, the introduction of ITZ layer requires different types of discretization approach especially for introducing micro-crack initiation, advancing front approach was used [20] and Goodman type element was also considered for modelling ITZ layer.

Several models have been created by different researchers considering the concrete as a three-layer material for different numerical analysis, nonetheless, studies utilising this mesoscale model for non-destructive evaluation by ultrasonic wave attenuation technique is limited. The aim of this paper is to emphasise the need for finite element modelling of dynamic wave propagation inside the concrete. Further, this study delineates a procedure to create a 2-D mesoscale model of concrete with ITZ layers and voids which are distributed randomly through the mortar layer based on certain conditions. Besides, the effect of the random distribution of aggregates in concrete on attenuated wave signals was investigated.

2. ANALYTICAL MODELLING IN ABAQUS

2.1 Aggregate size distribution

Grading of aggregates was completed using Fuller curve. Grading of aggregates generally refers to particle size distribution of aggregates i.e. the cumulative percentage of aggregates passing through a particular sieve. In the study, Fuller curve was used for grading the aggregates as depicted in Equation 1.

$$P(d) = (d/d_{max})^n \quad (1)$$

where $P(d)$ is a cumulative percentage of aggregates passing a sieve, d_{max} is the maximum size of the aggregate particle, n is an exponent of 0.45 - 0.70.

2.2 Aggregate building in concrete specimen

In the present study, a 2-D concrete specimen of 100 x 100 mm cross-section was considered. As concrete consists of 60 to 80% percentage of aggregates, size and shape of the aggregates highly influence on the properties of concrete in hardened as well as the fresh

state. Based on the grain size, greater than 4.75 mm is considered as a coarse aggregate. In the view of the reliable concrete model, the aggregate was modelled from 4.75 mm to the maximum size of 20 mm in different sizes. Grain shape of coarse aggregate was considered as a round for simplicity as assumed by several authors in the earlier research studies [21-23].

2.3 Random aggregate cum void generation process

Random generation of aggregates was adopted inside the mortar by random aggregate generation process. It is imperative to note that coarse aggregate total percentage was fixed at 40% and the aggregate was randomly generated. This model is a modified version of random aggregate generation process in which in addition to the aggregates, 2% voids were also generated to achieve more reliable model.

2.4 Random placement of aggregates and voids algorithm

Step 1: The coordinates were generated for the coarse aggregates from highest diameter to the lowest diameter. A random coordinate $C(x,y)$ was generated such that it makes the aggregate or voids lie within the boundary of the specimen. This can be checked to ensure confident by the condition that the coordinate value lies between the minimum C_{min} and maximum C_{max} coordinate value.

$$C_{min}(x_i,y_i) = C(0,0) + r_i + \gamma_1 \quad (2)$$

$$C_{max}(x_i,y_i) = C(l,b) - r_i - \gamma_1 \quad (3)$$

$$C_i = C_{min} + \eta(C_{max} - C_{min}) \quad (4)$$

Where C_i is a random coordinate for the i[th] particle, η is any value between 0 and 1, r is the radius of the particle, l is the length of the specimen (100 mm), b is the breadth of the specimen (100 mm), γ_1 is the minimum distance between the aggregate surface and the boundary of the specimen.

Step 2: The random coordinate for the next highest diameter particle is generated such that it doesn't overlap with the previously generated particle and also the minimum spacing between the surfaces of aggregates γ_2 is maintained.

$$\text{For } j = 1 \text{ to } n, \quad (5)$$

$$d > r_i + r_j + \gamma_2$$

$$j = j + 1$$

where d is the distance between the coordinate of i[th] particle and the coordinate of the j[th] particle, n is the total number of coordinates previously generated.

It is imperative to confirm that the newly generated particle doesn't overlap with any of the previously generated particles. If the condition is not satisfied, then Step 1 repeats for the same particle before moving to the next particle.

Step 3: Once all the aggregate coordinates are fixed, the random coordinates for voids are generated by repeating Step 1 by replacing γ_1 as γ_3 and in Step 2 by replacing γ_2 as γ_4,

where, γ_4 is the minimum distance between the surfaces of voids.

Step 4: If the algorithm is unable to generate the coordinate for the last few particles either during the placement of aggregates or voids, it represents that there is no enough space left to place the remaining particle satisfying the given condition in the current configuration. In that case, the trial can be restarted for a new configuration of particles.

Step 5: Even after a reasonable number of trials, if all the particles are unable to be placed, then the values of $\gamma_1, \gamma_2, \gamma_3$ and γ_4 are reduced and a new check is started

In order to understand the influence of voids more effectively, 2% were considered and randomly distributed. As discussed by different studies, the influence of interfacial transition zone was also taken into consideration to understand their effect on UPV.

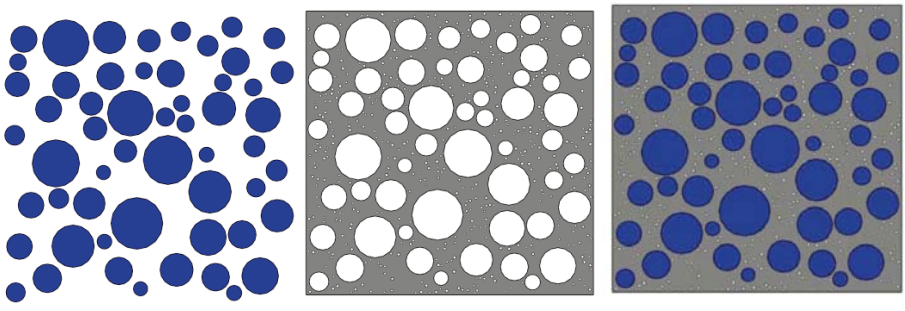

a. Aggregate b. Mortar with pores c. Concrete assembly

Figure 1: Mesoscale model of concrete

3. FINITE ELEMENT ANALYSIS

3.1 Modelling in ABAQUS/CAE

Characteristics of the media considered for the propagation of wave should be chosen in such a way that the delamination and the defects in the material can be characterised and segregated separately so that the proximity and the size of the defect can be visualised properly through analysis. Even though concrete is considered as a homogeneous medium in earlier studies, it consists of different layered arrangements [10,24]. In this study, concrete is considered as a three-layered material consisting of mortar, aggregate and ITZ layers. The significance of considering ITZ as a separate layer has been emphasised in different studies since they have a significant contribution and they are the most critical layer contributing to the micro-mechanical properties of concrete [25-26]. Subsequently, in order to understand the influence of ITZ on UPV, 2-D models were developed with ITZ layer and without ITZ layer and analysis were made separately and the influence of UPV was reported. Several studies reported the usage of ITZ in mesoscale modelling, the thickness of ITZ was reported between 10 to 20 μm experimentally [23,27]. Modelling ITZ as a micron thickness layer can result in numerical instability and difficulty in the computational process due to the need of fine meshes to define and characterise ITZ from rest of the layers. This resulted in considering ITZ layer thickness from 0.2 to 0.8 mm by different researchers [22,28-29]. The thickness of ITZ layer was taken as 0.5 mm and Young's modulus and strength of ITZ layer were taken as 75% of mortar [29]. In this study, Young's modulus, density and poison's ratio of aggregate, and mortar were taken as 70 GPa, 2500 kg/m^3, 0.2 and 25.5 GPa, 2200 kg/m^3, 0.2 correspondingly. In this study 3-noded triangle plane strain elements were considered for analysis. Figure 2 shows the ITZ considered in the model.

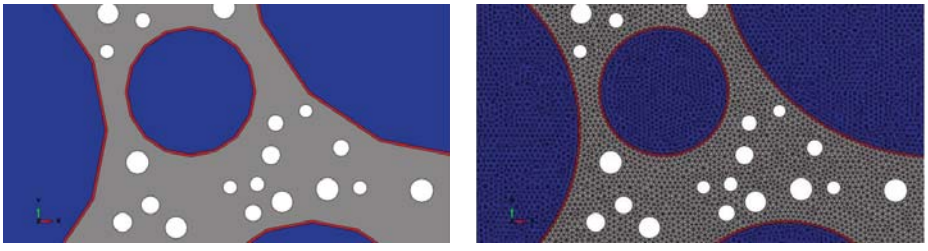

a. ITZ Layer (red colour) b. Triangular mesh of 0.2mm element size

Figure 2: Concrete model with aggregates, ITZ layer, mortar and voids

3.2 Time increment and spatial discretization: Stability analysis

For any dynamic problem considered in the finite element analysis, responses are computed in terms of step time. Each step can be divided into several increments depending upon the computational requirements. Time and space elements should be discretized properly in order to achieve numerical stability in wave propagation problem. The minimum wavelength with respect to a particular frequency need to be captured, the size of the elements should be chosen with care. In general, 10 elements per wavelength is used for more accurate modeling [30].The frequency of UPV used in this study is 150 kHz, correspondingly wavelength λ was calculated as19.65 mm, based on which the minimum size of the element was considered as 2 mm approximately. Nonetheless, the thickness of ITZ layer considered in the study was 0.5 mm consequently minimum element size of 0.5 mm was adopted in this study. Corresponding total step time was calculated as $50\mu s$ with each step increment of $0.01\ \mu s$. Since small deformations of elements are assumed, the common approximation used in wave propagation studies is that the critical time step is the transit time of the fastest wave in the smallest element. Hence the stability criterion is given by Equation 6.

$$\frac{\Delta t}{h} C_{max} \leq \frac{1}{\sqrt{2}} \quad (6)$$

where Δt denotes the time step, h the smallest element size, and C_{max} the fastest wave in the medium. For an infinite homogeneous medium, Courant condition poses necessary as well as sufficient condition for stability. In this study, time step was taken to its maximum value satisfying the stability criteria.

3.3 Wave propagation and loading

Proper history response was obtained after loading the model. Load configuration used in the study is shown. Loading was done exactly in the middle on one edge of the specimen with the receiver placed at direct opposite edge. In order to have a relatively good approximation of measurement made in the laboratory. Further, probe surface contact diameter of 22.3 mm was used during loading.

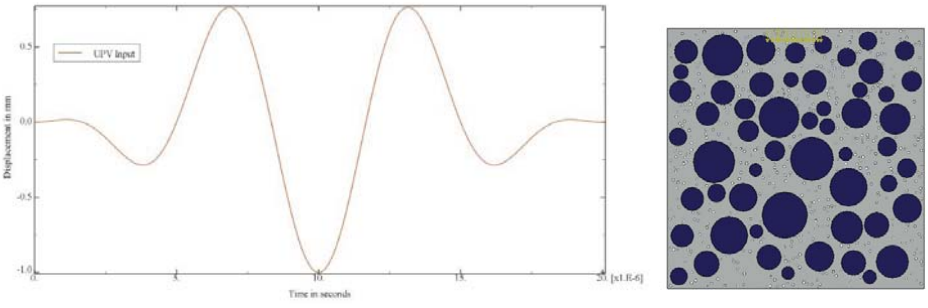

Figure 3: a) The ultrasonic pulse modelled as 3-cycle Hanning windowed tone burst with center frequency of 150 kHz, b) Position of transmitter during UPV attenuation

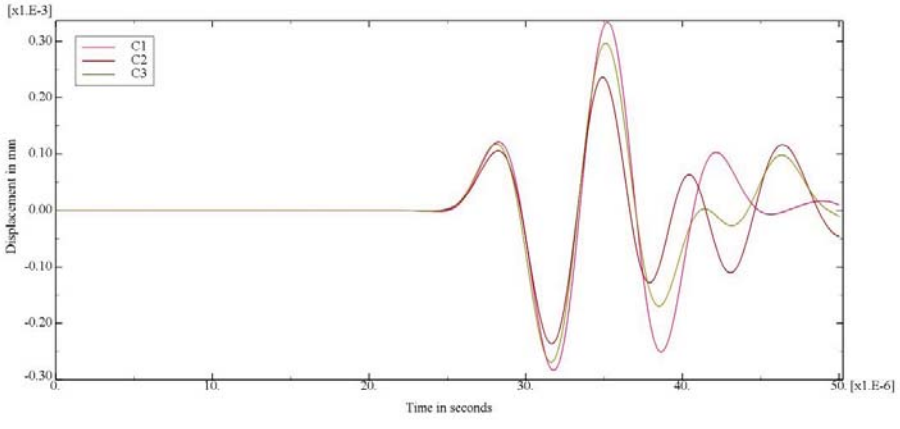

Figure 4: Displacement vs. Time curve obtained for UPV

The ultrasonic pulse is modelled by a 3-cycle Hanning windowed tone burst with center frequency 150 kHz given as a nodal force on the mid-nodes (22.3 mm) from the transmitter edge as shown. The transient Hanning windowed tone burst normally used in wave propagation simulations is given by Equation 7.

$$Y(t) = \begin{cases} \cos(2\pi ft)\left[1 - \cos\left(\left(\frac{2\pi f}{N}\right)t\right)\right], & 0 \le t \le \frac{N}{f} \\ 0, & \text{elsewhere} \end{cases} \quad (7)$$

Where f is the excitation frequency and N is the number of cycles. The transient wave used in this study is shown in Figure 3.

3.4 Experimental study

Concrete with cement content 360 kg/m^{3}was designed as per Indian standard with same aggregate proportion compared with the model. After 28 days of standard moist curing, tested for ultrasonic pulse velocity as per the procedure described in IS 13311-92. Average pulse velocity was compared with analytical observations.

4. RESULTS AND DISCUSSION

The main focus of this study is to simulate ultrasonic pulse in 2-D concrete with randomly generated aggregate throughout the mortar and voids. The developed concrete model (namely C1 as shown in Figure 5) was initially considered for UPV simulation. Figure 6 depicts the propagation of UPV in the developed 2-D model. Based on travel time and path length, the velocity of ultrasonic waves was observed as 4.82 km/sec. According to the Indian standard IS 13311 (Part-1)-1992 specified velocity criteria for concrete quality grading, it is found be excellent quality concrete.

Concrete with a similar proportion of coarse aggregate was cast and UPV test was performed as per IS 13311-92. However, in laboratory UPV testing for similar proportion concrete average velocity was found 4.1 km/sec. As per classification, it falls under good quality concrete. Although the developed models showed higher value, compared to the experimental results, the variations are found to be considerable. As the developed model considered the uniform size aggregate and other limitations are the responsible for the variation in the observation. However, it shows appropriate results compared to earlier models where concrete was modelled without ITZ and uniform aggregate distribution (only one or two sizes of aggregates were considered for coarse aggregate [31]). As mentioned earlier section, additionally, two concrete models were modelled with a different distribution of aggregates (namely C2, and C3). These models were developed for a constant percentage of aggregates as used in C1. It means coarse aggregates percentage was fixed at 40% and aggregates were generated randomly in such a way that the position of aggregates generated was made to change according to Fuller curve as described by Equation 1 to understand the effect of aggregate distribution on UPV. Therefore, totally three concrete were modelled with different configurations (C1, C2 and C3) with the same quantity of aggregate (40%) which are distributed differently in a random manner in each case as shown in Figure 5.Since the presence of aggregates and its distribution is one of the influential parameters that can manipulate UPV result in reality.

Although, a well-proportioned concrete with a different distribution of aggregates, the observed velocity from the model was 4.86 km/s and 4.88 km/s for C2 and C3 respectively. It is interesting to note the very minute variation in the observed velocities. It is because of the same quantity of coarse aggregates was considered in the developed model. Therefore, in this study position of the aggregates were varied (C1, C2, C3) for same proportion and UPV observations are almost similar. It may be due to least influence of ITZ as aggregate quantity considered as constant.

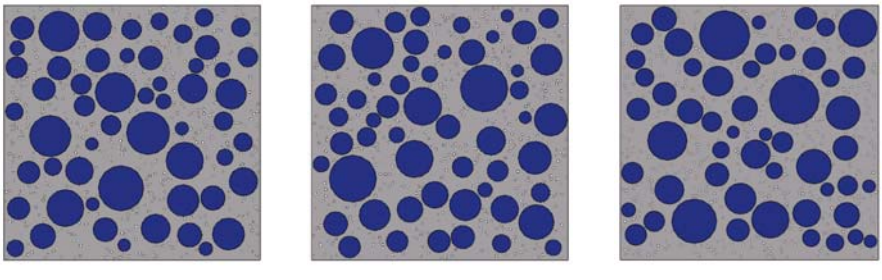

a. Configuration 1 (C1) b. Configuration 2 (C2) c. Configuration 3 (C3)

Figure 5: Three different configurations of 2-D models considered in the study

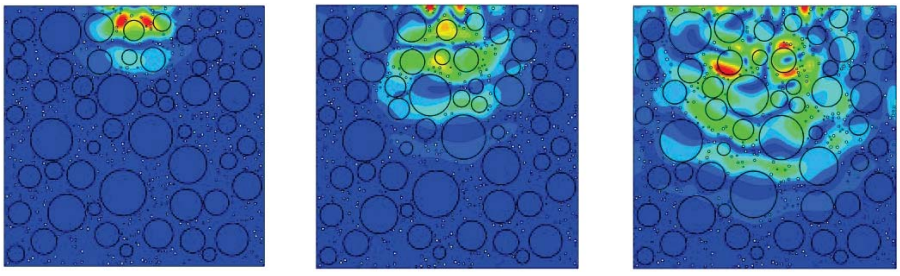

Figure 6: Propagation of ultrasonic wave in concrete

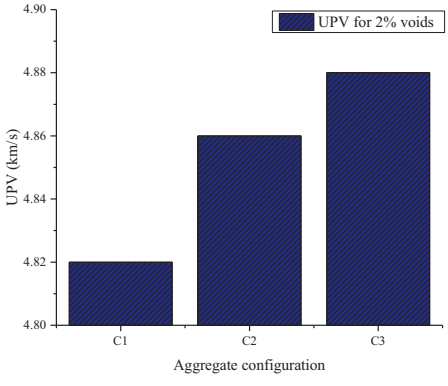

Figure 7: UPV results obtained for different aggregates configuration

Further investigation on the various quantity of aggregate in the developed model throw lights on the variation of aggregates and influence of ITZ. Moreover, abrupt changes in ITZ layer and exact thickness in the modelling properties leads to more reality wave propagation similar to experimental observations. Figure 7 depicts the results obtained from above simulation.

Comparison of the concrete model with experimental observations clearly shows that size and distribution of aggregates need to be taken care in order to obtain a proper model that can depict and consider the influence of aggregate in UPV that correspondingly illustrates the reality in actual modelling. Further, the size of the voids considered was less than the capability of capturing such small voids by analysis establishing the need of analysis using dynamic waves with varied frequency ranges. The influence of distribution and different sizes of voids and influence of different proportion and shape of aggregates on UPV in 2-D as well as in 3-D models are suggested as the future scope of this study.

5. CONCLUSION

This study is an approach towards the non-destructive evaluation of concrete by ultrasonic wave attenuation. The developed new algorithm in order to consider different size aggregates, ITZ and voids in concrete for UPV wave attenuation showed comparable observation with the quality of concrete. The effectiveness of the current model was compared with the previous model and the influence of the distribution of aggregate in the

concrete was found to be minimum. This method can be further extended in order to investigate the influence of different percentage of voids, the effect of different proportion and shape of aggregates on UPV in 2-D as well as in 3-D mesoscale models of concrete.

6 REFERENCES

[1] Benouis, A. and Grini, A., 'Estimation of concrete ' s porosity by ultrasounds', *Physics Procedia.*21 (2011) 53–58.

[2] Drozdz, M.B., 'Efficient finite element modelling of ultrasound waves in elastic media', Department of Mechanical Engineering, Imperial college of science technology and medicine, PhD Thesis (2008).

[3] Ludwig, R. and Lord, W., 'A finite-element formulation for the study of ultrasonic NDT systems', *IEEE transactions on ultrasonics, ferroelectrics and frequency control*. 35 (6) (1988) 809–820.

[4] Xu, H. and Wen, H.M., 'A computational constitutive model for concrete subjected to dynamic loadings', *International Journal of Impact Engineering.*91 (2016) 116–125.

[5] Xu, P.B., Xu, H. and Wen, H.M., '3D meso-mechanical modeling of concrete spall tests', *International Journal of Impact Engineering*. 97 (2016) 46–56.

[6] Han, D., Zhu, J., Li, L. and Pang, H., 'Verification and application of two-dimensional slice identification method in three-dimensional mesostructure under different aggregate gradations and packing algorithms', *Construction and Building Materials*. 102 (2016) 843–851.

[7] Abyaneh, S.D., Wong, H.S. and Buenfeld, N.R., 'Simulating the effect of microcracks on the diffusivity and permeability of concrete using a three-dimensional model'. *Computational Materials Science*. 119 (2016)130–143.

[8] Ma, H., Xu, W. and Li, Y., 'Random aggregate model for mesoscopic structures and mechanical analysis of fully-graded concrete', *Computers and Structures*. 177 (2016) 103–113.

[9] Wang, L., Bao, J. and Ueda, T., 'Prediction of mass transport in cracked-unsaturated concrete by mesoscale lattice model', *Ocean Engineering*. 127 (2016)144–157.

[10] Huang, Y.J., Yang, Z.J., Chen, X.W. and Liu, G.H., 'Monte Carlo simulations of meso-scale dynamic compressive behaviour of concrete based on X-ray computed tomography images', *International Journal of Impact Engineering*. 97 (2016) 102–115.

[11] Zhou, W., Tang, L., Liu, X., Ma, G. and Chen, M., 'Mesoscopic simulation of the dynamic tensile behaviour of concrete based on a rate-dependent cohesive model', *International Journal of Impact Engineering*. 95 (2016) 165–175.

[12] Zhou, X.Q. and Hao, H., 'Mesoscale modelling of concrete tensile failure mechanism at high strain rates', *Computers and Structures*. 86 (2008) 2013–2026.

[13] Liu, L., Shen, D., Chen, H. and Xu, W., 'Aggregate shape effect on the diffusivity of mortar : A 3D numerical investigation by random packing models of ellipsoidal particles and of convex polyhedral particles', *Computers and Structures*. 144 (2014)40–51.

[14] Li, B., Mao, J., Nawa, T. and Liu, Z., 'Mesoscopic chloride ion diffusion model of marine concrete subjected to freeze-thaw cycles', *Construction and Building Materials*. 125 (2016) 337–351.

[15] Shahbazi, S. and Rasoolan, I., 'Meso-scale finite element modeling of non-homogeneous three-phase concrete', *Case Studies in Construction Materials.* 6 (2017) 29-42.

[16] Bazant, Z.P., Tabbara, M.R., Kazemi, M.T. and Pijaudier-Cabot, G., 'Random particle model for fracture of aggregate fiber composites', *Journal of Engineering Mechanics.*116 (1990)1686–1705.

[17] de Schutter, G. AND Taerwe, L., 'Random particle model for concrete based on delaunay triangulation', *Materials and Structures*. 26 (1993) 67–73.

[18] Leite, J.P.B., Slowik, V. AND Mihashi, H., 'Computer simulation of fracture processes of concrete using mesolevel models of lattice structures', *Cement and Concrete Research*. 34 (2004) 1025–1033.

[19] van Meir, J.G.M., van Vliet, M.R.A. and Wang, T.K., 'Fracture mechanics in particle composites: statistical aspects in lattice type analysis', *Mechanics of Materials*. 34 (2002) 705–724.

[20] Wang, Z.M., Kwan, A.K.H. and Chan, H.C. 'Mesoscopic study of concrete I: Generation of random aggregate structure and finite element mesh', *Computers & structures*. 70 (1999) 533–544.

[21] Wriggers, P. and Moftah, S.O., 'Mesoscale models for concrete : Homogenisation and damage behaviour', *Finite Elements in Analysis and Design*. 42 (2006) 623–636.

[22] Kim, S. and Al-rub, R.K.A., 'Cement and Concrete Research Meso-scale computational modeling of the plastic-damage response of cementitious composites', *Cement and Concrete Research.*41 (2011) 339–358.

[23] Tasong, W.A., Lynsdale, C.J. and Cripps, J.C., 'Aggregate-cement paste interface Part I . Influence of aggregate geochemistry', *Cement and Concrete Research*. 29 (1999)1019–1025.
[24] Wang, X.F., Yang, Z.J., Yates, J.R., Jivkov, A.P. and Zhang, Ch., 'Monte Carlo simulations of mesoscale fracture modelling of concrete with random aggregates and pores', *Construction and Building Materials*. 75 (2015) 35–45.
[25] Nilsen, A.U. and Monterio, P.J.M., 'Concrete: A three phase material', *Cement and Concrete Research.* 23 (1993) 147-151.
[26] Scrivener, K.L. and Technik, D.B., 'The Interfacial Transition Zone (ITZ) Between Cement Paste and Aggregate in concrete', *Interface Science* 12(2004)411–421.
[27] Xiao, J., Li, W., Corr, D.J. and Shah, S.P., 'Effects of interfacial transition zones on the stress – strain behavior of modeled recycled aggregate concrete', *Cement and Concrete Research*. 52 (2013) 82–99.
[28] Zhou, X.Q. and Hao, H.,. 'Modelling of compressive behaviour of concrete-like materials at high strain rate', *International Journal of Solids and Structures.* 45 (2008) 4648–4661.
[29] Song, Z. and Lu, Y., 'Mesoscopic analysis of concrete under excessively high strain rate compression and implications on interpretation of test data', *International Journal of Impact Engineering*. 46 (2012) 41–55.
[30] Seron, F.J., Sanz, F.J., Kindelan, M. and Badal, J., 'Finite-element method for elastic wave propagation', *Communications in applied numerical methods*. 6 (1990) 359–368.
[31] Subair, M., Moorthi, P.V.P., Aniruddha, T., Sanket, R. and Bahurudeen, A. 'Influence of cement-aggregate influence on evaluation of ultrasonic pulse velocity test for rigid pavement', *International conference on transportation planning and implementation methodologies for developing countries*, IIT-B, India, December, 2016, 88-89.

Temporal Evolution of Microstructure, Chemical and Mechanical Properties of Tricalcium Silicate

Aleena Alex[(1)], Pijush Ghosh[(1)]

[(1)]Nanomechanics and Nanomaterials Laboratory, Indian Institute of Technology Madras, India

ABSTRACT

Hydration of cement clinkers, tricalcium and dicalcium Silicates (C_3S and C_2S) play a major role in determining the final strength and durability of concrete. Both these minerals contain molecules such as calcium oxide and silicon dioxide in varying proportions and contribute to the strength development. However, they differ in terms of crystal structure, hydraulic activity and mechanical properties. Hence in this work, temporal evolution of physical and mechanical properties of one of these cement clinkers (tricalcium silicate/C_3S) and its hydration products are monitored over time and quantified at nano scale. To assess the individual contributions to mechanical strength pure form of the mineral is used. Mechanical properties of the hydrating phases are determined using Nanoindentation. Scanning Electron Microscopy (SEM) is used for imaging and microstructure analysis. The chemical reactions taking place in the mix and the various product formations are tracked over time via Raman Spectroscopy. The study aims at exploring the fundamental mechanisms governing the different stages of hydration and evaluating the influence of these mechanisms in determining the final strength. This understanding is crucial in engineered cement design with enhanced properties.

Keywords: Cement clinkers, early age hydration, microstructure, tricalcium silicate (C_3S), Raman spectroscopy, SEM, Nanoindentation.

1 INTRODUCTION

Hydration of cement is a complex process which is a combination of various chemical reactions taking place simultaneously resulting in the development of unique microstructures. Often, for simplicity the hydration of cement is decoupled and the hydration of individual clinkers is investigated independently for the development of hydration models. In this study the pure triclinic form of tricalcium silicate (C_3S) is selected. There are various kinetic models describing hydration and growth. All these models attempt to explain the heat evolution curve of C_3S hydration which consists of mainly four stages namely- a) Initial wetting (first few minutes), b) induction period (first few hours), c) acceleration (1-10 days), and d) deceleration (10-28 days and continued) [1-4]. Concentric growth models are the earliest and simplest of these [5-7]. It suggests that the inner core is reduced and replaced by the hydration products. Recent studies have proposed that C-S-H needles nucleate on the grain surface and grow outward [8]. This growth is fast at the initial stages (after the induction period for the first few days) and then slows down. Once the surface is completely covered with these needles and there is no further scope of growth outward (at about 10-15 days of hydration) inner product starts to accumulate within the initial grain boundary as shown in Figure 1. This study focuses on the development of hydration product over a period of time (5 hours to 28 days) using three methods. Raman Spectroscopy to monitor the

chemical changes, SEM to track the development of microstructure, and Nanoindentation (NI) to monitor the mechanical properties.

Grid indentation techniques have been well established for ordinary portland cement (OPC) [9-13]. However they are yet to be applied for the hydrated pure clinkers. Also, most of the indentation studies have been conducted on the fully hydrated cement and partially hydrated are yet to be explored. The individual phase properties obtained from NI have then been used to develop representative volume elements (RVEs) through multi-scale modelling and estimate mechanical properties [14-17]. For a thorough understanding of the chemistry of hydration, microstructure evolution and mechanical property development, spectroscopic, imaging, and indentation techniques need to be combined. The observations from all the three techniques need to corroborate and complement each other.

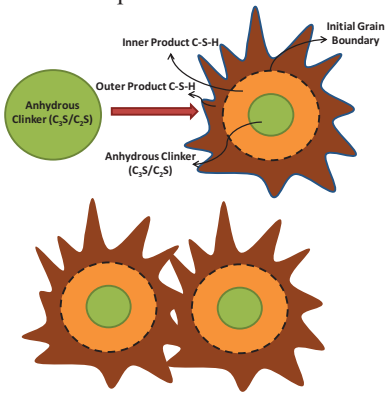

Figure 1: Schematic diagram of hydrating C_3S/C_2S grain. When two grains are close enough an interfaces formed in between which is a combination of C-S-H and pores.

2 RAMAN SPECTROSCOPY

Raman Spectroscopyhas been applied in cement science from as early as 1970's to the present day [18-22]. The most common variation namely OPC has remained elusive to the application of Raman spectroscopy due to the high amount of background signal. However, the pure form of constituent materials (Clinkers) respond to Raman scattering and their signature bands have been documented [18-22]. The major bands associated with C_3S hydration are reported in Table 1.

Table 1: Band assignments for Raman Spectra

Wavenumber (cm^{-1})	Assignment	Indicative of:
715, 1090	ν_4 (CO_3^{2-}) and ν_1 (CO_3^{2-})	$CaCO_3$
812, 843, 852, 883, 894, 903, 916	ν_1 or ν_3 (SiO_4^{2-})	C_3S
523, 539	ν_4 (SiO_4^{2-})	C_3S
600-730	Symmetric bending Si-O-Si (Q^2 and Q^3)	C-S-H

C_3S pastes were prepared by mixing the powder with deionised water at a ratio of 2:1. No special sample preparation technique was used for the specimens used for the Raman spectroscopy. The samples were stored in a sealed contained prior to testing. The chemical reaction taking place in the system can be represented as follows.

$$C_3S + H_2O \rightarrow C - S - H + Ca(OH)_2 \quad (1)$$

There is also the possibility of atmospheric carbonation resulting in the formation of $CaCO_3$.Wavelength of 1064 nm was used as the excitation signal. The results obtained are shown in Figure 2. Hydration is tracked over a period of 5 hours to 28 days. It is observed that at the end of 5 hours (end of induction period) the product C-S-H formation initiates. At the end of 2 days there is a discernible broad peak from 600-730 c^4m^{-1} which corresponds to the development of Q^2 and Q^3 [SiO_4^{2-}] in C-S-H. With the development of C-S-H over time the sharp peaks corresponding to Silicate vibrations in C_3S ranging from 812 to 916 cm^{-1}, reduces. The development of C-S-H slows down after 14 days which is consistent with the deceleration period of hydration. The major peaks corresponding to $Ca(OH)_2$ appears before 500 $cm^{-1}$and hence are not recorded in this study.

For further studies on microstructure and mechanical properties we have chosen two states of hydration-2nd and 14th day- because the distinguishable C-S-H peak is observed on 2nd day and after 14th days there is no significant change in the C-S-H peak intensity.

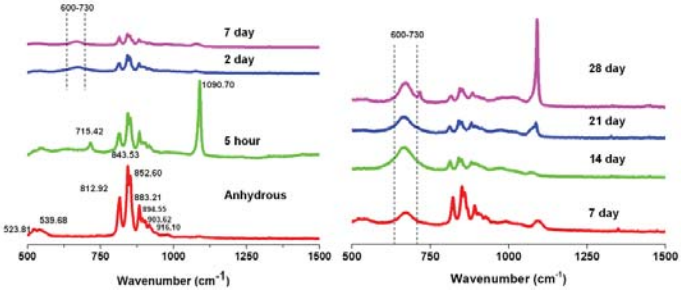

Figure 2: Hydration of C_3S monitored using Raman Spectroscopy from 5 hour to 28 days.

3 MICROSTRUCTURE ANALYSIS AND MECHANICAL PROPERTIES

The development of microstructure was captured using SEM. In order to investigate the microstructure and mechanical properties of C_3S at particular days of hydration, it should be ensured that the hydration is stopped at the desired number of days. Sample preparation is a crucial step for both these investigations. There are different techniques to stop the hydration like oven drying, solvent exchange, and vacuum or freeze drying. The merits and demerits of these techniques have been extensively researched [23]. Among the different techniques, solvent exchange using Isopropyl Alcohol (IPA) was adopted for this investigations. This is because solvent exchange causes minimal micro structural damage to the samples.

C_3S was mixed with deionised water in the ratio 2:1 and mixed thoroughly until a homogenous paste is obtained. The paste is then cast in a cylindrical mould of about 2 cm in height and 1.5 cm in diameter. The mould is properly sealed to prevent atmospheric contamination. The samples are placed in a desiccator for curing. After the samples have cured for the desired number of days, the moulds are removed and the samples are cut to thin slices of about 0.5 cm in height. They are placed in IPA for the next four days. During this period, water remaining in the pores of partially hydrated C_3S is removed and replaced with IPA, thus preventing further hydration. The IPA solution is periodically changed. At the end of four days the samples are removed and placed in a desiccator for the IPA to evaporate. These samples are then stored in sealed air-tight bags before used for further experimentation.

The samples were observed under a SEM. An anhydrous C_3S grain and the hydrating C_3S grains are shown in Figure 3. The product is seen forming as concentric needles projecting out from the underlying grain. The interface between two grains is observed as an intertwined network of these needles (Figure 4). The density of these interfaces varies with respect to the

stage of hydration. For instance, in 2nd day hydrated sample, where C-S-H formation has just initiated, the needles are typically shorter and the base of the needle can be observed in the SEM image. However for a 14 day hydrated sample the needles have grown in length and they have become dense on the surface, making it difficult to see their base. The average distance from the surface of one grain to the next interconnected grain as observed from at least 20 SEM images was 1.2 µm for the 2nd day hydrated sample and 2.2 µm for the 14th day hydrated sample.

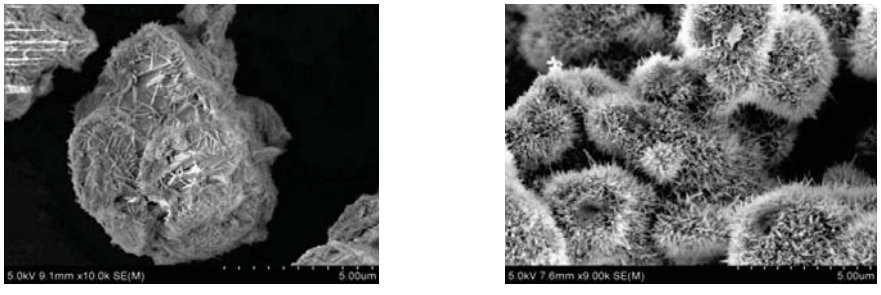

(a) (b)

Figure 3: (a) An anhydrous C_3S grain and (b) Hydrating C_3S grains

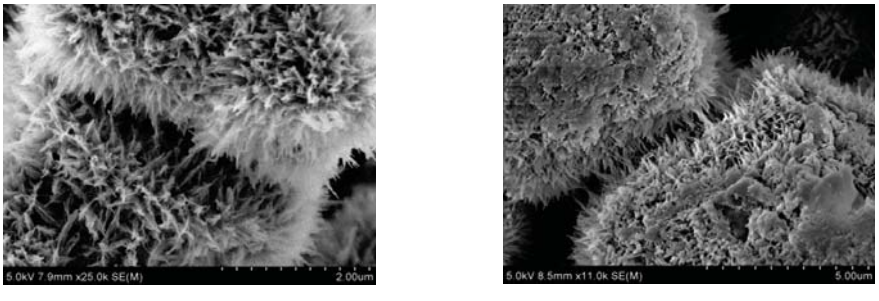

(a) (b)

Figure 4: SEM Images of (a) 2 day and (b) 14 day hydrated C_3S 2-grain Interfaces

The cut and dried sample are impregnated with epoxy and polished in two stages (Coarse polishing and Fine Polishing) before they are used for nanomechanical testing. This is because maintaining a very low roughness to indentation depth ratio is crucial for the reliability of Nanoindentation results [9]. The polished samples are indented in a 15x15 grid with each point at a distance of 10 µm apart. Reduced Modulus (E_r) is calculated from the slope of the initial part of unloading curve as.

$$E_r = \frac{1}{\beta}\frac{\sqrt{\pi}}{2}\frac{S}{\sqrt{A}} \quad (2)$$

where β is a constant specific to the geometry of the indentation tip, S=dP/dh (Stiffness) calculated from the initial portion of unloading curve and A is the projected contact area.

Hardness (*H*) is calculated as (*P/A*) where *P* is the maximum load. E_r and *H* for the two samples are plotted as a probability distribution function (PDF) in Figure 5. It can be observed that as the hydration proceeds there is a reduction in the volume of phases with higher modulus and hardness as they get converted to low density (LD) C-S-H. This is in agreement with the increasing product formation as observed from both Raman spectroscopy and SEM images.

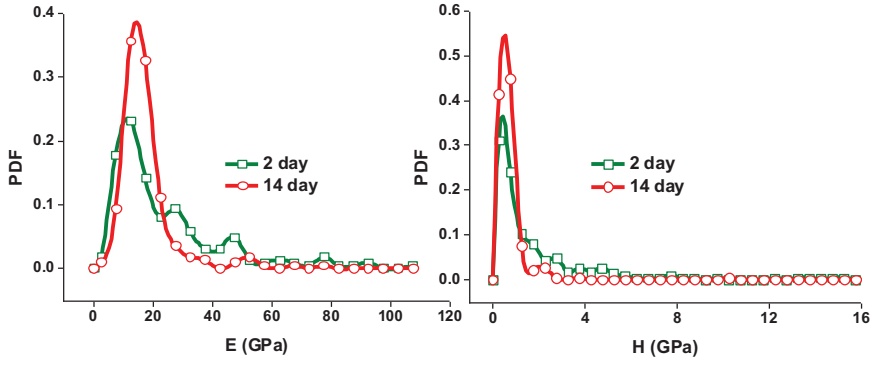

Figure 5: Reduced Modulus *(E_r)* and Hardness *(H)* of (a) 2nd day and (b) 14th day hydrated C_3S

4 CONCLUSIONS

- By stopping hydration at various stages, it is possible to track the changes in C-S-H microstructure and mechanical properties.
- From Raman spectroscopy, it is observed that C-S-H formation in C_3S paste initiates at 5 hours and a discernible peak is observed at 2nd days at 600-730 cm^{-1}. Hydration slows down after 14th days.
- C_3S-C_3S grain interfaces are observed in SEM as a network of intertwined needles which grow in length and density over the period of hydration.
- Nanomechanical testing showed a reduction in the higher density phases and formation of lower density C-S-H over a period of 2 days to 14 days of hydration.
- The observations from microstructure and mechanical properties over the period of hydration can be used for the multi scale modelling of hydrating phases.

5 ACKNOWLEDGEMENT

We thank the faculties and operators in charge of SEM facility used from the Dept. of Chemical Engineering. We also thank Ms. L. Pradipakanti Devi and Dr. Dilip K Satapathy, Dept. of Physics, IITM for their guidance with the use of Raman spectroscopy.

The authors also wish to acknowledge the support from department of science and technology (DST), India for the financial support through Project File Number SB/S3/CEE/017/2015.

6 REFERENCES

[1] Bullard, J. W., Jennings, H. M., Livingston, R. A., Nonat, A., Scherer, G. W., Schweitzer, J. S., Scrivener, K. L. and Thomas, J. J., 'Mechanisms of cement hydration',*Cem. Concr. Res.*, **41**(12) (2011) 1208–1223.

[2] Thomas, J. J., Biernacki, J. J., Bullard, J. W., Bishnoi, S., Dolado, J. S., Scherer, G. W. and Luttge, A., 'Modeling and simulation of cement hydration kinetics and microstructure development',*Cem. Concr. Res.*, **41**(12) (2011) 1257–1278.
[3] Kumar, A., Bishnoi, S. and Scrivener, K. L., 'Modelling early age hydration kinetics of alite',*Cem. Concr. Res.*, **42**(7)(2012) 903–918.
[4] Scrivener, K. L. and Nonat, A., 'Hydration of cementitious materials, present and future',*Cem. Concr. Res.***41**(7) (2011) 651–665.
[5] Kondo, R. and Ueda, S., 'Kinetics and Mechanisms of the Hydration of Cements', Proceedings of the Fifth International Symposium on the Chemistry of Cement, Tokyo, 1968, 203–248.
[6] Pommersheim, J.M. and Clifton, J.R., 'Mathematical modeling of tricalcium silicate hydration', *Cem. Concr. Res.* **9** (1979) 765–770.
[7] Pommersheim, J.M., Clifton, J.R. and Frohnsdorff, G., 'Mathematical modeling of tricalcium silicate hydration. II. Hydration sub-models and the effect of model parameters', *Cem. Concr. Res.***12** (1982) 765–772.
[8] Scrivener, K. L., Juilland, P. and Monteiro, P. J. M., 'Advances in understanding hydration of Portland cement', *Cem. Concr. Res.***78** (2015) 38–56.
[9] Constantinides, G., Ravi Chandran, K. S., Ulm, F. J. and Van Vliet, K. J., 'Grid indentation analysis of composite microstructure and mechanics: Principles and validation',*Mater. Sci. Eng. A.***430**(1-2) (2006) 189–202.
[10] Constantinides, G. and Ulm, F.-J., 'The nanogranular nature of C–S–H',*J. Mech. Phys. Solids*.**55**(1) (2007) 64–90.
[11] Ulm, F. J., Vandamme, M., Bobko, C., Alberto Ortega, J., Tai, K. and Ortiz, C., 'Statistical indentation techniques for hydrated nanocomposites: Concrete, bone, and shale',*J. Am. Ceram. Soc.***90**(9) (2007) 2677–2692.
[12] Hu, C. and Li, Z., 'A review on the mechanical properties of cement-based materials measured by nanoindentation',*Constr. Build. Mater.***90** (2015) 80–90.
[13] Mondal, P., Shah, S. P. and Marks, L., 'Short communication A reliable technique to determine the local mechanical properties at the nanoscale for cementitious materials', *Cem. Concr. Res.***37** (2007) 1440–1444.
[14] Masoero, E., Del Gado, E., Pellenq, R. J. M., Ulm, F. J. and Yip, S., 'Nanostructure and nanomechanics of cement: Polydisperse colloidal packing',*Phys. Rev. Lett.***109**(15)(2012).
[15] Masoero, E., Jennings, H. M., Ulm, F. J., Del Gado, E., Manzano, H., Pellenq, R. J. M. and Yip, S.,'Modelling cement at fundamental scales: From atoms to engineering strength and durability',*Comput. Model. Concr. Struct.*, **1** (2014) 139–148.
[16] Ioannidou, K., Kanduč, M., Li, L., Frenkel, D., Dobnikar, J. and Del Gado, E., 'The crucial effect of early-stage gelation on the mechanical properties of cement hydrates',*Nat. Commun.*, **7** (2016) 12106, 2016.
[17] Ioannidou, K., Krakowiak, K. J., Bauchy, M., Hoover, C. G., Masoero, E., Yip, S., Ulm, F.-J., Levitz, P., Pellenq, R. J.-M. and Del Gado, E., 'Mesoscale texture of cement hydrates',*Proc. Natl. Acad. Sci.***113**(8) (2016) 2029–2034.
[18] Bensted, J., *Cem. Concr. Res.***59** (1976) 140.
[19] Potgieter-Vermaak, S. S., Potgieter, J. H. and Van Grieken, R., 'The application of Raman spectrometry to investigate and characterize cement, Part I: A review',*Cem. Concr. Res.***36**(4) (2006) 656–662.
[20] Kirkpartick, R. J., Yarger, J. L., McMillan, P. F., Yu, P. and Cong, X.,'Raman spectroscopy of C-S-H, tobermorite, and jennite', *Adv. Cem. Based Mater.***5**(3-4) (1997) 93–99.
[21] Kiefer, W., Mazzolini, A. P. and Stoddart, P. R., 'Recent Advances in linear and nonlinear Raman spectroscopy I',*J. Raman Spectrosc.***38** (2007) 1538–1553.
[22] Black, L.,'Raman spectroscopy of cementitious materials',*Spectrosc. Prop. Inorg. Organomet. Compd.***40** (2009) 72–127.
[23] Zhang, J. and Scherer, G. W.,'Comparison of methods for arresting hydration of cement',*Cem. Concr. Res.***41**(10) (2011) 1024–1036.

Trainable WEKA Phase Segmentation on SEM/BSE Images of Slag Blended Cement Pastes

Natalia M. Alderete[1,2], Yury A. Villagrán Zaccardi[1,2] and De Belie Nele[1]

[1]Labo Magnel, Ghent University, Tech Lane Ghent Science Park, Campus A, Technologiepark Zwijnaarde 904, B-9052 Gent, Belgium

[2]LEMIT and CONICET, 52 entre 121 y 122 s/n, 1900 La Plata, Argentina

ABSTRACT

Scanning electron microscopy with backscattered electrons (SEM/BSE) is a powerful technique that allows the visualization of polished cross sections with good reproducibility and level of detail. It is widely used to study the microstructure of cement-based materials and identify different phases in the cement paste. However, in some cases it is difficult to distinguish between some phases due to a similar grey level, as in the case of slag and portlandite. Then, X-ray elements mapping is necessary to help in the differentiation according to composition, but it can be quite time consuming and tedious with standard detectors. A machine learning tool, trainable WEKA segmentation (TWS), can be used to train a classifier by means of pixel grey values and segment the different phases automatically without any assistance of compositional mapping, transforming the problem into a pixel classification issue. The trained models can be improved by adjusting each class. The application of the model to the images results in a segmented image that can be used for quantification. In this paper TWS is applied for segmenting SEM/BSE images without the need of elements mapping. Slag blended cement pastes at different ages are studied. Results are compared with image analysis through elements mapping and selective dissolution. From this comparison, some information regarding the image density of the portlandite is derived.

Keywords: Image analysis, trainable WEKA segmentation, phases, slag, portlandite

1 INTRODUCTION

Image segmentation is a powerful tool to separate sections of interest for image analysis. The main challenge of this technique is to obtain a reliable set of features that represent each segmented section/phase of the image. To deal with this task several approaches have been developed, as graph-based methods, region merging techniques, mapping image pixels to some feature space, etcetera. A review on image segmentation methods can be found in [1]. Particularly the waikato environment for knowledge analysis (WEKA) project aims to provide a comprehensive collection of machine learning algorithms and data processing tools to researchers and practitioners alike, and its workbench includes algorithms for image classification [2]. Trainable WEKA segmentation (TWS) is a plug-in, included in free

licensed Fiji environment that combines a collection of machine learning algorithms with a set of selected image features to produce pixel-based segmentations [3]. The image segmentation by pixel classification is based on the fact that all images are composed by pixels which are represented by a numeric value. A set of input pixels that are manually labelled into a specific class is later used as the training set for a selected classifier (algorithm that implements classification). The critical issue lies in an accurate segmentation of the images, but as TWS works interactively, adjustment of the model can be made after each training. The trained models (classifiers and clusters) can be improved by adjusting each class, as necessary, to achieve a good segmented image.

Once the classifier is trained, it can be used to classify either the rest of the input pixels or a completely new image automatically [3]. The defined model is then applied to the rest of the images, and a segmented image is one of the outputs. This machine learning tool has already been successfully used for different purposes, such as quantification of reactive oxygen species [4], prediction of solar radiation [5], monitoring the population of solitary bees [6]. Its strength relies on the ability to solve supervised and unsupervised learning problems based on a user defined number of image features.

Scanning electron microscopy with backscattered electrons (SEM/BSE) is a powerful technique that can be applied for the visualization of polished cross sections with good reproducibility and level of detail. Images from SEM/BSE are a widely used to study cement pastes [7]. One of the main reasons for this is that from SEM/BSE images it is possible to quantify, by image analysis, different constituents. However, for pastes with some supplementary cementitious materials (SCMs), additional information may be required from elemental (energy-dispersive X-ray spectroscopy) EDS mapping to achieve a reliable analysis. For the case of slag, SEM/BSE images may be combined with Mg maps to distinguish the slag from the portlandite, due to a similar grey level. Then, X-ray elements mapping is necessary to help in the differentiation according to composition, but this can be quite time consuming and tedious with standard detectors. Good resolution normally requires an image acquisition time of up to 10 h [8].

The aim of this work is to introduce a machine learning tool, TWS, to cement paste image analysis. SEM/BSE images of pastes with slag at four different hydration ages were analysed. TWS was used to segment five classes (Portlandite “CH”, slag particles “Slag”, calcium silicate hydrate “CSH”, anhydrous cement “Cement”, and pores “Pores”) by means of a training set for a selected classifier. Results were compared with two other independent techniques: selective dissolution (SD) and segmentation from EDS mapping, to validate the models. Furthermore, an estimation of the evolution of CH image density could be made considering the results from TWS and thermogravimetric analysis (TGA).

2 MATERIALS, SAMPLE PREPARATION AND SEM/BSE IMAGES ACQUISITON

Ordinary Portland cement was used to prepare the pastes with a water/binder (*w/b*) ratio of 0.4, and a 40 wt.% slag. Dry materials were first homogenized and then mixed with tap water using a laboratory mixer at 1600 rpm. Cylindrical moulds of 33 mm in diameter were used to cast the pastes and seal-cure them for 1, 7, 28, and 90 days.

From the cylinders, discs of approximately 2.5 mm in thickness were cut and kept immersed in isopropanol for 7 days to stop the hydration (with replacement at 1 and 3 days).

The discs were then kept in vacuum desiccators for 7 days to remove the isopropanol. Epoxy-impregnated paste discs were polished and coated with a 15 nm conductive carbon layer for SEM/BSE image analysis.

The SEM/BSE images were acquired at a magnification of 400x. Each image consists of 1280 x 1024 pixels which corresponds to a total area of 305 x 228 μm^2. A mean of 13 images were taken from each sample.

An EDTA extraction method was used for SD, following the guidelines provided in [9]. The consumption of portlandite was measured by TGA in accordance with the guiding principles described in [10].

3 DEVELOPING A MACHINE LEARNING TOOL FOR SEM/BSE IMAGES

3.1 Model generation

As mentioned before, for the model generation TWS uses machine learning algorithms and image features to produce segmentations. Descriptions and possible settings of each step can be found in [11]. In this work, to allow phase identification, it was decided to distinguish among five classes: CH, Slag, CSH, Cement and Pores. Some traces were input to each class to characterize them and then normally the classifier could be trained for all images. However, since grey levels for the same class were different from age to age, if a single classifier model were created for all ages, the trained classifier would account different features at different ages. To ensure reliability in the results, images were divided in groups corresponding to each age (1d, 7d, 28d, and 90d). Then, one image of each group was used to build up the corresponding model and train the corresponding classifiers.

After each model was created, images from the corresponding group were segmented into classified images. Furthermore, based on the applied model, the probability that each pixel belongs to each class can be displayed on a 32-bit hyperstack. Then, probability maps in grey scale for each class are obtained with values between 1-white (100% chance the pixel belongs to that class) and 0-black (0% chance the pixel belongs to that class). These probability maps are particularly important since they give the user the freedom to define the level of confidence desired for each data set. They also show graphically the probability distribution of each class. Additionally, it is possible to generate a receiver operating characteristic (ROC) graph, which allows the visualization, organization and selection of classifiers based on their performance [10]. A scheme of the described steps for the model generation, application and evaluation is shown in Figure 1.

3.2 Relative area amount for the different classes

As mentioned before, TWS provides the probability of each pixel to correspond to a particular class. Then the amount of pixels that belong to each class can be quantified by means of a histogram with a certain probability level. It is important to mention that a particular pixel could have high probabilities of belonging to more than one class simultaneously, depending of the outcome of the classifier. Consequently, the sum of the areas for all phases may not correspond to the total amount of pixels. The relative amount of pixels belonging to each group reflects the relative area of each phase. In principle, a 75% of probability of each pixel belonging to a particular class was chosen as an acceptable limit. Choosing a higher value than 75% can lead to disregard a sensitive amount of information; on

the other hand, choosing a lower value would lead to a higher value of uncertainty. However, it should be noticed that when selecting the 75% level of probability, certain features with low probability of belonging to any class are left out of the counting. This leads to slight underestimations of constituents since not all pixels are considered.

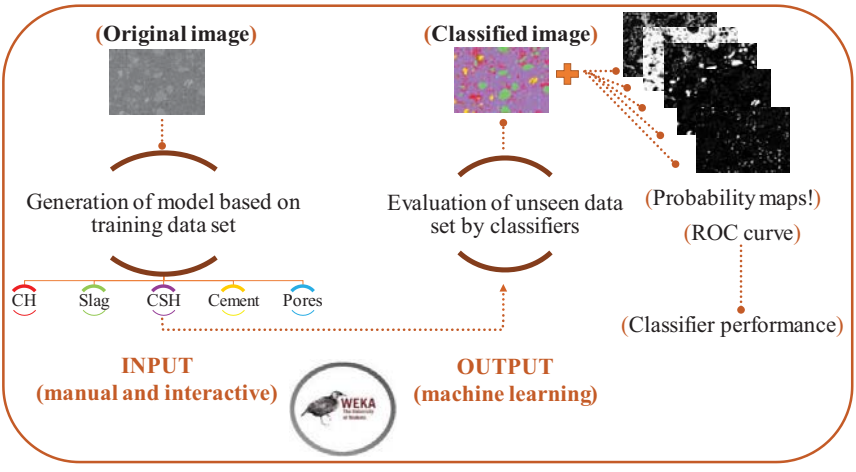

Figure 1: Scheme of steps for the model generation, application and evaluation

One way to address the underestimation issue is to increase the amount of pixels considered for the quantification, including pixels with 70% or 60% probability of belonging to a particular class, although in this case some features may be counted in erroneous classes and precision would certainly decrease. Another method could be to scale the number of pixels per class to sum the total amount of pixels in the image, i.e., transform results to their equivalent 100%. Although, this would imply the assumption that all classes increase linearly with the increase in probability, which may not be the case. For cement paste SEM/BSE images, some phases are certainly more homogeneous than others and therefore they are harder to be accounted for when having a more spread probability distribution.

The distribution of probability of each class was considered to determine which classes have the highest precision (and can be considered with 95% of probability) and which classes should be considered at 75% to include the most of the information possible. Figure 2 shows the probability distribution of each class for a classified image at 1 day of hydration. It was observed that Cement, Pores and CH are the classes with the highest precision, although CH is less precise than slag in relative terms. Arrows ‘a’ and ‘b’ point to the curves from CSH and Slag, which still comprise pixels below 95%. Then, for those two classes, the relative amount obtained at 75% was transformed into the equivalent 100%, to account for the not included data. For the other classes, the precision of each class was enough to consider the pixels at 95% of probability.

This approach shows that the level of probability has to be decided on a probability distribution basis. A high level of probability may be chosen (95% for example) for all classes if none of them has a marked curve after that level. If a verification of such curves is not made, important data could be left out of the quantifications.

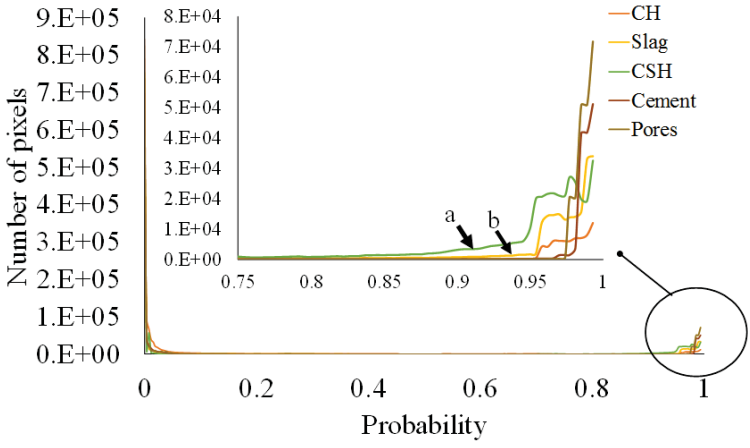

Figure 2: Probability distribution of each class

Figure 3 shows the results of the four models (1d, 7d, 28d, and 90d) quantified as relative amount of area for each class, considering the corrections mentioned above. Variation of phases with time show the progress in the reaction of the slag used.

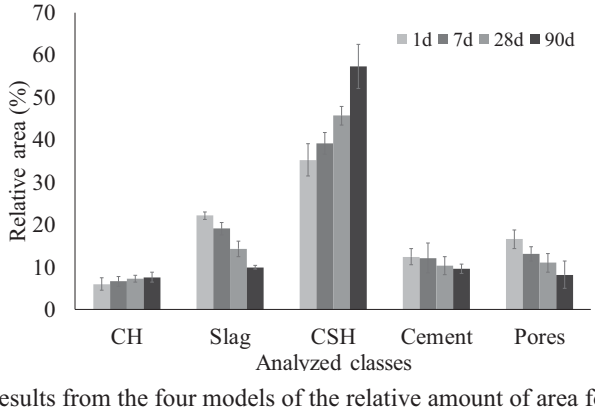

Figure 3: Results from the four models of the relative amount of area for each class

4 COMPARISONS WITH OTHER EXPERIMENTAL TECHNIQUES AND DISCUSSIONS

4.1 Quantification of slag by TWS compared with selective dissolution and SEM mapping results

In order to validate the results from the segmentation, comparisons were made of the quantified amounts of slag with other techniques. Figure 4 shows the correlations between the

amount of unreacted slag quantified by selective dissolution (in blue squares) and the amount quantified by SEM images based on EDS full element maps (red circles) compared with TWS results. A good correlation is observed in both cases, however, it seems that TWS generally overestimates the amount of slag in comparison with both techniques, or that slag content is underestimated with those techniques. For SEM/BSE mapping, previous studies have shown that underestimation is possible on the basis of difficulties to account for the smallest slag particles [12]. However, especially for the case of selective dissolution, results at 1 day are particularly higher than results from TWS or SEM mapping. This may be attributed to incomplete correction procedure of the dissolved part of slag and the undissolved aluminosilicate hydrates [13].

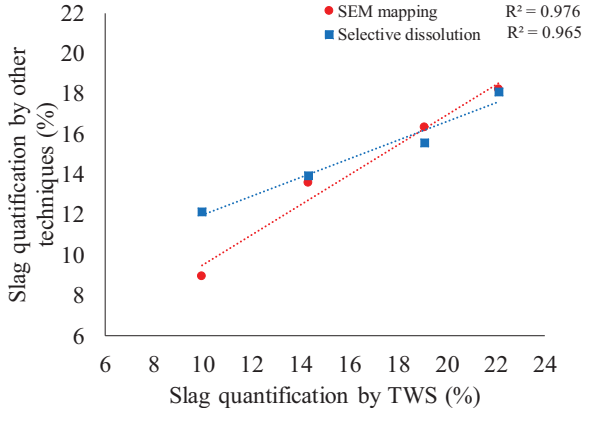

Figure 4: Correlation between amounts of unreacted slag obtained by TWS and other techniques

4.2 Estimation of CH image density

In theory, the stereology principles state that area fractions in 2D cross-sections are equal to 3D volume fractions [14]. Although, 2D cross-sections tend to be underestimated and 2D thickness of features tend to be overestimated [15]. This issue, however, is overcome with enough data from a fairly large representative area. Then, results for relative area of each class from TWS are equal to their volume fraction in the paste. Thus they can be expressed in cm^3 per 100 cm^3 of paste. Based on the CH relative volume and the TGA data (% expressed in weight), results were used to estimate the CH image density and its variation with time considering the measured density of the paste at different ages. Calculations lead to a relation between the density of the CH and the density of the paste as shown in Equation 1. Therefore, with the data from TWS, the image density of the CH can be estimated at different ages. Figure 5 shows (a) the correlation factor found between the density of the paste and the image density of the CH, and (b) the evolution with time of the CH image density calculated with the described method. These values are naturally lower than the density of calcium hydroxide crystals. They cannot account for the actual density of the phase, but only serve as a relationship between the mass and the area observed in the image, named in this case "image density".

$$\frac{\text{TGA results}}{\text{TWS results}} = \frac{\frac{g_{CH}}{g_{paste}}}{\frac{cm^3{}_{CH}}{cm^3{}_{paste}}} = \frac{(g_{CH}) \cdot [cm^3{}_{paste}\ ]}{(cm^3{}_{CH}) \cdot [g_{paste}]} = \frac{\rho_{CH}}{\rho_{paste}} = \quad \text{a (1)}$$

Then: $\rho_{CH} = a \cdot \rho_{paste}$

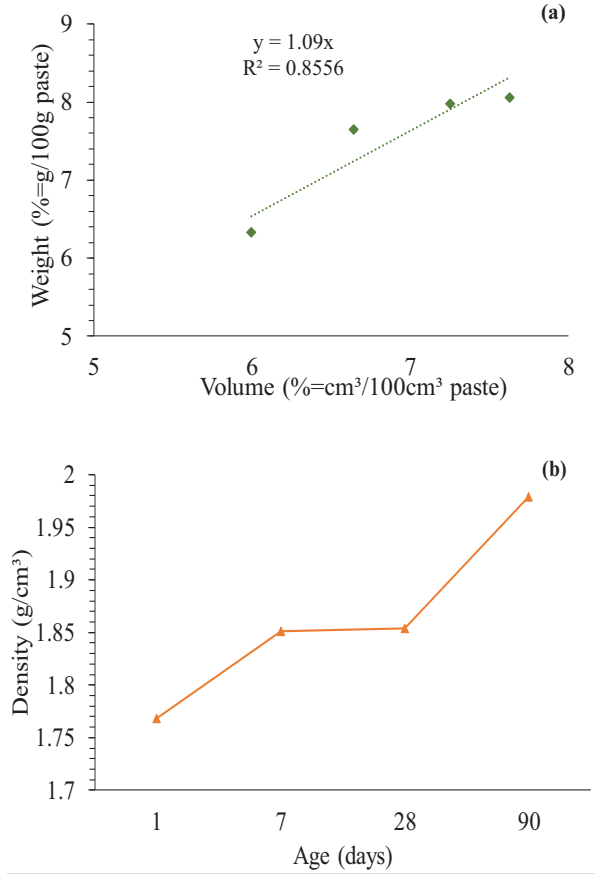

Figure 5: (a) Correlation factor between the density of the paste and the image density of the CH, (b) evolution with time of the CH image density

In theory, the density of the of CH is 2.25g/cm^3 [16]. Although, the density of CH measured on a white cement paste of 0.5 *w/b* at 21 days using ptychographic X-ray computed tomography was found to be of 2.12 ± 0.06 g/cm^3 [17]. The authors attributed this lower-than-expected density to porosity below the spatial resolution and to partial decalcification of the

calcium hydroxide due to the carbonation. The estimation of the image density using the TWS data gives a value of 1.98 g/cm^3 for a slag-blended paste at 90 days. In spite the low value, it was possible to estimate the progress of the CH densification as a function of time.

5 CONCLUSIONS

- A machine learning tool, TWS, was introduced to slag blended cement paste image analysis. It was found to be a useful tool for images segmentation, without the need of element mapping for the distinction among phases.
- When obtaining the probability maps form each designed class, attention should be paid to the chosen level of probability of the different trained classes. It is necessary to assess the probability distribution to identify the precision of each classifier in order not to disregard significant data.
- Validation of the results was made with two other independent techniques: selective dissolution and SEM/BSE mapping. TWS showed a good correlation with both techniques, especially with SEM/BSE mapping. In this sense, it implies significant reduction of time for image acquisition when no mapping is required.
- The potential of TWS has also been shown through the estimation of the CH content and its evolution with time. Although more work is necessary to link the CH image density to the physical density in structure of the paste, the TWS technique shows potential for the evaluation of the density of the constituents of cement pastes.

6 REFERENCES

[1] Pal N. and Pal S., 'A review on image segmentation techniques', *Pattern Recognition* **26** (9) (1993) 1277-1294.

[2] M. Hall, E. Frank, G. Holmes, B. Pfahringer, P. Reutemann, I.H. Witten, The WEKA data mining software: an update, SIGKDD Explorations 11 (2009) 10–18.

[3] Arganda-Carreras, I., Kaynig, V., Rueden, C., Schindelin, J., Cardona, A., Seung, H., 'Trainable_Segmentation: Release v3.1.2 [Data set] ', Zenodo (2016) http://doi.org/10.5281/zenodo.59290

[4] Sekulska-Nalewajko J., Gocławski J., Chojak-Kozniewska J., Kuzniak E., 'Automated image analysis for quantification of reactive oxygen species in plant leaves', *Methods* **109** (2016) 114–122.

[5] Yadav A., Malik H., Chandel S., 'Selection of most relevant input parameters using WEKA for artificial neural network based solar radiation prediction models', *Renewable and Sustainable Energy Reviews* **31** (2014) 509–519.

[6] Hart N. and Huang L., 'Monitoring populations of solitary bees using image processing techniques', *Int. J. Computer Applications in Technology* **50** (1) (2014) 45-50.

[7] Scrivener K., Bazzoni A., Mota B., Rossen E., 'A Practical Guide to Microstructural Analysis of Cementitious Materials' *CRC Press* (2015) 351–418 (Taylor & Francis Group, Boca Raton, 2016)

[8] Kocaba V., Gallucci E., Scrivener K., 'Methods for determination of degree of reaction of slag in blended cement paste' *Cem. Concr. Res.* **42** (2012) 511-525

[9] Lumley J., Gollop R., Moir G., Taylor H., 'Degrees of reaction of the slag in some blends with Portland cements', *Cem. Concr. Res.* **26** (1996) 139–151.

[10] Durdziński1 et al., 'Outcomes of the RILEM round robin on degree of reaction of slag and fly ash in blended cements' (2017), in preparation.

[11] Arganda-Carreras I., Kaynig V., Schindelin, J., Cardona, A., Seung, H., Trainable Weka Segmentation: A Machine Learning Tool for Microscopy Image Segmentation,
[12] Kocaba V., Gallucci E, Scrivener K., 'Methods for determination of degree of reaction of slag in blended cement pastes', *Cem. Concr. Res.* **42** (2012) 511–525.
[13] Scrivener K., Lothenbach, B., De Belie N. et al., 'TC 238-SCM: hydration and microstructure of concrete with SCMs', *Mater Struct* (2015) **48** (4) (2015) 835–862, doi:10.1617/s11527-015-0527-4
[14] Russ J., Dehoff R., 'Practical Stereology', 2nd Edn. (Kluwer Academic Press, New York, 2000).
[15] Scrivener K., 'Backscattered electron imaging of cementitious microstructures: understanding and quantification', *Cem. Concr. Compos.* **26** (2004) 935–945
[16] Desgranges L., Grebille D., Calvarin G., Chevrier G., Floquet N., Niepce J.-C., 'Hydrogen thermal motion in calcium hydroxide: $Ca(OH)^2$', *Acta Crystallographica* **49** (1993) 812–817
[17] Trtik P., Diaz A., Guizar-Sicairos M., Menzel A., Bunk O., 'Density mapping of hardened cement paste using ptychographic X-ray computed tomography', *Cem. Concr. Compos.* **36** (2013) 71–77

Using the Pitzer Model to Predict Aqueous Solution Compositions of Portland Cements Blended with Supplementary Cementitious Materials

Dale P. Prentice[(1)], Susan A. Bernal[(1)], Mark Bankhead[(2)], Martin Hayes[(2)], John L. Provis[(1)]

[(1)] Immobilisation Science Laboratory, Department of Materials Science & Engineering, University of Sheffield, UK

[(2)] National Nuclear Laboratory, Warrington, UK

ABSTRACT

Thermodynamic modelling can be used to predict how changes in cement chemistry will affect the nature of the hydration products and corresponding aqueous pore solutions. Current geochemical thermodynamic models primarily use the Debye-Hückel or Davies equations as the basis for determining activity coefficients of aqueous species. Using these equations, good results in predicting the aqueous phase compositions within pure cement systems are obtained; however, for blended cements these simplified equations may provide inaccurate results as pore solution chemistry can become more complex. Using the Pitzer model to determine activity coefficients in blended cement systems can improve the accuracy of simulated aqueous compositions, as long as a suitable parameter database can be made available and validated. The Pitzer model has fitted parameters which describe binary and ternary ion interactions to provide ion-specific activity coefficients for use at high ionic strength, as opposed to the non-specific values provided by the Debye-Hückel or Davies equations. The availability of accurate predicted aqueous solution compositions enables the simulation of phase assemblage of the hydrated blended cements, and the prediction of the main binding phase compositions is improved due to the more accurate simulation of interactions of aqueous ions.

Keywords: Thermodynamic modelling, Pitzer, aqueous solution, GEMS, blast furnace slag, C-A-S-H.

1 INTRODUCTION

Within the construction industry the use of supplementary cementitious materials (SCMs) has become more prevalent as time progresses. Including SCMs as a partial replacement for Portland cement (PC) within cements has been shown to enhance and contribute to the mechanical and durability properties of the hydrated materials. Management of nuclear fuel cycle wastes by cementation has also benefitted from these properties, and particularly the influence that SCMs such as blast furnace slag (BFS) have on the internal chemistry of these cements. Most notably, the use of PC: BFS blends have become the basis of industrial processes applied in the UK for encapsulating intermediate level nuclear waste.

Alongside altering the physical properties of the cement, SCMs have a noticeable impact on the hydration products formed and the pore solution chemistry. This impact on the chemistry during hydration is heavily dependent on the initial composition of the precursor

material used. Considering BFS in particular, the blast furnace process and the location from which the iron ore is sourced can lead to significant differences in the varying oxides and sulfides within the slag glass. This can pose an issue for the nuclear industry within the UK as sources of BFS have been forced to change due to issues with continuity of supply [1].

Thermodynamic modelling of cements offers the opportunity to predict which phases are formed based on the nature of the precursor material and the degree of hydration. Accurate modelling of cement phases and pore solutions relies on an accurate solid solution model depicting the main phase formed during hydration of PC:BFS, which is the calcium aluminium silicate hydrate (C-A-S-H) phase [2]. Multiple software packages such as PHREEQC and GEM Selektor offer a means of testing these materials. In this study GEM Selektor (GEMS) was used to utilise the predictive power of thermodynamic modelling [3]. Using GEMS it is possible to determine the phase assemblage of hydrated cement and pore solution [4].

Thermodynamic modelling relies on solubility data of the materials involved, and the application of activity coefficients to provide a non-ideal mixing correction [5]. The Debye-Hückel or Davies equations are most commonly used in these models to determine the activity coefficients of ions in solution[4]. Using the Davies method, activity coefficients are not ion specific, but generalised to all ions of a given charge, and a single dominant electrolyte must be specified. Methods such as specific ion interaction theory (SIT) or the Pitzer model [6] can determine activity coefficients specifically for each ion species for which interaction parameters are available, although this parameterisation is often a non-trivial exercise.

This study considers improving solid solution modelling of the C-A-S-H phase for the accurate simulation of cement hydration. An altered C-A-S-H model based on the C(-N)-A-S-H solid solution model [7] has been used to define the main hydrate phase within PC:BFS cements. In addition, the Pitzer method has been used as an alternative to the Debye-Hückel method for determining activity coefficients.

2 MATERIALS AND METHODS

A key phase in hydrated PC:BFS cement is the C-A-S-H phase which is comprised of Ca-O 'sheets' that encompass alumina-substituted silicate chains. Between these chains, an interlayer containing aqueous cations (e.g. K^+) provides charge balancing ions. The structure formed as a result resembles that of a disordered tobermorite-like phase [2]. Varying calcium to silicon ratios (Ca/Si) and aluminium to silicon ratios (Al/Si) affect the structure of the C-A-S-H phase, therefore due to the variation of this phase; an end-member solid solution model is required to correctly define its formation through hydration.

Table 1 C-A-S-H end-member model properties, adapted from Myers et al. [7] and Kulik[8].

End-member	Composition	$\Delta_f H$ (kJ/mol)	$\Delta_f G$ (kJ/mol)	$\text{Log}_{10}(K_{SO})$	Ref.
5CA	$(CaO)_{1.25}(Al_2O_3)_{0.125}$ $(SiO_2)_1(H_2O)_{1.625}$	-2491	-2293	-10.75	[7]
INFCA	$(CaO)_1(Al_2O_3)_{0.15625}$ $(SiO_2)_{1.1875}(H_2O)_{1.65625}$	-2551	-2343	-8.9	[7]
T2C	$(CaO)_{1.5}(SiO_2)_1(H_2O)_{2.5}$	-2721	-2465	−11.6	[7]
T5C	$(CaO)_{1.25}(SiO_2)_{1.25}(H_2O)_{2.5}$	-2780	-2517	−10.5	[7]
TobH	$(CaO)_{1.25}(SiO_2)_{1.5}(H_2O)_{2.5}$	-2831	-2570	−7.9	[7]
JenD	$(CaO)_{1.5}(SiO_2)_{0.67}(H_2O)_{2.5}$	-2400	-2170	−3.66	[8]

2.1 C-A-S-H end-member model

For this study a previously created C(-N)-A-S-H solid-solution model used for modelling alkali-activated-slag [7] has been adapted to better represent the C-A-S-H phase in PC:BFS cements. The sodium-containing end-members within the C(-N)-A-S-H model have been removed as sodium takes a less prevalent role in PC:BFS hydration, and a higher Ca/Si ratio end-member has been included as higher Ca/Si ratios are observed in PC:BFS cements. The revised C-A-S-H model is summarised in Table 1.

2.2 Thermodynamic modelling

Thermodynamic modelling is an extension of the law of mass action (LMA) approach which utilises the concentration of ionic species required to create a stable solid product. It requires a mass action constant (log *K*) of the aqueous complexes, solids and gases at the specified temperature. The *K* value is a constant used for determining the concentration at which the dissociated aqueous species will be at equilibrium with the solid phases or complexes present. Using this value for the phases of interest, the composition of the system is calculated iteratively by performing mass and charge balances. The commonly-used concentration-based formulation of the mass action constant considers an ideal solution, however cement is not an ideal solution, and therefore activity coefficients are required to apply a realistic non-ideality correction to the equations (Equations 1 and 2).

$$K_{SO} = \{Ca^{2+}\}^{1}\{SiO_3^{2-}\}^{1.1875}\{AlO_2^{-}\}^{0.3125}\{H_2O\}^{1.65625} \quad (1)$$

where $\{X\} = \gamma_X[X]$

Methods such as the Debye-Hückel equation use ionic strength and the charge of the specific ions as variable factors in calculating the respective activity coefficients for ions in solution. The extended Debye-Hückel (Equation 2) method for determining activity coefficients has been used extensively for thermodynamic modelling [5].

$$log_{10}\gamma_i = \frac{-A_\gamma z_i^2\sqrt{I}}{1 + \dot{a}B_\gamma\sqrt{I}} + b_\gamma I + log_{10}\frac{X_{jw}}{X_w} \quad (2)$$

Here, γ_i and z_i are the activity coefficient and charge of the i^{th} aqueous species respectively, A_γ and B_γ are temperature and pressure dependent coefficients, I is the effective molal ionic strength, $\dot{a}$ is the ion size parameter, $b\gamma$ describes short-range interactions between ionic aqueous species within an electrolyte solution, X_{jw} is the molar quantity of water, and X_w is the total molar amount of the aqueous phase.

For PC:BFS systems it is often assumed that the aqueous species is dominated by KOH , therefore the corresponding values of $\dot{a}$ (3.67 Å) and b_γ (0.123 kg/mol) [9] are used when modelling cement systems. The water activity is determined through osmotic coefficients. The extended Debye-Hückel equation is effective for molal ionic strength up to ~1 molal and PC: BFS cements tend to fall within that range (~1 – 2 molal) at younger ages. During longer curing times, this ionic strength may increase as more sulfide is released from the slowly-reacting slag grains, therefore an ion-specific method, such as the Pitzer model, for determining activity coefficients may be required at higher ionic strengths.

Software such as GEMS not only calculates the mass balance of the system but also determines whether the Gibbs free energy is at a global minimum (Equation 3), indicating that the system is no longer capable of further spontaneous change.

$$\sum_i \nu_i \Delta_f G^\circ = -RT\ln K_{SO} \quad (3)$$

2.3 Pitzer aqueous solution modelling

The Pitzer aqueous solution model is an ion-specific approach to determining the activity coefficients of aqueous species. This method considers the binary and ternary interactions between ions. Ion-specific interaction constants have been fitted based on the general Equation 4 which provide a broad overview of how the activity coefficients are formulated (more information can be found in [10]).

$$\ln\gamma_M = z_M^2 F + \sum_a m_a(2B_{Ma} + IC_{Ma}) + \sum_c m_c\left(2\Phi_{Mc} + \sum_a m_a\psi_{Mca}\right) + \sum_a\sum_{<a'} m_a m_{a'}\psi_{aa'I} + |z_X|\sum_c\sum_a m_c m_a C_{ca} \quad (4a)$$

$$\ln\gamma_X = z_X^2 F + \sum_c m_c(2B_{cX} + IC_{cX}) + \sum_a m_a\left(2\Phi_{Xa} + \sum_c m_c\psi_{Xac}\right) + \sum_c\sum_{<c'} m_c m_{c'}\psi_{cc'X} + |z_X|\sum_c\sum_a m_c m_a C_{ca} \quad (4b)$$

This approach incorporates the use of a virial coefficient expansion. An initial term which encompasses the system as a whole, in this case the Debye-Hückel term (F) is followed by the second virial coefficient which considers the interaction between pairs of aqueous species (B's, C's and Φ's)and finally the third virial coefficient which calculates ternary species interactions (ψ's).

This provides the basis for the activity coefficients for cationic species, γ_M and anionic species, γ_X. In Equation 3, m_c is the molality (mol/kg solvent) of cation c, with charge z_c. Subscripts *M, c* and *c'* refer to cations. Similarly, the subscripts *X, a* and *a'* refer to anions. The summation index, c, denotes the sum over all cations in the system. The double summation index, $c<c'$, relates to the sum over all interactions with non-similar cations. Equivalent definitions correspond to the summation indices for anions. Coefficients obtained for *B*'s and *C*'s are obtained from binary interaction data, whereby only binary ionic interactions were measured. Ternary species interactions are accounted for using the ψ and Φ coefficients.

2.4 Model parameters

Applicability of the Pitzer model and parameter set for optimising C-A-S-H modelling was tested against the solution results created by L'Hôpital et al. [11-12]. The study considered different Ca/Si, Al/Si and KOH levels within an aqueous solution to test how alkaline conditions affect the structure and solubility of C-A-S-H. A summary of the reaction environments can be seen in Table 2.

Table 2 Precursor molar ratios of components used for testing the Pitzer method for determining activity coefficients [11-12].

Ca/Si	Al/Si	KOH (M)
1	0.05	-
1	0.1	-
1	0.2	-
1.2	0.05	-
1.2	0.1	-
1.2	0.2	-
1.4	0.05	-
1.4	0.1	-
1.4	0.2	-
1.6	0.05	-
1.6	0.1	-
1.6	0.2	-

Ca/Si	Al/Si	KOH (M)
1	0.05	0.05
1	0.05	0.1
1	0.05	0.25
1.2	0.05	0.05
1.2	0.05	0.1
1.2	0.05	0.25
1.4	0.05	0.05
1.4	0.05	0.1
1.6	0.05	0.05
1.6	0.05	0.1
1.6	0.05	0.25

Table 3 Pitzer parameters used for modelling the systems studied by L'Hôpital et al. [11-12]. The Pitzer parameter types are fitting values which combine to provide the *B*, *C*, and Φ values found in Equation 4 [6].

Ion interactions			Parameter value	Pitzer parameter type	Reference
C	*a*	*c'*			
Ca^{2+}	OH^-		-0.1421	$\beta_{ca}^{(0)}$	[13]
Ca^{2+}	OH^-		-0.2303	$\beta_{ca}^{(1)}$	[14]
Ca^{2+}	OH^-		-5.7200	$\beta_{ca}^{(2)}$	[14]
Ca^{2+}	-	K^+	0.0320	θ_{cc}	[6]
Ca^{2+}	-	H^+	0.0920	θ_{cc}	[6]
K^+	OH^-		0.1611	$\beta_{ca}^{(0)}$	[15]
K^+	OH^-		0.1370	$\beta_{ca}^{(1)}$	[15]
K^+	OH^-		0.0041	C_{ca}^{Φ}	[14]
K^+	$HSiO_3^-$		0.2080	$\beta_{ca}^{(0)}$	[16]
K^+	$HSiO_3^-$		0.34	$\beta_{ca}^{(1)}$	[16]

The structure and formation of the C-A-S-H phase within PC:BFS cements are heavily linked with the solid-solution interaction with alkalis, and most prevalently potassium within the silicate chain interlayer [11]. Therefore, including Pitzer parameters of potassium interactions with other aqueous ions in the solution is important alongside the ions forming the C-A-S-H phase, as seen in Table 3. Calcium and potassium ions were the focus of this study as there are many publications calculating the Pitzer parameters for these ions.

3 RESULTS AND DISCUSSION

3.1 Impact on Activity Coefficients

At lower ionic strengths (0 – 2 m/mol kg^{-1}), the Pitzer parameters have a small effect on the activity coefficients in the solutions considered. The addition of KOH on the overall ionic strength of the solution is evident from the relatively large increase from 0.06 to 2 m/mol kg^{-1} seen in Figure 1.

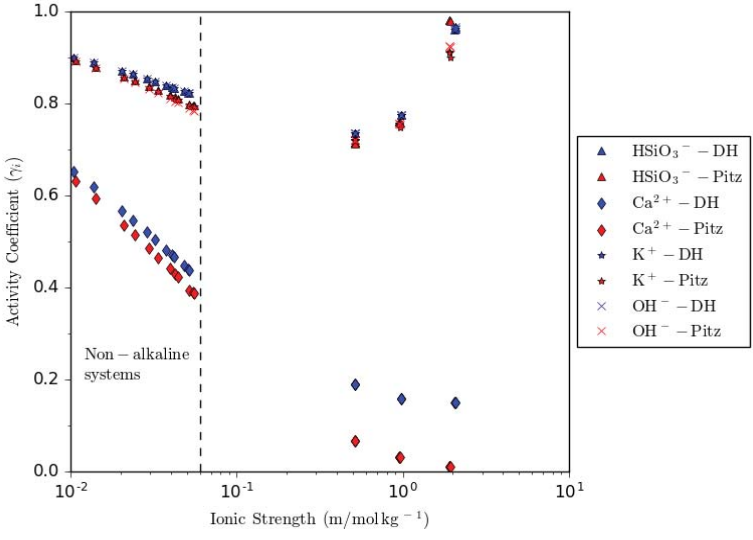

Figure 1 Effect of ionic strength and activity coefficient method used to determine the activity coefficients for K^+, Ca^{2+} and $HSiO^{3-}$.

The Pitzer activity coefficients become lower than those from the Debye-Hückel method for each of the ions measured. However, there was minimal difference between the activity coefficients obtained for K^+, OH^- and $HSiO^{3-}$ ions between the two methods even at the higher end of the ionic strength range. There was a noticeable difference for the Ca^{2+} ions. Calcium ion activity coefficients at the higher ionic strength range become 10 times smaller using the Pitzer equations compared with those from the Debye-Hückel method.

3.2 Effect on C-A-S-H composition

The Pitzer method provides good agreement with the experimental data for systems not containing KOH. At the higher alkali levels the Ca/Si ratios were consistently over-predicted as highlighted in Figure 2. A higher Ca/Si in the higher pH environment created by the alkaline material causes the over-compensation of calcium within the C-A-S-H phase as the higher $Ca(OH)_2$ rich end-members become more stable in higher alkaline environments despite less calcium availability in the system.

The Al/Si values simulated displayed poor agreement with the measured results except for the Al/Si values of the KOH solutions which were all maintained at 0.05 Al/Si (Figure 3). At the lower (Al/Si 0.06 to 0.08) levels which did not contain KOH, the simulations greatly over-predicted the levels of aluminium within the C-A-S-H phase. Measured Al/Si values

above 1.0 were scattered; both over-predicted and under-predicted for different systems using this C-A-S-H model and activity coefficient method.

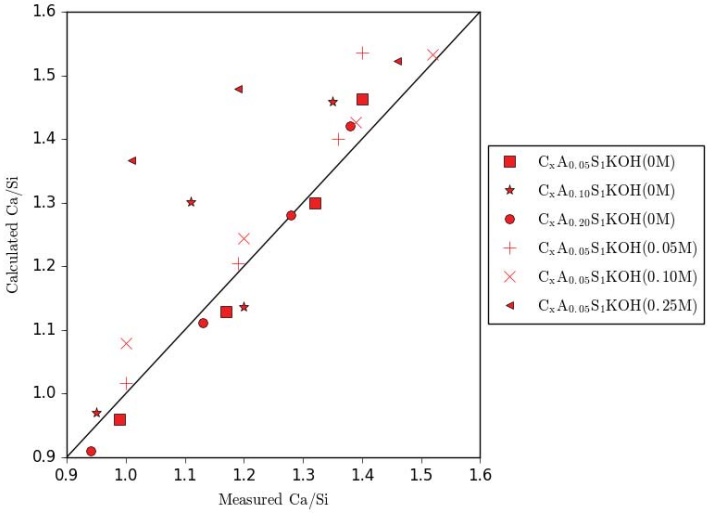

Figure 2 Simulated Ca/Si values compared to experimental C-A-S-H composition data ([11-12]). The *x* within the legend denotes varying levels of calcium molar ratios within the precursor material.

The composition of the C-A-S-H phase was most accurately described for formulations containing no KOH within the Ca/Si range of 1.2 to 1.5. At lower Ca/Si and Al/Si this method was not as accurate at simulating the overall structure of the C-A-S-H phase. There was little variation between the two Al/Si ratio end-members used; therefore the ability to describe a large range as 0.05 to 0.2 Al/Si was problematic.

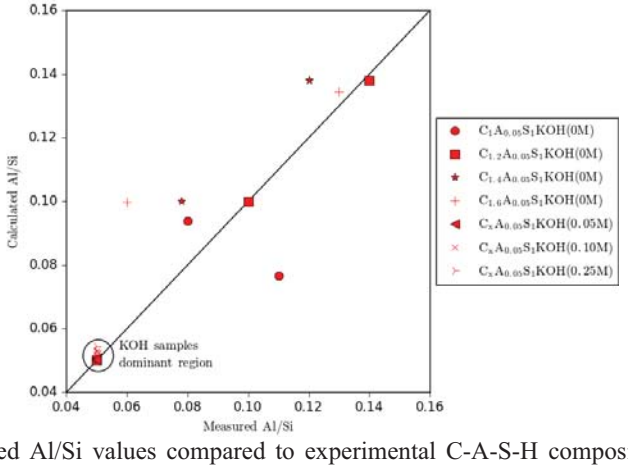

Figure 3 Simulated Al/Si values compared to experimental C-A-S-H composition data[11-12].

3.3 Aqueous solution analysis

For ease of comparison, pore solutions whereby the formulations contained Al/Si = 0.05 were compared. Prediction of the aqueous solution was adequate for the Ca^{2+}, OH^-, K^+, and Al^{3+} ions then solution as the majority of predicted values were within ± 1 order of magnitude of the measured values (Figure 4), which was considered acceptable. Simulated levels of silicon in the solution were consistently outside of the acceptable bounds for added KOH containing systems. This, along with the problems in Al/Si and Ca/Si ratios described above, may also be related to the assumption in the calculations here that dissolved silicate species are all present as monomers; further work should involve more detailed consideration of silicate polymerisation chemistry.

Greater amounts of silicon were predicted to be in the aqueous phase in the higher-alkali formulations due to the higher uptake of calcium within the C-A-S-H phase. This is most evident in the KOH-containing systems, whereby less calcium is observed in the aqueous solution which corresponds to the higher Ca/Si values observed in Figure 2. Mid-range KOH levels (0.05 and 0.1 M) improved the accuracy of the aqueous aluminium simulated, because the aluminium containing end-members are also used as lower calcium containing end-members. These lower calcium containing end-members were used instead of the TobH or T2C end-members and provided a good fit for the medium-KOH range. Prediction of the OH^- ion concentrations increased and became less accurate at higher KOH levels.

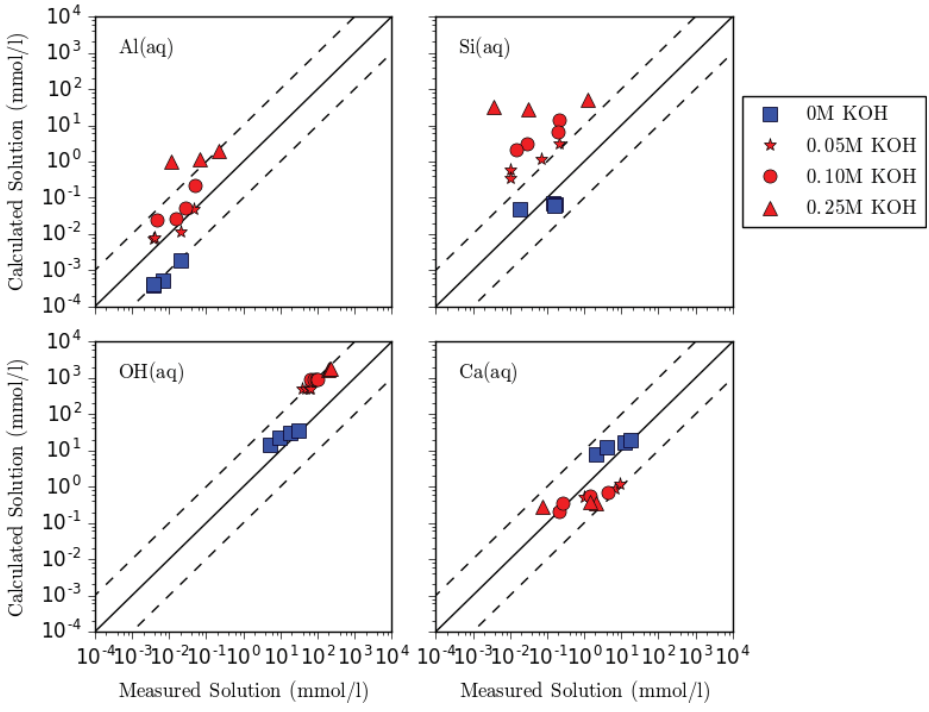

Figure 4 Simulated elemental concentrations in the aqueous phase compared to experimental pore solution composition data for synthetic C-A-S-H ([11-12]). Formulations with Al/Si = 0.05 were plotted. The dotted lines show ± 1 order of magnitude deviation from the solid $y = x$ line.

4 CONCLUSIONS

Using data from the literature it was possible to compare the efficacy of using calcium and potassium Pitzer parameters for simulating C-A-S-H hydration using an adapted end-member model. Prediction of the Ca/Si ratio was more effective within systems with no or less added KOH but both conditions led to similar difficulties simulating the Al/Si ratio. A lack of Pitzer parameters describing the specific ion interactions of Al-Si, Ca-Si and Al-K, and the need to include polymeric or ion-paired silicate species, may be the cause of why this method has not been entirely effective. Potassium containing end-members and a wider-range of aluminium containing end-members in the solid solution may be needed for improving this modelling approach.

5 ACKNOWLEDGEMENTS

This research was performed in part at the MIDAS Facility, at the University of Sheffield in collaboration with the National Nuclear Laboratory.

6 REFERENCES

[1] M. J. Angus, I. H. Godfrey, M. Hayes, and S. Foster, "Managing change in the supply of cement powders for radioactive waste encapsulation – twenty years of operational experience," Proceedings of an International Conference, Phoenix, March, 2010 (Waste Management, 2010).

[2] I. G. Richardson, A. R. Brough, R. Brydson, G. W. Groves, and C. M. Dobsont, "Location of aluminum in substituted calcium silicate hydrate (C-S-H) gels as determined by ^{29}Si and ^{27}Al NMR and EELS," *J. Am. Ceram. Soc.*, vol. 76, pp. 2285–2288, Mar. 1993.

[3] D. A. Kulik, T. Wagner, S. V. Dmytrieva, G. Kosakowski, F. F. Hingerl, K. V. Chudnenko, and U. R. Berner, "GEM-Selektor geochemical modeling package: revised algorithm and GEMS3K numerical kernel for coupled simulation codes," *Comput. Geosci.*, vol. 17, pp. 1-24, Aug. 2012.

[4] B. Lothenbach and F. Winnefeld, "Thermodynamic modelling of the hydration of Portland cement," *Cem. Concr. Res.*, vol. 36, no. 2, pp. 209–226, Feb. 2006.

[5] D. Damidot, B. Lothenbach, D. Herfort, and F. P. Glasser, "Thermodynamics and cement science," *Cem. Concr. Res.*, vol. 41, no. 7, pp. 679–695, Jul. 2011.

[6] K. S. Pitzer, "Activity Coefficients in Electrolyte Solutions: Ch 3,Ion interaction approach: theory and data correlation," 2nd Edn (CRC Press, Inc., Boca Raton, 1991)

[7] R. J. Myers, S. A. Bernal, and J. L. Provis, "A thermodynamic model for C-(N-)A-S-H gel: CNASH_ss. Derivation and validation," *Cem. Concr. Res.*, vol. 66, pp. 27–47, Dec. 2014.

[8] D. A. Kulik, "Improving the structural consistency of C-S-H solid solution thermodynamic models," *Cem. Concr. Res.*, vol. 41, no. 5, pp. 477–495, May 2011.

[9] H. C. Helgeson, D. H. Kirkham, and G. C. Flowers, "Theoretical prediction of the thermodynamic behavior of aqueous electrolytes by high pressures and temperatures, IV; calculation of activity coefficients, osmotic coefficients, and apparent molal and standard relative partial molal properties to 600°C," *Am. J. Sci.*, vol. 281, pp. 1249–1516, Dec. 1981.

[10] C. E. Harvie and J. H. Weare, "The prediction of mineral solubilities in natural waters: The Na-K-M-Ca-Cl-SO_4-H_2O system from zero to high concentration at 25°C," *Geochim. Cosmochim. Acta*, vol. 44, no. 7, pp. 981–997, Mar. 1980.

[11] E. L'Hôpital, B. Lothenbach, K. Scrivener, and D. A. Kulik, "Alkali uptake in calcium alumina silicate hydrate (C-A-S-H)," *Cem. Concr. Res.*, vol. 85, pp. 122–136, Mar. 2016.

[12] E. L'Hôpital, B. Lothenbach, D. A. Kulik, and K. Scrivener, "Influence of calcium to silica ratio on aluminium uptake in calcium silicate hydrate," *Cem. Concr. Res.*, vol. 85, pp. 111–121, Jan. 2016.

[13] J. Duchesne and E. J. Reardon, "Measurement and prediction of portlandite solubility in alkali solutions," *Cem. Concr. Res.*, vol. 25, no. 5, pp. 1043–1053, Apr. 1995.

[14] D. L. Parkhurst and C. A. J. Appelo, "Description of input and examples for PHREEQC version 3 — acomputer program for speciation , batch-reaction , one-dimensional transport ,

and inverse geochemical calculations.",U.S. Geological Survey Techniques and Methods, book 6, 2013.

[15] P. M. May, D. Rowland, G. Hefter, and E. Königsberger, "A generic and updatable Pitzer characterization of aqueous binary electrolyte solutions at 1 bar and 25 °C," *J. Chem. Eng. Data*, vol. 56, no. 12, pp. 5066–5077, Nov. 2011.

[16] J. L. Provis, P. Duxson, G. C. Lukey, F. Separovic, W. M. Kriven, and J. S. J. Van Deventer, "Modeling speciation in highly concentrated alkaline silicate solutions," *Ind. Eng. Chem. Res.*, vol. 44, no. 23, pp. 8899–8908, Oct. 2005.

Microstructural and Morphological Studies of Ordinary Portland Cement Paste and Fly Ash based Geopolymer in the presence of Chloride Ions

Pavithra Parthasarathy[(1)], Asad Hanif[(1)], Hongyu Shao[(1)] and Zongjin Li[(1, 2)]

[(1)]Department of Civil and Environmental Engineering, The Hong Kong University of Science and Technology, Hong Kong SAR, China

[(2)]Institute of Applied Physics and Materials Engineering, University of Macau, Macau

ABSTRACT

This paper presents the microstructural and morphological studies carried on ordinary portland cement paste and fly ash based geopolymer in the presence of chloride ions. Cement and geopolymer pastes were made with seawater and the resulting reaction products were analysed for phase composition, hydration degree, microstructural, and morphological features. The experimental results showed that in seawater cement paste, Friedel's salt was formed as hydration product co-existing with C-S-H and $Ca(OH)_2$. Chloride ions present in seawater promoted the Friedel's salt formation and increased the $Ca(OH)_2$ content. However, it was found that the presence of Friedel's salt decreased at later age. In geopolymer samples, use of seawater enhanced the formation of C-A-S-H phase. Microstructure of the seawater cement paste and geopolymer samples are much denser and smoother than the normal water cement paste and geopolymer samples. Presence of chloride ions in seawater densified the microstructure of seawater cement paste samples. For geopolymer samples, presence of the C-A-S-H phase made its microstructure denser and the chloride ions present in seawater was immobilized by fly ash.

Keywords: Chloride ion (Cl^-), seawater, cement hydration, geopolymer, microstructure.

1 INTRODUCTION

World's population increased by 10% last decade. The United Nations estimates that by 2050 there will be an additional increase in population of about 3.5 billion. This tremendous growth of population will greatly affect the people who live in developing countries. Several problems will be faced due to the population growth. One among them is the shortage of fresh water throughout the world. It is estimated that by 2050, more than half of the world population will not be able to get enough fresh water for their daily use. With the increasing infrastructure development, the need of fresh water to make concrete is also increasing. Several billion tons of water is used in concrete production yearly. The use of seawater in the place of fresh water will save fresh water and further helps in the water shortage problem. Also, coastal areas like Hong Kong which have limited access to fresh water would be economically benefited using seawater.

Previous studies on the use of seawater in concrete focus on strength characteristics, durability studies, and reinforcement corrosion. Use of seawater in concrete accelerates the early age strength and decreases the pore volume. Strength increased due to the formation of Friedel's salt, which reduced the pore volume [1-2] of concrete. Use of supplementary

cementing materials like fly ash, slag, and metakaolin in addition with sea water has been reported to improve the performance of concrete. Addition of metakaolin increased the chloride resistance of concrete, when samples are mixed with seawater [3]. Use of blast furnace slag in concrete increases the corrosion resistance of steel bar against the chloride ions present in seawater [4]. Porosity and pore size decrease with age when seawater is used for making self-compacting concrete [5].

Although studies were made on use of seawater in concrete and cement paste, majority of them focuses on strength development and corrosion resistance improvement. Very few studies were found on the effect of seawater on cement hydration and its microstructure. Further, the influence of chloride ion in seawater, on the microstructure of cement is still not clear. The objective of this paper is to investigate the presence of chloride ion on the microstructure of cement pastes. Additional study was also carried on fly ash based geopolymer to understand the effect of seawater on geopolymers.

2 MATERIAL AND METHODS

Ordinary Portland cement (OPC) and locally available fly ash were used in this study. Chemical composition of cement and fly ash used are shown in the Table 1.

Table 1: Chemical composition of raw materials used

Description	SiO_2	Al_2O_3	CaO	Fe_2O_3	SO_4	MgO	K_2O	TiO_2	MnO
OPC	19.92	4.29	64.94	2.72	5.74	1.26	0.84	0.29	-
Fly ash	46.62	18.21	12.67	11.59	2.46	4.79	1.52	0.97	0.13

Cement paste samples with a w/c ratio of 0.4 was used for study. Two sets of samples were prepared for the study, one set of samples were prepared by using seawater and another set with normal water. Prepared samples were then water cured in laboratory condition till 28 days. Hydration process of samples for corresponding age was stopped by storing it in acetone. Geopolymer samples were prepared with fly ash as raw material activated by alkaline solution. Sodium hydroxide and sodium silicate solution was used as alkaline solution to activate fly ash with sodium silicate to sodium hydroxide ratio of 2. Locally available seawater was used for preparing alkaline solution for seawater geopolymer samples and portable water was used for alkaline solution preparation for normal geopolymer samples. Prepared samples were cured in ambient temperature till the day of testing.

The crystalline phases of the cement paste and geopolymers were characterised by the X-ray diffraction (XRD, PANanalytical X'pert) using Cu-Kα radiation (1.541874 Å, 40 mA, 40 kV). The degree of hydration of cement paste and geopolymers were determined by a thermogravimetric analyser (TGA 7). The analysis was carried from room temperature to 800˚C in N_2 atmosphere with a heating rate of 10˚C/min. Bond details, chemical band shifts in cement paste, and geopolymer samples were investigated by Fourier transform infrared (FTIR) spectroscopy. Microstructure and morphological features of samples were observed using scanning electron microscopy (SEM, JEOL 6300).

3 RESULTS AND DISCUSSION

3.1 Phase composition

Figure 1 shows the XRD patterns of 7 and 28days normal water cement paste (NC7 & NC28) and seawater cement paste (SC7 & SC28) samples. Phases of $Ca(OH)_2$, C_3S and C_2S

were identified at peaks around 18, 28, 29, 32, 34, 38, 47, 50, and 54˚. Low intensity peaks of Friedel's salt ($3CaO.Al_2O_3.CaCl_2.10H_2O$) located around 11 and 39˚ are seen for 7day seawater sample. However, the peak at 39˚ was absent for 28 day seawater sample. This is due to the increased reactivity of C_3S phase with age. As shown in Figure 1, intensity of C_3S phase observed at 29˚ decreases with age, this is due to the utilisation of C_3S phase to form the reaction products C-S-H and $Ca(OH)_2$. Formation of these new reaction products destabilise the presence of Friedel's salt leading to the absence of Friedel's salt phase with age. Also, chloride ions bounded by Friedel's salt get released to the surface of concrete as it destabilises, which may result in strength decline of seawater concrete samples in later days as reported by [1,2].

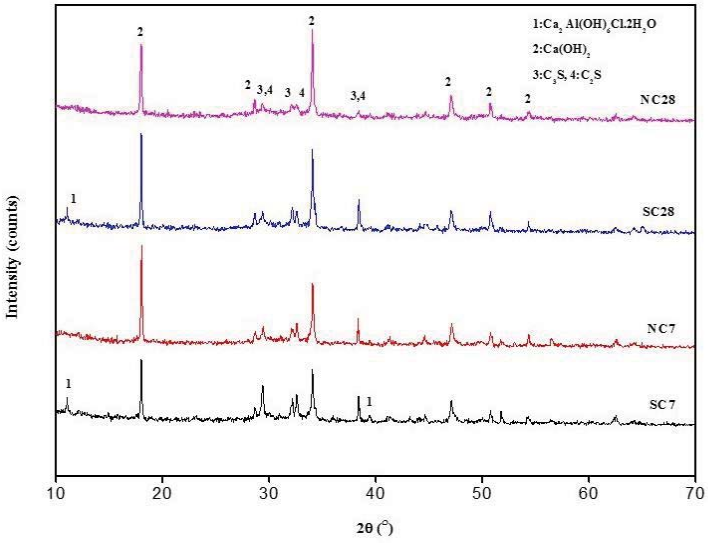

Figure 1: XRD pattern of 7day and 28day normal water and seawater cement paste samples

Figure 2 shows the XRD pattern of 28day normal water geopolymer (NG) and seawater geopolymer (SG) samples. Phases of SiO_2 and N-A-S-H were identified for normal water geopolymer located around 20, 26, 42, 44, 50˚. For seawater geopolymer samples, along with the existing SiO_2 and N-A-S-H phase, an additional C-A-S-H phase was observed around 38˚. From Figure 2, it can be seen that the intensity of N-A-S-H phase around 44˚ increased for seawater geopolymer samples with decrease in intensity of SiO_2 phase located around 20, 42˚.

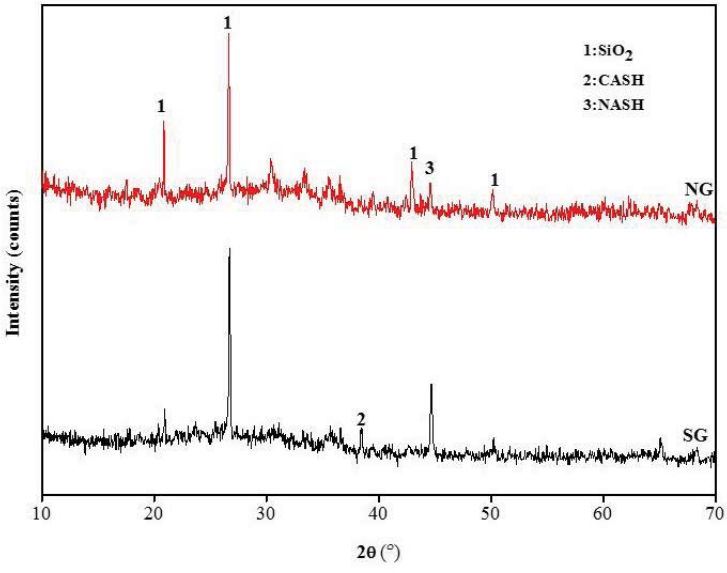

Figure 2: XRD pattern of normal water and seawater geopolymer samples

3.2 Thermal analysis

Figure 3 shows the thermogravimetric test results of cement pastes. From the Figure 3 it can be observed that the weight loss of seawater cement pastes around 310˚C is due to presence of Friedel's salt, this phase is absent in normal water pastes. This observation further confirms the presence of Friedel's salt in seawater cement paste samples in addition to XRD results. The peak observed in the temperature region of 400˚C is due to dehydroxylation, where chemical decomposition of $Ca(OH)_2$ take place. Greater derivative weight loss in this temperature range shows higher decomposition of $Ca(OH)_2$. Seawater cement paste samples shows higher decomposition of $Ca(OH)_2$ in comparison with normal water samples. Higher decomposition of $Ca(OH)_2$ takes place due to higher content of $Ca(OH)_2$ in cement hydration for seawater samples. From this it can be concluded that seawater promotes the formation of $Ca(OH)_2$ phase in hydration process. This is due to presence of chloride ions in seawater which accelerates the cement hydration to give increased content of $Ca(OH)_2$ phase. Similar observation was made by [6].

Figure 4 shows the thermogravimetric test results of geopolymers. No noticeable difference in weight loss is observed between seawater and normal water geopolymer samples. This could be attributed to the slow reactivity of fly ash. Fly ash geopolymers are normally heat cured in oven to accelerate the reaction process. But in this study geopolymer samples were cured in ambient temperature and it is possible that, the fly ash was not fully reacted at the time of testing.

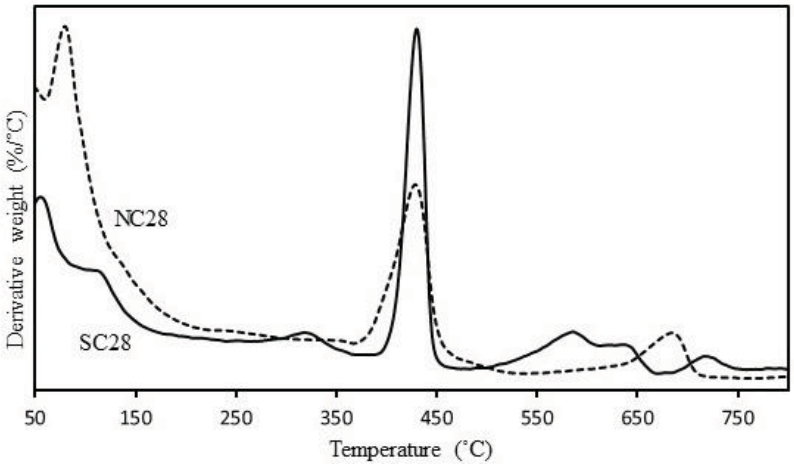

Figure 3: Derivative weight loss curve for normal water and seawater cement pastes samples

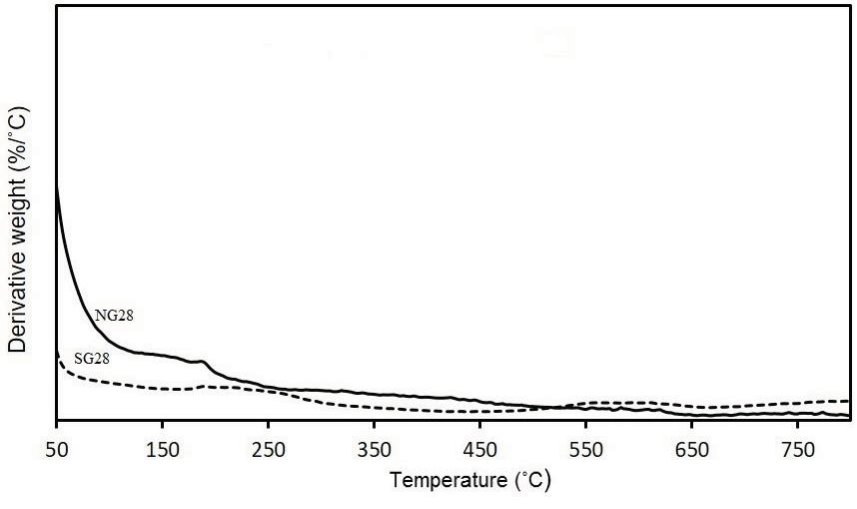

Figure 4: Derivative weight loss curve for normal water and seawater geopolymer samples

3.3 IR analysis

Figure 5 shows the FTIR spectrum of normal water and seawater cement paste samples for 7 and 28 day. The notations used in the figures are explained earlier in section 3.1. There was no significant difference in results observed for normal water and seawater cement paste samples. The intensity of IR spectrum decreases with age which refers to change in concentration of bands. Change in concentration may takes place due to presence of some additional functional group and it doesn't deal with band swift or new bond formation.

The presence of sharp peak around 3600 cm^{-1} is due to stretching vibration of O-H bond present in $Ca(OH)_2$. The broad band observed in the region around 3400 cm^{-1} is because of

asymmetrical stretching of O-H or H-O-H bond present in water molecules. Vibration of band at 1650 cm-^{1} is the bending of H-O-H bond present in water molecules. Also, bands observed at frequencies of 1480, 872 and 712 cm^{-1} are attributed to carbonates present in cement paste respectively. The vibration of band around 950 cm^{-1} is due to stretching of Si-O bond, likewise the presence of band around 520 and 450 cm-^{1} is because of bending vibration of Si-O bond [7].

Figure 6 shows the FTIR spectrum of normal water and seawater geopolymer samples. The bond information and the mode of vibration mentioned above holds well for geopolymer samples also. Significance difference found in IR analysis of geopolymer samples is the presence of additional peak at 1490 cm^{-1} for normal water geopolymer sample. This peak corresponds to the C=O bonding group present in carbonates. Absence of this group in seawater samples implies that the intensity or concentration of carbonates is low in seawater geopolymer samples. From this observation, it can be inferred that use of seawater reduces the concentration of carbonates formed in geopolymers. However, detailed investigation is needed here. Presence of chloride ions from seawater doesn't seem to have influence on the FTIR spectrum.

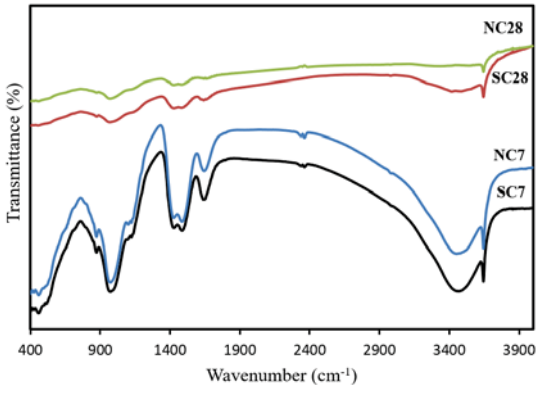

Figure 5: FTIR spectrum for 7 day and 28 day normal water and seawater cement paste samples

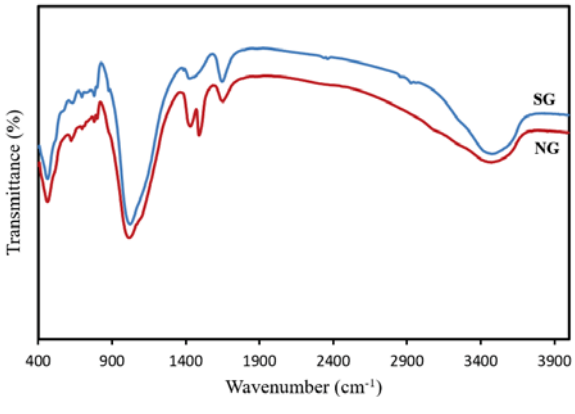

Figure 6: FTIR spectrum for normal water and seawater geopolymer samples

3.4 Microstructure and morphological characterisation

Figure 7 shows the SEM images of normal water and seawater samples. Figure 7(a) and 7(b) show the 7 day and 28 day microstructural images of normal water cement paste samples. Presence of needle shaped crystals attributed to ettringite is found in microstructure of samples. From Figure 7(b) it can be observed that the extent of this crystal formed decreased for 28day sample. Ettringite (AFt) is formed in early age of cement paste due to reaction of C-A-S (calcium aluminate silicate) with gypsum. C-A-S is formed because of hydration process between C_3A and water. It is to be noted that C_3A has high reactivity.

Figure 7(c) and 7(d) show the 7 day and 28 day SEM images of seawater cement paste samples. Hexagonal shaped structure was observed for 7day seawater samples. These crystals were identified as Friedel's salt from EDX analysis and based on observation made earlier [8]. The presence of these crystals in seawater samples further confirms the presence of chloride phase in cement hydration products with the use of seawater.

Friedel's salts are formed in cement paste due to presence of chloride ions in seawater. The chlorides are chemically bonded in the cement structure thus immobilising the movement of this ions. Friedel's salt is a rarely occurring AFm phase in cement hydration products. The mechanism of Friedel's salt formation can be explained as follows, presence of chloride ions in cement system readily replaces the sulphates from monosulfoaluminate (AFm) phase to form Friedel's salt. There are several chemical formulas for Friedel's salt based on the state of water. The following equation shows one such formation of Friedel's salt in cement hydration,

$$2Cl^- + 3CaO.Al_2O_3.CaSO_4.10H_2O \rightarrow 3CaO.Al_2O_3.CaCl_2.10H_2O + SO_4^{2-}$$

However, no such crystals were observed in the 28day seawater cement paste samples. The microstructure of seawater samples is more uniform and condenses with less presence of crystalline ettringite phase. This signifies the use of seawater makes the microstructure of cement paste samples denser. Friedel's salt act as crack bridger and fills the pores present in cement matrix (as shown in Figure 7c) to form denser microstructure.

Microstructure of geopolymer samples are shown in Figure 7(e) and 7(f). Flower like pattern of chabazite crystals are seen in seawater geopolymer samples (Figure 7(f)). This further confirms the presence of C-A-S-H phase in seawater geopolymers as chabazite is the crystal having C-A-S-H network. Such crystals were not observed in normal geopolymer samples. These crystals filled the tiny pores present in the geopolymer matrix which made the microstructure denser. The rhombohedral morphology of such crystal effectively filled the voids present making the structure more uniform and smooth. In normal water geopolymer samples elongated fibre like feature confirming to zeolite (N-A-S-H phase) are present. Presence of chloride ions are not detected in geopolymer samples with the use of seawater. This may be due to immobilization of chloride ions present in seawater by fly ash. The SEM results observed are well in consistent with the XRD and TGA results and gives clear idea about the phases found in cement paste and geopolymer samples with the use of seawater.

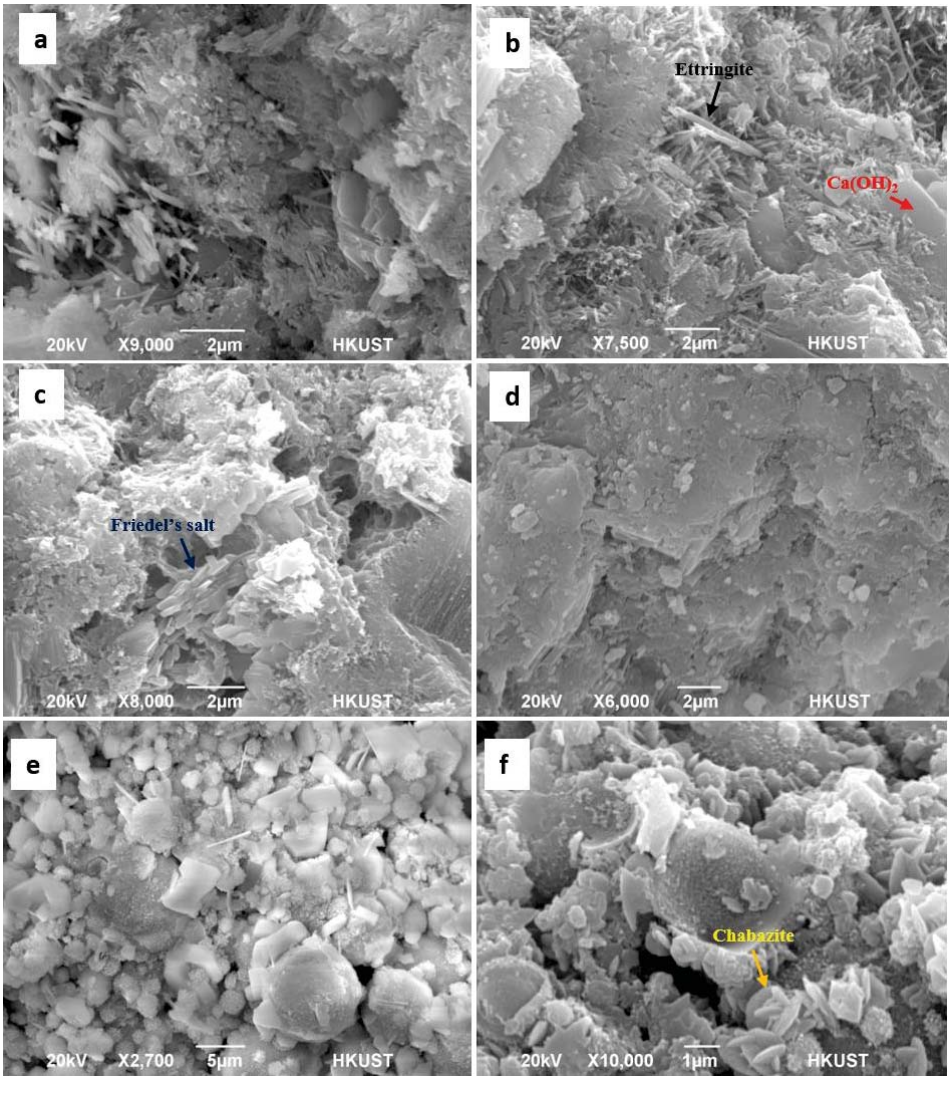

Figure 7: SEM images of (a) 7 day normal water cement paste (b) 28 day normal water cement paste (c) 7 day seawater cement paste (d) 28 day seawater cement paste (e) normal water geopolymer sample (f) seawater geopolymer sample

4 CONCLUSIONS

In this study, the presence of chloride ions on reaction products, hydration rate, microstructure, morphological properties of cement paste and fly ash based geopolymer samples were studied. Based on the results obtained, following conclusions are drawn:

- use of seawater resulted in formation of Friedel's salt in cement paste samples. In case of fly ash based geopolymer samples, use of seawater enhanced the formation of C-A-S-H phase.

- C-S-H, $Ca(OH)_2$, and Friedel's salt were the hydration phases identified in seawater cement paste samples. Phases of N-A-S-H and C-A-S-H were observed for seawater fly ash based geopolymer samples.
- use of seawater increased the $Ca(OH)_2$ content in earlier age of cement paste.
- microstructure of both cement paste and fly ash based geopolymer samples were observed to be denser and smoother with the use of seawater. This is because presence of chloride ions densified the microstructure of cement paste by formation of Friedel's salt. In geopolymer samples, formation of chabazite filled the micro-pores present in the matrix to result in denser microstructure.
- presence of chloride ions were not detected in the fly ash based geopolymer samples. This could be because of immobilization of chloride ions present in seawater by fly ash.

5 ACKNOWLEDGEMENTS

The authors would thank Materials characterization and Preparation Facility (MCPF) at The Hong Kong University of Science and Technology (HKUST) for testing and analysis of the samples.

6 REFERENCES

[1] Wegian, F. M., 'Effect of seawater for mixing and curing on structural concrete', *The IES Journal Part A: Civil & Structural Engineering*. 3(4) (2010) 235-243.

[2] Katano, K., Takeda, N., Ishizeki, Y. and Iriya, K., 'Properties and application of concrete made with sea water and un-washed sea sand', Proceedings of Third International conference on Sustainable Construction Materials and Technologies.

[3] Shi, S., Shui, Z., Li, Q. and Geng, H., 'Combined effect of metakaolin and sea water on performance and microstructures of concrete', *Construction and Building Materials,* 74 (2015) 57-64.

[4] Nishida, T., Otsuki, N., Ohara, H., Garba-Say, Z. M. and Nagata, T., 'Some considerations for applicability of seawater as mixing water in concrete', *Journal of Materials in Civil Engineering,* 27(7) (2015).

[5] Erniati, Tjaronge, W., Zulharnaj, and Irfan, U. R., 'Porosity, pore size and compressive strength of self-compacting concrete using sea water', *Procedia Engineering,* 125 (2015), 832-837.

[6] Li, Q., Geng, H., Shui, Z. and Huang, Y., 'Effect of metakaolin addition and seawater mixing on the properties and hydration of concrete', *Applied Clay Science,* 115 (2015), 51-60.

[7] Trezza, M. A., 'Hydration study of Ordinary Portland Cement in the presence of Zinc Ions', *Materials research,* 10(4) (2007), 331-334.

[8] Liu, J., Tang, K., Pan, D., Lei, Z., Wang, W. and Xing, F., 'Surface chloride concentration of concrete under shallow immersion conditions', *Materials*, 7 (2014), 6620-6631.

Reactivity of Slag-Cement Blends by Thermogravimetric Analysis

Kira Weise, Frank Roeser, Neven Ukrainczyk and Eduardus A. B. Koenders

TU Darmstadt, Institute of Construction and Building Materials, Darmstadt, Germany

ABSTRACT

In this paper, the reactivity of slag-cement blends was investigated by thermogravimetric (TG) analysis. Two types of slags were investigated with various replacement rates (3%, 5%, 10%, 20%, 30%, 40%, 80%, and 95% by mass) of slag in cement. Two water binder ratios were used, w/b = 0.45 and 0.35. The reaction was stopped at four different time points: after 1 day, 7, 14, and 28 days. A simple correlation was presented to predict $Ca(OH)_2$ content as a function of slag amount and reaction time.

Keywords: Slag, blended cement, reactivity, hydration, thermogravimetric.

1 INTRODUCTION

The use of ground granulated blast furnace slag (GGBFS or slag) as a substitute for cement clinker can improve technical properties, including workability, strength, and durability [1,2]. Setting time increases with the increase in slag content. In general, slag decreases the hydration rate of blended cement. Gao et al. (2005) investigated the effect of slag on interface zone between aggregate–cement paste using XRD, SEM, and micro-hardness measurements [3]. They concluded that a) the pozzolanic reaction rate was in direct proportion to the specific surface area of slag, b) slag significantly decreased the content and the mean size of $Ca(OH)_2$ crystals in the aggregate–mortar ITZ, which made the microstructure of ITZ more dense, and c) the ITZ weak zone almost vanished in concrete with 40% slag of 425 m^2/kg specific surface area, and completely vanished in concrete with 20% slag with 600 m^2/kg surface area, strengthening the cementitious matrix. Compressive strength developments depend upon the slag replacement percentage and the concrete age [4]. The amorphous part of slag reacts slowly and it takes time to increase pH from the hydration of Portland cement to dissolve the glassy slag parcels at early age. Thus, incorporation of slag slows down the early strength development. However, slag concrete had higher compressive strength than ordinary Portland cement concrete (OPC) after slag hydration and pozzolanic reaction was almost accomplished. Higher slag replacement percentage had higher ultimate strength. Cheng et al. (2005) also reported the beneficial influence of slag on the rapid chloride permeability (RCPT) and water permeability of concrete [4].

Some research results show the reaction behaviour and the resulting products of cement-slag blends based on the composition of the starting materials [5]. Chen and Brouwers presented a model to predict the composition and properties of the pastes, such as porosity. From the oxide composition of the cement and slag, conclusions can be drawn about the constituents of the hydration products. The hydration products formed can be C-S-H phases, hydrotalcite (M_5AH_{13}), ettringit ($C_6AS_3H_{32}$), and calcium aluminate hydrate (C_4AH_{13}). Stephant and Chomat (2015). note that the formation of these phases strongly depends on the alumina and magnesium content of the slag [6]. They also obtained the degree of hydration of the individual constituents by means of nuclear resonance spectroscopy and combined into an

overall degree of reaction. Furthermore, they used thermogravimetric analyzes to determine the content of calcium hydroxide and chemically bound water in the samples. The chemically bound water shows an approximate linear correlation to the degree of hydration, independent of the content of the slag. Contrary to the theory of Chen and Brouwers, Stephant and Chomat (2015) observed no consumption of the calcium hydroxide by slag, after one year. In this paper, the reactivity of slag-cement blends was investigated by thermogravimetric (TG) analysis, for two different water binder ratios, wide variety of replacements ratios and after 1, 7, 14, and 28 days of hydration.

2 EXPERIMENTAL

For the preparation of the samples, drinking water was used. The cement used by Holcim is a Portland cement CEM I 52.5 R-SR3 / NA. Two different slags from different plants were used in the present work, with a chemical composition shown in Table 1 and 2, respectively. The Slag1, originates from Dyckerhoff factory in Amöneburg. The Slag2 was kindly provided by Heidelberg cement and originates from the Dillinger Hütte.

Table 1: Chemical Analysis of Slag1 and Slag2

Slag1												
CaO	**SiO_2**	**Al_2O_3**	**MgO**	**S^{2-}**	**TiO_2**	**K_2O**	**Na_2O**	**Fe_2O_3**	**MnO**	**Cl^-**	**SO_3**	**Mn_2O**
42.44	35.85	11.38	6.00	1.25	0.78	0.37	0.22	0.41	0.255	0.014	0.17	0.283

Slag2										
CaO	**SiO_2**	**Al_2O_3**	**MgO**	**S**	**TiO_2**	**K_2O**	**Na_2O**	**Fe**	**Mn**	**Cl**
41.22	36.18	12.13	7.23	1.06	0.74	0.55	0.39	0.22	0.21	0.04

Slag1 has a slightly higher C/S ratio (1.18) than Slag2 with 1.14. Furthermore, the proportions of alumina and magnesium oxide in Slag1 are slightly lower. On the other hand, Slag1 has higher values of manganese and iron oxide. However, the deviations of the chemical compositions of the slags are small. The Blaine values of the materials used as reported by the manufacturers are listed in Table 3. Slag2 has a greater fineness than Slag1 and the Portland cement fineness is between the two slags.

Table 2: Fineness (Blaine values) of used raw materials

	CEM I 52.5 R	**Slag1**	**Slag2**
Blaine-Wert [cm^2/g]	4400	4000	4600

In the series of experiments, nine different replacement rates (3%, 5%, 10%, 20%, 30%, 40%, 80%, and 95% by mass) of slag in cement. Water binder ratio was set to w/b = 0.45 and 0.35. Furthermore, five exchange rates (10%, 20%, 40%, 60%, and 80% by mass) with a w/b value of 0.45 were used with the second Slag2 for comparison. Pastes were mixed with a mortar mixer from MAT Mischanlagentechnik GmbH for one minute at 60 Hz to obtain a homogeneous material. For the easier processing, the w/b value of 0.35 had to be achieved by use of superplasticizer. The spread for mortar according to DIN EN 1015-3, but without the 15-times lifting of the spreading table, was fixed between 15 and 20 cm. The pastes were filled into the plastic moulds, sealed, and stored at 20ºC.

The reaction was stopped at four different time points: after 1 day, 7, 14, and 28 days. For this, the hardened samples were hand-milled by washing twice with 5 ml of acetone. Device "STA 449 F5 Jupiter" from NETZSCH was used for thermogravimetric analysis of the samples. The crucible consists of alumina and was filled with 40–50 mg of sample powder. Nitrogen was used as an inert gas in the sample chamber. The samples were first heated to 40°C and kept isothermal at this temperature for 30 minutes. Subsequently, each sample was heated to 1000°C at a constant heating rate of 20°C per minute. The temperature range for determining the mass loss is set by means of the derivation of the TG curve (= DTG curve). According to [7] all mass losses observed below 600°C were normalized to the mass at 600°C. Stephant and Chomat (2015) normalize their measurements to 550°C.

3 RESULTS

Figure 1 shows example of TG results with Slag1 w/b value of 0.45 after 28 days. The blue curve shows a slag content of 10%, the red of 40%, while the green 80% by weight. When looking at the DTG curve, two very distinct peaks can be observed at around 100 °C (release of loosely bond water) and at approximately 450°C attributed to portlandite decomposition. In the case of slag blends, a second peak can also be seen in the temperature range from 150 to 200°C, which overlaps with the peak that has its maximum value at 100°C.

With increase in slag content, an approximate linear relationship with the content of calcium hydroxide is observed for both w/b ratios (Figure 2 and 3). This can be explained on the one hand by the decreasing proportion of calcium hydroxide-producing portland cement, and on the other hand, can also be attributed to the pozzolanic reaction of slag. In addition, the analysis of the total calcium hydroxide content of the samples clearly shows considerable increase from the first to the seventh day. Whereas, from this point in time until the 28th day it is almost constant. This observation is independent of the w/b value as well as of the slag replacement rate.

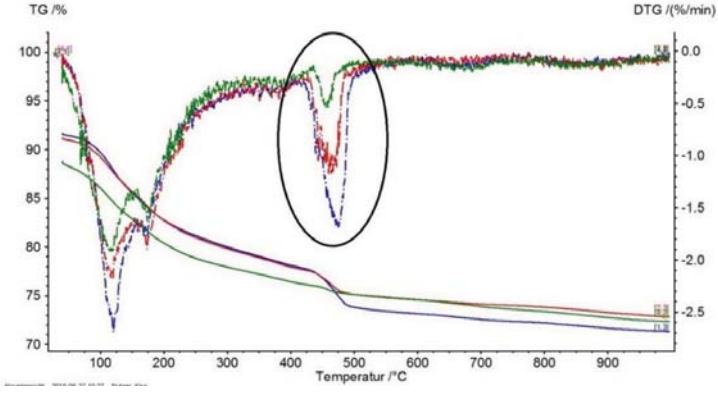

Figure 1: Thermogravimetric (TG) results - 10, 40, 80 M.-% (w/b = 0.45, 28 days, Slag1).

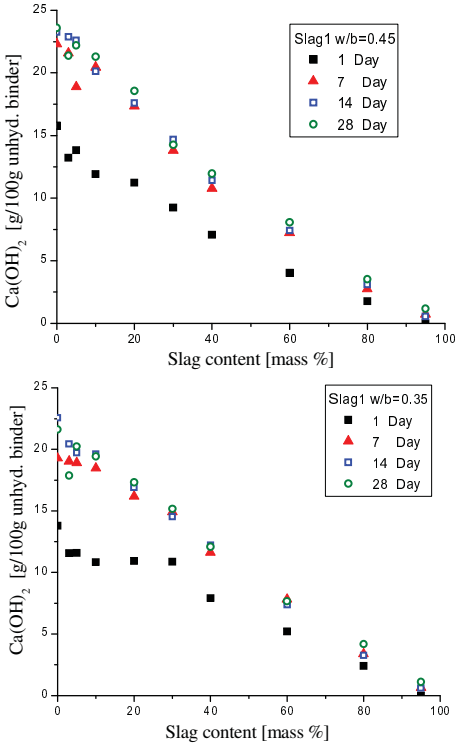

Figure 2: $Ca(OH)_2$ content as a function of Slag1 content and hydration time: w/b=0.45 (top) and w/b=0.35 (bottom)

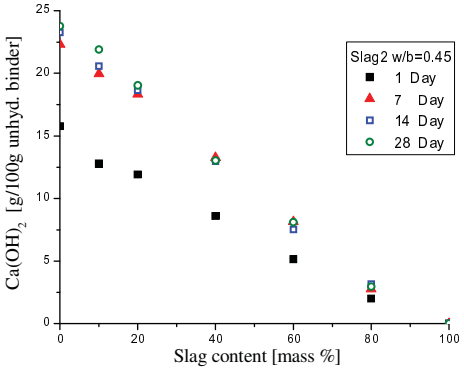

Figure 3: $Ca(OH)_2$ content as a function of slag replacement and hydration time (Slag2, w/b=0.45).

When comparing the effect of w/b ratio, it can be seen that the calcium hydroxide content is lower at the w/b value of 0.35 with replacement rate of 20% than at a w/b value of 0.45. This can be attributed to the fact that more water is available to the Portland cement at higher w/b value for hydration and thus more calcium hydroxide is formed. The calcium hydroxide content of both w/b values is approximately the same for times above 14 days. When both slags are compared (Figure. 4), it can be seen that Slag2 generally has slightly higher calcium hydroxide contents. This can be explained by the fact that Slag2 is finer ground than Slag1 and thus makes the blend more reactive. The difference is most pronounced at a replacement rate of 40%.

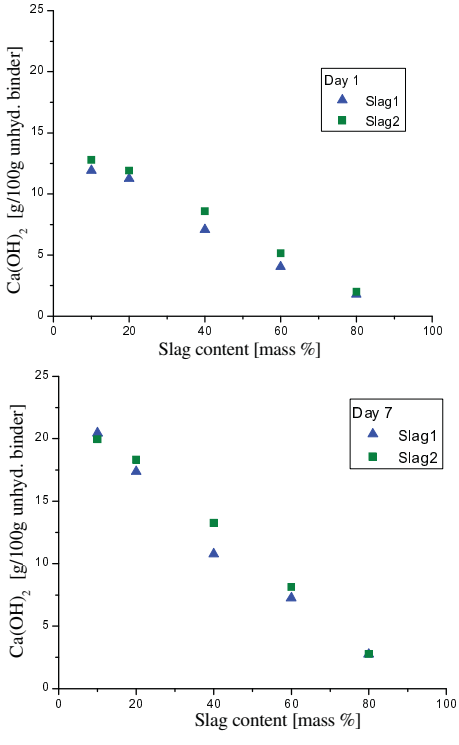

Figure 4: $Ca(OH)_2$ content as a function of slag replacement, Slag1 versus Slag2 (w/b=0.45): 1 day (top) and 7 days (bottom)

It is also interesting to quantify consumption of calcium hydroxide, i.e. to determine whether slag has pozzolanic properties. Figure 5 shows the consumption of calcium hydroxide by both the type of slags. However, as slag and cement interact between each other during hydration, more methods are needed to separate their individual effects. In addition, a greater amount of water is available to the Portland cement in the samples (w/b = 0.35), with an increase in replacement rate. On the other hand, at a w/b value of 0.45, Portland cement requires a theoretical w/c value of about 0.4 for the complete hydration, and thus sufficient water is present even without the addition of slag. For reactivity analyses, the reference (PC) sample was used to determine the calcium hydroxide content, with a correction factor corresponding to the proportion of Portland cement in the blended mixture. It was assumed

that this is linear to the proportion of the slag. Subsequently, the difference between the calcium hydroxide content formed by the Portland cement and the amount actually present in the sample could be used to calculate the proportion of the consumed calcium hydroxide due to pozzolanic reaction. However, this approach assumes that the reaction kinetics of cement (and slag) is not affected by mutual interactions, so the interpretation should be limited to this simplification.

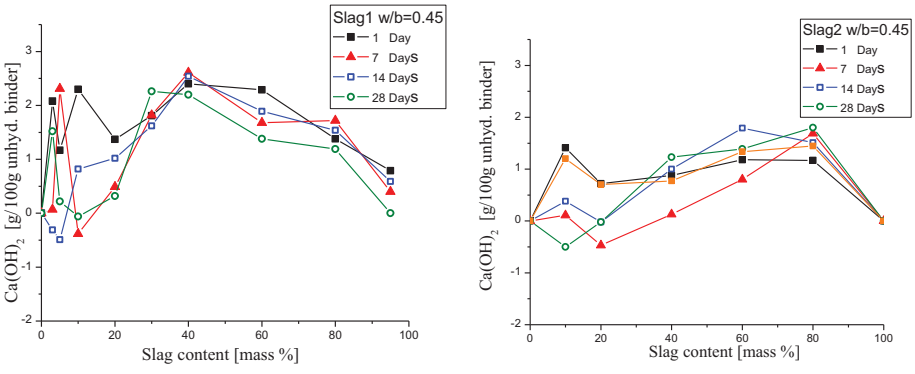

Figure 5: Consumption of $Ca(OH)_2$ (w/b = 0.45): Slag1 (left) and Slag2 (right).

The consumption values are generally positive, which means that there is a pozzolanic consumption of calcium hydroxide by slag. This indicates to the pozzolanic characteristics of the slag, but could also be related to inhibition of cement reaction by slag addition. Negative values for consumption of CH could mean that the slag itself produces calcium hydroxide or that more calcium hydroxide is produced from the Portland cement reaction by the presence of slag. According to the data in the literature, the second seems more probable due to the nucleation effect of the slag that accelerates the hydration rate. When looking at the samples of Slag1 and the w/b value of 0.45, it is noticeable that the consumption of calcium hydroxide to 40% by weight tends to increase and then decrease again. Up to this replacement rate, the increase in the slag content seems to cause the consumption of calcium hydroxide. If the slag content is increased by more than 40%, the consumption decreases because there is a relatively low proportion of portland cement that forms calcium hydroxide. The effect is similar to the results on the consumption of calcium hydroxide from the investigations of Chen and Brouwers [5].

In many studies the chemically bound water of paste samples is used to calculate a general degree of hydration. The chemically bound water is released by thermogravimetric analysis to a temperature range of about 50-600°C [7]. In this paper the mass loss of the chemically bound water in the temperature range from 40 to 600°C was considered. The values normalized to the mass fraction at 600 ° C are shown in Figure 6 for both slags. The greatest increase in chemically bound water (BW) takes place up to the seventh day. Up to this point, the graphs show declining values with increasing slag content. This can be explained by the fact that the reaction of the slag is much slower than that of Portland cement. With further hydration time, the BW increases further, but not as strongly as before. In addition, it can be observed that, with low slag contents, up to about 20% by mass, more or as much chemically bound water is present as in the reference mixtures. At higher replacements, the quantity of Portland cement does not seem to be sufficient to activate the slag in the same way until the 28th day.

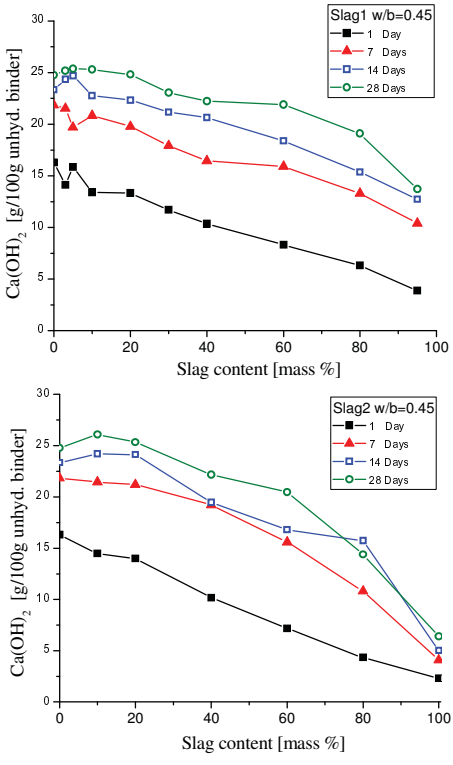

Figure 6. Chemically bounded water (w/b = 0.45): Slag1 (top) and Slag2 (bottom).

It was very noticeable in the evaluation of the measurements that the calcium hydroxide content of the blended mixes increases linearly with slag content, within the first 28 days. The temporal effect of the calcium hydroxide can be approximately by logarithmic function dependence. From these observations, the idea emerged to represent the calcium hydroxide content in the paste sample using a regression analysis. For this purpose, the data of the calcium hydroxide (normalized to 600°C) were used for both slags according to the two w/b values (Table 3). The selected regression model has the following form:

$$CH = \beta_0 + \beta_1 \, Slag + \beta_2 \log(t) \quad (1)$$

Where CH is $Ca(OH)_2$ content in g/100g unhydrated binder, Slag denotes the slag content of the original mixture in mass % and t indicates the hydration time in days.

Table 3: Parameters estimated by regression analysis of calcium hydroxide content.

Slag	**w/b**	β_0	β_1	β_2	R^2
Slag1	0.35	15.56	-0.19	1.66	0.9556
Slag2	0.45	16.73	-0.22	1.83	0.9462
Slag2	0.45	18.14	-0.22	1.45	0.9604

As expected, the parameter β_1 is negative, since the CH content decreases in the sample as the proportion of slag increases. β_2 is positive in the time interval, up to 28 days, since the content of calcium hydroxide increases over time. The initial value β_0 is greater at a higher w/b value, as by increasing the w/b value, more calcium hydroxide is formed by the portland cement. β_2 is greater at a higher w/b value since more calcium hydroxide can be formed in the course of time from the portland cement. For Slag2, β_0 is greater than for HS 1. This could result from the fact that Slag2 is finer ground. The same consideration would also explain the smaller value of β_2, since more calcium hydroxide is consumed by finer slag. It is also interesting that the parameter β_1 is -0.22 for both slags with a w/b value of 0.45. This means that the calcium hydroxide content decreases by 0.22 g per 100 g of unhydrated binder when the slag content is increased by a mass percentage. The value is smaller for the lower w/b of 0.35. This result suggests that the activity of the slag reaction is reduced at a lower w/b value. The simple regression analysis rests on a strong simplification of the reactions in Portland cement blends. It is not universally valid because the complex reactions of both starting materials are influenced by many other factors. However, it shows fundamental tendencies and summarizes some results from the thermogravimetric analyzes of this work.

4 CONCLUSION

In the present study, the reactivity of slag-cement blends was investigated by thermogravimetric (TG) analysis. Further complementary quantitative measurements are needed to be able to make more accurate statements about products formed, and to separate their reactivities. Identification of hydration products would simplify and specify the assignment of the measured mass changes in different temperature intervals.

A simple correlation was presented in this work to predict CH content as a function of slag content and reaction time. The experimental results of this paper could be used for calibration of more advanced models which should include slag-cement individual reactivities as well as other hydration products of cement-blends.

As slag has regional variability in the reactivity properties due to differences in its production, it would be desirable to incorporate the reactivity of the starting materials into the concrete mix design. As a result, the potential of additives such as, for example, the slag analyzed here could be used more efficiently. Against the background of the extensive environmental benefits and the growing relevance of resource conservation, this would be of particular interest to the construction industry.

REFERENCES

[1] Shi, C., Qian, J. (2000) High performance cementing materials from industrial slags a review. Resour. Conserv. Recycl. 29, 195-207.

[2] Song, H.-W., Saraswathy, V., (2006) Studies on the corrosion resistance of reinforced steel in concrete with ground granulated blast-furnace slagdan overview, J. Hazard. Mater. 138 226-233.

[3] Gao JM, Qian CX, Liu HF,Wang B, Li L (2005) ITZ microstructure of concrete containing GGBS. Cement and Concrete Research 35 (7) 1299–1304.

[4] Cheng A, Huang R, Wu JK, Chen CH (2005) Influence of GGBS on durability and corrosion behavior of reinforced concrete. Materials Chemistry and Physics 93 404–411.

[5] Chen, W., Brouwers, H.J.H., The hydration of slag, part 2: reaction models for blended cements, Journal of Materials Science 42 (2007) 2 444–464.

[6] Stephant, S, Chomat, L, (2015) Influence of the slag content on the hydration of blended cements, 14th International Congress on the Chemistry of Cement, At Beijing.

[7] Scrivener, K, Snellings, R, Lothenbach, B, A Practical Guide to Microstructural Analysis of Cementitious Materials, CRC Press Taylor & Francis Group, 2

Modelling Early Age Hydration Kinetics of C_3S Blended with Different Particle Size Distributions

Shiju Joseph[(1)], Shashank Bishnoi[(2)], Koen Van Balen[(1)], Ozlem Cizer[(1)]

[(1)]Department of civil engineering, KU Leuven, Belgium

[(2)]Department of civil engineering, IIT Delhi, India

ABSTRACT

Early age hydration kinetics of tricalcium silicate (C_3S) is studied extensively because of its predominant effect in the early age hydration of ordinary Portland cement (OPC). This paper focuses on modelling the effect of mixing different particle size distributions (PSD) on the hydration kinetics in the early ages. Three different PSDs of alite were mixed in different proportions and isothermal calorimetry was carried out on those mixes. The experimental results were then used to validate recently developed densification and volumetric growth model (DVG) hypothesis. Microstructural modelling platform, CemRS were used to simulate the DVG model taking into account the PSDs of alite mixed. Simulation results shows that it was able to capture the effect of PSDs and their blends without the need to vary the simulation parameters.

Keywords: Alite, hydration, modelling, kinetics

1 INTRODUCTION

Alite (impure tricalcium silicate) typically constitutes around 50-70% in ordinary Portland cement (OPC), and its predominant effect on early age hydration kinetics of OPC leads to extensive studies on pure tricalcium silicate (C_3S) [1][2]. The main hydration peak of C_3S is generally divided as the period of high dissolution, induction period, acceleration period, deceleration period and the period of low hydration. The period of high dissolution and induction period is not in the scope of this paper.

Modelling hydration kinetics of C_3S is of prime interest in order to understand the reaction mechanism involved. Results from experiments and modelling suggests that the main hydration peak of alite hydration is driven by nucleation and growth mechanism[3]. The objective of this paper is to investigate the effect of mixing different particle size distributions of C_3S on recently developed Densified volumetric growth (DVG) hypothesis[4].

2 EXPERIMENTAL PROTOCOL

Pure tricalcium silicate of three different fineness (Ac, An &Af) purchased from SARL mineral research processing has been used for this study. The different fineness was obtained by sieving through 32 and 63 μm sieves. The material was characterized using X-Ray diffraction technique (Figure 1). The peaks corresponds well with triclinic tricalcium silicate. Malvern Mastersizer 2000 was used to determine the particle size distribution (PSD) using laser diffraction technique (Figures 2 and 3). It could be noted that Ac is the coarsest and Af is the finest of the three fractions.

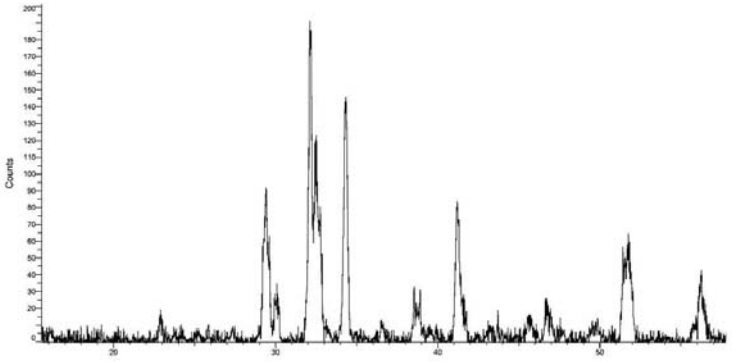

Figure 1: XRD measurement of C_3S (CuKα)

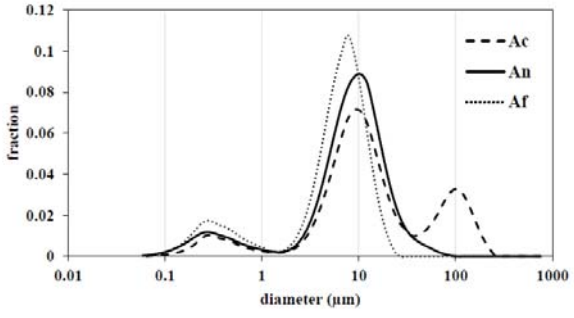

Figure 2: Laser diffraction result of three different PSD of C_3S (derivative)

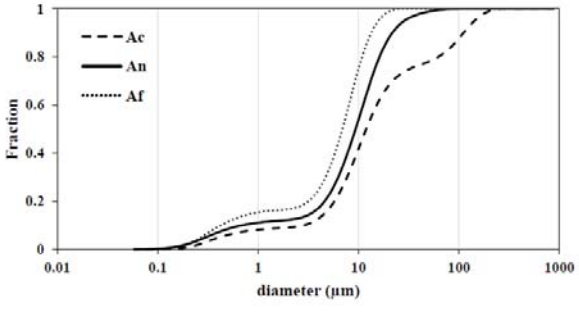

Figure 3: Laser diffraction result of three different PSD of C_3S (cumulative)

Pastes were prepared with the three C_3S fractions at a water to cement ratio (w/c) of 0.5. The preparation of the pastes was conducted in a temperature controlled room of 20ºC using deionized water. The prepared pastes were transferred to ampoules and was kept in TAM air isothermal calorimeter to monitor the heat of hydration. The heat of hydration of the three pastes (Ac, An and Af) at 20°C is given in Figure 4. It could be seen that the maximum heat release at the main peak of hydration depends upon the fineness, which is expected.

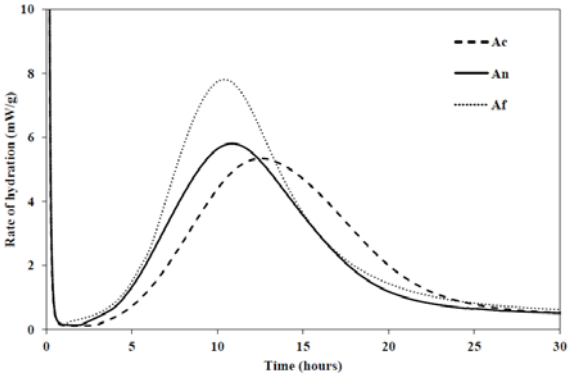

Figure 4: Result from isothermal calorimeter for the three C_3S PSD Ac, An and Af

To study the effect of mixing of PSDs, different PSD of C_3S was dry-mixed as per table 1. Heat of hydration was monitored at 20°C and 0.5 w/c following the same procedure as above and are recorded in Figure 5. It could be seen that main peak of hydration has a dependence on the fineness of the particles. Also it could be noted that the induction period ends sooner for finer particles.

Table 1: Mix compositions

	Ac	**An**	**Af**
M1	1/2	-	1/2
M2	1/3	1/3	1/3
M3	1/3	2/3	-
M4	-	2/3	1/3
M5	-	1/3	2/3
M6	2/3	1/3	-

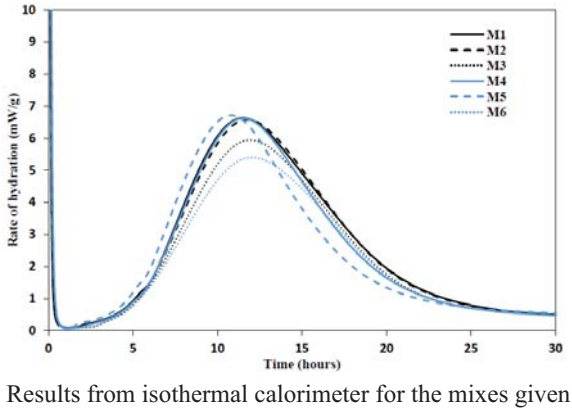

Figure 5: Results from isothermal calorimeter for the mixes given in Table 1

3 SIMULATION

Modelling platform CemRS, which was developed from adaptation of some basic concepts of vector microstructural modelling platform μic [5], was used as the simulation platform in this work. Particle size distributions obtained by laser diffraction is an input, and mathematical model DVG hypothesis is the reaction mechanism. DVG hypothesis is a modified nucleation and growth mechanism with a time dependent outer growth rate of C-S-H and densification of C-S-H dependent on its internal surface area. Detailed description and theory about CemRS and DVG hypothesis could be found elsewhere [4][6].

The parameters of Set #3 of table 1 from [4] was used for simulations. As there are no additional fillers in these simulations, a11f and a12f are not applicable. The input particle size distributions for the different mixes for CemRS is calculated from the original results of Ac, An and Af. The results from simulation and experiments are compared in Figure 6. It should be noted that as modelling the induction period is out of the scope of this paper, the peaks are shifted along the x-axis. There is a good fit despite not changing the parameters for individual particle size distributions. Small deviations are expected as there are different experimental errors which could deviate the results such as errors from laser diffraction, errors from isothermal calorimetery, errors due to improper mixing etc. The ability of the model to capture the effect of mixing different PSDs further validates the hypothesis and suggests that this model is ideal for capturing the effect of fineness.

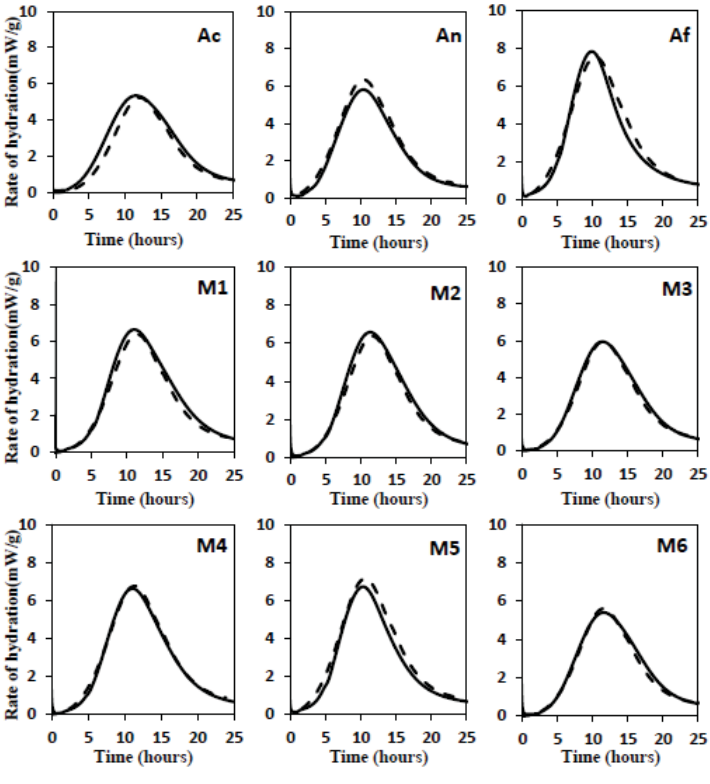

Figure 6: Comparison of the rate of heat evolution on the different mix proportions of PSDs on the simulation (dashed) and experiments (line)

4 CONCLUSION

Pure triclinic tricalcium silicate of three different fineness were dry mixed at different proportions to study the effect of particle size distribution on hydration kinetics. The effect of fineness on hydration kinetics is studied using isothermal calorimeter. DVG model [4] has been used to model the effect of fineness. Results from simulations were able to capture the effect of different fineness of C_3S along with its mixes with different proportions. There was no need to vary the coefficients of simulations for simulating the different mixes. This is an additional validation for the previously published model.

REFERENCES

[1] K. L. Scrivener, P. Juilland and P. J. Monteriro, "Advances in understanding hydration of Portland cement," *Cement and Concrete Research,* Vol. 78, pp. 38-56, 2015.

[2] J. Bullard, H. Jennings, R. Livingston, A. Nonat, G. Scherer, J. Schweitzer, K. Scrivener and J. Thomas, "Mechanisms of cement hydration," *Cement and concrete research,* Vol. 41, pp. 1208-1223, 2011.

[3] J. Thomas, J. Biernacki, J. Bullard, S. Bishnoi, J. Dolado, G. Scherer and A. Luttge, "Modelling and simulation of cement hydration kinetics and microstructural development," *Cement and concrete research,* Vol. 41, pp. 1257-1278, 2011.

[4] S. Joseph, S. Bishnoi, K. Van Balen and O. Cizer, "Modeling the effect of fineness and filler in the early-age hydration of tricalcium silicate," *J Am Ceram Soc,* Vol. 100, no. 3, pp. 1178-1194, 2017.

[5] S. Bishnoi and K. L. Scrivener, "mic: A new platform for modelling the hydration of cements," *Cement and concrete research,* Vol. 39, pp. 266-274, 2009.

[6] S. Joseph, S. Bishnoi, K. van Balen and O. Cizer, "CemRS: fast and efficient modelling platform for the simulation of cementitious systems," in *International RILEM Conference Materials Systems and Structures in Civil Engineering 2016 (MSSCE 2016) on Service Life of Cement-Based Materials and Structures*, Lyngby Denmark, 2016.

Micro-Analytical Characterisation of Concrete Deterioration due to Acid Attack in a Sewage Treatment Plant

Ramaswamy K. P.[1,2], Sivakumar R.[1], Manu Santhanam[1] and Ravindra Gettu[1]

[1]Dept. of Civil Engineering, Indian Institute of Technology Madras, Chennai – 600036, India

[2]Dept. of Civil Engineering, TKM College of Engineering, Kollam – 691005, India

ABSTRACT

Concrete being alkaline is susceptible to attack by aggressive solutions. This is a huge problem especially in sewage treatment plants, where structures constructed with concrete come into contact with a variety of both organic (such as acetic acid) and inorganic (such as sulphuric acid) acids that are produced by bacteria. The present study attempts to investigate the nature of concrete degradation that has occurred in a sewage treatment plant, possibly due to acid attack. Concrete samples were collected from various deteriorated locations in the sewage treatment plant. The microstructural alteration was studied from the collected samples using characterisation techniques such as X-ray diffraction, mercury intrusion porosimetry, scanning electron microscopy coupled with energy dispersive spectroscopy and X-ray micro-tomography. The test results depicted decalcification, indicating formation of gypsum, loss of portlandite, formation of silica gel, removal of the surface layers and extensive cracking. It is thus evident that the concrete structures in these locations have been subjected to attack by aggressive aqueous solutions.

Keywords: Acid attack, characterisation, concrete, degradation, decalcification, sewage

1 INTRODUCTION

Concrete is susceptible to attack by acids because of its alkaline nature [1-5]. Of particular concern is the progressive dissolution of hydrated cementitious phases, resulting in the formation of a degraded layer on the surface [1, 6-7]. Concrete can come into contact with acids in varied situations, predominantly in industrial environments. Sewage treatment plants (STPs), which treat domestic sewage and concrete sewer lines that transport the sewage, should also be taken into consideration. The degradation that occurs in a STP is a result of the combined attack by sulphuric acid and organic acids such as acetic acid [8]. This sulphuric acid is produced biogenically because of the bacterial action of *thiobacilli* [9-10]. Even though such degradation occurs at a very slow rate of 1 – 5 mm per year over a long period of time, the effects could be devastating [9]. This also causes corrosion of steel if the acid permeates through the concrete cover depth. Since the degraded layer formed is soft and porous, it provides an excellent stratum for the growth of bacteria. This helps in causing further deterioration of concrete in these environments. Hence, the present study attempts to

investigate the concrete deterioration in a sewage treatment plant by employing a set of material characterisation techniques.

2 CASE STUDY

A site visit to Nesapakkam sewage treatment plant in Chennai, India was conducted to investigate the possible locations where acid attack can occur. The collection and treatment of wastewater for the city of Chennai has been divided into five zones. The STP visited is situated in Zone 4, which lies in the south-west of the city and is the smallest zone. There are 27 pumping stations to collect the wastewater in this zone. This collected wastewater is then conveyed to the treatment facility at Nesapakkam, which consists of three treatment plants. The first plant of 23 MLD capacity, built in 1974, has been considered for this study. The wastewater collected in this plant is treated by Activated Sludge Process (ASP). The general layout of the plant is shown in Fig. 1. Fig. 2 shows the concrete deterioration from various locations of the plant, such as the screen and grit chamber, primary clarifier and aeration tank.

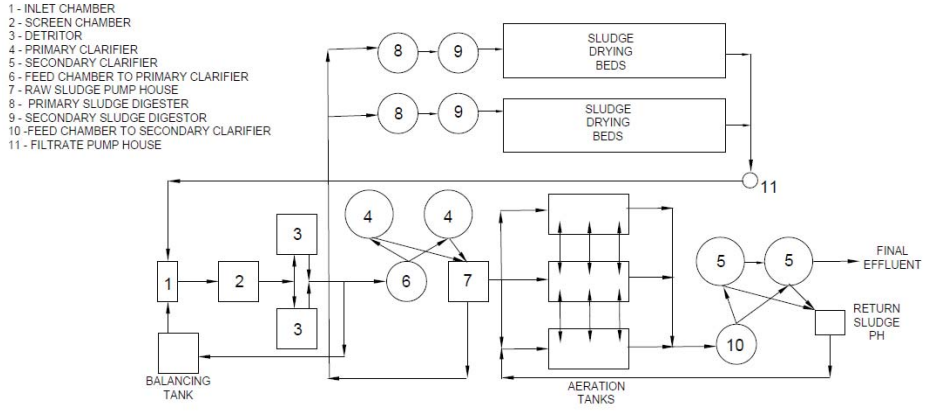

Fig. 1: Layout of the Nesapakkam sewage treatment plant

(a) Screening and grit chamber

(b) Primary clarifier

(c) Concrete deterioration in primary clarifier

(d) Aeration tank

Fig. 2: Concrete deterioration in various locations of Nesapakkam sewage treatment plant

3 METHODOLOGY FOR THE STUDY

3.1 Sample collection

The concrete samples were collected from various deteriorated locations of the plant, such as screen and grit chamber (which is always in contact with the raw flowing sewage), the primary clarifier and the secondary clarifier. Even though deterioration was observed in the aeration tank, samples could not be collected due to practical difficulties. All samples were collected by using a hammer and chisel from the zone that is subjected to alternate wetting and drying.

3.2 Test Methods

Material characterisation techniques were used to ascertain the nature of concrete deterioration. The details of the test methods used are given below.

3.2.1 X-ray diffraction (XRD)

X-ray diffraction analysis was performed on the collected samples for the identification of reaction products. The thin slices of concrete samples were immersed in iso-propanol for 3 days and subsequently dried. In order to prepare the sample for testing, mortar chunks were

further separated from the concrete sample. The samples so collected were crushed gently using a mortar and pestle, and sand grains separated as much as possible using sieves. The powdered sample passing through 75 μm was then taken for the testing. The XRD analysis was performed using an X'Pert Pro PANalytical diffractometer. The scanning range adopted was over the 2θ range from 5-65°. Cu-K_α radiation was used to generate X-rays with test settings of 45 kV voltage and a current of 30 mA. The identification of crystalline phases was carried out using the software, X'Pert HighScore Plus with ICSD database.

3.2.2 Mercury intrusion porosimetry (MIP)

In order to investigate the variation in porosity, MIP studies were conducted on the samples using a PASCAL 140/440 Series Porosimeter. Hydration/reactions of samples were stopped using a solvent exchange process using iso-propanol, as explained earlier. Mortar chunks were then extracted from the concrete and dried samples of mass 0.5-1 g were used for testing. A pressure upto 400 MPa (which corresponds to a pore size of 3.7 nm diameter) was used during the test. The porosity and pore structure related parameters of samples collected were compared with the porosity of mortar of M30 concrete made in laboratory conditions (sample named as C1).

3.2.3 Scanning electron microscopy (SEM)

To study the morphology of the deteriorated concrete samples and to confirm the elemental composition of the reaction products, SEM studies were carried out with energy dispersive spectroscopy (EDS). The machine, Inspect F, which has a field emission gun with high vacuum in the secondary electron mode, fitted with EDS detector was used. Flat samples cut using a diamond saw was immersed in iso-propanol for 3 days followed by drying. The samples were air blown to remove the loose particles. The samples were then sputter coated with gold for 90 seconds to avoid charging of samples during the imaging.

3.2.4 X-ray tomography (X-CT)

X-ray Computed Tomography (CT) is a powerful non-destructive technique used by material researchers to study the microstructure without physically cutting the specimen open. The technique has proven to be an apt technique to characterize the microstructure and deterioration associated with attack in cementitious materials due to aggressive solutions [11-14]. The tomography test setup at IIT Madras used for imaging, 'v|tome|x s' is a high resolution equipment consisting of both micro and nano focus X-ray tubes. The basic principles and detailed working procedure of X-ray CT are detailed in Ramaswamy et al. (2015) [15]. Cubical samples of approximately 10 mm were cut using a diamond saw. Solvent exchange process using iso-propanol (3 days immersion of samples) was used for the specimen conditioning followed by drying in desiccator. The dried specimens were then taken for CT imaging. A voltage of 70 kV and current of 200 μA was maintained during the test. Microfocus X-ray tube was used for generating the X-rays. After the detector calibration, the specimen was rotated 360° and a total of 900 radiograph images were captured during the complete rotation of specimen in the stage, to reconstruct the three-dimensional image using the software Phoenix datos|x 2.2.1. The 3D image was further sectioned to get the required 2D slice images (top and front view images) using the software Volume Graphics Studio Max 2.1.

4 RESULTS AND DISCUSSIONS

4.1 X-ray diffraction (XRD)

Fig. 3 (a) shows the XRD diffractogram of the sample taken from screen and grit chamber (S/GC). From the diffractogram, it is clearly visible that there is gypsum (reaction product) formed along with calcite. Quartz is also observed in the diffractogram, which could be due to crushing of sand grains from the mortar while preparing the sample. Further, it is observed that portlandite has been consumed completely in the attack due to decalcification by acids (both sulphuric and organic acids). Even though the screen and grit chamber hold only raw sewage, the effect of the attack is more pronounced here because of the continuous flow, which will remove the deteriorated layers and expose the fresh surface for attack. These findings are in agreement with a study conducted by Moradian et al. [16] who also observed very high damage in the entrance channel, which is the first structure in any STP. Similar conclusions regarding the grit chamber have been drawn by O'Connell et al. [17]. Fig.3 (b) shows the XRD diffractogram of the white precipitate obtained from the primary clarifier sample (PC1). Gypsum was observed as the primary and dominant reaction product along with trace amounts of quartz. This gypsum might have formed primarily due to the reaction between sulphuric acid and portlandite, suggesting that the primary clarifier is also susceptible to biogenic sulphuric acid attack. Portlandite is completely absent in the system. This could be due to the decalcification of portlandite to form gypsum on reacting with sulphuric acid or dissolution of portlandite due to the formation of soluble calcium salts on reaction with organic acids. The precipitate formed on the exposure of Ordinary Portland Cement (OPC) mortar immersed in 1% sulphuric acid (mineral acid) for a period of 1 month in laboratory condition was also analysed. It was confirmed that the reaction products were the same as found in the primary clarifier. Another interesting observation is that the precipitate samples collected from the outer layers were devoid of calcite, indicating that the calcite of acid attacked samples could only be present in the inner layers. This could be due to solubility of the calcite in acid solutions or the lesser availability of calcium hydrates (especially portlandite) to form calcite in the outer layers. The formation of calcite in the inner layers could have a role in limiting the kinetics of alteration and this needs to be addressed further.

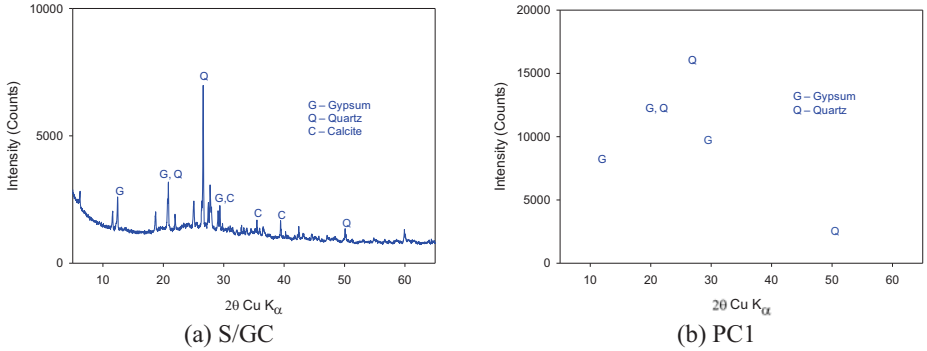

(a) S/GC (b) PC1

Fig. 3: XRD diffractograms of the samples collected

4.2 Mercury intrusion porosimetry

The variation in porosity due to acid attack was evaluated using mercury intrusion porosimetry (MIP). It can be noted that there is considerable increase in cumulative intruded volume due to the deterioration. This reinforces the fact that leaching leads to an increase in porosity due to decalcification of hydrated products and salt formation.

The various MIP related parameters are obtained from the test results and are presented in Table 1. The intruded volume and porosity was found to be higher for all the samples collected from the sewage treatment plant when compared to the reference sample (M30 concrete sample named C1). This indicates the severity of attack experienced by these concrete structures. The intruded volume and the porosity were highest for the samples collected from the screen and grit chamber. This could be due to the high organic content of the samples resulting in the dissolution of hydrates by organic acids and due to the flowing action of sewage in the screen and grit chamber. The bulk density was found to be low due to increase in porosity. The samples collected from the primary clarifier also showed higher porosity but lower than that of the screen and grit chamber samples. The porosity and intruded volume of the sample collected from secondary clarifier (sample named PC2) was found to be even lower and this could be due to the lower organic load present in the sewage at that location and relatively lower flow velocity of the sewage. As a result, bulk density was found to be higher.

Table 1: Summary of parameters based on MIP results

Results	S/GC	PC1	PC2	C1
Total intruded volume (mm^3/g)	266.7	108.5	74.4	54.9
Bulk density (g/cm^3)	1.38	1.77	2.07	2.34
Porosity by Hg intrusion (%)	36.90	19.24	15.41	12.84
Threshold diameter (μm)	*	1.43	1.00	0.06

* Threshold diameter could not be calculated as large sized pores were present

4.3 Scanning electron microscopy

Secondary electron imaging on the sample collected from the primary clarifier (PC1) shows the presence of gypsum, which is also confirmed by X-ray diffractogram. Thick deposits of gypsum crystals (shown in Fig. 4(a)) could be seen around the siliceous aggregates. The gypsum crystals were hexagonal-shaped with a columnar structure. The average size of the crystal was found to be 19 μm. It was observed that these thick gypsum deposits were noted on the void areas and in interfacial transition zones (ITZ) around the aggregates. This reinforces the fact that portlandite, which could be abundantly present in these areas, decalcified and converted to the final end product, gypsum. Energy dispersive spectroscopy (EDS) was done over the highlighted area shown in Fig. 4(a) and the spectrum confirms the product as gypsum with prominent peaks of Ca, S and O.

Fig. 4(b) shows another area of interest in which white gel-like deposits were observed along with gypsum. The EDS results show strong peaks of Si and O with traces of Al, S and Ca. This could be due to the amorphous gel formation after the decalcification of CSH gel and aluminate hydrates along with the gypsum formation. The gel thus formed is found to contain Al also. The imaging of the sample collected from the secondary clarifier is shown in Fig.4(c).

It shows a magnified image of the interfacial transition zone (ITZ) around the aggregates. The ITZ was found to be porous due to formation of gypsum (as confirmed by EDS).

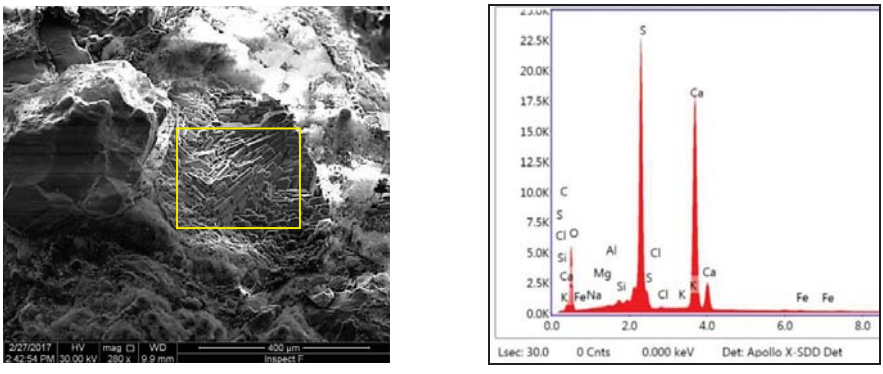

(a) Morphology of PC1 (left) and corresponding EDS (right) showing gypsum

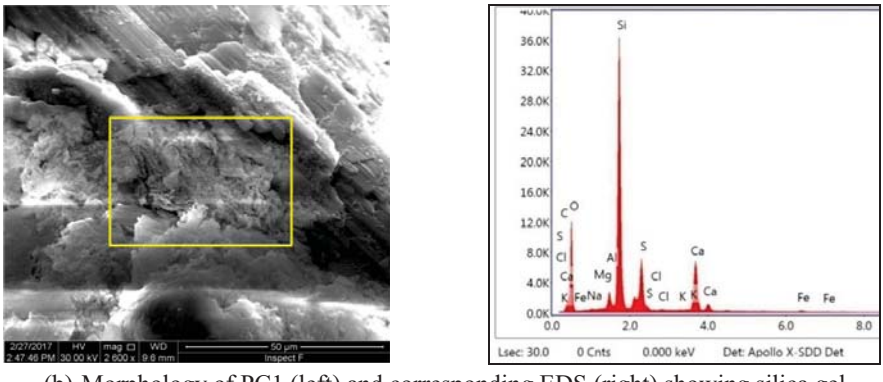

(b) Morphology of PC1 (left) and corresponding EDS (right) showing silica gel

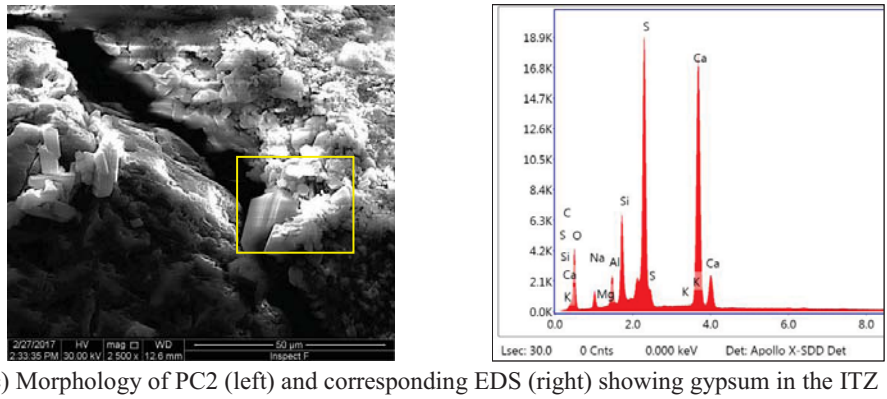

(c) Morphology of PC2 (left) and corresponding EDS (right) showing gypsum in the ITZ

Fig. 4: SEM micrographs of the samples

4.4 X-ray tomography

X-ray CT imaging was done to understand the alteration in the microstructure and to view the macro porosity of the samples investigated. Fig. 5(a) shows the top view, front view slice images and a 3D image of the samples collected from the screen and grit chamber (S/GC) of sewage treatment plant. The sample was found to be porous with macro voids identifiable from the images. More importantly, the paste was found to be very dark. The lower grayscale values of the pixels in the images suggest that the paste has been decalcified to a greater extent, comprising of silica gel. The 3D rendered image shows the outer surface that has degraded due to the combined action of abrasion due to the flowing sewage and the action of acids.

The sample collected from the primary clarifier (PC1) is shown in Fig. 5(b). The slice images showed the microstructural zonation. An outer degraded layer and a relatively lesser deteriorated layer could be noted. The paste of outer layer appeared darker when compared to the inner layer. Macro voids was observed in these samples also. Traces of gypsum deposits (as thin layer) could be noted from the front view slice image.

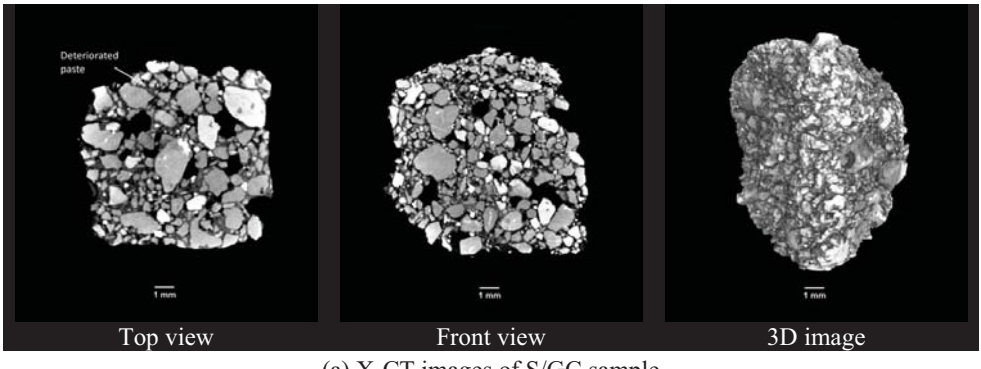

(a) X-CT images of S/GC sample

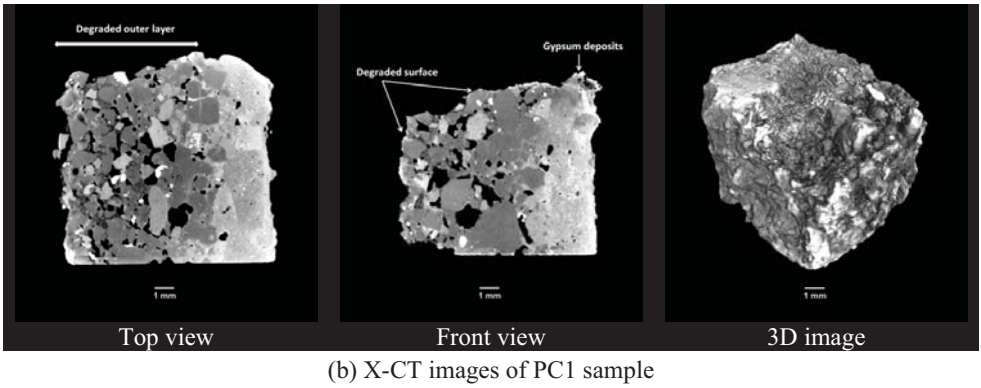

(b) X-CT images of PC1 sample

Fig. 5: X-ray tomography images of samples

5 CONCLUSIONS

The nature of deterioration of the concrete structures in a sewage treatment plant has been investigated by using micro-analytical characterisation techniques. It can be concluded that the deterioration is primarily due to the acids present in wastewater. The deterioration could also be due to other aggressive chemicals present such as chlorides and sulphates. The X-ray diffraction study revealed the main reaction product to be gypsum and was marked by the absence of portlandite. The loss of portlandite was attributable to the decalcification due to sulphuric acid to form gypsum. Also, the action of organic acids on portlandite could cause its progressive dissolution to form soluble salts. The SEM images with EDS show gypsum bound with amorphous silica gel rich in aluminium. The porosimetry results showed higher intruded volume and porosity for all the samples, which indicate the deterioration in microstructure. X-ray microtomography images also revealed the deteriorated microstructure of the samples collected. Further, the X-ray microtomography images indicate severe deterioration in the samples collected from the screen and grit chamber. The observed porosity suggests that, in addition to the aggressiveness of the solutions, the continuous flow of sewage plays a major role in accelerating the attack.

6 ACKNOWLEDGEMENTS

The authors thank the Centre for Non-Destructive Evaluation, Indian Institute of Technology Madras for the assistance provided in scanning the X-ray tomography images.

7 REFERENCES

[1] Pavlík, V., 'Corrosion of hardened cement paste by acetic and nitric acids Part I: Calculation of corrosion depth', *Cement and Concrete Research*, vol. 24, no. 3, pp. 551–562, 1994.

[2] Magniont, C., Coutand, M., Bertron, A., Cameleyre, X., Lafforgue, C., Beaufort, S., and Escadeillas, G., 'A new test method to assess the bacterial deterioration of cementitious materials', *Cement and Concrete Research*, vol. 41, no. 4, pp. 429–438, 2011.

[3] Allahverdi, A., Škvára, F., 'Acidic corrosion of hydrated cement-based materials: Part 1. Mechanisms of the phenomenon', *Ceramics-Silikáty*, vol. 44, pp. 114–120, 2000a.

[4] Zivica, V., Bajza, A., 'Acidic attack of cement based materials - A review (Part 1): Principle of acidic attack', *Construction and Building Materials*, vol. 15, pp. 331–340, 2001.

[5] Allahverdi, A., Skvara, F., 'Acidic corrosion of hydrated cement based materials: Part 2: Kinetics of the phenomenon and mathematical models', *Ceramics-Silikáty*, vol. 44, pp. 152–160, 2000b.

[6] Pavlík, V., 'Corrosion of hardened cement paste by acetic and nitric acids Part II: Formation and chemical composition of the corrosion products layer', *Cement and Concrete Research*, vol. 24, no. 8, pp. 1495–1508, 1994.

[7] Pavlík, V., 'Corrosion of hardened cement paste by acetic and nitric acids Part III: Influence of water/cement ratio', *Cement and Concrete Research*, vol. 26, no. 3, pp. 475–490, 1996.

[8] Bertron, A., Escadeillas, G., and Duchesne, J., 'Cement pastes alteration by liquid manure organic acids: Chemical and mineralogical characterization', *Cement and Concrete Research*, vol. 34, no. 10, pp. 1823–1835, 2004.

[9] Monteny, J., Vincke, E., Beeldens, A., De Belie, N., Taerwe, L., and Van Gemert, D., 'Chemical , microbiological and in situ test methods for biogenic sulfuric acid corrosion of concrete', *Cement and Concrete Research*, vol. 30, pp. 623–634, 2000.

[10] De Belie, N., Monteny, J., Beeldens, A., Vincke, E., Van Gemert, D., and Verstraete, W. 'Experimental research and prediction of the effect of chemical and biogenic sulfuric acid on

different types of commercially produced concrete sewer pipes', *Cement and Concrete Research*, vol. 34, no. 12, pp. 2223–2236, 2004.

[11] Wan, K., Xu, Q., Li, L., Sun, W., '3D porosity distribution of partly calcium leached cement paste', *Construction and Building Materials*, vol. 48, pp. 11–15, 2013.

[12] Rougelot, T., Burlion, N., Bernard, D., Skoczylas, F., 'About microcracking due to leaching in cementitious composites: X-ray microtomography description and numerical approach', *Cement and Concrete Research*, vol. 40, no. 2, pp. 271–283, 2010.

[13] Koenig, A., Dehn, F., 'Main considerations for the determination and evaluation of the acid resistance of cementitious materials', *Materials and Structures*, vol. 49, pp. 1693 – 1703, 2016.

[14] Dyer, T., 'Influence of cement type on resistance to organic acids', *Magazine of Concrete Research*, vol. 69, no. 4, pp. 175-200, 2016.

[15] Ramaswamy, K. P., Santhanam, M., Murugan, M., 'Characterization of cement paste modified with nano-materials using X-ray computed microtomography', *3rd International Conference on Modeling and Simulation in Civil Engineering*, pp. 279-289, 2015.

[16] Moradian, M., Shekarchi, M., Pargar, F., Bonakdar, A., and Valipour, M., 'Deterioration of concrete caused by complex attack in sewage treatment plant environment', *Journal of Performance of Constructed Facilities*, vol. 26, no. 1, pp. 124–134, 2012.

[17] O'Connell, M., McNally, C., and Richardson, M. G., 'Biochemical attack on concrete in wastewater applications: A state of the art review', *Cement and Concrete Composites*, vol. 32, no. 7, pp. 479–485, 2010.

Author Index

Conference organised by

The Indian Institute of Technology Madras, Chennai, India

In Association with

RILEM, the International Union of Laboratories and Experts in Construction Materials, Systems, and Structures

With the Support of

ICI, the Indian Concrete Institute

ACI, the American Concrete Institute

NCSHS, the National Centre for Safety of Heritage Structures

NIGIS, the NACE International Gateway India Section

ISAP, the International Society for Asphalt Pavements

TRG, the Transportation Research Group of India

The Masterbuilder

Typeset and printed by aksharaa muthra aalayam, Anna Salai, Teynampet, Chennai. 600 018, India.
Ph. 044 - 24364303. Cell: 9282134542, E-mail: murali.aks@gmail.com, Website: aksharaa.co.in

Advances in Construction Materials and Systems

Vol. 2

Proceedings of an International Conference (ICACMS)

Chennai, INDIA

September 3 - 8, 2017

Edited by Manu Santhanam, Ravindra Gettu, Radhakrishna G. Pillai and Sunitha K. Nayar

RILEM Proceedings PRO 118 Vol. 2

ISBN : 978-2-35158-194-0
ISBN : 978-2-35158-190-2 (Set)
e-ISBN : 978-2-35158-191-9
2017 Edition

The conference covers several themes related to construction materials and systems, with the objective of providing the state of the art coverage on cement and asphalt concrete, heritage materials, and building systems. The themes selected for the conference are reflective of the scientific coverage provided by the different Technical Clusters within RILEM. The 250+ papers received from academics and industry professionals from more than 50 countries across the world are assembled into 4 volumes. The first volume deals with the papers from the invited (keynote) speakers, while the remaining three volumes, arranged in appropriate sub-sections, deal with the specific themes of the conference as follows.

- Advances in supplementary cementing materials
- Concrete durability and performance specifications
- Early age behavior and rheology of cementitious systems
- Special concrete and applications
- Advances in characterization of construction materials
- Sustainable building systems
- Bituminous binders and mixtures
- Repair and conservation of heritage structures
- Corrosion control and monitoring in concrete structures
- Repair materials and repair systems for concrete structures

RILEM Publications S.a.r.l.
4 avenue du Recteur Poincaré
75016 Paris - France
Tel: + 33 1 42 24 64 46
Fax: + 33 9 70 29 51 20
E-mail : dg@rilem.net